



Organic Rankine Cycle (ORC) Power Systems

Technologies and Applications

Edited by Ennio Macchi and Marco Astolfi

Woodhead Publishing Series in Energy:
Number 107

Organic Rankine Cycle (ORC) Power Systems

Technologies and Applications

Edited by

Ennio Macchi

Marco Astolfi



AMSTERDAM • BOSTON • CAMBRIDGE • HEIDELBERG
LONDON • NEW YORK • OXFORD • PARIS • SAN DIEGO
SAN FRANCISCO • SINGAPORE • SYDNEY • TOKYO
Woodhead Publishing is an imprint of Elsevier



Woodhead Publishing Series in Energy

- 1 **Generating power at high efficiency: Combined cycle technology for sustainable energy production**
Eric Jeffs
- 2 **Advanced separation techniques for nuclear fuel reprocessing and radioactive waste treatment**
Edited by Kenneth L. Nash and Gregg J. Lumetta
- 3 **Bioalcohol production: Biochemical conversion of lignocellulosic biomass**
Edited by Keith W. Waldron
- 4 **Understanding and mitigating ageing in nuclear power plants: Materials and operational aspects of plant life management (PLiM)**
Edited by Philip G. Tipping
- 5 **Advanced power plant materials, design and technology**
Edited by Dermot Roddy
- 6 **Stand-alone and hybrid wind energy systems: Technology, energy storage and applications**
Edited by John K. Kaldellis
- 7 **Biodiesel science and technology: From soil to oil**
Jan C. J. Bart, Natale Palmeri and Stefano Cavallaro
- 8 **Developments and innovation in carbon dioxide (CO₂) capture and storage technology Volume 1: Carbon dioxide (CO₂) capture, transport and industrial applications**
Edited by M. Mercedes Maroto-Valer
- 9 **Geological repository systems for safe disposal of spent nuclear fuels and radioactive waste**
Edited by Joonhong Ahn and Michael J. Apted
- 10 **Wind energy systems: Optimising design and construction for safe and reliable operation**
Edited by John D. Sørensen and Jens N. Sørensen
- 11 **Solid oxide fuel cell technology: Principles, performance and operations**
Kevin Huang and John Bannister Goodenough
- 12 **Handbook of advanced radioactive waste conditioning technologies**
Edited by Michael I. Ojovan
- 13 **Membranes for clean and renewable power applications**
Edited by Annarosa Gugliuzza and Angelo Basile
- 14 **Materials for energy efficiency and thermal comfort in buildings**
Edited by Matthew R. Hall
- 15 **Handbook of biofuels production: Processes and technologies**
Edited by Rafael Luque, Juan Campelo and James Clark

- 16 **Developments and innovation in carbon dioxide (CO₂) capture and storage technology Volume 2: Carbon dioxide (CO₂) storage and utilisation**
Edited by M. Mercedes Maroto-Valer
- 17 **Oxy-fuel combustion for power generation and carbon dioxide (CO₂) capture**
Edited by Ligang Zheng
- 18 **Small and micro combined heat and power (CHP) systems: Advanced design, performance, materials and applications**
Edited by Robert Beith
- 19 **Advances in clean hydrocarbon fuel processing: Science and technology**
Edited by M. Rashid Khan
- 20 **Modern gas turbine systems: High efficiency, low emission, fuel flexible power generation**
Edited by Peter Jansohn
- 21 **Concentrating solar power technology: Principles, developments and applications**
Edited by Keith Lovegrove and Wes Stein
- 22 **Nuclear corrosion science and engineering**
Edited by Damien Féron
- 23 **Power plant life management and performance improvement**
Edited by John E. Oakey
- 24 **Electrical drives for direct drive renewable energy systems**
Edited by Markus Mueller and Henk Polinder
- 25 **Advanced membrane science and technology for sustainable energy and environmental applications**
Edited by Angelo Basile and Suzana Pereira Nunes
- 26 **Irradiation embrittlement of reactor pressure vessels (RPVs) in nuclear power plants**
Edited by Naoki Soneda
- 27 **High temperature superconductors (HTS) for energy applications**
Edited by Ziad Melhem
- 28 **Infrastructure and methodologies for the justification of nuclear power programmes**
Edited by Agustín Alonso
- 29 **Waste to energy conversion technology**
Edited by Naomi B. Klinghoffer and Marco J. Castaldi
- 30 **Polymer electrolyte membrane and direct methanol fuel cell technology Volume 1: Fundamentals and performance of low temperature fuel cells**
Edited by Christoph Hartnig and Christina Roth
- 31 **Polymer electrolyte membrane and direct methanol fuel cell technology Volume 2: In situ characterization techniques for low temperature fuel cells**
Edited by Christoph Hartnig and Christina Roth
- 32 **Combined cycle systems for near-zero emission power generation**
Edited by Ashok D. Rao
- 33 **Modern earth buildings: Materials, engineering, construction and applications**
Edited by Matthew R. Hall, Rick Lindsay and Meror Krayenhoff
- 34 **Metropolitan sustainability: Understanding and improving the urban environment**
Edited by Frank Zeman
- 35 **Functional materials for sustainable energy applications**
Edited by John A. Kilner, Stephen J. Skinner, Stuart J. C. Irvine and Peter P. Edwards

-
- 36 **Nuclear decommissioning: Planning, execution and international experience**
Edited by Michele Laraia
- 37 **Nuclear fuel cycle science and engineering**
Edited by Ian Crossland
- 38 **Electricity transmission, distribution and storage systems**
Edited by Ziad Melhem
- 39 **Advances in biodiesel production: Processes and technologies**
Edited by Rafael Luque and Juan A. Melero
- 40 **Biomass combustion science, technology and engineering**
Edited by Lasse Rosendahl
- 41 **Ultra-supercritical coal power plants: Materials, technologies and optimisation**
Edited by Dongke Zhang
- 42 **Radionuclide behaviour in the natural environment: Science, implications and lessons for the nuclear industry**
Edited by Christophe Poinssot and Horst Geckeis
- 43 **Calcium and chemical looping technology for power generation and carbon dioxide (CO₂) capture: Solid oxygen- and CO₂-carriers**
Paul Fennell and E. J. Anthony
- 44 **Materials' ageing and degradation in light water reactors: Mechanisms, and management**
Edited by K. L. Murty
- 45 **Structural alloys for power plants: Operational challenges and high-temperature materials**
Edited by Amir Shirzadi and Susan Jackson
- 46 **Biolubricants: Science and technology**
Jan C. J. Bart, Emanuele Gucciardi and Stefano Cavallaro
- 47 **Advances in wind turbine blade design and materials**
Edited by Povl Brøndsted and Rogier P. L. Nijssen
- 48 **Radioactive waste management and contaminated site clean-up: Processes, technologies and international experience**
Edited by William E. Lee, Michael I. Ojovan, Carol M. Jantzen
- 49 **Probabilistic safety assessment for optimum nuclear power plant life management (PLiM): Theory and application of reliability analysis methods for major power plant components**
Gennadij V. Arkadov, Alexander F. Getman and Andrei N. Rodionov
- 50 **The coal handbook: Towards cleaner production Volume 1: Coal production**
Edited by Dave Osborne
- 51 **The coal handbook: Towards cleaner production Volume 2: Coal utilisation**
Edited by Dave Osborne
- 52 **The biogas handbook: Science, production and applications**
Edited by Arthur Wellinger, Jerry Murphy and David Baxter
- 53 **Advances in biorefineries: Biomass and waste supply chain exploitation**
Edited by Keith Waldron
- 54 **Geological storage of carbon dioxide (CO₂): Geoscience, technologies, environmental aspects and legal frameworks**
Edited by Jon Gluyas and Simon Mathias
- 55 **Handbook of membrane reactors Volume 1: Fundamental materials science, design and optimisation**
Edited by Angelo Basile

-
- 56 **Handbook of membrane reactors Volume 2: Reactor types and industrial applications**
Edited by Angelo Basile
- 57 **Alternative fuels and advanced vehicle technologies for improved environmental performance: Towards zero carbon transportation**
Edited by Richard Folkson
- 58 **Handbook of microalgal bioprocess engineering**
Christopher Lan and Bei Wang
- 59 **Fluidized bed technologies for near-zero emission combustion and gasification**
Edited by Fabrizio Scala
- 60 **Managing nuclear projects: A comprehensive management resource**
Edited by Jas Devgun
- 61 **Handbook of Process Integration (PI): Minimisation of energy and water use, waste and emissions**
Edited by Jiří J. Klemesš
- 62 **Coal power plant materials and life assessment**
Edited by Ahmed Shibli
- 63 **Advances in hydrogen production, storage and distribution**
Edited by Ahmed Basile and Adolfo Iulianelli
- 64 **Handbook of small modular nuclear reactors**
Edited by Mario D. Carelli and Dan T. Ingersoll
- 65 **Superconductors in the power grid: Materials and applications**
Edited by Christopher Rey
- 66 **Advances in thermal energy storage systems: Methods and applications**
Edited by Luisa F. Cabeza
- 67 **Advances in batteries for medium and large-scale energy storage**
Edited by Chris Menictas, Maria Skyllas-Kazacos and Tuti Mariana Lim
- 68 **Palladium membrane technology for hydrogen production, carbon capture and other applications**
Edited by Aggelos Doukelis, Kyriakos Panopoulos, Antonios Koumanakos and Emmanouil Kakaras
- 69 **Gasification for synthetic fuel production: Fundamentals, processes and applications**
Edited by Rafael Luque and James G. Speight
- 70 **Renewable heating and cooling: Technologies and applications**
Edited by Gerhard Stryi-Hipp
- 71 **Environmental remediation and restoration of contaminated nuclear and NORM sites**
Edited by Leo van Velzen
- 72 **Eco-friendly innovation in electricity networks**
Edited by Jean-Luc Bessede
- 73 **The 2011 Fukushima nuclear power plant accident: How and why it happened**
Yotaro Hatamura, Seiji Abe, Masao Fuchigami and Naoto Kasahara. Translated by Kenji Iino
- 74 **Lignocellulose biorefinery engineering: Principles and applications**
Hongzhang Chen
- 75 **Advances in membrane technologies for water treatment: Materials, processes and applications**
Edited by Angelo Basile, Alfredo Cassano and Navin Rastogi

-
- 76 **Membrane reactors for energy applications and basic chemical production**
Edited by Angelo Basile, Luisa Di Paola, Faisal Hai and Vincenzo Piemonte
- 77 **Pervaporation, vapour permeation and membrane distillation: Principles and applications**
Edited by Angelo Basile, Alberto Figoli and Mohamed Khayet
- 78 **Safe and secure transport and storage of radioactive materials**
Edited by Ken Sorenson
- 79 **Reprocessing and recycling of spent nuclear fuel**
Edited by Robin Taylor
- 80 **Advances in battery technologies for electric vehicles**
Edited by Bruno Scrosati, Jürgen Garche and Werner Tillmetz
- 81 **Rechargeable lithium batteries: From fundamentals to applications**
Edited by Alejandro A. Franco
- 82 **Calcium and chemical looping technology for power generation and carbon dioxide (CO₂) capture**
Edited by Paul Fennell and Ben Anthony
- 83 **Compendium of Hydrogen Energy Volume 1: Hydrogen Production and Purification**
Edited by Velu Subramani, Angelo Basile and T. Nejat Veziroglu
- 84 **Compendium of Hydrogen Energy Volume 2: Hydrogen Storage, Transmission, Transportation and Infrastructure**
Edited by Ram Gupta, Angelo Basile and T. Nejat Veziroglu
- 85 **Compendium of Hydrogen Energy Volume 3: Hydrogen Energy Conversion**
Edited by Frano Barbir, Angelo Basile and T. Nejat Veziroglu
- 86 **Compendium of Hydrogen Energy Volume 4: Hydrogen Use, Safety and the Hydrogen Economy**
Edited by Michael Ball, Angelo Basile and T. Nejat Veziroglu
- 87 **Advanced district heating and cooling (DHC) systems**
Edited by Robin Wiltshire
- 88 **Microbial Electrochemical and Fuel Cells: Fundamentals and Applications**
Edited by Keith Scott and Eileen Hao Yu
- 89 **Renewable Heating and Cooling: Technologies and Applications**
Edited by Gerhard Stryi-Hipp
- 90 **Small Modular Reactors: Nuclear Power Fad or Future?**
Edited by Daniel T. Ingersoll
- 91 **Fuel Flexible Energy Generation: Solid, Liquid and Gaseous Fuels**
Edited by John Oakey
- 92 **Offshore Wind Farms: Technologies, Design and Operation**
Edited by Chong Ng & Li Ran
- 93 **Uranium for Nuclear Power: Resources, Mining and Transformation to Fuel**
Edited by Ian Hore-Lacy
- 94 **Biomass Supply Chains for Bioenergy and Biorefining**
Edited by Jens Bo Holm-Nielsen and Ehiaze Augustine Ehimen
- 95 **Sustainable Energy from Salinity Gradients**
Edited by Andrea Cipollina and Giorgio Micale
- 96 **Membrane Technologies for Biorefining**
Edited by Alberto Figoli, Alfredo Cassano and Angelo Basile
- 97 **Geothermal Power Generation: Developments and Innovation**
Edited by Ronald DiPippo

-
- 98 **Handbook of Biofuels' Production: Processes and Technologies (Second Edition)**
Edited by Rafael Luque, Carol Sze Ki Lin, Karen Wilson and James Clark
- 99 **Magnetic Fusion Energy: From Experiments to Power Plants**
Edited by George H. Neilson
- 100 **Advances in Ground-Source Heat Pump Systems**
Edited by Simon Rees
- 101 **Absorption-Based Post-Combustion Capture of Carbon Dioxide**
Edited by Paul Feron
- 102 **Advances in Solar Heating and Cooling**
Edited by Ruzhu Wang and Tianshu Ge
- 103 **Handbook of Generation IV Nuclear Power Reactors**
Edited by Igor Pioro
- 104 **Materials for Ultra-Supercritical and Advanced Ultra-Supercritical Power Plants**
Edited by Augusto Di Gianfrancesco
- 105 **The Performance of Photovoltaic Systems: Modelling, Measurement and Assessment**
Edited by Nicola Pearsall
- 106 **Structural Materials for Generation IV Nuclear Reactors**
Edited by Pascal Yvon
- 107 **Organic Rankine Cycle (ORC) Power Systems: Technologies and Applications**
Edited by Ennio Macchi and Marco Astolfi

Woodhead Publishing is an imprint of Elsevier
The Officers' Mess Business Centre, Royston Road, Duxford, CB22 4QH, United Kingdom
50 Hampshire Street, 5th Floor, Cambridge, MA 02139, United States
The Boulevard, Langford Lane, Kidlington, OX5 1GB, United Kingdom

Copyright © 2017 Elsevier Ltd. All rights reserved.

No part of this publication may be reproduced or transmitted in any form or by any means, electronic or mechanical, including photocopying, recording, or any information storage and retrieval system, without permission in writing from the publisher. Details on how to seek permission, further information about the Publisher's permissions policies and our arrangements with organizations such as the Copyright Clearance Center and the Copyright Licensing Agency, can be found at our website: www.elsevier.com/permissions.

This book and the individual contributions contained in it are protected under copyright by the Publisher (other than as may be noted herein).

Notices

Knowledge and best practice in this field are constantly changing. As new research and experience broaden our understanding, changes in research methods, professional practices, or medical treatment may become necessary.

Practitioners and researchers must always rely on their own experience and knowledge in evaluating and using any information, methods, compounds, or experiments described herein. In using such information or methods they should be mindful of their own safety and the safety of others, including parties for whom they have a professional responsibility.

To the fullest extent of the law, neither the Publisher nor the authors, contributors, or editors, assume any liability for any injury and/or damage to persons or property as a matter of products liability, negligence or otherwise, or from any use or operation of any methods, products, instructions, or ideas contained in the material herein.

ISBN: 978-0-08-100510-1 (print)

ISBN: 978-0-08-100511-8 (online)

Library of Congress Cataloging-in-Publication Data

A catalog record for this book is available from the Library of Congress

British Library Cataloguing-in-Publication Data

A catalogue record for this book is available from the British Library

For information on all Woodhead Publishing publications
visit our website at <https://www.elsevier.com/>



Working together
to grow libraries in
developing countries

www.elsevier.com • www.bookaid.org

Publisher: Joe Hayton

Acquisition Editor: Sarah Hughes

Editorial Project Manager: Lucy Beg

Production Project Manager: Omer Mukthar

Designer: Greg Harris

Typeset by TNQ Books and Journals

Related titles

Geothermal Energy: An Alternative Resource for the 21st Century
(ISBN 978-0-44452-875-9)

Geothermal Reservoir Engineering, 2e
(ISBN 978-0-12383-880-3)

Concentrating Solar Power Technology
(ISBN 978-1-84569-769-3)

Theoretical basis of the Organic Rankine Cycle

1

E. Macchi

Politecnico di Milano, Milan, Italy

1.1 Introduction

It is well known that gas and steam cycles play a dominant role in large-scale stationary power generation. Open-cycle gas turbines (often combined with steam cycles) are widely used, especially where low-cost natural gas is available, while steam cycles are the preferred solution when the energy source characteristics, typically coal or nuclear, require a closed-cycle power plant.

However, there is a large variety of energy sources (see Fig. 1.1) for which neither gas nor steam cycles offer a technically and/or economically viable solution to generate electric power. When the temperature and/or the thermal power available from the energy source is limited, it becomes attractive to adopt a different class of prime movers, universally known with the acronym ORC (Organic Rankine Cycle).

This volume focuses on ORC, aiming to provide the reader with a comprehensive overview of all aspects of this fascinating new field in the power generation industry. It is organized into three main parts.

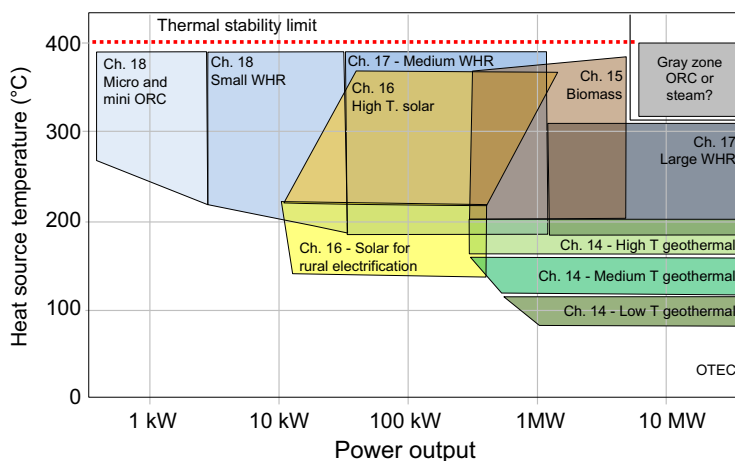


Figure 1.1 A representation of ORC applications fields in the heat source temperature-power output plane.

Part 1 of the volume is devoted to the fundamental bases of the technology:

- This introduction explains why the ORC technology is the unrivaled technical solution for producing electricity (or coproducing electricity and heat) from a wide-ranging variety of energy sources and illustrates the guidelines for selecting the proper fluid and the proper cycle for each application.
- In Chapter 2, the founder of Ormat, which is the undisputed world leading company in ORC, illustrates the exciting and successful history of ORCs, from the pioneering applications to the latest developments.
- Chapter 3 illustrates the possible technical options for ORC applications, in terms of thermodynamic cycles (from simple one pressure level to multipressure solutions), plant layouts, and main component characteristics.
- Chapter 4 provides a theoretical basis and a thorough review of the most up-to-date methods and available tools for calculating the thermodynamic and transport properties of working fluids for ORC.
- Chapter 5 addresses the topic of thermal stability of working fluids, a fundamental aspect in ORC applications, since thermal stability sets the limit to the maximum temperature of the thermodynamic cycle, strictly related to its conversion efficiency.
- Chapter 6 illustrates the basic principles of the dynamic modeling of ORC systems and how these models can be the basis for a reliable control of ORC, particularly in applications characterized by fast variations of operating conditions.
- Chapter 7 illustrates the most up-to-date methods to optimize an ORC system, both in terms of thermodynamic performance and economic aspects. A few examples demonstrate the intrinsic worth of these advanced design approaches.

Part 2 of the volume addresses the theoretical foundations behind the design methods and the performance prediction of the two key classes of components present in ORC systems. The first five chapters are dedicated to expansion machines (the “heart” of any ORC, whereby the working fluid converts its thermodynamic energy into mechanical work), while the last chapter illustrates the processes occurring in the heat exchangers, whereby the working fluid exchanges thermal energy with the heat source and sink or between two streams of the power cycle. In more detail:

- Chapter 8 describes the various options of turbine architecture which can be adopted in ORC plants and outlines the fluid-dynamic methods to design a turbine, spanning from the more classical to the most advanced ones.
- Chapter 9 deals with the design of axial-flow turbines, by far the most adopted solution in all power conversion systems, including ORC. New correlations for predicting the efficiency, specifically developed for the peculiar characteristics of ORCs, are presented for single and multistage solutions.
- Chapter 10 illustrates the features of radial inflow turbines, a widely adopted solution for large-scale, low–medium temperature applications, which, due to its capability of variable geometry, offers relevant advantages when coupled to heat sources which vary their conditions during the plant life.
- Chapter 11 describes the features of multistage outflow turbines, a technical solution which recently experienced a booming success especially in the geothermal field. The outflow turbine is particularly suited for ORCs, since it can handle large expansion ratios, thanks to the diameter increase during the expansion.

- Chapter 12 deals with the various solutions of volumetric expanders, describing the large variety of technological solutions, mostly derived from compressors in the refrigerating and air-conditioning industry.
- Chapter 13 describes the equations which govern the thermo-fluid-dynamic phenomena occurring in the heat exchangers present in ORC, as well as the correlations to be applied for predicting the heat transfer coefficients and the pressure drops. In addition, it illustrates the most common technical solutions for heat exchangers adopted by ORC manufacturers.

Part 3 deals with the most significant fields of application of ORCs, in a power range which spans over four orders of magnitude, from less than 1 kW micro-cogenerators to power plants with outputs above 10 MW, adopted in geothermal and heat recovery applications. [Fig. 1.1](#) describes the large variety of applications in the power output maximum temperature plan, where an upper limit is set to the maximum temperature, related to the thermal stability of organic fluids. It is worth noting that ORC characteristics (i.e., the capability of generating power with reasonable conversion efficiency at relatively low temperature and of requiring simple plant layouts and low-cost, efficient expanders at low power output), match very well with the features of most renewable sources, such as, geothermal, solar, and biomass. A “gray zone” is also indicated, in a range of power output and temperatures where the competition between ORC and steam cycle becomes uncertain. When the available heat source increases its temperature, steam takes advantage of its higher chemical stability and can reach efficiencies higher than ORC working fluids, moreover, large power outputs can justify the adoption of a more expensive turbine and a more complex plant layout.

All chapters listed below depict the state-of-the art and list some representative applications of ORCs in the exploitation of the energy sources. More specifically, they deal with:

- Chapter 14 discusses the main features of geothermal energy sources, and focuses on the increasing ORC role in exploiting high-, medium-, and low-temperature geothermal sources. One of the main advantages of the so-called binary cycles is their capability of having zero-impact on the environment, since the geothermal brine, after releasing heat to the ORC working fluid, is re-injected underground.
- Chapter 15 describes ORC applications with a variety of biomass energy sources. The most conventional applications involve a solid biomass boiler, a synthetic oil loop and an ORC, generally condensing at temperatures which make it possible to cogenerate heat and electrical energy. This explains the large diffusion of these plants in combination with district heating networks.
- Chapter 16 deals with ORC applications in the solar energy field. After a description of the characteristics of solar energy and of the various solutions adopted to concentrate the sun rays on receivers, the main advantages of adopting ORCs in this field are outlined. In opposition to the previous renewable sources (geothermal and biomass), where the ORC application reached a full commercial maturity, the application of ORCs in Concentrating Solar Power (CSP) plants is still at a demonstration stage. A promising application could be small CSP systems based on ORC for rural electrification.
- Chapter 17 describes ORC applications for waste heat recovery systems. Several industrial processes release, to the environment, a large amount of heat at temperatures which are suitable for producing electrical energy by an ORC. One interesting application is also heat recovery from prime movers fueled by fossil fuels, such as, Diesel engines and gas turbines. The applications span from relatively low power output to large plants.

- Chapter 18 deals with a relatively new application field for ORCs, called micro systems. These systems, are capable of generating heat (and cold, in so-called trigeneration applications) and electricity in households or small commercial units, in the optic of so-called smart grid applications. This field, which is still in a demonstration phase, demands low investment cost and maintenance, is capable of primary energy saving, and produces low emissions.

1.2 The unique features of Organic Rankine Cycles

It can be useful to initiate the introduction of a volume dedicated to ORC by discussing the reasons which support the following statement:

ORCs are the unrivalled technical solution for generating electricity from low-medium temperature heat sources of limited capacity.

First we will demonstrate the thermodynamic bases that prevents the use of any gas as a working fluid for low/medium temperature, say below 400-500°C, power cycles. We will then explain, mostly discussing turbomachinery issues, why water is not an appropriate working fluid for low/medium power output Rankine cycles. Finally, we will discuss the main issues related to the selection of the working fluid and the cycle arrangement.

1.3 Why air (or any other gas) is not an appropriate working fluid for a power cycle operating with low-medium temperature heat sources

Let's start by discussing some basic concepts of the thermodynamics of power cycles.

1.3.1 *The only thermodynamic processes which are technologically feasible in a power cycle*

All thermodynamic power cycles operate with a working fluid that experiences a series of processes. For heat sources "external" to the power cycle, two possibilities exist:

1. "open" cycles, whereby the working fluid is air, introduced into the cycle at environment conditions and released to the environment at the end of the process
2. "closed" cycles, whereby an arbitrary working fluid performs a cyclic series of transformations.

In both cases, *only two types* of processes are technologically feasible in power plants:

1. *nearly-adiabatic transformations*, where the fluid-dynamic process (either compression or expansion) is so fast that the working fluid exchanges heat in nearly negligible quantity
2. *nearly-isobaric transformations*, where the working fluid exchanges heat, either flowing at nearly constant pressure along the surfaces of a heat exchanger, or mixing with environment air (in an open-cycle).

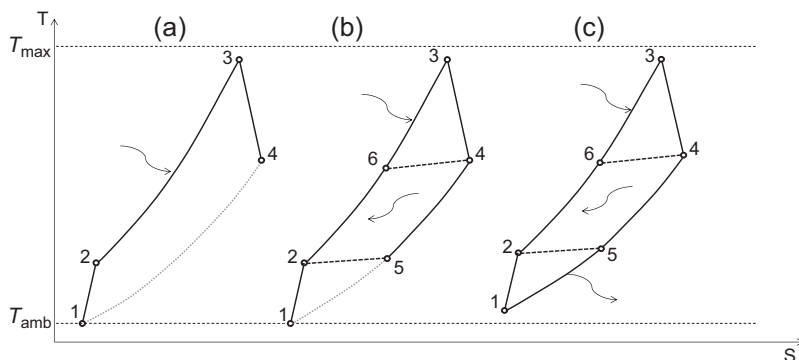


Figure 1.2 Temperature—entropy diagram of a power cycle having environment air as a working fluid. (a) simple cycle, open loop (b) recuperated cycle, open loop (c) recuperated cycle, closed loop Fig. 1.8 (a) Mach number of the absolute (V) and relative (W) velocity at stator exit (b) peripheral speed (c) vapour quality at turbine exit (d) Ratio between exit and inlet volume flow rate.

The former type of transformation occurs in components such as expanders (turbines or volumetric expanders), compressors, pumps, valves, piping, etc. The latter occurs in heat exchangers (evaporators, superheaters, recuperators, condensers, etc.) or in the discharge of working fluid to the environment. In the first case, the working fluid may (or may not) exchange mechanical work, in the second case, the exchange involves heat. The simultaneous exchange of heat and work in a single process is not feasible in practice.¹

1.3.2 The poor air (or any other gas) power cycle performance at low T_{max} temperature

Given the limitations discussed in Section 1.3.1, when the working fluid is air, the cycle assumes the shape shown in Fig. 1.2; two nearly-adiabatic transformations (1–2: compression and 3–4 expansion) and two nearly-isobaric transformations (2–3: heat introduction and 4–1: heat rejection). The addition of a recuperator (Fig. 1.2(b)) improves the cycle performance. Other plant arrangements, say by introducing intercooling in the compressor and/or reheating in the expansion phase are not of interest for relatively small-scale power plants.

Figs. 1.2(a) and (b) represent two “open” cycles, without and with a recuperator, respectively. The adoption of a “closed” cycle (Fig. 1.2(c)) with another gas as a working fluid requires an additional heat exchanger and increases the minimum cycle temperature, without any thermodynamic advantage.

The “thermodynamic quality” of air (or any other gas) cycles is rather poor. Actually, as shown in Fig. 1.3, the efficiency of a gas cycle is negative up to about $T_{max} < 250^{\circ}\text{C}$.

¹ With few exceptions, generally related to internal combustion engines, where active cooling is required since the working fluid reaches very high temperatures that cannot be sustained by components’ materials (say, first stages of gas turbines, or parts of internal combustion reciprocating engines).

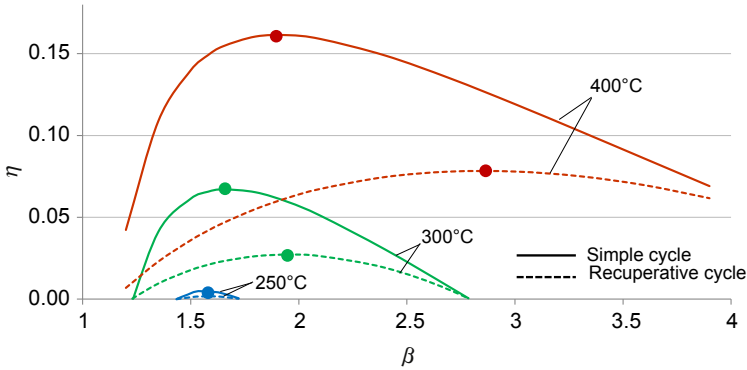


Figure 1.3 Net efficiency of simple and recuperated air cycle as a function of β for three different maximum temperatures.

Even at 400°C, the simple cycle efficiency hardly reaches 8%. The recuperated cycle efficiency is higher, but still remains relatively low. An explanation of such poor performance can be found by means of the second-law analysis, as discussed in the next section. Results are obtained with the following assumptions:

- Environment temperature, $T_{\text{amb}} = 15^\circ\text{C}$
- Compression polytropic efficiency, $\eta_{\text{pol},c} = 0.85$
- Expansion polytropic efficiency, $\eta_{\text{pol},t} = 0.85$
- Sommatory of relative pressure losses $\sum \Delta p_i / p_i = 10\%$
- Thermal losses = 1% of heat input
- Mechanical/electrical efficiency = 95%
- Recuperator minimum temperature difference = 10% of ideal temperature difference
- Primary heat exchanger minimum temperature difference = 10°C

1.3.3 The second-law analysis of air power cycles (with reference to a constant temperature heat source)

The second-law² analysis is the most powerful tool for understanding the rationale of a power cycle and the potential efficiency gains that can be achieved by improving its layout and/or its components' performance.

Let's consider the simple cycle represented in Fig. 1.2, working at an optimum pressure ratio as calculated in Fig. 1.3. Referring to a constant temperature T_{max} heat source and environment temperature T_0 , the cycle efficiency can be expressed by:

$$\eta = \eta_{\text{rev}} - \sum_1^N \Delta \eta_i$$

² Sometimes referred to as "exergy" or "entropy" analysis.

where η_{rev} is the ideal (“Carnot”) cycle efficiency, given by:

$$\eta_{\text{rev}} = 1 - \frac{T_0}{T_{\text{max}}}$$

$\Delta\eta_i$ is the efficiency penalties related to the various irreversibilities, given by:

$$\Delta\eta_i = T_0 \sum_1^N \frac{\Delta S_i}{Q_{\text{in}}}$$

where ΔS_i is the entropy increase caused by the i th irreversibility, N is the total number of irreversible processes taking place in the power cycle and in energy source and sink, Q_{in} is the heat input to the power cycle. The various efficiency penalties occurring in air power cycles at different T_{max} at optimum pressure ratio are represented in Fig. 1.4.

The following energy penalties are represented:

$\Delta\eta 1$ = pressure losses

$\Delta\eta 2$ = fluid-dynamic losses in compressor

$\Delta\eta 3$ = heat transfer losses in the heat introduction process

$\Delta\eta 4$ = fluid-dynamic losses in expansion

$\Delta\eta 5$ = losses due to mixing of hot air to atmosphere

$\Delta\eta 6$ = heat losses to the environment

$\Delta\eta 7$ = mechanical/electrical losses

$\Delta\eta 8$ = heat transfer losses in the recuperator

It can be seen that the efficiency losses are so large compared to the cycle efficiency (the bottom element of the bar diagram) that the air cycle performance is always quite poor, even at $T_{\text{max}} = 400^\circ\text{C}$.

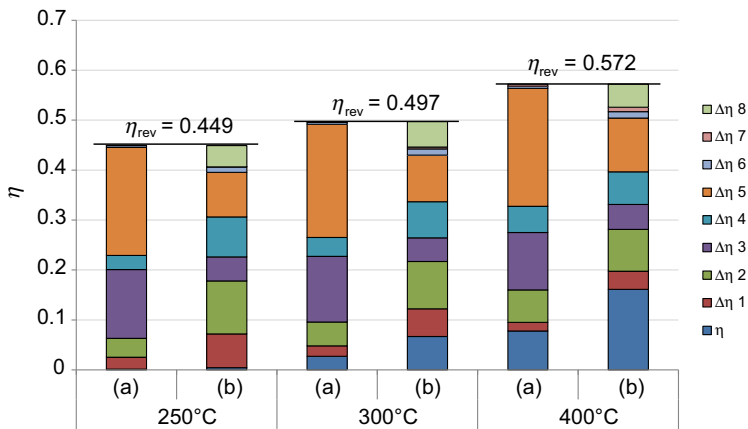


Figure 1.4 Second-law efficiency losses of gas cycles at various T_{max} (250°C, 300°C, and 400°C). (a) Simple cycle, (b) recuperative cycle. The pressure ratio is optimized for each cycle and the results are obtained using the same assumptions as Fig. 1.3.

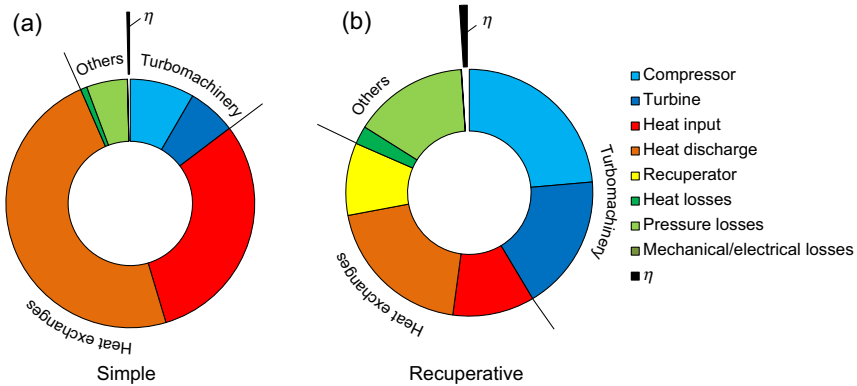


Figure 1.5 Cycle efficiency and second-law efficiency losses of a gas cycle at $T_{\max} = 250^{\circ}\text{C}$ and optimized pressure ratio. All values are in percentage of the reversible efficiency.

(a) Simple cycle, (b) recuperative cycle.

Let's consider the case of $T_{\max} = 250^{\circ}\text{C}$, where the cycle efficiency is very low (almost zero for a simple cycle, and less than 2% for the recuperative one). As shown in Fig. 1.5(a), it can be noted that the highest efficiency penalties take place in heat exchanges with the heat source and sink; the addition of turbomachinery and other losses results in a sum of efficiency losses which is almost equal to the reversible efficiency. The adoption of a recuperator changes the distribution among various efficiency penalties, decreasing the ones related to heat exchange with the heat source and sink, but increasing all the others and adding the one occurring in the recuperator; the result is still a very low cycle efficiency.

1.3.4 The advantages of substituting a gas cycle with a Rankine cycle

We have seen in the previous section that a gas cycle operating between 250°C and 15°C , under reasonable assumptions on components performance, cannot reach an acceptable efficiency. When compared to gas cycles, the adoption of a Rankine cycle brings about several thermodynamic advantages. In particular, the variable temperature heat exchanges with the source and sink respectively, are substituted (partially or totally) by constant temperature processes. Moreover, the compression takes place in the liquid phase, with the significant advantage that the compression work is dramatically reduced and the turbine work is close to the cycle useful work; the combined effect of these two circumstances is a strong decrease of the efficiency losses related to turbomachinery irreversibilities.

To demonstrate the merits of Rankine versus gas cycles, let us now consider a simple saturated Rankine cycle, operating with the same heat source and sink temperatures, and with components' performances similar to ones assumed for the air cycles of Fig. 1.3. We select three working fluids which have different

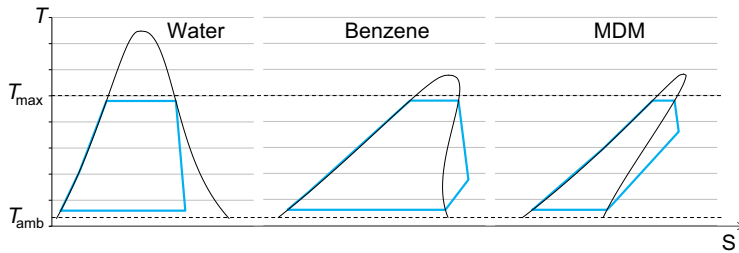


Figure 1.6 Temperature–entropy diagrams of saturated Rankine cycles having working fluids of different molecular complexity.

molecular complexities and a critical temperature well above the evaporation temperature:

- Water (a simple molecule, 3 atoms)
- Benzene (an intermediate complex molecule, 12 atoms)
- MDM (a highly complex molecule, 37 atoms octamethyltrisiloxane)

Increasing the molecular complexity, the molecular heat capacity increases due to the contribution of atoms vibration. This yields three main effects on the power cycle: (1) the inclination of the saturated vapor curve in the T-S diagram is different from that of simple molecule, hence the expansion occurs in “dry” conditions, (2) the increased importance of the liquid preheating phase with respect to the evaporation phase, and (3) the increased importance of the desuperheating phase in the heat rejection.

These effects are evident in Fig. 1.6, which shows the different “shape” of the power cycle:

- For water, the expansion takes place inside the Andrew’s curve, with unacceptably low vapor qualities in the last part of the expansion. The heat introduction occurring in the liquid preheating phase is relatively small compared to the one in the evaporation phase. The whole heat release occurs in the condenser in an isothermal process.
- For benzene, the saturated vapor curve is nearly vertical, so that the expansion curve takes place in the superheated region. The temperature at the turbine exit is close to the condensation temperature, so that most of heat release to the environment takes place at condensation temperature. The heat introduction occurring in the liquid preheating phase is much larger than the one in the evaporation phase.
- For MDM, the temperature drop across the turbine is very low, thus causing the heat release to the environment to occur mostly with significant temperature differences. The heat introduced in the evaporation phase is only a small fraction of the total heat introduced in the cycle.

If we calculate the performance of the three saturated cycles represented in Fig. 1.6, we obtain the results described in Fig. 1.7, which represents the cycle efficiency and the efficiency penalties for four different options:

Upper figure:

1. Nonrecuperated cycles, ideal components
2. Nonrecuperated cycles, real components

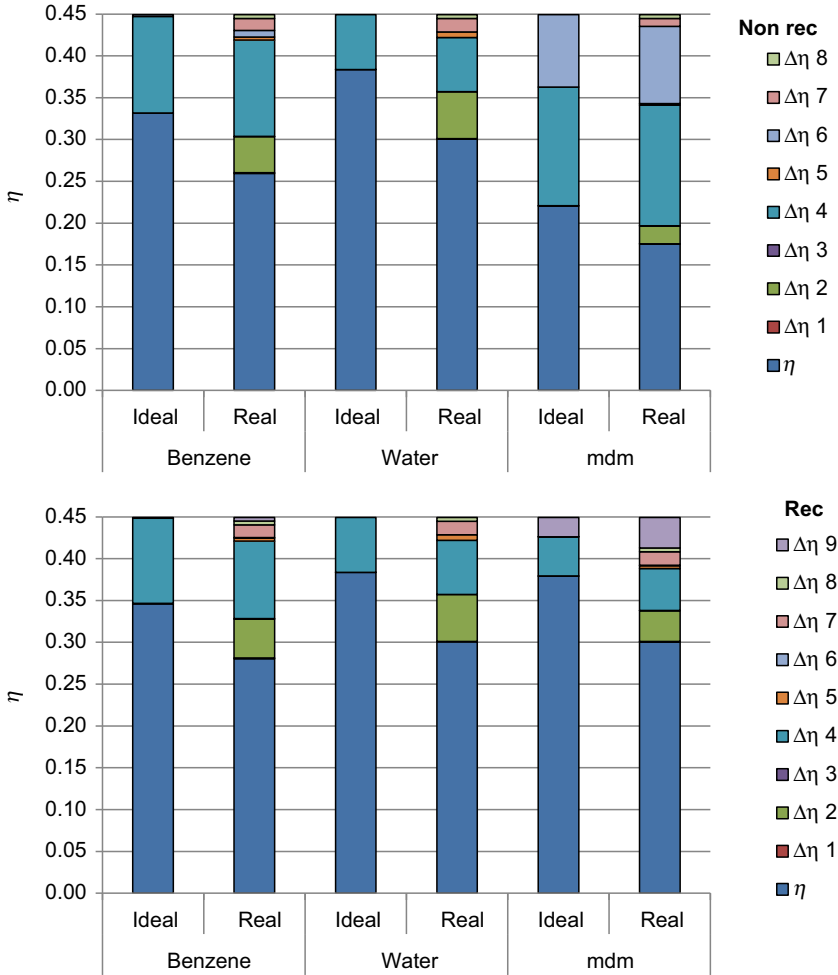


Figure 1.7 Cycle efficiency and second-law efficiency penalties of the three saturated Rankine cycles at $T_{\max} = 250^\circ\text{C}$.

Lower figure:

3. Recuperated cycles, ideal components
4. Recuperated cycles, real components

All the results are obtained with the following assumptions.

- Environment temperature, $T_0 = 15^\circ\text{C}$
- Condensation temperature, $T_c = 30^\circ\text{C}$
- Evaporation temperature = 240°C
- Pump polytropic efficiency, $\eta_{\text{pol},p} = 0.85$

- Expansion polytropic efficiency, $\eta_{\text{pol},t} = 0.85$
- Pressure losses = 10% of evaporation pressure
- Thermal losses = 1% of heat input
- Mechanical/electrical efficiency = 95%

The following efficiency penalties are represented:

$\Delta\eta_1$ = fluid-dynamic losses in pump

$\Delta\eta_2$ = fluid-dynamic losses in turbine

$\Delta\eta_3$ = pressure losses

$\Delta\eta_4$ = heat transfer losses in the liquid preheating

$\Delta\eta_5$ = heat transfer losses in the evaporation process

$\Delta\eta_6$ = heat transfer losses in the heat rejection to environment

$\Delta\eta_7$ = mechanical/electrical losses

$\Delta\eta_8$ = heat losses to the environment

$\Delta\eta_9$ = heat transfer losses in the recuperator

In the first option, where ideal components are used, the only efficiency penalties are given by the heat exchange with the heat source (in the liquid preheating phase, $\Delta\eta_4$) and sink, $\Delta\eta_6$. The best performance is obtained by the simplest molecule (water) for which the heat transfer to the environment is fully reversible and the weight of heat introduction under finite temperature difference is minimum. The worst is by the complex molecule (MDM), where both heat exchanges involve large quantities and occur under large temperature differences. The intermediate complex fluid (benzene) exhibits a performance intermediate between these two extremes.

In the second option, where we consider real components, the efficiency decreases for the three fluids in a similar manner. The largest efficiency penalty increase is due to fluid-dynamic losses in the turbine, which are more relevant for water, due the largest ratio between turbine work and heat input.

If we compare the results of the third option versus the first one, we can see that the presence of a recuperator³ significantly improves the performance of benzene and MDM cycles, which becomes similar, in the range of 85% of the Carnot efficiency.

Eventually, if we consider the fourth option, the most realistic one, we find that the performance of real cycles are similar for the three fluids.⁴ The achievable efficiency for saturated cycles is of the order of 65–70% of the Carnot cycle. The distribution of the energy penalty changes with the fluid complexity. MDM has a significant efficiency loss in the recuperator, but a lower penalty for the liquid preheating.

In conclusion, it can be stated that saturated Rankine cycles can achieve excellent thermodynamic performance, independent of the complexity of the adopted working fluid; the “shape” of the cycle changes, but the attainable efficiency is similar.

³ For steam, a counter flow recuperator is not possible. However, cycle efficiency could be improved by bleeding some steam during the expansion to preheat the condensate. This is a common practice in large scale steam cycles.

⁴ The slightly lower cycle efficiency for steam is due to the absence of the recuperator, but, as already pointed out, a significant improvement can be achieved by regenerative bleeding.

1.4 Why water is not the right working fluid for power cycles fed by energy sources of limited capacity

We found in the previous section that, in terms of cycle efficiency, water can be an excellent working fluid for saturated Rankine cycles. Water is the choice working fluid for large-scale Rankine cycles operating with high temperature energy sources in a wide variety of efficient cycle configurations, from the saturated cycles of nuclear power stations to the coal fired ultra-supercritical cycles. However, the thermodynamic properties of steam lead to multistage, capital-intensive turbines as well as to complex plant schemes and to liquid formation during the expansion; these constraints make steam a working fluid not suitable for low temperature-low power output applications.

On the contrary, the rationale of ORCs is to make technically feasible and economically attractive the power generation for moderate-temperature, dispersed energy sources. This is obtained by selecting a proper working fluid, capable of obtaining a simple plant arrangement and a low-cost turbine without liquid formation during the expansion.

1.4.1 The steam turbine issue for steam cycles

Let's consider a saturated steam cycle with an axial-flow turbine. For the evaporating pressures of interest, a single-stage impulse turbine would require the features represented in Fig. 1.8 where the following are highlighted:

1. High supersonic flows at stator exit and transonic or supersonic flows at rotor inlet
2. High peripheral speed
3. High liquid content at turbine discharge
4. High volumetric flow rate ratio between outlet and inlet conditions.

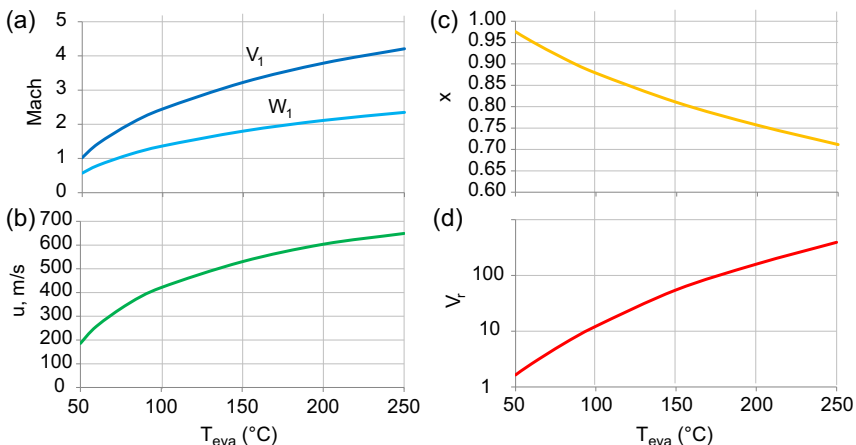


Figure 1.8 Some relevant features which make a single impulse stage turbine an unfeasible solution for saturated steam cycle with heat source temperatures above 100 $^{\circ}\text{C}$.

Let's briefly comment on the influence of turbine performance on each of these features⁵:

1. Supersonic velocity at stator exit: for M_{V1} above ≈ 1.4 , converging–diverging interblade channels must be adopted, with a negative influence on turbine efficiency caused by shock losses, particularly in off-design conditions. Transonic or supersonic relative velocity at rotor inlet (M_{W1} above ≈ 0.8) causes significant losses, with boundary layer–shock interaction in the rotor blades.
2. High peripheral speeds yield high centrifugal stresses in the rotating components; it would be safe to adopt values of the mean peripheral speed u below ≈ 300 m/s.
3. High liquid content in the expansion are detrimental for the efficiency as well as for the integrity of the turbine blades; vapor quality below ≈ 0.9 should be avoided.

The adoption of a reaction instead of an impulse stage could help the first two points, but would require even higher peripheral speeds. Moreover, a reaction stage must face the problems related to high volumetric expansion ratios across the rotor blade. For V_r above ≈ 4 , both the geometry of the rotor blade (high flare angles) and the shape of the velocity triangles (large increase of axial velocity components across the rotor blade) cause penalties on turbine efficiency.

Thus, to obtain a reasonable level of efficiency and a safe mechanical design of a steam turbine, it is necessary to adopt a multistage machine. However, the volumetric variation along the stages requires either the adoption of a multishaft machine and/or of a single-shaft turbine with a large variation of specific speed. Furthermore, for a small power output, the small volumetric flow rate at the turbine inlet requires highly partialized admission stages and/or very high rotational speed, as shown in Fig. 1.9. It can be seen that critical throat areas as small as 100 mm^2 and rotational speeds as high as 100,000 rpm result from power outputs below 1000 kW and evaporation temperatures higher than 200°C .

In conclusion, a steam turbine operating within a reasonable temperature range of evaporating and condensing temperatures requires complex and costly solutions, incompatible with power plants of limited power output. The adoption of a different working fluid, having larger molecular mass, higher molecular complexity, lower critical pressure, and temperature than water can solve most of the issues present in the turbine design.

1.5 Thermodynamic issues related to the choice of working fluid

1.5.1 Heat sources

The simplest classification of heat sources refers to their heat capacity, which influences their temperature variation during the heat release. Two options are considered:

- Infinite heat capacity, whereby heat is released at a constant temperature
- Finite heat capacity, whereby heat is released at a variable temperature.

⁵ For more details, refer to Chapter 9.

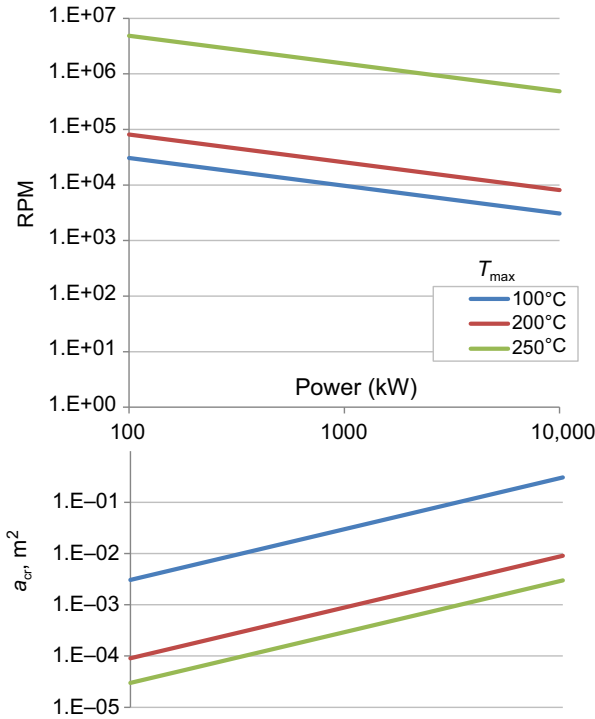


Figure 1.9 Critical throat area of steam turbines and speed of revolution as a function of evaporating temperature and power output.

1.5.1.1 Constant temperature heat sources

For these heat sources, the obvious reference ideal power cycle is the Carnot cycle, while the real cycle that better matches is a Rankine saturated cycle. The working fluid variables that influence the performance of saturated Rankine cycles are: (1) the molecular complexity (identified by the number of atoms), (2) the critical temperature and (3) the molecular mass. As previously discussed, the “shape” of a saturated Rankine cycle is mainly related to the working fluid molecular complexity; the higher the molecular complexity, the higher the need for the recuperator to decrease the efficiency penalties related to the economizer as well as to vapor desuperheating. With an ideal recuperator, both simple and complex molecules can achieve ideal cycle efficiencies in the range of 85% of a Carnot cycle operating between the same evaporation and condensation temperature. For real cycles, this figure drops to about 65–70%.

To discuss the influence of the working fluid properties on performance of saturated cycles, let’s consider the following six fluids, selected to discuss separately the influence of the various properties.

Fluid	Chemical formula	MDM	Number of atoms	T_{crit} , (°C)	p_{crit} (bar)
Fluids with similar complexity, different MDM, and similar T_{crit}					
Iso-pentane	$(CH_3)_2-CH-CH_2-CH_3$	72,14878	17	187	33.8
R365mfc	$CF_3-CH_2-CH_2-CHF_2$	148,0745	14	187	32.7
Fluids with similar complexity, similar MDM, and different T_{crit}					
Benzene	Cycle $= (CH)-$	78,11184	12	289	49.1
Iso-butane	$(CH_3)_2-CH-CH_3$	58,1222	14	135	36.3
Fluids with different complexity, different MDM, and high T_{crit}					
MDM	$C_8H_{24}O_2Si_3$	236,5315	37	291	14.2
Water	H_2O	18,01527	3	374	221
Benzene	Cycle $= (CH)-$	78,11184	12	289	49.1

Fig. 1.10(a), representing the cycle efficiency of the six fluids as a function of the evaporating temperature, indicates that the performances are similar for all fluids, irrespective of the molecular mass and the molecule complexity, as long as the evaporation temperature reaches values close to the critical temperature. Fig. 1.10(b), representing the expansion isentropic enthalpy drop, shows the main advantage of heavy molecules versus steam; the enthalpy drops of organic fluids are one order lower than the steam ones, with relevant advantages in the turbine design (lower peripheral speeds and lower number of stages). Fig. 1.10(c) points out that the volume ratio across the expansion is significantly increasing with the evaporating temperature for all fluids, reaching values greater than 100 for evaporating temperatures above 200°C. This means that one must face large expansion ratios, hence problems related to transonic and supersonic flows and high number of stages, independent of the working fluid characteristics, for saturated cycles having a significant temperature span between evaporation and condensation.

1.5.1.2 Variable temperature heat sources

Let's consider a variable temperature heat source releasing heat in the interval $(T_{max1} - T_{max2})$,⁶ while, as in the previous section, the temperature of the heat sink coincides with the condensation temperature of the cycle.⁷ Different from the previous

⁶ In some cases, it is appropriate to assume $T_{max2} = T_0$, in others, say for geothermal brines or exhaust gases, an opportune minimum temperature limit of the heat source must be considered.

⁷ Assuming $T_0 = T_c$, the condensation phase is considered a reversible process; hence, no efficiency penalties are associated with irreversibilities related to the difference between condensation and environment temperature.

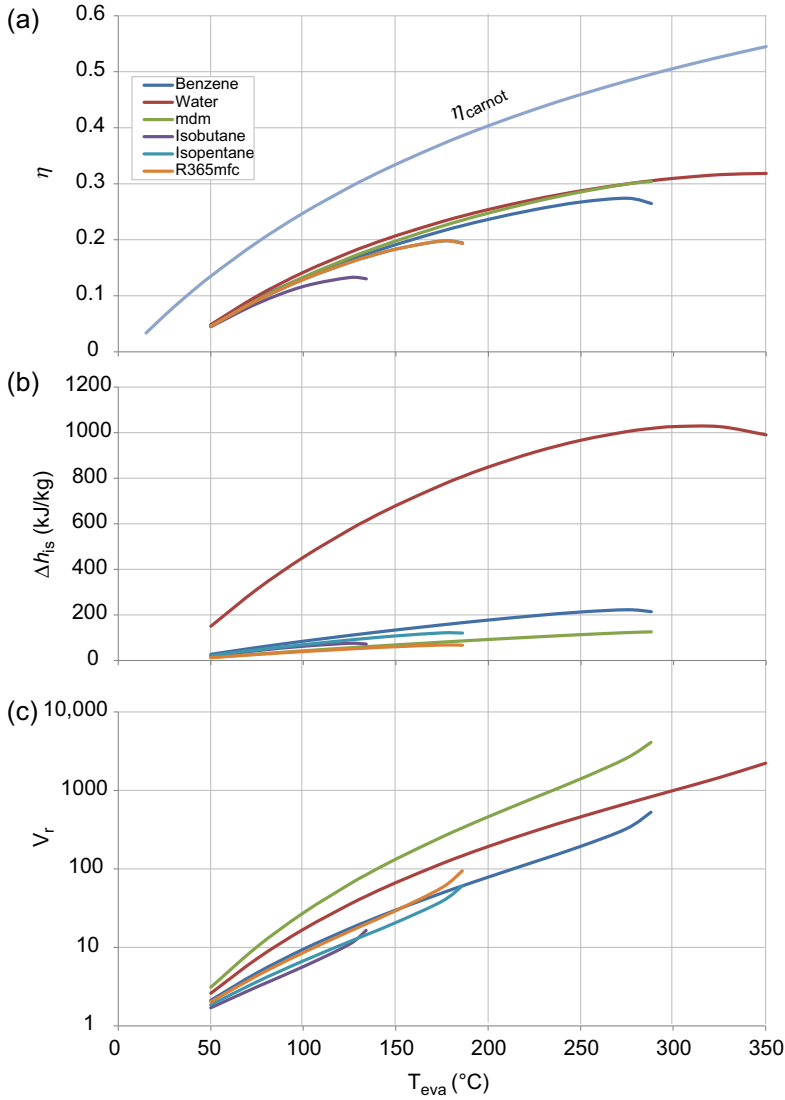


Figure 1.10 Trends of (a) plant efficiency, (b) isentropic enthalpy drop in expansion, and (c) volume ratio across the expansion, as a function of the evaporation temperature.

case, the “thermodynamic quality” of a power cycle is not related solely to the cycle efficiency; it is also related to its capability to cool the heat source down to $T_{\max 2}$. The efficiency of an ideal (reversible) cycle is given by:

$$\eta_{\text{rev}} = 1 - \frac{T_0}{\overline{T}_{\max}}$$

$$\text{where : } \bar{T}_{\max} = \frac{\int_{T_{\max 1}}^{T_{\max 2}} d\dot{Q}}{\int_{T_{\max 1}}^{T_{\max 2}} \frac{d\dot{Q}}{T}}$$

If the heat source is a flow of a fluid having constant specific heat c_p and mass flow rate \dot{m} ,

$$\bar{T}_{\max} = T_{\ln(T_{\max 1}, T_{\max 2})} = \frac{T_{\max 1} - T_{\max 2}}{\ln(T_{\max 1}/T_{\max 2})}$$

the resulting reversible efficiency η_{rev} is represented in Fig. 1.11 as a function of $T_{\max 1}$ and $T_{\max 2}$.

The ideal power P_{rev} achievable from the heat source is given by:

$$P_{\text{rev}} = \dot{m} c_p (T_{\max 1} - T_{\max 2}) \eta_{\text{rev}}$$

The ratio η_{rec} between the real and the ideal power

$$\eta_{\text{rec}} = P/P_{\text{rev}}$$

accounts for the quality of the ORC and is lower than η_{rev} for two reasons: (1) efficiency penalties related to the various irreversibilities occurring in ORC components (turbomachines, heat exchangers, pressure losses, etc.) and (2) an inability to cool the heat source down to $T_{\max 2}$.

While for constant temperature heat sources the best real cycle solution is always a saturated cycle, for variable temperature heat sources, various configurations should be considered, including superheated cycles, supercritical cycles, and multipressure level cycles. Chapter 3 of this volume analyses these options while a numerical example is provided at the end of Chapter 7. A brief discussion, is given here.

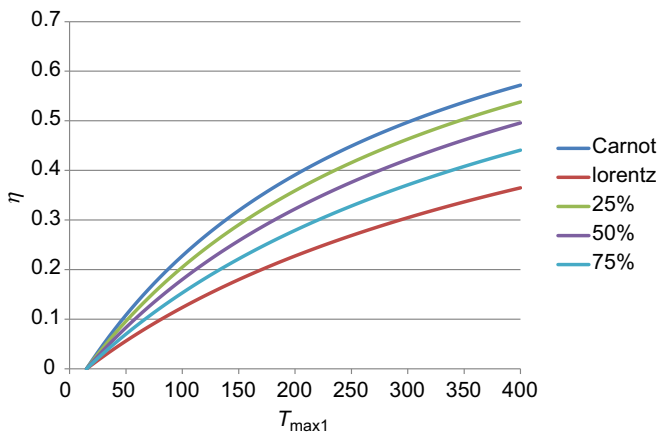


Figure 1.11 Variation of η_{rev} for variable temperature heat sources as a function of the interval of temperatures at which the heat is available. The % indicate the ratio $\frac{(T_{\max 1} - T_{\max 2})}{(T_{\max 1} - T_0)}$.

As in the previous case, the thermodynamic performance of a working fluid is primarily influenced by two parameters:

- Critical temperature
- Molecular complexity

but a further degree of freedom, the turbine inlet pressure must also be considered. The situation is illustrated in Fig. 1.12, which compares the performance of two working fluids (benzene and iso-butane) having a similar molecular complexity but a different critical temperature.

It can be seen that benzene (high critical temperature) experiences increasing cycle efficiency η with increasing pressure; saturated and superheated cycles have similar values, i.e., superheating does not provide any advantage to cycle efficiency. A different situation occurs for η_{rec} ; superheated cycles are penalized by the reduced capability of using the available heat for pressure above 10 bar, while saturated cycles

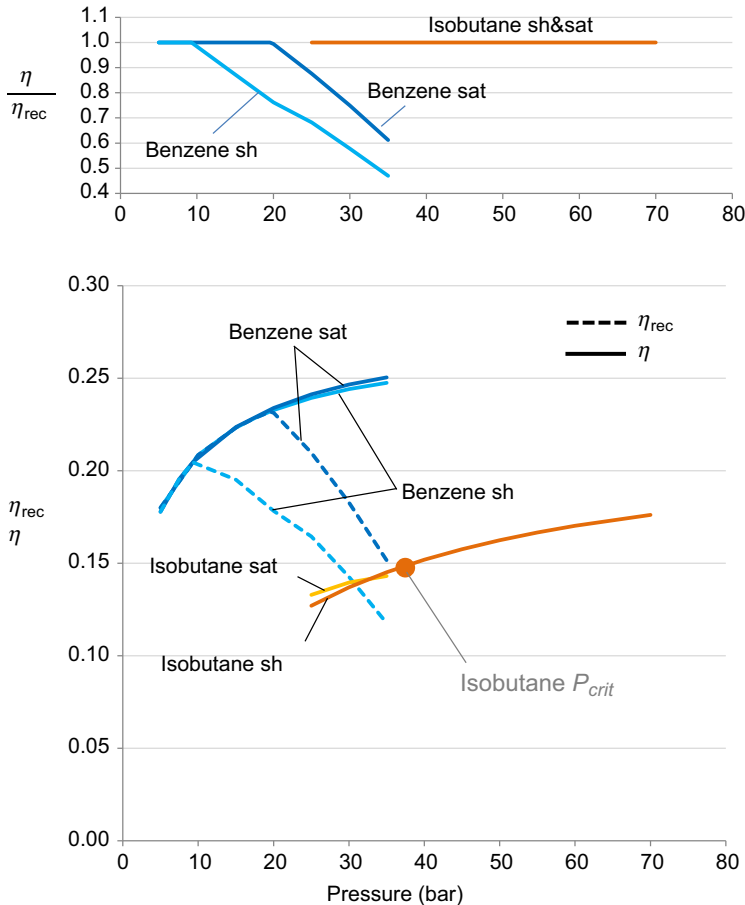


Figure 1.12 Efficiency of Organic Rankine Cycles (ORCs) as a function of the turbine inlet pressure. Heat source temperatures: $T_{max1} = 300^\circ\text{C}$, $T_{max2} = 120^\circ\text{C}$. Two fluids are considered: iso-butane ($T_{crit} = 135^\circ\text{C}$) and benzene ($T_{crit} = 289^\circ\text{C}$), which have a similar molecular complexity.

obtain the optimum value at about 20 bar, with much better performance. Above this pressure, the reduced capability of cooling the heat source is more important than the increase in cycle efficiency. A different situation occurs for the isobutene cycle, which continuously increases its efficiency with pressure, also above the critical value, without affecting the heat recovery. However, the irreversibilities related to the large temperature differences in heat introduction process are so high, that the cycle efficiency is always much lower for isobutene than for pentane. This example confirms a general rule, that the best working fluid for variable temperature heat sources should have a critical temperature close to $T_{\max 1}$.

The following example, illustrated in Fig. 1.13, deals with the influence of molecular complexity, i.e. number of atoms: we consider two fluids, MDM and methanol, which have a similar critical temperature, but a different number of atoms, 27 and 6 respectively.

The methanol results are similar to the ones discussed in the previous case for benzene, with the difference that in this case, the superheated cycle has a better performance in terms of cycle efficiency versus pressure. However, the heat recovered from the heat source starts decreasing at a lower pressure, so the final results are similar for

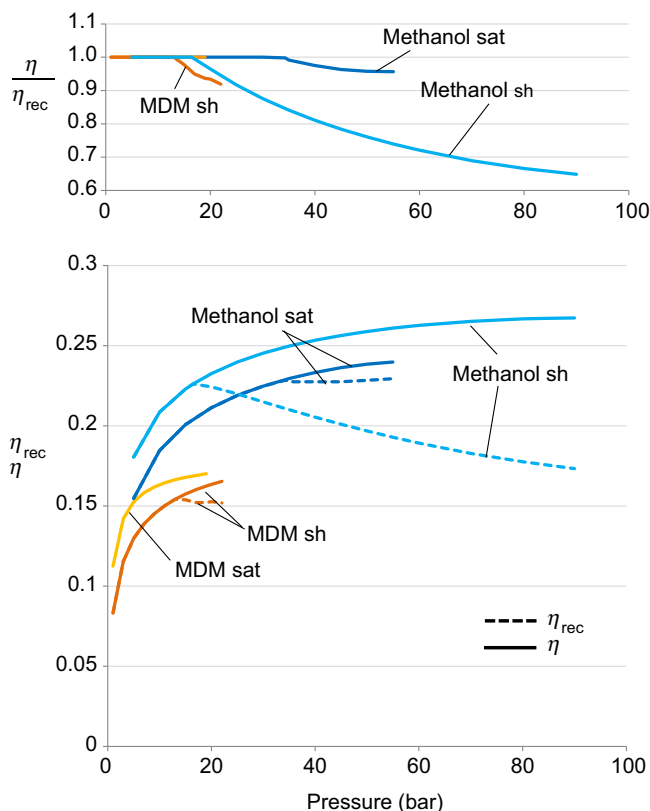


Figure 1.13 Efficiency of Organic Rankine Cycles (ORCs) as a function of the turbine inlet pressure. The heat source temperatures are $T_{\max 1} = 300^{\circ}\text{C}$ and $T_{\max 2} = 120^{\circ}\text{C}$. The two fluids considered are methanol (low complexity) and MDM (high complexity), which have a similar critical temperature.

methanol and benzene. A different situation occurs for the more complex fluid (MDM); since the cycle is not recuperative,⁸ the cycle efficiency is quite poor. Even if the temperature differences in the primary heat exchanger are lower than for methanol, the high losses related to the high temperature at the turbine outlet are more relevant and penalize the cycle performance.

It is of interest to point out that in the example considered, the different cycles: (1) saturated cycle with benzene, (2) superheated cycle with methanol, and (3) saturated cycle with methanol yield very similar results in terms of generated electricity. The choice among these cases cannot be based on simple thermodynamic analysis, as performed here, but should be obtained by more sophisticated methods, which account for realistic components' performance and cost, as discussed in Chapter 7 of this volume.

1.6 Criteria for the selection of the working fluid

As already discussed, the possibility of selecting the proper working fluid is the most important degree of freedom in ORC design. As shown in the following Table 1.1, which summarizes the characteristics of a large number of candidate working fluids, the choice is quite wide. The choice is even larger, if the search includes fluid mixtures.

The choice of fluid affects the thermodynamic cycle, the performance and cost of components (expander and heat exchangers), the plant layout, the safety requirements, etc. This circumstance was recognized by the refrigerating and air-conditioning industry much earlier than by the power sector; indeed, most of the requirements are the same for the three sectors.

1.6.1 General requirements shared with the refrigerating and air-conditioning industry

Some of the following requirements are obvious. The working fluid should be:

- *commercially available at a reasonable specific cost.* This aspect becomes particularly relevant for large size plants; a typical example is represented by multiMW geothermal plants, where a large working fluid inventory is required and the working fluid cost represents a significant share of the total plant investment cost
- *nonflammable.* Hydrocarbons, which are flammable working fluids, are often adopted, but they bring about relevant complications and additional costs
- *nontoxic:* again, a toxic working fluid (say, ammonia) is sometimes adopted, but has obvious disadvantages
- *compatible with materials* (lubricating oils, elastomers, metals etc.)
- *environmental benign.* Two main indexes account for the fluid acceptance:
 - Ozone Depletion Potential (ODP): is defined as the ratio of global loss of ozone due to given substances over the global loss of ozone due to the release of the same mass of CFC-11.

⁸ The recuperator would not improve the overall situation, since the heat it could recover is “free” anyway, being provided by the variable temperature heat source, that in presence of the recuperator, would waste a fraction of its heat.

Table 1.1 List of organic working fluids available in Refprop Database

	fluid	chemical formula	MDM	natoms	T_{crit} , °C	p_{crit} , bar	T_{min} , °C	T_{max} , °C	p_{max} , bar	H	F	I	GWP
Linear alkanes	propane	$CH_3-CH_2-CH_3$	44.10	11	96.7	42.5	-188	376.9	10000	1	4	0	4-6
	iso-butane	$(CH_3)_2-CH-CH_3$	58.12	14	135	36.3	-159	301.9	350	1	4	0	
	butane	$CH_3-(CH_2)_2-CH_3$	58.12	14	152	38	-138	301.9	690	1	4	0	
	neo-pentane	$(CH_3)_3-C-CH_3$	72.15	17	161	32	-16.6	276.9	2000	1	4	0	
	iso-pentane	$(CH_3)_2-CH-CH_2-CH_3$	72.15	17	187	33.8	-161	226.9	10000	1	4	0	
	pentane	$CH_3-(CH_2)_3-CH_3$	72.15	17	197	33.7	-130	326.9	1000	1	4	0	
	iso-hexane	$(CH_3)_2-CH-(CH_2)_2-CH_3$	86.18	20	225	30.4	-154	276.9	10000	2	3	0	
	hexane	$CH_3-(CH_2)_4-CH_3$	86.18	20	235	30.3	-95.3	326.9	1000	2	4	0	
	heptane	$CH_3-(CH_2)_5-CH_3$	100.20	23	267	27.4	-90.6	326.9	1000	1	3	0	
	octane	$CH_3-(CH_2)_6-CH_3$	114.23	26	296	25	-56.8	326.9	1000	1	3	0	
	nonane	$CH_3-(CH_2)_7-CH_3$	128.26	29	321	22.8	-53.5	326.9	8000	1	3	0	
	decane	$CH_3-(CH_2)_8-CH_3$	142.28	32	345	21	-29.7	401.9	8000	1	2	0	
	dodecane	$CH_3-(CH_2)_{10}-CH_3$	170.33	38	385	18.2	-9.55	426.9	7000	1	2	0	
Cyclo alkanes	cyclo-pentane	cycle $(CH_2)_5$	70.13	15	239	45.7	-93.4	326.9	2000	1	3	0	
	cyclo-hexane	cycle $(CH_2)_6$	84.16	18	280	40.8	6.32	426.9	800	1	3	0	
	methyl-cyclo-hexane	cycle $(CH_2)_6-CH_3$	98.19	21	299	34.7	-126	326.9	5000	1	3	0	
	n-propyl-cyclo-hexane	cycle $(CH_2)_6-CH_2-CH_2-CH_3$	126.24	27	358	28.6	-95	376.9	500	1	3	0	
Alkene and alkynes	1-butene	$CH_3-CH=CH-CH_3$	56.11	12	145	40.1	-141	276.9	500	1	4	0	
	2-methyl-1-propene	$CH_3-C(CH_3)=CH_2$	56.11	12	146	40.1	-185	251.9	700	1	4	0	
	trans-2-butene	$CH_3-CH=CH-CH_3$	56.11	12	155	40.3	-106	251.9	500	1	4	0	
	cis-2-butene	$CH_3-CH=CH-CH_3$	56.11	12	163	42.3	-139	251.9	500	1	4	0	
	benzene	cycle $=CH-$	78.11	12	289	49.1	5.55	476.9	5000	2	3	0	
	methyl-benzene	cycle $=CH-CH_3$	92.14	15	319	41.3	-95.2	426.9	5000	2	3	0	
Alcohols and ketons	dimethyl ether	CH_3-O-CH_3	46.07	9	127	53.4	131.7	525	400	1	4	1	
	acetone	$(CH_3)_2-C=O$	58.08	10	235	47	178.5	550	7000	1	3	0	
	methanol	CH_3-OH	32.04	6	240	82.2	175.6	620	8000	1	3	0	
	ethanol	CH_3-CH_2-OH	46.07	11	242	62.7	250	650	2800	1	3	0	
Refrigerant fluids	R125	CF_3-CHF_2	120.02	8	66	36.2	172.5	500	600	1	0	0	3500
	R218 (perfluoro propane)	$CF_3-CF_2-CF_3$	188.02	11	71.9	26.4	125.5	440	200	1	0	0	8830
	R143a	CF_3-CH_3	84.04	8	72.7	37.6	161.3	650	1000	1	4	0	4470
	R32	CH_2F_2	52.02	5	78.1	57.8	136.3	435	700	1	4	1	675
	R1234yf	$CH_2=CH-CF_3$	114.04	9	94.7	33.8	220	410	300	1	4	0	4
	R134a	CF_3-CH_2F	102.03	8	101	40.6	169.9	455	700	1	0	1	1430
	R227ea	$CF_3-CH_2F-CF_3$	170.03	11	102	29.3	146.4	475	600	1	0	1	3220
	R161	CFH_2-CH_3	48.06	8	102	50.1	130	400	500	1	4	0	12
	R1234ze	$CHF=CH-CF_3$	114.04	9	109	36.3	168.6	420	200	1	4	0	
	perfluoro butane	$CF_3-(CF_2)_2-CF_3$	238.03	14	113	23.2	189	500	300	1	0	0	
	R152a	CHF_2-CH_3	66.05	8	113	45.2	154.6	500	600	1	4	1	124
	perfluoro cycle propane	cycle $-(CF_2)_3-$	200.04	12	115	27.8	233.4	623	600	2	0	0	10300
	R236fa	$CF_3-CH_2-CF_3$	152.04	11	125	32	179.5	500	400	1	0	0	9810
	R236ea	$CF_3-CF_2-CHF_2$	152.04	11	139	34.2	242	500	600	1	0	0	9810
	R245fa	$CF_3-CH_2-CHF_2$	134.05	11	154	36.5	171.1	440	2000	2	1	0	1030
	R1233zd	$CF_3-CH=CHCl$	130.50	9	166.45	36.237	-78	276.85	1000	2	0	0	1
	R365mfc	$CF_3-CH_2-CH_2-CHF_2$	148.07	14	187	32.7	239	500	350	0	4	1	794
siloxanes	MDM	$C_8H_{18}OSi_2$	162.38	27	246	19.4	273	673	300	1	4	0	
	MDM	$C_8H_{18}O_2Si_3$	236.53	37	291	14.2	187.2	673	300	1	3	1	
	D4	$C_8H_{18}O_2Si_4$	296.62	40	313	13.3	300	673	300	1	2	0	
	MD2M	$C_{10}H_{20}O_2Si_4$	310.69	47	326	12.3	205.2	673	300	1	2	1	
	D5	$C_{10}H_{20}O_2Si_5$	370.77	50	346	11.6	300	673	300	1	2	0	
	MD3M	$C_{12}H_{26}O_2Si_5$	384.84	57	355	9.45	192	673	300	1	1	0	
	D6	$C_{12}H_{26}O_2Si_6$	444.92	60	373	9.61	270.2	673	300	1	2	0	
	MD4M	$C_{14}H_{34}O_2Si_6$	458.99	67	380	8.77	300	673	300	1	1	0	
	ammonia	NH_3	17.03	4	132	113	-77.7	426.9	10000	3	1	0	
	water	H_2O	18.02	3	374	221	0.01	1727	10000	0	0	0	

For each fluid, the following are reported: (1) the main fluid properties (MDM, natoms, T_{crit} , and p_{crit}), (2) their thermodynamic limits (T_{min} , T_{max} , and p_{max}) due to thermal stability and availability of experimental data, and (3) safety information according to NFPA classification (H, Health; F, Flammability; I, Instability; each index range from 0-no hazard to 4-maximum hazard) and (iv) Global Warming Potential (GWP) index.

- Global Warming Potential (GWP): it compares the amount of heat trapped by a certain mass of the gas in question to the amount of heat trapped by an equal mass of carbon dioxide.

Actually, it is practically impossible to satisfy all these requirements with an organic fluid suitable for ORC applications. The refrigerating and air-conditioning industry adopted for many decades CFC (chloro-fluoro-carbons), known as “freons” which were ideal for many aspects (not flammable, not toxic, low cost, and good thermodynamic characteristics), but were progressively banned because of their large ODP. For this reason, CFCs are not listed in the table. Afterward, a new family of refrigerants was developed, known as Hydro Fluoro Carbons (HFCs), nonozone-depleting, nonflammable, recyclable, and of low toxicity. They are used worldwide, but nowadays, new legislations are asking for GWP much lower than those exhibited by HFCs. So the problem is still unsolved and in most cases, the ORC manufacturers must renounce to some of the qualities listed above. More information about working fluid selection process is reported in Chapter 7.

1.6.2 A specific requirement for Organic Rankine Cycles: thermal stability

Differently from the air conditioning and refrigerating industry, which operate at low temperatures, most ORC applications require the working fluid to withstand relatively high temperatures in cyclic conditions. The issue of thermal stability, as well as compatibility with high temperature metals, becomes therefore of utmost importance. For this reason, Chapter 5 of this volume is dedicated to this topic.

1.6.3 Requirements on thermodynamic properties to be optimized

From a thermodynamic point of view, the ideal working fluid for ORC should have:

- *suitable critical parameters (temperature, and pressure)* for the application. For example, for saturated cycles, the critical temperature should be high enough to permit evaporation at a proper temperature, but low enough to obtain condensing pressures higher than the atmospheric one, or proper turbine size, etc.
- *suitable molecular complexity (number of atoms per molecule) for the application*: The number of atoms per molecule influences:
 - the “shape” of the Andrews curve and consequently the power cycle. In particular, a complex molecules causes:
 - “dry” expansion (a positive effect)
 - large fractions of heat input at variable temperature (a positive effect for variable temperature heat sources)
 - small temperature drops in the expansion phase (a negative effect)
 - the requirement of a large recuperator (a negative effect for investment cost)
- *suitable molecular mass*: large molecular mass is beneficial for the turbine design, since the molecular mass is inversely proportional to the turbine enthalpy drop, thus heavy molecules require lower number of stages and/or lower peripheral speeds and mechanical stresses. On the contrary, high molecular mass has a negative effect on heat transfer coefficients, thus on the size and cost of heat exchangers.

History of Organic Rankine Cycle systems

2

L.Y. Bronicki
ORMAT co-founder

2.1 Introduction

The history of the Organic Rankine Cycle (ORC) development spreads from the early 19th century until the ORC power systems became a substantial niche market in the 21st century power industry. The ORC history is intertwined with the empirical development of steam engines. Carnot's attempt to understand the empirical development led to the foundation of thermodynamics; however, the disconnect between the theory and the practice continued for many decades. The focus of this chapter will be on those ORC developments that were original and led to sustainable commercialization, or at least to meaningful demonstrations. As for the other examples of ORC systems or cycle variations they may be found in very comprehensive studies by [Colonna et al. \(2015\)](#), [Angelino et al. \(1984\)](#), [J.R. Owen \(1975\)](#), and the detailed references included therein.

2.2 Learning by doing: from steam engine to thermodynamics

The history of ORC systems is quite long, starting in the first half of the 19th century, about 100 years after the invention of the steam engine. Its progress overlaps the formative period of the development of thermodynamics, as Cardwell states in his book *From Watt to Clausius* ([Cardwell, 1971](#)):

The major topics of nineteenth-century physics were energy, thermodynamics and field theory...the second of these three, thermodynamics, originated substantially (but not of course wholly) in the power technologies of the eighteenth and early nineteenth centuries—...the men who created thermodynamics used the ordinary thought processes common to all men of science; and the materials they worked with and the problems they faced were all derived from the scientific and technological advances of the time. Thermodynamics was formulated in response to the intellectual challenges that were posed by the rapid improvements made in the heat engines and the accompanying advances in the science of heat that took place between about 1790 and 1865, one of whose root causes was the rapid progress made in power technology during this period ever since Newcomen's first engine of 1712 and Watt's invention of 1765.

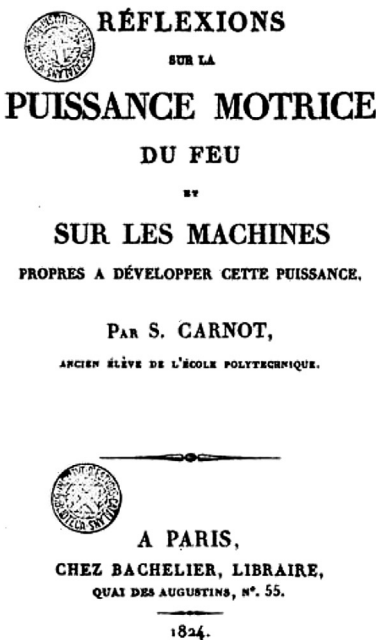
In his treatise, published in 1824, Sadi Carnot already suggested to use other substances as substitutes for water. He recognized several promising directions in the

practical development of heat engines, which, if given the attention they deserved when published, could have brought much sooner the development of ORC systems, internal combustion systems, and combined cycles.

For Carnot, the analysis of a power system cannot be limited to the vapor pressure, or even to the thermal efficiency (called by Carnot “the economy of the combustible”). The concluding paragraph of his famous treatise makes this so clear and so relevant today that it deserves quotation in full (Fig. 2.1):

The economy of the combustible is only one of the conditions to be fulfilled in heat engines. In many cases it is only secondary. It should often give precedence to safety, to strength, to the durability of the engine, to the small space which it must occupy, to small cost of installation, etc. To know how to appreciate in each case, at their true value, the consideration of convenience and economy which may present themselves; to know how to discern the more important of those which are only accessories to balance them properly against each other, in order to attain the best results by the simplest means: such should be the leading characteristics of the man called to direct, to co-operate towards one useful end, of whatsoever sort it may be.

Sadi Carnot Reflections on the Motive Power of Fire, Paris 1824, (Carnot, 1826)



‘On ne doit pas se flatter de mettre jamais à profit, dans la pratique, toute la puissance motrice des combustibles. Les tentatives que l’on ferait pour approcher de ce résultat seraient même plus nuisibles qu’utiles, si elles faisaient négliger d’autres considérations importantes. L’économie du combustible n’est qu’une des conditions à remplir par les machines à feu ; dans beaucoup de circonstances, elle n’est que secondaire, elle doit souvent céder le pas à la sûreté, à la solidité, à la durée de la machine, au peu de place qu’il faut lui faire occuper, au peu de frais de son établissement, etc. Savoir apprécier, dans chaque cas, à leur juste valeur, les considérations de convenance et d’économie qui peuvent se présenter, savoir discerner les plus importantes de celles qui sont seulement accessoires, les balancer toutes convenablement entre elles, afin de parvenir par les moyens les plus faciles au meilleur résultat, tel doit être le principal talent de l’homme appelé à diriger, à coordonner entre eux les travaux de ses semblables, à les faire concourir vers un but utile de quelque genre qu’il soit.’

Figure 2.1 Carnot concluding remarks, 1824.

Carnot's book was forgotten until Clapeyron, drew attention to it in 1834, and in 1850 Clausius used those of Carnot's ideas selected by Clapeyron in defining entropy and formulating the Second Law of Thermodynamics.

Perhaps one of the truest indicators of Carnot's greatness is the skill with which he abstracted, from the highly complicated mechanical contrivance that was the steam engine (even as early as 1824), the essentials, and the essentials alone, of his argument. Nothing unnecessary is included and nothing essential is missed. It is, in fact, very difficult to think of a more efficient piece of abstraction in the history of science since Galileo taught men the basis of the procedure. Carnot's practical engineering ideas were neglected, leading to a "divorce" between practice and theory. Power system practice and thermodynamics developed separately for half a century.

It is not difficult to understand why *Réflexions* was a failure. To the engineer, the postulation of the ideal engine and the reversible cycle must have seemed closer to the more imaginative passages in the Greek poetry than to the needs of power engineering. Poncelet and others had advised French engineers to keep practical requirements always in mind and to avoid being too abstract and theoretical. There was always the example of the Cornish engines, whose extremely high standards of performance had been achieved by careful attention to details and whose designers seemed to have made little use of abstract theory. In fact, Carnot had very little to teach the engineers of his time; the superiority of the high-pressure condensing steam engine had been established, so had the advantages of expansive operation, and by 1824 engineers knew well enough that, all things considered, there was no better working substance than steam. We must conclude that Carnot's message was essentially for engineers of a later generation with the resources of a more advanced technology (Carnot, 1826). Technology of steam turbines and internal combustion engines converged with the science of thermodynamics only at the end of the 19th century; ORC systems had to wait till the 1930s.

2.3 From steam engine to ORC, progress based on practical engineering and not on theory

The early 19th century was a period of intense development of the steam reciprocating engines. Developments of ORC systems were based on existing steam reciprocating engines. The use of alternative fluids can be traced back to the pressure limitations of the boilers at that time, which limited top cycle temperatures so that the criteria for choice of nonaqueous fluids were mainly based on vapor pressure considerations. The difficulty to achieve acceptable condenser vacuum, due to inadequate sealing techniques, resulted in comparatively high heat sink temperatures. Utilizing the heat rejected in the condensation process is where use of organic working fluids has its origin. Davy (Wilson and Radwan, 1977) suggested to employ liquids that could be vaporized at a low temperature in a boiler heated by the condensate and use the vapor produced in another engine. In 1829 Ainger (Ainger, 1830) suggested cascading cycles of different boiling point liquids—the boiler for each liquid serving as the

condenser for the fluid next higher in the series, with external heat supply being required only for vaporizing the highest boiling point liquid. The first commercial application of significance of an organic fluid was the 1853 Du Trembley system of combined vapors (Jameson, 1858; Guthrie, 1970) applied to ship propulsion and employing ether as the secondary fluid that was vaporized by condensing steam. Whilst there was an improvement in thermal efficiency, leakage of ether was a continuous problem and interest in the scheme waned after the loss by fire of one of the several vessels fitted with the system. A further practical application to marine propulsion toward the end of the 19th century was the “Zephyr” system for small launches developed by Yarrow in about 1888 concomitant with similar launches by Escher Wyss and in particular an ingenious patented system by Ofeldt (Thurston, 1902); the relation between the three is not known. Naphtha (petrol) was employed as both the working fluid, the lubricant, and the fuel. The system demonstrated quick starting, fewer manpower requirements, and lower machinery weight than comparable steam engines. The fact that it did not use steam enabled the launches to evade the regulations requiring a qualified engineer as the operator. This may have been one of the reasons for their commercial success; they sold by the hundreds up to around 1900 when the internal combustion engine began to be reliable and lighter. The system is shown in Fig. 2.2:

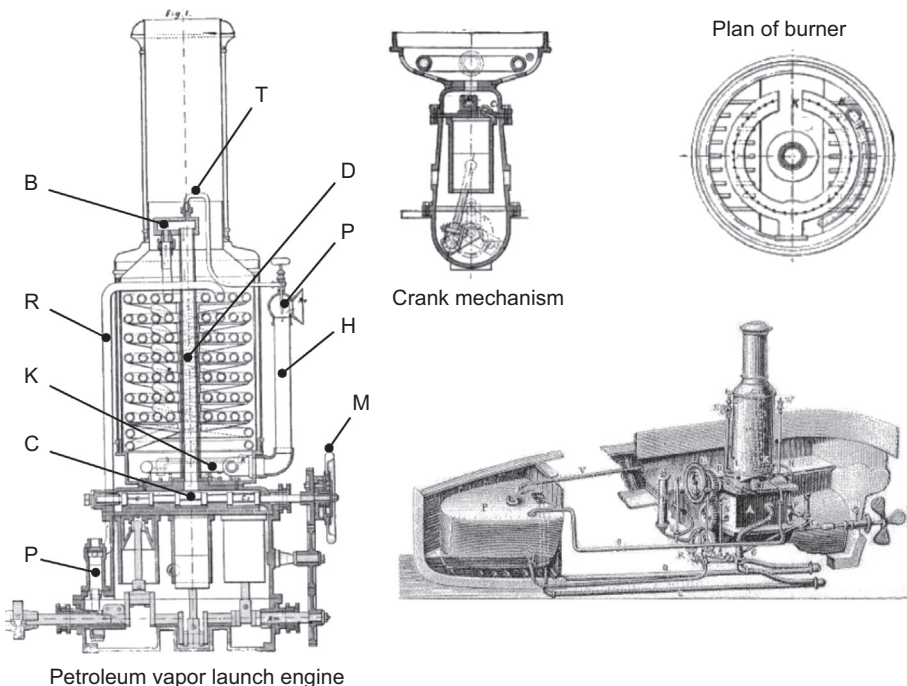


Figure 2.2 Escher Wyss – Ofeldt petrol launch, 1880.

Petrol is pushed into the helical tube boiler by pump P, through pipe R. When vaporized, it enters B, where most of it descends through pipe D to the engine valve chest. The valves C were driven by the three gears external to the engine; the wheel M controlled the valves to allow forward and reverse running. A portion of the vapor is diverted from B through tube T at the top, and is squirted through injector P, entraining air from the condenser and driving the petrol/air mixture down pipe H to the ring burner K, which heats the boiler tubes.

The exhaust petrol vapor, on leaving the engine, was condensed in “tubes outside the launch” that were under water, and returned to the tank in the bows. Condensation did not create a vacuum, and the back pressure on the engine pushed the condensed petrol forward and up into the bow tank.

The boiler pressure varied between 14 and 70 psi (100 and 480 Pa), regulated by the burner control valve attached to injector P. There was no throttle between boiler and engine. Petrol consumption was said to be between 17 and 20 pints (8 and 9.5 L) per hour, generating 6 horsepower (around 4.5 kW) at 233 rpm, which corresponds to a thermal efficiency of 4.6–5.4%. The launch would carry two people at about 5.5 knots. The petrol acted as lubricant as well as working fluid.

Frank W. Ofeldt not only developed the petrol launch but also built the Alco Vapor power plant for launches. The fluid was a mixture of water and alcohol. The evidence is contradictory as to whether “alcohol” in this context means “ethanol” or “methanol.”

The design was similar to the naphtha launches, but the ingenious principle of using the fuel as the working fluid and burning only the losses from the condenser air ejector was abandoned. See [Fig. 2.3](#) for the basic layout of the alco-vapor launch from Ofeldt's US patent No. 551,226.

Other alternative working fluids considered included ether, chloroform, ammonia, carbon disulfide, and sulfur dioxide. However, rapid improvements in the design and construction of engines and of high steam pressure (i.e., temperature) were a trend of this period, and this together with the emergence of the steam turbine with its ability to overcome the expansion limitations of the steam engine effectively curtailed the development of nonaqueous working fluid Rankine cycle systems using fuels for the time being.

For half a century there were few applications of ORC, all using solar energy rather than fossil fuels. In 1904 Willsie built two solar ORC engines using sulfur dioxide. One was a 6-horsepower (4.5 kW) installation in St. Louis, Missouri, and the other a 15-horsepower (11 kW) system in Needles, California. In 1907 F. Shuman, built a solar ORC engine, using a flat solar collector of 110 m² to boil ether at temperatures around 80°C and drive a 3.5 HP (2.6 kW) engine.

In the 1940s a 1 HP (0.75 kW) solar ORC system driving a water pump was “mass produced” and commercialized by the Italian company Somor ([Fig. 2.4](#)). Based on a clever design of Daniel Gasperini and Ferruccio Grassi, the system used a refrigeration piston compressor. The fluid was sulfur dioxide (a common refrigerant at the time) and included also an ingenious heliostat driven directly by a transmission from the engine assuring an angular velocity of slightly above 15 deg./hour. When the collector came out of focus the speed of the engine would slow, bringing the

collector back in focus. Tens of units were manufactured in Lecco, Italy, and sold. This was the first modern commercial ORC unit.

2.4 Rebirth of the ORC: integrating thermodynamics and system design

2.4.1 *University of Naples*

The first to employ an organic fluid in a real turbine system was Prof. [Luigi D'Amelio \(1935\)](#), who was also the first to consider the advantages of high molecular mass fluids to reduce the RPM and number of turbine stages rather than focus on vapor pressure only. D'Amelio undertook experiments using ethyl chloride at the University of Naples in the 1930s. D'Amelio's work led to a small solar-driven pump in 1935. Later, in the 1940s, D'Amelio designed a geothermal plant at Citara, Ischia Island, using ethylene as a working fluid. The plant operated for a few years and was decommissioned in the early 1950s. Apart from a publication at a solar energy conference in 1958, where the turbomachinery advantages of heavy molecular mass fluids were presented ([Fig. 2.5](#)), little notice seems to have been taken of this work at the time. Although in the 1930s others proposed the use of organic fluids such as diphenyl and diphenyl oxide for use in topping cycle steam plants, for reasons based only on vapor pressure considerations, there is no information on any such system ever built ([Dow, 1926](#); [Findlay, 1934](#)).

2.4.2 *National Physical Laboratory of Israel*

Between 1958 and 1961 clear criteria for selection of motive fluids were developed at the National Physical Laboratory of Israel in Jerusalem, in the framework of a small engine project, as part of a program to harness solar energy initiated in 1955.

Following D'Amelio's consideration of molecular mass (in addition to vapor pressure), careful attention was paid by Tabor and Bronicki to other fluid properties. The analysis of the losses, which drastically reduced the efficiency, as compared to Carnot efficiency in small engines, led to the conclusion that a turbine was preferable to a piston engine because of the efficiency. The physical properties of the fluid were chosen according to criteria that depend on the characteristics of the heat source and heat sink, as well as on the power output ([Tabor and Bronicki, 1961, 1964](#)). Unfortunately, in the 1950s detailed properties of fluids were available for a limited number of fluids only. For most of the fluids only sparse data was available. What was available were methods to calculate the properties over a range of conditions from a few data points ([Reid and Sherwood, 1958](#)). Doing that, including calculating thermodynamic diagrams, was very time consuming, but it was found that most of the properties could be related to information readily available, i.e., (1) boiling point (from which it was possible to calculate the pressure temperature relationship); (2) molecular mass (for calculating enthalpy and efflux velocity); (3) number of atoms in the molecule, which controls the wetness (below 10 atoms in the molecule) or dryness (above 10) of the

isotropic expansion; and (4) thermal and chemical stability. This enabled a quick selection of candidate fluids before undertaking long calculations of their properties. In addition, a practical working fluid has to be stable and noncorrosive under prolonged heating in contact with conventional materials. Fluids that were known to be unstable were rejected, but many fluids had to be tested because of lack of information for the conditions considered (150°C). Freons, for which all properties were well established, did not pass these tests at 150°C. Condition (3) was very important

Ing. Prof. LUIGI d'AMELIO
*Incaricato dell'insegnamento di Macchine termiche e idrauliche
 nel R. Istituto Superiore d'Ingegneria di Napoli*

234

LO SFRUTTAMENTO DELLE ENERGIE NATURALI IN LIBIA PER FORZA MOTRICE

L'IMPIEGO DI VAPORI AD ALTO PESO MOLECOLARE IN PICCOLE TURBINE

E L'UTILIZZAZIONE DEL CALORE SOLARE PER ENERGIA MOTRICE

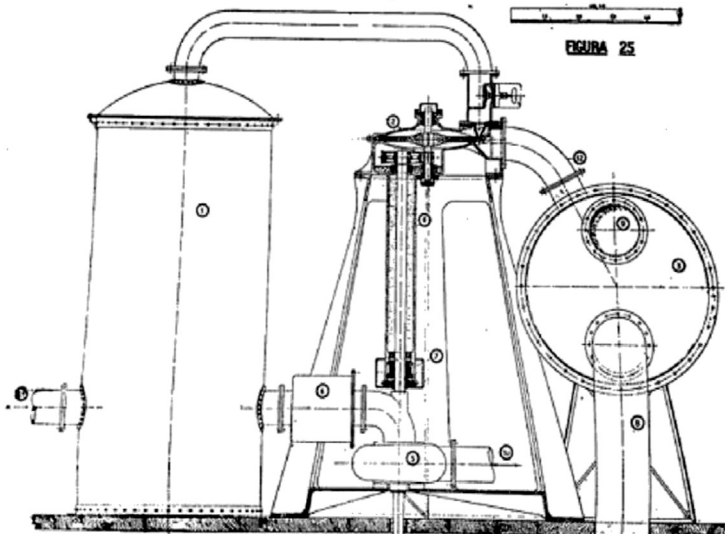


Figure 2.5 D'Amelio solar turbine, 1934.

June 26, 1962

H. Z. Tabor et al
Vapor turbines

3,040,528

Filed March 21, 1960

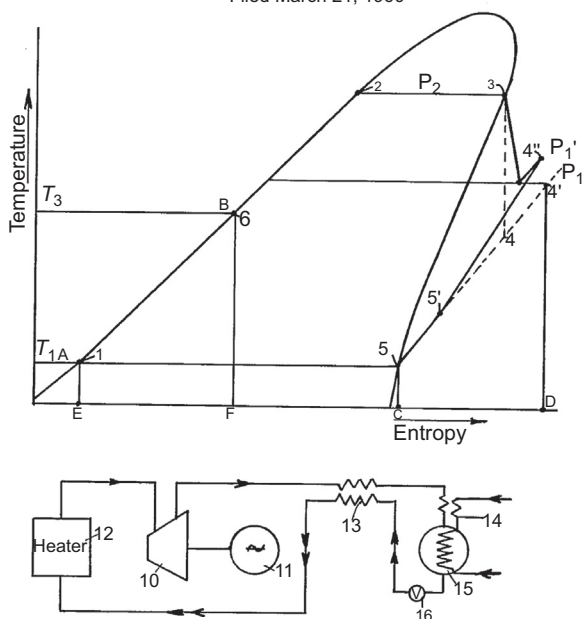


Figure 2.6 Recuperated Rankine cycle, 1961.

because when high molecular mass was desired, it is most often associated with large molecules leading to dry expansion. This superheat avoids blade erosion but leads to high irreversibility loss. A new Rankine cycle (Tabor and Bronicki, 1961) was introduced (Fig. 2.6), using a recuperator, which improved the cycle efficiency in such a manner that the result is largely independent of the fluid used, in addition to “correcting” the shape of the T-S diagram. The recuperator feedback also recoups part of the internal heat losses.

A 3 kW turbine was designed and built using mono-chlorobenzene. The turbine was part of a complete solar plant including solar collectors and heat storage and was demonstrated in 1961 at the UN Conference on New Energy Sources in Rome (Fig. 2.7) (Tabor and Bronicki, 1961).

This work led to the establishment of Ormat (discussed later in more detail).

2.4.3 Politecnico di Milano

The Italian activity in the field of ORCs started in the 1970s at Politecnico di Milano, under the scientific guidance of Prof. G. Angelino (1984). He led a team of scientists, including Ennio Macchi and Mario Gaia, studying the possibility of using organic fluids instead of water to power the Rankine cycle, initially for automotive, space, and solar applications.



Figure 2.7 3 kW turbogenerator with solar collectors, heat storage, and standby boiler, 1961.

The realization of the first prototypes was carried out by Gemmindustria (Milano), a mechanical shop belonging to Mario Gaia's family.

The first turbine (1976) had an output of 4 kW; heat source hot water (90–70°C) heat sink: cold water (15–25°C), working fluid: perchloroethylene in a saturated cycle.

This was the proof that it is possible to design a high-efficiency, low-mechanical stress turbine, even at very low power output.

A medium temperature ORC followed in 1978, with an output of 35 kW, the heat source was thermal oil (280°C) from a parabolic trough, cold sink: water (25–32°C), working fluid: Flutec PP3 (C8F16) in recuperated cycle. This unit was operated in Australia.

Among the configurations designed in the period 1976–80, there was also an original radial outflow turbine, using perfluorodecaline as working fluid (Fig. 2.8).

These efforts led to the establishment in 1980 of Turboden, by Mario Gaia, while Angelino and Macchi continued supporting Turboden with scientific research. Later Angelino and Invernizzi (1993) identified and tested a family of cyclic polymethylsiloxanes, which are fully nontoxic, moderately flammable, and stable up to 400°C operating temperatures.

A more recent cooperation between Turboden and Politecnico di Milano produced a 500 kW prototype, developed for ENEL, based on a supercritical cycle (working fluid R134a). The real geothermal application would be on a much larger scale (5–10 MW). See more details about Turboden later in the chapter.

2.4.4 Lappeenranta University of Technology

From the early 1980s, Professor Jaakko Larjola led the development of high-speed hermetic sealed (Larjola, 1984) turbogenerators in the hundreds of kW range, in which the



Figure 2.8 Prof. Mario Gaia's technology assessment for a radial outflow turbine working with perfluorodecaline, 1980.

turbine, generator, and pump share the same shaft supported by motive fluid bearings (Fig. 2.9).

The first complete 100 kW ORC system using R114 was operated and tested during 1983–85, with operating speed 30,000 rpm, 66 mm tilting pad bearings lubricated by the working fluid vapor (Fig. 2.10).

A second prototype was installed in industry, and was using waste heat; it was similar to the first prototype, but bearings were tilting pad bearings lubricated with liquid working fluid, and output 75 kW. It was made and tested during 1986–89.

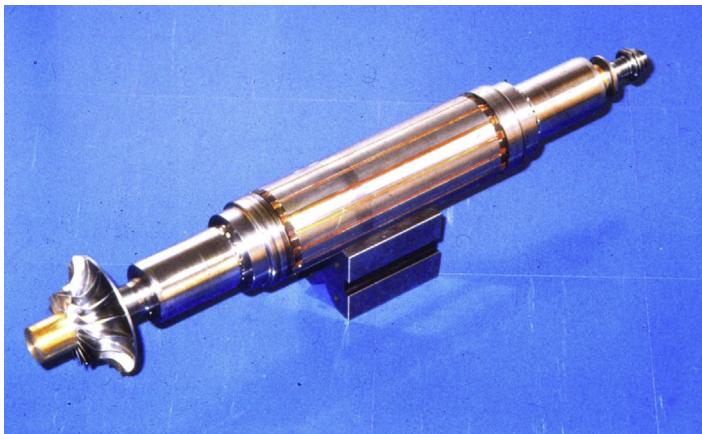


Figure 2.9 Inflow radial turbine with generator and feed pump, 1984.



Figure 2.10 Complete 100 kW ORC, 1984.

A third prototype was a 25 kW hermetic ORC made in 1990 for subsea operation, to load batteries in a research submarine (Jokinen et al., 1998). The knowledge acquired in these developments was later utilized in commercial units that were marketed starting from the early 2000s by Tri-O-Gen Company in the Netherlands (Larjola, 1988).

2.4.5 Various demonstration units

In the 1960s, development of a solar space system began in the United States by Aerojet General, Rockeddyne, General Electric (GE), and Sundstrand Aviation Corp. Sundstrand developed a 600 kW plant using waste heat from two 6600 kW diesel generating sets (Parsad, 1980). The fluid used was toluene. Four such plants were built; one plant operated for 8000 h and produced 4,000,000 kWh. Later Mechanical Technology Inc. built a 600 kW hermetically sealed unit that operated for some time in Torrance, California (Sternlicht, 1984).

Several other organizations in the United States have developed ORC systems funded by various government agencies, and some of these for automotive applications as a consequence of the 1970 Clean Air Act, which prompted the development of alternative prime movers to the automotive internal combustion engine. General Motors experimented with an organic reciprocating engine in 1954 although the work was not reported until 10 years later.

Thermo Electron Corporation developed an ORC System using FL-85, 85% tri-fluorethanol, as motive fluid. One application was the recovery of heat from diesel engine exhausts on a Mack truck. This truck with the ORC has been operated on the highway for over 25,000 miles and the ORC improved the truck fuel economy by more than 15% (Schad, 1981).

In 1975 Barber-Nichols built a 1 kW ORC using Freon 113 coupled to flat plate collectors that provided heat at 91°C. Later, in 1985, he built a geothermal plant of two 700 kW units (Fig. 2.11) using evaporative condensers cooling and a turbine of



Figure 2.11 Barber-Nichols 700 kW units, 1985.

his design and manufacture in Susanville. As of 2015 the plant is still in operation (Prigmore and Barber, 1974).

In the mid-1970s, GE built a 3 kW ORC fuel fired unit for Mobile Homes. It used a refrigeration compressor as an expander and other refrigeration hardware. The project never made it beyond laboratory tests and was abandoned.

In the United Kingdom, studies of ORC were started in about 1955. A 150 HP (110 kW) demonstration system was built and tested by Clarke Chapman and Co. (Owen, 1975) before developments were abandoned.

In 1979 the French company Bertin built a 50 kW solar ORC in Mexico using FC75, and in 1990 a 2.5 MW water cooled plant in Indonesia using N-pentane (Copeau, 1979).

In 1980 a 5 MW plant was built at Raft River, Idaho, using 143°C brine. The plant was decommissioned because of turbine failures and overall underperformance of the plant (DiPippo, 2012).

In 1982 Fluor Engineers built a plant of nominal 70 MW gross in Heber, California, using a single turbine and a mixture of isobutane with 10% isopentane. The inlet brine temperature was 182°C, water cooled. The parasitic losses, mainly of the fluid pump, were 23.4 MW (33%). Because of numerous mechanical equipment failures, the plant was decommissioned (DiPippo, 2012).

In 1984 the French utility EDF operated a hybrid 20 MW plant consisting of a 15.5 MW steam cycle and a 5 MW anhydrous ammonia bottoming unit (Jeumotte, 1983).

2.4.6 New cycles proposed

Since 1977 Prof. Ian K. Smith has worked on thermodynamics of organic fluids. In 1995, together with his colleague Nikola Stosic at City University in London (Smith, 1972), he developed the trilateral flash cycle (TFC) system (Fig. 2.12).

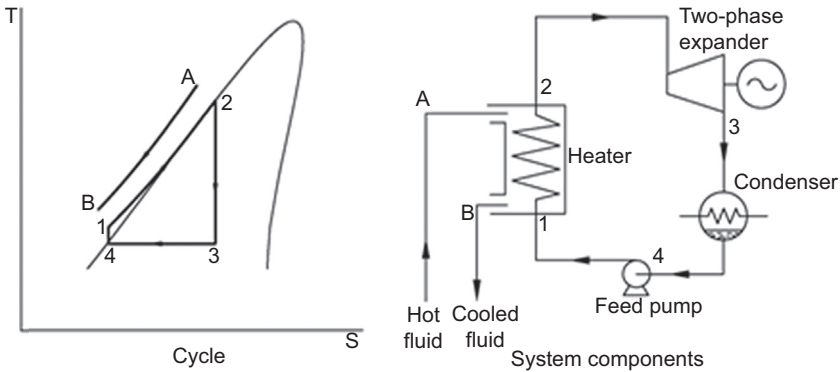


Figure 2.12 Smith triangular cycle, 1995.

This was a binary system based on the expansion of the working fluid from saturated liquid into wet vapor by the use of screw expanders as an alternative to turbines. The unique feature of the screw expander was their specially developed rotor profile, which was based on the mathematical theory of gearing and resulted in nearly pure rolling relative motion and very small contact forces between the male and female rotors (Smith and da Silva, 1994). This enabled the expander to operate without the need for timing gear to avoid rotor contact, while the liquid content of the refrigerant in the working chamber was sufficient to act as the lubricant. In addition, they found that only a minimal amount of lubricating oil was required to be dissolved in the working fluid, which did not affect the thermal properties of the fluid significantly. Some of the cold working fluid leaving the feed pump was directed to the bearings, where frictional heating evaporated the working fluid, leaving oil to build up in the bearing housing to lubricate the bearings. Consequently, the need for internal shaft seals and an external lubrication system was eliminated and the cost of the screw expander was greatly reduced. This system was capable of recovering more power from liquid-dominated brines than an ORC system due to better matching of the cooling of the brine to the heating of the working fluid in the primary heat exchanger. The maximum power that one machine can generate is on the order of 1–3 MW per unit, depending on the type of system and the brine and cooling conditions. These screw expanders were shown to be nearly as efficient as turbines when expanding dry vapor, and they can be coupled directly to a generator without an intermediate gearbox. They have similar characteristics as two-phase expanders when their efficiencies are not significantly reduced. The trilateral flash cycle, with this latter feature, enables improvements to be made in the conversion of heat to power, in order of 30% over conventional ORC systems, from brines (sensible heat) in the 100–140°C temperature range.

In addition to this, they later proposed a combined screw turbine combination, whereby hot hydrocarbons, heated in the liquid phase, are first expanded in a screw expander to an intermediate temperature, followed by separation of the liquid and vapor phases. The vapor is then further expanded in a turbine and the separated liquid

combined with the vapor condensate to preheat the compressed liquid. Using hydrocarbons such as N-pentane and n-pentane, this system was shown to recover power from liquid resources in the 180–200°C temperature range with high efficiency.

Smith and Stosic's screw expander technology (Smith and da Silva, 1994) is implemented under license by ElecraTherm in Carson City, Nevada, in their ORC systems. More details about ElecraTherm appear later in the chapter.

In 1984 Alexander Kalina patented the Kalina cycle for power generation using water-ammonia mixtures as the working fluid (DiPippo, 2004). The major difference from other ORCs is that the working fluid is a binary mixture of water and ammonia; evaporation and condensation occur at variable temperature. Therefore, irreversibility in the heat exchangers is reduced. For sensible heat sources this leads to improved thermodynamic performance, but the plant is more complex than a basic binary plant, and maintaining, as well as controlling, the concentration over the different sections of the plant and load varying over time is challenging. As a result, despite the appealing concept, over the last 30 years very few plants were built and very little is known of their performance.

Energent Corporation developed a Variable Phase Cycle, a triangular cycle similar to the I. K. Smith from which it differs, in that the near-saturation working fluid is expanded through a two-phase nozzle that partially, or fully, vaporizes the working fluid. The resulting two-phase jet is then sent through an axial wheel, some of the flow remains in liquid form, therefore the mass flow rate remains high with a low jet velocity that results in low turbine speed. The work on efficient two-phase expansion was first undertaken at the NASA Jet Propulsion Laboratory for powering long-term unmanned space missions using a radioactive decay heat source. Although this method was ultimately not chosen by NASA for space missions, Energent has built and tested a prototype for geothermal and waste heat recovery (Fig. 2.13).

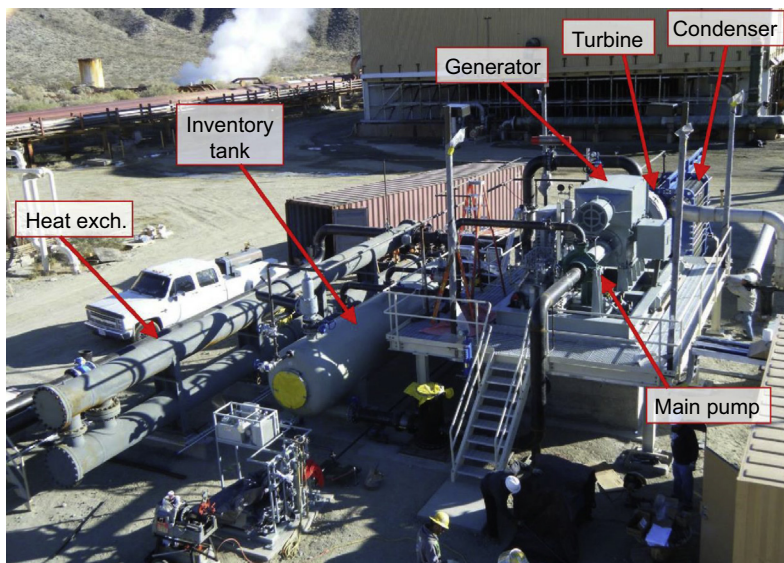


Figure 2.13 Energent 1 MW geothermal plant, 2003.

2.5 Early commercial plants

1. In 1952 at Kiabukawa in Congo, a small 200 kW ORC unit (Fig. 2.14) used water at 91°C from a spring and supplied electric power to a mine for a number of years (DiPippo, 2012).
2. 1966, Ormat 0.6 kW solar turbogenerator (Fig. 2.15) using dichlorobenzene driving an electrical submerged irrigation pump in Mali, Africa.
3. 1967 a 500 kW geothermal plant, using R12, was started in Paratuka, Kamtchatka in the USSR, now Russia (DiPippo, 2012; Gokhshtein et al., 1966),
4. 1979, at the Kashima steel Works, Kawasaki, Japan, completed a 2900 kW ORC system for process heat recovery using Freon 11 (Yamashita, 1979). In another steel mill at Kimitsu, Mitsui and Thermo Electron built an 11.5 MW ORC using Fluorinol 85 (Hirakawa and Suzuki, 1983).
5. 1979, Ormat build a 150 kW solar pond power unit (Fig. 2.16) (see details in paragraph 6.1 on Ormat).
6. 1979, McCabe built a commercial 12.5 MW cascading ORC with two fluids, isopentane and isobutane, in East Mesa, California (Fig. 2.17). The cooling water for the condensers was cooled in evaporation ponds. The plant was designed by J. Hilbert Anderson and used York expanders; it operated for a number of years (DiPippo, 2012).
7. 1982, Ormat installed 15 kW geothermal power unit on a well drilled by CFE (Mexican utility) using Freon 113.
8. 1982, Ormat completed a 5 MW solar pond power plant (Fig. 2.18) (see details in paragraph 6.1 on Ormat), which operated for seven years.

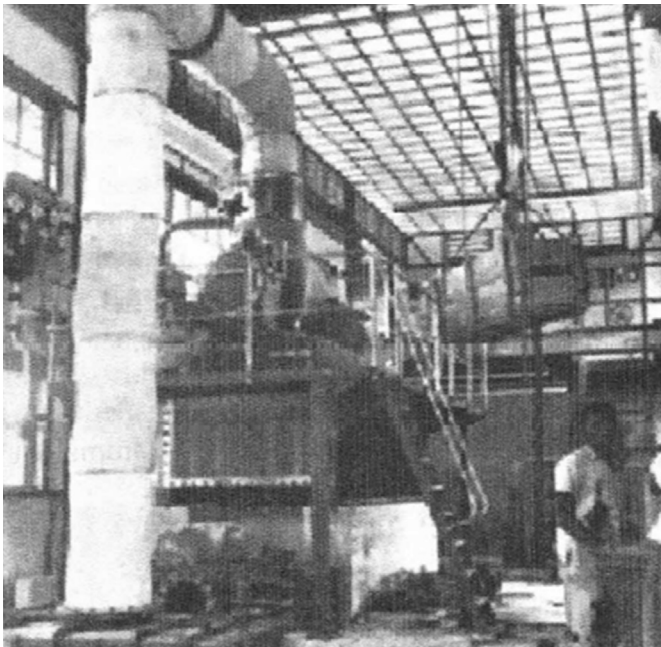


Figure 2.14 Kiabukawa 200 kW unit, 1952.



Figure 2.15 Ormat 0.6 kW solar pump in Mali.

9. 1984, a Turboden 35 kW turbine operating from solar collectors (Figs. 2.19 and 2.20) was installed in Perth Australia (see details in paragraph on Turboden).
10. 1984, Ormat a 600 kW (net) geothermal ORC using Freon 114 and driving an induction generator (Fig. 2.21). The well temperature is 95°C, the cooling water for the condenser is at 10–25°C. As of 2015 the unit is still operating at full power after 31 years of continuous operation.
11. 1984, the Ben Holt Company built an air-cooled plant (Fig. 2.22) with the process designed by Richard Campbell (1989) using Rotoflow radial inflow expanders (Holm, 1981) and isobutane fluid. Power output was 8 MW net from a brine temperature of 165°C and an annual average dry bulb air temperature of 7°C. In 1990 two identical 14 MW net units were added. Combined sales of the three units were more than 40 MW net in the winter. The units operated reliably until they were reconditioned in 2015.



Figure 2.16 The 150 kW solar pond and power unit at the Dead Sea, Israel.



Figure 2.17 McCabe 12.5 MW cascading ORC, 1979.

Ben Holt Company designed another two 15 MW net units at Steamboat near Reno in Nevada.

In the early stages of the Ben Holt Co.'s process design of the Mammoth geothermal binary cycle power plant, the general feeling was that a plant using conventional water cooling would be best. The initial capital cost of a water-cooled plant would have been lower, but a number of factors led to the choice of air-cooled condensers.

A major consideration was the location of the power plant. Mammoth Lakes, California, is a year-round mountain resort area with world-class skiing in the winter. As such, it was important to minimize the visual impact of the plant. Air-cooled condensers with their low



Figure 2.18 The 5 MW solar pond power plant at the Dead Sea, Israel.

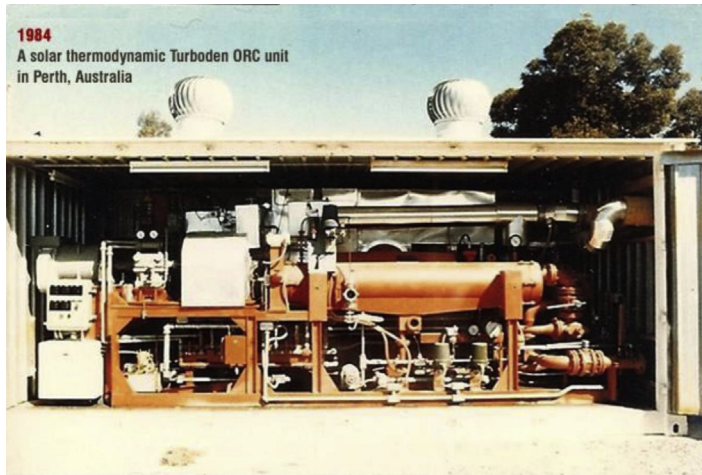


Figure 2.19 35 kW four-stage turbine, operating from solar collectors in Perth, Australia, 1984.

profile have a distinct advantage over a water-cooled plant with a highly visible cooling tower plume. A second concern regarding the cooling tower plume was that the plume could deposit water droplets on the nearby highway, potentially causing icing problems during the winter months.

Another major consideration was that the price of electricity was the same at 3 a.m. on a cold winter night as it was at 3 p.m. on a hot summer afternoon. Because an air-cooled plant can take advantage of low air temperatures—whereas a water-cooled plant must be throttled back to prevent freezing—power production and, therefore, in cases where the power purchase agreement is not peak weighted, the revenue from an air-cooled plant are higher during winter.



Figure 2.20 Concentrating solar collectors providing hot oil to the 35 kW ORC, 1984.

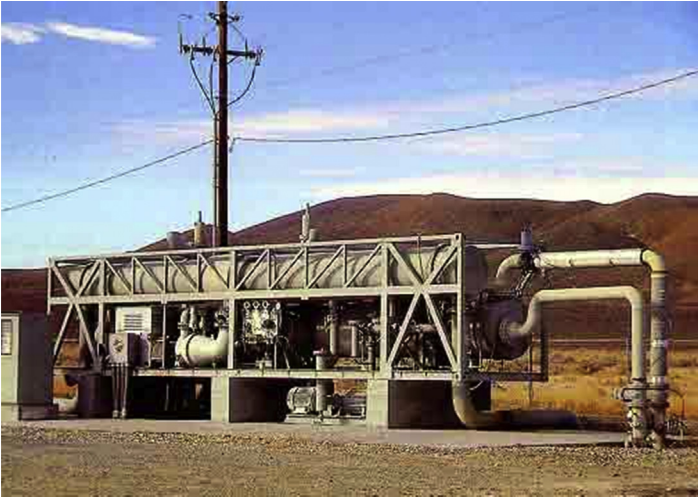


Figure 2.21 600 kW geothermal ORC at Wabuska, Nevada.

Other considerations included the ongoing cost of chemical treatment for a water-cooled plant, plus the lack of a good cooling water source in the area. This latter consideration has proven particularly important with the severe drought conditions California has faced since the plant was put in operation.

When these considerations were taken all together, the choice of air over water cooling was clear.

12. Many prototypes of Micro H&P for domestic application were built, unfortunately none led to commercialization ([Colonna et al., 2015](#); [Micro H&P](#)).
13. For automotive applications, except for GM and Thermo Electron units tested in the 1970s, mentioned earlier, automotive manufacturers like Cummins, Honda, Bosh, and others, are involved in R&D.



Figure 2.22 Ben Holt Mammoth 36 MW air-cooled geothermal plant, 1984.

2.6 Commercialization of ORC systems, present status

2.6.1 Established dedicated ORC manufacturers

2.6.1.1 Ormat

Ormat was founded by Lucien and Dita Bronicki in 1964 with an agreement with National Preparedness Leadership Initiative (NPLI) to implement Lucien's work and the right to use the patented new cycle. The company is a pure player in renewable energy, a leading vertically integrated company engaged in the geothermal and recovered energy power business. It designs, develops, owns, and operates geothermal and recovered energy-based power plants predominantly using ORC units designed and manufactured by it. About 100 US patents cover its original technology.

Since 2004 Ormat Technologies Inc., headquartered in Reno, Nevada, has been a public company traded on the New York Stock exchange. Worldwide it employs more than 1000 people. As of 2015, Ormat has built more than 3000 ORC units up to 4 kW, and approximately 500 modules in the power range of 1–25 MW, totaling more than 2000 MW.

From the onset, the development in Ormat was closely following Carnot's teachings: *"The economy of the combustible (Efficiency) is only one of the conditions to be fulfilled in heat engines. In many cases it is only secondary...appreciate in each case, at their true value, the consideration of convenience and economy ...discern the more important of those which are only accessories to balance them properly against each other, in order to attain the best results by the simplest means"* (Carnot, 1826). Attaining economically the maximum useful power from a given heat source and heat sink requires balancing between the cycle design with minimum irreversible losses and the system design to maximize the ratio of useful power output to parasitic losses, i.e., the power used to circulate the motive fluid in the system and to move the heat from and into the cycle. This is achieved by using the fluid properties as free design parameters to optimize the cycle and the turbine configurations. In the case of solar energy, the heat source (the collector output) and heat sink may be considered isothermal. In most other cases the source is nonisothermal (sensible heat).

Properties such as ratio of latent heat of vaporization to sensible heat of preheating were the criteria for the choice of fluid to optimize the heat amount extracted by the cycle from the source. Vapor pressure as a function of temperature was the criterion that enabled using gravity feed rather than pump on small units and reduced blade and piping size on large systems. Molecular mass was an important criterion for the choice of fluids for small units to reduce the rotational velocity and increase the size of blades for better efficiency.

Ormat's first unit was a solar-powered ORC of 600 W hermetically enclosed like a domestic refrigerator, using dichlorobenzene as the motive fluid as well as lubricant. It powered an electric water pump in Mali in 1966 (see Fig. 2.15, paragraph 5.2).

As no orders for solar units came in, Ormat identified a niche market opportunity in power for remote unattended telecommunication repeaters created by the introduction of transistors instead of electronic tubes, which drastically reduced the power

requirements and dramatically increased the reliability. Now the “Achilles heel” of the repeater was the diesel generator associated with batteries in a charge-discharge mode, which was the main factor of low availability of the repeater station, short life of batteries, and high diesel engine maintenance costs.

Ormat’s hermetically sealed units (Bronicki, 1988) in the power range of 200 W to 4 kW, powered by natural gas, Liquefied petroleum gas (LPG), or kerosene filled this need. The fluids used were mixtures of dichloro and trichloro benzene isomers. The turbine was a 20,000 RPM radial inflow supersonic turbine with a brushless alternator on the same shaft supported by bearings lubricated by the motive fluid. The low vapor pressure in the system allowed to use gravity feed rather than a pump. About 3000 of such units were sold, many of the 120 units installed in 1975 on the Trans-Alaska pipeline were still in operation in 2015 without overhaul (Fig. 2.23).

A radioisotope-powered dual fluid 400 W demonstration unit was built, diphenyl and dichlorobenzene in a cascading configuration, but was not commercialized (Bronicki, 1966).

The energy crisis of 1973 gave value to previously neglected low temperature heat sources. In 1975 a 150 kW ORC powered by a solar pond was built at the Dead Sea followed by a 5000 kW plant. The fluid used was Freon 114 in a recuperated cycle between 85°C and 27°C. This plant operated for seven years (Bronicki et al., 1980). See Fig. 2.18.

In 1985 Ormat delivered a 70 kW ORC for a solar pond built with Ormat assistance by the US Bureau of Reclamation in El Paso, Texas (Fig. 2.24). The unit used Freon 113 and operated for 17 years providing both electricity and heat to a food processing factory.

Both projects were successful technically, but the drop in oil prices made the technology uneconomical.



Figure 2.23 One of the 60 Remote Gate Valve Stations powered by two 600 W ORCs in Alaska, 1976. As of 2015 most of the units were still in operation.

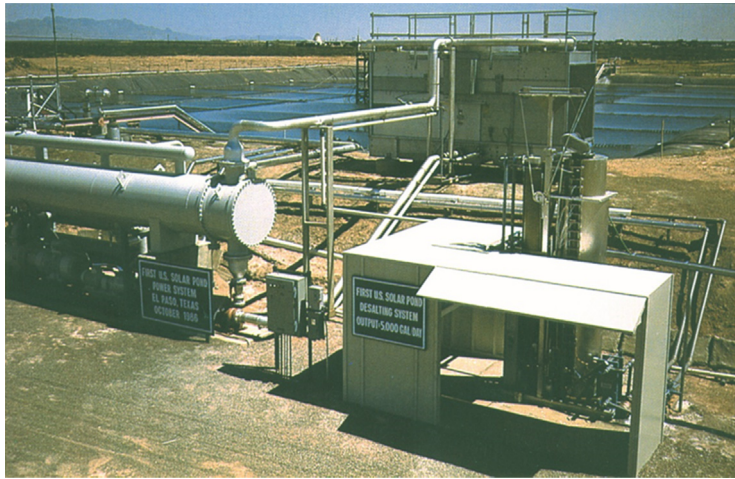


Figure 2.24 The 70 kW heat and power solar pond unit in El Paso.

Again, Ormat had to find another application; this time it was waste heat recovery from the exhaust of gas turbine compressor stations (Bronicki and Schochet, 2005) (Fig. 2.25), cement plants (Legman, 2002) (Fig. 2.26), LNG regasification plants (Fig. 2.27), and geothermal hot brines (Fig. 2.29).

The deregulation of the electricity market in the United States in the 1980s opened the electricity market to renewable energy independent power producers and enabled Ormat to participate in this new market utilizing its mature technology of ORC units where it successfully competed with conventional steam turbine systems. Initially, Freons (11, 113, and 114) were used, but for applications above 100°C Freons were



Figure 2.25 6.5 MW ORC out of the 10 units on Northern pipeline compressor stations, 2006.



Figure 2.26 1 MW ORC recovering heat in the Heidelberger Zement plant, 1999.



Figure 2.27 4 MW ORC operating on an LNG regasification plant, 2010.

abandoned because of inadequate stability and later even for low temperatures because of high GWP. Today, straight hydrocarbons are used, mainly pentanes as well as butanes and hexanes, which are flammable but highly stable and noncorrosive. Neither toluene nor benzene have been used, as they are carcinogenic. Axial transonic two- and three-stage turbines were used (Fig. 2.28).



Figure 2.28 15 MW three-stage axial turbine during assembly in Ormat.

Cascaded integrated two- and three-level plants (Krieger and Kaplan, 2000) were developed to overcome the drawback of the supercritical cycle where the high-pressure fluid pump consumes a substantial portion of the gross power. In many cases, the cascaded two- or three-level ORC has a higher net efficiency than the supercritical cycle despite the higher gross cycle efficiency of the latter (Fig. 2.29) (Bronicki, 2008).



Figure 2.29 36 MW three-level ORC, phase 1 of the 72 MW McGinness Hills complex, 2012.

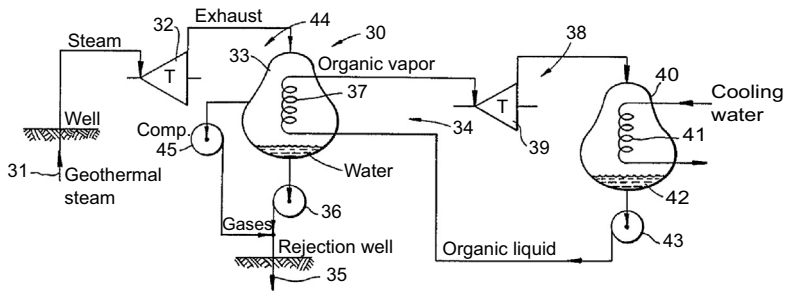


Figure 2.30 First geothermal combined cycle plant comprising ten 3.5 MW Modules in Hawaii, 1993.

Another configuration developed is the geothermal combined cycle, using a back-pressure steam turbine as a topping unit (Figs. 2.30 and 2.31) (Legman, 2000).

A 100 MW geothermal power plant (Fig. 2.32) consisting of four 25 MW modules is the largest ORC-based power plant in operation. In spite of operating in a steam-dominated resource, it is more efficient than a steam flash plant under the same conditions.



Figure 2.31 130 MW geothermal combined cycle power plant in Upper Mahiao, Philippines, 1996.

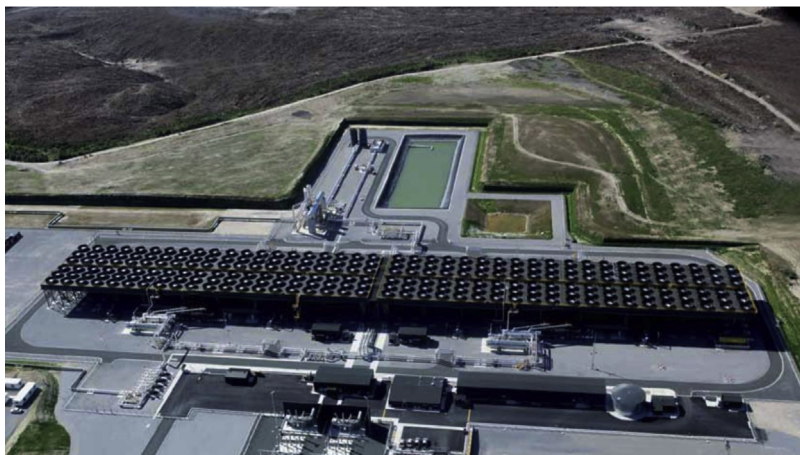


Figure 2.32 100 MW pure ORC geothermal power plant in New Zealand, 2013.

The largest geothermal plant in Indonesia is currently being built utilizing the combined cycle configuration with an output of 330 MW.

2.6.1.2 *Turboden*

Mario Gaia founded Turboden in 1980, with the specific company object of researching, designing, manufacturing, commissioning, and servicing organic Rankine cycle turbogenerators (Gaia, 2011).

Turboden is a private company. In 2009 United Technology Corporation acquired 51% of Turboden's shares.

In 2013 Mitsubishi Heavy Industries acquired the UTC quota. Italian quota holders continue to be in charge of management. Like Ormat, Turboden is a pure player in renewable energy and manufactures its own turbines.

In the first years of activity (indicatively from 1980 to 1997), the ORC turbogenerators by Turboden were small power (3–100 kW), for solar (low and medium temperature), geothermal, and heat recovery applications (Fig. 2.19 and 2.33) (Bini and Viscuso, 2011).

In 1988 two geothermal units of 100 kW each were successfully commissioned in Zambia (Fig. 2.34). The working fluid utilized was tetrachloroethylene, and thanks to the low temperature of the source (around 100°C) and the low pressure of the working fluid, the ORC unit could operate by gravity, without a circulation pump.

Starting from 1988, Turboden decided to concentrate in medium-high temperature applications and realized a first 3 kW ORC unit powered by wood logs (Fig. 2.35). A siloxane fluid was utilized for the first time in an ORC unit, thanks to its favorable thermodynamic properties, health and environment friendliness.

In 1995, in a steel mill, a 1 MW cascaded system (with two different working fluids), followed by the first industrial unit for biomass application, was installed. This unit produced 300 kW from thermal oil at 300°C and supplied hot water at



Figure 2.33 Turboden made a four-stage 35 kW turbine, 1984.



Figure 2.34 Two Turboden Geothermal Power ORCs of 100 kW each in Zambia, 1988.

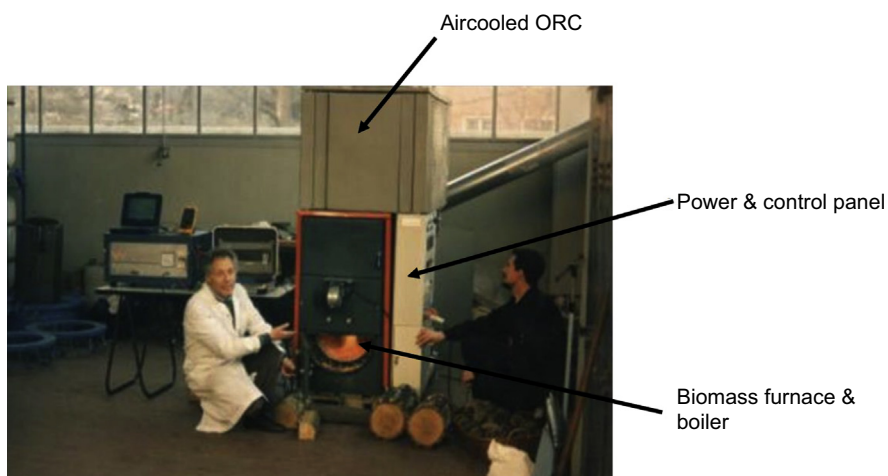


Figure 2.35 Wood Log Powered 3 kW ORC, 1988.

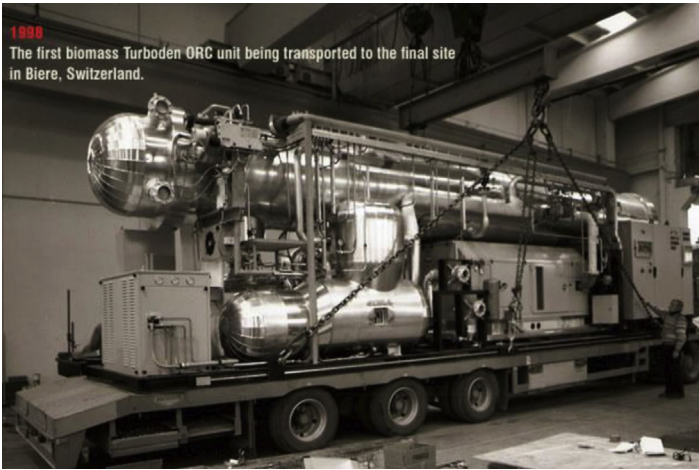


Figure 2.36 300 kW biomass unit in Biere, Switzerland, 1998.

80°C in cogenerative mode to a Swiss Army training center (Fig. 2.36). A two-stage axial turbine was used.

From 2000 to 2009, Turboden experienced an exponential growth installing biomass fueled ORC plants in Austria, Germany, Italy, and other North European countries. The favorable feed in tariffs available in those countries helped the penetration in this market.

In fact, most Turboden units in operation are in biomass applications (both CHP and “power only”), where Turboden is the undisputed leader. The following Table 2.1 (updated June 2016) reflects Turboden’s ORC units presently in operation and under development.

Table 2.1 Turboden plants in operation and under development

	In Operation	Under Development
Biomass	230	45
Geothermal	8	2
Waste heat recovery	20	6
Waste to energy	8	0
Solar	1	3
TOTAL	267	56

The average size is around 1.5 MW electric. Most of these units are fed by thermal oil at a temperature around 300°C and feature an efficiency of 18–25%.

During the last five years Turboden increased the size of its ORCs and widened its portfolio to larger heat recovery, geothermal (Fig. 2.37) and biomass (Fig 2.38) plants,



Figure 2.37 5.6 MW geothermal plant in Durnhaar, Germany, 2013.



Figure 2.38 6 MW Biomass ORC during installation in Fraser Lake, Canada, 2015.

with power units exceeding 5 MW. Besides the traditional scheme using thermal oil as heat carrier, a number of units for heat recovery from gaseous sources using different heat carriers or direct exchange were successfully put in operation.

In 2014 Turboden installed four large biomass plants in Canada. The units are fed by thermal oil at 315°C and feature gross conversion efficiency of 25% (net 23.6%). Working fluid: cyclopentane.

2.6.2 New entrants (in alphabetical order)

2.6.2.1 *Adoratec*

Power equipment packager Adoratec in Germany built a number of plants for developers.

2.6.2.2 *Atlas Copco*

Atlas Copco Group is a global industrial group of companies headquartered in Sweden. Its compressor division is a leader in equipment for the process industry. Between other products it manufactures expanders. Its involvement in ORC systems started by supplying the expanders' trains only, itself or through its subsidiary Maffy Trench.

In 2012 it got involved in complete systems: a 2 MW (using 134a) for heat recovery and a 22.5 MW (using n-butane) geothermal plant. As of 2015, Atlas Copco is constructing one 3.6 MW (using isobutane) and two 22.5 MW plants (Colonna et al., 2015).

2.6.2.3 *ElectraTherm*

ElectraTherm Incorporated in 2005 and is headquartered in Reno, Nevada.

Power + Generator generates clean electricity from low-grade waste heat utilizing ORC and proprietary technologies.

The machines are fully packaged (Fig. 2.39), with outputs up to 110 kW for distributed power generation from low-grade waste heat (77–122°C) utilizing water cooled ORC and proprietary technologies; it licenses two patents from the City University of London and has an additional seven patents issued or in application.

The Power + Generator uses a closed-loop ORC to create pressure by boiling a working fluid into a gas. The working fluid is a hydrofluorocarbon called R-245fa (1,1,1,3,3-pentafluoropropane), a nonflammable, nontoxic liquid with a boiling point slightly below room temperature, about 15°C. The gas expands and turns a twin screw expander that drives a generator to produce electricity.



Figure 2.39 ElectraTherm 110 kW power generator, 2014.

The twin screw expander offers distinct advantages for low-temperature small-scale ORCs, such as simple and compact design, low-speed operation with the ability to handle heat input variations and dual phase flow of the working fluid, significant part load capability, no gear box or oil pump, attractive payback, and proven technology.

The 35 kW unit fits well with 500 kW gensets, the 65 kW unit fits well with 800 kW engines, and a 110 kW unit, well suited for 1–2 MW engines.

In addition to waste heat from internal combustion engines, ElectraTherm's Power + Generator utilizes waste heat from biogas/biomass plants, wastewater treatment plants, landfills, flares and geothermal hot brines. As of 2015, 50 machines were installed in 11 countries around the world.

2.6.2.4 Exergy

Exergy is an Italian company that features radial outflow turbine technology (Fig. 2.40). The company was founded by Claudio Spadacini in the late 1990s as a power plant engineering service provider and entered the ORC market after 2005 as ORC power plant supplier.

In 2009 the application of Exergy started the development of its own technology by applying to commercial ORCs the multistage radial outflow turbine. The radial outflow technology was conceived and applied in the early 20th century by Ljungstrom (counter-rotating) and Parsons (single-rotating) to expand steam. The choice to use the radial outflow turbine with steam demonstrated serious limitations, mainly due to the huge complications suffered by the multidisk radial outflow turbine when the market moved from counter pressure toward full-condensing configuration. These issues meant no significant development of such type of turbines, which were phased out for steam applications by axial turbines. The radial outflow turbine is intrinsically able to develop a low-enthalpy head, which is typical of an organic Rankine cycle, but on



Figure 2.40 3.5 MW geothermal plant in Turkey, 2015.



Figure 2.41 900 kW ORC using 180°C hot water from a steel plant, 2014.

the other side shows some unique characteristics when applied to ORC. The high efficiency of the machine is combined with the better overall cycle efficiency as a result of higher pressure ratio and volumetric ratio made possible by the increasing cross-section area throughout the expansion ([Spadacini et al., 2011](#)) ([Fig. 2.42](#) and [Fig. 2.43](#)).



Figure 2.42 5 MW ORC operating from thermal oil at 300°C, 2015.



Figure 2.43 Exergy 1 MW radial outflow rotor, 2015.

The radial outflow turbine was launched into the marketplace in 2010; the first unit was commissioned in 2011 and in 2015 counted a portfolio of approximately 150 MW in geothermal, heat recovery, biomass, and solar applications (Fig. 2.42).

In 2015 Exergy started a geothermal power plant in Turkey. The plant uses steam/brine at 105°C, it is water cooled and produces 3.5 MW gross, in a steel mill a unit has produced 1 MW since 2014 (Fig. 2.41), and the construction of a 5 MW unit in a glass plant has just been started.

2.6.2.5 General Electric (GE)

In the 1970s GE developed a 3 kW ORC for mobile homes, a project that it quickly terminated. Now GE has two ORC product lines.

In 2010 GE Energy Infrastructure bought a subsidiary of Calnetix Inc. to manufacture the Clean Cycle 125 kW ORC systems (Fig. 2.44). The Clean Cycle 125TM Integrated Power Module is used to recover exhaust heat from GE Jenbacher gas engines and other applications. As of early 2011, more than 100 such modules have been manufactured (Colonna et al., 2015).

In 2000 GE Power system acquired Rotoflow (Holm, 1981), a manufacturer of radial expanders for the process industry and geothermal power plants. GE now has the ORegen ORC product line for waste heat recovery (Burrato, 2013).

In 2013 GE supplied to NRgreen in Alberta, Canada, a 17 MW gross/14 MW net heat recovery plant on the Windfall compressor station. The GE ORegen utilizes cyclopentane in a recuperated cycle (Ormat patent) (Fig. 2.45). The project was supported by a \$7 million grant from the Alberta Climate Change and Emissions Management Corporation (Del Turco et al., 2011).

On the same Alliance Pipeline, four other compressors use Ormat 7 MW units that have been operating successfully since 2007.

GE is planning four additional 17 MW (gross) units (Colonna et al., 2015).

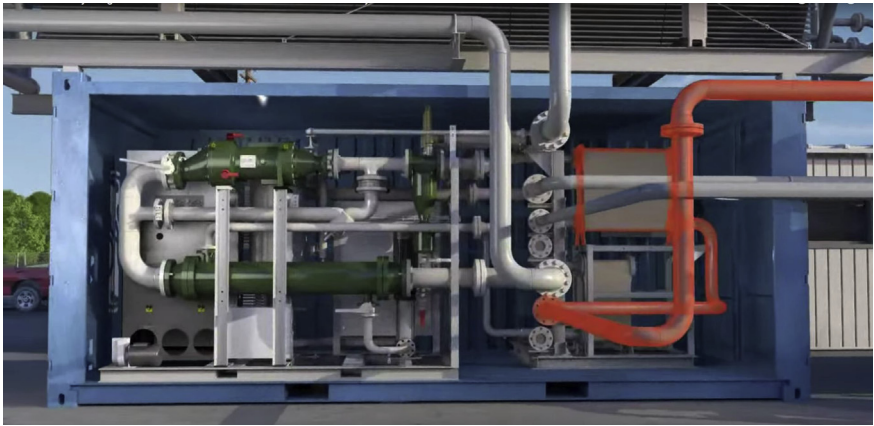


Figure 2.44 Clean Cycle 150 kW unit, 2010.

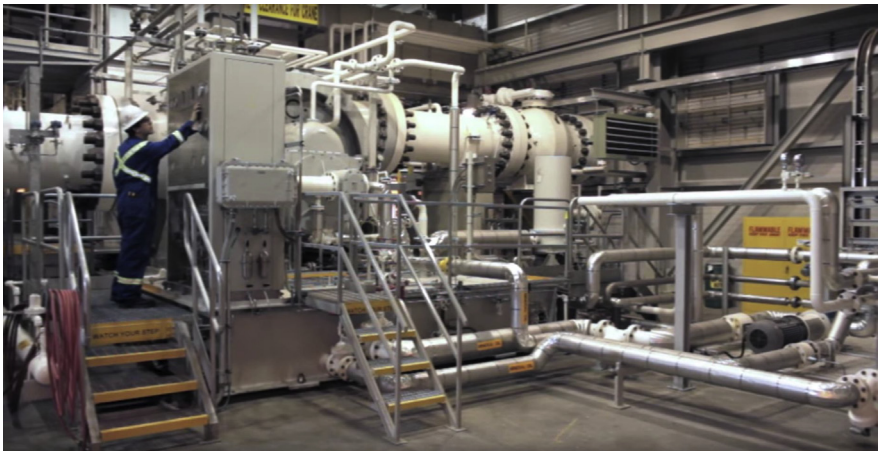


Figure 2.45 GE 14 MW ORegen installation in the Windfall Compressor Station of the Alliance Pipelines, in Alberta, Canada, 2013.

2.6.2.6 *GMK*

GMK was founded by the Rostock University in Germany. Since 2000, about 30 ORC systems up to 2 MW have been manufactured. Most of the units are in the range of 40 kW using a special expander directly driving a 50 Hz generator. They are used for heat recovery from biogas engines and biomass incineration plants.

2.6.2.7 *Triogen Company (Triogen)*

Established in 2001 to produce hermetically sealed ORC units based on Lappeenranta University patents using toluene as a motive fluid and lubricant for the bearings.



Figure 2.46 160 kW Triogen biogas ORC, 2014.

By 2014, about 30 water cooled 160 kW units were manufactured for heat recovery from biogas engines (Fig. 2.46) and biomass incineration plants (van Buijtenen, 2009).

2.6.2.8 Turbine air systems (TAS)

TAS build a number of units and power plants for geothermal applications using a supercritical cycle (Figs. 2.47 and 2.48) (Colonna et al., 2015), such as pioneered by Ben Holt, but using a fluorinated hydrocarbon motive fluid and turbines manufactured by others.

As of 2015 TAS discontinued the ORC product line.

2.6.2.9 United Technologies/Pratt and Whitney

United Technologies (UTC) developed an interesting 200 kW water-cooled PureCycle power unit (Fig. 2.49) using Carrier refrigeration hardware. J. Brasz and his team (Brasz, 2011) developed the most detailed, thorough and successful adaptation of a refrigeration compressor as an expander for an ORC system. The motive fluid was R245fa. Many small installations using one or two PureCycle units were very successful such as the one at Chena Hot Springs in Alaska (Brasz and Holdmann, 2005). About 100 such units were built (Colonna et al., 2015) before UTC decided to abandon this product line like GE did for the mobile home ORC in the 1970s.



Figure 2.47 TAS 2 MW Dixie Valley Geothermal Unit using Barber Nichols Turbine, 2003.



Figure 2.48 TAS 22 MW plant in Neal Hot Springs, Nevada, 2012.

2.6.2.10 Various new entrants

There are a large number of diversified proposals for small ORCs, all of them with a limited number of units, that have not yet reached economic competitiveness (Colonna et al., 2015). One example is ENOGIA (Enogia) (Fig. 2.50), which, in 2012, built a 10 kW skid-mounted hermetic oil-free turbine/generator ORC that uses waste heat from a biogas engine generator CHP water loop enhancing the plant efficiency.



Figure 2.49 UTC 200 kW water-cooled PureCycle in Chena Hot Springs, Alaska.



Figure 2.50 Enogia 10 kW ORC Package, 2015.

2.7 Software development

In the last 30 years the development of engineering software enabled taking full advantage of the flexibility of ORC to optimize the utilization of low and moderate temperature heat sources. In addition to available general purpose software packages, some manufacturers developed their own ad hoc programs. Thermal engineering software developers such as [Thermoflow Inc.](#) in the United States, and [Asimptote](#) in the Netherlands now offer specific packages for ORC. In academia the work on ORC continues especially at the Politecnico di Milano, the ORC group of University of Liege in Belgium, and most actively by Professor Piero Colonna and his team at the Delft University of Technology in the Netherlands.

2.8 Summary

As of 2015 only two companies had succeeded in commercializing the ORC technology in a sustainable way over many decades, Ormat and Turboden while a third company, Exergy, on the basis of recent installations will likely join them. While the ORC market is still a niche market, it provides an opportunity of sustainable business, especially for pure play companies who have the perseverance and the technical innovation culture to pursue the market.

References

- Angelino, G., Gaia, M., Macchi, E., 1984. A review of Italian activity in the field of Organic Rankine Cycles. In: Proceedings of the International VDI Seminar on ORC, Zurich 1984, in VDI Berichte, vol. 539. VDI Verlag, pp. 465–482.
- Ainger, A., 1830. Quarterly journal of science. Literature and Arts Volume 7 New Series 186–189.
- Angelino, G., Invernizzi, C., 1993. Cyclic methyisiloxanes as working fluids for space power cycles. Journal of Solar Energy—Transactions of the ASME 115 (3), 130–137.
- Adoratec official website: www.adoratec.com.
- Atlas Copco — Expanders, official website: www.atlascopco-gap.com.
- Asimptote official website: www.asimptote.com.
- Bronicki, L.Y., 1988. Experience with high speed organic Rankine cycle turbomachinery. In: Proceedings of Conference on High Speed Technology, No. ENTE D-15. Lappeenranta University of Technology, pp. 44–61.
- Bronicki, L., September 1966. Rankine cycle power unit operating with isotopic heat sources. In: UKAEA/ENEA Symposium on Industrial Applications for Isotopic Power Generators. Harwell.
- Bronicki, L.Y., Lev-Er, J., Porat, Y., 1980. Large solar power plants based on solar ponds. In: 11th World Energy Council Conference. Munich.
- Bronicki, L.Y., Schochet, D.N., 2005. Bottoming organic cycle for gas turbines. In: ASME TurboExpo 2005, Reno.

- Bronicki, L.Y., 2008. Advanced power cycles for enhancing geothermal sustainability, 1,000 MW deployed worldwide. In: Power and Energy Society General Meeting – Conversion and Delivery of Electrical Energy in the 21st Century, 2008 IEEE.
- Bini, R., Viscuso, F., 2011. High efficiency (25%) ORC for power-only generation mode in the range 1–3 MW: an already proven technology also available for partially cogenerative applications. In: ORC2011 – 1st International Seminar on ORC Power Systems - Delft (NL), September 22–23.
- Burrato, A., 2013. OReGen to waste heat recovery: development and applications. In: ASME ORC2013 – 2nd International Seminar on ORC Power Systems - Rotterdam (NL), October 7–8.
- van Buijtenen, J., 2009. The Tri-O-Gen Organic Rankine Cycle: development and perspectives. *Journal of the Institution of Diesel and Gas Turbine Engineers* 13 (1).
- Brasz, J., 2011. Low temperature/small capacity ORC system development. In: Keynote Lecture at the ORC2011-1st International Seminar on ORC Power Systems – Delft (NL), September 22–23.
- Brasz, J., Holdmann, G., 2005. Power Production from a Moderate Geothermal Resource *Transactions – Geothermal Resources Council*, vol. 29, pp. 729–733.
- Colonna, P., Casati, E., Trapp, C., Mathijssen, T., Larjola, J., Turunen-Saaresti, T., Uusitalo, A., October 2015. Organic Rankine Cycle power systems: from the concept to current technology, applications, and an outlook to the future. *Journal of Engineering for Gas Turbines and Power* 137, 100801–1.
- Cardwell, D.S.L., 1971. *From Watt to Clausius, the Rise of Thermodynamics in the Early Industrial Age*. Heinemann Educational Books Ltd., London.
- Carnot, S., 1826. In: Mendoza, E. (Ed.), *Reflexions sur la Puissance Motrice du feu*. Bachelier Libraire Paris 1824. English translation: “Reflections on the motive power of fire”. Dover publications, Inc., New York, 1960.
- Copreau, C., 1979. Thermodynamic power conversion unit. In: *Societe Bertin 78370 Plaisir Fr.*
- Campbell, R.G., October 1989. Construction and planned operation of a hybrid power plant. *GRC Transactions*. Campbell, 1989, Volume 13, <http://pubs.geothermal-library.org/lib/grc/1001831.pdf>.
- D’Amelio, L., 1935. *l’Impiego di Vapore ad Alto Peso Molecolare in Piccola Turbina*. Universita di Napoli.
- Dow, H.H., 1926. Diphenyl-oxide bi-fluid power plants. *Mechanical Engineering* 48 (8), 815–818.
- DiPippo, R., 2012. *Geothermal Power Plants*, third ed. Elsevier Ltd.
- DiPippo, R., 2004. Second Law assessment of binary plants generating power from low-temperature geothermal fluids. *Geothermics* 33, 565–586.
- Energent official Web site: www.Energent.net.
- ElectraTherm official website: www.electratherm.com.
- Exergy, Official website: www.orc.com.
- Enogia official website: www.enogia.com.
- Findlay, W.S., 1934. Some suggestions for diphenyl heat engines. *The Power Engineer* 29 (336), 89–91.
- Guthrie, J., 1970. Bizarre. “Ships of the Nineteenth Century”. Hutchinson, pp. 193–196.
- Gokhshtein, D.P., Smirnov, G.F., Kirov, V.S., 1966. Some features of binary cycle systems with non-aqueous vapours. In: ASME Paper No. 66-GT-84.
- Gaia, M., 2011. 30 years of ORC development. In: Keynote Lecture at the ORC2011 – 1st International Seminar on ORC Power Systems – Delft (NL), September 22–23.
- GE official Website: www.ge-distributedpower.com.

- GE buys Calintex, October 1, 2010. BloombergBusiness.
- GMK, Gesellschaft für Motoren und Kraftanlagen GmbH, website: www.GMK.de.
- Hirakawa, T., Suzuki, T., May 1983. 14 MW ORC plant installed at Nippon Steel. Modern Power Systems 2.
- Holm, J., 1981. The application of turboexpanders for energy conservation. Transactions of the IMechE.
- Jameson, J.W., 1858–59. On the performance of the screw steamship 'Sahel' fitted with Du Trembley's combined vapour engine and of the sister ship 'Oasis' fitted with steam engines worked expansively and provided with partial surface condensation. Minutes of proceedings of the Institution of Civil Engineers 18, 233–294.
- Jokinen, T., Larjola, J., Mikhaltsev, I., 1998. Power unit for research submersible. In: ElecShip 98, International Conference on Electric Ship, pp. 114–118.
- Jeumotte, A.L., 1983. Le cycle binaire pour centrale électrique a refroidissement sec. In: Rev. Gen. Therm. Fr. No 255, Mars 1983.
- Kalina, I.A., 1984. Combined cycle system with novel bottoming cycle. Journal of Engineering for Gas Turbines and Power – Transactions of the ASME 106, 737–742.
- Krieger, Z., Kaplan, U., 2000. US Patent 6009711 Apparatus and Method for Producing Power Using Geothermal Fluid.
- Larjola, J., 1984. ORC-plant with high-speed gas lubricated turbogenerator. In: VDI Berichte – Proceedings of the International VDI Seminar, vol. 539. VDI Verlag, pp. 697–705. 173.
- Larjola, J., 1988. ORC power plant based on high speed technology. In: Proceedings of the Conference on High Speed Technology No. ENTE D-15. Lappeenranta University of Technology, pp. 63–77.
- Legman, H., May 2002. Recovery of waste heat in cement industry by ORC. In: Trans. IEEE, 2002, Jacksonville.
- Legman, H., 2000. The 60 MW Mokai Geothermal Project. GRC, Reno.
- Micro H&P official website: www.microchap.info.
- Owen, J.R., June 1975. The Organic Rankine Cycle – a Review of Applications and Factors Affecting Working Fluid Selection Research Memorandum ML 76. The City University Department of Mechanical Engineering, London.
- Ormat Technologies Inc. Official website: www.ormat.com.
- Parasad, A., 1980. Field testing of a 600 kW organic Rankine cycle waste recovery. In: EnergyTechnology: Proceedings of the Energy Technology Conference, vol. 1, pp. 482–494.
- Prigmore, D.R., Barber, R.E., 1974. Prototype solar powered Rankine cycle system providing residential air conditioning and electricity. In: Proc. 9th IECEC, pp. 326–333, 205. Sargent.
- Reid, R.C., Sherwood, T.K., 1958. The Properties of Gases and Liquids, Their Estimations and Correlations. McGraw-Hill Inc.
- Sternlicht, B., 1984. Development prospects for Organic Rankine Cycles and heat pumps. In: Proceedings of the International VDI Seminar on ORC, Zurich 1984, in VDI Berichte, vol. 539. VDI Verlag.
- Schad, J.L., 1981. Comparison of organic rankine working fluids. In: Conference on Use of Organic Fluids for Waste Heat Recovery in Ships and Industry. City University London.
- Smith, I.K., August 1972. A Program to Determine the Thermodynamic Properties of Organic Fluids in the Saturated, Superheated and Supercritical States. The City University, Research Memorandum ML 42.

- Smith, I.K., da Silva, M., 1994. Development of the trilateral flash cycle. Part 2: increasing power output with working fluid mixtures. *Proceedings of the Institution of Mechanical Engineers, Part A: Journal of Power and Energy* 208 (2), 135–144.
- Spadacini, C., Centemeri, L., Xodo, L.G., Astolfi, M., Romano, M.C., Macchi, E., 2011. A new configuration for organic Rankine cycle power systems. In: *ORC2011 – 1st International Seminar on ORC Power Systems – Delft (NL)*, September 22–23.
- Thurston, R.H., 1902. Series vapour and waste heat engines as supplementary to single vapour engines. *Journal of Franklin Institute* 154 (4), 291–314.
- Tabor, H., Bronicki, L., 1961. Small turbine for solar energy power package. In: *Proc. U.N. Conf. On New Sources of Energy, Rome*, vol. 4, p. 68.
- Tabor, H., Bronicki, L., 1964. Establishing Criteria for Fluids for Small Vapor Turbines. *SAE Technical Paper*, 640823.
- Turboden official website: www.turboden.eu.
- Del Turco, P., Asti, A., Del Greco, A., Bacci, A., Landi, G., Seghi, G., 2011. The ORegen waste heat recovery cycle: reducing the CO₂ footprint by means of overall cycle efficiency improvement. In: *Proceedings of ASME Turbo Expo 2011. Vancouver (CA)*, June 6–10, pp. 547–556.
- Triogen B.V., Official website: www.triogen.nl.
- TAS official website: www.tas.com.
- Thermaflow official website: www.thermaflow.com.
- Wilson, S., Radwan, M.S., 1977. Appropriate thermodynamics for heat engine analysis and designs. *International Journal of Mechanical Engineering Education* 5 (1).
- Yamashita, A., 1979. Power generation system by heat recovery from converter cooling water. *The Sumitomo Search No. 25*. May 1981.

Technical options for Organic Rankine Cycle systems

3

M. Astolfi

Politecnico di Milano, Milan, Italy

Organic Rankine Cycles (ORCs) are a technology suitable for the exploitation of many different energy sources and are particularly suitable for medium—low temperature heat sources and/or for small available thermal power. In both fields, the efficiency is limited: in the first case because of the low efficiency of the ideal Carnot or the ideal Lorentz cycles, and, in the second case, because of the limited efficiency of some key components, like the expander and the pumps which are penalized by miniaturization. Due to their limited power output ORCs, use plant layouts less complex than common steam Rankine cycles. Compared to large recuperative steam cycles, two or three pressure levels cycles are rarely proposed on the market, with the exception of the geothermal field, where the high cost of the heat source (exploration and drilling are capital intensive activities) makes profitable the use of more expensive but also more efficient plants. Another reason for ORC simplicity is related to the thermodynamic properties of the working fluids; high complexity fluids show small temperature drops along the expansion, with a temperature at turbine discharge higher than those attainable in steam plants. Recuperative cycles are usually adopted in these cases instead of regenerative bleedings with a less complex design and a simplex control of the plant. Finally, the maximum power output for each single expander is generally limited to 15 MW_{el} leading to volume flow rates which are rarely so large to require a cross-over and case splitting in two or more turbine groups. In conclusion, ORCs compared to other closed cycle power systems have an intrinsically simpler plant layout characterized by a limited number of components: an easy operation, a small thermal inertia, and a great flexibility in off-design conditions.

In this chapter, a description of the main components of ORC plants is presented, along with a brief overview of the cycle configurations that are commonly used or proposed in the literature for ORC applications. Further information can be found in a comprehensive review papers by [Colonna et al. \(2015\)](#) and [Lecompte et al. \(2015\)](#).

3.1 Equipment list

Any ORC cycle is made mainly by four classes of components: (1) the heat exchangers, (2) the expander, (3) the pump, and (4) the generator unit. Beside them, many other components are usually required for a safe and stable operation of the system and for its control. A short list of the components usually present on ORCs is presented in this chapter while a detailed description can be found in the other chapters of this book.

3.1.1 Heat exchangers

These components are used for: (1) the heat introduction process in the so-called Primary Heat Exchanger (PrHE), (2) for the heat release to the environment in the condenser, and (3) for the internal recovery of the thermal energy available from the hot vapor discharged by the turbine in the recuperator. The architecture of the PrHE varies depending on the application, the type of fluids, and the operating conditions of the thermodynamic cycle. For subcritical cycles it consists of the economizer, the evaporator, and possibly the superheater. For supercritical cycles (where phase transition occurs continuously) or when mixtures are used it is arranged as a once-through heat exchanger.

Because of the low efficiency of ORC, particular attention must be paid to the heat exchangers design, since they typically contribute for the largest fraction of power block cost. For all heat exchangers, the design must take into account the trade-off between different opposite effects: the increasing of surface is positive from a thermodynamic point of view, since it allows minimizing the entropy generation and achieving higher performances, on the other hand it leads to more expensive equipment with a contrasting effect on the Levelized Cost Of Electricity. Carbon steel is the most common material for these components even if other alloys can be used in presence of particular fluids and corrosion issues. Please refer to Chapter 13 for a detailed description of the heat exchanger configurations and their modeling principles.

3.1.1.1 Shell and Tubes

Shell and Tubes (S&T) are the most common heat exchanger in the ORC field and they are used for the economizer and the superheater components when the hot stream is a liquid.¹ As reported in Fig. 3.1, they are made by a bundle of tubes enclosed in a shell: one stream flows in the tubes one or more times (in the latter case, the header is separated in different chambers by horizontal baffles) while the other one flows in the shell,

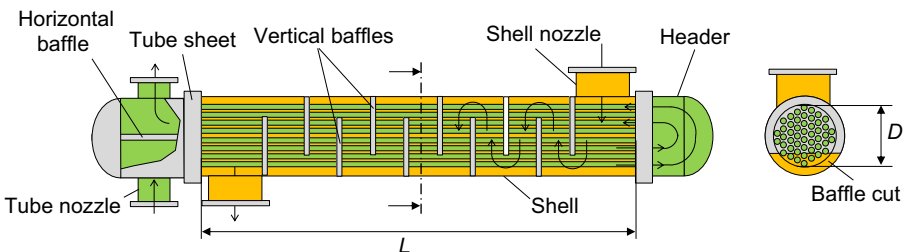


Figure 3.1 Shell and Tubes heat exchanger.

¹ In most of the ORC applications the hot fluid in the PrHE is a liquid: this is obvious for geothermal brines and solar power plants but it is true also for biomass combustion and WHR where often a loop of heat transfer fluid (pressurized water, steam, or oil) is used to limit the risk of working fluid decomposition at high temperatures.

almost perpendicular to the tube bundle following a path defined by the vertical baffles arrangement (Kakac, 2002).

The position of the hot and the cold fluid depends on their nature and the operating conditions. The high pressure fluid (generally the working fluid) flows in the tubes in order to limit the heat exchanger weight and cost. However, if the hot stream presents fouling and scaling issues, like in geothermal applications, it is preferable to let it flows in the tubes. In this way, the maintenance of the heat exchangers is easier and cheaper, as mechanical cleaning can be used. These techniques consist in conveying bodies made by a matter of brushes or scrapers, called pigs, into the tubes. Pigs are pushed by compressed air or pressurized water and they remove incrustations by friction. In this case the high pressure working fluid is located in the shell side in contrast with common design principles resulting in a more expensive heat exchanger with a thicker vessel. Alternatively the geothermal brine can be placed in the shell side and the scaling removal is realized with chemical compounds.

S&T design relies on TEMA standards (TEMA, 2007) which defines the standard sizes for the shells, the tubes, and the headers. If the heat transfer surface exceeds one or more limit (maximum shell diameter and maximum tubes length) different units in parallel and/or in series are used. Alternatively if a very high L/D ratio is required, the hairpin S&T heat exchanger, reported in Fig. 3.2, is usually adopted since it allows for a large thermal duty in a single unit with an almost perfect counter current disposition.

3.1.1.2 *Evaporators and water cooled condensers*

For large size plants with a liquid hot source, evaporators are usually arranged as a kettle reboiler (see Fig. 3.3). These components are formed by a two-pass tube bundle where the hot fluid flows, surrounded by a plenum of liquid working fluid in equilibrium with its own vapor. The working fluid enters in a separate section in subcooled conditions² and it is heated up to saturated state by mixing with the saturated liquid. On the top of the heat exchanger, a demister unit is always present to remove the droplets of liquid that are dragged by the vapor flow and that can be dangerous for the turbine

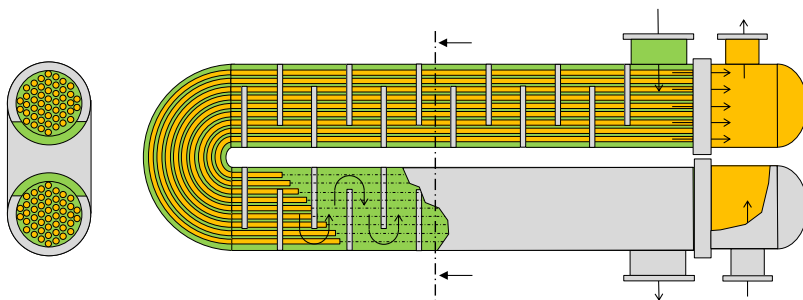


Figure 3.2 Hairpin Shell and Tubes heat exchanger.

² Evaporation must be avoided in the economizer due to the strong increase of pressure drops and the reduction of heat transfer coefficients.

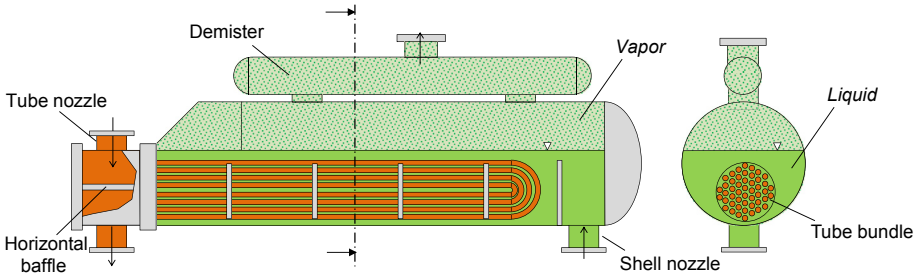


Figure 3.3 Kettle reboiler heat exchanger.

blades (Kakac, 1991). These components are usually more expensive than classical S&T because of the thicker shell and the large amount of fluid contained but they are the most common solution in big power plants due to the possibility to control the quality of vapor and the level into the heat exchanger.

A similar configuration is used for water cooled condensers. Cold water can be available from the environment (rivers, lakes, seas, and boreholes) or it can be a heat transfer fluid for district heating or industrial thermal users in a cogenerative back-pressure configuration. In the first case, there is usually no limitation on the mass flow rate of cooling flow but the temperature increment of water is limited, by regulation, in order to protect the environment. In the second case, the thermal power to be delivered is usually fixed and the power plant is controlled to meet this requirement. A last option is to use evaporative tower technology which allows to considerably reducing the condensation temperature compared to air cooled systems with a limited consumption of water.

Fig. 3.4 depicts the generic layout of a water cooled condenser where the cold water flows in the tubes and the vapor in the shell. The vapor enters from the top, hits an impingement plate and it is distributed on the whole tube bundle. Vapor comes into contact with the cold tubes, it condensates and it is eventually subcooled. The drops of liquid fall onto the tubes underneath and meet with the vapor to perform a partial heat and mass transfer. If a sufficient volume is guaranteed under the bank of tubes, the liquid has a residence time long enough to return in a saturated liquid condition in equilibrium with the vapor. This volume is called condenser hot well and its level

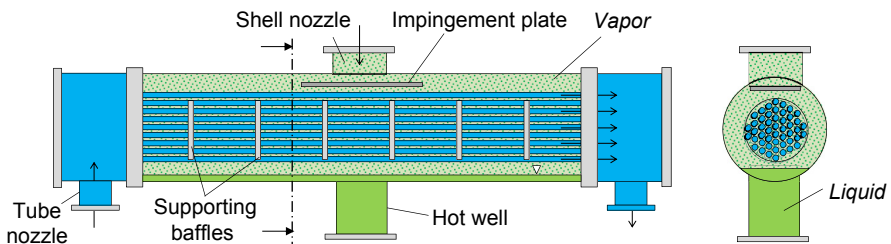


Figure 3.4 Water cooled condenser heat exchanger.

(as for the level in the kettle reboilers) is one of the control parameters of a Rankine cycle. The level must be in a well-defined range, between a minimum level in order to prevent pump cavitation and a maximum level that prevents some tubes from remaining submerged, which would result in condensate subcooling and detrimental effects on the efficiency of the plant.

3.1.1.3 Air cooled condensers

If water is not available as a cooling medium, ambient air is the only option. Taking in mind that air shows a very low heat transfer coefficient and that the condenser has to reject to the environment a large fraction of the power input, it is evident that the design of the air cooled condenser (ACC) can greatly affect the plant economics, with a share of power block cost at around 20%. A large surface provides a reduction in the condensation pressure and an increase in the power output but it leads to a higher equipment cost, a larger footprint, and to a higher fans electric consumption. The design of this component is derived from the heating, ventilation, and air conditioning (HVAC) industry. With reference to [Fig. 3.5](#), an ACC is formed by a couple of copper finned tube banks made by a few (up to five) rows and multiple passes. Ambient air is conveyed by a series of fans placed on the top of the unit. Small tube diameters and advanced fin designs can give large benefits in terms of total weight and internal volume (it is important to reduce the amount of fluid charged in the plant). Finally a solution which is offered by [LU-VE \(2013\)](#) consists in a “wet and dry” ACC. The condenser is provided by one or two water sparkling systems for each side. Demineralized water is sprayed on the tube bank if the air temperature becomes too high with the aim of maintaining the cooling capacity while limiting the fan consumption. In this way, the duty of the condenser is dramatically improved thanks to the contribution of water evaporation with relevant energy advantages. Usually the transition from dry to wet operation is set to 20°C.

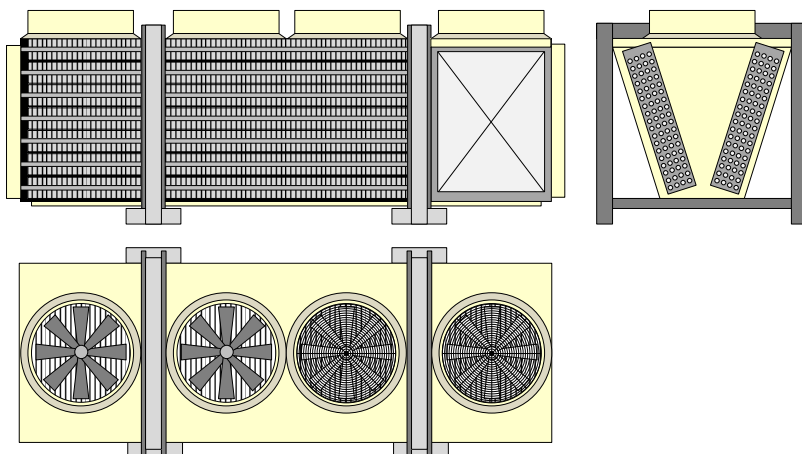


Figure 3.5 Air cooled condenser sketch.

3.1.1.4 Recuperator

The recuperator is a component particularly important in high temperature applications and in those cases characterized by a high minimum temperature of the heat source. Usually, for high temperature sources, complex working fluids are used involving small temperature drops along the expansion and a large thermal power available at turbine discharge. A recuperative preheating of the pumped liquid is important to obtain high efficiencies, limiting the temperature differences in the PrHE and reducing the heat released to the environment. The recuperator is usually designed as a finned tubes heat exchanger in order to improve the heat transfer coefficient on the tube external side where vapor flows. This technology is derived from the HVAC industry and the recuperator is realized by several liquid circuits arranged on different staggered rows forming a tube bank. Tubes are finned with continuous metallic plates; organic liquid flows perpendicular to the vapor and multi-pass paths are usually adopted. The external–internal surface ratio is generally around 15–17. Fins are usually realized in copper except for aggressive fluids like ammonia, while tube material depends on the operating temperature. For temperatures below 200°C, tubes are made with copper while for higher temperatures cupronickel 90/10 is used. The recuperator is placed just after the turbine diffuser in order to reduce pressure losses in the piping between the two components as shown in Fig. 3.6.

3.1.1.5 Braze plate and plate fin

For small scale applications, instead of S&T heat exchangers, plate-fins or brazed plate heat exchangers can be used since they are more economical and they show high global heat transfer coefficients.

3.1.2 Expander

The expander is the key component of an ORC and depending on the size of the plant and the working fluid properties the expander type can completely change. More

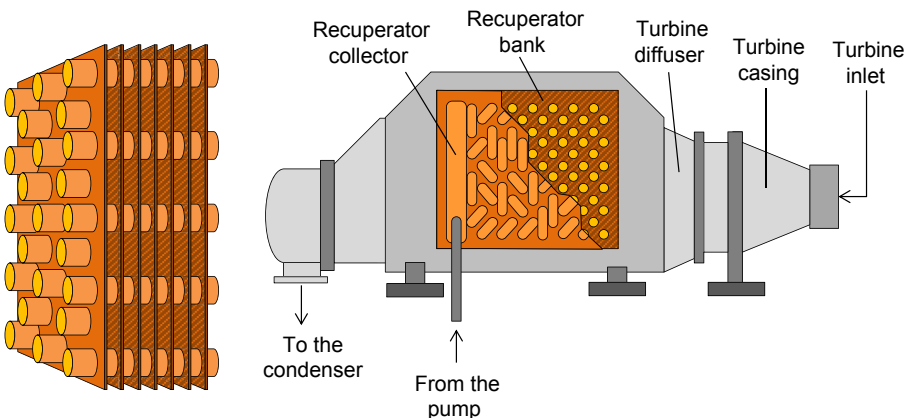


Figure 3.6 Schematic representation of regenerator finned tube bank typical and its disposition ant turbine outlet.

details can be found from Chapters 8 to 12. Expanders can be mainly divided in two categories: (1) turbomachines and (2) volumetric or positive displacement devices.

3.1.2.1 *Turbomachines*

Turbomachines are formed by a sequence of stages, each one made by a stator and a rotor. In the stator, the fluid accelerates in converging (or converging–diverging) static channels. After, it enters in the rotor where it is possibly further expanded and deflected exchanging momentum with the turbine blades. Rotor disks are connected to the turbine shaft. Depending on the relative motion of the fluid respect to the shaft the turbines can be classified as: (1) axial, (2) radial inflow or centripetal, and (3) radial outflow. A detailed description of these components is reported in Chapters 9, 10, and 11 respectively. Turbomachines are suitable for medium/large power plants and their typical power output span is between 100 kW and 15 MW. Axial turbines for power output higher than 0.5 MW are the most common choice in the ORC field; they are developed by both [Ormat](#) and [Turboden](#). However, smaller sizes show strong efficiency penalization due to the very small blades and/or the need for partial admission. Radial inflow turbines have been mainly produced by [Atlas Copco](#) for big plants and by [GE Calnetix](#) for small applications. This latter case is particularly interesting since the turbine is equipped with magnetic bearings and rotates at very high RPM. If the expansion is characterized by a very high volume ratio and a large volumetric flow rate radial outflow, turbines are suggested thanks to the possibility to use prismatic blades and arrange several stages on the same rotor disk. These machines are commercialized by [Exergy](#).

3.1.2.2 *Volumetric expanders*

If the power output is below 100 kW the design of an efficient turbomachine is very challenging and the use of positive displacement devices can be advantageous. In these machines, pockets of fluid are trapped during the rotation, they are expanded and then discharged. Volumetric expanders are deeply analyzed in Chapter 12 and among them the scroll and the screw configurations are the most used in experimental and commercial devices like [ElectraTherm](#) and E-Rational [<http://e-rational.net/>]. These components are cost-effective since they are derived from the refrigerant compressor market and they can benefit by large scale economies. In addition, they can expand a two phase fluid with less erosion issues compared to a turbine. The main limit of these devices is the difficulty in realizing multiple stage expansion and the low efficiency in the presence of a high volume ratio. Both effects limit the maximum evaporation temperature of the cycle, in particular if a high critical temperature fluid is used.

3.1.3 *Pumps*

ORC pumps are usually variable speed multistage centrifugal pumps and their design is relatively common because of their wide use in both the chemistry and refinery fields. Depending on the cycle configuration, fluid selection and cycle design parameters, the pump might show a consumption which is a relevant share of the turbine gross power output (up to 20–30% in supercritical cycles with high critical pressure fluids). In this case, the pump efficiency is a crucial parameter and the component

has to be carefully designed in order to achieve high cycle efficiency. The effect is even more pronounced for small size application where the pump efficiency is greatly penalized.

3.1.4 Generators, gear boxes, and power electronic systems

The generator converts mechanical power into electricity; it usually rotates at grid frequency and it is directly connected to the expander. However, in the ORC field, the variability of working fluids and applications leads to expanders having very different optimal rotational speeds. Large plants usually require slow machines while micro ORCs require superfast radial inflow turbines. In the first case, it is possible to use a generator rotating at 1500, 1000, or 750 RPM depending on the number of pole pairs. Alternatively, a gear box can be used between the turbine shaft and the generator shaft. The same component can be used for applications that require a fast turbine but above certain gear ratio the use of the gear box is not convenient because of the high mechanical losses. For very high optimal rotational speed, the generator is usually directly connected to the turbine and it produces electric power with a frequency higher than the grid one; an AC/DC + DC/AC power conditioning system is eventually used to correct the frequency.

3.1.5 Noncondensable gas removal

The pressure in the condenser can be above or below the ambient pressure depending on the critical properties of the fluid and on the condensation temperature. Once the thermodynamic condition at turbine inlet are fixed, the reduction of the condensing pressure generally leads to a higher power production with advantages for cycle performances but, on the other hand, it entails a larger condenser surface, a more complex turbine and a higher auxiliary consumption with a nonunivocal effect on the plant economics. Generally, in the ORC field, the working fluid and the cycle parameters are selected in order to avoid very low condensing pressure but in some cases a high vacuum in the condenser may be profitable in spite of air leakage concerns. The increase of noncondensable gases in the condenser leads to a progressive increment of the back pressure of the turbine with detrimental effects on the power output. Furthermore corrosive phenomena may occur in the high temperature plant sections because of the high oxygen content. In common steam cycles, a deaerator is used to remove noncondensable gases, with a stream of superheated steam taken from the turbine; gases and vapor are vented to the atmosphere from the top of the stripping column. In the ORC field however, a deaerator cannot be used because organic fluids cannot be released into the environment due to: (i) their high Global Warming Potential (GWP); (ii) safety reasons related to their flammability or toxicity; (iii) or their relevant cost. If the condensing pressure is below the ambient one, devices for the removal of noncondensable gases are required. A common solution is to use a vacuum pump that removes a mixture of organic fluid vapor and noncondensable gases from the condenser shell as reported in Fig. 3.7(a). The mixture can flow through a treatment unit formed by activated carbon filters that absorbs the organic molecules. Alternatively, for big plants or

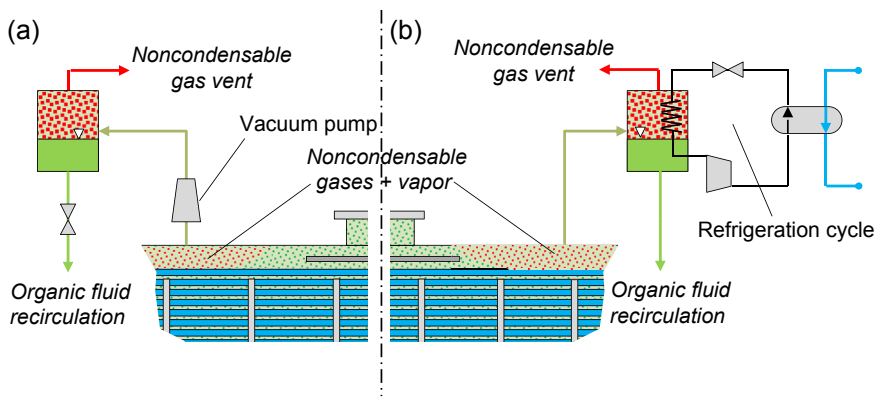


Figure 3.7 Schematic representation of two noncondensable gas removal systems with (a) a vacuum pump and with (b) a refrigeration cycle.

for expansive fluids, it is important to limit the working fluid loss; in this case the organic fluid–air mixture flows into a vessel and the liquid phase is separated from the vapor. Because of the higher pressure, the liquid is more concentrated in the organic fluid while the vapor phase has a high content of noncondensable gases. Liquid is recirculated into the condenser while gases are vented. An alternative solution (see Fig. 3.7(b)) is to use a batch system formed by a vent valve that convoys a mixture of vapor and gas into a vessel where a refrigeration cycle is used to reduce the temperature. The liquid vapor equilibrium is obtained again with a larger concentration of noncondensable gases in vapor phase that are vented while the almost pure organic fluid in liquid phase is recirculated.

3.1.6 Balance of plant and instrumentation

Balance of Plant (BOP) includes all the components required to complete the installation and to operate the plant. The piping between the components, the valves, the bypass connection, and the instrumentation are part of the BOP, and their cost can be a considerable share (25–30%) of the equipment cost.

Instrumentation is required to control the plant, to characterize the performance of components, and to plan maintenance. It would be good practice to ensure that pressure and temperature measures are available at the inlet and outlet section of each component, with the aim of monitoring the heat transfer coefficients of the heat exchangers and the efficiency of the expander during operation.

3.2 Plant layouts

In the ORC field, only a few plant layouts are commonly used on the market while other configurations are proposed in the scientific literature for specific applications. ORC cycles can be divided into two main categories, namely *single pressure level*

cycles and *multi pressure levels cycles*; *single pressure level cycles* can be further divided into *subcritical* and *supercritical* (or *transcritical*) cycles, while only subcritical configurations are adopted for *multi pressure levels cycles*. Besides these two main groups, two other cycles are the triangular cycle and the complete flash cycle, which are proposed mainly for solar power applications.

3.2.1 Single pressure level cycles

The single pressure level cycle is the simplest plant layout and it requires a small number of components: a pump, a PrHE, a turbine, and a condenser. A recuperator is optional and it is used when it is not possible to cool the heat source down to ambient temperature due to technical reasons. In Fig. 3.8, the basic plant layout for a recuperative single level cycle is presented. Fluid in saturated liquid condition (1) is extracted from the condenser (a) hotwell and its pressure is increased by a pump (b) to the maximum cycle pressure (2). If a recuperator (c) is present, fluid is heated up by cooling down the hot fluid discharged by the turbine (7). Working fluid enters the PrHE (3) where it absorbs heat from the heat source. Depending on the size of the plant, the configuration, and the working fluid, the PrHE can be formed by a single once-through heat exchanger or by different units. In particular, if the cycle is a supercritical

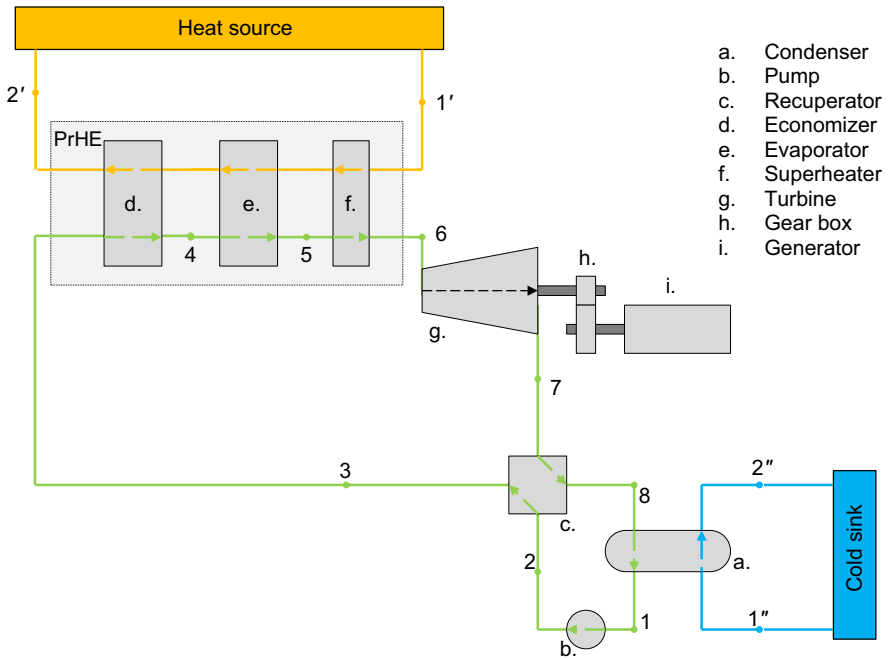


Figure 3.8 Plant layout for a single pressure level cycle. A once-through Primary Heat Exchanger is used for supercritical cycles while for subcritical cycles a division between economizer, evaporator, and superheater is usually adopted.

one or if a mixture of fluid is used, the once-through heat exchanger is the only option; conversely, for big subcritical power plants a physical division in economizer (d), evaporator (e), and possibly superheater (f) is usually adopted. After the turbine control valve, the high pressure and high temperature fluid (6) is expanded in a turbine (g) or in a volumetric expander down to a pressure slightly higher than the condensation one. Mechanical work is extracted and converted into electrical power by the generator (i), which is connected to the turbine shaft. If the rotational speed of the turbine is different from the grid frequency, a generator with a number of pole pairs greater than one, a gear box (h), or a power electronic system can be adopted. Expanded fluid possibly flows through the recuperator and it is eventually condensed.

Its simplicity and attainable efficiencies make this kind of cycle the first option for many different applications, from geothermal to solar energy, from waste heat recovery to biomass combustion. This configuration is divided into two families based on the same plant layout, but notably different in maximum attainable efficiency and leveled costs of electricity; these families are the subcritical and the supercritical cycles.

3.2.1.1 Subcritical cycles

A subcritical cycle has a maximum pressure that is lower than the critical one. Working fluid passes through an evaporation process that is isothermal if the fluid is a pure compound or it presents the characteristic glide in temperature if a blend is used. Subcritical cycles are the most common configuration for large geothermal binary plants with low brine temperatures, for biomass combustion, in Waste Heat Recovery (WHR) applications and domestic cogeneration. If the working fluid has a critical temperature higher than the heat source maximum temperature, the use of superheating is generally detrimental since it entails a reduction of the working fluid mass flow rate and the power production. In this case, the saturated cycle is the optimal solution from both a thermodynamic and economic point of view (Astolfi et al., 2014a,b). On the contrary, if a low critical temperature fluid is used, superheating is strongly recommended because it allows an increase in the average temperature in the heat introduction process without limiting the exploitation of the heat source. The design of the superheater needs to be carefully optimized in order to effectively reduce the plant LCOE. Generally, high critical temperature fluids are preferable while low critical temperature fluids are used when there is the necessity to maintain a condensing pressure higher than the ambient one or if limitations in both the volumetric flow rate and the expansion volume ratios are present. Fig. 3.9 depicts the Temperature-Heat (T-Q) and the Temperature-specific Entropy (T-s) diagrams for a slightly superheated subcritical cycle working with pentane fluid.

Depending on the heat source, each component in Fig. 3.8 can be formed by different components in series or parallel. Fig. 3.10 depicts an ORC for onboard WHR in the automotive sector, in subcritical configuration. Truck engines have efficiencies of around 30–35% and many automotive WHR studies aim to considerably reduce fuel consumption. Engines release heat into the environment from different components, namely the Exhaust Gases Recirculation (EGR), the Charge Air Cooler (CAC), and the Exhaust flue gas Cooler (EC). Each stream is characterized by heat

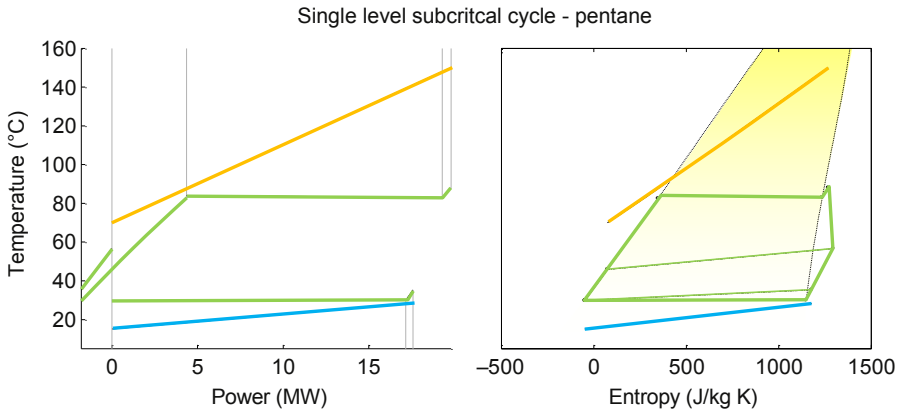


Figure 3.9 T-Q diagram (left) and T-s diagram (right) for a subcritical recuperative cycle with pentane.

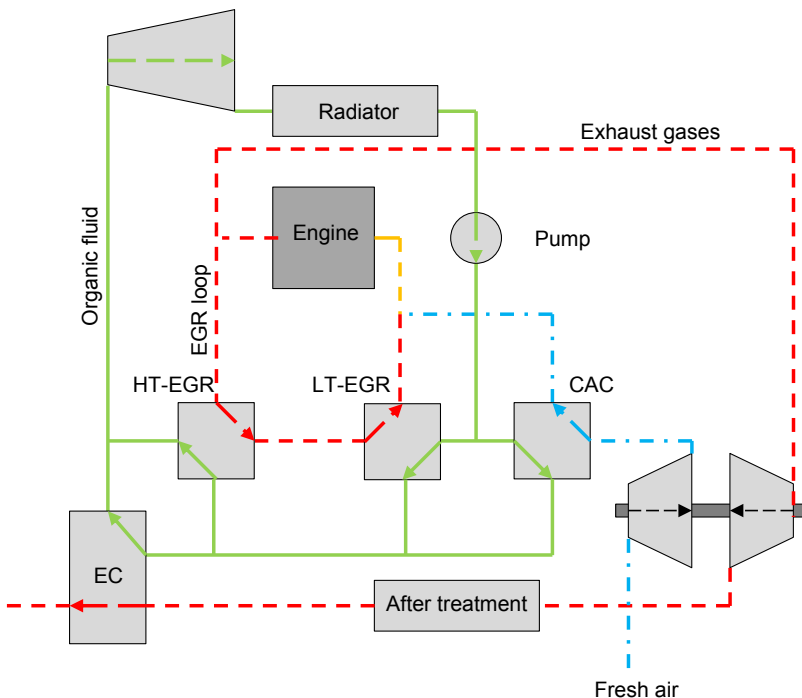


Figure 3.10 Plant layout for a single pressure level cycle Organic Rankine Cycle (ORC) integrated with a truck engine able to recover heat from the Exhaust Gases Recirculation (EGR), the Charge Air Cooler (CAC), and the Exhaust flue gas Cooler (EC) heat exchangers. Figure rearranged from Teng, H., Regner, G., Cowland, C., 2007. Waste heat recovery from heavy duty diesel engines by Organic Rankine Cycle. Part I: hybrid energy systems of diesel and rankine engines. In: SAE Technical Papers.

available at different temperatures. An ORC can be suitable to recover heat from all of these streams using two economizers and two evaporators in parallel and releasing heat to the environment with a radiator.

3.2.1.2 Supercritical cycles

A supercritical or transcritical cycle is a cycle with a maximum pressure higher than the critical one. Working fluid is heated up from subcooled liquid to superheated vapor with a smooth transition above the critical point. The phase change is gradual and all the physical and thermodynamic properties vary without discontinuity in the heat introduction process.³ Supercritical cycles are interesting because they can achieve a higher efficiency compared to the subcritical ones if a finite heat capacity source is available. With a proper selection of the working fluid and a correct optimization of cycle parameters, it is possible to obtain a heating curve that matches the variable temperature heat source, reducing the overall logarithmic temperature difference and the efficiency losses due to heat introduction process with finite temperature differences. Fig. 3.11 depicts the T-Q and the T-s diagrams for a supercritical cycle working with R134a and it is possible to appreciate the strong reduction of temperature difference in the PrHE compared to the subcritical case.

Despite the higher attainable efficiencies, supercritical cycles generally have higher pressures than the subcritical cycles and more expensive devices are required. Multi-stage centrifugal pumps are used because of the higher cycle pressure, and their efficiency should be carefully considered because their power consumption can be a relevant share of the gross power production (up to 30% in supercritical cycles with

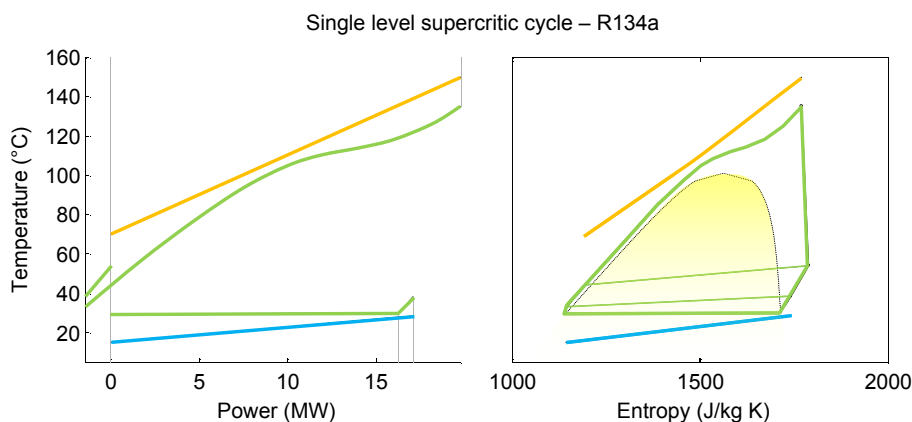


Figure 3.11 T-Q diagram (left) and T-s diagram (right) for a supercritical cycle working with R134a.

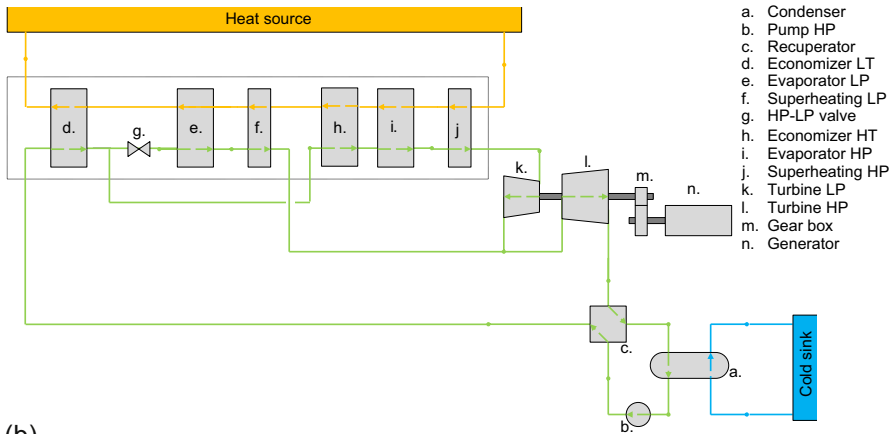
³ For low complexity fluids a large fraction of the heat is introduced in proximity of the critical point where the specific heat shows a marked peak. Supercritical transition is instead more smooth for high complexity fluids characterized by similar values of specific heat in liquid and vapor phase.

high critical pressure fluids). Furthermore, the cost of the heat exchanger is increased because of the higher thickness of metal, especially in geothermal applications where the working fluid is placed in the shell side. Supercritical cycles are studied in several publications (Zhang and Jiang, 2012; Walraven et al., 2012; Saleh et al., 2011; Karellas and Schuster, 2008; Shengjun et al., 2011; Guo et al., 2011), mainly for geothermal applications and heat recovery from industrial processes where the glide in temperature of heat source is compatible with the shape of a supercritical transition. Experimental activities have been performed in Livorno by Enel, Turboden, and Politecnico di Milano on a 500 kW_{el} supercritical cycle with R134a for geothermal applications (Astolfi et al., 2013). The experimental activity has demonstrated the great flexibility of this kind of cycle with a really stable operation. Off-design is controlled by varying the speed of revolution of the pump and it has been demonstrated that the cycle is able to smoothly switch from a supercritical to a subcritical operation according to the heat source maximum temperature and mass flow rate without showing instability. Another example is the cycle proposed by Exergy (Spadacini et al., 2011) which is a 1 MW_{el} high efficiency supercritical cycle for heat recovery or biomass combustion application. The particular features of this cycle are the use of an innovative radial outflow turbine and the use of PP1 as a working fluid which is a high complexity perfluorinated fluid never used before in the ORC field. The last example is the 7.5 MW WHR ORC designed by Mistral and installed at the foothills of the Rocky Mountains; heat is recovered from a gas turbines installed in a natural gas pipeline pumping station it drives a butane supercritical cycle with a maximum temperature of 250°C and pressure of 45 bar. A customized two-stage Atlas Copco turboexpander with the two wheels rotating at different velocities is used in this plant in a very advanced configuration.

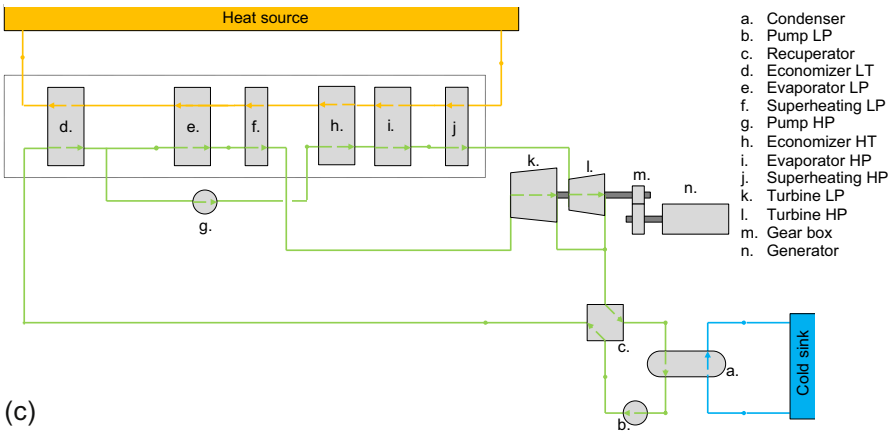
3.2.2 Multi pressure levels cycles

This kind of cycle is so far rarely adopted even if it can achieve higher efficiency compared to subcritical single level cycles and it performs similar to the supercritical ones. The adoption of two (or more) pressures of evaporation allows a better match between the temperature profiles in the PrHE but it requires a more complicated plant layout and a more expensive equipment (two turbines, larger heat transfer surfaces, etc.). Due to this reason they are proposed only in particular applications where the efficiency of power conversion is extremely important or the fixed cost of heat source greatly overcomes the cost of the power block. An example of applications where two or more pressure level cycles might be profitable are deep geothermal reservoirs with high exploration and drilling costs, and industrial waste heat recovery from plants like cement and steel production industries. In this last field, power outputs can be large as 10 MW_{el}, and ORCs must compete with steam Rankine cycles. From a general point of view, a two pressure level cycle can be arranged in many different configurations. Fig. 3.12 depicts three different plant layouts but others can be obtained by combining different PrHE configurations and turbine arrangements. In the plant layout on Fig. 3.12(a), the fluid is pumped to the cycle maximum pressure and, after the recuperator, it flows into a low temperature economizer where it is heated up to a temperature

(a)



(b)



(c)

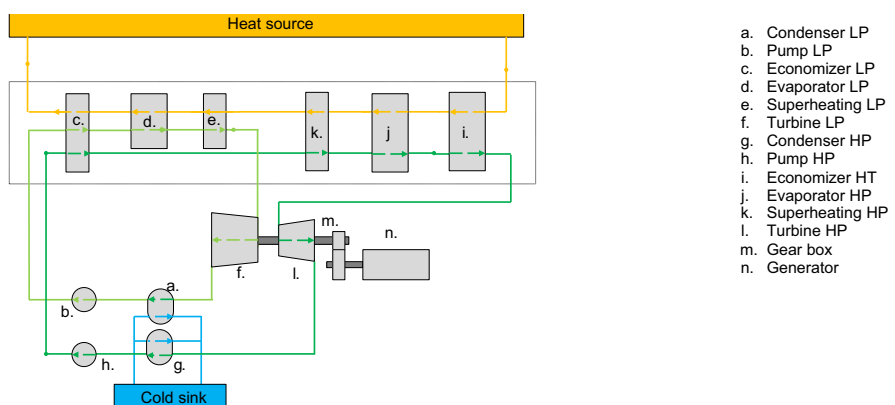


Figure 3.12 Plant layout schemes for three generic two pressure levels cycles: (a) single pump and turbines in series, (b) two pumps and turbines in parallel, (c) tandem configuration.

close to the low temperature evaporation level. The total mass flow rate is hence divided into two streams: one flows in the high temperature economizer and it is eventually evaporated at high pressure while the other flows through an isenthalpic valve where its pressure is reduced down to the low pressure level. Superheating can be present on both evaporation levels instead of using a saturated vapor turbine admission. Turbines are arranged in series. Radial outflow turbines present a particular advantage in the case of two or more pressure levels. Thanks to the increasing radius, they can handle the increasing flow rate with fewer difficulties than axial turbines; prismatic blades can be used and both high pressure and low pressure stages are on the same disc. More details about this configuration are reported in Chapter 11. In the plant layout in Fig. 3.12(b) two different pumps are used, the first one pumps the whole mass flow rate up to the low evaporation level pressure while the other increments the pressure only of the fluid going to high temperature level. With respect to the first solution, more expensive equipment is used, with the advantage of a more precise plant control. In this case, turbines are arranged in parallel and streams are mixed before entering into the recuperator; this configuration can be profitable for big power plants where it is difficult to handle the whole low pressure volume flow rate in a single machine. Finally, Fig. 3.12(c) depicts the *tandem configuration* basically formed by two separated single level cycles working with different evaporation temperatures and with turbines mounted on the same shaft. This configuration is more expensive than the previous ones because of the need for more components but it has the advantage of independently controlling the two cycles. A comparison between the one level and the two pressure level cycles for geothermal application is reported in Chapter 7.

The T-Q and the T-s diagrams for two cycles differing in turbines arrangement are shown in Fig. 3.13.

3.2.3 Trilateral cycles

Other cycle configurations are proposed in the literature in order to further increase the plant efficiency. These cycles try to reproduce as closely as possible, the ideal Lorentz cycle. The cycle closest to the ideal cycle is a triangular cycle with a two phase flow expansion starting from a saturated liquid condition (Smith, 1993, 1994). Heat capacity of the working fluid is almost constant because heat is introduced in conditions far from

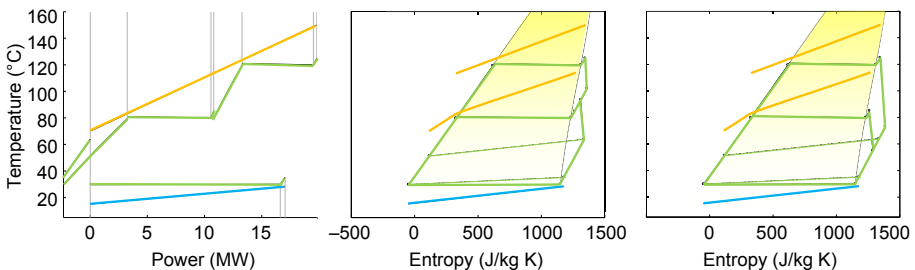


Figure 3.13 T-Q diagram for a pentane two pressure levels cycle for geothermal applications, T-s diagrams with turbines in series and parallel configurations.

the critical point thus entailing the possibility to maintain an almost constant temperature difference in the whole PrHE. The idea is fascinating but it entails a number of difficulties that are mainly related to the expander design and operation. The first problem is related to two phase flow expansion with a presence of droplets of liquid which causes the erosion of metal surfaces and limits the peripheral speed. Screw expanders are the suggested components for this kind of applications; they are widely studied for HVAC applications to replace the lamination valve and to increase the COP of the cycle. Experimental activities carried out so far have pointed out some technical limits in their use but they are currently commercialized by Helies Power [<http://www.heliexpower.com/>] for steam applications. More details about their architecture, their operation, and the maximum attainable efficiencies are discussed in Chapter 12. The other limit is related to the small built in volume ratio of common volumetric expanders and thus the low maximum temperatures attainable with this cycle; the working fluid must be selected taking this aspect into account. Furthermore, it is crucial to use fluids with a critical temperature close to the maximum temperature of the cycle in order to increase the density of the saturated vapor resulting from the flash stage. These constraints entail that the flash trilateral cycles are suitable for the exploitation of medium–low temperature heat sources using a small–medium complexity fluid.

With the aim of exploiting heat sources with a relevant temperature variation, the overall expansion can be divided into more than one device. Screw expanders difficulty handle two phase flow at the intake port because of the phase stratification which leads to a noncorrect feeding of the device. A proposed solution consists in an almost triangular two pressure levels cycle (Smith et al., 2005). This plant layout is reported in Fig. 3.14; the working fluid is expanded from a condition close to saturated liquid at

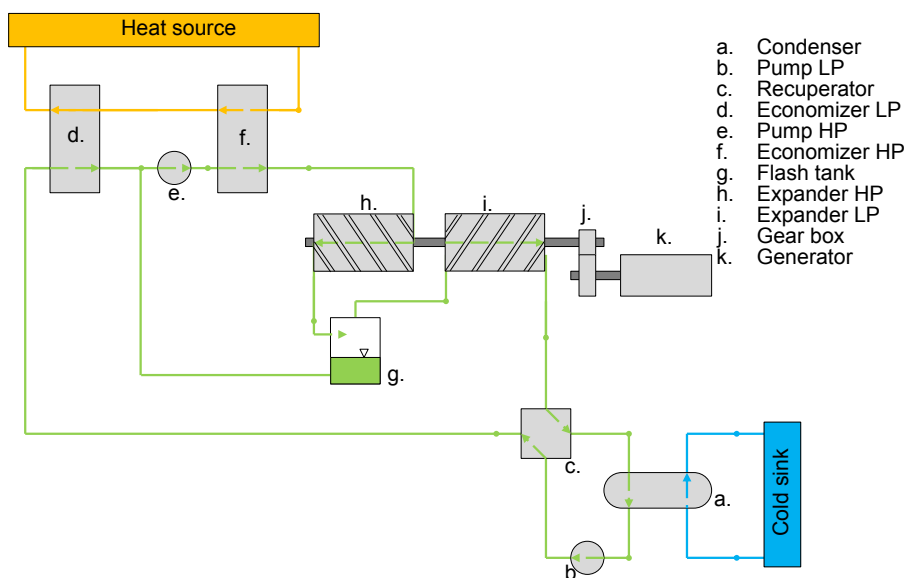


Figure 3.14 Plant layout scheme of a flash trilateral cycle as proposed by Smith (1993).

the maximum cycle temperature by a high pressure screw expander that discharges a two phase fluid with a vapor content function of fluid complexity and expansion pressure ratio. A flash stage is hence required to separate the vapor from the liquid phase. Vapor is expanded from saturated condition down to the condensing pressure, it flows possibly in a recuperator and it is eventually condensed. Liquid from the condenser hotwell is pumped to a pressure greater than the flash one; it is heated in a low temperature economizer and mixed with the liquid coming from the flash stage. The high pressure pump feeds the high temperature economizer where fluid is brought again close to saturated liquid conditions.

This cycle allows the exploitation of a variable temperature heat source, minimizing the entropy generation in the heat introduction process and thus achieving higher efficiencies. Despite the good potential of this plant layout, a number of issues have to be faced and this solution is far from to be available on the market. The T-Q and the T-s diagram for the flash trilateral cycle are reported in Fig. 3.15.

Finally a Complete Flashing Cycle (CFC) is proposed (Casati et al., 2013) with the aim to approximate a trilateral cycle in high temperature applications, for example solar energy exploitation using advanced solar collectors. This cycle generally uses a high complexity fluid like a siloxane or a long chain hydrocarbon exploiting the overhanging shape of the Andrews curve. For these fluids, lamination from saturated liquid to saturated vapor conditions is almost isentropic and it results in small temperature and pressure drops. The T-s diagram is reported in Fig. 3.16; heat is introduced to the fluid in the liquid state up to a temperature close to the saturated one where it is throttled, crossing the two phase region and reaching a saturated vapor or a slightly superheated vapor condition. Fluid expands in a turbine, it flows in the recuperator, and it eventually condenses.

Eventually, an interesting characteristic of this class of cycles is represented by the possibility to design solar power plants with the working fluid flowing directly into the solar field. The working fluid during the heating process is always liquid and so it can be easily handled in conventional solar collectors; DSG collectors are not required,

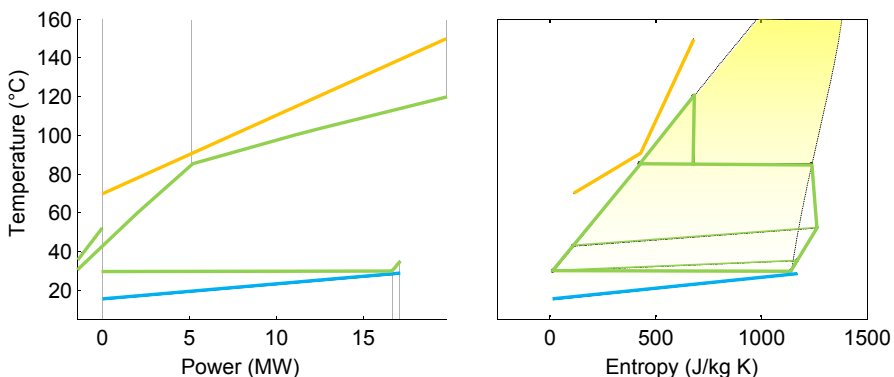


Figure 3.15 T-Q and T-s diagrams for the flash trilateral cycle.

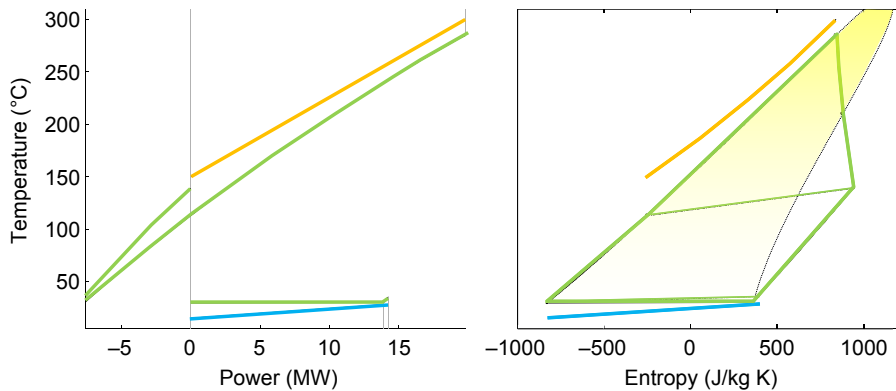


Figure 3.16 Throttled admission Complete Flashing Cycle (CFC) cycle for high temperature applications.

limiting the issues related to an increase of pressure drops, thicker and more expensive collector tubes, and additional hazard protections due to the presence of high pressure vapor in the solar field. Furthermore, heat storage can be realized directly with the hot working fluid. The most suitable solution is a solid medium heat storage formed by a vessel filled with rocks or small metal balls ([Herrmann et al., 2002](#)); in charging mode, hot fluid enters the heat storage tank from the top, it flows in the gaps between the particles heating the solid medium. In discharging mode, the flux is inverted and heat is released to the working fluid. The main advantage of this solution is the reduced amount of fluid compared to the conventional two tanks storage or liquid thermocline storage with considerable economic benefits considering the high cost of organic fluids. [Fig. 3.17](#) depicts the basic layout for the CFC while an example of the use of this concept for small and low temperature solar plant is reported in [Astolfi \(2015\)](#).

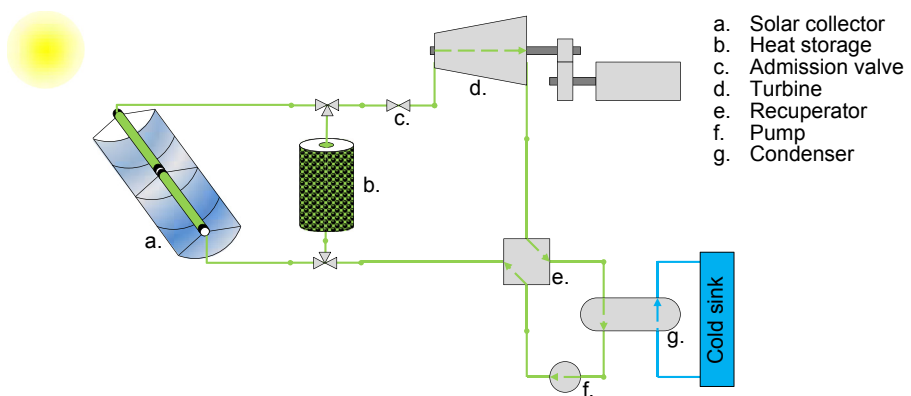


Figure 3.17 Direct CSP plant based on a Complete Flash Cycle; the working fluid is used in both the solar field and the thermal storage.

3.3 Use of mixtures versus pure fluids

In some applications, the use of a mixture of fluids instead of a pure fluid allows obtaining a higher efficiency and a higher power production thanks to the minimization of irreversibilities of the heat transfer process under finite temperature differences. The main effect in using mixtures is represented by a phase transition process which is isobaric but not isothermal. A certain increment in temperature is obtained during evaporation while the temperature decreases in condensation. This peculiarity allows reducing the temperature difference in both the PrHE and the condenser thus reducing the second law losses in these components with an overall increase of net power production as shown in the two T-Q diagram in Fig. 3.18. The nonisothermal phase transition can be explained considering an isobaric Vapor–Liquid Equilibrium diagram for a general mixture where a low boiling temperature fluid A is mixed with a high boiling temperature fluid B⁴ as reported in Fig. 3.18. The bubble line represents the locus of temperatures at which the first bubble of fluid is formed while the dew point is determined by the formation of the first drop. The values of T_{dew} and T_{bubble} are the same at the two extremities namely for pure A or pure B component, in the rest of the VLE diagram instead the two temperatures are different and the gap between them represents the temperature glide during phase transition.⁵

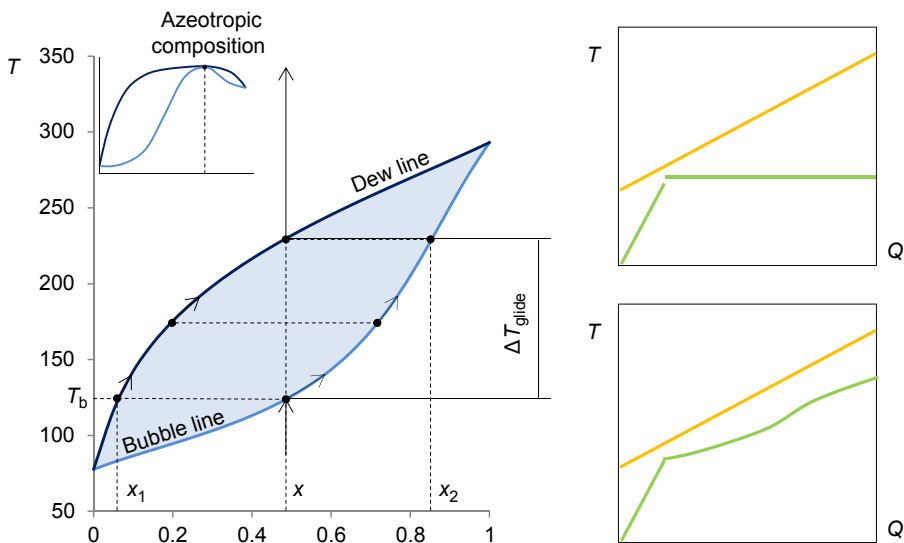


Figure 3.18 VLE diagram for a binary mixture and T-Q diagrams for pure fluid (top) and mixture (bottom).

⁴ With reference to an isobaric VLE diagram the high boiling temperature fluid is the compound with the higher saturation temperature thus the fluid which is less volatile. For isothermal VLE, the more volatile fluid shows the higher saturation pressure.

⁵ An exception is the presence of an azeotropic point which entails no differences in composition between the vapor phase and the liquid phase. These points are not interesting from this point of view.

The temperature glide during phase transition depends on the nature of the fluids and on the composition; high temperature glides can be obtained for a mixture of fluids having noticeably different critical temperatures or fluids of different chemical classes. As explained in Chapter 7, the huge number of fluid combinations and the mixture composition are additional variables for the optimization process, leading to a problem that cannot be faced with an enumerative approach. A preselection among the available mixtures is always required, checking miscibility, verifying the trends of VLE data in the range of temperature of interest, and finding information about the chemical stability of the blend. The use of mixtures of fluids in ORC systems is investigated in some papers (Chang et al., 2012; Brüggemann et al., 2012; Colonna and Angelino, 1998) that aim at highlighting the potential advantage of a nonisothermal phase transition in efficiency increase.

Despite the advantages achievable with mixtures, their use as working fluid in binary ORCs is still extremely limited because of a number of difficulties which make these solutions less practical and affordable than the use of a pure fluid. The main issues are related to fluid composition variation and limitation of film transfer coefficients.

- *Composition variation*: if a leakage of fluid occurs, the vapor which is vented to the environment has a concentration of the more volatile component higher than the nominal one and so a differential refill is required in order to restore the original composition. This requires additional cost for the fluid analysis, a more expensive fluid storage area, and possible malfunctioning of the plant if the leakage is not rapidly revealed.
- *Reduction of heat transfer coefficient*: the film transfer coefficients in phase transition are lower for mixtures than for pure fluids (Bivens and Yokozeki, 1992; Gu and Bart, 1999). By using mixtures, it is possible to reduce the ΔT_{min} in the heat exchangers thus increasing the UA parameter respect to an isothermobaric process. In addition, the overall heat transfer coefficient U is smaller leading to a more marked increase of the heat exchanger surface. A reduction of U close to $\sim 30\%$ was obtained for a toluene–methanol mixture using Aspen software and Huron Vidal mixing rules. For any new mixture a detailed bibliographic review is required but, unfortunately, there is a very little availability of experimental data on transport properties, which entails relevant difficulties in a reliable estimation of heat exchangers cost.

Please refer to Chapter 4 for further details regarding fluid and mixture thermophysical and transport property calculations.

References

- Astolfi, M., Bini, R., Macchi, E., Paci, M., Pietra, C., Rossi, N., Tizzanini, A., 2013. Testing of a new supercritical ORC technology for efficient power generation from geothermal low temperature resources. In: Rotterdam: 2nd International Seminar in ORC Power Systems.
- Astolfi, M., Romano, M., Bombarda, P., Macchi, E., 2014a. Binary ORC power plants for the exploitation of medium-low temperature geothermal sources. Part A thermodynamic optimization. *Energy* 66.

- Astolfi, M., Romano, M., Bombarda, P., Macchi, E., 2014b. Binary ORC power plants for the exploitation of medium-low temperature geothermal sources. Part B techno-economic optimization. *Energy* 66 s.l.
- Astolfi, M., 2015. Techno-economic Optimization of Low Temperature CSP Systems Based on ORC with Screw Expanders. *Energy Procedia* 69 s.l.
- Brüggemann, D., Heberle, F., Preißinger, M., 2012. Zeotropic mixtures as working fluids in Organic Rankine Cycles for low-enthalpy geothermal resources. s.l. *Renewable Energy* Vol. 37.
- Bivens, D.B., Yokozeki, A., 1992. Heat Transfer of Refrigerant Mixtures. Purdue: s.n.
- Casati, E., Galli, A., Colonna, P., 2013. Thermal energy storage for solar-powered organic Rankine cycle engines. *Solar Energy* 96 s.l.
- Chang, K.C., Baik, Y.J., Lee, Y.S., Yoon, H.K., Kim, M., 2012. Power enhancement potential of a mixture transcritical cycle for a low-temperature geothermal power generation. s.l. *Energy* Vol. 47.
- Colonna, P., Angelino, G., 1998. Multicomponent Working Fluids For Organic Rankine Cycles (ORCs). s.l. *Energy* Vol. 23.
- Colonna, P., Casati, E., Trapp, C., Mathijssen, T., Larjola, J., Turunen-Saaresti, T., Uusitalo, A., 2015. Organic Rankine cycle power systems: from the concept to current technology, applications and an outlook to the future. *Journal of Engineering for Gas Turbines and Power* 137 s.l.
- Atlas Copco. (Online) www.atlascopco.com.
- ElectraTherm. (Online) electratherm.com.
- Exergy. (Online) www.exergy-orc.com.
- GE, Calnetix. <http://www.calnetix.com>.
- Gu, J., Bart, H.-J., 1999. Decrement Estimation of the Heat Transfer Coefficient in Mixture Boiling. s.l. *The Canadian Journal Of Chemical Engineering* Vol. 77.
- Guo, T., Wang, H., Zhang, S., 2011. Comparative analysis of natural and conventional working fluids for use in transcritical Rankine cycle using low-temperature geothermal source. *International Journal of Energy Research* 35.
- Herrmann, U., Geyer, M., Kearney, D., 2002. Overview on thermal storage systems. s.l.: FLABEG Solar Int. GmbH. In: Workshop on Thermal Storage for Trough Power Systems.
- Kakac, S., 1991. Boilers, Evaporators and Condensers. Wiley & Sons s.l.
- Kakac, S., 2002. Heat Exchangers Selection, Rating and Thermal Design, second ed. CRC press. s.l.
- Karellas, S., Schuster, A., 2008. Supercritical fluid parameters in organic Rankine cycle applications. *International Journal of Thermodynamics* 11.
- Lecompte, S., Huisseune, H., van den Broek, M., Vanslambrouck, B., De Paepe, M., 2015. Review of organic Rankine cycle (ORC) architectures for waste heat recovery. *Renewable and Sustainable Energy Reviews* 47, 448–461. <http://dx.doi.org/10.1016/j.rser.2015.03.089>.
- LU-VE, 2013. Dry and Spray Catalogue. LU-VE Contardo s.l.
- Ormat. (Online) www.ormat.com.
- Saleh, B., Koglbauer, G., Wendland, M., Fischer, J., 2011. Working fluids for low-temperature organic Rankine cycles. *Applied Thermal Engineering* 31.
- Shengjun, Z., Huaixin, W., Tao, G., 2011. Performance comparison and parametric optimization of subcritical Organic Rankine Cycle (ORC) and transcritical power cycle system for low-temperature geothermal power generation. *Applied Energy* 88 s.l.
- Smith, I.K., Stosic, N., Kovacevic, A., 2005. An improved system for power recovery from higher enthalpy liquid-dominated fields. *Proceedings World Geothermal Congress* 28 s.l.

- Smith, I.K., 1993. Development of the trilateral flash cycle system Part 1: fundamental considerations. Proceedings of the Institution of Mechanical Engineers Part A: Journal of Power and Energy 207 s.l.
- Smith, I.K., 1994. Development of the trilateral flash cycle system Part 2: increasing power output with working fluid mixtures. Proceedings of the Institution of Mechanical Engineers, Part A: Journal of Power and Energy 208 s.l.
- Spadacini, C., Centemeri, L., Xodo, G.L., Astolfi, M., 2011. A new configuration for Organic Rankine Cycle power systems. In: Delf: 1st International Seminar on ORC Power Systems. TEMA, 2007. Tema Standards – The Ninth Edition.
- Teng, H., Regner, G., Cowland, C., 2007. Waste heat recovery from heavy duty diesel engines by Organic Rankine Cycle. Part I: hybrid energy systems of diesel and rankine engines. In: SAE Technical Papers.
- Turboden. (Online) www.turboden.eu.
- Walraven, D., Laenen, B., D'haeseleer, W., 2012. Comparison of Thermodynamic Cycles for Power Production from Low-temperature Geothermal Heat Sources. Energy Conversion and Management s.l.
- Zhang, F.Z., Jiang, P.X., 2012. Thermodynamic analysis of a binary power cycle for different EGS geofluid temperatures. Applied Thermal Engineering 48, 476–485 s.l.

Organic fluids for Organic Rankine Cycle systems: classification and calculation of thermodynamic and transport properties*

I.H. Bell, E.W. Lemmon

National Institute of Standards and Technology, Boulder, CO, United States

4.1 Overview of thermophysical properties of fluids and their application to Organic Rankine Cycle systems

In Organic Rankine Cycles (ORC), thermodynamic and transport properties (collectively thermophysical properties) are needed in all aspects of the design process, from fundamental cycle analysis, through design of heat exchangers and working components, to detailed dynamic modeling of expansion devices. Without accurate models for the thermophysical properties of the fluid(s) in use, none of the other modeling can proceed.

In order to analyze the cycle performance (efficiency, power generation, etc.) of the classical four-component ORC (evaporator, expander, condenser, and pump) with simplified component models, transport properties are not needed. In order to carry out any cycle analysis, the thermodynamic properties of the working fluid must be well characterized with an equation of state (EOS) of reasonable accuracy, as described in the following sections. Furthermore, if it is desired to carry out detailed analyses of the components in the cycle, transport properties are required.

In this chapter, first a discussion of the modeling of the thermodynamic properties of pure fluids is carried out, followed by the modeling of the thermodynamic properties of mixtures, and finally, analyses are presented for the modeling of the transport properties of both mixtures and pure fluids. We close with a discussion of interpolation methods and their use to obtain significant increases in computational speed.

* Contribution of NIST, an agency of the US government; not subject to copyright in the United States.

4.2 Classification of fluids

ORCs have a number of different types of heat sources and sinks, working fluids, and cycle configurations. A number of different types of fluids can be found in these systems:

- Heat transfer fluids (such as water, oils, gaseous fluids or mixtures, or aqueous solutions).
- Brines (as the heat source in geothermal systems).
- Humid air (as the source fluid and/or sink fluid for the ORC system).
- Molten salts (for instance in solar power tower systems).
- Pure working fluids [such as *n*-pentane or hydrofluoroolefins (HFO)]
- Mixtures of fluids as the working fluid (such as mixtures of hydrocarbons, mixtures of HFO, etc.)

The analysis described here focuses on pure fluids and mixtures, as the models used for these fluids are the most complex to evaluate. For the other fluids (aside perhaps from humid air), the models used to evaluate their properties are quite simple, as they are often implemented as polynomials in temperature.

One of the motivations for the use of mixtures in an ORC is to better match the temperature glide between the heat source stream, heat sink stream, and the working fluid, in order to reduce heat transfer irreversibilities. For instance, if the heat source and sink streams are water or air, they exhibit a change in temperature (temperature glide) as they absorb or reject heat (but without changing phase from gas to liquid or vice versa). A pure fluid experiences no change in temperature as it evaporates or condenses at constant pressure, while many mixtures have a temperature glide as they change phase (evaporation or condensation) at constant pressure. Proper selection of the mixture can allow for an improvement in the matching of temperature profiles, a decrease in the heat transfer irreversibilities, and an increase in the system efficiency of 20% as shown in one study ([Heberle and Brüggemann, 2015](#)).

4.3 Thermodynamic properties of pure fluids

4.3.1 Equations of state

An EOS is used to describe the relationship between thermodynamic properties. It can be written in a number of different formulations or based on a number of sets of different independent variables. Any two independent variables could be used in the EOS, but the most convenient set of independent variables are temperature and pressure as they are easily measureable quantities. Practical concerns generally result in the use of temperature and density as the independent variables of equations of state, as described below.

4.3.2 Ideal-gas equation of state

Those with a recollection of their first chemistry class will remember their first contact with equations of state, that of the ideal-gas law. This EOS is quite simple to

implement and understand, it gives the relationship between pressure, temperature, and density for an ideal-gas in the limit of zero pressure; in this limiting case, the molecules of gas are entirely noninteracting. This EOS is given by

$$p = \rho RT$$

where p is the pressure in Pa, R is the ideal-gas constant in J/mol/K, and ρ is the molar density in mol/m³. Alternatively, the compressibility factor Z ($Z = 1$ for an ideal-gas) can be written as

$$Z = \frac{p}{\rho RT}.$$

This form is introduced for extension to the more complex equations of state.

4.3.3 Cubic equation of state

While ideal-gas equations of state are quite adequate for technical purposes in the low-pressure dilute gas phase, they cannot be used to model vapor–liquid equilibria, properties in the liquid phase, or gaseous properties near the critical point. For these needs, cubic equations of state were developed, with the earliest being that of [van der Waals \(1873\)](#), which can be expressed as

$$p = \frac{RT}{V - b} - \frac{a}{V^2}.$$

where a is an attractive parameter and b is the excluded volume. Other authors in the following decades (in fact, continuing to today) attempted to overcome some of the known limitations of the van der Waals EOS. Two of the cubic equations of state that have stood the test of time and have found wide usage are those of Peng–Robinson ([Peng and Robinson, 1976](#)) and Soave–Redlich–Kwong ([Soave, 1972](#)).

The Peng–Robinson (PR) and Soave–Redlich–Kwong (SRK) equations of state represented a significant step forward in the representation of the phase behavior of pure fluids, but they too have known limitations. While they fare well for vapor–liquid equilibria, in the liquid phase, the SRK EOS yields predictions for liquid densities that are in error by as much as 30% for polar fluids like water (at 298 K and 0.1 MPa). For that reason, more-accurate multiparameter equations of state were developed over the last few decades.

4.3.4 Multiparameter fundamental equation of state

To achieve higher fidelity predictions of the thermodynamic properties of pure fluids, covering the entire fluid surface from dilute gas to the melting line, multiparameter equations of state were developed. These multiparameter equations of state are

significantly more complex to implement than simple cubic equations of state, but they can, when properly constructed, yield much higher accuracy.

One of the first entrants in this field was the Benedict–Webb–Rubin (BWR) EOS (Benedict et al., 1940) containing 12 terms. This formulation was subsequently extended to increase the number of terms in the so-called modified-Benedict–Webb–Rubin (mBWR) EOS (Jacobsen and Stewart, 1973) containing 32 fixed terms. A family of 12 mBWR equations of state was developed under the auspices of the International Union of Pure and Applied Chemistry, from the 1970s to the 1990s. These mBWR equations of state were a major step forward in the high-fidelity reproduction of the thermodynamic properties of fluids. The mBWR EOS is explicit in pressure, given by the form

$$Z = \frac{p}{\rho RT} = 1 + \sum_i n_i \tau^{t_i} \delta^{d_i} + \sum_i n_i \tau^{t_i} \delta^{d_i} \exp(-\gamma_i \delta^2)$$

where $\tau = T_c/T$, $\delta = \rho/\rho_c$, ρ_c is the critical density of the fluid, and T_c is the critical temperature of the fluid. These equations of state can be converted to the Helmholtz-explicit formulations presented below by the use of the conversion routines presented by Span (2000). The mBWR equations of state are generally employed in their Helmholtz-energy converted form because they are more readily added into existing thermophysical property libraries.

Over the last few decades, a major shift has occurred in the formulation of high-accuracy equations of state. While cubic equations of state are still largely used in many technical domains (petroleum engineering being only one of many), so-called fundamental Helmholtz-energy-explicit equations of state (HEOS) have come to dominate the high-accuracy formulations in use for the calculation of thermodynamic properties of fluids.

Unlike the ideal-gas, cubic, and mBWR equations of state, the fundamental HEOS uses the Helmholtz-energy potential A (where $A = U - TS$) as the fundamental property of the EOS. The Helmholtz energy is only one of the four fundamental properties, the other three being the Gibbs energy, internal energy, and enthalpy. This can be expressed in a nondimensionalized form as

$$\alpha = \frac{A}{RT} = \alpha^0(\tau, \delta) + \alpha^r(\tau, \delta)$$

The primary motivation for this style of fundamental EOS is that all other thermodynamic properties of interest can be obtained through derivatives of the Helmholtz-energy potential. For instance, the pressure can be obtained from

$$p = \rho RT \left(1 + \delta \left(\frac{\partial \alpha^r}{\partial \delta} \right)_\tau \right).$$

Likewise, all other thermodynamic properties can be obtained in a similar fashion.

The parameter α^0 is the ideal-gas part of the nondimensionalized Helmholtz-energy potential and α^r is the residual part. The forms of α^0 and α^r vary, but in general the ideal-gas part is given by the form

$$\alpha^0(\tau, \delta) = -1 + \ln \frac{\rho T}{\rho_0 T_0} + \frac{h_0^0}{RT} - \frac{s_0^0}{R} + \frac{1}{T} \int_{T_0}^T \frac{c_p^0(T)}{R} dT - \int_{T_0}^T \frac{c_p^0(T)}{RT} dT$$

where the isobaric heat capacity $c_p^0(T)/R$ must be integrated to obtain the ideal-gas nondimensionalized Helmholtz energy. The constants h_0^0 and s_0^0 are selected to yield the desired values for enthalpy and entropy at the reference state given by ρ_0 and T_0 . Enthalpy and entropy are relative properties (relative to the reference state); changing the values of h_0^0 or s_0^0 offsets the enthalpy and entropy values by a constant amount, but these changes will not shift the differences in enthalpy or entropy between two states (i.e., for the calculation of the mechanical work of expansion of a turbine).

The ideal-gas constant-volume specific heat capacity c_v^0 can be obtained from a second derivative of the ideal-gas Helmholtz-energy term from

$$c_v^0 = -R\tau^2 \left(\frac{\partial^2 \alpha^0}{\partial \tau^2} \right)_\delta$$

and the ideal-gas isobaric heat capacity can be then obtained from $c_p^0 = c_v^0 + R$. The residual part is in general given by a form similar to

$$\begin{aligned} \alpha^r(\tau, \delta) = & \sum_i n_i \tau^{t_i} \delta^{d_i} + \sum_i n_i \tau^{t_i} \delta^{d_i} \exp(-\gamma_i \delta^{l_i}) \\ & + \sum_i n_i \tau^{t_i} \delta^{d_i} \exp\left(-a_i(\delta - \varepsilon_i)^2 - b_i(\tau - \beta_i)^2\right). \end{aligned}$$

The equations of state for ordinary water (Wagner and Pruss, 2002) and carbon dioxide (Span and Wagner, 1996) include so-called nonanalytic terms that yield a nonanalytic value directly at the critical point. These terms represent a significant challenge from the standpoint of implementation and fitting of equations of state, and are not included in any other EOS. Furthermore, a large amount of experimental data are required in the near-critical region to fit these terms.

The details of the derivatives required to obtain other thermodynamic variables are described in Span (2000) or Lemmon and Jacobsen (2005). A subset of the most commonly used thermodynamic variables is

$$\frac{u}{RT} = \tau \left[\left(\frac{\partial \alpha^0}{\partial \tau} \right)_\delta + \left(\frac{\partial \alpha^r}{\partial \tau} \right)_\delta \right]$$

$$\frac{s}{R} = \tau \left[\left(\frac{\partial \alpha^0}{\partial \tau} \right)_{\delta} + \left(\frac{\partial \alpha^r}{\partial \tau} \right)_{\delta} \right] - \alpha^0 - \alpha^r$$

$$\frac{h}{RT} = \tau \left[\left(\frac{\partial \alpha^0}{\partial \tau} \right)_{\delta} + \left(\frac{\partial \alpha^r}{\partial \tau} \right)_{\delta} \right] + \delta \left(\frac{\partial \alpha^r}{\partial \delta} \right)_{\tau} + 1$$

where u is the mole-specific internal energy, s is the mole-specific entropy, and h is the mole-specific enthalpy. The EOS for a given fluid is expressed as a set of coefficients and exponents that are needed in the various terms that comprise the ideal-gas and residual parts of the nondimensionalized equations of state.

4.3.5 Vapor–liquid equilibrium

For pure fluids, the saturated equilibrium state is the stable equilibrium of one liquid state with one vapor state. Vapor–liquid equilibrium can be expressed as the set of equations

$$p'(T_s) = p''(T_s)$$

$$g'(T_s) = g''(T_s)$$

which represents the equality of pressure p and specific Gibbs energy g between liquid (') and vapor (') states. Many authors have proposed means of solving this set of equations. The classical algorithm ([Span, 2000](#)) for solving the equilibrium conditions is the use of an iterative scheme to determine the pressure that yields equal Gibbs energies for both phases for a given saturation temperature T_s . This method involves significant iteration of the EOS to obtain density as a function of temperature and pressure for each of the liquid and vapor states at each step in the overall iteration.

An alternative to the pressure-iterative methodology of Span is the use of the classical Newton–Raphson two-dimensional system solver as described by [Akasaka \(2008\)](#). In this method, a two-dimensional system of equations for equality of pressure and Gibbs energy is constructed with the liquid density ρ' and vapor density ρ'' as the independent variables to be obtained. This method reduces the amount of iteration, and is still quite simple to implement.

A less well-known method for calculating the vapor–liquid equilibrium conditions is the use of the algorithm in [Kretzschmar et al. \(1990\)](#). This method uses derivatives of the Maxwell-loop conditions in order to arrive at the phase-equilibrium solution. Testing with this method has demonstrated its stability and efficiency. It is currently the algorithm implemented in CoolProp ([Bell et al., 2014](#)) to carry out vapor–liquid equilibria calculations for pure fluids. In contrast to the methods presented above, the Maxwell-loop criterion method can still converge to the correct solution starting from poor initial guesses for the liquid and vapor densities, even quite close to the critical point for well-constructed equations of state.

4.3.6 Flash routines

As described previously, most equations of state in common use are formulated such that the independent variables are temperature and density, and any other desired output variable can be obtained as a single direct evaluation of the EOS. This can be expressed as the mapping

$$T, \rho \rightarrow Y$$

where Y is the property of interest.

In many applications, other independent variables are more natural. For instance, in cycle analysis and dynamic analysis of ORC systems, pressure and enthalpy are the most natural independent variables. For other applications, such as the detailed analyses of positive-displacement expanders, the most natural set of independent variables would be temperature and internal energy.

At the numerical level, the evaluation of a call in the form $Y = f(x_1, x_2)$, where x_1 and x_2 are the independent variables in use, first requires a mapping to the independent variables of the EOS, followed by a direct evaluation of the EOS. This can be summarized as the mapping

$$x_1, x_2 \rightarrow T, \rho \rightarrow Y$$

If either x_1 or x_2 are temperature or density, the problem simplifies to a one-dimensional problem, where only one variable must be determined. Otherwise, both of the independent variables of the EOS must be obtained.

From the standpoint of speed, the following (highly approximate) guide can be used to estimate the computational speed for a single-phase input:

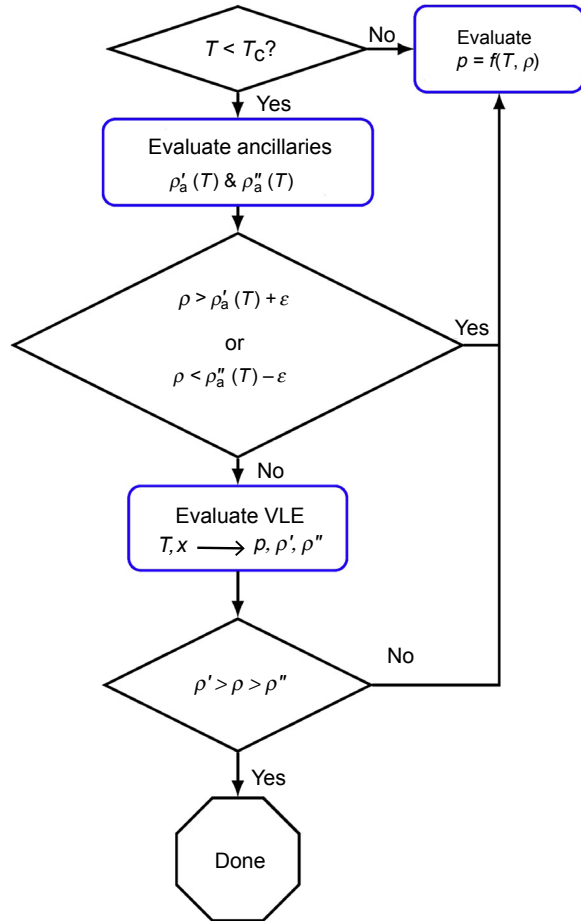
1. Temperature and density (1 computational unit).
2. Temperature and pressure (2 computational units).
3. Density and pressure (4 computational units).
4. Temperature and entropy (10 computational units).
5. Density and one of entropy, enthalpy, or internal energy (10 computational units).
6. Pressure and one of entropy, enthalpy, or internal energy (10 computational units).
7. Enthalpy and entropy (200 computational units).

These computational speed values are meant primarily as a rule-of-thumb, to guide the user towards selecting more favorable independent state variables.

4.3.7 Temperature–density inputs

A “blind” flash call where the location on the phase diagram is unknown is problematic because even just by knowing the independent variables of the EOS, it is not possible to know a priori whether the inputs correspond to a liquid, vapor, supercritical, or two-phase equilibrium state. For instance, even if temperature and density are known for a pure fluid, a multistep process must be carried out to determine whether the inputs

Figure 4.1 Flowchart of the steps required for a flash call using temperature and density as input values (ε is a small value corresponding to the uncertainty in the ancillary curve).



correspond to a homogeneous state for which the pressure can be explicitly calculated for the given temperature and density as demonstrated in Fig. 4.1. The ancillary equations are simple curves that are provided to give good estimates of the vapor pressure and liquid and vapor densities of the fluid. The parameter x is the vapor quality, ρ' refers to the saturated liquid density, and ρ'' refers to the saturated vapor density.

4.3.8 Pressure–enthalpy inputs

The amount of computational effort involved to carry out a flash call varies greatly depending on the set of input variables provided. For instance, one of the common sets of input variables are pressure and enthalpy, which are needed in a wide range of mechanical system modeling simulations. For these inputs, the problem is more complex because neither of the inputs overlap with the independent variables of the

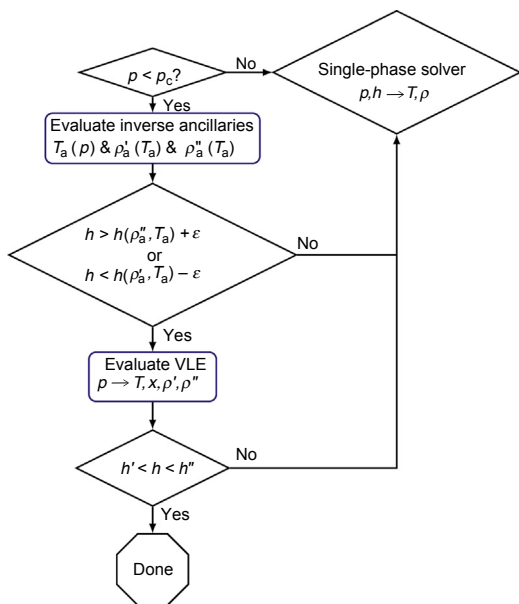


Figure 4.2 Flowchart of the steps required for a flash call with pressure and enthalpy as input values (ϵ is a small value corresponding to the uncertainty in the ancillary curve).

EOS. Hence, the algorithm must do a two-dimensional iteration in order to obtain the temperature and density from the pressure and enthalpy. For instance, for pressure and enthalpy as independent variables, most flash routines employ a logic similar to that shown in Fig. 4.2.

4.3.9 Using initial estimate values

For input variables that have less overlap with the independent variables of the EOS, the additional computational effort can be significant. For instance, when enthalpy and entropy are provided, there are a number of challenges to constructing an efficient flash algorithm:

- The ancillary equations (and the vapor–liquid equilibrium routines) utilize temperature as the independent variable, with pressure or density as outputs.
- The general shapes of the enthalpy–entropy curves along the saturated liquid and vapor curves are not the same, and can have multiple local maxima or minima, a consequence of the size of the molecule and its polarity. For instance, in Fig. 4.3, the saturation curves for acetone demonstrate a unique solution for the saturated enthalpy for a given value of entropy, while for D4 (the siloxane octamethylcyclotetrasiloxane), there are multiple potential solutions for the saturated enthalpy for entropies in a wide range of values.
- A simple determination of whether the point is above the critical temperature or pressure is not possible.

As a result, the computational throughput of calculating pressure as a function of enthalpy and entropy can be on the order of 100 times slower than an evaluation of pressure as a function of temperature and density.

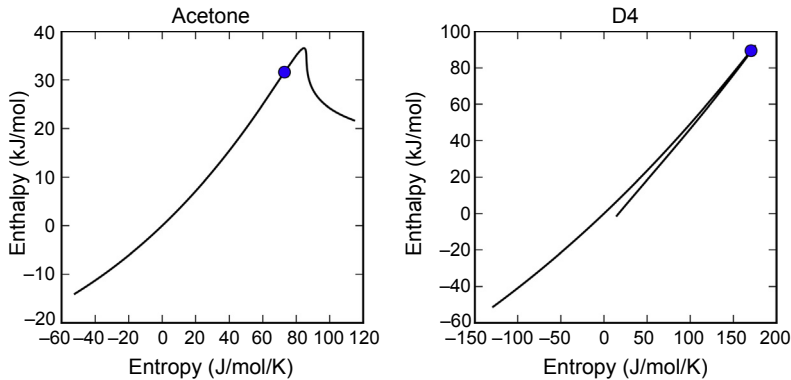


Figure 4.3 Saturation curves in enthalpy–entropy coordinates for acetone and D4 (Octamethylcyclotetrasiloxane); circle shows critical point.

There are a number of ways in which the flash calculation routines can be accelerated. The first opportunity to speed up the calculations is if the phase of the fluid is already known. For instance, if all the inputs are known to be in the gas phase (for instance for a dry-expanding fluid in an expander), the flash routine can be instructed to skip the logic that determines whether the inputs are two-phase or single-phase.

A second level of optimization is possible when good initial estimates for the independent variables used in the EOS are available, and no phase change is expected in the vicinity of the estimated state. In this case, the flash routine can entirely skip the phase calculation and use the initial estimate as a starting point for the iterative solver. Situations where initial estimate values are available are surprisingly common, for instance in carrying out steady-state cycle simulations. In this case, at intermediate iterations marching towards the solution, the previous iteration's values can be used as starting estimates for the flash routine. The computational speedup can be quite significant when good estimates are provided and the inputs are particularly challenging (for instance with enthalpy and entropy).

4.3.10 IAPWS-IF97 as an alternative solution for water

While water is under some definitions of the word not strictly “Organic” in the sense of ORCs, it is one of the most heavily studied and used fluids throughout the technical spheres. For this reason, researchers under the auspices of the *International Association for the Properties of Water and Steam* (IAPWS) developed both an exceptionally high-accuracy reference EOS in temperature and density (Wagner and Pruss, 2002) as well as the industrial formulation IAPWS-IF97 (IAPWS, 2007).

The motivation for the IAPWS-IF97 formulation is that the scientific formulation of the EOS for water is exceptionally accurate, complex, and as a result, slow to evaluate. Furthermore, many calculations of practical interest use temperature and pressure as independent variables, and the iteration required to calculate $\rho = f(T, p)$ adds significant

computational overhead with the scientific formulation. IAPWS-IF97 demonstrates one potential means of achieving higher computational speeds and convenience for pure fluids when temperature and pressure are the desired independent variables. The methods presented below that use interpolation tables are likely a better choice as a general solution.

In the IAPWS-IF97 formulation, the fluid surface for water is divided up into five regions, and in four of the five regions, an EOS explicit in Gibbs energy as a function of temperature and pressure is fit. In one of the regions (region 3), an equation explicit in Helmholtz energy as a function of temperature and density is constructed. The advantage of the IF97 formulation is that for temperature and pressure as independent variables, other outputs can be directly evaluated. Furthermore, a number of backwards equations are provided for doing inverse calculations, for instance for several regions, inverse equations are constructed that give temperature and pressure as a function of (for instance) entropy and enthalpy. If the backwards equations are used, further iteration can refine the solution and yield a backwards evaluation that is consistent with the forward evaluation with temperature and pressure as inputs.

4.4 Thermodynamic properties of mixtures

The use of mixtures has been proposed in order to allow the possibility of matching variable-temperature heat sources and sinks with the glide of the working fluid in the heat exchanger in order to decrease heat exchange irreversibilities. As with pure fluids, a variety of models are available for the calculation of mixture thermodynamic properties.

4.4.1 Cubic equations of state

Valderrama (2003) and Wei and Sadus (2000) each provide a comprehensive review of the state-of-the-art development of cubic equations of state. Perhaps the most commonly used cubic EOS is the SRK formulation. For mixtures, this model can be expressed by

$$p = \frac{RT}{V - b_m} - \frac{a_m \cdot \alpha(T_R, \omega)}{V(V + b_m)}$$

where a_m and b_m arise from a weighting of the a and b parameters from the pure fluids. Several different combination models are available for a_m and b_m ; the reader is advised to refer to the review of Valderrama for more information.

The use of cubic equations of state is convenient because they are themselves easy to implement. For applications where higher accuracy is required, cubic equations of state are insufficient. For these higher accuracy applications, as with pure fluids, multi-parameter Helmholtz-energy-explicit models can be used.

4.4.2 Multiparameter mixture models

The extension of the pure-fluid Helmholtz-energy-explicit models to mixtures of fluids began in the middle of the 1990s, in parallel efforts carried out in the USA and in Germany, in the works of [Lemmon \(1996\)](#), [Lemmon and Jacobsen \(1999\)](#), and [Lemmon and Tillner-Roth \(1999\)](#). In the beginning, emphasis was placed on the study of blends of refrigerants and natural gas mixtures.

In recent years, these multiparameter mixture models have been extended to cover a much wider range of mixture components and applications. The GERG 2004 ([Kunz et al., 2007](#)) and GERG 2008 ([Kunz and Wagner, 2012](#)) models were developed to extend the range of natural gas mixtures that could be modeled with these Helmholtz-energy-based models. More recently, the work of [Gernert et al. \(2013, 2014, 2015\)](#) extended the Helmholtz-energy-explicit models to mixtures relevant for the study of carbon capture and storage systems.

The multiparameter mixture models are all based on a similar formulation to that of the pure fluids. As in the GERG model, the ideal-gas contribution to the nondimensionalized Helmholtz energy is given by

$$\alpha^0(\rho, T, \bar{x}) = \sum_{i=1}^N x_i [\alpha_{oi}^0(\rho, T) + \ln x_i]$$

where the x_i are the mole fractions of the mixture components (and \bar{x} is the vector of mole fractions) and the residual part is the summation of an ideal-mixing part and an excess Helmholtz-energy contribution

$$\alpha^r(\delta, \tau, \bar{x}) = \sum_{i=1}^N x_i \alpha_{oi}^r(\delta, \tau) + \Delta \alpha^r(\delta, \tau, \bar{x})$$

where, for mixtures, $\tau = T_r(\bar{x})/T$ and $\delta = \rho/\rho_r(\bar{x})$. The reducing functions $\rho_r(\bar{x})$ and $T_r(\bar{x})$ are described in the following section.

The excess term $\Delta \alpha^r(\delta, \tau, \bar{x})$ can be thought of as a term that captures the departure from ideal-mixing behavior, though the parameters in the reducing functions can also strongly shape the thermodynamic surfaces. The excess term can be given in the form

$$\Delta \alpha^r(\delta, \tau, \bar{x}) = \sum_{i=1}^{m-1} \sum_{j=i+1}^m \left[x_i x_j F_{ij} \alpha_{ij}^r(\delta, \tau) \right].$$

In this case, there are departure functions α_{ij}^r associated with each binary pair forming the mixture. These departure functions are only available for mixtures for which a significant amount of experimental data are available. For mixtures with some but not extensive data, a generalized function is currently available ([Kunz and Wagner, 2012](#)), and the parameter F_{ij} can be fitted to determine how much the generalized function

contributes to the mixture. Otherwise, for the ij binary pair, the parameter F_{ij} is set to zero, removing the excess contribution to the Helmholtz energy. For binary pairs in similar families, a new generalized departure function α_{ij}^F could be developed, as was done for some alkane mixtures (Kunz and Wagner, 2012) or water-based binary mixtures (Gernert and Span, 2015).

4.4.3 Reducing functions

In the pure-fluid equations of state, the critical temperature T_c and density ρ_c are the reducing parameters. In the case of mixture models, a composition-dependent reducing function is used. All the libraries implementing these high-accuracy mixture models (REFPROP, CoolProp, TREND; see Section 4.9) use the reducing parameter model from the GERG formulation. In this model, the reducing temperature formulation is given by

$$T_r(\bar{x}) = \sum_{i=1}^N \sum_{j=1}^N x_i x_j \beta_{T,ij} \gamma_{T,ij} \frac{x_i + x_j}{\beta_{T,ij}^2 x_i + x_j} (T_{c,i} \cdot T_{c,j})^{0.5}$$

and the reducing density is given by

$$\frac{1}{\rho_r(\bar{x})} = \sum_{i=1}^N \sum_{j=1}^N x_i x_j \beta_{v,ij} \gamma_{v,ij} \frac{x_i + x_j}{\beta_{v,ij}^2 x_i + x_j} \frac{1}{8} \left(\frac{1}{\rho_{c,i}^{1/3}} + \frac{1}{\rho_{c,j}^{1/3}} \right)^3.$$

The pair of reducing functions have four adjustable parameters: $\beta_{T,ij}$, $\gamma_{T,ij}$, $\beta_{v,ij}$, and $\gamma_{v,ij}$. These four parameters govern the shape of the reducing function, and, assuming sufficient experimental data are available, can be fitted to the data for a binary mixture.

This process of fitting the interaction parameters was carried out by the researchers that developed the GERG 2004 model (Kunz et al., 2007), the GERG 2008 model (Kunz and Wagner, 2012), and the EOS-CG model (Gernert and Span, 2015). Other researchers fitted the interaction parameters for refrigerant mixtures (Akasaka 2013, 2014; Lemmon and Jacobsen, 2004).

Similarly, researchers at the National Institute of Standards and Technology have invested significant effort in fitting interaction parameters for a wide range of binary mixtures. These interaction parameters were ultimately implemented into the REFPROP thermophysical property library, which as of publication contains the binary interaction parameters for approximately 670 binary mixtures.

In the case that the interaction parameters are unknown for a binary mixture, a few simple estimation models can be used in their place. The first model is the Lorentz–Berthelot model; in which, all four of the adjustable parameters ($\beta_{T,ij}$, $\gamma_{T,ij}$, $\beta_{v,ij}$, and $\gamma_{v,ij}$) are set equal to 1, and F_{ij} is set equal to 0. This results in a quadratic mixing rule. A second possible estimation scheme is linear mixing.

In this scheme, the parameters $\beta_{T,ij}$ and $\beta_{v,ij}$ are set equal to 1, and the parameters $\gamma_{T,ij}$ and $\gamma_{v,ij}$ are given by

$$\gamma_{v,ij} = 4 \frac{\left(\frac{1}{\rho_{c,i}} + \frac{1}{\rho_{c,j}}\right)}{\left(\frac{1}{\rho_{c,i}^{1/3}} + \frac{1}{\rho_{c,j}^{1/3}}\right)^3} \quad \text{and} \quad \gamma_{T,ij} = \frac{1}{2} \frac{T_{c,i} + T_{c,j}}{(T_{c,i} \cdot T_{c,j})^{0.5}}$$

with F_{ij} set to 0. This yields, as the name implies, a linear reducing temperature (and reducing volume) between the pure component critical temperatures (and specific volumes).

Fig. 4.4 shows the reducing temperature for a hydrogen–propane mixture for three reducing function parameter models. The default model includes the fitted parameters in the GERG 2008 model, which in this case were fitted to experimental data. It is currently not possible to generically recommend the use of linear mixing or quadratic mixing rules when no other information is available.

Other estimation schemes have been developed to predict the interaction parameters for mixtures with little or no experimental data. The scheme of [Lemmon and McLinden \(2001\)](#) for instance can be used to predict the interaction parameters for mixtures of refrigerants and refrigerant-like fluids, such as many of the working fluids proposed for ORCs.

Some of the estimation schemes will miss important mixture behavior, such as the appearance of azeotropy, if the mixture parameters are assumed to all be 1, linear mixing rules are used, or if the mixture interaction parameters are incorrectly predicted. For instance, Fig. 4.5 shows a pressure–mole fraction plot for a mixture of refrigerant R32 and propane that demonstrates that when the interaction parameters appropriately

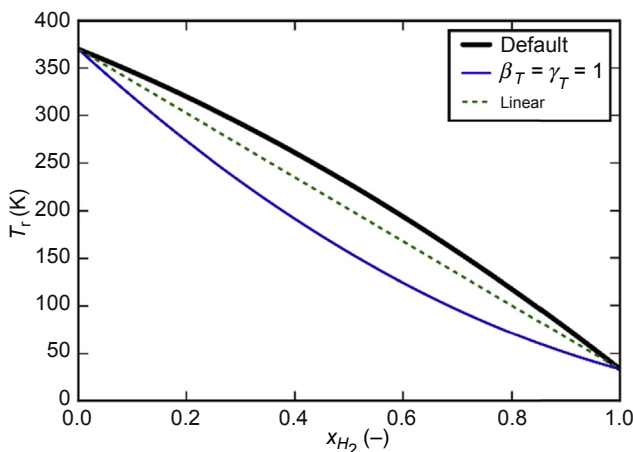


Figure 4.4 Reducing temperature for a hydrogen–propane mixture with three different reducing-parameter sets (default values are taken from [Kunz and Wagner \(2012\)](#)).

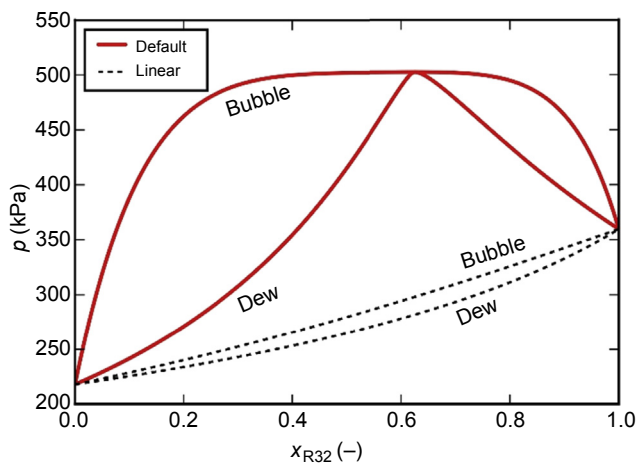


Figure 4.5 Pressure-mole fraction plot for a mixture of refrigerant R32–propane for default and linear mixing interaction parameters at 250 K (interaction parameters taken from REFPROP).

fit, the presence of an azeotropic composition at a refrigerant R32 mole fraction of approximately 0.63 is found, whereas when the interaction parameters are predicted with the linear mixing model, an azeotropic composition is not found.

This (admittedly extreme) example demonstrates that the use of simple mixing rules (linear, Lorentz–Berthelot, etc.) can yield entirely incorrect conclusions about important features such as temperature glide and azeotropy. The user of these mixture models (particularly when the interaction parameters are predicted) should confirm that the behavior of the EOS matches that of experimental data whenever possible.

4.4.4 Mixture thermodynamics

While a thorough coverage of mixture thermodynamics based on the Helmholtz-energy-explicit mixture models is beyond the scope of this work, a broad overview of the use of these mixture models will be presented here. For detailed information about the use of these models, the reader is directed to the work of [Kunz et al. \(2007\)](#) or [Kunz and Wagner \(2012\)](#) (the GERG model), the work of [Michelsen and Møllerup \(2007\)](#), and the further extension of the GERG model by [Gernert et al. \(2014, 2015\)](#).

4.4.4.1 Phase equilibria

As with pure fluids, for mixtures there exists a stable equilibrium between liquid and vapor phases, and metastable states. We will only discuss the stable equilibrium of a liquid phase with a gas phase. The determination of vapor–liquid equilibria is based on thermodynamic and mechanical equilibria, or alternatively expressed as equality of temperature, pressure, and the fugacities of each component in the mixture between the vapor and liquid phases.

Other equilibria are also possible, including equilibria with solid phases, multiple liquid phases, etc. An example of the potential for a wide range of possible phase equilibria is the formation of hydrates (Jäger et al., 2013). In most ORC systems, the only phase equilibria that is encountered is vapor–liquid equilibria (VLE).

The numerical routines needed to carry out these VLE calculations are complex, and a large body of literature has been developed to tackle this problem (Gernert et al., 2014; Gernert and Span, 2015; Jäger et al., 2013; Kunz et al., 2007; Kunz and Wagner, 2012). Fundamentally, the general VLE problem can be divided into a number of simplified cases that are supported in most thermophysical property libraries (REFPROP, CoolProp, TREND):

- Bubble point: A liquid phase with the bulk composition in equilibrium with an infinitely small amount of vapor.
- Dew point: A vapor phase with the bulk composition in equilibrium with an infinitely small amount of liquid.
- T - P flash: Temperature and pressure are known, and the compositions of the liquid and vapor are determined.

4.4.4.2 Flash routines

The determination of the phase of a mixture (two-phase, vapor, liquid) is significantly more complex than the similar determination for pure fluids. To begin with, the vapor–liquid equilibria calculations are more complex, and furthermore, unlike pure fluids, it is not possible to directly know the critical pressure for mixtures as it is not necessarily coincident with the maximum pressure along the saturation curve. In addition, implementation of the elements required to carry out the flash calculations for mixtures requires significant additional labor to implement complicated composition derivatives.

An additional complexity of mixture modeling arises with the consideration of phase stability. To use the stability criteria, a guess is made for the number of phases in existence (usually two, liquid and vapor). If the phases can be shown to be stable in this configuration, the mixture is at a stable vapor–liquid equilibrium state. Otherwise, the inputs correspond to a single-phase state, and the single-phase routines are employed.

The flash calculations proceed in a similar fashion to pure fluids. A determination is first made of whether the inputs are single-phase or two-phase with either a direct evaluation of the vapor–liquid equilibria conditions or stability routines. If the inputs are single-phase, an iterative solver is used to determine the temperature and density. Otherwise, the VLE iterative solver or stability routines yield all necessary thermodynamic variables.

4.5 Transport properties of pure fluids

While thermodynamic properties are undeniably important from the standpoint of cycle design and analysis, transport properties (here viscosity and thermal

conductivity) are also of importance in order to properly design, simulate, and optimize components of the cycle, most especially heat exchangers. The transport property models tend to be divided into two families — those that deal with pure fluids and those that deal with mixtures (which are often treated as some sort of weighted combinations of the properties of pure fluids). Furthermore, in the unfortunately common situation that there is little or no experimental transport property data for a fluid, predictive schemes must be used, such as extended corresponding states (ECS) methods for predicting viscosity and thermal conductivity of pure fluids and mixtures.

4.5.1 Viscosity

The viscosity of a fluid is a measure of its resistance to shear force, or alternatively, its ability to transfer momentum. The theory (Sengers, 1985) states that the viscosity of a pure fluid should be infinite at the critical point, while in fact, nearly all viscosity formulations, aside from those of carbon dioxide (Vesovic et al., 1990) and water (Huber et al., 2009) do not include this critical-point divergence. The reason for this behavior is two-fold:

- There are very few fluids that have sufficient measurements of the viscosity in the critical region.
- The size of the region around the critical point where the critical enhancement of viscosity is significant is very small [see, for instance, the critical enhancement of water (Huber et al., 2009), where the critical enhancement is greater than 2% only in the range of temperature $0.9982T_c < T < 1.0057T_c$].

In the literature, a number of different formulations have been proposed for the viscosity of a pure fluid, but in recent years, most of the literature has settled on the following empirical formulation

$$\mu = \mu^{(0)}(T) + \mu^{(b)}(T, \rho) + \mu^{(c)}(T, \rho)$$

where the total viscosity μ is broken into three contributions, $\mu^{(0)}$ from the dilute gas in the limit of zero density, the critical region contribution $\mu^{(c)}$, and a background contribution $\mu^{(b)}$ that arises from effects that are governed by neither the dilute-gas-limit behavior nor the critical region behavior. As described above, the critical-region contribution is typically neglected ($\mu^{(c)} = 0$).

The dilute gas (or zero-density) contribution can be treated by kinetic gas theory (Hirschfelder et al., 1967), yielding

$$\mu^{(0)} = \frac{(26.692 \times 10^{-3}) \sqrt{MT}}{\sigma_\mu^2 \Omega^{(2,2)}}$$

where M is the molar mass in kg/kmol, T is the temperature in K, σ_μ is the size parameter of the Lennard–Jones model in nm, and $\Omega^{(2,2)}$ is the empirical collision integral of Neufeld et al. (1972) for the Lennard–Jones potential. In practice, the

dilute-gas contribution to the viscosity is typically correlated with simple polynomial or rational polynomial forms as a function of temperature.

There is much less theory that can be used to handle the background contribution to the viscosity, though an attempt has been made by [Chung et al. \(1988\)](#). The background contribution $\mu^{(b)}$ is usually divided into two contributions; one from the so-called initial-density part derived from the Rainwater–Friend theory ([Friend and Rainwater, 1984](#); [Rainwater and Friend, 1987](#)) and another from the residual viscosity contribution. This yields a form for the background viscosity of

$$\mu^{(b)} = \mu^{(R-F)} + \Delta\mu_r.$$

The Rainwater–Friend theory is used to arrive at the slope of the viscosity versus density in the limit of zero-density. This so-called initial-density term is expressed by

$$\mu^{(R-F)} = B_\mu \rho \mu^{(0)}$$

where an updated version of the second viscosity virial coefficient B_μ (which is only a function of temperature) has been correlated in the work of [Vogel et al. \(1998\)](#) as a function of an energy-based reduced temperature.

The residual viscosity term $\Delta\mu_r$ is typically described with an entirely empirical formulation, sometimes guided by free-volume terms proposed by [Batschinski \(1913\)](#) and [Hildebrand \(1971\)](#). In recent years, symbolic regression has been used to determine an appropriate functional form for the residual-viscosity term for several fluids, including normal hydrogen ([Muzny et al., 2013](#)), *n*-hexane ([Michailidou et al., 2013](#)), *n*-heptane ([Michailidou et al., 2014](#)), and benzene ([Avgeri et al., 2014](#)).

4.5.2 Thermal conductivity

The thermal conductivity of a fluid is a measure of the ease of transfer of heat through the fluid; it is treated in a similar fashion to that of viscosity. The total thermal conductivity is divided into contributions arising from the zero-density, background, and critical components.

In the zero-density limit, kinetic theory ([Millat et al., 1996](#)) can guide the behavior of the correlation, but in engineering correlations, the zero-density contribution to the thermal conductivity is given by a short polynomial (or rational polynomial) in temperature (or reduced temperature).

The critical enhancement term is usually based on the model of [Olchoway and Sengers \(1989\)](#). This form is relatively simple to implement, though it does require derivatives of pressure at two different temperatures and is dependent on the viscosity model employed. As a result, well-constructed equations of state and viscosity formulations must already exist.

The critical enhancement for thermal conductivity is effective over a much wider range than for the viscosity. For instance, [Fig. 4.6](#) shows the critical enhancement term along the critical isochore for propane with the thermal conductivity formulation

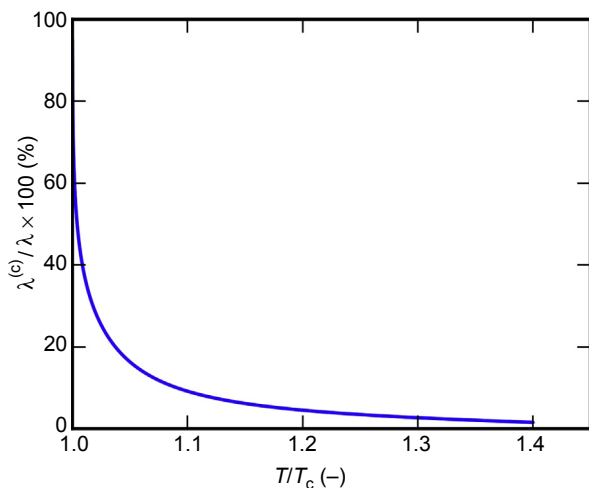


Figure 4.6 Critical contribution to the total thermal conductivity along the critical isochore for propane.

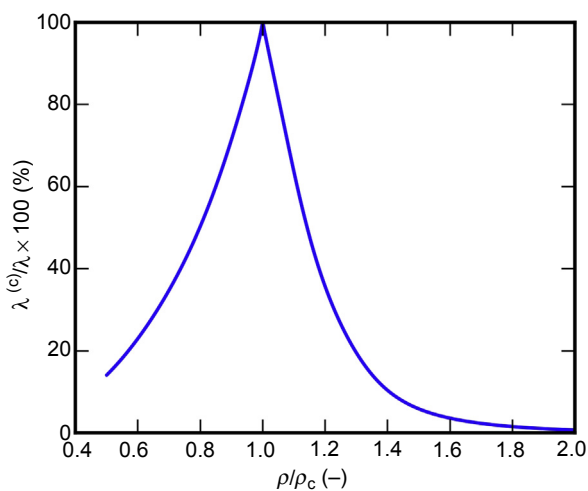


Figure 4.7 Critical contribution to the total thermal conductivity along the critical isotherm for propane.

of [Marsh et al. \(2002\)](#), and [Fig. 4.7](#) shows the same contribution along the critical isotherm. Even at a reduced temperature of 1.15 times the critical temperature, the critical enhancement still contributes more than 6% to the total thermal conductivity. In reduced density (see [Fig. 4.7](#)), the impact of the critical enhancement term is evident over an even wider range.

As in the viscosity, theory ([Sengers, 1985](#)) predicts that the thermal conductivity should diverge directly at the critical point.

4.5.3 Extended corresponding states

There are many pure fluids for which the amount of experimental transport-property data available is quite limited, but for which reasonable estimates of viscosity and thermal conductivity are still required. One means of dealing with this limitation is through the use of ECS. The concept of ECS is to derive the transport properties for a fluid of interest from the properties of a reference fluid that is well studied, and for which high-accuracy transport property correlations already exist. A number of authors have contributed to the development of the extended-corresponding-states formulation for transport properties (Ely and Hanley, 1981, 1983; Huber and Ely, 1992; Klein et al., 1997; McLinden et al., 2000) and a similar formulation can be used for the thermodynamic properties.

For the application of ECS to pure fluids, the viscosity and thermal conductivity are divided into contributions for the zero-density limit, a background contribution, and the critical contribution (thermal conductivity only). The dilute gas portion is treated using theory, both for viscosity (Hirschfelder et al., 1967) and thermal conductivity (Hirschfelder et al., 1967). For the critical enhancement of thermal conductivity, the model of Olchowy and Sengers (1989) is employed, using fitted parameters, or default values if insufficient data are available.

The remaining part, the background contribution, is treated with ECS. A so-called conformal state is found for the reference fluid that yields the desired mapping onto the fluid of interest (Klein et al., 1997; McLinden et al., 2000). The background part for the fluid of interest is then given by the background contribution of the reference fluid evaluated at the conformal state point.

The application of ECS is quite complex, and a fully worked-out example of the use of ECS can be found in the work of Bell et al. (2014).

4.6 Transport properties of mixtures

The database of correlations and experimental datasets for transport properties of mixtures is in general far less developed than for pure fluids. One of the challenges stems from the fact that transport property models are dependent on thermodynamic-property models. Thus, in order to develop a mixture transport property model, the following prerequisite steps must be carried out:

1. Development of pure-fluid equations of state for each pure component.
2. Development of transport property formulations for each pure component.
3. Development of a thermodynamic-property model for the mixture.
4. Development of a transport property formulation for the mixture.

As a result, the development of transport properties of mixtures tends to lag those of thermodynamic properties.

4.6.1 Viscosity and thermal conductivity

The technical report of Chichester and Huber (2008) summarizes the state-of-the-art in mixture property predictions as implemented into the NIST REFPROP library. In that

report, a description of the use of ECS for mixtures is presented; this ECS-based formulation is used to predict the viscosity and thermal conductivity of mixtures as implemented in REFPROP.

Other models have also been proposed for the viscosity and thermal conductivity of liquids. The work of Poling et al. (2001) discusses the models available in the literature for the viscosity and thermal conductivity of mixtures of liquids. No general theory is presented by Poling that can be used over the entire fluid surface including liquid, gas, and supercritical states.

For viscosity, friction theory (Quiñones-Cisneros et al., 2000, 2001) can be used to provide predictions of the viscosity of mixtures of fluids with an accuracy generally better than 10%. The disadvantage of this method is that the models for all of the constituent components must also be based on the use of friction theory, while most of the reference correlations for viscosity are not friction-theory based.

4.7 Surface tension

The surface tension is a measure of the strength of an interface formed between a liquid and its environment. This interface itself is a result of the intermolecular interactions experienced by molecules on the interface.

4.7.1 Pure fluids

In the recent literature, the surface tension of pure fluids has exclusively been modeled by equations of the form

$$\sigma = \sum_i a_i \left(1 - \frac{T}{T_c}\right)^{n_i}$$

where the surface tension σ is in N/m, T_c is the critical temperature in K, and T is the temperature in K. Values for the coefficients a_i and n_i are fluid-specific and can be found in the literature for the fluid of interest. Extensive work has been carried out by Mulero and coworkers (Cachadiña et al., 2015; Mulero and Cachadiña, 2014; Mulero et al., 2012, 2015) to fit surface tension curves for large families of fluids, covering nearly all the fluids in REFPROP 9.1. Additional data are available in the work of Jasper (1972) for a wide range of fluids.

4.7.2 Mixtures

The literature for predictive models for the surface tension of mixtures has been summarized in the work of Poling et al. (2001). They describe several models for the surface tension of fluids that are available in the open literature. Fundamentally, these models are divided in three categories:

- Thermodynamically-based models, like those of Sprow and Prausnitz (1966).
- Rough estimation methods, like linear or quadratic weighting of the pure-fluid surface tensions.
- Empirical relationships, like that of the Macleod–Sugden correlation (Poling et al., 2001).

4.8 Interpolation methods

As described previously, many applications, especially dynamic modeling, require the use of pressure and enthalpy as the independent variables in flash calculations. The flash calculation to obtain temperature and density from pressure and enthalpy is challenging, and computationally quite expensive. As a result, more efficient models to evaluate thermophysical properties of mixtures and pure fluids are needed, and interpolation methods can be of use.

There exist a wide range of approaches for interpolation methods that can be employed. One of the fastest methods for the calculation of thermodynamic and transport properties is to generate polynomial (often spline) curves that cover the entire fluid surface, generally in a piecewise fashion (IAPWS, 2015). Alternatively, functional forms such as multivariate rational polynomial (Aute and Radermacher, 2014) forms may be used. The second family of methods involves the use of regularly spaced grids in the independent variables; often density and pressure are logarithmically spaced though most other variables can be linearly spaced. Bilinear, bicubic, or higher-order interpolation can be used for a locally consistent formulation with these regularly spaced grids. Alternatively, the Tabular Taylor Series Extrapolation (TTSE) method can be used, which extrapolates the tabulated values from grid cells.

Each of these types of interpolation have their strengths and weaknesses. Some, especially the polynomial interpolation methods and the spline-based interpolation methods, require extensive work to construct the interpolation data for a given fluid. They are in that sense tailored for one particular fluid. The table-based methods, while somewhat slower than the spline-based interpolation methods, are straightforward to understand and to implement, and will be further discussed here.

4.8.1 Tabular interpolation

In the tabular interpolation schemes described here (both bicubic and TTSE), the first step is to generate a set of tabulated data that are regularly spaced in the independent variables. These data should also include partial derivatives of the other, non-tabulated thermodynamic variables with respect to the independent variables of the table.

The total set of variables that should be covered by the tables are:

- pressure
- temperature
- enthalpy
- entropy
- density
- internal energy
- viscosity (cannot be an independent variable of the table)
- thermal conductivity (cannot be an independent variable of the table)

The tables are constructed in two parts: one for the homogeneous, single-phase portions of the fluid, and another along the saturation boundary. For pure fluids, the saturation boundary can be calculated from the vapor–liquid equilibrium routines. For mixtures of fixed composition, the phase envelope can be constructed from the

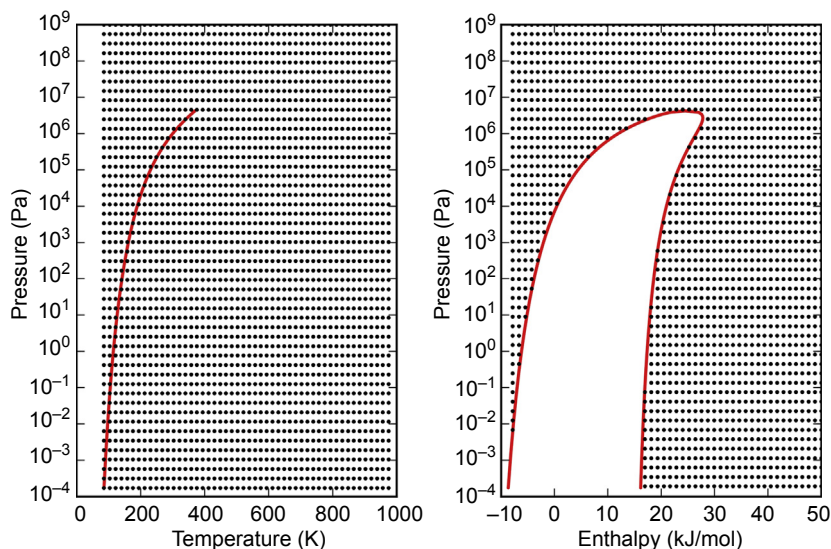


Figure 4.8 Tabulated grid points for pressure—temperature and pressure—enthalpy for propane; each dot represents one point in the single-phase domain for a 50×50 grid.

low-pressure dew-point line, through the critical region, and to the high density bubble-point line. This so-called phase envelope defines the line between single-phase and two-phase states for mixtures.

For instance, in the single-phase portion of the fluid surface, two sets of tables can be constructed: one with pressure and enthalpy as independent variables, and another with pressure and temperature as independent variables, as shown in Fig. 4.8. These variables are advantageous for a number of reasons. Pressure—temperature and pressure—enthalpy are the most commonly used pairs of independent variables; if other variables are desired, for instance temperature and density, they can be obtained from a one-dimensional bisection to find the correct cell in the table. Other common inputs such as enthalpy and entropy can also be handled as a one-dimensional bisection in the nontabulated variable.

4.8.2 Tabular Taylor-series extrapolation

TTSE can be used to evaluate inputs in the single-phase domain of the fluid of interest. This method is based on a Taylor-series expansion in two variables around a given data point. Mathematically this can be expressed as

$$\begin{aligned}
 z = z_{ij} &+ \Delta x \left(\frac{\partial z}{\partial x} \right)_{y,ij} + \Delta y \left(\frac{\partial z}{\partial y} \right)_{x,ij} + (\Delta x)^2 \left(\frac{\partial^2 z}{\partial x^2} \right)_{y,ij} + (\Delta y)^2 \left(\frac{\partial^2 z}{\partial y^2} \right)_{x,ij} \\
 &+ \frac{1}{2} \Delta x \Delta y \left(\frac{\partial^2 z}{\partial x \partial y} \right)_{ij}
 \end{aligned}$$

where z is the output parameter of interest, and x and y are the independent variables, $\Delta x = x - x_i$ and $\Delta y = y - y_j$.

For a given set of inputs that are the same as the independent variables of the table, interval bisection is used to find the nearest nodes in both variables. While a counter-intuitive result, interval bisection is faster than a direct lookup of the cell when the inputs are logarithmically spaced due to the computational overhead of using transcendental functions (most especially the logarithm in this case).

Determination of the node to be used becomes more problematic near the two-phase boundary in the single-phase region. In this case, if interval bisection predicts a node that is in the two-phase region, the node is shifted out of the two-phase region.

4.8.2.1 *Bicubic interpolation*

One of the disadvantages of the TTSE method is that there are discontinuities in the output values as inputs shift the selected node for extrapolation. One of the ways around this problem is through the use of bicubic interpolation, which allows for a smooth surface over the entire range that the table is constructed. The bicubic interpolation method requires the same tabular interpolation data that are used by the TTSE method (values and derivatives at the grid points), and in each cell the output variable z is given by a function of the independent variables x and y

$$z = \sum_{i=0}^3 \sum_{j=0}^3 a_{ij} \hat{x}^i \hat{y}^j$$

where the variables \hat{x} and \hat{y} are normalized variables for the grid cell. For speed considerations, the coefficients a_{ij} are determined as part of the initialization of the table. Even so, the bicubic interpolation method is in general approximately 10% slower than the TTSE method due to the additional evaluations required.

4.8.2.2 *Spline-based tabular look-up interpolation*

A newer entrant into the field of interpolation methods is that of Spline-based tabular look-up (SBTL). This method, as developed by Kunick and coworkers (IAPWS, 2015), is based on constructing biquadratic spline functions for each cell in the tabulated data. The coefficients for each of the cells are obtained as part of a global optimization that enforces continuity of values and derivatives at each cell boundary. Furthermore, input and output transformation is used to scale the variables onto a rectangular grid that allows for noniterative cell determination. Construction of the biquadratic splines for a given fluid is somewhat complex, and the software FluidSplines was developed to facilitate this process.

For water, the SBTL method demonstrates approximately a 10-fold speed improvement over the use of IAPWS-IF97 (with iterative refinement of the solution). For applications with demands for very high accuracy, the SBTL method is one of the most computationally efficient options.

4.9 Libraries available

Many libraries exist that implement some subset of the thermophysical property models. The list provided here emphasizes libraries that are based on the highest-accuracy formulations available in the literature, are under active development, and have transparent documentation of the models used.

4.9.1 REFPROP

The REFPROP property library ([Lemmon et al., 2013](#)) developed at the National Institute of Standards and Technology is the state-of-the-art library for the thermophysical properties of pure fluids and mixtures. It comprises all the highest-accuracy and technical equations of state in the open literature, as well as additional parameters for mixture models not in the open literature. Furthermore, it includes the most comprehensive models available for the transport properties of pure fluids and mixtures. It is developed in FORTRAN, and interfaces are available for many programming languages and environments of practical interest.

4.9.2 CoolProp

The CoolProp library ([Bell et al., 2014](#)) is a C++-based open-source library of thermophysical properties that emulates much of the functionality of REFPROP. Additionally, CoolProp has properties of humid air, incompressible fluids, and brines, as well as tabular interpolation (TTSE and bicubic), for both pure fluids and mixtures (from REFPROP).

4.9.3 TREND

A newer entrant into the field of thermophysical property libraries is the TREND 2.0 library ([Span et al., 2015](#)) developed by the Chair of Thermodynamics at the Ruhr-Universität Bochum, Germany. This FORTRAN-based library has specialized routines for the evaluation of mixture thermodynamics, and includes routines for the formation of, and equilibrium with, solids of H₂O and CO₂ and various hydrates (CO₂, nitrogen, oxygen, argon, carbon monoxide, methane, ethane, and propane).

4.9.4 FluidProp

FluidProp is a thermophysical property library currently developed by Asimptote, which includes a free version and add-ons with additional functionality. It implements many cubic equations of state as well as a SAFT (statistical associating fluid theory) variant. It includes wrappers to a number of programming environments of interest, and permits interfacing to REFPROP as an add-on.

4.9.5 Zittau/Goerlitz libraries

The above libraries are quite general, while the libraries developed at the Zittau/Goerlitz University of Applied Sciences are specialized; developed for fast evaluation, multithreaded applications, and other similar considerations. User-friendly interfaces are available for many popular engineering environments. Furthermore, specialized libraries for the evaluation of mixtures of flue gases and humid air are available.

Acknowledgments

The authors would like to acknowledge the contributions of Arno Laesecke of the National Institute of Standards and Technology and Stefan Herrig of the Ruhr-Universität Bochum.

References

- Akasaka, R., 2008. A Reliable and useful method to determine the saturation state from Helmholtz energy equations of state. *Journal of Thermal Science and Technology* 3, 442–451.
- Akasaka, R., 2014. A thermodynamic property model for the R-134a/245fa mixtures. In: 15th International Refrigeration and Air Conditioning Conference at Purdue, July 14–17, 2014.
- Akasaka, R., 2013. Thermodynamic property models for the Difluoromethane (R-32) + trans-1,3,3,3-tetrafluoropropene (R-1234ze(E)) and difluoromethane + 2,3,3,3-tetrafluoropropene (R-1234yf) mixtures. *Fluid Phase Equilibria* 358, 98–104.
- Aute, V., Radermacher, R., 2014. Standardized polynomials for fast evaluation of refrigerant thermophysical properties. In: International Refrigeration and Air Conditioning Conference at Purdue University.
- Avgeri, S., Assael, M.J., Huber, M.L., Perkins, R.A., 2014. Reference correlation of the viscosity of benzene from the triple point to 675 K and up to 300 MPa. *Journal of Physical and Chemical Reference Data* 43, 033103.
- Batschinski, A., 1913. Untersuchungen über die innere Reibung der Flüssigkeiten. *Zeitschrift für Physikalische Chemie* 84, 643–706.
- Bell, I.H., Wronski, J., Quoilin, S., Lemort, V., 2014. Pure and pseudo-pure fluid thermophysical property evaluation and the open-source thermophysical property library CoolProp. *Industrial & Engineering Chemistry Research* 53 (6), 2498–2508.
- Benedict, M., Webb, G.B., Rubin, L.C., 1940. An empirical equation for thermodynamic properties of light hydrocarbons and their mixtures. *Journal of Chemical Physics* 8, 334–345.
- Cachadina, I., Mulero, A., Tian, J., 2015. Surface tension of refrigerants—selection of data and recommended correlations. *Journal of Physical and Chemical Reference Data* 023104.
- Chichester, J.C., Huber, M.L., 2008. NISTIR 6650: Documentation and Assessment of the Transport Property Model for Mixtures Implemented in NIST REFPROP (Version 8.0). National Institute of Standards and Technology (NIST).
- Chung, T.-H., Ajlan, M., Lee, L.L., Starling, K.E., 1988. Generalized Multiparameter correlation for nonpolar and polar fluid transport properties. *Industrial & Engineering Chemistry Research* 27, 671–679.

- Ely, J.F., Hanley, H.J.M., 1981. Prediction of transport properties. 1. viscosity of fluids and mixtures. *Industrial & Engineering Chemistry Fundamentals* 20 (4), 323–332.
- Ely, J.F., Hanley, H.J.M., 1983. Prediction of transport properties. 2. Thermal conductivity of pure fluids and mixtures. *Industrial & Engineering Chemistry Fundamentals* 22 (1), 90–97.
- Friend, D.G., Rainwater, J.C., 1984. Transport properties of a moderately dense gas. *Chemical Physics Letters* 107, 590–594.
- Gernert, G.J., 2013. A New Helmholtz Energy Model for Humid Gases and CCS Mixtures (Ph.D. Dissertation). Ruhr-Universität Bochum.
- Gernert, J., Jäger, A., Span, R., 2014. Calculation of phase equilibria for multi-component mixtures using highly-accurate Helmholtz energy equations of state. *Fluid Phase Equilibria* 375, 209–218.
- Gernert, J., Span, R., 2015. EOS-cg: a Helmholtz energy mixture model for humid gases and CCS mixtures. *Journal of Chemical Thermodynamics* 274–293.
- Heberle, F., Brüggemann, D., 2015. Thermo-economic evaluation of organic Rankine cycles for geothermal power generation using zeotropic mixtures. *Energies* 8 (3), 2097–2124.
- Hildebrand, J., 1971. Motions of molecules in liquids: viscosity and diffusivity. *Science* 174, 490–493.
- Hirschfelder, J.O., Curtiss, C.F., Bird, R.B., 1967. *Molecular Theory of Gases and Liquids*. John Wiley and Sons.
- Huber, M.L., Ely, J.F., 1992. Prediction of viscosity of refrigerants and refrigerant mixtures. *Fluid Phase Equilibria* 80, 239–248.
- Huber, M.L., Perkins, R.A., Laesecke, A., Friend, D.G., Sengers, J.V., Assael, M., Metaxa, I.M., Vogel, E., Mareš, R., Miyagawa, K., 2009. New international formulation for the viscosity of H₂O. *Journal of Physical and Chemical Reference Data* 38 (2), 101–125.
- IAPWS, 2015. Guideline on the Fast Calculation of Steam and Water Properties With the Spline-based Table Look-up Method (SBTL). IAPWS (In Press).
- IAPWS, 2007. Revised Release on the IAPWS Industrial Formulation 1997 for the Thermodynamic Properties of Water and Steam. IAPWS.
- Jacobsen, R.T., Stewart, R.B., 1973. Thermodynamic properties of nitrogen including liquid and vapor phases from 63 K to 2000 K with pressures to 10,000 bar. *Journal of Physical and Chemical Reference Data* 2 (4), 757–922.
- Jäger, A., Vinš, V., Gernert, J., Span, R., Hrubý, J., 2013. Phase equilibria with hydrate formation in H₂O + CO₂ mixtures modeled with reference equations of state. *Fluid Phase Equilibria* 338, 100–113.
- Jasper, J.J., 1972. The surface tension of pure liquid compounds. *Journal of Physical and Chemical Reference Data* 1, 841–1009.
- Klein, S.A., McLinden, M.O., Laesecke, A., 1997. An improved extended corresponding states method for estimation of viscosity of pure refrigerants and mixtures. *International Journal of Refrigeration* 20, 208–217.
- Kretzschmar, H.-J., Zschunke, T., Klinger, J., Dittman, A., 1990. An alternative method for the numerical calculation of the Maxwell criterion in vapour pressure computations. In: *Properties of Water and Steam: Proceedings of the 11th International Conference*.
- Kunz, O., Klimeck, R., Wagner, W., Jaeschke, M., 2007. The GERG-2004 Wide-range Equation of State for Natural Gases and Other Mixtures. VDI Verlag GmbH.
- Kunz, O., Wagner, W., 2012. The GERG-2008 wide-range equation of state for natural gases and other mixtures: an expansion of GERG-2004. *Journal of Chemical & Engineering Data* 57, 3032–3091.

- Lemmon, E.W., 1996. A Generalized Model for the Prediction of the Thermodynamic Properties of Mixtures Including Vapor-Liquid Equilibrium (Ph.D. Dissertation). University of Idaho, Moscow.
- Lemmon, E.W., Huber, M.L., McLinden, M.O., 2013. NIST Standard Reference Database 23: Reference Fluid Thermodynamic and Transport Properties-REFPROP, Version 9.1. <http://www.nist.gov/srd/nist23.cfm>.
- Lemmon, E.W., Jacobsen, R.T., 1999. A generalized model for the thermodynamic properties of mixtures. *International Journal of Thermophysics* 20 (3), 825–835.
- Lemmon, E.W., Jacobsen, R.T., 2005. A new functional form and new fitting Techniques for equations of state with application to Pentafluoroethane (HFC-125). *Journal of Physical and Chemical Reference Data* 34 (1), 69–108.
- Lemmon, E.W., Jacobsen, R.T., 2004. Equations of state for mixtures of R-32, R-125, R-134a, R-143a, and R-152a. *Journal of Physical and Chemical Reference Data* 33 (2), 593–620.
- Lemmon, E.W., McLinden, M.O., 2001. Method for estimating mixture equation of state parameters. In: *Thermophysical Properties and Transfer Processes of New Refrigerants*, Paderborn, Germany.
- Lemmon, E.W., Tillner-Roth, R., 1999. A Helmholtz energy equation of state for calculating the thermodynamic properties of fluid mixtures. *Fluid Phase Equilibria* 165, 1–21.
- Marsh, K.N., Perkins, R.A., Ramires, M.L.V., 2002. Measurement and correlation of the thermal conductivity of propane from 86 K to 600 K at pressures to 70 MPa. *Journal of Chemical & Engineering Data* 47, 932–940.
- McLinden, M.O., Klein, S.A., Perkins, R.A., 2000. An extended corresponding states model for the thermal conductivity of refrigerants and refrigerant mixtures. *International Journal of Refrigeration* 23, 43–63.
- Michailidou, E.K., Assael, M.J., Huber, M.L., Abdulagatov, I.M., Perkins, R.A., 2014. Reference correlation of the viscosity of n-heptane from the triple point to 600 K and up to 248 MPa. *Journal of Physical and Chemical Reference Data* 43, 023103.
- Michailidou, E.K., Assael, M.J., Huber, M.L., Perkins, R.A., 2013. Reference correlation of the viscosity of n-hexane from the triple point to 600 K and up to 100 MPa. *Journal of Physical and Chemical Reference Data* 42 (3), 331041–331042.
- Michelsen, M.L., Møllerup, J.M., 2007. *Thermodynamic Models: Fundamentals & Computational Aspects*. Tie-Line Publications, Holte, Denmark.
- Millat, J., Vesovic, V., Wakeham, W., 1996. In: Millat, J., Dymond, J.H., de Castro, C.A.N. (Eds.), *Transport Properties of Fluids: Their Correlation, Prediction and Estimation*. Cambridge University Press, New York, pp. 29–64.
- Mulero, A., Cachadiña, I., 2014. Recommended correlations for the surface tension of several fluids included in the REFPROP Program. *Journal of Physical and Chemical Reference Data* 43, 231041–0231048.
- Mulero, A., Cachadiña, I., Parra, M.I., 2012. Recommended correlations for the surface tension of common fluids. *Journal of Physical and Chemical Reference Data* 41 (4), 431051–4310513.
- Mulero, A., Cachadiña, I., Sanjuán, E.L., 2015. Surface tension of alcohols. Data selection and recommended correlations. *Journal of Physical and Chemical Reference Data* 44 (3). Available at: <http://scitation.aip.org/content/aip/journal/jpcrd/44/3/10.1063/1.4927858>.
- Muzny, C.D., Huber, M.L., Kazakov, A.F., 2013. Correlation for the viscosity of normal hydrogen obtained from symbolic regression. *Journal of Chemical & Engineering Data* 58 (4), 969–979.

- Neufeld, P.D., Janzen, A.R., Aziz, R.A., 1972. Empirical equations to calculate 16 of the transport collision integrals $\Omega(l,s)^*$ for the Lennard-Jones (12-6) potential. *Journal of Chemical Physics* 57 (3), 1100–1102.
- Olchowy, G.A., Sengers, J.V., 1989. A simplified representation for the thermal conductivity of fluids in the critical region. *International Journal of Thermophysics* 10 (2), 417–426.
- Peng, D.-Y., Robinson, D.B., 1976. A new two-constant equation of state. *Industrial & Engineering Chemistry Fundamentals* 15 (1), 59–64.
- Poling, B.E., Prausnitz, J.M., O'Connell, J.P., 2001. *The Properties of Gases and Liquids*, fifth ed. McGraw Hill.
- Quiñones-Cisneros, S.E., Zeberg-Mikkelsen, C.K., Stenby, E.H., 2000. The friction theory (f-theory) for viscosity modeling. *Fluid Phase Equilibria* 169, 249–276.
- Quiñones-Cisneros, S.E., Zeberg-Mikkelsen, C.K., Stenby, E.H., 2001. One parameter friction theory models for viscosity. *Fluid Phase Equilibria* 176, 1–16.
- Rainwater, J.C., Friend, D.G., 1987. Second viscosity and thermal-conductivity virial coefficients of gases: extension to low reduced temperature. *Physical Review A* 36, 4062–4066.
- Sengers, J.V., 1985. Transport properties of fluids near critical points. *International Journal of Thermophysics* 6 (3), 203–232.
- Soave, G., 1972. Equilibrium constants from a modified Redlich-Kwong equation of state. *Chemical Engineering Science* 27 (6), 1197–1203.
- Span, R., 2000. *Multiparameter Equations of State - An Accurate Source of Thermodynamic Property Data*. Springer.
- Span, R., Eckermann, T., Herrig, S., Hielscher, S., Jäger, A., Thol, M., 2015. *TREND. Thermodynamic Reference and Engineering Data 2.0*.
- Span, R., Wagner, W., 1996. A new equation of state for carbon dioxide covering the fluid region from the Triple point temperature to 1100 K at pressures up to 800 MPa. *Journal of Physical and Chemical Reference Data* 25, 1509–1596.
- Sprow, F.B., Prausnitz, J.M., 1966. Surface tensions of simple liquid mixtures. *Transactions of the Faraday Society* 62, 1105–1111.
- Valderrama, J., 2003. The state of the cubic equations of state. *Industrial & Engineering Chemistry Research* 42, 1603–1618.
- van der Waals, J.D., 1873. *On the Continuity of the Gaseous and Liquid States*. Universiteit Leiden, Leiden, The Netherlands.
- Vesovic, V., Wakeham, W.A., Olchowy, G.A., Sengers, J.V., Watson, J.T.R., Millat, J., 1990. The transport properties of carbon dioxide. *Journal of Physical and Chemical Reference Data* 19, 763–808.
- Vogel, E., Küchenmeister, C., Bich, E., Laesecke, A., 1998. Reference correlation of the viscosity of propane. *Journal of Physical and Chemical Reference Data* 27, 947–970.
- Wagner, W., Pruss, A., 2002. The IAPWS formulation 1995 for the thermodynamic properties of ordinary water substance for general and scientific use. *Journal of Physical and Chemical Reference Data* 31, 387–535.
- Wei, Y.S., Sadus, R.J., 2000. Equations of state for the calculation of fluid-phase equilibria. *AIChE Journal* 46 (1), 169–196.

Thermal stability of organic fluids for Organic Rankine Cycle systems

5

C.M. Invernizzi¹, D. Bonalumi²

¹University of Brescia, Brescia, Italy; ²Politecnico di Milano, Milan, Italy

5.1 Introduction

The net power of a heat engine, having set the available thermal power \dot{Q}_{in} , depends strictly on the conversion efficiency η according to (see [Invernizzi, 2013](#)):

$$\dot{W} = \dot{Q}_{in}\eta \quad (5.1)$$

with $\eta = \eta(T_H, T_0, \dot{S}_G)$ a function of the maximum temperature of the heat source T_H , of the ambient temperature T_0 , and of the entropy generated in the system per unit time \dot{S}_G .

Firstly, having set T_0 , the higher the T_H , the higher the conversion efficiency. Then, with T_H and T_0 set, the greater the \dot{S}_G , the lower the conversion efficiency. One of the most important contributions to the generated entropy \dot{S}_G is the temperature difference between T_H and the maximum operative temperature T_{H1} of the engine (for instance, the evaporation temperature).

Therefore, when the thermal power \dot{Q}_{in} is available at a high temperature, it is essential that the working fluid in the heat engine be used safely at the highest maximum temperature T_{H1} , close to T_H .

By way of a simple example, with reference to an ideal heat engine and assuming the temperature difference $\Delta T_H = (T_H - T_{H1})$ as the only reason for thermodynamic irreversibility, [Fig. 5.1](#) reports the conversion efficiency as a function of \dot{S}_G for different values of T_H and ΔT_H . Assuming $T_H = 400^\circ\text{C}$, when $\Delta T_H = 50$ and 100°C , the efficiency is about 94% and 87% of the ideal maximum attainable value respectively.

While the logarithmic mean temperature differences in the high-temperature heat exchangers can be reduced by selecting small pinch-point temperature differences or selecting suitable thermodynamic cycles (for instance, supercritical ones), the operating maximum temperature is limited by the thermal stability and it is an unavoidable physical and chemical characteristic of every single working fluid.

Heat sources at relatively high temperatures are plentiful. According to the European Project Heat Recovery in Energy Intensive Industries, for example, the potential electricity generation from the recovery of waste heat in energy intensive industries in Europe is between 13,000 and 20,000 GWh/year (depending on the yearly

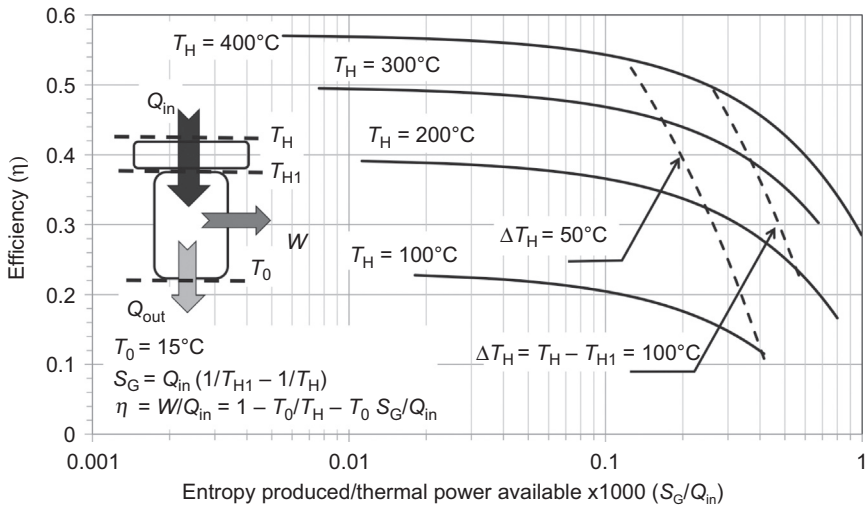


Figure 5.1 Conversion efficiency for an ideal (internally reversible) heat engine as a function of the entropy produced by a heat transfer irreversibility at high temperature. The heat is available at the temperature T_H and the engine operates between T_0 and $T_{H1} < T_H$.

operating hours). The temperature at which this heat is available is mostly above 350°C (HREI DEMO Observatory, 2013).

Generally, no matter how, a thermal decomposition modifying the physical and thermodynamic properties of the working fluid negatively affects the design performances (useful power and efficiency) of the engine.

Just as a theoretical example, with reference to Fig. 5.2, we assumed: (1) a siloxane as the working fluid (hexamethyldisiloxane, $\text{H}_3\text{C}-\text{Si}-\text{O}-\text{Si}-\text{CH}_3$), (2) a

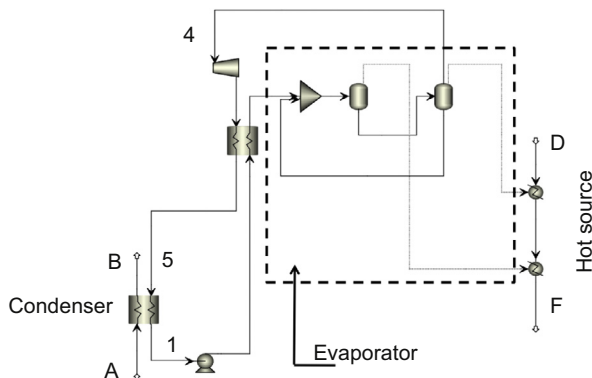


Figure 5.2 A simplified plant scheme for an Organic Rankine Cycle recovering heat from a heat transfer oil. The evaporator is modeled in a way to assure saturated vapor at point “4” in every working conditions. The used computational program was Aspen Plus (a registered trademark of Aspen Technology, Inc.).

condensation temperature of 40°C (condensation pressure $P_C = 0.115$ bar), (3) an evaporation pressure of 17 bar (evaporation temperature of 237.12°C), and (4) reasonable efficiencies for the turbine and pump. Under these conditions, the net power could be about 60 kW for a unit mass flow rate of thermal oil in the evaporator (supposed available between $T_D = 400^\circ\text{C}$ and $T_F = 300^\circ\text{C}$, see Fig. 5.2).

Owing to the relatively low condensation pressure, if the fluid slightly decomposes, a very small quantity of methane is sufficient (for example a molar fraction of 0.5 per thousand) to compromise the heat transfer at the condenser (see Fig. 5.3(b)). Because of the very low dew temperatures of methane, the dew temperature for the hypothetical resulting mixture corresponds to that of pure hexamethyldisiloxane, while the bubble temperature (fixed a pressure value) is much lower (about 25°C in this case, see Fig. 5.3(a)). As a consequence, in the numerical example, the cold temperature approach

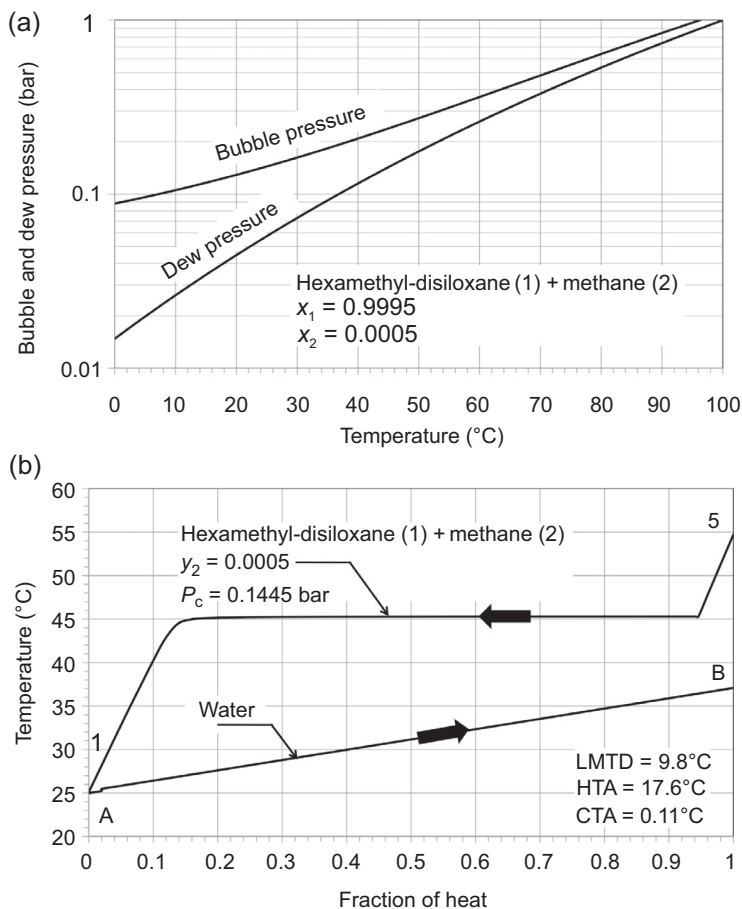


Figure 5.3 (a) Bubble and dew curves for a mixture of hexamethyldisiloxane and methane. (b) Heat transfer diagram in the condenser of the cycle in Fig. 5.2 operating in “off-design” conditions.

vanishes and the engine cannot work, notwithstanding, in the considered case, an increase of P_C of about 26% in comparison with the base case. Although the example considers an extreme situation, it is representative of what can happen in a real engine.

Furthermore, in certain particular cases even a minor degradation of the working fluid can compromise the engine's operation and, even worse, damage essential components if the decomposition is accompanied by a corrosive action and deposition of a chemically active carbonaceous residue. That said, some very slight fluid decomposition is unavoidable and the engine must be designed to prevent the massive decomposition that can jeopardize its operation.

5.2 The thermal and the thermochemical stability of working fluids

5.2.1 The thermal stability

In accordance with the Standard ASTM No D6743-11 ([Standard Test](#)), the thermal stability of a working fluid is its “heat resistance”, or, the capability to preserve unchanged all its main physical properties because of the heating. As a general rule, the greater the thermal stability, the greater the maximum temperature at which the fluid can be used.

The thermal degradation of a working fluid occurs when the temperature breaks the molecular bonds, thereby forming new compounds (the products of decomposition), which have either lower or higher boiling points.

For example, among the products of thermal decomposition of toluene (C_7H_8 , a well-known working fluid), at about 340°C, there is methane, C2 and C3 alkanes and alkenes (in the gaseous phase), and biphenyls (as a major degradation product in the liquid phase) ([Cole et al.](#)).

As the degradation of a working fluid increases exponentially with the temperature, according to ([Spurlin, 2015](#)), an increase of 10°C in the bulk temperature can double the rate of decomposition, halving the operating life of the fluid.

However, above a threshold temperature, there is always thermal degradation of the working fluid and (having fixed the operating conditions) the residence time then affects the quantity of degraded mass. For example, in [Andersen and Bruno \(2005\)](#), at 315°C and 41 bar, samples of n-pentane and toluene, in different cells in 316L stainless steel, and following residence periods from 40 h to 15 days, show a “half-life” of 4.7 and 3.3 years respectively.

Moreover, the pressure has a sensible effect both on the decomposition percentage and on the distribution of the decomposition products. In [Fig. 5.4](#), by way of example, the decomposed mole fraction is represented as a function of the reciprocal of the temperature for cyclopentane at two different pressures. The results are from a total Gibbs free energy equilibrium calculation and the assumed products of decomposition are inferred from [Ginosar and Petkovic \(2011\)](#). At 300°C, for a reaction pressure from 1 to 40 bar, the decomposed mole flow rate fraction $(\dot{n}_{in} - \dot{n}_{out})/\dot{n}_{in}$ falls by about one-third.

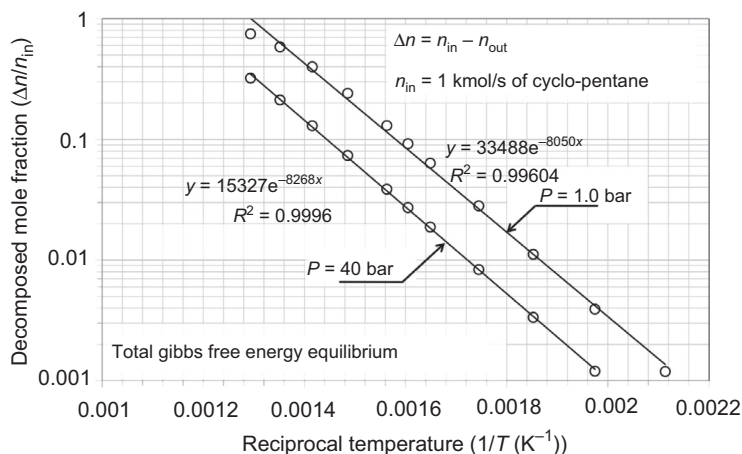


Figure 5.4 Results of chemical equilibrium in a Gibbs reactor for cyclopentane and its assumed decomposition products. The used computational program is Aspen Plus (a registered trademark of Aspen Technology, Inc.).

Both low and high boiling degradation products jeopardize the heat transfer processes. The low boiling compounds could reduce the available NPSH (Net Positive Suction Head) of the circulation pumps (Spurlin, 2015), change the flash point of the working fluid (with safety problems), and raise the condensation pressure to unacceptable values. The high boiling compounds can increase the fluid viscosity. As they cannot easily be removed from the system, in time, they can form tar deposits.

In an inert environment, the bond dissociation energies of the compound are a fairly good indication of its thermal stability. As a general rule, for example, hydrogen forms strong bonds with carbon, fluorine, nitrogen, and oxygen. A single bond between two atoms is weaker than a double or a triple bond (the alkene $H_2C=CH_2$ and the alkyne $HC\equiv CH$ have a carbon–carbon dissociation energy bond of about 2 and 2.5 times stronger respectively than that of the alkane H_3C-CH_3). The methyl H_2C-H bond (≈ 450 kJ/mol) is one of the stronger C–H bonds, but, essentially, it is weaker than the energy bond of C–F (≈ 530 kJ/mol). Silicon forms strong bonds with oxygen (≈ 798 kJ/mol) and carbon (≈ 435 kJ/mol).

In a plant, the working fluid is in contact with numerous materials and substances: metals, plastics and lubricants, air, and water (hard to remove completely from a plant). In these real operating conditions, its thermal stability may worsen dramatically. So, in practical cases, it is better to characterize a working fluid in terms of its “thermochemical stability” rather than its “thermal stability”.

5.2.2 The thermochemical stability

For instance, according to Saaski and Owzarski (1977, pp. 2–31), the decomposition rate of refrigerant R-11 (trichlorofluoromethane, CCl_3F), increases for catalytic effects

by a factor of 3 and of 20 in the presence of Inconel and 18-8 stainless steel respectively, in comparison with platinum. In [Ginosar and Petkovic \(2011\)](#), the decomposition products of cyclopentane at 300°C increased by a factor of about 1.84 in the presence of air. Even Inconel 617, after exposure to helium (a noble gas) with small quantities of impurities (7.14 ppm in volume of hydrogen, 0.021 ppm of water, 0.76 ppm of methane, 0.47 ppm of carbon monoxide, and 0.089 ppm of nitrogen), for 10,000 h, shows appreciable corrosion at temperatures between 650 and 900°C ([Lee et al., 1981](#)).

As a further example, methylene chloride (CH_2Cl_2), in a quartz cell, decomposes at 1% per hour at 415°C; in the presence of AISI 430F stainless steels, the same decomposition rate occurs at 250°C ([Santacesaria et al., 1974, 1975](#)).

It is therefore essential to test a working fluid not only alone but also in the presence of some of the materials that are foreseen in the plant.

5.3 The evaluation of thermal stability

A consolidated method for testing the chemical stability of materials and working fluids, the so-called “sealed tube test”, was worked out by ASHRAE for refrigerants and is described in the ANSI/ASHRAE Standard 1997–2002.

Generally, glass tubes are charged with the refrigerant, air, moisture, (in predetermined quantities), oil, and metal strips. The tubes are sealed hermetically and then aged at elevated temperatures for a specified time. A comparison between the tubes and a control tube (in terms of color and physical appearance of the fluids and of the metal surfaces) gives preliminary information about the thermochemical stability. A chemical analysis of the fluids (gas and liquids) and the metal strips can then complete the information on their mutual compatibility and on the thermochemical stability of the refrigerant. An example of an extended analysis based on the ASHRAE sealed tube test for the new hydrofluoroolefins, HFO-1234yf and HFO-1234ze is available ([Rohatgi et al., 2012](#)).

Besides the sealed tube test, specific “component” and “system tests” have been developed for the refrigerants too. The component tests are conducted in large pressure vessels in the presence of the component, a lubricant, and the refrigerant. The system tests are carried out on complete systems working in well controlled or under severe working conditions. An “on-tap” analysis of the products and of the rate of the chemical reactions gives information about the chemical stability of the fluids involved. These component and system tests also provide useful data on the life and performance of the systems and components themselves ([ASHRAE Handbook, 1994](#), Chapter 5).

Another static test method, for the thermal stability of organic heat transfer fluids, is described in ASTM Standard ([Standard Test](#)). The Standard specifies how the test must be managed, by test cells, in the absence of oxygen and water and stipulates that the boiling range of the heated sample fluid be evaluated (by gas chromatography analysis) and then compared to the boiling range of the pure, unused fluid.

In the ASTM Standard (Vapor Pressure) a procedure to set the decomposition temperature for pure fluids or liquid mixtures is described. The method makes use of an isoteniscope¹ and, as the initial decomposition temperature is assumed to be that temperature at which (1) the curve (in a plane vapor pressure, reciprocal absolute temperature) first departs from linearity or (2) when the isothermal rate of pressure rise is 6.7 kPa/h.

The Standard (Vapor Pressure) was used in Blake et al. (1961) to test lubricating oils and hydraulic fluids. Various different types of isoteniscopes were used in Johns et al. (1962a,b) and Fabuss et al. (1963) to find organic structures stable at 550°C. Here, the authors assumed as their criterion for defining thermal stability, the temperature at which the rate of decomposition of the fluid samples was equal to 1 mol percent per hour.

From our point of view, the vast quantity of results presented in the previous papers can be summed up as, all the aromatics are more thermally stable than the corresponding saturated compounds. Silicones are seen to be more thermally stable than silanes (Blake et al., 1961). For example, among the considered paraffin hydrocarbons, octacosane [$\text{CH}_3(\text{CH}_2)_{26}\text{CH}_3$], shows a thermal decomposition temperature of 350°C. Correspondingly, an equivalent branched paraffin hydrocarbon should be less stable than octacosane. Among the aromatic hydrocarbons investigated, *p*-quaterphenyl is shown to be better than the best aliphatic by at least 100°C. Polyaromatic ethers and aromatic amines all appear extremely stable, at least as much as the polyaromatic hydrocarbons. Aliphatic silanes exhibit thermal decomposition temperatures similar to those of better aliphatic hydrocarbons. Aromatic silanes are about 80–100°C more stable than aliphatic silanes. Silicones (Dow Corning 710 and 550 silicones fluids) show a thermal decomposition temperature of about 350–380°C.

Perfluorination and perchlorination of aromatic rings increase the thermal stability. For example, perfluorobenzene C_6F_6 was found to be stable in the vapor phase, even at 670°C (Johns et al., 1962a).

Decomposition generally occurs at lower temperatures in the liquid phase than in the vapor phase. For example, naphthalene had a decomposition temperature of about 620–650°C at atmospheric pressure in the vapor phase, while its decomposition temperature was about 570°C in the liquid phase (Johns et al., 1962a).

Apparatus for static tests is described in Andersen and Bruno (2005). Some reaction cells (various bars in stainless steel 316 of 6.4 cm length, 0.64 cm OD, and 0.18 cm ID) are inserted into a thermal block made of AISI 304, with the possibility of varying the temperature between 375 and 500°C. It is then possible, measuring decomposition by means of gas chromatography at different temperatures and different residence times, to evaluate the decomposition reaction rate constant k (see Eq. (5.2)) of the fluid under test.

¹ The isoteniscope is a device used to measure the vapor pressure of liquids. The manometer and the sample of the fluid whose vapor pressure is being measured are both immersed in a thermostatic bath. The liquid and the vapor of the sample are kept at a constant temperature, avoiding any thermal gradient.

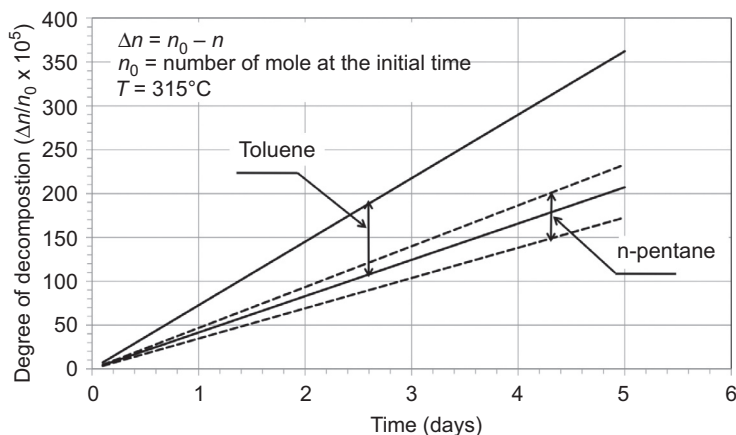


Figure 5.5 Degree of decomposition as a function of time for toluene and for n-pentane at 315°C.

The results are from Andersen Wendy, C., Bruno Thomas, J., 2005. Rapid screening of fluids for chemical stability in organic Rankine cycle applications. *Industrial and Engineering Chemistry Researches* 44, 5560–5566.

The procedure was applied in Andersen and Bruno (2005) to n-pentane, 2-methylbutane (isopentane), 2,2-dimethylpropane (neopentane), toluene, and benzene at 315°C. The branched pentanes were less stable than n-pentane. For toluene (boiling temperature of 111°C) and n-pentane (boiling temperature of 36.1°C) the decomposition reaction constant is about $(6.6 \pm 1.8) \times 10^{-9} \text{ s}^{-1}$ and $(4.7 \pm 1.8) \times 10^{-9} \text{ s}^{-1}$ respectively. The degree of decomposition as a function of time for toluene and n-pentane at 315°C is given in Fig. 5.5. Given the measurement uncertainties, according to the Andersen and Bruno (2005), the two fluids seem quite similar.

Apart from the static methods, dynamic circuits (closed hermetic circuits either in a natural or in forced circulation loops) can also be used to test thermal stability of the working fluids. In a dynamic loop, the main goal has to be to test the working fluid under the same conditions as a real operating system. Usually, the dynamic circuits are designed with liquid and with noncondensable gas sampling devices, where fluid samples can be periodically drawn off for chemical analysis. An example of a very simple scheme of a closed dynamic circuit can be found in Fig. 5.6 (Gamba, 1977).

Niggemann (1969) presented various results about the technological aspects, for the development of an Organic Rankine power conversion system capable of long term operation in a space environment. The working fluids considered are biphenyl and the eutectic mixture of biphenyl and biphenyl ether. In order to investigate the thermal degradation of the working fluids, four hermetically sealed test loops with sampling valves were designed and built.

For the duration of 6250 h at about 370°C, after recurrent analysis, the eutectic mixture of biphenyl and biphenyl ether showed no significant changes in several

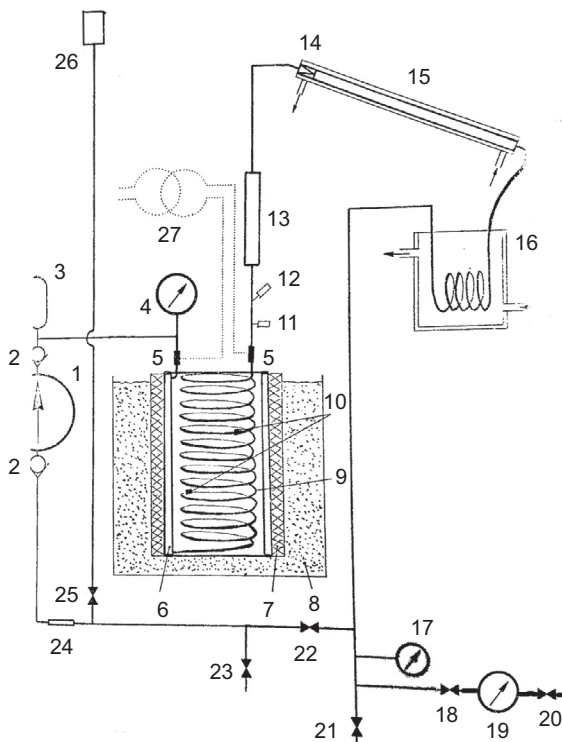


Figure 5.6 Scheme of a simple closed dynamic circuit. (1) membrane pump, (2) nonreturn valves, (3) hydro-pneumatic accumulator, (4) pressure gauge, (5) connection terminals of the electrical transformer, (6) annular chamber, (7) fiberglass, (8) sand, (9) coil, (10) thermocouples for the thermostat controller, (11) thermocouple for the measure of the temperature of the fluid, (12) thermocouple for the measure of the metal tube, (13) container for metal samples, (14) throttling hole, (15) condenser, (16) subcooler, (17) pressure gauge to measure the condensation pressure, (18) connecting valve between the circuit and the vacuum gauge, (19) vacuum pump, (20) connecting valve between the vacuum gauge and the vacuum pump, (21) emptying valve, (22) valve, (23) loading valve, (24) dielectric joint in Teflon, (25) connecting valve, (26) liquid tank, and (27) a 4 kW single-phase electrical transformer.

From Gamba, M., 1977. *Experimental Analysis of the Thermal Stability of Two Organic Fluids: Freon 113 and PP2*. (Degree thesis). Politecnico di Milano (in Italian).

important physical properties (viscosity at different temperatures, refractive index at 82°C, specific gravity at 25°C, and freezing point).

After 6000 h operation at the maximum temperature of 370°C, the degradation of the eutectic mixture was less than 0.1%.

A chemical analysis of the noncondensable gases produced by the decomposition revealed the presence of hydrogen, methane, ethane, and propane (the expected degradation products) and nitrogen, oxygen, carbon monoxide and carbon dioxide as a result of the entry of air into the loop and of the consequent oxidation of the working fluid at

elevated temperatures. Meanwhile, the liquid samples revealed benzene, phenol, different high boilers terphenyls, and ethers aromatic products.

As a further example, a preliminary design for a recovery Rankine engine to be installed on a standard truck is described in [Di Nanno et al. \(1983\)](#). The thermal stability of the chosen working fluid (RC-1, a mixture of 60 mol% pentafluorobenzene and 40 mol% hexafluorobenzene) was tested in a dynamic loop for 442 h at 370°C, 653 h at 430°C, and 532 h at 480°C. At the same time, static tests in glass sealed capsules were carried out at 480°C. The results of all dynamic tests showed no significant thermal degradation in RC-1 fluid constituents.

On the other hand, in [Ragaller et al. \(1987\)](#), a sample of about 16 g of RC-1 in static tests, after 1000 h at 430°C, revealed a degradation of approximately 7.5%. The primary degradation products were perfluoro-biphenyl, isomers of nonafluoro-biphenyl, HF and F₂ (two highly reactive gases). At 480°C, after 100 h, about 30% of the sample decomposed.

Finally, as a further example, [Cole et al. \(1987\)](#) and [Havens et al. \(1987\)](#) describe the results of a study into the thermal stability of toluene as a working fluid in space power modules with an intended electrical power of 4 kW. The dynamic circuit (including a regenerator) simulates supercritical turbine inlet conditions of 400°C and 42 bar. The selected materials (300 series stainless steel, Viton and Teflon) were all compatible with toluene and suitable to the condensation pressure, which was slightly greater than the ambient pressure, ensuring a limited reentry of air.

The circuit worked for 3410 h mainly at 400°C and among the decomposition products were: (in the gaseous phase) hydrogen, methane, ethane, propane, nitrogen, carbon monoxide, and carbon dioxide (the latter being evidence of a small air leak); benzene, biphenyl, bibenzyl, and other two and three rings aromatic hydrocarbons (among the liquid products). The authors have concluded that toluene degradation, in these working conditions, does not seem to be a significant issue.

It is worth mentioning the work involved in selecting the working fluids for heat pipes. The fluid in a heat pipe acts as a heat transfer fluid, in accordance with the repeated evaporations and condensations of a thermodynamic closed cycle. Heat pipes are often hermetically sealed devices with a small internal volume in which even a minimum decomposition of the working fluid can compromise proper operation by clogging the fluid circulation.

The operating temperature ranges of the heat pipes are extremely wide (from cryogenic temperatures to several thousand degrees Celsius). The working fluids used are simple (monoatomic or diatomic) gases or simple organic compounds in the cryogenic range, and organic and inorganic fluids or liquid metals in the greater temperature ranges.

As an example, [Saaski and Owzarski \(1977\)](#) summarizes the results of a quest for stable two-phase heat transfer fluids for the temperature range 100–350°C. After a wide general survey of previously available data on the thermal stability of working fluids, the authors present the results of compatibility tests in heat pipes using a capsule made of carbon steel (A-178) and aluminum alloy 6061. The considered working fluids are: various aromatic hydrocarbons (toluene, naphthalene, biphenyl, and *o*-terphenyl), two halogenated aromatic hydrocarbons (monochloro-naphthalene, 1-fluoro-naphthalene), and inorganic molecular fluids (carbon disulfide, tin

tetrachloride, titanium tetrachloride, and antimony trichloride). The fluids were subjected to operating pressures of about 1 or 2 bar above their boiling point (corresponding to operative temperatures from about 60 to 300°C) for varying periods of time, up to 3500 h. The couplings of tin tetrachloride–aluminum at 159°C, antimony trichloride–aluminum at 227°C, and monochloronaphthalene–carbon steel at 266°C were found to be totally incompatible. The remaining fluids and envelopment combinations always generated noncondensable gases, but without blocking the functionality of the devices.

The fluids considered so far have been especially aromatic hydrocarbons (toluene and biphenyl), saturated, linear or branched and cyclic hydrocarbons (n-pentane, isopentane, cyclopentane), siloxanes, perfluorocarbons and refrigerants (hexafluorobenzene and hydrofluorocarbons).

As a general rule, the static tests are more stressful for the working fluid under investigation than the dynamic ones. In fact, in a static test, small quantities of fluid are confined at high temperature throughout the duration of the test.

However, the results from both the static and the dynamic tests (at least in relatively analogous conditions) are roughly in agreement. Basically, aromatic substances are more thermally stable than the corresponding saturated compounds; a minimum thermal decomposition is always present above certain temperatures and no organic fluid can safely withstand temperatures above 400°C. In any case, the nature of the containing walls and the presence of lubricating oil play a dominant role.

The results of different test procedures are hard to compare. By way of example, the decomposition temperature of perfluorobenzene in a gaseous phase is assumed to be 670°C (Johns et al., 1962a). On the other hand, according to Ragaller et al. (1987) at a temperature of 480°C, 30% of the fluid sample decomposed.

Static tests are helpful for a systematic investigation of the thermochemical stability of potential working fluids and, in a relatively straightforward way, they can test the influence of different materials and substances too. In Section 5.4, a particular static system to study thermochemical stability of working fluids is presented and described.

5.4 A system for the measurement of thermal stability

Experimental apparatus for the evaluation of thermal stability of working fluids was developed by Invernizzi in 1990. Since this time, many results were presented. The thermal degradation threshold of various refrigerants is discussed in Calderazzi and di Paliano (1997) and in Angelino and Invernizzi (2003); that of a fluoroether (HFE-7100) is discussed in Invernizzi and Pasini (2000); results for several siloxanes are presented in Angelino and Invernizzi (1993); and in Angelino et al. we consider toluene and some tri-methylbenzenes.

A new version of the apparatus has been developed at the Department of Mechanical and Industrial Engineering at the University of Brescia.

The method is based on measuring the pressure and temperature of an appropriate quantity of the liquid, confined within a container at a constant volume. First, the vapor

pressure of the de-gassed “virgin” fluid is measured; this then serves as the reference. Then, the fluid sample is subjected to different constant test temperatures (at preset time intervals, typically 70–100 h), monitoring the pressure of the cylinder at constant volume which contains the fluid. After the permanence of the fluid sample at the test temperature, the vapor pressure curve is re-measured each time. Decomposition of the fluid is revealed by: (1) any variation in the pressure over time during the permanence of the sample at constant temperature; and (2) a difference in the vapor pressure compared to reference values. Where necessary, chemical analysis may be carried out on the fluid samples at the end of each test.

The hydraulic circuit is shown in Fig. 5.7. The system concept is illustrated in Fig. 5.8.

The thermostatic bath (B) is used for the preliminary de-gassing operations and to measure the vapor pressure. Its temperature is controlled electronically and can vary between -40°C and $+50^{\circ}\text{C}$, with a resolution of 0.1°C and a stability of 0.2°C . For temperatures greater than 50°C , vapor pressure values are measured with the test cylinder in a muffle kiln (F). The kiln is also used for the thermal “stress” tests. The temperature of the muffle kiln can be controlled electronically and set between 70 and 1000°C , with a resolution of 1°C and a degree of stability of around 2°C .

The whole circuit is made in AISI 316L stainless steel. The cylinder has an internal volume of about 150 cm^3 . One end of the cylinder containing the fluid sample is sealed by TIG welding; the other end is used for inserting the loading tube, which connects the cylinder with the rest of the circuit, and for inserting a blind tube which holds the temperature sensor.

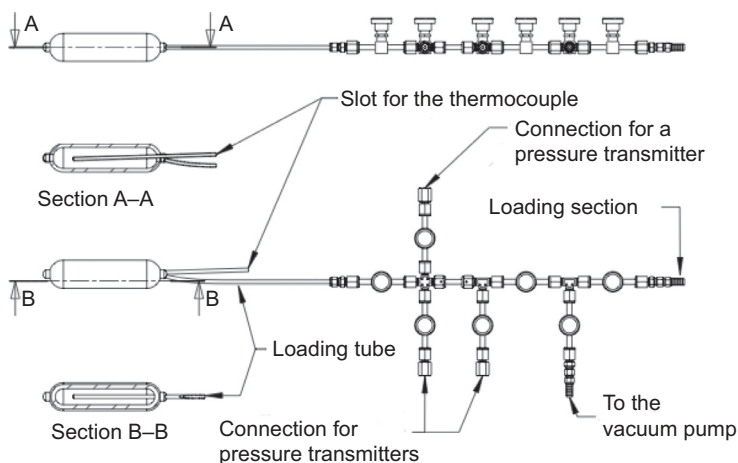


Figure 5.7 Details of the test hydraulic circuit. The sections “A–A” and “B–B” show the hydraulic connections and the housing of the temperature sensor.

From Pasetti, M., November 25, 2013. Thermal Stability of Working Fluids for Organic Rankine Cycles. Final Report. Department of Mechanical and Industrial Engineering, University of Brescia. Work Order CM-RI-100034 (in Italian), with permission of Turboden Srl.

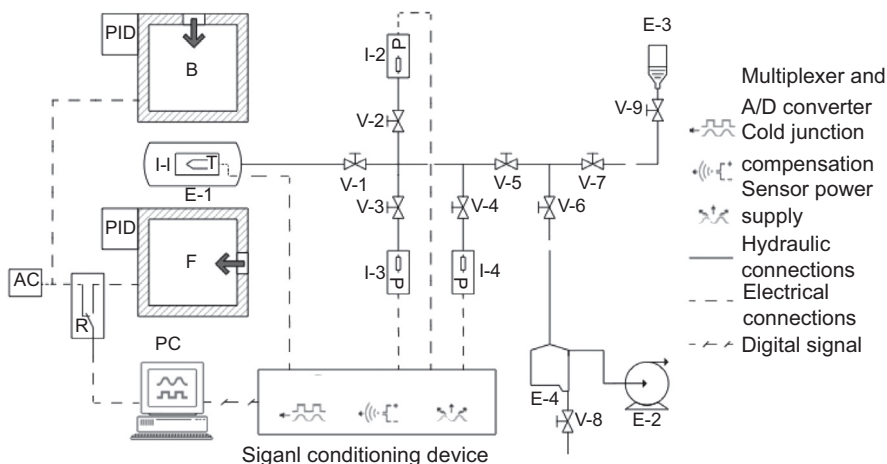


Figure 5.8 Schematic layout of the experimental apparatus: (F) muffle furnace, (B) thermostatic bath, (AC) AC power, (R) security relay for the power supply of the furnace, (PID) temperature control panel, (PC) personal computer for data acquisition and for the system control, (E-1) sample cylinder, (E-2) vacuum pump, (E-3 and E-4) vacuum trap, (V-1, V-2, V-3, V-4, V-5, V-6, and V-7) bellows valves, (V-8) Hoffman clamp, (V-9) Pyrex tap, (I-1) thermocouple, and (I-2, I-3, and I-4) pressure transmitters.

From Pasetti, M., November 25, 2013. Thermal Stability of Working Fluids for Organic Rankine Cycles. Final Report. Department of Mechanical and Industrial Engineering, University of Brescia. Work Order CM-RI-100034 (in Italian), with permission of Turboden Srl.

The connectors and the valves are made from AISI 316 or AISI 316L steel. The bellows valves have a maximum operating pressure of around 60 bar. All the connections are equipped with metal packing that guarantees tight sealing properties, both under pressure and under vacuum, whatever the fluid. At the height of the pressure transmitters, there are stop valves that prevent damage to the instruments once the pressure within the circuit has passed the maximum limit of the measuring device. The intercept valves are closed manually, but an alarm from the control system signals when the need arises.

The pressure is measured using mechanical deformation instruments, with silicon piezoresistive sensors. The technical characteristics of all the instruments installed can be found in [Table 5.1](#). An electronic card, equipped with an integrated system that compensates for the cold joint, is responsible for the acquisition and A/D (Analog to Digital) conversion of signals originating from the thermocouple.

The sampling and recording of data downstream from the process of acquisition and A/D conversion of the signal is carried out by an application created within the context of LabVIEW programming. The digital signals from the acquisition cards are sampled and the averages recorded at intervals of 1 min. Apart from acquiring and recording data, the application is also responsible for the system control, and cutting off power to the kiln whenever the pressure or temperature values reach the safety levels imposed by the operator.

Table 5.1 Technical characteristics of the chosen measuring instruments

Instruments for the measure of pressure	
Manufacturer and model	BCM sensor 131(I)
Measured quantity	Absolute pressure
Measuring principle	Mechanical deformation Piezoresistive silicon
Output signal	4–20 mA (two-wire conduction)
Process connection	Conical thread GAS NPT
Instrument full scale (FSO)	1 bar, 10 bar, 50 bar
Accuracy	0.1% FSO
Operating temperature range	–40 to 125°C
Compensated temperature range	–10 to 60°C
Temperature drift	Span: 0.03% FSO/°C Zero: 0.03% FSO/°C
Maximum allowed pressure	150% FSO
Instruments for the measure of temperature	
Manufacturer and model	Gefran TC1M
Measuring principle	Thermocouple of type K
Measuring range	–40 to 1050°C
Accuracy for $T \in (-40 \text{ to } 333^\circ\text{C})$	$\pm 2.5^\circ\text{C}$
Accuracy for $T > 333^\circ\text{C}$	$\pm 0.0075T$

1) BCM is the name of the company that provided us the sensors. 2) GAS NPT = National Pipe Thread for Gas 3) FSO = Full Scale Output
 From Pasetti, M., November 25, 2013. Thermal Stability of Working Fluids for Organic Rankine Cycles. Final Report. Department of Mechanical and Industrial Engineering, University of Brescia. Work Order CM-RI-100034 (in Italian), with permission of Turboden Srl.

The quantity of fluid that is loaded each time is calculated on the basis of the maximum temperature the fluid sample is expected to experience, making sure that the pressure at the maximum test temperature is no higher than the scale limit of the pressure transmitters present. With a specific volume as close as possible to the critical value and compatible with the maximum pressure limit, the maximum extent of the vapor pressure can be measured.

The assumed values $u_s(P)$ for the compound uncertainties on the pressure measurements and $u_s(T)$ for the temperature measurements, are assumed equal to the uncertainties reported in Table 5.1. In all the subsequent Figures, the composed uncertainties are extended to the 95% of confidence.

In the following, we present some representative vapor pressure measurements, then we discuss several examples of thermal stability results.

5.4.1 Some examples of vapor pressure measurements

As reference values of vapor pressure are fundamental in our procedure for a proper evaluation of the level of thermal degradation of a working fluid, we show some of the results of measured vapor pressure curves for significant fluids from the new version of the apparatus.

Perfluoro-n-hexane. In Fig. 5.9 the vapor pressure for perfluoro-n-hexane (C_6F_{14} , $T_{cr} = 176.4^\circ C$, $P_{cr} = 18.02$ bar) between -20 and $170^\circ C$ is reported. For comparison, the Figure reports some data from the literature too (Dias et al., 2005; Stiles and Cady, 1952; Crowder et al., 1967; Mousa, 1978) Taking into account the accuracies and the uncertainties of our measurements, the results are acceptable across the whole temperature range.

The perfluorocarbons are considered thermochemically very stable and, also for their chemical inertness and not flammable, are used as heat transfer fluids. They were already proposed in the past as working fluids in high temperature (250 – $300^\circ C$) Organic Rankine Cycles (ORCs) (see, for example Bombarda and Invernizzi (2015)).

Cyclopentane. In Fig. 5.10 some measured values of the vapor pressure are reported and they are compared with literature values (Benson, 1941; Aston et al., 1943; Mokbel et al., 1995). Cyclopentane (C_5H_{10} , $T_{cr} = 238.6^\circ C$, $P_{cr} = 45.1$ bar) was considered as a working fluid in high-temperature geothermal binary plants and is used in heat recovery Rankine engines with size power from a few MW up to 17 MW, see for example Zia et al. (2013) and Burrato (2013).

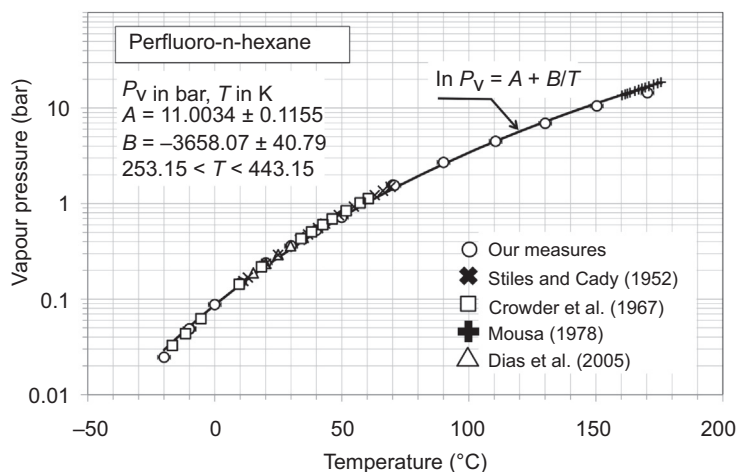


Figure 5.9 Vapor pressure of perfluoro-n-hexane. A comparison among our measured values and literature values.

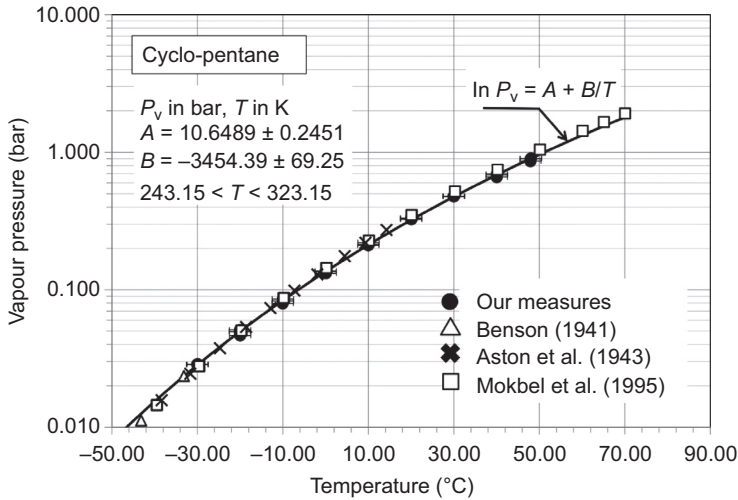


Figure 5.10 Vapor pressure of cyclopentane. A comparison among our measured values and literature values. In this case the measured values are limited to the subatmospheric portion of the vapor pressure curve.

From Pasetti, M., November 25, 2013. Thermal Stability of Working Fluids for Organic Rankine Cycles. Final Report. Department of Mechanical and Industrial Engineering, University of Brescia. Work Order CM-RI-100034 (in Italian), with permission of Turboden Srl.

Titanium tetrachloride. Measured vapor pressure values are in Fig. 5.11 with the data from Pike and Foster (1959) as a comparison. Titanium tetrachloride (TiCl_4 , $T_{\text{cr}} = 364.85^\circ\text{C}$, $P_{\text{cr}} = 46.61$ bar) belongs to the halides family. Halides were proposed as good working fluids in heat pipes in the temperature range $200\text{--}400^\circ\text{C}$ (see Bombarda and Invernizzi, 2015). Titanium tetrachloride is liquid at room temperature and, from a strictly thermodynamic point of view, it is an almost ideal working fluid as it has a high molecular weight (189.69) and a molecular complexity parameter² near zero ($\sigma \approx 2$). It is not inflammable, but, unfortunately, it is very reactive with water, releasing hydrogen chloride (toxic and corrosive).

The three fluids we considered in our example belong to very different families, and the results show the versatility of the measuring apparatus designed (albeit, within the rather high margins of uncertainty offered by the instruments available).

5.4.2 The quantification of the decomposition

As usual, the decomposition of the fluid produces gases with lower boiling temperatures; the first evidence of decomposition is the increase in the vapor pressure at relatively low temperatures. In fact, generally, having fixed the temperature, even the

² The molecular complexity of a working fluid can be correlated with the slope of the vapor limit curve and may be evaluated by the parameter $\sigma = (T_{\text{cr}}/R) [dS_{\text{SV}}/dT]_{T_{\text{cr}}} = 0.7$. It is basically a function of molar heat capacity and of the acentric factor ω (see Invernizzi, 2013, Chapter 2, Section 2.5, pp. 109–111).

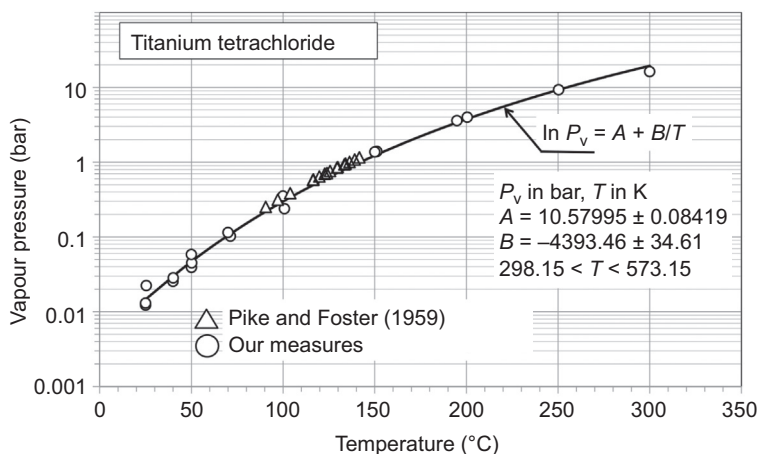


Figure 5.11 Vapor pressure of titanium tetrachloride. A comparison among our measured values and literature values.

Data are from Macchi, E., Bonalumi, D., Invernizzi, C., Iora, P., September 2014. Experimental Results of Thermal Stability of TiCl_4 , Material Selection and a Technical and Economical Analysis. Polytechnic of Milan – Group of Energy Conversion Cycle. ENEA Report RdS/PAR2013/269 (in Italian), with permission of ENEA.

smallest decomposition will raise the vapor pressure P above the value for the “virgin” (unused) fluid (the reference value, P_V) by a quantity ΔP , which is very clear at any pressure below the atmospheric value.

Fig. 5.12 reports values of vapor pressure for a sample of perfluoro-*n*-hexane, measured after its permanence at different temperatures for 80 h each time. In the subatmospheric range, there is a clear increase in the measured vapor pressures as an effect of a partial thermal degradation of the fluid. At $T = -20^\circ\text{C}$, for example, the ratio $(P - P_V)/u(\Delta P)$, with $u(\Delta P)$ the uncertainty of the calculated difference $\Delta P = (P - P_V)$, is 0.381 after 80 h at 200°C and rises to 2.76 after 80 h at 400°C . As long as the decomposition is small, the overpressure in the vapor pressure tends to fall, increasing the corresponding saturation temperature (see Fig. 5.12(a) and (b)).

A second indication of a thermochemical degradation in progress is the trend of the pressure over time, at every mean test temperature. For instance, in Fig. 5.13(a) and in Fig. 5.13(b), the pressure trends during the test time interval of a sample of perfluoro-*n*-hexane are reported, at mean temperatures of 350°C and of 400°C respectively. At the mean temperature of 350°C , the mean pressure increases slightly (about 0.6 mbar/h), and at 400°C , the pressure increases at a rate of about 3 mbar/h. In both cases, the pressure rise, bearing in mind the instrumental uncertainty, is detectable and significant.

On the other hand, a massive decomposition leads to an important pressure increase over time during the test. In Fig. 5.14, for example, the pressure of a sample of perfluoro-*n*-hexane, at the mean test temperature of 450°C increases in 80 h from 45.3 to 48.1 bar.

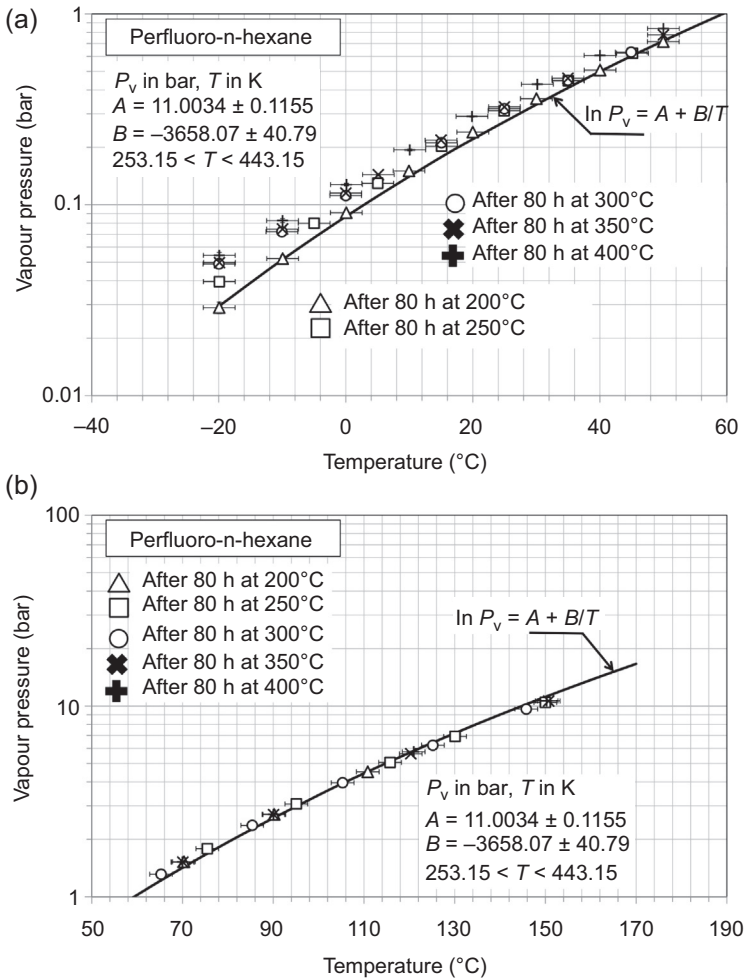


Figure 5.12 Measured vapor pressures of a sample of perfluoro-n-hexane after its permanence for 80 h at different test temperatures. The basic reference line is that obtained by a fitting of the measured values for the virgin fluid (see Fig. 5.9).

In Fig. 5.15, vapor pressure values for a pure commercial sample of cyclopentane and for the same sample after 70 h permanently at 240 and 340 $^{\circ}\text{C}$ are compared. The vapor pressure difference $\Delta P = (P - P_v)$ at about 10 $^{\circ}\text{C}$ after 70 h at 340 $^{\circ}\text{C}$ is about 47 mbar. It is less than the estimated uncertainty $u(\Delta P)$, but, nonetheless, appreciable. This pressure difference, though not statistically significant (owing to the relatively high uncertainty on the temperature), is still an indication of a low thermochemical degradation. Actually, in Ginosar and Petkovic (2011) the authors, in their dynamic loop with cyclopentane, at a maximum temperature of 350 $^{\circ}\text{C}$, after about 350 h, found total decomposition products of 1516 ppm. So, our system seems capable of revealing even minimal rates of decomposition.

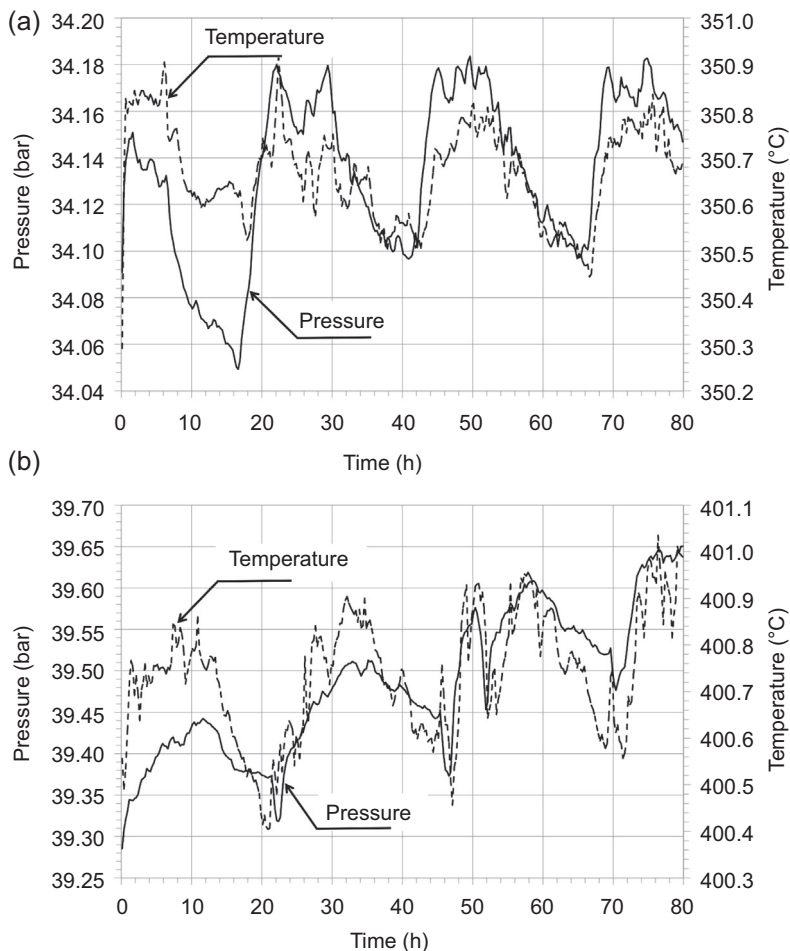


Figure 5.13 Trends in temperature and pressure in 80 h at two different test mean temperatures (350 and 400°C – Figure 5.13 (a) and (b) respectively) for a sample of perfluoro-n-hexane.

Fig. 5.16(a) reports temperature and pressure trends during a thermal stability test. The pressure increased by 2.5% in about 15 h (a mean rate of 0.17% per hour). The consequence of the thermal decomposition on the vapor pressure is shown in Fig. 5.16(b).

Therefore, measuring vapor pressure and monitoring the pressure trend during tests at different temperatures, over a significant number of hours, provides useful information on the thermodynamic stability of a potential working fluid. However, quantifying the decomposition is impossible without a chemical analysis of the decomposition products, in the gas phase and the residual liquid. Decomposition takes place at any temperature, but only when the pressure (at a preset mean test temperature) increases drastically, can we say that the fluid has decomposed in a massive and unacceptable

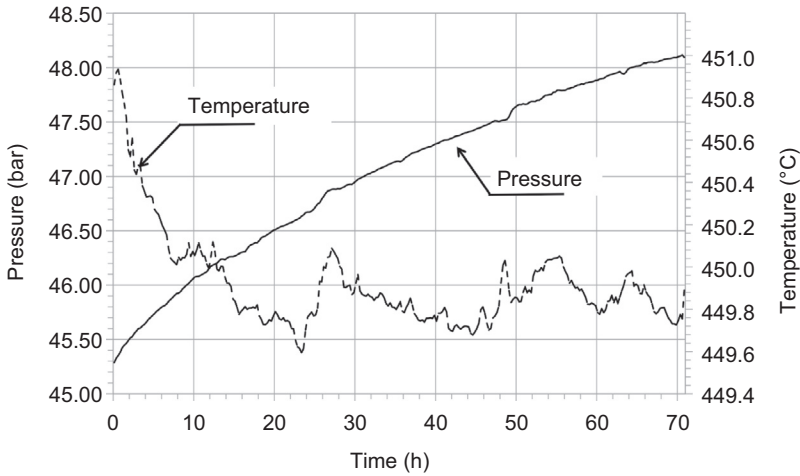


Figure 5.14 Trends in temperature and pressure in 80 h at a test mean temperature of 450°C for a sample of perfluoro-n-hexane.

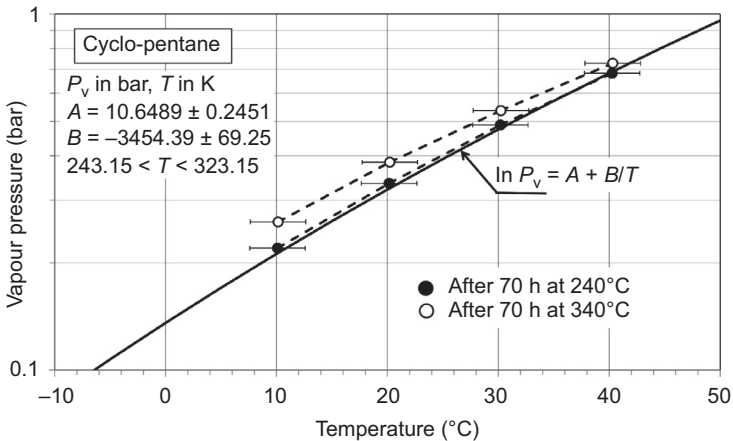


Figure 5.15 Vapor pressure as a function of temperature for a sample of cyclopentane before and after some decomposition tests.

Data are from Pasetti, M., November 25, 2013. Thermal Stability of Working Fluids for Organic Rankine Cycles. Final Report. Department of Mechanical and Industrial Engineering, University of Brescia. Work Order CM-RI-100034 (in Italian), with permission of Turboden Srl.

way. Generally speaking, this also corresponds to a dramatic variation in the vapor pressure curve.

It is well-known that (Benson, 1960, Chapter II, p. 14), assuming a first-order reaction, the rate of the reaction (decomposition) is proportional to the concentration of

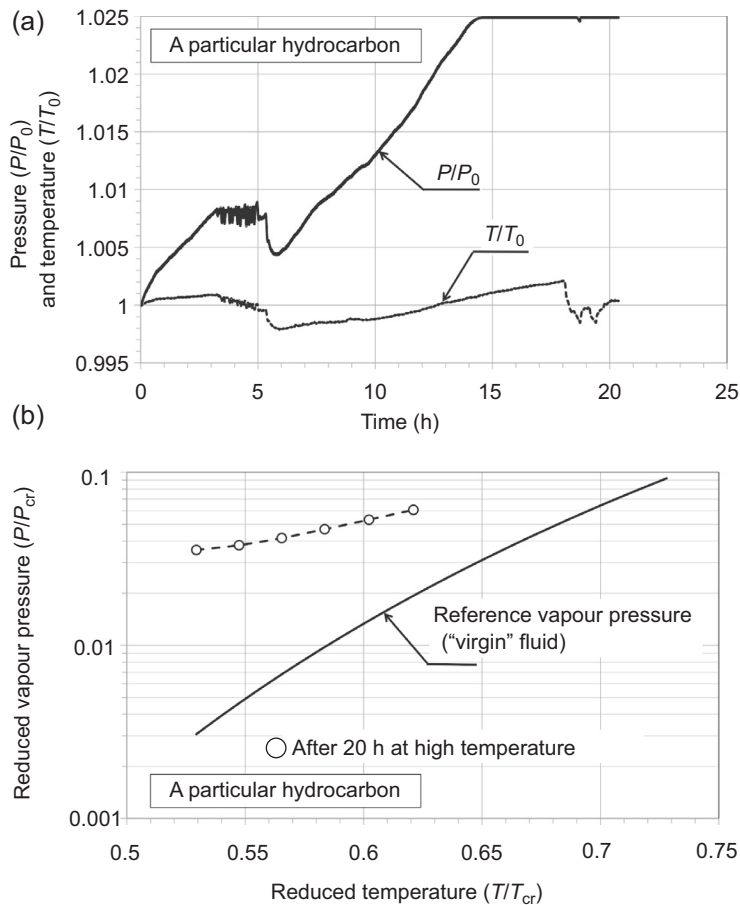


Figure 5.16 (a) Temperature and pressure trends for a hydrocarbon undergoing a massive thermal decomposition. (b) A comparison between the vapor pressure curves for the unused fluid after its thermal decomposition.

By courtesy of Turboden Srl.

only one of the reacting substances. Assuming the number of mole n of the fluid under investigation, we can write

$$\frac{dn}{dt} = -kn \quad (5.2)$$

with

$$k = A \exp(B/T) \quad (5.3)$$

The variable n is the number of mole of the substance at time t , $dn/dt = v$ is the velocity reaction, and k is said to be the rate constant of the reaction (in m/s for a first-order reaction). Assuming $\alpha = \Delta n/n_0$ as the degree of dissociation over time Δt , the integration over time of Eq. (5.2) gives

$$\frac{\ln(1 - \alpha)}{\Delta t} = -k \quad (5.4)$$

From composition analyses used to determine at least one degree of dissociation α at different temperatures, the Eqs. (5.3) and (5.4) enable us to estimate the decomposition rate at any temperature.

In any case, after the permanence of the fluid sample at the test temperature, decomposition generally manifests itself via the formation of “noncondensable” gases and, consequently, the subatmospheric vapor pressure P is generally higher at the P_V of a quantity ΔP , due to the presence of noncondensable products of the decomposition. Or

$$P = P_V + \Delta P \quad (5.5)$$

in the hypothesis where all moles of decomposition products are in the gas phase, at sufficiently low pressures (Pasetti et al., 2014)

$$\begin{aligned} \Delta P &\approx \frac{n_D RT}{V_G} \\ &\approx \frac{n_D RT}{V - V_L} \\ &\approx \frac{n_D RT}{V(1 - V_L/V)} \\ &\approx \frac{n_D RT}{V} \\ &\approx \frac{n_D}{n_0} \frac{RT \bar{\rho}}{MW} \end{aligned} \quad (5.6)$$

or

$$\Delta P \propto \frac{\Delta n}{n_0} \frac{RT}{MW} \bar{\rho} \quad (5.7)$$

and

$$\alpha = \frac{\Delta n}{n_0} \propto \frac{\Delta P MW}{RT \bar{\rho}} \quad (5.8)$$

The mean density $\bar{\rho}$ can be estimated once the loaded mass is known as well as the volume V of the cylinder. Roughly speaking, it can be assumed that $\bar{\rho} \approx \rho_{cr} = P_{cr}MW/(z_{cr}RT_{cr})$.

Defined $\bar{\beta}$ as

$$\bar{\beta} = \frac{1}{N} \sum_i^N \frac{\Delta P_i}{P_{cr}} \frac{T_{cr}}{T_i} z_{cr} \quad (5.9)$$

mean value for several points, at subatmospheric total pressure P and with the sum extended to just those values where $\Delta P/u$ (ΔP) > 1.0, we can, therefore, assume

$$\alpha = \frac{\Delta n}{n_0} \propto \bar{\beta} \quad (5.10)$$

and also

$$\frac{\ln(1 - \alpha)}{\Delta t} \propto \frac{\ln(1 - \bar{\beta})}{\Delta t} = -k^* \quad (5.11)$$

The coefficient k^* , the “quasirate” constant of the reaction, can therefore be assumed to be a parameter which, roughly speaking and to enable a comparison between fluids, provides an indication of resistance to thermal decomposition.

Fig. 5.17 reports the parameter k^* obtained from thermal stability measures on titanium tetrachloride and perfluoro-n-hexane.

The “quasiconstant” of the velocity reaction k^* increases exponentially with the test temperature. The values for TiCl_4 (taken at temperatures of 400, 500, and 550°C) are, on average, higher than the values of k^* for C_6F_{14} (calculated at temperatures of 300, 350, and 400°C). However, TiCl_4 is much more reactive with humidity and, given the difficulties encountered when loading it into the circuit, we cannot exclude the presence of air in the circuit at the start of the tests. It is interesting to note, however, that the coefficient B is around one-third lower than that of C_6F_{14} , indicating a greater resistance to temperature rise (a greater heat stability).

At 400°C, $k^* \approx 3.8 \times 10^{-9} \text{ s}^{-1}$ per C_6F_{14} and at 450°C the fluid has decomposed to a large extent (see Fig. 5.14). The reaction of thermochemical decomposition is a catastrophic phenomenon, and it may take just 20–30°C to set it off.

5.5 Conclusions

The thermal stability of working fluids for ORC is an essential design parameter but it is very difficult to define it in absolute terms. Most of the organic fluids show some

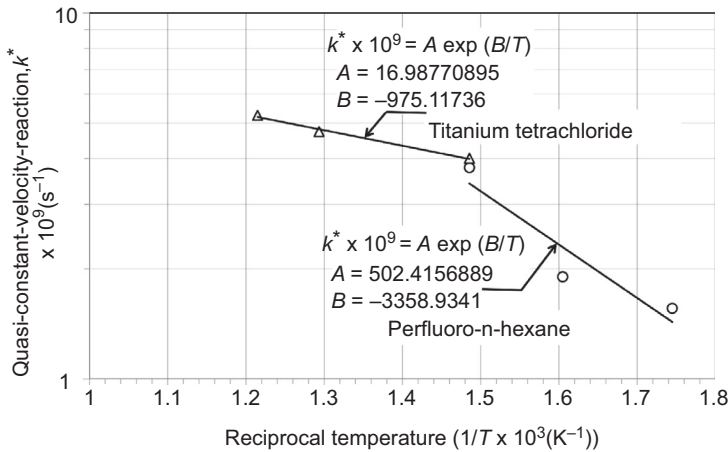


Figure 5.17 “Quasiconstant” velocity reaction as a function of temperature for two working fluids.

Data for titanium tetrachloride are from Macchi, E., Bonalumi, D., Invernizzi, C., Iora, P., September 2014, Experimental Results of Thermal Stability of TiCl_4 , Material Selection and a Technical and Economical Analysis. Polytechnic of Milan – Group of Energy Conversion Cycle. ENEA Report RdS/PAR2013/269 (in Italian), with permission of ENEA, with permission of ENEA.

thermal degradation above typical temperatures and, as a matter of fact, they are all useless above 350–400°C.

As discussed and repeatedly reaffirmed, it is difficult to associate an absolute value to the thermochemical stability of working fluids; the thermal resistance is affected, for example, by the presence of containment materials, air, humidity, and lubrication oils.

In spite of this, in Table 5.2 we collect some data for typical substances, now in use or proposed as working fluids in Rankine cycles. The listed fluids are representative of well-known chemical classes and the values of the reported maximum operative temperatures are only indicative of their own practical thermochemical stability. Just as an example, consider that perfluoropropane (refrigerant 218, $\text{CF}_3\text{CF}_2\text{CF}_3$), according to Fielder (1963), at 500°C, decomposes at a rate of 1% in 100 h; perfluoro-n-hexane (another linear fluorocarbon), decomposes at a rate 10 times greater at 450°C (see Fig. 5.14).

The acceptable decomposition level depends of the specific application and no matter how, a relative comparison among different suitable working fluids is possible only by resorting to the same experimental procedure.

Pyrolysis data and data from tests using sealed tubes may give some indications. In a plant there are various materials and very different working conditions even for a single plant. So, in a strict sense, only tests in dynamic loops and in operative conditions as close as possible to the real ones can ensure significant practical results.

Table 5.2 Estimated maximum functional temperature for some representative working fluids for Rankine cycles

Fluid	T_{\max} (°C) ^a	T_{cr} (°C) ^b	P_{cr} (bar) ^c	T_{B} ^d	σ ^e
Hydrocarbons					
Pentane	300	196.55	33.7	36.06	7.08
Cyclopentane	300	238.54	45.15	49.25	3.53
Toluene	350–400	318.6	41.263	110.6	9.63
Chlorobenzene	320 ^f /660 ^g	359.5	45.191	131.75	8.52
Biphenyl	400	499.85	33.8	255	33.38
Diphenyl oxide	400	493.65	30.8	258	34.72
Downtherm A	400	497.2	31.34	257	34.8
Fluoro-compounds and refrigerants					
R134a	350–370	101.06	40.593	−26.07	−2.34
R245fa	300	154.01	36.51	15.14	2.84
R23	400	25.86	48.2	−82.1	−7.84
R32	570–590 ^h	78.4	57.8	−51.65	−8.5
Fluorinol 85	250–300	233	55.2	75	
Perfluorohexane	400	175.55	18.7	56.6	27.95
Perfluoropropane (R218)	500 ⁱ	71.85	26.75	−39	6.31
Hexafluorobenzene	350–400	243.58	32.75	117.96	12.6

Continued

Table 5.2 Continued

Fluid	T_{\max} (°C) ^a	T_{cr} (°C) ^b	P_{cr} (bar) ^c	T_{B} ^d	σ ^e
Siloxanes					
Linear (MM...MD ₂ M)	300	[245.6326.25]	[19.39,12.27]	[100.52,194.35]	[29,63]
Cyclic (D ₄ ...D ₆)	350	[313.35,372.63]	[13.32,9.61]	[175.0.244.99]	
Some inorganics and organic compounds					
Pyridine	350–400	346.8	56.3	115.2	4.5
Carbon dioxide	650–700 ^j	30.98	73.77		
Titanium tetrachloride	550	365.95	46.61	134.8	1.99

^aMaximum operative temperature.^bCritical temperature.^cCritical pressure.^dNormal boiling temperature.^eParameter of molecular complexity: $\sigma = (T_{\text{cr}}/R) (dS/dT)_{v,0.7}$.^fAccording to Curran (1979).^gIn a heated silica vessel (Cullis and Priday, 1954).^hIn a straight heated Inconel 600 pipe, (Ito et al., 2014).ⁱAt 500°C, according to Fielder (1963), in an Inconel bomb, the fluid degrades at a rate of 1% in 100 h.^jAccording to the proposal by Parma et al. (2011), with stainless steel 316-type. In Magnox reactors, high oxidation rates of mild steel structural components compelled to reduce maximum temperatures from 410 to 360–380°C (Shropshire, 2004).

The right compromise can be found combining, in static tests, both the measure of chemical composition (if considered important) and the analysis of meaningful physical properties (such as the vapor pressure).

On the other hand, only static tests allow a methodical analysis of thermal stability of families of potential working fluids. The dynamic circuits are usually designed for single definite working fluids and it is unlikely that one circuit suits different fluids.

Resorting to static tests and to chemical analysis allows the rate constant of the decomposition reaction to be estimated in a consistent way too. Nevertheless, isothermal measurements of pressure variations and subsequent evaluation of vapor pressure give limiting operating temperatures. In any case, having identified a fluid, the final test must be carried out in a prototypical dynamic real circuit. Dynamic circuits, if appropriately designed, could also give information about heat transfer parameters of working fluids.

Nomenclature

Symbols, acronyms, and subscripts	
α	Dissociation degree
$\bar{\beta}$	Parameter proportional to dissociation degree (see Eq. 5.9)
η	Efficiency
k	Reaction rate constant
M	Mass (kg)
MW	Molecular weight
\dot{n}	Mole flow rate (mol/s)
n_D	Number of moles of decomposition products
n_0	Initial number of moles
Δn	Number of decomposed moles
P	Pressure (bar)
P_c	Condensation pressure (bar)
\dot{W}	Mechanical power (W)
\dot{Q}	Thermal power (W)
R	Universal gas constant (8.3143 J/molK)
T	Temperature (°C or K)
T_h	Temperature of the heat source (°C or K)
T_0	Ambient temperature (°C or K)
\dot{S}_G	Entropy generated per unit time owing to a thermodynamic irreversibility (W)

Continued

Symbols, acronyms, and subscripts	
V	Volume (m^3)
V_G	Volume occupied by gas (m^3)
V_L	Volume occupied by liquid (m^3)
ρ	Density (kg/m^3)
ρ_{cr}	Density of the critical point (kg/m^3)
$\bar{\rho}$	Mean density (kg/m^3)
ID	Internal diameter
OD	Outer diameter
ORC	Organic Rankine Cycle
in	Inlet
out	Outlet
LMTD	Logarithmic mean temperature difference ($^{\circ}\text{C}$)
HTA	Hot temperature approach ($^{\circ}\text{C}$)
CTA	Cold temperature approach ($^{\circ}\text{C}$)

References

- Andersen, P.C., Bruno, T.J., 2005. Thermal decomposition kinetics of RP-1 rocket propellant. *Industrial & Engineering Chemistry Research* 44, 1670–1676.
- Andersen Wendy, C., Bruno Thomas, J., 2005. Rapid screening of fluids for chemical stability in organic Rankine cycle applications. *Industrial and Engineering Chemistry Researches* 44, 5560–5566.
- Angelino, G., Invernizzi, C., 1993. Cyclic methylsiloxanes as working fluids for space power cycles. *Journal of Solar Energy Engineering* 115, 130–137. ISSN:0199-6231.
- Angelino, G., Invernizzi, C., 2003. Experimental investigation on the thermal stability of some new zero ODP refrigerants. *International Journal of Refrigeration* 26, 51–58.
- Angelino, G., Invernizzi, C., Macchi, E., 1991. Organic working fluid optimization for space power cycles. In: Angelino, G., De Luca, L., Sirignano, W.A. (Eds.), *Modern Research Topics in Aerospace Propulsion*. Springer Verlag, New York, pp. 296–326. ISBN: 0387974172.
- HREII DEMO Observatory, September 2013. EU Paper: ORC Waste Heat Recovery in European Energy Intensive Industries. LIFE ENV/IT/000397.
- 1994 ASHRAE Handbook, 1994. *Refrigeration Systems and Applications*. SI Edition. American Society of Heating, Refrigerating and Air Conditioning Engineers, Atlanta, GA, 30329.
- Aston, J.G., Fink, H.L., Schumann, S.C., March 1943. The heat capacity and entropy, heats of transition, fusion and vaporization and the vapor pressures of cyclopentane. Evidence for a non-planar structure. *Journal of the American Chemical Society* 65 (3), 341–346.

- Benson, S.W., 1960. *The Foundations of Chemical Kinetics*. McGraw-Hill, New York.
- Benson, S.W., July 1941. Micromethod for identification of volatile liquids. Vapor pressures of cyclopentane and the pentenes. *Industrial and Engineering Chemistry* 13 (7), 503–504.
- Blake, E.S., Hammann, W.C., Edwards, J.W., Reichard, T.E., Ort, M.R., 1961. Thermal stability as a function of chemical structure. *Journal of Chemical and Engineering Data* 6 (1), 87–98.
- Bombarda, P., Invernizzi, C., 2015. Binary liquid metal – organic Rankine cycle for small power distributed high efficiency systems. *Proceedings of Institution of Mechanical Engineering, Part A* 229 (2), 192–209.
- Burrato, A., 2013. OReGen™: GE Waste Heat Recovery System to Reduce CO₂, Emissions and Increase Plant Efficiency. *Technology Insights*. http://site.ge-energy.com/businesses/ge_oilandgas/en/techinsights/introduction.html.
- Calderazzi, L., di Paliano, P.C., 1997. Thermal stability of R-134a, R-141b, R-131I, R7146, R-125 associated with stainless steel as a containing material. *International Journal of Refrigeration* 20 (6), 381389.
- Cole, R.L., Demirgian, J.C., Allen, J.W., August 10–14, 1987. Predicting toluene degradation in Organic Rankine-Cycle engines. In: *Intersociety Energy Conversion Engineering Conference*. Philadelphia, Pennsylvania. Paper No. 879075.
- Crowder, G.A., Taylor, Z.L., Reed, T.M., Young, J.A., 1967. Vapor pressures and triple point temperatures for several pure fluorocarbons. *Journal of Chemical and Engineering Data* 12 (4), 481–485.
- Cullis, C.F., Priday, K., 1954. The thermal decomposition of aromatic compounds. I. Chlorobenzene. *Proceedings of the Royal Society of London. Series A, Mathematical and Physical Sciences* 224 (1158), 308–321.
- Curran, H.M., September 1979. The Use of Organic Working Fluids in Rankine Engines. Hittman Associates, Inc. Contract No. DE-AC03–79CS-30202.
- Di Nanno, L.R., DiBella, F.A., Koplow, M.D., December 1983. An RC-1 Organic Rankine Bottoming Cycle for an Adiabatic Diesel Engine. Thermo Electron Corporation, Waltham, Massachusetts, 02254. DOE/NASA/0302–1, NASA CR-168256, TE4322-251-83.
- Dias, A.M., Gonçalves, C.M.B., Caço, A.I., Santos, L.M.N.B.F., Pineiro, M.M., Vega, L.F., coutinho, J.A.P., Marucho, I.M., 2005. Densities and vapor pressures of highly fluorinated compounds. *Journal of Chemical and Engineering Data* 50, 1328–1333.
- Fabuss, M.A., Borsanyi, A.S., Fabuss, B.M., Smith, J.O., 1963. Thermal stability studies of pure hydrocarbons in a high pressure isothermoscope. *Journal of Chemical and Engineering Data* 8 (1), 64–69.
- Fielder, W.L., July 1963. Thermal Decomposition of Some Linear Perfluoroalkanes in an Inconel Bomb. NASA. Technical Note D-1744.
- Gamba, M., 1977. Experimental Analysis of the Thermal Stability of Two Organic Fluids: Freon 113 and PP2 (Degree thesis). Politecnico di Milano (in Italian).
- Ginosar Daniel, M., Petkovic Lucia, M., 2011. Guillen Donna Post, thermal stability of cyclopentane as an organic Rankine cycle working fluid. *Energy and Fuels* 25, 4138–4144.
- Havens, V.N., Ragaller, D.R., Sibert, L., Miller, D., 1987. Toluene stability space station Rankine power system. In: *Intersociety Energy Conversion Engineering Conference*, Philadelphia, Pennsylvania, August 10–14, 1987. Paper No. 879161.
- Invernizzi, C., 1990. Thermal stability investigation of organic working fluids: an experimental apparatus and some calibration results. *La Termotecnica XLIV*, 69–76 (in Italian).
- Invernizzi, C.M., 2013. *Closed Power Cycles – Thermodynamic Fundamentals and Applications*. Springer-Verlag, London.

- Invernizzi, C., Pasini, A., 2000. Thermodynamic performance of a new working fluid for power cycles. *La Termotecnica LIV*, 87–92 (in Italian).
- Ito, M., Dang, C., Hihara, E., July 14–17, 2014. Thermal decomposition of lower-GWP refrigerants. In: *Proceedings of the 15th International Refrigeration and Air Conditioning Conference at Purdue*. Purdue University. Paper No. 2591.
- Johns, I.B., McElhill, E.A., Smith, J.O., 1962a. Thermal stability of organic compounds, industrial & engineering chemistry. *Product Research and Development* 1 (1), 2–6.
- Johns, I.B., McElhill, E.A., Smith, J.O., 1962b. Thermal stability of some organic compounds. *Journal of Chemical and Engineering Data* 7 (2), 227–281.
- Lee, J.C., Campbell Jr., J., Wright, D.E., January 1981. Closed-cycle gas turbine working fluids. *Transaction of the ASME. Journal of Engineering for Power* 103, 220–228.
- Macchi, E., Bonalumi, D., Invernizzi, C., Iora, P., September 2014. Experimental Results of Thermal Stability of TiCl_4 , Material Selection and a Technical and Economical Analysis. ENEA Report RdS/PAR2013/269. Polytechnic of Milan – Group of Energy Conversion Cycle (in Italian).
- Mokbel, I., Rauzy, E., Loiseleur, H., Berro, C., Jose, J., 1995. Vapor pressures of 12 alkylcyclohexanes, cyclopentane, butylcyclopentane and trans- decahydronaphtalene down to 0.5 Pa. Experimental results, correlation and prediction by an equation of state. *Fluid Phase Equilibria* 108, 103–120.
- Mousa, A.H.N., 1978. Study of vapor pressure and critical properties of perfluoro-n-hexane. *Journal of Chemical and Engineering Data* 23 (2), 133–134.
- Niggemann, R.E., April 15, 1969. Quarterly Progress Report No. 12. Organic Rankine Cycle Technology Program. Aviation Division Sundstrand Corporation. Report No. SAN-651–96.
- Parma, E.J., Wright, S.A., Vernon, M.E., Fleming, D.D., Rochau, G.E., Suo-Anttila, A.J., Al rashdan, A., Tsvetkov, P.V., May 2011. Supercritical CO_2 Direct Cycle Gas Fast Reactor (SC-GFR) Concept. Sandia National Laboratories, Albuquerque. New Mexico 87185 and Livermore, California 94550. SAND2011–2525.
- Pasetti, M., November 25, 2013. Thermal Stability of Working Fluids for Organic Rankine Cycles. Final Report. Department of Mechanical and Industrial Engineering, University of Brescia. Work Order CM-RI-100034 (in Italian).
- Pasetti, M., Invernizzi, C.M., Iora, P., 2014. Thermal stability of working fluids for organic Rankine cycles: an improved survey method and experimental results for cyclopentane, isopentane and n-butane. *Applied Thermal Engineering* 73 (1), 764–774.
- Pike, F.P., Foster, C.T., 1959. Vapor pressure and boiling point of titanium tetrachloride. *Journal of Chemical and Engineering Data* 4 (4), 305–306.
- Ragaller, D., Sibert, L., Cole, R.L., Demirgian, J.C., Allen, J.W., August 10–14, 1987. Degradation of the organic Rankine-cycle fluid RC-1. In: *Intersociety Energy Conversion Engineering Conference*. Philadelphia, Pennsylvania. Paper No. 879074.
- Rohatgi, N.D.R., Clark, R.W., Hurst, D.R., March 2012. Material Compatibility and Lubricants Research for Low GWP Refrigerants – Phase I: Thermal and Chemical Stability of Low GWP Refrigerants with Lubricants. Final Report. Spauschus Associates, Inc., Sylva, NC, 28779. AHRTI Report No. 09004-01.
- Saaski, E.W., Owzarski, P.C., June 1977. Two-Phase Working Fluids for the Temperature Range 50 to 350°C. Sigma Research, Inc., Richland, Washington. CR-135255.
- Santacesaria, E., Morini, A., Carrá, S., November 1974. Researches on thermal decomposition of methylene chloride. *La Chimica e l'Industria* 56 (11), 747–753.
- Santacesaria, E., Morini, A., Carrá, S., 1975. Influence of metallic surfaces on decomposition of methylene chloride. *La Termotecnica* 29 (8), 443–449.

- Shropshire, D.E., April 25–29, 2004. Lessons learned from GEN I carbon dioxide cooled reactors. In: Proceedings of ICONE 12. Twelfth International Conference on Nuclear Engineering. Arlington, Virginia. Paper No. ICONE12-49380.
- Spurlin, M. Conrad Gamble, Ander Beain, Defining Thermal Stability, Solutia Inc., St. Louis. Document downloaded from: <http://www.therminol.com>.
- Standard Test Method for Thermal Stability of Organic Heat Transfer Fluids. ASTM Standard No: D6743–11. (2015).
- Stiles, V.E., Cady, G.H., 1952. Physical properties of perfluoro-n-hexane and perfluoro-2-methylpentane. *Journal of the American Chemical Society* 74 (15), 3771–3773.
- Standard Test Method for Vapour Pressure-Temperature Relationship and Initial Decomposition Temperature of Liquids by Isoteniscope. ASTM Standard No: D2879–10.
- Zia, J., Sevincer, E., Chen, H., Hardy, A., Wickersham, P., Kalra, C., Laursen, A.L., Vandeputte, T., January 2013. High-Potential Working Fluids for Next Generation Binary Cycle Geothermal Power Plants. Phase 3 and Final Report: Fluid/Cycle Downselection and Experimental Validation. Department of Energy (DOE), Washington DC. Document ID 307132, IAC Number HD-225824, Contract Number DE-EE002769.

Dynamic modeling and control of Organic Rankine Cycle plants

6

F. Casella

Informazione e Bioingegneria, Politecnico di Milano, Milan, Italy

6.1 Introduction

Organic Rankine Cycle (ORC) systems can be employed for different types of applications, with different cycle configurations, and using different types of components. This gives rise to a large number of different control problems, each of them having its own unique feature. The aim of this chapter is to present a methodological framework that allows ORC designers to master this problem, and to give general guidelines for the analysis of the system dynamics and for the successful design of control systems that meet the end user's specifications.

ORC systems find applications in many different areas. More traditional ones include low-temperature geothermal power generation, heat recovery from industrial processes, power production from biomass, and cogeneration for district heating. Among the more innovative ones, we can mention solar thermal power generation, power generation in off-grid systems, or heat recovery from internal combustion engines onboard vehicles.

Many applications, in particular the more traditional ones, are inherently stationary or quasistationary. The heat input is constant or very slowly changing and never deviates too much from the design value during the system operation. On the other hand, the electrical power output is often used to feed local loads, reducing the consumption of electrical power provided by the AC grid. If power is exported to the grid, it is not usually subject to any stringent requirement. In these cases, the dynamic behavior of the system is of no particular interest, and the design of the control system is usually not critical. The success of innovative applications of ORC systems, instead, often relies much more on dynamic and control performance. For example, the recovery of waste heat in internal combustion engines onboard vehicles requires to handle very fast, with very large variations of the heat input, on a scale which is unheard of in conventional power generation applications.

There are numerous aspects which can influence the dynamic behavior, the control objectives, and the control system design of an ORC system.

The first aspect is the cycle configuration. The two most commonly used ones are the standard Rankine cycle and the regenerative Rankine cycle, where the turbine exhaust fluid is used to preheat the evaporator feed flow via a recuperator. More complex configurations might be chosen for specific applications. For example, an ORC

generator coupled to a modern turbo-charged Diesel engine could have two evaporators in parallel, one recovering the high-temperature heat from the exhaust gas recirculation loop, while the other one recovers heat from the lower temperature exhaust.

The dynamic behavior and the control strategies of ORC plants are also determined by the choice of their components.

If a volumetric expander is employed, the vapor mass flow rate through it is roughly proportional to the rotational speed and to the vapor density at the inlet, and also depends on the valve timing. Conversely, if a turbine is used, the mass flow rate does not depend on the rotational speed and is roughly proportional to the pressure at the inlet. As a consequence, the dynamic response of the pressure and of the mechanical power in the two cases is completely different.

The mass flow rate through a volumetric feed pump mainly depends on its rotational speed only, while it also depends on the pressure difference in the case of turbo-pumps. The speed of response of the vapor generator is determined by mass and energy storage, which is proportional to the fluid volume and to the heat capacitance of the walls; as a consequence, compact devices such as plate or shell-and-plate heat exchangers lead to a faster dynamic response than shell-and-tube heat exchangers.

AC/AC converters are usually employed on medium- and low-size machines, whose rotational speed is too large to be reduced by gears to the rotational speed of synchronous machines rotating at the AC network frequency. This gives one extra degree of freedom, because the expander rotational speed can be controlled to its optimal value depending on the operating conditions. In the case of larger machines with a lower rotational speed that permits the use of mechanical gears, one can opt for a direct connection of the synchronous generator with the AC grid. This choice can be less expensive and more efficient at the design operating point, because the AC/AC converter losses are avoided; on the other hand, as the rotational speed of the expander is fixed, off-design operation can be significantly penalized.

Finally, in many cases the system is built in a way that introduces additional constraints on variables of interest for the dynamic behavior. For example, compact ORC machines can have the turbine, electrical generator, and main pump placed on the same axis, to simplify the design and reduce losses; in this case, the rotational speed of the turbo-pump, which is determined by the AC/AC converter, can be used to control the feed flow, and the system needs to be designed so that the turbine always operates close to optimal conditions also during reduced load operation. Another example is given by ORC systems coupled to internal combustion engines, where one could decide to put the expander on the same shaft of the engine, in order to reduce the costs and losses of an extra electrical generator and motor pair.

Stated in high-level terms, the basic control objectives are the same for all ORC systems, always operate the system safely, while obtaining the highest possible conversion efficiency. Off-grid power generation applications have additional requirements regarding the voltage and frequency of the generated power, which must remain within prespecified bounds. However, how these high-level requirements translate into actual control strategies depends essentially on the specific system configuration.

For example, in systems with a high temperature heat sources, including solar ones, the control of the vapor generator outlet temperature is crucial, as too high

temperatures could lead to the decomposition of the fluid; in other cases, e.g., where a primary loop with thermal oil is employed, this task could become less critical or even absent.

Another example is the role of the feed flow; in most cases, this manipulated variable is used to control the degree of superheating at the evaporator outlet, but this assumes that the hot well of the condenser is large enough and there is enough fluid in the system to avoid underflow or overflow at all times. However, in some designs with very bulky evaporators and without the need to control the superheating, thanks to a thermal oil loop, the condenser hot well can be comparatively small, to save on the cost of the working fluid; in this case, the feed flow must be used to control the level in the hot well.

Summing up, when dealing with the dynamics and control of ORC plants, it is essential to understand the specific application at hand, with its system configuration and operational objectives, as they may lead to completely different control requirements and control system strategies. Understanding the dynamics of the process is a key factor, in particular for innovative applications where the system does not always operate close to the design point. Dynamic modeling plays a very important part here, as will be discussed in [Section 6.2](#). There are no consolidated best practices or ready-made recipes for the control of innovative ORC systems, but it is possible to envision a systematic, model-based approach, that will be discussed in the remainder of this chapter.

6.2 Dynamic modeling and simulation for control design

6.2.1 *Role of dynamic modeling in the design process*

Understanding the process dynamics is the key to successful control design. As discussed in the [Section 6.1](#), there are many different possible configurations for an ORC plant, each with its own unique dynamic behavior and control requirements, and no established best practices how to deal with them.

Waiting until the first physical prototype of a new ORC system is available, to gain insight in the process dynamics exclusively by empirical means, is in general not a wise strategy. First of all, performing all the kinds of experiments that are required to support the control design procedure can be expensive, time-consuming, and possibly dangerous, as it might be easy to damage the prototype by, e.g., causing fluid decomposition because of too high temperature, or damaging the rotating machinery because of overspeed.

Secondly, but not less important for innovative systems with highly dynamic behavior and tight operational constraints, the dynamics of the plant might turn out to be unfavorable for the design of a controller that meets the specification. Typical causes for this scenario are too slow open-loop dynamics, insufficient control authority of the actuators, and nonminimum phase dynamics (i.e., inverse responses and pure time delays) that limits the achievable bandwidth of closed-loop controllers.

In order to avoid these problems, dynamic modeling and simulation is an essential tool in all the phases of the system design. On one hand, it allows all the experiments required for high-performance control design at a very low marginal cost. On the other hand, it allows recognition of system designs that are inherently difficult to control, and help to improve them during the early design stages, while the costs associated to design changes are still comparatively low.

System-level models are needed to carry out these activities, which aim at reproducing the overall system behavior resulting from the interaction of its components, rather than focusing on their detailed individual behavior. When tackling a new system, the starting point is usually a fairly detailed system model, which is built in a modular fashion by connecting system-level component models. These components are often derived or calibrated with the results of sophisticated component models used for design. For example, simplified one-dimensional models can be derived for heat exchangers with complex geometry (e.g., plate heat exchangers), by tuning suitable correction factors to obtain the same design performance, and by using simplified correlations to describe the off-design performance. The level of detail should be appropriate for control studies, so that the static performance is captured with sufficient accuracy, and the dynamics on the time scales relevant for the controller designed are correctly described, while irrelevant phenomena (such as, e.g., pressure wave propagation in heat exchangers) can be neglected. The component models used for this purpose should be validated against experimental data, or any other source of trusted reference data.

This kind of model can be used to explore the dynamic behavior of the plant, understanding its main features, such as speed of response, presence of endogenous oscillatory behavior, inverse response dynamics and delays, more or less pronounced nonlinear behavior, coupling between the various control inputs and controlled outputs, etc. To this end, one can study the response of the system to small step changes in the control inputs around different operating points or, if the modeling tools allows it, obtain a linearized approximation of the system dynamics around on-design and off-design operating points and then study its dynamic behavior in the frequency domain, e.g., by means of Bode diagrams of the transfer functions.

Using this model as a reference, it is then possible to derive further simplified and compact models that can be used directly for model-based control design. This can be done directly, e.g., by computing a linearization of the detailed model and then using model-order reduction techniques on the linear model to reduce its complexity, or indirectly, by writing first-principles based models with strong simplifying assumptions, whose validity can then be assessed against the results of the more detailed model, or whose parameters can possibly be tuned in order to match the detailed model's response.

Finally, once the control design has been finalized, the detailed model can be used to test the closed-loop performance of the controller by simulation. When doing so, it is essential that the plant model is more accurate and detailed than the simplified model used for the control design, in order to assess the robustness of the controller design with respect to unmodeled dynamics.

6.2.2 *Introduction to object-oriented modeling*

The detailed dynamic modeling of systems such as ORCs is preferably carried out using a modular paradigm, in which the overall system model is obtained by the connection of submodels representing the individual components of the cycle: heat exchangers, pumps, expanders, control valves, electrical generators, etc.

For run-of-the mill engineering activities, it is essential that the modeling tool features a comprehensive library of ready-made components that can be used out of the box to assemble the model of any possible plant configuration that one could come across in a reasonable amount of time. For research and development activities, it is more important to have a flexible modeling tool that allows customization of existing models or possibly to add completely new ones. It is also very important to be able to understand the modeling assumptions and the limits of validity of the models.

As of the time of this writing, contrary to other more mature sectors such as steam or nuclear power plants, there are no established and comprehensive tools for dynamic modeling of ORC system. Furthermore, as the field of ORC systems is far from being mature, research and development activity plays a much more prominent role than standard engineering design. In this kind of scenario, Equation-based Object-Oriented (EOO) modeling turns out to be particularly suitable to address the problem of dynamic modeling and simulation.

In the framework of EOO modeling, one can start to define models of individual physical components (e.g., a turbine), or even of the behavior of a part of a component (e.g., the flue-gas side of an evaporator). This is accomplished by first defining the interface of the component to the outside world in terms of physical connectors, each characterized by quantities that are relevant to the physical domain. For example, a turbine model has one mechanical connector, containing its rotation angle and the cut torque applied to it, and two thermo-fluid connectors, each containing the pressure, mass flow rate, specific enthalpy, and possibly composition (in the case of fluid mixtures) of the fluid going through it; the primary side of a heat exchanger will have two thermo-fluid ports at the inlet and outlet, and one or many (in the case of distributed parameter models) thermal ports, each containing a temperature and a heat flow, that represent the thermal exchange at the channel wall boundaries. Then, one defines the internal variables and parameters of the component, and writes differential-algebraic equations that relate these variables among themselves and with the connector variables.

Once these basic building blocks have been defined by means of equations, one can build a system model by connecting submodels, possibly using a graphical user interface with drag-and-drop metaphor. Each connection set corresponds to extra equations that are added to the set of equations of the individual building blocks, stating that the effort variables (such as pressure, temperature, or angle) are equal, and that the sum of flow variables (such as mass flow, heat flow, or torque) is zero.

The EOO modeling paradigm is declarative, meaning that one can write the constitutive equations of each component as they are, without worrying about how and in which order they will be solved. It is also acausal, in the sense that the variables of the interface connectors are, per se, neither inputs nor outputs. In other words, the basic

models are not written with their solution in mind. On the one hand, this allows models to be written in a way that is easier to understand, as the individual equations (mass, momentum, energy balances, constitutive equations, and physical correlations) can be written as they are on paper. On the other hand, the models thus obtained are very flexible, because they can be reused in different contexts where the very same equations hold, but the way they are solved differs, in terms of which variables are solved for in which equations and in which order, due to different boundary conditions.

Once the system model has been assembled, EOO simulation tools analyze the structure of the overall system, sort the equations, apply symbolic simplifications where possible, and eventually automatically generate efficient code to solve the equations. For further details on this process, the interested reader is referred to [Cellier and Kofman \(2006\)](#).

The de facto standard of EOO modeling and simulation is the Modelica language ([Mattsson et al., 1998](#); [Fritzson, 2014](#)), which is defined and developed by the nonprofit Modelica Association. Several simulation tools exist that can process a system model written in Modelica and produce executable simulation code, both commercial (Dymola, SimulationX, Wolfram SystemModeler, MapleSim) and open-source (OpenModelica, JModelica). At least in principle, the Modelica code is portable among all these different tools, though the ability of each of them to provide efficient and robust simulation code may vary. Moreover, all Modelica tools are constantly being improved from this point of view, so that one can expect to get better and better quality of the simulation executable code starting from the same Modelica source code simply by using newer versions of these tools, without the need to change the model code themselves.

The high-level declarative modeling approach allows the tailoring of all of the details of the component models to the requirements of a specific ORC system, possibly also embedding proprietary information (e.g., heat transfer correlations or efficiency curves), in a very convenient way, leaving the effort of generating efficient simulation executable code to the Modelica tool of choice. The typical development pattern is that one that starts with writing a basic library of reusable components, which are validated against experimental data and/or reference models, and then widens its scope by adding more specialized components over time during new projects, whilst reusing existing validated models wherever possible.

6.2.3 *Modelica models of Organic Rankine Cycle systems*

Two Modelica libraries of reusable components for the dynamic modeling of ORC systems are reported in the literature. One is based on the ThermoPower library ([Casella and Leva, 2005](#); [Casella and Leva, 2006](#)), which was originally developed for the modeling of steam-cycle based models and later on extended to the modeling of ORC system by adding a Modelica interface to external fluid property computation software such as RefProp ([Lemmon et al., 2013](#)), FluidProp ([Colonna et al., 2010](#)), and CoolProp ([Bell et al., 2014](#)) by means of the ExternalMedia library ([Casella and Richter, 2008](#)).

The application of this library to a 150 kW toluene-based ORC system is reported in [Casella et al. \(2013\)](#). The top-level view of the system model is shown in [Fig. 6.1](#), where the main components of the system are connected by means of thermo-fluid connectors and mechanical connectors. Note that in this specific system design, the main pump, the turbine and the electrical generator are connected on the same shaft. The three bypass components at the center of the diagram represent the flow of organic fluid that is used for the lubrication of the turbine-pump component (about 30% of the total prefeed pump flow), which are eventually discharged in the condenser and, for a minor part, at the turbine outlet.

Some components are directly written by means of equations. For example, a specific turbine model was developed in this case, assuming sonic choked conditions in the stator throat and constant isentropic efficiency, as not enough data was available in this case to model the changes of efficiency with the operating conditions. The equation-based modeling approach allows to turn the model equations directly into code. An excerpt of such code is reported in [Table 6.1](#), to give a feeling of how well-written Modelica code can be self-explanatory and self-documenting.

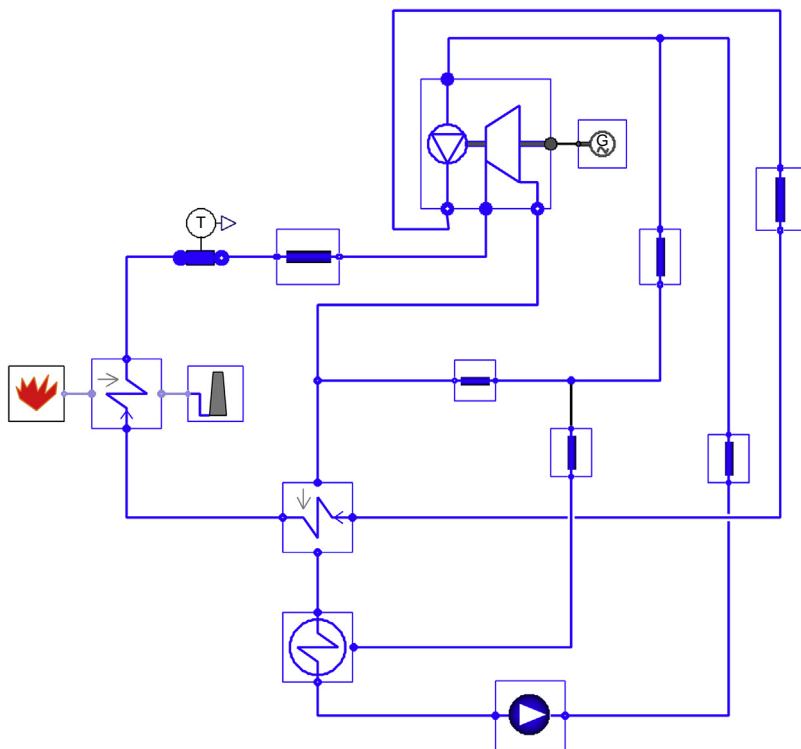


Figure 6.1 Top-level view of an Equation-based Object-Oriented (EOO) Organic Rankine Cycle (ORC) system model.

Table 6.1 Modelica code of the turbine equations

```

vapor_in = Medium.setState_ph(pin,hin);
hiso = Medium.isentropicEnthalpy(pout, vapor_in);
hin - hout = eta_iso * (hin-hiso) "Computation of outlet
enthalpy";
sin = Medium.specificEntropy(vapor_in);
hin = ht + 1/2*ct^2;
ht = Medium.specificEnthalpy(Medium.setState_ps(pt,sin));
ct = Medium.velocityOfSound(Medium.setState_ps(pt,sin));
rhot = Medium.density(Medium.setState_ps(pt,sin));
w = rhot * At * ct;
Pm = eta_mech * w * (hin-hout) "Mechanical power from the
vapor";
Pm = - tau * omega "Mechanical power balance";
u = D/2 * omega;
Phi = (hin-hiso)/(u^2);
eta_iso = (a[1]*Phi^2 + a[2]*Phi + a[3]);
// Mechanical boundary conditions
shaft_a.phi = phi;
shaft_b.phi = phi;
shaft_a.tau + shaft_b.tau = tau;
der(phi) = omega;
// vapor boundary conditions and inlet vapor properties
pin = inlet.p;
hin = inStream(inlet.h_outflow);
hout = outlet.h_outflow;
pout = outlet.p;
w = inlet.m_flow;
inlet.m_flow + outlet.m_flow = 0 "Mass balance";

```

Other components, such as the evaporator and recuperator, can be built by re-using and customizing existing models from the ThermoPower library. For example, the evaporator model, shown in Fig. 6.2 is obtained by connecting a 1-dimensional, 2-phase, finite-volumes fluid flow model, a 1-dimensional ideal gas finite volumes flow model and a wall model together. The coupling element represent the counter-current heat exchange configuration, which could also be more complex, as in the case of twopass shell-and-tube heat exchangers. The one-dimensional fluid flow models contain a replaceable fluid model and a replaceable heat transfer model, which can be redeclared to fit the specific modeling needs; this is another very useful feature of EOO modeling languages and of Modelica in particular. In this case, the fluid model was changed from the default IAPWS IF97 water-steam model to the RefProp model of toluene accessed by the ExternalMedia library, while specific heat transfer correlations were developed based on the know-how of the system designers.

Another model defined in terms of submodels is the integrated pump and turbine model found at the top left of the diagram in Fig. 6.2, which was obtained by connecting a general-purpose pump from the ThermoPower library to the custom turbine model presented above, via their mechanical shaft connector, see Fig. 6.3. This model

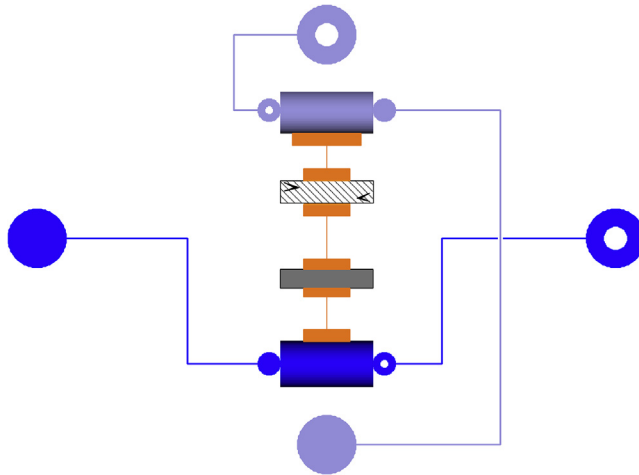


Figure 6.2 Equation-based Object-Oriented (EOO) diagram of the integrated pump and turbine component.

exposes a mechanical shaft connector to the outside that can be connected to different types of electrical generator models, depending on the purposes of the study.

Another Modelica library for the dynamic modeling of ORC systems is the ThermoCycle library (Quoilin et al., 2014). Contrary to the previous case, this library was developed from the grounds up with ORC applications in mind.

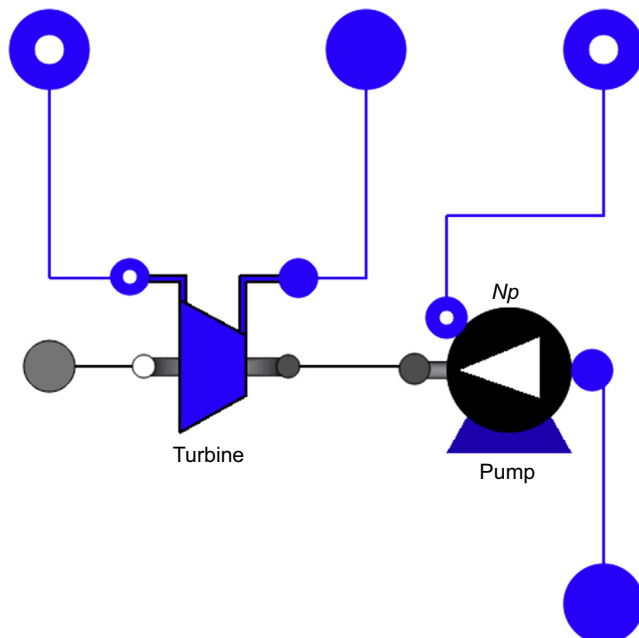


Figure 6.3 Equation-based Object-Oriented (EOO) diagram of the turbo-pump model.

6.2.4 Modeling assumptions for dynamic models of Organic Rankine Cycle systems

In this section, the typical modeling assumptions that can be made to derive modular models of ORC systems are discussed.

6.2.4.1 Vapor generator

The vapor generator in ORC systems of moderate or small size is usually of a once-through type. Depending on the specific design, plate, shell-and-plate or shell-and-tube heat exchangers can be used. For the purpose of dynamic modeling, the flow configuration can be roughly approximated as an equivalent one-dimensional counter-current one. It might be necessary to introduce some corrections to take into account the fact that the heat transfer is less efficient than in an ideal counter-current configuration (such as concentric pipes); this is usually accomplished by introducing a correction factor in the heat transfer coefficients, that is calibrated in order to match the steady-state performance of the dynamic model with detailed design models, or with experimental data, when available.

Although the velocity of the two phases in the evaporation section might be somewhat different, homogeneous-flow models are usually employed, as the additional complication of accounting for the phase slip is usually not balanced by a significant improvement of the accuracy of the computed transients.

The one-dimensional flow models are usually discretized using the finite volume method (Casella and Leva, 2006), taking into account mass and energy storage in the fluids and in the wall in-between, although the finite element method can also be employed, if a simple counter-current exchange configuration is assumed (Schiavo and Casella, 2007). A critical issue with all these models are the numerical artefacts induced by the phase change in the models. The basic structure of the mass balance equation for a finite volume model is shown in Eq. (6.1)

$$\frac{V}{N} \left(\frac{\partial \rho}{\partial p} \frac{dp}{dt} + \frac{\partial \rho}{\partial h} \frac{dh}{dt} \right) = w_{\text{in}} - w_{\text{out}} \quad (6.1)$$

where V is the total volume of the flow channel, N the number of finite volumes, ρ is the density, p is the pressure, h is the specific enthalpy, and w_{in} and w_{out} are the inlet and outlet mass flow rates. When the state (p , h) enters or leaves the saturation dome, the two partial derivatives (in particular the first) can change by several orders of magnitude, causing flow rate pulses or bumps that are completely non-physical. This phenomenon can be limited by taking a large enough value of N , e.g., 20 or 40, so that the effect of the discontinuity of the model is multiplied by a small factor. However, this increases the computational weight of the model, so there is a trade-off between having small artefacts and long simulation times. There are some strategies to limit these issues, see, e.g., Bonilla et al. (2010), Quoilin et al. (2014), or Casella (2006); the latter being used by the ThermoPower models (these can be helpful to obtain good enough transients with a limited number of volumes).

Detailed heat transfer correlations can be used in these models; however, this can be unnecessarily cumbersome, and possibly require the knowledge of proprietary data. An alternative that is often used is to consider simple correlations that can be tuned to match design or experimental data. Simulation artefacts can also arise due to discontinuities in the heat transfer correlations between the single-phase and two-phase regions. Suitable regularizations need to be introduced in order to produce smooth transients.

Large size ORC systems, such as those found in geothermal plants, use kettle-type boilers. In this case, the organic fluid side is well approximated by a zero-dimensional, lumped-parameter model, accounting for the overall mass and energy balances and assuming thermodynamic equilibrium between the liquid and the vapor phases, which is guaranteed by the continued formation and upward motion of vapor bubbles forming on the hot tube walls. On the other side, the hot fluid side and the tube walls still need to be represented by a one-dimensional, distributed model, which is basically the same as in once-through evaporator models. The overall model thus has a structure similar to the one shown in Fig. 6.2, where the bottom component represents, in this case, a zero-dimensional volume model of a two-phase mixture at thermodynamic equilibrium.

6.2.4.2 *Recuperator*

The recuperator, if present, can also be of different types, but can usually be represented as an equivalent one-dimensional counter-current heat exchanger. In most cases, the hot side and the cold side stay within the one-phase region, so there are no particular problems in this component.

6.2.4.3 *Condenser*

If the focus of the dynamic simulation is on the operation of the steam generator and turbine, a widely used modeling assumption is to assume that the condenser operates at fixed (or at least prescribed) values of temperature and pressure. This allows us to describe the ORC cycle as an open cycle; the feed flow comes out of a fixed (or prescribed) pressure and temperature generator, and the turbine (or the hot side of the recuperator) discharges into another fixed (or prescribed) pressure generator. Besides skipping all the computational workload of the condenser simulation, which might be significant, this configuration is numerically robust with respect to the fact that the component models might not conserve the mass with great accuracy, due to discretization errors or to inaccuracy in the partial derivatives shown in Eq. (6.1). If the condenser design and possibly the condenser control is an essential part of the system design effort, then appropriate condenser models must be used, taking in due consideration potential problems in the lack of conservation of the total mass of the closed circuit. If the condensation takes place in a homogeneous-flow pattern, where the steam fraction gradually decreases as the organic fluid flow advances towards the condenser outlet, then one-dimensional models similar to the evaporator models can be used. If shell and tube condensers are used instead, then a one-dimensional model of the coolant flow and of the Nusselt-type condensation on the pipe surface must be coupled with zero-dimensional, lumped-parameter models of the vapor contained in the shell and

of the subcooled liquid in the condenser hot well. In the latter case, one can usually neglect the heat transfer between the steam and liquid volumes, as the separation surface is quite small and the velocity of the fluid at the phase boundary is negligible.

6.2.4.4 Expanders

Depending on the specific system design and size, a volumetric expander or a turbine can be used as an expander. The residence time of the fluid in such components is very small, compared the heat exchangers, so that purely algebraic (quasi-static) system level models are usually employed.

In principle, the first and second performance laws must be described, the first relating to the pressures, flow rate, and rotational speed of the machine, the second relating to the isentropic efficiency of the machine with pressure, flow, and rotational speed. Different descriptions of these two curves can be given, depending on the specific machine and on the information available. For example, if a turbine with choked first stage nozzles is employed, then the first characteristic curve can be described by modeling an isentropic flow to the throat and assuming the speed of sound there, see [Table 6.1](#); if a multi-stage turbine is employed that does not work in choked flow conditions, one may use Stodola's ellipse law instead. As for the efficiency curves, if the data are available, one might employ two-dimensional maps, giving the efficiency as a function of the pressure ratio and rotational speed. For some types of machines, it is possible to use one-dimensional curves of the form $\eta_{\text{iso}} = f(v/c_0)$, where v is the blade speed and c_0 is the velocity corresponding to a single-stage isentropic expansion between the inlet conditions and the outlet pressure. In case volumetric expanders are used, the first performance law can be described by computing the ideal flow as the product between the fluid density at the inlet flange, the number of strokes per second and the displacement of the machine, multiplied by a volumetric efficiency that is determined from design or experimental data.

When designing completely new machines, one can think of using more detailed models, closer to the physics of the machine. In the case of multistage turbines, one might write stage-by-stage equation-based models that take into account the blade geometry and compute the flow stage-by-stage. In the case of volumetric expanders, one might use a dynamic model that takes into account the actual filling and emptying of the expander variable volume, as well as the detailed behavior of the admission and discharge valves and of their control system. These models can be directly employed within the overall system model, or used to tune system-level models as the ones mentioned previously.

6.2.4.5 Pumps

Pump models are also described in terms of two performance maps. The first one is usually provided by the manufacturer as head versus volume flow curves at different rotational speeds. If the curve is only provided at the nominal speed, one can use models that derive approximated curves at other speeds by means of the kinematic similarity principle. The second performance map can be provided either in terms of efficiency curves on the head-flow plane, or in terms of power consumption curves as a function of flow and speed; the similarity principle can also be used here. All these

curves can be described in terms of interpolating functions, such as polynomials or splines, and used within equation-based models. In the context of Modelica models, one can use ready-made library models, where the functions describing the first and second characteristic curve are replaceable, and can be redeclared to one's own choice.

6.2.4.6 Control valves

The behavior of control valves can be described by means of standard equations that correlate the valve opening, the boundary conditions, and the flow through the component. The ISA S75/IEC 60534 standards provide correlations for incompressible fluids (liquid phase), compressible fluids (vapor phase), and flashing valves (liquid inlet, two-phase outlet), that can be readily implemented directly as algebraic equations in an EOO model. If the process dynamics itself turns out to be fast, the dynamic behavior of the valve positioning servo-system becomes important to determine the closed-loop dynamic behavior of the system, so it should be included in the model. Unfortunately, in most cases it is difficult or impossible to gain access to any information about the servo-positioner dynamics, so simple first-order or second-order linear systems, possibly with some speed saturation, can be used to take these dynamics into account. In case detailed information is available and turns out to be crucial for the system's dynamic performance, one can use the EOO modeling capabilities to set up high-fidelity models of the actuators as well.

6.2.4.7 Sensors

Some sensors, most notably temperature sensors, might have a significantly delayed response. If the time scale of this response is not negligible when compared to the closed-loop response time, then it should be included in the model, to accurately reproduce the closed-loop dynamics. First- or second-order low-pass linear systems are usually employed for this purpose.

6.2.4.8 Electrical/mechanical generation

If the ORC system goal is to generate electrical power, there are two possible configurations. For larger machines, one can employ synchronous generators, rotating at sub-multiples of the AC frequency, possibly through a mechanical gear. Ultimately, this boils down to prescribing a fixed rotational speed at the turbine flange. In the case of smaller machines that have a too high rotational speed, the use of an AC/AC converter is mandatory. If one is not interested in the design of the power electronics, it is possible to assume that the AC/AC converter is equipped with a speed control algorithm, which opens and closes the electrical gates to ensure a power flow that will keep the rotational speed at equilibrium at the set point value. This behavior can be described at the system level by a simple component that prescribes the rotational speed to be equal to the set point (possibly with some low-pass filtering in-between to mimic the delay in the set point response), and connecting it to the turbine shaft connector. In principle, one could also employ more detailed object-oriented models of the power electronics and of the distribution network and loads, possibly using existing libraries of Modelica models of

power systems. This could be interesting for the study of small isolated networks powered by ORC generators, where one has to make sure that the frequency and voltage of the supplied power is always adequate. However, this kind of model can be quite computationally intensive, so it makes sense to use them only if strictly required.

6.3 Control design work-flow

6.3.1 Conventional work-flow

The conventional work-flow for control system design starts from a mechanical design of the system which is complete or almost complete. This means that the choice of the fluid, the design of the thermodynamic cycle, and the mechanical design of the main components (turbomachinery, heat exchangers) has already been carried out, and is taken as input data for the control design process.

The first step is to formulate the high-level goals of the control systems, i.e., operating the system safely at the maximum possible efficiency, in terms of some controlled variables following some suitable set points. This might be the output of some optimization carried out on a static model of the system that can also compute off-design steady-state operating points. The number of controlled variables must correspond to the number of manipulated variables, in order to match the degrees of freedom in the process operating point.

The next step is to understand the dynamics between the manipulated variables and the controlled variables. One can start analyzing the dynamic response of the controlled variables to small changes of the manipulated variables around some steady state operating points. This can be done by actually simulating the response of the latter to small step changes of the former, or possibly by having the simulation tool compute a linearized model of the system around the design point and computing the transfer functions. The computation of linearized models is a powerful and useful feature; in this context, however, one has to be careful that the modeling artefacts mentioned in [Section 6.2.4](#) do not make the results invalid. If the equilibrium around which the model is linearized happens to coincide with the transition of the two-phase boundary from one volume to the next, then the result of the linearization process will describe the artefact instead of the dynamics of interest. It is therefore important to always check that the step response of the linearized system is similar to the step response of the full model, for small enough step changes; if not, one can try to change the equilibrium point a bit to avoid linearizing the artefacts.

Several aspects can be taken into consideration:

- *Response times.* By looking at the step responses and/or at the transfer functions, one can understand what the dominant time constants of the system are, as well as what the fastest and slowest output variables are.
- *Coupling.* By computing the Relative Gain Array (RGA) matrix (and possibly the dynamic RGA matrix, in the frequency range comprising the crossover frequencies of the control loops), one can get an indication of the degree of coupling of the different control loops, based on the linearized system dynamics. If, by suitably coupling the manipulated and controlled variables, an RGA close enough to unity can be obtained, it means that the control

problem can be successfully solved by using a fully decentralized control system, with N independent controllers, each taking care of its controlled output by acting on the coupled manipulated variables. If the RGA can only be approximately brought to block-diagonal form, it means that the variables corresponding to each block will have to be dealt with by centralized controllers, which determine all the manipulated variables simultaneously, based on all the controlled variable measurements. In the worst case, a single centralized controller is needed to take care of all the controlled variables. Decentralized controllers are simpler to design and operate, so they are preferred whenever possible; on the other hand, centralized controllers can achieve superior performance if this is really required.

- *Nonlinear behavior.* If one wants to employ linear controllers, for which systematic and well-understood control design techniques exist, the performance is guaranteed only if the process dynamics is also linear or close to linear. One can determine how nonlinear the process is by repeating the analysis around different off-design operating points, and comparing the step responses or frequency responses. The greater the differences, the more it will be necessary to resort to nonlinear control techniques, such as, gain scheduling, to successfully solve the control problem.
- *Alternative manipulated variables.* If the variability of the dynamic response with the operating point is very high, one can use the model to explore alternative manipulated variables. For example, exchanging a valve with a prescribed flow source (where the prescribed flow is the new manipulated variables instead of the valve opening) might reveal a more favorable input–output dynamic behavior. Later on, the actual control system could employ a cascaded structure, whereby a fast, low-level local flow controller acts on the valve opening to obtain the required flow rate, and its set point is used as a virtual control variable by the high-level controller.
- *Nonminimum phase response.* The dynamic analysis might reveal a dynamic response characterized by right-half plane transmission zeros in the transfer function of the system. For single-input, single-output systems, this corresponds to an inverse dynamic response to step changes of the input, i.e., in the initial phase of the transient, the controlled variable goes in the opposite direction with respect to its final steady-state value. Such zeros impose fundamental limitations on the bandwidth of feedback controllers, which means lower bounds on response and settling times, and also limitations to the disturbance rejection capabilities. These limitations are intrinsic in the process dynamics, no matter how good or sophisticated the controller is. It is very important to spot these limitations early on in the design process, because they might affect the control performance up to the point of making it impossible to meet the dynamic performance specifications.

Based on the results of this first analysis, one can choose the most appropriate control strategies and control techniques, according to the principle that the simple working solution should always be preferred. For example, a system which is never operated too far from the design point and is never subject to demanding transients might be satisfactorily controlled by simple decentralized Proportional-Integral-Derivative controllers. If the nonlinearity of the dynamic behavior across the expected range of operation is substantial, gain-scheduling techniques might be necessary to guarantee satisfactory performance in all operating conditions. If the RGA is very far from unity, multivariable controllers should be employed.

In the case of systems subject to very strong external disturbances, the use of feed-forward action could be essential to meet the performance specification. A notable case is the one of ORC systems used for heat recovery in internal combustion engines,

where the thermal load to the evaporator can change drastically and very quickly, causing very large fluctuations in the process variable. In this case, the load is actually determined in a very tight way by the internal combustion engine controller, so this information can be used to compute feedforward actions that may improve the controller performance substantially.

For all types of model-based controllers, detailed (albeit system-level) modular models are usually too cumbersome to be used directly. One way to use them to obtain low-order models that can be employed for model-based design is to first have the tool compute the linearized dynamics, and then use some linear model-order reduction technique (e.g., balanced truncation) to reduce the number of state variables to a manageable one. The other option is to write down drastically simplified first-principle models, whose validity can be assessed a posteriori by comparing their behavior with the reference model, and which may contain some parameters that can be tuned to better match their response to the reference model.

The performance of the control system can then be assessed by an extensive simulation campaign, using the reference EOO model of the plant as a virtual test bed.

6.3.2 Advanced and integrated work-flows

As already noted in previous sections of this chapter, for ORC systems there are lots of design alternatives and no consolidated best practices or rules. For innovative systems where dynamic performance is a key requirement, the conventional work-flow presented in the previous section, whereby the mechanical design is a given input for the control design, may fall short of meeting the performance specifications, due to limitations in the achievable dynamic performance that are inherent in the process dynamics and cannot be overcome simply by means of smarter controller design (See [Section 6.3.1](#)). One such limitation that was previously mentioned in this chapter, could be the presence of nonminimum phase dynamics in the process; another one can be lack of control authority, i.e., the min–max range of some actuators is too small to meet the design specifications, because of the large inertia of the process.

In all these cases, meeting the specifications of the dynamic behavior of the system not only requires design of the control system, but also modification of the mechanical design of the process, to make its dynamics more favorable.

A first, rather crude, way to do so is to foresee one (or more) iterations in the design process. Once the control system performance has been thoroughly assessed and some process-induced limitations highlighted, the system can return to the mechanical drawing board, with some indication of possible measures to improve the situation. For example, one might try to increase the fluid velocity in a heat exchanger to reduce the residence time and thus make its dynamic response faster, or decide to change some actuators in order to gain more control authority, which might involve some process design changes, e.g., changing some pipe diameters.

One can try to make this approach more systematic by means of optimization tools. One example is reported in [Pierobon et al. \(2014\)](#), where the design of an ORC bottoming cycle for a gas-turbine electrical generator on an oil rig is

considered. The electrical grid onboard the rig is isolated from the mainland, so the generators must be able to withstand the connection and disconnection of large electrical loads (docking ships) while keeping the frequency of the system within acceptable bounds. In that paper, a two-stage multiobjective optimization was performed. In the first stage, the static design of the system is optimized with respect to efficiency and volume, finally obtaining the Pareto front of alternative solutions that are never dominated by each other, and that characterizes the optimal trade-off between the two conflicting objectives. Having done this, the system designs on the Pareto front are used to automatically parameterize dynamic models of the system, whose controllers are tuned using simple heuristic rules. This allows to automatically check the frequency transient corresponding to the ship docking and undocking with all Pareto-optimal designs, and to discard those which fail to meet the specification on the maximum power system frequency variation onboard the oil rig. In the presence of nonminimum phase dynamics, one could even skip the actual design of the controller and only consider the position of the right-hand side plane transmission zeros of the open-loop transfer function of the system, trying for example, to maximize their distance from the real axis, or to constrain their distance from the real axis to be greater or equal to a certain threshold.

An even more comprehensive approach can be undertaken, based on EOO languages and tools. The idea is to write equation-based models that describe the equipment design process. One can then build the system model by connecting the components and add equations prescribing the design objectives, e.g., the net power output, the condensation temperature, and the evaporator pressure. The solution of such a model yields a complete description of all the key quantities in the thermodynamic cycle (pressures, temperatures, and power flows), as well as the parameters of the mechanical design of the equipment, such as, the number, length, and diameter of the tubes in a shell and tube heat exchanger. In a second step, one can remove the equations prescribing the design objectives and add the equations that prescribe the design parameters obtained at the first step instead. In this case, the solution of the model equations allows one to compute the off-design operating points of the system. All of these results can then be used to parameterize and initialize a dynamic model of the system, in order to analyze its dynamic response; the results of the third step can be used to design the control system and assess the closed-loop performance of the system in on-design and off-design conditions.

This process can be described in terms of an algorithm, or function, whose inputs are the design objectives, and whose outputs are performance indicators of the system, including dynamic ones. This function can be passed to derivative-free, global optimization algorithms (e.g., genetic algorithms) that can be used to optimize the on-design, off-design, and dynamic performance of the system simultaneously, while taking into account operational constraints, e.g., avoiding dangerously high temperatures in the organic fluid, as well as mechanical design constraints, e.g., the minimum blade height or the maximum rotational speed in the turbine. This approach is currently being investigated by some researchers, including the author of this chapter, and might result in powerful integrated design tools in the future.

6.4 Conclusions

ORC systems are extremely diversified in terms of applications, operating conditions, size, and type of equipment. Each different configuration has a different dynamic behavior and might need different control strategies, based on the process dynamics and on the application requirements. There are no established design rules or best practices in this field, and it may be possible that there will never be any, given the huge variety of possible scenarios.

Future innovative ORC applications, such as solar and automotive, will have more and more challenging dynamic requirements. In order to meet these requirements, it is essential to understand the process dynamics by means of dynamic models during the design phase. EOO tools are optimally placed for this task, and have already been successfully demonstrated in this field. The insight and data obtained from these models can be used to select the most appropriate control strategy, to help tuning the controller parameters, and to assess the closed-loop dynamic performance in on-design and off-design scenarios.

Future integrated design and optimization tools based on EOO models might allow one to tackle the integrated optimal design of the thermodynamic cycle, equipment, and control system, yielding the best possible combinations of on-design, off-design, and dynamic performance, fulfilling at the same time all the constraints of the mechanical design and operational parameters of the system.

References

- Bell, I.H., Wronski, J., Quoilin, S., Lemort, V., 2014. Pure and pseudo-pure fluid thermophysical property evaluation and the open-source thermophysical property library CoolProp. *Industrial & Engineering Chemistry Research* 53 (6), 2498–2508.
- Bonilla, J., Yebra, L., Dormido, S., 2010. Mean densities in dynamic mathematical two-phase flow models. *Computer Modeling in Engineering & Sciences* 67 (1), 13–38.
- Casella, F., 2006. Object-oriented modelling of two-phase fluid flows by the finite volume method. In: *Proceedings 5th MATHMOD Vienna, Vienna, Austria, February 8–10, 2006*.
- Casella, F., Leva, A., 2005. Object-oriented modelling & simulation of power plants with Modelica. In: *Proceedings 44th IEEE Conference on Decision and Control and European Control Conference 2005, Pages 7597–7602, Seville, Spain, December 12–15, 2005*. IEEE, EUCA.
- Casella, F., Leva, A., February 2006. Modelling of thermo-hydraulic power generation processes using Modelica. *Mathematical and Computer Modeling of Dynamical Systems* 12 (1), 19–33.
- Casella, F., Mathijssen, T., Colonna, P., van Buijtenen, J., 2013. Dynamic modeling of organic cycle power systems. *Journal of Engineering for Gas Turbines and Power* 135 (4), 042310–1–12.
- Casella, F., Richter, C.C., 2008. ExternalMedia: a library for easy re-use of external fluid property code in Modelica. In: Bachmann, B. (Ed.), *Proceedings 6th International Modelica Conference, Pages 157–161, Bielefeld, Germany, March 3–4, 2008*. Modelica Association.

- Cellier, F.E., Kofman, E., 2006. Continuous System Simulation. Springer-Verlag.
- Colonna, P., van der Stelt, T.P., Guardone, A., 2010. FluidProp (Version 3.0): A Program for the Estimation of Thermophysical Properties of Fluids. A program since 2004. <http://www.fluidprop.com/>.
- Lemmon, E.W., Huber, M.L., McLinden, M.O., 2013. NIST Standard Reference Database 23: Reference Fluid Thermodynamic and Transport Properties-REFPROP version 9.1.
- Fritzson, P., 2014. Principles of Object Oriented Modeling and Simulation with Modelica 3.3. Wiley IEEE Press.
- Mattsson, S.E., Elmqvist, H., Otter, M., 1998. Physical system modeling with Modelica. Control Engineering Practice 6 (4), 501–510.
- Pierobon, L., Casati, E., Casella, F., Haglind, F., Colonna, P., 2014. Design methodology for flexible energy conversion systems accounting for dynamic performance. Energy 68, 667679.
- Quoilin, S., Desideri, A., Wronski, J., Bell, I., Lemort, V., 2014. Thermocycle: a modelica library for the simulation of thermodynamic systems. In: Proceedings 10th International Modelica Conference, Pages 787–797, Lund, Sweden, March 10–12, 2014. The Modelica Association.
- Schiavo, F., Casella, F., June 2007. Object-oriented modelling and simulation of heat exchangers with finite element methods. Mathematical and Computer Modeling of Dynamical Systems 13 (3), 211–235.

Thermodynamic and technoeconomic optimization of Organic Rankine Cycle systems

7

M. Astolfi¹, E. Martelli¹, L. Pierobon²

¹Politecnico di Milano, Milan, Italy; ²Technical University of Denmark, Lyngby, Denmark

7.1 Design of Organic Rankine Cycles and their optimization

Organic Rankine cycles (ORCs) are power systems based on the use of a suitable organic compound as working fluid within a Rankine cycle. In the basic layout configuration the plant is quite simple because it does not require regenerative bleedings and it allows for dry expansion. However, the design of the expander may be challenging because of the thermophysical properties of heavy and complex fluids. In this section an overview of ORC design criteria and optimization is first presented, after the available commercial softwares are listed, pointing out their peculiarities and their limits. Finally a few examples of state-of-the-art numerical analysis are presented. A complete description of ORC technology is out of the scope of this chapter and the main information can be found by the reader in the other chapters of this book. However, it is important here to briefly list the main characteristics of this technology to give the basis for a better understanding of this chapter.

- ORCs have a good flexibility and they are the most suitable solution for the exploitation of many different energy sources. Most of the information about the fields of application for ORCs is reported in Chapters 1 and 14–18 of this book. The most common energy sources for ORCs are renewable energies like solar energy, hot geothermal brines, biomass, and waste heat recovery from industrial processes or engines. The different natures of these energy sources, the different maximum temperatures and operation constraints entail a nonunivocal design of ORCs that usually requires solutions that are custom designed rather than commercial off-the-shelf standard products as better explained in this chapter.
- ORCs use a suitable compound as working fluid within the cycle instead of water. Organic fluids appreciably differ one from the other in both thermodynamic and physical properties. This strongly affects both the plant layout and the design of each component with relevant effects on cycle efficiency and system cost. Thermodynamic properties of organic fluids and the main differences versus water are discussed in Chapters 1 and 4. The number of possible working fluid candidates is huge, leading to a large dimension of the optimization problem.
- ORCs can be designed in various cycle configurations. Some of them are widely used, whereas others are innovative or oriented to very specific applications. For a given energy

source different layouts lead to different installation costs and different efficiencies with a nontrivial selection of the best option. Available plant configurations are listed and described in detail in Chapter 3 and briefly summarized in this chapter.

- Reliable thermodynamic and economic optimizations require the use of efficiency correlations for the machines, a reliable estimation of heat transfer coefficients and a trustworthy cost correlation for each component. This is a big challenge and it represents the main barrier for the achievement of reliable results. This issue is accentuated in the ORC field because the same component developed for more common applications like steam cycles can be dramatically different when working with a highly complex molecule. In particular, expanders (both turbine and volumetric machines) are the key components in ORC technology and their design is greatly affected by working fluid properties and cycle parameters: the definition of efficiency and cost correlations is still partially an open task because of the lack of numerical simulation tools and experimental data.

In conclusion, because of the peculiarities of ORCs, their design and optimization are very challenging tasks and require a good knowledge of organic fluid thermodynamic properties, component design criteria, and cost correlations. In following sections the main information about ORC design criteria and optimization is reported.

7.1.1 Organic Rankine Cycle design steps

ORCs are a widely studied technology. Many different research centers and universities are oriented toward the design, the optimization, and the dynamic simulation of this kind of system. Many of these institutions are also involved in experimental campaigns to test new devices, new working fluids, or new cycle configurations. Regarding the numerical analysis of an ORC, several steps are required to select the optimal working fluid and the best cycle configuration, taking into account not only nominal performance indexes, but also economic aspects, off-design efficiency, the dynamic behavior of the plant, or the plant volume or weight. A schematic view of the design and optimization process for a generic ORC is reported in Fig. 7.1: three different stages can be highlighted: (1) analysis of the problem, (2) working fluid and cycle configuration selection, and (3) system optimization.

These steps can be faced progressively, and wrong assumptions in the first ones compromise the achievement of a good result at the end of the process. For this reason the entire process is iterative and requires robust algorithms to obtain the optimal solution in a reasonable computational time without incurring in local minimum. In addition, depending on the application, the economical context, the technological boundaries and several other constraints may bind the final design.

7.1.2 Problem analysis

The problem analysis requires a detailed description of the heat source and the heat sink and the evaluation of all the technical constraints and both environmental and safety issues. Technical constraints mainly concern component choice or plant

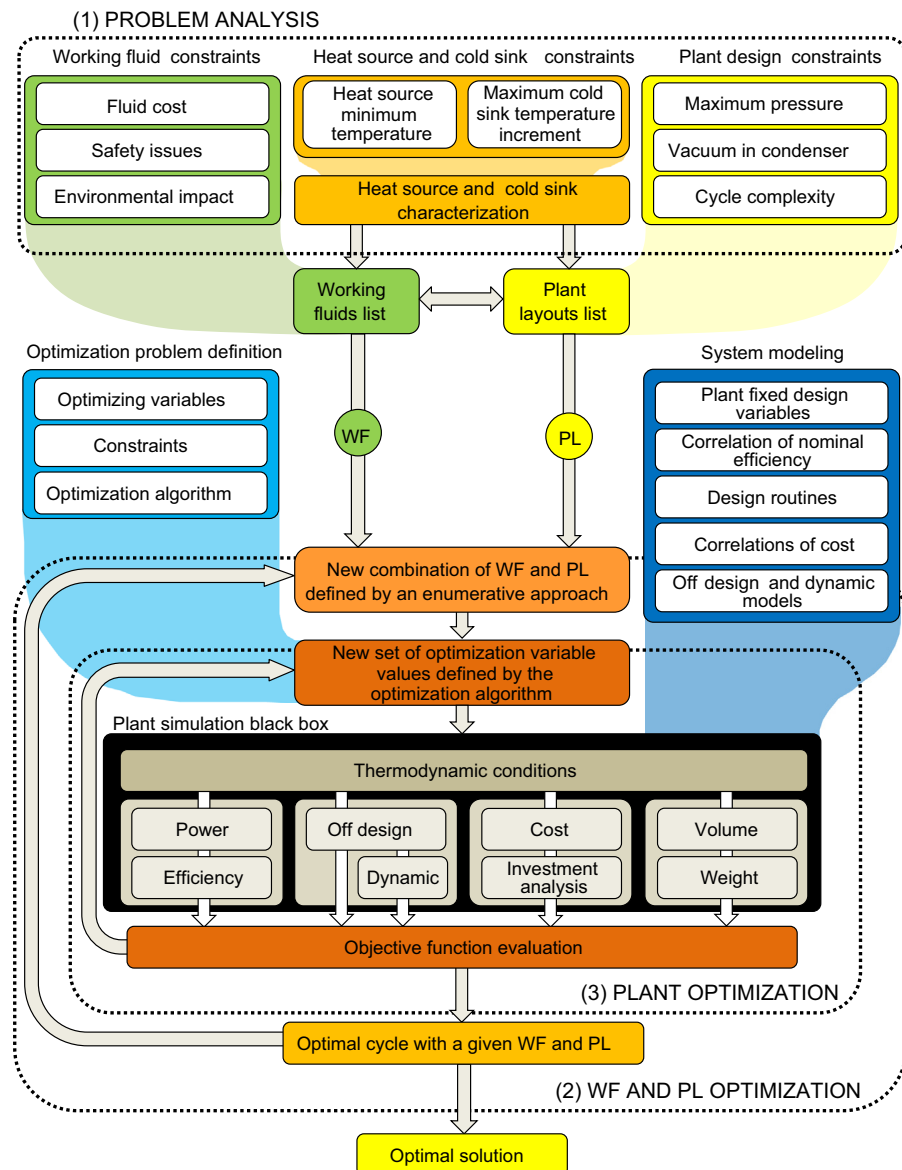


Figure 7.1 Steps required for the design and optimization of organic Rankine cycles from the analysis of the problem to the definition of the optimal combination of working fluid and cycle configuration. *PL*, plant layout; *WF*, working fluid.

layout, whereas the others limit the use of some chemical classes of fluids. Regarding the hot and cold sink characterization it is possible to list the following observations, whereas considerations about working fluid and plant layout selection are reported in later sections.

- The heat source in the ORC field can be often represented as a liquid or a gaseous hot stream available at a temperature higher than the ambient one. This is clearly the case for geothermal hot brines and waste heat recovery from hot gases but it is valid even for solar and biomass energy exploitation, in which a heat-transfer fluid (HTF) loop is commonly used to avoid local hot spots that can induce fluid decomposition. In all these cases the heat source has a variable temperature and it can be cooled down to a certain temperature limit, which is generally higher than the ambient temperature. Independently of the heat source it is crucial to know (i) the mass flow rate, (ii) the heat capacity as function of temperature, (iii) the maximum temperature and (iv) the presence of additional constraints on the minimum temperature of the heat source. The maximum temperature is often an exogenous variable of the problem, whereas in the case of an HTF loop it can be optimized from a technoeconomic point of view. Depending on the nature of the HTF (synthetic oil, pressurized water, steam) various constraints related to maximum allowable pressure should be considered as well. Isothermal heat sources are rarer and they can be found in waste heat recovery applications if steam is used as the HTF and in the geothermal field for two-phase hot geothermal brines. In the last case the presence of noncondensable gases (mainly CO_2) can greatly affect the temperature–heat released profile of the heat source. This trend is not easily described by a polynomial curve and the numerical solution of the vapor–liquid equilibrium is required in several sections of the heat exchanger to locate the exact pinch-point temperature difference in the PrHE (primary heat exchanger). In other cases the heat source can be formed by different hot streams at different temperatures and with different heat capacities: typical examples are two-phase geothermal sources, where heat can be recovered by both the liquid and the mixture of vapor and noncondensable gases, and WHR (waste heat recovery) from automotive engines, where heat is available from the exhaust gas recirculation, the charge air cooler, and the exhaust flue gas cooler. A preliminary analysis can be carried out using the pinch analysis: all the hot streams are aggregated in a composite curve that represents the equivalent heat source, and the ORC is designed to meet the pinch-point temperature difference with respect to this curve that can present discontinuities and sharp slope variations. The optimal solution obtained has the maximum higher efficiency but it may require a very complex plant layout with several heat exchangers in series and in parallel. Starting from this configuration it is possible to sketch a simpler plant layout having a similar efficiency but a lower equipment cost.

Regarding the heat source minimum temperature a number of technical reasons can limit its value above the ambient one. For geothermal applications the limit is related to the precipitation of salts present into the geothermal brine. Independently of the plant layout (the hot water can be obtained from the flash of the geothermal fluid or by the use of a submerged pump into the well) the geothermal brine contains a high percentage of salts which can greatly vary from case to case. These compounds are mainly carbonates, sulphates and nitrates of alkaline metals like sodium and calcium and their composition is strictly related to the kind of rocks surrounding the geothermal reservoir. Depending on chemical species and their concentration there is an operative temperature limit below which salts start precipitating with the formation of scaling on heat exchanger surfaces and entailing a reduction of heat transfer coefficients and an increase of pressure drops. This limit, also called reinjection temperature limit, is pretty difficult to define and its evaluation requires the exact knowledge of the brine composition and the calculation of the chemical species equilibrium at different temperatures. On the basis of Enel experience in geothermal energy exploitation this technical limit is fixed to 70–75°C (Rossi, 2013) for most of the geothermal plants nowadays in operation in Nevada and Arizona. Another consequence of an excessive cooling down of the geothermal brine is the premature depletion of the reservoir whose temperature

is progressively reduced during the plant life time. A temperature reduction of around $1\text{--}2^{\circ}\text{C}$ per year was reported in operating plants exploiting a geothermal brine with an initial maximum temperature of 150°C involving a gradual reduction of cycle performances during the plant lifetime.

In heat recovery applications hot gases are usually obtained from combustion processes or from the cooling of hot devices like endothermic engines, steel furnaces and cement production kilns. In the first case the lower limit of exploitation of the heat source is related to the minimum temperature allowable at the stack to avoid condensation of acid and corrosive compounds that are present in the flue gas. Depending on the fuel used and on the excess of air in combustion, this temperature can vary in a range of $80\text{--}180^{\circ}\text{C}$. In the case of biomass combustion hot gases usually do not release heat directly to the working fluid and generally an HTF is used in loop circulation between the biomass boiler and the ORC. In this case the lower temperature limit is set according to the specifications of pollutant removal units placed after the heat recovery and the requirements of air preheating. If the hot stream is a hot liquid or a clean or a dry gas it can be ideally cooled down to ambient temperature without any drawbacks and the lower limit is set by a technoeconomic optimization of the whole system.

In solar thermal power plants the lower temperature limit of the heat source is mainly related to physical properties of the HTF, usually synthetic oil, which flows into the collectors of the solar field. From a general point of view once fixed the thermal input to the ORC, reducing the temperature of the HTF at the solar field inlet leads to different contrasting effects. The solar collectors work with a lower average tube wall temperature limiting the heat losses to the ambient, thus reducing the required area of the solar collectors. On the other hand the HTF temperature variation is larger, the mass flow rate is reduced, and this leads to a different design of the solar field with a lower number of longer loops. The pressure drop increases because of both the longer path and the increase in HTF viscosity at low temperatures (generally lower than 50°C) with a non-univocal effect on solar field pump consumption. Furthermore the cycle efficiency is reduced because of the lower average temperature of heat introduction. The selection of the optimal temperature limit for an indirect solar power plant is hence the result of a trade-off between several opposite effects.

- The cooling medium is generally ambient air or water, depending on the installation site. Required data in this case are (1) the heat sink temperature, (2) the heat capacity, and (3) constraints in the maximum temperature increase due to environmental protection regulations. Generally, the mass flow rate is not limited and it is a result of the system overall design; however, in some cases it can be bounded and this information needs to be considered as a problem constraint: this is the case of a CHP (combined heat and power) plant where the heat released at the condenser is used for district heating or industrial processes.

It is important to emphasize that in some case the temperature, the mass flow rate, the composition of the heat source, and the temperature of the cooling medium may change during plant operation, with a consequent change in plant efficiency. For applications that work always at nominal conditions, like in the geothermal field or CSP (concentrating solar power) with large thermal storage and water-cooled condensation, it is common to use average values for these quantities, whereas in other cases this approach may introduce relevant inaccuracy into the economic evaluation of the plant. In these cases, like highly discontinuous WHR, domestic CHP generators, and the air-cooled power plants, the off-design conditions and possibly the dynamic behavior must be accounted for in the system optimization.

7.1.3 Choice of working fluid and cycle configuration

The most important stage is definitely the correct choice of both working fluid and cycle configuration. Making the wrong choice at this stage entails a poor cycle performance compared to the maximum attainable with a more suitable fluid. Of the same importance is the choice of cycle configuration.

The various combinations of working fluid and plant layout are usually investigated with an enumerative approach to limit the number of discontinuities in the objective function and to obtain more reliable results. This exhaustive approach is the strategy commonly used in most of the publications but in some papers other methodologies are proposed, even if not directly applied to the ORC field. Synthesis optimization aims at directly optimizing the plant configuration (Biegler et al., 1997; Chen et al., 2015). The number of components and the connection between them are defined as variables for the optimization routine: the streams are handled using binary variables with the possibility of excluding automatically some components or changing the order of the heat exchangers coupled with the heat source. This type of approach is extremely flexible and general, but it entails a more challenging optimization problem, which is intrinsically harder to be solved because the objective function presents a relevant number of discontinuities and local minimum. Other studies (Hattiangadi, 2013; Lampe et al., 2013) consider the fluid choice directly as a variable in the problem: the idea is to optimize the fluid chemical composition and the plant design at the same time, thus reducing the number of simulations required by the exhaustive study of a certain problem. The main limit of this strategy consists in working fluid characterization: multiparameter equations of state cannot be used because of the large number of required additional variables, and usually simpler cubic or PC-SAFT equations of state are adopted with a strong reduction in solution accuracy. Furthermore the working fluid resulting from the optimization might be a nonexistent fluid with critical properties similar but not equal to those of any other commercial fluid. In this case two solutions are possible: (1) selecting the commercial fluid closer to the optimal one and optimizing the system again or (2) synthesizing the desired fluid. This methodology is demonstrated in Papadopoulos et al. (2011) but it entails uncertain costs, which are surely higher than the purchase of a widely used commercial fluid.

The exhaustive enumerative analysis on all the combinations of working fluids and plant layouts, however, can be extremely time-consuming and at this stage a good predesign analysis is always required with the aim of reducing the domain of the possible solutions. Technical limits and environmental and safety issues can be taken into account to exclude some working fluids and some cycle configurations or to fix some design parameters and reduce the computational time required by the optimization procedure. For instance, the maximum cycle pressure or the necessity to avoid vacuum into the condenser can affect the choice of cycle configuration, limiting the investigation to just some plant layouts or some working fluids. In other applications, like the heat recovery from engine exhaust gases in the automotive field, a light plant and a small occupied volume are required, pushing the choice toward simple plant layouts having a limited number of components. Remote applications, like small solar plants in rural contexts and WHR from pumping stations along pipelines, need instead simplicity, reliability, and low

maintenance cost. At the end of this stage a number of promising working fluids and plant layouts for the exploitation of a given heat source are preselected. In the following sections the main considerations about working fluid and plant layout choice are listed.

7.1.3.1 *Working fluid choice*

ORCs can be designed using a huge number of possible working fluids: this is obviously a great advantage that makes these systems suitable for almost every heat source but, on the other hand, make the resolution of the optimization problem inevitably more difficult. Organic fluids can be selected from various chemical classes like hydrocarbons (alkanes, alkenes, etc.), refrigerant fluids (partially fluorinated and perfluorinated compounds), and siloxanes. Limiting the choice to well-known fluids, the number is around 100, with fluids differing remarkably from one another. In addition, in some applications, the use of mixtures can be profitable and the composition needs to be optimized depending on the temperature profile of the hot and the cold sources: the use of compound blends entails an additional degree of freedom and leads to a remarkable increase in the size of the problem. Only a small number of pure fluids are commonly used in commercial systems (mainly toluene, pentane, butane, R134a, R245fa, and light siloxanes) because ORC manufacturers tend to keep the choice among a limited number of well-known fluids already used in previous installations. However, from a general point of view there are no reasons to exclude from the analysis a certain fluid if its thermodynamic and physical properties are accurately described by a well-calibrated equation of state (EoS). In the case of a mixture, instead a validation of experimental data from a reference is always required to obtain reliable results. As explained further on in this chapter the knowledge of fluid properties is crucial for the correct design of both cycle and components. For additional information about EoS please refer to Chapter 4.

Depending on the application, the number of candidate working fluids can be greatly reduced considering not only thermodynamic properties but even the thermal stability, the cost, the environmental impact, the safety issues, and the technological limits on different components.

Thermal stability and material compatibility

Organic fluids exposed to high temperature tend to decompose, entailing a maximum cycle temperature limit around 350–400°C. Hydrocarbons and halogenated compounds with a molecule backbone chain formed by carbon atoms are subject to cracking and pyrolysis processes at temperatures higher than their critical point. These processes form light residual molecules and solid particles, with a consequent increase in the fouling resistance on heat exchanger surfaces, damage to the turbine blade surfaces, and a notable change in the fluid thermodynamic properties.

The thermal stability limit for most of the fluids used in ORCs is around 350–400°C, even if for low-boiling-temperature fluids a lower limit is usually considered. The threshold of thermal stability is evaluated by experimental activities in which the saturation pressure of the fluid is measured after a permanence from 5 to 50 h at high temperatures and comparing the obtained values with the nominal ones. The

departure from nominal data is evaluated during and after the exposure to high temperatures because for some fluids the degradation starts during the cooling process. Different campaigns are usually performed for different temperatures and different times of permanence at (Invernizzi and Angelino, 2003). A difference of 1% with respect to nominal data after a permanence of 50 h is assumed as the threshold for the definition of the temperature stability limit. Please refer to Chapter 5 for further details. Inevitably, the exploitation of a high-temperature heat source excludes all those fluids that cannot tolerate such high temperatures or otherwise it requires the use of an HTF loop between the heat source and the working fluid.

Cost, environmental impact, and safety concerns

Working fluid inventory cost may represent a noticeable share of the total equipment cost and in many case it can represent more than 10% of the total plant cost. The specific cost of organic fluids changes appreciably depending on the chemical class and the market size. Working fluid purchase cost (fluid in the cycle plus the volume of the makeup vessel) is not generally considered in system optimization because it requires the estimation of the volume of the plant and a preliminary sizing of all the heat exchangers and the piping. This level of detail is usually obtained with very specific tools and a long computational time, which is usually noncompatible with the optimization of the entire system. However, from personal communications with manufacturers and organic fluid producers the following aspects can be highlighted:

- The share of the working fluid cost on the total plant cost is not always negligible and it can reach 10% of the plant cost, without the balance of plant cost (BOP), if a nonflammable and nontoxic fluid is used.
- A wide cost difference is highlighted between flammable and nonflammable fluids: flammable fluids, mainly all the linear and cyclic hydrocarbons, cost around US\$2.50/kg in 2015, whereas the others, like refrigerant fluids, cost at least US\$15.00/kg. R134a is the only exception, because it is produced in large amounts for the air conditioning market, and its cost is around US\$5.00/kg. Heavy perfluorinated fluids are extremely expensive (more than US\$100.00/kg), because they are usually sold in small quantities and their market is limited.
- Another difference is the density of these compounds in the liquid phase: flammable fluids are relatively light ($\sim 600 \text{ kg/m}^3$), whereas fluorinated compounds have a density that is approximately twice that of hydrocarbons, entailing for the same plant volume a larger amount of fluid.¹
- Using a nonflammable fluid (eg, R245fa vs. pentane) leads to a fluid cost at least 12 times higher than using a flammable fluid, with a relevant impact on power block economics. On the other hand, the use of flammable fluids requires additional safety protection, an expensive antifire system and additional authorizations, which make the whole project more expensive. In most of the cases these additional costs are not so high to level off the economic advantage of using a cheaper fluid, and hydrocarbons are widely used for stationary ORC applications. Nevertheless, all these considerations are strongly site dependent and the additional costs vary greatly from country to country, and a general conclusion cannot be stated. For example, in Europe a series of strict normative regulations, the 96/82/EC and the 2012/18/UE, also called

¹ The hypothesis of a constant value of system volume is reasonably correct when kettle reboilers and pool-condensing heat exchangers are used, but may lead to inaccurate results for supercritical cycles with once-through heat exchangers.

Seveso II–III Directives,² regulate the use of flammable and toxic compounds in the industrial field. As a result, the installation of ORCs using dangerous working fluids is strongly discouraged because they need more expensive equipment, require a longer authorization process, and have to face strong NIMBY (not in my backyard) reactions.

- Similar considerations regard the impact of the accidental release of a working fluid into the environment, usually represented by two indexes: the ozone depletion potential (ODP) and the global warming potential (GWP). The first index represents the potential of a molecule of a certain compound to deplete the ozone (O₃) layer that protects us from UV radiation. Most dangerous compounds are free radical catalysts and, among them, atomic chlorine (Cl) and bromine (Br) are the most active: a single radical of these species can activate a sequence of reactions that can destroy more than 100,000 molecules of ozone. Halogen compounds, like chlorofluorocarbons, hydrochlorofluorocarbons, and bromofluorocarbons, were widely used in the 1970s and 1980s as refrigerant fluids, propellants for aerosols, and solvents, but they have been banned since 1996 in most developed countries because of their high ODP. Despite their exceptional thermodynamic properties they should never be used for ORC applications.

The second index represents the impact of a molecule of a certain compound on the greenhouse effect, which is considered the main cause of global warming. Many of the organic fluids used in ORCs have a very high GWP: in particular, fluorinated compounds (hydrofluorocarbons HFC), which are used as fluids in refrigeration and automotive air conditioning, show a GWP index that can exceed 2000, with a consequent issue if they are accidentally released into the environment during operation or at the end of plant life. Refrigerant fluids with a high GWP are not yet banned from ORC applications, but Europe has forbidden the use of R134a in the automotive sector since 2013, whereas the United States is going to discourage its use after 2016. For this reason many chemical companies like Honeywell (Honeywell) have invested great efforts in the past years in producing low-GWP drop-in fluids for the refrigerants R134a and R245fa, which are called R1234yf and R1233zd, respectively.

In addition to hydrocarbons and fluorocarbons, siloxanes have been intensively studied for high-temperature applications. From a chemical point of view they are formed by long (and often cyclic) chains of Si–O and Si–C groups and they are characterized by both high complexity and high molecular mass. They are virtually nontoxic and have negligible GWP and ODP, but some of them are flammable, and their use is considered hazardous in both Europe and Canada. Fig. 7.2 depicts the various chemical classes of organic fluids in terms of GWP index and flammability index as defined by the National Fire Protection Association (Jones, 2009).

Effects on component sizing and cycle design

Organic fluids differ appreciably in molecular weight and molecular complexity and they cover a large range of critical temperatures and critical pressures. These differences strongly affect the configuration of the cycle and the design of the main components. The influence of the various parameters on the expander design is taken as an example and the main considerations are listed below. The effect of each parameter

² The Seveso Directive was adopted by the European Union after the Seveso disaster in 1976, which involved a small chemical plant in the north of Italy. A relevant amount of TCDD, an extremely toxic compound (National Fire Protection Association Health Hazard 4), was released into the environment, causing a frightening exposure to the population.

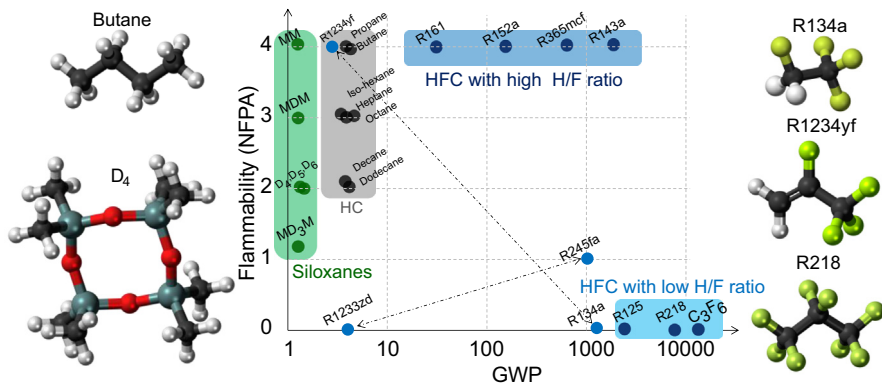


Figure 7.2 Organic fluids commonly used in organic Rankine cycles as a function of their global warming potential (GWP) and flammability index (from 0, nonflammable, to 4, extremely flammable). Molecular structures were provided by various authors using Discovery Studio Visualizer. *NFPA*, National Fire Protection Association. H/F is the ratio between hydrogen and fluorine atoms.

on the component design is presented considering the other values constant, but it is important to emphasize that the different effects usually sum each other.³

- *Molecular mass*: A fluid with high molecular mass shows small enthalpy drops in expansion but also a low speed of sound. On one hand, it would be possible to realize the expander as a turbine with a small number of stages (at limit only one) and with a small loading coefficient. This helps the design of the machine and leads to compact and relatively cheap machines. On the other hand, the presence of supersonic flows requires a nonconventional design of turbine blades with converging–diverging nozzles and the possible presence of shock waves with a penalty on expansion efficiency. From a technoeconomic point of view the number of stages is selected considering the trade-off between the attainable increase in efficiency and the increment of component cost.
- *Molecular complexity*: The higher the molecular complexity is, the higher the volume ratio across the expansion is for a fixed pressure ratio. For an axial turbine this leads to difficulties in handling in a single stage the increase in volume flow rate (high flaring angles and supersonic flows) and the need for a multistage machine with a higher investment cost. On the other hand, a fluid with high complexity allows for a dry expansion starting from saturated vapor without a blade erosion issue and in conclusion a longer life of the component. In addition, high-complexity fluids show small temperature drops across the expansion with the necessity of adopting a recuperator to recover the heat available at turbine discharge to preheat the pumped liquid.
- *Critical properties*: In a saturated Rankine cycle, once the evaporation and the condensation temperature are selected, the pressure ratio and the volume ratio across the expansion increase with the critical temperature of the fluid because of the exponential dependency of

³ In theory the effect of each fluid property can be analyzed separately from the others; however, for fluids in the same chemical class, an increase in complexity usually results in a heavier fluid with a higher critical temperature and a lower critical pressure, so cross-effects need to be always considered.

pressure and temperature on saturation. Furthermore, increasing the critical temperature generally results in a higher volume flow rate with an increase in the low-pressure component dimension and cost. In large power output applications, if an axial or a radial outflow turbine is used, the high volume ratio can be handled, increasing the number of stages of the turbine and accounting for the corresponding incremental cost. In other applications the expander is usually a single-stage machine that is strongly penalized when the volume ratio is above a certain limit. For example, for small and micro ORC applications (small CSP power plant, automotive ORC, and domestic cogenerative units) the cost of the expander is a relevant share of the system cost and the use of single-stage radial inflow turbines or a volumetric expander (screw or scroll) is preferable with respect to multistage turbines. These expanders show a low efficiency for volume ratios above 7–10 (depending on the expander architecture) and so the choice of high critical temperature fluids leads to a limitation of the evaporation temperature and thus a cycle efficiency penalization. On the other hand, the selection of a high-critical-temperature fluid for very small applications may be profitable because it leads to high volume flow rates and it allows designing the turbine with a reasonable size, a higher efficiency, and possibly a direct connection with the generator. A last consideration regards the content of noncondensable gases: for a given condensation temperature, the higher the critical temperature is, the lower the condensing pressure is, with a potential increase in air leakage into the condenser, a reduction of system performance, and the necessity to install a vacuum pump or a batch system for gas removal.⁴

The heat exchanger design is influenced by fluid characteristics as well, but the effect in this case is less marked than for the expander. Different pure organic fluids show similar heat transfer coefficients, whereas the use of mixtures involves a remarkable penalty on phase transition with an increase in heat exchanger surface and cost (Bivens and Yokozeki, 1992; Gu and Bart, 1999).

7.1.3.2 Plant layout choice

In ORCs the single-level subcritical saturated cycle is the most common choice. However, other plant layouts are intrinsically more suitable for some heat sources. For example, when the heat source temperature is variable, supercritical cycles and multiple pressure level cycles are more adequate; because they allow for a better match among the heat source and the working fluid temperature profiles, they can reach higher efficiency. As a drawback they generally show an investment cost higher than that of the single-level saturated cycle, because of the larger heat transfer surfaces. In addition, supercritical cycles usually have a high maximum pressure with a consequent increase in both the pump consumption and the thickness of the heat exchanger walls, whereas a multilevel cycle requires a higher investment cost and a more complex plant control.

The use of a recuperator is common in ORC but this option must always be carefully evaluated: on one side, it allows the recovery of part of the thermal energy available at turbine discharge to preheat the working fluid; on the other, it entails pressure drops on both sides (and a consequent penalty on power production), a larger heat transfer area, and a higher equipment cost. The use of the recuperator is usually

⁴ Remember that a deaerator cannot be used in ORC systems because the organic fluids usually have a high GWP and they cannot be vented into the atmosphere.

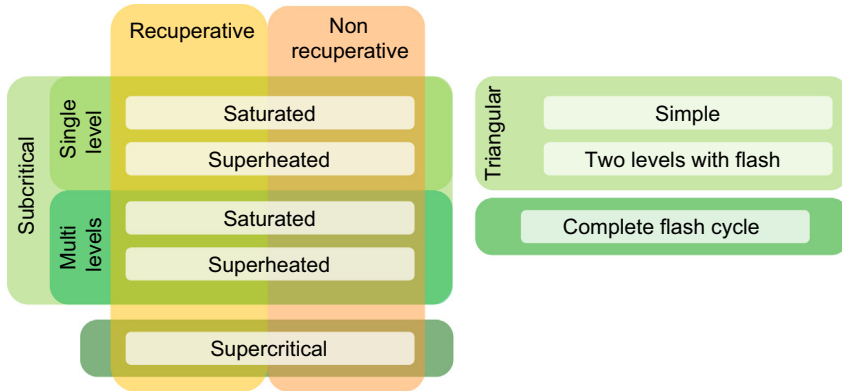


Figure 7.3 Available organic Rankine cycle plant configurations.

suggested in the case of heat sources that cannot be cooled down below a certain minimum temperature: in this case it is possible to increase the working fluid mass flow rate and the power output. The optimal design of this component depends on the heat source constraints and the fluid characteristics; among them the molar complexity of the fluid plays a relevant role because the more complex the fluid is, the smaller the temperature drop in expansion is and the larger the heat available at the recuperator is.

Two other cycle layouts are proposed in the literature with the aim of minimizing the temperature differences in the PrHE: in both of them the fluid remains in the liquid state during the heat introduction process, allowing for an easier design of the PrHE and a direct storage in the case of solar plants.

- The triangular cycle (Smith, 1993, 1994) and the flash triangular cycle (Smith et al., 2005) are considered an option for medium to low heat sources, but they require a two-phase expansion starting from the saturated liquid state. For this reason volumetric expanders are the only reliable option, with a consequent limitation in maximum volume ratios across the expansion and maximum power output.
- The complete flash cycle is a promising solution for medium to high temperature sources like high-concentration CSP and biomass. The hot and high-pressure liquid coming from the PrHE totally vaporizes across an isenthalpic valve and it is eventually expanded in a turbine. The throttling process is irreversible, but for some high-complexity and high-critical-temperature fluids (eg, siloxanes and long-chain fluorinated hydrocarbons) the process is almost isentropic with a small penalty on cycle efficiency (Casati et al., 2013).

Fig. 7.3 depicts a classification of the various plant layouts available in the ORC field, whereas a more detailed description of these configurations is reported in Chapter 3.

7.2 System optimization

For each combination of working fluid and plant layout, an optimization of the system should be performed to define the best ORC system according to a certain objective function. This is the third step in ORC study and, as for the second one, it is crucial

to fairly compare different solutions and different assumptions. For a generic system several parameters must be defined to calculate all the thermodynamic points and evaluate the plant efficiency and the power output: most of them can be optimized with the aim of maximizing or minimizing a selected figure of merit. Among them, some are defined a priori on the base of the designer experience or problem constraints, whereas others are varied by a suitable numerical algorithm. The optimization variables can be bounded or unbounded and a set of linear constraints can be generally defined between them. Furthermore, nonlinear constraints can be implemented if some limit cannot be directly expressed as a function of the optimization variables: these limits are usually accounted as penalty factors on the objective function to penalize those solutions that do not respect one or more limits.

In the optimization of an ORC it is necessary to define:

- the objective function
- the optimizing variables
- the models of the plant components and the simulation tools
- the optimization approach and the optimization algorithm

7.2.1 Objective function

The objective function for an optimization problem is the figure that is maximized or minimized during the optimization process. For ORCs two main classes of objective functions can be defined, if the goal is to maximize the plant performance or to minimize the cost of the produced electrical power. Because usually a higher efficiency is achieved with more expensive equipment, the optimal cycles obtained with the two different objective functions can be significantly different.

7.2.1.1 Technothermodynamic optimization

Many publications are focused on the optimization of ORC from a thermodynamic point of view, because this analysis allows obtaining accurate results even without sophisticated efficiency correlations and it does not require cost functions. A list of relevant studies following this approach is given in [Table 7.1](#).

Various objective functions can be considered as representative of the thermodynamic performance of an ORC system but all of them are equivalent in terms of trend and optimal cycle configuration even if the absolute value changes according to the evaluated quantity. [Fig. 7.4](#) depicts the Sankey diagram of a general two-pressure-level ORC exploiting a hot source (top stream, ts) throughout a loop of HTF (medium stream, ms) and releasing heat to the cooling medium (bottom stream, bs). It is possible to define:

- *Net power output*: This is calculated as the difference between the gross turbine power output and the power consumption of the working fluid pumps and the auxiliaries of the system:

$$W_{el}^{net} = W_{el}^{gross} - \sum_{\substack{LP \\ HP}}^j W_{el}^{pump, wf, j} - \sum_{\substack{ts \\ ms \\ bs}}^j W_{el}^{pump, j} \quad (7.1)$$

Table 7.1 Relevant publications on organic Rankine cycle thermodynamic optimization

References	Heat source	\dot{Q}_{in} or W_{el} or m_{hs}	Types of cycles	Considered fluids	Machine efficiency	Fixed variables	Optimization variables	Optimization function	Component sizing	Optimal cycles
Invernizzi and Bombarda (1997)	Geothermal brine at 100–300°C	—	Sub-SA rec/no-rec	R11, R114, R245ca, R245fa, R236fa, R134a, HFE-245fa, <i>n</i> -butane, <i>n</i> -pentane, <i>n</i> -perfluoropentane	$\eta_{is,turb} = 75\%$ $\eta_{wf,pump} = 50\%$	$\Delta T_{pp,PrHE} = 20^\circ\text{C}$ $\Delta T_{sh} = 10^\circ\text{C}$ $\Delta T_{pp,rec} = 20^\circ\text{C}$ $T_{cond} = 40^\circ\text{C}$ $\Delta p_i = 0$	p_{eva}	Plant exergy efficiency	—	—
Invernizzi et al. (2007)	WHR: MGT flue gas at 250–350°C	—	Sub-SA rec	HFC-43-10mee, HCFC-123, <i>n</i> -pentane, CFC-113, 2,2-dimethylbutane, 2,3-dimethylbutane, <i>n</i> -hexane, hexafluorobenzene, MM, pentafluorobenzene, <i>n</i> -heptane, <i>c</i> -hexane, MDM, <i>n</i> -octane, D4, MD2M	$\eta_{is,turb} = 75\%$ $\eta_{wf,pump} = 60\%$	$\Delta T_{mL} = 30^\circ\text{C}$ $\Delta T_{pp,rec} = 20^\circ\text{C}$ $T_{cond} = 30^\circ\text{C}$ $\Delta p_i = 0$	T_{eva}	Net power	Considerations on turbine design for power outputs 25–100 kW _{el}	—
Tchanche et al. (2009)	Solar: water at 75–115°C as HTF	2 kW _{el}	Sub-SA no-rec	RC318, R114, R113, R12, R123, R134a, R141b, R152a, R32, R407C, R500, ethanol, methanol, propane, isobutane, <i>n</i> -butane, <i>n</i> -pentane, cyclohexane, NH ₃ , water	$\eta_{is,turb} = 70\%$ $\eta_{wf,pump} = 80\%$ $\eta_{mec-el} = 63\%$	$\Delta T_{ap,PrHE} = 15^\circ\text{C}$ $\Delta T_{pp,PrHE} = 6^\circ\text{C}$ $T_{cond} = 35^\circ\text{C}$ $\Delta p_i = 0$	—	—	Considerations on turbine outlet volume flow rate, volume flow ratio, and cycle pressures	$T_{HTF} = 90^\circ\text{C}$ and $T_{eva} = 75^\circ\text{C}$: <i>n</i> -butane ^c : $\eta_{cycle} = 4.24\%$ $\eta_{II} = 24.8\%$
Dai et al. (2009)	WHR: gas at 145°C	1100–1400 kW _{th} (15.95 kg/s)	Sub-SA rec/no-rec	NH ₃ , butane, isobutane, R11, R123, R141B, R236EA, R245CA, R113, water	$\eta_{is,turb} = 85\%$ $\eta_{wf,pump} = 60\%$	$\Delta T_{pp,PrHE} = 8^\circ\text{C}$ $\Delta T_{pp,rec} = 5^\circ\text{C}$ $T_{cond} = 25^\circ\text{C}$ $\Delta p_i = 0$	p_{eva} $T_{in,turb}$	Plant exergy efficiency	—	R236ea: $T_{eva} = 87.7^\circ\text{C}$ $\eta_{cycle} = 11.53\%$ $\eta_{plant} = 7.88\%^a$ $\eta_{II} = 35.43\%$ Isobutane: $T_{eva} = 87.1^\circ\text{C}$ $\eta_{cycle} = 11.52\%$ $\eta_{plant} = 7.79\%^a$ $\eta_{II} = 35.05\%$

Lakew and Bolland (2010)	WHR: air at 80–200°C	6–18 MW _{th} (100 kg/s)	Sub-SA no-rec	R134a, R123, R245fa, R227ea, <i>n</i> -pentane, propane	$\eta_{is,turb} = 80\%$ $\eta_{wf,pump} = 80\%$ $\eta_{mec-el} = 90\%$	$\Delta T_{pp,PrHE} = 10^\circ\text{C}$ $\Delta T_{pp,cond} = 5^\circ\text{C}$ $T_{cond} = 20^\circ\text{C}$ $\Delta p_i = 0$	p_{eva}	Net power	Turbine (SP, single stage turbine), total HE area	$T_{ha} = 80\text{--}160^\circ\text{C}$: R227ea $T_{ha} \approx 200^\circ\text{C}$: R245fa
Schuster et al. (2010)	Generic source at 210°C	—	Sub-SA/sup rec/no-rec	Water, R134a, R227ea, R152a, RC318, R236fa, R245fa, isobutene, isopentane, isohexane, cyclohexane, R365mfc	$\eta_{is,turb} = 80\%$ $\eta_{wf,pump} = 85\%$	$p_{max} = 1.03 \times p_{crit}$ (sup cases) $\Delta T_{pp,PrHE} = 10^\circ\text{C}$ $\Delta T_{SH} = 2^\circ\text{C}$ $\Delta T_{pp,rec} = 10^\circ\text{C}$ $T_{cond} = 20^\circ\text{C}$ $\Delta p_i = 0$	Sub: T_{eva} Sup: $T_{in,turb}$	Net plant efficiency	Heat exchangers area	Sup: R365mfc and isopentane: $T_{max} \approx 180^\circ\text{C}$ $\eta_{plant} \approx 14\%$ Sub: R245fa and isobutene: $T_{eva} \approx 140^\circ\text{C}$ $\eta_{plant} \approx 13.2\%$
Quoilin et al. (2011a,b)	Solar: with HTF at $\sim 150^\circ\text{C}$	$\sim 60 \text{ kW}_{th}$	Sub-SA rec	<i>n</i> -Pentane, SES36, R245fa, R134a	$\eta_{scroll-exp}^c$: calc $\eta_{wf,pump} = 70\%$ $\eta_{HTF,pump} = 70\%$	$\Delta T_{SH} = 10^\circ\text{C}$ $\Delta T_{pp,PrHE} = 8^\circ\text{C}$ $\Delta T_{pp,rec} = 8^\circ\text{C}$ $\Delta T_{pp,cond} = 8^\circ\text{C}$ $\Delta T_{sc,cond} = 5^\circ\text{C}$ $\Delta p_{HEs} = 7.5 \text{ kPa}$	T_{eva} ΔT_{HTF}	Net plant efficiency	Scroll expander (given geometry), plate PrHE area, recuperator area, condenser area	SES36: $T_{eva} = 169^\circ\text{C}$ $\eta_{cycle} = 13.1\%$ $\eta_{plant} = 7.9\%$ <i>n</i> -pentane: $T_{eva} = 189^\circ\text{C}$ $\eta_{cycle} = 11.9\%$ $\eta_{plant} = 7.0\%^b$
Zhang and Jiang (2012)	Geothermal brine at 100–200°C	$\sim 310 \text{ kW}_{th}$ 730 kW_{th} (1 kg/s)	Sub-SA/sup no-rec	R134a, R245fa, isobutene, isopentane	$\eta_{is,turb} = 85\%$ $\eta_{wf,pump} = 85\%$	$\Delta T_{pp,PrHE} = 4^\circ\text{C}$ $\Delta T_{cond} = 35^\circ\text{C}$ $T_{ca} = 26^\circ\text{C}$ $\Delta p_i = 0$	T_{eva}	Plant exergy efficiency	—	$T_{geo} = 100^\circ\text{C}$: R134a ($T_{eva} = 68^\circ\text{C}$) $T_{geo} = 150^\circ\text{C}$: R134a (sup) $T_{geo} = 200^\circ\text{C}$: R245fa (sup)

Continued

Table 7.1 Continued

References	Heat source	\dot{Q}_{in} or \dot{W}_{el} or \dot{m}_{hs}	Types of cycles	Considered fluids	Machine efficiency	Fixed variables	Optimization variables	Optimization function	Component sizing	Optimal cycles
Walraven et al. (2012)	Geothermal brine at 100–150°C	$\sim 310 \text{ kW}_{th}$ 460 kW_{th} (1 kg/s)	Sub/sup Rec/no-rec bleed/ no-bleed 1-Pr. Lev. versus multi-Pr. Lev.	R12, R22, R41, R32, R115, R124, R125, R134a, R142b, R152a, R218, R227ea, R236ea, R236fa, R245fa, R1234yf, R1234ze, RC318, C4F10, C5F12, CF3I, SF6, ethane, propane, isobutane, propylene, DME, CO ₂ , N ₂ O, others	$\eta_{is,turb} = 85\%$ $\eta_{wf,pump} = 80\%$	$\Delta T_{pp,PrHE} = 5^\circ\text{C}$ $\Delta T_{cond} = 25^\circ\text{C}$ $\Delta p_i = 0$	$T_{in,turb}$ p_{max}	Plant exergy efficiency	—	$T_{geo} = 125^\circ\text{C}$, no $T_{lim,geo}$: R227eaSup, no-rec $\eta_{II} \sim 55\%$ $T_{geo} = 125^\circ\text{C}$, $T_{lim,geo} = 75^\circ\text{C}$: R1234yfSup, rec $\eta_{II} \sim 41\%$
Astolfi et al. (2014a,b)	Geothermal brine at 120–180°C Reinjection temperature 70–15°C	$\dot{m}_{geo} = 100 \text{ kg/s}$	Sub-SA/SH, sup rec/ no-rec	54 organic fluids	$\eta_{is,turb} = 85\%$ $\eta_{wf,pump} = 70\%$	$\Delta T_{pp,PrHE} = 3^\circ\text{C}$ $\Delta T_{pp,rec} = 5^\circ\text{C}$ $\Delta T_{pp,cond} = 0.5^\circ\text{C}$ Pressure drops of heat exchangers	$T_{in,turb}$ p_{max}	Specific net power, plant efficiency	PrHE area, recuperator area, condenser area	$T_{geo} = 120^\circ\text{C}$, C4F10 Sub, SA, rec $\eta_{plant} \sim 9.62\%$ $T_{geo} = 150^\circ\text{C}$, RC318 Sup, rec $\eta_{plant} \sim 12.79\%$ $T_{geo} = 180^\circ\text{C}$, R1234yf Sup, rec $\eta_{plant} \sim 15.28\%$
Martelli et al. (2015)	Biomass-fired boiler with oil loop	$\sim 8 \text{ MW}_{th}$ oil at 300°C	Sub-SA/SH rec/no-rec	Toluene, MDM	Turbine design model (stage-by-stage) and optimization $\eta_{is,turb} = 82\text{--}87\%$ $\eta_{wf,pump} = 80\%$	Pressure drops of heat exchangers	p_{eva} ΔT_{SH} $\Delta T_{pp,PrHE}$ $\Delta T_{pp,REG}$ p_{COND} $\omega_{turbine}$ B_{stages}	Net plant efficiency	Heat exchangers and turbine	Toluene Sub-SH, rec $\eta_{plant} = 21.9\%$ MDMSub-SH, rec $\eta_{plant} = 21.3\%$

HE, heat exchanger; HTF, heat-transfer fluid; PrHE, primary heat exchanger; WHR, waste heat recovery.

(a) Heat available from WHR and geothermal brine calculated by considered cooling of the heat source to ambient temperature. (b) Includes solar collector thermal efficiency. (c) Optimal fluid considering constraints on component design.

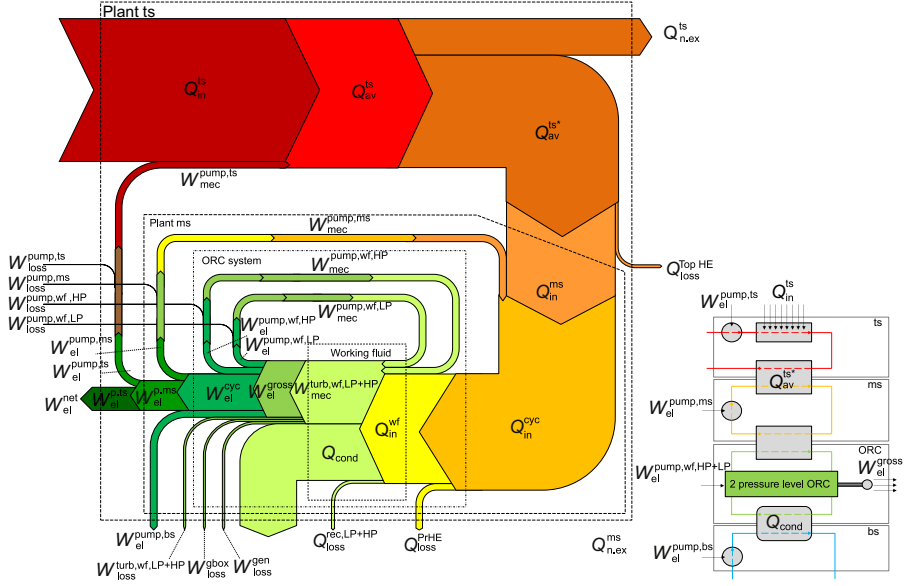


Figure 7.4 Sankey diagram for the energy balance of a two-pressure-level organic Rankine cycle (ORC) exploiting a hot source through a heat-transfer fluid loop. *ts*, top stream (hot source); *ms*, medium stream (HTF loop), *bs*, bottom stream (cooling medium).

- *Plant efficiency*: This is equal to the ratio between the net power output and the maximum available thermal power:⁵

$$\eta_{\text{plant}} = \frac{W_{\text{el}}^{\text{net}}}{Q_{\text{in}}^{\text{ts}}} \quad (7.2)$$

- *Second law efficiency*: This is calculated by dividing the net power output by the exergy of the heat source or the maximum power output attainable with a reversible cycle:

$$\eta_{\text{II}} = \frac{W_{\text{el}}^{\text{net}}}{W_{\text{rev}}} \quad (7.3)$$

where W_{rev} can be calculated as the exergy variation in the heat source when it is totally exploited. In the case of a constant heat capacity stream and negligible pressure drops, the reversible power can be obtained with the Lorenz efficiency:

$$W_{\text{rev}} = Q_{\text{in}}^{\text{ts}} \left(1 - \frac{T_{\text{amb}}}{T_{\text{mIn,ts}} \left| \begin{array}{c} T_{\text{in,ts}} \\ T_{\text{out,lim,ts}} \end{array} \right|} \right) \quad (7.4)$$

⁵ Please consider that using the cycle thermodynamic efficiency (i.e., the net power output $W_{\text{el}}^{\text{net}}$ divided by the heat input to the cycle $Q_{\text{in}}^{\text{wf}}$) may lead to relevant errors. Using this figure as the objective function may result in a poor exploitation of the heat source and a low power production.

Specific power: This is calculated as the ratio between the net power production and the mass flow rate of the heat source, which is proportional to the maximum available thermal power or the heat source exergy variation. This figure can be used only if the heat source is characterized by a fixed mass flow rate (e.g., geothermal brines, WHR) instead of a fixed heat input (e.g., biomass, CSP):

$$W_s = \frac{W_{el}^{net}}{m_{ts}} \quad (7.5)$$

7.2.1.2 Need for component efficiency correlations

It is important to emphasize that the thermodynamic optimization may lead to unfeasible results if technological constraints and curves of efficiency are not used during the plant design. An explicative example is a comparison between two subcritical saturated Rankine cycles working with two complex fluids that differ in critical temperature. Consider performing a thermodynamic optimization, assuming the same isentropic expansion efficiency and varying only the evaporation temperature: for a given heat source the optimal cycles are very similar, they have almost the same optimal evaporation temperature and they reach almost the same efficiency. However, the high-critical-temperature fluid shows a larger volume ratio across the expansion and extreme volume flow rate at the discharge section with a possible penalty on the expander efficiency.⁶ In this case, the assumption of a fixed expander efficiency leads to an unfair comparison because the power produced by the cycle working with the high-temperature fluid is overestimated. In the worst case the expansion obtained has a volume ratio so high that it cannot be handled with decent efficiency with a conventional expander (an axial/radial outflow turbine with a reasonable number of stages, a single-stage radial inflow turbine, or a volumetric expander) causing an excessive increase in capital cost. To handle this problem a set of additional constraints should be used to bind the maximum volume ratio and/or the maximum volume flow rate. In addition, it is strongly suggested to use efficiency curves for the machines with the aim of considering the detrimental effects of large volume ratios and/or small dimensions on the component performance. Maps of efficiency in this fashion are difficult to obtain and are usually derived from numerical simulation and real data operation. A correlation derived from a long experience in ORC turbine design is reported in Chapter 9 for axial turbines, whereas a first attempt for a screw expander is reported in Astolfi (2014).

The same considerations can be made for other components, such as the pumps whose efficiency should be defined as a function of the volume flow rate, whereas the fans of an air-cooled condenser (ACC) are usually off-the-shelf components and their nominal efficiency can be derived from the manufacturer's datasheet.

⁶ When adopting fluids with large volumetric expansion ratios, if a single shaft is considered for all stages (thus same rotational speed), an efficiency penalty occurs even if a large number of stages is adopted due to the impossibility of selecting the optimal rotational speed for each stage.

7.2.1.3 Technoeconomic optimization

Technoeconomic optimizations are generally more complex than thermodynamic optimizations because they require the use of reliable cost correlations, the knowledge of heat transfer coefficients, and a realistic predesign of the expander. A list of relevant publications on this topic is reported in Table 7.2.

The objective function of a technoeconomic optimization is not univocal because it depends on the application investigated. Different objective functions can be defined depending on the type of heat source and on the assumptions at the basis of the financial evaluation of the investment. A brief summary of the possible economic objective functions is here proposed, starting from the more exhaustive to the simplest one.

- *Capital budgeting analysis or investment appraisal:* This approach is the most general, and it is based on the analysis of the investment and the calculation of the IRR (internal rate of return), which is a parameter commonly used in capital budgeting because it allows comparing plants with different investment costs, different power productions, and different variable costs. It is defined as the “rate of return” that makes the NPV (net present value)⁷ equal to zero at the end of the plant life and it is equal to the maximum acceptable rate of return. First the total cost of the plant is calculated as an overnight cost, rescaling the expenses incurred during the years of construction to the night before the first startup. This value represents the negative y intercept of the curves represented in Fig. 7.5, which shows the capital budgeting analysis applied to two different investments. Each year part of the investment is covered by the cash flow minus the O&M (operation and maintenance) costs. The cash flow can be an actual income derived by the selling of the electricity produced or the savings due to the reduction of purchased electricity. Discounted present values (DPVs) are used to take into account the effect of the time value of money on future earnings:

$$DPV = \frac{FV}{(1 + r)^t} \quad (7.6)$$

where FV is the value of a future cash flow, t is the year, and r is the discount rate.

From the analysis of the trend of the NPV during the life of the plant it is possible to evaluate the payback time of the investment and the final NPV. IRR is hence calculated varying r in order to set to zero the NPV at the end of plant life. The higher the value of IRR is, the higher the profitability of the investment is. In Fig. 7.5 the capital budgeting analysis for two plants differing in investment ($A = \$20$ million, $B = \$40$ million) and power production ($A = 18$ MW, $B = 30$ MW) is reported. Common hypotheses are the selling price of electricity ($\$0.03/\text{kWh}_{\text{el}}$) and the hours of operation ($7000 \text{ h}_{\text{eq}}/\text{year}$). The solid lines correspond to $r = 3.5\%$, and the dashed lines are obtained using the corresponding values of IRR. It is possible to note that plant B shows a higher NPV at the end of its lifetime but its IRR is notably lower than that of plant A.

⁷ The NPV, namely the value or the magnitude of an investment, is not a suitable financial indicator because it does not give any information about the risk of a certain investment. A large NPV can be obtained for investments characterized by a more expensive plant cost and a longer payback time, which might be actually less profitable than another one with a lower NPV.

Table 7.2 Relevant publications on organic Rankine cycle technoeconomic optimization

References	Heat source	\dot{Q}_{in} or \dot{W}_{el} or \dot{m}_{hs}	Types of cycles	Considered fluids	Machine efficiencies	Fixed variables	Optimization variables	Optimization function	Component sizing	Optimal cycles
Hettiarachchi et al. (2007)	Geothermal brine at 70–90°C	10 MW _{el}	Sub-SA no-rec	PF5050, R123, ammonia, <i>n</i> -pentane	$\eta_{is,turb} = 85\%$ $\eta_{wf,pump} = 75\%$ $\eta_{mec-el} = 96\%$ $\eta_{ew,pump} = 80\%$	$T_{cw} = 30^\circ\text{C}$ $\Delta p_i = \text{calc}$	T_{eva} T_{cond} u_{geo} u_{cw}	Specific heat exchange area: m ² /kW	Heat exchangers area	NH ₃ : $T_{eva} = 76.9^\circ\text{C}$ $T_{cond} = 43.0^\circ\text{C}$ $\eta_{cycle} = 8.9\%$ $\eta_{plant} = 0.8\%^a$ $\alpha = 0.34 \text{ m}^2/\text{kW}$
Quoilin et al. (2011a,b)	WHR: gas at 180°C with HTF	$\dot{m}_{gas} = 0.3 \text{ kg/s}$	Sub-SA no-rec	R245fa, R123, <i>n</i> -butane, <i>n</i> -pentane, R1234yf, Solkatherm	$\eta_{scroll-exp: calc} \eta_{wf,pump} = 60\%$ $\eta_{HTF,pump} = 60\%$ $\eta_{mec-el} = 70\%$	$\Delta T_{pp,PrHE} = 10^\circ\text{C}$ $\Delta T_{sh} = 5^\circ\text{C}$ $\Delta T_{pp,cond} = 10^\circ\text{C}$ $\Delta T_{sc,cond} = 5^\circ\text{C}$ $T_{cw} = 15^\circ\text{C}$ $\dot{m}_{cw} = 0.5 \text{ kg/s}$ $\Delta p_{eva} = 10 \text{ kPa}$ $\Delta p_{cond} = 20 \text{ kPa}$	T_{eva}	Net power	Scroll expander (given geometry), plate PrHE area, condenser area	R245fa: $T_{eva} = 113.5^\circ\text{C}$ $\eta_{cycle} = 7.78\%$ $\eta_{plant} = 5.13\%$ R123: $T_{eva} = 111.8^\circ\text{C}$ $\eta_{cycle} = 8.41\%$ $\eta_{plant} = 5.00\%$ <i>n</i> -Butane: $T_{eva} = 133.2^\circ\text{C}$ $\Delta T_{pp,PrHE} = 7.5^\circ\text{C}$ $\eta_{plant} = 4.47\%$ $CS = 2136 \text{ €/kW}$ <i>n</i> -Pentane: $T_{eva} = 139.9^\circ\text{C}$ $\Delta T_{pp,PrHE} = 4.0^\circ\text{C}$ $\eta_{plant} = 3.88\%$ $CS = 2505 \text{ €/kW}$
Shengjun et al. (2011)	Geothermal brine at 90°C	$\dot{m}_{geo} = 1 \text{ kg/s}$	Sub-SA/Sup no- rec	R123, R245ca, R245fa, <i>n</i> - butane, isobutane, R236ea, R236fa, R152a, R227ea, R134a, R143a, R218, R125, R41, R170, CO ₂	$\eta_{is,turb} = 80\%$ $\eta_{wf,pump} = 75\%$ $\eta_{mec-el} = 96\%$	$\Delta T_{pp,PrHE} = 5^\circ\text{C}$ $\Delta T_{pp,cond} = 5^\circ\text{C}$ $T_{cw} = 20^\circ\text{C}$ $\Delta p_i = 10 \text{ kPa}$	Sub: T_{eva} p_{cond} Sup: $T_{in,turb}$ p_{max} p_{cond}	Specific heat exchange area (α): m ² / kW COE (only heat exchangers cost, function of operating pressure, considered)	Heat exchangers area	R152a: $T_{eva} = 74^\circ\text{C}$ $T_{cond} = 27.9^\circ\text{C}$ $\alpha = 1.64 \text{ m}^2/\text{kW}$ R152a: $T_{eva} = 60^\circ\text{C}$ $T_{cond} = 27.9^\circ\text{C}$ COE = 53 €/MWh

Astolfi et al. (2014a,b)	Geothermal brine at 120–180°C Reinjection temperature 70–15°C	$m_{\text{geo}} =$ 100 kg/s	Sub SA/SH, sup rec/no-rec	54 organic fluids	$\eta_{\text{is,turb}} = \text{calculated}$ $\eta_{\text{wf,pump}} = 70\%$	Pressure drops of heat exchangers	$T_{\text{in,turb}}$ p_{max} T_{cond} $\Delta T_{\text{pp,PrHE}}$ $\Delta T_{\text{pp,cond}}$ $\Delta T_{\text{pp,rec}}$	Total specific plant cost	Turbine, PrHE area, recuperator area, condenser area	$T_{\text{geo}} = 120^\circ\text{C}$, R16 Sup, SH rec + GearBox $C_s = 3750 \text{ €/kW}$ $T_{\text{geo}} = 150^\circ\text{C}$, R134a Sup, rec $C_s = 2500 \text{ €/kW}$ $T_{\text{geo}} = 180^\circ\text{C}$, R152a Sup, rec $C_s = 1900 \text{ €/kW}$
Martelli et al. (2015)	Biomass-fired boiler with oil loop	$\sim 8 \text{ MW}_{\text{th}}$ oil at 300°C	Sub-SA/SH rec/ no-rec	Toluene, MDM	Turbine design model (stage- by-stage) and optimization $\eta_{\text{is,turb}} = 82\text{--}87\%$ $\eta_{\text{wf,pump}} = 80\%$	Pressure drops of heat exchangers and economic assumptions	p_{eva} ΔT_{SH} $\Delta T_{\text{pp,PrHE}}$ $\Delta T_{\text{pp,REG}}$ p_{COND} ω_{turbine} B_{stages}	Annual profit	Heat exchangers and turbine	Toluene Sub-SH, rec $\eta_{\text{plant}} = 15\text{--}21\%$ depending on electricity price MDM Sub-SH, rec $\eta_{\text{plant}} = 9\text{--}20\%$ depending on electricity price

COE, cost of electricity; *HTF*, heat-transfer fluid; *PrHE*, primary heat exchanger; *WHR*, waste heat recovery.

(a) Heat available from WHR and geothermal brine calculated by considered cooling of the heat source to ambient temperature.

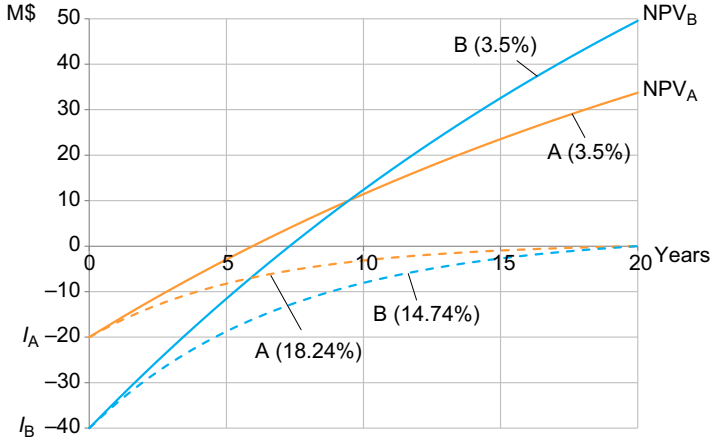


Figure 7.5 Capital budgeting analysis for two different WHR plants, internal rate of return (IRR) is reported in brackets for the dotted lines, genetic algorithms, NPV , net present value.

This approach requires the assumption of the price of electricity to compare different solutions and it is, for this reason, site dependent, and general conclusions are hard to obtain.

Furthermore the use of IRR as an index for plant profitability has some drawbacks because its maximization involves distortions in the achieved solutions. With an optimization of IRR, low PBT (payback time) investments look more profitable than other ones that can reach, at the end of the plant lifetime, an NPV notably higher. A general suggestion is to consider a maximization of NPV at the end of plant life with a constraint on the minimum PBT.

- *Levelized cost of electricity*: The levelized cost of electricity (LCOE) is expressed in US dollars for kWh_{el} produced and it represents, for a given technology, the minimum electricity price that allows the project to break even at the end of its lifetime. It is an economical index that accounts for all the plant life expenses related to the construction, the operation, and the maintenance. It is calculated by Eq. (7.7) and it does not require the definition of the price of electricity:

$$\text{LCOE} = \frac{\sum_{t=1}^n \frac{I_t^f + O \& M_t^f + FC_t^v + O \& M_t^v - M_t^f}{(1+r)^t}}{\sum_{t=1}^n \frac{E_t}{(1+r)^t}} \quad (7.7)$$

where the terms with superscript f are related to yearly fixed expenses and superscript v denotes variable expenses calculated by multiplying the energy production for the specific variable cost:

- I_t^f is the fixed investment cost for the year t of operation.
- $O \& M_t^f$ is the fixed O&M cost.
- $FC_t^v = \text{fc}^v E_t$ is the fuel consumption cost for the production of an amount E_t of energy; fc^v is the specific cost in $\text{US}\$/\text{kW}_{\text{el}}$.

- $O\&M_t^v = o\&m^v E_t$ is the O&M cost for the production of an amount E_t of energy; $o\&m^v$ is the corresponding specific cost in US\$/kW_{el}.
- $MI_t^v = mi^v E_t$ is the monetary incentive for the production of an amount E_t of energy; mi^v is the specific incentive in US\$/kW_{el}.

Another way to evaluate the LCOE consists in normalizing the whole life of a power plant to an equivalent year of operation with the possibility of comparing technologies that differ from one another in terms of capital cost and power output (NETL, 2011). This approach requires the evaluation of two terms: the first is a fixed cost related to the investment cost and the fixed yearly O&M costs and the second is related to the variable cost of energy production accounting for fuel consumption, the variable O&M costs, and the monetary incentives for renewable technologies. The fraction of capital cost at the first year is calculated by Eq. (7.8):

$$I^f = I_{TOT} CCF \quad (7.8)$$

where CCF is the first-year capital charge factor, which usually ranges between 10% and 15% depending on the financial risk assumptions and the lifetime of the plant. This quantity is also called the levelized capital charge rate.

The LCOE is hence calculated as the specific cost of the energy produced and it represents the slope of the straight line connecting the origin of axes with the final point of total expense of a plant for 1 year of operation as shown in Fig. 7.6:

$$LCOE = \frac{C^f + C^v}{E} = \frac{C^f + c^v E}{E} = \frac{[I_{TOT} CCF + O\&M^f] + [(fc^v + o\&m^v - mi)E]}{E} \quad (7.9)$$

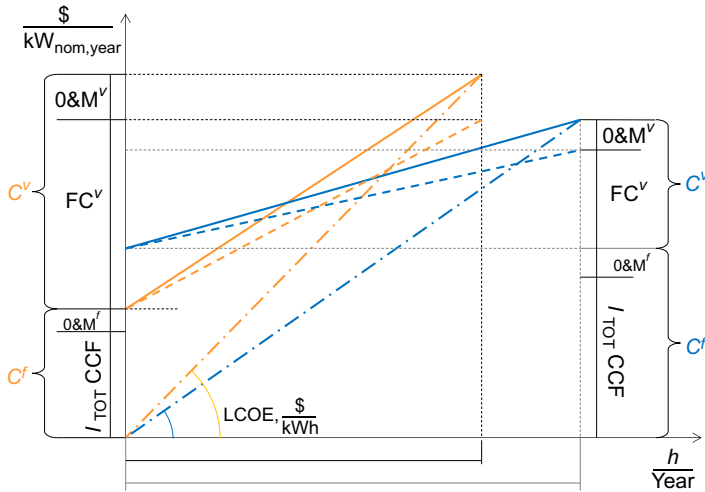


Figure 7.6 Levelized cost of electricity (LCOE) graphical representation for two power plants. CCF, capital charge factor; O&M, operation and maintenance; FC, fuel consumption cost.

Different plants can be compared in terms of LCOE without any assumption on price of electricity and plants with a lower LCOE are intrinsically more competitive on the market than the others.

- *Specific cost of the plant:* This is the most intuitive index and it is calculated simply by dividing the total cost of the plant (cost of the power block plus the cost of the heat source) by the net power of the system. It is proportional to the LCOE if the variable costs related to fuel consumption are not considered, such as in solar and geothermal energy, and O&M costs are neglected.

7.2.1.4 Need for reliable cost correlations

Information about the equipment cost, the BOP, and the fixed investment cost related to the exploitation of a certain heat source should be known with a good accuracy to obtain reliable final results in technoeconomic optimization. Rough errors in the calibration of the cost correlation may lead to results far from the optimal in terms of both final LCOE and cycle design. In addition, if technological constraints are not considered, optimal solutions might entail configurations that are almost infeasible from a technical point of view. For instance, if the air condenser cost function largely underestimates the component cost, the optimization routine will push both approach-point and pinch-point temperature differences to their lower bounds, achieving a higher power production but entailing an extremely wide heat exchanger surface. Another example is related to turbine cost correlation when high critical temperature fluids are used: low condensing temperatures lead to very low condensing pressures and an exponential increase in both the volume flow rate and the mean diameter at the turbine last stage. Furthermore, the isentropic volume ratio is increased, requiring a higher number of stages and a more expensive component. If the turbine cost correlation does not take into account the number of stages and their dimension, the optimization algorithm will push the condensation temperature to very low values to exploit a higher enthalpy drop and increase the power production, but will lead to an extremely expensive design for the turbine.

Equipment cost

Despite the importance of obtaining reliable cost correlations, this topic is not widely discussed in scientific literature, and general, capital cost functions are difficult to find. Furthermore, available data usually refer to a very specific field or to a small range of temperatures and pressures. Engineering companies and component manufacturers are the only ones who can provide affordable data but the economic information is generally kept strictly reserved and data are rarely conveyed.

Three main references are usually adopted to obtain cost correlations; they propose different approaches and some more details about them are further reported to give to the reader a general overview:

- *Perry's Chemical Engineers' Handbook* (Green, 1997) is a widely used handbook about chemical engineering processes and it contains a chapter about equipment cost correlations. Various approaches are proposed by this text and we refer to the exponential method, which

is commonly used in engineering for fast cost estimations. The cost of a component is calculated starting from the cost of a similar component, knowing its size or its capacity. A power factor is used to account for scale economies attainable with larger equipment, which generally shows a lower specific cost. The reference formula is reported in Eq. 7.10:

$$C = C_0 \left(\frac{q}{q_0} \right)^n \quad (7.10)$$

where C_0 and q_0 are respectively the capital cost and the capacity of the reference component and q is the capacity of the component whose cost is unknown. Exponent n introduces a deviation from the linear trend considering size effect on the equipment cost and for this reason it is generally lower than unity. For instance, typical values for motors or generators are around 0.6–0.7, whereas for air-cooled condensers they are close to unity because of the modularity of this component. An intrinsic drawback of this approach is related to the definition of just one reference point and one exponent. Therefore, errors in their estimation introduce high deviation of the calculated cost especially for a component size far from the reference.

- *Analysis, Synthesis, and Design of Chemical Processes* (Turton et al., 2012) is another common textbook for the design of chemical and synthesis processes. It presents a detailed methodology for the calculation of equipment cost for many components of interest in the ORC field. The approach followed is more accurate compared to Perry's and results do not present drifts for values far from the reference. In Turton, the base cost functions are obtained by using the capital equipment-costing program CAPCOST (CAPCOST), which is based on the module factor approach originally introduced by Guthrie (Guthrie, 1969, 1974) and later modified by Ulrich (Ulrich, 1984). The final cost is split into three contributors: a base cost related to the component's most important quantity (surface for heat exchangers, volume flow rate for pumps, etc.), an incremental factor due to pressure, and a last factor if a material different from carbon steel is used. Data are regressed and cost correlations are presented in the logarithmic form reported in Eq. (7.11):

$$\log_{10}(C_p^0) = K_1 + K_2 \log_{10}(A) + K_3 [\log_{10}(A)]^2 \quad (7.11)$$

where C_p^0 is the base equipment cost for a component operating at ambient pressure and made of carbon steel and A is the capacity or the size of the component. Lower and upper bounds for each correlation are declared.

The effects of pressure and labor are taken into account by multiplying the base cost for a certain bare module factor F_{BM} calculated with Eq. 7.12:

$$F_{BM} = B_1 + B_2 F_M F_P \quad (7.12)$$

where F_M and F_P are the material and the pressure factor, respectively.

Different material factors are listed for each component depending on the material used for the construction. Data proposed by Turton are calculated as the average of values from reference (Guthrie, 1969; Ulrich, 1984). Pressure factor instead is calculated with the formula reported in Eq. 7.13:

$$\log_{10}(F_P) = Y_1 + Y_2 \log_{10}(P) + Y_3 [\log_{10}(P)]^2 \quad (7.13)$$

where P is the pressure in bar gauge inside the tube or inside the shell, depending on the side where the high-pressure fluid is placed. Pressure factors are always greater than unity and extrapolation outside of the validity range should be done with caution. Correction is applied only for fluid pressure of 5 bars greater than the ambient.

Finally the cost of a general component results from Eq. (7.14):

$$C_{BM} = F_{BM} C_p^0 \quad (7.14)$$

- The NETL (National Energy Technology Laboratory) report (Loth et al., 2002) is the result of a work funded by the US government and it follows an approach similar to Turton for the estimation of base equipment cost. Data are provided as curves of capital cost against size for various components. The claimed accuracy in the report is $+50\%/-30\%$ and it is recommended for order of magnitude cost estimations. In the NETL report, ICARUS Process Evaluator software is also used and some results for shell-and-tube (S&T) heat exchangers are reported.

Bulk material and installation labor costs are estimated with a series of multiplicative factors to take into account foundations, insulation, instrumentation, and other expenses. Depending on the type of streams handled, different values are proposed, varying the temperature and the pressure. The final cost of a general component is calculated by Eq. (7.15):

$$C_{BM} = C_p^0 (1 + F_{DL}) \sum_{i=1}^n (1 + a_i (1 + b_i)) \quad (7.15)$$

where C_p^0 is obtained graphically from the charts in the report, F_{DL} is the distributive labor factor equal to 0.2 for heat exchangers and other ORC components, and a_i and b_i are the distributive factors for bulk material and labor for the different n terms previously mentioned. Finally, multiplicative factors for converting carbon steel to other alloys cost are considered.

The previous references are adequate for the estimation of the cost of common components like S&T heat exchangers, plate fin or brazed plate heat exchangers, pumps, and generators. Unfortunately a very small bibliography is available about expanders and there is no availability of cost correlation that enjoys widespread support. Some information can be obtained from steam turbine drivers, whose cost is usually a function of power output; however, the mere use of these correlations in the ORC field may result in large errors. Let us consider two saturated cycles working with two fluids having different critical temperatures: for the same evaporation and condensation temperature they would produce approximately the same power but the high critical temperature fluid has a turbine with a larger frontal dimension and more stages (both the volume flow rate and the volume ratio are higher) with obviously a higher cost. A general cost correlation for ORC turbines should take into account a fixed cost that depends on the engineering design cost plus a cost that depends on the estimated number of stages N_{st} and their dimension (the diameter D or the SP of the last stage can be used as representative of the frontal dimension of the turbine) as reported in Eq. (7.16):

$$C_{turb} = K_1 W^{\alpha_1} + K_2 SP^{\alpha_2} N_{st}^{\alpha_3} \quad (7.16)$$

where the coefficients K and the exponents α should be calibrated on real data. A similar cost correlation for medium-size axial turbines (range 500–2000 kW) has been proposed by Martelli and Capra (2015).

Other capital costs

In most applications the sum of the equipment costs (plus the BOP) is a small share of the overall plant cost because relevant expenses are needed to actually exploit the heat sources, in other cases instead the heat source cost is almost nil and the hot stream is directly available. For example, the exploitation of solar energy needs the installation of solar collectors and thermal storage, geothermal energy requires expensive explorative campaigns and drilling activities, and biomass combustion needs a wood storage, a biomass boiler, and a gas treatment unit. On the other hand, exploitation of industrial WHR is generally inexpensive and the cost of additional components is almost negligible with respect to the ORC power block. The ratio between the “cost of the heat source” and the cost of the power block plays a relevant role in the system optimization: if the heat source is very expensive the optimal technoeconomic solution is pushed toward the maximum efficiency because of the need to pay back a high investment; in contrast, for cheap energy sources it is probable that the cycle efficiency is penalized in favor of a lower equipment cost.

7.2.1.5 Other objective functions

In some cases the aforementioned objective functions are not suitable to realistically describe the operation of the ORC mainly because the average operating conditions are different from the nominal ones (off-design and dynamic simulations can add a great value to the analysis) or because of the need to concurrently consider different quantities in the optimization, like the plant weight or volume.

Off-design and dynamic behavior

In some applications, like geothermal energy, WHR from continuous industrial processes, or a CSP plant with a large solar multiple and a large storage, the ORC works very close to the nominal conditions. Off-design operations are limited to daily startup and shutdown and generally a deep analysis of the off-design performances is not required, especially if water is used as the cooling medium. In contrast, if an ACC is used, the condensation pressure and thus the power output may vary noticeably between day and night in a location with a large atmospheric temperature range and through the year depending on the season. If the variation in temperature is not dramatic it is common to use an average value and account for off-design penalization by reducing the number of equivalent working hours. For other applications, like the exploitation of solar energy in plants without storage and cogenerative power plants controlled by the thermal user's needs, the evaluation of the off-design/part-load performance is a topic of crucial importance.

In these cases it is opportune to introduce into the objective function information about the actual operation of the plant throughout a representative time span. This analysis can be carried out with a steady-state off-design calculation or by introducing dynamic analysis of the whole system. The governing equations for heat exchangers and pumps are usually well known, whereas the main uncertainty is related to the definition of off-design curve for the turbine performance because this information is owned by manufacturers and data are rarely conveyed. In the case of systems having very fast variations in the operating conditions, like automotive ORC for heat recovery from flue gases and cogenerative ORC for domestic applications, dynamic simulations can add further details accounting for the effects of transient behavior on the overall performances. Modelica software ([Modelica](#)) in the Dymola environment ([Dymola](#)) is the most used tool for the dynamic simulation of power systems thanks to the work of Casella ([Thermo Power](#)), and it provides a detailed component library, including heat exchangers and turbines, suitable for ORC power systems. More details about dynamic simulation are reported in Chapter 6.

Using information about the off-design and the dynamic behavior of the system during its optimization allows one to reach a more robust result, selecting those fluids and those plant configurations that are more suitable for the exploitation of a given energy source throughout the whole lifetime and operating conditions. An example of combined optimization of design and part-load behavior is reported at the end of this chapter.

Other parameters of interest: weight, volume, and environmental impact

From a general point of view, the optimization of an ORC system may aim at the minimization of different quantities that usually push the solution in different directions. An example is the design of an ORC for automotive or naval application ([Pierobon et al., 2013](#)): in this case it is certainly of primary importance to have a high efficiency or a low LCOE but on the other hand it is also crucial to limit the system volume and weight because the space is scarce. The two goals would drive the solution to different designs: the maximization of efficiency requires large heat exchanger surfaces, multi-stage turbines, and bulky components; on the opposite side, minimizing the volume of the system leads to higher efficiency losses because of the high temperature differences in the heat-transfer process. The objective function should consider all these terms with different weights and the result of the optimization process is not a single solution but a locus of minimum, called a Pareto front. Solutions for the Pareto front have roughly the same value for the overall objective function but a different breakdown of the different terms. Among these solutions further selection can be done considering additional limits that allow excluding some results and identifying a small number of promising configurations ([Wang et al., 2013](#); [Gerber and Marechal, 2012](#)).

7.2.2 Optimizing variable definitions and cycle design model

Independent of the selection of the working fluid and plant layout, it is necessary to define the set of independent decision variables to be varied by the optimization

algorithm. From a general point of view, each single parameter of the cycle components could be optimized, including geometrical details typically considered in the engineering design study (eg, diameter and length of heat exchanger tubes, fin height and density, fluid velocities, etc.). However, this approach is not recommended for the following reasons:

- The larger the number of optimization variables is, the more challenging the optimization problem is in terms of required computational time, with the risk of finding just a local minimum/maximum.
- To properly assess the effects of the optimization variables on the performance and costs of the cycle, accurate models of the equipment units are necessary. The optimization variables must be selected in agreement with the level of detail of the adopted performance and cost models and the relevance to the objective function.

One explicative example is the choice of pressure drops in each component of the cycle and in the piping. Most of the studies consider fixed pressure drops assuming typical values according to the type of component (heat exchanger, valve, pipe, etc.) and the type of fluids flowing in it. Other publications, instead, perform the design of heat exchangers to better estimate the pressure drops across the main heat exchanger, the regenerator, and the condenser ([Pierobon et al., 2013](#)). Pseudo-one-dimensional models like the Bell–Delaware method ([Kuppan, 2000](#); [Shah and Sekulic, 1998](#)) for S&T heat exchangers can be used, and variables like velocity of the streams, baffle and tube spacing, tube diameter, and baffle cut are optimized, allowing for the calculation of the actual pressure drops and the heat transfer coefficients and eventually a more reliable estimation of the heat exchanger surface and cost. Although this approach is really promising, because in theory it allows one to achieve the best trade-off between heat transfer coefficient and pressure drops of the heat exchangers, it is highly risky because of the size and the complexity of the numerical problem. The development of an ad hoc optimization algorithm is hence required, such as that developed in [Capra and Martelli \(2015\)](#) for the simultaneous optimization of the cycle and turbine design. In addition, if the focus of the work is the thermodynamic cycle itself and not the design of the heat exchangers, it is sufficient to assume typical values of pressure drops and heat transfer coefficients. Similarly, if the main goal is to find the optimal thermodynamic cycle (pressures and temperatures), typically pressure drops, evaporator subcooling temperature difference, thermal loss of heat exchangers, mechanical efficiency of rotating machines, and electric efficiency of generators/drivers are fixed by the designer on the basis of the best design practice.

The variables that are typically optimized when optimizing the efficiency of the cycle (thermodynamic optimization) are the evaporation and the condensation temperatures, the superheating degree, and the degree of regeneration. Technoeconomic optimization instead entails a larger problem because of the need to optimize the pinch-point temperature differences of the heat exchangers. [Fig. 7.7](#) depicts the quantities that should be defined for the complete definition of a single-level supercritical ORC and [Table 7.3](#) reports a list of assumptions that can be used for fixed design parameters in ORC optimization.

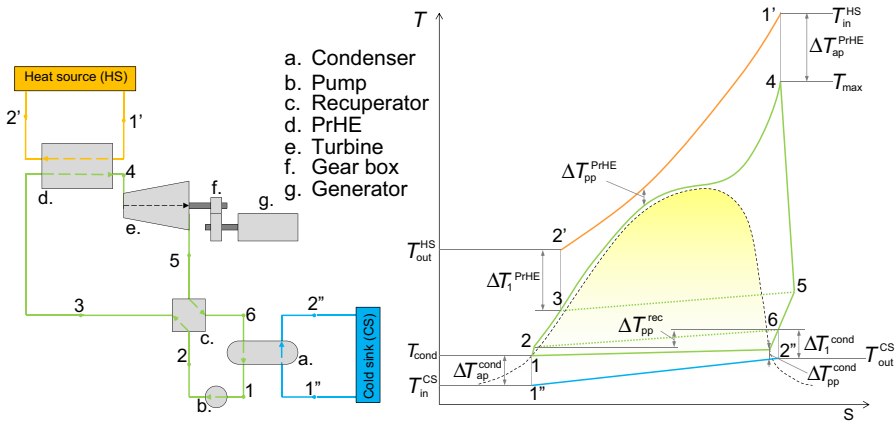


Figure 7.7 Supercritical plant layout and T-s diagram with the definition of the quantities usually required for the definition of the thermodynamic cycle. *PrHE*, plate heat exchanger.

The variables that can be generally optimized for an ORC are listed in the following, with a short description on the effects they have on the cycle assessment depending on the cycle layout and the working fluid properties.

- Condensation temperature or condensation pressure:** This parameter defines the temperature and pressure at the condenser inlet. Reducing this parameter leads to an increase in the gross power output thanks to a larger turbine pressure and enthalpy drops with benefits on the cycle efficiency. On the other hand, it entails an increase in the condenser auxiliary consumption that can be a relevant share of the gross power for air-cooled plants exploiting a low-temperature heat source. From a pure thermodynamic point of view, if water is used as the cooling medium, the condensation temperature can be fixed to an opportune value according to the ambient temperature, the condenser configuration, the limit temperature increment, or the need to avoid high vacuum in the condenser and the consequent limitation of noncondensable gas leakage. In contrast, if an ACC is used, the condensation temperature should be optimized considering that the lower its value is, the higher the airflow rate and the fan consumption are. In a technoeconomic optimization, instead, the variation in the condensation temperature entails two contrasting effects on the LCOE, and the optimal value for this variable is the result of a trade-off between an increase in power production and a greater equipment cost caused by larger heat transfer surfaces and bigger fans. In addition, reducing the condensing pressure leads to higher working fluid volume flow rates and higher volume ratios across the expansion with a turbine having a bigger size and a larger number of stages.
- Cycle maximum pressure:** The maximum pressure of the cycle can be defined from the evaporation temperature for subcritical cycles⁸ and the turbine inlet pressure for the supercritical cycles. This parameter strongly affects the cycle thermodynamic efficiency, the working fluid mass flow rate, the PrHE heat transfer area, and the turbine efficiency and design.

⁸ The common choice is to use the evaporation temperature directly as optimization variable for subcritical cycles because of the more marked effect on cycle performance.

Table 7.3 Main fixed assumptions related to pressure drops, heat exchangers, heat losses, and component efficiency

<i>Temperature differences and pressure drops</i>		
ΔT_{cond}^a	0–0.3°C	Condensation
Δp_{des}	1–2%	Desuperheating
Δp_{eco}	30–60 kPa	Economizer
ΔT_{eva}^a	0–1°C	Evaporation
$\Delta p/p_{\text{sh}}$	1–2%	Superheating
$\Delta p/p_{\text{PrHE}}$	4–10%	Supercritical PrHE
$\Delta p/p_{\text{rec,HS}}$	2–4%	Recuperator hot side
$\Delta p_{\text{rec,CS}}$	30–60 kPa	Recuperator cold side
ΔT_{sc}	1.5°C	Subcooling at evaporator inlet
<i>Heat losses from heat exchangers</i>		
Q_{loss}	1%	Percentage of transferred heat
<i>Component efficiency^b</i>		
$\eta_{\text{is,expander}}$	0.70–0.85 (turbines at optimal speed) 0.65–0.80 (volumetric expanders for $V_r \approx V_{r,\text{built-in}}$)	
$\eta_{\text{mec, expander}}$	0.93–0.97	
$\eta_{\text{el, gen}}$	0.94–0.98	
η_{gearbox}	0.93–0.97	
η_{pump}	0.50–0.70	
η_{fan}	0.60–0.70	
$\eta_{\text{mec,pump/fan}}$	0.94–0.98	
$\eta_{\text{el,mot}}$	0.93–0.97	

PrHE, primary heat exchanger.

^aFor once-through heat exchangers with flow in phase transition (evaporation and condensation) it is convenient to express the pressure drop as an equivalent temperature drop in analogy with the HVAC field.

^bComponent efficiencies range between a minimum and a maximum value representative of small and big machines, respectively. More details can be found in Chapters 9–12.

This parameter must always be optimized independent of the figure of merit selected as the objective function.

- *Turbine inlet temperature (superheating degree)*: This parameter sets the maximum temperature of the cycle. It affects the power production in a nonunivocal way (especially if the heat source can be cooled down to ambient temperature) and even in thermodynamic optimization it should be optimized (Astolfi et al., 2014a,b; Capra and Martelli, 2015).
- *Pinch-point temperature difference in the recuperator*: This parameter influences the recuperator effectiveness. The optimization of this parameter is important in the presence of a

limit on the heat source minimum temperature because a proper recuperator design allows the best compromise between cycle efficiency and the complete exploitation of the available energy source to be obtained.

- Outlet temperature of the hot stream:** This variable sets the temperature profile of the heat source in the PrHE. From a thermodynamic point of view, the lower the value of this variable is (compatibly with a minimum pinch-point temperature difference and the limits in the minimum heat source temperature), the higher the plant power production is, thanks to an increase in heat input, a lower mean logarithmic temperature difference in the heat-transfer process, and a lower consumption of heat source auxiliaries (e.g. circulation pump, fans, etc). In technoeconomical optimization, instead, the usual trade-off between cost and efficiency can be highlighted but different results are achieved depending on the economic value of the heat source. Fig. 7.8 shows the result of the PrHE technoeconomic optimization of an R134a supercritical ORC in the geothermal field: the graph on the left is obtained with a high cost of exploration and drilling, the graph on the right with a relatively inexpensive geothermal resource. For expensive heat sources, the technoeconomic optimization almost coincides with the thermodynamic optimization because it is crucial to have a high-power production to pay back the large investment cost. The heat source is totally exploited with small temperature differences in the heat-transfer process. A similar consideration is valid for CSP technology in which the solar collectors have a relevant share of the plant cost. On the other hand, for very inexpensive heat sources, like WHR from industrial processes, the optimal plant has generally an efficiency lower than the maximum attainable, a nontotal exploitation of the heat source, a lower power production, but also larger mean logarithmic temperature differences and a reduced cost of the PrHE with contrasting effects on LCOE. It is important to emphasize that in subcritical cycles the location of the PrHE pinch point is easy to find because it is usually either at the beginning of the evaporation process or at the cold end of the economizer, depending on the temperature of the heat source. More attention needs to be paid in the case of a supercritical cycle because the exact location of the pinch point is not known a priori: the suggested approach is to discretize the PrHE in several sections by using a fixed increment of enthalpy. It is interesting that this method is more

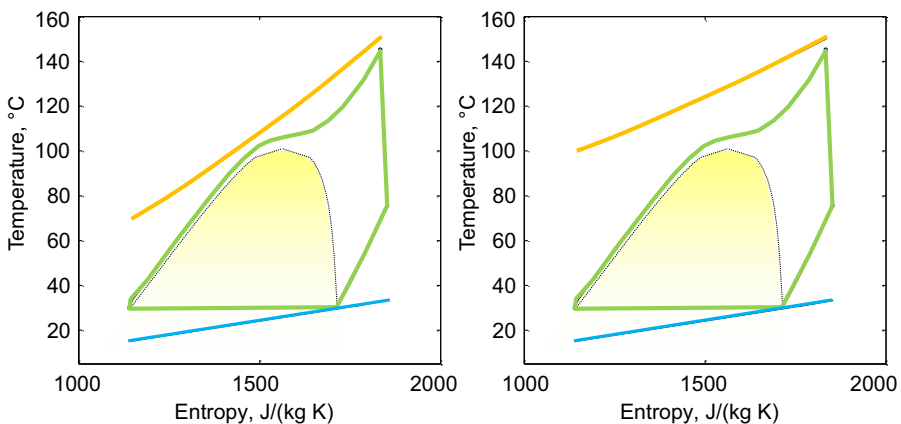


Figure 7.8 A supercritical cycle optimized (left) for an expensive geothermal source and (right) for a cheap heat source: minimization of levelized cost of electricity is obtained by a reduction in power production and cost of the primary heat exchanger.

reliable than using a fixed increment of temperature, because in a supercritical transition (even for complex fluids) a large amount of heat is introduced in proximity to the critical point, and the second approach may lead to a poor resolution and an inaccurate calculation of the required heattransfer surface.

- *Outlet temperature of the cooling medium:* This defines the minimum temperature difference between the saturated vapor in the condenser and the cooling air or the cooling water. By increasing this parameter, a lower cooling medium flow rate is needed with reduced fan/pump consumption, but the condenser has a higher heat transfer area leading to a higher equipment cost.
- *Mass flow rate ratios or pinch-point temperature difference in the PrHE for multilevel pressure cycles:* The mass flow rate of working fluid, which is generated in the PrHE, can be determined by solving the energy balance equations of the different PrHE sections. If the objective function is thermodynamic, the optimal pinch-point value is trivial and equal the lower bound value, whereas, if the objective function is economic (LCOE or NPV), the pinch-point temperature difference is worth optimizing to find the best trade-off between cost of the heat transfer area and efficiency. If the cycle features multiple pressure levels, a pinch-point temperature difference should be defined for each pressure level. Then the flow rates of each pressure level shall be determined with the heat cascade approach of pinch analysis, consisting in solving the energy balance equations of each temperature zone of the PrHE defined by the evaporation levels (Martelli et al., 2011). The optimization of the pinch-point temperature differences of the evaporation levels allows one to adjust the ratios between the mass flow rates of fluid evaporated in the different levels so as to improve the heat recovery factor and cycle efficiency. For this reason, in multiple-pressure-level cycles, pinch-point temperature differences in the evaporation levels should always be optimized or alternatively the ratio between the mass flow rates flowing in the various levels of multilevel cycles.

A summary of the suggested optimization variables usually considered for the three general cycle configurations on the basis of the objective function is reported in Table 7.4.

It is important to note that most of the optimization variables can be defined in different ways, for instance, the maximum temperature of a subcritical superheated cycle can be defined directly by its value or by defining an approach-point temperature difference with respect to the hot source inlet condition or finally by selecting a temperature increment in superheating. The same considerations can be made for the maximum and the minimum pressure of the cycle and, from a general point of view, all the definitions are perfectly equivalent. However, a smart selection of the set of independent variables allows defining the linear constraints between the parameters, helping the optimization algorithm to reach the final solution with a better precision and a reduced computational time.

7.2.3 Numerical approaches for the plant simulation

The calculation of the objective function requires the calculation of all the thermodynamic points of the cycle and the evaluations of the dimension and the cost of main components. As already mentioned it is crucial to use reliable tools for the estimation of fluid thermodynamic properties, whereas for the simulation of the system conceptually different approaches are available.

Table 7.4 Suggested optimization variables depending on the cycle configuration and the objective function

	One pressure level		Two pressure levels		Flash trilateral	
	Technothermodynamic	Technoeconomic	Technothermodynamic	Technoeconomic	Technothermodynamic	Technoeconomic
T_{cond}		X		X		X
$p_{\text{max,LP}}$	X	X	X	X	X	X
$\Delta T_{\text{sh,LP}}$	X	X	X	X		
$\Delta T_{\text{pp,rec,LP}}$		X		X		X
$p_{\text{max,HP}}$			X	X	X	X
$\Delta T_{\text{sh,HP}}$			X	X		
$\Delta T_{\text{pp,rec,HP}}$				X		
M_r			X	X		
$T_{\text{out,HS}}$		X		X		X
$\Delta T_{\text{pp,cond}}$		X		X		X
n	2	6	5	10	2	6

- The sequential modular (SM) approach is based on the solution of the problem following a block diagram or a sorted list of components. This approach is also called procedural or casual programming: each component constitutes a module that receives input data and calculates the output results that will be available to following components. If the flow diagram is straightforward the algorithm provides the results after a once-through calculation. The simulation of an ORC is instead an iterative process because of the mutual dependency among the variables of the cycle. After each iteration, the guess variables are updated to new values with a successive substitution approach, and the calculation is repeated until convergence is reached. This strategy generally suffers from long execution times and it may fail to reach the real solution for complex systems with multiple recycles of mass flow rate and energy. Aspen Plus ([AspenPlus](#)) and ThermoFlex ([Thermoflex](#)) are common examples of software based on this approach: they provide a graphical interface whereby different components can be connected to build the whole system. The main advantage of ThermoFlex is the ability to easily perform off-design simulations and the availability of economics data banks. Unfortunately, in ThermoFlex there are a small number of available working fluids; and the accuracy of EoS for organic fluids is not sufficient for the analysis of ORC technology especially in the case of supercritical cycles. The ability to link ThermoFlex with Refprop helps to cover this limitation but not all the Refprop fluids are available and the code gets really slow with a strong increase in computational time. Other than these issues, ThermoFlex allows performing simple optimizations varying a limited number of parameters. Aspen Plus is a software for the modeling of both chemical processes and power systems. The main advantage of Aspen is the ability to use a large variety of working fluids with a good accuracy. The Aspen Plus fluids data bank is definitely the most complete among commercial softwares and it allows selecting several different EoSs for the calculation of fluid thermodynamic properties. Some of them are relatively simple, like Peng–Robinson or Redlich–Kwong, whereas others ones are extremely advanced, with the possibility of describing the thermodynamic properties with a really good accuracy on experimental data. In addition Aspen Plus implements several mixing rules methodologies for the estimation of the behavior of blends formed by two or more components, ensuring the ability to perform reliable design of ORC working with mixtures. Finally it is possible to calibrate ad hoc EoSs for fluids or mixtures if experiential data are available. One of the drawbacks of this software is the difficulty in creating user-defined components. For instance, the turbine component in the basic version is described just with a fixed isentropic efficiency and it is not possible to link its performance to fluid properties and other cycle parameters. Another limit regards the off-design and the dynamic analysis, which is pretty challenging, requiring the definition of all the governing equations and the fixed parameters of the system.
- The equation oriented (EO) approach consists in writing the model of the ORC system as a system of nonlinear equations representing the constitutive relationship of each component of the cycle (i.e., the mass and energy balances, the operation mode). The set of equations is eventually handled by the simulation tool that analyzes the problem, makes symbolic simplifications, and solves them with a nonlinear solver. This approach is more general and it can address most of the limits of the SM strategy because it allows one to easily simulate the thermodynamic cycle. The main limit of this approach is the availability of a robust, fast, and reliable solution algorithm: at the first iteration most of the variables are unknown and the solution process is strongly affected by the initialization point. Engineering Equation Solver ([EES software](#)) is probably the most used software based on the EO approach: it solves systems with up to 24,000 nonlinear equations and it implements high-accuracy Refprop EoSs for more than 100 fluids of interest for the ORC field. Another big advantage of this software

is the availability of single- and multiple-variable optimizations with a remarkable reduction of problem computational time. Another example of this approach is represented by the equation-based object-oriented (EEO) method, which is based on declarative or acasual programming and all the equations are written with the aim of describing the problem rather than considering how the system will be solved. This leads to large advantages in code flexibility and readability. The Modelica ([Modelica](#)) language is the present standard of EEO modeling and it can be used by several simulation tools (e.g., Dymola and OpenModelica) that allow one to write reusable components and provide a graphical user interface for the assembly of the plant layout.

In addition to these two standard approaches, many researchers have developed customized cycle models with the aim of obtaining a faster code and to control each step of the system simulation. ORC plant layouts are less complex than big steam ranking cycles and chemical and industrial processes and the calculation of the thermodynamic points often does not require any iterative procedure and the results can directly calculated.⁹ Any programming language able to call fluid propertied routines is suitable for this purpose and in the literature many studies have been done with Matlab, Fortran, C++, and Visual Basic.

7.2.4 Optimization approaches

The final step consists in the choice of the optimization approach, which acts on the optimization variables with the aim of optimizing the objective function. Similar to process engineering, optimization approaches can be classified into three main categories ([Biegler et al., 1997](#)):

- Equation oriented approach

In the EO approach, the optimization problem and plant models are solved simultaneously because the model equations are included as constraints in the optimization problem. Thus, there is no distinction between independent decision variables and dependent variables, or between model equations and technoeconomic constraints. Typically, the resulting optimization problem is a nonlinear program (NLP) and it is tackled with gradient-based optimization algorithms, such as sequential quadratic programming (SQP) or interior point (see, eg, [Walraven et al., 2014](#)). Because of the nonconvexity of the objective function and constraints and the large number of variables, the optimization algorithm may return a local minima or even an infeasible solution, if the starting point is not good.

- Black-box approach

In the black-box approach, the optimization algorithm explores the space of independent design and, for each sampled solution, a cycle simulation/design routine (the black box) works out the cycle design and the relevant performance indexes. Compared to the EO approach, such black-box strategy may considerably increase the probability of determining the global optimum because the optimization level considers only the independent decision variables (a few) and the design specification constraints, because all the dependent variables and unit equations are hidden into the design model (black box). Moreover, in the black box the designer can easily implement any correction to the design variables to solve possible

⁹ This is not true if correlations of efficiency are used for the expander. In this case the simulation requires an iterative process, which is usually faster than the resolution of a system of tens of equations.

inconsistencies. Finally, within the black box it is also possible to use external codes for calculating the design or the performance of some specific cycle components. Only inequality constraints are typically defined at the optimization level because all the equality constraints can be included in the black-box function by decreasing the number of independent variables. The black box can consist in any of the tools for the plant simulation presented earlier.

- Infeasible path approach

In the infeasible path approach (Biegler and Cuthrell, 1985) some of the model (flow-sheet, cycle, etc.) equations are “opened” (they must not be necessarily guaranteed at each sampled solution) and included as constraints in the optimization problem. It is advantageous to open the equations corresponding to closed loops (called “recycle equations,” associated with recycles of material/energy streams or information like in the case of a recuperator), as they slow down the convergence rate of the fixed-point solvers used in the SM simulation codes. Thus, the main advantage is the saving of computational time required for each black-box evaluation (simulation of the cycle/flowsheet). On the other hand, the intermediate solutions sampled by the optimization algorithm are in general infeasible, as they do not meet the opened constraints and feasibility is guaranteed only when the optimization algorithm reaches convergence. Furthermore, in addition to the independent decision variables, additional auxiliary variables (called “tear variables”) must be optimized with an increase in the computational time of the optimization algorithm.

For the aforementioned advantages and the relatively fast convergence of the cycle simulations, the black-box approach is widely adopted for the optimization of ORCs, as reviewed by Martelli et al. (2015). On the other hand, owing to the complex modeling equations of the cycle components, the resulting performance indexes returned by the simulation solver may be noisy and nonsmooth (discontinuous or nondifferentiable).

7.2.4.1 Single-objective optimization algorithms

In the following we assume that a single most relevant objective function can be defined and the problem can be stated as a single-objective optimization problem. Moreover, as typically occurs in ORC design optimization problems arising with the black-box approach, we assume that the problem features only inequality constraints:

$$\min f(x)$$

$$\text{s.t. } g(x) \leq 0$$

$$Ax \leq b$$

$$l \leq x \leq u,$$

where x is the vector of decision variables, $g(x)$ is the vector of nonlinear inequality constraints, A and b are the matrix and the right-hand-side vector of the linear inequality constraints, and l and u denote the lower and upper bounds on the decision variables.

When selecting the optimization algorithm for the black-box approach, the following features should be taken into consideration:

- features of the objective function and constraints (nondifferentiability, discontinuity, numerical noise),
- type of constraints,
- number of variables of the optimization problem
- parallel computing capability: possibility of parallelizing the evaluations (i.e., simulations) of the sampled solutions using multiple cores.

Concerning the smoothness of the objective function and constraints, if all the functions are smooth and do not show numerical noise, even gradient-based NLP algorithms, such as SQP, are suitable. However, the functions returned by simulation solvers are generally noisy (the numerical noise is generated by the tolerances of the convergence loops within the simulation), nondifferentiable, and even discontinuous. If functions are affected only by numerical noise and there is not a risk of unexpected crashes of the simulation solver, techniques exploiting approximations of the gradients (e.g., implicit filtering; [Gilmore and Kelley, 1995](#)) or models of the functions (i.e., model-based derivative-free methods; [Conn et al., 2009](#)) can still be adopted and keep a sufficiently good convergence rate. On the other hand, if the functions exhibit steep angle points and/or step-type discontinuities (as often happens in the techno-economic optimization of ORCs) and/or unexpected failures of the simulation, very robust direct-search methods must be adopted. These methods are able to determine an improving solution without relying on gradients and/or models (e.g., interpolation or regression polynomials, surrogates, etc.) of the objective function and constraints. Indeed, the function discontinuities make the function gradients and the function models useless for determining the most promising search directions. As a penalty for the lack of information on the function gradients, the convergence rate of direct-search methods is orders of magnitude lower than that of gradient-based methods and this issue limits the applicability to problems with at most a few tens of variables (30 is already considered a challenging figure, requiring several thousands of function evaluations).

The existing local and global direct-search methods applicable to black-box problems can be subdivided into six main classes:

- **Simplicial-search methods**
Simplicial-search methods employ a simplex of points, which is iteratively expanded, contracted, and rotated so as to improve the objective function of its vertices. Well-known examples are the simplex algorithm by [Nelder and Mead \(1965\)](#) for unconstrained optimization and the complex algorithm of [Box \(1965\)](#) for constrained optimization. Although the simplex of points may cover most of the feasible region, simplicial-search algorithms must be regarded as local search techniques as they do not extensively explore the whole space and, on multimodal functions, may prematurely converge to local minima ([Martelli and Amaldi, 2014](#)).
- **Random-search and simulated-annealing methods**
Random-search methods are stochastic global search methods that rely solely on the random sampling of a sequence of solutions in the feasible region of the problem. These

methods have been attracting attention for global optimization since 1960 because of their ability to tackle problems whose mathematical structure is difficult to analyze (e.g., black-box functions) and the existence of asymptotic convergence results (if the method satisfies a certain set of conditions, the sequence of iterates converges to a global optimum with a probability of 1). Examples are the controlled random-search algorithms by [Price \(1983\)](#) and [Kaelo and Ali \(2006\)](#). Simulated annealing algorithms are essentially random-search methods in which the new solutions, generated according to a sequence of probability distributions (e.g., the Boltzmann distribution) or a random procedure (e.g., a hit-and-run algorithm), may be accepted even if they do not lead to an improvement in the objective function. The candidate solution is accepted with a probability p calculated by the following equation:

$$p = \min\left\{1, e^{(f_{\text{best}} - f_{\text{new}})/T}\right\} \quad (7.17)$$

where T is called the “temperature” parameter, f_{best} denotes the best value found so far, and f_{new} is the function value of the new solution. The temperature parameter is decreased monotonically with f_{best} to realize a probability distribution that progressively accepts only improving solutions. The best known methods for constrained real variable black-box problems are those proposed by [Romeijn and Smith \(1994\)](#), [Wah and Wang \(1999\)](#), and [Hedar and Fukushima \(2004\)](#).

- Population-based methods

The class of population-based algorithms is quite broad as it contains all the metaheuristic search methods that make use of a population of solutions to orient the exploration. Such class comprises not only the well-known genetic algorithms but also other evolutionary methods, such as differential evolution, memetic algorithms, ant colony, particle swarm, and scatter search ([Simon, 2013](#)). Genetic algorithms (GAs) and differential evolution techniques have been attracting attention from the first publication of [Holland \(1975\)](#). Although originally developed for integer problems, many authors have extended their use to continuous variables problems. The basic idea is to apply laws inspired by natural evolution, such as inheritance, mutation, selection, and crossover, to simulate the evolution of a population of solutions (called individuals). This class of methods seems to work well on multimodal black-box functions for their exceptional exploration capability. However, similar to other evolutionary algorithms, GAs are capable of quickly finding promising regions of the search space but may take a relatively long time to reach the optimal solution. Among the available algorithms, the covariance matrix adaptation evolution strategy (CMAES) ([Hansen et al., 2003](#)) and the ϵ constrained differential evolution method ([Takahama and Sakai, 2006](#)), best codes respectively in the 2005 and 2006 Institute of Electrical and Electronic Engineers Congress on Evolutionary Computation Benchmark, proved to be very effective in engineering black-box problems.

When using evolutionary algorithms, attention should be paid to the selection of the algorithm parameters, such as number of individuals, probability of mutation, type of crossover, etc. The convergence rate and the accuracy of the returned solution strongly depend on these parameters. On the other hand, unfortunately, no general guidelines can be given because the optimal algorithm setup is problem specific (i.e., it depends on the number of optimization variables and on the features of the problem functions and constraints). Thereby, these parameters have to be tailored to each optimization problem by performing several computational tests and analyzing the results. It is also important to note that, because the evolutionary algorithms have random operators, results are different at each run. Thus, to

assess the accuracy of the results and the reliability of the algorithm, the optimization should be repeated several times (at least 5–10 times), keeping the best solutions.

- Dividing rectangle (DIRECT) methods

DIRECT algorithms, like the DIRECT (Jones et al., 1993) and the multilevel coordinate search (MCS) (Huyer and Neumaier, 1999), are global optimization methods that mimic a sampling technique. The feasible region is divided into a number of hyperrectangles with a single sample solution. In each iteration, new hyperrectangles are formed by dividing the most promising ones and then sampling one point for each new hyperrectangle. Potentially optimal hyperrectangles either have low function values at the sample points or are large enough (i.e., unexplored) to be good targets for global search. The algorithms typically stop when the hyperrectangle size is below a certain value set by the user or the maximum number of function evaluations is reached.

- Directional direct-search methods

In directional direct-search methods, at each iteration the search around the current solution is carried out along a set of directions that is rich enough to guarantee convergence to stationary points. Depending on the set of directions, such methods can be further subdivided into three main types: generalized pattern search (GPS; Audet and Dennis, 2003), generating set search (Kolda et al., 2006a,b), and mesh adaptive direct search (Audet and Dennis, 2006). GPS methods (Audet and Dennis, 2003) generate a sequence of iterates with nonincreasing objective function values where each iteration is either an optional so-called “search step” or a so-called “poll step.” In the search step, the objective function is evaluated at a finite number of solutions lying on a mesh to try to find one that yields a lower objective function value than the current solution. Any strategy, including genetic algorithms, may be used to search for a better solution. The search step is optional and not essential for the convergence guarantees. The poll step consists in the exploration of the neighboring mesh points around the current best solution. To guarantee the convergence on continuously differentiable functions, the set of poll directions must positively span the solution space. Typically the coordinate directions (ie, the vectors of the canonical basis and their negative counterpart) are adopted. Although convergence to stationary points is proved for continuously differentiable problems (Audet and Dennis, 2003), for nonsmooth problems GPS methods may not converge to a stationary point (minimum), as pointed out by (Kolda et al., 2003) and (Martelli and Amaldi, 2014).

- Hybrid methods

Several hybrid strategies have been developed by coupling the aforementioned algorithms so as to overcome their drawbacks. Among the hybrid techniques, it is worth mentioning PGS-COM (Martelli and Amaldi, 2014), which was specifically developed to deal with nonsmooth constrained black-box problems arising in process and energy engineering. The general idea is to combine the positive features of constrained particle swarm, generating set search, and complex. It has been successfully applied to the optimization of ORCs (Martelli et al., 2015; Capra and Martelli, 2015), heat recovery steam cycles (Nord et al., 2014), CO₂ capture processes (Gatti et al., 2014), and heat exchanger networks (Mian et al., 2015).

The interested reader can find a more detailed review and comparison of direct-search derivative-free methods for bound-constrained problems in Rios and Sahinidis (2013) and for constrained nonsmooth problems in Martelli and Amaldi (2014).

Last but not least, an important feature of black-box optimization algorithms is the possibility of parallelizing the evaluations of the black-box functions (i.e., cycle simulations). Indeed today’s computers have multiple cores, which can be exploited by

assigning to each one the simulation of a cycle design solution. Ideally, if the algorithm is specifically written for parallel computing without sequential procedures, this expedient allows decreasing the required computational time by a factor equal to the number of available cores. In practice, the time savings is lower, depending on the algorithm coding and machine architecture (e.g., for Matlab implementations of PGS-COM and generating set search (GSS) on a standard desktop PC, a factor of about 2 with four cores, a factor of about 5 or 6 with eight cores; [Martelli and Amaldi, 2014](#)). Whereas simplicial-search and random-search algorithms are sequential and not suitable for parallel computing, directional-search and population-based algorithms are typically coded for parallel computing.

7.2.4.2 Classification of problem constraints

As far as constraints are concerned (typically inequality constraints, as motivated earlier), to select the best optimization algorithm, it is necessary to distinguish the various types of constraints. Here we refer to the classification presented [Le Digabel and Wild \(2015\)](#)

- Quantifiable versus nonquantifiable constraints

“A quantifiable constraint is a constraint for which the degree of feasibility and/or violation can be quantified. A nonquantifiable constraint is one for which the degrees of satisfying or violating the constraint are both unavailable” ([Le Digabel and Wild, 2015](#)) (i.e., it is a binary 0–1 constraint). An example could be the 0–1 output (i.e., failure/convergence reached) of a convergence routine of the cycle simulation solver.

- Relaxable versus unrelaxable

“A relaxable constraint is a constraint that does not need to be satisfied in order to obtain meaningful outputs from the simulations in order to compute the objective and the constraints. An unrelaxable constraint is one that must be satisfied for meaningful outputs to be obtained” ([Le Digabel and Wild, 2015](#)). In the design optimization of ORCs, examples of relaxable constraints are desired specifications in terms of efficiency or costs whose slight violation can be allowed. Examples are specifications in terms of desired output power, minimum desired gas stack temperature, maximum desired investment cost, maximum desired number of turbine stages, etc. Another example is the constraint that limits the liquid fraction along the expansion with the aim of reducing blade erosion and efficiency penalization. For wet fluids (simple molecules) it is sufficient to set a constraint on the steam quality at turbine outlet, whereas for dry fluids (complex molecules) it is necessary to constrain the maximum liquid fraction reached across the whole expansion.

Unrelaxable constraints guarantee the physical feasibility of the cycle: examples are those which guarantee the feasibility of the heat transfer in the heat exchangers (positive pinch-point temperature differences) and those which force the superheat temperature to be greater than or equal to the evaporation temperature, the regenerator outlet temperature to be lower than the evaporation temperature, or the evaporator pressure to be higher than the condenser pressure. For instance, if the power output is optimized for a subcritical ORC, the evaporation temperature and the turbine inlet temperature must be selected as optimization variables. The evaporation temperature lower bound is close to the condensing temperature, whereas the upper bound is either the temperature of the heat source or the critical temperature of the fluid. The

turbine inlet temperature has the same lower and upper bounds as the evaporation temperature in order to also reproduce saturated cycles. Thus, to avoid meaningless solutions, it is crucial to add an unrelaxable linear constraint among these two variables that keeps the maximum temperature of the cycle always greater equal than the evaporation temperature and prevents the optimization algorithm from exploring meaningless solutions. The same consideration is valid for the evaporation temperature levels of double pressure level cycles.

- A priori versus simulation based

“An a priori constraint is a constraint for which feasibility can be confirmed without running a simulation. A simulation-based constraint (or simulation constraint) requires running a simulation to verify feasibility” (Le Digabel and Wild, 2015). Typically a priori constraints are expressed as algebraic equations (linear or nonlinear). In the optimization of the design of ORCs, examples are the linear constraints that force the superheat temperature to be greater than or equal to the evaporation temperature and the evaporator pressure to be higher than the condenser pressure. Simulation-based constraints are all those requiring the simulation of the cycle to determine the involved variables, such as the constraint on the minimum desired gas stack temperature, minimum desired vapor fraction at turbine outlet, maximum desired investment cost, maximum desired number of turbine stages, etc.

- Known versus hidden constraints

“A known constraint is a constraint that is explicitly given in the problem formulation. A hidden constraint is not explicitly known to the solver” (Le Digabel and Wild, 2015). A hidden constraint typically appears when the simulation crashes.

The use of constraints on both the optimization variables and the calculated quantities is crucial to obtain a feasible solution and to reduce the computational time. It is worth noting that only a few direct-search algorithms are specifically designed to deal with constraints. Most methods, like CMAES, DIRECT, and MCS, were developed for bound-constrained problems (where variables have lower and upper bounds) and then they are extended to handle different types of constraints with the penalty approach:

$$f_p(x) = f(x) + \sum_i [k_i(\max\{0, g_i(x)\})]^2 \quad (7.18)$$

where $f(x)$ is the original objective function, $g_i(x) \leq 0$ are the inequality (linear or nonlinear) constraints, k_i are the penalty coefficients, and $f_p(x)$ is the penalized objective function minimized by the optimization algorithm.

Although widely used for its simplicity, the penalty approach has the following drawbacks.

- There is no standard methodology for the definition of the penalty coefficients k_i . Different weights for the penalties can be set depending on the importance of the constraint. However, values that are too large may affect the search algorithm effectiveness, driving it far from the global optima, whereas those that are too small risk leading to infeasible solutions as the constraint violation is not sufficiently penalized. Thus, a final check of the violation of the constraints is recommended.
- The penalty approach does not avoid the violation of the unrelaxable constraints; hence, if unrelaxable constraints guarantee the physical feasibility/meaning of the system and such constraints are handled with the penalty approach, the values returned by the black box

(cycle simulation) may be meaningless and/or may fail, driving the optimization algorithm toward useless solutions.

- The whole space defined by the upper and lower bounds is explored, without taking into account of the explicitly known constraints, with a penalty in terms of computational time.
- Information about the geometry of the feasible region defined by the explicitly known constraints is not exploited to guide the optimization and generate promising sample points/search directions.
- The penalty approach is not suitable for dealing with nonquantifiable constraints and hidden constraints, as the violation of the constraint cannot be quantified.

In summary the penalty approach is suitable only for quantifiable relaxable constraints.

To deal with unrelaxable constraints, hidden constraints, and nonquantifiable constraints, the extreme barrier approach is typically adopted: if a sampled solution does not meet the unrelaxable constraints or the black-box solver fails to return a meaningful value, an extremely high (ideally infinite) value of the objective function is assigned to the sampled solution. This strategy prevents infeasible solutions from being considered promising by the optimization algorithm. On the other hand, the approach generates large step-type discontinuities of the objective function, which can be properly handled only by certain optimization algorithms, like CPSO (Hu and Eberhart, 2002) and MADS. A similar approach consists in rejecting the infeasible solution and trying to replace it by iteratively generating new solutions, as done in the complex algorithm and in the controlled random search algorithm. Another possible approach to handling unrelaxable constraints is called the “repair method” and consists in accepting the infeasible solutions and then progressively moving them toward the feasible ones, as done by the GENOCOP III GA (Michalewicz and Nazhiyath, 1995).

Other optimization algorithms have been specifically developed to deal with a priori linear constraints (such as PSwarm by Vaz and Vicente 2009, GSS by Kolda et al. 2006a, simulated annealing by Romeijn and Smith 1994, PGS-COM by Martelli and Amaldi 2014), and/or nonlinear constraints (such as Wah and Wang, 1999, Kolda et al. 2006b) at the algorithm level with specific mathematical techniques.

7.2.4.3 Multiobjective optimization algorithms

If the problem features multiple conflicting objective functions (e.g., energy efficiency and investment cost) and it is not possible to assign relative weights and sum the objectives so as to define a single relevant objective to be minimized/maximized, the problem shall be formulated as a multiobjective optimization problem:

$$\min\{f_1(x), f_2(x), f_3(x), \dots\}$$

$$\text{s.t. } g(x) \leq 0$$

$$Ax \leq b$$

$$l \leq x \leq u$$

where x is the vector of decision variables; $f_i(x)$ denotes the different, typically conflicting, objective functions; $g(x)$ is the vector of nonlinear inequality constraints; A and b denote the linear inequality constraints; and l and u denote the lower and upper bounds on the decision variables.

For this class of problems, the optimality condition is called “Pareto optimality” (Miettinen and Norwell, 1999): a solution \bar{x} is Pareto optimal (also called “nondominated”) if there does not exist another feasible solution such that $f_i(x) \leq f_i(\bar{x})$ for all i and that $f_j(x) < f_j(\bar{x})$ for at least one index j . Briefly, a solution is Pareto optimal if there does not exist another feasible solution that yields an improvement in one (or more) objective without causing the degradation of at least one other objective. The set of Pareto optimal solutions is called the Pareto front.

The available multiobjective optimization methods capable of determining the set of Pareto optimal solutions can be classified in three categories (Marler and Arora, 2004):

- methods with a priori articulation of preferences
- methods with a posteriori articulation of preferences
- population-based evolutionary algorithms

It is worth noting that the methods of the first two classes convert the multiobjective problem into a sequence of single-objective problems that can be solved with the optimization algorithms described in the previous section.

Methods with a priori articulation of preferences allow the user to specify preferences, which can be articulated in terms of goals or the relative importance of different objectives. Most of these methods include coefficients that can either be set to reflect decision-maker preferences or be continuously altered so as to find the complete set of Pareto optimal solutions. The weighted-sum approach is an example of this class of methods. The basic idea is to assign relative weights to the objective functions and then to minimize the weighted sum of the objective functions. By varying the weights, it is attempted to find the whole Pareto front. However, the weighted-sum method fails to find the Pareto optimal solution on nonconvex portions of the Pareto front, as proven in Messac et al. (2000).

Methods with a posteriori articulation of preferences aim directly at determining the representation of the whole Pareto optimal set as it is impossible for the decision-maker to assign relative weights to the objective functions. Examples are the normal boundary intersection method (Das and Dennis, 1998) and the normalized normal constraint method (Messac et al., 2003), which overcome the deficiencies of the weighted-sum approach.

The last class of techniques includes a large variety of evolutionary algorithms that have been adapted for multiobjective optimization. The most popular paradigm consists in using a selection operator based on Pareto domination and a reproduction operator. The nonsorting GA NSGA-II (Kalyanmoy, 2000, 2001) is an example of such a paradigm. The algorithm starts with a random solution population P of size N . Then, the standard GA operators (i.e., selection, crossover, and mutation) are used to create a child population Q from P with the same size N . Once N child solutions are generated, the parent and child populations (thus $2N$ solutions) are sorted according to the principle of “non-Pareto domination” and solutions are ranked by assigning each of them a

fitness equal to its nondomination level. Finally, the new population is generated by taking the first N elements of the sorted fitness levels. The process is repeated until either all elements of the population have fitness level equal to 1 (i.e., all solutions stay on the Pareto frontier) or a predetermined number of function evaluations are reached. The algorithm is suitable for nonsmooth and noisy black-box problems as it does not use derivative information.

Evolutionary algorithms adopting the same paradigm but different reproduction operators are

- differential evolution approaches (e.g., [Sarker and Abbass, 2004](#)),
- immune-based approaches ([Coello and Cortés, 2005](#)),
- particle swarm optimizer approaches ([Wang and Yang, 2009](#)), and
- probabilistic model-based methods ([Igel et al., 2007](#)).

A quite comprehensive review of the main evolutionary algorithms can be found in [Aimin et al. \(2011\)](#).

As for single-objective evolutionary algorithms, attention should be paid when selecting the algorithm parameters. Indeed, the convergence rate, the extension, and the accuracy of the Pareto front strongly relate to these parameters.

7.2.4.4 Example of algorithm selection

In the Matlab environment ([Natick, 2013](#)), several different nonlinear optimization algorithms are readily available calling functions (*fmincon*, *fminsearch*, *patternsearch*, *ga*, etc.). However, these algorithms have considerably different convergence properties, as previously explained, and a careful selection is necessary to obtain good results. Here we compare the performance of two different algorithms on two test cases: (i) the thermodynamic optimization with fixed turbine efficiency and (ii) the technoeconomic optimization of a two-pressure-level geothermal cycle working with pentane. The thermodynamic optimization features a limited number of variables and smooth and non-noisy functions. On the other hand, economic optimizations present nonsmooth functions because a stage-by-stage turbine model is used, the recuperator can be automatically suppressed by the optimization routine, and different pinch points may activate within the PrHE.

We compare the performance of the SQP algorithm ([Nocedal and Wright, 2006](#)), implemented by the Matlab *fmincon* function, and the *genetic algorithm* of the Matlab function *ga* ([Goldberg, 1989](#)). The default options are used with the same tolerance on the final optimality condition.

For the thermodynamic optimization, five variables are considered: the two evaporation temperatures, the degree of superheating for both levels, and the mass flow-rate ratio. The objective function to be maximized is the net electric power. The global optimum is double checked with an extensive sensitivity analysis. In [Fig. 7.9A](#) the trend of the optimal solutions is reported against M_r and the two dotted lines define a range of $\pm 0.5\%$ error. The maximum is found in correspondence to a mass flow ratio close to 0.4, corresponding to a net power output slightly higher than $8.4 \text{ MW}_{\text{el}}$ and a $\Delta T_{\text{pp,PrHE}}$

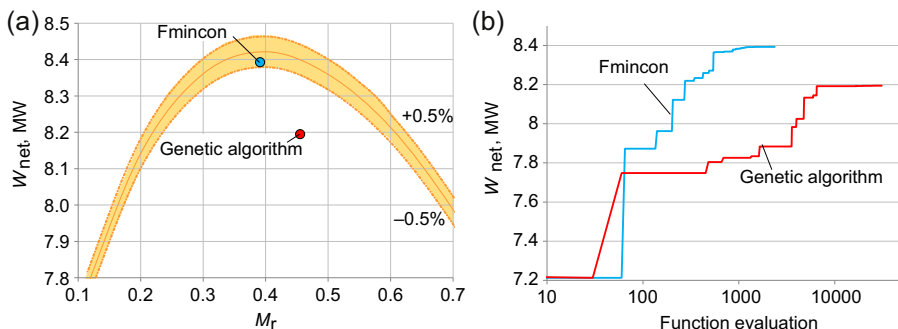


Figure 7.9 Comparison between the final solutions achieved by the three optimization algorithms and the reference solution for the considered test case. *Dotted lines* represent an error of $\pm 0.5\%$.

equal to the lower bound in both pressure levels. The markers denote the solutions found by the two different algorithms.

The same starting point is passed to the two algorithms. It is fairly close to the global optimum: both evaporation temperatures are close to the optimal value and superheating is initialized at 10°C , on the low side of its variability range defined by the lower and upper bounds. As a result the objective function value (net power output) of the starting point is 12% lower than the optimal value. Fig. 7.9B depicts the trend of the net power against the function evaluation number. Whereas SQP (*fmincon*) can quickly find a close-to-optimal solution with a limited number of function evaluations, thanks to the exploitation of the function gradients and Hessians, which provide useful information as the problem is smooth and nonnoisy, the *genetic algorithm* has a very slow convergence rate because of the lack of gradient information and the need of sampling a larger number of points before finding an improving solution. As result the SQP can reach a solution very close to the real optimum and the small difference is due to the presence of pressure drops in the superheaters that are accounted even if the cycle converges to a saturated configuration.

The second example is the technoeconomic optimization applied to the same reference case: in addition to the optimization variables already considered, the condensing temperature, the pinch-point temperature differences in both the condenser and the recuperator, and the outlet temperature of geothermal brine are also optimized. The number of stages, and so the cost of each turbine, change according to the volume ratio, which is strictly related to the values of evaporation temperatures and pressure of condensation. This discrete change leads to discontinuities and nondifferentiabilities of the objective function.

The plot of specific cost is displayed in Fig. 7.10 as a function of the two evaporation temperatures (while maintaining fixed the other variables).

It is possible to notice that the objective function presents at least three local minimum and several discontinuity lines represented in Fig. 7.10 by *dotted lines*.

Computational results indicate that SQP is not suitable for this type of problem as it returns a solution far from the global optimum (10% higher objective function value).

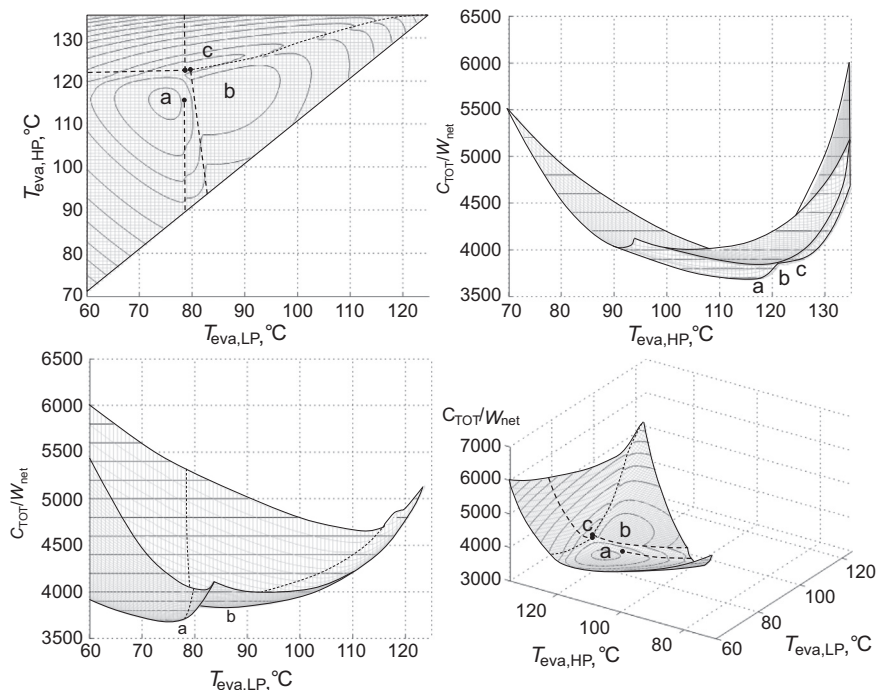


Figure 7.10 Surface of the objective function for the technoeconomic test case. Local minima are labeled with letters b and c, and the global optimum is labeled with letter a. *Dotted lines* show the presence of discontinuities.

Indeed it relies on the information provided by the gradient and hessian of the objective function but such information is misleading owing to the function's nonsmoothness. Another issue of SQP is due to the type of its search strategy. SQP is a local optimization algorithm, which moves from the starting point by finding close improving solutions with the risk of finding just the local minima close to the starting solution. To overcome this limitation, local search methods are typically used in combination with multistart approaches (i.e., consisting in starting local optimization algorithms from multiple starting points chosen according to probabilistic criteria).

GA requires a considerable number of function evaluations because of the poor convergence rate but, eventually, it finds the global minimum. In addition, a better selection of the algorithm parameters (size of the population, migration and mutation factors) may lead to a faster convergence rate or more accurate solution. The advantages of GA over SQP in this test case are two: (1) GA is a global optimization method whose search strategy allows one to explore the whole feasible region with a lower risk of being trapped in local minima and (2) GA does not use derivatives and so it is able to cope with nonsmooth functions.

The examples indicate that:

- Selecting the wrong optimization algorithm may lead to strongly suboptimal solutions, making optimization useless.

- It is not possible to define an optimization algorithm that works for all problems. The optimization algorithm selection must be tailored for each problem taking into account the key features of the problem and the advantages/disadvantages of the algorithms. Although evolutionary algorithms can handle almost any type of problem because of the very robust search strategy, their convergence rate is significantly lower than deterministic algorithms (either derivative-free or gradient-based) and their convergence properties strongly depend on the algorithm setup parameters. Hence their use should be limited to problems that cannot be successfully tackled with more efficient approaches, such as nonsmooth optimization problems.

7.3 Numerical examples

Three numerical examples of state-of-the art optimization applied to ORCs are presented. The first deals with the optimization of ORCs for a medium-temperature geothermal brine, investigating the effect of different assumptions about the turbine design on the final results; a technoeconomic optimization is carried out, highlighting the most promising working fluids and cycle layouts. The second test case is focused on biomass combustion and the effect of the optimization of a part-load control strategy on the overall design of the plant. The last example deals with a multiobjective optimization of ORC for WHR applications.

7.3.1 *Technoeconomic analysis of organic Rankine cycle plants in the geothermal field*

In this section a comparison between subcritical, supercritical, and two-pressure-level cycles is performed considering both technothermodynamic and technoeconomic optimizations. The importance of using reliable correlations for the estimation of turbine efficiency and cost is highlighted. The black-box optimization approach is adopted: the optimization variables are controlled by direct-search optimization algorithms and the ORC design and simulation are performed by a Matlab routine. Further details can be found in [Astolfi \(2013\)](#). All the assumptions related to pressure drops and component performances are reported in [Table 7.3](#). The heat source is modeled as a 100 kg/s geothermal brine with a maximum temperature of 150°C and reinjection temperature limit of 70°C. To obtain general trends all the fluids available in Refprop are used in this analysis.

7.3.1.1 *Technothermodynamic optimization*

In many studies the efficiency of the turbine is kept fixed without any further consideration about the turbine design, the number of stages, and the necessity of using a gearbox or a power electronic system. This assumption is approximately valid only if the rotational speed is optimized and the number of stages is selected without any technoeconomic evaluation. In fact, a very high overall efficiency can always be obtained by optimizing the rotational speed and by increasing the number of stages, thus limiting the volume variation and the enthalpy drop across each single row. In the simulations, first a fixed isentropic efficiency equal to 85% is assumed as

representative of average performance in the geothermal field; later a comparison is proposed considering two cases: (1) a direct connection with the generator at 3000 RPM and (2) the possibility of optimizing the turbine rotational speed. As already mentioned before, for large volume ratios (i.e., fluids with very high critical temperature), the assumption of a fixed value of efficiency might lead to an overestimation of net power production or a very expensive turbine with several stages.

The results for the subcritical configuration with turbine efficiency equal to 85% are reported in Fig. 7.11, in which the trend of specific power (calculated as the ratio between net plant power and brine flow rate) is displayed against a reduced temperature parameter. This parameter is defined as the ratio between the critical temperature of the fluid and the maximum temperature of the geothermal brine in Kelvin degrees. Reporting the results against this quantity is useful to compare solutions with different temperatures of the geothermal source and to define general criteria in fluid and cycle selection.

Each marker is representative of the optimal solution for a subcritical cycle configuration obtained by acting on two variables: the evaporation temperature and the superheating temperature increment. Using fluids with a low critical temperature (e.g., R218) entails a limitation of power output mainly because of the low evaporation temperature and the correction of the pinch-point temperature difference in the

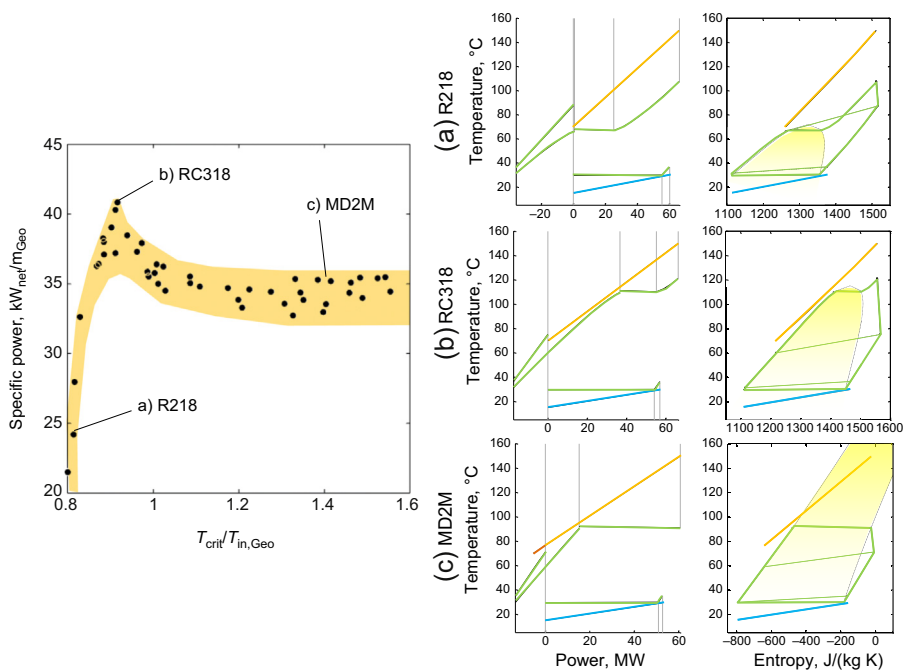


Figure 7.11 Specific power for subcritical cycles optimized by varying evaporation temperature and superheating temperature difference. The T-Q diagram and the T-s diagram are proposed for three fluids representative of a low-critical-temperature fluid (R218), a high-critical-temperature fluid (MD2M), and the optimal fluid (RC318).

recuperator to avoid boiling in the preheating process. As a result, the temperature differences in both recuperator and PrHE are larger than the minimum, and the maximum temperature of the cycle is limited to maintain a lower outlet temperature from the turbine. In this way it is possible to exploit the whole available heat in the recuperator without increasing the duty and the efficiency losses of the condenser. It is also evident that subcritical superheated cycles working with fluids with critical temperature lower than the brine temperature tends toward supercritical cycles. On the other hand, for fluids with a critical temperature higher than the brine maximum temperature (e.g., MD2M) the adoption of superheating is detrimental. Because the effect of fluid thermodynamic properties on turbine efficiency is not considered, all these cycles show almost the same performance because they work between the same temperatures of condensation (assumed) and evaporation (optimized). They basically refer to the same ideal Carnot efficiency and show similar second law efficiency as already described in Chapter 1. The optimal working fluid is RC318, whose optimal evaporation temperature is pushed toward the upper bound, and possible advantages are achievable by the adoption of a higher maximum pressure. The specific power for optimal supercritical cycles is reported in Fig. 7.12 and compared with the previous results: supercritical cycle can reach higher performances for low-critical-temperature fluids thanks to a better matching between the heat source and the working fluid in the PrHE. The efficiency increment is larger for low-critical-temperature fluids where no limitation of the recuperator is now considered.

Finally, two-pressure-level cycles are considered even if they are rarely proposed for the exploitation of geothermal brines. With this plant layout it is possible to reduce the efficiency losses in the heat introduction process and achieve a remarkable increase in power production with respect to the subcritical single-level cycles. Fig. 7.14A depicts the optimal results for the two-pressure-level cycles in comparison with both single-level subcritical and supercritical cycles: the results are obtained by acting on five variables, namely, the two evaporation temperatures, the superheating increments, and the ratio between the high-pressure and the low-pressure mass flow rates. The maximum specific power is close to that of the supercritical cycle but the same result is achieved with a more complex plant layout and a more complex operation because the liquid levels must be controlled in the condenser and in both evaporators.

From a thermodynamic point of view and with a fixed turbine efficiency supercritical cycles lead to higher performances compared to both single-level and two-level subcritical cycles.

With a direct coupling with the generator, the assumption of turbine fixed efficiency can lead to large errors and misleading final results, as can be noticed by observing Fig. 7.13A, in which the expander performance is reported for the subcritical optimal solutions.¹⁰ A very high efficiency can be obtained for a large number of fluids but it is possible to notice that for some low-critical-temperature fluids and for high-

¹⁰ It is important to emphasize that these values are obtained with a different combination of evaporation temperature and superheating temperature increment with respect to the previous case because the optimization is carried out considering the effects of cycle parameters on the turbine efficiency. In some cases, it is convenient to reduce the evaporation temperature to increase the turbine efficiency.

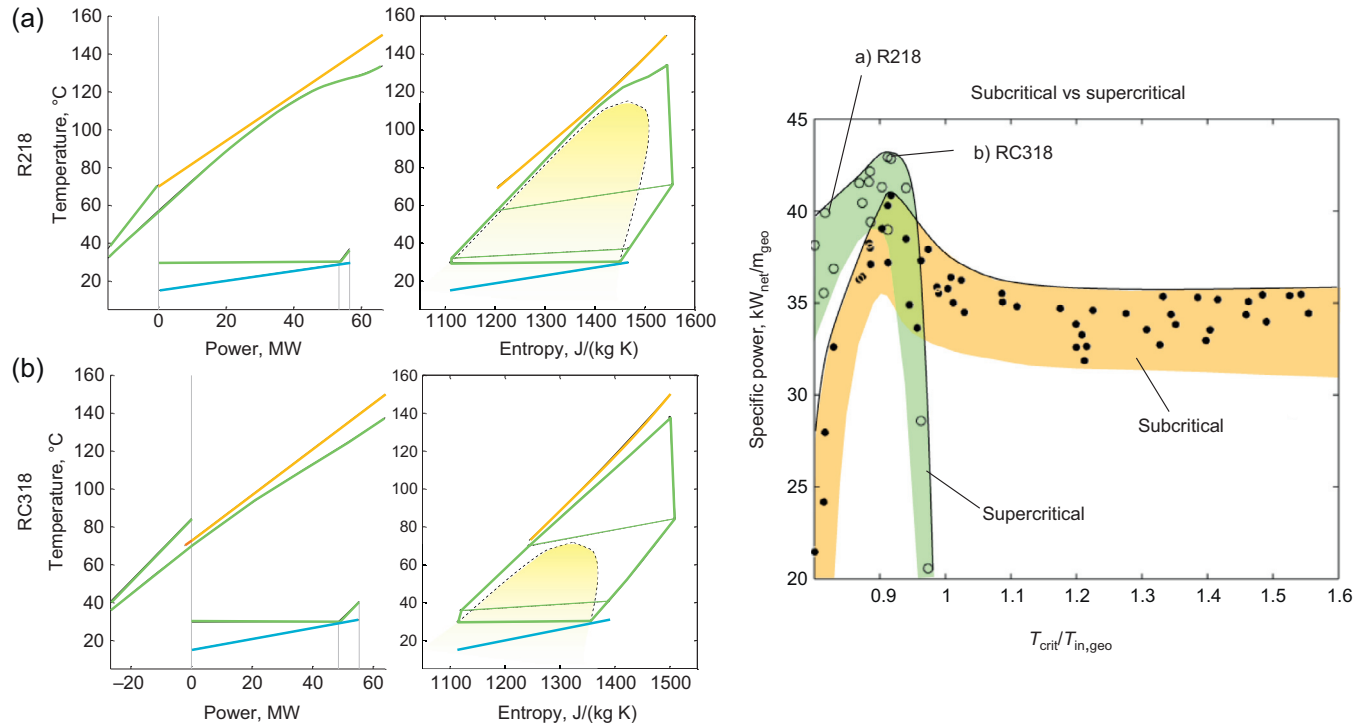


Figure 7.12 Comparison between performance achievable for supercritical and subcritical single-level cycles.

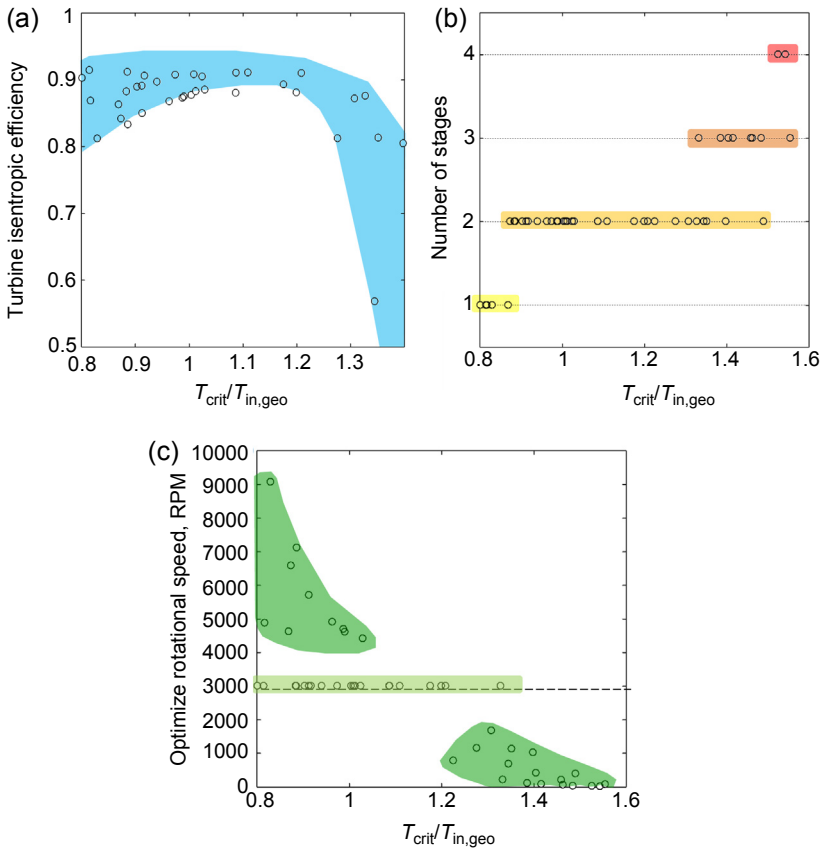


Figure 7.13 (A) Maximum attainable isentropic turbine efficiency for a direct coupling with the generator, (B) number of stages of the turbine, and (C) optimized rotational speed. Results refer to the subcritical cycle.

temperature fluids the turbine isentropic efficiency drops because of the nonoptimized rotational speed. In addition, for high-critical-temperature fluids the volume ratio is large and multistage turbines should be adopted (see Fig. 7.13B). The optimal results are reported in Fig. 7.14B: for some fluids it is possible to obtain a higher power production with respect to the previous case thanks to the increased turbine efficiency; for others instead the assumption of fixed turbine efficiency may lead to a large overestimation of system performance if a direct coupling with the generator is considered.

The same cases are analyzed optimizing the rotational speed. Always with reference to the subcritical cycle it is possible to observe how the optimal rotational speed is equal to 3000 RPM for many solutions, but faster turbines are needed for low-critical-temperature fluids and low rotational speeds are required for high-critical-temperature fluids, as reported in Fig. 7.13C. For the turbines with optimal rotational speed different from grid frequency, the efficiency of the gearbox or the power electronic system is accounted for in the computation of final results displayed in Fig. 7.14C.

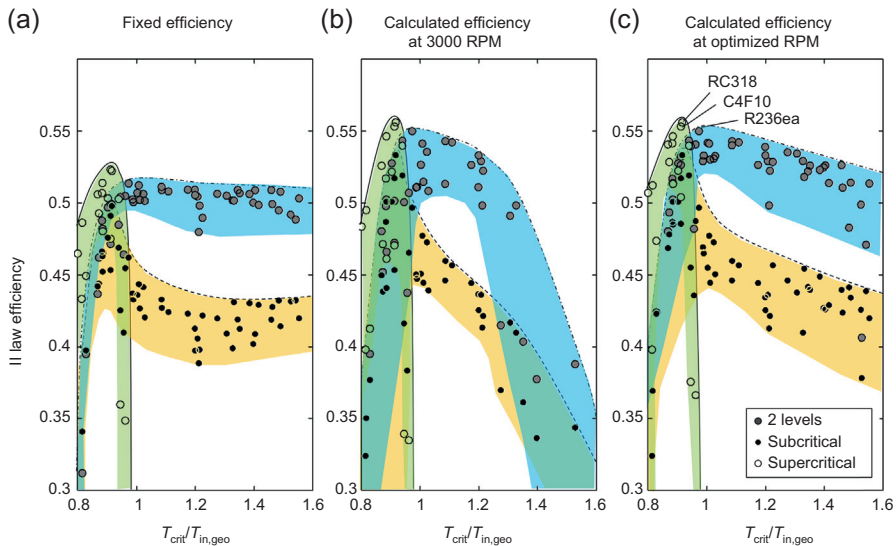


Figure 7.14 Comparison between the optimal cycles from a thermodynamic point of view with different hypotheses on turbine efficiency.

Optimized turbine efficiencies are obviously higher with respect to those solutions with direct coupling with the generator but a decrease in performance is highlighted for high-critical-temperature fluids characterized by multistage turbines because of the trade-off between stages with very different optimal rotational speeds. This effect is even larger for two-pressure-level cycles for which the rotational speed is determined considering both turbines on the same shaft. It can be noticed that the optimal cycle is always in supercritical configuration using a fluid with a critical temperature close to the inlet temperature of the geothermal brine. The maximum attainable efficiency is obtained for a supercritical cycle working with RC318.

7.3.1.2 Technoeconomic optimization

The technoeconomic optimization is carried out with the aim of minimizing the specific cost of the plant; thus this approach requires the optimization of the heat exchanger surfaces and the turbine while considering a fixed cost for the realization of the geothermal well. In geothermal fields the cost of the exploration campaigns, the drilling, and the construction of all the required infrastructures is a relevant share of the final plant cost (up to 50%). In this case a fixed cost of US\$16.2 million in 2015 dollars is assumed considering a favorable thermal gradient (ΔT_{geo}) of 50°C/km (Bombarda, 2011).

A preliminary economic optimization was carried out with four fluids having very different thermodynamic properties to validate the correlations adopted under a wide range of conditions and to verify the influence of the various parameters that mainly

affect the final optimal solution. The fluids considered were R134a, ammonia, water, and D5 (a medium-large weight siloxane). R134a, despite its GWP, is commonly used as a refrigerant fluid and as a working fluid for supercritical regenerative cycles. Ammonia is rarely used in power plants because of its flammability and toxicity but, thanks to its thermodynamic properties, gives the possibility of obtaining a compact design of the components and may be profitable from an economic point of view. Water is the most common fluid used for power generation, but it is not competitive for medium- to low-temperature heat sources and small sizes, mostly because of the uneconomical turbine design. Finally, D5 is considered to investigate the difficulties that can occur when using complex fluids with a high critical temperature. A supercritical recuperative cycle is used for R134a, the selected configuration for ammonia and water consists of a subcritical superheated cycle with the adoption of a gearbox, and a subcritical superheated cycle is adopted, allowing the solver to converge to a saturated configuration acting on ΔT_{sh} , for D5. The optimization algorithm aims at minimizing the specific cost of the plant, acting on a number of variables (from 6 to 10) dependent on the cycle configuration (see Table 7.4). Rotational speed of the turbine is always optimized.

In Table 7.5, the calculated efficiencies and values of the optimized parameters resulting from the thermodynamic and from the economic optimization are reported, and in Fig. 7.15 the comparison between the specific costs obtained in thermodynamic and in economic optimizations is presented for the four investigated fluids. Wide stacked bars represent absolute component cost repartition and narrow bars show the change in total plant- and power block-specific cost.

Final results for R134a show a lower T_{cond} than the value adopted in the thermodynamic optimization, with a consequent increase in both air condenser area and fan consumption. The optimal maximum pressure decreases, whereas $\Delta T_{ap,PrHE}$ and $\Delta T_{pp,PrHE}$ increase, leading to a higher value of $\Delta T_{mln,PrHE}$ and a reduction of PrHE cost, but also reducing the cycle efficiency. Thanks to the optimization of $\Delta T_{pp,rec}$, geothermal brine is completely exploited in both cases. The main effect of economic optimization is a reduction in absolute total plant cost reflected in the lower value of both total plant-specific costs (−12.65%) and power block-specific costs (−27.14%). With ammonia for fluid the economic optimization reduces the condensing temperature with an almost constant evaporating pressure and a resulting increase in power production. Power block cost increases because of the lower ΔT_{mln} in the condenser, whereas it remains almost constant for the PrHE. Both power block- and total plant-specific costs are reduced thanks to the higher power output. In this case, the adoption of a speed reducer is advantageous and the mechanical losses associated with this component are more than compensated for by the increased turbine efficiency. The optimal rotational speed is around 11,000 RPM. In both cases component cost repartitions show that PrHE, condenser, and turbine cover almost 75% of the total power block cost. The final specific cost is lower for R134a, thanks to its higher efficiency. With water, the optimized cycle shows a low evaporation temperature to respect the constraint on minimum vapor quality at turbine discharge. The turbine is more expensive than for both R134a and ammonia because of the

Table 7.5 Thermodynamic and Technoeconomic results for four fluids exploiting a 150°C geothermal brine

	R134a		Ammonia		Water		D5	
	Thermodynamic	Technoeconomic	Thermodynamic	Technoeconomic	Thermodynamic	Technoeconomic	Thermodynamic	Technoeconomic
System efficiency								
Cycle efficiency	13.30%	12.74%	11.50%	11.93%	9.30%	9.48%	13.13%	9.42%
Plant efficiency	13.26%	12.70%	10.67%	11.25%	9.26%	9.30%	10.38%	6.41%
Recovery efficiency	100.0%	100.0%	93.21%	94.71%	100.0%	98.54%	79.38%	68.54%
Plant II law	0.5411	0.5182	0.4354	0.4591	0.3778	0.3794	0.4234	0.2617
General results								
$W_{\text{net plant}}$	8879.4	8504.6	7145.8	7534.2	6200.2	6226.4	6948.4	4294.8
Specific cost PB	1592.4	1160.3	1241.2	1154.1	1726.2	1672.6	6981.8	3490.9
Specific cost TOT	3827.0	3342.7	3796.7	3570.9	4760.0	4679.9	11,321.4	8170.4
Design parameters								
$T_{\text{cond}}, ^\circ\text{C}$	30	24.29	30	24.29	30	30.65	30	54.43
$T_{\text{eva}}, ^\circ\text{C}$, or p_{eva}	47.9 bars	41.45 bars	86.37	86.74	71.17	72.95	99.72	107.74
$\Delta T_{\text{ap,PrHE}}, ^\circ\text{C}$	10.98	17.82	4.5	4.47	4.5	2.0	50.28	42.26
$\Delta T_{\text{pp,rec}}, ^\circ\text{C}$	5	11.85	5	5	—	—	5	17.67

Continued

Table 7.5 Continued

	R134a				Ammonia				Water				D5			
	Thermodynamic		Technoeconomic		Thermodynamic		Technoeconomic		Thermodynamic		Technoeconomic		Thermodynamic		Technoeconomic	
System efficiency																
$\Delta T_{pp,PrHE}$, °C	3		8.08		3		3.73		3		2.48		3		2	
$\Delta T_{pp,cond}$, °C	1		2.20		1		1.91		1		2.31		1		10	
$T_{out,geo}$, °C	70		70		70		74.27		70		71.21		70		95.20	
$\Delta T_{mln,PrHE}$, °C	7.51		15.34		17.16		18.47		21.86		20.31		14.67		12.32	
Turbine results																
Turbine efficiency	0.899		0.8993		0.8976		0.8955		0.8845		0.8841		0.8803		0.8865	
Number of stages	2		2		4		4		5		5		3		2	
Rotational speed	3000		3000		11,343.4		11,771.9		1605.6		1681.8		74.7		175.7	
Size parameter (m)	0.1601	0.249	0.168	0.262	0.0987	0.1538	0.0962	0.1604	0.8701	1.8575	0.831	1.7997	5.166	16.822	3.513	7.056
Specific speed	0.0927	0.1354	0.093	0.137	0.079	0.1356	0.0751	0.141	0.0834	0.2228	0.0823	0.2237	0.060	0.200	0.087	0.176

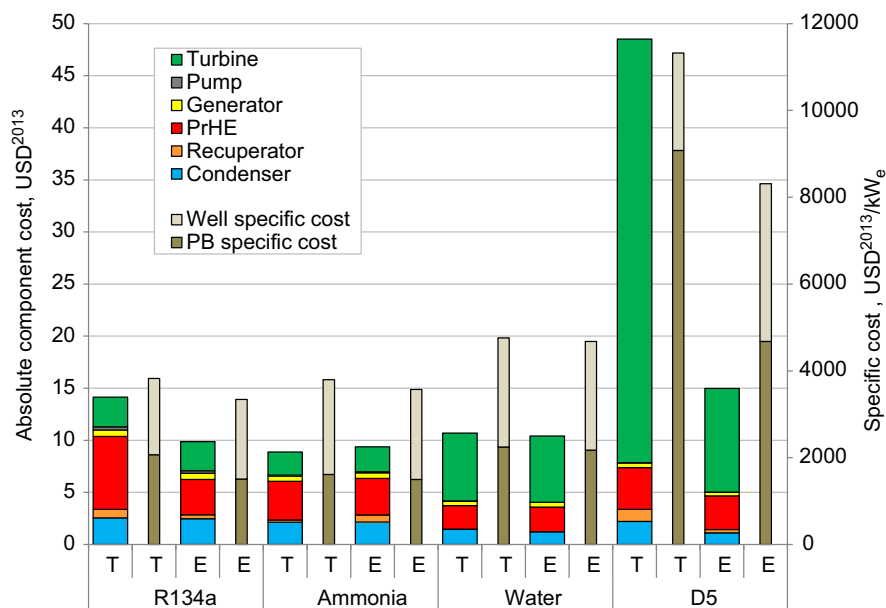


Figure 7.15 Absolute cost repartition (left axis) and specific cost (right axis) achievable for four test fluids exploiting a 150°C geothermal brine. *PrHE*, primary heat exchanger; T, thermodynamic optimization; E, technoeconomic optimization.

larger number of stages and the larger size parameter. The optimization algorithm has a small possibility of changing this solution: an increase in evaporation temperature entails a reduction in recovery efficiency and a nontotal exploitation of the geothermal source; in addition expansion would not respect the vapor quality limit (set at 0.93) with a strong penalty on turbine performance. Both condensing temperature and evaporation temperature are slightly increased with the aim of reducing turbine cost while maintaining a good power production. D5 was selected as representative of high-complexity fluids. It features an overhanging saturation line and the optimization numerically converges to a saturated cycle, which is the most advantageous configuration also from the economic point of view. The main difficulty found in using high-critical-temperature fluids is the very low condensing pressure and the consequent very high volume flow rate at turbine exhaust, causing a high cost of this component. For this fluid, the turbine is largely the most expensive component, and economic optimization leads to an increase in both evaporation and condensing pressure, with the main goal of reducing the turbine size. Recovery rate drops because of the higher evaporation temperature, entailing a lower plant efficiency and power production. The overall power block cost and total plant-specific costs decrease, but reach values that are more than twice those of R134a and ammonia.

In conclusion, water and D5 are economically unsuitable for medium- to low-temperature geothermal sources. In particular, water is indicated more for high-temperature heat sources with net power of at least 10 MW, to reduce criticalities in the design of the first turbine stage. On the other hand, D5 and other siloxanes and complex hydrocarbons are attractive for high-temperature cogenerative applications, where the higher condensing temperature and pressure lead to a favorable size of the last turbine stage.

The technoeconomic optimization routine is applied to all the considered fluids with the three cycle configurations already used in the previous case.

In Fig. 7.16A, the decrement of total specific cost attainable with an economic optimization is reported and it is possible to notice that a relevant reduction in specific cost, larger than US\$200/KW_{el} (2015 dollars) is always possible but more marked results are highlighted using high- or low-critical-temperature fluids. In particular for fluids with a $T_{in,geo}/T_{crit}$ parameter lower than unity the optimal cycle is still supercritical but the efficiency is strongly penalized owing to a reduction in maximum pressure and temperature.

Fig. 7.16B depicts the total specific cost for various combinations of plant layouts and working fluids: it is possible to note a rather regular trend of the total plant-specific cost with respect to the $T_{in,geo}/T_{crit}$ parameter. The minimum is found in the range between 0.8 and 0.9, where several cycles with different fluids can achieve good economics. For values of $T_{in,geo}/T_{crit}$ lower than 0.8, the cost of optimized solutions rapidly increases because of the reduction in plant performance as already found from the thermodynamic analysis. For values above 0.9, cost rises as well, because of the lower efficiency and the strong increase in turbine cost, which mainly affects the final solution. Two-pressure-level cycles show a lower cost than

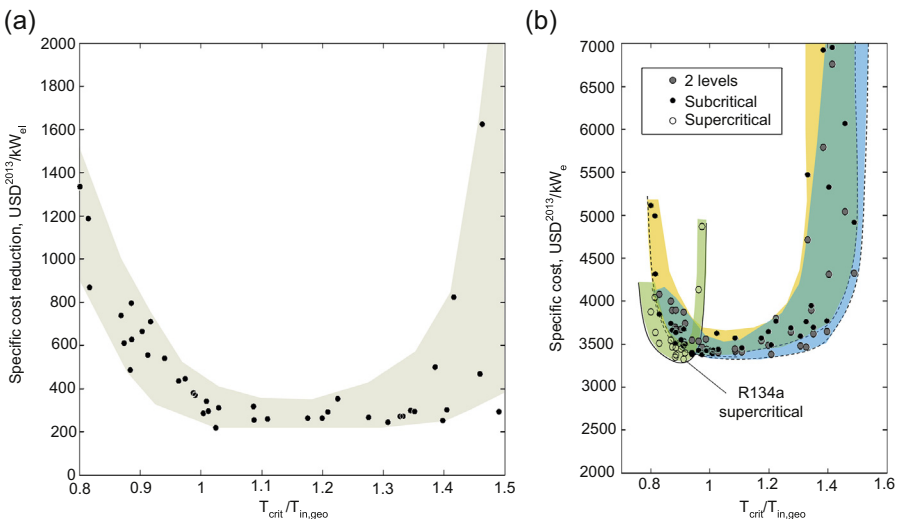


Figure 7.16 (A) Reduction of plant-specific cost attainable and (B) specific power output variation with a technoeconomic optimization versus a technothermodynamic optimization.

the subcritical single-level ones thanks to a higher power production and a larger number of optimization variables, which allows exploring a wider range of solutions. These cycles have a specific cost competitive with the supercritical cycles but the higher BOP and the use of more expensive components affect the final solution. The optimal solution is an R134a supercritical regenerative cycle with no gearbox. For this fluid, a well-designed two-stage turbine directly joined with the generator can be used.

7.3.2 Optimization of biomass-fired combined heat and power Organic Rankine Cycles

This section concerns the optimization of the design of a biomass-fired ORC plant for CHP production. The scheme of the ORC plant is reported in Fig. 7.17. It is made of a biomass-fired boiler; a loop of hot oil transferring heat from the boiler to the cycle; a heat exchanger in which the working fluid is preheated, evaporated, and superheated; a turbine; a regenerator; and a condenser, which supplies thermal power to a residential district heating network through a water loop. A turbine bypass stream has been added to increase the operational flexibility. Because the turbine bypass connects the boiler outlet directly to the condenser inlet, it allows reducing the turbine power and increasing the condenser thermal power at a fixed boiler load.

The district heating network presented in (Tańczuk and Ulbrich, 2013) is considered as a test case: the plant must supply 5.3 MW of thermal power to the district heating network for 4290 full-load equivalent operating hours with the yearly heat-load duration shown in Fig. 7.18.

As clearly indicated by the heat-load duration curve, if the electricity selling price is not sufficiently high compared to the fuel cost, the plant will have to operate at part load for most of the year. Hence, rather than designing the plant for the maximum efficiency or minimum LCOE at full load (e.g., using large heat transfer areas to accommodate the full-load heat duty and multiple turbine stages for the full-load pressure ratio), it may be more advantageous to adopt a less costly design targeted at the average expected part-load operating conditions. Moreover, the selection of the cycle design variables should be adjusted so as to improve the plant flexibility in terms of minimum load and part-load efficiency. For these reasons, it is important to take into account the expected part-load operation early at the design stage through an approach capable of simultaneously optimizing the design and part-load operation.

Martelli et al. (2015) and Capra and Martelli (2015) devise a problem decomposition and two-stage algorithm for coping with the simultaneous design/part-load optimization problem.

Given

- the heat-load duration curve of the district heating network and required delivery/return water temperatures;
- the main economic assumptions including electricity selling price, heat selling price, fuel cost, and the levelized capital charge rate (LCCR; defined as the amount of revenue per

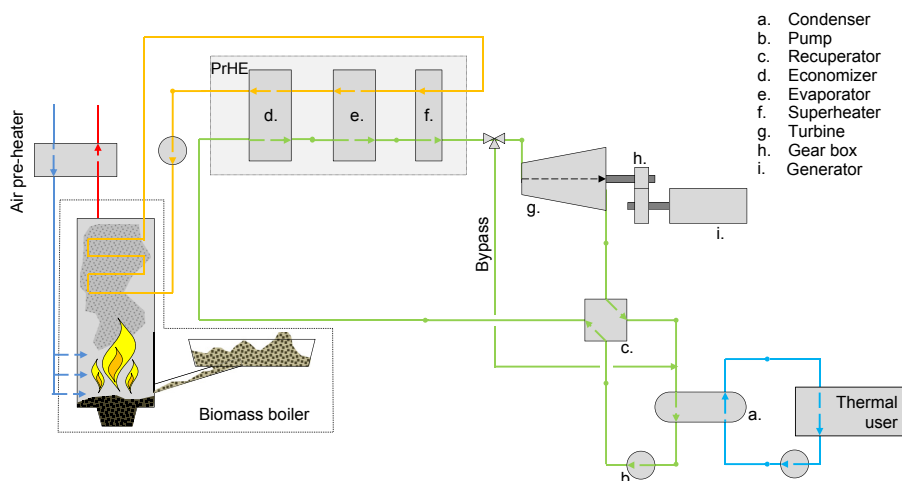


Figure 7.17 Scheme of the organic Rankine cycle plant considered. *PrHE*, primary heat exchanger.

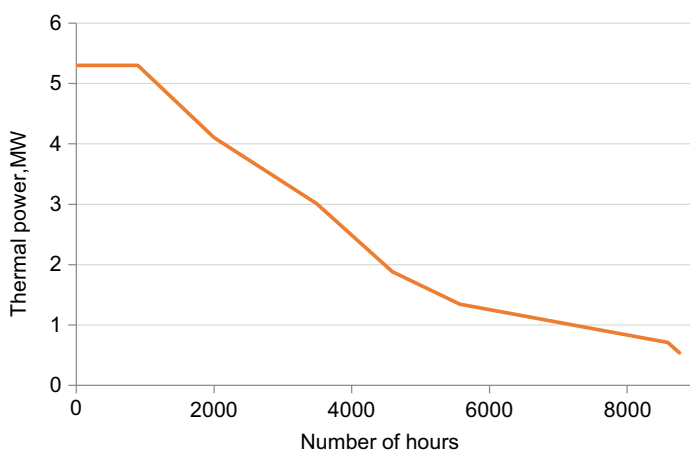


Figure 7.18 Original heat-load duration curve of the district heating network presented by (Tańczuk and Ulbrich, 2013) and considered as a test case in (Capra and Martelli, 2015).

unit of investment cost that is needed to pay the carrying charges on that investment) (EPRI, TAG, 1993) necessary to convert the total investment cost into an annual cost; and

- accurate thermodynamic and cost models of the main equipment units (i.e., boiler, turbine, main heat exchanger, regenerator, etc.) to predict their performance and investment costs as functions of the cycle design variables,

the optimization algorithm simultaneously optimizes

- the key plant design variables (plant size, evaporation pressure, condensation pressure, superheating degree, regenerator pinch-point temperature difference, main heat exchanger temperature difference);

- the key turbine design variables (turbine rotational speed, number of stages and expansion ratio of each turbine stage); and
- the part-load control strategy (mass flow rates, pressures and temperatures of each stream of the cycle) for all the operating conditions expected on the basis of the heat-load duration curve,

to achieve the maximum annual profit, including capital and operating costs.

The simultaneous design/part-load optimization problem can be stated as follows:

$$\max_{x_D, x_{O,t}} P(x_D, x_{O,t})$$

$$\text{s.t. } g_D(x_D) \leq 0$$

$$g_O(x_D, x_{O,t}) \leq 0$$

$$h_O(x_D, x_{O,t}) = 0$$

$$lb_D \leq x_D \leq ub_D$$

$$lb_O \leq x_{O,t} \leq ub_O$$

$$x_D \in \mathcal{R}^{n_D}$$

$$x_{O,t} \in \mathcal{R}^{n_O}$$

where x_D , lb_D , ub_D and g_D label respectively the set of design variables (plant size, evaporation design pressure, condenser design pressure, design superheating degree, design pinch-point temperature difference of regenerator, main heat exchanger, turbine rotational speed, and expansion ratio of each turbine stage), the lower and upper bounds on the design variables, and the design constraints (the heat transfer feasibility within the heat exchangers and the maximum load, specific speed, or volumetric expansion ratio of the turbine stages, see (Martelli et al., 2015) for further details). Instead $x_{O,t}$, lb_O , ub_O , h_O , and g_O denote respectively the part-load operation variables (mass flow rates, pressures, and temperatures of the plant streams in each time period t), the upper and lower bounds on the part-load variables, and the equations of the part-load model of the cycle (i.e., equations describing the off-design behavior of heat exchangers, turbine, pumps, etc.) (Capra and Martelli, 2015). P denotes the annual profit of the plant and it depends on both design and operating variables:

$$\begin{aligned} (x_D, x_{O,t}) = & \sum_{t \in \Theta} \text{GM}_t(x_D, x_{O,t}) - \left(C_B(x_D) + C_P(x_D) + \sum_{j \in \Phi} C_j(x_D) \right) \\ & \cdot \text{LCCR} - C_M(x_D) \end{aligned} \quad (7.19)$$

where GM is the gross margin (depending on both design and operating variables); Θ is the set of expected operating periods of the year; C_B is the cost of civil works, contingencies, engineering, and procurement; C_P is the cost of permits; C_M is the fixed O&M cost; C_j is the investment cost of the j th equipment unit (boiler, turbine, etc.); and Φ is the set of equipment units of the cycle. It is worth noting that C_B , C_P , C_M , and C_j depend only on the design variables x_D .

It is worth optimizing the plant size because, depending on the economic data, it may be profitable to oversize or undersize the plant with respect to the peak heat load demand. If oversized so as to increase the production of electricity, the surplus condensation heat can be wasted through an auxiliary heat exchanger, whereas, if slightly undersized to save capital cost, it is possible to use the turbine bypass to satisfy the peak demand of heat.

Tackling Eq. (7.19) is quite challenging because (1) of the relatively large number of variables and constraints, (2) the optimization algorithm may converge to a local optimum because of the nonconvexity of the objective function and constraints, and (3) the cycle design model and turbine design algorithm described in (Martelli et al., 2015) (required to compute the plant investment costs C_B , C_P , C_M , and C_j within the objective function) are nondifferentiable and discontinuous black-box functions (see Fig. 7.19), which would jeopardize the use of efficient gradient-based

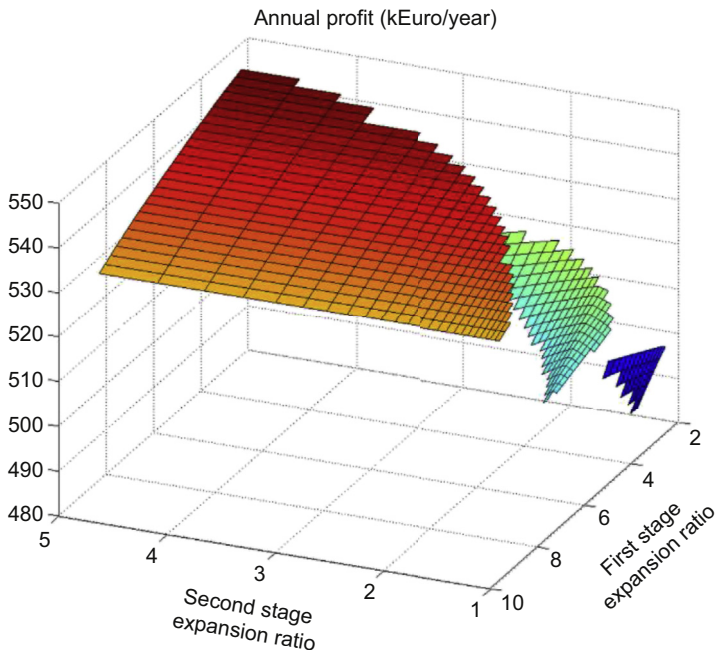


Figure 7.19 Three-dimensional plot of the annual profit of the organic Rankine cycle plant considered in (Martelli et al., 2015) as a function of the first- and second-stage pressure ratio. It is important to note that the function has step-type discontinuities corresponding to the activation of turbine stages (which imply an increase in investment cost).

optimization algorithms. For these reasons, solving directly the optimization problem is really computationally expensive and may return very poor solutions.

To overcome these issues, a two-level decomposition of the problem has been devised. The design variables are optimized at the upper level and, for each fixed set of design variables, the part-load operation variables are optimized at the lower level for each expected operating period of the year. The corresponding two-level algorithm is shown in Fig. 7.20. At the upper level, the black-box optimization algorithm PGS-COM (Martelli and Amaldi, 2014) varies the design variables x_D looking for the solution with maximum annual profit. For each design solution x_D sampled by PGS-

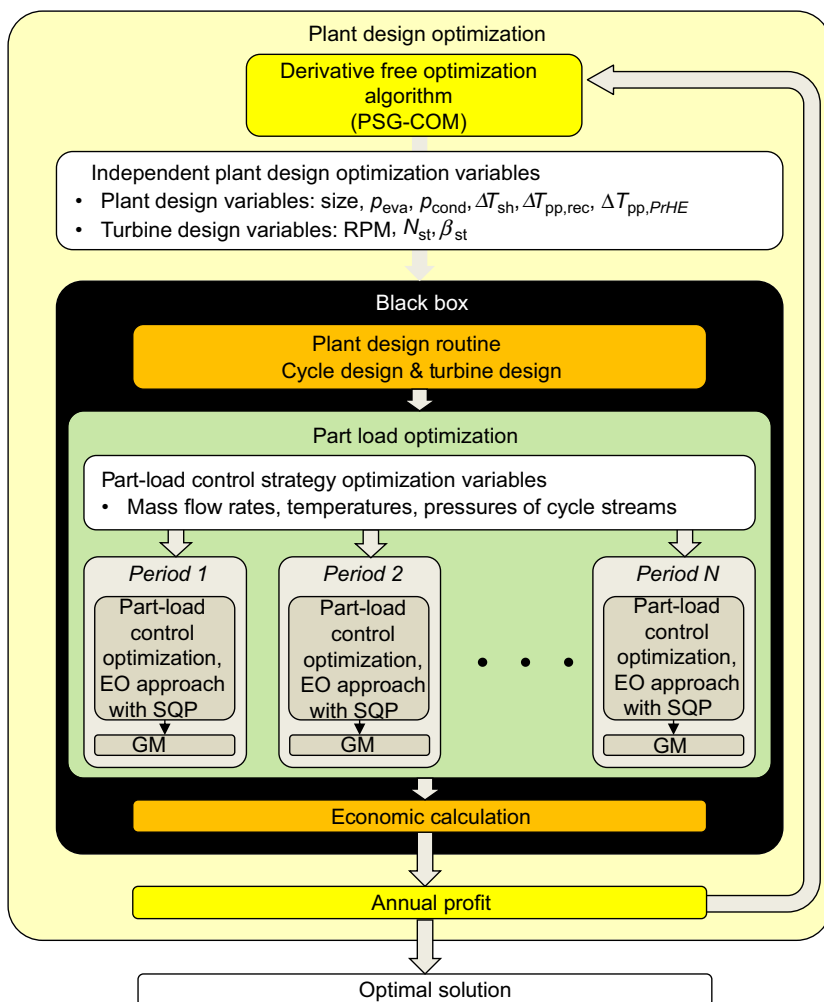


Figure 7.20 Block-flow scheme of the optimization methodology proposed in (Capra and Martelli, 2015). *EO*, equation oriented; *GM*, gross margin; *SQP*, sequential quadratic programming.

COM, first the cycle and turbine are designed and their investment costs are assessed with the black-box routine described in (Martelli et al., 2015), then the plant part-load operation problem is optimized for a discretized number (5–10) of heat demands expected over the year (the values and the corresponding durations of the discretized heat demands are selected so as to approximate the yearly heat-load duration curve of the district heating network). At this point, the annual profit can be computed and its value is returned to the upper-level optimizer, PGS-COM, which uses such information to proceed and determine the next point x_D to sample.

Whereas the design (upper level problem) is optimized with the black-box approach, the part-load optimization problem (lower level problem) is tackled with the equation oriented approach: the equations of the part-load model are constraints of the optimization problem, which maximizes the gross margin GM gained by the plant in each operating period by varying all the cycle operating variables. The part-load optimization problem is optimized adopting the EO approach because all the involved functions (constraints and objective) are continuous and twice differentiable, thus the efficient gradient-based SQP algorithm can be used, and the design solution can be passed as the starting point to quickly find solutions with decreasing loads (see the procedure in Capra and Martelli, 2015).

The optimization is performed considering two working fluids already adopted in commercially available biomass-fired ORCs, i.e., MDM and toluene, and three different electricity prices (80, 110, and 140€/MWh) to show the effect of such parameters on the optimal cycle design and part-load control strategy. Moreover, the cycles found with the simultaneous design/part-load optimization algorithm (cases “PL”) are compared with those obtained by considering only the operation at full load for the expected number of equivalent hours [cases “PR” found in (Martelli et al., 2015) with the design optimization algorithm]. For the sake of brevity, only the computational results relative to toluene are reported here (see Table 7.6) and the reader is referred to (Capra and Martelli, 2015) for the results concerning MDM.

Results indicate that there is a substantial advantage in considering part-load operation early at the design stage of the plant. In particular, to save capital costs, the design/part-load optimization algorithm selects slightly undersized cycles and uses the turbine bypass to satisfy the peak load. Moreover, to save on heat exchanger areas, it prefers higher condensation pressures, lower superheating degrees, and larger pinch-point temperature differences compared to the cases optimized considering only full-load operation. It is worth noting that such design choices allow one to save capital costs without significantly penalizing the part-load efficiency of the plant.

Another relevant feature of the cycles found by the simultaneous design/part-load optimization algorithm is the advantage of adopting slightly higher evaporation pressures than the optimal values for full-load operation. The reason is the optimal part-load operation strategy, which consists in the sliding-pressure mode at high loads and a combination of sliding pressure and throttling at low loads where the sliding-pressure mode (the most efficient strategy) cannot be applied because premature evaporation occurs in the regenerator. Because part-load operation is considered already at the design stage, the optimization algorithm can adopt high design values of the

Table 7.6 Optimized Organic Rankine Cycle design solutions with toluene

Designs with toluene	PL-140	PR-140	PL-110	PR-110	PL-80	PR-80
Evaporation pressure, kPa	2578.91	2190.1	2757.14	2136	1706.96	998.7
Evaporation temperature (dependent variable), K	551.38	535.4	559.61	540.52	496.98	489.9
Condenser thermal power (cycle size), kW	5144.74	5300	4709.4	5300	4702.74	5300
Superheating degree, K	11.85	29.8	7.82	31.63	38.58	75.0
Pinch-point temp. diff. PrHE, K	2.72	1.0	2.52	1	5.01	8.3
Pinch-point temp. diff. regenerator, K	4.8	4.67	7.84	7.34	21.47	20.1
Condenser pressure, kPa	59.51	41.05	55.29	44.93	137.67	66.79
Pinch point temp. diff. of condenser (dependent variable), K	13.43	2.09	11.41	5	44.02	18.43
Turbine rotational speed, RPM	20,000	20,000	20,000	20,000	19,862	20,000
Number of turbine stages (dependent variable)	2	2	2	2	1	1
Pressure ratio of first stage	4.76	5.139	5.77	4.86	12.40	18.081
Pressure ratio of second stage	9.1	10.381	8.64	9.77	—	—
Nominal electric efficiency (design load), %	18.07	21.01	19.38	20.60	13.06	15.04
Nominal power output (design load), kW	1394.7	1706.5	1358.8	1661.4	830.13	1110.90
Fuel thermal input LHV basis (design load), kW	7720.4	8122.1	7012.2	8065.4	6358.64	7384.51
ORC mass flow rate (design load), kg/s	13.52	13.69	11.65	13.62	12.10	13.25
Oil mass flow rate (design load), kg/s	60.25	48.87	78.43	46.91	22.46	29.05
Investment cost, k€	5071.2	5346.0	4807.0	5261.4	4159.39	4.593
Actual annual profit (part-load operation), k€/year	632.63	611.16	453.37	414.22	284.76	233.53
Actual payback time, years	9	9	12	13	15	18

A comparison between designs “PR” computed in [Martelli et al. \(2015\)](#), considering the full-load equivalent hours of the heat user, and designs “PL” determined with the two-stage algorithm for the simultaneous optimization of design and part-load operation is presented. Note that the actual annual profit has been estimated by simulating the annual part-load operation of the ORC plant indicated by the heat-demand duration curve. *ORC*, Organic Rankine Cycle; *LHV*, lower heating value; *PrHE*, primary heat exchanger.

evaporation pressure so as to extend the load range in which the sliding-pressure mode can be adopted.

Thanks to the aforementioned expedients, the ORC plant designs optimized considering also part-load operation lead to a considerably higher annual profit (up to 22% higher) compared to the designs optimized considering only full-load operation for the given number of equivalent hours.

7.3.3 Multiobjective optimization of Organic Rankine Cycles in offshore waste heat recovery applications

As discussed earlier, ORCs are particularly suitable for WHR from industrial processes. An interesting application is their use in offshore oil and gas (O&G) platforms. The majority of O&G facilities use medium-size gas turbines to supply the electricity on board. The main design criterion is the plant reliability because a failure of the power system entails an enormous economic loss for the platform operator. Compactness, low weight, and dynamic flexibility are crucial aspects to minimize the installation costs. Thereby, the yearly energy conversion efficiency of offshore power stations is typically low, ranging between 20% and 30%. Given their high modularity and simplicity, ORCs have been proposed to recover the thermal energy of offshore gas turbines.

In most studies available in the literature, i.e., (Bhargava, 2014; Pierobon, 2013), a performance indicator (net power output or thermal efficiency) is optimized considering the working fluid and cycle parameters as optimization variables. However, such approach is often inadequate for offshore applications. Other criteria, e.g., the volume and weight of the WHR unit or the economic revenue, are as important as or even more than the performance of the system itself. Therefore, a multiobjective optimization approach is more effective to design the ORC as the resulting Pareto front allows the plant designer to select the system layout giving the best compromise between the objective functions.

This optimization approach has been used by Pierobon (2014) for the design of an ORC unit enhancing the energy conversion efficiency of the Draugen offshore O&G platform, located 150 km from Kristiansund, in the Norwegian Sea. As shown in Fig. 7.21, the power station comprises three SGT500 gas turbines for a total capacity of 50 MW. To enhance the reliability and diminish the risk of failure of the power system, two turbines run at a time, covering 50% of the load each. The third one is kept on standby, allowing for maintenance work. Despite the low performance, this strategy ensures the necessary reserve power for peak loads and the safe operation of the engines.

For this case study, suitable objective functions are the NPV, the weight (or the volume) of the ORC unit, and the CO₂ emissions. Accordingly, the set of optimization variables shall comprise both cycle parameters, e.g., condensing and evaporating pressure, and geometric quantities related to the components design, e.g., tube length and tube diameter. This approach allows estimating the weight and dimensions of the ORC unit. Part-load models can be used to evaluate the CO₂ emissions over the entire year

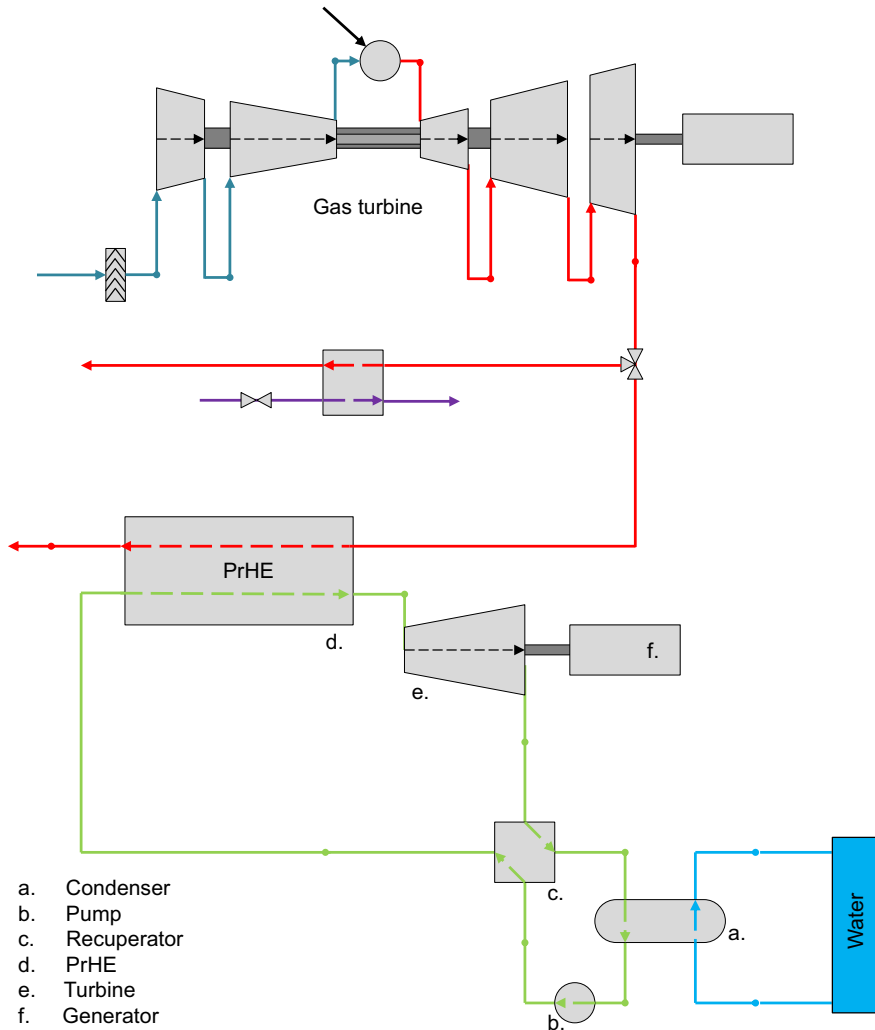


Figure 7.21 Simplified layout of the power system on the Draugen offshore oil and gas platform. The organic Rankine cycle module recovers the thermal power released with the exhaust gases of one engine, in this case gas turbine A. *PrHE*, primary heat exchanger.

and the profitability of the investment. The reader can refer to [Pierobon \(2014\)](#) for a theoretical and mathematical description of the optimization problem.

[Fig. 7.22](#) shows the steps of the optimization process. The routine starts by acquiring the array of parameters and the first set of optimization variables. Subsequently, the cycle calculation is performed by evaluating the thermodynamic states at the inlet and at the outlet of each component. The pressure drops in the heat exchangers are initially neglected. At this point, the heat exchangers are designed. Thus, the pressure drops and the component weights can be estimated. The cycle

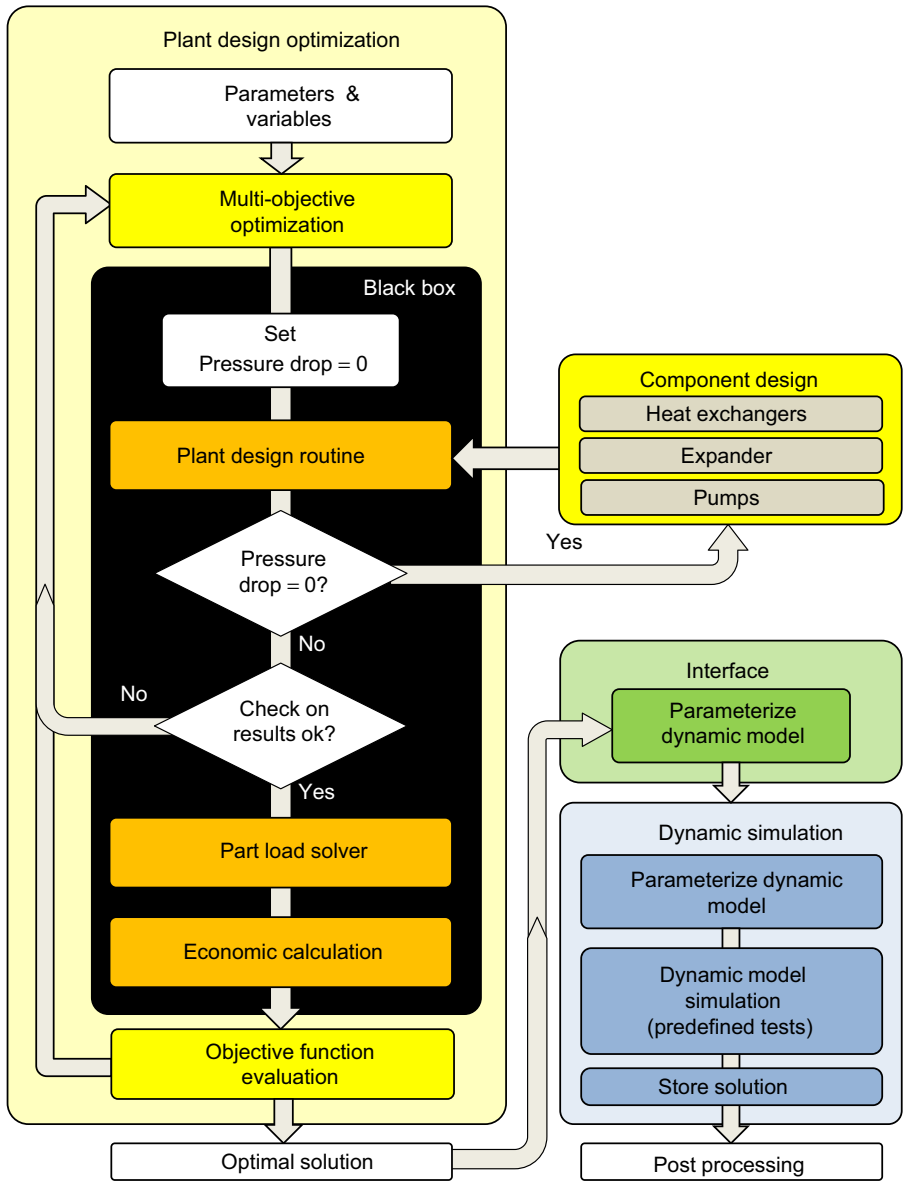


Figure 7.22 Multiobjective optimization approach. The results of the design optimization can be used as inputs for the dynamic simulations of the power system. *HE*, heat exchanger; *S&T*, shell and tube.

calculation is thus run again accounting for the pressure losses in the heat exchangers. The results are then checked with respect to the first and second principle of thermodynamics. If the test on the results is positive, a yearly part-load simulation is

performed to compute the CO₂ emissions and the NPV. The process continues until the average change in the spread of the Pareto front is lower than the specified tolerance. The constraints on the dependent variables, e.g., the fluid velocities in the heat transfer equipment, can be treated as barrier functions by properly accounting for their contribution in the objective functions.

Fig. 7.23 shows the results of such optimization approach. A two-dimensional prospect of the Pareto fronts is given for six working fluids. Each point in the Pareto front corresponds to an optimal design of the ORC system. The average daily CO₂ emissions of the offshore power station are related to the weight of the ORC module. All curves present a hyperbolic trend. Larger heat transfer areas (i.e., weight) allow recuperating more heat from the gas turbine. Moreover, the heat transfer irreversibility is lowered, thus improving the energy conversion efficiency of the power system. The curve is, however, nonlinear. At the extremes of the graphs, small increments in one variable give large variations of the second metric. On the rightmost side, this is because the heat transfer area of the heat exchangers grows hyperbolically with the logarithmic mean temperature difference. Such variable relates to the optimization parameters and strongly affects the thermal efficiency of the combined cycle unit. Therefore, a small increment in performance entails a much higher weight of the WHR module.

Fig. 7.24 shows the trends relating the NPV to the weight of the ORC unit for each fluid candidate. The graph shows the presence of a design for which the economic revenue is maximized. Each curve starts with a relatively steep positive gradient. After the maximum NPV is achieved, the curves drop linearly, showing lower economic revenues. The NPV is a function of the plant cost and the value associated with the fuel savings. Starting from low weights, small increases in energy conversion efficiency of the power station improve the NPV significantly. Subsequently, enhancing the performance of the bottoming cycle modules is not beneficial as the total investment cost becomes excessively large.

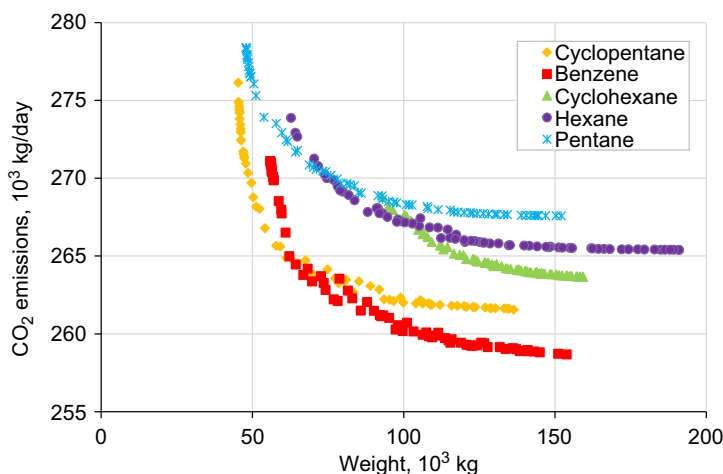


Figure 7.23 Pareto fronts for six working fluids. The CO₂ emissions (first objective function) are related to the weight of the organic Rankine cycle module (second objective function).

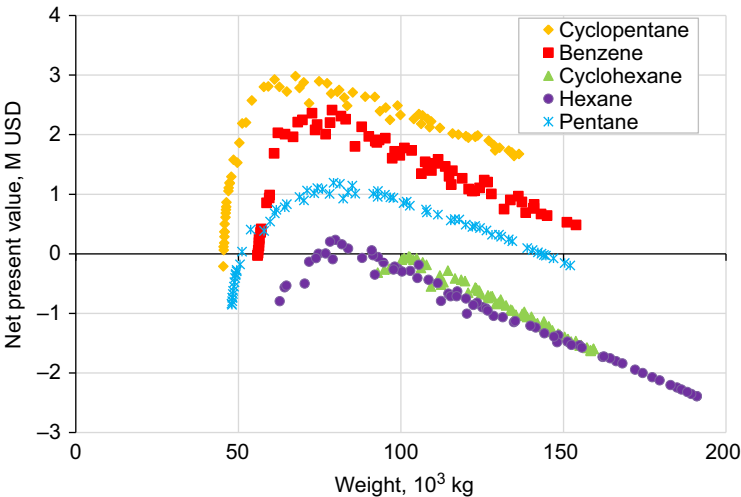


Figure 7.24 Pareto fronts for six working fluids. The net present value (third objective function) is related to the weight of the organic Rankine cycle module (second objective function).

This case study shows that the multiobjective optimization, here solved using the NSGA-II procedure, is a valuable approach to define the optimal working fluids and the ORC design when a number of conflicting criteria have to be satisfied. In the case study, the optimal design should be the one giving the highest NPV. On the other hand, having a Pareto frontier allows selecting the optimal design based on other indicators, e.g., a weight constraint and/or a desired level of system performance. This approach can be extended further to include dynamic criteria in the design phase or to understand the effect of the optimization variables on the plant dynamics. For instance, one may test the dynamic response of the system for each design of the Pareto. This enables assessing the dynamic flexibility of the power station for different designs of the WHR unit. In this way, design candidates that do not respect transient metrics, e.g., rise time, can be excluded already in the design phase, thus avoiding problems during commissioning; see [Pierobon et al. \(2014\)](#).

Acronyms

BOP	balance of plant
bs	bottom stream
CFC	chlorofluorocarbons
CHP	combined heat and power
Cs	specific cost, USD/kW _{el}

EoS	equation of state
GWP	global warming potential
HFC	hydrofluorocarbons
HP	high pressure
HS	heat source
HTF	heat transfer fluid
IRR	internal rate of return
LCOE	levelized cost of electricity, USD/MWh or USD/kWh
LP	low pressure
ms	medium stream
NPV	net present value
ODP	ozone depletion potential
ORC	organic Rankine cycle
PB	power block
PrHE	primary heat exchanger
RPM	rotations per minute
ts	top stream
USD	US dollar
WHR	waste heat recovery

Nomenclature

C	cost, USD
p	pressure, bar
Q	thermal power, kW or MW
rec/no-rec	recuperative/nonrecuperative cycle configuration
s	specific entropy, kJ/kgK
SA	saturated or slightly superheated cycle
SH	superheated cycle
SP	stage size parameter, m
Sub	subcritical cycle

Continued

Sup	supercritical cycle
T	temperature, °C
W	power, kW or MW
η	efficiency

Subscripts

amb	ambient conditions
ap	approach point
cond	condensation (condition) or condenser (plant component)
crit	critical condition
des	desuperheating section of condenser (plant component)
eco	economizer (plant component)
el	electrical
eva	evaporation (conditions) or evaporator (plant component)
exp	expansion
II	second law
in	inlet condition
is	isentropic process
lim	limit in reinjection condition
loss	dispersion to the environment
mec	mechanical
mln	mean logarithmic
PrHE	primary heat exchanger
pp	pinch point
r	ratio
rec	recovery (efficiency) or regenerator (plant component)
sc	subcooling
sh	superheater (plant component)
th	thermal
wf	working fluid

References

- Aimin, Z., Bo-Yang, Q., Li, H., Shi-Zheng, Z., Ponnuthurai, N.S., Zhang, Q., 2011. Multi-objective evolutionary algorithms: a survey of the state of the art. *Swarm and Evolutionary Computation* 1 (1) s.l.
- AspenPlus, [Online]. www.aspentech.org.
- Astolfi, M., Romano, M., Bombarda, P., Macchi, E., 2014a. Binary Orc power plants for the exploitation of medium-low temperature geothermal sources. Part A thermodynamic optimization. *Energy* 66.
- Astolfi, M., Romano, M., Bombarda, P., Macchi, E., 2014b. Binary Orc power plants for the exploitation of medium-low temperature geothermal sources. Part B techno-economic optimization. *Energy* 66 s.l.
- Astolfi, M., 2013. An Innovative Approach for the Techno Economic Optimization of Organic Rankine Cycles (Ph.D. thesis). s.l.
- Astolfi, M., 2014. Techno-economic optimization of low temperature CSP systems based on ORC with screw expanders. *Energy Procedia* 69 s.l.
- Audet, C., Dennis, J.E., 2003. Analysis of generalized pattern searches. *SIAM Journal on Optimization* 13.
- Audet, C., Dennis, J.E., 2006. Mesh adaptive direct search algorithms for constrained optimization. *SIAM Journal on Optimization* 17 (2), 188–217 s.l.
- Bhargava, R.K., 2014. Thermo-economic evaluation of ORC system in off-shore applications. In: *ASME Turbo Expo 2014: Turbine Technical Conference and Exposition*. American Society of Mechanical Engineers s.l.
- Biegler, L.T., Cuthrell, J.E., 1985. Improved infeasible path optimization for sequential modular simulators – II: the optimization algorithm. *Computers and Chemical Engineering* 9 s.l.
- Biegler, L.T., Grossmann, I.E., Westerberg, A.W., 1997. *Systematic Methods of Chemical Process Design*. Prentice Hall.
- Bivens, D.B., Yokozeki, A., 1992. *Heat Transfer of Refrigerant Mixtures*. Purdue: s.n.
- Bombarda, P., 2011. *Estimating Cost of the Geothermal Power Technologies: Main Aspects and Review*. Bruxelles: s.n.
- Box, M.J., 1965. A new method of constrained optimization and a comparison with other methods. *Computer Journal* 8 (1) s.l.
- CAPCOST, [Online]. <http://www.capcost.ca/>.
- Capra, F., Martelli, E., 2015. Numerical optimization of CHP Organic Rankine Cycles – Part B: simultaneous design & part-load optimization. *Energy* 90 (Part 1), 329–343 s.l.
- Casati, E., Galli, A., Colonna, P., 2013. Thermal energy storage for solar-powered organic Rankine cycle engines. *Solar Energy* 96 s.l.
- Chen, C.L., Li, P.Y., Chen, H.C., Lee, J.Y., 2015. Synthesis of transcritical ORC-integrated heat exchanger networks for waste heat recovery. In: *12th International Symposium on Process Systems Engineering and 25th European Symposium on Computer Aided Process Engineering*. Elsevier: s.l (Vol. part A).
- Coello, C.A., Cortés, N.C., 2005. Solving multiobjective optimization problems using an artificial immune system. *Genetic Programming and Evolvable Machines* 6 (2) s.l.
- Conn, A.R., Scheinberg, K., Vicente, L.N., 2009. *Introduction to Derivative Free Optimization*. MPS-SIAM Series on Optimization: s.l.
- Dai, Y., Wang, J., Gao, L., 2009. Parametric optimization and comparative study of organic rankine cycle (ORC) for low grade waste heat recovery. *Energy Conversion and Management* 50, 576–582 s.l.

- Das, I., Dennis, J.E., 1998. Normal-boundary intersection: a new method for generating the Pareto surface in nonlinear multicriteria optimization problems. *SIAM Journal on Optimization* 8, 631–657 s.l.
- Dymola, [Online]. www.dymola.com.
- EES software, [Online]. <http://www.fchart.com/ees/>.
- EPRI. TAG, June 1993. Technical Assessment Guide (Electric Supply). Electric Power Research Institute, Palo Alto. EPRI Report TR-102275.
- Gatti, M., Martelli, E., Maréchal, F., Consonni, S., 2014. Multi-objective optimization of a Rectisol process. *Computer Aided Chemical Engineering* 33, 1249–1254 s.l.
- Gerber, L., Marechal, F., 2012. Environomic optimal configurations of geothermal energy conversion systems: application to the future construction of Enhanced Geothermal Systems in Switzerland. *Energy* 45, 908–923 s.l.
- Gilmore, P., Kelley, C.T., 1995. An implicit filtering algorithm for optimization of functions with many local minima. *SIAM Journal on Optimization* 5 s.l.
- Goldberg, D.E., 1989. *Genetic Algorithms in Search, Optimization & Machine Learning*. Addison-Wesley: s.l.
- Green, D.W., 1997. *Perry's Chemical Engineers' Handbook*, seventh ed. Mc-Graw Hill: s.l.
- Gu, J., Bart, H.-J., 1999. Decrement estimation of the heat transfer coefficient in mixture boiling. *The Canadian Journal of Chemical Engineering* 77 s.l.
- Guthrie, K.M., 1969. Data and techniques for preliminary capital cost estimating. *Chemical Engineering* 24.
- Guthrie, K.M., 1974. *Process Plant Estimating Evaluation and Control*. Craftsman Book Co., Solana Beach.
- Hansen, N., Muller, S.D., Koumoutsakos, P., 2003. Reducing the time complexity of the derandomized evolution strategy with covariance matrix adaptation (CMA-ES). *Evolutionary Computation* 11 (1), 1–18 s.l.
- Hattiangadi, A., 2013. *Working Fluid Design for Organic Rankine Cycle (ORC) Systems* (thesis). TU Delft.
- Hedar, A.R., Fukushima, M., 2004. Derivative-free filter simulated annealing method for constrained continuous global optimization. *Journal of Global Optimization* 35 (4), 521–549 s.l.
- Hettiarachchi, H.D.M., Golubovic, M., Worek, W.M., Ikegami, Y., 2007. Optimum design criteria for an Organic Rankine Cycle using low-temperature geothermal heat sources. *Energy* 32, 1698–1706 s.l.
- Holland, J., 1975. *Adaptation in Natural and Artificial Systems*. University of Michigan Press, Ann Arbor.
- Honeywell, [Online] Solstice-yf data sheet. www.honeywell.com.
- Hu, X., Eberhart, R., 2002. Solving constrained nonlinear optimization problems with particle swarm optimization. In: *Proceedings of the 6th World Multiconference on Systemics, Cybernetics and Informatics*. Orlando, USA.
- Huyer, W., Neumaier, A., 1999. Global optimization by multilevel coordinate search. *Journal of Global Optimization* 14, 331–355 s.l.
- Igel, C., Hansen, N., Roth, S., 2007. Covariance matrix adaptation for multi-objective optimization. *Evolutionary Computation* 15 (1) s.l.
- Invernizzi, C., Angelino, G., 2003. Experimental investigation on the thermal stability of some new zero ODP refrigerants. *International Journal of Refrigeration* 26, 51–58.
- Invernizzi, C., Bombarda, P., 1997. Thermodynamic performance of selected HCFs for geothermal applications. *Energy* 22, 887–895 s.l.
- Invernizzi, C., Iora, P., Silva, P., 2007. Bottoming micro-Rankine cycles for micro-gas turbines. *Applied Thermal Engineering* 27, 100–110 s.l.

- Jones, D., Perttunen, C., Stuckman, B., 1993. Lipschitzian optimization without the Lipschitz constant. *Journal of Optimization Theory and Application* 79, 157–181 s.l.
- Jones, B., 2009. *Fundamentals of Fire Fighting Skills*, second ed. National Fire Protection Association, Sudbury, MA.
- Kaelo, P., Ali, M.M., 2006. Some variants of the controlled random search algorithm for global optimization. *Journal of Optimization Theory and Applications* 130 (2) s.l.
- Kalyanmoy, D., 2000. A Fast Elitist Non-dominated Sorting Genetic Algorithm for Multi-objective Optimization: NSGA-II. *Parallel Problem Solving from Nature PPSN VI*. Springer Berlin Heidelberg: s.l.
- Kalyanmoy, D., 2001. *Multi-objective Optimization Using Evolutionary Algorithms*, 16. John Wiley & Sons: s.l.
- Kolda, T.G., Lewis, R.M., Torczon, V., 2003. Optimization by direct search: new perspectives on some classical and modern methods. *SIAM Review* 45, 385–482 s.l.
- Kolda, T.G., Lewis, R.M., Torczon, V., 2006a. Stationarity results for generating set search for linearly constrained optimization. *SIAM Journal on Optimization* 17, 943–968 s.l.
- Kolda, T.G., Lewis, R.M., Torczon, V., 2006b. A Generating Set Direct Search Augmented Lagrangian Algorithm for Optimization with a Combination of General and Linear Constraints s.l, SANDIA Report SAND2006–5315.
- Kuppan, T., 2000. *Heat Exchanger Design Handbook*. Marcel Dekker Inc.
- Lakew, A., Bolland, O., 2010. Working fluids for low-temperature heat source. *Applied Thermal Engineering* 30, 1262–1268 s.l.
- Lampe, M., Stavrou, M., Gross, J., Bardow, A., 2013. Integrated process and working fluid optimization for Organic Rankine Cycle (ORC) using PC-SAFT. In: *2nd International Seminar on ORC Power Systems*. Rotterdam.
- Le Digabel, S., Wild, S., 2015. A Taxonomy of Constraints in Simulation-Based Optimization. *Les cahiers du GERAD*: s.l vols G-2015-57.
- Loth, H.P., Lysons, J., White, C.W., 2002. *Process Equipment Cost Estimation – Final Report*. Department of Energy – United States of America: s.l.
- Marler, R.T., Arora, J.S., 2004. Survey of multi-objective optimization methods for engineering. *Structural and Multidisciplinary Optimization* 26, 369–395 s.l.
- Martelli, E., Amaldi, E., 2014. PGS-COM, a hybrid method for non-smooth black-box constrained optimization. *Computers and Chemical Engineering* 63.
- Martelli, E., Amaldi, E., Consonni, S., 2011. Numerical optimization of heat recovery steam cycles: mathematical model, two-stage algorithm and applications. *Computers & Chemical Engineering* 35 (12) s.l.
- Martelli, E., Capra, F., Consonni, S., 2015. Numerical optimization of CHP organic rankine cycles – Part A: design optimization. *Energy* 90 s.l.
- Messac, A., et al., 2000. Ability of objective functions to generate points on nonconvex Pareto frontiers. *AIAA Journal* 38, 1084–1091 s.l.
- Messac, A., Ismail-Yahaya, A., Mattson, C.A., 2003. The normalized normal constraint method for generating the Pareto frontier. *Structural and Multidisciplinary Optimization* 25, 86–98 s.l.
- Michalewicz, Z., Nazhiyath, G., 1995. Co-evolutionary algorithm for numerical optimization with nonlinear constraints. *Proceedings of the Second IEEE International Conference on Evolutionary Computation* 647–651. IEEE Press: s.l.
- Mian, A., Martelli, E., Marechal, F., 2015. Framework for the multiperiod sequential synthesis of heat exchanger networks with selection, design, and scheduling of multiple utilities. *Industrial & Engineering Chemistry Research* 55, 168–186 s.l.

- Miettinen, M., Norwell, M., 1999. *Nonlinear Multiobjective Optimization*. Kluwer Academic Publisher, Massachusetts.
- Modelica, [Online]. www.modelica.org.
- Nelder, J.A., Mead, R., 1965. A simplex method for function minimization. *The Computer Journal* 7 s.l.
- NETL, 2011. *Quality Guidelines for Energy System Studies. Cost Estimation Methodology for NETL Assessments of Power Plants Performance*. U.S. Department of Energy.
- Nocedal, J., Wright, S.J., 2006. *Numerical Optimization*, second ed. Springer Series in Operations Research. Springer Verlag: s.l.
- Nord, L.O., Martelli, E., Bolland, O., 2014. Weight and power optimization of steam bottoming cycle for offshore oil and gas installations. *Energy* 76, 891–898 s.l.
- Papadopoulos, A., Linke, C., Stijepovic, M., Seferlis, P., Voutetakis, S., 2011. Computer-aided design and selection of optimum working fluids and ORC systems for power generation from low enthalpy heat sources. Delft. In: 1st International Seminar in ORC Power Systems.
- Pierobon, L., et al., 2014. Design methodology for flexible energy conversion systems accounting for dynamic performance. *Energy* 68 s.l.
- Pierobon, L., Nguyen, T.-V., Larsen, U., Haglind, F., Elmegaard, B., 2013. Multi-objective optimization of organic Rankine cycles for waste heat recovery: application in an offshore platform. *Energy* 58, 538–549 s.l.
- Pierobon, L., 2013. Optimization of organic Rankine cycles for off-shore applications. In: ASME Turbo Expo 2013: Turbine Technical Conference and Exposition. American Society of Mechanical Engineers: s.l.
- Pierobon, L., 2014. *Novel Design Methods and Control Strategies for Oil and Gas Offshore Power Systems*. Technical University of Denmark (Danmarks Tekniske Universitet), Department of Mechanical Engineering (Institut for Mekanisk Teknologi), Thermal Energy (Termisk Energi): s.l.
- Price, W.L., 1983. Global optimization by controlled random search. *Journal of Optimization Theory and Application* 40 (3) s.l.
- Quoilin, S., Orosz, M., Hemond, H., Lemort, V., 2011a. Performance and Design optimization of a low-cost solar organic Rankine cycle. *Solar Energy* 85, 955–966 s.l.
- Quoilin, S., Declaye, S., Tchanche, B.F., Lemort, V., 2011b. Thermo-economic optimization of waste heat recovery Organic Rankine Cycles. *Applied Thermal Engineering* 31, 2885–2893 s.l.
- Rios, L., Sahinidis, N., 2013. Derivative-free optimization: a review of algorithms and comparison of software implementations. *Journal of Global Optimization* 56 (3), 1247–1293 s.l.
- Romeijn, H.E., Smith, R.L., 1994. Simulated annealing for constrained global optimization. *Journal of Global Optimization* 5 (2) s.l.
- Rossi, N., 2013. Testing of a new supercritical ORC technology for efficient power generation from geothermal low temperature resources. In: *Proceedings of ASME ORC 2013 Conference*. Rotterdam.
- Sarker, R., Abbass, H., 2004. Differential evolution for solving multi-objective optimization problems. *Asia Pacific Journal of Operational Research* 21 (2) s.l.
- Schuster, A., Karellas, S., Aumann, R., 2010. Efficiency optimization potential in supercritical organic Rankine cycles. *Energy* 35, 1033–1039 s.l.
- Shah, R.K., Sekulic, D.P., 1998. Chapter 17-Heat exchangers. In: Hartnett, J.P., Cho, Y.I., Rohsenow, W.M. (Eds.), *Handbook of Heat Transfer*. McGraw-Hill, New York.

- Shengjun, Z., Huaixin, W., Tao, G., 2011. Performance comparison and parametric optimization of subcritical Organic Rankine Cycle (ORC) and transcritical power cycle system for low-temperature geothermal power generation. *Applied Energy* 88 s.l.
- Simon, D., 2013. *Evolutionary Optimization Algorithms*. Wiley: s.l, ISBN 978-0-470-93741-9.
- Smith, I.K., Stosic, N., Kovacevic, A., 2005. An improved system for power recovery from higher enthalpy liquid-dominated fields. In: *Proceedings World Geothermal Congress* s.l.
- Smith, I.K., 1994. Development of the trilateral flash cycle system Part 2: increasing power output with working fluid mixtures. In: *Proceedings of the Institution of Mechanical Engineers, Part A: Journal of Power and Energy* s.l.
- Smith, I.K., 1993. Development of the trilateral flash cycle system Part 1: fundamental considerations. In: *Proceedings of the Institution of Mechanical Engineers Part A: Journal of Power and Energy* s.l.
- Takahama, T., Sakai, S., 2006. Constrained optimization by the ϵ constrained differential evolution with gradient-based mutation and feasible elites. In: *Proceedings of the Second IEEE International Conference on Evolutionary Computation* s.l.
- Tańczuk, M., Ulbrich, R., 2013. Implementation of a biomass-fired co-generation plant supplied with an ORC (Organic Rankine Cycle) as a heat source for small scale heat distribution system — a comparative analysis under Polish and German conditions. *Energy* 62 s.l.
- Tchanche, B.F., Lambrinos, G., Frangoudakis, A., Papadakis, G., 2009. Low-grade heat conversion into power using organic Rankine cycles — a review of various applications. *Renewable and Sustainable Energy Reviews* 15, 3963–3979, s.l.
- The MathWorks, Inc. MATLAB Version 8.1.0.604, 2013. Natick: s.n.
- Thermo Power, [Online]. www.thermopower.sourceforge.net.
- Thermoflex, [Online]. www.thermoflex.com.
- Turton, R., Bailie, R.C., Whiting, W.B., Shaeiwitz, J.A., Bhattacharyya, D., 2012. *Analysis, Synthesis, and Design of Chemical Processes*, fourth ed. Prentice Hall: s.l.
- Ulrich, G.D., 1984. *A Guide to Chemical Engineering Process Design and Economics*. John Wiley and Sons, New York.
- Vaz, A.I.F., Vicente, L.N., 2009. PSwarm: a hybrid solver for linearly constrained global derivative-free optimization. *Optimization Methods and Software* 24, 669–685 s.l.
- Wah, B.W., Wang, T., 1999. Constrained simulated annealing with applications in nonlinear continuous constrained global optimization. In: *Proceedings of the IEEE International Conference on Tools with Artificial Intelligence* s.l.
- Walraven, D., Laenen, B., D'haeseleer, W., 2012. Comparison of thermodynamic cycles for power production from low-temperature geothermal heat sources. *Energy Conversion and Management* s.l.
- Walraven, D., Laenen, B., D'haeseleer, W., 2014. Optimum configuration of shell-and-tube heat exchangers for the use in low-temperature organic Rankine cycles. *Energy Conversion and Management* 83 s.l.
- Wang, Y., Yang, Y., 2009. Particle swarm optimization with preference order ranking for multi-objective optimization. *Information Sciences* 179 (12) s.l.
- Wang, J., Yan, Z., Wang, M., Li, M., Dai, Y., 2013. Multi-objective optimization of an organic Rankine cycle (ORC) for low grade waste heat recovery using evolutionary algorithm. *Energy Conversion and Management* 71 s.l.
- Zhang, F.Z., Jiang, P.X., 2012. Thermodynamic analysis of a binary power cycle for different EGS geofluid temperatures. *Applied Thermal Engineering* 48, 476–485 s.l.

Fluid dynamic design of Organic Rankine Cycle turbines

8

G. Persico¹, M. Pini²

¹Politecnico di Milano, Milan, Italy; ²Delft University of Technology, Delft, The Netherlands

8.1 Introduction

Organic Rankine Cycle (ORC) power systems are nowadays a mature and cost-effective technology for the efficient exploitation of energy sources characterized by low-to-medium temperature levels (Colonna et al., 2015). For source temperature levels below 350°C (Colonna et al., 2015; Gaia, 2011), the adoption of molecularly complex and heavy organic fluids instead of steam opens the way for the technical implementation of the Rankine Cycle, simplifying the design of the components (especially the turbo-expander) and the assembly of whole system. This makes these sources exploitable with a cost-competitive and reliable technology (Verneau, 1978; Angelino et al., 1984). As widely documented in the literature (Macchi, 2013), the expander crucially influences the performance, the power control capability, and the cost (capital and operative) of the overall ORC power system.

For the typical power size of ORCs, which ranges from a few kW_{el} up to some MW_{el}, the selected machine is usually a turbine [for smaller scale ORCs volumetric machines could also be considered (Oudkerk et al., 2013)]. Therefore, once the thermodynamics of the fluid expansion is defined, the design of the expander has to rely on turbomachinery aerodynamics. From this perspective, ORC turbines often present highly unconventional configurations, since the specific character of organic fluids has a dramatic effect on the turbine flow physics and performance. These features need to be carefully considered in the design phase.

As a general consideration, the specific enthalpy drop along the turbine expansion line is inversely proportional to the molecular weight of the fluid. This determines some relevant advantages in case of organic fluids. At first, the specific work exchange required to the turbine is relatively small (with respect to corresponding steam units) and can be disposed in a single or a few stages; this leads to compact turbomachinery configurations, providing layout simplifications and cost savings. A second advantage stands out for small capacity systems, as the target power output can be achieved with a relatively large mass flow rate, resulting in larger turbine size with respect to the miniaturized configurations of the corresponding steam ones (Quoilin et al., 2013).

Despite the small enthalpy drop, the expansion ratio remains very large. As a result, the low number of stages is beneficial for the machine size but implies a high expansion ratio per stage; in organic fluids, the high expansion ratio couples

with a generally low speed of sound, leading to transonic and supersonic turbines in ORC power systems. As a result, shock waves and choked flow conditions commonly affect ORC turbine aerodynamics, complicating the design and operation of ORC systems.

The complexity of the ORC turbine design is further amplified by the nonideal thermo-physical behavior of organic fluids in the conditions of interest. Part of the expansion process usually takes place in close proximity to the saturated vapor curve or even close to the critical point. In such thermodynamic conditions, severe real gas effects arise and complex multiparameter equations of state are necessary for a proper description of the caloric and volumetric characteristics of the fluid, as well as for the accurate estimate of transport properties.

For the reasons discussed above, the fluid-dynamic design of ORC turbines is particularly challenging, and it is further complicated by the very few available experimental data regarding flows of organic fluids, especially in the thermodynamic conditions of interest.¹ In this context, simplified design tools based on empirical loss models and flow angle correlations are still relevant in the preliminary design phase, but should be combined to advanced design techniques based on high-fidelity flow models to achieve reliable prediction of turbine performance. These advanced tools are especially crucial to obtain the highest turbine performance in both design and off-design conditions.

The design path of ORC turbines offers optimization challenges at many levels, and proceeds step-by-step as the fidelity level (and complexity) of the computational model increases. The final turbine layout is then usually a complex combination of the outcomes provided by each optimization step, starting from the preliminary choice of the machine architecture and of the stage arrangement (Pini et al., 2013), to the through-flow design (Petrovic et al., 2001; Larocca, 2008; Pasquale et al., 2013), up to the detailed blade shape definition (Pierret & Van Den Braembussche, 1999; Rai, 2000). Thanks to the progressive increase of computational capability and the recent development of optimization techniques, both low-fidelity (for preliminary design) and high-fidelity (for aerodynamic design) solution methods can now be applied systematically within optimization algorithms to identify the best configuration at each level of the design path. An analysis of the machine with the most realistic flow model, including three-dimensional flow structures, turbulence effects, and (possibly) unsteadiness, finally assesses the entire procedure.

The end-to-end fluid-dynamic design process for an ORC turbine is schematically depicted in Fig. 8.1, which also serves as an outline for the present chapter. The present essay reviews all the design steps, in their basic concepts and formulations, highlighting the specific features required by their application in the ORC context. The rational connection between the preliminary design methods and the most advanced shape optimization tools in searching for the optimal turbine configuration is discussed, providing examples of ORC turbine design.

¹ Systematic experiments on supersonic flows on organic fluids have been performed only very recently (Spinelli et al., 2013).

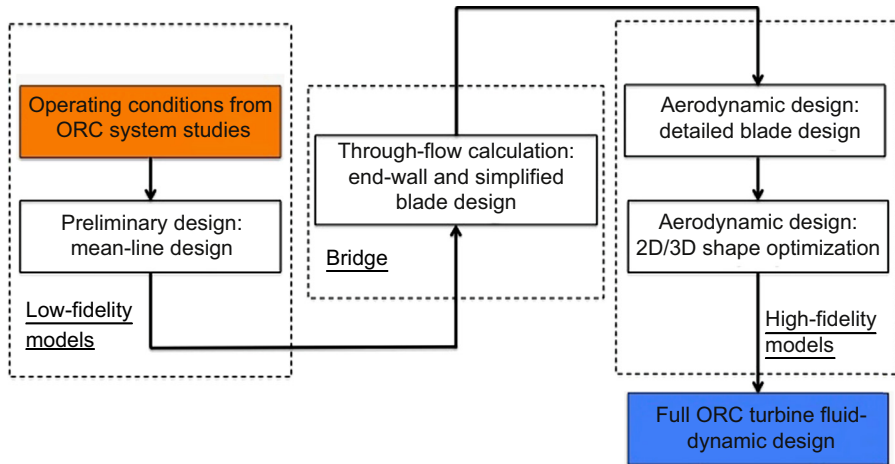


Figure 8.1 Schematic of the fluid-dynamic design process for an Organic Rankine Cycle (ORC) turbine.

8.2 Review of Organic Rankine Cycle turbine architectures

Over the years, the flexibility and scalability of turbo-expanders led to a multiplicity of configurations, which make them adaptable in diverse branches of applications. However, in some application areas the variety of possible architectures is not entirely exploited. For instance, while hydraulic turbine technology includes impulse and partial admission machines (Pelton), reaction radial machines (Francis, Deriaz) and reaction axial machines (Kaplan, bulb), for steam and gas turbines the multistage axial-flow configuration covers the largest share of the market² (even though the radial-inflow turbine is preferred in specific application areas, such as that of micro gas turbines).

This consideration is not valid for ORC Power Systems. ORCs are applied for the exploitation of diverse energy sources, including waste heat and renewables, featuring a wide range of operational conditions; therefore, several configurations were historically adopted for the power plant and, especially, for the turbine. The application range is so large that also volumetric expanders are presently considered for very small capacity systems (that, however, is not discussed in this essay).

ORC turbine technology has always included both radial inward machines (Hoffren et al., 2002) and axial-flow machines (Gaia, 2011; Verneau, 1978; Colonna et al., 2008), and recently, the novel multistage radial-outward configuration has been proposed (Spadacini et al., 2011; Pini et al., 2013; Casati et al., 2014) and successfully

² As a matter of fact, the target in the steam and gas turbine technology is large power concentration, and the axial-flow turbine best matches the related combined requirements of large flow rate and large enthalpy drop.

implemented. If a design paradigm has to be chosen for ORC turbines, this has to be found in the small enthalpy drop across the whole machine and the low speed of sound of the fluid; these two main features lead to compact machines characterized by a low number of stages and highly supersonic flows. A rough classification is proposed in the following, on the basis of the open literature only, bearing in mind that the indications reported cannot cover the whole technical scenario, and counter-examples might be found.

8.2.1 Radial-inward or centripetal turbines

For low electric power output (from tens to hundreds of kW_{el}), but with some relevant examples of machines reaching a few MW_{el} of power capacity for geothermal applications, whose ORC turbines feature relatively low fluid volume ratios), the combined effect of low work exchange and low flow rates suggests the selection of single-stage radial inward machines (Fig. 8.2), characterized by a centripetal stator and a centripetal (or mixed-flow) rotor. The very large expansion ratio (which may reach the order of 100 in some applications) can be divided only between the two cascades, normally keeping a low reaction degree to avoid extreme flow conditions in the rotor blade row. This implies highly supersonic flows at the stator exit (Mach number greater than 2.5), requiring converging–diverging blade configurations (Hoffren et al., 2002; Marconcini et al., 2012; Rinaldi et al., 2015). The design of converging–diverging centripetal stators is critical; classical techniques developed for supersonic plane or cylindrical nozzles can be adapted to radial turbine configuration (Uusitalo et al., 2014), even though strong shocks may establish in the semibladed diverging region and at the trailing edge. However, this methodology represents a crucial step for the aerodynamic design process, as profiles constructed in this way provide a baseline configuration for the application of systematic shape

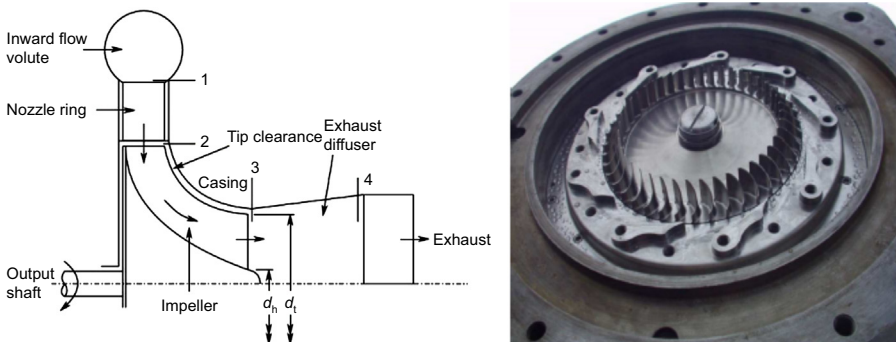


Figure 8.2 Meridional scheme (left) and picture (right) of a radial-inflow turbine. Note that mixed-flow rotors (to which the scheme refers) are commonly used in conventional applications, while radial inward rotors are often implemented for Organic Rankine Cycles (as shown in the picture).

Picture on the right reproduced under the courtesy of Triogen B.V., The Netherlands.

optimization procedures; these latter techniques have been demonstrated by [Pasquale et al. \(2013a,b\)](#), and are discussed in [Section 8.5.2](#). However, even after optimization, relatively low performance at both design and off-design conditions has to be accepted (with respect to steam or gas turbine applications), as well as a relevant rigidity of operation due to highly supersonic conditions and converging–diverging configurations.

8.2.2 Axial turbines

When the target power ranges from a few hundreds of kW_{el} to a few MW_{el} , the flow rate required increases as well as the specific speed of the machine. For these high specific speed applications, the axial-flow configuration ([Fig. 8.3](#)) becomes competitive with the radial-inflow turbine, providing the opportunity to increase the number of stages and, thus, to reduce the stage loading. However, as the enthalpy drop is still small as well as the target power with respect to other energy conversion technologies, compactness is still a relevant issue for the whole ORC power system. Hence, the number of stages tends to remain very low (up to three in usual applications, also considering rotor-dynamic issues of overhanging machines). As a result, considering the large stage expansion ratio, the axial channel undergoes severe spanwise enlargements across each cascade (especially in the last stages), with a negative impact on performance. Furthermore, considering the low speed of sound, and the small reaction degree of each stage (to avoid too severe supersonic conditions in the rotor), highly supersonic conditions are still found at the stator exit, and converging–diverging stators are still used ([Macchi, 1977](#); [Macchi et al., 1980](#); [Colonna et al., 2008](#)). These axial stators are prone to the same critical features affecting their radial inward counterpart; however, it will be shown in this chapter how a systematic optimization of these supersonic cascades with advanced tools ([Pini et al., 2014b,c](#); [Rodriguez-Fernandez and Persico, 2015](#)) is

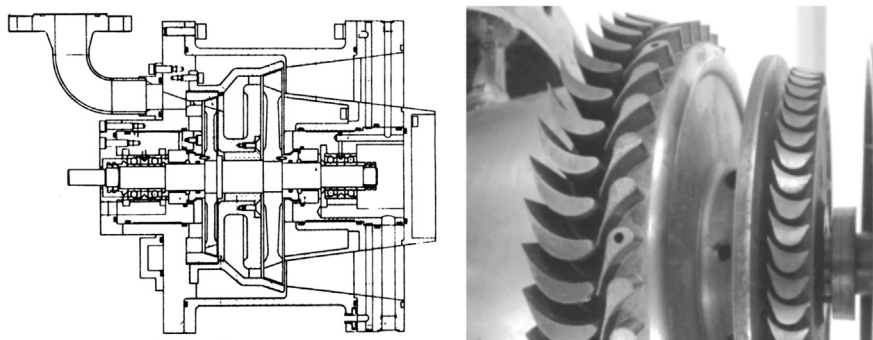


Figure 8.3 Meridional scheme (left) and picture (right) of a two-stage axial-flow turbine for Organic Rankine Cycle (ORC) applications. The machine was designed by the research team of Politecnico di Milano for an ORC application with monochlorobenzene ([Osnaghi et al., 1979](#)). Note the impulse style of the first rotor and the converging–diverging shape of the supersonic second stator.

Picture on the right taken at Laboratorio di Fluidodinamica delle Macchine of Politecnico di Milano, Italy.

able to dramatically reduce the shock losses, not only in design conditions but also in a wide range of operative conditions.

8.2.3 *Radial-outward or centrifugal turbines*

In addition to these classical turbine configurations and with the aim to overcome, at least partially, the aforementioned limitations of ORC turbines for both small and large power capacity, a novel turbine configuration was recently proposed, which implies a radical departure in design philosophy. The radial-outflow, or centrifugal, turbine architecture, firstly conceived by [Ljungstrom \(1949\)](#), actually represents a valid alternative over traditional solutions. Firstly, the centrifugal architecture can better accomplish the large volumetric flow ratio across ORC turbines, as the inherent increase of passage area along the flow path limits the flaring angle and prevents the onset of significant spanwise flow components. Secondly, many stages can be disposed in a relatively compact machine, thus avoiding supersonic flow conditions and providing a favorable compromise between compactness and performance. These advantages provide a considerable increase of aerodynamic performance at nominal point and greater flexibility at partial loads, as asserted in ([Pini et al., 2013](#); [Spadacini et al., 2011](#)). Additionally, the low enthalpy drop typical of ORC machines avoids the use of Ljungstrom counter-rotating solution³ and allows classic stator-rotor stage assembly with lesser mechanical complexity, as shown in [Fig 8.4](#). The industrial exploitation of this novel machine configuration in the ORC market is presently ongoing ([Spadacini et al., 2011](#)) and it is receiving scientific ([Pini et al., 2013](#); [Casati et al., 2014](#)), as well as industrial recognition (Chapter 11). As shown in the example discussed in [Section 8.4.2](#), some initial exercises of design suggest less critical aerodynamics, no choking conditions, and relatively high performance for radial outflow ORC cascades ([Persico et al., 2013](#)), even though specific issues arise due to apparent forces, which affect both the blade-to-blade and secondary flows of centrifugal rotors ([Persico et al., 2015](#)). In such a nonconventional context, the ongoing research on centrifugal turbine blades is opening a long path of development for this class of machine.

8.2.4 *Hybrid architectures*

Despite the potential of the radial-outflow architecture, there is no still clear evidence of the superiority of this arrangement if compared to an axial machine featuring the same number of stages and characterized by similar reaction degrees, stage loading and flow regimes throughout the cascades.⁴ One of the shortcomings of the radial-outflow turbine is the presence of the downstream volute that may introduce additional fluid-dynamic penalties not present in axial turbines and is rather critical at off-design conditions. The highest performance could then be achieved by resorting

³ Conceived to provide the high specific work exchange required by the steam technology.

⁴ Even though the centrifugal layout allows to accommodate more stages than the axial one, opening the way to exploit larger overall pressure ratio without overloading the stages.

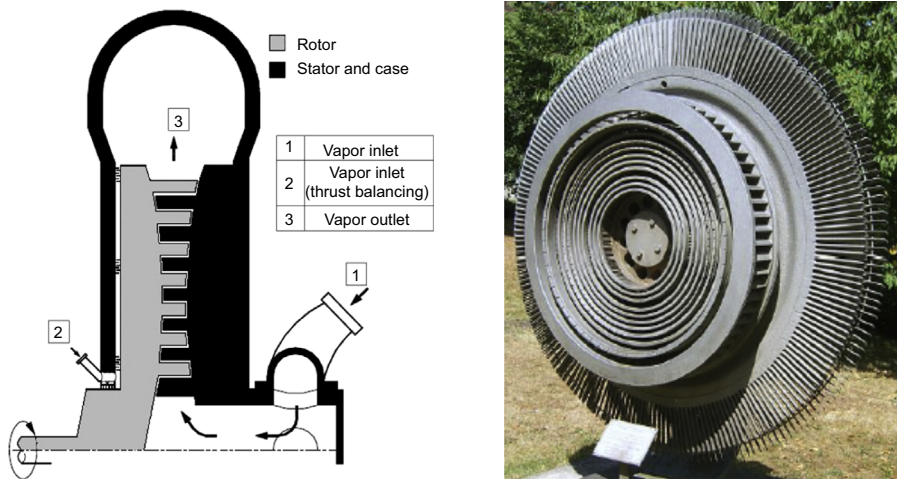


Figure 8.4 Meridional scheme (left) and picture (right) of a radial-outward turbine, originally conceived for steam applications with counter-rotating blade rows, and recently proposed for ORC applications implementing a conventional stator-rotor configurations.

to hybrid architectures, in which the first part of the expansion, i.e., when the volumetric flow ratios are larger due to the nonideality of the fluid flow, may be accomplished in centrifugal stages, while axial disks are retained to handle the remaining expansion occurring entirely in the (almost) ideal thermodynamic region. To the authors' knowledge, this turbine concept is currently under consideration by the major ORC manufacturers.

For small-scale applications, a possibly disruptive alternative may be constituted by a hybrid architecture integrating a first radial-inward stage and a second axial stage. This configuration would allow splitting of the expansion ratio between two stages, thereby relieving the issue of formation of strong shock waves affecting classical centripetal turbines and considerably augmenting the performance both at design and off-design.

8.3 Mean-line preliminary design

The plethora of the technical solutions available for ORC turbines and the variety of applications in which they have to operate indicate that the design of ORC turbines demands an open-minded approach.

The first and crucial step of the whole procedure is, therefore, the selection of the machine architecture (axial-flow with or without partial admission, radial-inflow, radial-outflow, or hybrid). This can be done by resorting to statistical data (such as the Balje diagrams) or to overall machine correlations. The most relevant example of such an approach in ORC technology was proposed in [Macchi \(2013\)](#) and is discussed in another chapter of this book (Chapter 9).

Once the general machine configuration has been selected, the design procedure needs to rely on fluid-dynamic concepts. However, as the actual flow configuration within a turbine is extremely complex, and probably even more for the case of an ORC, the modeling of the flow field has to be approached step-by-step. In the current turbomachinery technology, distinction is made between low-fidelity and high-fidelity models:

- Low-fidelity models are constructed using simplified approaches, so that they require the implementation of correlations to predict losses and flow angles (in terms of deviations from blade geometrical angles).
- High-fidelity models are based on sufficiently complex flow schemes to directly predict the most relevant flow features (even though some effects, such as that of turbulence and flow unsteadiness, are still approached in simplified ways).

To mark the distinction between low-fidelity and high-fidelity models from a design perspective, in the following the techniques based on low-fidelity models will be classified as ‘preliminary’ design methods, while the ones based on high-fidelity models will be referred to as ‘aerodynamic’ design methods. In the present section, the basics of the preliminary design are discussed, focusing on the impact of the ORC specific features at this level of the design. [Section 8.5](#) will focus on aerodynamic design, while [section 8.4](#) will present the throughflow model, which can be regarded as the bridge between low and high fidelity approaches. A schematic of the full design process for an ORC turbine is depicted in [Fig. 8.1](#).

8.3.1 Mean-line concept

The preliminary turbine design is mostly based on the so-called mean-line flow model. The mean-line model, also known as the one-dimensional approach, assumes uniform and unidirectional flow at inter-blade passages (referring to the midspan values, in general); the model is formulated with a lumped-parameter approach, only focusing on inlet and exit conditions of each cascade, regardless of the detailed shape of the blade. Thanks to these dramatic simplifications, the mean-line model allows quick determination of how to subdivide the thermodynamic process as well as the fluid-dynamic evolution over the entire machine; for this reason, the preliminary design is often the most crucial step of the whole procedure. In other terms, a highly-efficient ORC turbine can be realized if and only if the mean-line analysis gives a realistic and highly-efficient preliminary design. Provided that the architecture is selected on the basis of statistical diagrams, such as the one of Balje for compressible flow turbines or to correlations constructed specifically for ORC turbines (Chapter 9), the output of the mean-line design provides the machine layout in terms of size, angular speed, stage number, blade heights, and velocity diagrams.

In fact, if the preliminary design would be entirely reliable, the aerodynamic design would be limited to the identification of the blade shapes that guarantee the expected outcomes in terms of efficiency and work exchange. This is actually the case in some turbomachinery applications (for example axial-flow fans, thanks to

the reliability of the NACA database of experiments). This is not the case for ORC turbines, which often feature a highly nonconventional configuration. In the case of turbines, some studies document a good agreement between the results of such preliminary calculations and performance measurements (Wilson, 1984; Craig and Cox, 1971). However, this analysis cannot leave aside the specific knowledge available for different architectures. For supersonic radial inward turbines, a preliminary design procedure was developed at NASA in the 1990s (Glassman, 1995). For supersonic axial-flow turbines, the approach proposed in Macchi and Perdichizzi (1981) and based on the Craig & Cox model (Craig and Cox, 1971), with supersonic corrections, was found to be sufficiently reliable when applied in an industrial environment.⁵ Finally, acceptable reliability of preliminary design calculations was also found for slightly transonic centrifugal turbines, as demonstrated by comparisons against high-fidelity Computational Fluid-Dynamics (CFD) performed by the authors themselves (Persico et al., 2013, 2015).

The design exercises presented at the end of this chapter will show how a systematic optimization can considerably improve the preliminary predictions; however, these latter are still the foundation of the design process of an ORC turbine. Several solvers were developed and are currently in use by both companies and research institutes for carrying out ORC turbine development. Just a few examples are AXTUR (developed at Politecnico di Milano (Macchi and Perdichizzi, 1981)), zTurbo (developed at Politecnico di Milano with Technical University of Delft (Pini et al., 2013; Casati et al., 2014)), and TURAX [developed at Denmark Technical University with Politecnico di Milano (Meroni et al., 2016)].

The general approach of the mean-line model is now discussed, following the procedure used by the authors themselves for developing zTurbo, which has no a priori limitations in terms of the working fluid, flow regime, and turbine architecture.

8.3.2 Mean-line formulation

A preliminary design tool solves the balance equations of mass, energy, and momentum, alongside a loss model to evaluate entropy generation. Once the flow angles are determined, the deviation angle model allows an estimation of the blade geometric angles. With respect to conventional applications, a tool for ORC turbines has to deal with fluids with arbitrary thermodynamic behavior. In practice, instead of directly implementing the equations of state in the solving procedure, the solver could either interrogate an external library (such as RefProp, FluidProp, or CoolProp) or use a Look-up-Table, constructed with one of the aforementioned libraries. The balance equations have to be formulated in a general form, considering specific features, to properly treat both subsonic and supersonic flows in both the stationary and rotating frames of reference.

⁵ Pro-veritate opinion of Prof. Ing. Mario Gaia at the third International Symposium of ORC Power Systems, Brussels, October 12–14, 2015

Table 8.1 Main input data for mean-line model of a turbine stage

Boundary conditions	Geometrical constraints	Design variables
Inlet/outlet TD conditions	Blade minimum thickness	Reaction degree
Mass flow rate	Maximum flaring angle	Blade angle/throat
Stage expansion ratio	Hub/tip clearance	Blade chord
Target power	Stator/rotor gap	Angular speed

The calculation scheme for a single turbine stage can be schematized in a few steps, briefly summarized in the following:

1. Three classes of data need to be assigned, synthetically organized in Table 8.1. At first, thermodynamic conditions, stage expansion ratio, and mass flow rate are provided as inputs (these data are customary given by the thermodynamic analysis). Other relevant input parameters are the geometric quantities related to manufacturing constraints, which are not the object of design. Finally, values for the design variables need to be assigned; these are the reaction degree, the blade chords, the blade outlet angles, and the rotational speed. This makes the proposed approach a ‘direct’ method, as it evaluates the flow once the geometry is assigned. It will be shown that this method, if coupled with a systematic optimization algorithm, provide a highly flexible design tool, capable of exploring more configurations than that provided by inverse design tools.
2. By means of the stage reaction degree, the stator outlet velocity and the corresponding isentropic Mach number can be calculated. A distinction has to be made, at this level, between subsonic and supersonic nozzles. In the case of subsonic flow, the thermodynamic conditions in the nozzle throat are retrieved by solving the balance equations for the mass (Eq. (8.1)) and the momentum in the tangential direction (Eq. (8.2)), between the geometric throat and the downstream nonbladed zone:

$$\rho_{th} \cdot v_{th} \cdot o = \rho_1 \cdot v_1 \cdot pi \cdot \cos(\alpha_1) \quad (8.1)$$

$$v_{th} \cdot \sin(\alpha_{th}) = v_1 \cdot \sin(\alpha_{out}) \quad (8.2)$$

where the subscripts 1 and th indicate the discharge and throat sections respectively, o and pi are the throat width and the cascade pitch, ρ is the density, v is the velocity magnitude, and α is the flow angle.

In the case of supersonic nozzles, isentropic expansion can be assumed from the inlet section (where total conditions are given) up to sonic conditions at the choked throat. Correspondingly, the system of equations to be solved reads:

$$\begin{cases} s = s(p_{T,in}, T_{T,in}) \\ h_{th} = h_{T,in}(p_{T,in}, T_{T,in}) - \frac{1}{2} c(h_{th}, s)^2 \\ \dot{m} = \rho_{th}(h_{th}, s) \cdot c(h_{th}, s) \cdot A_{th} \end{cases} \quad (8.3)$$

where s and h are entropy and enthalpy, p and T are pressure and temperature, c is the speed of sound, \dot{m} is the flow rate, the subscript T stands for total quantities, and the subscript in indicates the cascade inlet section. By solving the continuity equation (Eq. (8.3)), the throat passage area A_{th} can be evaluated, and, if the throat width is assigned, the blade height can be computed. In both cases, the outflow angle is estimated by applying a proper deviation correlation (Sawyer, 1972). The blade number can be evaluated with a standard loading criterion [the Zweifel one (Zweifel, 1945), for example, which provides the optimal solidity as a function of the flow deflection across the cascade⁶].

3. The isentropic stage calculation discussed above provides the first guess for an iterative procedure to estimate the cascade losses. Several loss models are available, such as those proposed by Ainley and Mathieson (1957), Craig and Cox (1971), and Traupel (1977) for axial machines (also applicable to centrifugal machines), and NASA (Glassman, 1995) for radial inward machines. Specific corrections for supersonic flows and postexpansions downstream of the throat are also to be considered. The introduction of loss coefficients allows the prediction of entropy generation within the cascades with the following generalized expression:

$$\Delta s = s_{out} - s_{in} = s(P_{out}, h_{out}) - s_{in} = s\left(P_{out}, h_{out, is} + \zeta \frac{V_{out}^2}{2}\right) - s_{in} \quad (8.4)$$

thus correcting the isentropic estimates of flow velocities and blade heights.

The same calculation scheme is applied to rotors by solving the balance equations (conservation of mass and rothalpy) in the rotating frame of reference. The outcomes of the single-stage calculation procedure discussed above are.

- the velocity diagrams
- the shape of the meridional channel
- the estimate of stage performance.

When multistage turbines are of concern, the procedure is repeated for every stage, once the number of stages and the expansion ratio per stage is known. The repartition of the expansion among the stages is critical for ORC turbines (of axial and centrifugal architecture), due to the large overall expansion ratio and the low number of stages (Macchi, 1977). In the common practice of axial-flow multistage turbomachinery, simplified assumptions are usually made at a preliminary level, by keeping constant a number of quantities among all the stages. Typical assumptions are that the stages share the same reaction degree⁷ and all the rows share the same blade discharge angles. As a result, the velocity diagrams remain unchanged among the stages and the so-called repeating-stage arrangement is obtained.

Notably, these simplified strategies cannot be directly translated to ORC axial-flow turbines, considering that a few stages can be installed and that the fluid volumetric behavior is highly nonideal. In the case of centrifugal turbines the situation is even more critical, as the peripheral speed varies in the streamwise direction, and this

⁶ The solidity might also be adjusted in the aerodynamic design phase, if relevant improvements can be achieved.

⁷ Commonly around 0.5, which would ensure close-to-optimal stage efficiency (Dixon and Hall, 2010).

necessarily leads to different velocity triangles per stage. Some general design guidelines are proposed in the [section 8.3.3](#), based on the open literature and on the authors' experience.

8.3.3 Guidelines for a preliminary design of multistage Organic Rankine Cycle turbines

Several studies show that for axial-flow ([Macchi, 1977; Macchi et al., 1980](#)) and centrifugal ([Pini et al., 2013; Casati et al., 2014](#)) turbines, significant benefits can be achieved by accepting different levels of loading (and, hence, very different expansion ratio and work exchange) for the different stages. Three main cases can be considered (single-stage centripetal turbines are obviously excluded from the analysis):

1. For axial ORC turbines with an extremely large expansion ratio (more than 100), the dramatic volumetric ratio can be handled only by using partial admission in the first stage, which also exchanges a considerable fraction of the overall turbine work. However, impulse stages also provide lower efficiency with respect to reaction ones ([Dixon and Hall, 2010](#)); therefore, it is convenient to use a reaction style for the following stages, renouncing the simplification provided by the repeated stage strategy.
2. For axial-flow turbines with a large expansion ratio (standard for ORC), partial admission may not be necessary and the volumetric expansion is compensated with a proper change in blade span and mean diameter between the first and the last stages. As a result, the first stage is characterized by 'insufficient' peripheral speed; to achieve an acceptable amount of work exchange by the first stage, a low reaction degree has to be used. Reaction stages are, instead, used in the last stages of the machine to gain efficiency. So no stage repetition is suggested in this case.
3. For centrifugal turbines, the effects of the volumetric expansions are mitigated by the inherent increase in cross section offered by the radial-outflow configuration. So, partial admission is never required and the increase in blade span is limited with respect to axial machines; a further advantage comes from the fact that the repartition of the work and expansion ratio among the stages is less critical, as more stages can be installed with respect to axial machines. However, the peripheral speed strongly changes along the machine, with two main implications: the first stages suffer for insufficient peripheral speed and the repeated stage strategy can never be used as it is. Some parameters, such as the reaction degree and the cascade discharge angles, can actually be kept constant, but the velocity diagrams and, hence, the blade design differ anyway, stage-by-stage. However, studies ([Pini et al., 2013; Casati et al., 2014](#)) indicate that even for centrifugal turbines with a few stages, a smooth evolution of the meridional channel can be achieved, by designing the machine without imposing any kind of simplification, namely by performing the design optimization at each stage differently.

8.3.4 Optimal preliminary design of Organic Rankine Cycle turbines

The design procedure outlined previously often leads to suboptimal turbine solutions, though proper design choices are made. With the aim of identifying the turbine configuration that maximizes a selected merit function, the mean-line solver has to be

integrated with an optimization procedure. A systematic optimization is required to consider several aspects, which adapt a general mathematical process to the preliminary turbine design:

1. the definition of the so-called fitness function to be maximized
2. the independent variables and their range of variation, namely the design space
3. the constraints bounding the solutions space, geometrical and fluid-dynamic
4. the optimization algorithm.

These four features are now considered in detail, starting from the definition of the fitness function. A turbine fluid-dynamic optimization is typically aimed at the maximization of the efficiency, which may be formulated as

$$\eta_{T\chi} = f(\Psi, \phi, M, Re, Sh, \chi) = \frac{\Delta w}{\Delta h_{TS} - \chi \frac{C_{out}^2}{2}} \quad (8.5)$$

where χ stands for the fraction of discharged kinetic energy recovered downstream of the last stage ($\chi = 0$ means total-static efficiency, $\chi = 1$ means total-total efficiency). The functional dependence of the efficiency on the work and flow coefficients Ψ and Φ and from the Mach and Reynolds numbers M and Re is explicitly reported; the dependence also includes the term Sh , synthetically indicating the turbine shape. Part of these parameters determines the design space of the problem, the other part constitutes the set of design constraints. The constraints can be geometrical (see Table 8.1) or related to the flow regime (Mach number at the stator exit and at rotor inlet) if the designer wants to eliminate some supersonic flow effects (converging–diverging ducts and unique incidence effects). For each design variable reported in Table 8.1, a range of variation has to be prescribed, thus defining the design space that the optimization algorithm can explore searching for the optimum.

As discussed in Section 8.3.3 about multistage turbines, the real potential of a systematic preliminary optimization is achieved by prescribing separate optimization variables for each stage. As a result, in the case of multistage turbines, the number of independent variables can exceed 20. For such a problem, a robust optimization algorithm is needed. In the experience of the authors, evolutionary optimization strategies based on a single-objective genetic algorithm (GA) are suitable for the mean-line fluid-dynamic design. These algorithms perform well in the case of nonsmooth fitness functions, spanning the whole design space and avoiding to converge to local optima possibly found during the search.

8.4 Bridge between preliminary and aerodynamic design: throughflow model

When a preliminary turbine layout is available, the definition of the blade geometry can be approached. As ORC turbines are highly nonconventional, the adoption of common blade profiles is questionable and a specific aerodynamic design is highly

recommended. In this way, both the reliability of the design procedure and the performance of the machine can be improved.

Unfortunately, the connection between preliminary and aerodynamic design is often not straightforward, as low-fidelity and high-fidelity models are constructed in completely different ways. Notably, the output of a preliminary design does not provide the entire set of input information required by the aerodynamic design. From this perspective, the application of some ‘intermediate’ models can be beneficial for a proper set-up of the aerodynamic design. The most relevant intermediate technique is the throughflow model, which incorporates part of the fluid-dynamic complexity while retaining some low-fidelity features. For this reason, it is considered as the logical bridge between mean-line and aerodynamic models of turbine flows. This section discusses the concept, the formulation and the application to design of the throughflow model.

8.4.1 Throughflow concept

The key simplification of the throughflow model, suggested by the inherent annular geometry of turbomachines, assumes a two-dimensional axisymmetric flow problem in the meridional (e.g., axial/radial) plane. To aid the reader in the comprehension of the logical connection between the different models, a representation of mean-line, throughflow, and aerodynamic models is provided in Fig. 8.5 for a multistage centrifugal ORC turbine.

Fig. 8.5 shows how a very complex three-dimensional turbine configuration (left), is progressively simplified up to a mean-line model (right). The throughflow model (center) is ‘intermediate’ in the sense that, having neglected any azimuthal variation, the blades do lose their actual shape and are replaced by mean flow surfaces; the inclination of these mean surfaces determines the local flow direction and has to be imposed by assigning a volume force field. The blockage effects connected to the blade thickness (generally relevant and even crucial for converging–diverging bladed ducts) can also be taken into account through a proper source term. Notably, the throughflow model does not reproduce the viscous losses, as the most relevant viscous effects are not

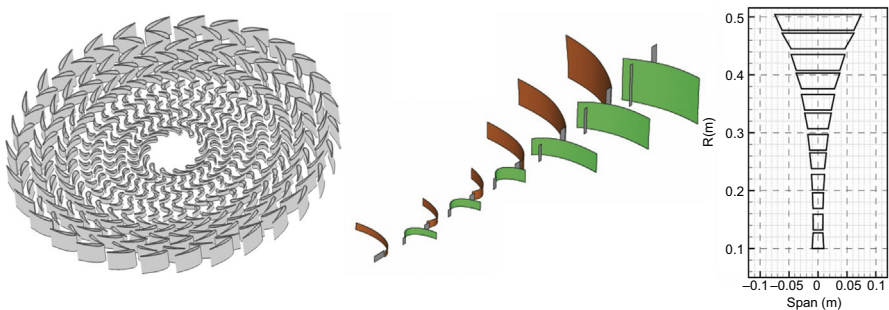


Figure 8.5 Aerodynamic (left), throughflow (center), and mean-line (right) models of a multistage radial-outflow turbine.

represented (blade boundary layers, wakes, secondary, and tip leakage flows). Therefore, losses are still introduced via correlations, giving a low-fidelity character to throughflow solvers.

Nevertheless, the throughflow model provides a dramatic improvement with respect to the mean-line representation from the design perspective. As a matter of fact, the throughflow representation allows extending along the blade span the mean-line information available from the preliminary design; it actually provides the spanwise evolution of flow properties and velocity diagrams, while needing only very rough information about the blade geometry (simplified camber-line and thickness distributions). Moreover, the computational cost of throughflow calculation is also very limited (never exceeding a few minutes on a standard PC), thus it is inherently suitable for systematic application within optimization strategies. For these reasons throughflow solvers are intensively applied in gas and steam turbine technology (Denton and Dawes, 1999), and in the authors' opinion they could be of relevant interest also in the context of ORC turbines, which feature large blade spans and large flaring angles in the last stages.

Classical techniques for the computation of the flow field in the meridional plane, such as the radial equilibrium equation (Smith, 1966), the streamline curvature method (Novak, 1967), and the matrix throughflow method (Marsh, 1966) are still in use, but suffer from severe limitations in treating transonic flow conditions and in solving the detailed flow field inside the bladed regions. Numerical solution strategies borrowed from CFD have been exploited to generalize the throughflow formulation, resulting in much more robust and reliable methods for turbomachinery analysis and design (Damle et al., 1998; Simon and Leonard, 2005; Persico and Rebay, 2012). This so-called CFD-based throughflow model allows the capturing of the onset of choking, shock waves, and supersonic postexpansions (although in the axisymmetric simplification). The generality of this technique is particularly attractive for ORC turbines, always featuring transonic or supersonic flows. To the knowledge of the authors, the unique example of CFD-based throughflow solver already applied to ORC turbines is TzFlow, developed at Politecnico di Milano (Persico and Rebay, 2012). In the following Section 8.4.2 the main features of the TzFlow solver are discussed.

8.4.2 Throughflow formulation

Mathematically, the throughflow model is obtained by averaging the three-dimensional inviscid flow equations in the azimuthal direction and by introducing proper source terms to account for the averaged effects of the blades. Swirl, blockage, and losses induced by the actual cascade aerodynamics cannot be computed directly but are represented by suitably defined volume forces. The resulting system of equations can be synthetically written as:

$$\frac{\partial u}{\partial t} + \frac{\partial f^x}{\partial x} + \frac{1}{r} \frac{\partial(rf^r)}{\partial r} + \frac{s^r}{r} + s^{\nabla b} = s^v \quad (8.6)$$

The variable (u) and flux function (f) vectors are defined as.

$$u = \begin{bmatrix} \rho \\ \rho e_0 \\ \rho v_x \\ \rho v_r \\ \rho v_\theta \end{bmatrix}, \quad f^x = \begin{bmatrix} \rho v_x \\ \rho h_0 v_x \\ \rho v_x^2 + P \\ \rho v_r v_x \\ \rho v_\theta v_x \end{bmatrix}, \quad f^r = \begin{bmatrix} \rho v_r \\ \rho h_0 v_r \\ \rho v_x v_r \\ \rho v_r^2 + P \\ \rho v_\theta v_r \end{bmatrix} \quad (8.7)$$

where ρ denotes the density, P is the pressure, v_x , v_r , and v_θ are the cylindrical components of the velocity vector, and e_0 and h_0 are the stagnation internal energy and enthalpy respectively. Pressure P and temperature T have to be evaluated as functions of the variables u (and vice-versa) by means of arbitrarily complex equations of state. This can be done either by interrogating an external thermodynamic library or by resorting to a LuT approach (Pini et al., 2014a). In the system (8.6) several volume forces appear, defined as:

$$s^r = \begin{bmatrix} 0 \\ 0 \\ 0 \\ -(\rho v_\theta^2 + P) \\ \rho v_r v_\theta \end{bmatrix}, \quad s^{\nabla b} = \frac{1}{b} \frac{\partial b}{\partial x} \begin{bmatrix} \rho v_x \\ \rho h_0 v_x \\ \rho v_x^2 \\ \rho v_r v_x \\ \rho v_\theta v_x \end{bmatrix} + \frac{1}{b} \frac{\partial b}{\partial r} \begin{bmatrix} \rho v_r \\ \rho h_0 v_r \\ \rho v_x v_r \\ \rho v_r^2 \\ \rho v_\theta v_r \end{bmatrix} \quad (8.8)$$

$$s^v = \begin{bmatrix} 0 \\ \rho(\mathbf{L} + \mathbf{D}) \cdot \omega r \mathbf{e}_\theta \\ \rho(\mathbf{L} + \mathbf{D}) \cdot \mathbf{e}_x \\ \rho(\mathbf{L} + \mathbf{D}) \cdot \mathbf{e}_r \\ \rho(\mathbf{L} + \mathbf{D}) \cdot \mathbf{e}_\theta \end{bmatrix}$$

The source term s^r is a typical feature of cylindrical coordinates.⁸ The source term $s^{\nabla b}$ takes into account the effects of the blade thickness in both the tangential and radial direction, through a “blockage factor” of the annular channel defined as:

$$b(x, r) = \frac{N[\theta_p(x, r) - \theta_s(x, r)]}{2\pi} \quad (8.9)$$

⁸ Axisymmetric models always benefit from formulation in cylindrical coordinates, as the gradients in the azimuthal direction are null.

where the difference $\theta_p - \theta_s$ is the local angular distance between the suction and the pressure side of the blades, and N is the blade number in the annular cascade. The source term s^v contains the blade force, and the associated power exchange, representing the actual aerodynamic forces exchanged between the flow and the blades. The blade force accounts for both the swirling imparted by the blade to the flow and the loss mechanisms activated in the flow process. The former ‘inviscid’ force acts orthogonally to the local flow surface and is renamed L , while the latter ‘friction’ force is aligned to the local flow surface and is renamed D .⁹

The magnitude of the inviscid force field is determined by requiring that, in the bladed regions, the flow remains parallel to the mean flow surface; in TzFlow, this immersed tangential condition is satisfied by resorting to a penalty formulation (Persico and Rebay, 2012).

To account for the magnitude of the friction force component, a classical formulation (Horlock, 1971) is used, namely, $D = T\nabla s \cdot \mathbf{t}$, where \mathbf{t} is the unit vector tangent to the local velocity. The key advantage of the above formulation is that the friction force can be easily computed once the entropy rise across each zone is known from loss correlations, and a smooth functional form is assumed to redistribute the overall entropy rise from the inlet to the outlet of each cascade.

The set-up of a throughflow calculation from the outcome of a mean-line design is a relatively direct procedure. As blade spans and flow angles are known from mean-line analysis, simplified assumptions can be made on the spanwise evolution of the blade angles (e.g., constant blade angle, free-vortex configurations, etc.) and conventional functional forms can be used for the blade camber lines (e.g., piecewise cubic functions that satisfies the inlet and outlet flow angles). Similarly, simplified thickness distributions can be used (extracted from database of profiles) that would provide a realistic picture of the interblade channel shape.

Fig. 8.6 provides an example of the outcome of throughflow calculations, showing the distributions of thermodynamic and flow quantities for the turbine presented in Fig. 8.5.

Fig. 8.6 clarifies the potential provided by a computational model that properly accounts for the local flow properties in the axial/radial plane. Notably, the progressive expansion of the flow along the several stages can be appreciated, as well as the alternated distribution of high and low absolute and relative Mach numbers in the stators and in the rotors of each stage. If the blade span is limited, spanwise variations are negligible and the information provided by the mean-line model is representative of the entire flow; this is visible in the first three stages of the machine. However, when the flaring becomes relevant, as in the last three stages of the machine, relevant spanwise gradients arise and their evaluation and ‘control’ at throughflow level can be crucial for the subsequent aerodynamic design. A relevant example is the last stator of the machine modeled in Fig. 8.6; a visible, local area of supersonic flows is found close to the end-walls, which might produce a local increase of loss, with respect to the mean-line value.

⁹ The flow surface is primarily defined by the blade mean surface and modified at the leading and trailing edges to account for the effects of incidence and deviation, see (Persico and Rebay, 2012) for a specific discussion of this problem.

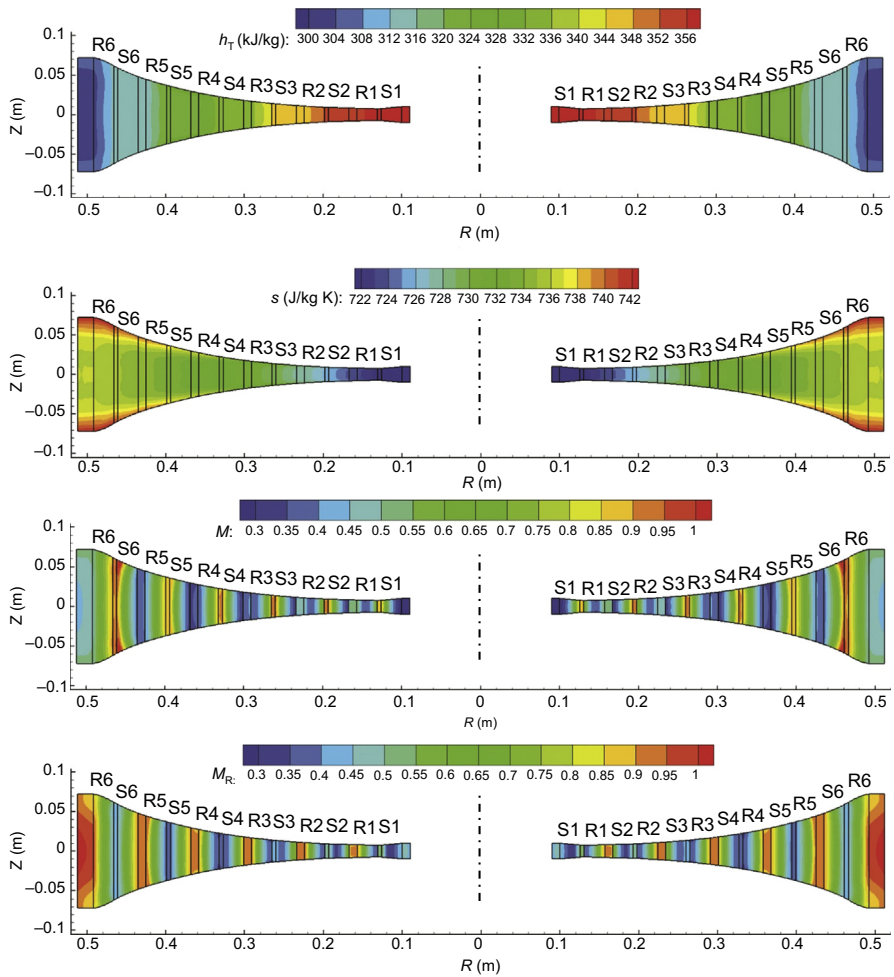


Figure 8.6 Distributions of total enthalpy, entropy, and absolute/relative Mach number on the meridional plane for a multistage centrifugal ORC turbine.

These supersonic flows are caused by the combination of the pressure gradient established along the blade and the one established on the curved endwall profile. Proper design of the camber-line and of the local endwall profile can indeed limit this over-speed, minimizing the spanwise gradients and improving the turbine performance.

8.4.3 Throughflow or spanwise design guidelines

The previous example indicates that relevant information can be achieved by applying the throughflow model to ORC turbines, which feature large flaring angles in the last stages (or in their unique stage, if single-stage machines are of concern). However, the

application to radial machines provides a very partial view of the real potential of the throughflow model in the design phase. For radial turbines, the peripheral speed does not change in spanwise direction and the same velocity diagram is preserved along the whole blade span (unless the blades are modified on purpose by the designer); in such a configuration, spanwise effects can arise only in high-flaring blade rows. Conversely, axial and mixed-flow machines feature radial equilibrium effects and spanwise variation of peripheral speed, which both contribute in modifying the velocity diagrams along the span. The throughflow model allows quantification of the impact of this spanwise variation, providing guidelines for the spanwise design of the blades. Some relevant indications achievable with throughflow calculations, in particular for axial-flow turbines, can be summarized as follows:

- Impact of using dihedral blades (i.e., constant blade profile along the span) on velocity diagrams away from the midspan.
- Improvements provided by the use of twisted blades (whose aerodynamic design and manufacturing, demand a relevant increase of costs).
- In the case of using dihedral blades, the subsequent spanwise variation of incidence, to evaluate if incidence effects need to be mitigated with specific design criteria.
- Spanwise distribution of Mach numbers and flow angles, to predict if specific design constraints are not satisfied away from the midspan.
- Spanwise disuniformity of work exchange and losses, and their effect on the distribution of thermodynamic quantities (such as total enthalpy, entropy, and pressure), and if these effects should be reconsidered in the preliminary design.
- Combination of all the aforementioned features with large flaring angles in the last stages of the turbine.

8.4.4 Optimal spanwise design

The throughflow model can also be used to control the spanwise variations by implementation within an optimization algorithm, whose outcome is the optimal blade mean surface. One of the authors has already performed an exercise of throughflow design, by combining TzFlow with an evolutionary algorithm (Pasquale et al., 2013a,b). As the throughflow model is constructed around a simplified representation of the geometry, the optimization also has to be approached in a simplified way. Furthermore, when setting the throughflow design, most of the limitations and constraints imposed by the application and/or by the designer are already satisfied by the mean-line design. Therefore, the design space that needs to be explored is much reduced, and is limited to a few quantities representative of the spanwise variation around mean values.

With reference to the four main features of optimization procedures previously discussed, the following considerations can be proposed for a systematic throughflow design:

- Typical choices for the design variables are the blade angles of each cascade in a few relevant spans (at least two, at the tip and at the hub).
- Regarding the constraints, as already discussed, the main geometrical constraints are handled in the frame of mean-line design; however, other relevant fluid-dynamic quantities need to be

constrained. Notably, as throughflow solvers make use of CFD techniques, it is not possible to assign the pressure ratio and the flow rate; in general, the pressure ratio is assigned via boundary conditions, and the flow rate results from the calculation. As a result, a specific constraint has to be applied to the flow rate to guarantee that the outcome of the optimization is consistent with the target of the machine under consideration.

- Several options are available for the definition of the fitness function in the context of the throughflow design, commonly related to the minimization of the spanwise variation of work exchange (and hence that of total enthalpy), as well as the minimization of discharge kinetic energy and the entropy production. These different objectives can also be combined in a unique fitness function, assigning different weights to the different functions to be minimized, so to achieve an optimal compromise between nonconcurrent goals.
- For the optimization algorithms, a conventional evolutionary strategy is suitable for this kind of optimization, considering the inherent low-cost of the throughflow calculation (a few minutes for a standard PC for an entire multistage turbomachine).

The definition of an optimal blade mean surface, combined with a standard trend for the blade thickness, leads to the definition a ‘first guess’ for the three-dimensional shape of the blade. In this way, the outcome of the throughflow design provides most of the necessary inputs for the construction of the high-fidelity model used for aerodynamic design, which is considered in the following section.

8.5 Aerodynamic design

Once velocity diagrams and thermodynamic quantities are determined along the whole blade span, the detailed shape of the blades is obtained by the aerodynamic design, which represents the last step of the design procedure.¹⁰ For conventional machines featuring specific classes of profiles, the aerodynamic design can be a relatively simple procedure, limited to the proper selection of the profiles from a database.¹¹

However, such a consideration does not hold for ORC turbines, as their nonconventional configuration results in a substantial lack of well-established design criteria. Furthermore, the supersonic flow regime of ORC turbine cascades might suggest the implementation of converging–diverging blade rows, whose design requires specific techniques. For these reasons, the present-day aerodynamic design of ORC turbine blades cannot rely on simplified rules, and demands the application of high-fidelity flow models. Therefore, it is the most ‘expensive’ phase of the process, in terms of acquisition/development of high-fidelity solvers, as well as of computational cost involved in their systematic application.

In general, the aerodynamic design of flow devices could be directly performed at a three-dimensional level. However, this is not usually done for turbomachinery, as a number of choices made at the preliminary level reduces the design

¹⁰ In fact, a final calculation with fully three-dimensional and unsteady flow models including turbulence and real gas effects might also be performed as assessment of the design at the end of the procedure.

¹¹ A procedure for constructing the three-dimensional shape of blades from optimal throughflow surfaces is discussed in (Pasquale et al., 2013a,b).

space. This limitation, far from being a weakness, is instead the reason for the effectiveness of the step-by-step design procedure discussed in this chapter. To determine the blade shape, the common approach is to identify the shape of one or a few blade profiles to be stacked along the blade axis, so to satisfy the design flow angle and to guarantee (or improve) the performance estimated at the preliminary/throughflow level.

Hence, the aerodynamic design of turbomachinery is devoted to the determination of the shape of a succession of profiles; this requires high-fidelity models but can be approached with a succession of quasi-three-dimensional blade-to-blade flow models, with a relevant reduction of computational cost with respect to fully three-dimensional methods. In the specific field of ORC turbines, dihedral (prismatic) blades are often used and, therefore, only one profile has to be optimized.

The development of design techniques for turbomachinery profiles has been a relevant research area for the last 50 years, for application in propulsion and energy systems. Different approaches have emerged between turbines and compressors, between axial and radial machines, and between compressible and incompressible flow machines. For the present discussion, only techniques for compressible flow turbines are of interest, considering the specific features required by the different architectures.

The design of turbine blades for high-speed flows has to combine the concepts developed for high-speed nozzles with that of aerodynamic profiles. Especially for ORC turbine cascades, that often feature supersonic flows, the control of the flow passage area is crucial to guarantee the target of expansion ratio. At the same time, the detailed shape of the profile has to be carefully determined, especially in the front and rear semi-bladed regions, where the flow is confined on one side only and severe pressure gradients may arise, with the potential onset of shocks and subsequent boundary layer separations. As a result, the aerodynamic design of ORC turbines involves three substeps:

- A preliminary definition of the bladed channel to match the cascade requirements, such as the expansion ratio and the gauging angle.
- A proper redefinition of the profile shape in the front and rear part of the suction side to ensure regular accelerations of the flow, thus avoiding abrupt overspeeds.
- A final optimization of the resulting profile by means of automated design methods.

These first two points are described in [Subsection 8.5.1](#) while the final step is treated separately in [Subsection 8.5.2](#).

8.5.1 Geometrical representation of Organic Rankine Cycle turbine blades

The shape of a turbine blade has to be chiefly accomplished in order to minimize aerodynamic losses. With reference to the nomenclature introduced in [Fig. 8.7](#), presented for a radial ORC turbine cascade but also valid for axial configurations, common design guidelines can be drawn:

1. The camber-line of a single blade is entirely defined by assigning a functional form (circular, elliptic, or parabolic) satisfying the inlet blade angle β_{in} , the outlet blade angle β_{out} , the stagger angle γ , and the axial/radial chord c_{rad} .

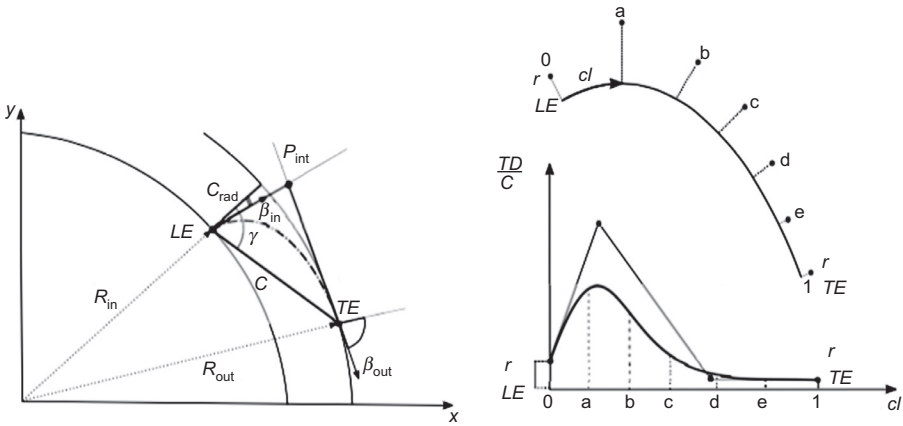


Figure 8.7 Left: camber-line construction of a centrifugal turbine blade using B-Splines. Right: definition of the blade thickness distribution by B-Splines (bottom) and its normal application to the camber-line (top).

2. The pressure (PS) and the suction (SS) side are built by specifying a thickness distribution (TD) as a function of the chord and applying it normal to the camber-line.
3. The leading-edge (LE) and trailing edge (TE) are accomplished by connecting the PS and the SS in such a way that C^2 continuity is guaranteed.
4. The cascade configuration is finally obtained by positioning a second blade at a distance equal to the pitch. This makes it possible to compute the area distribution and the gauging-angle,¹² which are crucial parameters to assess the flow expansion and flow deviation.

In current ORC turbine practice, the first three steps are accomplished by means of parametric curves/surfaces. The key idea is to adopt Computer-Aided Design (CAD) techniques, in which lines and surfaces are expressed by a succession of weighted basis functions. Examples of curves suitable for proper geometry representation are Bezier lines, Chebyshev polynomials, and B-Splines. Nowadays, B-Splines and their generalization, NonUniform Rational B-Splines (NURBS), represent the standard for curve and surface description in computer graphics and CAD softwares (Farin, 2002).

The use of basic functions leads to a ‘parametrization’ of the geometry, in the sense that complex shapes (like the ones of turbine blades) can be described with a relatively low number of parameters, namely the control points, the knot sequence, and the weight that identifies each piece of the shape. A very synthetic discussion of B-Splines is now provided, to show how geometry parametrization techniques can be exploited to obtain a satisfactory geometrical representation of the blade shape.

¹² The gauging angle depends on the ratio between the cascade throat and the pitch, $gau = \arccos(o/pitch)$.

8.5.1.1 Blade geometry parametrization

A B-Spline curve can be defined as a piecewise line whose smoothness and continuity can be ensured by proper construction conditions. A B-Spline curve can be described as a weighted sum of basis functions of order n as follows:

$$x(u) = \sum_{j=0}^L d_j N_j^n(u) \quad (8.10)$$

where d_j , with $j = 0, \dots, L$, are the control points, and $N_j^n(u)$ are the corresponding n -degree B-Spline bases. These can be defined recursively in the form:

$$N_j^k(u) = \frac{u - u_{j-1}}{u_{j+k-1} - u_{j-1}} N_j^{k-1}(u) + \frac{u_{j+k} - u}{u_{j+k} - u_j} N_{j+1}^{k-1}(u) \quad (8.11)$$

$$N_j^0(u) = \begin{cases} 0 & \text{if } u_{j-1} \leq u < u_j, \\ 1 & \text{otherwise} \end{cases}$$

where u_j , with $j = 0, k$ is the knot sequence. Notice that $k = L + n - 1$.

The illustration of the blade construction starting from the outputs provided by the mean-line design is given in Fig. 8.7 using B-Splines. The camber-line is completely established by the inlet blade angle β_{in} , the outlet blade angle β_{out} , the stagger angle γ , the radial chord c_{rad} , and the LE position. The TE position is uniquely defined by the LE, γ , c_{rad} , and an additional third point resulting from the intersection of the inlet and outlet lines. These two lines follow the direction of β_{in} and β_{out} , respectively, which are defined in an axial/radial reference of framework. Using three control points (one placed at LE, one at TE, and the last at the intersecting point), the camber-line assumes a quadratic shape, and by changing the weight value of the intersecting control points, the ensemble of the quadratic curves can be represented, i.e. $w_{int} = 1.0$ parabolic, $w_{int} > 1.0$ hyperbolic, $w_{int} < 1.0$ elliptic (also circular). Moreover, although scarcely utilized, even more than three control points can be specified to construct a higher degree camber-line curve. In conclusion, all of these options ensure a high level of flexibility in selecting the most appropriate camber-line shape. The SS and PS are also NURBS curves, whose control points are found by assigning a TD as a function of the camber-line position. Bottom right Fig. 8.7 shows an example of a TD (parameterized by four control points) for the suction side, and, on top, the application of this TD normal to the camber-line. As anticipated, the SS is retrieved by means of a parametric curve having the set of points $0, a, b, \dots, 1$ as control points. It is worth mentioning that specifying the TD allows to distribute and control the fluid-dynamic loading along the profile.

Parametric curves/surfaces are also applied to fit existing blade geometries. This is particularly useful when turbine blades need to be redesigned for performance improvement. Specifically, by applying a proper interpolation technique (such as least squares), a parametric representation of the baseline blade shape can be achieved,

determining the coordinates of control points, the knot sequence, and the weights of the B-spline line that best fits the original shape. The specific formulation of B-Splines gives wide freedom to the designer, who can control the shape of the final interpolated B-Spline not only through the position of the control points but also through the knot sequence. For examples, the knot sequence can be used to automatically adjust the position of the control points that serve as design variables of the optimization problem. In this way, one can identify areas prone to optimization and thus assign a different number of control points for each region during the interpolation process. This is a crucial feature especially for ORC turbine blades, which often exhibit a complex converging–diverging shape and, therefore, may benefit significantly from optimization in local areas downstream of the throat, as it will be shown in the design examples.

The baseline blade can be parametrized by a unique B-Spline or with a multiplicity of them (for example using different parametrization lines for the pressure and suction sides of the blade). In any case, special care has to be taken for the trailing edge, as a circular (or elliptic) arc is best suited in this region. Thanks to the flexibility of B-Splines, the parametrization curve can be constrained to pass through the first and last data points of the trailing edge region, which can be expressed as a circular arc. Continuity and regularity between B-Splines and the circular arc can be ensured by imposing the same derivative.

8.5.1.2 Design remarks for Organic Rankine Cycle turbine blades

The cascade shape resulting from the previous design procedure are usually classified in three main types, depending on the flow regime. Minor or major modifications of the initial geometry can be made according to the recommendations outlined in the following.

1. Transonic cascades

Designed to discharge sonic or weakly supersonic flows with $M < 1.1$. Bladed channels are shaped as converging ducts, and the discharge flow angle is directly controlled by the gauging angle, applying classical correlations like the ones of [Ainley and Mathieson \(1957\)](#) available from steam and gas turbine technology.

The aerodynamic design of these cascades is not critical, as their working parameters are relatively close to that of high-pressure steam and gas turbines.

However, the application of this class of profiles is very limited in ORC technology. Radial-inward and axial ORC turbines always operate with supersonic cascades, with Mach number much larger than 1.1. Only centrifugal turbines for ORC applications can operate with transonic blade rows, although profiles for the nonconventional radial-outward configuration require specific adaptation techniques [such as conformal transformation, see [\(Persico et al., 2013\)](#)].

2. Supersonic converging cascades

Designed to discharge supersonic flows with $1.1 < M < 1.4$. For plane nozzles, a converging–diverging duct is required to achieve a Mach number larger than 1. In the case of turbine cascades, an alternative solution is possible, by adopting a purely converging

bladed duct and accepting a supersonic postexpansion in the semibladed region downstream of the (sonic) throat at the exit of the bladed duct. This configuration guarantees a certain flexibility in the case of the partial load of the turbine, even though shocks do occur in the rear suction side of the blade and at the trailing edge. However, if the Mach number is limited to 1.4, these shocks are relatively weak and have a limited impact on the cascades performance. This consideration, in combination to the design simplification provided by the use of converging blades with respect to converging–diverging ones, makes preferable to adopt converging postexpanding turbine cascades for $M < 1.4$ (Osnaghi, 2013). In the ORC technology, such an operating condition could only occur for multistage axial and centrifugal turbines.

When designing a supersonic converging blade row, the geometric deflection has to be carefully studied, as the postexpansion imparts a further rotation to the flow in the meridional direction, downstream of the trailing edge of the blade, and increases with the discharge Mach number. The design gauging angle must, therefore, be corrected by predicting the supersonic deviation. This can be done in a relatively simple way, by applying classical one-dimensional models to the supersonic semibladed region, which provide an acceptable estimate of both shock losses and flow deflection imposed by the postexpansion (Osnaghi, 2013; Traupel, 1977).

Once these estimates are performed, the aerodynamic design of the blades can be done by resorting to the techniques available for high-speed steam and gas turbines. A classic design method for the rear suction side of the blade, namely the semibladed region downstream of the sonic throat, was proposed by Deich et al. in 1965, and is schematically reported in Fig. 8.8. The method suggests adopting a brief convex part (indicated by the line B-C) just downstream of the throat (indicated by the line A-B), followed by a longer concave section that is finally filleted to the trailing edge. Such a configuration should optimize the interaction between the blade surface and the expansion fan generated at the trailing edge of the adjacent blade.

3. Supersonic converging–diverging cascades

Designed to discharge supersonic flows for $M > 1.4$. When the discharge Mach number is higher than 1.4, the postexpansion involves strong shocks and the corresponding supersonic deviation of the flow is so large that purely converging cascades become inefficient. For these cases, converging–diverging cascades have to be considered. This configuration is a typical feature of ORC turbines, and is highly unconventional outside of ORC technology; it is applied only for control stages for small-scale steam turbines. The design of such cascades first requires an evaluation of the dimension of the sonic throat to be generated within the bladed channel. The design of the converging duct upstream of the throat is, in general, not critical and very simple techniques can be used (e.g., circular or elliptic arcs). Conversely,

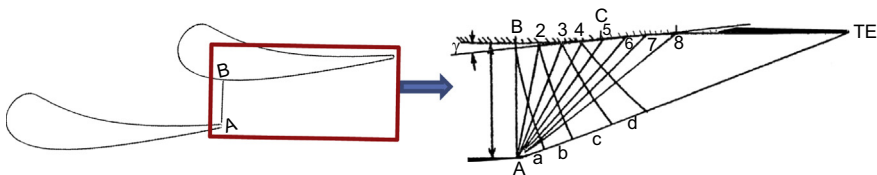


Figure 8.8 Design scheme for the rear suction side of converging postexpanding cascades.

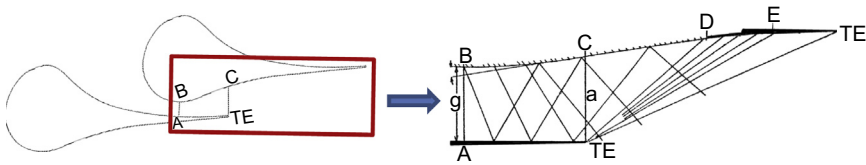


Figure 8.9 Design scheme for the diverging part of supersonic cascades.

the design of the diverging part downstream of the throat, both internal and external to the bladed channel, is very critical and, if not properly considered, may lead to a dramatic reduction of efficiency, especially at off-design conditions. A very rough design technique for the rear suction side, proposed by [Deich et al. \(1965\)](#) and represented in [Fig. 8.9](#), suggests implementing a convex region for the diverging section of the bladed channel (from the sonic throat A-B to the discharge section TE-C). The rear suction side in the semibladed region should, instead, be shaped as a first rectilinear sector C-D, followed by a concave part D-E which is finally filleted to the trailing edge region.

Alternative and more general solutions are nowadays possible for the design of the diverging part. An inverse design technique for plane converging–diverging nozzles based on the Theory of Characteristics ([Guardone et al., 2013](#)) has been adapted to the design of highly supersonic cascades ([Uusitalo et al., 2014](#)).

All these methods are meant to provide an initial shape of the blade, ensuring acceptable performance. Once this ‘first guess’ is available, the refined aerodynamic design is by far the most complex phase of the whole design process, demands a proper optimization procedure, and is crucial to achieve high-performance machines. The following [Subsection 8.5.2](#) discusses how the detailed design of the blade can be approached systematically by applying shape optimization techniques. Dedicated examples are presented to demonstrate the capabilities of advanced techniques to provide a relevant margin of improvement with respect to classical design methods, even at off-design conditions.

8.5.2 Automatic design of Organic Rankine Cycle turbine blades by shape-optimization techniques

Optimal aerodynamic design of ORC turbines demands high-fidelity flow models. Simplifications have to be limited as much as possible (although not totally, as is usual in the calculation of industrial flows) to retain the actual flow complexity. To this end, the modeling and simulation techniques commonly referred to as CFD are best suited to support the detailed aerodynamic design.

In this section, the CFD models suitable for the simulation of the flow within ORC turbines are discussed, as well as the way in which they can be exploited in the framework of aerodynamic design. Finally, three examples of advanced design techniques applied to an ORC turbine cascade are discussed, to demonstrate the potential of shape optimization in this context.

8.5.2.1 *Computational Fluid-Dynamics modeling for Organic Rankine Cycle turbine flow simulation*

CFD aims at integrating the Navier–Stokes equations on multidimensional domains, solving explicitly the mass, momentum and energy balance equations expressed in differential form, and making use of numerical approximation techniques. These equations include time derivatives (unsteady evolution), transport terms (convection), and diffusion terms (viscous effects and heat conduction), resulting in a nonlinear second order system of four (two-dimensional) or five (three-dimensional) differential equations. For such a complex system, a generalized analytical solution method is not available. Numerical methods are therefore required to carry out an approximate solution of the system on a computational mesh, which discretizes the computational domain.

The mathematical complexity of the Navier–Stokes system is further amplified by the nonlinear character of the equations, which makes them prone to massive instability. The onset of this large-scale instability is triggered when the inviscid terms become sufficiently larger than the viscous ones (namely, for sufficiently high Reynolds numbers), and is referred to as transition to Turbulence. The chaotic flow condition that establishes for higher Reynolds numbers is identified as turbulent flow.

Turbulence affects turbomachinery flows, including those within ORC turbines, due to the high flow velocity that makes the Reynolds number overcome the transition limit in all the cases of industrial relevance. The proper simulation of turbulent instabilities, although nowadays possible also for turbomachinery flows (Sandberg et al., 2015), demands computational costs in the order of months on massively parallel machines, due to the dramatic grid resolutions in space and time required to reproduce the extremely wide range of scales appearing in turbulent flows. Such a cost is not affordable for industrial calculations, especially for those oriented to optimization procedures.

A classic alternative solution consists of reproducing the effects of turbulence, by resorting to statistical operators, intuitive physical modeling, and dimensional analysis. At first, the Reynolds decomposition between mean and fluctuating (e.g., turbulent) components is introduced and applied to the Navier–Stokes equations, resulting in the so-called Reynolds-Averaged Navier–Stokes equations (RANS, in the Favre formulation valid for compressible flows). In these equations, which represent the time-average of the differential balance of mass, momentum, and energy, new terms appear due to the nonlinearity of the original Navier–Stokes equations. These terms cannot be evaluated directly, hence proper ‘closure’ models are required to solve the system.

Several classes of turbulence models were proposed, from simple algebraic models [such as the one of Baldwin–Lomax (Baldwin and Lomax, 1978)], to more advanced models based on one [Spalart–Allmaras (Spalart and Allmaras, 1992)] or two [k-epsilon (Launder and Sharma, 1974), k-omega (Wilcox, 1988)] differential equations, up to models for each turbulent term [Reynolds stress models (Speziale, 1991)]. The interested reader is referred to the books of Pope (2000) for a general discussion of Turbulence modeling and Wilcox (2006) for a review of the most relevant

turbulence models available for CFD. For turbomachinery flows (hence also for ORC turbines), an optimal compromise between computational cost, mathematical complexity, and reliability has been found for the k - ω model, both in the standard and in the Shear Stress Transport formulation proposed in [Menter \(1993\)](#). The k - ω model allows to solve the flow in the near-wall region, and hence is able to simulate the boundary layer development even in the presence of severe pressure gradients. This is of paramount importance for turbines blades, which are exposed to severe acceleration in the front part and to diffusion in the rear suction side. Furthermore, the model also predicts with acceptable accuracy the onset of separation. All of these phenomena are features of ORC turbines, due to the high expansion ratio of the cascades and the onset of shocks, which might induce local boundary layer separation.

As final brick for constructing a reliable flow model for ORC turbines, arbitrary equations of state must be prescribed to account for the thermodynamic behavior of the fluid. This can be done by implementing a generalized thermodynamic treatment, either by resorting to external libraries ([Colonna and Rebay, 2004](#)) or Look-up-Tables ([Pini et al., 2014a](#)), coherently with the approach proposed for the preliminary design.

The resulting RANS system for ORC application is therefore constructed with four or five balance equations, two turbulence model equations, plus the thermodynamic model. From a mathematical perspective, the RANS system shares the same difficulty of the original Navier–Stokes system. However, the grid resolution required by a RANS calculation is of several orders of magnitude smaller than the one required by the original Navier–Stokes system, opening the way for the systematic application of CFD in the industrial context. A rough estimate of the computational cost can be proposed; less than one day for steady three-dimensional calculations, and less than 1 h for steady two-dimensional calculations on standard PCs. A further reduction of at least one order of magnitude can be achieved by resorting to high-performance parallel computing.

8.5.2.2 *Computational Fluid-Dynamics-based turbomachinery design*

In the computational framework discussed in [section 8.5.2.1](#), CFD becomes a tool suitable for routine application within turbomachinery design procedures. However, CFD is inherently an analysis tool, and its application for design demands a rational strategy to ‘guide’ the designer towards an optimal configuration. Furthermore, because of the complexity of the problem and the large number of design variables, the designer can have only a limited vision (and control) of the optimization process. Therefore, an efficient and reliable aerodynamic optimization has to rely on algorithms that automatically drive the design towards the optimal configuration. Furthermore, despite the authors recommend the application of systematic optimization methods along the whole design chain, the aerodynamic optimization is far more complex with respect to preliminary optimization, and it has a comparatively larger impact.

In the last decades, several CFD-based shape optimization procedures were proposed, which can be classified into inverse design methods ([Demeulenaere et al., 1997](#)), adjoint-based gradient methods ([Peter and Dwight, 2010](#)), and stochastic methods, such as evolutionary algorithms (EAs) ([Coello, 2000](#)). Inverse design

methods are attractive as they should allow identification of the geometry that satisfies a prescribed flow condition. However, in practice, the feasibility of the computed shape is not always guaranteed, and the implementation of geometrical constraints is difficult in an inverse framework. Furthermore, these methods require the complete reformulation of the CFD problem, which involves relevant coding and mathematical difficulties when the flow model is particularly complex, as in ORC turbines. Probably for these reasons, the authors are not aware of the application of the inverse method for ORC turbines.

Alternatively, optimization can be pursued by minimizing a certain objective function, using direct CFD methods in combination with sensitivity derivatives (deterministic methods) or EAs (stochastic methods). These two methods share the general formulation of the optimization problem (design variables and constraints, simulation tools, and fitness function), but search for the minimum using a completely different approach.

Deterministic gradient-based design techniques identify the optimal configuration using a relatively low number of steps, providing an efficient way to calculate the gradient. In general the aerodynamic design of turbomachinery requires a large number of design variables, while relatively simple objective functions are to be minimized; for such problems the adjoint approach represents the most suitable and effective technique to compute the gradient (Peter and Dwight, 2010). Adjoint-based deterministic methodologies hence represent one of the most interesting choices for the optimization of turbomachinery blades.

Stochastic evolutionary design techniques search for the optimal shape by resorting to GA, often coupled to surrogate models to reduce the overall computational cost of the optimization procedure (Verstraete et al., 2010). Even though their computational cost remains higher than that achievable with the efficient adjoint solutions, stochastic methods allow the exploration of a wide range of feasible solutions, identifying the best individual solution (i.e., global minimum in some circumstances), and is inherently suitable to handle multiobjective optimization problems (Pierret et al., 2006).

Regardless of the automated design method, any shape optimization strategy requires the definition of the usual four main “bricks”:

1. the set of design variables (and their constraints)
2. the flow model
3. the fitness function (or functions, in case of a multiplicity of nonconcurrent objectives).
4. the optimization strategy.

Out of these four bricks, deterministic and stochastic methods differ for the optimization strategy; the remaining three elements are shared and are discussed with a uniform approach in the following. The two optimization strategies are discussed in Subsections 8.5.2.3 and 8.5.2.4, with the support of dedicated exercises of design, applied to the same supersonic cascade.

1. Design variables

With regard to the selection of the design variables, these can be either all the control points defining the two sides of the blade profile, the TD (as explained in 8.5.1.1), or a subset of them. Most commonly, a subset of the control points' coordinates can be left free to change in a specified range. Notably, the identification of the variable control points and the

definition of the boundaries within that they can move, are the most crucial optimization parameters; they determine the *design space* of the optimization procedure, namely the space which has to contain the blade geometry.¹³ If properly assigned, the design space allows pursuit of shape-optimization, preserving the general operation parameters of the cascade (flow angle, flow rate, etc.).

2. Flow model

For turbine design, the flow model is set by the specific CFD configuration selected (inviscid/viscous/turbulent flow, subsonic/transonic/supersonic flow regime, two-dimensional/quasi-three-dimensional/three-dimensional fluid domain), as discussed in [Section 8.5.2.1](#). In ORC turbines, models including the effects of turbulence are recommended, even though inviscid models remain of interest due to the relevance of shocks (captured in a reliable way even by inviscid flow solvers); obviously, ORC turbine flow solvers must include a rigorous treatment of compressible flows, including the capturing of sonic throats, shocks, and expansion fans. For the purposes of profile design, which is the primary aim of the aerodynamic design, quasi-three-dimensional flow models can be used, solving blade-to-blade slices delimited spanwise by two slip conditions. As a result, the computational cost is similar to that of a two-dimensional model, namely a few minutes.

3. Fitness function

The objective functions are usually defined to achieve an improvement of cascade performance. This can be done directly, by minimizing the entropy production of the cascade (assuming adiabatic flows in ORC turbines, the entropy production is only due to loss mechanisms). As an alternative, indirect definitions can be proposed, by considering the specific features of the flow configuration. In the case of ORC turbine cascades, which operate in highly supersonic flow conditions (especially for radial-inflow and axial-flow machines), shock losses may play a dominant role in the cascade performance. As demonstrated by the proposed design examples reported in the following, the minimization of pressure gradients downstream of the cascade (and hence of the shock strength) can be as effective as the direct minimization of the entropy production.

In the following both deterministic and stochastic shape-optimization methods are presented, and their application to determine the optimal blade shape of a supersonic ORC cascade is discussed. The main differences between the methods, in terms of flexibility, convergence rates, and computational costs, are acknowledged. Furthermore, it is finally shown how the two methods, although following very different convergence paths, lead to a similar outcome in terms of optimal blade shape and performance.

8.5.2.3 *Adjoint-based gradient optimization of a supersonic Organic Rankine Cycle turbine cascade*

Gradient-based optimization techniques are particularly suited to solve optimization problems involving minor geometrical modifications between the initial and the optimal blade shape, as frequently occurs in turbomachinery. When using such

¹³ The proper identification of the design space is more relevant for stochastic optimization methods than for deterministic ones, as the former demand a systematic sampling within the entire design space; however, also for deterministic methods the identification of constraints for the blade geometry is eventually needed in order to provide a feasible blade geometry.

Table 8.2 Desired and undesired characteristics of the continuous and discrete adjoint method

	Continuous	Discrete
Ease of development	–	+
Accuracy of the gradients	–	+
Ability to handle arbitrary fitness functions	–	+
Ability to handle nondifferentiability	–	+
Computational cost (CPU usage and storage)	+	–
Flexibility in solution	+	–

algorithms, the cost of computing the gradient is not negligible and largely affects the overall optimization expense. As a consequence thereof, [Jameson \(1998\)](#) pioneered the use of the *adjoint method* in aerodynamics to compute the sensitivities of a given functional with respect to a certain set of design variables. Traditionally, the adjoint method is classified depending on the approach followed to derive the adjoint equations. In the *continuous adjoint formulation* the flow governing equations are first linearized and then discretized to obtain a suitable form of the adjoint equations to be integrated numerically. The contrary holds for the *discrete adjoint formulation* in which the discretized form of the Navier–Stokes equations is linearized via Automatic Differentiation, as extensively reported in [Giles and Duta \(2003\)](#) and [Mader et al. \(2008\)](#). Both approaches have been extensively investigated for a variety of aerodynamic optimization problems. On the basis of these works, the Pros (+) and the Cons (–) of the two methods are summarized in [Table 8.2](#).

For the case of ORC applications, the discrete adjoint formulation is arguably much more convenient. The formulation of the optimization problem can involve a multiplicity of objective functions (e.g., entropy production or shock strength minimization) that can only be handled by using the discrete adjoint. Furthermore, the use of complex thermo-physical models may cause problems of nondifferentiability, that are solvable only by Automated Differentiation. At the same time, the high computational cost of the discrete adjoint can be partly alleviated through a massively parallel resolution of the adjoint equations. For such reasons, only the discrete adjoint is considered hereinafter.

In mathematical terms, the gradient of the cost functional J , or of any constraint J , is retrieved by sequentially solving the following system of equations:

$$\left(\frac{\partial \mathbf{R}}{\partial \mathbf{u}}\right)^T \mathbf{v} = -\left(\frac{\partial J}{\partial \mathbf{u}}\right)^T \quad (8.12)$$

$$\left(\frac{dJ}{d\alpha_{\text{geo}}}\right)^T = \left(\frac{d\mathbf{X}}{d\alpha_{\text{geo}}}\right)^T \left[\left(\frac{\partial J}{\partial \mathbf{X}}\right)^T + \left(\frac{\partial \mathbf{R}}{\partial \mathbf{X}}\right)^T \mathbf{v} \right] \quad (8.13)$$

The first relation represents the adjoint system of equation, valid for any kind of physical flow model (inviscid, viscid, or turbulent with arbitrary EoS). Its solution \mathbf{v} , i.e., the adjoint vector, can be found by either a direct algorithm, as in Pini et al. (2014b,c), or by a time-marching scheme. Once solved, the second equation allows cheap determination of the sensitivities of the quantity of interest, with respect to changes of the design variables α_{geo} , for instance the control points of CAD curves/surfaces as in Section 8.5.2.3. The first left-hand term of the second equation accounts for the rate of grid perturbation as α_{geo} are moved. An effective way to account for this term is described in Pini et al. (2014b,c).

For a certain blade shape, the flow solution, the adjoint solution, and the objective function gradient are calculated at each optimization step. If unconstrained optimization is of concern, the gradient vector is then converted into physical displacement of the design variables by means of a gradient method (e.g., steepest descent or conjugate gradient). Finally the blade geometry is updated and the process restarts until convergence. The termination criterion is usually expressed in terms of (relative) difference between the objective functions at two successive design steps.

The described design algorithm has been successfully applied by the authors to redesign a converging–diverging ORC turbine cascade operating with siloxane MDM under supersonic conditions. The original blade geometry, shown in Fig. 8.10 was designed by means of the method of characteristics for the diverging part. The optimization process aimed at maximizing the performance of the cascade operating with an expansion ratio of eight starting from a superheated condition ($P_{\text{T,in}} = 8$ bar, $T_{\text{T,in}} = 272^\circ\text{C}$) close to the saturation line, resulting in a discharge Mach number higher than 2.

The blade parameterization, with a total of 22 control points, was constructed by fitting the original blade geometry with two B-Spline curves (one for the suction and one for the pressure side) as reported in 8.5.1.1. However, only the subset of 10 control points marked in red was definitively used for the optimization. This

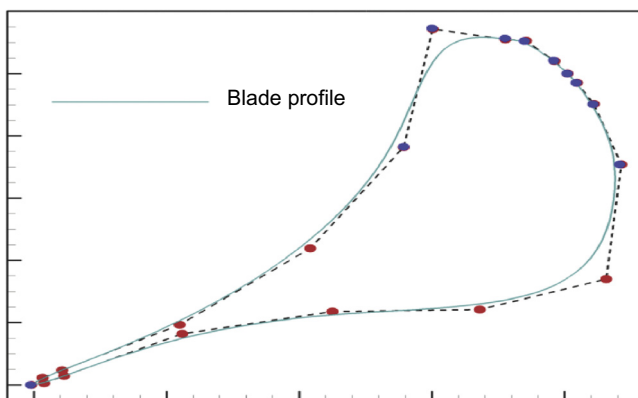


Figure 8.10 Control points distribution of the supersonic Organic Rankine Cycle cascade. *Red dots* indicate the points moved throughout the design process.

Table 8.3 Results of the shape optimization of the supersonic ORC cascade

Blade	J	Y (%)	m_{flow}	α_{flow} (degrees)	Mach_{mix}
Baseline	0.078	11.78	1	74.95	1.95
Optimized	0.014	3.6	0.92	76.68	1.98

resulted from a preliminary sensitivity analysis performed with the adjoint that revealed a minor influence of the remaining points with respect to the cost functional defined as:

$$J = \left[\frac{\sum_{i=1}^{n_{\text{ob}}} (M_i - M_{\text{mix}})^2}{n_{\text{ob}}} \right]^{\frac{1}{2}} \quad (8.14)$$

where M_i is the Mach number at each node of the outflow bound, and M_{mix} is the mixed-out averaged value. For supersonic ORC cascades, but also true for transonic ORC cascades, the major entropy production is due to the strong shock wave forming on the rear suction side of the blade (i.e., the geometry portion controlled by the red control points), giving rise to a high nonuniform flow downstream of the cascade. As a result, enforcing flow uniformity, as is the intent of (8.14), indirectly entails a reduction of fluid-dynamic losses and can be regarded as an effective strategy to improve performance of ORC turbines.

This design exercise was carried out using an inviscid flow model, which was found sufficiently accurate, compared to fully turbulent simulations, and by resorting to look-up tables constructed via the approach proposed in [Pini et al. \(2014a\)](#). The convergence was achieved after 15 iterations, corresponding to 30 min on a dual-core Intel I5. The main results, reported in [Table 8.3](#), showed a significant performance enhancement (an eight-point gain in total pressure loss coefficient Y on the basis of inviscid simulations, corrected to a six-point gain by subsequent turbulent CFD simulations) at the expense of a decrease of mass flow rate, caused by a slight reduction of the throat width. Nonetheless, the mass flow rate can be readily adjusted by increasing the blade span with very minor implications in terms of fluid-dynamic losses. As it can be observed in [Fig. 8.10](#), the reduction of the rear suction side curvature provided by the optimization enabled suppression of the severe shock forming in the downstream mixing zone of the original geometry.

In the presence of nontrivial constraints, for instance, a prescribed outflow angle, the authors suggest the use of constrained optimization algorithms (e.g., quasinewton methods like BFGS). These algorithms require, additionally, the sensitivities of the constraints, that can be computed using the same adjoint infrastructure.

8.5.2.4 Evolutionary stochastic optimization of a supersonic Organic Rankine Cycle turbine cascade

Alternatively or in combination with gradient methods, stochastic techniques are a further relevant class of shape optimization algorithms. Among them, EAs and in particular GAs are particularly attractive as they: (1) deal with smooth-less objective functions, (2) introduce constraints easily, and (3) treat multiobjective optimization, only needing the application of analysis solvers (Reeves and Rowe, 2002). In this perspective, they are termed nonintrusive design algorithms. Furthermore, GAs sample the whole design space and, in case of optimization problems with multiple local optima, they identify promising regions of the design space where the global optimum might be located.¹⁴

However, to exploit the advantages of stochastic methods, thousands of evaluations of the direct computational model of interest are required. To tackle the resulting computational burden, which might become unaffordable for CFD-based design, surrogate-based optimization strategies were developed (Powell, 1970). Surrogate models are mathematical expressions (i.e., analytical functions) of increasing complexity which approximate the actual trend of the objective function (Simpson et al., 2001). The surrogate has to be trained along the process so that its minimum progressively approaches the real physical function. In these strategies, the GA operates on the surrogate only (to find its minimum); hence, the reliability of the surrogate is the key-feature of the whole optimization process.

In Surrogate-Based Optimization, the surrogate model is first built by interpolation on an initial database of configurations tested by CFD, it is then constructed by a Design of Experiments (DoE) technique. Then, the GA finds the minimum of the surrogate. The surrogate constructed with the initial database has a limited reliability, which can be improved following either Local (Surrogate-Based Local Optimization, SBLO) or Global (Surrogate-Based Global Optimization, SBGO) strategies.

The SBLO strategy improves the surrogate by resorting to a trust region approach, based on the calculation of the trust region ratio ρ . For the general iteration k , ρ^k is defined as:

$$\rho^k = \frac{f(x_c^k) - f(x_{\text{opt}}^k)}{\tilde{f}(x_c^k) - \tilde{f}(x_{\text{opt}}^k)} \quad (8.15)$$

in which f is the real (CFD) objective function, \tilde{f} is the surrogate model, x_c is the center of the trust region (optimum of iteration $k - 1$), and x_{opt} is the optimal configuration identified at the iteration k . ρ^k evaluates how reliable is the improvement of the fitness function at the k -th iteration with respect to the previous one. If ρ^k is positive, the design space is shrunk to a smaller 'trust region', centered in x_{opt} . Then a new database

¹⁴ Hybrid optimization is possible, combining GAs with gradient method to efficiently find the global optimum.

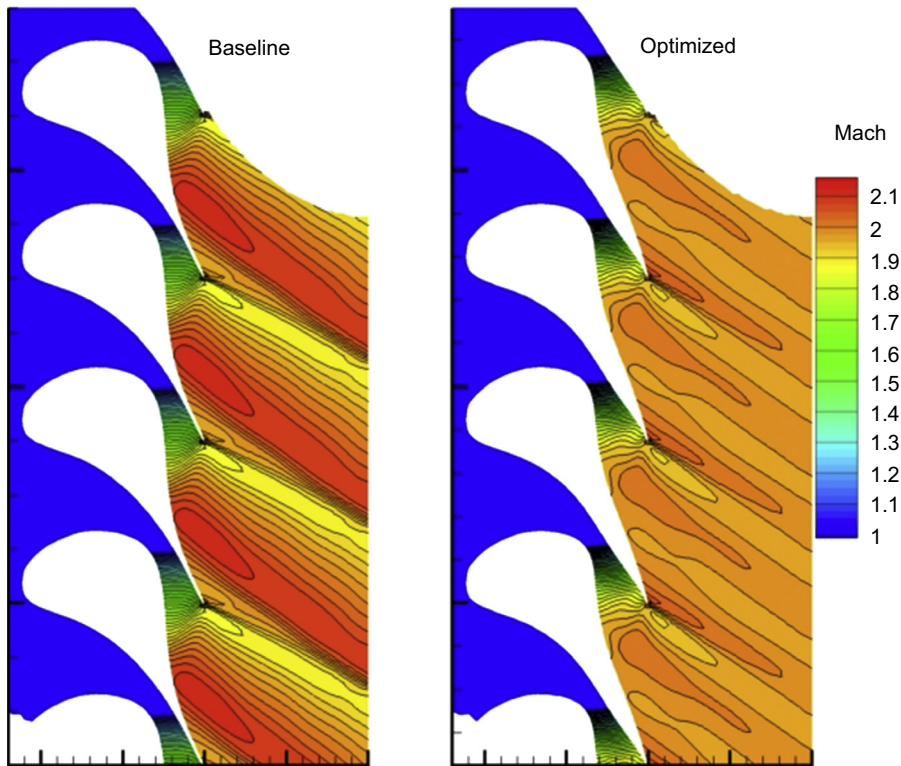


Figure 8.11 Mach number contour for the original and optimized supersonic Organic Rankine Cycle cascade. The greater flow uniformity is clearly visible in the right picture.

of CFD runs is performed, selected by the DoE within the new trust region, as schematically shown in the left frame of Fig. 8.12. The Surrogate is then interpolated, a new optimization is performed with the GA, and a new trust region ratio is evaluated. By iterating the procedure the center of the trust region is guided towards the actual optimum, mimicking the deterministic action of the gradient.

On the contrary, the SBGO strategy improves the surrogate by progressively adding the optima achieved in the previous iterations to the initial database, as represented in the right frame of Fig. 8.12. SBGO is far cheaper than SBLO, as only one DoE has to be performed at the beginning of the process, although there is no guarantee of convergence. However, in the experience of the authors, SBGO most often converges to an optimal configuration very close to the one achieved by SBLO, when applied to shape optimization of turbine blades.

In the following, an exercise of evolutionary design is reported, considering the same converging–diverging blade optimized in Section 8.5.2.4, by applying both SBLO and SBGO strategies.

The blade was parametrized as a unique B-spline composed of 30 control points (with a circular trailing edge), by using the methodology presented in Section 8.5.2.3;

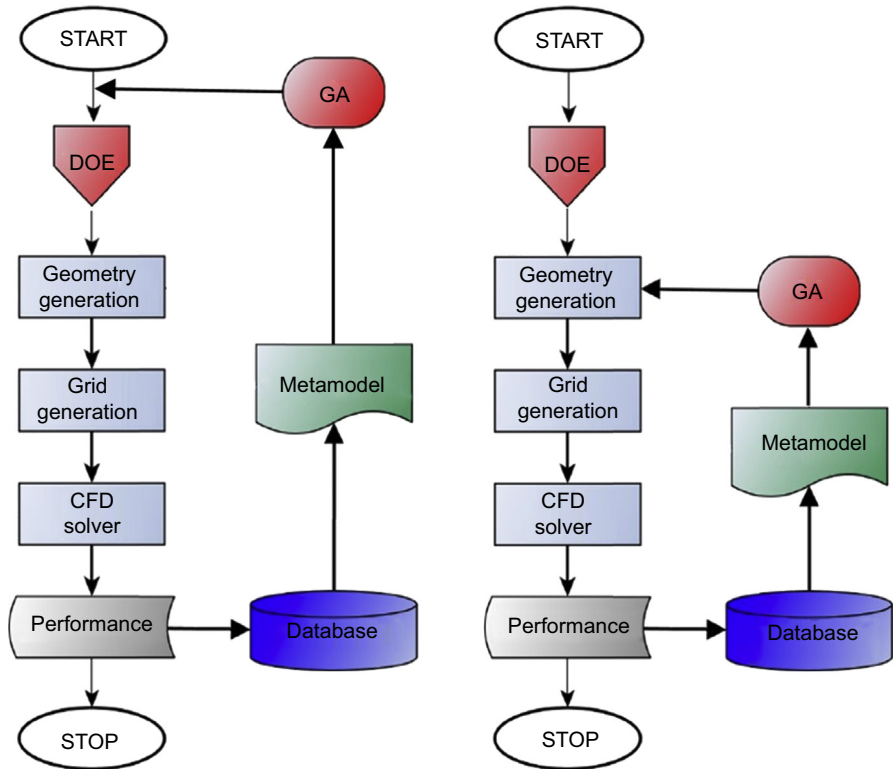


Figure 8.12 Flow charts of surrogate-based local (left) and global (right) optimization strategies.

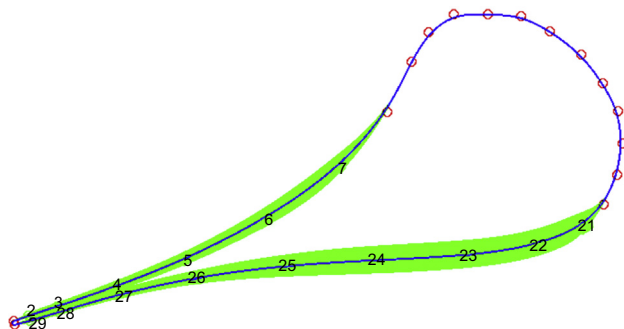


Figure 8.13 Movable control points and related design space (green area).

15 control points were left free to move within the specified design space, as depicted in Fig. 8.13. The trailing edge width was kept fixed for structural reasons.

CFD calculations were carried out on structured grids in the order of 10^5 hexahedral cells, using a quasi-three-dimensional flow model featuring the LuT approach and the

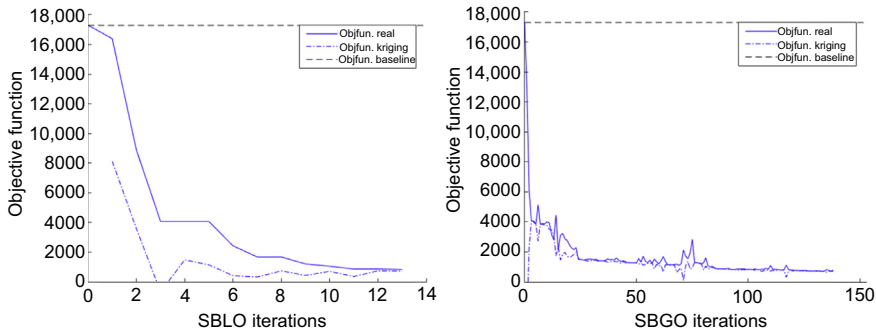


Figure 8.14 Convergence history for SBLO and SBGO techniques.

k-omega SST turbulence model. High-resolution numerical schemes were applied for the integration of the RANS system. The reliability of the CFD model used here was previously assessed against experiments performed by one of the authors on a research turbine stage installed at Politecnico di Milano (Persico et al., 2012).

The optimizations were performed by resorting to a NonDominated Sorting GA, set with 200 generations, a probability of crossover and mutation of 80% and 2%, respectively, and elitism. Kriging was used as a surrogate model to approximate objective function.¹⁵ Latin Hypercube was used as the DoE, composed (as a rule of thumb) of a number of individuals equal to five times the number of variables (namely 75 CFD runs). The objective function was still defined according to Eq. (8.14).

The convergence histories of the SBLO and SBGO techniques, reported in Fig. 8.14, show that the two methods provide the same significant minimization of the objective function (which is reduced by 95% with respect to the baseline value). Both the methods exhibit a smooth convergence process in which the surrogate model quickly matches the real flow tendency; this provided the conclusion that both the trust region and the training procedures are appropriate for the present design problem. The resulting optimal blade configurations were also very similar. The cost of the optimizations were about 0.5 days for SBGO and 2.5 days for the SBLO on a 15 processor Cluster.

The advantages provided by the optimization are clearly visible when comparing the baseline (left) and optimized (right) configurations reported in Fig. 8.15. The minimization of the pressure oscillations downstream of the cascade leads to a noteworthy weakening of the main shock strength. Hence, the severe pressure gradient observed in the baseline case is significantly reduced and the weaving path of the blade wakes is almost eliminated. As a result, the overall entropy generation is also reduced in the optimized case and the total pressure losses of the cascade drop from 15% to 9%, with the flow rate remaining within 1% of the design value.

¹⁵ The Kriging technique is based on a set of interpolation methods, sometimes called Gaussian Processes, and was originally developed for geostatistic problems and nowadays widely used in many engineering fields.

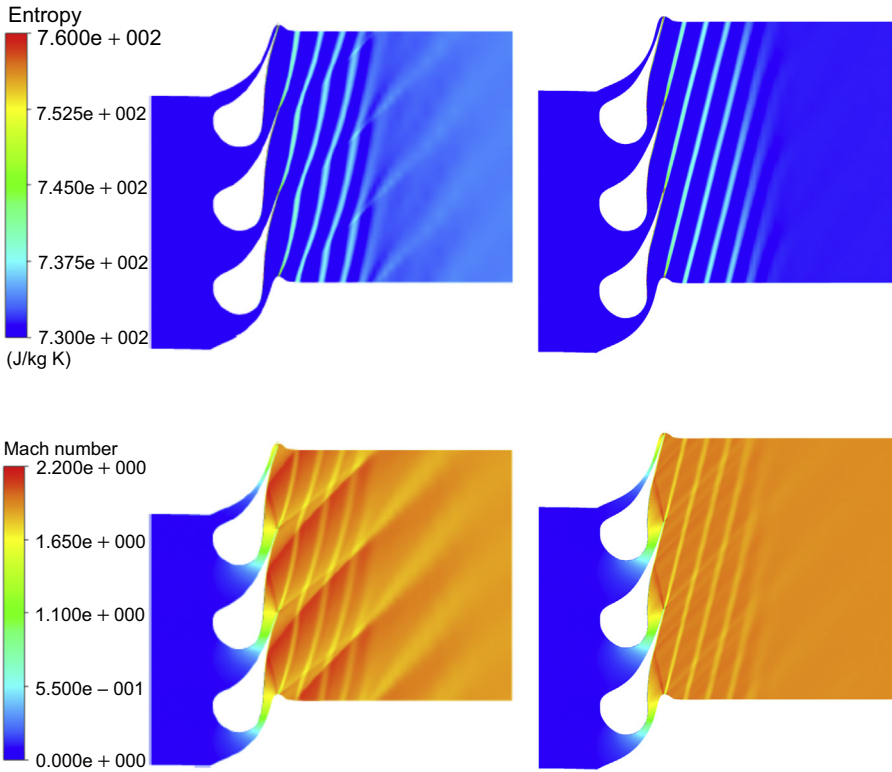


Figure 8.15 Entropy (top) and Mach number (bottom) contours for the baseline (left) and optimized (right) supersonic Organic Rankine Cycle turbine cascade.

These features reproduce those achieved by the adjoint-based gradient method. The optimal blade shapes determined with the two techniques are indeed very similar; both methods enhance the divergence of the channel within the bladed region, making the rear suction side almost straight in the semibladed region. Such a configuration differs significantly from the one resulting from the use of simplified techniques (see subsection 8.5.1.2), proving that shape optimization allows significant improvements in turbine performance.

8.5.2.5 Robust multipoint optimization of a supersonic Organic Rankine Cycle turbine cascade

The automatic character of shape-optimization techniques offers the opportunity to introduce a further element of flexibility in turbine design, including the aleatory variation of operating conditions or the uncertainties in the flow models (e.g., closure parameters of turbulence or thermo-physical models) within the design procedure. This opens the way to achieve turbine configurations which are ‘robust’

with respect to such variations. This is of primary importance for ORC applications, especially for waste-heat recovery systems that are particularly exposed to fluctuations in operating conditions.

Both gradient and evolutionary methods described in [Sections 8.5.2.3 and 8.5.2.4](#) can be adapted to a robust configuration, with minor modifications. A standard way, which was proved to be very effective by the authors, consists of formulating the “robust” objective function J as a weighted sum of the N objective functions J_i evaluated for the i -th operating condition:

$$J = \sum_{i=1}^N w_i J_i \quad (8.16)$$

where w_i are the weight coefficients accounting for the relevance of each single point (in terms of probability or operation time). Such weights can be accurately deduced via uncertainty quantification algorithms, as proposed in [Pini et al. \(2014c\)](#), once a probability density function (e.g., uniform, normal, etc.) for the input variables is established.

The robust design here presented were applied to the same supersonic turbine cascade considered before, using both gradient ([Pini et al., 2014c](#)) and evolutionary methods. Once again, the two methodologies led to similar results, which are briefly summarized in the following.

To cover a sufficiently wide range of operating conditions, representative of ORC turbines, the cascade backpressure was raised by a factor two. Three operating conditions were used to evaluate the multipoint objective functions, namely the design one (1 bar), the maximum one (2 bar), and an intermediate one (1.5 bar), all of them having the same weight. The increase of static backpressure for supersonic converging–diverging cascades strengthens the shocks and may cause a dramatic rise in the loss coefficient.¹⁶

This actually occurs for the original cascade configuration, as it is shown in [Fig. 8.16](#). The same is found for the blades optimized in [Sections 8.5.2.3 and 8.5.2.4](#). When, instead, the robust multipoint optimization is carried out, the shock strength is significantly weakened even for the highest pressure (central frame of [Fig. 8.16](#)) and the loss coefficient undergoes only a slight increase with respect to that resulting at the design backpressure.

This represents a very significant result, not achievable with any of the simplified design methods discussed in this chapter and it is specifically relevant for ORC turbines subject to strong nonlinear variations of the operating conditions.

¹⁶ It is worth noting that this behavior is truly valid as long as the relative flow at the inlet of the subsequent rotor is subsonic. In the case of rotor supersonic inflow, the occurrence of shock waves at the blade leading-edge as well as the onset of the so-called unique incidence effects make the performance of the stator cascade less sensible to the static backpressure.

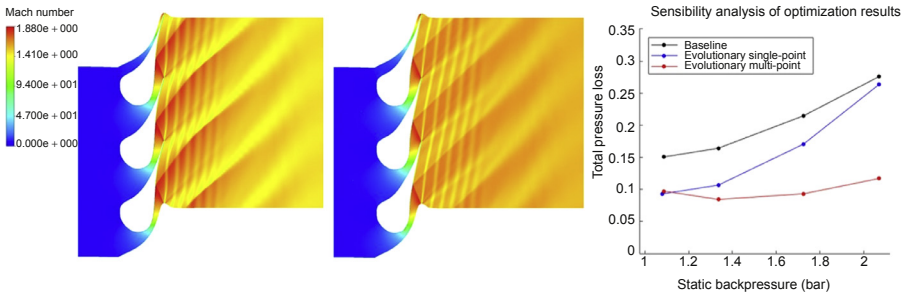


Figure 8.16 Mach number contours for baseline (left) and robust-optimized (center) cascades for the highest backpressure. Dependence of loss coefficient on operating condition (right).

8.6 Conclusions

This chapter has reviewed the most relevant techniques currently available for the design of ORC turbines, showing how these methods can be combined in a coherent design path to create optimal turbine configuration in terms of architecture and blading shape. The formulation of each different model has been presented, giving proper emphasis to the specific features required by ORC turbine models. The mean-line model for preliminary design, the throughflow model for spanwise design, and the CFD model for aerodynamic design have been documented in detail, also providing indications for constructing proper interfaces between each design step.

Alongside the basics of the turbine models, some relevant design remarks for ORC turbines have also been highlighted. In particular, the inappropriateness of the repeated stage strategy for any ORC turbine architecture has been explained, the relevance of spanwise design in the last turbine stages has been justified, and the specific techniques for designing converging–diverging blade rows have been discussed.

By specific choice of the authors, no inverse design methods have been presented. Conversely, and in line with the most recent advances in computational capabilities, it has been shown how direct methods originally developed for analysis purposes can be effectively exploited for design, once incorporated within automatic optimization strategies. The application of systematic optimization at any level of the design chain is recommended and detailed indications have been provided throughout the chapter for constructing efficient optimization procedures for each turbine design step.

The chapter has furthermore highlighted some of the most advanced aerodynamic shape optimization techniques, emphasizing their specific requirements in terms of geometry representation and flow modeling. The potential for shape optimization has been demonstrated by applying two very different optimization procedures to the same supersonic ORC turbine cascade, originally designed by means of classical techniques for converging–diverging blade rows. Notably, both the methods provide dramatic improvements in the cascade performance (loss coefficient reduced by 40%) and lead to a very similar outcome in terms of optimal blade shape.

The flexibility and the automatic character of these techniques opens the way for the so-called robust design, namely the formulation of the optimization problem in a statistical framework. Eventually, this enables to explicitly consider the variability of some operating or physical parameters of the turbine in the design process. Given the specific operation of ORC turbines, which often run at part-load conditions, a dedicated example has been presented to show how a blade configuration providing almost constant performance in a relatively wide operation range can be determined, by applying shape optimization tools. Such a result clearly demonstrates the potential of optimization over traditional design methods.

The discussion and the results presented in this chapter suggest that, even though highly loaded and featuring high-flaring angles, ORC turbines can exhibit relatively high efficiency if designed with proper methods. Especially for emerging technologies, such as mini-ORC power systems (i.e., below 50 kW_{el}), the use of advanced design tools will be instrumental for achieving acceptable performance of the turbine, thus making the ORC technology viable for a variety of applications.

References

- Ainley, D.G., Mathieson, G.C.R., 1957. A Method of Performance Estimation for Axial-flow Turbines. Technical Report No. R&M 2974. Aeronautical Research Council, London.
- Angelino, G., Gaia, M., Macchi, E., 1984. A review of Italian activity in the field of organic Rankine cycles. In: International VDI-seminar (ORC-hp-technology, Working Fluid Problems), Zürich, Switzerland, September 10–12, pp. 465–482.
- Baldwin, B.S., Lomax, H., 1978. Thin Layer Approximation and Algebraic Model for Separated Turbulent Flows. AIAA Paper 78-257.
- Casati, E., Vitale, S., Pini, M., Persico, G., Colonna, P., 2014. Centrifugal turbines for mini-organic rankine cycle power systems. *ASME Journal of Engineering for Gas Turbines and Power* 136 (12), 122607.
- Coello, C., 2000. A updated survey of GA-based multiobjective optimization techniques. *ACM Computing Surveys* 32 (2), 109–143.
- Colonna, P., et al., 2015. Organic rankine cycle power systems: from the concept to current technology, applications, and an outlook to the future. *ASME Journal of Engineering for Gas Turbines and Power* 137 (10), 100801–100819.
- Colonna, P., Rebay, S., 2004. Numerical simulation of dense gas flows on unstructured grids with an implicit high resolution upwind Euler solver. *International Journal for Numerical Methods in Fluids* 46.
- Colonna, P., Harinck, J., Rebay, S., Guardone, A., 2008. Real-gas effects in organic Rankine cycle turbine nozzles. *Journal of Propulsion and Power* 24 (2), 282–294.
- Craig, H., Cox, H., 1971. Performance estimation of axial flow turbines. *Proceedings of the Institution of Mechanical Engineers* 185 (1), 407–424.
- Damle, S.V., Dang, T.Q., Reddy, D.R., 1998. Throughflow method for turbomachines applicable for all flow regimes. *Journal of Turbomachinery* 119 (2), 256–262.
- Deich, M., Filippov, G., Lazarev, L., 1965. Atlas of axial turbine blade cascades. C.E. Trans 4563–4564 (CEGB Information Services).

- Demeulenaere, A., Leonard, O., Van Den Braembussche, R., 1997. A two-dimensional Navier-Stokes inverse solver for compressor and turbine blade design. *Journal of Power and Energy* 211 (4), 299–307.
- Denton, J.D., Dawes, B., 1999. Computational fluid dynamics for turbomachinery design. *Proceedings of IMechE* 213 (Part C).
- Dixon, S.L., Hall, C.A., 2010. *Fluid Mechanics and Thermodynamics of Turbomachinery*, fifth ed. Elsevier Butterworth-Heinemann, Burlington, MA.
- Farin, G., 2002. *Curves and Surfaces for CAGD: A Practical Guide*, fifth ed. Morgan Kaufmann Publishers Inc., San Francisco, CA, USA.
- Gaia, M., 2011. 30 Years of organic rankine cycle development. In: *First International Seminar on ORC Power Systems*, Delft, The Netherlands, September. 11–23. Keynote Lecture. <http://www.orc2011.nl/content/keynote>.
- Giles, M.B., Duta, M.C., 2003. Algorithm developments for discrete adjoint methods. *AIAA Journal* 41 (2), 198–205.
- Glassman, A.J., 1995. Enhanced Analysis and Users Manual for Radial-Inflow Turbine Conceptual Design Code RTD. NASA Report 195454.
- Guardone, A., Spinelli, A., Dossena, V., 2013. Influence of molecular complexity on nozzle design for an organic vapor wind tunnel. *Journal of Engineering for Gas Turbines and Power* 135 (4), 42307.
- Hoffren, J., Talonpoika, T., Larjola, J., Siikonen, T., 2002. Numerical simulation of real-gas flow in a supersonic turbine nozzle ring. *ASME Journal of Engineering Gas Turbines Power* 124 (2), 395–403.
- Horlock, J.H., 1971. On entropy production in adiabatic flow in turbomachines. *Journal of Basic Engineering* 93, 587–593.
- Jameson, A., 1998. Aerodynamic design via control theory. *Journal of Scientific Computing* 3 (3), 233–260.
- Larocca, F., 2008. Multiple objective optimization and inverse design of axial turbomachinery blade. *Journal of Propulsion and Power* 24 (5), 1093–1099.
- Lauder, B.E., Sharma, B.I., 1974. Application of the energy dissipation model of turbulence to the calculation of flow near a spinning disc. *Letters in Heat and Mass Transfer* 1 (2), 131–138.
- Ljungstrom, F., 1949. The development of the Ljungström steam turbine and air preheater. *Proceedings of the Institution of Mechanical Engineers* 160 (1), 211–223.
- Macchi, E., Perdichizzi, A., 1981. Efficiency prediction for axial-flow turbines operating with nonconventional fluids. *Journal of Engineering for Gas Turbine and Power* 103 (4), 718–724.
- Macchi, E., Bassi, G., Bollina, E., Perdichizzi, A., Osnaghi, C., 1980. Cnrm thermal heat pump - 2. Turbomachinery development. In: *XV International Congress of Refrigeration*, Venezia 23–29 September 1979.
- Macchi, E., 1977. Design criteria for turbines operating with fluids having a low speed of sound. *Von Karman Institute for Fluid Dynamics* 2, 1–64.
- Macchi, E., 2013. The choice of working fluid: the most important step for a successful organic rankine cycle (and an efficient turbine). In: *Second International Seminar on ORC Power Systems*, Rotterdam, The Netherlands, October 7–8. Keynote Lecture. <http://www.asme-orc2013.nl/content/keynote>.
- Mader, C.A., Martins, J.R.R.A., Alonso, J.J., van der Weide, E., 2008. Adjoint: an approach for the rapid development of discrete adjoint solvers. *AIAA Journal* 46 (4), 863–873.
- Marconcini, M., Rubecchini, F., Arnone, A., Del Greco, A.S., Biagi, R., 2012. Aerodynamic investigation of a high pressure ratio turbo-expander for organic rankine cycle applications. *Proceedings of the ASME Turbo Expo* 8.

- Marsh, H., 1966. A Digital Computer Program for the Through-Flow Fluid Mechanics in an Arbitrary Turbomachine Using a Matrix Method. Tech. Rep. 3509. Aeronautical Research Council.
- Menter, F.R., 1993. Zonal Two Equation K- ω Turbulence Models for Aerodynamic Flows. AIAA Paper 93-2906.
- Meroni, A., La Seta, A., Andreasen, J.G., Pierobon, L., Persico, G., Haglind, F., 2016. Combined Turbine and Cycle Optimization for Organic Rankine Cycle Power Systems—Part A: Turbine Model. *Energies* 9 (5), 313.
- Novak, R.A., 1967. Streamline curvature computing procedures for fluid flow problems. *Journal of Engineering for Gas Turbines and Power* 89, 478–490.
- Osnaghi, C., Angelino, G., Bassi, F., Bollina, E., Ferrari, P., Gaia, M., Giglioli, G., Macchi, E., Perdichizzi, A., 1979. Progetto e realizzazione di un motore a fluido organico con espansione a turbina da accoppiarsi con un impianto solare a media concentrazione. In: *Proceedings of the II Seminario Informativo dell'attività del sottoprogetto 'Energia Solare'*, Milano, pp. 432–443 (in Italian).
- Osnaghi, C., 2013. Teoria delle Turbomacchine. Esculapio.
- Oudkerk, J., Quoilin, S., Declaye, S., Guillaume, L., Winandy, E., Lemort, V., 2013. Evaluation of the energy performance of an organic rankine cycle-based micro combined heat and power system involving a hermetic scroll expander. *ASME Journal of Engineering for Gas Turbines and Power* 135 (4), 042306.
- Pasquale, D., Persico, G., Rebay, S., 2013a. Optimization of turbomachinery flow surfaces applying a CFD-based throughflow method. *ASME Journal of Turbomachinery*. ISSN: 0889-504X 136 (3 (March)), 031013 (11 pages).
- Pasquale, D., Ghidoni, A., Rebay, S., 2013b. Shape optimization of an Organic Rankine Cycle radial turbine nozzle. *Journal of Engineering for Gas Turbines and Power* 135 (4), 42308.
- Persico, G., Rebay, S., 2012. A penalty formulation for the throughflow modeling of turbomachinery. *Computers & Fluids*. ISSN: 0045-7930 60, 86–98.
- Persico, G., Mora, A., Gaetani, P., Savini, M., 2012. Unsteady aerodynamics of a low aspect ratio turbine stage: modeling issues and flow physics. *Journal of Turbomachinery* 134 (6).
- Persico, G., Pini, M., Dossena, V., Gaetani, P., 2013. Aerodynamic design and analysis of centrifugal turbine cascades. In: *ASME Paper GT2013-95770, Proceedings of the 2013 ASME Turbo Expo, Turbine Technical Conference & Exposition, June 3–7, 2013, San Antonio, Texas, USA*.
- Persico, G., Pini, M., Dossena, V., Gaetani, P., 2015. Aerodynamics of centrifugal turbine cascades. *ASME Journal of Engineering for Gas Turbines and Power*. ISSN: 1528-8919 137 (11 (November)), 112602 (11 pages).
- Peter, J., Dwight, R., 2010. Numerical sensitivity analysis for aerodynamic optimization: a survey of approaches. *Computers & Fluids* 39, 373–391.
- Petrovic, M.V., Dulikravich, G.S., Martin, T.J., 2001. Optimization of multistage turbines using a through-flow code. *Journal of Power and Energy* 215 (5), 559–569.
- Pierret, S., Van Den Braembussche, R., 1999. Turbomachinery blade design using a Navier-Stokes solver and artificial neural network. *Journal of Turbomachinery* 121 (2), 326.
- Pierret, S., Coelho, R., Kato, H., 2006. Multidisciplinary and multiple operating points shape optimization of three-dimensional compressor blades. *Structural and Multidisciplinary Optimization* 33 (1), 61–70.
- Pini, M., Persico, G., Casati, E., Dossena, V., 2013. Preliminary design of a centrifugal turbine for ORC applications. *ASME Journal of Engineering for Gas Turbines and Power* 135, 042312.

- Pini, M., Spinelli, A., Persico, G., Rebay, S., 2014a. Consistent Look-up Table interpolation method for real-gas flow simulations. *Computers & Fluids*. ISSN: 0045-7930 107, 178–188.
- Pini, M., Persico, G., Pasquale, D., Rebay, S., 2014b. Adjoint method for shape optimization in real-gas flow applications. *ASME Journal of Engineering for Gas Turbines and Power*. ISSN: 1528-8919 137 (3 (March)), 032604 (13 pages).
- Pini, M., Persico, G., Dossena, V., 2014c. Robust adjoint-based shape optimization of supersonic Turbomachinery cascades. In: *ASME Paper GT2014-27064, Proceedings of the 2014 ASME Turbo Expo, Turbine Technical Conference & Exposition*, June 16–20, 2014, Dusseldorf, Germany.
- Pope, S.B., 2000. *Turbulent Flows*. Cambridge University Press.
- Powell, M.J.D., 1970. A new algorithm for unconstrained optimization. In: Rosen, J., Mangasarian, O., Ritter, K. (Eds.), *Nonlinear Programming*. Academic Press, New York, pp. 31–65.
- Quoilin, S., Broek, M.V.D., Declaye, S., Dewallef, P., Lemort, V., 2013. Techno-economic survey of organic Rankine cycle (ORC) systems. *Renewable Sustainable Energy Rev* 22, 168–186.
- Rai, M., 2000. Aerodynamic design using neural networks. *AIAA Journal* 38 (1), 173–182.
- Reeves, C.R., Rowe, J.E., 2002. *Genetic Algorithms: Principles and Perspectives: A Guide to GA Theory*. Kluwer Academic Publishers, Norwell, MA, USA.
- Rinaldi, E., Pecnik, R., Colonna, P., 2015. Unsteady RANS simulation of the off-design operation of a high expansion ratio ORC radial turbine. In: *3rd International Seminar on ORC Power Systems*, Brussels, Belgium, 12–14 October 2015.
- Rodriguez-Fernandez, P., Persico, G., 2015. Automatic design of ORC turbine profiles using evolutionary algorithms. In: *Proceedings of the Third International Seminar on ORC Power Systems*, October 12–14, 2015, Brussels, Belgium.
- Sandberg, R.D., Michelassi, V., Pichler, R., Chen, L., Johnstone, R., 2015. Compressible direct numerical simulation of low-pressure turbines-part I: methodology. *Journal of Turbomachinery* 137 (5) art. no. 051011.
- Sawyer, J., 1972. *Gas Turbine Engineering Handbook*. Gas Turbine Publications, Stamford, CT.
- Simon, J.F., Leonard, O., 2005. A throughflow analysis tool based on the Navier–Stokes equations. In: *6th European Turbomachinery Conference*.
- Simpson, T., Poplinski, J., Koch, P.N., Allen, J., 2001. Metamodels for computer-based engineering design: survey and recommendations. *Engineering With Computers* 17 (2), 129–150.
- Smith, L.H., 1966. The radial-equilibrium equation of turbomachinery. *Journal of Engineering Power* 88.
- Spadacini, C., Centemeri, L., Xodo, L., Astolfi, M., Romano, M., Macchi, E., 2011. A new configuration for organic Rankine cycles power systems. In: *First International Seminar on ORC Power Systems*, Delft, The Netherlands, September 11–23.
- Spalart, P.R., Allmaras, S.R., 1992. A One-Equation Turbulence Model for Aerodynamic Flows. *AIAA Paper* 92-0439.
- Speziale, C.G., 1991. Analytical methods for the development of Reynolds-stress closures in turbulence. *Annual Review of Fluid Mechanics* 23.
- Spinelli, A., Pini, M., Dossena, V., Gaetani, P., Casella, F., 2013. Design, simulation, and construction of a test rig for organic vapors. *ASME Journal of Engineering for Gas Turbines and Power* 135 (4), 042304.
- Traupel, W., 1977. *Thermische Turbomaschinen*. Springer-Verlag, Berlin.

- Uusitalo, A., Turunen-Saaresti, T., Guardone, A., Grönman, A., 2014. Design and flow analysis of a supersonic small scale ORC turbine stator with high molecular complexity working fluid. In: ASME Turbo Expo 2014: Turbine Technical Conference and Exposition.
- Verneau, A., 1978. Emploi des fluids organiques dans les turbines solaires (The use of organic fluids in the solar turbines). *Entropie* 82, 9–18.
- Verstraete, T., Alsalihi, Z., Van Den Braembussche, R., 2010. Multidisciplinary optimization of a radial compressor for microgas turbine applications. *ASME Journal of Turbomachinery* 132 (2), 031004.
- Wilcox, D.C., 1988. Re-assessment of the scale-determining equation for advanced turbulence models. *AIAA Journal* 26 (11), 1299–1310.
- Wilcox, D.C., 2006. *Turbulence Modeling for CFD*. DCW Industries Inc.
- Wilson, D., 1984. *The Design of High-Efficiency Turbomachinery and Gas Turbines*. MIT Press, Cambridge, MA.
- Zweifel, O., 1945. The spacing of turbo-machine blading especially with large angular deflection. *Brown Boveri Review* 32 (1), 436–444.

Axial flow turbines for Organic Rankine Cycle applications

9

E. Macchi, M. Astolfi

Politecnico di Milano, Milan, Italy

9.1 The role of axial-flow turbines in the power generation sector

All statistical data prove that the axial-flow turbine is by far the preferred solution to convert the potential energy of a fluid working within a thermodynamic power cycle into mechanical energy; actually, most of the electricity produced worldwide is obtained by electric generators driven by axial-flow turbines. As is well known, about 70% of electricity in the world is produced in power plants fueled by fossil fuels (carbon, natural gas, and oil), either in gas turbine or in turbine cycles; all of these power plants adopt multistage axial flow turbines. A similar choice is made for power cycles of nuclear reactors, which produce roughly 12% of the world's electricity. If we sum the contribution of geothermal turbines, biomass steam turbines, hydro axial-flow turbines, and wind turbines, we find out that approximately 90% of the energy produced worldwide comes from axial-flow turbines.

Such a wide range of applications, proves that the axial-flow turbines, by properly selecting their design parameters, fit well practically all situations as reported in Fig. 9.1:

- Working fluid: can be a gas (the most common are the combustion products in gas turbines), a vapor (the most common is steam, either superheated or wet), or a liquid (the most common is water).
- Temperature: can be as high as 1400°C, as in the first stages of modern gas turbines; can be close to ambient temperature, as in the last stages of a steam turbine; or can be much lower than ambient temperatures, as in cryogenic plants.
- Pressure: can be very high (above 300 bar, as in Ultra Super Critical (USC) steam plants), or very low (a few hundredths of a bar, like in the last stage of a steam cycle, condensing at a low temperature).
- Overall pressure ratio: can be as high as several thousands, as in USCs, or as low as 1.0002 in wind turbines.
- Overall enthalpy drop: can be as high as 3000 kJ/kg or as low as a few tenths of J/kg in wind turbines.
- Volume flow rates: from several thousands of m³/s, as in the last stage of large steam turbines to a few hundredths of m³/s, as in high pressure stages of small steam turbines.
- Volume ratios: from some thousands (in Ultra Supercritical Cycles of modern steam power stations) to unity (hydro turbines).
- Speed of revolution: from over 100,000 rpm for micro gas turbines to a few rpm for large wind turbines.
- Outer diameters: from a few centimeters, as in micro-turbines to over 100 m, in multiMW wind turbines.

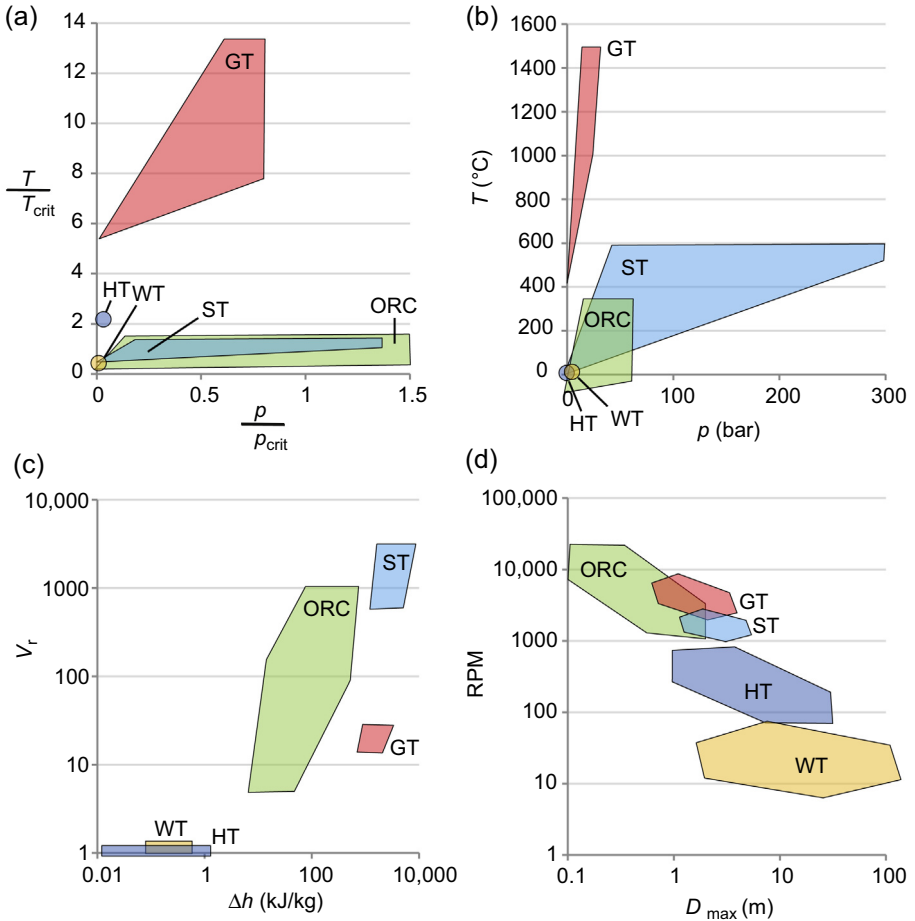


Figure 9.1 Range of application of commercial axial flow turbines: Gas Turbine (GT), Steam Turbine (ST), Hydro Turbine (HT), and Wind Turbine (WT).

Of course, the axial flow turbine characteristics vary for the different applications: wind turbines have a few (two or three) rotor blades, without stator blades or a diffuser; Kaplan hydro turbines have centripetal adjustable stator blades followed by an axial flow rotor and a diffuser; aero-derivative gas turbines have a multishaft arrangement, with various stages rotating at different speeds; and large-scale industrial gas turbines have three or four stages on the same shaft. Both the last two families have air-cooled blades, which require peculiar aerodynamic design features. Eventually, steam turbines exhibit a large variety of solutions, generally with a single-shaft arrangement and a large number of stages. Generally speaking, all the quoted applications are mature technologies, with hundreds or thousands of models in operation and with well-established, sophisticated design procedures. On the other hand, in the Organic Rankine Cycle (ORC) field, because of the great variety of applications, off-the-shelf

components are not available and each expander is generally customized depending on the working fluid and cycle design parameters. In the scientific literature, there is little availability of numerical data and it is difficult to estimate the maximum attainable efficiency of a turbomachine without performing a predesign of the component.

This chapter aims at defining a set of general correlations for the estimation of axial-flow turbine efficiency in the ORC field. A dedicated numerical tool is used for the optimization of several hundreds of turbines and the results are presented in specific parameters (SP , V_r and N_s) according to similarity rules. The analysis is carried out for single, two, and three stages turbines. For each case, a correlation of efficiency at optimal rotational speed is calibrated in function of the equivalent single stage SP and the total isentropic V_r . Three sensitivity analyses are proposed in order to highlight the effects of each single parameter on stage efficiency. Finally, the effect of fluid choice on turbine performance and dimension is discussed with a numerical example.

9.2 The peculiarities of the design procedures of Organic Rankine Cycle turbines

9.2.1 The selection of input parameters is part of the turbine design procedure

The design procedure of a “conventional” turbine (either a gas, steam, or hydraulic turbine) initiates after a series of input data have been defined by considerations not strictly involved with turbine design, these include: the working fluid, the total thermodynamic conditions ahead of the turbine, the outlet static pressure, and the mass flow rate. Often, also the speed of revolution and the number of stages are known in advance, on the ground of previous experience on similar machines.

On the contrary for ORCs, it is a common situation to design the turbine for each specific application. As a rule, before commencing the turbine design, a number of important decisions have to be made, first of all, the working fluid, then the power cycle arrangement (subcritical or supercritical, saturated or superheated, recuperated or not, etc.). These choices are not straight forward, but require optimization procedures, as dealt with in Chapter 7. The “quality” of the results of these optimizations relies on the availability of reliable correlations capable of predicting with reasonable accuracy the performance and cost of the main components, in particular of the turbine. In other words, the choice of the working fluid and of the thermodynamic conditions at turbine inlet and outlet is not a design step that can be done independently from their influence on the turbine characteristics.

9.2.2 Why simple correlations of efficiency prediction proposed for gas and steam turbines do not apply to Organic Rankine Cycle turbines

Various correlations, charts, and diagrams for the estimation of axial turbine efficiency are proposed in the literature but usually they lack some variables of crucial interest in the ORC field. The use of complex and heavy fluids entails a design of ORC turbines

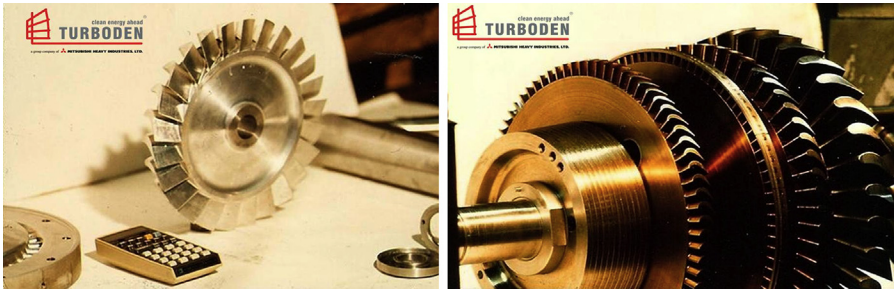


Figure 9.2 Two Organic Rankine Cycle axial-flow turbines designed in the late 1970s (Gaia, 2011).

which is different from either gas or steam turbines. Organic fluids generally operate at moderate temperatures and show a small isentropic enthalpy drop in expansion leading to the design of compact turbines with a reduced number of stages and low loading coefficients (k_{is}). Peripheral speed is generally not a critical issue while in gas and steam turbines this is the key limiting factor in the selection of stage number due to both mechanical stresses and high temperatures. On the other hand, organic fluids usually have large volume ratios per stage and a low speed of sound. Both these aspects make the design of an ORC turbine a quite challenging task which cannot be faced without the support of specific optimization software. Simple correlations such as Smith diagrams (Smith, 1965) and Baljé and Binsley plots (Baljé and Binsley, 1968) cannot completely catch these ORC turbine peculiarities. As already demonstrated by Macchi (1977), Macchi and Perdichizzi (1977), and Lozza et al. (1981), a rigorous design of an axial flow turbine should take into account real blade dimensions and the effects of Mach numbers especially if supersonic flows are present. These aspects are crucial for organic fluids, where blades are characterized by a large height variation, large flaring angles, and supersonic velocities. In particular in Macchi (1977) the effect of both the volume ratio and the specific speed is analyzed for different single stage turbines operating with heavy and complex fluids while in Lozza et al. (1981) a sensitivity analysis is carried out varying the number of stages for turbines with two different size parameters. A further step ahead is provided in the work of Macchi and Perdichizzi (1977) with the definition of a map of efficiency for single stage turbines at optimized rotational speed as a function of size parameter and volume ratio. The purpose of this Chapter is to propose an efficiency correlation for single, two, and three stage axial-flow turbines at optimized rotational speed in a wide range of volume ratios and dimensions.

Fig. 9.2 reports two examples of ORC turbines designed according to this methodology.

9.3 Methodology

9.3.1 Similarity rules and selection of independent variables

Except for some biomass applications, in the ORC field, each turbine is designed ex novo because each plant differs in the available thermal power and in the temperature

of both the heat source and the cooling medium. Turbines in ORC can operate with different fluids in a large range of pressure and volume ratios, size, and power output. For these reasons, it is interesting to adopt a nondimensional approach which allows comparing optimal turbine designs on the basis of specific parameters. According to similarity rules (Dixon et al., 1998), the results achieved for a certain turbine stage can be extended to any other case if the stages respect the following conditions (Macchi and Perdichizzi, 1977):

- They have the same specific speed.
- The geometric similarity is fully verified, namely all the geometrical ratios are equal.
- The flow is fully turbulent so that the Reynold number effects are negligible.
- The Mach numbers are similar.
- The volumetric behavior of the two fluids is the same, namely the volume flow rate variation across the stage is equal for the two fluids. This condition is verified if the two fluids are incompressible or if they are ideal gas with the same pressure ratio and the same heat capacity ratio.

ORC turbines range from micro scale to large machines and so the geometrical similarity cannot be always verified because of the presence of technological constraints such as the minimum trailing edge thickness and the minimum tip clearance gap. Very small turbines are intrinsically less efficient because of the increase of secondary and leakage losses. On the other hand, the high value of volume ratios affect the turbine stage design which requires converging–diverging blades and relevant variation of blade height in a single row with detrimental effects on stage efficiency.

The parameters suggested as independent variables for a parametric analysis are the size parameter SP and the volume ratio V_r , while the specific speed N_s will be optimized for each case. The physical significance of SP, V_r , and N_s and their influence on the turbine efficiency will be discussed later.

$$SP = \frac{V_{out,is}^{0.5}}{\Delta h_{is}^{0.25}} \quad (9.1)$$

$$V_r = \frac{V_{out,is}}{V_{in}} \quad (9.2)$$

$$N_s = \frac{RPM}{60} \frac{V_{out,is}^{0.5}}{\Delta h_{is}^{0.75}} \quad (9.3)$$

9.3.2 Simplifying assumptions of fluid behavior

In order to obtain efficiency maps with sufficient detail and covering a large range of ORC applications, hundreds of turbines have been optimized. Independent variables range between a minimum and a maximum value, which is 0.02–1 m for SP and 1.2–200 for V_r .

The optimizations presented in the following sections are realized assuming a complex ideal gas with a γ value equal to 1.05 as representative of a generic organic fluid. We found this simplifying hypothesis appropriate for the scope of the present analysis, i.e., to obtain a quite accurate preliminary prediction of turbine efficiency for a large

variety of ORC cycles and working fluids. The test cases at the end of this chapter confirm the validity of this assumption. Of course, in the final turbine design a proper Equation of State (EoS) should be considered.

In this study, Reynolds numbers are not considered as independent variables since for an Re greater than 10^6 the effect on stage performance is negligible, while the influence of Mach numbers on blade geometry, flow angles, and losses are accounted for. Even if the Mach numbers resulting from the adopted ideal gas assumption differ from the real ones, these deviations cause minor effects on the predicted stage efficiency (Macchi and Perdichizzi, 1977).

9.3.3 The Axtur code

All the results presented in the following sections are obtained with Axtur tool, an *in house* optimization code for axial flow and radial outflow turbines developed by Macchi and Lozza at the Energy Department of the Politecnico di Milano. The code is based on a pseudo 1D approach and both the blade channels geometry and velocity triangles are defined at the mean diameter for each blade row. Blade heights are hence obtained from the continuity equation and the actual blade geometry is considered in the efficiency losses calculation. Efficiency loss for each row is computed using correlations from the literature, to take into account the presence of the boundary layer, supersonic flows, flow angle variations, and other losses. Fig. 9.3 depicts the main

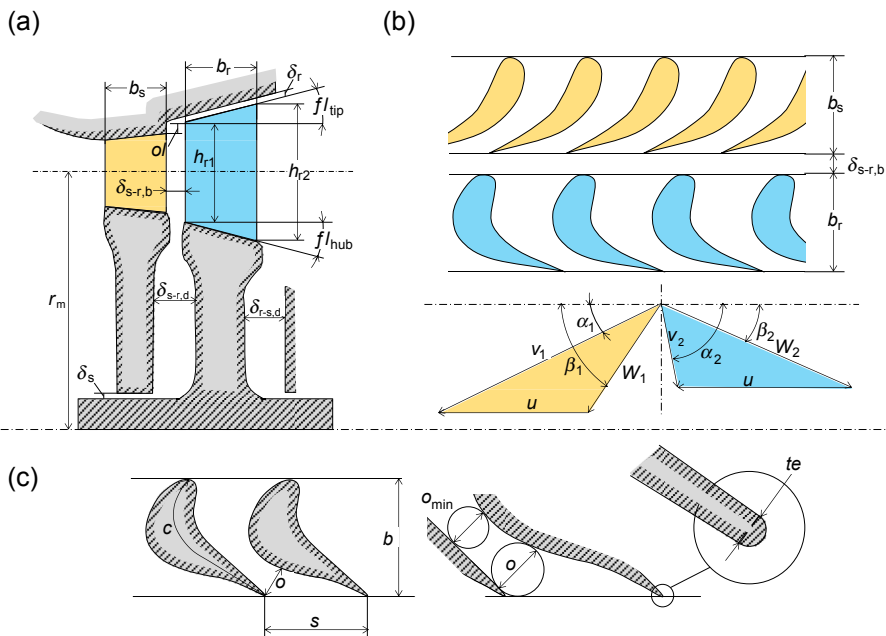


Figure 9.3 Notation used in Axtur for the blade geometry (a and c) and the velocity triangles (b). In the velocity triangle, the V vector represents the absolute velocity, while W is the velocity relative to the rotor blade, and the u vector is the peripheral speed. Subscripts 1 and 2 refer to the inlet and the outlet of the rotor blade respectively.

quantities used to describe an axial turbine stage; in Fig. 9.3(a) the stator and the rotor stage are represented in the meridional plane, in Fig. 9.3(b) the blade-to-blade plane is shown with a representation of velocity triangles, and finally, Fig. 9.3(c) depicts a converging–diverging blades used by the code when $Ma > 1.4$, otherwise $o = o_{\min}$ and post expansion is considered.

Axtur, starting from a feasible initial point, performs multivariable constrained optimizations for turbines with a maximum stage number equal to three. Every stage is fully defined by nine parameters. Three of them define stage quantities: the stage isentropic loading coefficient (k_{is}), the isentropic degree of reaction (r^*), and the isentropic volume ratio (V_r). The other six parameters (three for each row) are representative of stage geometrical ratios (o/s , o/b , and b/r_m). These parameters are the optimization variables of the problem and they can be varied by the optimization algorithm between a lower and an upper bound whose values are defined according to the limits of the correlations used to compute the efficiency losses.

In addition, nonlinear constraints are considered for other variables of interest, like maximum Mach numbers, maximum number of blades, flaring angles, and for other technological limitations. Penalty factors are introduced if nonlinear constraints are not respected.

For a single stage, Axtur optimizes the total-to-static efficiency corrected by the fraction of kinetic energy recovered by the diffuser according to Eq. (9.4).

$$\eta = \frac{W}{\Delta h_{T-S} - \varphi_E \frac{v_{2,a}^2}{2}} \quad (9.4)$$

where φ_E is the efficiency of the diffuser; it is assumed that 50% of the kinetic energy of the discharge absolute velocity axial component can be recovered.

The approach is not completely rigorous because the recovery of kinetic energy entails a reduction of the pressure at turbine discharge and so a higher pressure drop and a higher power production while here, the effect is accounted for by subtracting the same term from the denominator. As proven by Macchi (1977), the approximation is generally valid and does not affect the quality of the solution in terms of turbine efficiency. For a multistage turbine, the code maximizes the power output imposing $\varphi_E = 1$ for all the stages except the last one, but introducing annulus losses between blade rows.

The results provided by Axtur consist in a complete characterization of blade geometry in both blade-to-blade and meridional planes and velocity triangles. Furthermore, the breakup of the efficiency losses is reported considering the following effects:

- Profile loss (Craig and Cox, 1971): due to the blade shape and effects related to friction, fluid vane deflection, and boundary layer dissipation. This loss mainly depends on blade pitch (s), blade axial chord length (b), trailing edge thickness (te) and roughness of blade surface, angular deflection ($\Delta\alpha$, $\Delta\beta$), and relative velocity ratio.
- Secondary losses (Craig and Cox, 1971): caused by secondary flow structures mainly described by passage vortex, horseshoe vortex, trailing edge vortex, and corner vortex. These losses are affected by the same parameters which have influence on profile losses plus blade height (h).

- Annulus losses (Craig and Cox, 1971), or Kacker and Okapuu (1981): due to the passage of fluid in the gap between two blade rows. This loss is calculated for all the stages except for the last one.
- Leakage losses (Craig and Cox, 1971): caused by the unwanted passage of fluid above the blade tip whose expansion does not contribute to power production. This kind of loss is mainly related to radial clearance (δ_r), blade length (c), and blade overlap (ol). They can be null for the first stator blades only.
- Disk windage losses: due to the velocity gradient in the clearance between stator and rotor disk walls. They are strongly affected by rotational speed and by both absolute disk clearance (δ_{s-r} , δ_{r-s}) and disk diameter.
- Kinetic energy loss: it is the fraction of kinetic energy of discharge velocity which cannot be recovered with the diffuser. Usually it is defined with a coefficient (ϕ_c) smaller than unit respect to the kinetic energy of the axial component.

Exit flow angles are computed according to the following correlations, depending on the flow condition: (1) subsonic flow Ainley and Mathieson (1951), (2) Supersonic flow after expansion Vavra (1969), (3) Supersonic flow with converging–diverging nozzle Deich et al. (1965). Experimental data from Deich et al. (1965) are used for accounting additional losses related to the supersonic flows at the blade exit, while an empirical correlation introduced by Macchi (1977) accounts for losses related to relative transonic velocities at the rotor inlet.

9.4 The proposed efficiency correlation

9.4.1 Single stage turbines

The first step of the analysis is focused on single stage turbines; the effects of small SP and large V_r are investigated for different speeds of revolution (namely different N_s) to catch the penalizations due to miniaturization of blade geometry and supersonic flows. More than five hundred turbines were optimized, with varying SP, V_r , and N_s . It is important to remember that, according to similarity rules, the results here obtained are representative of any other turbine stage with the same set of independent parameters. Different volumetric fluid behavior and molar mass affect variables like speed of revolution, pressure ratio, temperature and enthalpy drop and mass flow rate but they have small influence on the final optimal design, on the geometrical aspect and the isentropic efficiency.

In Fig. 9.4 each point represents the maximum efficiency attainable for any combination of SP, V_r , and N_s . It is possible to notice that for each couple of SP and V_r parameters an optimal specific speed is found, while detrimental effects on the efficiency can be highlighted, increasing the V_r and decreasing the SP. As a general consideration, there is a large range in SP and V_r where the optimal specific speed is between 0.1 and 0.15, as already pointed out in Macchi (1977). For small SP and for high V_r the optimal N_s decreases down to 0.05. This is justified by the presence of lower and upper bounds on some geometrical dimensions like minimum blade height and maximum h/D ratio at the discharge section. In these cases, an N_s value

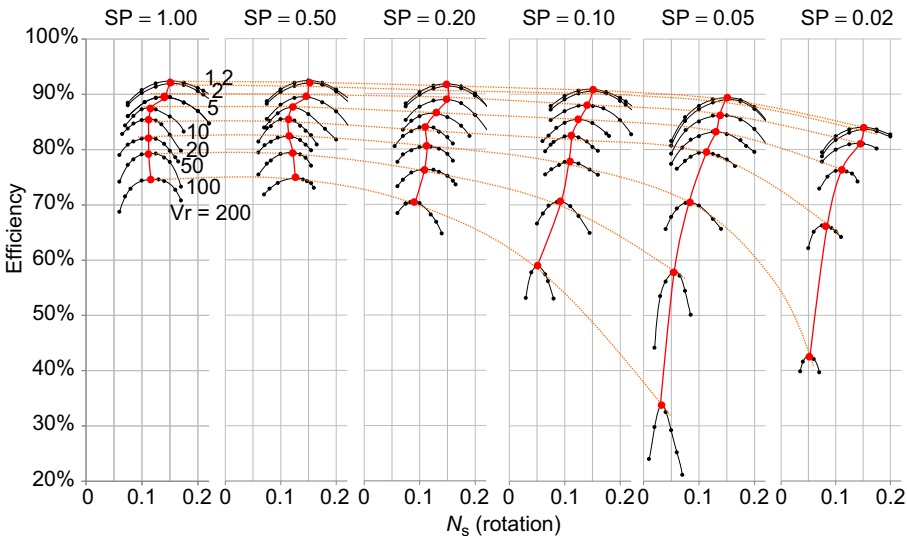


Figure 9.4 Results for the single stage turbines. Black markers (•) are representative of the optimal turbine configuration for each combination of SP, V_r , and N_s . Red markers identify the turbine designs at optimized rotational speed for each combination of SP and V_r .

above 0.1 entails an almost unfeasible design of the blade with a strong increase of secondary losses due to fluid leakages and high flaring angles. The maximum point for every curve is representative of the maximum attainable efficiency at optimized rotational speed and optimal results are collected in a contour map reported in Fig. 9.5.

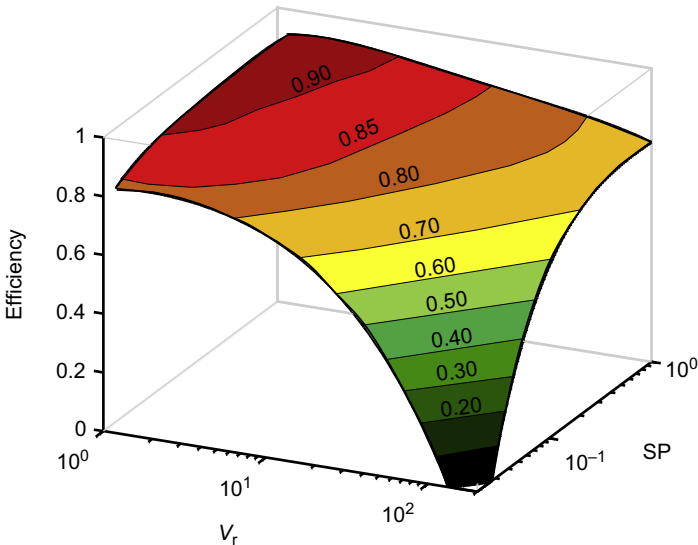


Figure 9.5 Map of efficiency for a single stage turbine at optimal N_s .

For a better understanding of the effects occurring in the definition of optimized stage geometry, three parametric analyses are proposed in the following. The first focuses on the effect of N_s at fixed SP and V_r , while the other two are carried out varying one by one V_r and SP at optimized rotational speed.

9.4.1.1 Effect of N_s

The first analysis regards the optimization of N_s for a single stage turbine at fixed SP and V_r equal to 0.4 m and 4 respectively (similar results are obtained for any other SP and V_r combination). Results are reported in Fig. 9.6. In this case, both the volume flow rate at turbine exit and the isentropic enthalpy drop are constant and so the N_s parameter has a direct effect on the speed of revolution and turbine mean diameter. At low specific speed the turbine stages have a large mean diameter because of the necessity to maintain the optimal u velocity above a certain value and to reduce the stage loading. Stages in this region have small h/D parameters and they are affected by high leakage and secondary losses. Velocity triangles are representative of impulse stages with an almost axial absolute velocity V_2 , thus the kinetic losses are minimized. Disk windage

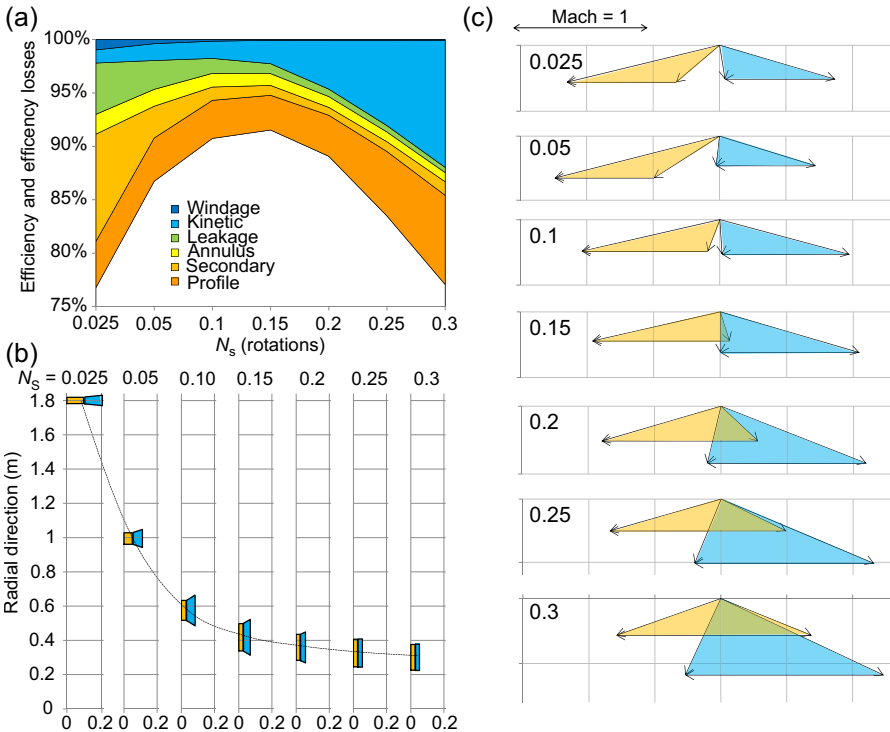


Figure 9.6 Results of the parametric analysis varying N_s for a single stage turbine with SP = 0.04 and $V_r = 4$. (a) Efficiency losses breakup, (b) blade profiles, and (c) velocity diagrams. Mach numbers for inlet and outlet triangles are calculated using the fluid Speed of Sound (SoS) at the stator and rotor outlet sections respectively.

loss is noticeable because of the large diameter interested by this dissipation effect. Increasing the rotational speed allows for a reduction in the stage mean diameter, with a consequent reduction of both the secondary and the leakage losses thanks to higher blades and a larger h/D ratio. On the other hand, the distorted shape of the velocity triangles entails high values of discharge velocity which cannot be maintained in an axial direction. As a consequence, kinetic energy losses increase because of the high value of V_2 and the presence of a tangential component which cannot be recovered by the diffuser. The trade-off between these opposite effects leads to the presence of an optimum value of N_s which yields the maximum efficiency. An optimal N_s value is equal to about 0.15, corresponding to well-proportioned turbine stages and an almost 50% reaction velocity triangle with an axial absolute velocity at the turbine outlet.

9.4.1.2 Effect of V_r at optimized N_s

Optimized results for single stage turbines, with different V_r and a fixed SP equal to 0.05, are presented in Fig. 9.7. The breakdown of efficiency losses shows that the maximum attainable efficiency is a decreasing function of V_r . For really low volume ratios, namely values below about 2, velocity triangles are subsonic, the load is limited and 50% reaction stages with high efficiency can be designed, h/D ratio is

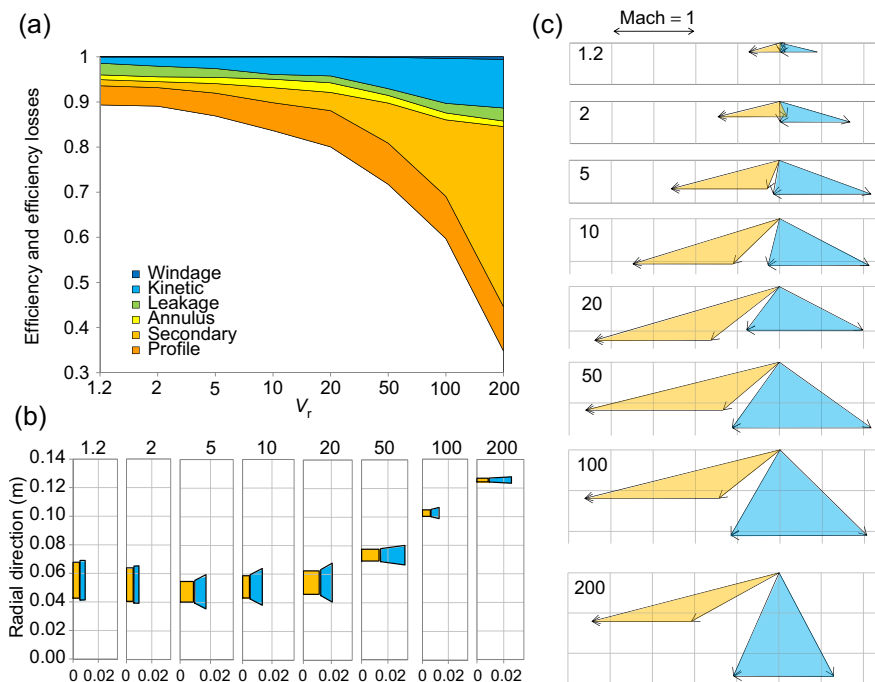


Figure 9.7 Results of the parametric analysis for different single stage turbines having the same SP = 0.05 m at the optimal specific speed. (a) Efficiency losses breakup, (b) blade profiles, and (c) velocity diagrams.

favorable, no flaring is required and both secondary and profile losses are small. Increasing V_r , Mach numbers greater than unit are obtained, in particular for V_1 and W_2 velocities, with an increase of profile losses. Converging–diverging stator nozzles are required for V_r above 5, while they are also needed for rotor blades values beyond 10. For a V_r greater than 20, a velocity close to the sonic one is obtained at W_1 with serious issues related to shock waves at the rotor inlet. A loss coefficient, which takes this effect into account, contributes to penalize the overall efficiency.

Velocity triangles become more and more distorted due to the necessity to handle higher volume flow variations and contextually maintaining a velocity vector V_2 close to the axial direction and limiting M_{W1} . Increasing the volume ratio involves a higher isentropic enthalpy drop and optimized stages with a higher peripheral speed u and a larger mean diameter in order to limit the stage load. Solutions move toward impulse stages with very small blade heights and high secondary losses due to an unfavorable h/D ratio; finally disk windage loss increases due to a larger surface facing the phenomena. In conclusion, adopting V_r higher than 5 for a small SP single stage turbine entails a strong limitation in the attainable efficiency and multistage turbines should be considered in order to contain the loading coefficient on each stage.

9.4.1.3 Effect of SP at optimized N_s

The last sensitivity analysis is realized for different single stage turbines with the same $V_r = 20$ but different SP and the results are reported in Fig. 9.8. Size parameter is varied from 0.02 to 1 m which is a value representative of turbines close to the maximum size of normal ORC expanders. All the stages work with the same isentropic enthalpy drop but they notably differ in volumetric flow rate because of the quadratic dependence on the SP. Small size parameters lead to very small volume flow rates at the turbine inlet section with a reduced passage area. Due to geometrical limits on minimum blade height and minimum δ_r/h ratio, the mean diameter gets smaller with an

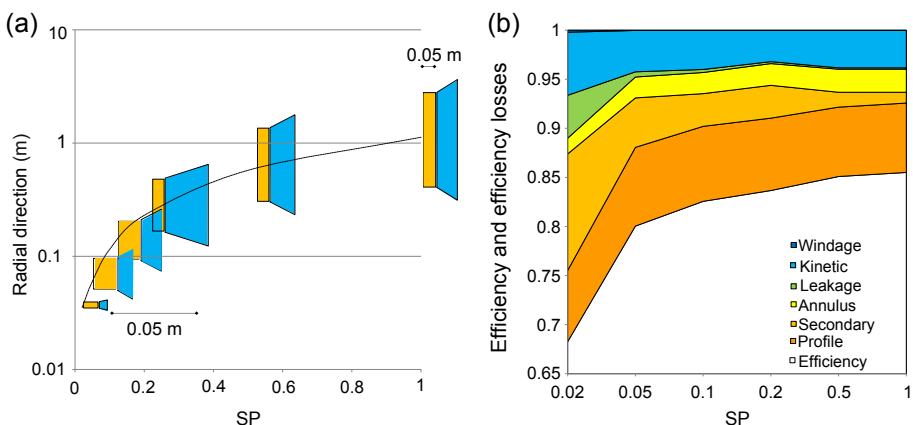


Figure 9.8 Results of the parametric analysis for different single stage turbines having the same $V_r = 20$ at the optimal specific speed. (a) Blade profiles and (b) efficiency losses breakup.

increase of rotational speed in order to maintain the optimal value of specific speed. These two effects result in a strong efficiency drop for small turbines with a considerable increase of secondary and leakage losses. Similar results are obtained for smaller V_r , even if the efficiency drop related to small SP is less marked.

9.4.2 Multistage turbine

In the previous section 9.4.1, single stage turbines have been considered highlighting that their efficiency is strongly penalized by high volume ratios with an even more marked reduction at small size parameters. In the ORC field, multistage turbines are commonly adopted because they can achieve a higher efficiency exploiting the repartition of the whole volume flow variation on two or more stages. In this work, only two and three stage turbines are considered because in most of the applications the benefit in adopting a higher number of stages is limited with an increase of component cost and a higher cost of electricity. For common applications, axial turbines are usually overhung with a rolling bearing on the generator side of the shaft. This design allows an easy inspection of the turbine during maintenance operations and it is generally preferred even if it limits the number of stages to three because of rotodynamic issues. For turbines directly coupled to generator, a rotodynamic analysis performed by Spadacini et al. (2013) shows that for a number of stages greater than three, the natural frequencies of the turbine shaft get closer to 50–60 Hz with the risk of resonance during normal operation. A technical solution to increase the number of stages and the overall volume ratio without incurring these problems is represented by radial outflow turbines (see Chapter 11 for further details).

The results for the two stage turbine are obtained by optimizing the rotational speed for each turbine, and are presented in terms of V_r and SP, calculated for the overall expansion as though it is exploited by a single stage. In Fig. 9.9(a) the increment of efficiency attainable with a two stage turbine instead of a single stage turbine is displayed. Increases of efficiency are not constant over the considered range of SP and V_r .

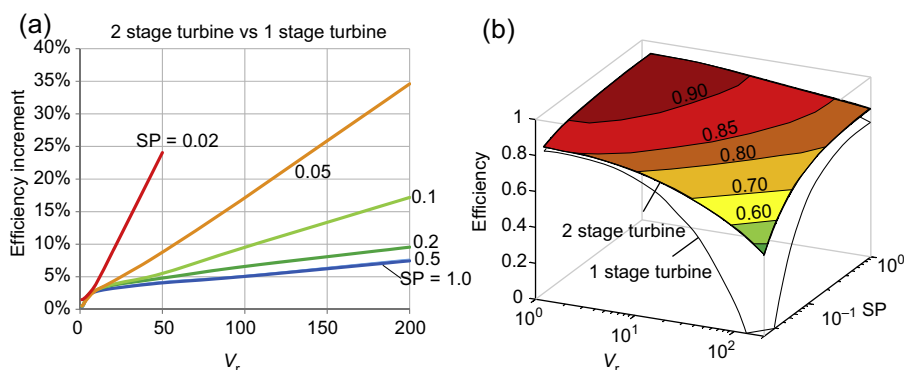


Figure 9.9 Efficiency increases attainable adopting a two stage turbine instead of a single stage turbine (a), graphical representation of maps of efficiency for single stage and two stage turbines (b).

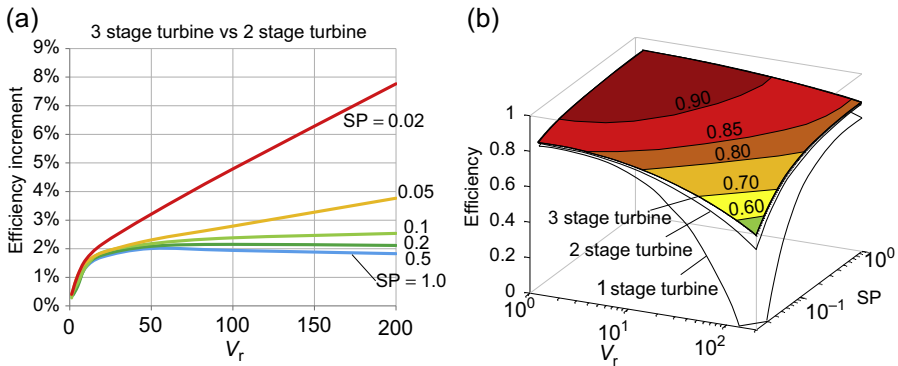


Figure 9.10 Efficiency increases attainable adopting a three stage turbine instead of a two stage turbine (a), graphical representation of maps of efficiency for single stage, two stage turbines and three stage turbines (b).

The most relevant increments are obtained for high overall volume ratios and a small SP. For a V_r equal to 5, the efficiency increment is greater than 2 percentage points independent of the SP value; an increment that usually justifies a more expensive device with the adoption of a two stage turbine. Benefits are obviously larger for higher V_r and the efficiency increase reaches values above 10% for medium-small machines and volume ratios greater than 50. The last observation regards the possibility to extend the domain of the solution; in particular for an SP lower than 0.02 m and V_r of 100 and 200 it is not possible to design a full-admission single stage turbine with a reasonable efficiency. The high load on such a small stage and the presence of geometric constraints entail a nonfeasible execution of the optimization algorithm with variable values always outside of the efficiency losses correlation limits. This problem does not arise for two stage turbines and the whole range of SP and V_r is explored.

Similar considerations can be achieved by comparing two stage and three stage turbines. Results are reported in Fig. 9.10. The attainable efficiency increase is lower than in the previous case but, once again, notable advantages are highlighted for high volume ratios and small turbines.

9.4.3 Numerical correlations of efficiency

The set of data of maximum attainable turbine efficiency are regressed with an OLS (Ordinary Least Square) regression performed in *Gretl*. The most suitable terms function of SP and V_r are selected and a process of exclusion of the less influencing ones is carried out in order to obtain the maximum value of the adjusted R^2 coefficient. All the proposed correlations have a functional form reported in Eq. (9.5) while the numerical values of the retrieved coefficients can be found in Table 9.1.

$$\eta = \sum_{i=0}^{15} A_i F_i \quad (9.5)$$

Table 9.1 Regressed coefficients to be used in the correlation of turbine efficiency for single, two, and three stage turbines

Stages number		1 stage	2 stages	3 stages
<i>n</i>	<i>F_i</i>	<i>A_i</i>		
0	1	0.90831500	0.923406	0.932274
1	ln(SP)	−0.05248690	−0.0221021	−0.01243
2	ln(SP) ²	−0.04799080	−0.0233814	−0.018
3	ln(SP) ³	−0.01710380	−0.00844961	−0.00716
4	ln(SP) ⁴	−0.00244002	−0.0012978	−0.00118
5	<i>V_r</i>	—	−0.00069293	−0.00044
6	ln(<i>V_r</i>)	0.04961780	0.0146911	—
7	ln(<i>V_r</i>) ²	−0.04894860	−0.0102795	—
8	ln(<i>V_r</i>) ³	0.01171650	—	−0.0016
9	ln(<i>V_r</i>) ⁴	−0.00100473	0.000317241	0.000298
10	ln(<i>V_r</i>) ln(SP)	0.05645970	0.0163959	0.005959
11	ln(<i>V_r</i>) ² ln(SP)	−0.01859440	−0.00515265	−0.00163
12	ln(<i>V_r</i>) ln(SP) ²	0.01288860	0.00358361	0.001946
13	ln(<i>V_r</i>) ³ ln(SP)	0.00178187	0.000554726	0.000163
14	ln(<i>V_r</i>) ³ ln(SP) ²	−0.00021196	—	—
15	ln(<i>V_r</i>) ² ln(SP) ³	0.00078667	0.000293607	0.000211
Adjusted <i>R</i> ²		0.99790	0.99935	0.99954

9.5 Model validation

In this section an example of the capabilities of the proposed correlations is provided. In particular, the aim is to show how the volume ratio and the dimension of a real turbine stage can affect the turbine performance. To validate the proposed methodology, two fluids (R125 and hexane) are considered and two turbine sizes (isentropic power of 5 MW and 250 kW) are analyzed. Both fluids expand from a temperature of 155°C down to a pressure equal to the saturation at 30°C as representative of a low temperature heat source application with a cooling water condenser. A supercritical cycle is considered for R125 with a turbine inlet pressure of 36.2 bar while a saturated cycle is imposed for hexane according to its high critical temperature and the overhanging saturated vapor line which allows for a dry expansion. In [Table 9.2](#), the main thermodynamic properties of the fluids are reported with other data of direct interest for the evaluation of turbine efficiency.

Table 9.2 Characteristics of the considered fluids and the main results of the analysis

	R125		Hexane	
Critical properties				
MM	120.02		86.18	
T_{crit} (°C)	66.02		234.67	
p_{crit} (bar)	36.18		30.34	
Expansion data				
W_{is} (kW)	5000	250	5000	250
p_{in} (bar)	36.200		8.290	
p_{out} (bar)	15.685		0.250	
ΔT_{sh} (°C)	88.980		0	
m (kg/s)	237.71	11.89	40.78	2.04
$V_{\text{out, is}}$ (m ³ /s)	3.79	0.19	55.24	2.76
Specific parameters				
V_{r}	2.293	2.293	34.389	34.389
SP (m)	0.162	0.036	0.397	0.089
$\eta_{\text{is}}^{\text{correlation}}$	0.903	0.877	0.833	0.799
Axtur results				
$\eta_{\text{is}}^{\text{Axtur}}$	0.907	0.872	0.828	0.795
RPM	6000	31,000	5500	2800
N_{s}	0.111	0.129	0.104	0.118
D (m)	0.420	0.086	0.900	0.180

Both R125 and hexane show real gas effects at the turbine inlet with a compressibility factor equal to 0.85 and 0.79 respectively while a behavior closer to ideal gas is founded at turbine discharge with values of 0.91 and 0.99. The overall expansion coefficients (γ) are different from the value assumed for the ideal gas in the previous sections and are equal to 1.10 and 1.06. The two turbine stage differ in both the V_r and the SP. The expansion of R125 shows a very limited variation of density because of the high condensation pressure and the high degree of superheating. On the contrary, hexane according to the corresponding state principle (Poling et al., 2001) has a lower condensing pressure (a vacuum pump is required at the condenser to remove air leakage) and a larger volume flow rate variation across the turbine. Hexane mass flow rate is lower than the R125 but the SP is larger because of the very low density at the turbine outlet section. Using the correlation of efficiency previously described,

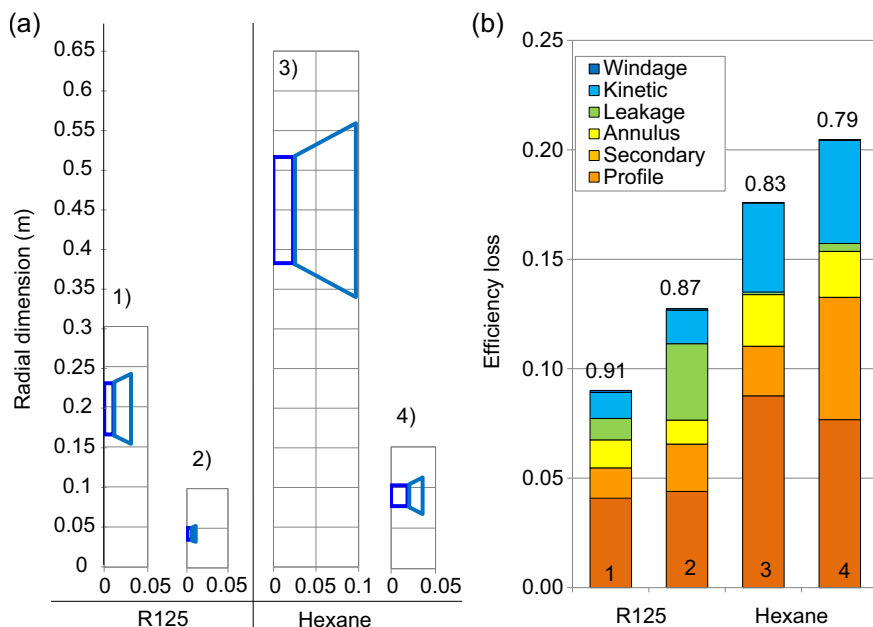


Figure 9.11 Graph (a) meridional plane for the four turbines: (1) R125 big size application, (2) R125 small size application, (3) hexane big size application, and (4) hexane small size application. Graph (b) breakdown of efficiency losses for the four cases.

the turbine efficiency is calculated; the R125 turbine shows a very high (90%) efficiency while for hexane, the presence of supersonic flows and the limitation of flaring angles plays a detrimental role in the final efficiency, which is close to 83%. In this case, the positive effect of a larger SP is not sufficient to compensate for the difficulties in realizing a high V_r stage. Reducing the size of the turbines in the presence of geometrical constraints (minimum o/s and maximum o/b) bound the final solution and leads to a decrement of about 3 points of efficiency, confirming the overall trend presented in previous analyses. The meridional planes of the four turbines are reported in Fig. 9.11(a) while Fig. 9.11(b) depicts the breakdown of efficiency losses. R125 turbines are affected by high leakage losses because their small blade heights while the turbine working with hexane are penalized by relevant profile losses and kinetic energy losses. The four turbines are hence designed in Axtur considering real fluid properties computed with Refprop (Lemmon et al., 2013) (i.e., compressibility effects, Mach numbers, etc.) and optimizing the rotational speed. It is possible to highlight a good accordance among the efficiencies calculated with the two methods confirming the validity of the proposed approach. The optimal rotational speed, the optimal N_s and the resulting optimal diameter are reported in table as well.

Only for the large size dimension turbine working with hexane a three stages turbine is selected in order to highlight once again the advantages attainable by a repartition of the total volume ratio in different stages. Results are displayed in Fig. 9.12.

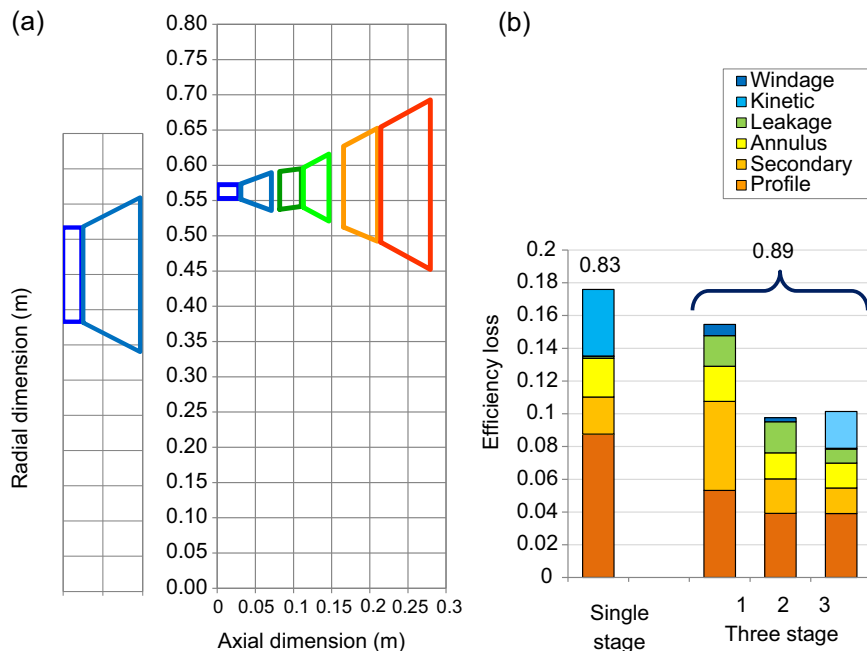


Figure 9.12 Comparison between the single stage and the three stage turbine working with hexane in the meridional plane (a) and the breakdown of the efficiency loss (b).

In this case, the three stages have a volume ratio around 3.2 which is compatible with the achievement of very high efficiency. The stage loading drops from 3.65 for the single stage turbine to an average value close to 3 thanks to the enthalpy drop repartition, while the mean peripheral speed is reduced (diameter increases but the rotational speed is reduced) with a limitation of velocities and supersonic flows issues. The degree of reaction increases with a consequent reduction of the profile losses; however, the lower blade height leads to an increase of both the secondary and the leakage losses in the first two stages. The increase of total turbine efficiency is more than 6 percentage points as confirmed by the correlation of efficiency proposed above.

9.6 Conclusions

In this Chapter three correlations of performance are provided for axial turbines with a maximum number of stages equal to three. This study aims to complete the work done in previous publications about the estimation of maximum efficiency attainable with 1D optimization techniques. The correlations can be used for a preliminary estimation of turbine performance in the numerical optimization of ORC, even if the results are affected by inaccuracy mainly related to the quality of efficiency losses correlations and the simplified volumetric behavior assumed in the generation of the performance maps.

On the basis of the present analyses the following conclusions can be addressed about ORC turbines:

- Rotational speed must be always optimized since relevant efficiency decrements are highlighted for values lower and higher than the optimal one. The use of slow generators with more than two couple of poles is recommended for large turbines while a gearbox or a power electronic system is required for small size machines having an optimal rotational speed higher than 3000 RPM.
- Geometrical similarity cannot always be verified because of the presence of geometrical constraints related to blade machining and limits of loss correlations. Decreasing the size of the turbine, the efficiency is reduced mainly because of the increasing of profile and leakage losses.
- Isentropic volume ratio strongly affects stage design and efficiency. A single stage turbine with high V_r is penalized because of the presence of big flaring angles, supersonic flows, and high kinetic losses and it is advantageous to split the expansion into two or more stages.
- The contemporary presence of small SP and high V_r strongly penalizes the attainable efficiency of single stage machines and suggests the adoption of multistage solutions.

Nomenclature

Variables		
A	Coefficients for the efficiency correlations	(—)
B	Axial chord	(m)
B	Pressure ratio	(—)
H	Efficiency	(—)
F	Terms of the efficiency correlations	(—)
φ_E	Kinetic energy recovery factor	(—)
Γ	Ratio of specific heats	(—)
k_{is}	Isentropic load coefficient	(—)
H	Enthalpy or blade height	(m)
h/D	Blade height—blade mean diameter ratio	(—)
M	Mass flow rate	(kg/s)
N_s	Specific speed	(—)
O	Blade channels throat	(m)
P	Pressure	(bar)
R	Radius	(m)
ρ	Density	(kg/m ³)
S	Blade step	(m)

Continued

SP	Size Parameter	(m)
T	Temperature	(°C)
V	Volume flow rate	(m ³ /s)
V	Absolute velocity	(m/s)
U	Mean peripheral speed	(m/s)
V_r	Volume ratio	(—)
W	Power	(kW)
W	Relative velocity	(m/s)
Subscripts		
Crit	Critical property	
Eva	Evaporation	
Cond	Condensation	
Is	Isentropic	
Re	Real	
T-S	Total to static	

References

- Ainley, D.C., Mathieson, G.C.R., 1951. A Method of Performance Estimation for Axial-flow Turbines, Vol. R&M 2974. British Aeronautical Research Council.
- Baljè, O.E., Binsley, R.L., 1968. Axial turbine performance evaluation: part B - optimization with and without constraints. *ASME Journal of Engineering for Power* 349–360.
- Craig, H.R.M., Cox, H.J.A., 1971. Performance estimation of axial flow turbines. *Proceedings of the Institution of Mechanical Engineers* 185, 407–423, 32/71.
- Dixon, S.L., Eng, B., 1998. *Fluid Mechanics, Thermodynamics of Urbomachinery*, fifth ed. Elsevier.
- Deich, M.E., Filippov, G.A., Lazarev, L.Y., 1965. *Atlas of Axial Turbine Blade Characteristics*. Mashinostromie Publishing House, Moscow.
- Gaia, M., 2011. 30 Years of Organic Rankine Cycle Development. In: *Delft: 1st International Seminar on ORC Power Systems*.
- Gretl. (Online) www.gretl.sourceforge.net/.
- Kacker, S.C., Okapuu, U., 1981. A Mean Line Prediction Method for Axial Flow Turbine Performance Prediction. paper 81-GT-58. ASME.
- Lozza, G., Macchi, E., Perdichizzi, A., 1981. On the Influence of the Number of Stages on the Efficiency of Axial Flow Turbines. vols. paper 82-GT-43. ASME.
- Lemmon, E.W., Huber, M.L., McLinden, M.O., 2013. NIST Standard Reference Database 23: Reference Fluid Thermodynamic and Transport Properties-REFPROP: Version 9.1. National Institute of Standards and Technology, Standard Reference Data Program.

- Macchi, E., 1977. Design Criteria for Turbines Operating With Fluids Having Low Speed of Sound.
- Macchi, E., Perdichizzi, A., September 1977. Theoretical Prediction of the Off-design Performance of Axial-flow Turbines. Martinus Nijhoff Publishers, pp. 1867–1896.
- Poling, E.B., Prausnitz, J.M., O'Connell, J.P., 2001. Properties of Gases and Liquids, fifth ed. McGraw-Hill Education.
- Smith, M.H., 1965. A simple correlation of turbine efficiency. Journal of Royal Aeronautical Society 69, 467.
- Spadacini, C., Rizzi, D., Saccilotto, C., Salgarollo, S., Centemeri, L., 2013. The radial outflow turbine technology: impact on the cycle thermodynamics and machinery fluid- and rotor-dynamic features. In: Rotterdam: 2nd International Seminar on ORC Power Systems.
- Vavra, M.H., 1969. Axial Flow Turbines. Von Karman Institute for Fluid-dynamics, Brussels vol. Lecture series 15.

Radial inflow turbines for Organic Rankine Cycle systems

10

P. Valdimarsson

pvald ehf and Reykjavik University, Reykjavik, Iceland

10.1 Radial inflow turbines: what are they?

The flow in a radial inflow turbine is as the name implies, in a radial direction, towards the center of the rotor. These turbines are sometimes built with cantilever blades, so that both the inflow and outflow from the rotor blades are in a radial direction. The 90 degrees radial inflow turbine is more common, where there is a 90 degrees change of flow direction in the rotor, and the flow leaves the rotor in an axial direction.

The radial inflow turbine is very common. The diesel engine turbocharger is usually a radial inflow turbine mounted back to back to a radial outflow compressor. A small turbocharger will have very high rotational speed, but as both the turbine and the compressor are similar components with similar dimensions, they can be designed for a common (high) rotational speed.

Even the hydraulic Francis turbine, found in hydroelectric power plants all over the world is a radial inflow turbine.

The radial inflow turbine has a sister component, the radial outflow compressor. The radial outflow compressor has the same 90 degrees change of flow direction. The flow enters the compressor wheel in an axial direction at the hub, and leaves the wheel in a radial direction. The mechanical design is in many ways similar and some subassemblies are common.

10.2 Radial inflow turbines: who makes them?

The market leader in producing radial inflow turbines for Organic Rankine Cycle (ORC) plants is Atlas Copco (Agahi and Mohr, 2015). GE Rotoflow (Hawkins, et al., 2012) was very active in the market some years ago, and seems to be strengthening its appearance again. Cryostar (Marcuccilli and Thiolet, 2010) as well produced radial inflow turbines for ORC cycles. Both these companies have produced a large number of radial inflow turbines for other industries. To the knowledge of the author, neither Samsung (Hanwha) Techwin (http://energy.hanwhatechwin.com/product/product_list.asp?cid=578&clvl=1) nor MAN Turbo (<http://turbomachinery.man.eu/products/expanders>) have made radial inflow turbines for ORC plants, even if they are producing radial inflow turbines for other markets.

Fixed geometry turbines are a different product, even if they are as well installed in ORC plants and compete with the radial inflow turbine in that sense. Ormat (Bronicki, et al., 2014) has been the market leader in plants with fixed geometry axial turbines. Turboden (Rizzi, et al., 2015) is also a large player in the market, mainly in plants for combustion biomass as heat source. Both these companies have hundreds of references. Exergy (Spadacini, et al., 2014) is a new entry in the market, and has produced some fixed geometry radial outflow turbines.

10.3 Thermodynamic fundamentals

The main function of the turbine is to convert the enthalpy of the working fluid into shaft work. The largest amount of enthalpy which can be taken from the fluid is the so-called isentropic enthalpy drop, which is the reduction in enthalpy which an ideal reversible expansion could reach.

The available enthalpy is converted to kinetic energy, both in the stationary inlet guide vanes (IGV) as well in the turbine rotor wheel. This kinetic energy is then transferred over to the turbine wheel.

A cross section through a radial inflow turbine with cantilever blades is shown in Fig. 10.1.

Three thermodynamic stations are shown on Fig. 10.1. Station 1 is where the fluid flows into the nozzle guide vane cascade. The leading edge of the inlet nozzle guide vane is designed so that the angle of attack for the flow is correct at the design point. The flow direction is usually close to being radial.

The flow area between the nozzle guide vanes is smaller at the nozzle guide vane outflow than at the inflow, thus accelerating the flow, as long as the flow velocity does not reach the speed of sound.

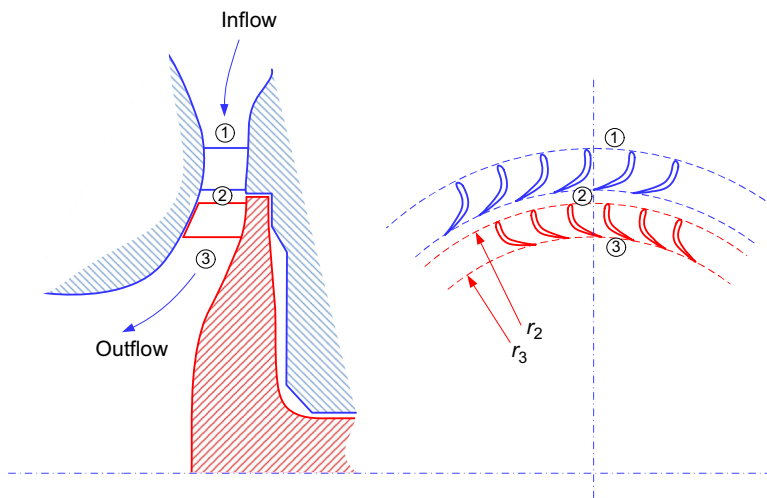


Figure 10.1 Cross sections through a cantilever bladed radial inflow turbine. Station 1: Stator inflow; Station 2: Stator outflow/rotor inflow; Station 3: Rotor outflow.

If the pressure ratio over the nozzle guide vanes is sufficiently high, and the nozzles have correct geometry, the flow at the nozzle outlet may become supersonic (supercritical). A supercritical nozzle has different geometry than a subcritical (converging–diverging nozzle, also known as Laval nozzle), with sonic velocity occurring at the throat of the supersonic nozzle. Variable nozzle geometry is used to control the flow by changing the throat cross sectional area, exactly in the same way as for the subsonic nozzle.

Station 2 is at the nozzle guide vane outflow, which is at the same time the rotor inflow. The direction of the accelerated flow at Station 2 has now a substantial tangential component. The velocity vector of this flow, measured relative to a stationary coordinate system is c_2 , following the naming convention that velocities measured relative to a stationary coordinate system have the letter c , whereas velocities measured relative to a coordinate system rotating with the rotor have the letter w . U is the peripheral velocity of the rotor blade.

The stator and rotor blades and the blade inflow and outflow vectors are shown in Fig. 10.2, together with the rotor blade inlet and outlet velocity triangles.

The vector c_2 and the vector w_2 are both describing the same flow, one (c_2) seen from a stationary system of reference, and the other (w_2) seen from a system of reference moving with the rotor blade leading edge at the velocity U_2 . Note that the trailing edge of the rotor blade moves at a velocity U_3 , which is smaller than the leading edge peripheral velocity U_2 . This is because the distance from the center of rotation to the leading edge r_2 is larger than the distance to the trailing edge r_3 .

The Euler turbine equation relates the power transferred between the flow and blade row by means of angular velocity, direction change of fluids' tangential velocity, and the geometry of the turbine.

The equation is derived from the change in angular momentum of the fluid going through the rotor blade row.

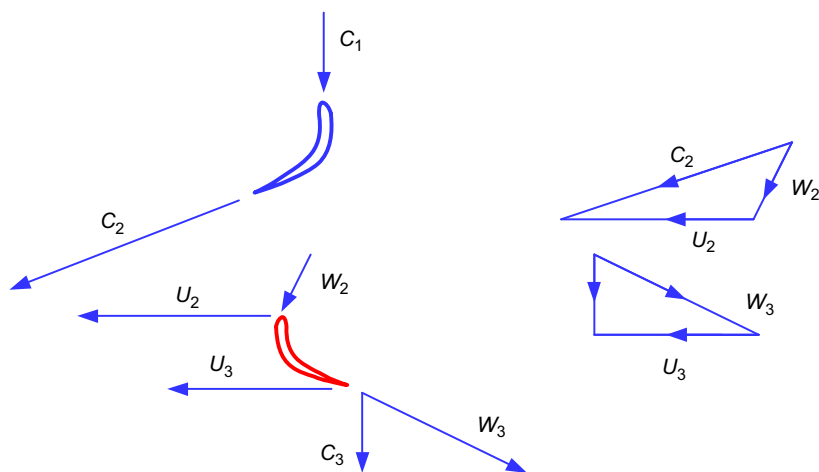


Figure 10.2 Flow vectors and velocity triangles in a cantilever bladed radial inflow turbine. Station 1: Stator inflow; Station 2: Stator outflow/rotor inflow; Station 3: Rotor outflow.

The angular momentum is the linear momentum of the fluid flow in the tangential direction multiplied with the momentum arm, which is equal to the distance to the center of rotation of the rotor.

A change in linear momentum will be equal to the external force on the flow. Similarly, the change of angular momentum of the fluid flow in the rotor blade row is then equal to the torque which the flow causes on the rotor:

$$\tau = \dot{m} \cdot (c_{\phi,2} \cdot r_2 - c_{\phi,3} \cdot r_3)$$

where ϕ denotes the tangential velocity component.

The power which the turbine produces is then obtained by multiplying this torque with the rotor angular velocity:

$$\dot{W} = \tau \cdot \omega = \dot{m} \cdot \omega \cdot (c_{\phi,2} \cdot r_2 - c_{\phi,3} \cdot r_3)$$

Note:

1. The power output will be larger if the radius of the blade row leading edge is large and the radius of the rotor blade trailing edge is small, which is the fact in the radial inflow turbines.
2. The outflow velocity from the rotor blade trailing edge has kinetic energy, which is lost and dissipated in the turbine exhaust system. The enthalpy available for accelerating the flow through the turbine stator and rotor is limited, and thus the trailing edge outflow velocity should be as low as possible.

The main components of a 90 degrees radial inflow turbine are shown on [Fig. 10.3](#).

Here the radius of the outflow from the rotor is considerably smaller than the radius of the inflow to the rotor.

The IGV shown are movable, so that the geometry of the nozzle guide vane row can be changed during operation of the turbine. This is beneficial, and will be discussed in more detail in Chapter 10.4.

A 90 degrees inward radial flow cross section together with flow vectors and velocity triangles is shown on [Fig. 10.4](#).

The flow vectors and velocity triangles are similar to the previous example with the cantilever blade radial turbine. The geometry of the 90 degrees inward radial flow turbine allows however, a larger difference between the rotor blade row inflow and outflow radii. It can be seen from the Euler turbine equation that this is a great advantage of the 90 degrees turbine.

The inlet and outlet pressure for an ORC turbine are usually determined outside of the turbine. The inlet pressure is the same as the vaporizer pressure, which is determined by the characteristics of the heat source and of the selected working fluid. The outlet pressure is determined by the condenser performance, which is in turn influenced by environmental variables such as air temperature and humidity. An exhaust diffuser will allow a lower pressure than the condenser pressure at the blade outflow, thereby increasing the available enthalpy drop for the turbine.

The exhaust diffuser is well shown on [Fig. 10.4](#), and station 4 is the diffuser outlet.

A sample calculation is made for expansion of Isobutane. The inlet temperature is 103.5°C and the inlet pressure 20.8 bar absolute. The condenser pressure is 5.23 bar absolute. An h-s diagram for this expansion is shown in [Fig. 10.5](#).

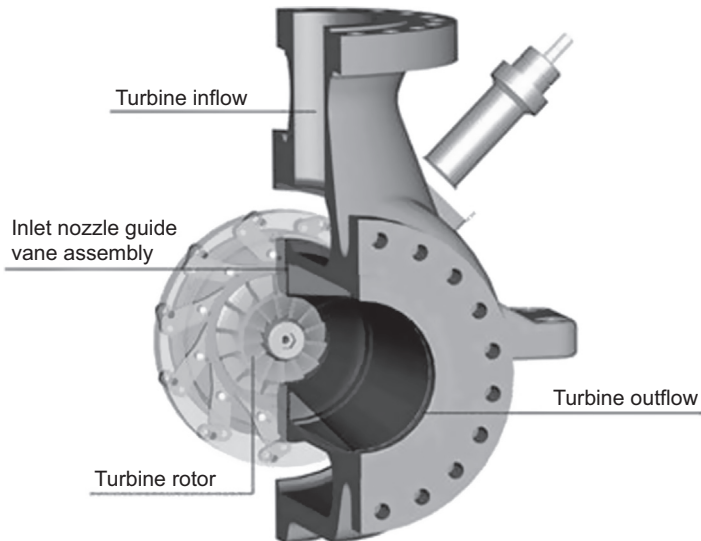


Figure 10.3 Main components of a radial inflow turbine.

Valdimarsson, P., 2014, New development in the ORC technology. "Short Course VI on Utilization of Low- and Medium-Enthalpy Geothermal Resources and Financial Aspects of Utilization", organized by United Nations University -Geothermal Training Program and LaGeo, El Salvador, March 23-29, 2014 ISBN 978-9979-68-339-1 <http://www.os.is/gogn/unu-gtp-sc/UNU-GTP-SC-18-18.pdf>.

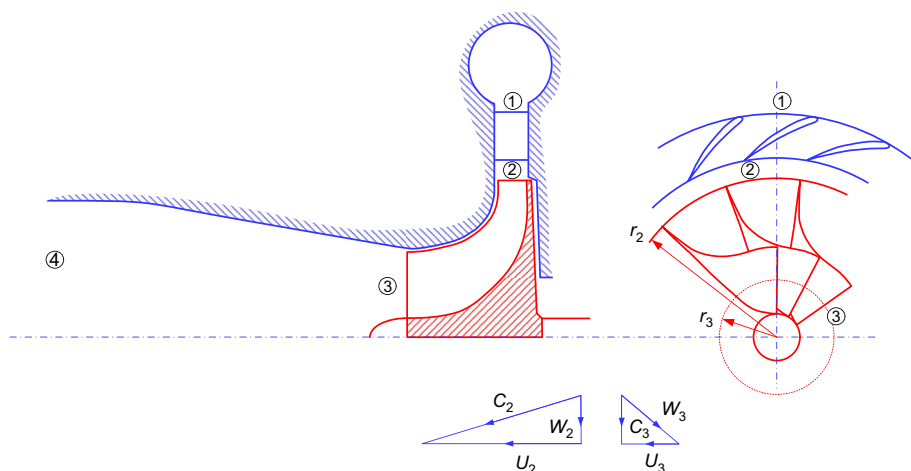


Figure 10.4 Flow vectors and velocity triangles in a 90 degrees radial inflow turbine. Station 1: Stator inflow; Station 2: Stator outflow/rotor inflow; Station 3: Rotor outflow.

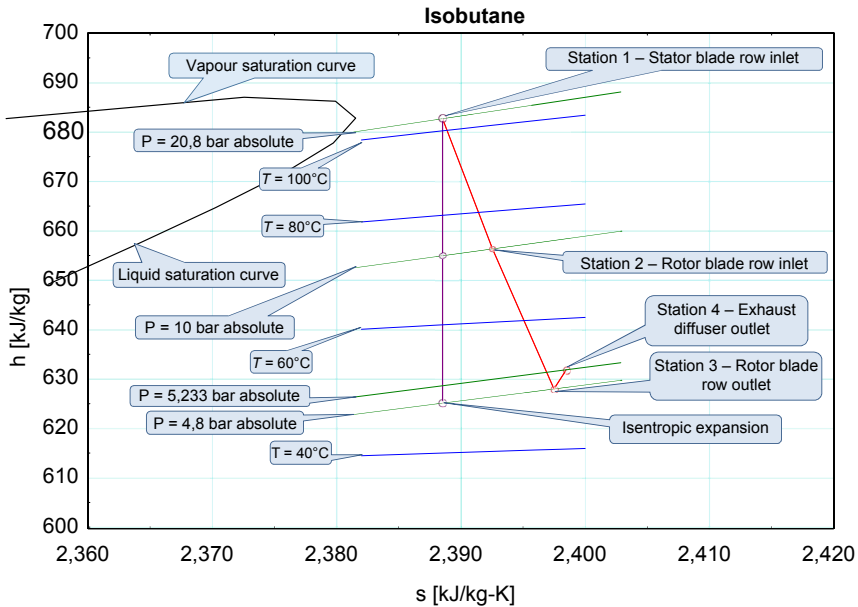


Figure 10.5 An h-s diagram of a sample expansion of isobutane in a 90 degrees inward radial flow turbine.

10.4 Variable geometry nozzle guide vanes in the radial inflow turbine

The radial turbine can be controlled by means of variable geometry IGV. By adjusting the guide vanes, or “nozzles”, the flow cross section, or “gap”, as well as the tangential velocity at the guide vane can be modified. This ensures that the angle of attack of the flow on the leading edge of the rotor blade is kept correct, even if the flow changes. The turbine rotational speed is usually constant, so the blade tangential velocity can be assumed to be constant for all flows and loads.

Thereby, the performance curve of a radial turbine in terms of a constant isentropic efficiency and rotational speed across the entire performance map can be considered optimal. The efficiency performance curve only decreases slightly under off-design conditions.

A turbine with fixed geometry does not have this flexibility. If the flow changes, then the velocity out of the nozzle guide vanes will change and the angle of attack on the blade leading edge will not be correct, resulting in losses. This can be partly compensated for, if the first turbine stage is an impulse stage, by using a partial admission nozzle ring. Then a part of the nozzle ring is not used if the flow is reduced, thereby maintaining correct flow velocity for the remainder of the nozzle ring. This does not help if the flow increases, nor does it help the later turbine stages.

Therefore, radial turbine design is an excellent match for the requirements of an ORC-based power plant.

The technology is also perfectly suited for climate zones with considerable seasonal variations in ambient temperature, leading to deviations in condensing pressure in facilities where air-cooled condensers are used.

Another usage scenario includes block heat and power plants with combined heat and power (CHP) generation. In this case, the power plant is not only producing electricity for the grid, but also heat, usually for a district heating scheme. District heating is supplying heat to buildings, so obviously the heat to deliver is dependent on the outside temperature. District heating is a demanding customer, the distribution grids are not as far-reaching as the electric grids, and usually the CHP plant is the only producer of heat for the district heating grid. The flow from a geothermal well is constant. The heat needed for a district heating system is dependent on the weather, so the heat available to generate electricity is reduced during the cold season.

Overall, a stable performance curve is beneficial for all applications, in which the process is run under off-design conditions as well as processes, in which off-design conditions differ significantly from initial operating conditions.

The nozzle guide vanes have a pivot point, around which the nozzle guide vane is turned. An actuation ring is attached to the nose of each vane, so that all the nozzle guide vanes are turned in unison when the actuator ring is moved. The movement of the nozzle guide vanes changes the flow area for the working fluid between the vanes, thus ensuring constant fluid velocity even if the volume flow changes. The contour profile of the vanes is then designed in such a way that the direction of the flow vector from the vane trailing edge is adjusted to ensure a correct angle of attack at the rotor blade leading edge at all times.

The assembly is shown on [Fig. 10.6](#).

The traditional method of controlling a turbine is by throttling the gas entering the turbine. The pressure at the inflow to the (fixed) nozzle guide vanes in a traditional turbine is then variable, with the result that the design flow velocity at the outflow of the nozzle guide vanes can only be upheld for the design valve position.

If the valve has to be moved, the inflow pressure to the nozzle guide vanes will change with the result that the angle of attack on the leading edge of the rotor blade will be suboptimal, leading to loss of efficiency and power production.

The variable nozzle guide vanes eliminate the need for a turbine control valve.

The ability of the inward radial flow turbine to be controlled by variable geometry nozzle guide vanes is a large benefit in an ORC plant.

Environmental conditions will influence the performance of the ORC plant cold end, so that the turbine outflow (condenser) pressure is not the same in all seasons and for all weather conditions. Then the pressure difference over both the stator and rotor blade rows changes, and the enthalpy available for conversion into kinetic energy of the fluid changes as well. The variable geometry nozzle guide vanes compensate for this by changing the flow area through the vanes, thereby keeping the turbine efficiency high despite this change of operating conditions.

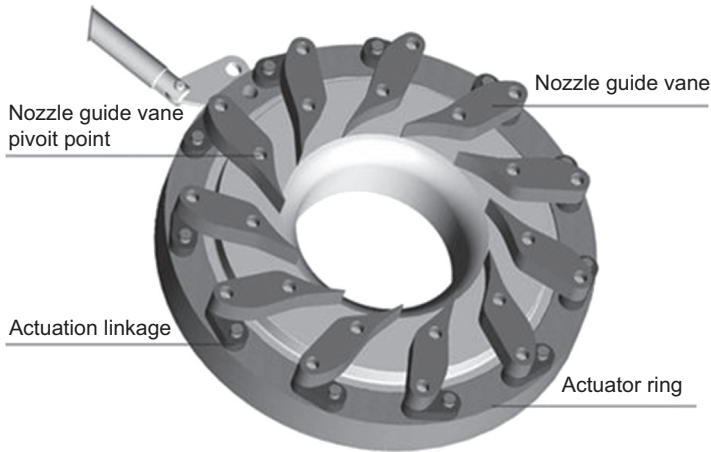


Figure 10.6 A variable geometry nozzle guide vane assembly in a 90 degrees inward radial flow turbine.

Valdimarsson, P., 2014, New development in the ORC technology. “Short Course VI on Utilization of Low- and Medium-Enthalpy Geothermal Resources and Financial Aspects of Utilization”, organized by United Nations University -Geothermal Training Program and LaGeo, El Salvador, March 23-29, 2014 ISBN 978-9979-68-339-1 <http://www.os.is/gogn/unu-gtp-sc/UNU-GTP-SC-18-18.pdf>.

The conditions at the hot end will influence the turbine operation. The vaporizer pressure in the ORC plant is optimized for given source fluid properties. If the properties of the source fluid change, then another vaporizer pressure may become optimal. This would typically happen in a geothermal application, where the reaction of the field to exploitation is not as originally expected.

The setback here is that the source fluid from the field does not have the (high) temperature which was initially expected. Then the plant is running at a condition very different from the design condition. Almost certainly a new and lower vaporizer pressure will help, and then the benefit of being able to run the existing turbine at high efficiency at the new conditions becomes extremely valuable.

What can be done if the turbine does not have a variable geometry inlet guide vanes? Three alternatives are obvious:

1. Run the turbine as it is, with low efficiency.
2. Re-blade the nozzle guide vane row, with associated downtime and cost.
3. Install a new turbine, with even more downtime and higher costs.

The variable geometry nozzle guide vanes thus have two main benefits in an ORC plant:

1. They ensure a high yearly energy production of the ORC plant by keeping efficiency high under varying climatic conditions.
2. They reduce the risk for the plant owner by being able to adjust to changing properties of the heat source for the plant.

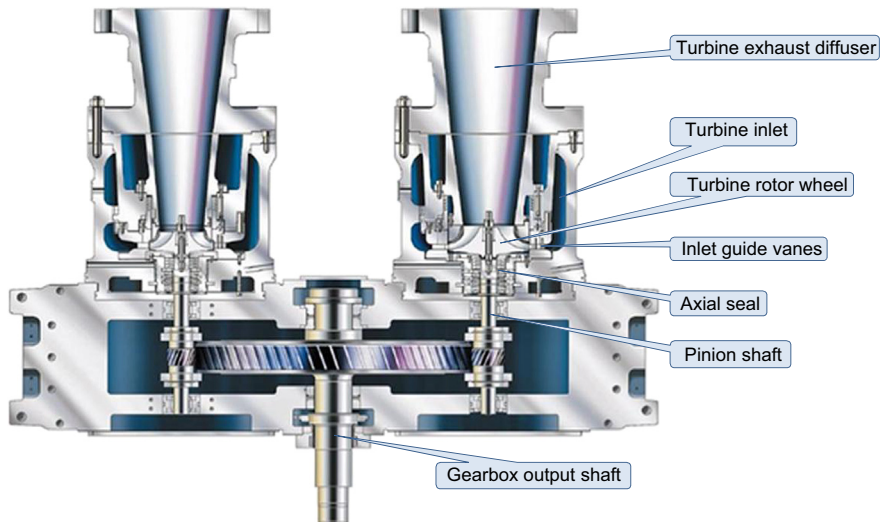


Figure 10.7 Section through two parallel inward radial flow turbines with integral gear technology.

The figure is rearranged from: <http://www.atlascopco-gap.com/fileadmin/download/brochure/driving-expander-technology.pdf>.

10.5 Gearbox and integral gear technology

Industrial applications involve usually either a generator or an electric motor. Then a gearbox will be necessary to connect the radial turbine to a synchronous rotational speed of the generator or the motor. The same gearbox can have more than one compressor or turbine mounted, making it possible to run single-stage expansion with more than one turbine in parallel, or by having more than one turbine mounted in series on the same gearbox for multistage expansion.

The turbine wheel can be mounted directly on the gearbox pinion. This “Integral Gear Technology” eliminates the need for a special driveshaft from the turbine to the gearbox, making the turbine–gearbox assembly sturdy, reliable, and maintenance friendly.

A section through two turbines with integral gear technology mounted on the same gearbox is shown on Fig. 10.7.

10.6 Advantages of radial turbines compared to axial or impulse turbines in Organic Rankine Cycle-based waste heat recovery processes

As opposed to the radial turbine design described in Chapter 10.4, an axial turbine can only be controlled by means of a throttling valve at the machine inlet. When the flow is

changed from the design volume flow, then the angle of attack at the blade leading edge will change, which leads to reduced efficiency.

As a countermeasure, tolerances towards angle of attack changes in axial turbines can be increased by modifying the profile of the rotor blade, e.g., by increasing the radius at the blade leading edge.

But this also leads to a diminished aerodynamic efficiency of the entire stage.

Under these conditions, the impulse turbine design is also inferior to radial turbines with variable IGV; the option of partial admission of the blades is hardly more than “damage control”.

10.7 Radial turbines support higher pressure ratios and broader areas of application

Due to their design, radial turbines can achieve much higher pressure ratios per stage than axial turbines. In practice, pressure ratios up to 10 are common for single-stage radial turbines. In order to achieve the same pressure ratio, an axial design turbine would require three to four stages.

These performance features make radial turbines the first choice for ORC-based, trans-critical waste heat recovery (WHR) applications with their high temperature levels and exclusively sensible heat transfer processes.

The largest destruction of exergy in an ORC power plant is in the heat transfer process between the source fluid and the working fluid in preheaters and vaporizers, and to a lesser extent between the working fluid and the cooling fluid in the condenser. The selection of working fluid and pressure level is a result of a minimization of these losses. Usually the source fluid flow and temperature is given and cannot be influenced by the ORC plant designer. The operating conditions for the turbine at the design point is determined at the same time.

The turbine pressure ratio is then given, and the turbine design parameters are defined. The turbine manufacturers can now determine the size of the turbine, number of stages, turbine rotational speed, and so on from their available product portfolio.

10.8 Large turbines

Atlas Copco presently produces radial inflow turbines with up to roughly 14 MW power. The maximum power for each turbine is of course dependent on the ORC plant cycle, so the maximum can be stretched a bit if the ORC cycle is favorable. A turbine with a larger wheel has been developed, extending this limit to roughly 18 MW, again depending on the ORC cycle.

In cases where a process requires more than one turbine stage, these can be mounted on a single gearbox. This integral design approach, also commonly used in multistage radial compressors, can be suited towards individual customer and process requirements.

Atlas Copco has delivered such turbines for a power plant in Pamukören, Turkey in four identical ORC plants. Each plant has two parallel turbines on a common gearbox,



Figure 10.8 Two parallel inward radial flow turbines mounted on a common gearbox with integral shaft technology.

delivering a total of 22 MW, or 11 MW for each turbine. Such a turbine pair is shown on Fig. 10.8; the photo was taken before the turbines were insulated.

10.9 Sturdiness and reliability

The variable geometry IGV designed by Atlas Copco have proven to be reliable. The clamping of the guide vanes is done by balancing the gas forces acting on the assembly, and is thus self-adjusting.

The turbine shaft serves the function of a pinion shaft of the gearbox, thereby increasing the compactness and sturdiness of the design. This is especially suited as a cost-efficient solution in ORC-based power plant applications where a single turbine alone cannot transfer the entire power provided by the process. The same applies to processes with multiple pressure levels.

Industry standard seals have been used in the turbines from Atlas Copco. Their selection is discussed in Chapters 10.10 and 10.11.

The conclusion of this is that the inward radial flow turbine design from Atlas Copco is extremely reliable and requires little maintenance, even if this is a high performance design with advanced features.

This high reliability and low maintenance has been verified in hundreds of turbines which have been made by Atlas Copco and delivered not only to ORC plants, but also to applications with similar (and not quite so similar) fluids such as natural gas condensate removal, liquid natural and petroleum gas, air separation, and so on.

The Atlas Copco integrally geared design allows the combining of up to eight compressor and expander stages on a single gearbox.

10.10 Advantages of gas-lubricated mechanical face seals: optimal turbine efficiency

For the gas-side shaft seal in radial turbines for ORC-applications, gas-and oil-lubricated mechanical face seals are both viable alternatives. Both designs offer minimal leakage

and the smallest possible overhang of the turbine rotor, thereby facilitating an optimal degree of rotor dynamics. Gas-lubricated mechanical face seals (or dry face seals) rely on inert sealing gas to prevent the already minimal leakage of process gas to be released into the environment. Together with the appropriate process configuration, this also helps to prevent contamination of the working fluid with inert gas.

However, in this process, the residual leakage of the working fluid mixes with the flow of sealing gas. This may require an additional step in the process to separate both gases in a seal gas recovery unit.

Afterwards, the leaked process gas is reinserted into the ORC process. The elimination of working fluid leakages is not only a priority from a plant operator's perspective, but the process gases, e.g., refrigerants, are costly materials that also add to the emission of greenhouse gases.

This is in sharp contrast to the underlying promise of sustainability achieved through geothermal power generation.

The advantages of dry face seals include maximum rotational speeds for optimal turbine efficiency. Their main disadvantage, especially when it comes to ORC-based applications, is the loss of working fluid with the seal gas. If the seal is good, this loss may be acceptable, but cost-intensive sealing gas recovery units will be necessary.

10.11 Advantages of oil-lubricated mechanical face seals: maximum leakproofness

As an alternative, oil-lubricated mechanical face seals in ORC-based processes offer a maximum degree of leakproofness. This design option also eliminates the need for a costly and work-intensive sealing gas recovery unit.

But the use of oil-lubricated mechanical seals is not without downsides; compared to gas, oil is a highly viscous fluid. Used as a sealant medium, it creates a high level of friction between the rings rotating with the turbine shaft and the static rings along the sealing gap. This ultimately leads to increased heat generation at the seal, limiting the maximum rotational speed of a turbine combined with an oil-lubricated face seal. For this reason, a turbine based on such a design may fall short of achieving its maximum efficiency. This method also requires a sealing oil system, which may necessitate degassing of process gas released from the oil. In summary, the initial cost advantage of oil-lubricated seals compared to dry face seals with a sealing oil recovery unit is minimal.

For this reason, neither of the two options is inherently superior to the other. Choosing the right sealing system thereby requires consideration of all project parameters to weigh all the pros and cons of each option.

10.12 The track records

Atlas Copco has been manufacturing inward radial flow turbines and outward radial flow compressors for decades. There are hundreds of inward radial flow turbines

made by Atlas Copco in operation today on fields such as natural gas condensate removal, liquid natural and petroleum gas, and air separation, in addition to ORC power plants. The number of installed outward flow radial compressors is even greater.

Atlas Copco is building ORC power plants with its own radial inflow turbines, but has also sold a number of turbines to other ORC companies.

In a paper by [R. Bertani \(2015\)](#), the number of geothermal ORC plants is estimated at roughly 290, with the average plant size of 6.3 MW. In papers by [S. Quoilin et al. \(2013\)](#) it is stated that the number of ORC units in WHR (20%) is roughly equal to the number in geothermal (22%), and the number of ORC units in biomass plants (57%) is roughly equal to the sum of geothermal and WHR. Quoilin also estimates the average power of an ORC unit to be around 3 MW. If both Bertani and Quoilin are right, then the total number of ORC units worldwide should be around 1300.

This leads to an estimate of 1000–1500 turbines in ORC plants worldwide, thereof almost 300 in geothermal plants. It is interesting that the number of inward flow radial turbines delivered by Atlas Copco for all industries in the same order of magnitude (rough estimate of the production of Atlas Copco during the last years are around 120 radial compressors and turbines per year).

Atlas Copco has been delivering inward radial flow turbines for binary and ORC power plants since 1977, and made the first geothermal ORC turbine in 1982 (13.4 MW). The turbines delivered are in the range of 3–13 MW. Atlas Copco has a special position in the market by routinely producing large turbines, presently up to roughly 13 MW.

It can be concluded that the inward radial flow turbine has a very long and good track record.

References

- Agahi, R., Mohr, F., 2015. Evaluation of inflow radial turbo expander field performance for a 25 MW geothermal organic rankine cycle train. In: 39th Geothermal Resources Council Annual Meeting – Geothermal: Always On, GRC 2015, Reno, NV, 20–23 September 2015. GRC Trans. 39, 805–807.
- Bertani, R., April 2015. Geothermal power generation in the world 2010–2014 update report. In: Proceedings World Geothermal Congress 2015. Australia, Melbourne, pp. 19–25.
- Bronicki, L., Nett, C.N., Nordquist, J., 2014. Electricity generation from fuel cell waste heat using an Organic Rankine Cycle. In: ASME 2014 12th International Conference on Fuel Cell Science, Engineering and Technology, FUELCELL 2014 Collocated with the ASME 2014 8th International Conference on Energy Sustainability, Boston, MA, June 30–July 2, 2014.
- Hawkins, L., Zhu, L., Blumber, E., Mirmobin, P., Erdlac Jr., R., 2012. Heat-to-electricity with high-speed magnetic bearing/generator system. In: Geothermal Resources Council Annual Meeting 2012 – Geothermal: Reliable, Renewable, Global, GRC 2012, Reno, NV, September 30–October 3, 2012. GRC Trans. 36 (2), 1073–1078.
- Maruccilli, F., Thiolet, D., 2010. Optimizing binary cycles thanks to radial inflow turbines. In: Proceedings World Geothermal Congress 2010, Bali, Indonesia, 25–29 April 2010. <http://www.geothermal-energy.org/pdf/IGAstandard/WGC/2010/2640.pdf>

- Quoilin, S., et al., June 2013. Techno-economic survey of Organic Rankine Cycle (ORC) systems. *Elsevier Renewable and Sustainable Energy Reviews* 22, 168–186.
- Rizzi, F., Di Schio, C.R., Santarossa, S., 2015. Hybrid ORC waste heat recovery system and solar thermal plant in Morocco. In: *IEEE-IAS/PCA Cement Industry Technical Conference, IAS/PCA CIC 2015*, West Toronto, Canada, 26–30 April 2015.
- Spadacini, C., Xodo, L., Quaia, M., Frassinetti, M., Rizzi, D., 2014. The geothermal radial outflow turbine. In: *Geothermal Resources Council Annual Meeting – Geothermal: A Global Solution*, GRC 2014, Portland, OR, September 28–October 1, 2014. *GRC Trans.* 38, 755–757.

Radial outflow turbines for Organic Rankine Cycle expanders

11

C. Spadacini, D. Rizzi

Exergy S.p.A., Olgiate Olona (VA), Italy

11.1 Introduction

The Organic Rankine Cycle (ORC) market is expanding and there is rising interest about it in the scientific community. In terms of system performance, turbines are the most important and critical component of ORC systems (Macchi, 2013).

Most of the R&D (research and development) activities, in the past decades, have concentrated on the thermodynamics of the cycle, fluid dynamics of heavy fluids, and organic fluid selection and stability. In particular, the work of Politecnico di Milano and University of Delft, two of the most active universities in the ORC field, has been dedicated to the study of the heavy fluid, in general, and siloxanes in particular (Angelino and Invernizzi, 1993). Another important portion of the research load has been oriented towards the fluid-dynamics of heavy fluids, such as the BZT (Bethel-Zel'dovich-Thompson) effect (Colonna et al., 2006).

However, only a few theoretical academic studies have been done to evaluate the arrangement of the most important component, the turbine. Among them is a paper by Angelino (1984), which covers the history of ORC research at Politecnico di Milano, and no mention is made of turbine configurations, other than axial turbines.

The two ORC market leaders, Ormat and Turboden, in the last decades, have also spent much of their effort in R&D and IP (Intellectual property) on ORC fluid and fluid-dynamics, but have never investigated nor implemented turbine configurations other than axial turbines. In the USA, few applications have featured high speed radial inflow expanders developed for the oil and gas sector.

The improvement of ORC systems has been limited by those two configurations due to a number constraints (detailed in the rest of the chapter), including:

- For radial inflow turbines, the limitation is volumetric expansion ratio and volumetric exhaust flow.
- For axial turbines, the constraints relate to blade height (i.e., h/D), limiting the volumetric expansion ratio.

These issues have been overcome against a significant increase in system complexity:

- Double stage radial inflow in series for high volumetric expansion ratio (GE ORegen).
- Double stage radial inflow in parallel for high volumetric exhaust flow (Atlas Copco Energas).
- Double-casing axial turbine in series at different RPM (Turboden; Bini, 2008).



Figure 11.1 First multistage 1 MW_e Exergy radial outflow turbine in 2010 (Spadacini et al., 2011).

An interesting innovation in this panorama is the ORC radial outflow turbine (ROT) developed by Exergy (Fig. 11.1), which has several unique characteristics qualifying this unconventional configuration as advantageous for many ORC applications, as it ideally matches the process conditions typical for these kinds of uses, mainly and typically in the multiMW power plants.

In fact, it has been demonstrated (Macchi, 2013; Frassinetti et al., 2013) that this machine is competitive with both axial and radial inflow turbines. These solutions are usually adopted in ORC applications, with the overhung configuration, as they create compact machines and reduce sealing problems (Salucci et al., 1983).

In order to better understand its potential and limits, this chapter describes the features of the ORC ROT, through mechanical, thermodynamic, and fluid-dynamic fundamentals.

The following paragraphs, provide readers with an overview of the traditional turbine arrangements and a detailed description of the ROT basics.

A comparison of the presented ROT with an axial ORC turbine in overhung configuration directly coupled with a generator is presented. This analysis highlights differences in fluid-dynamic losses and explains the higher efficiency of ROT compared with the axial overhung turbine. Finally the typical configurations allowed by the radial outflow technology are presented.

A brief history of this particular configuration is provided as an introduction.

11.2 The history of the radial outflow configuration

The history of the ROT includes the Parsons and Ljungström turbine.

11.2.1 Parsons turbine

In 1884, Parsons designed his first steam turbine. Rather than using a single stage impulse machine, he chose to follow the path of the multistage reaction turbine (Meher-Homji, 2000)

This decision arose due to several reasons, including higher efficiency and lower speeds. The lower speeds allowed him to avoid speed reducers so that his machines could be more flexible and therefore have a wider market.

As he wished to enter the power generation and ship propulsion markets, he focused on a reaction steam turbine with an axial configuration.

The first Parsons turbine produced about 7.5 kW (10 hp) at 18,000 rpm.

Initially he used brass straight blades but later he used curved blades attached to steel disks. His later designs used an increasing drum diameter and multiple compounded turbines in series (Meher-Homji, 2000).

Parsons sold over 300 marine turbo generators before he closed his partnership with Clarke Chapman in 1889 in a legal dispute that resulted in Parsons not being allowed to use his own axial reaction multistage turbine on the market (Meher-Homji, 2000).

For this reason, he decided to focus his work on a compound ROT that he patented.

After considerable difficulty, Parsons finally got the power industry to buy into his steam turbine turbo generator designs and soon his turbines started to replace reciprocating engines at central stations. In 1893, he managed to purchase his original patents and again offered his multistage axial reaction design. Soon his multistage designs were producing 25,000 kW and became the norm for central power stations all over the world. By 1923, Parsons had installed a set up to 50,000 kW (Meher-Homji, 2000).

Therefore, with his innovative turbines Sir Charles Parsons revolutionized the naval propulsion market too.

In 1893, he began working on a small turbine for a ship called “Turbinia”; he equipped the ship with a single ROT engine turning a single screw (Fig. 11.2).

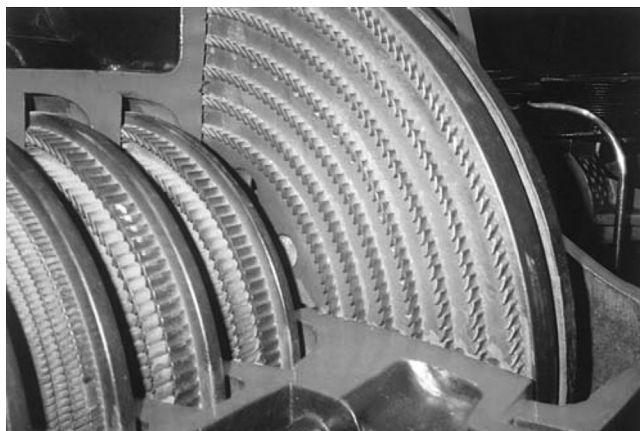


Figure 11.2 A radial outflow Parsons turbine (Meher-Homji, 2000).

After recovering his axial flow turbine patents, Parsons replaced the engine of the ship with a three-stage axial flow design. The engine developed 2300 hp and allowed the Turbinia to attain a speed of 34 knots (Meher-Homji, 2000).

For Sir. Parsons, the radial outflow configuration was the way to continue manufacturing turbines and selling them on to the power production and propulsion markets, when he could not employ the axial multistage turbine, which resulted to be more performant for other applications.

11.2.2 Ljungström turbine

The Ljungström turbine owes its name to the Swedish engineers Birger and Fredrik Ljungström who patented it in 1908. This turbine type was produced by Svenska Turbinfabriks Aktienbolaget Ljungström, which they established in 1913.

In respect to all other turbines, it has a unique feature; it is a multistage counter-rotating centrifugal steam turbine. It consists of two discs facing each other, connected with two independent shafts, with crowns of blades installed alternately on both of them.

As shown in Fig. 11.3, the working fluid (it was steam) is introduced into the central compartment through ports and slots and it flows through the counter-rotating blades of the two discs towards the periphery. Such a turbine was mainly used for power generation, but there are also some applications in railway engineering because of their favorable mass-to-power ratio (Fig. 11.4).

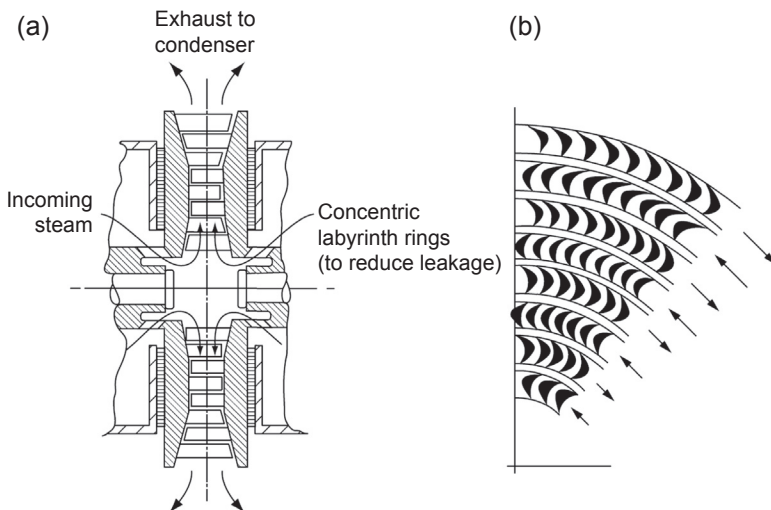


Figure 11.3 Schematic drawing of a Ljungström turbine (Dixon, 1998). (a) Meridional section through turbine and (b) Blading arrangement and directions of rotation.

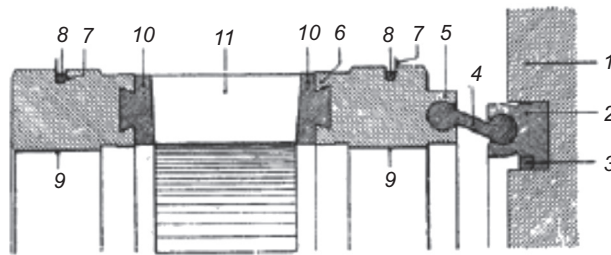


Figure 11.4 Stodola Loewenstein “steam and gas turbines”.

Peter Smith reprint 1945.

11.3 Radial outflow configuration: considerations about particular features and comparison with the most traditional alternative

The most common expander types used in ORC are axial flow turbines, radial inflow turbines, and ROTs.

Organic fluids have a very high molecular weight. The main effects of a high molecular weight on expander design are: low enthalpy drop along expansion, high volumetric ratio, and low speed of sound.

Thanks to this, ORC turbines can be designed with only a few stages (even only one single stage) and are characterized by both a low stage load coefficient and a low peripheral speed, with the possibility to realize low-stress and high efficiency blade profiles. However, difficulties in stage design can arise because of the high volume flow ratio along the expansion. For these fluids, to realize the whole expansion in a single reaction stage often entails a blade height difference, which strongly penalizes stage efficiency due to the formation of nonnegligible radial velocity components. In addition, Organic fluids have low speed of sound and therefore a high Mach number. In single stage impulse machines the high Mach number is combined with high deflection blades that generally result in high efficiency losses.

The typical configuration for an ORC turbo generator is a machine with an expander directly connected to a generator; sometimes, a gearbox is used between the expander and the generator to obtain different rotational speeds. In order to simplify the mechanical configuration of the system and to reduce costs of investment, operation, and maintenance due to the presence of a gear, the ROT is usually directly connected to the generator with coupling. In any case, for both solutions, all machines usually have a cantilever rotor to simplify the machine and To minimize leakage of organic fluid into the external environment, all machines usually have a cantilever rotor to have one shaft seal.

The crossing flow (Fig. 11.5) relative to the axis of rotation of the machine, defines the turbine type. When the flow is parallel to the axis of rotation, the machine is denoted as an axial flow turbine, and when the flow is perpendicular to the axis of rotation, the machine is denoted as a radial flow turbine. In particular, when the flow moves from outside to inside the machine, it is defined as a radial centripetal

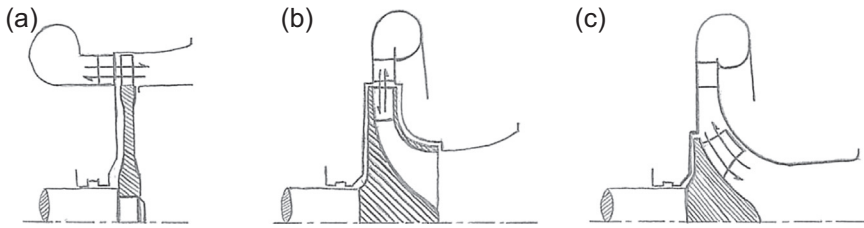


Figure 11.5 Crossing Flow. (a) axial; (b) radial; (c) mix.

turbine (or radial inflow turbine), and when the flow moves from the inside to the outside of the machine, it is defined as a radial centrifugal turbine (or ROT). Finally, when both radial and axial flow velocity components are present, the machine is denoted as mixed flow.

Figs 11.6 and 11.7 show the typical arrangement of a multistage ROT in a cantilever configuration. In the inlet duct, the flow is axial across the inlet nose the flow becomes radial. The working fluid flow passes through the alternate stator and rotor blade rows, where mechanical energy is extracted. Before the turbine outlet, the working fluid passes through a radial diffuser to recover a part of the exhaust kinetic energy. Stator blade rings are fixed on a disk called a stator disk and the rotor blade rings are fitted on another disk called the rotor disk. The rotor disk is joined to the shaft and transmission flange to transmit power from the blade to the generator through coupling. Bearings installed on the turbine casing support the shaft. A mechanical seal between the rotor disk and bearings is required to isolate the working fluid from the external environment. This arrangement allows more stages in one disk; this is the best solution in a rotor cantilever configuration because it minimizes the rotor weight and distance between the rotor center of gravity and bearings.

To better understand the particular features of the ROT, some considerations about turbomachinery fluid-dynamics and about thermodynamics are necessary.

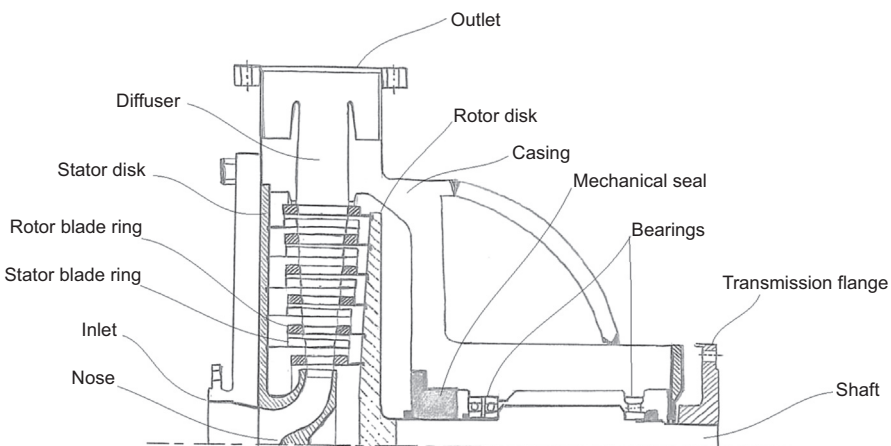


Figure 11.6 Multistage radial outflow turbine.



Figure 11.7 Multistage radial outflow turbine.
Courtesy of Exergy SpA.

The fluid-dynamic differences of ROTs, when compared to other turbines, is due to the increase in a radius through the blade rows. In fact, the flow streamlines through the blade rows of an axial flow turbine have essentially a constant radius, whereas there is a substantial reduction in radius through the radial inflow turbine, while in a ROT there is a substantial increase in a radius through the blade rows.

For a fluid-dynamic analysis of ROT and to understand the differences compared to the other turbine types, the construction of velocity diagrams is a fundamental tool. For generality to axial or either inlet and outlet radial turbines, the velocity triangles will be constructed in stream surfaces passing through the machine. By definition, a stream surface has no mass flow crossing it and no fluid velocity normal to it. Considering an orthogonal coordinate system (m, θ) where θ is the polar angle of a cylindrical coordinate system (Fig. 11.8), for an ideal axial flow stage, the meridional coordinate, m , is identical to the axial coordinate, z . The same is true at the rotor exit of an ideal radial inflow stage. Upstream of the rotor in an ideal radial inflow stage, the meridional coordinate m , is identical to the radial coordinate, r . Upstream and downstream of the rotor in an ideal radial outflow stage, the meridional coordinate m is identical to the radial coordinate r .

In Fig. 11.9, the velocity diagrams on a stream surface for a general turbine stage is shown. Subscript 0 refers to the inlet nozzle section, subscript 1 to the nozzle exit section or rotor inlet section, and subscript 2 to the rotor exit section. The velocity in the stationary coordinate system, the absolute velocity, is designated as C . The velocity in the rotating coordinate system, the relative velocity, is designated as W . The tangential velocity is designated as U .

The meridional velocity component combines the axial and radial velocity component, which is identical in either coordinate system:

$$W_m = C_m = \sqrt{C_z^2 + C_r^2}$$

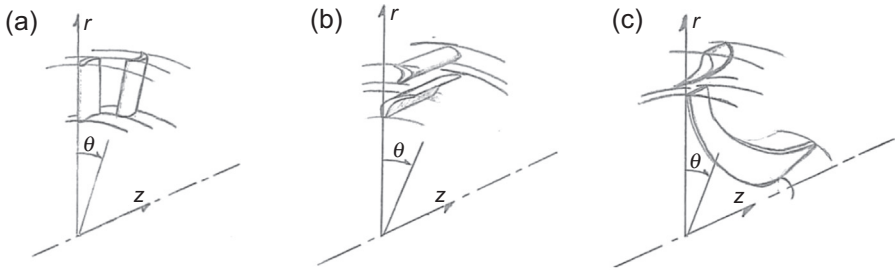


Figure 11.8 Cylindrical coordinate system. (a) axial turbine; (b) ROT; (c) radial inflow turbine.

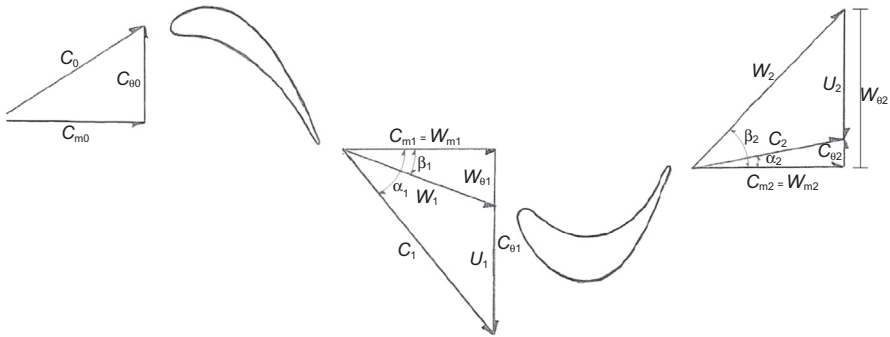


Figure 11.9 Velocity diagrams on a stream surface.

If ω is the angular velocity of the rotating coordinate system. The relative tangential velocity components is:

$$W_\theta = C_\theta - \omega r$$

The velocities are given by:

$$C = \sqrt{C_m^2 + C_\theta^2} \quad W = \sqrt{W_m^2 + W_\theta^2}$$

The flow angle with respect to the tangential direction in the stationary coordinate system, α , is given by:

$$\tan \alpha = \frac{C_m}{C_\theta}$$

The flow angle with respect to the tangential direction in the rotating coordinate system, β , is given by:

$$\tan \beta = \frac{C_m}{W_\theta}$$

The angles at the inlet and exit sections of blade rows are the first step to define the shape of the profile.

In an axial turbine stage, both in the inlet and in the outlet rotor section, the coordinate r increases from the hub to the tip blade, then the absolute and relative tangential velocity components change. In particular, the local blade speed at the hub coordinate is less than the local blade speed at the tip coordinate. This different velocities from hub to tip induce a different shape of velocity diagrams. For this reason, when the tangential speed difference is not negligible, for maximize the efficiency twisted blade are necessary.

In the radial inflow turbine, in the inlet rotor section, the coordinate r is constant, while in the rotor exit section, the coordinate r increases from the hub to the tip blade, then the absolute and relative tangential velocity components change. In the radial inflow turbine, to maximize the efficiency, a difficult rotor blade shape is necessary.

In the ROT stage, being the peripheral velocity constant along the blade span, velocity triangles at the hub and tip do not change, and the blades are prismatic instead of twisted. For this reason, the simple shape of a prismatic blade is enough to maximize the efficiency of the stage.

A further important geometric characteristic that affects the fluid dynamics of the turbines, is the aspect ratio of the blade rows, defined as:

$$Ar = \frac{h}{c}$$

where h is the height of blade and c is the cord of the blade profile.

The height of the blade rows, at any station, is a function of the flow passage area. For the calculation of the flow passage area, it is necessary to know the absolute meridional velocity (C_m) (Fig. 11.10) and the volumetric flow (\dot{V}). In axial turbines, the flow passage area is an annulus area at any station, in ROTs the flow passage area is a cylindrical area at any station, in radial inflow turbines, the flow passage area is usually

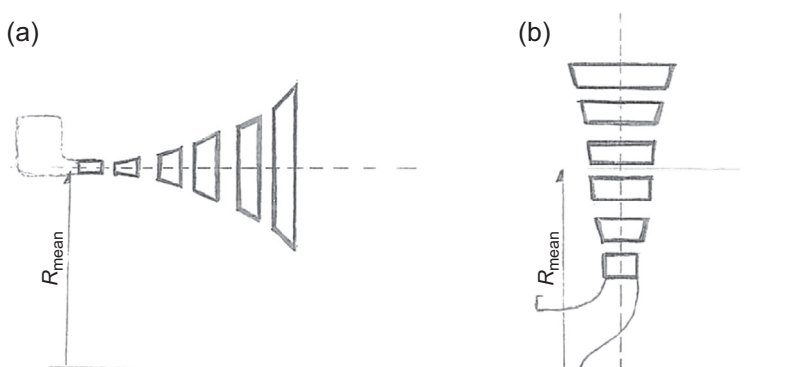


Figure 11.10 Meridional plane. (a) axial turbine; (b) radial outflow turbine.

a cylindrical area at the inlet and outlet nozzle stations while is an annulus area at rotor exit station.

For the annulus area, there are more methods to approach the problem to define the geometrical characteristics of the section, for example, it is possible start from the mean diameter to calculate the inner and outer diameter. The blade height will be the half the difference between the outer and inner diameter.

For the cylindrical area, the diameter defines the height of the cylinder and the blade height.

The organic fluids generally show high expansion ratios with small volumetric flows at the inlet section and low enthalpy drops (Poling et al., 2000). For this reason in ORC axial turbines, if the mean diameter is constant, the blade height of the first stage is very low while the blade height of last stage is very high. This fact entails low efficiencies across the machine: first stages are characterized by high secondary losses and in extreme cases may require partial admission, on the other hand last stages suffer from high h/D ratios with the need to have twisted blades, resulting in a more complex design and risk of supersonic flows. The machine mean diameter is selected according to the rotational speed and the fluid speed of sound, with the aim of maximizing the efficiency. In ORC ROTs, the diameter increases along the expansion process thus allowing for a more efficient expansion. Considering the same mean diameter of the machine, the blade height of the first stage is greater than the axial turbine because the radius is considerably smaller than the mean diameter; while the blade height of last stage is smaller than axial turbine because the radius is greater than the mean diameter. This means that it is possible to have lower blades at the last stage, leading to evident mechanical advantages, and higher blades at the first stages, thus reducing the end wall and leakage losses. For these reasons, as initial stages have a better aspect ratio, they do not need partial admission, avoiding additional losses related to this aspect. As a consequence, the possibility to manage higher volumetric flow ratio, allows a higher pressure at the turbine inlet while keeping the same condensing pressure, therefore giving the opportunity to increase the thermodynamic cycle efficiency.

In radial inflow turbine, nozzle is placed at maximum diameter while exit rotor station is placed at the lower machine diameter. In ROT, nozzle is placed at minimum diameter while exit rotor station is placed at maximum machine diameter.

To understand the fluid-dynamic advantages of the radial outflow configuration the following turbine design factors must be taken into account: degree of reaction, stage loading, flow coefficient.

The stage loading is a measure of the work output of the stage, defined as:

$$\Psi = \frac{\Delta W}{U^2}$$

It is often used in conjunction with the flow coefficient, defined as:

$$\phi = \frac{C_m}{U}$$

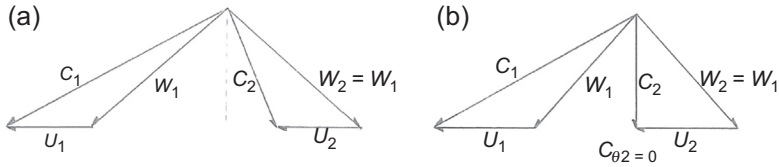


Figure 11.11 Velocity diagrams for a zero reaction stage. (a) generic; (b) pure axial leaving velocity.

The degree of reaction of a turbine stage is the fraction of the fluid static enthalpy drop which occurs in the rotor. The basic design of the turbine starts from the choice of the reaction: zero reaction, 50% reaction, and axial leaving velocity (variable reaction).

It should be emphasized however, that the designer is not limited to these three types and that in a three-dimensional design of the turbine reaction may vary continuously along the blades.

In an impulse stage, the degree of the reaction is zero (Fig. 11.11), meaning that the gas expands and accelerates in the stator passages, and then is merely deflected at a constant thermodynamic state by the moving rotor blades. From the definition, if the reaction is zero, then:

$$W_1 = W_2 \quad \tan \beta_1 = \tan \beta_2 \quad \beta_1 = \beta_2$$

Velocity triangles for this zero reaction stage are shown:

The specific work output is:

$$\begin{aligned} \Delta W &= UC_m(\tan \alpha_1 + \tan \alpha_2) \\ &= UC_m(\tan \beta_1 + \tan \beta_2) \\ &= 2UC_m \tan \beta_2 \end{aligned}$$

and the blade loading coefficient is:

$$\Psi = \frac{\Delta W}{U^2} = \frac{2C_m}{U} \tan \beta_2$$

in particular, if $\alpha_2 = 0$ and the leaving velocity is axial, then

$$\tan \beta_2 = \frac{U}{C_m} \quad \text{and} \quad \Psi = 2$$

the change in tangential velocity is twice the blade speed.

Stages having a 50% degree of reaction are used where the stator and the rotor for a turbine equally share the enthalpy drop. If there is equal enthalpy drop across the rotor and stator, then $R = 0.5$ and the velocity triangles are symmetrical, as it is shown in Fig. 11.12.

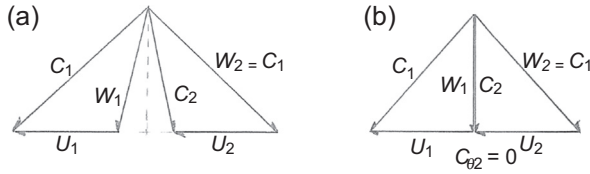


Figure 11.12 Velocity diagrams for this 50% reaction stage. (a) generic; (b) pure axial leaving velocity.

$$\text{Then } \alpha_1 = \beta_2 \quad \alpha_2 = \beta_1 \quad \text{and} \quad \tan \beta_2 - \tan \beta_1 = \frac{U}{C_m}$$

The specific work output is:

$$\begin{aligned} \Delta W &= UC_m(\tan \alpha_1 + \tan \alpha_2) \\ &= UC_m(\tan \beta_1 + \tan \beta_2) \\ &= UC_m\left(2 \tan \beta_2 - \frac{U}{C_m}\right) \end{aligned}$$

and

$$\Psi = \frac{\Delta W}{U^2} = \frac{2C_m}{U} \tan \beta_2 - 1 = \frac{2C_m}{U} \tan \alpha_1 - 1$$

in particular, if $\alpha_2 = 0$ and the leaving velocity is axial, then:

$$\tan \beta_2 = \frac{U}{C_m} \rightarrow \Delta W = U^2 \quad \text{and} \quad \Psi = 1$$

The change in tangential velocity across the rotor is then equal to the blade speed.

In both cases, the best efficiency is obtained when the flow leaves axially, in this way the specific work of impulse stage is equal to $2U^2$, while for the 50% reaction degree stage the specific work is only U^2 . It is also clear, however, that flow velocities are higher in the impulse stage which will lead to larger viscous losses. Altogether, the more specific work of impulse stage is also less efficient.

A useful presentation of stage performance based on the stage loading and coefficients is the Smith chart shown in Fig. 11.13. Although first published in 1965, this is very widely used today (Moustapha et al., 2003).

It is an empirical correlation based on some 70 turbine tests. These were all stages of constant axial velocity (in axial turbine), with a reaction between 0.2 and 0.6, and a relatively high aspect ratio in the region of 3–4. The efficiency values have been normalized to exclude tip leakage loss, and therefore are higher than would be expected for similar turbines in actual operation. However, it has been demonstrated

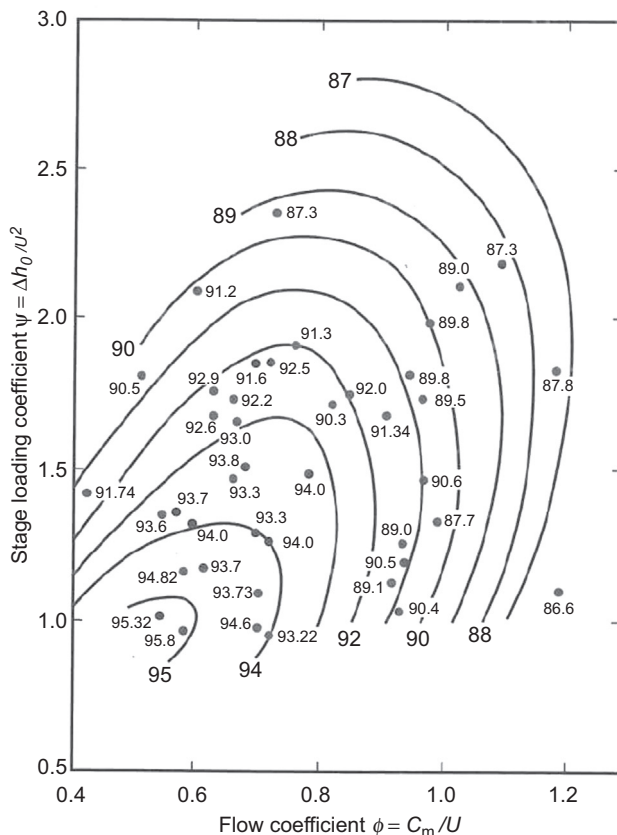


Figure 11.13 Smith chart of turbine stage efficiency (Smith, 1965).

that the trends shown are accurate even for turbine stages significantly different from those originally used, and the Smith chart is extensively used to indicate suitable choices of loading and flow coefficients for preliminary design. The Smith chart does not give a good indication of the actual efficiency of a given design, but the comparison between blade rows of different loading and flow coefficients is generally found to be quite reliable (Moustapha et al., 2003).

When Ψ increases, the deflection angle ($\beta_2 - \beta_1$) must increase. High turning blades invariably have a larger surface area in contact with the fluid, and therefore have larger friction losses. Furthermore, as the amount of turning done by the fluid in the blade passage increases, the scope for secondary flow generation and the associated losses also increases. As the flow coefficient increases at a constant loading coefficient, the deflection angle decreases but the mass flow rate and therefore the axial component of velocity increases, leading to a general increase in velocity levels through the stage. Therefore, for any given loading coefficient there is an optimum flow coefficient value where the efficiency is at a maximum in the Smith chart. Clearly the best efficiency occurs at small values of loading and flow coefficients.

In the preliminary turbine design, if the enthalpy drop across the machine is defined, when the number of stages and design reaction of stages are selected, only the mean diameter or rotational speed can be chosen.

$$\omega r_{\text{mean}} = U = \sqrt{\frac{\Delta h_{\text{is,tot}}}{2(1 - \chi)N_{\text{stage}}}}$$

where r_{mean} is the mean the radius of the machine, χ is the reaction of stages, and N_{stage} is the number of stages.

In order to simplify the mechanical configuration of the system and to reduce the costs of investment, operation, and maintenance due to the presence of a gear, it is preferable to have the expander directly connected to the generator. For this reason, the generator, with a number of poles and grid frequency, determines the speed of the expander. The maximum rotational speed available with conventional synchronous generators (two poles) is 3000 RPM if the frequency grid is 50 Hz, and 3600 RPM if the frequency grid is 60 Hz.

This speed is satisfactory for axial turbines and ROTs because the design can be used more for stages. The radial inflow turbine arrangement is different; usually there is just one stage with a 50% degree and therefore the required tip speed of the rotor is very high. It is possible to obtain high tip speed and high efficiency only with a gearbox (to increase a rotational speed).

ROT allows several stages fitted on the same disk, then more stage than axial turbine are available in cantilever rotor solutions (Spadacini et al., 2013). For this reason it is possible to choose a better reaction degree, consequently stage loading and flow coefficients are smaller and therefore maximize the efficiency.

Since the work done on the fluid depends directly on the change in fluid angular momentum across the rotor, the ROT has a minimum disadvantage relative to the other turbines due to its lower rotor inlet radius.

The well-known general Euler equation for turbomachinery, ignoring minor negligible losses, provides a formulation of the specific work for a single stage as (Stodola and Lowenstein, 1927):

$$L_{\text{eu}} = U_1 C_{\theta 1} - U_2 C_{\theta 2}$$

As a result, in order to maximize the specific work of a single stage, $C_{\theta 1}$ must be much bigger than $C_{\theta 2}$. The highest specific work of a single stage is thus achieved by the radial inflow configuration, which intrinsically, has a higher peripheral velocity at the inlet and a lower one at the outlet.

The Bernoulli equations extended to the radial stage are:

$$\text{Total enthalpy upstream nozzle} \quad H_0 = h_0 + \frac{C_0^2}{2} = h_1 + \frac{C_1^2}{2}$$

$$\text{energy balance over the moving blade} \quad h_1 + \frac{W_1^2}{2} - \frac{U_1^2}{2} = h_2 + \frac{W_2^2}{2} - \frac{U_2^2}{2}$$

$$\text{or} \quad h_1 - h_2 = \left[\frac{W_2^2}{2} - \frac{W_1^2}{2} \right] - \left[\frac{U_2^2}{2} - \frac{U_1^2}{2} \right]$$

where H is the total enthalpy, and h static is the enthalpy.

This means that in evaluating the relative exit speed, the centrifugal term $\left[\frac{U_2^2}{2} - \frac{U_1^2}{2} \right]$ must be taken into account.

It should be observed that in any case as it must be $h_2 \leq h_1$, depending from the reaction degree consequently; it follows that in any case

$$W_2 \geq \sqrt{W_1^2 + (U_2^2 - U_1^2)}$$

Therefore the specific work obtainable from the radial outflow configuration is lower than the one from a radial inflow or even a purely axial one. Nevertheless this effect can be reduced by using several stages and so reducing the term $(U_2^2 - U_1^2)$.

It can be written:

$$(U_2^2 - U_1^2) = \omega^2 R_{av} C_r$$

where R_{av} is the mean radius of the rotor stage, and C_r is the radial chord of rotor stage. Therefore, a lower radial chord is better to reach a lower term.

The expansion line is summarized in Fig. 11.14.

Another key component to the turbine is the diffuser that converts the kinetic energy (high velocity) of the working fluid into pressure by gradually slowing (diffusing) the gas velocity. The diffuser increases power due to lower pressure at downstream last rotor row than the exhaust one at the very end of the machine.

The design of a high efficiency diffuser is easier in the radial outflow since the increase in section, necessary to get a good recovery of kinetic energy, is helped by the change in cross section along the radius.

Radial diffusers have two major categories. They can be either vaneless or vaned. Vaneless diffusers have a wider operating range, lower efficiency, and lower pressure recovery than vaned diffusers.

A vaneless diffuser, in its most simple form, is just made by two parallel plates, leading to an increase in the flow area as the radius increases. Vaneless diffusers are used where a large operation range is needed and the manufacturing costs must be kept to a minimum. On the other hand, vaned diffusers, which can be divided to subcategories based on the design principle or geometry, change the mean flow path radius. Better efficiency can be achieved with vaned diffusers, but they narrow the operating range significantly and are much more expensive to manufacture. Vaned diffusers are typically used with higher pressure ratios.

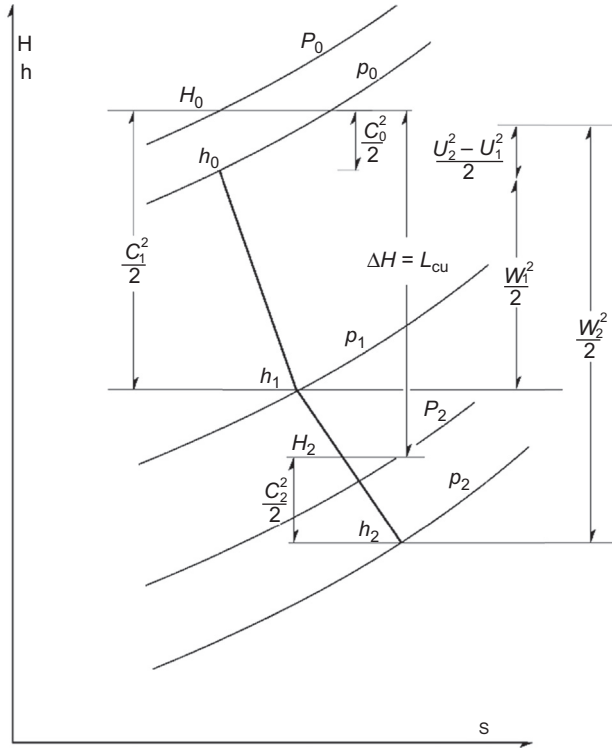


Figure 11.14 Radial outflow turbine stage expansion.

A vaneless diffuser has a simple geometry consisting of two parallel or almost parallel walls. The diffuser walls form an annular passage from the turbine rotor exit to some outlet diameter. The diffuser inlet may or may not be pinched, which means that the diffuser height is smaller than the channel height at the last rotor blade ring. Different inlet geometries of vaneless diffusers are possible. The most important design criteria affecting the performance of the vaneless diffuser are the channel width and the radius ratio of the diffuser inlet and outlet.

The conservation of mass and angular momentum yield are applied:

$$rC_{\theta} \approx \text{constant}$$

$$q_m = \rho C_r 2\pi r b$$

where C_{θ} is the tangential velocity, r is the radius, q_m is the mass flow, ρ is the density, C_r is the radial velocity, and b is the diffuser width. The definition of the absolute flow angle α in the diffuser is:

$$\tan \alpha = \frac{C_{\theta}}{C_r}$$

A maximum recovery factor is obtained with a low α angle and a high radial ratio. The common exhaust diffuser employed in axial turbines is annular. In the radial diffuser, if the discharge radius is substantially greater than the inlet radius, then the swirl component can be substantially recovered. For this reason the efficiency of a radial diffuser is greater than an axial diffuser, mostly in off design conditions.

To perform the above mentioned comparison, a common case study has been used for both configurations. The boundary conditions are in [Table 11.1](#).

ROTs and axial turbines have the same mean radius and rotational speeds (3000 RPM) but have a different number of stages, five and three respectively, according to what the main ORC manufacturers offer. For each stage, the degree of reaction, stage loading, and flow coefficients are selected in order to maximize the efficiency of the blade profile, based on the Smith chart. Inputs and results are in [Table 11.2](#).

The enthalpy drop of the fluid is divided into several stages for the single-disk/multistage configuration; the ROT is characterized by a better recovery factor and by lower stage work coefficients. This results in a subsonic or at most a transonic expansion (in spite of the low speed of sound of organic fluids), instead of a supersonic

Table 11.1 Boundary conditions for common case study

Fluid (—)	Pentane
Turbine inlet pressure (bar)	8
Turbine inlet temperature (°C)	116.2
Turbine outlet pressure (bar)	1.3
Turbine mass flow rate (kg/s)	50

Table 11.2 Boundary conditions for common case study

		Axial	Radial outflow
Enthalpy drop	(kJ/kg K)	68.88	68.88
Rotational speed	(rpm)	3000	3000
Number of stages	(—)	3	5
R min/mean/max	(mm)	322.7/360/397.7	272/360/448
U mean	(m/s)	113	113
R min/mean/max	(—)	0.1/0.1/0.1	0.45/0.47/0.5
Ψ min/mean/max	(—)	1.8/1.8/1.8	1.03/1.07/1.09
Φ min/mean/max	(—)	0.59/0.68/0.76	0.43/0.45/0.47
Blade height min/mean/max	(mm)	28.2/49.7/74.6	41.9/46.5/55.1
Exhaust energy	(kJ/kg K)	3.76 (5.5%)	2.55 (3.7%)
Mechanical power	(kW)	2853.35	3023.14

one typical of the other configuration. It also results in a higher fluid-dynamic efficiency both in nominal and off-design conditions, thanks to:

- lower stage loading and work coefficients
- higher reaction of the stages
- better aspect ratio of the stages
- lower exhaust energy. (Considering the radial diffuser the performance will be improved thanks to low velocity leaving).

It easy to understand that the radial outflow configuration has the best efficiency.

Fig. 11.15 shows the axial stages (red points) and the radial outflow stages (green points) on the Smith chart, for a comparison of stage efficiencies.

An in-house made 1D code has been used to design the two machines: the code simulates the expansion of the working fluid in the turbine and it uses reliable losses model

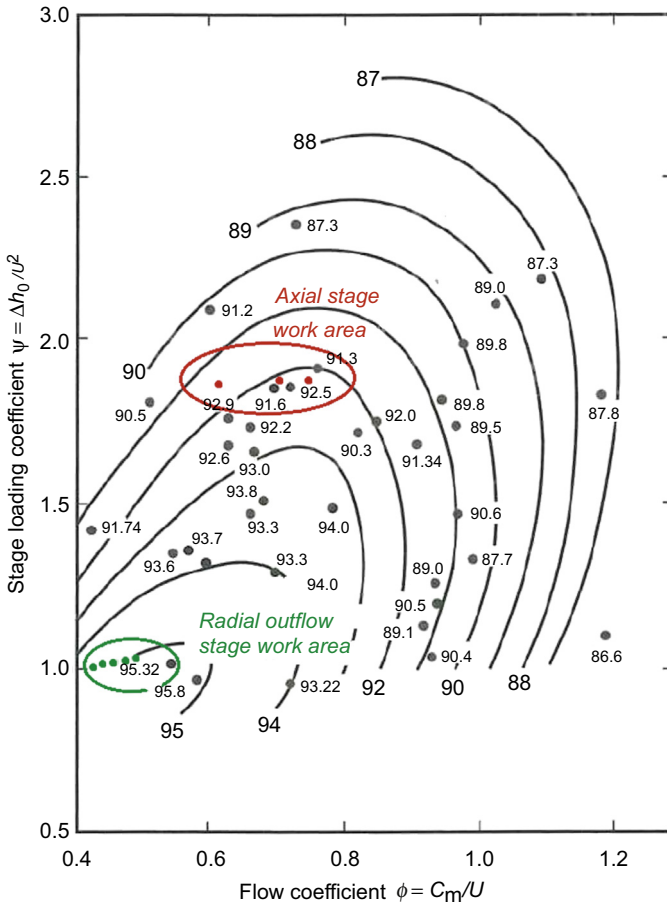


Figure 11.15 Comparison on Smith chart of turbine stage efficiencies.

from reference (Ainley and Mathieson, 1951; Dunham and Came, 1970; Kacker and Okapuu, 1981; Daily and Nece, 1960, Egli, 1935); thermodynamic properties are calculated with Refprop 9.1 (NIST, 2013).

According to the 1D code, the ROT and axial turbine have an isentropic efficiency of 87.78% and 82.85% respectively. In particular, profile losses, trailing edge losses, and endwall losses are lower in the ROT, leakage losses are lower in the axial turbine (disk/diaphragm was considered), and disk friction losses are similar between the two cases.

The mechanical construction of the multistage ROT is unique. Fig. 11.16 shows a section through a machine; the illustration includes the end of the turbine shaft, upon which the turbine disk and transmission flange are mounted. It can be seen that the face of the disc contains a number of circumferential grooves. Each groove carries a blade ring, shown to a larger scale in Fig. 11.16, in which, is the: rotor and stator disks, stator and rotor blade rings, supporting rings, expansion ring, a caulking wire, and packing strips (fin). Rotor blade rings are interleaved from the stator blade ring, and flow leakage is checked by the thin fins.

The forces to which rotor blade rings are subjected during normal turbine operation, particularly centrifugal force, produce bending moments, which tend to flex or deflect the parts, particularly the blades. The bending moment produces stresses of such magnitude that it has heretofore been considered necessary, in view of the character of known methods of blade attachment (process of production), to consider the blades as beams freely supported at their ends. This must be taken into account when calculating stresses for the purpose of determining the proper dimensions for the blades.

The bending moment produces stresses that are of much magnitude that it has heretofore been considered necessary. Stress calculation considers the blades as beams freely supported at their ends. The dimension of the blades must consider mechanical stress and process of production.

The expansion ring is characterized by low stiffness. The expansion ring is so thin that it can act only as a guide, and the centrifugal forces must be taken up by the strength of supporting ring. With unequal heating of the rotor disk and of the blade ring, the ends of the expansion ring are also at different temperatures, and they expand with a slight twisting of the ring, so that only a small force is exerted on the blades.

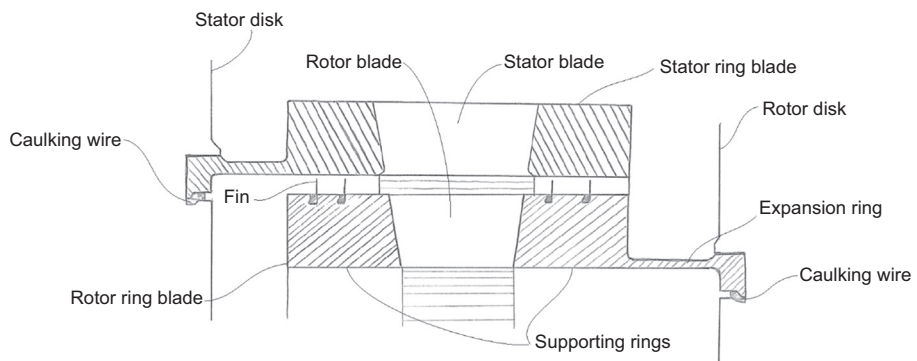


Figure 11.16 Blade rings detail with fins in order to limit fluid leakage.

For this reason, multistage ROT is the best solution where fast start up is mandatory.

The single-disk/multistage configuration minimizes static and dynamic loads on the bearings, owing to the reduced distance between the bearings and the turbine's center of gravity.

For these reasons, the radial outflow configuration improves the rotor dynamic. Due to the better rotor dynamic, the shaft vibration is minimized, and this therefore decreases the maintenance and extends the useful life of the rotating components. In other words, a shaft section smaller than the mechanical seal sizing leads to a longer life of the component.

11.4 Other configurations of the radial outflow turbine in Organic Rankine Cycles

11.4.1 *The radial–axial configuration*

The radial–axial configuration (Fig. 11.17) allows all of the strengths of the ROT (i.e., no partial admission required, no twisted blades, axial disk/multistage arrangement, and all the others strengths described previously) to be retained. It also allows the removal of the limitations created by the low specific work. In fact, placing the axial stage after the radial stage can produce a high percentage of work.

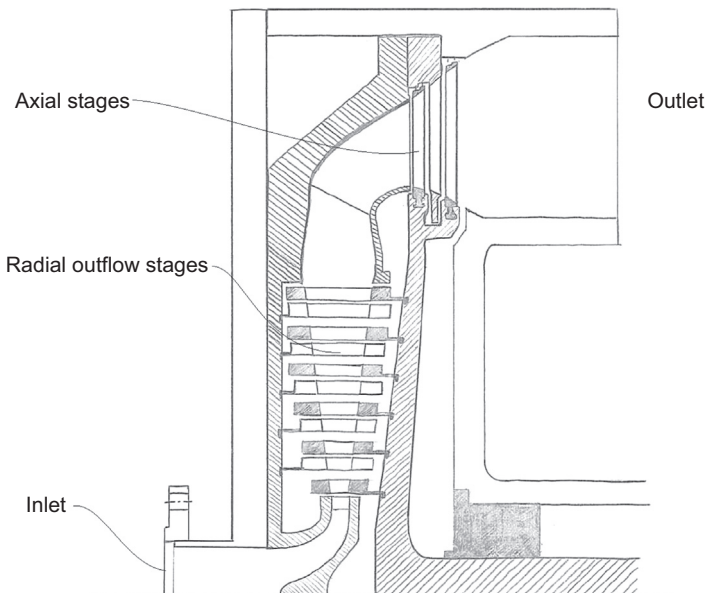


Figure 11.17 The radial–axial configuration.

This configuration is particularly useful for applications with a middle to high enthalpy drop, such as, biomass plants, Concentrated Solar Power (CSP) plants, or some high temperature geothermal plants.

11.4.2 The multipressure radial outflow turbine

The multipressure ROT allows multiple admissions and/or extractions in the same machine.

Multiple extractions give the opportunity to perform more efficient cogenerative cycles, because only a part of the working fluid is used as a thermal input for utilities, while the other part can continue its expansion for providing electricity.

On the other hand, an interesting application of multiple admissions is in geothermal power plants. It is well documented that binary geothermal power plants have the possibility to be developed as multipressure level cycle systems and for many geothermal resources; a system designed in this way can deliver a significant increase in the power output, in comparison to a single pressure level system (Di Pippo, 2005). These cycle configurations enable the recovery of heat from the geothermal source by vaporizing the organic fluid at multiple pressure and usually reduce both the thermal irreversibility associated with such heat exchange and increase the cycle efficiency. The concept recalls the combined cycles.

As represented in Figs. 11.18 and 11.19, a single pressure level cycle is intrinsically simpler and usually less expensive than a multipressure level system. However, the advantage in the efficiency offered by the latter gives a favorable payback, thus making it the preferred option in the geothermal field.

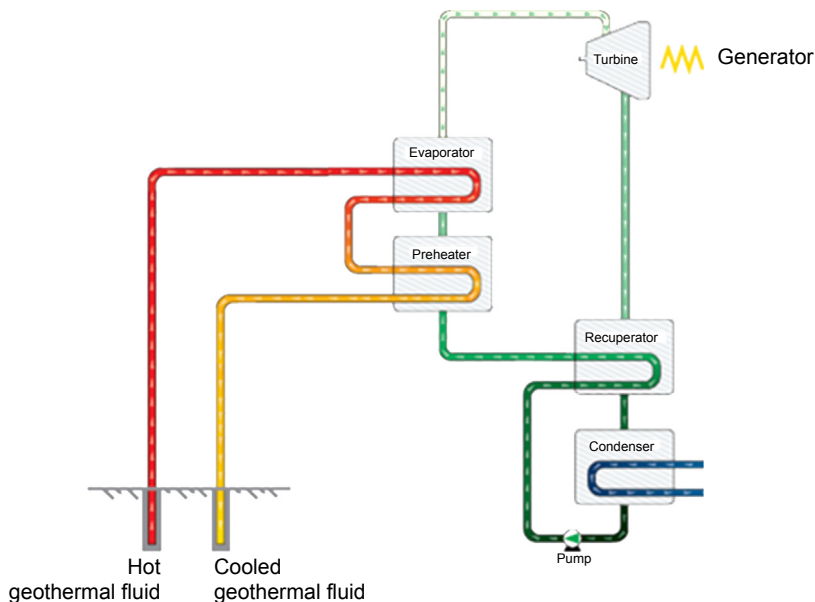


Figure 11.18 Process flow diagram of a regenerative 1 pressure level cycle.

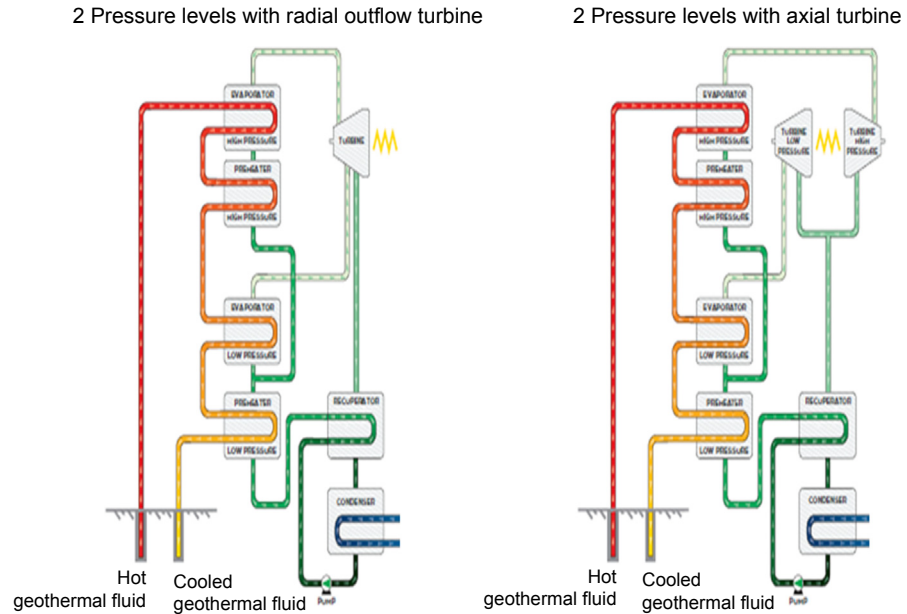


Figure 11.19 Process flow diagram of a regenerative 2 pressure level cycle.

Multipressure level geothermal binary systems require at least one turbine per pressure level to expand the organic vapor, and these turbines are normally installed with an overhung configuration (Di Pippo, 2005).

The ROT gives the possibility to employ a different solution.

In order to expand multipressure flows in the same axial turbine, it would be necessary to enlarge the space between the disks, allowing a second flow to be inserted to mix with the primary flow; the mixed flow would then expand in the remaining stages.

As a consequence, the shaft length of the axial turbine must increase, resulting in several rotor dynamic problems for the overhung configuration, as the distance between the center of gravity of the turbine disks and the bearings consequently increases. However, it does not appear possible to design such a turbine. Having a single-disk/single stage configuration, the radial inflow turbine does not allow multiple pressure entries.

A different scenario is instead provided by the ROT; its unique single-disk/multi-stage configuration makes it possible to enlarge the spacing between the stages (Figs 11.20 and 11.21), allowing a low pressure flow to enter the turbine, whilst still maintaining an overhung configuration without any negative rotor dynamic consequences.

The ROT can therefore allow multiple pressure levels cycles to be expanded over a single turbine.

The major advantages related to this configuration are the techno-economical savings associated with a lower number of turbines to be installed per plant. This minimizes the plant overall costs, and reduces the amount of rotating equipment, spare

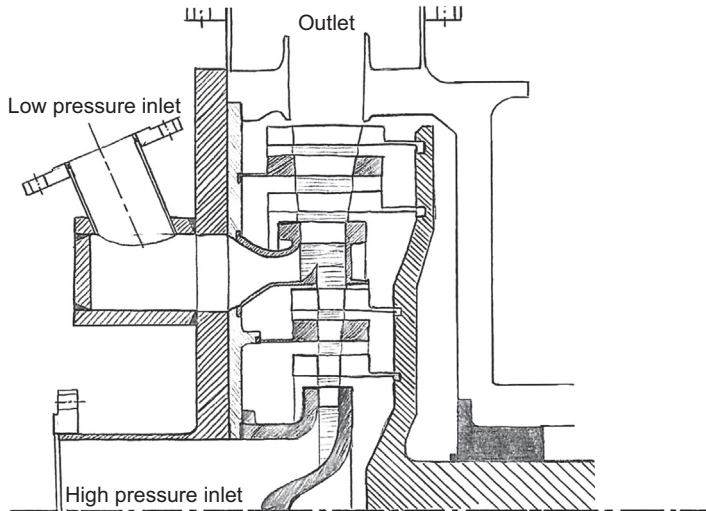


Figure 11.20 Schematic drawing of the multipressure radial outflow turbine.



Figure 11.21 Double pressure level radial outflow turbine.
Courtesy of Exergy.

parts and maintenance. Furthermore the plant layout is more compact, reducing the amount of foundations, control equipment, and control complexity.

11.5 Conclusion

At the operative conditions typical for ORCs, fluids with a high molecular weight lead to enthalpy drops, volumetric flows, and volumetric ratios significantly lower than steam; this makes possible to reconsider the ROT configuration for ORC applications where the intrinsic limits of this type of technology are no longer relevant.

If compared to traditional organic fluid turbines, meaning overhung axial turbines, the overhung ROT demonstrates several mechanical and fluid-dynamic differences hereby summarized.

The multistage radial outflow configuration in the ORC has the following features:

- Partial compensation of the requirement of increasing sections, caused by the volumetric flow increase during expansion of the fluid, thanks to the increasing radius, meaning higher blades in the first stages and lower blades in the last stages.
- Initial stages with better aspect ratio blading and no need for partial admission, leading to efficiency improvements.
- Blade section is constant and prismatic, as the peripheral speed is constant in the entire passage section.
- Grade of reaction is constant along the blade, thus it is possible to have all impulse stages, reducing mechanical stress on the last ones. This is not possible in axial turbines, especially in the last stages where the different speed between tip and hub rotor is huge and so it is not possible to avoid twisted blades with a strong variation of reaction degree along the blade height.
- Enthalpy drop is divided into several stages thus limiting the involved speeds, both absolute and relative. In comparison to the steam or gas turbine, ORC fluids are characterized by a low speed of sound; this fact limits the acceptable peripheral speed, to avoid shock waves losses.
- Radius and therefore has a good recovery of kinetic energy. Moreover the tangential velocity component can be recovered with good efficiency also in off design conditions.

Differently from the disk/diaphragm axial turbine, in an ROT, more than one rotor stage can be arranged on a single overhanging disk, providing some advantages:

- Better rotor dynamic thanks to the minor mass and to the reduced distance between the bearings and barycenter.
- Due to mechanical features it permits fast start up, and it is the best solution when this is mandatory, for example in CSP plants without large thermal energy storage.
- Smaller shaft section.
- Single coupling between disk and shaft.
- Simpler dynamic balance.
- Minor static and dynamic load on the bearings.
- Strain on shaft seal sizing is lower, leading to a longer life of the component.

References

- Angelino, G., Gaia, M., Macchi, E., 1984. A review of Italian activity in the field of organic Rankine cycles. In: Proc. of the International VDI-seminar Held in Zurich, 10–12 September 1984. VDI Berichte 539, VDI Verlag, Dusseldorf.
- Angelino, G., Invernizzi, C., August 1993. Cyclic methylsiloxanes as working fluids for space power cycles. *Journal of Solar Energy Engineering*, Transactions of the ASME 115/135.
- Ainley, D.G., Mathieson, G.C.R., 1951. A Method of Performance Estimation for Axial-Flow Turbines. R&M 2974, Aeronautical Research Council, London.
- Bini, R., Duvia, A., 2008. Apparatus for Generating Electric Energy Using High Temperature Fumes. European patent application n. EP 1 998 013 A2.

- Colonna, P., Rebay, S., Harinck, J., Guardone, A., 2006. Real-gas effects in ORC turbine flow simulations: influence of thermodynamic models on flow fields and performance parameters. In: European Conference on Computational Fluid Dynamics, ECCOMAS CFD 2006.
- Daily, J.W., Nece, R.E., March 1960. Chamber dimension effects on induced flow and frictional resistance of enclosed rotating disk. *Transactions of the ASME, Journal of Basic Engineering* 217–232.
- Di Pippo, R., 2005. *Geothermal Power Plants: Principles, Applications and Case Studies*. Elsevier.
- Dixon, S.L., 1998. *Fluid Mechanics and Thermodynamics of Machinery*. Elsevier.
- Dunham, J., Came, P.M., July 1970. Improvements to the Ainley-Mathieson method of turbine performance prediction. *Transactions of the ASME, Journal of Engineering for Power* 252–256.
- Egli, A., 1935. The leakage of steam through labyrinth glands. *Transactions of the ASME* 57, 115–122.
- Frassinetti, M., Rizzi, D., Serafino, A., Centemeri, L., Spadacini, C., 2013. Operational results of the world's first orc radial outflow turbine, and its future development. In: Proc. of 2nd Int. Sem. on ORC Power Systems, October, Rotterdam.
- Horlock, J.H., 1966. *Axial-Flow Turbines*. Butterworths, London.
- Kacker, S.C., Okapuu, U., 1981. A Mean Line Prediction Method for Axial Flow Turbine Efficiency. Paper No. 81-GT-58. ASME, New York.
- Macchi, E., 2013. The choice of working fluid: the most important step for a successful organic Rankine cycle (and an efficient turbine). In: Proc. of 2nd Int. Sem. on ORC Power Systems, October, Rotterdam.
- Meher-Homji, C.B., 2000. The historical evolution of turbomachinery. In: Proc. of the 29th Turbomachinery Symposium, September, Houston (TX).
- Moustapha, H., Zelesky, M.F., Baines, N.C., Japiske, D., 2003. *Axial and Radial Turbines. Concepts ETI*.
- NIST, 2013. Reference Fluid Thermodynamic and Transport Properties—REFPROP Version 9.1.
- Poling, B.E., Prausnitz, J.M., O'Connell, J.P., 2000. *The Properties of Gas and Liquids*. McGraw-Hill.
- Salucci, B., Centemeri, L., Caniato, G., 1983. Bench testing of a 500 kW organic Rankine cycle plant. In: Proc. of the Third International Seminar on the Results of EC Geothermal Energy Research, November, Munich.
- Smith, M.H., 1965. A simple correlation of turbine efficiency. *Journal of Royal Aeronautical Society* 69, 467.
- Spadacini, C., Centemeri, L., Xodo, L.G., Astolfi, M., Romano, M.C., Macchi, E., 2011. A new configuration for organic Rankine cycle power systems. In: Proc. of 1st Int. Sem. on ORC Power Systems, September, Delft.
- Spadacini, C., Rizzi, D., Saccilotto, C., Salgarollo, S., Centemeri, L., 2013. The radial outflow turbine technology: impact on the cycle thermodynamics and machinery fluid- and rotor-dynamic features. In: Proc. of 2nd Int. Sem. on ORC Power Systems, October, Rotterdam.
- Stodola, A., Lowenstein, L.C., 1927. *Steam and Gas Turbines*. McGraw-Hill, New York.
- Traupel, W., 1966. *Thermische Turbomaschinen*. Springer-Verlag, Berlin.

Positive displacement expanders for Organic Rankine Cycle systems

12

V. Lemort, A. Legros

University of Liège, Liège, Belgium

12.1 General introduction

The expansion machine is one of the four main components of an Organic Rankine Cycle (ORC) system. The expander performance largely influences that of the whole system. Moreover, the expander is a crucial component for the control of the ORC system. The purpose of the present chapter is to understand the principle of operation of major technologies of displacement expanders, to list their technical limitations, to introduce performance indicators, and to understand the interaction between the ORC system and the expander.

12.1.1 Definition

A positive displacement (or “volumetric”) expander is an expansion machine in which the working fluid pressure is decreased by increasing its volume.

The displacement expander usually comprises a stator and one or several rotors connected to the expander shaft. Their relative position, which varies with the shaft rotating angle, defines a series of working chambers in which the fluid is trapped. The high-pressure fluid forces the rotors to move and a moving boundary work is done by the fluid on the rotors. The volume of the working chambers increases and the fluid pressure decreases. Energy transferred, under the form of mechanical work, results in a decrease of the fluid energy. The movement of the rotors is usually transformed into a rotating movement of a shaft so that shaft work can be recovered.

It seems that the growing interest in positive displacement expanders is following that in ORC systems. The technical maturity and the market of displacement expanders in ORC systems is nothing compared with displacement compressors used in HVAC&R (Heating, Ventilation, Air-Conditioning and Refrigeration) and the compressed air industry. Even if some technologies of large-scale displacement expanders have been developed and commercialized for decades, there are still intense research and development activities conducted to develop displacement expanders that meet the requirements of ORC systems. Positive displacement expanders typically equip ORC systems with power lower than 150 kWe (see Fig. 12.18).

12.1.2 Major differences among positive displacement expanders

Positive displacement expanders differ by the technology of stator and rotors and hence the type of mechanism used to create the variation of the volume of the working chambers and the timing of suction, expansion, and discharge phases. Major technologies of positive displacement expanders are the piston, the twin-screw, the scroll, the vane, and the roots expanders. However, many other designs have been imagined and patented for the last two centuries. Also each technology gathers a large number of variants.

Major technologies of expanders will be described in [section 12.2](#). However, at this stage, the major distinctions among technologies will be listed.

12.1.2.1 Type of motion of moving elements

The first distinction among displacement machines concerns the type of motion of the moving elements, i.e. the rotors. As shown in [Fig. 12.1](#), there exist three main types of motion: reciprocating, orbital, and rotary motions. Each type of motion is associated with different technologies of expanders.

12.1.2.2 Internal expansion

Most of the expander technologies usually exhibit a built-in volume ratio and thus comprise an internal expansion phase (“expansive machines”). In contrast, the roots expander does not allow for the internal expansion of the working fluid (“nonexpansive machine”). At the end of the suction process, the high-pressure chamber is immediately put into communication with the low-pressure side of the machine. That will be illustrated later in [Fig. 12.11](#).

12.1.2.3 Presence of valves

The timing of suction, expansion, and discharge can be imposed either by valves (such as in piston expanders) or by the geometry of the machine itself (vane, scroll, screw,

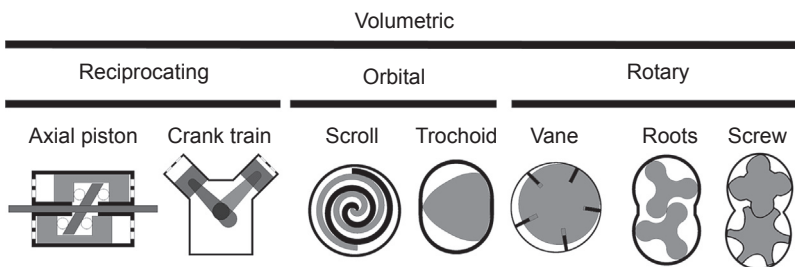


Figure 12.1 Classification of positive displacement expanders according to the type of motion of the rotors.

and roots). Valves can also be used to control the displacement of the machine or its built-in volume ratio (for instance, in screw machines). The absence of valves simplifies the design and increases the reliability of the machine. The absence of supply and exhaust valves also eases the inversion of the machine from the compressor mode to the expander mode.

12.1.2.4 Open-drive versus semi-hermetic and hermetic machines

In an open-drive machine, the expander shaft goes through the casing (by means of adequate seals). Since the expander shaft is apparent, it can be connected by the user either to a generator or to a device supplied by mechanical power.

In a hermetic machine, a tight envelope permanently encloses the expander and the electrical generator. No access to the expander shaft is made possible. The machine power output is electrical. The cooling of the generator is ensured by the working fluid.

In a semi-hermetic machine, the bolted envelope can be opened for servicing the elements it comprises.

12.1.2.5 Oil-lubricated versus oil-free

The design of the expander can prevent any contact between the moving elements delimiting the chambers that contain the working fluid. This is the case for some scroll and screw expanders (synchronized machines). The absence of contact allows for oil-free operation, which is beneficial for the overall Rankine cycle system, but usually a penalty for the expander itself (oil tends to seal the leakage paths). In such oil-free machines, the bearings are generally lubricated by grease.

The contact between moving elements requires lubrication, which can be solid or liquid. The latter mode of lubrication is the most common and usually relies on oil. Solid lubrication can be ensured by adequate materials.

Oil can circulate with the working fluid through the entire ORC system or be separated and driven back to the expander supply by means of an external circuit. The oil separator at the outlet of the expander can be bulky and not adapted for some applications, such as mobile ones, where compactness is an issue.

12.2 Description of major types of displacement expanders

There exists a large panel of positive displacement expanders. Some existing but less known concepts are sometimes revived, while new concepts are still proposed. Among all of the concepts, the most popular ones are the piston, the scroll, the twin-screw, and the vane expanders. These concepts are described in [section 12.2](#). Less common technologies are also briefly mentioned, such as the roots and the single-screw expanders.

12.2.1 Piston expanders

12.2.1.1 Principle of operation

A reciprocating expander, or piston expander, is made up of one or several cylinders in which pistons move in a reciprocating fashion from the Top Dead Center (TDC) to the Bottom Dead Center (BDC). Fluid enters and leaves the cylinder through orifices equipped with valves. Fig. 12.2 displays the machine diagram and the associated pressure-volume diagram (“indicator diagram”) for two typical designs of machine. The indicator diagram has been idealized in order to only account for the under-compression/expansion and over-compression/expansion losses described hereunder (such a diagram is often called a “theoretical” or “hypothetical” indicator diagram). In the machine diagram, “suc” and “dis” respectively indicate the suction and discharge orifices.

At position 1, the cylinder volume is minimal and equal to the clearance volume V_0 . The piston starts its downward stroke (it moves from the TDC towards the BDC). Since the supply port is open, the fluid at the supply pressure (in the absence of pressure losses through the port) enters the cylinder. The admission process (1 to 2) extends during a fraction of the stroke, also called the cut-off or length of admission.

In position 2, the cylinder volume is equal to Volume Inlet Closing V_{IC} . In this position, the supply valve closes. The increase of volume from position 1 to 2 is equal to the expander displacement V_s . From position 2, the mass of fluid trapped inside the cylinder behaves as a closed system (in the absence of internal leakage flows) and the expansion phase starts. As the piston keeps on moving towards position 3, the fluid pressure decreases from the supply pressure P_{su} to the pressure at the end of the expansion $P_{in,expan}$. In position 3, the exhaust port opens and the discharge process is initiated. The distance travelled by the piston from the TDC to the BDC is the stroke S . The associated increase of volume is the stroke displacement or “maximal” displacement $V_{s,max}$.

Similarly to other displacement machines, according to the expansion built-in volume ratio and the pressure at the exhaust of the expander, three situations may occur: either the pressure at the end of the expansion $P_{in,expan}$ is higher than the pressure P_{ex} in the exhaust pipe (under-expansion), or it is equal, or it is lower (over-expansion). The expansion built-in volume ratio is defined as the ratio between the volume at the end of the expansion process and the volume at the end of the suction process:

$$\begin{aligned}
 r_{v,in,expan} &= \frac{V_3}{V_2} \\
 &= \frac{V_c}{V_{IC}} \text{ (crossflow)} \quad \text{or} \quad \frac{V_{EC}}{V_{IC}} \text{ (uniflow)}
 \end{aligned} \tag{12.1}$$

In the case of under-expansion, some fluid leaves the machine to decrease the pressure down to the exhaust pressure (evolution 3 to 4 in Fig. 12.2 left and evolution 3 to 5 in Fig. 12.2 right). In Fig. 12.2 left, the piston has just reached the BDC and starts to move upward. The fluid remaining inside the cylinder is pushed out of the machine

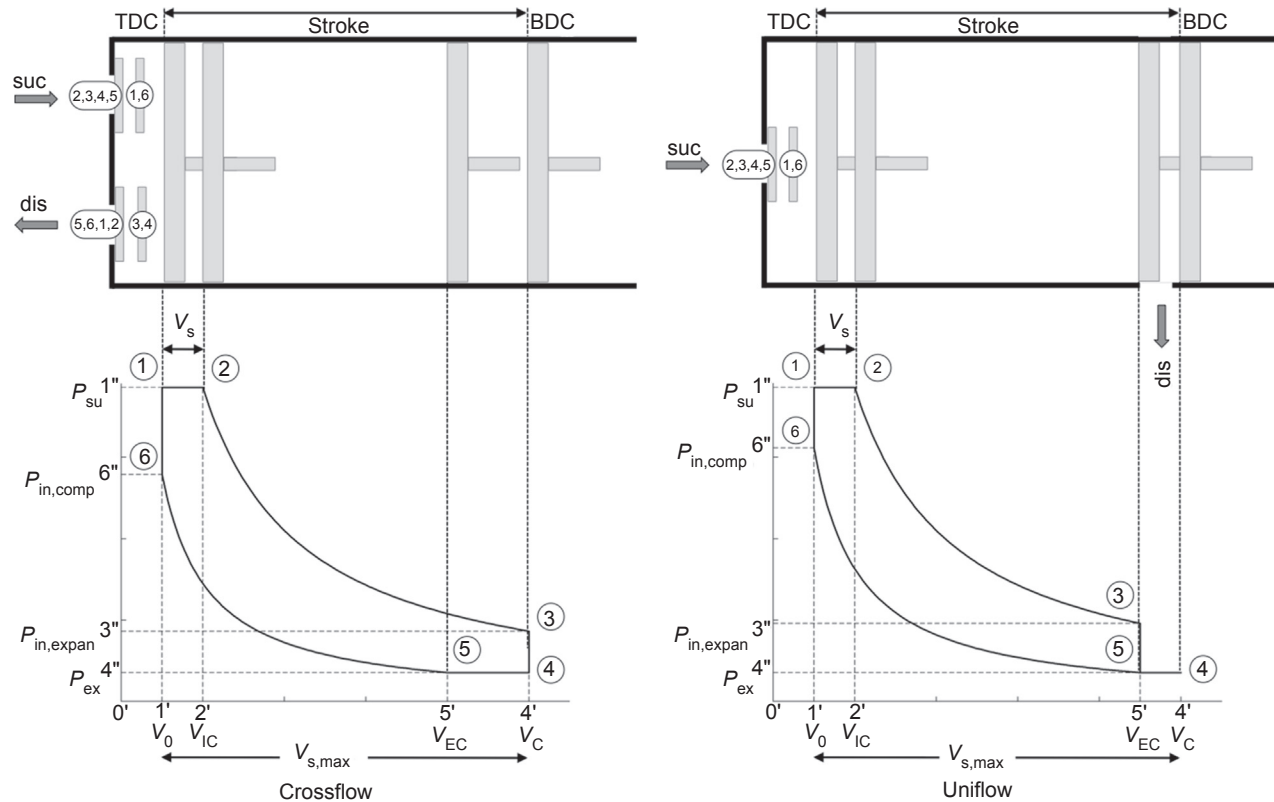


Figure 12.2 Machine diagram and associated indicator diagram of crossflow (left) and uniflow (right) piston expanders. *TDC*, Top Dead Center; *BDC*, Bottom Dead Center.

from 4 to 5. In Fig. 12.2 right, the piston continues its descent towards BDC (position 4) and moves again towards TDC from 4 to 5.

From position 5 (volume V_{EC}), the mass trapped inside the cylinder behaves again as a closed system and as the piston continues its upward movement towards the TDC, the pressure is increased from P_{ex} up to $P_{in,comp}$ (evolution 5 to 6). Similarly to the expansion process, the pressure $P_{in,comp}$ at the end of the compression process can be lower, equal, or higher than the supply pressure (Fig. 12.3). The compression built-in volume ratio is here defined as the ratio between the volume at the beginning of the compression process and the volume at the beginning of the suction process (clearance volume).

$$r_{v,in,comp} = \frac{V_5}{V_6} = \frac{V_{EC}}{V_0} \quad (12.2)$$

In some machines, the suction process starts before the piston has reached the TDC. For instance, Oudkerk et al. (2015) tested a machine with symmetrical supply port opening and closing timings with respect to the TDC.

In the case of under-compression, when the inlet valve opens (position 6), fluid enters into the cylinder yielding an increase of the pressure up to the supply pressure (evolution 6 to 1). In the case of over-compression, some fluid leaves the cylinder until the cylinder pressure and the supply pressure equalize.

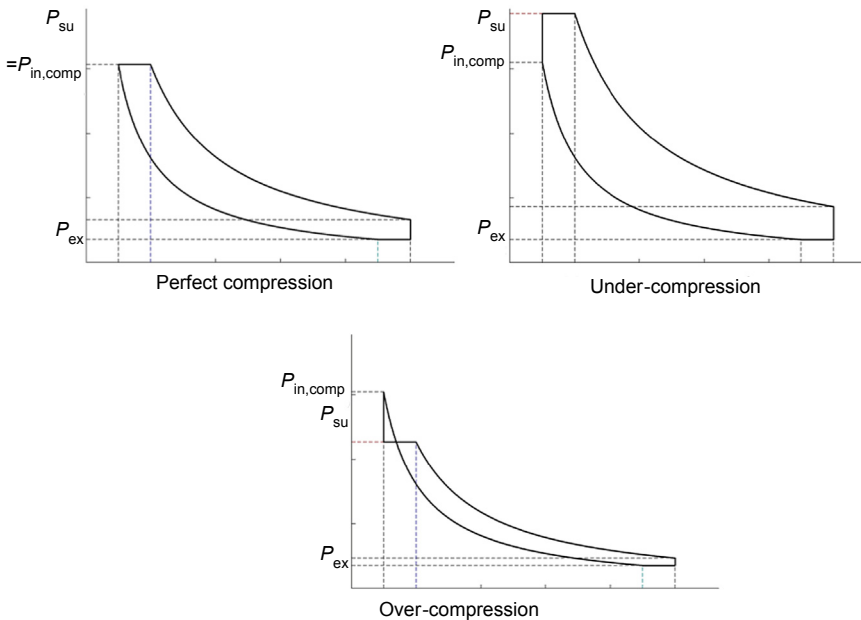


Figure 12.3 Theoretical indicator diagram of a piston expander. Illustration of perfect compression, under-compression, and over-compression losses.

12.2.1.2 Mechanical aspects

Main types of valves used in piston expanders are poppet valves, sleeve valves, and rotary valves. Both supply and exhaust valves can be actuated in order to control the volume at the end of the supply process (V_{IC}) and at the end of the discharge process (V_{EC}). Another simple and reliable mechanism for controlling the length of admission or “cut-off” (i.e., the expander displacement) consists of using two poppet valves in series and adjusting the time of opening overlap (Syniuta and Palmer, 1974; Demler, 1976).

Piston expanders can also be characterized by the fluid flow configuration inside the cylinder. In uniflow expanders (illustrated in Fig. 12.2 right), the supply port is located close to the cylinder head while the exhaust port is located at the opposite cylinder extremity and usually consists of an opening on the cylinder wall covered or uncovered by the piston. As shown in Fig. 12.2 right, from position 5 (after the equalization of pressures), the piston continues its downward movement until reaching the BDC (position 4). The upstroke starts then and the piston moves towards position 5, from which the exhaust ports are covered again. In crossflow expanders both the supply and exhaust ports are located on/close to the cylinder head (Fig. 12.2 left). Multiflow expanders are based on a combination of the two previous configurations: the exhaust ports can be located at both extremities of the cylinder (Daccord et al., 2013).

The uniflow configuration presents some advantages. The supply and exhaust processes being spatially dissociated, the cylinder head is not cooled down during the exhaust process, which results in less cooling down of the working fluid during the suction process and less risk of fluid condensation (Plattel, 1993). Also the uniflow configuration tends to simplify the design of the expander because of the use of exhaust port openings instead of actuated valves. In uniflow expanders, the compression phase starts earlier during the upward stroke resulting in a higher compression work. Such machines are generally characterized by a higher clearance volume in order to prevent over-compression (Daccord et al., 2013). Over-compression can also be prevented by the use of relief valves (Jakuba and McGeehan, 1975). The crossflow configuration yields a lower compression work. As a consequence, for the same stroke and expander (cut-off) displacements, the machine produces a larger power than uniflow expanders (Syniuta and Palmer, 1974). However, theoretical isentropic effectiveness of the machine is lower because of the larger under-compression loss. The mass flow rate admitted by the machine is also larger because of the wider gap between the pressure at the end of the compression and the supply pressure. Note that the indicator diagram displayed in Fig. 12.2 right could also be obtained with a crossflow expander provided that the timing of the exhaust valve was symmetrical about BDC (Demler, 1976).

There are two main families of mechanisms used to transform the rotating shaft motion into a reciprocating piston motion: crank train and swash/wobble plate mechanisms. The crank train mechanism, used in radial piston expanders, is similar to the mechanism used in internal combustion engines and relies on the use of a crankshaft connected to pistons (Fig. 12.4). This type of mechanism leads to bulkier machines than axial-type machines.

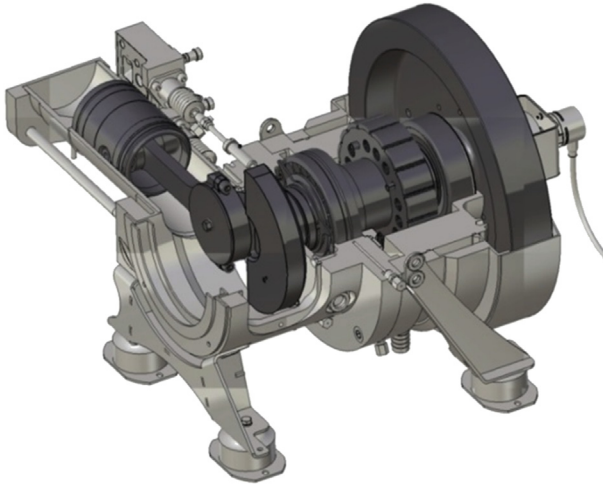


Figure 12.4 View of a crank train piston expander (Daccord et al., 2013).

The swash and wobble plate mechanisms are used in axial piston expanders (Fig. 12.5). In such expanders, several pistons are parallel to the machine shaft. The pistons' rods are connected to a plate that is tilted with respect to the expander shaft. Since the plate is attached to the shaft, the rotation of the latter yields a reciprocating motion of the pistons. If the piston rods are rigidly connected to the plate, the piston head must rotate. This is not the case for swash plate and wobble plate axial piston expanders. In the former case, the extremities of the piston rods are sliding on the rotating plate. In the latter case, these extremities are connected with ball joints to a wobbling plate. The wobbling of the latter plate can be created by using, for instance, a plate rotating with the shaft and bearings between both plates to allow for their relative



Figure 12.5 View of a double-acting axial piston expander.

Reproduced with permission of Daccord, R., Sager M., A piston expander for exhaust heat recovery on heavy commercial vehicles. In: Presentation given at the 2nd Automotive ORC Consortium Workshop, Denver, November 19 and 20, 2015.

motion (Grip, 2009). Axial piston expanders, which are similar to mobile air conditioning piston compressors, are more compact than expanders with crank train mechanisms. For this reason, they present a large interest for ORCs used for waste heat recovery from cars and trucks engines. In a similar way to what is done in mobile air conditioning compressors, the tilt angle could be adjusted in order to modify the piston stroke and hence the expander displacement.

12.2.1.3 Technical limitations

In theory, piston expanders could cover a range of displacements similar to what is achieved in internal combustion engines. In practice, displaced volume flow rates for ORC applications currently range from approximately 1.25 to 75 l/s.

Piston expanders can typically operate under high supply pressures and temperatures. For instance, Seher et al. (2012) reported tests conducted on a single-cylinder double-acting oil-free piston expander supplied by steam at 32 bar/380°C and producing 14 kW. A single-cylinder piston expander fed by steam at 36 bar/350°C was also tested by Daccord et al. (2013) and produced around 2.5 kW.

Piston expanders are characterized by large built-in volume ratios (values up to 15 can typically be met on the market). Hence they can perform efficiently under large pressure ratios. For instance, Daccord et al. (2013) reported the operation of an axial piston expander under a pressure ratio of 50. Usually, design considerations indicate that it is not worth increasing the volume ratio too much, since the additional work produced becomes of the same order of magnitude than the additional mechanical losses.

12.2.2 Scroll expanders

12.2.2.1 Principle of operation

Scroll expanders belong to the family of orbiting machines. They are composed of two involutes, one being the central symmetry of the other. Generally, one involute is fixed while the other one shows an orbiting movement. Their relative position defines a series of chambers, most of them having a crescent-shape layout (Fig. 12.6). These chambers act as suction, expansion or discharge chambers.

Fig. 12.6 displays the evolution of the fluid inside the machine and Fig. 12.7 the associated theoretical indicator diagram. In position 1, the suction chamber located in the center of the machine and in communication with the supply port is at its minimal volume (“clearance volume”). From this position, its volume increases

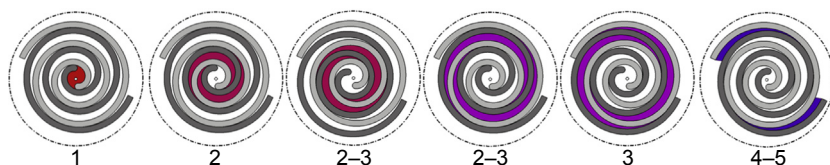


Figure 12.6 Principle of operation of a scroll expander.

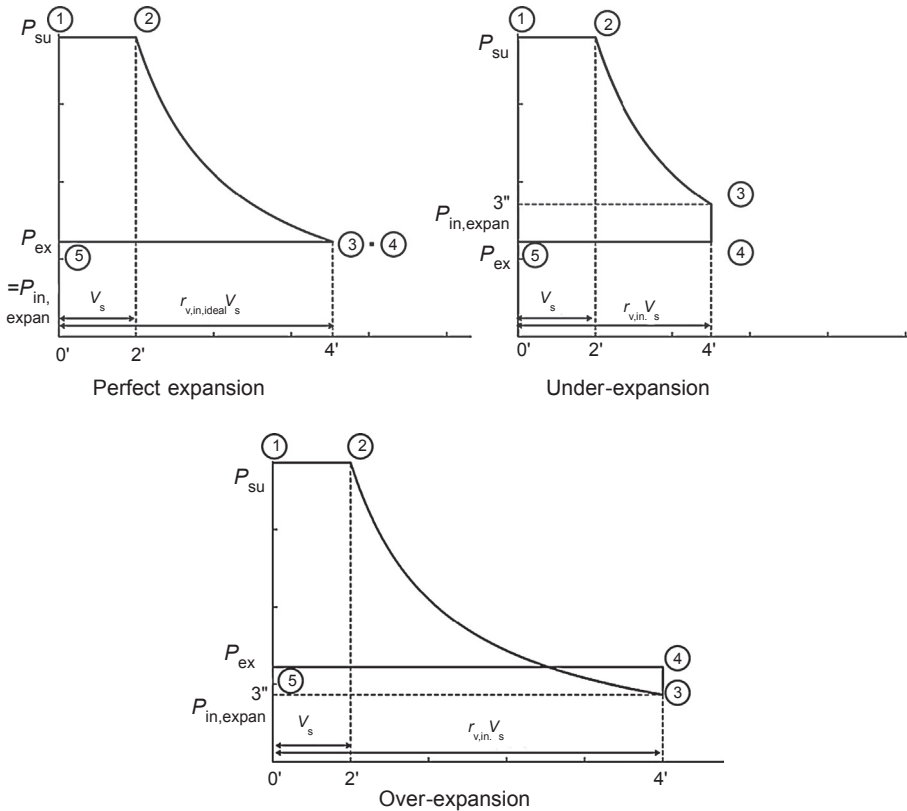


Figure 12.7 Theoretical indicator diagram of a scroll expander. Illustration of under-expansion and over-expansion losses.

over one entire shaft revolution (evolution 1 to 2). The fluid at the supply pressure fills the chamber through the supply port.

In position 2, the suction chamber divides itself into three chambers. Two of them become expansion chambers and form two different expansion paths. The third one forms the new suction chamber whose volume is the clearance volume. This clearance volume is not represented in Fig. 12.7. Since the fluid pressure inside the clearance volume is equal to the supply pressure, this clearance volume does not impact the machine performance. The pair of expansion chambers exists for at least a fraction of one full revolution but it can also take several turns to disappear. The number of full revolutions during which the pair of expansion chambers exists is closely related to the built-in volume ratio of the machine. As shown in Fig. 12.6, several pairs of expansion chambers can simultaneously exist. During their existence, the volume of the expansion chambers increases (evolution 2 to 3), so that the fluid pressure decreases from P_{su} to $P_{in,expan}$.

At the end of the expansion process the expansion chambers become the discharge chambers. This happens when the expansion chambers open up to the exhaust line

(position 3). Similarly to the piston expander, the pressure at the end of the expansion process is either equal (perfect expansion), higher (under-expansion), or lower (over-expansion) than the exhaust pressure. In the two latter cases, some fluid has to leave or enter the machine to equalize the pressure (evolution 3 to 4). The associated irreversibility decreases the isentropic effectiveness of the machine.

For a last full shaft revolution, the volume of the discharge chambers will slightly increase first and finally decrease towards zero. The fluid, at the exhaust pressure (in the absence of pressure losses), is expelled inside the carter of the machine and exits through the exhaust port (evolution 4 to 5).

12.2.2.2 *Mechanical aspects*

The expansion of the fluid drives the moving involute. However, the motion is not circular but it is actually orbital. To prevent the rotational movement of the moving involute and to convert this orbiting movement into a rotating shaft movement, anti-rotation mechanisms must therefore be used and associated with an eccentric shaft. Anti-rotation mechanisms exist in various ways and are adapted to different kinds of scroll machines. In refrigeration scroll machines, an Oldham ring is often used. However when compactness and high speed are required, the Oldham ring is not good enough and eccentric ball thrust bearings are used. A third mechanism is also used in scroll machines; it consists of three additional shafts that guide the mobile involute.

Scroll expanders can be compliant or kinematically rigid. Compliance allows for a degree of freedom in a given direction. This degree of freedom can be along the radial or axial direction, or even both. Such a mechanism allows the scroll expander to adapt itself to the operating conditions, leading to an increased efficiency. Kinematically rigid expanders cannot adapt when transient conditions happen, especially in the presence of liquid fluid or debris, which can cause damage when they are trapped between the involutes.

Finally, scroll machines are highly reliable components due to a very low number of moving elements. Maintenance is also rather low. Some scroll machines may need a tip seal (whose mechanism is explained in [section 12.3.1.1](#)) replacement but most of the time, the machine is designed to require no maintenance at all.

12.2.2.3 *Technical limitations*

Scroll expander major limitation is the maximal fluid temperature allowed at the expander supply. Currently, high temperature scroll expanders work with temperatures up to approximately 215°C ([Lemort et al., 2006](#)). Approximately the same limit is also found on the exhaust temperature of open-drive air scroll compressors. Operation at high temperature leads to high thermal expansion, increasing the internal leakage of the machine. The seal material must also endure such temperature levels and therefore requires proper selection.

Pressure does not appear to be a limiting factor. However, increased pressure leads to higher loads on the bearings of the machine. HVAC&R scroll compressors typically operate with pressure ratios up to 11. Larger pressure ratios yield low performance

because of under-compression losses. A pressure ratio of 15 in expander mode has been reported in the literature (Lemort et al., 2006).

Scroll machine maximal speed is roughly 10,000 rpm continuous and 12,000 rpm at peak. This maximal speed is, among other things, limited by the anti-rotation mechanism. Such a limit is typically found with automotive air-conditioning scroll compressors.

There exist scroll expanders on the market with displacements varying approximately from 12 cm³ up to 73 cm³. HVAC&R scroll compressors available on the market show displacements ranging commonly from 3 to 850 cm³, with built-in volume ratios close to 3, which means expander displacements ranging approximately from 1 cm³ to 283 cm³. The current trend in the HVAC&R industry is to increase the compressor displacement leading to a competition between screw and scroll machines.

HVAC&R scroll compressors built-in volume ratio ranges from 1.5 to 3.5, whereas higher volume ratios are met in air compressors (up to 4). Scroll expanders usually have moderate built-in volume ratios, between 3.5 and 5. Scroll expanders are therefore more dedicated to organic fluids than to water. Scroll expanders may achieve higher volume ratios if they are comprised of variable wall thickness involutes. No commercial machines already exist, but studies have been published regarding prototypes. A means of increasing the volume ratio also consists in associating two expanders in series (Kane et al., 2009).

Finally, this type of expander can work with wet expansion, especially if the scroll is compliant.

12.2.3 Twin-screw expanders

Currently, most of the screw expanders are twin-screw machines. Scientific and technical literature also mentions the use of single-screw expanders but to a lesser extent.

12.2.3.1 Principle of operation

A twin-screw expander is made up of two intermeshing helically toothed rotors (the male and the female rotors) housed in a casing. The rotors and the casing delimit a series of working chambers that evolve from one extremity of the rotors

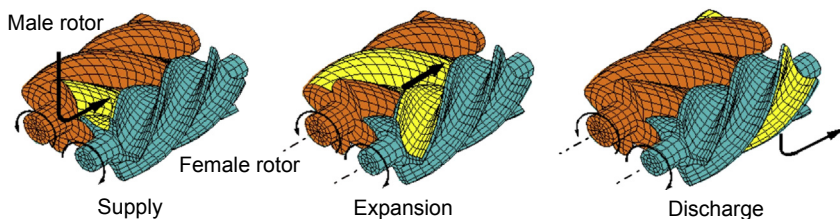


Figure 12.8 Principle of operation of a twin-screw expander. Reproduced with permission of A. Brümmer (2011).

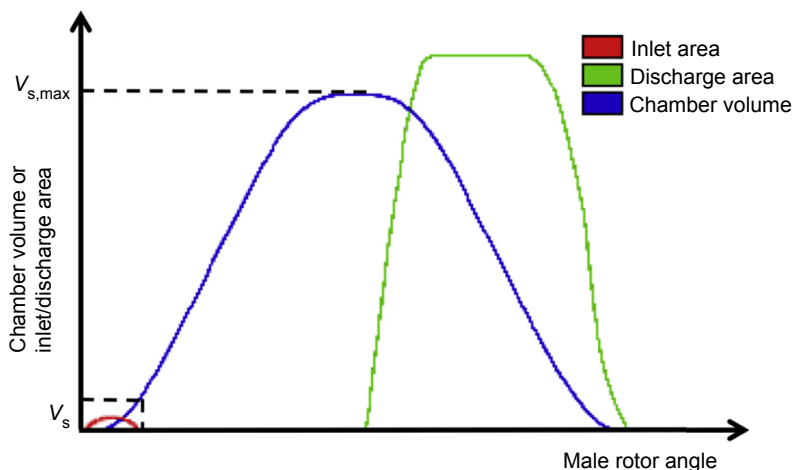


Figure 12.9 Variation of the chamber volume with the shaft rotation angle.

Adapted from Brümmer, A., 2012. Energy efficiency – waste heat utilization with screw expanders. Pumps, Compressors and Process Components.

to the other one (Fig. 12.8). The casing comprises a suction port and a discharge port, located at both extremities of the rotors. The location and the shape of the two ports allow for the communication of the chambers with the supply and the discharge lines respectively. The same chamber becomes, successively, a suction chamber, an expansion chamber, and finally a discharge chamber. Fig. 12.9 provides the evolution of the chamber volume with the machine rotating angle. The limitations of the supply and exhaust ports on the casing are named the high-pressure control edge and the low-pressure control edge respectively (Brümmer, 2012). At the initial angular position of the machine shaft, the chamber volume is equal to zero. A screw expander presents no clearance volume. As the male rotor rotates, the volume of the chamber increases until reaching a maximum value and then decreases towards zero.

The supply port allows for the filling of the chamber with the high-pressure fluid during a fraction of the ascending part of the curve in Fig. 12.9 (delimited by the supply control edge). This fraction depends on the size and shape of the supply port. Expansion starts as soon as the chamber is not in communication with the supply port. The chamber reaches the discharge port as soon as its volume is at its maximum. In this shaft angle position, the exhaust control edge is reached. The volume then decreases until the chamber disappears. The discharge process extends over the entire descending portion of the curve in Fig. 12.9.

The built-in volume ratio is equal to the ratio between the maximum volume $V_{s,max}$ and the expander swept volume V_s . The volume ratio is not a function of the geometry of the rotors. It depends on the angular position of the high-pressure control edge. The lower the angular position of the control edge the larger the built-in volume ratio and the smaller the swept volume. Hence, for given rotor dimensions, a compromise has to be found between increasing the swept volume

and the built-in volume ratio. A similar compromise has to be found when selecting the cut-off ratio in piston expanders.

12.2.3.2 Mechanical aspects

There are two types of twin-screw expanders: synchronized (oil-free) and unsynchronized (oil flooded) machines. In unsynchronized machines, there is a hydrodynamic contact between the male and the female rotors. This hydrodynamic contact is ensured by lubricating oil. The presence of oil imposes a limit on the machine circumferential speed and hence on the hydrodynamic losses. In contrary, in synchronized machines, external timing gears prevent any contact between the rotors. As a consequence, the machine can be run without oil. The absence of a liquid phase in the working chambers yields larger internal leakage flows. The relative impact of these internal leakage flows can be reduced by increasing the rotor's circumferential speed u (tip speed).

12.2.3.3 Technical limitations

Since twin-screw expanders comprise purely rotating components, high rotational speed can be achieved. Ng et al. (1990) reported an achieved rotational speed of 21,000 rpm.

There is little published information about the range of capacity of twin-screw expanders. However, according to Stosic et al. (2011), compressors can deliver between 10 l/s and 10,000 l/s of compressed gas. With future improvement in machining, smaller clearance between screw components could be achieved leading to smaller capacity screw expanders.

Screw expanders typically show maximum built-in volume ratios of 5. However, the literature reports a volume ratio of 8 (Brümmer, 2012).

12.2.4 Vane expanders

A vane expander consists in a cylindrical housing (stator) in which a cylindrical rotor is in motion. The rotor is offset from the center of the housing as seen in Fig. 12.10. Slots are spread out all over the rotor and allow the insertion of vanes that are pushed out by a spring or similar mechanisms. The vanes are pressed against the housing and define chambers. The chamber in communication with the admission port is referred to as the suction chamber. When that chamber is no longer in contact with the suction port, the expansion process begins, and ends when the chamber faces the exhaust port, becoming then a discharge chamber.

12.2.4.1 Mechanical aspects

The vane expander is a relatively simple machine. The most complex part is the vane mechanism. Several publications have been written about the dynamics of those vanes, studying the impact of the mechanisms that press the vane against the housing. Two mechanisms exist: the vane position is maintained either by a spring or by the working fluid pressure. Spring-assisted vane expanders show better volumetric performance because the vane is always pushed against the housing but the friction losses are higher

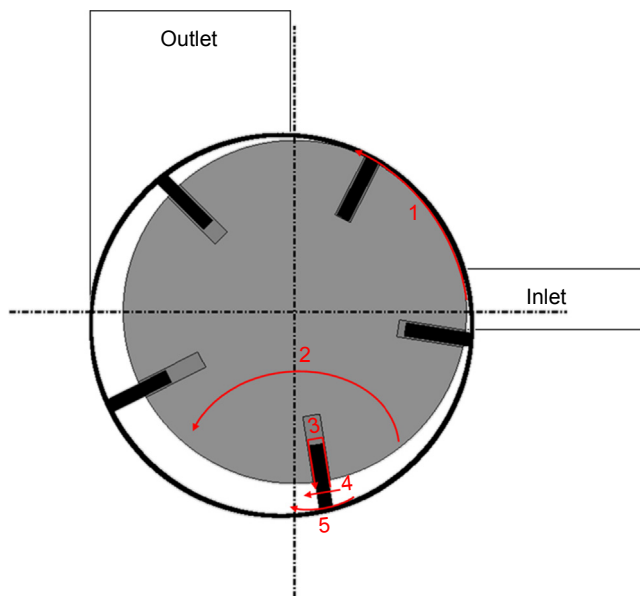


Figure 12.10 Representation of a 5-vane expander and indication of the leakage paths. (1) rotor-housing gap; (2) rotor-end plate gap; (3) vane groove gap; (4) vane-end plate gap; and (5) vane-housing gap.

than in the pressure-assisted expander. Therefore, the latter mechanism achieves better isentropic effectiveness (Jia et al., 2011).

12.2.4.2 Technical limitation

Similarly to most volumetric expanders, vane machines are often limited in temperatures. Thermal expansion becomes predominant and friction in the vanes increases significantly and may lead to a lock up of the vane, which most of the time ends with its destruction. This limit in temperature results in a limit in the pressure ratio. According to the literature, pressure ratio can vary from 3 to 7. Temperature limits are not so often reported in literature. However, Badr et al. (1985) report a maximal allowable operating temperature of 140°C.

Vane expanders have been studied since the 1970s and their displacements vary from 3 to 40 cm³ with a maximal rotational speed of 4000 rpm (Badr et al., 1985). Due to the high inertia brought by the offset of the rotor, vane expanders are usually limited to small to medium rotational speeds.

The volume ratio can be adapted by modifying the geometry of the machine. Reducing the periods of time of communication with the supply and exhaust ports will affect the volume ratio. However, in practice, the diameters of the intake and discharge pipes result from a pressure drop consideration. An increase in the number of vanes results in an increase in the volume ratio, but that number is closely related to the rotor size and mechanical strength. Also friction losses tend to increase with the

number of vanes. Built-in volume ratios encountered in practice are in the range of 2–8.5 (Badr et al., 1985).

12.2.5 Other machines

The expanders presented in sections 12.2.1 through 12.2.4 do not constitute an exhaustive list of all expander technologies. Some other technologies may be interesting for ORC systems, but their use is scarcer than for the previous ones. This section provides a brief introduction to those other expanders.

12.2.5.1 Roots expanders

Roots expanders are not frequently encountered. Technical and scientific literature about those machines is scarce. Roots expanders are very similar in shape to a screw expander. They consist of two meshing male rotors similar to a twin-screw expander. The rotor can be twisted along the axial direction or not. Roots expanders differ from twin-screw expanders mainly by their built-in volume ratio, which is equal to 1. This leads to a rectangular indicator diagram, as presented in Fig. 12.11.

The fluid entering the machine is trapped in a suction chamber comprised between the housing and the rotors. When the chamber comes into contact with the exhaust port, the fluid is released to the exhaust line. A rotor with two lobes will have four suction chambers per rotation. Roots expanders show power ranging approximately from 1 to 30 kW with a maximal rotational speed of roughly 20,000 rpm. They are typically equipped with timing gears.

12.2.5.2 Trochoidal expanders

The trochoidal expander geometry is obtained by the trajectory of a point fixed to a circle that is rolling inside or outside of a second circle. The most known trochoidal

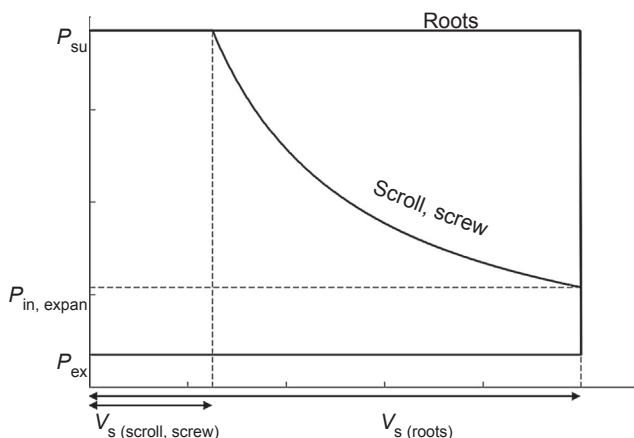


Figure 12.11 Comparison of theoretical indicator diagrams for machines with and without internal expansion.

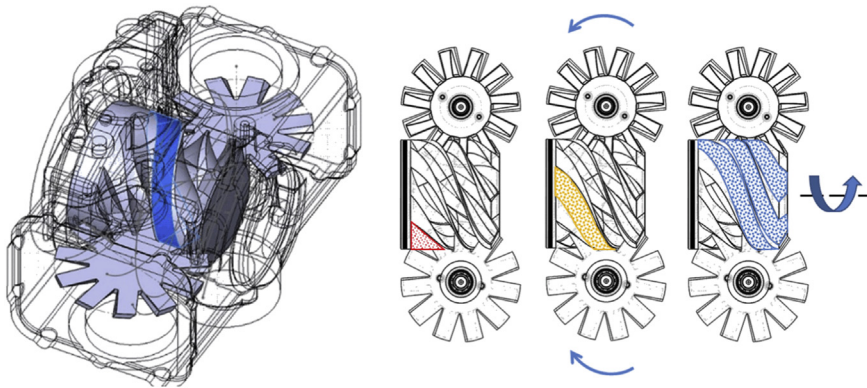


Figure 12.12 Principle of operation of a single-screw expander: assembly and working chamber (left); and expansion process (right).

Reproduced with permission of D. Ziviani.

geometry is the Wankel geometry. Some pumps, called gerotor pumps, also use the trochoidal curves. Therefore gerotor expanders are sometimes described in the literature. This type of expander can be operated under a high-pressure ratio.

12.2.5.3 Single-screw expanders

A single-screw expander is made up of a central rotor with helical grooves meshing with two toothed gate rotors (Fig. 12.12). This meshing delimits a working chamber on each side of the rotor, resulting in symmetrical and simultaneous evolution of the fluid with respect to the central rotor rotation axis (Ziviani et al., 2015a). Consequently, a better balance of radial and axial loads is achieved, increasing the bearing lifespan.

Currently, most of the screw expanders used in ORCs are twin-screw machines. However, single-screw expanders are available on the market and there is an increasing number of research works presented in the literature (Wang et al., 2011; He et al., 2013; Ziviani et al., 2015a). Single-screw machines are also commercialized in compressor mode for HVAC&R applications.

According to He et al. (2013), single-screw expanders could cover powers ranging from 1 to 200 kW. Volume ratios of 7 could be achievable with such machines.

12.3 Thermodynamics of displacement expanders

12.3.1 Major losses in displacement expanders

Major losses in displacement expanders, penalizing the overall isentropic effectiveness, are the under-expansion/over-expansion losses, under-compression/over-compression losses, internal leakages, supply and exhaust pressure losses,

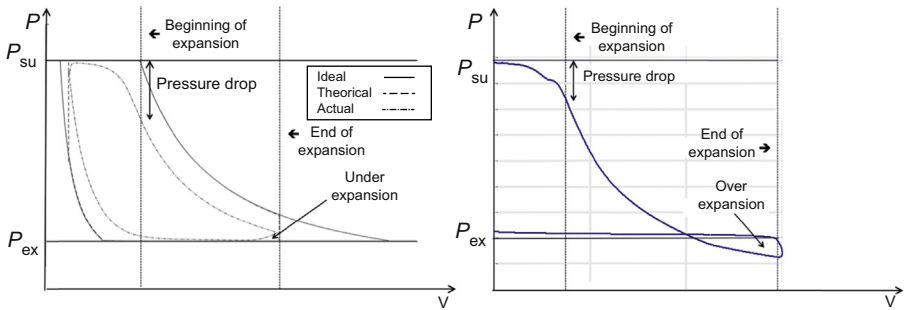


Figure 12.13 Actual indicator diagrams (drawn by simulation). Piston expander (left) and scroll expander (right).

heat transfer, and friction losses. These losses result in a deformation of the indicator diagram with respect to the theoretical one introduced previously. This is represented in Fig. 12.13, which shows the actual indicator diagrams for two particular cases: a piston expander characterized by under-expansion losses (left) and a scroll expander characterized by over-expansion losses (right). Both diagrams show the pressure drops encountered during suction and discharge processes (in the piping and in the orifices). It can also be observed that the pressure decrease/increase at the beginning of the discharge process is not sudden, as it is assumed in the theoretical diagram. Actually, the diagram is deformed due to the progressive opening of the discharge ports and the resulting flow limitation at the beginning of the discharge process.¹ Heat transfers and leakage flows also tend to deform the indicator diagram.

Losses associated with the mismatch between the internal and external pressure ratios have been described in section 12.2. The present section focuses on other types of losses.

12.3.1.1 Internal leakages

Internal leakage flows constitute another major source of losses in displacement expanders. They often strongly modify the shape of the indicator diagram. Leakages are due to the pressure gradients that are applied across leakage paths resulting from clearances between moving elements. The number and shapes of the leakage paths (and their crank-angle evolution) depend on the technology of displacement expanders.

In scroll expanders, there are two types of leakage: radial and flank ones. Fig. 12.14 illustrates those different types. Radial leakage, numbered 1 in Fig. 12.14, flows from one chamber to the radially consecutive one, going over the involute whereas flank leakage, numbered 2, takes place in the gap formed by the walls of both involutes. Leakages tend to slightly decrease the pressure in the first

¹ In the case of scroll expanders, the discharge chamber volumes first slightly increase before decreasing.

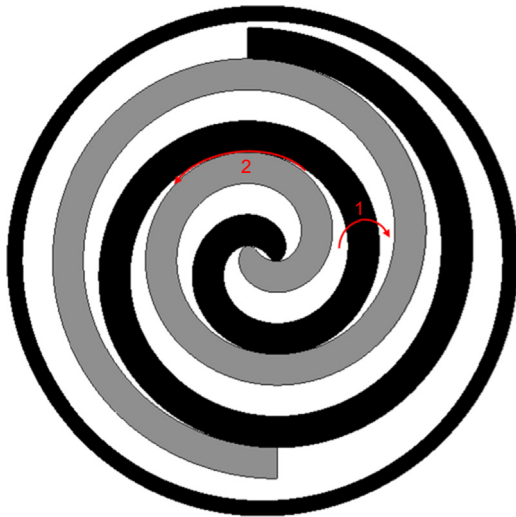


Figure 12.14 Leakage paths in scroll expanders. (1) Radial gap and (2) flank gap.

chambers and increase it in the last ones, which may result in a slightly larger output power, but a lower isentropic effectiveness. The increase in the output power can be explained by the increase in the mass flow rate that enters the machine. Radial leakages can be reduced either by the use of compliant systems or by nestling tip seals in spiral grooves in each involute.

In piston expanders, fluid can leak through the piston rings. In uniflow configurations, the leakage flow can be recovered in the exhaust pipe. Fluid can also leak through the valves from the supply pipe into cylinders and it can leak along the poppet valves' stems.

There are four different leakage paths in twin-screw expanders: the blowhole; the clearance between male and female rotors (profile meshing clearance); the clearances between rotors lobes and the casing (housing gaps); and the clearances between the rotors extremities and the casing (front gaps) (Lee et al., 2001; Kaneko and Hirayama, 1985). These leakage paths are represented in Fig. 12.15.

Vane expanders are usually characterized by five different leakage paths, which are presented in Fig. 12.10 (Bingchun et al., 2008). The first leakage path, numbered 1 in Fig. 12.10, occurs between the supply and exhaust ports, through the gap between the rotor and its housing (stator). Leakage path 2 results from the gap between the rotor and the end plate. Leakage paths 3 through 5 take place around the vanes. Leakage path 3 is due to the small clearance between the vane and its groove. Leakage 4 occurs between the vane and the end cover. Finally, path number 5 is the clearance between the vane and the housing.

12.3.1.2 Heat transfer

The fluid exchanges heat with the physical boundaries (expander casing, walls of the chambers) through finite temperature differences, resulting in an increase or a decrease

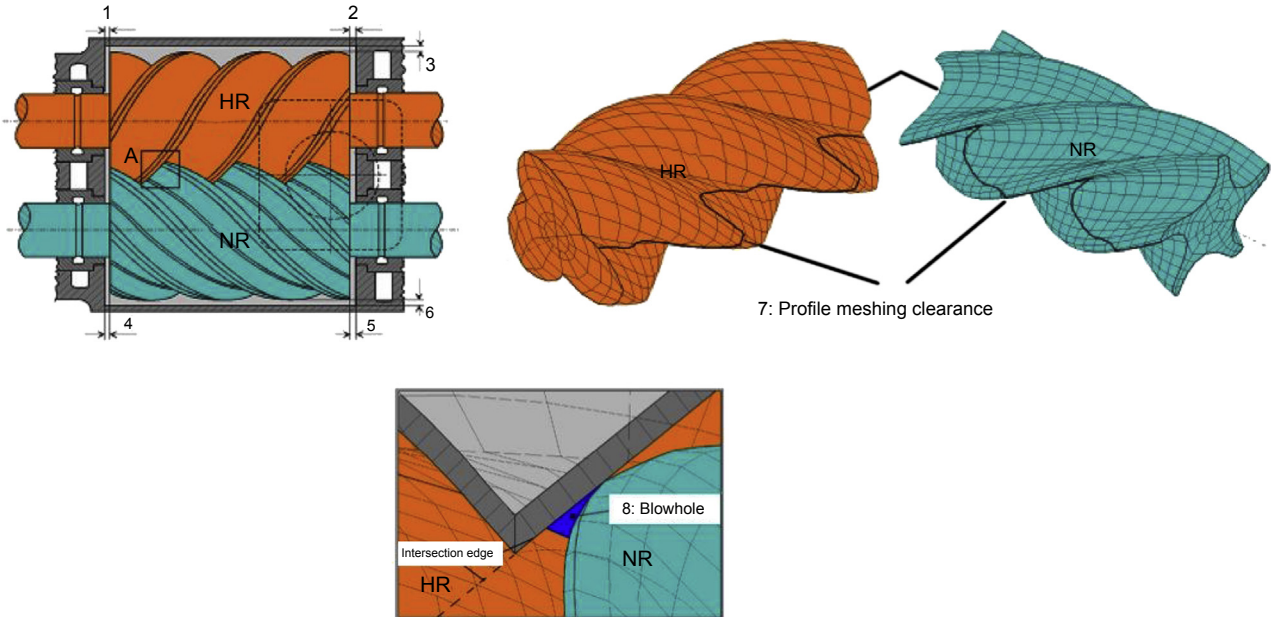


Figure 12.15 Leakage paths in twin-screw expanders. (1), (2), (4), and (5) front gaps; (3) and (6) housing gaps; (7) profile meshing clearance; and (8) blowhole.
 Reproduced with permission of [A. Brümmer \(2011\)](#).

of its temperature. If the working fluid is a vapor, condensation may eventually appear. In the absence of adequate insulation, the expander casing also exchanges heat with the environment and cannot be considered as adiabatic. The heat transfers do not have any significant impact on the indicator diagram. Heat transfers mostly influence the fluid discharge temperature, but do not modify the internal work significantly.

12.3.1.3 Friction losses

Vane expanders present a trade-off between leakage and friction losses. Indeed, if the vane is not sufficiently pressed against the housing, leakages are large and friction losses are limited. On the other hand, if the force acting on the vane is high, the leakage mass flow rate is small but the friction losses are important.

Friction losses are therefore a major concern in vane expander and vane material must be thoroughly studied in order to reduce the leakage as much as possible. The addition of oil in the working fluid also helps to decrease the friction between the vane and the housing.

Friction losses are usually the second most important loss in scroll expanders. The biggest friction losses result from the force that tends to separate the two involutes, called the axial force. That force acts on the anti-rotation mechanism causing high friction. Depending on the architecture of that anti-rotation mechanism, friction can be lowered.

12.3.1.4 Losses associated with the presence of a clearance volume

As explained in a previous section, recompression may occur in piston expanders when the exhaust valve is closed before reaching TDC. As a function of the pressure at the end of the recompression phase, under-compression or over-compression losses occur. Wankel expanders have a clearance volume and show similar indicator diagrams than piston expanders ([Antonelli and Martorano, 2012](#)).

Losses associated with recompression can also occur in vane expanders, depending on the position of the supply and exhaust ports. The design of those ports will define the working process of the machine. Some vane expanders use only one supply and one exhaust port ([Robertson, 1977](#)) whereas other ones are equipped with a second couple of ports ([Bingchun et al., 2008](#)).

Losses associated with the presence of a clearance volume occur neither in scroll nor in screw expanders.

12.3.1.5 Pressure drops

Pressure drops occur during both the suction and the discharge processes. Pressure drops decrease the pressure at the beginning of the expansion process and increase it at the beginning of the discharge process. As a consequence, the area of the actual indicator diagram is smaller than that of the theoretical one and the power produced by the machine is reduced. Pressure drops result from flow restrictions in supply and exhaust ports. This can be due to the valves opening characteristics in piston

expanders or to some overlapping of the moving elements and the supply/exhaust ports in other machines.

Other distributed and singular pressure drops encountered by the fluid between the working chambers supply and exhaust orifices and the machine supply and exhaust ports should also be considered: friction in internal piping, bends, etc.

In twin-screw machines, the supply port cross-sectional area is zero at the initial shaft rotating angle and then progressively increases. At the beginning of the supply process, due to this reduced flow area and choked flow regime, the entering mass flow rate is limited. Consequently, it takes some time for the chamber pressure to approach the supply pressure.

At the end of the expansion and compression processes, the pressure equalization processes do not exactly occur at a constant machine volume. This is due to the restricted flow passage for the flow entering or exiting the machine. Such phenomenon is visible in [Fig. 12.13](#).

12.3.2 Displaced mass flow rate

In the ideal case, a displacement expander displaces a constant volume flow rate of fluid. This volume flow rate depends on the machine swept volume or displacement V_s (m³), the rotational speed N (Hz), and the working cycle frequency i (—). The latter is defined as the number of cycles represented in the indicator diagram described by the machine during one entire revolution of its shaft. The theoretical volume flow rate is given by:

$$\dot{V}_s = i \cdot N \cdot V_s \quad (12.3)$$

12.3.2.1 Expander displacement

In the case of piston expanders, the displacement is a fraction X_{IC} of the maximal displacement (“stroke” displacement):

$$V_s = V_{IC} - V_0 = X_{IC} \cdot V_{s,max} \quad (12.4)$$

In twin-screw expanders, in a similar way to piston expanders, the expander displacement is also a fraction of a maximal displacement. In both machines, a compromise has to be found between maximizing the expander displacement and the built-in expansion volume ratio. In piston expanders, the maximal displacement is easily found by multiplying the stroke by the piston cross-sectional area. For screw expanders, expressing the crank angle evolution of the chamber volume as a function of rotors characteristics is less trivial. The interested reader should refer to the work of [Stosic et al. \(2005\)](#) for twin-screw machines and [Ziviani et al. \(2015b\)](#) for single-screw machines. For scroll and vane expanders, analytical expressions of the expander displacement V_s and of the crank angle evolution of the suction, expansion, and discharge chambers’ volumes, involving geometrical characteristics of the machine, can also be derived. The reader should refer to the

Table 12.1 Working cycle frequency for major types of expanders

Type of machine	Working cycle frequency
Single-acting piston	Number of cylinders
Double-acting piston	Twice the number of cylinders
Scroll	1
Single-screw	Twice the number of grooves on the main rotor
Twin-screw	Number of teeth of the male rotor
Vane	Number of vanes
Roots	Twice the number of lobes per rotor

work conducted by [Lemort \(2008\)](#) for the scroll machines and by [Badr et al. \(1985\)](#) for the vane machines.

12.3.2.2 Working cycle frequency

The working cycle frequencies of the major types of expanders are given in [Table 12.1](#).

12.3.2.3 Mass flow rate

The theoretical mass flow rate displaced by the expander is defined as the ratio between the swept volume flow rate and the specific volume of the fluid at the expander supply.

$$\dot{M}_{\text{th}} = \dot{V}_s / v_{\text{su}} \quad (12.5)$$

The actual fluid mass flow rate differs from this theoretical value, because of:

- Pressure drops during the suction process.
- Heat transfer during the suction process.
- The presence of a clearance volume (not in all expanders' technologies). At the start of the suction process, a quantity M_{comp} of fluid is trapped in the clearance volume, in a thermodynamic state different from the one at the expander supply.
- Internal leakages between the expander components. Internal leakages flow from the high-pressure expander inlet to the low-pressure expander outlet.

As a consequence of the three first types of losses, the specific volume v_{su}^* at the end of the suction phase (and hence, at the beginning of the expansion phase) is different from v_{su} .

In the most general case, the mass flow rate displaced by the expander is expressed by:

$$\dot{M} = \dot{M}_{\text{in}} + \dot{M}_{\text{leak}} \quad (12.6)$$

In the absence of clearance volume (screw and vane expanders), the internal mass flow rate is computed as:

$$\dot{M}_{\text{in}} = \dot{V}_s / v_{\text{su}}^* \quad (12.7)$$

The latter equation is still applicable to scroll expanders, since the clearance volume at the beginning of the suction process contains fluid at the supply pressure (minus eventual pressure drops).

For piston expanders, the mass flow rate entering into/leaving the cylinder to increase/decrease the pressure from the pressure at the end of the compression up to/down to the supply pressure (with a correction to take into account the supply pressure drop) must be taken into consideration. In this case, the net mass flow rate entering the expander can be computed as the difference between the flow rate of fluid that is expanded and the flow rate of fluid that is compressed. The proposed expression (Eq. (12.8)) of the mass flow rate as a function of the volume flow rates relies on the approximation that the fluid specific volume at the start of the compression is equal to the one in the discharge line (v_{ex}).

$$\dot{M}_{\text{in}} = \dot{M}_{\text{expan}} - \dot{M}_{\text{comp}} \cong \dot{V}_{\text{IC}} / v_{\text{su}}^* - \dot{V}_{\text{EC}} / v_{\text{ex}} \quad (12.8)$$

12.3.3 Produced mechanical or electrical power

12.3.3.1 Theoretical internal power

The theoretical (or “hypothetical”) internal work produced by the working fluid is obtained by adding up the suction work and the expansion work and by subtracting the discharge work and compression work:

$$W_{\text{in,th}} = W_{\text{suc}} + W_{\text{expan}} - W_{\text{dis}} - W_{\text{comp}} \quad (12.9)$$

The theoretical internal work corresponds to the areas 1234561 and 123561 of the theoretical indicator diagrams depicted in Fig. 12.2 left and right. For crossflow machines, the suction, expansion, discharge and compression works are respectively represented by areas 122'1'1, 234'2'2, 44'5'54 and 55'1'65. For uniflow machines operating with the diagram shown in Fig. 12.2 (right), the discharge work is not present. The expansion work is represented by area 235'2'2. The theoretical internal work can also be found by summing the areas 1''233''1'', 3''344''3'' (crossflow machines) or 3''354''3'' (uniflow machines), 4''566''4'' and 6''611''6''. Hence, for crossflow machines, the theoretical internal work can be approximated by:

$$\begin{aligned} W_{\text{in,th}} \cong & \dot{M}_{\text{expan}} \cdot (h_{\text{su}} - h_{\text{in,expan}}) + V_c \cdot (P_{\text{in,expan}} - P_{\text{ex}}) \\ & - \dot{M}_{\text{comp}} \cdot (h_{\text{in,comp}} - h_{\text{ex}}) - V_0 \cdot (P_{\text{su}} - P_{\text{in,comp}}) \end{aligned} \quad (12.10)$$

where h_{su} (J/kg) is the specific enthalpy at the expander supply, $h_{\text{in,expan}}$ (J/kg) is the specific enthalpy at the end of the internal expansion, and h_{ex} (J/kg) is the specific enthalpy at the expander exhaust.

In the case of ideal scroll, screw, and vane expanders, the indicator diagram is given in Fig. 12.7. Such machines are characterized by a discharge process extending to a chamber volume equal to zero. Consequently, the compression work is equal to zero in Eq. (12.9). The theoretical internal work is equal to the area 123451 in Fig. 12.7. This area corresponds to the sum of the areas corresponding to the suction and expansion works (122'0'1 and 234'2'2, respectively), minus the area corresponding to the discharge work (544'0'5). The theoretical internal work can also be found by summing the areas 1233''1 and 3''3453''. Hence, the theoretical internal work can be computed by:

$$\begin{aligned} W_{\text{in,th}} &= M_{\text{in}} \cdot (h_{\text{su}} - h_{\text{in,expan}}) + r_{\text{v,in}} \cdot V_{\text{s}} \cdot (P_{\text{in,expan}} - P_{\text{ex}}) \\ \Leftrightarrow W_{\text{in,th}} &= M_{\text{in}} \cdot (h_{\text{su}} - h_{\text{in,expan}}) + v_{\text{in,expan}} \cdot (P_{\text{in,expan}} - P_{\text{ex}}) \end{aligned} \quad (12.11)$$

Roots expanders do not show any internal expansion. The internal work is the difference between the suction and discharge works. The integration of the indicator diagram, shown in Fig. 12.11, is straightforward because of its rectangular shape:

$$W_{\text{in,th}} = V_{\text{s}} \cdot (P_{\text{su}} - P_{\text{ex}}) \quad (12.12)$$

The theoretical internal (or “indicated”) power can be computed by introducing the working cycle frequency and the expander shaft rotational speed:

$$\dot{W}_{\text{in,th}} = i \cdot N \cdot W_{\text{in,th}} \quad (12.13)$$

12.3.3.2 Actual internal power

The actual cycle differs from the theoretical cycle because of other irreversibilities than the under-compression/expansion and over-compression/expansion losses. As a consequence of all these irreversibilities, the actual indicator diagram differs from the theoretical one (see Fig. 12.13). The actual indicator diagram can be predicted by using a detailed simulation model of the expansion machine. It can also be directly measured (at least, portions of the diagram) provided that internal pressure measurements are feasible. The actual internal work, or “indicated” work, can be retrieved by integrating the area underneath the pressure–volume curve in this indicator diagram.

$$W_{\text{in}} = \oint P dV \quad (12.14)$$

The actual internal power can be computed using [Eq. \(12.13\)](#). The ratio between the actual and the theoretical internal works (or powers) is the internal effectiveness (or “diagram factor”). It gives an indication of the impact of all these irreversibilities:

$$\varepsilon_{\text{in}} = \frac{\dot{W}_{\text{in}}}{\dot{W}_{\text{in,th}}} \quad (12.15)$$

12.3.3.3 Shaft power

The shaft power is obtained by deducing the mechanical losses from the internal power:

$$\dot{W}_{\text{sh}} = \dot{W}_{\text{in}} - \dot{W}_{\text{loss,mec}} \quad (12.16)$$

The expander mechanical efficiency is defined as:

$$\eta_{\text{mec}} = \frac{\dot{W}_{\text{sh}}}{\dot{W}_{\text{in}}} = \frac{\dot{W}_{\text{in}} - \dot{W}_{\text{loss,mec}}}{\dot{W}_{\text{in}}} \quad (12.17)$$

12.3.3.4 Electrical power

If the expander drives a generator, the performance of the latter must be taken into account. The electrical power produced by the generator is equal to the shaft power minus the generator losses:

$$\dot{W}_{\text{el}} = \dot{W}_{\text{sh}} - \dot{W}_{\text{loss,el}} \quad (12.18)$$

The generator efficiency is defined as:

$$\eta_{\text{el}} = \frac{\dot{W}_{\text{el}}}{\dot{W}_{\text{sh}}} \quad (12.19)$$

12.3.3.5 Overall expander energy balance

For an open-drive machine, the energy balance across the expander can be expressed as:

$$\dot{W}_{\text{sh}} = \dot{M} \cdot (h_{\text{su}} - h_{\text{ex}}) - \dot{Q}_{\text{amb}} \quad (12.20)$$

where \dot{M} (kg/s) is the mass flow rate displaced by the expander and is defined by [Eq. \(12.6\)](#) and \dot{Q}_{amb} (W) are the ambient losses from the casing.

For a hermetic expander, the energy balance is:

$$\dot{W}_{\text{el}} = \dot{M} \cdot (h_{\text{su}} - h_{\text{ex}}) - \dot{Q}_{\text{amb}} \quad (12.21)$$

12.4 Performance of displacement expanders

12.4.1 Performance indicators

12.4.1.1 Volumetric performance

Different performance indicators can be used to express the performance of a volumetric expander. The filling factor is defined as the ratio between the mass flow rate entering the expander and the theoretical mass flow rate, as given by Eq. (12.22). Some authors use the inverse of the filling factor, named the volumetric effectiveness ε_v .

$$\phi = \frac{\dot{M}}{\dot{M}_{th}} = \frac{1}{\varepsilon_v} \quad (12.22)$$

In contrast to volumetric compressors, supply pressure losses and internal leakages have antagonistic effects on the filling factor; the former tends to decrease it, while the latter increases it. Also, fluid heating up during suction will decrease the filling factor while cooling down will increase it. To better understand the impact of the different losses on the filling factor, the latter can be decomposed according to Eq. (12.23).

$$\phi = \frac{\dot{M}}{\dot{M}_{th}} = \frac{\dot{M}}{\dot{M}_{in}} \frac{\dot{M}_{in}}{\dot{V}_{IC}/v_{su,th} - \dot{V}_{EC}/v_{ex}} \frac{\dot{V}_{IC}/v_{su,th} - \dot{V}_{EC}/v_{ex}}{\dot{M}_{th}} = \phi_1 \cdot \phi_{P,T} \cdot \phi_0 \quad (12.23)$$

The first factor ϕ_1 quantifies the impact of internal leakages and is always larger than unity (see Eq. (12.6)). The second factor takes into account the impact of supply pressure drop and heat transfer (usually cooling down), which modify the fluid specific volume. $v_{su,th}$ is the specific volume at the beginning of the expansion process in the absence of pressure drop and heat transfer. In the presence of a clearance volume, it differs from v_{su} . If pressure losses are the predominant phenomenon, the value of $\phi_{P,T}$ is lower than unity. The third factor ϕ_0 is equal to unity for all machines that do not show any clearance volume. For piston expanders (Eq. (12.24)), its value is generally lower than unity in the case of over-compression and higher than unity in the case of under-compression.

$$\phi_0 = \frac{V_{IC} \cdot v_{su}/v_{su,th} - V_{EC} \cdot v_{su}/v_{ex}}{V_{IC} - V_0} \quad (12.24)$$

Even if the analysis of the filling factor is not straightforward for expanders, machines without clearance volume showing a filling factor much larger than unity are characterized by important internal leakages.

12.4.1.2 Power performance

To assess the performance of an expander, the power it produces (for given fluid supply conditions and a given discharge pressure) is compared to the power that would

be produced in the case of a reference evolution of the fluid through the expander. The reference evolution is typically the adiabatic and reversible (i.e., isentropic) one.

The ratio of the power produced by the expander and the power it would produce if the expansion of the fluid was isentropic is named the isentropic effectiveness. According to the system boundary that is considered, several definitions of the isentropic effectiveness can be considered:

- The internal isentropic effectiveness or (“indicated efficiency”):

$$\varepsilon_{s,in} = \frac{\dot{W}_{in}}{\dot{M}(h_{su} - h_{ex,s})} \quad (12.25)$$

where $h_{ex,s}$ (J/kg) is the specific enthalpy at the exhaust of the expander if the expansion was isentropic from the supply state to the discharge pressure.

- The shaft/electrical isentropic effectiveness

$$\varepsilon_{s,el} = \frac{\dot{W}_{sh,el}}{\dot{M}(h_{su} - h_{ex,s})} \quad (12.26)$$

As an example, Fig. 12.16 shows the measured shaft isentropic effectiveness of an oil-free open-drive scroll expander integrated into an ORC system working with R245fa. The isentropic effectiveness is drawn as a function of the pressure ratio imposed on the expander for different rotational speeds. It can be observed that the effectiveness goes through a maximum value because of under-expansion and over-expansion losses. The optimal pressure ratio varies with the rotational speed due to the other losses.

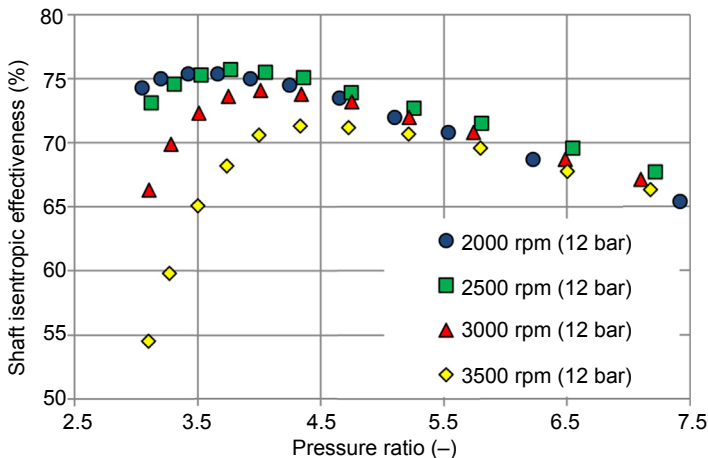


Figure 12.16 Measured shaft isentropic effectiveness of an open-drive scroll expander fed by R245fa (Declaye et al., 2013).

To better assess the relative impact of each source of losses in a positive displacement expander, the electrical isentropic effectiveness can be disaggregated in the following way (Ng et al., 1990):

$$\begin{aligned}\varepsilon_{s,el} &= \frac{\dot{M}_{in}}{\dot{M}} \frac{\dot{W}_{in}}{\dot{W}_{in,th}} \frac{\dot{W}_{sh}}{\dot{W}_{in}} \frac{\dot{W}_{el}}{\dot{W}_{sh}} \frac{1}{\phi_{P,T}} \frac{1}{\phi_0 \dot{M}_{th} (h_{su} - h_{ex,s})} \dot{W}_{in,th} \\ &= \left(\frac{1}{\phi_1 \phi_{P,T}} \varepsilon_{in} \eta_{mec} \eta_{el} \right) \varepsilon_{s,th}\end{aligned}\quad (12.27)$$

The leakage contribution ϕ_1 to the filling factor quantifies the impact of internal leakages. The specific volume contribution $\phi_{P,T}$ to the filling factor quantifies the impact of supply pressure drop and heat transfer on the volumetric performance. The internal efficiency ε_{in} is an indicator of the irreversibilities that deform the pressure–volume diagram (pressure drops, etc.). The mechanical efficiency η_{mec} quantifies the impact of the mechanical losses and the electrical efficiency η_{el} is an indicator of the performance of the generator. The theoretical isentropic effectiveness $\varepsilon_{s,th}$ quantifies the impact of under-compression, over-compression, under-expansion, and over-expansion losses. It varies with the built-in compression and expansion volume ratios and with the pressure ratio imposed on the machine (ratio between the ORC evaporating and condensing pressures). Hence, the expression in brackets in Eq. (12.27) represents all losses not represented in the theoretical indicator diagram.

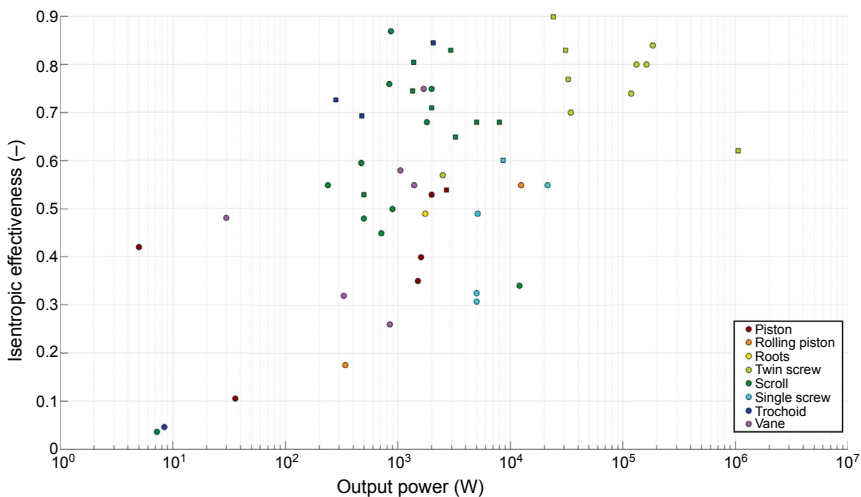


Figure 12.17 Evolution of the maximal measured isentropic effectiveness with the maximal measured output power for 67 machines described in the literature (circles denote mechanical power/isentropic effectiveness and squares electrical power/isentropic effectiveness).

12.4.2 Typical achieved performance

The performance of 67 machines described in 57 scientific papers has been analyzed and Fig. 12.17 shows the evolution of the maximal isentropic effectivenesses achieved by the machines with their maximal output powers. There is a general trend between the isentropic effectiveness and the produced power. Screw machines typically produce the largest powers, with high effectiveness. Over the range of 100 W to 10 kW, scroll machines show the best performance. Piston and vane expanders cover the same range of powers, but with lower performance. Single-screw expanders produce lower powers than twin-screw expanders and with lower effectiveness. The literature reports few machines producing powers lower than 100 W. Hence, it is difficult to draw conclusions.

12.5 Integration of displacement expanders into Organic Rankine Cycle systems

12.5.1 Selection of the expander technology

12.5.1.1 Capacity

As explained by Persson (1990), each expansion machine technology is characterized by an optimal peripheral velocity (or “tip speed”) that is fairly independent of the machine size for a given geometry and technology of machine. This tip speed u (m/s) can be simply expressed as a function of the rotor diameter D (m) and rotational speed N (Hz) by:

$$u = \pi \cdot D \cdot N \quad (12.28)$$

In displacement machines, the existence of an optimal tip speed results from antagonistic effects: the power loss associated with internal leakages decreases with the tip speed while the power losses associated with the supply pressure drop, discharge pressure drop and friction increase with the tip speed (Persson, 1990). According to Brümmer (2012), the tip speed commonly ranges between 20 and 40 m/s for unsynchronized twin-screw expanders and between 60 and 120 m/s for synchronized ones. Much lower values are typically reached for piston and scroll machines.

The expander displacement is related to the rotor diameter. The ratio V_s/D^3 is a dimensionless parameter that is independent of the machine size for a given technology and geometry (Persson, 1990). Combining Eq. (12.3) (assuming $i = 1$) and Eq. (12.28), the following relationships can be derived:

$$N = \sqrt{\frac{\left(\frac{V_s}{D^3}\right) u^3}{\pi^3 \dot{V}_s}} \quad (12.29)$$

$$D = \sqrt{\frac{\pi \dot{V}_s}{\left(\frac{V_s}{D^3}\right) u}} \quad (12.30)$$

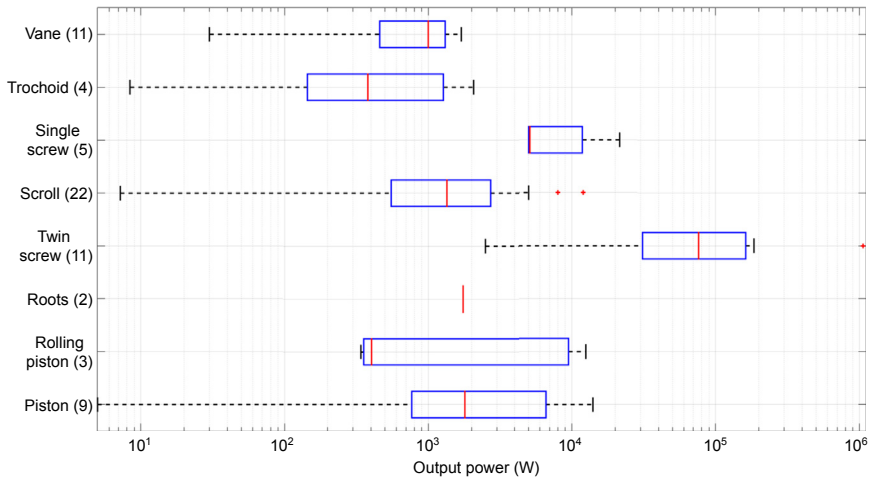


Figure 12.18 Ranges of power produced by major technologies of expanders. Based on the analysis of reported performance of 67 machines published in technical literature.

These relationships, proposed by [Persson \(1990\)](#), indicate that for a given technology and geometry of machine operating at its optimal tip speed, the rotational speed increases when the expander swept volume flow rate decreases, and the rotor diameter increases when the expander swept volume flow rate increases. For machines with orbital rotor motion, the diameter should be replaced by twice the eccentricity in previous relationships. The rotational speed is limited by rolling-element bearings and the diameter is limited by manufacturing constraints. As a consequence, each technology of expansion machine can cover a range of swept volume flow rates and hence power outputs.

[Fig. 12.18](#) shows the range of power outputs produced by a sample of 67 machines, described in the literature, in a box and whisker plot. The left and right extremities of the box respectively indicate the first and third quartiles q_1 and q_3 . The red band inside the box indicates the median. The whiskers correspond to the lowest and highest data still within respectively $q_1 - 1.5 \cdot (q_3 - q_1)$ and $q_3 + 1.5 \cdot (q_3 - q_1)$. The red points indicate the outliers. From this Figure, it can be observed that scroll and piston expanders approximately cover the same range of powers. Twin-screw expanders cover larger powers and fill the gap between turbomachines and other technologies of expanders. Single-screw machines cover a smaller range of powers, roughly between the ranges covered by scroll and twin-screw machines. The survey comprises only two roots expanders. Vane and trochoidal expanders compete with scroll and piston for output powers up to approximately 2 kW. However, according to [Antonelli and Martorano \(2012\)](#), much larger powers could be achieved by Wankel expanders. Rolling piston expanders seem to be able to cover as large powers as the scroll and the piston. However, few publications are available on this technology.

[Fig. 12.19](#) displays the range of the maximal rotational speeds achieved for each technology of expanders. Most of the expanders are operated at speeds lower than

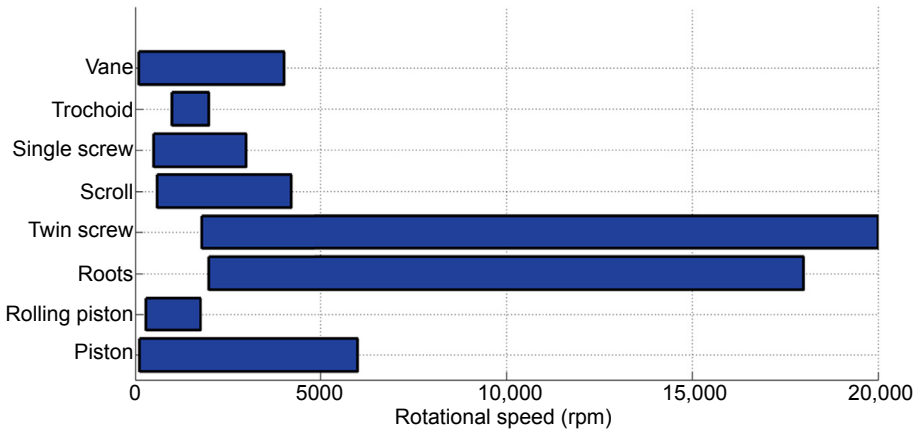


Figure 12.19 Ranges of rotational speeds achieved by major technologies of expanders. Based on the analysis of reported performance of 67 machines published in technical literature.

6000 rpm. Twin-screw and roots expanders can achieve much larger rotational speeds, which tends to increase the machine compactness.

12.5.1.2 Technical limitations

Besides the limitations on the power output range, technical limitations must be taken into consideration such as maximal allowable operating pressure and temperature, ability to operate without lubricating oil, and maximal achievable built-in volume ratio.

In contrary to turbomachines, scroll, twin-screw (Ng et al., 1990; Smith et al., 2009), and single-screw (He et al., 2013) expanders tolerate the admission of a large amount of working fluid in liquid state. This is due to the low velocity of the liquid phase inside the machine yielding no risk of erosion of the rotors/stator. Piston expanders can also ingest working fluid in the two-phase state (Daccord et al., 2013). This advantage of displacement expanders over turbomachines is a major asset for their use in ORC systems operating with wet fluids or in trilateral cycles.

12.5.2 Expander preliminary design

The preliminary design of a positive displacement expander consists in selecting its displacement, rotational speed, and built-in expansion ratio.

The working parameters of the ORC system that must be known for sizing the machine are the mass flow rate, the supply pressure and temperature, and the exhaust pressure. Using a simulation model of the expander, the swept volume flow rate can be deduced. In the absence of such a model, this volume flow rate can be roughly approximated by assuming a filling factor equal to unity: $\dot{V}_s \cong v_{su} \cdot \dot{M}$.

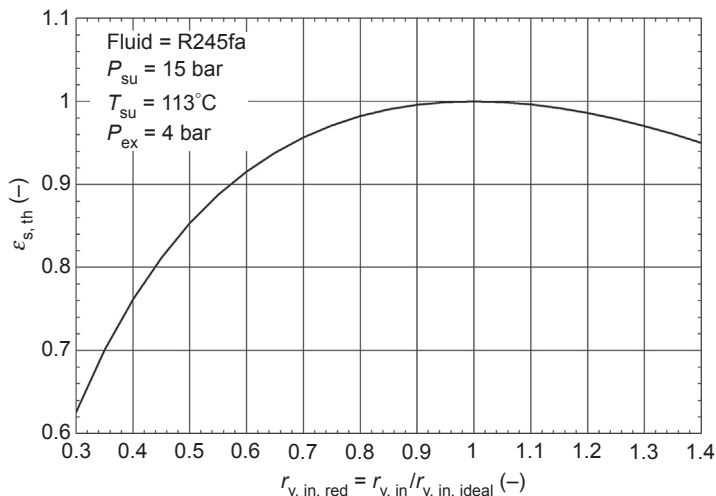


Figure 12.20 Evolution of the theoretical isentropic effectiveness with the ratio of actual to ideal built-in volume ratios.

Knowing the supply pressure (evaporating pressure) and temperature, and the exhaust pressure (condensing pressure), which are imposed by the ORC system, the built-in expansion volume ratio could be selected in order to get a perfect expansion (no under-expansion and over-expansion losses). However, selecting a built-in volume ratio slightly lower than the ideal one does not yield a significant decrease in produced work. This is shown in the example given in Fig. 12.20 where the theoretical isentropic effectiveness is drawn as a function of the ratio between the actual and the ideal built-in volume ratios. In this simulation, reducing by 20% the volume ratio from its ideal value yields a decrease of the theoretical isentropic effectiveness of around 2%. In the meantime, the envelope size of the machine can be reduced.

12.5.3 Control

Controlling a positive displacement expander integrated inside an ORC system generally means adjusting the volume flow rate $\Phi \cdot V_s$ it displaces. For a fluid mass flow rate \dot{M} imposed by the ORC feed pump, this means controlling the expander supply pressure and hence the evaporating pressure. The evaporating pressure is one of the major variables controlled to optimize the ORC performance.

To adjust the volume flow rate, either the expander rotational speed N or its displacement V_s could be controlled. Controlling the speed of an expander coupled to a generator connected to the grid can be achieved by means of an inverter. Varying the speed of the expander also has an impact on its performance. Actually, at low speed, internal leakages play a significant role while at high speed, major losses are friction and pressure losses (the tip speed moves away from its optimal value). In

mobile applications, the speed can be controlled when the expander is not mechanically coupled to the engine shaft.

As explained in [Section 12.2](#), some expander technologies offer means of controlling the displacement V_s . This is the case for piston expanders (with variable cut-off mechanisms), twin-screw expanders, and single-screw expanders (with sliding valves). In single-screw and twin-screw expanders, a sliding valve can also be used to control the internal volume ratio.

In some applications, the expander is equipped with a by-pass valve in order to protect it, for instance, during the switch-on of the ORC system.

12.6 Conclusions

The selection of the type of expander and the definition of its preliminary design strongly depend on the characteristics of the ORC system into which it is integrated. The maximum allowable operating pressure and temperature of the expander should be compatible with the evaporating pressure and with the evaporator exhaust temperature. Also, the nominal pressure ratio imposed on the machine, i.e., the ratio between the evaporating and condensing pressures, will largely influence the definition of the built-in volume ratio and the selection of the expander technology. Compactness may also be an important criterion (for instance, for mobile applications). Finally, choosing a lubricated expander rather than oil-free will improve the performance of the expander, but increase the complexity of the ORC system.

As a consequence, the choice of the expander technology has to be conducted in parallel with the selection of the ORC architecture, operating conditions, and working fluid.

Acknowledgments

The authors would like to thank Rémi Daccord, Andreas Brümmer and Alexander Nikolov, Davide Ziviani, Abhinav Krishna and Matthew Fortini for the information they provided about piston, twin-screw, single-screw and roots expanders respectively.

References

- Badr, O., O'Callaghan, P.W., Probert, S.D., 1985. Multi-vane expanders: geometry and vane kinematics. *Applied Energy* 19, 159–182.
- Bingchun, Y., Shaoyi, S., Xueyuan, P., Ziwen, X., 2008. Modeling and experimental investigation on the internal leakage in a CO₂ rotary vane expander. In: *Proceedings of the International Compressor Engineering Conference at Purdue*, July 14–17, 2008.
- Brümmer A., *Energiewandlungsprinzip der Schraubenmaschine*, Schraubenmaschinen Nr. 14, p. A1-A4, TU Dortmund, 2011. ISSN 0945-1870.
- Brümmer, A., 2012. Energy efficiency — waste heat utilization with screw expanders. *Pumps, Compressors and Process Components* 120–126.

- Daccord, R., Melis, J., Kientz, T., Darmedru, A., Pireyre, R., Brisseau, N., Fonteneau, E., May 28, 2013. Exhaust heat recovery with Rankine piston expander. In: ICE Powertrain Electrification & Energy Recovery on.
- Declaye, S., Quoilin, S., Guillaume, L., Lemort, V., 2013. Experimental study on an open-drive scroll expander integrated into an ORC system working with R245fa, paper. *Energy* 15, 173–183.
- Demler, R.L., 1976. The application of the positive displacement reciprocating steam expander to the passenger car. SAE. Paper 760342.
- Grip, R.L., 2009. A Mechanical Model of an Axial Piston Machine. Licentiate Thesis, Department of Machine Design. Royal Institute of Technology, Stockholm, Sweden.
- He, W., Wu, Y., Peng, Y., Zhang, Y., Ma, C., Ma, G., 2013. Influence of intake pressure on the performance of single screw expander working with compressed air. *Applied Thermal Engineering* 51, 662–669.
- Jakuba, S., McGeehan, J.A., 1975. Component development of automotive reciprocating steam expanders. In: SAE Automotive Engineering Congress and Exposition, February 24–28, 1975.
- Jia, X., Zhang, B., Pu, L., Guo, B., Peng, X., 2011. Improved rotary vane expander for trans-critical CO₂ cycle by introducing high-pressure gas into the vane slots. *International Journal of Refrigeration* 34, 732–741.
- Kane, M., Creteigny, D., Favrat, D., Maquet, J., Octobre 29, 2009. Projet HTScroll, Nouveau système de cogénération à turbine spirale haute température, Rapport final. In: Département fédéral de l'environnement, des transports, de l'énergie et de la communication DETEC. Office fédéral de l'énergie OFEN.
- Kaneko, T., Hirayama, N., September 1985. Study on fundamental performance of helical screw expander. *Bulletin of JSME* 28 (243).
- Lemort, V., Teodores, I.V., Lebrun, J., 2006. Experimental study of the integration of a scroll expander into a heat recovery Rankine cycle. In: 18th International Compressor Engineering Conference, Purdue, USA.
- Lemort, V., 2008. Contribution to the Characterization of Scroll Machines in Compressor and Expander Modes (Ph.D. thesis). University of Liège, Belgium.
- Lee, W.S., Ma, R.H., Chen, S.L., Wu, W.F., Hsia, H.W., 2001. Numerical simulation and performance analysis of twin screw air compressors. *International Journal of Rotating Machinery* 7 (1), 65–78.
- Marco, Antonelli, Luigi, Martorano, September 2012. A study on the rotary steam engine for distributed generation in small size power plants. *Applied Energy* 97, 642–647.
- Ng, K.C., Bong, T.Y., Lim, T.B., 1990. A thermodynamic model for the analysis of screw expander performance. *Heat Recovery Systems & CHP* 10 (2), 119–133.
- Oudkerk, J.-F., Dickes, R., Dumont, O., Lemort, V., 2015. Experimental performance of a piston expander in a small-scale organic Rankine cycle. *IOP Conf. Series: Materials Science and Engineering* 90, 012066.
- Persson, J.G., 1990. Performance Mapping Vs Design Parameters for Screw Compressors and Other Displacement Compressor Types, 859. VDI Berichte, nr, Düsseldorf.
- Platell, P., 1993. Displacement expanders for small scale cogeneration. Licentiate thesis. KTH.
- Robertson, G.F., 1977. Experimental and Analytical Study of a Steam Vane Expander. Technical Memorandum. File No. TM 77–65. February 1, 1977. The Pennsylvania State University.
- Seher, D., Lengenfelder, T., Gerhardt, J., Eisenmenger, N., Hackner, M., Krinn, I., 11 October 2012. Waste Heat Recovery for Commercial Vehicles with a Rankine Process. In: Proceedings of the 21st Aachen Colloquium Automobile and Engine Technology, Aachen, Germany, pp. 7–9.

- Smith, I.K., Stosic, N., Kovacevic, A., 2009. Steam as the working fluid for power recovery from exhaust gases by means of screw expanders. In: *Proceedings of the International Conference on Compressors and Their Systems*. London, 2009.
- Stosic, N., Smith, I., Kovacevic, A., 2005. *Screw Compressors - Mathematical Modelling and Performance Calculation*. Springer, New York, p. 138. ISBN: 10 3-540-24275-9.
- Stosic, N., Smith, I.K., Kovacevic, A., Mujic, E., 2011. Review of Mathematical Models in Performance Calculation of Screw Compressors. *International Journal of Fluid Machinery and Systems*. Vol. 4, No 2.
- Syniuta, W.D., Palmer, R.M., 1974. Design features and initial performance data on an automotive steam engine Part II - reciprocating steam expander - design features and performance. In: *SAE Automotive Engineering Congress*, Detroit, Mich., February 25–March 1, 1974.
- Wang, W., Wu, Y., Ma, C., Liu, L., Yu, J., 2011. Preliminary experimental study of single screw expander prototype. *Applied Thermal Engineering* 31, 3684–3688.
- Ziviani, D., Desideri, A., De Paepe, M., van den Broek, M., Lemort, V., 2015a. Low-order models of a single-screw expander for organic Rankine cycle applications. In: *Proceedings of the 9th International Conference on Compressors and Their Systems*, City University London, September 7–9, 2015.
- Ziviani, D., Bell, I.H., De Paepe, M., van den Broek, M., 2015b. Update on single-screw expander geometry model integrated into an open-source simulation tool. *IOP Conf. Series: Materials Science and Engineering* 90, 012064.

Heat transfer and heat exchangers

13

A. Cavallini

Emeritus Professor, University of Padova (Italy)

13.1 Heat transfer in exchangers

In organic Rankine cycle (ORC) technology the heat exchangers involved are essentially boilers (both pool and once-through boilers), in which external heat is supplied to the cycle working fluid; condensers, in which the cycle working fluid rejects heat to the external ambient (air or water) or, in cogeneration, to a heat transfer carrier for external use; and regenerative heat exchangers, so dubbed because the transfer of heat takes place between the same working fluid in different internal stages of the thermodynamic cycle. In some cases there can also be, separate from boilers, preheaters, in which the liquid working fluid is heated by the external fluid before entering the boiler, and superheaters, to further raise the temperature of the working fluid in the vapor phase after evaporation.

All these exchangers are of the two-stream, direct-transfer, and indirect-contact type: heat is transferred between two fluid streams kept separated by a metallic structure (wall, plate, ...) without mixing. Heat losses to the surroundings can be usually assumed negligible; furthermore the cycle working fluid is a pure substance; these assumptions will be retained in the following and throughout this chapter, together with that of steady-state operation, unless otherwise stated.

Fig. 13.1 shows schematically the section view of a particular metallic wall separating the two fluid streams mutually transferring heat in a heat exchanger; without loss of generality, this particular case will be used in the following to treat the broad subject of heat transfer in exchangers.

As can be seen, it is basically a cylindrical wall (straight round tube), with fins inserted in both the inner and the outer surface. Finned tubes, if the case, are employed to reduce the thermal resistance between the surface and the adjacent fluid stream; in practical cases it is much more common to have fins on only one side of the metallic wall (i.e., the side controlling the heat transfer process), or to have unfinned surfaces on both sides. With finned surfaces, it is common practice to distinguish between the base or prime surface (that of the original round tube in Fig. 13.1), which is partly masked by the fins, and the fin surface, this last being less effective in the heat transfer process. In this case it is also possible to talk of the internal side (inside the tube, indexed i), the other then dubbed the external side (indexed e).

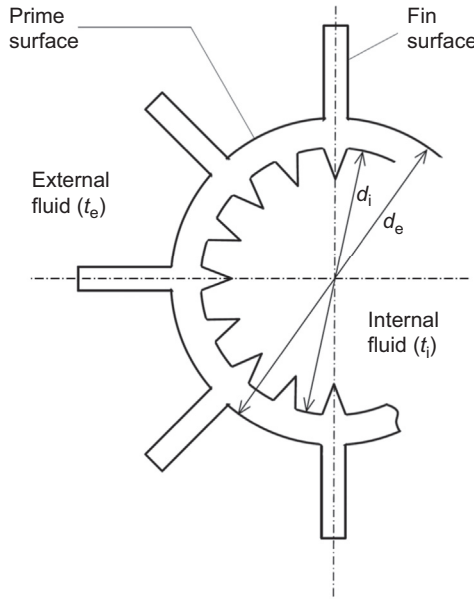


Figure 13.1 Heat transfer between two fluid streams separated by a double-finned cylindrical wall.

Relative to an elemental piece of the heat transfer wall of extension dz in the axial direction (circumferential uniformity is assumed to exist), the local heat transfer rate can be expressed as:

$$d\dot{Q} = U \cdot dA \cdot |(t_i - t_e)| \quad (13.1)$$

where A is the heat transfer area taken as reference (for ducts the most common choice is to refer to A_e , the external area of the wall); t_i and t_e are the local bulk (mixing cup) temperatures of respectively the internal and the external fluid stream; and U is the so-called overall heat transfer coefficient referred to area A , which can be derived from

$$\frac{1}{U \cdot dA} = \frac{1}{U_i \cdot dA_i} = \frac{1}{U_e \cdot dA_e} = \frac{1}{\Omega_i \cdot h_i \cdot dA_i} + \frac{r_{bw}}{dz} + \frac{1}{\Omega_e \cdot h_e \cdot dA_e} \quad (13.2)$$

and for both h_i and h_e uniform along the entire heat transfer wall:

$$U = U_i \frac{A_i}{A} = U_e \frac{A_e}{A} = \left(\frac{A}{\Omega_i \cdot h_i \cdot A_i} + A \cdot R_{bw} + \frac{A}{\Omega_e \cdot h_e \cdot A_e} \right)^{-1} \quad (13.3)$$

where h_i and h_e are the convective fluid-to-wall heat transfer coefficients on respectively the internal and external sides and Ω_i and Ω_e are the overall efficiencies

respectively of the finned-wall inner and outer surfaces: for unfinned surfaces $\Omega = 1$. This parameter will be treated in detail later in this section. R_{bw} is the conduction thermal resistance of the base wall; for a round tube $R_{bw} = \ln(d_e/d_i)/(2\pi \cdot Z \cdot \lambda_w)$; this term can often be neglected, as it is commonly much lower than the other resistances in series. r_{bw} in Eq. (13.2) is the conduction thermal resistance per unit length of the base wall; d_i and d_e are respectively the inner and outer diameter of the cylindrical prime wall; Z is the total axial length of the wall; and λ_w is the thermal conductivity of the prime wall material.

The last member of relationship (13.3) infers negligible fouling and negligible contact thermal resistances. Fouling resistance may build up on a heat transfer surface during operation, for deposition of a film or scale (particulate, precipitation, chemical reaction, biological fouling) or corrosion products. If the case, it can be accounted for by adding the relative fouling resistance term into the brackets of Eq. (13.3), expressed as (respectively for the internal and/or for the external surface) $\frac{R_{fou,i} \cdot A}{\Omega_i \cdot A_i}$ and/or $\frac{R_{fou,e} \cdot A}{\Omega_e \cdot A_e}$; R_{fou} is the so-called fouling factor, given in heat transfer manuals or textbooks with relation to the type of fluid stream and the operating conditions; see Table 13.1 for some representative values.

Contact resistance is related to the quality of the contact between the base of the fin and the prime surface on which it is inserted. Of course this resistance is nil for integral fins or brazed and fully soldered or welded ones; sometimes it may be relevant, and difficult to forecast, for fins attached to the prime surface by mechanical fit or tension winding (such as in the common tension-wound L-shaped finned tubes), or when tubes are simply expanded into the plate fin material (usually aluminum), without brazing or galvanizing.

Fins are evidently used to enhance the heat transfer rate from a prime surface by increasing the surface area typically by a factor ranging roughly from 3 to 20 times; however, it must be recognized that the added fin surface is less effective than the original prime surface in transferring heat with the adjacent fluid: heat flows by conduction along the fin, and this infers the existence of a temperature gradient, which brings the fin surface temperature closer and closer to that of the fluid as the fin tip is approached; of course, should it be possible to use a fin material with infinite thermal conductivity, in case of nil contact resistance the added fin surface would be as effective as the prime surface in the heat transfer with the adjacent fluid stream.

To take into account this reduced capability of the fin surface in the convective heat transfer process, the concept of overall efficiency Ω of a finned surface has been introduced.

For a full insight into the meaning of the overall efficiency Ω of a finned surface, reference can be made to one single longitudinal fin of uniform rectangular cross-sectional area depicted on the outside prime cylindrical surface of Fig. 13.1 (see Fig. 13.2). Let $\theta = |t - t_{fd}|$ be the local excess temperature of the fin surface, the difference between the variable fin surface temperature t and the (assumed constant) bulk fluid stream temperature t_{fd} , expressed positively; θ is decreasing from the value at the fin base θ_b to the tip value $\theta_{x=L} = \theta_t$. Under the following simplifying assumptions, the

Table 13.1 Representative design values of fouling factors for tubular exchangers

Fluid stream	Fouling factor ($\text{m}^2 \text{K/W}$)	
	velocity $\leq 1 \text{ m/s}$	velocity $> 1 \text{ m/s}$
Seawater, temperature $\leq 50^\circ\text{C}$	0.00009	
Seawater, temperature $> 50^\circ\text{C}$	0.00018	
Cooling tower water, untreated makeup, temperature $\leq 50^\circ\text{C}$	0.0005	
Cooling tower water, untreated makeup, temperature $> 50^\circ\text{C}$	0.0009	0.0007
Cooling tower water, treated makeup, temperature $\leq 50^\circ\text{C}$	0.00018	
Cooling tower water, treated makeup, temperature $> 50^\circ\text{C}$	0.00035	
City or well water, temperature $\leq 50^\circ\text{C}$	0.00018	
City or well water, temperature $> 50^\circ\text{C}$	0.00035	
River water, temperature $\leq 50^\circ\text{C}$ (average)	0.0005	0.00035
River water, temperature $> 50^\circ\text{C}$ (average)	0.0007	0.00035
Distilled or closed-cycle condensate	0.00009	
Organic liquids, organic heat transfer media	0.00018	
Fuel oil	0.0001	
Engine exhaust gas	0.0018	
Exhaust steam (oil-bearing)	0.0002	
Condensing and vaporizing medium organics	0.0001–0.0003	
Gases at low pressure (ambient air, ...)	0.0001	

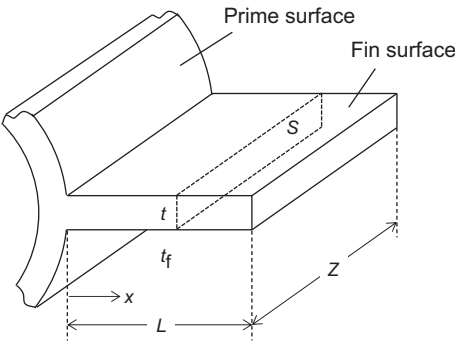


Figure 13.2 Longitudinal constant cross-section fin.

pattern of the surface excess temperature θ moving from the base to the tip of the fin can be readily obtained by simple algebra (Incropera, De Witt, 1996):

- Unidimensional heat conduction within the fin: the fin temperature is constant in any cross section normal to its axis.
- Uniform convective heat transfer coefficient on the fin surface, assumed equal to that pertaining to the residual base surface.
- Negligible convective heat transfer on the fin tip surface (adiabatic fin tip condition).

The solution for the excess temperature θ , normalized to its base value θ_b , yields:

$$\frac{\theta}{\theta_b} = \frac{\cosh[m(L-x)]}{\cosh(m \cdot L)} \quad (13.4)$$

where x is the distance from the base section, and the dimensional parameter (m^{-1} in SI units) $m = \sqrt{\frac{h \cdot P}{\lambda_f \cdot S}}$ (symbols are defined under Nomenclature, at the end of this chapter). For longitudinally long fins it is approximately $P/S \approx 2/\delta$, and therefore $m = \sqrt{2h/(\lambda_f \cdot \delta)}$. Fig. 13.3 illustrates the pattern of the normalized excess temperature ratio along the fin. The conduction heat transfer rate through the fin base cross section \dot{Q}_b is the total heat flow rate transferred under steady-state conditions between the fin and the surrounding fluid, $\dot{Q}_f = \dot{Q}_b$:

$$\dot{Q}_f = -\lambda_f \cdot S \cdot \left(\frac{d\theta}{dx} \right)_{x=0} = m \cdot \lambda_f \cdot S \cdot \theta_b \cdot \tanh(m \cdot L) \quad (13.5)$$

It is now possible to introduce the fin efficiency η_f , a measure of the capability of the fin to transfer heat with the surrounding fluid; it is defined as *the ratio of the actual fin*

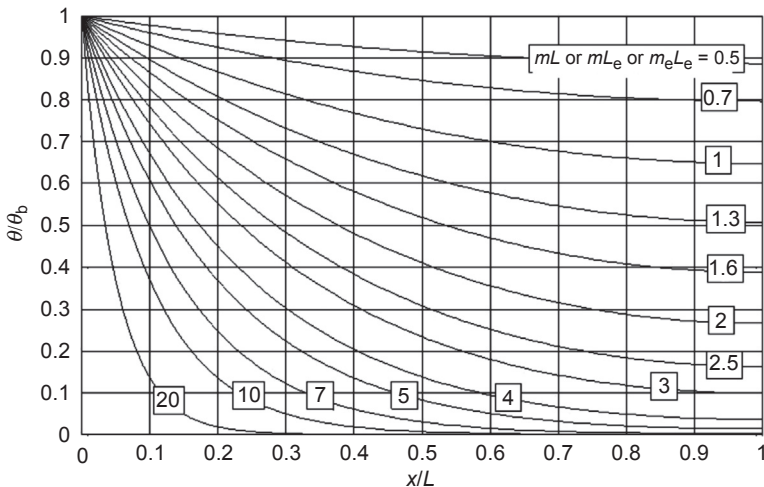


Figure 13.3 Dimensionless excess temperature in a longitudinal constant cross-section fin.

heat transfer rate \dot{Q}_f to the heat rate $\dot{Q}_{f,\max}$ that would exist if the entire fin surface were at the fin base temperature:

$$\eta_f = \frac{\dot{Q}_f}{\dot{Q}_{f,\max}} = \frac{m \cdot \lambda_f \cdot S \cdot \theta_b \cdot \tanh(m \cdot L)}{h \cdot A_f \cdot \theta_b} = \frac{\tanh(m \cdot L)}{m \cdot L} \quad (13.6)$$

It has been shown that the fin tip convective flow rate can be accounted for by using, in Eq. (13.6), in place of the real fin length L , a fictitious fin length L_e (the effective length) defined as $L_e = L + \delta/2$, with quite a good approximation; the convective coefficient related to the fin tip has been assumed equal to that pertinent to the fin flanks. The final expression of general use for the longitudinal fin efficiency is therefore:

$$\eta_f = \frac{\dot{Q}_f}{\dot{Q}_{f,\max}} = \frac{\tanh(m \cdot L_e)}{m \cdot L_e} \quad (13.7)$$

Fig. 13.4 illustrates the pattern of η_f versus the dimensionless group $(m \cdot L_e)$.

For the fin to transfer more heat rate than the prime surface it masks, the condition $\eta_f > S/A_f \approx \delta/(2L_e)$ must be satisfied (the excess temperature of the prime surface is considered the same as for the fin base, that is θ_b).

For other fin shapes, an exact analytical solution is possible only in a few cases under some idealized assumptions, and usually it involves higher mathematics, yielding complicated expressions scarcely useful even for computer calculations; this is, for example, the case for the rectangular cross-section circular radial fin, for which the analytical expression of the fin efficiency η_f involves considering modified Bessel functions; a graphical representation of this solution is given in Fig. 13.5.

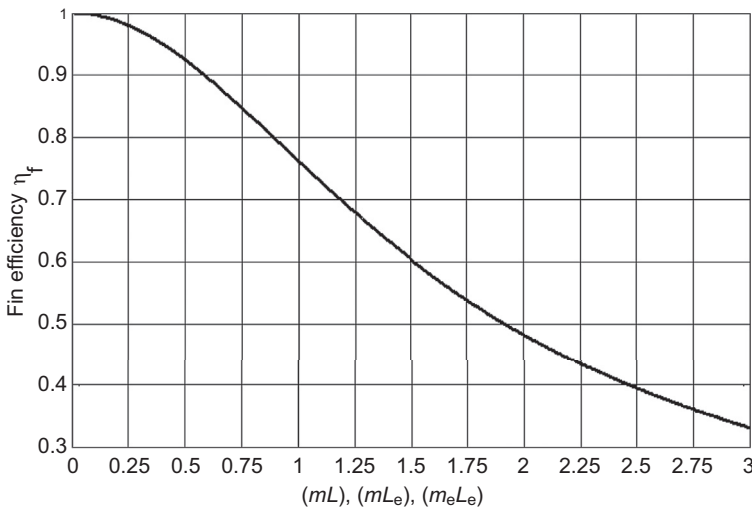


Figure 13.4 Thermal efficiency of a longitudinal constant cross-section fin.

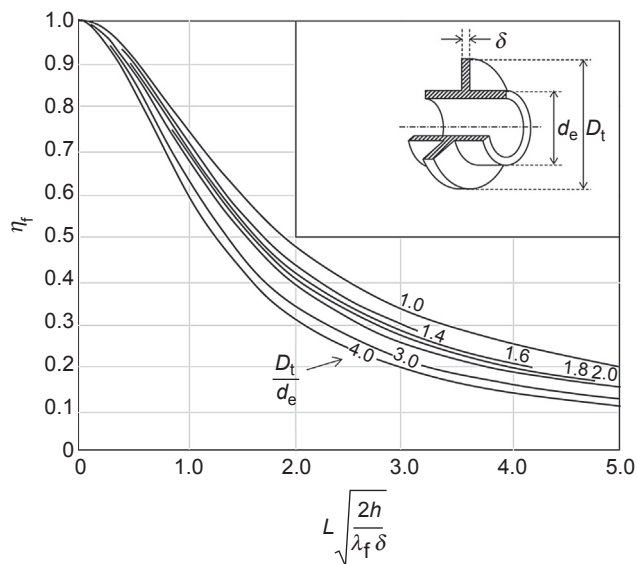


Figure 13.5 Thermal efficiency of a radial circular constant cross-section fin.

To go around this obstacle, simplified solutions are proposed in the technical literature for the approximate calculation of the efficiency of fins of different shapes, under substantially the same assumptions considered previously for the longitudinal rectangular cross-section fin. The method considered in the following consists in the definition, for any relevant fin shape, of fictitious effective values for the fin height L_e and (when applicable) for the fin thickness δ_e to be used to compute, first, an effective value of the dimensional parameter $m_e = \sqrt{2h/(\lambda_f \cdot \delta_e)}$, and then, applying an expression formally identical to the straight rectangular fin solution, to calculate the fin efficiency, with good approximation of the analytical or numerical results:

$$\eta_f = \frac{\tanh(m_e \cdot L_e)}{m_e \cdot L_e} \quad (13.8)$$

Table 13.2 summarizes some relevant results for computing thermal efficiencies of fins of various shapes.

From **Eq. (13.8)** it can be inferred that, at unchanged values of the other parameters, the fin efficiency is higher:

- When the thermal conductivity λ_f of the material it is made of is higher. Fins are usually made of copper or, most often, of aluminum (for cost and weight reasons).
- When the thickness δ_e is higher and the length L_e is lower. About fin thickness, it should be observed that the higher it is, generally the fewer fins can be accommodated on the same prime surface, with less total transfer area enhancement. About fin length, it must be considered that any successive increment in length is less effective in enhancing heat transfer to the surrounding fluid.

Table 13.2 Approximate solutions for fin efficiencies on circular tubes

Longitudinal fins of trapezoid profile	
	<p>Use Eq. (13.8) or (13.10) with: $\delta_e = 0.75 \cdot \delta_r + 0.25 \cdot \delta_t$; $L_e = L + 0.5 \cdot \delta_t$ where δ_r and δ_t ($\delta_r \geq \delta_t$) are the fin thicknesses respectively at the root and at the tip</p>
Transversal constant thickness rectangular fins (Schmidt, 1966)	
	<p>Use Eq. (13.8) or (13.10) with $\delta_e = \delta$ and: $L_e = d_e [0.5(1 + 0.35 \ln \gamma)(\gamma - 1)]$; $\gamma = 1.28 \frac{Y_l}{d_e} \sqrt{\frac{Y_t}{Y_l} - 0.2}$ valid for $1.2 < Y_t/d_e$ and $1 \leq Y_l/Y_t < 2$ Y_l, side in the flow direction; Y_t, side perpendicular to the flow direction δ, uniform fin thickness; d_e, external diameter of the base tube For square fins of side Y, $\gamma = 1.145(Y/d_e)$ For square fins of side $Y = 2d_e$, $L_e = 0.83 \cdot d_e$</p>
Transversal constant thickness circular fins (radial fins) (Schmidt, 1966)	
	<p>Use Eq. (13.8) or (13.10) with $\delta_e = \delta = \delta_r = \delta_t$ and: $L_e = \left(L + \frac{\delta}{2}\right) \left(1 + 0.35 \ln \frac{(2L + d_e)}{d_e}\right)$ valid for $L \leq d_e$ and $(L/\delta) > 2.5$ δ, uniform fin thickness; d_e, external diameter of the base tube; L, fin height</p>

Table 13.2 Continued

Radial fins of trapezoid cross section	
	<p>Use the same equations as for constant thickness radial fins, with $\delta_e = \frac{\delta_r + \delta_t}{2}$ where δ_r and δ_t ($\delta_r \geq \delta_t$) are the fin thicknesses respectively at the root and at the tip</p>
Continuous (adjacent) fins of constant thickness (Shah and Sekulić, 2003; HEDH, 2001; VDI Heat Atlas, 2010)	
	<p>Rough approximation: subdivide the total flat fin surface area equally among all the tubes of the concerned array; compute the fin efficiency using the formulas for a transversal constant thickness radial fin of equal surface area per tube</p> <p>Better approximation: for in-line tube arrangements, spot the rectangular or square portion of the total fin surface area pertinent to each (core) tube; compute the fin efficiency using formulas for constant thickness rectangular fins.</p> <p>For staggered-tube arrangements, the fin surface area pertinent to each (core) tube is an hexagon, for which Eq. (13.8) or (13.10) can be used with $\delta_e = \delta$ and:</p> $L_e = d_e [0.5(1 + 0.35 \ln \gamma)(\gamma - 1)];$ $\gamma = 1.27 \frac{p_t}{d_e} \sqrt{\frac{p_d}{p_t}} - 0.3 \text{ for } p_l \geq \frac{1}{2} p_t$ $L_e = d_e [0.5(1 + 0.35 \ln \gamma)(\gamma - 1)],$ $\gamma = 1.27 \frac{2p_t}{d_e} \sqrt{\frac{p_d}{2p_t}} - 0.3 \text{ for } p_l < \frac{1}{2} p_t$ <p>p_l, p_t, and p_d are respectively the longitudinal, transversal, and diagonal tube pitches, δ is the uniform fin thickness, and d_e is the external tube diameter (Fig. 13.18)</p>

- When the convective heat transfer coefficient h with the surrounding fluid is lower. Finned surfaces are always used with gases at low (for example, ambient air) or moderate pressure and generally on that side of a heat transfer wall that is controlling the overall heat transfer process (the side that displays a far or a significantly higher heat transfer resistance).

By relaxing the assumption of no fouling on the fin surface, [Young and Ward \(1957\)](#), assuming a thin uniform fouling layer deposition on the fin of thermal resistance per unit fin surface area R_{foul} , came out with a modified definition of the fin parameter m_e , to be used when fin fouling is envisaged, as follows:

$$m_e = \sqrt{\frac{2}{(h^{-1} + R_{\text{foul}}) \cdot \lambda_f \cdot \delta}} \quad (13.9)$$

For high longitudinal and transverse radial, rectangular, or continuous fins, experimental evidence suggests modifying the fin efficiency expression (13.8) into ([HEDH, 2001](#)):

$$\eta_f = \frac{\tanh(m_e \cdot L_e)}{m_e \cdot L_e} [1 - 0.058(m_e \cdot L_e)] \quad (13.10)$$

where the term in square brackets corrects for the nonuniform convective heat transfer coefficient along the fin surface.

It is now possible to define the overall efficiency Ω of a finned surface as *the ratio of the heat rate \dot{Q}_t from the total transfer area A [sum of the area associated with the array of fins A_{ft} plus the exposed (uncovered) area of the base (prime) surface A_{pu} , $A = A_{\text{ft}} + A_{\text{pu}}$] and the heat rate $\dot{Q}_{t,\text{max}}$ that would exist if the entire finned surface were at the prime surface temperature*. Assuming uniform equal convective heat transfer coefficient h both for the prime and the fin surfaces, one can write:

$$\Omega = \frac{\dot{Q}_t}{\dot{Q}_{t,\text{max}}} = \frac{A_{\text{pu}} \cdot h \cdot \theta_b + \eta_f \cdot A_{\text{ft}} \cdot h \cdot \theta_b}{A \cdot h \cdot \theta_b} = 1 - \frac{A_{\text{ft}}}{A} (1 - \eta_f) \quad (13.11)$$

and therefore the total heat transfer rate \dot{Q}_t can be expressed referring only to the prime surface temperature t_b :

$$\dot{Q}_t = \Omega \cdot A \cdot h \cdot |(t_{\text{fd}} - t_b)| \quad (13.12)$$

and consequently the finned surface thermal resistance (convective + conductive) is:

$$R_f = \frac{1}{\Omega \cdot A \cdot h} \quad (13.13)$$

as it appears in the general correlations (13.2) and (13.3) for both the internal and the external finned surfaces.

The finned geometry must be optimized, compromising among several appropriate criteria; to name only a few: total heat transfer enhancement, manufacturing complexity and cost, volume and weight of equipment, induced pressure losses for the fluid streams.

It is to be emphasized that sometimes the so-called design convective heat transfer coefficient h_d is presented in some sources of heat transfer data (manuals, manufacturers' technical bulletins, ...), directly derived from experimental tests, which includes the surface thermal efficiency ($h_d = \Omega \cdot h$) for whatever fin material is used; it may include also the penalty for fin contact effect and/or flow maldistribution. Of course, if the original experimental data are to be used with fins with the same geometry but made with a different material, then it is necessary to reduce the original data to calculate h and then the new value of η_f related to the new fin material.

13.2 Heat exchanger basics

A pipe-in-pipe (or tube-in-tube) is perhaps the simplest heat exchanger type, schematically represented in Fig. 13.6: one fluid stream flows inside the inner pipe, and the second fluid flows in the annulus formed by the two coaxial pipes. As shown in Fig. 13.6, two different basic flow configurations can be realized in this apparatus: in the counter-flow configuration the two fluids flow parallel to each other but in opposite directions, whereas in the parallel-flow configuration the two fluids flow in the same direction. The same Fig. 13.6 shows schematically the different temperature profiles of the two single-phase fluid streams along the heat exchanger, both in counter-flow and in parallel-flow configuration, whereas their inlet temperatures are assumed the same. It is immediately evident, at least for the case illustrated in Fig. 13.6, that the counter-flow configuration is more efficient, in that it makes the best use of the available temperature difference and obtains the highest change in temperature of each fluid. On the other hand, it is immediately evident too that, should at least one fluid keep at constant temperature along the heat transfer process (isobaric condensation or evaporation of a pure fluid), the two flow configurations bring about the same result, that is, they are equally efficient.

Under the same assumptions set forth at the beginning of the previous section, the first law of thermodynamics (no shaft work and negligible kinetic energy variations for the two fluid streams) for the total heat transfer rate \dot{Q} leads to the following balance equations:

$$\dot{Q} = \dot{M}_h \cdot (h_{h,in} - h_{h,out}) = \dot{M}_c \cdot (h_{c,out} - h_{c,in}) \quad (13.14)$$

and for no phase change in the exchanger,

$$\dot{Q} = \dot{M}_h \cdot \bar{c}_h \cdot (t_{h,in} - t_{h,out}) = \dot{M}_c \cdot \bar{c}_c \cdot (t_{c,out} - t_{c,in}) \quad (13.15)$$

Note that in Eq. (13.14) the symbol h is used for the specific enthalpy of the fluids.

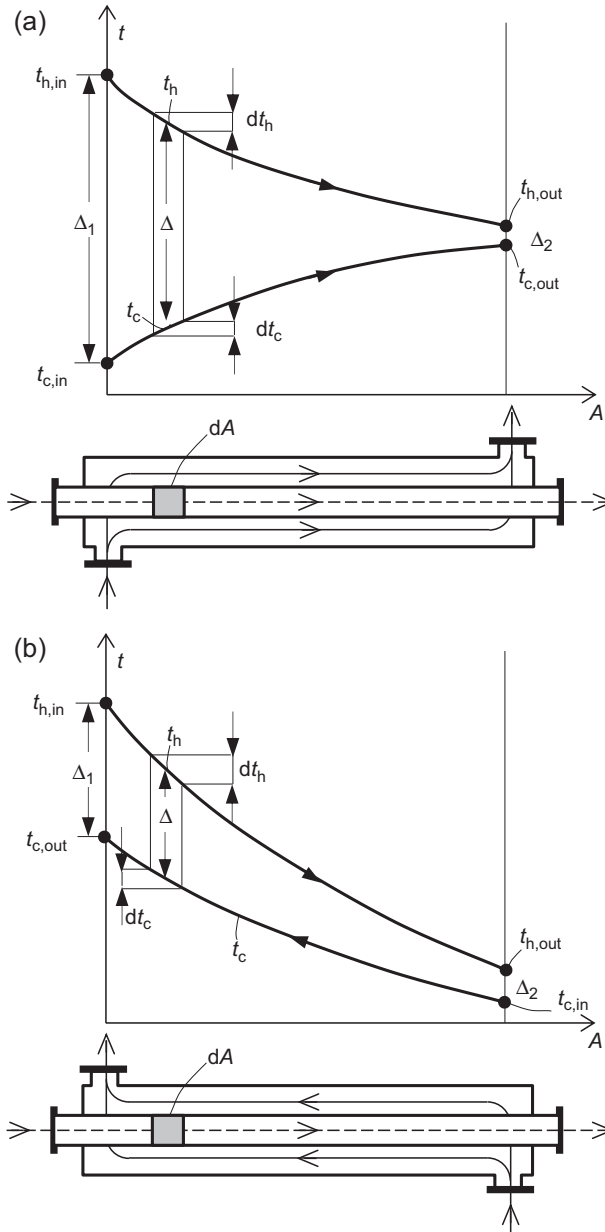


Figure 13.6 Temperature profiles in tube-in-tube heat exchangers (parallel flow and counter flow). (a) Cocurrent and (b) counter-current.

For the situation represented in Fig. 13.6, the local temperature difference between the two fluid streams $\Delta = t_h - t_c$ changes continuously along the heat transfer surface of the apparatus; the local elemental heat flow rate can be expressed as $d\dot{Q} = U \cdot dA \cdot \Delta$. When the overall heat transfer coefficient U keeps constant along the entire heat

transfer surface, and the specific heat capacities c_h and c_c of the two fluids can be considered constant in the relative temperature ranges, then the temperature difference Δ along the heat transfer surface varies according to the expression:

$$\Delta = \Delta_1 \cdot e^{-U \cdot M \cdot Ax} \quad (13.16)$$

where $M = (\frac{1}{C_h} - \frac{1}{C_c})$ for the counter-flow configuration and $M = (\frac{1}{C_h} + \frac{1}{C_c})$ for the parallel-flow configuration, Δ_1 is the temperature difference between the hot and the cold fluid at the end of the apparatus where the hot fluid enters the exchanger (Δ_2 is the temperature difference at the opposite end of the exchanger), and Ax is the heat transfer area from end 1 to the position considered. The same expression can be used when one fluid stream changes phase isothermally in the entire exchanger, by setting $1/\dot{C} = 0$ for this fluid.

Under the same assumptions it is possible to compute the total heat flow rate \dot{Q} transferred in the exchanger by the following rate equation:

$$\dot{Q} = U \cdot A \cdot \overline{\Delta t} \quad (13.17)$$

where $\overline{\Delta t}$ is the effective mean temperature difference. It can be easily shown that, with the assumptions put forward, for both the counter-flow and the parallel-flow configurations the value of the mean effective temperature difference can be calculated from the values Δ_1 and Δ_2 as follows:

$$\overline{\Delta t} = \frac{\Delta_1 - \Delta_2}{\ln(\Delta_1/\Delta_2)} = \Delta t_{LM} \text{ (logarithmic mean temperature difference : LMTD)} \quad (13.18)$$

This same expression holds true when one fluid stream evolves at constant temperature in the exchanger (isobaric condensation or evaporation of a pure fluid).

Owing to the symbols definition chosen, Eq. (13.17) is the same for both parallel flow and counter flow, but it should be remarked that the end Δt 's are different in the two cases, and therefore the final expressions are as follows:

$$\text{counter - flow: } \overline{\Delta t} = \Delta t_{LM,c-f} = \frac{(t_{h,in} - t_{c,out}) - (t_{h,out} - t_{c,in})}{\ln \frac{(t_{h,in} - t_{c,out})}{(t_{h,out} - t_{c,in})}}; \quad (13.19)$$

$$\text{parallel - flow: } \overline{\Delta t} = \Delta t_{LM,p-f} = \frac{(t_{h,in} - t_{c,in}) - (t_{h,out} - t_{c,out})}{\ln \frac{(t_{h,in} - t_{c,in})}{(t_{h,out} - t_{c,out})}} \quad (13.20)$$

Once the inlet and outlet temperatures of both fluid streams are consistently fixed, it can be observed that it is always $\Delta t_{LM,c-f} \geq \Delta t_{LM,p-f}$, where the equal sign holds only when one fluid stream evolves at a constant temperature in the exchanger, a situation

for which the two flow configurations are equally effective. Further, unlike the counter-flow configuration when both fluids change temperature in the apparatus, the parallel-flow configuration does not allow the cold fluid to be heated above the exit temperature of the hot fluid: this would make it negative the argument of the logarithm of Eq. (13.20) and would obviously be a violation of the second law of thermodynamics.

The logarithmic mean temperature difference is always less than the arithmetic mean temperature difference $\Delta t_{AM} = \frac{\Delta_1 + \Delta_2}{2}$; it is anyway easy to show that, if $0.62 \leq \Delta_1/\Delta_2 \leq 1.6$, then employing Δt_{AM} in place of Δt_{LM} brings about an error not exceeding 2%.

For the counter-flow configuration, when the flow heat capacities of the two fluid streams are equal, that is $\dot{C}_h = \dot{C}_c$, it results in $\Delta_1 = \Delta_2$; in this case clearly $\Delta t = \Delta_1 = \Delta_2$. The same result holds when both fluid streams evolve isothermally in the exchanger, no matter what the flow configuration is.

Counter flow and parallel flow are not the only possible flow configurations in a heat transfer apparatus. For example shell-and-tube heat exchangers (S&THXs) enable the realization of other flow configurations, in addition to counter flow and parallel flow. Such an exchanger is schematically represented in Fig. 13.7: quite a lot of small-diameter tubes (the tube bundle) can be accommodated in-line within a single much larger surrounding tube, dubbed the shell. Suitable subdivided headers usually at both ends of the shell distribute the tube-side fluid into the tubes. In this way, the tube-side fluid can cross the shell back and forth several times, whereas for the shell-side fluid a single pass through the shell is by far the most common arrangement; hairpin tubes (U-tubes) can also be used, with no baffled header at one end of the shell. In this way, within a single shell, a heat exchanger may combine both counter-flow and parallel-flow arrangements; it is to be observed that the presence of crosswise baffles of different shapes in the bundle does not substantially alter this somewhat idealized point of view. S&THXs are usually named according to the number of shell passes followed

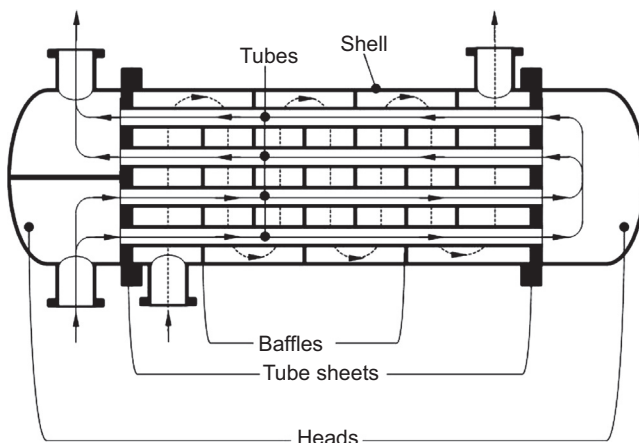


Figure 13.7 Shell-and-tube heat exchanger type 1–2.

by the number of tube passes; a 1–4 shell-and-tube exchanger is so arranged as to display one shell pass for the “external fluid” and four tube passes for the “internal fluid”. By far the most common situation is to have an even number of tube passes.

The temperature change pattern of shell-and-tube exchangers with dissimilar shell-and-tube passes is obviously of neither full counter-flow nor full parallel-flow type, except for the case when at least one of the fluids evolves isothermally in the entire exchanger, when all flow configurations give rise to the same temperature change pattern. With the additional assumption that the transfer area is equally distributed among all the tube passes, it is still possible to determine a suitable value of the mean average effective temperature difference $\overline{\Delta t}$ such that the total heat transfer flow rate can again be expressed by Eq. (13.17); $\overline{\Delta t}$ is somewhat between the values pertinent to the counter-flow and the parallel-flow (if compatible) configurations with the same end temperatures of the two fluids.

It is standard procedure to define a temperature correction factor, defined as $F_t = \overline{\Delta t} / \Delta t_{LM,c-f}$, where $\Delta t_{LM,c-f}$ is the log-mean temperature difference calculated as for the case of true counter flow with the same end temperatures for the two fluids, and F_t , usually given in graphs or, rarely, as an algebraic expression, for any flow configuration is a function of the two parameters R and P defined as:

$$R = \frac{\dot{C}_c}{\dot{C}_h} = \frac{(t_{h,in} - t_{h,out})}{(t_{c,out} - t_{c,in})}; \quad P = \frac{(t_{c,out} - t_{c,in})}{(t_{h,in} - t_{c,in})} \quad (13.21)$$

An example of a graphical representation of F_t is given in Fig. 13.8 for the multipass flow configuration 1–2; as it is often the case, the graph is the same irrespective of which fluid flows tube-side or shell-side. Without appreciable errors the same graph can be employed for the multipass configurations 1–4, 1–6, ..., that is, for any

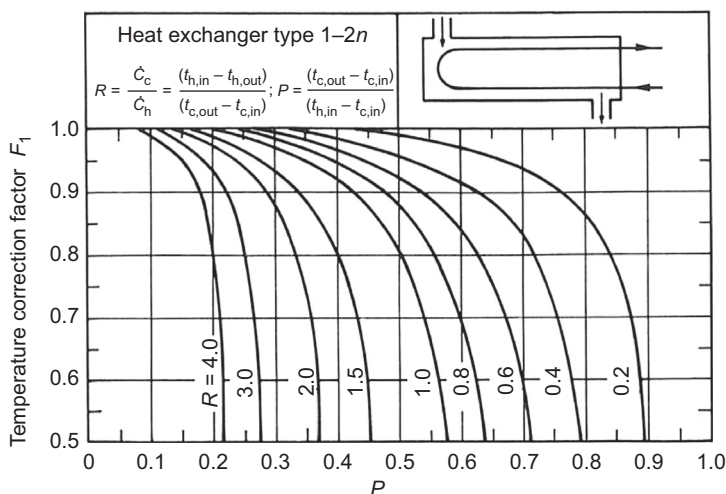


Figure 13.8 Temperature factor F_t for heat exchangers type 1–2n.

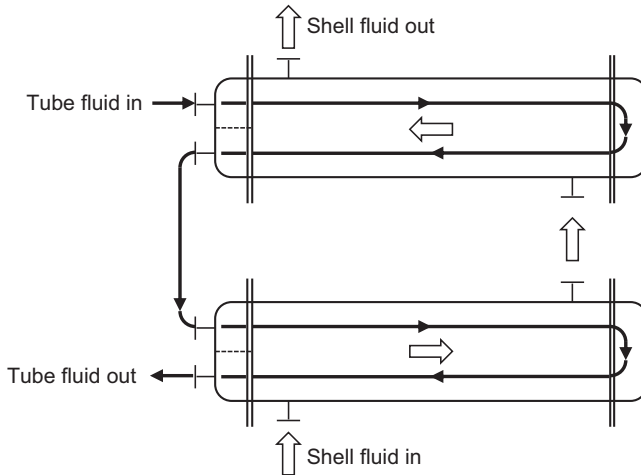


Figure 13.9 Two 1–2 shell-and-tube heat exchangers connected in series.

flow configuration with one shell pass and an even number of tube passes, and therefore the graph in Fig. 13.8 is marked 1–2 n . The same holds true for configurations dubbed 2–4 n , 3–6 n , ..., where, as told before, rather than having two or three fluid passes in the same shell, it is often preferred to connect in series two or three shell-and-tube exchangers of the 1–2 n type, as shown in Fig. 13.9; note that the two fluids should enter (and consequently leave) the series-connected shells at the two extreme ends, so to better approach full counter flow for better exploitation of the driving temperature difference; usual graphs or formulas found in textbooks or manuals are given for this situation. Of course S&THXs with equal numbers of shell-and-tube passes, as well as series-connected 1–1 exchangers, can enable both the counter-flow and the parallel-flow configuration, and these cases can be treated, as far as the temperature change pattern is concerned, like the pipe-in-pipe exchangers; shell-side fluid is always considered perfectly mixed in all thermal pattern derivations considered above.

It is common practice to take $F_t = 0.8$ as the lower limit for a heat exchanger to be conveniently used in a given application; should $F_t < 0.8$ result when designing a heat exchanger, a different flow configuration, closer to counter flow, should be considered.

When one gas stream at ambient or moderate pressure flows in a heat exchanger, generally the structured or compact surface needed in this case for an efficient heat transfer calls for cross-flow pattern configurations, which can be single or multipass, as for example schematically depicted in Fig. 13.10 for a typical gas heater.

Two ideal limit situations for both fluid streams must then be considered: the mixed case, when it can be assumed that the surface conformation permits perfect fluid mixing normal to the main flow direction and therefore the fluid temperature is uniform perpendicularly and varies only along the main direction of motion, and the perfectly unmixed case, when it can be assumed in the limit that the fluid is fully prevented from mixing normal to the main flow direction; in this case the fluid exit temperature is intended as the adiabatic mixed fluid temperature at the heat exchanger outlet. These

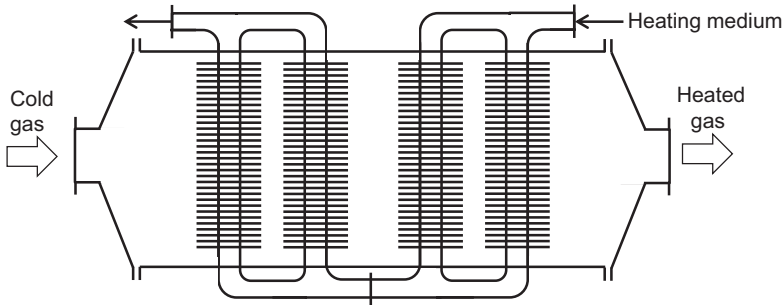


Figure 13.10 Sketch of a cross-flow heat exchanger (gas heater).

two extreme situations clearly give rise to different temperature change patterns, and generally the unmixed situation brings about a better thermal performance.

Even in the case of single or multipass cross-flow configurations, with the relevant assumption that the flow of both fluids is evenly distributed over the total flow area, it is possible to express the total heat transfer rate in the exchanger by relationship (13.17), where the appropriate value of the mean effective temperature difference is again calculated making use of the suitable temperature correction factor F_t (again a function of parameters R and P and of the flow configuration) to the logarithmic mean temperature difference for the ideal counter-flow configuration $\Delta t_{LM,c-f}$. For multipass unmixed arrangements, two extreme situations must further be considered, according to what can be assumed for the fluid between passes: either complete mixing or no mixing at all. Again the flow configuration does not play any role with respect to the temperature change pattern, should at least one fluid evolve isothermally in the entire exchanger.

Ultimately, under the assumptions set forth, it is always possible to express the total heat flow rate transferred in the exchanger by means of the transfer equation:

$$\dot{Q} = U \cdot A \cdot F_t \cdot \Delta t_{LM,c-f} \quad (13.22)$$

This approach, in heat exchanger design theory, is given the name of the F -correction factor method; it lends itself well to handling heat exchanger design problems, such as to determine the necessary transfer area A , given U , \dot{C}_c , \dot{C}_h , and the terminal fluids temperatures. Not so much for rating (sizing) problems, such as to determine the fluid exit temperatures given U , A , \dot{C}_c , and \dot{C}_h and the inlet fluid temperatures: in this case, with the exception of the trivial cocurrent flow configuration, the F -correction factor approach would require a trial-and-error solution procedure.

A more general approach of heat exchanger design theory is the so-called ε -NTU method: ε stands for thermal effectiveness of the heat exchanger, and NTU stands for number of transfer units.

The efficiency factor of the exchanger, effectiveness ε , is defined as follows, for streams without phase change:

$$\varepsilon = \frac{\dot{Q}}{\dot{Q}_{\max}} = \frac{\dot{C}_h (t_{h,in} - t_{h,out})}{\dot{C}_{\min} (t_{h,in} - t_{c,in})} = \frac{\dot{C}_c (t_{c,out} - t_{c,in})}{\dot{C}_{\min} (t_{h,in} - t_{c,in})} \quad (13.23)$$

where \dot{Q} is the actual heat rate transferred in the exchangers, and \dot{Q}_{\max} is the maximum heat rate that would be possible to transfer between two streams of fluid with the same heat capacity rates and inlet temperatures, in an ideal exchanger, this being an exchanger in perfect counter-flow configuration and with infinite transfer area. It is immediately recognized that the maximum possible heat transfer rate \dot{Q}_{\max} is that which would cause the stream with the smaller heat capacity rate, henceforth dubbed \dot{C}_{\min} , to leave the exchanger at the inlet temperature of the other stream. For the case when only one of the fluid streams evolves at constant temperature in the entire exchanger, the same definition of thermal effectiveness holds good, and \dot{C}_{\min} refers to the stream without change of phase; in Eq. (13.23) the member involving the heat capacity rate of the fluid with change of phase becomes indeterminate. The trivial case with isothermal change of phase for both fluid streams cannot be treated by this approach.

Finally the NTU for a transfer process in a heat exchanger and the capacity rate ratio r are defined as follows:

$$\text{NTU} = \frac{U \cdot A}{\dot{C}_{\min}}; \quad r = \frac{\dot{C}_{\min}}{\dot{C}_{\max}} \quad (13.24)$$

where \dot{C}_{\min} and \dot{C}_{\max} are respectively the smaller and the larger of the two magnitudes \dot{C}_h and \dot{C}_c ; $r = 0$ for the case of isothermal change of phase of one of the fluid streams.

Under the same assumptions made when treating the F -correction factor approach, it is generally possible for any flow configuration to express the thermal effectiveness ε as a function of the NTU and the capacity rate ratio r :

$$\varepsilon = f(\text{NTU}, r, \text{flow configuration}) \quad (13.25)$$

These correlations are reported, in the form of graphs and/or equations (sometimes approximate expressions), in heat exchanger textbooks and manuals; some of them, for the most important flow configurations pertinent to the subject of this book, are also given in the following.

For the two extreme cases of ideal flow configurations, that is, cocurrent (parallel) flow and counter-current flow, it is easy to find the exact analytical expressions for the functional dependence (13.25). The results are:

$$\text{Parallel-flow: } \varepsilon_{p-f} = \frac{1 - e^{-\text{NTU}(1+r)}}{1 + r} \quad (13.26)$$

$$\text{Counter-flow}(r < 1): \varepsilon_{c-f} = \frac{1 - e^{-\text{NTU}(1-r)}}{1 - r \cdot e^{-\text{NTU}(1-r)}}; \quad (13.27)$$

$$\text{Counter-flow}(r = 1): \varepsilon_{c-f} = \frac{\text{NTU}}{\text{NTU} + 1}$$

It should be observed that the condition $r = 1$ yields $(t_{h,\text{in}} - t_{h,\text{out}}) = (t_{c,\text{out}} - t_{c,\text{in}})$, that is, in counter-flow $\Delta_1 = \Delta_2$: under the assumption of constant specific heat

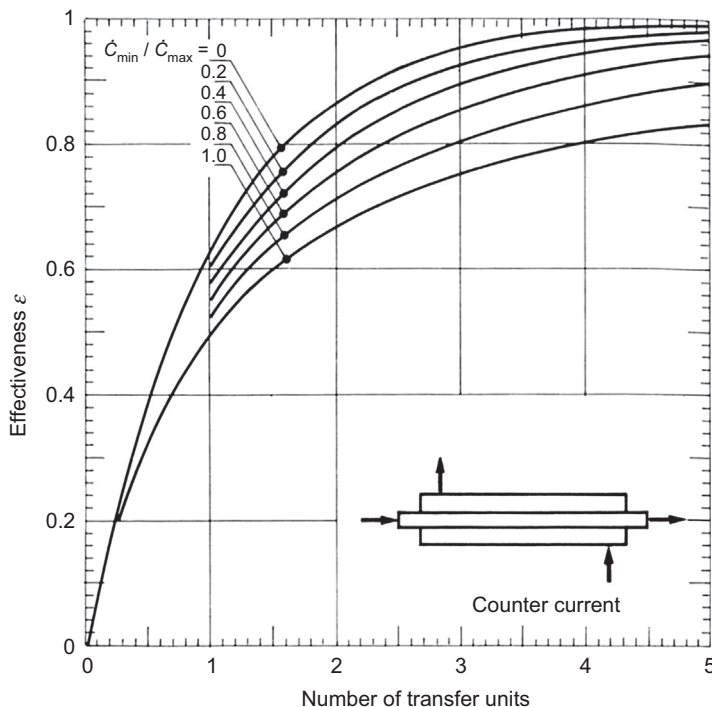


Figure 13.11 Effectiveness ε versus number of transfer units NTU for a counter-flow heat exchanger.

capacities for the two fluids, this means that the local temperature difference Δ keeps constant throughout the entire heat transfer surface.

Figs. 13.11–13.16 present the graphs of effectiveness ε on the vertical axis versus NTU on the abscissa with the capacity rate ratio r as the parameter of the various curves, for the most common heat-exchanger flow configurations. As can be inferred from the graph in Fig. 13.16, unlike for all the other cases considered in the previous figures, the mixed–unmixed cross-flow configuration is stream asymmetric, that is, the exchanger effectiveness ε (and the temperature correction factor F_t too) does not remain invariant by switching sides of the two fluid streams. Most exchangers considered in the following are stream symmetric.

From the graphs presented, some important conclusions can be drawn, not limited only to the flow configurations expressly examined:

- For the borderline case $r = 0$ all the flow configurations give the same value for the thermal effectiveness in relation to the NTU fulfilled:

$$\text{All flow configurations, } r = 0 \rightarrow \varepsilon = 1 - e^{-NTU} \quad (13.28)$$

This is the important case of condensation or boiling/evaporation of the ORC working fluid (a pure substance or an azeotropic mixture) in condensers and evaporators/boilers,

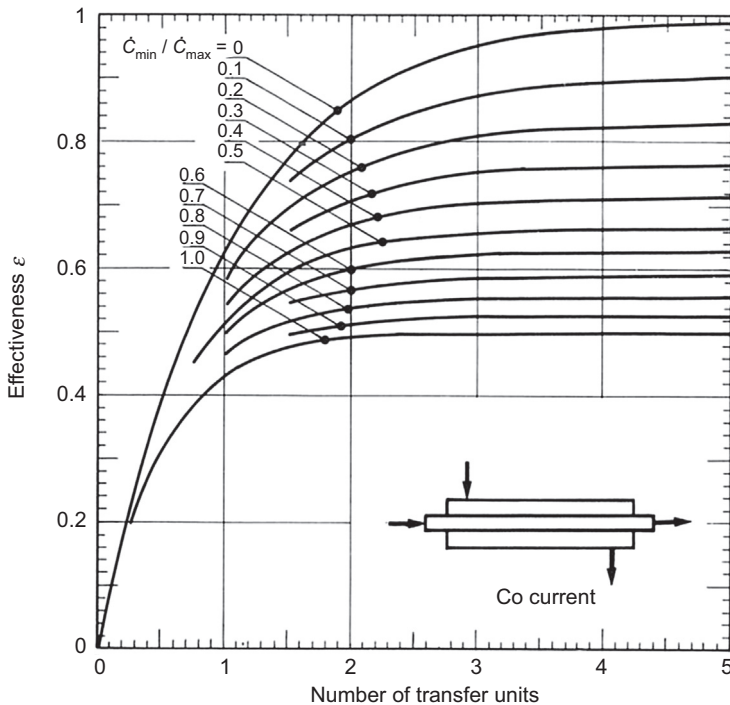


Figure 13.12 Effectiveness ε versus number of transfer units NTU for a parallel-flow heat exchanger.

when pressure variations can be neglected. It is to be considered that often in these apparatuses the heat transfer process is not limited only to change of phase, but also involves liquid heating or subcooling, or vapor superheating or desuperheating.

- For $0 < r \leq 1$ generally the effectiveness increases at increasing NTU for all values of r ; this fact, seemingly obvious and indeed true for all flow configurations considered in the graphs of Figs. 13.11–13.16, is not of general soundness: some particular flow configurations, such as cross flow with both fluids mixed, exhibit local conditions under which, at constant r , the effectiveness ε decreases with increasing NTU.
- At the same values of NTU and of the capacity rate ratio r , for any different flow configuration, the thermal effectiveness ε is always less ($r \neq 0$, $\text{NTU} \neq 0$) than the effectiveness obtained with the counter-flow configuration and larger than that obtainable with a parallel-flow configuration. The deviation from the effectiveness of the counter-flow configuration generally increases at increasing both r and NTU.
- It can be observed that the case $r = 1$ ($\dot{C}_h = \dot{C}_c$) is the most critical as far as the influence of the exchanger flow configuration on the process effectiveness is concerned; it is where, at the same value of NTU, the effectiveness values ε fall more apart from one another depending on the flow configurations. The graph in Fig. 13.17 shows for comparison the trends of ε versus NTU at $r = 1$ for all the flow configurations considered in the preceding graphs.
- For $\varepsilon < \sim 0.4$ the flow configuration does not have a big influence on the required NTU. At capacity rate ratio $r = 1$ (worst case for this comparison), the counter-flow configuration

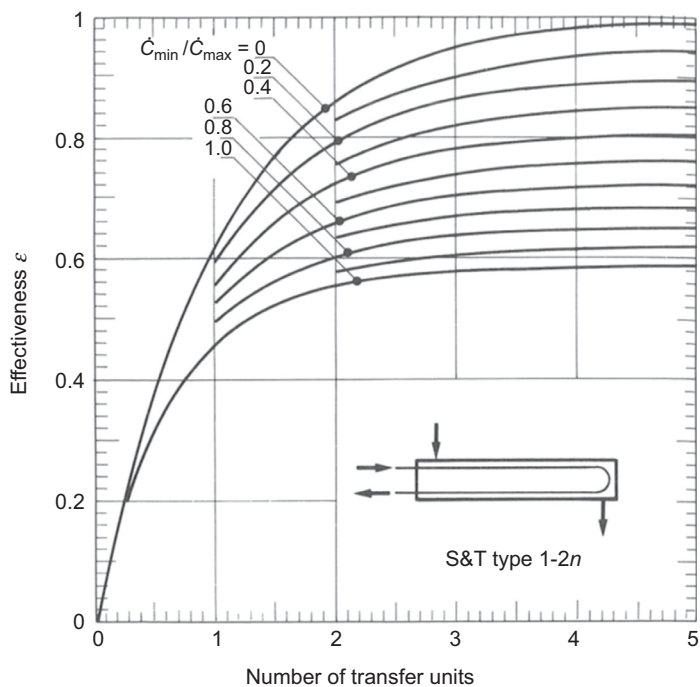


Figure 13.13 Effectiveness ε versus number of transfer units NTU for a 1–2 n heat exchanger. S&T, shell and tube.

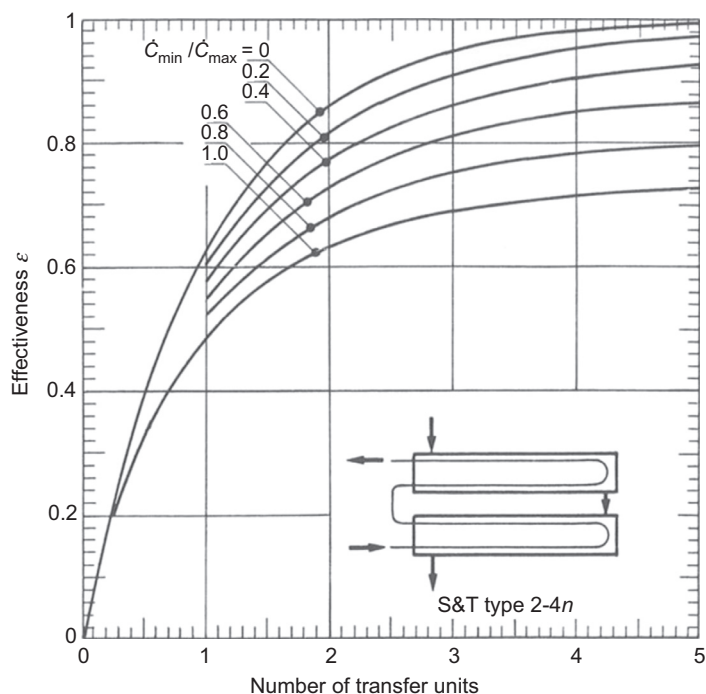


Figure 13.14 Effectiveness ε versus number of transfer units NTU for a 2–4 n heat exchanger. S&T, shell and tube.

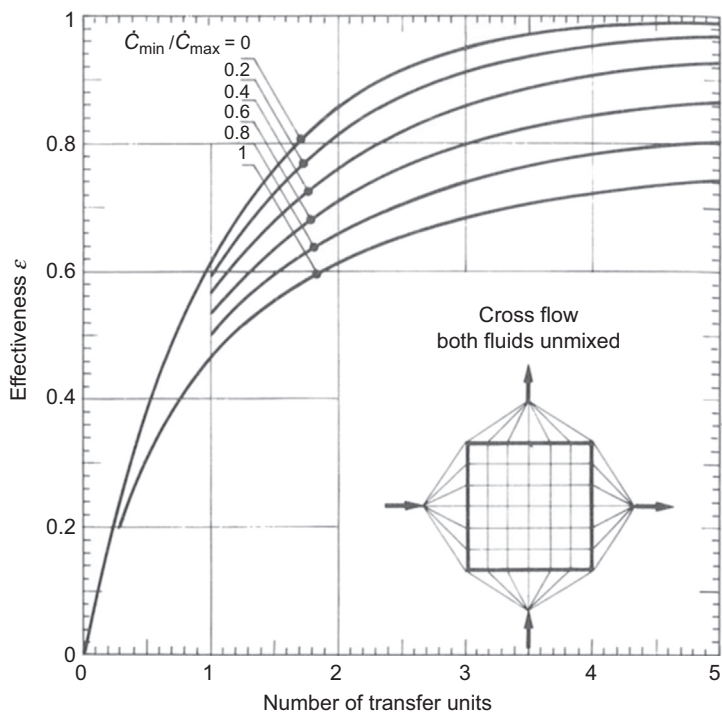


Figure 13.15 Effectiveness ε versus number of transfer units NTU for an unmixed–unmixed cross-flow heat exchanger.

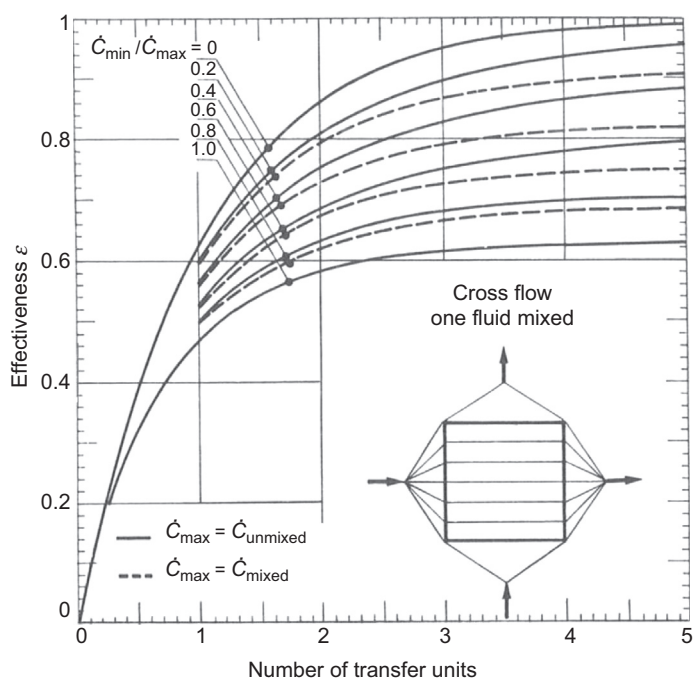


Figure 13.16 Effectiveness ε versus number of transfer units NTU for an unmixed–mixed cross-flow heat exchanger.

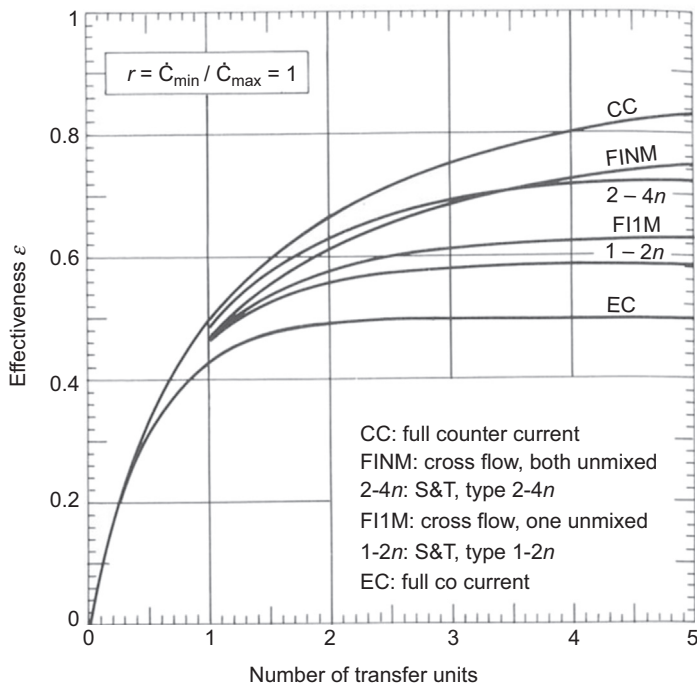


Figure 13.17 Effectiveness ε versus number of transfer units NTU for heat exchangers of different flow configurations at $r = \dot{C}_{\min}/\dot{C}_{\max} = 1$. S&T, shell and tube.

requires 0.67 transfer units, versus 0.80 for the cocurrent configuration, that is, at equal overall heat transfer coefficient U , a heat transfer surface 20% larger.

- It is to be mentioned that, because of the asymptotic nature of the $\varepsilon - \text{NTU}$ curves, when the value of the effectiveness ε is not far from the limit pertinent to the flow configuration considered, a small increase in ε can be obtained only at the expense of a considerable increase in NTU, that is in heat exchanger size.

The $\varepsilon - \text{NTU}$ method lends itself to a straightforward solution for both of the elementary problems of heat exchanger design theory, under the somewhat restrictive assumption set forth at the beginning of this section: sizing and rating.

Sizing: Given $\dot{C}_h, \dot{C}_c, t_{h,\text{in}}, t_{c,\text{in}}, U, A$, one can determine the required A . The effectiveness ε and the capacity rate ratio r can then be readily calculated; from the appropriate graph, the necessary number of heat transfer units NTU can then be evaluated, and finally the required heat transfer area is obtained from $A = \text{NTU} \cdot \dot{C}_{\min}/U$.

Rating: Given $\dot{C}_h, \dot{C}_c, t_{h,\text{in}}, t_{c,\text{in}}, U, A$, and the chosen flow configuration, one can determine the fluid outlet temperatures $t_{h,\text{out}}$ and $t_{c,\text{out}}$. The NTU and the capacity rate ratio r can be readily calculated. The effectiveness ε can then be readily computed from the appropriate graph or equation. The total heat flow rate can now be computed from the rate equation $\dot{Q} = \varepsilon \cdot \dot{C}_{\min} \cdot (t_{h,\text{in}} - t_{c,\text{in}})$, and subsequently the fluid outlet temperatures from $t_{h,\text{out}} = t_{h,\text{in}} - \dot{Q}/\dot{C}_h$ and $t_{c,\text{out}} = t_{c,\text{in}} + \dot{Q}/\dot{C}_c$.

Another useful feature of the ε – NTU method is that, when in a given heat exchanger the inlet fluid temperatures change from the design values and the quantities \dot{C}_h , \dot{C}_c , and U can be considered unmodified, the thermal effectiveness also stays unchanged and the new (steady-state) fluid exit temperatures can be immediately calculated accordingly.

13.3 Heat transfer and pressure drop in pipe flow

Heat transfer. As dictated by the theory of dimensional analysis, forced-convection heat transfer data in ducted flow without change of phase can be expressed by correlations involving three main dimensionless groups made up of all the base physical quantities playing a role in this phenomenon:

- the Nusselt number $Nu = \frac{h \cdot \ell}{\lambda}$, which comprises the convective heat transfer coefficient (local h or averaged over the entire heat transfer surface \bar{h}); it is the parameter one is generally looking for when designing or rating heat exchangers; it can be readily obtained once the relative Nusselt number has been calculated;
- the Reynolds number $Re = \frac{\rho \cdot w \cdot \ell}{\mu}$, a well-known fundamental parameter in flow dynamics;
- the Prandtl number $Pr = \frac{c_p \cdot \mu}{\lambda}$, which is a property of the fluid; for many common gases Pr is around 0.7, with moderate variations with both temperature and pressure.

The characteristic length ℓ appearing in both Nu and Re identifies the particular element within its similitude family. For flow inside ducts, it is usually chosen as the inner diameter $\ell \equiv d_i$ in the case of pipes of circular cross section. For pipes of different cross-section shape, it is most often the so-called hydraulic diameter (at times dubbed equivalent diameter) defined as $d_h = \frac{4a}{P_{\text{wet}}}$, where a is the flow cross-section area and P_{wet} the wet perimeter. Note that for a circular pipe $d_h = d_i$, whereas for an annulus it is $d_h = d_{\text{ei}} - d_{\text{ie}}$, the difference between the internal diameter of the external tube and the external diameter of the internal tube.

Other dimensionless quantities may appear in the mentioned correlations, to take into account specific effects, such as variable fluid properties, surface roughness, entrance effects,

The functional correlations among the dimensionless groups, presented in mathematical form, in some simple cases can be of theoretical derivations; most of the time they are of semiempirical origin, obtained by fitting sets of experimental data, limited to specified ranges for the independent dimensionless variables, to obtain simple mathematical expressions.

In ordinary straight pipes of circular cross section and in transition ($2300 < Re \leq 10,000$) or fully turbulent flow ($Re > 10^4$), by far the most common situation for heat exchangers of interest in this context, the Nusselt number \overline{Nu} referred to the value of \bar{h}_i averaged on the full tube inside transfer area can reliably be calculated by the Gnielinski correlation:

$$\overline{Nu} = \frac{(f/8)(Re - 1000)Pr}{1 + 12.7\sqrt{(f/8)}(Pr^{2/3} - 1)} \left[1 + \left(\frac{d_i}{Z} \right)^{2/3} \right] \quad [\ell \equiv d_i] \quad (13.29)$$

where f is the Moody friction factor for smooth pipes calculated by making use of the Filonenko correlation:

$$f = (1.82 \log_{10} Re - 1.64)^{-2} [\ell \equiv d_i] \quad (13.30)$$

The Gnielinski correlation is recommended within the following ranges for the independent variables:

$$0 < d_i/Z < 1, 0.6 < Pr < 2000, 2300 < Re < 10^6$$

The term of Eq. (13.29) in square brackets accounts for the entrance effect, where the fluid flow boundary layer is under thermal and hydrodynamic development.

Fluid properties in Eq. (13.29) are to be evaluated at the mean bulk condition between pipe entrance and exit. For large variations in the fluid physical properties, a multiplying correction factor CF can be applied to results obtained from correlation (13.29), as follows:

- for liquids: $CF = (Pr/Pr_w)^{0.11}$ (Pr evaluated at mean bulk fluid temperature, Pr_w at related wall temperature), valid for $(0.1 < Pr/Pr_w < 10)$;
- for gases: $CF = (T/T_w)^n$ [$n = 0$ if the gas is cooled; n depends on the type of gas, for heated gases, as specified in VDI Heat Atlas (2010)]; T is the absolute mean bulk gas temperature, T_w is the absolute related wall temperature].

For straight smooth circular tubes and turbulent flow, alternatively the simpler, but less accurate than Eq. (13.29), Dittus–Boelter correlation can be applied,

$$\overline{Nu} = 0.023 Re^{0.8} \cdot Pr^n \quad (13.31)$$

$$(\ell \equiv d_i; Re > 10,000; (Z/d_i) > 60; n = 0.3 \text{ for cooling; } n = 0.4 \text{ for heating})$$

where all fluid properties must be evaluated at the fluid mean temperature.

For smooth straight concentric annuli, according to Petukhov and Rozien as reported in Section 2.5.1 of HEDH (2001), the heat transfer coefficient can be obtained by a modification of Eq. (13.29) calculated using the hydraulic diameter $d_h = (d_{ei} - d_{ie})$ as the characteristic length ℓ to evaluate \overline{Nu} and Re , using d_h for d_i in the term (d_i/Z) and multiplying the result by a function of the diameter ratio (d_{ei}/d_{ie}) dependent on the boundary condition considered. For the relevant case of heat transfer only on the inner wall (outer wall isolated), it is:

$$\frac{\overline{Nu}_{\text{annulus}}}{\overline{Nu}_{\text{tube}}} = 0.86 \left(\frac{d_{ei}}{d_{ie}} \right)^{-0.16} \quad (13.32)$$

For smooth straight noncircular ducts in turbulent flow, as a rough approximation, the same correlations considered earlier for smooth straight circular tubes can be employed, by using the hydraulic diameter d_h of the duct in evaluating Nu , Re , and (d_i/Z) .

Correlations for computing the convective heat transfer coefficient in laminar or transition flow in ducts for different boundary conditions can be found in [HEDH \(2001\)](#) and [VDI Heat Atlas \(2010\)](#).

Pressure drop. In-pipe single-phase flow heat transfer can be enhanced with associated pressure drop penalization, by using internal finned surfaces or pipe inserts, such as twisted tapes or other turbulators of different shapes ([Shah and Sekulić, 2003](#)).

Frictional pressure drop for a fluid without change of phase in developed turbulent flow inside a straight duct can be computed by the classical expression:

$$\Delta p_{\text{frict}} = f \frac{Z}{d_h} \rho \frac{w^2}{2} \quad (13.33)$$

where density ρ and mean velocity w are evaluated at mean condition between inlet and outlet. The Moody friction factor f must not be confused with the Fanning friction factor, of frequent use in the United States, four times smaller. For smooth ducts (as ducts in drawn brass or copper can be considered, except when the inner diameter is on the order of 2 mm or less—minitubes) the friction factor f is a function of the sole Reynolds number Re and can be computed by the Blasius correlation:

$$f = \frac{0.3164}{Re^{0.25}} \quad (13.34)$$

$$(\ell \equiv d_h; 3,000 < Re < 100,000)$$

For rough ducts the friction factor depends additionally on the value of the so-called relative roughness $e_r = \frac{h_r}{d_h}$, where h_r is the equivalent absolute mean roughness height of the duct surface; a few values are presented in [Table 13.3](#). In this case the friction factor can be computed by the Colebrook–White implicit equation:

$$\frac{1}{\sqrt{f}} = -2 \log_{10} \left[\frac{2.51}{Re \cdot \sqrt{f}} + \frac{e_r}{3.71} \right] \quad (13.35)$$

$$(\ell \equiv d_h; 4,000 < Re < 10^8; 0 < e_r \leq 0.05)$$

When approximately $Re > 3500/e_r$, the flow is completely controlled by roughness, and f is independent of the Reynolds number. Then the Prandtl–von Kármán equation can be used:

$$\frac{1}{\sqrt{f}} = 1.14 + 2 \log_{10}(e_r) \quad (13.36)$$

Table 13.3 Absolute pipe roughness h_r

Surface material	Absolute roughness (m)
Aluminum, lead	$0.001\text{--}0.002 \times 10^{-3}$
Drawn brass, drawn copper	0.0015×10^{-3}
PVC, plastic pipes	0.0015×10^{-3}
Stainless steel	0.0015×10^{-3}
Steel, commercial pipes	$0.045\text{--}0.09 \times 10^{-3}$
Welded steel	0.045×10^{-3}
Rusted steel	$0.15\text{--}4 \times 10^{-3}$
Riveted steel	$0.9\text{--}9 \times 10^{-3}$
Galvanized steel	0.15×10^{-3}
Asphalted cast iron	0.012×10^{-3}
New cast iron	$0.25\text{--}0.8 \times 10^{-3}$
Worn cast iron	$0.8\text{--}1.5 \times 10^{-3}$
Smoothed cement	0.3×10^{-3}

An explicit equation closely matching results obtained with the Colebrook–White equation [Eq. (13.36)] is the one known as the Swamee–Jain equation:

$$f = \frac{0.25}{\left[\log_{10} \left(\frac{e_r}{3.7} + \frac{5.74}{Re^{0.9}} \right) \right]^2} \quad (13.37)$$

$$(\ell \equiv d_h; 5000 > Re > 10^7; 0.00004 > e_r > 0.05)$$

Pipe flow is not the only source of pressure losses in a heat exchanger; pressure losses in so-called flow singularities must be additionally considered to compute the fluid total pressure loss in the exchanger. Entrance and exit connections, manifolds, headers, and bends are the most common singularities one must consider in a tubular heat exchanger; pipe fittings, valves, strainers, in addition to bends of various shapes, are other singularities to be accounted for in pipes carrying the fluids into and out of the apparatus.

Pressure losses in singularities are calculated according to the general correlation:

$$\Delta p_{\text{frict}} = k \cdot \rho \frac{w^2}{2} \quad (13.38)$$

w being the fluid mean velocity at a specified reference location, ρ the fluid density, and k the loss coefficient dependent on geometry and flow dynamic conditions.

References [HEDH \(2001\)](#) and [VDI Heat Atlas \(2010\)](#) present extensive procedures and numerical data to compute loss coefficients for common singularities. Here the

Table 13.4 Bend pressure loss coefficients

Bend angle (degrees)	Ratio: $\frac{\text{Centerline radius of curvature } R_b}{\text{Internal pipe diameter } d_i}$						
	0.5	0.6	0.8	1	2	4	10
45	$k_b = 0.58$	0.47	0.37	0.27	0.17	0.11	0.09
90	$k_b = 0.84$	0.67	0.48	0.39	0.24	0.16	0.12
180	$k_b = 1.1$	0.86	0.63	0.50	0.31	0.22	0.17

case of round bends in circular cross-section tubes in turbulent flow will be treated in some detail as an exemplification and for the importance this component has in tubular heat exchangers (return bends).

In this case, according to Jayanti (www.thermopedia.com), the total loss coefficient is obtained as the sum of two factors, both dependent on the bend angle θ and the curvature ratio (R_b/d_i):

$$k = f \frac{\pi R_b}{d_i} \frac{\theta}{180^\circ} + k_b, \theta \text{ expressed in } (^\circ) \quad (13.39)$$

The first term of the second member in Eq. (13.39) is due to pipe friction: f is the friction factor calculated for a straight pipe of the same internal diameter as the round bend d_i ; R_b is the bend centerline radius of curvature; θ (degrees) is the bend angle. The second term k_b , the bend pressure loss coefficient due to the curvature effect that induces secondary flow development, is reported in Table 13.4 for three bend angles. Note that, according to other sources, even k_b is dependent on the Reynolds number (VDI Heat Atlas, 2010).

13.4 Heat transfer and pressure drop in external flow through banks of plain and finned tubes

Heat transfer. Banks of circular plain tubes (of external diameter d_e) crossed by a fluid at an approaching yaw angle of 90 degrees relative to the tubes' axis will be considered in the following. The arrangement of tubes within the bundle (in-line or staggered) plays an important role in this case; Fig. 13.18 illustrates the most usual tube layouts with equidistant tubes: p , the tube pitch, is the common distance between adjacent tubes, whereas, in relation also to the flow direction, the longitudinal tube pitch p_l , the transverse tube pitch p_t , and the diagonal tube pitch p_d must be considered.

Predicting procedures for heat transfer coefficients and frictional pressure gradients may require, in addition to the usual nondimensional quantities Nu , Re , Pr , (μ/μ_w) , ..., conveniently defined as specified later on, consideration of other dimensionless geometrical parameters, such as the relative transverse pitch $p_{r,t} = p_t/d_e$, the relative longitudinal pitch $p_{r,l} = p_l/d_e$, and the relative diagonal pitch $p_{r,d} = p_d/d_e$.

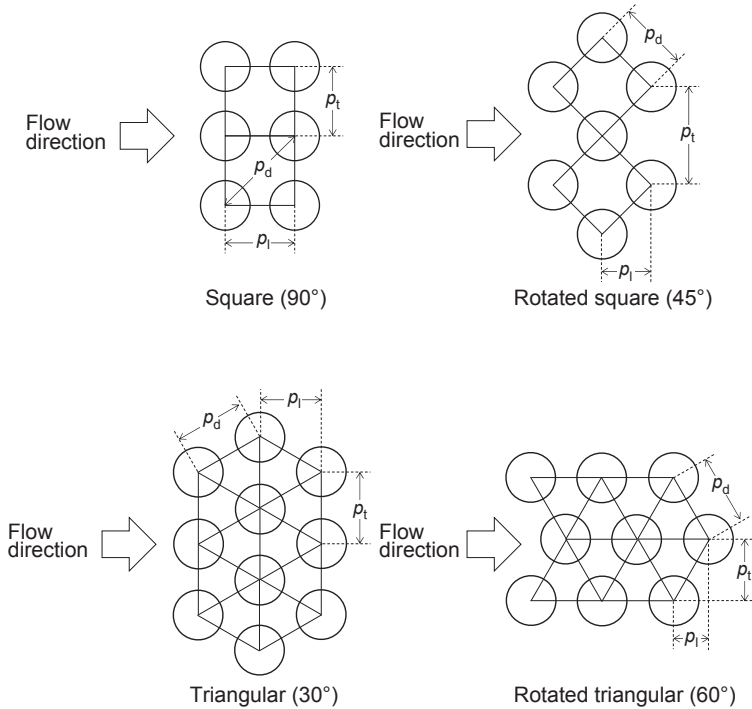


Figure 13.18 Tube layouts in bundles.

The mean heat transfer coefficient \bar{h} (averaged over the external surface of all tubes in the bundle) is considered here; it depends on the number of tubes in the direction of flow n_r (number of tube rows), as the level of turbulence affecting the core tubes increases downflow and because of the entrance and exit effects; the whole situation is governed by the bundle arrangement and its compactness (tube pitches).

In the presentation of nondimensional correlations authors usually take the external tube diameter as the characteristic length to be used in the Nusselt and Reynolds numbers, $\ell \equiv d_e$, whereas in the Reynolds number the maximum velocity w_{\max} experienced by the fluid in the bundle is taken as the reference velocity w , $w \equiv w_{\max}$. This maximum velocity takes place in the minimum flow area a_{\min} and can be calculated as:

$$w_{\max} = \frac{\dot{M}}{\rho \cdot a_{\min}} \quad (13.40)$$

Consequently the appropriate expression for the Reynolds number becomes:

$$Re_{w_{\max}} = \frac{\dot{M} \cdot d_e}{a_{\min} \cdot \mu} \quad (13.41)$$

where \dot{M} is the fluid total mass flow rate.

According to [HEDH \(2001\)](#), in the majority of practical applications, the tube arrays are chosen with equal distance p (the tube pitch) among the tubes; staggered

Table 13.5 Minimum flow areas for tube arrays with equal pitch p

Array type	p_t	p_l	p_d	$a_{\min} =$
Square (90 degrees)	p	p	$1.414 p$	$n_t (p - d_e)Z$
Triangular (30 degrees)	p	$0.866 p$	p	$n_t (p - d_e)Z$
Rotated square (45 degrees) $p/d_e \leq 1.71$	$1.414 p$	$0.707 p$	p	$2n_t (p - d_e)Z$
Rotated square (45 degrees) $p/d_e \geq 1.71$	$1.414 p$	$0.707 p$	p	$n_t (1.414 p - d_e)Z$

n_t is the number of tubes per row.

arrangements are either 45-degree-rotated square pitch or 30-degree (equilateral) triangular pitch, as shown in Fig. 13.18. In these cases, the expressions to compute a_{\min} are shown in Table 13.5.

According to ESDU International (ESDU, 1973), the Nusselt number for this case, related to the mean value of the convective heat transfer coefficient \bar{h} , can be evaluated as follows:

$$\overline{Nu} = k \cdot F \cdot Re_{wmax}^m \cdot Pr^{0.34} \left(\frac{Pr}{Pr_w} \right)^{0.26}$$

(13.42)

($\ell \equiv d_e$; $n_t \geq 6$ tubes per row; $(Z/d_e) > 5$; flow normal to tubes axes)

In Eq. (13.42), the factor F corrects for the number of tube ranks (number of tube rows in the direction of flow) being less than 8; when this number of tube ranks is exceeded, the mean value of the convective heat transfer coefficient \bar{h} can be regarded as practically constant. Table 13.6 gives the values of F .

The values of k and exponent m in Eq. (13.42), with the related validity ranges, are given in Table 13.7.

Banks of plain high-fin tubes in cross-flow. The convective heat transfer coefficient for gases at low or moderate pressure is usually 1 or 2 orders of magnitude lower than that for liquids or fluids with change of phase; for this reason, when the two streams in the exchanger are just a gas and a liquid (or a fluid with change of phase), on the gas side it is necessary to have a much larger transfer area, structured much more compactly than is possible to realize with circular tubes: high fin tubes are then used. This is the

Table 13.6 Values of F in Eqs. (13.42) and (13.44) (Rabas and Taborek, 1987)

Number of tube ranks	1	2	3	4	5	6	7	8 or more
F	0.65	0.77	0.84	0.90	0.94	0.97	0.99	1

Table 13.7 Values of k and exponent m for use in the ESDU correlation (13.42)

Range of Re_{wmax}	In-line banks		Staggered banks	
	k	m	k	m
$10 - 3 \cdot 10^2$	0.742	0.431	1.309	0.360
$3 \cdot 10^2 - 2 \cdot 10^5$	0.211	0.651	0.273	0.635
$2 \cdot 10^5 - 2 \cdot 10^6$	0.116	0.700	0.124	0.700

Valid for $1.2 \leq p_{r,i} \leq 4$ and $p_{r,i} \geq 1.15$.

case, for example, for air-cooled condensers, a common piece of equipment in ORC technology. Typical aluminum fins have density from 300 up to 800 fins per meter, 0.1–0.5 mm thickness, and up to 2.5 cm in height, with an increase in heat transfer surface up to 20 times the base surface. The convective heat transfer coefficient depends on fluid properties and velocity and on the overall geometry. A simple correlation to calculate the mean forced convection heat transfer coefficient in this case is the one developed by PFR Engineering Systems, Inc. (PFR, 1976), dealt with in the following.

For finned bundles with at least four tube ranks, the average Nusselt number is:

$$\overline{Nu} = k \cdot \left(\frac{A}{A_{tb}} \right)^{-0.17} \cdot Re_{wmax}^{0.633} \cdot Pr^{1/3} \quad (13.43)$$

$$(\ell \equiv d_e; 5 < (A/A_b) < 12; 5 \cdot 10^3 < Re_{wmax} < 10^5;$$

$$\text{staggered bundles } k = 0.29; \text{ in-line bundles } k = 0.19)$$

A_{tb} is the total area of the base surface, covered and uncovered by fin roots (the area of the base tubes without the fins).

For less than four tube rows, the result from Eq. (13.43) must be multiplied by a correction factor given in Table 13.8; note that, for a staggered tube bundle, the mean heat transfer coefficient increases with increasing number of rows, whereas for in-line tube bundles the contrary is true.

Table 13.8 Correction factor for Eq. (13.43) (Yudin and Tokhtarova, 1971)

Number of tube ranks →		1	2	3	4 or more
Correction factor	In-line	1.2	1.1	1.04	1
	Staggered	0.76	0.88	0.96	1

Table 13.9 Minimum flow areas for tube arrays with equal pitch p

Array type	p_t	p_l	p_d	$a_{\min} =$
Square	p	p	$1.414 p$	$n_t (p - d_e - 2n_f \cdot \delta \cdot L)Z$
Triangular	p	$0.866 p$	p	$n_t (p - d_e - 2n_f \cdot \delta \cdot L)Z$
Rotated square (45 degrees) $p/d_e \leq 1.71$	$1.414 p$	$0.707 p$	p	$2n_t (p - d_e - 2n_f \cdot \delta \cdot L)Z$
Rotated square (45 degrees) $p/d_e \geq 1.71$	$1.414 p$	$0.707 p$	p	$n_t (1.414 p - d_e - 2n_f \cdot \delta \cdot L)Z$

n_t is the number of tubes per row.

The maximum fluid velocity w_{\max} to be used in $Re_{w\max}$ must again be calculated according to Eq. (13.40), allowing for the presence of the fins in evaluating a_{\min} . Table 13.9 gives the correlations to compute a_{\min} for commonly used arrays of round fins of constant thickness δ , height L [$L = (D_t - d_e)/2$], and number of fins per unit length of tube n_f , when the tube pitch p is constant.

So far plain fins have been considered; modification to this basic surface geometry can bring about a substantial increase in the convective heat transfer coefficient with the gas stream (in certain circumstances, up to two-three times), which sure enough comes with a pressure drop penalization; when compactness is a premium, this solution is often implemented. The simple addition of holes on the plain surface (perforated fins) results in a heat transfer increase because of the wake mixing in the holes region. Heat transfer coefficients with wavy fins benefit from increased turbulence and secondary flow, which may be established. The augmentation in heat transfer coefficients obtained with offset strip fins and louvered fins is a consequence of the interrupted and repeated growth of boundary layers, with dissipation in the wake regions; of course slits should not hinder the conduction of heat transfer along the fin. Work has also been reported on enhancing plain fin performance using vortex generators. Heat transfer and pressure drop characteristics of those kinds of fins, commonly of the continuous type (each single fin embraces all tubes in the bundle) cannot be reported here because of space limitations; references (Wolverine-Thome, 2010; Kays and London, 1964) report extensive data and design correlations on this matter.

Banks of radial low-finned tubes in cross-flow. Plain round fins of this kind are on the order of 1.5 mm high, with densities n_f from about 630 to 750 fins per meter of base tube length. For this geometry, with fins of constant thickness δ , interfin spacing $s = \frac{1}{n_f} - \delta$, and diameter at the fin tip D_t , Rabas and Taborek (1987) suggest the following correlation:

$$\begin{aligned} \overline{Nu} = & 0.292 Re_{w\max}^m \left(\frac{s}{D_t} \right)^{1.115} \left(\frac{s}{L} \right)^{0.257} \left(\frac{\delta}{s} \right)^{0.666} \left(\frac{D_t}{d_e} \right)^{0.473} \left(\frac{D_t}{\delta} \right)^{0.772} \\ & \cdot Pr^{1/3} \left(\frac{Pr}{Pr_w} \right)^{0.26} \cdot F \end{aligned} \quad (13.44)$$

$$(\ell \equiv d_e; m = 0.585 + 0.0346 \ln(D_t/s); L < 6.35 \text{ mm};$$

$$1000 < Re_{w\max} < 25,000; (D_t/s) < 40; p_1 < p_t)$$

F is again the correction factor accounting for the number of tube rows in the direction of flow; as a rough approximation, values given in [Table 13.6](#) can be used, but correlation (13.44) is restricted to bundles of more than six tube rows in the flow direction.

Pressure drop in external flow normal to tube bundles with circular tubes. In this circumstance, pressure losses result from both skin friction and form drag effects, the former prevailing at low Reynolds numbers, and the latter taking over at increasing fluid velocity. In agreement with Gaddis ([VDI Heat Atlas, 2010](#)), the frictional pressure drop across a tube bundle can be calculated according to the expression:

$$\Delta p_{\text{frict}} = k \cdot N \cdot \frac{\rho \cdot w_{\max}^2}{2} \quad (13.45)$$

where N , the number of main resistances in the flow direction, is equal to the number of tube ranks ($N = n_r$) for in-line tube arrangement and for staggered tube arrangements with the narrowest cross section between adjacent tubes in the same row, that is, when $p_{r,l} \geq 0.5\sqrt{2p_{r,t} + 1}$, whereas $N = n_r - 1$ if, for staggered tube arrangements, the narrowest cross section lies in the diagonal between tubes in adjacent tube rows ($p_{r,l} < 0.5\sqrt{2p_{r,t} + 1}$). The loss coefficient k , for so-called ideal bundles, is a function of the already defined parameters $Re_{w\max}(\ell \equiv d_e)$, $p_{r,l}$, $p_{r,t}$. An ideal tube bundle postulates $n_r \geq 10$, $n_t \geq 10$ (number of tubes per row), $(Z/d_e) \geq 10$, uniform approaching free-stream velocity, and fluid properties constant with temperature. With a gas undergoing a pressure variation, density should be evaluated at mean conditions between inlet and outlet. Deviations from this ideal situation can be taken care of by suitable correction factors.

The analytical correlations even for the ideal loss coefficient are rather cumbersome; here only those for fully turbulent flow ($10^4 \leq Re_{w\max} \leq 3 \cdot 10^5$) will be given, dubbing the loss coefficient k_{turb} ; for more details, the original reference ([VDI Heat Atlas, 2010](#)) must be referred to.

The loss coefficient for an ideal bundle has two different analytical expressions, depending on the type of tube arrangement, as follows:

- in-line tube arrangement:

$$k_{\text{turb}} = \left\{ \left[\frac{0.22 + 1.2 \frac{(1 - 0.94/p_{r,l})^{0.6}}{(p_{r,t} - 0.85)^{1.3}}}{1} \right] \cdot 10^{0.47[(p_{r,l}/p_{r,t}) - 1.5]} + [0.03(p_{r,l} - 1)(p_{r,t} - 1)] \right\} \cdot Re_{w\max}^{-0.1(p_{r,l}/p_{r,t})} \quad (13.46)$$

$$(\ell \equiv d_e; 10^4 \leq Re_{w\max} \leq 3 \cdot 10^5; 1.25 \leq p_{r,t} \leq 3.0; 1.2 \leq p_{r,l} \leq 3.0)$$

- staggered tube arrangement:

$$k_{\text{turb}} = \left[2.5 + \frac{1.2}{(p_{r,t} - 0.85)^{1.08}} + 0.4 \left(\frac{p_{r,l}}{p_{r,t}} - 1 \right)^3 - 0.01 \left(\frac{p_{r,t}}{p_{r,l}} - 1 \right)^3 \right] \cdot Re_{w\max}^{-0.25}$$

$$\left(\ell \equiv d_e; 10^4 \leq Re_{w\max} \leq 3 \cdot 10^5; 1.25 \leq p_{r,t} \leq 3.0; 0.6 \leq p_{r,l} \leq 3.0; \right.$$

$$\left. \sqrt{(p_{r,t}/2)^2 + p_{r,l}^2} \geq 1.25 \right)$$
(13.47)

Correction factors F , to account for the nonideality of the real bundle and to be used as multipliers of the results yielded by the ideal correlations, are as follows:

Correction for temperature-variable fluid properties $F_{t,vfp}$. When the fluid dynamic viscosity varies consistently in the thermal boundary layer, in a turbulent flow regime, the correction factor is:

$$F_{t,vfp} = \left(\frac{\mu_w}{\mu} \right)^{0.14}$$
(13.48)

The bulk fluid physical properties are to be evaluated at mean conditions between inlet and outlet, whereas μ_w is the dynamic viscosity evaluated at the wall temperature where the mean bulk condition takes place (often the mean wall temperature is considered).

Correction for small number of tube rows (less than 10). Unlike in laminar flow, in the turbulent flow range, if the number of tube rows is between 5 and 10, this correction is negligible and can be ignored.

What has been reported so far provides an overall view of the procedures, the types of correlations, and the variables involved in the attempt to predict heat transfer and pressure drop performance of tube bank arrangements so much used in tubular heat exchangers. Of course, it has been possible to examine in detail only a very small part of all the different surface geometries and flow dynamic conditions that can be encountered in designing heat transfer apparatuses.

References (Kays and London, 1964; Kraus et al., 2001; Wolverine-Thome, 2010; VDI Heat Atlas, 2010; HEDH, 2001) report data and predicting procedures for heat transfer and pressure drop performance of a wide variety of unfinned and finned tube banks of different shapes and arrangements.

13.5 Evaporation and boiling heat transfer

13.5.1 Pool boiling on the outside of tubes and tube bundles

Pool boiling takes place on a surface of a heated wall immersed in a pool of liquid at or near its saturation temperature, when the surface temperature is brought above the

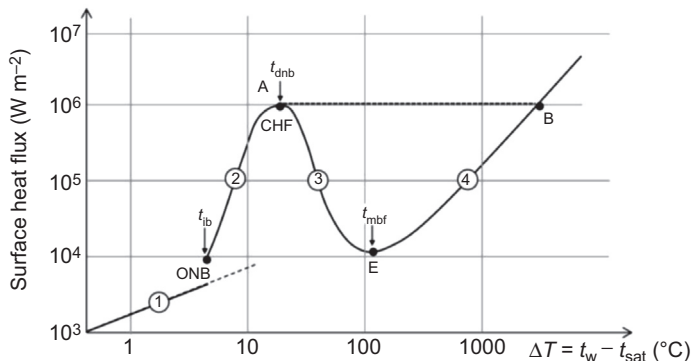


Figure 13.19 Pool boiling (Nukiyama) curve for water at atmospheric pressure. ONB: onset of nucleate boiling; CHF: critical heat flux.

liquid saturation temperature, and the motion of the liquid is the sole consequence of the heat transfer process, with no substantial external contribution.

Let's consider a horizontal single metallic round pipe immersed in a pure single-component liquid at or near saturation. By progressively increasing the uniform surface temperature of the tube t_w above the liquid saturation temperature t_{sat} , and measuring the heat flux \dot{q} , the log–log plot depicted in Fig. 13.19 is obtained (Nukiyama curve), where the numerical values on the axes, broadly referred to water at atmospheric pressure, are indicated only to give a general order of magnitude, as the phenomenon depends on a large number of variables, such as type of fluid, ambient physical conditions, type and microstructure of the surface,

It can be seen that the boiling curve of Fig. 13.19 presents four distinguishable heat transfer trends as the wall-to-saturation temperature difference $\Delta t = t_w - t_{sat}$ (dubbed the excess temperature in boiling) is increased:

Natural convection regime: At small excess temperature difference Δt , heat is transferred to a layer of superheated liquid by natural convection and is transported to the pool surface where evaporation takes place (region 1 in Fig. 13.19).

Nucleate boiling regime: When the surface temperature reaches the so-called incipient boiling temperature t_{ib} sufficient for boiling nucleation to occur, isolated bubbles start to form on the surface in some nucleation sites (small cavities trapping vapor). As the surface temperature is further increased above the fluid saturation temperature, more and more nucleation sites are activated, and the heat transfer becomes very effective, with most of the heat exchanged by direct transfer from the surface to the wetting liquid in motion; however, three competing mechanisms of heat transfer are present at the same time: bubble agitation, vapor–liquid exchange, and evaporation (region 2) (Thome-Wolverine, 2010). When the upper part of region 2 of the boiling curve of Fig. 13.19 is reached, vapor escapes the surface in the form of jets because of increased bubble formation, forming slugs traveling to the free surface; the heat transfer coefficient reaches a maximum value somewhat before the maximum heat flux is obtained. The role of the number of active nucleation sites explains why in this heat transfer regime the surface microstructure is an important factor in establishing the heat transfer performance of the heated wall. Nucleate boiling is the heat transfer regime sought after in the vast majority of natural convection industrial heat transfer apparatuses.

Transition boiling regime: By further increasing the wall temperature, the point of departure from nucleate boiling ($t_w = t_{\text{dnb}}$) is reached at which the heat flux gets to a maximum value \dot{q}_{max} , dubbed the critical flux, after which the phenomenon becomes unstable, characterized by a partial coverage of the heat transfer surface with a vapor layer and a resulting decrease in the heat flux due to limited liquid-to-surface contact and poor thermal conductivity of the vapor phase (region 3).

Film boiling regime: The heat flux reaches a minimum value (point E) at $\Delta t = t_{\text{mfb}} - t_{\text{sat}}$, where t_{mfb} is the so-called temperature of the minimum film boiling point (Leidenfrost point). For $t_w > t_{\text{mfb}}$ the heat flux increases again with Δt : the heat transfer surface is now completely masked by a stable vapor blanket, through which a significant heat transfer mechanism at increasing temperature difference becomes thermal radiation (region 4).

The accurate knowledge of the critical heat flux \dot{q}_{max} pertaining to point A is important in some situations when the heat flux is imposed as the external independent variable (nuclear reactor fuel elements, heating by an electrical resistance, ...). By increasing the heat flux past the critical value, the operating point on the boiling curve of Fig. 13.19 jumps abruptly from point A to point B, with a crucial sudden growth of the wall temperature from $t_A = t_{\text{dnb}}$ to t_B , with possible damage or even melting of the wall material. For this reason, point A is often termed the burnout point or thermal crisis.

Nucleate boiling correlations. As can be envisaged from the graph in Fig. 13.19, the dependence of heat flux \dot{q} on excess temperature Δt , at least in the central part of the nucleate boiling curve, can be well represented by a correlation of the type $\dot{q} \propto \Delta t^n$, that is, for the nucleate boiling convective heat transfer coefficient $h_{\text{nb}} = \dot{q}/\Delta t$, $h_{\text{nb}} \propto \Delta t^{n-1}$, or even $h_{\text{nb}} \propto \dot{q}^{\frac{n-1}{n}}$, where $n \approx 3$.

The simple Cooper dimensional correlation (Cooper, 1984) is as follows:

$$h_{\text{nb}} = 55 \cdot p_{\text{R}}^{0.12-0.4343 \ln R_{\text{p}}} \cdot (-\log_{10} p_{\text{R}})^{-0.55} \cdot M^{-0.5} \cdot \dot{q}^{0.67} \quad (13.49)$$

$$(0.001 < p_{\text{R}} \leq 0.9, 2 < M < 200 \text{ kg/kmol})$$

where h_{nb} is obtained in $\text{W}/(\text{m}^2\text{K})$, expressing the heat flux \dot{q} in W/m^2 , the surface roughness parameter R_{p} in micrometers, and the molecular mass M in kg/kmol ; p_{R} is the reduced pressure of the fluid (actual pressure divided by critical pressure). The roughness parameter R_{p} (maximum peak height) is defined as the largest peak height of a surface finish profile measured from the mean line: if unknown, the value $R_{\text{p}} = 1 \text{ } \mu\text{m}$ is suggested for metal unpolished surfaces.

Other commonly used correlations for the prediction of nucleate boiling heat transfer coefficients are the ones by Rohsenow (1962), Mostinski (1963), Stephan-Abdelsalam (1980), Gorenflo (1993), and Ribaski-Siaz Jabardo (2003): all of them are treated in Wolverine—Thome (2010).

As for predicting the critical heat flux \dot{q}_{max} for nucleate pool boiling on the upper surface of a large plain horizontal wall, the Zuber correlation (Zuber, 1959) can be employed, independent of the surface material:

$$\dot{q}_{\text{max}} = \frac{\pi}{24} H_{\text{lv}} \cdot \rho_{\text{v}} \left[\frac{\sigma \cdot g (\rho_{\text{l}} - \rho_{\text{v}})}{\rho_{\text{v}}^2} \right]^{0.25} \quad (13.50)$$

where H_{lv} is the latent heat of vaporization, ρ_l the liquid phase density, ρ_v the vapor phase density, σ the surface tension, and g the acceleration due to gravity. According to Linhard and Dühr, as reported in (HEDH, 2001), the leading constant of Eq. (13.50) should be increased to 0.149 (instead of $\pi/24$); furthermore the value of the critical heat flux as given by expression (13.50) and multiplied by a correction factor $F = 0.904$ applies to large horizontal tubes ($R' \geq 1.17$), whereas for small horizontal tubes ($0.12 \geq R' > 1.17$) of external diameter d_e , values obtained by expression (13.50) should be multiplied by a correction factor of $F = 0.94(R')^{-0.25}$, where the dimensionless heater radius is defined as $R' = \frac{d_e}{2} \left[\frac{g(\rho_l - \rho_v)}{\sigma} \right]^{0.5}$.

A roughened surface provides more cavities and crevices that can be activated as sites for vapor generation, and thus generally presents higher heat transfer coefficients in a nucleate boiling regime compared to smooth surfaces; however, fouling can nullify this benefit. Special enhanced structured surfaces providing stable augmentation of nucleate boiling heat transfer coefficients (even by more than 1 order of magnitude) have been patented and offered on the market in recent years. The integral low-finned tube, with continuous helical fins around the circumference, is one example of an enhanced surface. Other types of enhanced surfaces are obtained by coatings of porous material on the base heat transfer surface formed by various techniques, such as brazing or sinterization. Another technique consists of mechanical deformation of finned surfaces, thus creating double reentering artificial cavities acting as nucleation sites, able to activate at much lower wall superheat than plain surfaces do. For more information about enhanced boiling surfaces and some design criteria refer to (Wolverine—Thome, 2010) and specific product manufacturers.

Boiling in kettle reboilers: This takes place in bundles of horizontal tubes. At least at small and medium heat fluxes, the average boiling heat transfer coefficients in a tube bundle are consistently higher than that for a single tube of the same geometry and material under otherwise equal conditions. The main reason for this is the added convective contribution: any bundle tube is under the influence of the flow motion caused by heat transfer from the surrounding tubes and is therefore immersed in a high-velocity two-phase flow circulation, with some similarities to what happens in channeled flow boiling; the flow tends to become convection-dominated as the local vapor quality increases. This drives to express the average bundle boiling heat transfer coefficient for pure fluids \bar{h}_{bundle} as follows:

$$\bar{h}_{\text{bundle}} = h_{\text{nb},1} \cdot F_b + h_{\text{nc}} \quad (13.51)$$

where $h_{\text{nb},1}$ is the nucleate boiling heat transfer coefficient for an equal single tube under otherwise equivalent conditions; the factor F_b accounts for the effect of convective boiling; a simplified equation, dependent only on the bundle geometry, has been proposed by Taborek (HEDH, 2001) as follows:

$$F_b = 1 + 0.1 \left[\frac{0.785(D_B/d_e)}{C_1(p/d_e)^2} - 1.0 \right]^{0.75} \quad (13.52)$$

In Eq. (13.52), D_B is the bundle diameter of circle tangent to the outer tubes, p is the pitch of the equidistant tubes in the bundle, and $C_1 = 1$ for square (in-line or rotated) tube layouts and $C_1 = 0.866$ for triangular tube layouts. Finally, h_{nc} in Eq. (13.51) is the natural convection heat transfer coefficient in bundles for the liquid phase, which can be taken approximately as $h_{nc} = 1000 \text{ W/(m}^2\text{K)}$ for water and $h_{nc} = 250 \text{ W/(m}^2\text{K)}$ for hydrocarbons.

For kettle and internal reboilers, $F_b \approx 2$ is a common value; in this case, it can be appreciated that in a tube bundle the heat transfer coefficient can be more than double that for the single tube.

Palen in HEDH (2001) suggests more sophisticated methods to evaluate the terms in Eq. (13.51), extending its application even to zeotropic multicomponent mixtures.

Thome (Wolverine—Thome, 2010) suggests an asymptotic method to predict the local bundle boiling heat transfer coefficient h_{bundle} from the nucleate boiling heat transfer coefficient $h_{nb,1}$ and a convective boiling heat transfer coefficient h_{cb} : $h_{\text{bundle}} = \sqrt{h_{nb,1}^2 + h_{cb}^2}$, and presents some preliminary results even for bundles with enhanced tubes.

The critical heat flux for a tube bundle may occur by various mechanisms and can be considerably less than that for the single same tube under otherwise equivalent conditions. Palen (HEDH, 2001), in relation to smooth tube bundles, correlates the ratio of the bundle maximum heat flux $\dot{q}_{B,\text{max}}$ to the single-tube maximum heat flux $\dot{q}_{1,\text{max}}$ [Eq. (13.50) corrected for cylinders] as a function of a simple dimensionless geometry parameter Φ_B (bundle correction factor):

$$\frac{\dot{q}_{B,\text{max}}}{\dot{q}_{1,\text{max}}} = \Phi_B; \quad \Phi_B = 3.1 \frac{\pi D_B \cdot Z}{A}; \quad \text{if } \Phi_B > 1, \text{ use } \Phi_B = 1 \quad (13.53)$$

where Z is the length of tube bundle and A the total outside tube heat transfer surface area.

If the average design heat flux exceeds half of the bundle maximum heat flux, vapor release channels should be considered in the bundle to avoid vapor binding.

Information on thermal performance about boiling in enhanced tube bundles is rather scarce in the open literature, and no reliable general predicting method has been made available. The reader can refer to Wolverine—Thome (2010) for some discussion on this topic.

13.5.2 Flow boiling inside tubes

In-tube flow boiling occurs in once-through and recirculation boilers; it is a complicated phenomenon to predict, with quite a few variables playing a fundamental role. Let us start by considering the axial-symmetric case of a round vertical tube uniformly heated by a moderate heat flux along its total length, fed from below under steady-state conditions by a subcooled pure single-component liquid. Let us suppose that the heat flux is such that the tube inner wall temperature at the inlet is below the fluid saturation temperature: as the fluid proceeds along the tube (supposed long enough), it will be first heated, then vaporized, and finally superheated; along this process, quite different

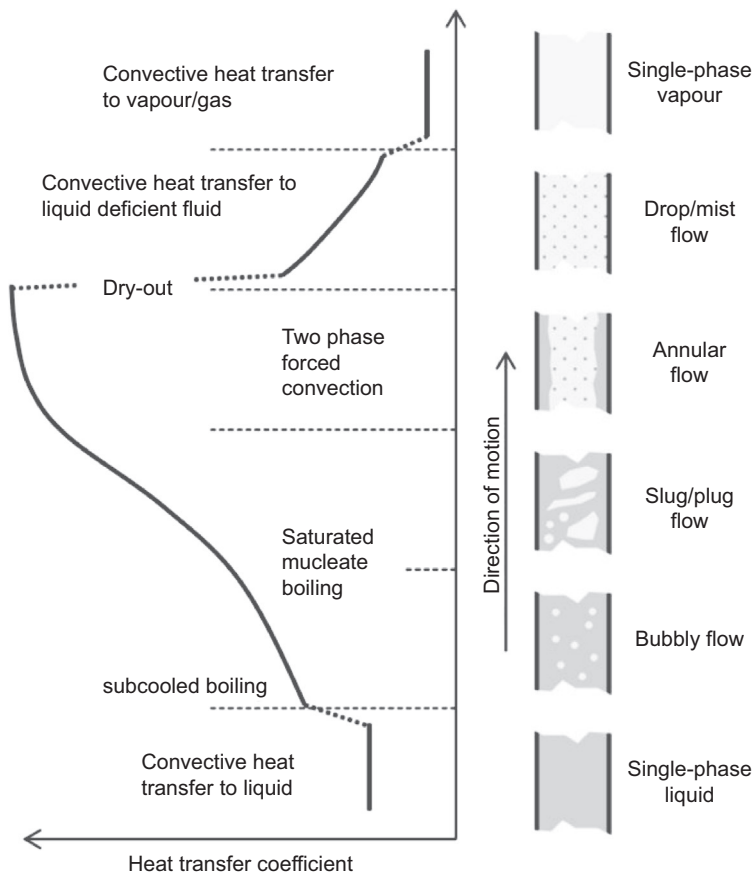


Figure 13.20 Convective flow boiling in a vertical tube.

flow patterns are present in the tube, each one characterized by specific heat transfer mechanisms, which will be briefly discussed here, referring to the sketch presented in Fig. 13.20.

Moving in the flow direction, at first the liquid is heated by forced convection; both the liquid mixing cup temperature and the pipe surface temperature increase; the local heat transfer coefficient can be computed by appropriate forced convection correlations for single-phase flow. The wall surface temperature t_w goes past the fluid saturation temperature t_{sat} , until the excess temperature $\Delta t = t_w - t_{sat}$ is sufficient to activate some nucleation sites on the pipe wall and some vapor formation takes place, even if the bulk fluid can still be subcooled: if this is the case, the region of subcooled boiling is present, first dubbed partial boiling, and then fully developed subcooled boiling. As the wall surface temperature further increases, the surface becomes fully covered by bubble sites and consequently the single-phase convective heat transfer mechanism loses importance.

The saturated nucleate boiling region is then reached, at the point where the thermodynamic mass vapor quality $x = 0$ (x is defined as the ratio between the vapor-phase mass flow rate and the total mass flow rate, calculated by an energy balance in the assumption of thermodynamic equilibrium); the mechanism of heat transfer is here the same as in fully developed subcooled boiling: vapor bubbles are generated from a thin liquid layer next to the surface, which is superheated to a sufficient degree to activate nucleation sites. In fully developed subcooled boiling and saturated nucleate boiling most likely the flow patterns are bubbly flow (bubbles dispersed or suspended as discrete elements in a liquid continuum) followed by slug flow (large bubbles separated by liquid “slugs”). As vapor production further progresses, the transition to an annular flow pattern can take place, with a high-velocity vapor core and a highly sheared annular thin liquid film forced to the pipe wall; now heat is very effectively taken away from the wall by forced convection and evaporation takes place at the liquid–vapor interface; most often nucleate boiling is completely suppressed because the wall temperature drops below the limiting value necessary to sustain nucleation at the given heat flux (Collier–Thome, 1996). Some liquid can be pulled out of the liquid annulus and travel with the vapor core in the form of small dispersed droplets (annular flow with entrainment). The annular flow regimes are characterized by very high heat transfer coefficients and referred to as the two-phase forced convective region.

Vapor quality continues to increase in the flow direction, until a condition is reached when the full evaporation of the liquid film occurs; at this point, known as dry-out, the heat transfer coefficient abruptly drops by 1 or even 2 orders of magnitude, with a sudden increase in the wall temperature at imposed heat flux. Beyond this point, up to the condition of single-phase vapor, a drop flow pattern takes place, and the region is dubbed liquid-deficient. In this region, which can extend beyond the thermodynamic equilibrium dry–saturated vapor point (calculated vapor quality $x = 1$), several heat transfer mechanisms should be accounted for: from the surface to liquid droplets, either impacting the wall (wet collision) or entering the boundary layer without wetting the wall (dry collision); convective heat transfer from the wall to the bulk vapor, and from the bulk vapor to droplets dispersed in the vapor core; and radiative heat transfer from the wall to the liquid droplets and to the bulk vapor. The problem is extensively discussed in Collier – Thome (1996), in which some correlations for predicting the heat transfer coefficients are presented, both of empirical nature and allowing or not for departure from thermodynamic equilibrium.

After reaching the condition of single-phase vapor, heat transfer takes place by forced convection, and the pertinent correlations can be fully applied.

The preceding discussion refers to a condition of moderate heat flux from the pipe wall to the boiling/evaporating fluid flow. Increasing the heat flux applied to the heating surface, at other conditions unchanged, the subcooled boiling region appears at a larger value of bulk liquid subcooling [saturation temperature minus bulk liquid temperature ($t_{\text{sat}} - t_{\text{bulk,i}}$)], the transition between saturated boiling and two-phase forced convective heat transfer is moved to higher values of vapor quality, and dry-out appears at a lower value of vapor quality, thus restricting the vapor quality range where the highly efficient two-phase convective heat transfer can take place.

At still higher values of imposed heat flux, the two-phase convective heat transfer region is no longer present, and the transition from the saturated nucleate boiling region leads to the new film boiling region at a point termed the DNB (departure from nucleate boiling), with the heat transfer surface completely blanketed by a vapor layer of low conductivity through which heat must be transferred to the evaporating liquid; a very drastic sudden deterioration in the heat transfer coefficient occurs at the DNB point; this situation is similar to what happens in pool boiling beyond the Leidenfrost point.

Improving further the imposed heat flux, DNB takes place at lower and lower mass vapor quality, until it may enter the subcooled liquid region, when the transition is directly from the heat transfer mechanism of subcooled nucleate boiling to that of film boiling.

In a horizontal tube subjected to the same experimental situation, heat transfer rates may be different from that discussed above for vertical tubes, to the extent that gravitation causes radial asymmetric flow patterns that of course affect the heat transfer behavior. Furthermore, in addition to the flow patterns already dealt with for vertical flow, stratified flow patterns (the two phases flow separately with a smooth or a wavy interface) can appear in some conditions. In bubbly, stratified, and intermittent (slug or plug) flow patterns in horizontal tubes, because of buoyancy, the tendency arises to segregate the vapor phase preferentially toward the top of the pipe; the upper tube surface may become unwetted, with a low local heat transfer coefficient; vapor segregation can be offset by increased mass flow rate. At high vapor qualities, annular flow is likely to occur, but with a lower thickness liquid film in the upper part of the tube than at the bottom, most susceptible to dry-out; as a consequence, critical heat fluxes are generally consistently lower in horizontal tubes than in vertical ones at otherwise identical conditions.

In two-phase flow, the heat transfer behavior is closely linked to the type of flow pattern: flow pattern maps have been developed to try to predict the two-phase flow pattern, given geometry and fluid and flow physical conditions; they are two-dimensional representations of the boundary lines (transitions) among the different types of flow patterns plotted against suitable dimensional or nondimensional coordinates, specifically for horizontal or vertical flow; for details refer to (Collier and Thome, 1996) or (HEDH, 2001).

Several correlations have been presented in the scientific literature to predict the local (circumferential averaged) heat transfer coefficient h_{sfb} in saturated flow boiling (convective and nucleate boiling regions); quite a lot of them are in the form of a combination of a nucleate boiling contribution and a convective contribution. Thus the Liu and Winterton correlation (Liu and Winterton, 1991) is an asymptotic expression as follows:

$$h_{\text{sfb}} = \sqrt{(S \cdot h_{\text{nb}})^2 + (F \cdot h_1)^2} \quad (13.54)$$

where h_{nb} is the nucleate boiling heat transfer coefficient calculated by the Cooper (13.49) correlation, and h_1 is the convective heat transfer coefficient calculated for the liquid only flowing in the same tube with local mass flow rate $\dot{M}_1 = \dot{M}(1 - x)$, to be

computed by the Dittus–Boelter correlation (13.31) with the Reynolds number $Re_1 = \frac{4\dot{M}_1}{\pi d_i \cdot \mu_l}$ and the liquid phase Prandtl number Pr_1 . S is the nucleate boiling suppression factor, less than unity because, under forced convection conditions, the temperature gradient in the liquid film next to the pipe wall is steeper than in nucleate pool boiling, thus keeping down the heat transfer nucleation contribution. F is the convective enhancement factor, larger than unity, because of the increased liquid velocity caused by the vapor formed in the evaporation process. The two factors are to be calculated as follows:

$$F = \left[1 + x \cdot Pr_1 \left(\frac{\rho_l}{\rho_v} - 1 \right) \right]^{0.35}; \quad S = \frac{1}{(1 + 0.055 F^{0.1} \cdot Re_1^{0.16})} \quad (13.55)$$

The correlation by Gungor and Winterton (1987) is also reported here for its simplicity and because explicitly it differentiates the horizontal flow situation from the vertical one:

$$\frac{h_{\text{sfb}}}{h_1} = (1 + 3000 \cdot Boi^{0.86}) \cdot S_2 + 1.12 \left(\frac{x}{1-x} \right)^{0.75} \left(\frac{\rho_l}{\rho_v} \right)^{0.41} \cdot F_2 \quad (13.56)$$

where h_1 is as defined before; Boi is the boiling number, $Boi = \frac{\dot{q}}{\dot{m} \cdot H_v}$, and Fr_1 is the liquid phase Froude number, $Fr_1 = \frac{\dot{m}^2}{\rho_l^2 \cdot g \cdot d_i}$. The two factors S_2 and F_2 are to be calculated as follows:

$$S_2 = Fr_1^{(0.1-2Fr_1)} \text{ if horizontal and } Fr_1 < 0.05; S_2 = 1 \text{ otherwise} \quad (13.57)$$

$$F_2 = Fr_1^{0.5} \text{ if horizontal and } Fr_1 < 0.05; F_2 = 1 \text{ otherwise} \quad (13.58)$$

The local flow pattern evaporation model of Kattan, Thome, and Favrat is fully described in Wolverine–Thome (2010). It is based on their original two-phase diabatic flow pattern map specific for horizontal evaporating flow; their flow boiling model covers fully stratified flows, stratified–wavy flows, intermittent flows, annular flows, and annular flows with partial dry-out. Later improvements to the model, also presented in Wolverine–Thome (2010), implemented heat transfer prediction methods also for mist flow and for the region separating mist flow from annular and stratified–wavy flow regimes.

Enhancement techniques for in-tube evaporation heat transfer include the use of twisted tape inserts, corrugated/fluted tubes, internally porous coated tubes, and, most of all, microfin tubes, both of helical and of herringbone inner-grooved types. Whereas the use of a twisted tape insert is mainly reserved to retrofit into existing plain tube bundles without retubing, microfin tubes are now the prevailing choice for enhanced boiling: fins are usually 0.1–0.3 mm in height and thus with an efficiency close to unity independent of the metal, shape, and average thickness. Helical

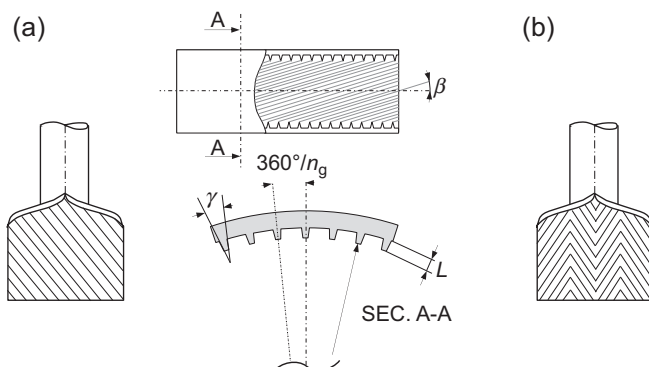


Figure 13.21 Low-fin tubes. (a) Microfin; (b) herringbone.

microfinned tubes are typically made of copper (but also available in stainless steel), with an outside diameter from 4 to 15 mm, a single set of 50–70 fins with helix angle from 6 to 30 degrees (18 degrees is most common), and triangular or trapezoidal fin shapes with an apex angle from 25 to 90 degrees; they are also available in the duo-height type, with alternating fins of different heights. Other microfinned surfaces are available, such as cross-grooved tubes that present an additional set of grooves with opposite helical orientation, whereas herringbone tubes are characterized by V-shaped grooves; see [Fig. 13.21](#).

Readers should be warned that quite often, in the presentation of heat transfer performance of microfin tubes, the design convective heat transfer coefficient is given and referred to a reference fictitious area, that of a cylinder with diameter either equal to the base-fin pipe diameter or equal to the pipe diameter measured at the fin tip; although this choice facilitates the comparison between the heat transfer performance of the microfin tube and that of a plain tube of equal internal diameter d_i , it may otherwise cause confusion as this procedure is not universally adopted.

Microfin tubes enhance the evaporation design heat transfer coefficient typically even by a factor of 3 to 5 at low mass velocities and in horizontal orientation compared to a plain tube of equivalent geometry at the same operating conditions; the heat transfer enhancement is less pronounced as the mass velocity increases or for vertical orientation, tending to the value of the internal transfer surface area ratio (1.4–2.5); on the other hand the penalization in terms of increased pressure drop is always quite low, making this geometry by far the best choice for effective flow boiling enhancement.

Procedures for predicting the heat transfer performance of enhanced tubes in flow evaporation are presented and discussed in [Wolverine–Thome \(2010\)](#).

13.6 Condensation heat transfer

13.6.1 External film condensation heat transfer

Surface condensation of a saturated or superheated pure (single-component) vapor in contact with a cooled surface takes place when the temperature of the surface t_w is

below the vapor saturation temperature t_{sat} , univocally dependent on its pressure: either dropwise or film-wise condensation may take place. In dropwise condensation the liquid forms on the surface as droplets of different sizes, drained by the action of gravity and, if the case, vapor shear; this mechanism takes place on hydrophobic surfaces, often obtained by suitable coatings, and it is extremely effective as far as heat transfer is concerned, with heat transfer coefficients around 1 order of magnitude higher than in film-wise condensation. Nevertheless dropwise condensation is difficult to promote, stabilize, and maintain, and therefore industrial heat transfer apparatuses are always designed referring to film-wise condensation, with the liquid condensate forming a continuous film on the cooled surface, drained by the action of gravity and, if the case, vapor shear.

Film-wise condensation heat transfer was first modeled by Nusselt in 1916, when he obtained the analytical solution to the problem of condensation of a saturated vapor on a vertical plain surface under the following assumptions (Nusselt, 1916):

- laminar flow and constant thermophysical properties for the condensate liquid film flowing on the surface;
- constant wall temperature t_w , and uniform saturation temperature $t_{\text{sat}} > t_w$ of the vapor (no thermal resistance at the condensate–vapor interface);
- negligible shear stress at the condensate–vapor interface;
- heat transfer across the condensate liquid film occurring only by conduction, with linear liquid temperature distribution. This means that the local condensation heat transfer coefficient can be computed as $h = \lambda_l / \delta$, where δ is the local thickness of the liquid condensate film.

Under these conditions it is possible to obtain the expression of the condensate film thickness as a function of the vertical position on the plate, and then the Nusselt number $\overline{Nu}_{\text{plate}}$ related to the average condensation heat transfer coefficient \bar{h}_{plate} for a plate of vertical dimension Z :

$$\overline{Nu}_{\text{plate}} = \frac{\bar{h}_{\text{plate}} \cdot Z}{\lambda_l} = 0.943 \left[\frac{\rho_l \cdot g (\rho_l - \rho_v) H_{lv} \cdot Z^3}{\mu_l \cdot \lambda_l (t_{\text{sat}} - t_w)} \right]^{0.25} \quad (13.59)$$

The same kind of analysis can be applied to the outer surface of a horizontal circular tube of external diameter d_e , yielding under the same assumptions, for the Nusselt number Nu_{tube} referred to the circumferential averaged heat transfer coefficient h_{tube} :

$$Nu_{\text{tube}} = \frac{h_{\text{tube}} \cdot d_e}{\lambda_l} = 0.729 \left[\frac{\rho_l \cdot g (\rho_l - \rho_v) H_{lv} \cdot d_e^3}{\mu_l \cdot \lambda_l (t_{\text{sat}} - t_w)} \right]^{0.25} \quad (13.60)$$

In external condensation on a bundle of horizontal tubes, the liquid condensate drains from the upper tubes to the lower ones, thus increasing the average condensate film thickness of the inundated lower tubes and consequently lowering the average condensation heat transfer coefficient; the effect is mitigated by the generation of ripples and promotion of turbulence caused by inundation. For a vertical tier of N

horizontal tubes, the Nusselt number \overline{Nu}_{Ntubes} , referred to the condensation heat transfer coefficient \overline{h}_{Ntubes} averaged over all the N tubes of the vertical tier, can be calculated using the expression:

$$\overline{Nu}_{Ntubes} = \frac{\overline{h}_{Ntubes} \cdot d_e}{\lambda_l} = N^{-m} \cdot Nu_{tube} \quad (13.61)$$

where Nu_{tube} is the Nusselt number for the upper noninundated tube of the tier, calculated by Eq. (13.60); for the exponent m , the rather conservative value $m = 0.25$ is often suggested; more realistic values, validated by experimental tests, are $m = 0.08$ or even $m = 0.04$.

So far the effect of shear at the liquid–vapor interface was considered negligible; at high vapor velocities, this may become the prevailing factor in determining the liquid film characteristics and therefore the heat transfer coefficients. Vapor shear reduces the film thickness and promotes turbulence, thus increasing heat transfer coefficients; further it contributes to the removal of the liquid film from the wall, and last it can modify the intertube flow modes (Wolverine–Thome, 2010).

Honda and coworkers (Honda et al., 1988) presented an analysis of the phenomenon able to predict the experimental data from various sources. For the shear controlled regime, namely for $Re_L > 200,000$, the shear dominated Nusselt number is calculated by the following expression:

$$Nu_{sh} = \frac{h_{sh} \cdot d_e}{\lambda_l} = a(1 + b \cdot E)^{0.5} B \cdot Re_L^{(1-m/2)} \cdot Re_f^{*-n} \quad (13.62)$$

$$E = [\dot{q} / (H_{lv} \cdot \rho_v \cdot w_{max,v})] Re_V^m; \quad B = (\rho_v / \rho_l)^{0.5} (v_v / v_l)^{m/2} Pr_l^{0.4};$$

$$Re_L = (w_{max,v} \cdot \rho_l \cdot d_e) / \mu_l; \quad Re_V = (w_{max,v} \cdot \rho_v \cdot d_e) / \mu_v; \quad Re_f^* = 2\Gamma / \mu_l$$

h_{sh} is here the condensation heat transfer coefficient for any single tube in the bundle; vapor velocity $w_{max,v}$ is to be computed referring to the local mass flux (immediately above the tube under consideration) and the minimum flow area; and Γ is the mass flow rate of condensate per unit length of tube, evaluated at its base and in the assumption of uniformly dispersed inundation. Values for the constants a and b and exponents m and n are reported in Table 13.10.

For the gravity and shear controlled regime ($Re_L < 200,000$) Honda and coworkers suggest using an asymptotic combination of Nu_{sh} and Nu_{gr} , this last being the Nusselt number calculated for the gravity-controlled regime, for which they present their own expression.

Table 13.10 Constants and exponents for Eq. (13.62)

Staggered tube layout	$a = 0.165(p_t/p_l)^{0.7}$	$b = 1.83$	$m = 0.4$	$n = 0.2$
In-line tube layout	$a = 0.053$	$b = 18.0$	$m = 0.2$	$n = 0.2$

Bundle condensation heat transfer can be enhanced by employing integral low-finned tubes (dubbed 2D, two-dimensional fins): fins are helical, with typical density ranging from 700 to 1500 fins per meter, 0.6–1.5 mm in height, and with thickness on the order of 0.3 mm.

Surface tension σ plays a very important role in condensation heat transfer on a 2D finned horizontal tube, inasmuch as it affects the flow dynamics of the liquid condensate on the tube surface. Local differences in pressure in the liquid condensate film, determined by curvatures of the liquid–vapor interface, promote a surface tension-driven flow of condensate from the fin tip toward the fin base, where drainage by gravity prevails. In addition, surface tension favors a retention of liquid among the fins in the lower part of the tube, as depicted in Fig. 13.22, hindering heat transfer in that area of the tube.

Honda et al. (1983) derived an expression for the liquid condensate retention (flooding) angle ϕ_R :

$$\phi_R = \cos^{-1} \left[\frac{4\sigma \cdot \cos(\gamma/2)}{\rho_l \cdot g \cdot s_t \cdot D_t} - 1 \right]; \quad \text{valid for } s_t < 2L \quad (13.63)$$

where L is the fin height, s_t is the interfin spacing at the fin tips, D_t is the tube diameter evaluated at the fin tip, and γ is the fin apex angle for a trapezoidal fin; for a rectangular fin, $\gamma = 0^\circ$. Note that, for $\frac{4\sigma \cdot \cos(\gamma/2)}{\rho_l \cdot g \cdot s_t \cdot D_t} \geq 2$, ϕ_R must be set equal to zero and the fin interspace is fully flooded. Integral low-finned tubes are more effectively utilized with low-surface-tension fluids; steam condensation would require larger fin spacing to limit the retention angle; these types of enhanced tubes are very seldom if ever utilized for steam condensation, also given the very high condensation heat transfer coefficients achieved with steam on smooth surfaces.

Beatty and Katz (1948) first presented a model for the prediction of condensation heat transfer coefficients on a single horizontal 2D low-finned tube. Their model is

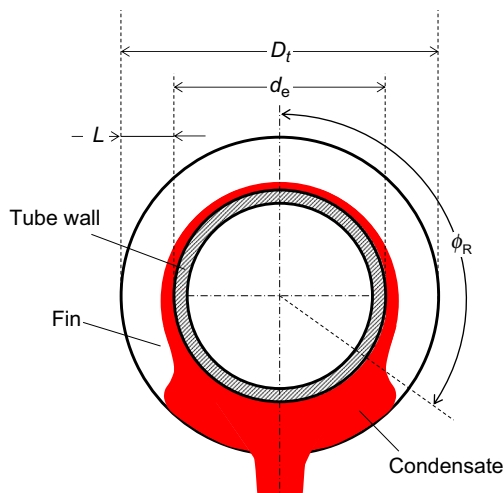


Figure 13.22 External condensation on low-fin tubes: flooding angle.

based on a Nusselt-type two-zone approach: for the prime interfin surface they applied the Nusselt theory for a horizontal plain tube, whereas for the fin flanks they considered the Nusselt analysis related to a vertical surface; they ignored the phenomenon of interfin liquid retention.

Later on, Webb et al. (1985) improved the Beatty and Katz model to predict the design heat transfer coefficient h_d referred to the total transfer area $A_{\text{tot}} = A_{\text{root}} + A_{\text{fin}}$, by assuming that surface tension, rather than gravity force, controls condensate drainage from the fin surface, and taking into consideration the effect of interfin flooding, too; their final correlations are reported in the following:

$$h_d = h \cdot \Omega$$

$$= \frac{\phi_R}{\pi} \left(h_{\text{root}} \frac{A_{\text{root}}}{A_{\text{tot}}} + \eta_f \cdot h_{\text{fin}} \frac{A_{\text{fin}}}{A_{\text{tot}}} \right) + \left(1 - \frac{\phi_R}{\pi} \right) h_{\text{flooded}}; \quad (13.64)$$

ϕ_R must be expressed in (rad)

$$h_{\text{fin}} = 0.943 \left[\frac{\lambda_l^3 \cdot \rho_l \cdot H_{lv}}{\mu_l (t_{\text{sat}} - t_w)} \right]^{0.25} \left[\frac{2\sigma}{L^2} \left(\frac{1}{p_f} + \frac{1}{\delta_{\text{root}}} \right) \right]^{0.25};$$

$$h_{\text{root}} = 1.514 \left(\frac{\mu_l^2 \cdot Re_{\text{root}}}{g \cdot \lambda_l^3 \cdot \rho_l^2} \right)^{-\frac{1}{3}};$$

$$h_{\text{flooded}} = \lambda_l \frac{2L + s}{L \cdot s} \text{ (for rectangular cross-section fins)}$$

$$Re_{\text{root}} = \frac{4\dot{M}_{\text{root}}}{\mu_l \cdot s_{\text{root}}}; \quad \dot{M}_{\text{root}} = \dot{M}_{\text{fin}} + h_{\text{root}} \cdot A_{\text{root}} \frac{t_{\text{sat}} - t_w}{H_{lv}};$$

$$\dot{M}_{\text{fin}} = h_{\text{fin}} \cdot \eta_f \cdot A_{\text{fin}} \frac{(\phi_R/\pi)(t_{\text{sat}} - t_w)}{\pi \cdot H_{lv}}; \quad (\phi_R \text{ in (rad)})$$

It may be appreciated that, in the unflooded zone, the convective heat transfer coefficient is calculated as a weighted average of the convective coefficient pertaining to the prime root surface A_{root} and that pertaining to the fin surface A_{fin} , with due account to the fin efficiency η_f at the condition of this zone. In the preceding equations Ω is the surface efficiency, ϕ_R the retention angle, Eq. (13.63), L the fin height, p_f the fin pitch, δ_{root} the fin thickness, s the fin interspace, t_w the temperature of the prime surface, \dot{M}_{root} the condensate flow rate leaving A_{root} , and \dot{M}_{fin} the condensate flow rate on fins.

The last term of Eq. (13.64) refers to the heat transfer rate across the condensate bridged zone; most of the time this contribution is small and can often be omitted from the calculation. For this reason a precise evaluation of h_{flooded} is not necessary. A rough expression is suggested here to compute the convective heat transfer

coefficient for the condensate bridged zone h_{flooded} : it is taken as equal to the specific conductance of a stationary uniform liquid film of thickness approximately equal to the ratio of the interfin volume to the heat transfer surface area (fin tip neglected), with unitary fin efficiency in this zone due to the reduced value of the convective coefficient; the expression given earlier is for a rectangular cross-section fin.

Vapor shear reduces thickness and promotes turbulence in the liquid film; furthermore it affects the intertube flow pattern: at very low vapor velocities, the condensate leaves the tube, forming equally spaced columns; when the vapor velocity increases, the columns break into droplets and a dispersed flow takes place. On the other hand, vapor shear seems not to influence the extension of the flooded portion of the tube.

Cavallini et al. (1996) experimented with the effect of vapor shear on the condensation heat transfer coefficient on single low-fin tubes. They observed that for vapor Reynolds numbers $Re_v = \frac{\rho_v \cdot w_{\text{max},v} \cdot D_t}{\mu_v}$ in the range 70,000–100,000, the vapor shear stress contribution to heat transfer starts to become evident above the sole gravity and surface tension contributions, whereas at the highest values of the vapor Reynolds number tested, around 300,000–350,000, vapor shear is the predominant active force governing condensate drainage. To reproduce this behavior, they proposed an asymptotic expression to compute the design heat transfer coefficient in the form:

$$h_d = \left(h_{\text{st}}^2 + h_{\text{fc}}^2 \right)^{0.5} \quad (13.65)$$

[design heat transfer coefficients referred to a fictitious cylindrical
reference surface of diameter D_t]

where the first asymptote h_{st} is the design heat transfer coefficient under stationary vapor conditions when shear stress effects are insignificant, and the second asymptote h_{fc} is the heat transfer coefficient when forced convection mechanisms are predominant and gravity and surface tension effects become negligible.

The first term h_{st} can be calculated by suitable models for stationary conditions, such as the model by Webb and coworkers presented earlier. The second term h_{fc} can be expressed as a function of the geometry of the 2D extended surface, of the so-called equivalent Reynolds number Re_{eq} , and of the liquid Prandtl number Pr_l :

$$Nu_{\text{fc}} = \frac{h_{\text{fc}} \cdot D_t}{\lambda_l} = C \cdot Re_{\text{eq}}^{0.8} \cdot Pr_l^{1/3} \quad (22,000 \leq Re_{\text{eq}} \leq 110,000; \quad 3 \leq Pr_l \leq 8) \quad (13.66)$$

with:

$$Re_{\text{eq}} = \left[(\rho_v \cdot w_{\text{max},v} \cdot D_t) / \mu_l \right] (\rho_l / \rho_v)^{0.5}; \quad Pr_l = (c_{pl} \cdot \mu_l) / \lambda_l;$$

$$C = 0.03 + 0.166(\delta_t / p_f) + 0.07(L / p_f)$$

where δ_t is the fin thickness at the tip, p_f the fin pitch, and L the fin height.

In horizontal bundle condensation, both shear and inundation effects must be accounted for. Cavallini et al. (1999) in this context suggested using the following simple expression to compute the average condensation heat transfer coefficient of the N th tube in a vertical tier, which refers to a single inundation factor:

$$h_{dN} = \left(h_{st}^2 + h_{fc}^2 \right)^{0.5} \left[N^{0.96} - (N - 1)^{0.96} \right] \quad (13.67)$$

[design heat transfer coefficients referred to a fictitious cylindrical
reference surface of diameter D_t]

where both h_{st} and h_{fc} are the values calculated for a single tube, Eqs. (13.64) and (13.66).

The adverse influence of liquid inundation in external condensation with 2D horizontal low-finned tubes can be cleared by using 3D integral low-finned tubes: tridimensional fins are in this case in the form of pins, rods, or spines, for example, obtained by cross-cutting or by notching conventional integral low-finned tubes; various types of 3D integral low-fin tubes are offered on the market. For more information regarding the heat transfer performance of this enhancing geometry, see (Cavallini et al., 1999, 2003) or (Wolverine—Thome, 2010).

13.6.2 In-tube flow condensation heat transfer

During condensation inside horizontal smooth tubes, the two-phase flow may be dominated by vapor shear or gravity forces. Whereas an annular flow pattern is associated with high vapor shear, stratifying, wavy, or slug flow appears when gravity is the controlling force; Dobson and Chato (1998), for example, took visual observations of this phenomenon and developed criteria for the transition boundaries among the various flow patterns.

In stratifying flow processes, when vapor shear at the liquid—vapor interface is negligible, a thick condensate layer appears at the bottom of the tube, through which heat transfer can be neglected, and a thin liquid film settles in the upper portion of the tube. Heat transfer through the thin film may be analyzed by the classical Nusselt theory, and the average heat transfer coefficient h over the entire circumferential tube wall can consistently be computed by the following expression:

$$h = \kappa \left[\frac{\lambda_l^3 \cdot \rho_l^2 \cdot g \cdot H_{lv}}{\mu_l \cdot d_i \cdot (t_{sat} - t_w)} \right]^{0.25} ; \quad \kappa = 0.728 \cdot \alpha^{0.75} ; \quad (13.68)$$

$$\alpha = \left\{ 1 + (\rho_v / \rho_l)^{2/3} [(1 - x) / x] \right\}^{-1}$$

where the leading parameter κ is given as a function of the void fraction α , for which the Zivi (1964) expression is here suggested. For a definition of α see Section 13.7.

In tube-side industrial condensers the conditions are such that the action of shear at the liquid–vapor interface cannot be neglected for most of the heat transfer surface, and therefore realistic tools for predicting heat transfer coefficients taking into account both gravity and shear are required. It has been recognized that the mechanism of heat transfer is influenced by the configuration of the two-phase flow; although sophisticated works are present in the scientific literature linking the heat transfer coefficient to the specific actual flow regime (Cavallini et al., 2002; Thome et al., 2003), a much simpler heat transfer performance predicting procedure is briefly outlined here, which proved reliable for the design of heat transfer apparatuses (Cavallini et al., 2006).

It was observed that, in flow condensation inside a horizontal pipe, the heat transfer coefficient is Δt -dependent only when gravity is the prevailing force in the determination of the flow pattern, whereas when annular flow or annular-mist flow is present, the heat transfer coefficient does not depend on the vapor excess temperature in condensation $\Delta t = t_{\text{sat}} - t_w$; furthermore it was possible to derive a unified procedure for the prediction of the heat transfer coefficient in all flow patterns falling in the gravity-dependent category [substantially wavy stratified and intermittent (slug) flow patterns]; a different procedure must be considered in the gravity-independent flow patterns, substantially annular flow. A simple criterion to establish the transition between the two flow pattern categories was found in terms of dimensionless vapor velocity J_v , whose transition value J_v^T can be expressed as a function of the Martinelli parameter X_{tt} , differently for two families of fluids, hydrocarbons and other refrigerants; all the aforementioned parameters are specified below. For $J_v > J_v^T$ the flow pattern is such that the heat transfer coefficient is Δt -independent and the specific predicting procedure should be applied; conversely, if $J_v \leq J_v^T$ the heat transfer coefficient is Δt -dependent, and a different predicting method must be used. The details of the predicting calculations are as follows, observing that h_A is the condensation heat transfer coefficient in the Δt -independent region, and h_D is the one in the Δt -dependent region:

$$X_{tt} = \left(\frac{\mu_l}{\mu_v} \right)^{0.1} \left(\frac{\rho_v}{\rho_l} \right)^{0.5} \left(\frac{1-x}{x} \right)^{0.9}; \quad J_v = x \cdot \dot{m} / [g \cdot d_i \cdot \rho_v (\rho_l - \rho_v)]^{0.5}$$

$$J_v^T = \left\{ [7.5 / (4.3 X_{tt}^{1.111} + 1)]^{-3} + C_T^{-3} \right\}^{-1/3};$$

$$C_T = 1.6 \text{ for hydrocarbons}$$

$$C_T = 2.6 \text{ for other refrigerants}$$

$$\Delta t - \text{independent flow regime} (J_v > J_v^T):$$

$$h_A = h_{LO} \left[1 + 1.128 x^{0.817} (\rho_l / \rho_v)^{0.369} (\mu_l / \mu_v)^{0.236} (1 - \mu_v / \mu_l)^{2.14} Pr_l^{-0.100} \right]$$

$$h_{LO} = 0.023 Re_{LO}^{0.8} \cdot Pr_l^{0.4} \cdot \lambda_l / d_i$$

$$(13.69)$$

Δt – dependent flow regime ($J_v \leq J_v^T$):

$$h_D = \left[h_A (J_v^T / J_v)^{0.8} - h_{\text{STRAT}} \right] (J_v / J_v^T) + h_{\text{STRAT}}; \quad Re_{\text{LO}} = \dot{m} \cdot d_i / \mu_l \quad (13.70)$$

$$h_{\text{STRAT}} = 0.725 \left\{ 1 + 0.741 [(1 - x)/x]^{0.332} \right\}^{-1} \\ \times [\lambda_l^3 \cdot \rho_l (\rho_l - \rho_v) g \cdot H_{lv} / (\mu_l \cdot d_i \cdot \Delta t)]^{0.25} + (1 - x^{0.087}) h_{\text{LO}}$$

Surface geometries for enhanced flow condensation are substantially the same integral finned geometries considered for enhanced in-tube boiling, that is, low-fin surfaces such as microfin, cross-grooved, and herringbone tubes. These geometries can display a condensation heat transfer coefficient enhancement ratio, compared to equivalent smooth tubes under the same operating conditions, far exceeding the mere area increase ratio, with modest pressure drop penalization, and this is more true when the fluid mass velocity in the channel is low. Generally speaking, microfin tubes show a heat transfer enhancement from 80% to 140%, with a pressure loss increase from 20% to 80%; cross-grooved tubes give a 25–30% higher heat transfer performance than microfin tubes with a pressure drop increase only 6–10% higher. With herringbone tubes, the best results are obtained at high mass velocities [above 300 kg/(m²s)], when they outperform the other types of low-fin tubes. Heat transfer enhancements are partly due to the simple increase in the effective transfer area, but additionally also to turbulence induced in the liquid film by the microfins, and to the surface tension effect on the condensate flow and drainage.

The first correlation presented in the literature to predict design heat transfer coefficients during pure vapor condensation inside copper low-fin, microfin, and cross-grooved tubes is the one by Cavallini et al. (1999); it is based on the Cavallini and Zecchin equation for smooth tubes (Cavallini and Zecchin, 1974). It has the form of a forced convection correlation referred to an equivalent Reynolds number Re_{eq} . With respect to the original correlation, two new nondimensional groups have been inserted; the first one, Rx , accounts for the area increase due to the presence of the helical low fins; for cross-grooved tubes the same expression is used referred to the first set of grooves, as the additional set does not significantly improve the heat transfer area. The Bond number Bo accounts for surface tension effects, whereas the product of the Bond number and the Froude number Fr directly represents the relative weight of shear and surface tension effects.

The calculation procedure can be summarized as follows:

$$Nu = \frac{h_d \cdot d_t}{\lambda_l} = 0.05 Re_{\text{eq}}^{0.8} \cdot Pr_l^{1/3} \cdot Rx^m (Bo \cdot Fr)^n \quad (13.71)$$

$$(Re_{\text{eq}} > 15,000; \quad 3 < Pr_l < 6.5; \quad 0.3 < Bo \cdot Fr < 508; \quad 7^\circ < \beta < 30^\circ)$$

[design heat transfer coefficient h_d referred to a fictitious cylindrical reference surface of diameter D_t]

$$Re_{eq} = 4\dot{M} \left[(1-x) + x(\rho_l/\rho_v)^{0.5} \right] / (\pi \cdot D_t \cdot \mu_l)$$

$$Rx = \{ [2L \cdot n_g (1 - \sin(\gamma/2))] / [\pi \cdot D_t \cos(\gamma/2)] + 1 \} / \cos \beta$$

$$Fr = w_{VO}^2 / (g \cdot D_t); \quad Bo = g \cdot \rho_l \cdot L \cdot \pi \cdot D_t / (8 \sigma \cdot n_g)$$

$$\text{Low - fin } (L/D_t \geq 0.04): m = 1.40 \quad n = -0.08$$

$$\text{Micro - fin } (L/D_t < 0.04): m = 2.00 \quad n = -0.26$$

$$\text{Cross - grooved}: m = 2.10 \quad n = -0.26$$

where n_g is the total number of grooves, β the spiral angle, and γ the fin apex angle (see Fig. 13.21).

It should be emphasized that vapor velocity w_{VO} must be always calculated with reference to the total two-phase mass flow rate and the properties of the vapor phase, referring to a circular cross section of diameter D_t , the diameter at the fin tip of the finned tube.

Quite often in air-cooled condensers, the tubes are leaned downward by a few degrees in the flow direction to favor condensate drainage; heat transfer correlations for horizontal tubes must be used in this circumstance too.

13.7 Pressure drop in two-phase flow

Similar to what happens in single-phase flow, in channeled flow the two-phase heat transfer coefficient can generally be increased at the expense of a growth in pressure drop. However, in two-phase heat transfer, different from what happens with a single-phase fluid, static pressure drop affects the fluid temperature profile in the exchanger, with related effects in its performance. Reliable pressure-drop-predicting procedures are needed for the correct design of condensers and boilers.

The total static pressure drop gradient of a channeled two-phase fluid flow is the sum of three contributions, namely:

$$\left(\frac{dp}{dz} \right)_t = \left(\frac{dp}{dz} \right)_{\text{grav}} + \left(\frac{dp}{dz} \right)_{\text{mom}} + \left(\frac{dp}{dz} \right)_{\text{frict}} \quad (13.72)$$

where z is the axial coordinate, oriented in the flow direction; $\left(\frac{dp}{dz} \right)_{\text{grav}}$ is the gravitational pressure drop gradient due to gravity, nil for horizontal flow, negative for upward flow, and positive for downward flow; $\left(\frac{dp}{dz} \right)_{\text{mom}}$ is the momentum or acceleration pressure drop gradient, which can be nil, positive, or negative; and $\left(\frac{dp}{dz} \right)_{\text{frict}}$ is the frictional pressure drop gradient, always negative; it is nil when ideal frictionless flow is assumed.

In two-phase (liquid/vapor) flow it is necessary to refer to a model for the flow structure to be able to analyze and try to work out predicting procedures for the various pressure drop components.

The homogeneous flow model is the simplest to think of: a unique single pseudo-fluid is considered, characterized by properties calculated as suitable intercorrelations among the liquid and the vapor phase properties. The rules for single-phase flow are then applied. Apart from some very dispersed types of flow, such as some mist flow patterns, this model is inadequate in most cases, and it will not be further dealt with here.

In most cases a separated flow model is considered: the liquid and vapor streams are supposed to flow separately in the channel, each at its own average velocity. In this context, the quantity (cross-sectional) void fraction becomes relevant, defined as the fraction of the total cross-flow area a occupied by the vapor phase, the rest of course being reserved to the flow of the liquid phase.

Once the void fraction α is known, the average liquid w_l and vapor w_v phase velocities can be computed as:

$$w_l = \frac{\dot{m}(1-x)}{\rho_l(1-\alpha)}; \quad w_v = \frac{\dot{m} \cdot x}{\rho_v \cdot \alpha} \quad (13.73)$$

where $\dot{m} = \dot{M}/a$ is the total mass velocity.

Among the many procedures proposed in the scientific literature to compute the void fraction, the correlation by Steiner (VDI Heat Atlas, 2010) is now widely used; it is derived from the Rouhani and Axelsson (1970) drift flux model, and for in-tube horizontal flow it reads:

$$\alpha = \frac{x}{\rho_v} \left\{ \left[1 + 0.12(1-x) \right] \left(\frac{x}{\rho_v} + \frac{1-x}{\rho_l} \right) + \frac{1.18(1-x)[g \cdot \sigma(\rho_l - \rho_v)]^{0.25}}{\dot{m} \cdot \sqrt{\rho_l}} \right\}^{-1} \quad (13.74)$$

In the separated flow model, the gravitational pressure drop gradient can be calculated as follows:

$$\left(\frac{dp}{dz} \right)_{\text{grav}} = \rho_{\text{tp}} \cdot g \cdot \cos \theta \quad (13.75)$$

where ρ_{tp} is the two-phase density $\rho_{\text{tp}} = \rho_l(1-\alpha) + \rho_v \cdot \alpha$, and θ is the angle between the flow direction and the gravity vector.

The expression of the acceleration pressure gradient is the following:

$$\left(\frac{dp}{dz} \right)_{\text{mom}} = -\frac{d}{dz} [\dot{m}(1-x) \cdot w_l + \dot{m} \cdot x \cdot w_v] = -\dot{m}^2 \frac{d}{dz} \left[\frac{(1-x)^2}{\rho_l(1-\alpha)} + \frac{x^2}{\rho_v \cdot \alpha} \right] \quad (13.76)$$

and this expression can be easily integrated between inlet and outlet of the channel.

For an evaporating flow in a constant sectional area duct the contribution of the momentum pressure gradient to the total static pressure gradient is negative, thus contributing to a loss in pressure in the flow direction. For a condensing flow in a constant sectional area duct it is the other way round, thus contributing to a pressure recovery in the flow direction.

As to the frictional pressure drop gradient, several methods have been proposed in the scientific literature since the pioneering work by [Lockhart and Martinelli \(1949\)](#), who first introduced the concept of two-phase multipliers, addressed too in many other frictional pressure gradient-predicting procedures ever since.

The Friedel correlation ([Friedel, 1979](#)) for in-tube flow, presented here, utilizes the two-phase multiplier Φ_{Fr} to predict the two-phase frictional pressure gradient from the frictional pressure gradient $\left(\frac{dp}{dz}\right)_{frict,LO}$ calculated for the liquid flowing alone in the same tube with total mass flux \dot{m} :

$$\left(\frac{dp}{dz}\right)_{frict} = \Phi_{Fr}^2 \cdot \left(\frac{dp}{dz}\right)_{frict,LO} \quad (13.77)$$

The frictional pressure gradient for the liquid is calculated as $\left(\frac{dp}{dz}\right)_{frict,LO} = -f_{LO} \dots f_{LO} \frac{1}{d_i} \frac{\dot{m}^2}{2\rho_l}$, with the single-phase friction factor f_{LO} calculated with the Blasius [Eq. \(13.34\)](#), with $Re = \frac{\dot{m} \cdot d_i}{\mu_l}$.

The two-phase flow multiplier is

$$\Phi_{Fr}^2 = E + \frac{3.24F \cdot H}{Fr_h^{0.045} We_1^{0.035}} \quad (13.78)$$

with

$$Fr_h = \frac{\dot{m}^2}{g \cdot d_i \cdot \rho_h^2}; \quad We_1 = \frac{\dot{m}^2 \cdot d_i}{\sigma \cdot \rho_h}; \quad \rho_h = \left(\frac{x}{\rho_v} + \frac{1-x}{\rho_l} \right)^{-1};$$

$$E = (1-x)^2 + x^2 \frac{\rho_l \cdot f_{VO}}{\rho_v \cdot f_{LO}}; \quad F = x^{0.78} (1-x)^{0.224};$$

$$H = \left(\frac{\rho_l}{\rho_v} \right)^{0.91} \left(\frac{\mu_v}{\mu_l} \right)^{0.19} \left(1 - \frac{\mu_v}{\mu_l} \right)^{0.7}$$

The single-phase vapor friction factor f_{VO} refers to the vapor phase flowing alone in the pipe with total mass velocity \dot{m} , calculated with the Blasius [Eq. \(13.34\)](#), where $Re = \frac{\dot{m} \cdot d_i}{\mu_v}$.

An extensive review of two-phase flow frictional pressure drop analyses and predicting procedures in various geometries is reported in [Wolverine—Thome \(2010\)](#), including flattened plain tubes, microfin tubes, corrugated tubes, plain tubes with twisted tape inserts, and plain and enhanced tube bundles.

13.8 Shell-and-tube heat exchangers

The S&THX is the most versatile type of heat transfer apparatus, and for this reason it is the most used in a variety of applications. By far the most common configuration of this exchanger basically consists of a bundle of parallel round tubes inserted longitudinally into a cylindrical round shell; the so-called tube-side fluid flows inside the tubes of the bundle, and the so-called shell-side fluid flows on the outside of the tubes within the shell, where usually appropriate transverse baffles establish a convenient flow pattern; see [Fig. 13.7](#). The main components of an S&THX are therefore the tube bundle with the tubesheets and the baffles, the shell with inlet and outlet nozzles, and the front- and rear-end heads.

The various types of S&THXs are commonly designated according to the Tubular Exchanger Manufacturers Association (TEMA) standard, as shown in [Fig. 13.23](#). This TEMA-type designation comprises three capital letters. The first letter describes the stationary head type at the front end of the apparatus, according to the first column of [Fig. 13.23](#): five different alternatives are possible. The second letter describes the heat exchanger shell, selected from the seven types shown in the middle column of [Fig. 13.23](#). Finally, the third letter, chosen from the eight alternatives shown in the third column of [Fig. 13.23](#), describes the stationary or floating head type at the rear end. For example, an AES TEMA-type S&THX is an exchanger with a channel and removable cover front head, a one-pass shell, and a floating head with backing device rear end.

The most common shell design with no change of phase is the single-pass E TEMA type, whereas the two-pass TEMA F type is less frequently used, with limited temperature variation of the shell-side fluid to restrain heat leakage across the longitudinal baffle and to limit thermal stresses; often, when this flow configuration is required to achieve high thermal effectiveness, it is preferred to use two single-shell-pass exchangers in series, even if this solution is more expensive. Split-flow shells, like TEMA types G and H, are mainly used as condensers or even evaporators, as in refrigeration technology. TEMA type K shell (kettle reboiler) is used for natural convection boiling heat transfer: the larger diameter of the shell compared to that of the tube bundle (up to double) favors vapor disengagement and high heat fluxes. The TEMA X shell, because of its low pressure drop, is used for gas heating or cooling applications (often with external finned tubes, for a balanced thermal design), or for low-pressure vapor condensation. The TEMA J shell is the preferred choice for vapor condensation, with two symmetrical inlets for the vapor phase and one central outlet for the liquid condensate.

Regarding the stationary head, TEMA type A (channel and removable cover) is the most frequently used, both with fixed-tubesheet and with U-tube and floating head

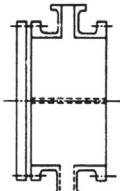
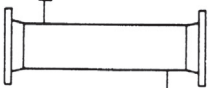
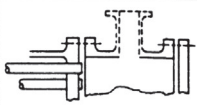
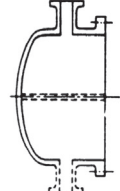
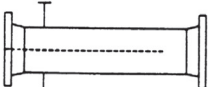

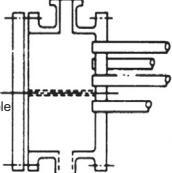
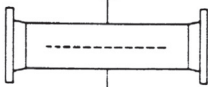
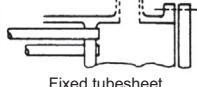
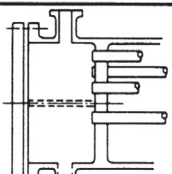
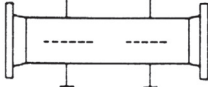
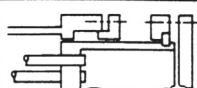
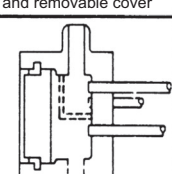
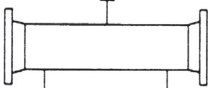
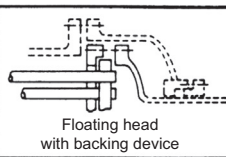
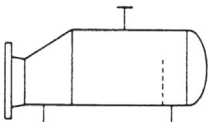
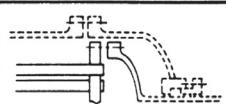
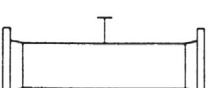
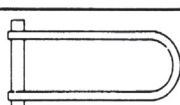
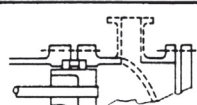
	Front end stationary head types		Shell types		Rear end head types
A	 Channel and removable cover	E	 One pass shell	L	 Fixed tubesheet like "A" stationary head
B	 Bonnet (integral cover)	F	 Two pass shell with longitudinal baffle	M	 Fixed tubesheet like "B" stationary head
C	 Removable tube bundle only Channel integral with tube-sheet and removable cover	G	 Split flow	N	 Fixed tubesheet like "N" stationary head
N	 Channel integral with tube-sheet and removable cover	H	 Double split flow	P	 Outside packed floating head
D	 Special high pressure closure	J	 Divided flow	S	 Floating head with backing device
		K	 Kettle type reboiler	T	 Pull through floating head
		X	 Cross flow	U	 U-tube bundle
				W	 Externally sealed floating tubesheet

Figure 13.23 TEMA shell-and-tube heat exchanger types.
Courtesy of TEMA, the Tubular Exchanger Manufacturers Association.

exchangers. In many circumstances, the bundle can be extracted from the shell for mechanical cleaning requirements; with low-fouling tube-side fluid, the TEMA type B head (bonnet—integral cover) can be preferred because it is less costly.

Channels integral with tubesheet and removable cover (TEMA types C and N) are sometimes used; type N permits only chemical cleaning of the tube bundle side.

Regarding the rear-end heads, considerations similar to those for the front-end heads apply; they can be either stationary or floating, the last arrangement providing allowance for thermal stresses between the tubes and the shell. TEMA types S and T (floating heads) apply to removable bundle designs, allowing mechanical cleaning of the shell-side heat transfer surface, made possible by choosing a square-pitch tube arrangement. The S-type floating head has a split backing ring to reduce the shell diameter required to extract the tube bundle, thus increasing the exchanger thermal performance. The P-type floating head is not recommended because of leakage problems of packed joints.

Round plain tubes, straight or U-shaped, are most often used in S&THXs, with external diameter ranging from 15 to 30 mm; smaller tubes provide higher shell-side heat transfer coefficients and a more compact apparatus, but are less suitable to mechanical cleaning. Finned tubes can be used to balance the tube-side and shell-side thermal resistances. On the shell side low transversal finned tubing can be used, with a fin density ranging from 250 to 1200 fins/m, with up to three times enhancement of the heat transfer surface with high overall efficiency.

Tubes are arranged either in a square or in an equilateral triangle layout, the former allowing mechanical cleaning of the tubes' outside surface in removable bundle exchangers. Tube pitch ranges from 1.25 to 2 times the tube external diameter, the minimum value dictated by the mechanical resistance of the tubesheets.

The tube bundle comprises transverse baffles designed to support the tubes between the two end tubesheets, to address the shell fluid along the appropriate flow pattern in the shell (plate baffles) or to promote turbulence (grid baffles); the most common are the single- and (less frequently) the double-plate segmental baffles illustrated in Fig. 13.24. Other plate baffles are the triple segmental and the disc-and-doughnut types, whereas the most common grid baffle is the rod type.

Segmental baffles direct the fluid in the bundle core at a right angle to the tubes, thus promoting mixing and turbulence and enhancing the heat transfer coefficient; this flow pattern can generate flow-induced vibration of the tubes, and this problem should be addressed at the design stage. Single segmental baffle spacing usually ranges from 0.2 to 1 internal shell diameter, and the window cut is commonly from 20% to 40% of the baffle diameter.

In some circumstances, such as low-pressure-drop requirements or an unsupported tube span that is too large, the exchanger can be built with no tubes in the window of single segmental baffles.

Other components often present in the tube bundle of an S&THX are the impingement baffles or plates, inserted downstream of the inlet nozzle to protect the peripheral tubes from high-velocity flow-induced erosion, cavitation, or vibration.

Moreover the tube bundle comprises the tubesheet(s), tie rods, and, if necessary, sealing strips and/or dummy tubes, inserted to obstruct the bypass flow around the

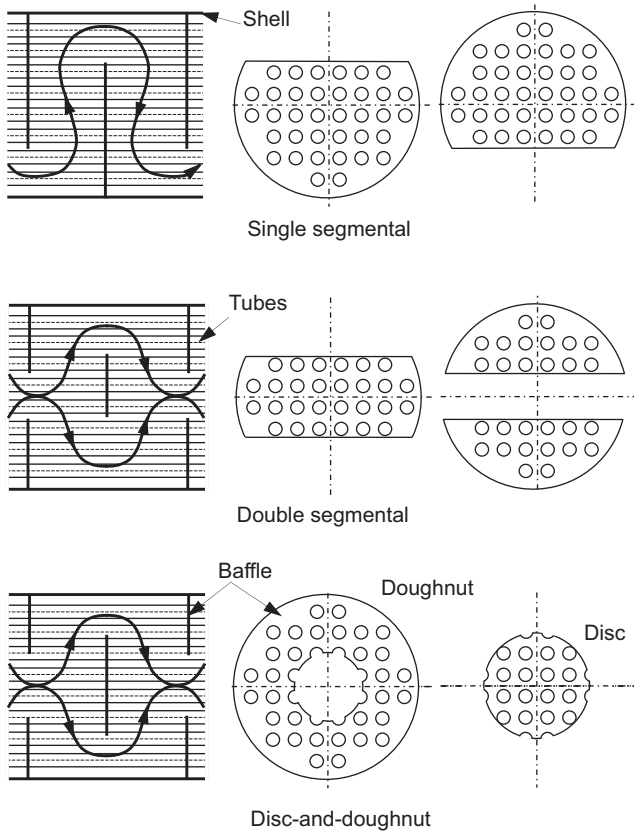


Figure 13.24 Segmental baffles in shell-and-tube heat exchangers.

bundle in the space between the outermost tubes and the shell inner wall; for the same reason, dummy tubes can also be inserted into the bundle to obstruct the bypass stream in flow lanes due to the omission of tubes for the presence of tube pass partitions in the exchanger heads.

TEMA specifies mechanical design and fabrication requirements for three classes of S&THXs: class R for the severe service environments of petroleum refineries and related industries, class C for the generally moderate service environments of commercial and general process industries, and finally class B, for the general chemical industry.

Quite often the design of S&THXs is accomplished using commercially available proprietary software offered by cooperative research organizations or developed by computer service companies (HTRI, Aspen Technology, ...). These are usually application-oriented programs incorporating design and cost analyses complying with codes and standards from various sources (TEMA, ASME, ISO, ...).

It is generally recognized that the best reference for thermal and hydraulic analysis of single-phase S&THXs available in the open literature is the so-called Bell–Delaware method as proposed by Taborek in 1983 (HEDH, 2001); it is a rating method

that predicts the thermal and hydraulic performance of a fully specified exchanger and the involved fluid streams.

Whereas the computation of both heat transfer and pressure drop performance is straightforward for the tube side, for the complex baffled shell-side geometry it is further complicated by the observation that fluid flows partly across and partly along the tubes, and that the unavoidable clearances create leakage and bypass flow paths in parallel to the main stream, each one with different effective heat transfer and pressure drop characteristics. Along with the main effective flow, which is related to flow across an ideal tube bundle, the Bell–Delaware method considers four additional parallel-flow paths:

- the leakage stream in the clearance orifices between the tube wall and the baffle holes;
- the bypass stream in the gap between the outer tubes of the bundle and the inner shell wall, which can be mitigated by the insertion of sealing strips;
- the leakage stream between the baffle edge and the inner shell wall;
- the bypass stream along the lanes in the direction of flow created by the omission of tubes in connection with the pass partition head baffles; these lanes can be blocked by inserting dummy tubes.

The mean value of the heat transfer coefficient for the whole tube bundle, to be applied to the total external surface of the tubes, is calculated by multiplying the ideal tube bank heat transfer coefficient (calculated as if the total shell-side stream flowed across the tube bundle) by suitable correction factors, accounting for the leakage and bypass streams considered earlier (baffle leakage correction factor and bundle bypass correction factor); in addition, other multiplying correction factors are considered, such as the baffle cut correction factor to account for the effect of the window flow on the heat transfer (where cross-flow is not present and the mean fluid velocity is usually different) and, if the case, the unequal baffle spacing correction factor, the laminar flow correction factor, and the wall viscosity correction factor.

As a rough indication, for a well-designed heat exchanger the combined effect of all these correction factors is on the order of 0.6, that is, the mean shell-side heat transfer coefficient is around 60% of that achievable if the total mass flow would cross perpendicularly an ideal tube bank of equal geometry.

As to the shell-side pressure drop, in the Bell–Delaware method it is computed as the sum of the inlet nozzle pressure drop, the bundle pressure drop, and the exit-side pressure drop; in turn the bundle pressure drop is calculated separately for the cross-flow zone, the window zone, the inlet baffle compartment, and the exit baffle compartment.

The Taborek approach of the Bell–Delaware method is reported in detail in [HEDH \(2001\)](#), [Wolverine–Thome \(2010\)](#), and [Shah and Sekulić \(2003\)](#).

[Table 13.11](#) presents typical values of convective heat transfer coefficients and fouling factors for well-designed S&THXs.

13.9 Air-cooled heat exchangers

Air-cooled heat exchangers (air-fin coolers/condensers) are an alternative to water-cooled S&THXs for the rejection of low-grade heat to the ambient sink to cool or,

Table 13.11 Typical film heat transfer coefficients and fouling factors for shell-and-tube heat exchangers (Shah and Sekulić, 2003)

Fluid	Heat transfer coefficient (W/(m ² K))	Fouling factor (m ² K/W)
No change of phase		
Liquid water	5000–7000	$1\text{--}2.5 \times 10^{-4}$
Liquid ammonia	6000–8000	$0\text{--}1 \times 10^{-4}$
Liquid light organics	1500–2000	$0\text{--}2 \times 10^{-4}$
Liquid medium organics	750–1500	$1\text{--}4 \times 10^{-4}$
Liquid heavy organics—heating	250–750	$2\text{--}10 \times 10^{-4}$
Liquid heavy organics—cooling	150–400	$2\text{--}10 \times 10^{-4}$
Liquid very heavy organics—heating	100–300	$4\text{--}30 \times 10^{-4}$
Liquid very heavy organics—cooling	60–150	$4\text{--}30 \times 10^{-4}$
Gas, $p \approx 1\text{--}2$ bars	80–125	$0\text{--}1 \times 10^{-4}$
Gas, $p \approx 10$ bars	250–400	$0\text{--}1 \times 10^{-4}$
Gas, $p \approx 100$ bars	500–800	$0\text{--}1 \times 10^{-4}$
Condensing pure single-component vapor—no noncondensables		
Water, ammonia, $p \approx 1$ bar	10,000–15,000	$0\text{--}1 \times 10^{-4}$
Water, ammonia, $p \approx 10$ bars	15,000–25,000	$0\text{--}1 \times 10^{-4}$
Light organics, $p \approx 1$ bar	2000–4000	$0\text{--}1 \times 10^{-4}$
Light organics, $p \approx 10$ bars	3000–4000	$0\text{--}1 \times 10^{-4}$
Medium organics, $p \approx 1$ bar	1500–4000	$1\text{--}3 \times 10^{-4}$
Boiling pure single-component liquid		
Water, $p < 5$ bars, $\Delta t < 25\text{K}$	3000–10,000	$1\text{--}2 \times 10^{-4}$
Water, $p > 5$ bars, $\Delta t < 20\text{K}$	4000–15,000	$1\text{--}2 \times 10^{-4}$
Light organics, $p < 20$ bars, $\Delta t < 20\text{K}$	1000–4000	$1\text{--}2 \times 10^{-4}$
Medium organics, $p < 20$ bars, $\Delta t < 20\text{K}$	1000–3500	$1\text{--}3 \times 10^{-4}$
Heavy organics, $p < 20$ bars, $\Delta t < 20\text{K}$	750–2500	$2\text{--}5 \times 10^{-4}$

Notations

p , pressure;

Δt , excess temperature in boiling (wall minus saturation);

Light organics, organics with liquid dynamic viscosity $\mu_l < 0.5 \times 10^{-3}$ Pa s;

Medium organics, organics with liquid dynamic viscosity $0.5 \times 10^{-3} \leq \mu_l < 2.5 \times 10^{-3}$ Pa s;

Heavy organics, organics with liquid dynamic viscosity $2.5 \times 10^{-3} \leq \mu_l < 50 \times 10^{-3}$ Pa s;

Very heavy organics, organics with liquid dynamic viscosity $\mu_l \geq 50 \times 10^{-3}$ Pa s.

- Heat transfer coefficients and fouling factors are based on area in contact with fluid.
- Allowable pressure drops are generally assumed as 0.5–1 bar, except for low-pressure gas and two-phase flow (5% of absolute pressure) and very viscous organics (1.5–2.5 bars).
- The presence of noncondensables in condensers, even if in small volume percentage, strongly penalizes condensation heat transfer coefficients, because of buildup of mass transfer (diffusion) resistance.
- Boiling/evaporation and condensation of multicomponent zeotropic mixtures, due to the presence of mass transfer resistance in relation to the amplitude of the boiling or condensation temperature range, exhibit lower heat transfer coefficients compared to single-component fluids or zeotropic multicomponent mixtures of similar nature.

more often, condense a process (working) fluid; they are gaining favor, because of the increasing cost and shortage of water and recent concerns about water pollution. Air cooling compared to water cooling presents additional advantages: reduced maintenance costs, air-side fouling that is easier to handle than water-side scaling and/or corrosion, and less danger of working fluid contamination. On the other hand, disadvantages of air cooling are the large heat transfer surface needed, space occupation, less effective cooling performance, seasonal variation of air temperature, and noise pollution.

Air fin exchangers basically consist of one or more bundles of outside finned tubes: the process fluid flows inside the tubes while the cooling air flows in cross-flow over the outside of the tubes, assisted by fans. The finned tubes are set between side frames, merging into header boxes at either end, which are provided with internal baffles to make possible multipass arrangements for the internal fluid.

In large multibundle units, bundles are grouped into bays (typically formed by two or three bundles connected in parallel) laid horizontally (for condensers tubes may be slightly sloped to assist in drainage). Air is moved across the tube bundles in a single cross-flow path by axial flow fans, installed within fan rings connected to the bay by plenum chambers. More often fans may be arranged for forced draft, that is, placed before the tube bundles along the upward flow direction, making fan maintenance easier. It is also possible to arrange fans for induced draft, that is, placed after the bundles along the flow direction: this arrangement gives a more even air distribution across the tubes and is less prone to hot air recirculation, although it is less energy efficient as the fans handle warmer air; additionally, the hood-shaped plenum protects the bundle from rain. If the case, airflow can be controlled by louvers or by using variable-pitch fan blades, variable-speed drives, or switching off the fans.

Still referring to large units, typically core tubes are carbon steel, stainless steel, or other metal alloy, 25.4 mm or more in external diameter, with spirally tension-wound aluminum fins about 13 or 16 mm in height and 0.3–0.5 mm in thickness, with density from 275 to 630 fins/m; low fin density must be chosen in dirty environments; typical extended surface effectiveness is on the order of 0.85. In some cases hot-dip galvanized steel tubes and fins are used, because they are more resistant to corrosion, with some degradation in thermal effectiveness. Tube rows in each bundle may be up to six, arranged in a staggered layout. Different tube passes may have different numbers of tubes; for example, in a condenser, one pass formed by several tube rows in parallel may serve as the condensing section, while the single last lower tube row may serve as the subcooler, with the liquid velocity increased because of the limited number of tubes in parallel; in addition, not all the tubes in a row must necessarily belong to the same tube pass.

Standard bundles range from 1.2 to 12.2 m in length and from 1.2 to 3.6 m in width; inlet and outlet nozzles of the bundle headers are connected to manifolds.

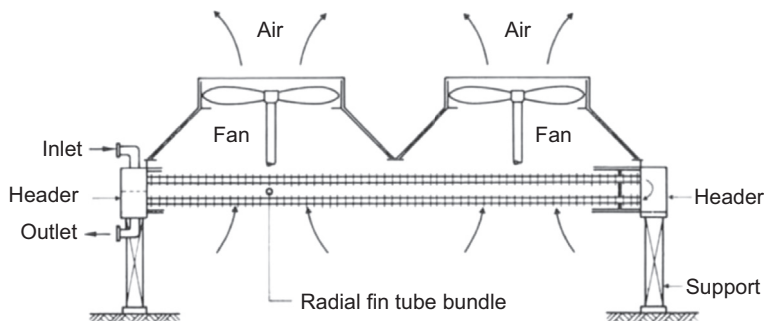


Figure 13.25 Sketch of an induced-draft air cooler (or air condenser).

Header boxes may be of different types according to the particular needs; they can be grouped into four classes, as follows:

- plug-type boxes, in which individual plugs are placed opposite each tube for inspection and cleaning;
- removable cover plate boxes, used when internal fouling is severe;
- completely welded construction boxes;
- manifold type boxes.

Air face velocity, which is calculated on the basis of the gross cross-sectional area for the airflow as if the tubes were absent, typically ranges from 1.5 to 3.5 m/s in air-fin exchangers.

Fig. 13.25 shows a sketch of an air-cooled heat exchanger.

In small, packaged units, copper tubes with aluminum-enhanced plate fins can be used. In these units, a vertical or sloped orientation for the tube bundles can be adopted, with reduced ground area requirement. Common arrangements are the so-called A-frame and V-frame units: in these cases, two tube bundles have one header box in common and face each other sloped in opposite directions, 30–45 degrees from the vertical, recalling the shape of either the letter A or the letter V; the A-frame type lends itself to forced-draft airflow, and the V-frame type is more suited to induced-draft airflow.

13.10 Gasketed and brazed plate heat exchangers

The gasketed plate heat exchanger (PHE) is a very important type of equipment for heat transfer between liquid streams inasmuch as it is a very compact apparatus with very high overall heat transfer coefficients and moderate pressure losses, able to fulfill full counter-flow enabling very small end temperature differences, single pass or multipass arrangements, low liquid holdup, and reduced fouling. It essentially consists of a large number of parallel stamped or embossed rectangular thin metal plates with suitable corrugations both to increase turbulence in the stream flow and to enable the formation of channels between adjacent plates; furthermore, corrugations

grant additional rigidity to the plates. The plates have ports at each corner and are fitted with suitable peripheral shaped elastomeric molded gaskets seated into provided grooves to prevent leaks. When the corrugated plates are clamped together by tie bolts in an external frame between a stationary and a follower thick end cover, the ports form appropriate manifolds to distribute the liquid streams into the channels formed between any two adjacent plates; the two streams flow in opposite directions through alternate channels in counter-flow. The plate spacing is established by the plate corrugation; among the very many corrugation patterns available on the market, most common by far is the chevron or herringbone corrugation pattern: when assembled as a unit, each alternate plate is rotated 180 degrees or, less often, presents a different chevron angle, thus corrugations on successive plates cross and contact one another at many points, forming tortuous channels promoting high turbulence (which in turn enhances heat transfer and reduces fouling: design fouling factors for PHEs can be taken by dividing the values given in Table 13.1 by 4). Chevron corrugation is geometrically characterized by a sinusoidal pattern of amplitude \hat{a} (typical values from 0.6 to 2.5 mm), wavelength (corrugation pitch) Λ (typical values from 7 to 15 mm), and wavenumber $X = 2\pi\hat{a}/\Lambda$, with crests and troughs oriented at a chevron angle ϕ against the herringbone axis (the bulk flow direction; $0^\circ < \phi < 90^\circ$); typical values of ϕ span from 30 to 70 degrees. Plates with $\phi < 45^\circ$ are dubbed soft, as they display lower frictional pressure drop, and plates with $\phi > 45^\circ$ are dubbed hard, with larger pressure drops. Additional geometric parameters used to establish the thermal and hydraulic performance of chevron-type PHEs are the ratio of developed (wavy) and projected areas for the plate Φ , dubbed the area enlargement factor, and the hydraulic or equivalent diameter D_h , defined as four times the volume between plates divided by the wetted surface between plates, which is calculated as $D_h = 4\hat{a}/\Phi$. The parameter Φ can be approximately calculated by the expression $\Phi \approx \frac{1}{6} \left(1 + \sqrt{1 + X^2} + 4\sqrt{1 + X^2/2} \right)$. A single chevron corrugation pattern can cover the full plate width, or it can be repeated two or more times.

Additional advantages of a gasketed PHE are that it can be easily disassembled for cleaning, maintenance, or inspection and that the number of plates in the same frame can be readily adjusted to meet different requirements. But the presence of gaskets is responsible for some limitations of gasketed PHEs: the maximum working pressure is usually limited to 10–16 bars (even if special constructions allow one to double this value); the maximum working temperature is limited by the gasket material (usually PHEs operate below 150°C, but again special gaskets can allow operations above this temperature); gasket material must be compatible with the fluid handled; gaskets may need replacement with time; and the presence of gaskets cannot guarantee perfect hermetic sealing, especially in the presence of gas phase, as in two-phase flow, or under vacuum operations.

To address to some extent these intrinsic limitations, and at the same time to maintain most of the unique features of PHEs, welded PHEs are now available on the market including, most important among this family of heat transfer apparatuses, brazed plate heat exchangers (BPHEs). In this type of heat exchanger, gaskets, tightening bolts, thick

end plates, and frame are eliminated: the pack of corrugated stainless steel plates, assembled with end covers and connections, is vacuum brazed at high temperature at all contact points among the plates to form an integral tight unit suitable for operating at higher temperature and pressure than conventional gasketed units; the usual brazing material is copper; nickel can be used too when ammonia is to be handled.

Specially designed plates, to limit pressure drop, make BPHEs suitable for use as evaporators and water-cooled condensers (see Fig. 13.26) in refrigeration and heat pump applications with so-called medium- or high-pressure refrigerants (packaged water chillers and heat pumps), with heat transfer capacity up to around 600 kW in a single unit, and maximum working pressure up to 40–45 bars; low-pressure refrigerants are penalized by too high a pressure drop. In ORC technology BPHEs can be used in the same kind of applications in medium- to small-size field erected plants and in packaged units (Fig. 13.26).

It is not possible to report general correlations or procedures for predicting the heat transfer and pressure drop performances of PHEs, because of the wide variety of corrugation patterns marketed; designers can be helped by resorting to proprietary data available from the various manufacturers.

Some simple predicting correlations, both for convective heat transfer coefficient and for frictional pressure drop in single- and two-phase flow, are presented in the following, limited to the chevron-type plate corrugation of common geometries.

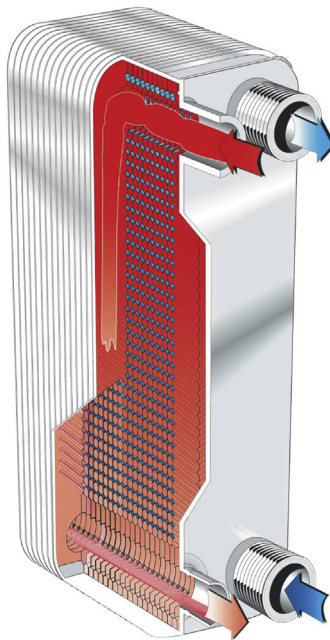


Figure 13.26 Brazed plate condenser.

(this illustration is the property of Alfa Laval Corporate AB and any use or reproduction is subject to approval by Alfa Laval Corporate AB).

Especially the correlations for boiling and condensation in BPHEs should be used with caution and regarded as a rough guide, because they are not supported by sufficiently broad experimentation. Some additional references to work appearing in the open literature on the subject are reported at the end of each section. The overall heat transfer coefficient for a PHE is calculated as if the plates were flat, with transfer area equal to the prime surface A_p .

13.10.1 Single-phase liquid flow (Martin, 1996)

The frictional pressure drop along one plate length L_p is given by:

$$\Delta p_{\text{frict}} = f \frac{L_p}{D_h} \frac{\dot{m}}{2\rho} \quad \text{with} \quad \dot{m} = \frac{\dot{M}}{2a \cdot W \cdot n_p} \quad (13.79)$$

where length L_p is measured between ports on the same side, W is the plate width measured between gaskets, and n_p is the total number of parallel channels.

The friction factor f is calculated by the expression:

$$f = \left[\frac{\cos \phi}{\sqrt{0.18 \tan \phi + 0.36 \sin \phi + f_0/\cos \phi}} + \frac{1 - \cos \phi}{\sqrt{3.8 f_{90}/\cos \phi}} \right]^{-0.5} \quad (13.80)$$

where f_0 and f_{90} are the limiting values of the friction factor with chevron wave patterns in phase at $\phi = 0^\circ$ and $\phi = 90^\circ$, respectively, to be calculated by the expressions:

- for laminar flow:

$$Re < 2000: \quad f_0 = 64/Re; \quad f_{90} = (1.8 \log_{10} Re - 1.5)^{-2}$$

- for turbulent flow:

$$Re \geq 2000: \quad f_0 = \frac{597}{Re} + 3.85; \quad f_{90} = \frac{39}{Re^{0.289}}$$

The pressure drops in the distributor and collector channels should be accounted for separately; they may not be negligible, mainly with soft plates.

The single-phase mean convective heat transfer coefficient h referred to the plate prime surface $A_p = L_p \cdot W \cdot \Phi$ can be calculated by the expression:

$$\overline{Nu} = \frac{\bar{h} \cdot D_h}{\lambda} = 0.122 Pr^{1/3} [f \cdot Re^2 \cdot \sin(2\phi)]^{0.374} \left(\frac{\mu}{\mu_w} \right)^{1/6} \quad (13.81)$$

with the bulk fluid properties evaluated at the arithmetic mean fluid temperature.

Additional references on this subject are [VDI Heat Atlas \(2010\)](#), [HEDH \(2001\)](#), and [Palm and Claesson \(2006\)](#).

13.10.2 Evaporating fluid (*Han et al., 2003a*)

According to these authors, the frictional pressure gradient during evaporation can be computed as:

$$\left| \left(\frac{dp}{dz} \right)_{\text{frict}} \right| = f_{\text{tp}} \frac{1}{D_h} \frac{\dot{m}_{\text{eq}}^2}{2\rho_l} \quad (13.82)$$

with the local equivalent mass velocity defined as $\dot{m}_{\text{eq}} = \dot{m} \left[1 - x + x \left(\frac{\rho_l}{\rho_v} \right)^{0.5} \right]$, and the two-phase local friction factor calculated as a function of the equivalent Reynolds number $Re_{\text{eq}} = \dot{m}_{\text{eq}} \cdot D_h / \mu_l$ according to:

$$\begin{aligned} f_{\text{tp}} &= c_1 \cdot Re_{\text{eq}}^{c_2} \quad \text{with } c_1 = 64,700 \left(\frac{\Lambda}{D_h} \right)^{-5.27} \cdot \phi^{-3.03}; \\ c_2 &= -1.314 \left(\frac{\Lambda}{D_h} \right)^{-0.62} \cdot \phi^{-0.47}; \phi \text{ expressed in (rad)} \end{aligned} \quad (13.83)$$

The local evaporation heat transfer coefficient can be calculated by the expression:

$$Nu = \frac{h \cdot D_h}{\lambda_l} = c_3 \cdot Re_{\text{eq}}^{c_4} \cdot Boi_{\text{eq}}^{0.3} \cdot Pr_l^{0.4} \quad (13.84)$$

where the local equivalent boiling number is defined as $Boi_{\text{eq}} = \frac{\dot{q}}{\dot{m}_{\text{eq}} \cdot H_{\text{lv}}}$ and

$$\begin{aligned} c_3 &= 2.81 \left(\frac{\Lambda}{D_h} \right)^{-0.041} \cdot \phi^{-2.83}; \\ c_4 &= 0.746 \left(\frac{\Lambda}{D_h} \right)^{-0.082} \cdot \phi^{0.61}; \phi \text{ expressed in (rad)} \end{aligned}$$

This procedure is based on tests performed for $\phi = 45, 55$ and 70° , $13 < \dot{m} < 34 \text{ kg/m}^2/\text{s}$, $2.5 < \dot{q} < 8.5 \text{ kW/m}^2$, and R-22 and R-410A as working fluids.

Additional references on this subject are [Longo et al. \(2015b\)](#), [Del Col et al. \(2015\)](#), [Ayub \(2003\)](#), and [Palm and Claesson \(2006\)](#).

13.10.3 Condensing fluid (*Han et al., 2003b*)

The frictional pressure gradient during condensation can be again expressed as:

$$\left| \left(\frac{dp}{dz} \right)_{\text{frict}} \right| = f_{\text{tp}} \frac{1}{D_h} \frac{\dot{m}_{\text{eq}}^2}{2\rho_l} \quad (13.85)$$

with the two-phase local friction factor calculated again as a function of the equivalent Reynolds number according to:

$$f_{tp} = c_5 \cdot Re_{eq}^{c_6} \quad \text{with } c_5 = 3520 \left(\frac{\Lambda}{D_h} \right)^{4.17} \cdot \phi^{-7.75};$$

$$c_6 = -1.024 \left(\frac{\Lambda}{D_h} \right)^{-0.0925} \cdot \phi^{-1.3}; \phi \text{ expressed in (rad)}$$

The local condensation heat transfer coefficient can be calculated by the expression:

$$Nu = \frac{h \cdot D_h}{\lambda_l} = c_7 \cdot Re_{eq}^{c_8} \cdot Pr_l^{1/3} \quad (13.86)$$

with

$$c_7 = 11.22 \left(\frac{\Lambda}{D_h} \right)^{-2.83} \cdot \phi^{-4.5}; c_8 = 0.35 \left(\frac{\Lambda}{D_h} \right)^{0.23} \cdot \phi^{1.48}; \phi \text{ expressed in (rad)}$$

This procedure is based on tests performed for $\phi = 45, 55$ and 70° , $13 < \dot{m} < 34$ kg/m²/s, and R-22 and R-410A as working fluids.

Additional references on this subject are [Longo et al. \(2015a\)](#), [Mancin et al. \(2012\)](#), [Ayub \(2003\)](#), and [Palm and Claesson \(2006\)](#).

Nomenclature

Roman

A	Heat transfer area (m ²)
a	Cross-sectional area (m ²)
\hat{a}	Corrugation amplitude (m)
Bo	Bond number = $\frac{(\rho_l - \rho_v)g \cdot \ell^2}{\sigma}$ (—)
Boi	Boiling number = $\frac{\dot{q}}{\dot{m} \cdot h_{lv}}$ (—)
\dot{C}	Flow heat capacity = $\dot{m} \cdot c_p$ (W/K)
c	Specific heat capacity (J/(kg K))
d, D	Diameter (m)
e_r	Relative roughness (—)
F	Correction factor (—); enhancement factor (—)
F_t	Temperature correction factor (—)

Continued

Fr	Froude number = $\dot{m}^2 / (\rho^2 \cdot g \cdot \ell)(-)$
f	Moody friction factor (-)
g	Acceleration due to gravity (m/s^2)
H_{lv}	Latent heat of vaporization (J/kg)
h	Convective heat transfer coefficient ($\text{W}/(\text{m}^2 \text{ K})$); specific enthalpy (J/kg)
h_r	Mean roughness height (m)
J_v	Dimensionless vapor velocity (-)
k	Pressure loss coefficient (-); leading constant (-)
L	Fin height (m); vertical dimension (m); plate length (m)
ℓ	Reference characteristic length (m)
M	Molecular mass (g/mol ; kg/kmol)
\dot{M}	Mass flow rate (kg/s)
m	Fin parameter = $\sqrt{\frac{h \cdot P}{k_f \cdot \delta}} (\text{m}^{-1})$; exponent (-)
\dot{m}	Mass velocity ($\text{kg}/(\text{m}^2 \text{ s})$)
Nu	Nusselt number = $h \cdot \ell / \lambda (-)$
NTU	Number of transfer units [Eq. (13.24)] (-)
n, N	Number of specified elements (-)
n	Exponent (-); number of specified elements (-)
n_f	Fin density (number of fins per unit length) (m^{-1})
P	Perimeter of fin cross section (m); dimensionless temperature parameter (-)
Pr	Prandtl number = $c_p \cdot \mu / \lambda (-)$
p	Pressure (Pa); pitch (m)
p_r	Relative pitch (-)
\dot{Q}	Heat transfer rate (W)
\dot{q}	Heat flux (W/m^2)
R	Heat transfer resistance (K/W); dimensionless temperature parameter (-)
R'	Dimensionless heater radius (-)
Re	Reynolds number = $\rho \cdot w \cdot \ell / \mu (-)$
R_b	Bend radius of curvature (m)
R_p	Surface roughness parameter (μm)
r	Flow heat capacity ratio = $\dot{C}_{\min} / \dot{C}_{\max} (-)$
r_{bw}	Thermal resistance per unit length (m K/W)
s	Interfin spacing (m)

S	Cross-sectional area (m^2); suppression factor (—)
t, T	Temperature ($^{\circ}\text{C}$, K)
U	Overall heat transfer coefficient ($\text{W}/(\text{m}^2 \text{ K})$)
W	Width (m)
We	Weber number $= \frac{\dot{m}^2 \cdot \ell}{\sigma \cdot \rho}$ (—)
w	Velocity (m/s)
X_{tt}	Martinelli parameter (turbulent–turbulent) (—)
x	Linear coordinate (m); thermodynamic vapor quality (—)
Z	Axial length (m)
z	Axial coordinate oriented in flow direction (m)

Greek

α	Void fraction (—)
β	Angle (degrees, rad)
γ	Angle (degrees, rad)
Δ	Local temperature difference ($^{\circ}\text{C}$, K)
Δt	Excess temperature ($^{\circ}\text{C}$, K)
$\overline{\Delta t}$	Effective mean temperature difference ($^{\circ}\text{C}$, K)
δ	Thickness (m)
ε	Effectiveness (—)
η	Efficiency (—)
θ	Excess temperature ($^{\circ}\text{C}$, K); angle (degrees, rad)
Γ	Mass flow rate of condensate per unit length of tube ($\text{kg}/(\text{m s})$)
λ	Thermal conductivity ($\text{W}/(\text{m K})$)
μ	Dynamic viscosity ($\text{kg}/(\text{m s})$)
ν	Cinematic viscosity (m^2/s)
ρ	Density (kg/m^3)
σ	Surface tension (N/m)
Ω	Overall efficiency of a finned surface (—)
ϕ	Angle (degrees, rad)
Φ	Area enlargement factor (—)
Λ	Chevron corrugation pitch (wavelength) (m)

Subscripts

AM	Arithmetic mean
B	Bundle
b	Refers to base; boiling; bend
c	Cold
c–f	Counter-flow
cv	Convective boiling
d	Diagonal; design
dnb	Departure from nucleate boiling
e	External
eq	Equivalent
f	Refers to fins
fc	Forced convection
fd	Of fluid
fou	Fouling
frict	Frictional
g	Grooves
gr, grav	Gravity; gravitational
h	Hot; hydraulic; homogeneous
i	Internal
ib	Incipient boiling
in	At inlet
LM	Logarithmic mean
LO	Liquid only (total flow assumed liquid)
l	Longitudinal; refers to liquid phase
lam	Laminar
max	Maximum
mfb	Minimum film boiling
min	Minimum
mom	Momentum
nb	Nucleate boiling
nc	Natural convection
out	At outlet

p	Of the prime surface; at constant pressure; plate
p-f	Parallel-flow
R	Reduced; retention
r	At root; relative; rows of tubes; ranks of tubes
STRAT	Stratified
sat	Saturated; at saturation
sfb	Saturated flow boiling
sh	Shear
st	Stationary
t	Total; at tip; tube; transverse; temperature
tp	Two-phase
turb	Turbulent
u	Uncovered
VO	Vapor only (total flow assumed vapor)
v	Refers to vapor phase
vfb	Variable fluid properties
w	At the wall
wmax	Maximum velocity

References

- Ayub, Z.H., 2003. Plate heat exchanger literature survey and new heat transfer and pressure drop correlations for refrigerant evaporators. *Heat Transfer Engineering* 24 (5), 3–16.
- Beatty, K.O., Katz, D.L., 1948. Condensation of vapors on outside of finned tubes. *Chemical Engineering Progress* 44 (1), 55–70.
- Cavallini, A., Zecchin, R., 1974. A dimensionless correlation for heat transfer in forced convection condensation. In: 6th Intl. Heat Transfer Conference, Tokyo, vol. 3, pp. 309–313.
- Cavallini, A., Doretti, L., Longo, G.A., Rossetto, L., 1996. A new model for forced convection condensation on integral-fin tubes. *Heat Transfer Engineering* 118, 689–693.
- Cavallini, A., Del Col, D., Doretti, L., Longo, G.A., Rossetto, L., 1999. Condensation heat transfer with refrigerants. *Two-Phase Modelling and Experimentation 1999*. Editions ETS Italy, pp. 71–88.
- Cavallini, A., Censi, G., Del Col, D., Doretti, L., Longo, G.A., Rossetto, L., 2002. Condensation of halogenated refrigerants inside smooth tubes. *International Journal of HVAC&R Research* 8 (no. 4), 429–451.

- Cavallini, A., Censi, G., Del Col, D., Doretti, L., Longo, G.A., Rossetto, L., Zilio, C., 2003. Condensation inside and outside smooth and enhanced tubes — a review of recent research. *International Journal of Refrigeration* 26, 373–392.
- Cavallini, A., Del Col, D., Doretti, L., Matkovic, M., Rossetto, L., Zilio, C., Censi, G., 2006. Condensation in horizontal smooth tubes: a new heat transfer model for heat exchanger design. *Heat Transfer Engineering* 27 (8), 31–38.
- Collier, J.G., Thome, J.R., 1996. *Convective Boiling and Condensation*, third ed. Clarendon Press, Oxford.
- Cooper, M.K., 1984. Saturated nucleate pool boiling: a simple correlation. In: 1st U.K. National Heat Transfer Conference, vol. 2, pp. 785–793.
- Del Col, D., Rossato, M., Chinellato, F., Muzzolon, A., Rossetto, L., 2015. Flow Boiling of R-32 inside a Brazen Plate Heat Exchanger. *International Congress of Refrigeration*. Yokohama, Japan.
- Dobson, M.K., Chato, J.C., 1998. Condensation in smooth horizontal tubes. *ASME Journal of Heat Transfer* 120, 193–213.
- ESDU International plc, 1973. Convective heat transfer during crossflow of fluids over plain tube banks. ESDU Data Item N 73031.
- Friedel, L., 1979. Improved friction pressure drop correlations for horizontal and vertical two-phase pipe flow. In: *European Two-phase Flow Group Meeting*, Ispra, Italy (paper E2).
- Gorenflo, D., 1993. Pool Boiling. V.D.I. Heat Atlas. VDI Verlag.
- Gungor, A.E., Winterton, R.H.S., 1987. Simplified general correlation for saturated flow boiling and comparison of correlations with data. *Chemical Engineering Research and Design* 65 (2), 148–156.
- Han, D.H., Lee, K.J., Kim, Y.H., 2003a. Experiments on the characteristics of evaporation of R-410A in brazed plate heat exchangers with different geometric configurations. *Applied Thermal Engineering* 23 (10), 1209–1225.
- Han, D.H., Lee, K.J., Kim, Y.H., 2003b. The characteristics of condensation in brazed plate heat exchangers with different chevron angles. *Physics Journal of the Korean Physical Society* 43, 66–73.
- Honda, H., Nozu, S., Mitsumori, K., 1983. Augmentation of condensation on horizontal finned tubes by attaching a porous drainage plate. In: *Proc. ASME-JESME Thermal Engng. Joint Conference*, vol. 3, pp. 289–296.
- Honda, H., Uchima, B., Nozu, S., Nakata, H., Fujii, T., 1988. Condensation of downward flowing R-113 vapour on bundles of horizontal smooth tubes. *The Japan Society of Mechanical Engineers* 54–502 (B), 1453–1460.
- Heat Atlas, V.D.I., Gesellschaft Verfahren, V.D.I., Chemieingenieurwesen (Eds.), 2010, second ed. Springer Verlag, Berlin.
- Incropera, F.P., DeWitt, D.P., 1996. *Fundamentals of Heat and Mass Transfer*, fourth ed. John Wiley and Sons, New York.
- Keys, W., London, A.L., 1964. *Compact Heat Exchangers*. Mc. Graw-Hill Book Company, New York.
- Kraus, A.D., Aziz, A., Welty, J., 2001. *Extended Surface Heat Transfer*. John Wiley & Sons, Inc., New York, NY.
- Liu, Z., Winterton, R.H.S., 1991. A general correlation for saturated and subcooled flow boiling in tubes and annuli, based on a nucleate pool boiling equation. *International Journal of Heat and Mass Transfer* 34 (11), 2759–2766.
- Lockhart, R.W., Martinelli, R.C., 1949. Proposed correlation data for isothermal two-phase two-component flow in pipes. *Chemical Engineering Progress* 45, 39–45.

- Longo, G.A., Righetti, G., Zilio, C., 2015a. A new computational procedure for refrigerant condensation inside herringbone-type brazed plate heat exchangers. *International Journal of Heat and Mass Transfer* 82, 530–536.
- Longo, G.A., Righetti, G., Zilio, C., 2015b. A new model for refrigerant boiling inside herringbone-type brazed plate heat exchangers (BPHEs). *International Journal of Heat and Mass Transfer* 91, 144–149.
- Mancin, S., Del Col, D., Rossetto, L., 2012. Condensation of superheated vapour of R-410A and R-407C inside plate heat exchangers: experimental results and simulation procedure. *International Journal of Refrigeration* 35, 2003–2013.
- Martin, H., 1996. A theoretical approach to predict the performance of chevron-type plate heat exchangers. *Chemical Engineering and Processing: Process* 35 (4), 301–310.
- Mostinski, I.L., 1963. Application of the rule of corresponding states for calculation of heat transfer and critical heat flux. *Teploenergetika* 4, 66.
- Nusselt, W., 1916. Die Oberflächenkondensation des Wasserdampfes. *Zeitschrift des Vereins Deutscher Ing.* 60, 541.
- Palm, B., Claesson, J., 2006. Plate heat exchangers: calculation methods for single- and two-phase flow. *Heat Transfer Engineering* 27 (4), 88–98.
- PFR Engineering Systems, Inc., 1976. Heat transfer and pressure drop characteristics of dry tower extended surfaces. Part II: data analysis and correlations. BNFL-PFR-7-102. Pfresh Start Films Inc - Marina Del Rey California.
- Rabas, T.J., Taborek, J.T., 1987. Survey of turbulent forced-convection heat transfer and pressure drop characteristics of low-finned tube banks in cross flow. *Heat Transfer Engineering* 8 (2), 49–62.
- Ribatski, G., Saiz Jabardo, J.M., 2003. Experimental study of nucleate boiling of halocarbon refrigerants on cylindrical surfaces. *International Journal of Heat and Mass transfer* 46, 4439–4451.
- Rohsenow, W.M., 1962. A method of correlating heat transfer data for surface boiling of liquids. *Trans. ASME* 74, 969–975.
- Rouhani, Z., Axelson, E., 1970. Calculation of volume void fraction in the subcooled and quality region. *International Journal of Heat and Mass Transfer* 13, 383–393.
- Shlünder, E.U. (Ed.-In-Chief), 2001. *Heat Exchanger Design Handbook*, Begell House, Inc., New York, Wallingford (UK).
- Shah, R.K., Sekulić, D.P., 2003. *Fundamentals of Heat Exchangers Design*. John Wiley & Sons, Inc., New York, NY.
- Shmidt Th, E., 1966. Verbesserte Methoden zur Bestimmung des Wärmeaustausches an Berippten Flächen. *Kältetechnik-klimatisierung* 14 (part 4).
- Stephan, K., Abdelsalam, M., 1980. Heat transfer correlations for natural convection boiling. *International Journal of Heat and Mass Transfer* 23, 73–87.
- Thome, J.R., *Engineering Data Book III*. Wolverine Tube, Inc., Decatur, US. Copyright 2004–2010.
- Thome, J.R., El Hajal, J., Cavallini, A., 2003. Condensation in horizontal tubes, part 2: new heat transfer model based on flow regimes. *International Journal of Heat and Mass Transfer* 46, 3365–3387.
- Webb, R.L., Rudy, T.M., Kedzierski, M.A., 1985. Prediction of condensation on horizontal integral-fin tubes. *Journal of Heat Transfer* 107, 369–376.
- Young, E.H., Ward, D.J., 1957. Fundamentals of finned tubes heat transfer. *The Refining Engineer* 29 (12).

- Yudin, V.E., Tokhtarova, L.S., 1971. Influence of number of transverse rows in finned tubes in staggered and in-line banks on their heat transfer and drag. *Energomashinostroeniye* 4, 41–42.
- Zivi, S.M., 1964. Estimation of steady state steam void fraction by means of the principle of minimum entropy production. *ASME Journal of Heat Transfer* 86c, 247–252.
- Zuber, N., 1959. Hydrodynamic aspects of boiling heat transfer. (Ph.D. thesis, U.C.L.A.). Also available as AEC tech. report AECU – 4439, Phys. and Math.

Geothermal energy exploitation with Organic Rankine Cycle technologies

14

C. Spadacini, L.G. Xodo, M. Quaia
Exergy S.p.A., Olgiate Olona (VA), Italy

14.1 Introduction: geothermal resource exploitation

Among the renewable energy resources, geothermal is the most interesting for reliable base-load energy production. Geothermal power plants are, in fact, characterized by very high annual capacity factor, availability, and reliability. Geothermal power plants exploit a resource that consists of a hot fluid coming from an underground reservoir by means of a steam turbine or a binary cycle.

This chapter will carry out an analysis of the geothermal power plant available technologies, and focus on the organic Rankine cycle (ORC) solution.

14.1.1 Resource classification

A geothermal reservoir is identified where a temperature gradient anomaly is combined with the presence of underground water trapped in a confined area with suitable characteristics of geology and permeability. Summarizing the main features, according to DiPippo (2005), the following characteristics are considered essential to making a hydrothermal geothermal resource viable:

- a large heat source
- a permeable reservoir
- a supply of water
- an overlying layer of impervious rock
- a reliable recharge mechanism

There are a number of correction methods in case the reservoir is lacking some of the listed features, such as increasing permeability by fracking and injecting water in the reservoir. The geological features must be naturally present, such as the heat source (which causes the gradient anomaly) and the impermeable rock layer above the reservoir (which confines the liquid source in the reservoir).

While attempting to exploit geothermal energy, the key point is the definition of the characteristics of the untapped geothermal fluid contained in the underground reservoir. Such definition is the leading factor for the design of a geothermal power plant, and its importance and proper characterization become evident while operating the plant.

The most important parameter for the classification of the geothermal resource is its enthalpy, which is the combination of temperature, pressure, and vapor fraction. A first classification of geothermal resources is based on vapor fraction (or quality) of the reservoir, which implies different technology of exploitation: vapor-dominated and liquid-dominated resources are identified (Smith, 1975).

A geothermal reservoir in which the geothermal fluid is contained in the state of steam is defined as vapor dominated. Typical temperature is in the range of 250–300°C and the fluid at the wellhead is superheated (dry) steam.

In the liquid-dominated fields, the geothermal fluid is contained in the liquid state. These fields are characterized by a broad range of temperatures, always associated with high pressure, which is necessary to keep the fluid in a liquid state. The liquid-dominated definition refers to the conditions of the fluid in the reservoir: at the wellhead, depending on temperature and pressure of the resource, the fluid will be liquid or biphasic. The liquid-dominated fields are the most numerous ones and those with the highest potential for exploitation in the future.

Nowadays most of the electricity produced from geothermal sources comes from vapor-dominated and high-enthalpy liquid-dominated fields but, due to the very complex geological process at the basis of these systems, the quantity of high-quality resources around the world is very limited (Stefansson, 2005).

The heterogeneous nature of the process of formation of the geothermal reservoirs leads to the creation of geothermal basins that are very different from each other in terms of chemical and thermophysical characteristics. In fact, the physical properties of the fluids, such as the enthalpy (temperature and pressure) and steam content, as well as the chemical properties, such as total gas content and dissolved salts and their composition, vary greatly. For these reasons, each geothermal ORC plant requires a completely new design starting from the choice of the working fluid and the cycle layout.

A typical classification of the liquid-dominated resources is based on the “bottom-hole” or “full-liquid” temperature T_{bh} , which represents the temperature of the geothermal fluid in the production zone of the reservoir (bottom-hole). In case it is not possible to measure this parameter, it can be defined as the equivalent temperature of a pressurized water flow having the same available heat content of the geothermal biphasic flow at the wellhead (Fig. 14.1); for this reason, the terms “enthalpy” and “temperature” in the classification of a geothermal resource are often used with the same meaning.

Classification of the fields is still under discussion; over the years many classifications based on bottom-hole temperature have been provided. The following Table 14.1 (Dickson and Fanelli, 2004) identifies different classifications, according to multiple references.

Regardless of the classification of the resource, due to the unstable nature of a geothermal system, an extensive study of the reservoir characteristics must be performed in order to optimize the plant design and minimize the risk, and only a continuous monitoring of the reservoir status and the resource characteristics grants high availability and productivity of a geothermal plant.

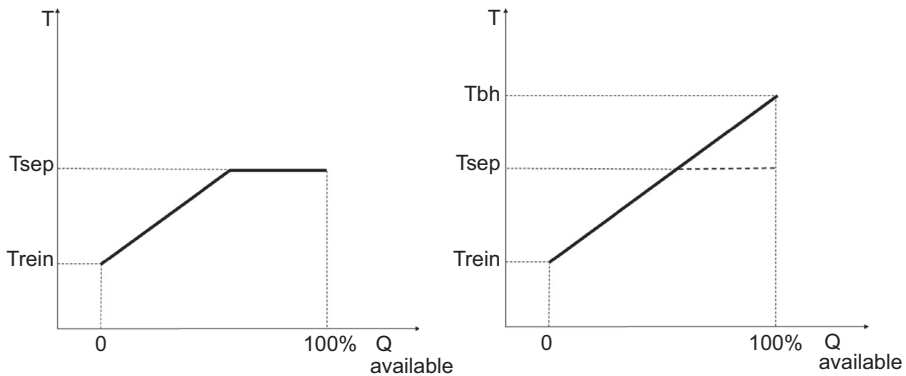


Figure 14.1 Representation of full-liquid or bottom-hole temperature.

Table 14.1 Resources classification according to enthalpy (Dickson and Fanelli, 2004)

Resource name	Temperature range (°C) of classification for the considered references				
	Muffler and Cataldi (1978)	Hochstein (1990)	Benderitter and Cormy (1990)	Nicholson (1993)	Axelsson and Gunnlaugsson (2000)
Low-enthalpy resources	<90	<125	<100	≤150	≤190
Medium-enthalpy resources	90–150	125–225	100–200	—	—
High-enthalpy resources	>150	>225	>200	>150	>190

14.1.2 Resources and plant locations

Geothermal reservoirs are located where the heat flow from the center of the earth is greater. These areas correspond with regions of relative motion between the earth’s plates (Fig. 14.2); as a consequence of these deep earthquakes, the magma contained below in the earth’s crust tends to reach the surface through active volcanoes and heat flow is in the same way facilitated toward shallow reservoirs.

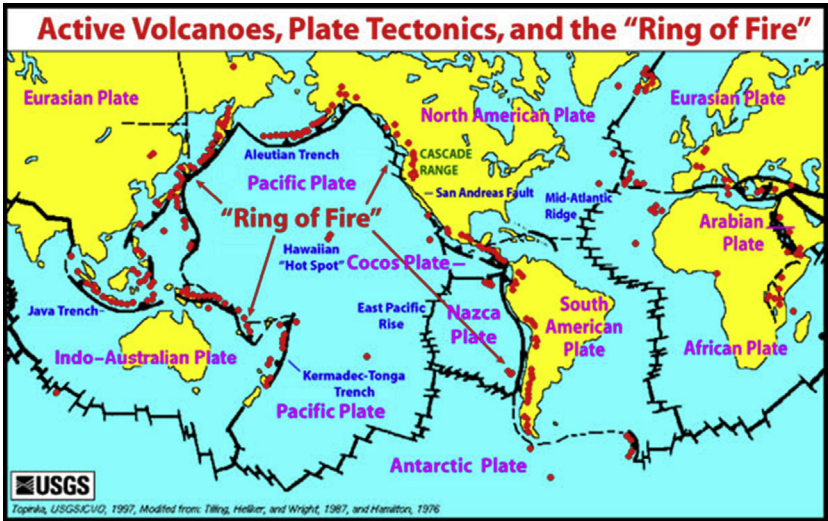


Figure 14.2 The ring of fire (USGS, 1997).

All of these items can be clearly recognized in Fig. 14.3, where main geothermal areas are shown; they generally match to a belt that runs along the edges of continents, the so-called *fire belt* of the earth, where volcanic activities still occur.

Geothermal resources exploitation for electric power production was conceptualized and studied by Prince Piero Ginori Conti at the beginning of the 20th century; on July 4, 1904 he installed the first experimental machine to demonstrate the possibility of exploitation of geothermal energy on a source located near Larderello, Tuscany, Italy. The experiment was conducted by transferring the geothermal energy

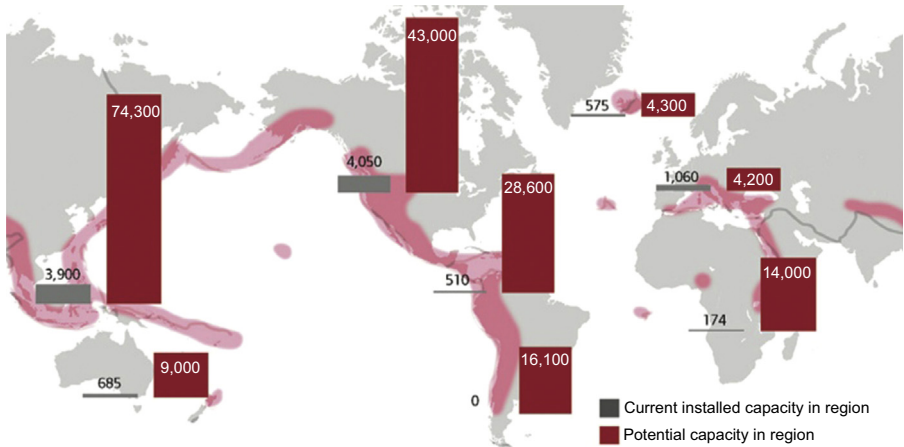


Figure 14.3 Distribution of geothermal potential along with the ring of fire (Islandsbanki, 2011).

to a binary water cycle, producing pure steam driving a piston engine coupled to a 10 kW dynamo generator and supplying five connected low-wattage light bulbs (UGI, 2007).

The first commercial geothermal power plant in the world—Larderello 1—was installed in 1913 and consisted of an indirect-cycle pure-steam process with a 250 kW backpressure steam turbine manufactured by Franco Tosi, providing electricity to all the chemical plants of the Boraciferous region and with the first electrical line transferring geothermal power to the near villages (i.e., Pomarance and Volterra).

The direct-cycle geothermal technology was experimented with in 1923, by testing a 23 kW turbine in Serazzano, near Larderello. Due to the very high chemical quality of the geothermal steam source, this unit ran without problems for almost two years.

Other installations followed in Italy, for a total of 123.9 MW (107 MW from binary units and 16.9 MW from backpressure steam turbines) at the end of 1943.

During the 1950s the commercial exploitation of geothermal sources began also in other regions of the world, mainly by exploiting high-temperature resources, thus by installing dry steam or single-flash steam turbines.

Beginning with the first pilot plants by Ormat in the early 1980s, an innovative configuration was engineered, tested, and commercialized targeting the exploitation of low-temperature geothermal resources: the ORC binary technology. This system has had good success in the geothermal market as it enables the commercial exploitation of resources otherwise not exploitable and as a competitive solution also for certain medium- to high-temperature resources.

A third binary configuration was also evaluated in the past—the Kalina cycle, utilizing a mixture of water and ammonia. Although from a theoretical point of view this cycle shows great thermodynamic performance, due to the greater complexity of the system and the related technical difficulties it did not encounter success as a commercial application.

Consequently, geothermal binary technology nowadays is substantially synonymous with ORC.

The geothermal development, started with binary technology, boosted with the exploitation of high-enthalpy resources with direct-steam technologies, which represent today more than 90% of the installed power.

Referring to the situation at the end of 2014, worldwide geothermal power plant installed capacity is 12.6 GW, for a total energy production of 73.5 TWh. [Table 14.2](#) shows a classification by continents, while [Fig. 14.4](#) shows the distribution among the main countries ([Bertani, 2015](#)).

Several areas appear to be underdeveloped if not unexploited, such as South America (Chile, where the first 40 MW project will be installed in 2016, and Peru), Africa (Ethiopia and Tanzania), Russia (Kamchatka peninsula), and China.

Further developments are predicted in Chile, Montserrat, Iran, and others, where geothermal projects will be completed in the coming five years. In Turkey at the end of 2014 there were plants in the development, design, and construction phases that would be online in 2015–17, doubling the installed capacity.

Table 14.2 Installed power and energy produced from geothermal resources per area, at the end of 2014 (Bertani, 2015)

Continent	Installed power (MWe)	Energy produced (GWh)
Africa	601	2,858
America	5,089	26,353
Asia	3,756	22,084
Europe	2,133	14,821
Australia	1,056	7,433
Total	12,635	73,549

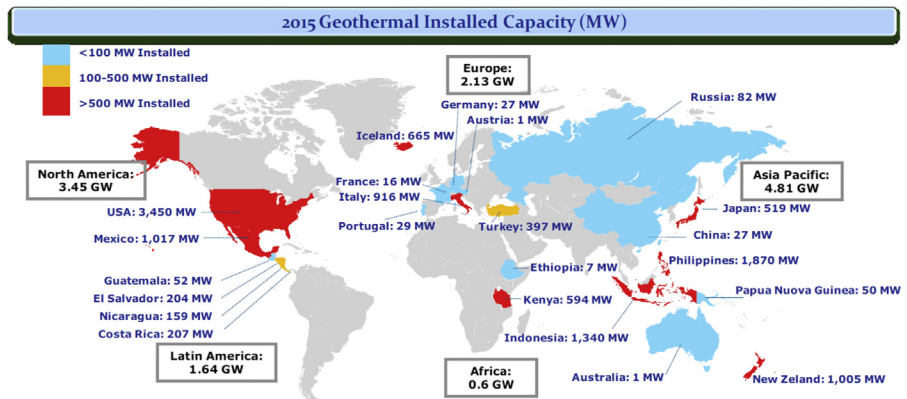


Figure 14.4 Installed capacity at the end of 2014 worldwide (Bertani, 2015).

A geothermal power plant is a risky and capital-intensive investment, with high expenditure and high risk in the first phases. The underdevelopment of certain areas derives from the difficulties in accessing this investment, due, for example, to political and economic instability and by technical challenges such as the location of the geothermal fields in remote areas.

Regarding the power plants’ technologies classification, these are essentially divided between binary and backpressure; single, double, or triple flash; or dry steam turbine. The installed capacity of each technology and its location is presented in Table 14.3. For a detailed description of these plant layouts, refer to the next paragraph.

14.1.3 Technological options, theoretical analysis

There are a number of ways to exploit a geothermal resource for power generation, depending on the fluid enthalpy and chemical characteristics. Considering the

Table 14.3 Installed capacity for each power plant technology, end of 2014 (Bertani, 2015)

Area	Dry steam	Single flash	Double flash	Triple flash	Hybrid	Back pressure	Binary	Total
Africa		543				48	11	602
Asia	484	2,514	525				236	3,758
Europe	795	796	273				268	2,133
Latin America		908	510			90	135	1,642
North America	1,584	60	881	50	2		873	3,450
Oceania		259	356	132		44	266	1,056
Total	2,863	5,079	2,544	182	2	181	1,790	12,640

classification based on steam quality of the geothermal resource, the geothermal fluid originating in vapor-dominated fields, which is dry superheated steam, is typically exploited with a direct expansion in steam turbine, while liquid-dominated resources are exploited in a number of configurations.

A geothermal well features a production curve having maximum pressure where flow is zero (closed valve) and maximum flow (choked flow) where pressure is minimum (Fig. 14.5). The shape of the production curve and the values of pressure and mass flow vary significantly from one reservoir to another. In particular, a geothermal well operating with a two-phase flow shows a different behavior at very low mass flow rate—a sharp reduction in pressure occurs and flow is reduced to zero.

The production pressure at wellhead is regulated in order to optimize power production; independently from the technology that is used to convert the geothermal energy, it is clear that decreasing the production pressure, the exergy of the heat source will decrease accordingly. Considering the exergy proportional to the enthalpy difference between turbine inlet and turbine outlet, neglecting the pressure drop between well-head and turbine inlet, a maximum is identified according to Fig. 14.6. A more detailed study on the relation (Section 14.1.3.1) between enthalpy head and inlet pressure is presented in the relevant paragraph.

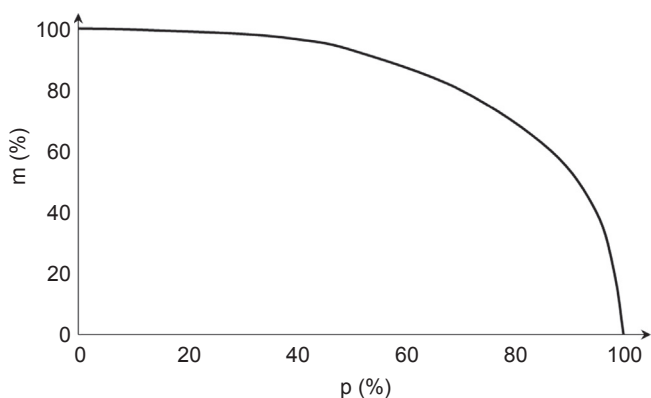


Figure 14.5 Typical geothermal well production curve.

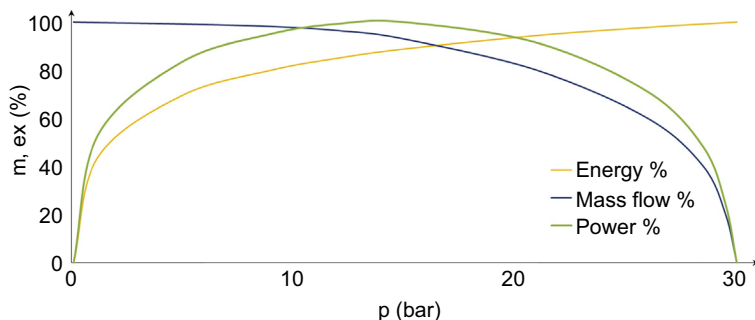


Figure 14.6 Optimization of well production pressure.

The exploitation of the geothermal fluid can occur in two ways:

- the vapor fraction (or the dry superheated steam) is expanded directly in a turbine
- the exploitation takes place by transferring the geothermal heat to a secondary low-boiling fluid that, vaporizing, expands in the turbine

It is generally preferred, when possible, to use a steam turbine to expand the vapor phase of the geothermal fluid; additionally, in some cases a hybrid configuration, including both the means of exploitation, is suggested as optimal.

This next section gives an overview of both direct and binary cycles, leaving the detailed analysis of a particular binary cycle using ORC in [section 14.1.3.2](#)

14.1.3.1 Direct cycles

The following discussion will analyze the direct use of geothermal steam for power production in terms of thermodynamics and technical and operational features.

A number of possible configurations are presented. A general description of the balance of plant (condenser, cooling tower, ejector), which is common to all the configurations, will be given at the end of the discussion.

Thermodynamics

In a vapor-dominated field, the steam turbine is operated directly by the steam produced by the well, which is typically superheated.

The pressure and the mass flow at wellhead must be balanced in order to maximize power production along the geothermal well production curve, such as in [Fig. 14.6](#). In fact, turbine power is calculated multiplying enthalpy head by mass flow; the increase in mass flow results in a proportional increase in power production, while pressure reduction at turbine inlet grants lower power production, as follows.

Defined a schematic such as [Fig. 14.7](#), where point 3 is turbine inlet (considering all the other eventual steam users negligible) and point 5 is turbine outlet (5_{is} for isentropic expansion), the theoretical power produced by the turbine is expressed as

$$W = \dot{m}\Delta h = W = \dot{m}_3(h_3 - h_5) = \dot{m}_3\eta_{is}(h_3 - h_{5,is})$$

where

$$\eta_{is} = \frac{h_3 - h_5}{h_3 - h_{5,is}}$$

As shown in [Fig. 14.8](#), the isenthalpic pressure reduction at wellhead (and, thus, turbine inlet) leads to higher value of enthalpy at turbine discharge, thus lower enthalpy head and power. As an example, the figure shows two different cases in which, given an available flow at 10 bar expanded to 1 bar, pressure drop at turbine inlet is, respectively, 2 and 4 bar, with a corresponding reduction in enthalpy head of 12%.

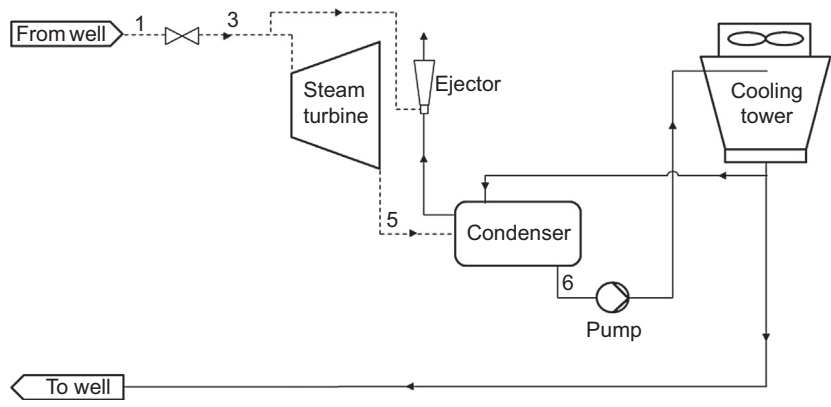


Figure 14.7 Dry steam plant, typical simplified flow diagram.

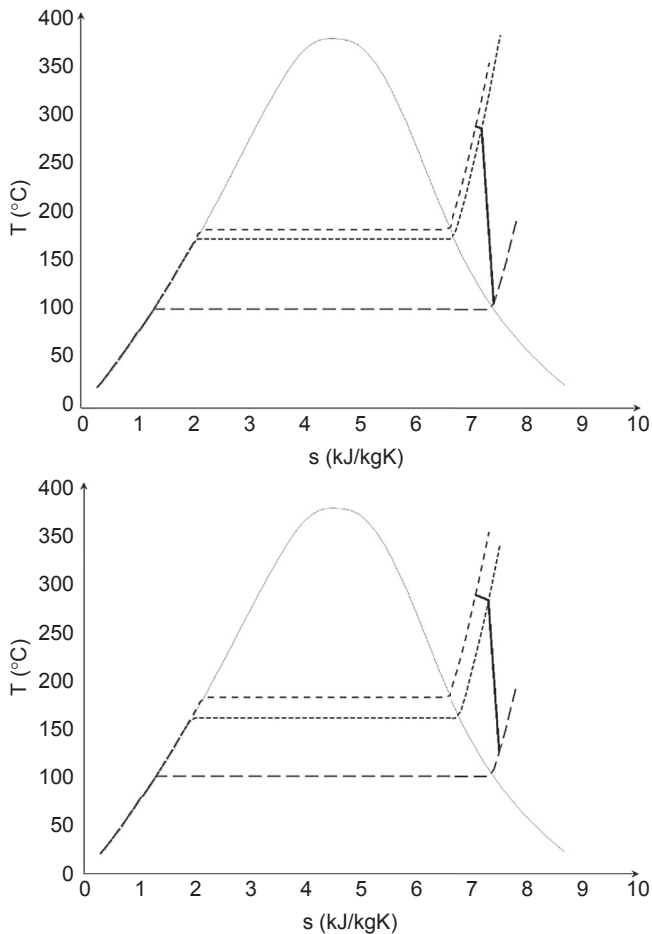


Figure 14.8 $T-s$ diagrams showing the effect of pressure drop at turbine inlet in a superheated vapor expansion.

In case the reservoir is liquid dominated, a separation of the vapor phase from the liquid phase is required before the utilization of steam in a direct cycle. Separation can be implemented in one or more stages, resulting in the so-called single-flash, double-flash, or multiple-flash configurations.

In a single-flash plant, the geothermal fluid is separated into vapor and liquid phase at a certain pressure—the steam feeds a steam turbine, while the brine (liquid phase) is reinjected or discharged (Figs. 14.9).

In a multiple-flash configuration the geothermal fluid is separated into vapor and liquid phase; the steam will feed a high-pressure (HP) steam turbine, while the liquid phase will be sent to a second separator after pressure reduction. Here it will be separated and admitted into a low-pressure (LP) steam turbine (Fig. 14.10). Eventually, a third pressure level can be foreseen—after the last separator the brine (liquid phase) will be reinjected or discharged.

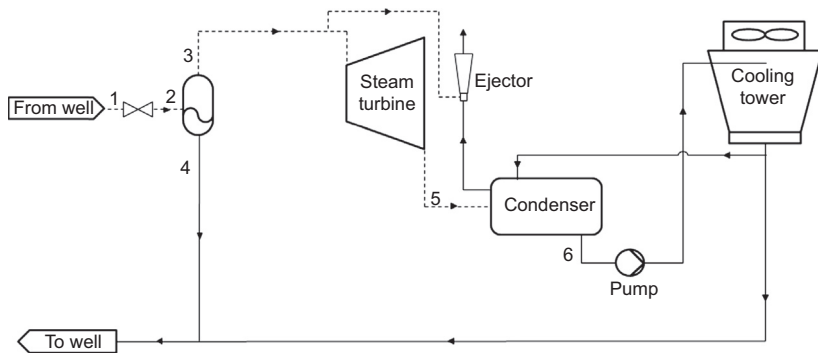


Figure 14.9 Single-flash cycle, typical simplified flow diagram.

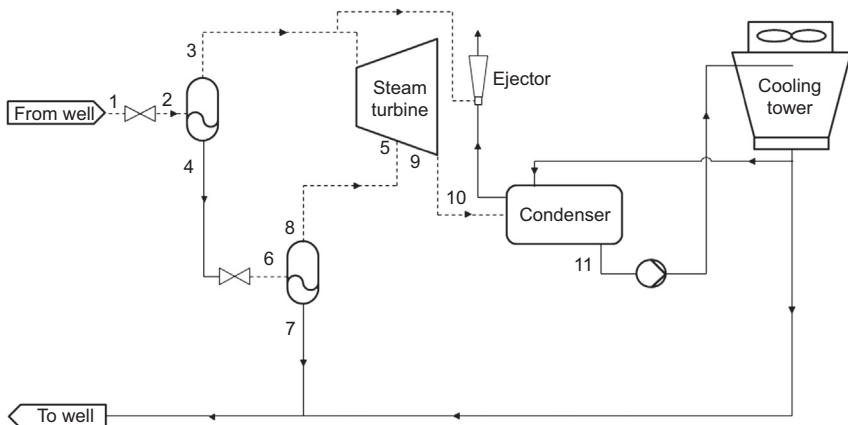


Figure 14.10 Double-flash cycle, typical plant simplified flow diagram.

As most of the cascade heat recovery cycles, the energy conversion efficiency increases while increasing the amount of heat recovery levels. Here follows an analysis of the two main configurations: single and double flash.

The power output of a single-flash configuration is calculated as follows: considering a total flow \dot{m}_1 feeding the plant, the vapor quality after separation can be expressed as

$$x_2 = \frac{h_1 - h_4}{h_3 - h_4} = f(h_1, p_1, p_2)$$

As a consequence, the power generated by the turbine is $W = \dot{m}_3(h_3 - h_5)$, where $\dot{m}_3 = \dot{m}_1 x_2$ and

$$\eta_{is} = \frac{h_3 - h_5}{h_3 - h_{5,is}}$$

resulting in

$$W = \dot{m}_1 \frac{h_1 - h_4}{h_3 - h_4} \eta_{is} (h_3 - h_{5,is})$$

With the same approach, the power output of a double-flash configuration can be calculated starting from the HP level.

Similarly, the mass flow to the LP turbine will be $\dot{m}_7 = \dot{m}_4 x_8 = \dot{m}_1 (1 - x_2) x_8$, where

$$x_8 = \frac{h_4 - h_6}{h_7 - h_6} = f(h_4, p_4, p_8)$$

As a consequence, the power generated by the two turbines is $W = \dot{m}_3(h_3 - h_5) + \dot{m}_7(h_7 - h_{10})$, where $\dot{m}_3 = \dot{m}_1 x_2$ and

$$\eta_{is,HP} = \frac{h_3 - h_5}{h_3 - h_{5,is}}, \quad \eta_{is,LP} = \frac{h_7 - h_{10}}{h_7 - h_{10,is}}$$

resulting in

$$W = \dot{m}_1 \left[\frac{h_1 - h_4}{h_3 - h_4} \eta_{is,HP} (h_3 - h_{5,is}) + \left(\frac{h_1 - h_4}{h_3 - h_4} + \frac{h_3 - h_1}{h_3 - h_4} \frac{h_4 - h_6}{h_7 - h_6} \right) \eta_{is,LP} (h_7 - h_{10,is}) \right]$$

The optimization of the systems is achieved by maximizing the specific work output of the plant. This can be calculated by neglecting pumps and other parasitic workloads, and deriving the specific work output with the separation temperature and equalizing it to zero.

Considering T_{bh} the bottom-hole temperature as defined previously and T_{sink} condensing temperature, the optimal single-flash temperature is:

$$T_{flash} \approx \frac{T_{bh} + T_{sink}}{2}$$

For a double-flash plant, with the same hypotheses:

$$T_{1st,flash} \approx \frac{2}{3}(T_{bh} + T_{sink}), \quad T_{2nd,flash} \approx \frac{1}{3}(T_{bh} + T_{sink})$$

The use of multiple separation levels has further benefits than the efficiency gain, as it grants better thermodynamics and technical solutions.

Given the theoretical analysis of the cycle, it is important to consider that the presence of noncondensable gases (NCGs) modifies the heat release curve of the geothermal steam, as the equilibrium between the phases at a certain temperature is granted at the corresponding partial pressure of water in the vapor phase. For the sake of clarity, given a certain separation pressure P_{sep} , the separation temperature T_{sep} is lower than the saturation temperature $T_{sat}(P_{sep})$, being $T_{sat}(P_{wat})$ where $P_{wat} = x_{wat} \cdot P_{tot}$ and x_{wat} is the molar fraction of water in the water/NCG mixture.

Regardless of the configuration upstream, steam turbines can be configured as back-pressure or full condensing, with considerable differences in terms of pressure at turbine outlet; the former is characterized by direct discharge in atmosphere, while the latter requires backpressure typically lower than one-tenth of atmospheric pressure. From a thermodynamic point of view, a condensing turbine offers the maximum power output, thanks to the high-enthalpy head, but the additional auxiliary consumption caused by this choice is not negligible.

In terms of cooling media, the typical full-condensing configuration is featured with a wet cooling tower feeding cold water to a condenser. The water-cooled condenser can be surface type, where the heat exchange is carried out without contact between the condensing vapor and the cooling water, or direct contact, where cold water is mixed with the condensing vapor and a single liquid outlet is obtained.

As shown in the relevant typical flow diagrams, the presence of noncondensable gases in the geothermal fluid requires the installation of an extraction system for these gases, generally connected to the condenser. Such systems are usually composed of vacuum pumps, steam ejectors, or more frequently a combination of the two, complicating the plant in terms of design, costs, and operations. The energy consumption of such systems is not irrelevant, being up to 15% of the power produced by the steam turbine.

Technical and operational features

The geothermal fluid is generally composed of a mixture of water and a number of chemical constituents, as listed in [Section 14.3.1.1](#). As some of the dissolved chemicals are either subject to deposits or aggressive against metals, scaling and corrosion are always expected on those parts. The nature of scaling and corrosion issues is described for both direct and binary cycles in ([Section 14.3.1.1](#)).

Furthermore, geothermal steam turbines usually expand saturated steam (in case of flash plant) or with a low degree of superheating (in case of dry steam plant), which expand in the two-phase region (as shown in the T-s diagrams of [Figs. 14.11 and 14.12](#)). In both cases there is a relevant presence of liquid droplets impacting on the turbine blades, with consequent erosion ([Fig. 14.15](#)).

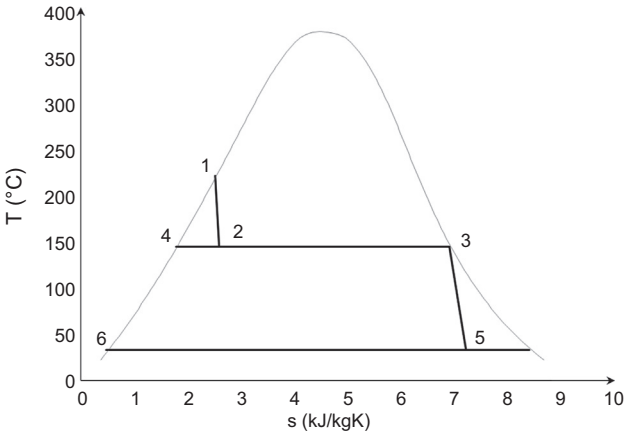


Figure 14.11 Single-flash cycle, typical T-s diagram.

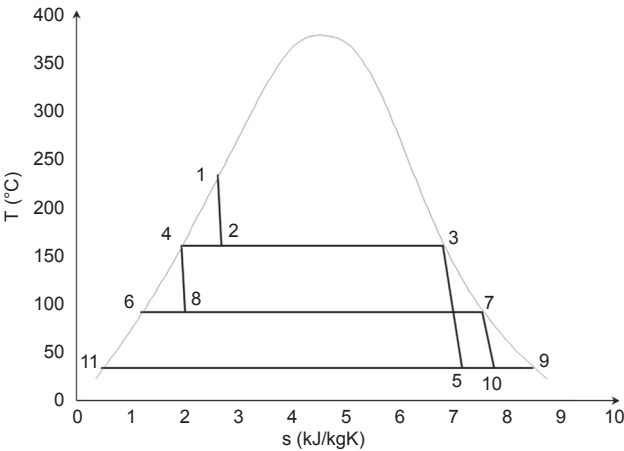


Figure 14.12 Double-flash cycle, typical T-s diagram.



Figure 14.13 Corroded (left) geothermal steam turbine blades (Sabatelli, 2013).



Figure 14.14 Scaling in geothermal steam turbine blades (Adiprana et al., 2010).

Geothermal steam turbines consequently suffer corrosion (Fig. 14.13) and creation of scaling point in the rotor blades (Fig. 14.14), due to the expansion of the geothermal steam. These phenomena affect the turbine efficiency along its useful life, necessitating regular intensive maintenance, including turbine shutdown, visual inspection of the rotor blades, and subsequent substitution of the damaged rotor blades.

Finally, steam turbines are generally coupled to wet condensing system and cooling towers. Such condensing system causes a limited energy consumption but most importantly it is characterized by evaporation losses. As such the reservoir balance is negative—not all the fluid extracted from the system is then reinjected. Furthermore, the management of the cooling water cycle can be a serious issue for projects in remote locations and in extremely cold conditions, respectively, due to the need for continuous operation and anti-icing measures.



Figure 14.15 Eroded turbine blade (Sabatelli, 2013).

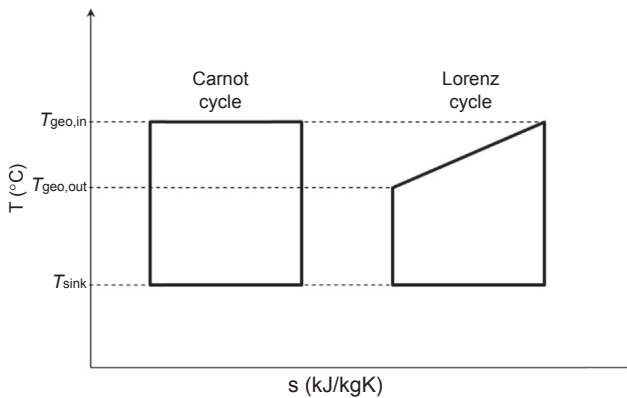


Figure 14.16 Carnot cycle and Lorenz cycle.

14.1.3.2 Binary cycles

The exploitation of a geothermal resource using binary technology is based on the utilization of a secondary fluid in the power cycle, which vaporizes in heat exchangers by receiving heat from the geothermal fluid.

While it is obvious that direct exploitation of the geothermal fluid can happen only by means of steam expansion in a turbine, the feed flow of a geothermal binary cycle is generally singular or in combination:

- liquid flow of brine or two-phase fluid, directly from the wells
- liquid flow of pressurized brine, separated in a pressurized vessel
- steam flow, including noncondensable gases, separated in a pressurized vessel or discharged by a topping system using steam turbine

As the liquid phase is involved, the distinguishing feature of a binary cycle is the ability to efficiently recover energy from a temperature-changing heat source.

The enthalpy and the noncondensable gases content of the geothermal fluid are the main drivers of the thermodynamic analysis and the design of geothermal binary plants; these characteristics combined with the wellhead conditions are the key parameters for the selection of the secondary organic fluid and working cycle.

Considering a theoretical full-liquid resource, which is cooled from a maximum temperature $T_{\text{geo,in}}$ to a minimum temperature $T_{\text{geo,out}}$ (considered as reinjection temperature), the theoretical cycle exploiting the resource is not the Carnot cycle, which assumes heat exchange at constant temperature, but the Lorenz cycle, which minimizes the thermal irreversibility associated to the heat transfer by means of coupling the hot fluid heat release curve and the organic fluid vaporization curve (Fig. 14.16).

The efficiency of the theoretical Lorenz and the Carnot cycles is expressed as while the T-s diagram for these two reversible cycles is reported in Fig. 14.16.

$$\eta_{\text{LOR}} = 1 - 2 \frac{T_{\text{sink}}}{T_{\text{mln}_{\text{geo,in-out}}}}; \quad \eta_{\text{CAR}} = 1 - \frac{T_{\text{sink}}}{T_{\text{heat source}}}$$

where $T_{\text{mln}_{\text{geo,in-out}}}$ is the mean logarithmic temperature of the geothermal heat source, T_{sink} is the temperature of the heat sink, and $T_{\text{heat source}}$ a general constant temperature at which heat is available for a Carnot cycle.

Lorenz efficiency corresponds to the efficiency of a Carnot cycle having the heat source temperature equal to the mean logarithmic temperature of the heat source.

The real conditions of the resource differ from the theoretical full-liquid conditions due to the presence of NCG and general coexistence of two phases at wellhead pressure. This feature of the geothermal resource creates an infinite combination of heat release curves, each one implying a different optimal conversion cycle. Fig. 14.17 shows the heat release curve of a pure steam flow and of a mixture of steam and noncondensable gases.

The next discussion is an overview of the main binary cycles used in geothermal application: binary Rankine cycle, Kalina cycle, and organic Rankine cycle.

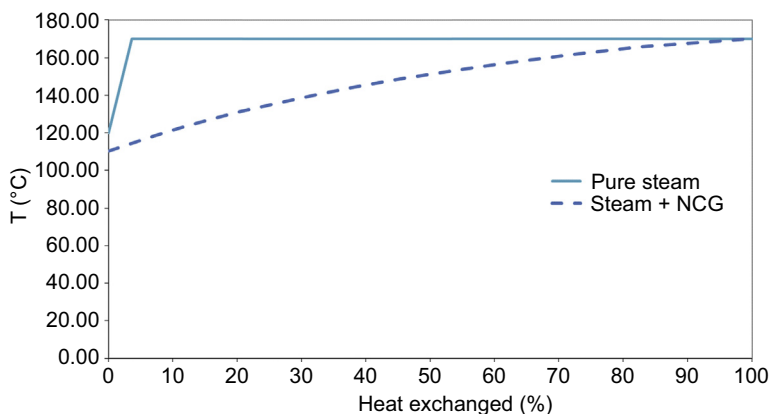


Figure 14.17 Typical heat release curves of pure steam and steam + NCG.

Pure water (Rankine cycle)

As described in the historical overview at the beginning of the chapter, binary cycles were originally conceived using pure water as working fluid. During early 20th century this was in fact the most popular configuration to exploit the Italian geothermal steam sources (UGI, 2007). The first plants exploited steam-dominated resources, extracting heat from the geothermal steam and operating a preferably superheated Rankine cycle (Fig. 14.18, left side), while the saturated vapor obtained from a separator in a liquid-dominated resource is preferably coupled with a saturated Rankine cycle (Fig. 14.18, right side).

Compared to the direct cycles, a water binary system has indeed some advantages but also some disadvantages. Firstly, the turbine does not suffer the typical corrosion, scaling, and erosion issues of those using geothermal steam. Secondly, the pure steam requires a much simpler noncondensable gas extraction system on the condenser, as

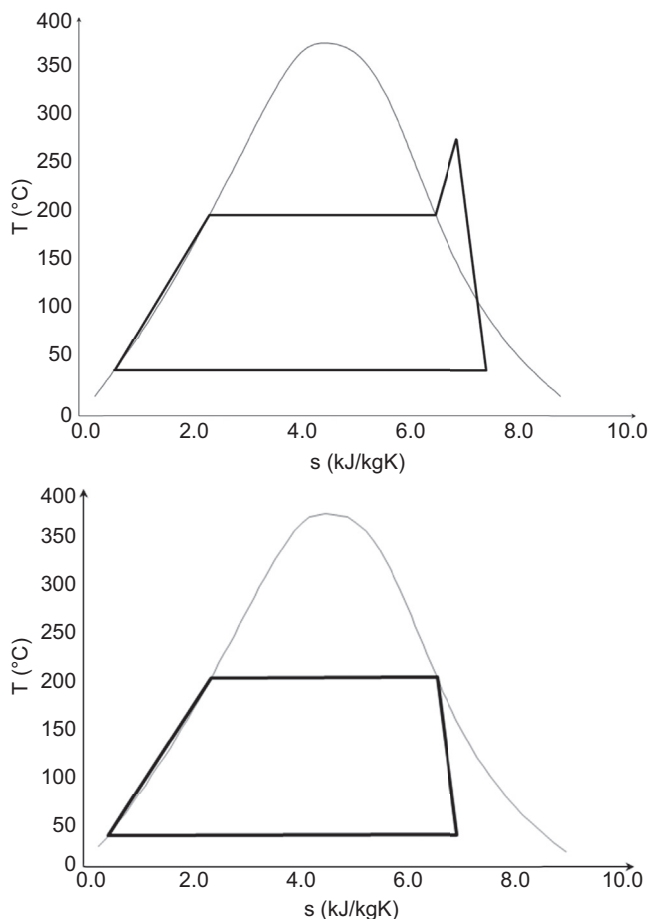


Figure 14.18 Pure water binary cycle, typical T-s diagrams.

the only NCGs present in the system are due to the minimum leakages. Conversely, the consumption of the feed pump is not negligible, the complexity increases, and thermal irreversibility features the heat exchange. We can conclude that the water binary cycle helps overcome some of the technological challenges of the geothermal plants, but some technical issues remain unsolved, such as of the impact of liquid droplet formation during expansion, the very-low pressure at the condenser, and the limitation on blade height at first and last stages, leading to limitations in operating pressures and turbine power (both in terms of minimum and maximum output).

Due to what has been presented herein, it is reasonable to conclude that water binary cycles were a configuration of interest when steam turbines were not yet technologically ready to expand the aggressive and corrosive geothermal steam.

Kalina

The indirect exploitation of geothermal sources may also occur with the so-called Kalina cycle, conceptualized during the mid-1980s by Dr. Alexander Kalina. The main feature of such a system is the adoption as secondary fluid of a mixture composed of water and ammonia, which has the ability to vaporize and condensate at variable temperature but constant pressure (Kalina, 1984).

Water and ammonia have similar molecular weight but quite different thermophysical characteristics as presented in Table 14.4.

When mixed, water and ammonia form a nonazeotropic mixture. In such a mixture ammonia is the more volatile component of the two, having a lower boiling and condensing temperature than water.

For a nonazeotropic mixture, temperature and composition continuously vary during boiling, as illustrated by the points **a** to **f** in Fig. 14.19.

Given the composition of a certain mixture, when the same starts to boil (point **a**), a vapor richer in the more volatile fluid—ammonia—is formed with a composition given in point **B**. Continuing in the boiling (point **c**), the temperature increases and the concentration of liquid and vapor changes as per points **d** and **e**. If full boiling is reached (point **f**), the mixture is a saturated vapor at dew point temperature and the vapor composition is the same as that in liquid phase at the beginning of the evaporation process.

Consequently, nonazeotropic mixtures such as ammonia-water evaporate at increasing temperature and condense at decreasing temperature, considering the transformation is happening at constant pressure. By properly designing the system, this

Table 14.4 Properties of water and ammonia

Name	Chemical formula	Molecular weight (kg/kmol)	Critical temperature (°C)	Critical pressure (MPa)	Boiling point at 1.013 bar (°C)	Freezing point at 1.013 bar (°C)
Ammonia	NH ₃	17.0	101.1	4.059	−33.3	−77.7
Water	H ₂ O	18.0	373.9	22.064	100.0	0.0

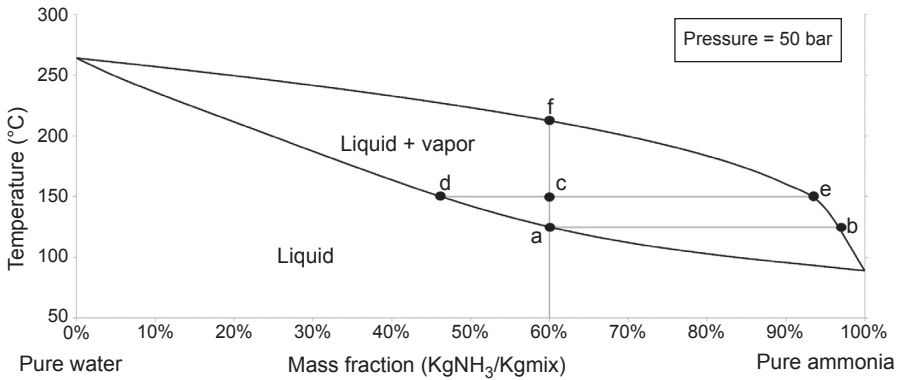


Figure 14.19 Isobaric phase transition in a nonazeotropic mixture (water-ammonia).

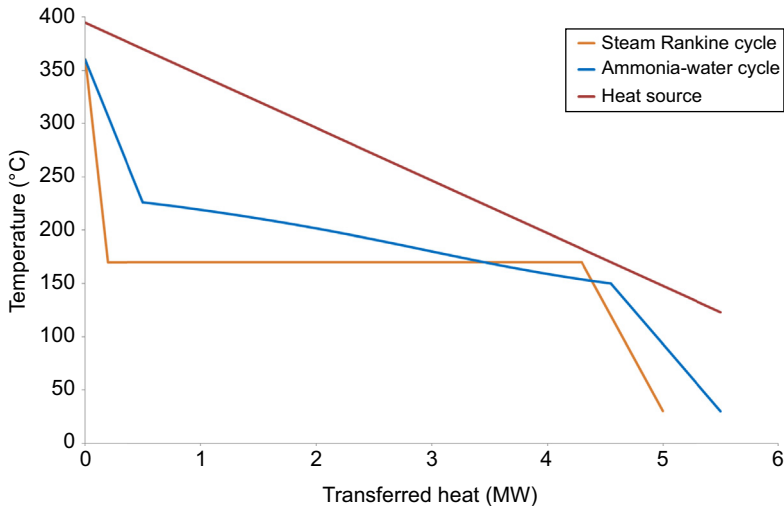


Figure 14.20 Comparison between T-Q diagrams of a Rankine and a Kalina cycle.

sliding evaporative behavior enables a good fit of the heat release curve of the geothermal fluid than a pure substance. This behavior is presented in Fig. 14.20.

For the same principle, the sliding condensing behavior may better match the heat release curve of the temperature-changing heat sink than a pure substance.

The Kalina cycle is generally designed as a superheated cycle with a regenerative section, as per Fig. 14.21; in fact, considering the unique features of this type of vaporization, superheating is adopted in order to avoid liquid drops in the turbine, and, consequently, a recuperator is foreseen to recover thermal energy at turbine discharge.

Kalina cycle has the possibility to vary the thermophysical properties of the working fluid in different parts of the cycle by changing the relative composition of the ammonia-water mixture; when configured as an absorption-condensation process, as

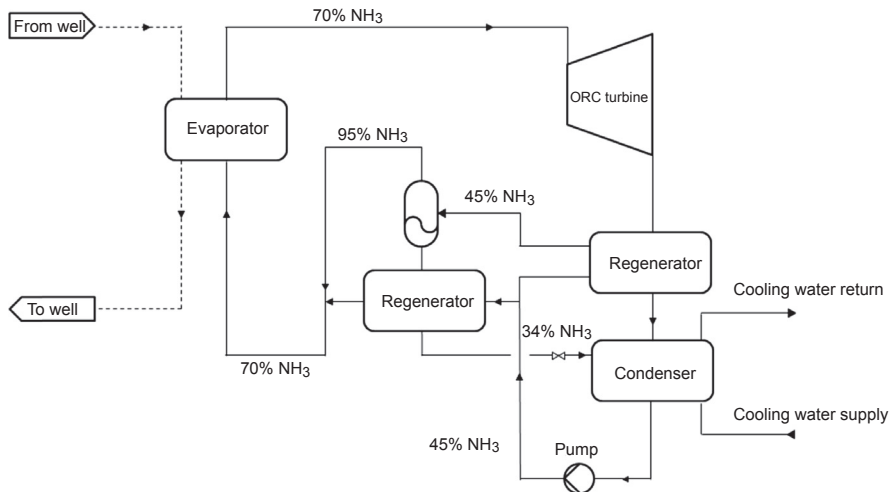


Figure 14.21 Typical simplified process flow diagram of a Kalina cycle.

per Fig. 14.21, the recirculation process reduces the turbine exhaust pressure and the exhaust temperature as well (Mlcak, 1996). On the other hand, adding a distillation column within the binary loop it clearly increases the plant complexity.

Although Kalina cycle presents some theoretical advantages when compared to ORC, this technology did not gain market favor. This technology has been applied only rarely on a geothermal resource, e.g., the 2 MW plant in Húsavík, Iceland, has encountered some serious issues and failures during its operation (Ásgeirsson, 2009).

The Húsavík unit was commissioned in June 2000 and exploits a brine source at 124°C, cooled to 80°C. The geothermal fluid is then used further for heating purposes, in the local district heating system. The process flow diagram of the plant is presented in Fig. 14.22, where the superheated cycle with a regenerative section and the absorption-condensation process can be identified.

The mixture is expanded in an overhung turbine designed and supplied by Kühnle, Kopp & Kausch. The turbine wheel operates at 11,226 rpm and has an integral gear on the shaft to couple the turbine to a 1500 rpm synchronous generator (Mlcak, 2001).

Some severe problems have been faced during the operation of the plant; of these the most important are the corrosion/erosion on the turbine and the difficulties in managing the working mixture. Regarding the first point, the phenomena happened between the turbine housing and the nozzles due to the wrong selection of the turbine materials, incompatible with ammonia, which led to the need to change it. As this remedy was unsuccessful, in 2004 it has been decided to change the turbine manufacturer to GE-Rotoflow. Even though it was provided with the highest quality materials, this turbine also suffered a big failure as a part of the turbine wheel was damaged, including turbine blades, shaft, nozzle vanes, and housing. The difficulties in managing the ammonia-water mixture led to the redesign of the separator (Ásgeirsson, 2009).

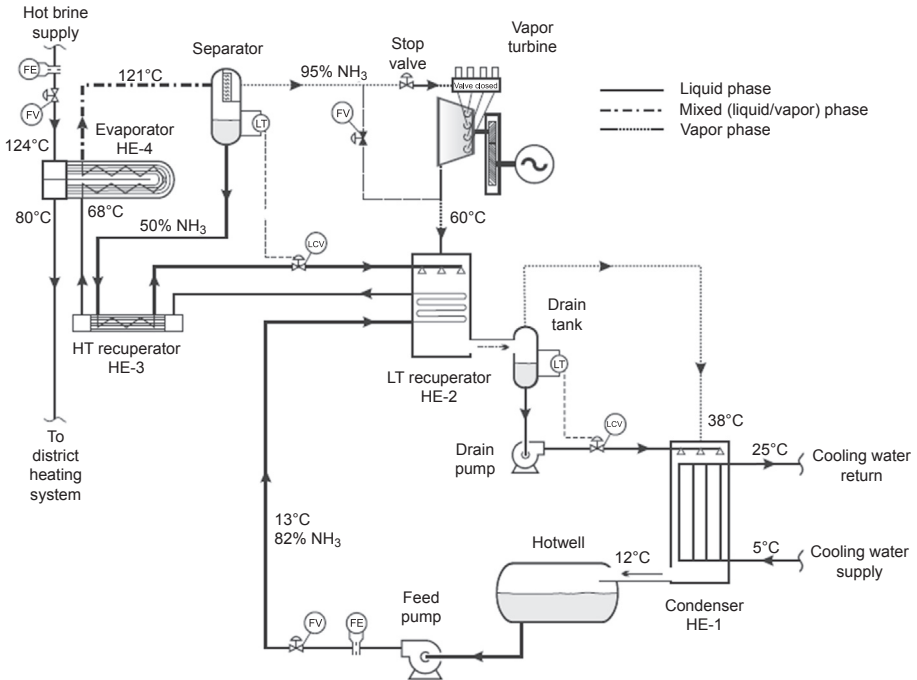


Figure 14.22 Process flow diagram of Húsavík Kalina cycle (Mlcak, 2001).

Organic Rankine cycle

Having different features than the other binary solutions, the ORC represents a broader family of thermodynamic cycles, thanks to the degree of freedom given by the choice of the working fluid.

As anticipated, passing from a theoretical resource to the real wellhead conditions of a geothermal resource, the main parameters influencing the cycle design are:

- geothermal fluid enthalpy (bottom-hole conditions)
- NCG content
- Wellhead conditions (pressure, mono- or biphasic)
- chemical composition of the fluid
- available resource size (producible power)

The main parameters to characterize the design of the ORC binary power plant for this resource are:

- working fluid and cycle selection (pressures and temperatures, superheating, regeneration)
- condensation temperature/pressure and cooling media
- turbine technology selection

The next section aims to describe more in detail the available solutions for applying ORC systems to geothermal power plants.

14.2 Geothermal ORC binary plants

14.2.1 Fluid selection

Given a certain geothermal resource in terms of fluid enthalpy, NCG content, wellhead conditions, chemical composition and quantity of available resource, and defined boundary conditions, a number of organic Rankine cycles are applicable, thanks to the many available degrees of freedom.

The working fluid of an ORC can be chosen according to a number of parameters:

- molecular weight (low or high)
- complexity (low or high), which leads, respectively, to wet and dry fluids (negative or positive saturation vapor curve)
- flammability (high, low, or none)

Working fluids for geothermal applications generally are low boiling, meaning that the evaporation takes place at higher pressure than water saturation pressure at the same temperature, as more extensively described in Chapter 7. Many low-boiling organic fluids are available in the market, such as chlorofluorocarbon (CFC), hydrochlorofluorocarbon (HCFC), hydrofluorocarbon (HFC), fluorocarbon (FC), hydrocarbon (HC), and the most recent hydrofluoroolefin (HFO). From a technical standpoint, the listed fluids are eligible but the CFC and HCFC fluids are banned due to their high ozone depletion potential (ODP) and traditional HFCs are progressively being phased out due to their high global warming potential (GWP) in favor of HFOs.

A number of thermophysical parameters define the behavior of the fluids: critical temperature and pressure and dry or wet expansion of the fluid (asymmetric or symmetric saturation vapor curve).

In [Table 14.5](#) the most important thermophysical characteristics ([REFPROP 9.0](#)) of the organic fluids currently used on the market are presented, compared with water.

The critical temperatures of these fluids vary from 100°C to 200°C, while the critical pressure is in the range of 30–40 bar. Latent heat and heat capacity are generally lower for HFC, and the only fluid featured with wet expansion is R134a ([Fig. 14.23](#)).

Analyzing the diagram in relative units ([Fig. 14.24](#)), it appears that normal- and isopentane have very similar shape, normal- and isobutane have quite different shape, R245fa is quite similar to butane, while R134a is different from all the other fluids. As such, given a thermodynamic cycle, it becomes evident that fluids with the same molecular weight will not necessarily perform with similar heat recovery efficiency while fluids with similar critical temperature are expected to do so. On the other hand, fluids with different molecular weight, complexity, and critical point will lead to different enthalpy heads, volumetric expansion ratios, and exhaust volumetric flows on the turbines. Furthermore, as the critical pressure and boiling points are different, these fluids will also operate at different operating pressure.

Table 14.5 Thermophysical characteristics of organic fluids and water

Name	Class	Chemical formula	Molecular weight (kg/kmol)	Critical temperature (°C)	Critical pressure (MPa)	Boiling point at 1.013 bar (°C)	Type of expansion
R134a	HFC	CH ₂ FCF ₃	102.0	101.1	4.059	−26.1	Wet
R245fa	HFC	CF ₃ CH ₂ CHF ₂	134.0	154.0	3.651	15.1	Dry
Isobutane	HC	C ₄ H ₁₀	58.1	134.7	3.629	−11.8	Dry
Butane	HC	C ₄ H ₁₀	58.1	152.0	3.796	−0.5	Dry
Isopentane	HC	C ₅ H ₁₂	72.1	187.2	3.378	27.8	Dry
Pentane	HC	C ₅ H ₁₂	72.1	196.6	3.370	36.1	Dry
Water	—	H ₂ O	18.0	373.9	22.064	100.0	Wet

HC, hydrocarbon; HFC, hydrofluorocarbon.

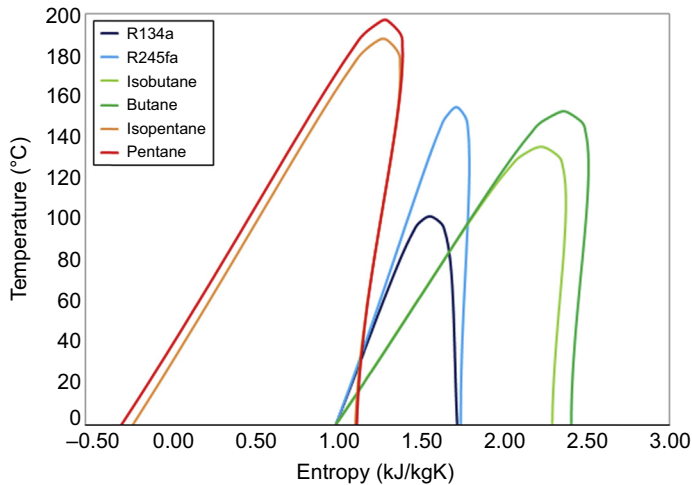


Figure 14.23 T-s diagram for typical organic fluids used in geothermal application.

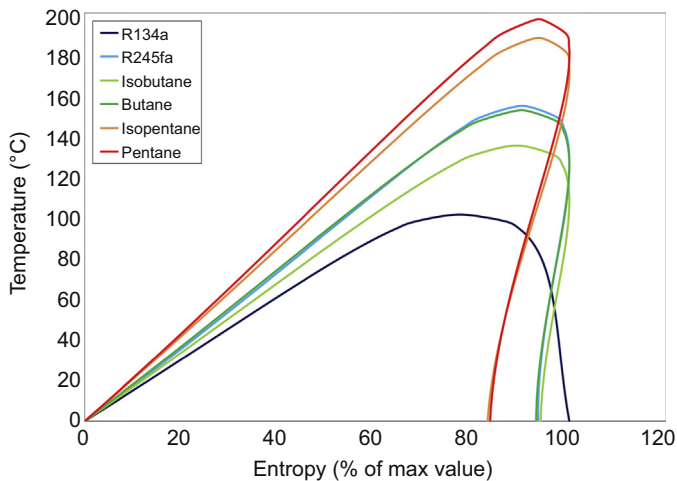


Figure 14.24 T-s diagram for typical organic fluids used in geothermal application (relative entropy).

14.2.2 Cycle selection

As anticipated in Par. 14.1.3, the binary cycles exploit heat from both vapor and liquid phase. Generally, the resource can be exploited adopting one of the following configurations:

1. Subcritical systems
 - a. Single pressure level system
 - b. Double pressure level system
 - c. Triple pressure level system

2. Supercritical

3. Bottoming and combined cycles: steam turbine + binary cycle

In order to present easier coverage of this analysis, before getting into the details of each configuration, a numerical example is presented, aiming to compare the three subcritical solutions and the supercritical configuration. The comparison is carried out using normal pentane as the working fluid for the subcritical cycles, as it is the most commonly applied fluid and has a broader range of application, and R134a for the supercritical cycle.

Three cases are presented: medium-high enthalpy (200°C), medium enthalpy (150°C), and low enthalpy (100°C) full-liquid flows, cooled to a reinjection temperature of 70°C (Fig. 14.25).

A more extensive numerical example of fluid cycle selection is given as a case study in (Section 14.2.3), where the remaining hypotheses at the basis of this comparison are listed.

The results will be discussed throughout the description of the cycle configurations that are presented following. Please refer to Chapter 3 for more details about the ORC plant configurations, their layouts, and their features.

- The **single-pressure-level** system is the simplest ORC configuration possible. The geothermal fluid, either in liquid or both phases, rejects heat to the organic fluid through the tubes of a number of heat exchangers, where the organic fluid is vaporized and fed to the turbine. Due to the typical shape of the preheating and vaporization curves, the single-pressure-level cycle fits very well resources with high steam content at ORC inlet, meaning a large part of the heat exchange is at almost constant temperature, or a low temperature difference between inlet and outlet of the geothermal liquid.
- The **double-pressure-level** system is composed of two “subcycles,” in which the organic fluid is vaporized and fed to the turbines in parallel at different pressure, namely high-pressure and low-pressure cycles. Typically, they are featured with two turbines in tandem configuration (or on a single integral gearbox) on a single generator unit. On the geothermal fluid side, the heat exchangers can be encountered both in series and in parallel in different stages of the cycle, depending on the optimal configuration for the given resource. A recent development is the two-level single-turbine configuration, developed with a single-disk radial outflow turbine, which eases the use of a single recuperator, condenser, pumping group, and low-temperature preheater, as the turbine discharges the entire flow, mixed inside the turbine after the second admission. As shown in the comparison at the beginning of this paragraph, the two-pressure-level system shows the maximum gain of approximately 14% over single-pressure-level system when applied to medium-enthalpy resources with high-temperature difference between ORC inlet and outlet, but maintains a good performance in all cases—with more than +10% with respect to the simplest plant layout; for this reason it is nowadays the most commonly adopted configuration for new plants exploiting medium-enthalpy resources.
- **Triple pressure level** systems consist of three subcycles in parallel, with the same philosophy as for the two-pressure-level system—the organic fluid cycles are substantially independently operated in parallel, while on the geothermal fluid side the flow encounters the heat exchangers in series and in parallel according to the best fit of the cycle to the available resource. The three-pressure-level cycle is always performing over others, even if not always significantly more than the two-pressure level; in the reference case of medium enthalpy with

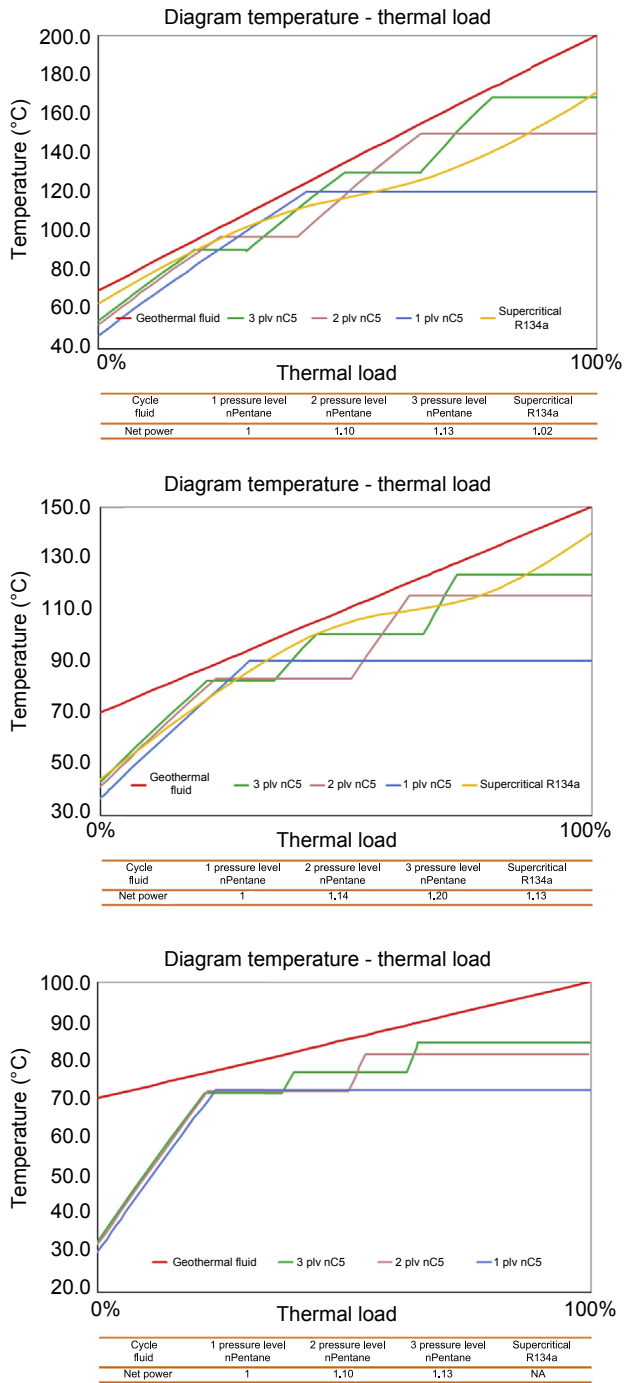


Figure 14.25 Multipressure and supercritical cycles comparison.

high-temperature drops of the geothermal fluid the increase in performance is +20% over the single-pressure-level system and +5% over the double-pressure-level system.

- When the organic fluid at turbine inlet is a supercritical fluid, which has passed through no traditional phase transition, the resulting cycle is named **supercritical**. The cycle is in fact not entirely over the critical point, as the condensing pressure and temperature are usually below the critical point (except if CO₂ is used). Supercritical systems are alternative to double- and triple-pressure-level cycles for medium-enthalpy-level resources, and are particularly indicated for reaching very low reinjection temperatures, thanks to the shape of the heating curve. The typical fluids used for this cycle are R134a and propane, due to the very low critical point. The aim of this cycle is to replicate the most similar cycle to the Lorenz cycle, thus is particularly interesting for geothermal fluids with high temperature difference between inlet and outlet to the system. The supercritical cycle is comparable in terms of performance for medium enthalpy resources to a multiple-pressure-level system, but shows no clear advantage when enthalpy is higher.

14.2.2.1 *Bottoming and combined cycles*

Combined systems are suited for resources with high enthalpy, and thus very high steam amount. The binary unit can run in parallel to the steam turbine, exploiting a geothermal liquid flow after separation, or in series, with the addition of a steam flow coming from the backpressure turbine. The former is the so-called “bottoming” configuration, in which the ORC exploits the heat contained in the brine flow after separation (Fig. 14.26).

The combined cycle configuration is usually the most efficient means of exploitation of a high-enthalpy resource and fits particularly well the resources with high noncondensable gases content—the aim is the maximization of the power output together with the reduction of the installation of low-pressure condenser with NCG extraction system (Fig. 14.27). Differently from the typical geothermal ORC system, the combined cycle is generally completely water cooled, taking advantage of the pure water coming from the condensing steam as a makeup for the cooling towers system.

14.2.2.2 *Regeneration*

Compared to high-temperature ORC, where regeneration is a common practice, geothermal binary systems are not always regenerative. The system is equipped with a regenerator in order to recover the thermal energy contained in the vapor at turbine discharge and to heat the liquid feed of the organic fluid to the preheater; at the same time, efficiency increases, and the amount of heat discharged to the condenser is reduced. The extent of the beneficial impacts of adding this component, which should be evaluated technically and economically, has to be defined case by case, evaluating the amount of the energy recovered and the impact of the additional pressure drops within the vapor and liquid streams, leading to a reduction in turbine enthalpy drop and an increase in pump consumption, and the cost of the component and the related modifications to the plant design.

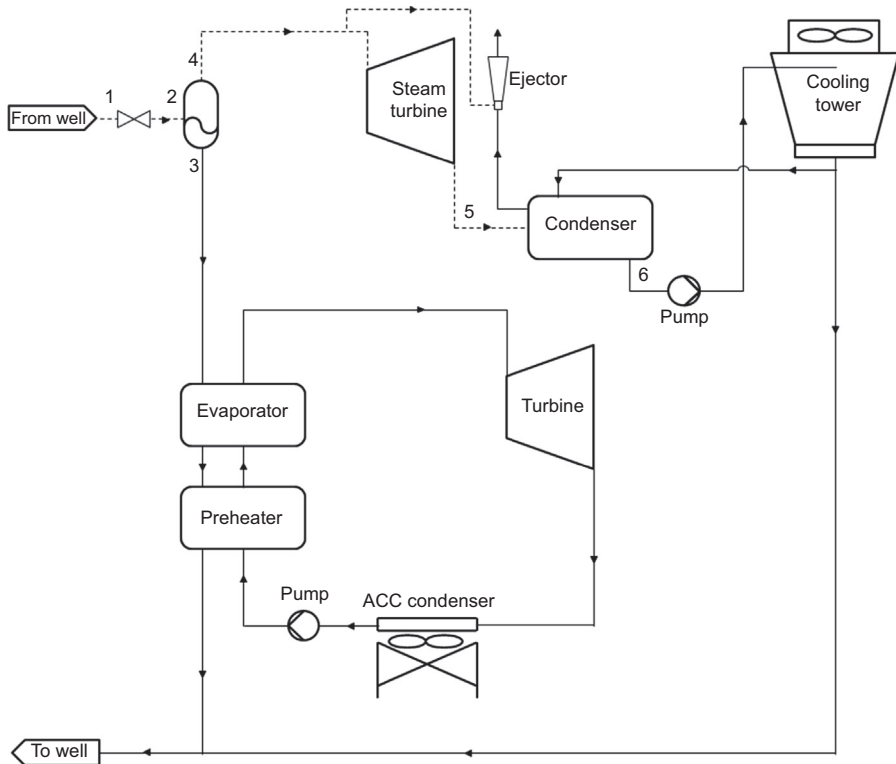


Figure 14.26 Bottoming cycle, plant typical simplified flow diagram.

Regeneration is usually less beneficial for a cycle when the molecular complexity of the organic fluid decreases (as the turbine outlet temperature gets lower) and when the reinjection temperature is limited by silica deposition, reservoir management, or other issues that may be encountered at low temperature. Multiple-level systems may be equipped with regenerator on high-pressure levels only.

Superheating is generally not beneficial in ORC geothermal applications, as the heat recovery efficiency of the cycle decreases.

14.2.2.3 Turbine technology

Considering the cycle configurations listed in this paragraph, the fluid and cycle shall match the turbine technology. As such, analysis of the following parameters becomes essential:

- enthalpy head
- volumetric and pressure ratio of the expansion
- exhaust volumetric flow

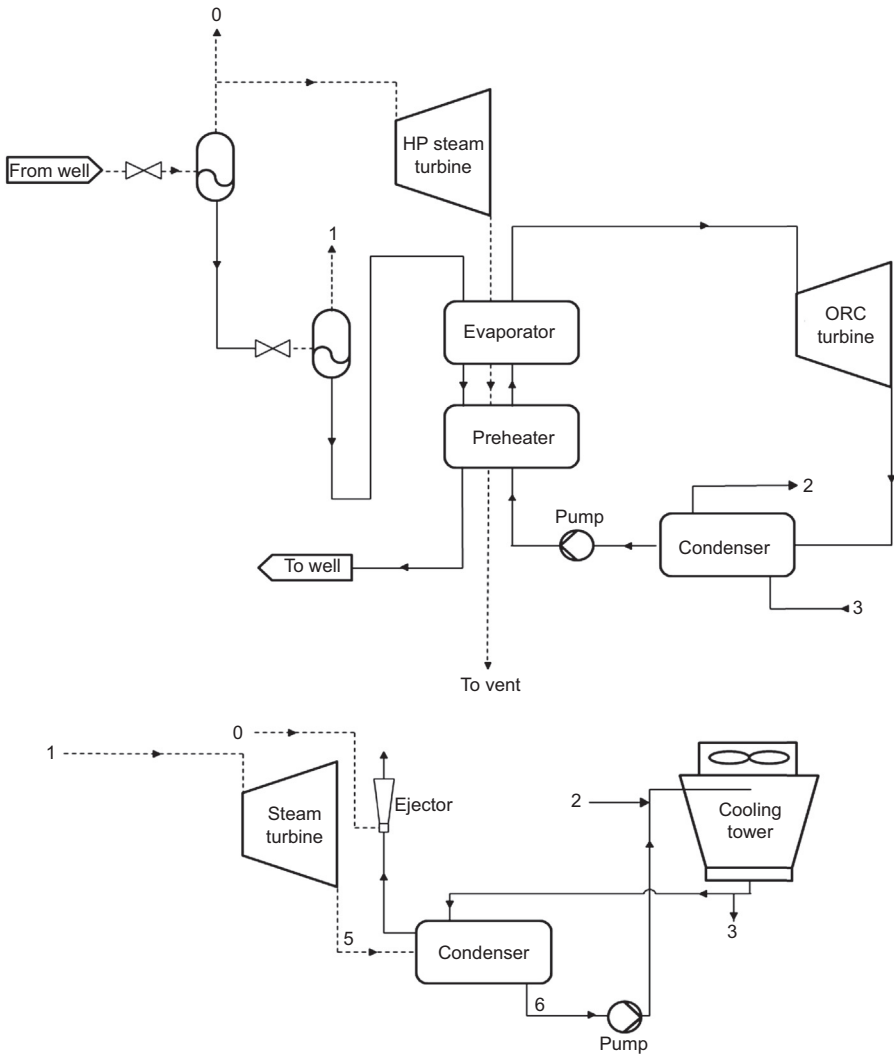


Figure 14.27 Combined cycle, plant typical simplified flow diagram.

The optimization of the overall heat recovery system is achieved by matching the operating conditions of the working cycle together with the turbine efficiency, thereby maximizing the plant power output:

- axial turbine
- radial inflow turbine
- radial outflow turbine
- scroll/screw expander

The selection of the turbine configuration according to the previous parameters is covered in detail in the relevant chapters of this book. ORC turbines for geothermal application are generally designed in overhung configuration, in order to maximize simplicity and minimize costs, while geothermal steam turbines are typically axial turbines between bearings, with a horizontal split case construction.

14.2.3 Fluid and cycle selection, a numerical example

The most used working cycles and organic fluids in ORC geothermal binary power plants are compared. The analysis is performed considering the exploitation of one of the most common geothermal resources and the possibility to cool it down to two different temperatures.

The analysis aims to understand which plant configuration is the most effective in order to maximize the production of the given resource and the different behavior of the systems analyzed, thus the differences in the design of the plant components.

The hypothesis of the analysis are the following:

Geothermal resource type	Brine — Pressurized water
Geothermal resource mass flow	Same for all the configurations
Geothermal resource temperature	150°C
Geothermal resource minimum temperature	70°C
Pinch point in the heat exchangers	5°C
Recuperator minimum temperature difference	15°C
Organic fluid condensing temperature	30°C
Turbine isentropic efficiency	82%
Pump isentropic efficiency	70%
Generator efficiency	97%
Pump motor efficiency	95%
Pressure drops within ORC loop (other than the turbine)	None
Fluid database	Nist REFPROP 9.0

Formalizing the mathematical problem:

$$\left\{ \begin{array}{l} \max[P_{\text{net}}] \\ iv = \{T_{\text{eva}}\} \\ T_{\text{rej}} \geq T_{\text{rej min}} \\ \Delta T_{\text{pp}} \geq \Delta T_{\text{pp, min}} \end{array} \right.$$

The goal is the maximization of the net power, and this is achieved by varying the independent variable evaporation temperature T_{eva} , considering the rejection temperature and pinch point constraints.

The organic fluids analyzed are:

- Pentane, normal- and iso-
- Butane, normal- and iso-
- R245fa
- R134a

While the working cycles analyzed are:

- 1 saturated pressure level—with or without recuperator
- 2 saturated pressure level—with or without recuperator on high- and low-pressure levels
- Supercritical—with or without recuperator

The results of the analysis, reported in [Tables 14.6 and 14.7](#), show that:

- Pentane is the most versatile fluid as it performs well in both subcritical cases while the other fluids tend to be less effective when the resource temperature variation is limited. This result is strictly connected to the fluids' thermophysical characteristics, and pentane appears to be well suited as it has the highest critical temperature but also the lowest critical pressure, which is an ideal match with this geothermal resource. On the other hand, pentane features the highest volumetric flows as well as high volumetric ratios and enthalpy drops along the fluid expansion in the turbine.
- Butane is better performing when the resource variation is greater, while it is not preferable or even suitable for heat recovery at high temperature and low degree of cooling, due to the low critical point. This behavior can be seen more greatly in isobutane, as it has a critical temperature that is much lower than butane.
- R245fa appears to be an effective fluid, with outputs similar to butane but when compared with this, it leads to comparable volumetric flows at turbine inlet, greater volumetric ratio and volumetric flows at turbine discharge, and significantly smaller (almost a half) enthalpy drops. As its cost per unit of volume is approximately 10–15 times greater than the hydrocarbons, R245fa is generally selected as operating fluid only in very limited applications, thus potentially when local acceptance, local regulations and fluid flammability, and associated risk are playing an important role.
- R134a with a supercritical cycle is well suited for recovering energy from resources at medium to low temperature and with a significant cooling, the conditions in which this configuration better match the geothermal fluid cooling curve. In fact the thermophysical characteristics of R134a, meaning low critical temperature and low latent heat, coupled with a supercritical cycle are not suited for heat recovery with high resource temperature and small cooling as the temperature difference between the hot and the cold fluid becomes too great. This behavior can be seen in [Figs. 14.28 and 14.29](#). As its cost per unit of volume is in the range of five times greater than the hydrocarbons, R134a is generally selected as operating fluid only in very limited applications, thus potentially when local acceptance, local regulations and fluid flammability, and associated risk are playing an important role.
- Multipressure level cycles are convenient when the resource temperature variation is relatively high; as a matter of fact, adding a further heat recovery loop facilitates the heated organic fluid to replicate the heat release curve of the geothermal fluid, and this can be noticed in [Figs. 14.30 and 14.31](#). The advantage of a multipressure system is instead quite

Table 14.6 Results of comparison for the 150–70°C resource

Cycle fluid	1 pressure nPentane	1 pressure isoPentane	1 pressure nButane	1 pressure isoButane	1 pressure R245fa	2 pressure nPentane	2 pressure isoPentane	2 pressure nButane	2 pressure R245fa	Supercritical R134a
Gross power	1	1.02	1.07	1.15	1.06	1.17	1.18	1.21	1.20	1.33
Net power	1	1.01	1.03	1.06	1.03	1.16	1.16	1.15	1.15	1.15
Gross efficiency (%)	11.3%	11.4%	12.0%	12.9%	11.9%	13.0%	13.1%	13.5%	13.4%	14.9%
Net efficiency (%)	11.1%	11.1%	11.2%	11.6%	11.3%	12.7%	12.7%	12.6%	12.6%	12.6%
Temp rej (°C)	71	70	70	70	70	70	70	70	70	70
Temp Turb in HP (°C)	90.2	90.7	99.1	108.7	99.6	115.5	116.1	121.0	121.3	140.0
Temp Turb in LP (°C)	—	—	—	—	—	83.9	84.8	93.3	94.1	—
Pr Turb in HP (bar)	4.7	5.9	15.0	23.3	12.5	8.3	10.1	22.5	19.8	47.8
Pr Turb in LP (bar)	—	—	—	—	—	4.1	5.1	13.4	11.1	—
Pr cond (bar)	0.82	1.09	2.83	4.05	1.78	0.82	1.09	2.83	1.78	7.70
UA HP ph	670	729	835	1086	845	623	676	820	809	—
UA LP ph	—	—	—	—	—	226	236	267	276	—
UA HP eva	1054	1051	988	900	983	798	791	726	722	2014
UA LP eva	—	—	—	—	—	691	679	615	615	—
UA HP recu	292	295	—	—	—	105	117	50	49	368

Continued

Table 14.6 Continued

Cycle fluid	1 pressure nPentane	1 pressure isoPentane	1 pressure nButane	1 pressure isoButane	1 pressure R245fa	2 pressure nPentane	2 pressure isoPentane	2 pressure nButane	2 pressure R245fa	Supercritical R134a
UA LP recu	—	—	—	—	—	28	32	13	12	—
UA HP cond	1909	1931	1663	1707	1670	1623	1649	1719	1697	1745
UA LP cond	—	—	—	—	—	1072	1055	976	982	—
UA TOT	3932	4014	3485	3693	3499	5167	5235	5185	5162	4127
v in HP (m ³ /kJ)	1.57	1.31	0.51	0.30	0.52	0.46	0.39	0.18	0.17	0.16
V in LP (m ³ /kJ)	—	—	—	—	—	0.62	0.50	0.19	0.20	—
V out HP (m ³ /kJ)	9.13	7.23	3.00	2.17	3.97	4.88	3.91	1.75	2.31	1.14
v out LP (m ³ /kJ)	—	—	—	—	—	3.07	2.38	3.11	1.31	—
v out/v in HP	5.80	5.52	5.86	7.23	7.66	10.61	10.00	9.79	13.35	7.01
v out/v in LP	—	—	—	—	—	4.94	4.77	5.12	6.65	—
dh is HP (kJ/kg)	64.2	61.1	69.2	68.0	36.0	87.16	82.75	85.49	44.19	42.53
dh is LP (kJ/kg)	—	—	—	—	—	58.12	55.71	64.38	33.64	—

Table 14.7 Results of comparison for the 150–110°C resource

Cycle fluid	1 pressure nPentane	1 pressure isoPentane	1 pressure nButane	1 pressure isoButane	1 pressure R245fa	2 pressure nPentane	2 pressure isoPentane	2 pressure nButane	2 pressure R245fa	Supercritical R134a
Gross power	1.00	1.00	0.99	—	0.97	1.03	1.03	0.99	0.98	0.99
Net power	1.00	1.00	0.93	—	0.93	1.02	1.02	0.93	0.93	0.87
Gross efficiency (%)	15.5%	15.6%	15.4%	—	15.1%	16.0%	16.0%	15.4%	15.2%	15.2%
Net efficiency (%)	15.0%	15.0%	14.0%	—	14.1%	15.4%	15.3%	13.9%	14.0%	13.1%
Temp rej (°C)	110	110	110	—	110	110	110	110	110	110
Temp Turb in HP (°C)	122.0	122.9	128.6	—	128.4	133.3	133.7	136.1	136.3	145.0
Temp Turb in LP (°C)	—	—	—	—	—	121.1	122.0	128.1	128.0	—
Pr Turb in HP (bar)	9.4	11.5	25.7	≈ P critical	22.75	11.7	14.0	29.2	26.4	45.7
Pr Turb in LP (bar)	—	—	—	≈ P critical	—	9.3	11.3	25.5	22.6	—
Pr cond (bar)	0.82	1.09	2.83	—	1.78	0.82	1.09	2.83	1.78	7.70
UA HP ph	317	338	393	—	388	236	252	323	306	—
UA LP ph	—	—	—	—	—	136	143	141	147	—
UA HP eva	737	723	623	—	626	499	488	421	417	888
UA LP eva	—	—	—	—	—	464	451	334	346	—

Continued

Table 14.7 Continued

Cycle fluid	1 pressure nPentane	1 pressure isoPentane	1 pressure nButane	1 pressure isoButane	1 pressure R245fa	2 pressure nPentane	2 pressure isoPentane	2 pressure nButane	2 pressure R245fa	Supercritical R134a
UA HP recu	192	193	210	—	203	60	65	22	23	176
UA LP recu	—	—	—	—	—	42	46	15	15	—
UA HP cond	918	917	902	—	909	713	722	825	797	877
UA LP cond	—	—	—	—	—	592	589	497	520	—
UA TOT	2164	2171	2128	—	2126	2741	2756	2578	2571	1941
v in HP (m ³ /kJ)	0.54	0.46	0.21	—	0.20	0.23	0.20	0.10	0.10	0.18
V in LP (m ³ /kJ)	—	—	—	—	—	0.24	0.20	0.08	0.08	—
v out HP (m ³ /kJ)	6.70	5.33	2.42	—	3.22	3.60	2.90	1.51	1.94	1.14
V out LP (m ³ /kJ)	—	—	—	—	—	2.94	2.33	3.25	1.27	—
v out/v in HP	12.30	11.66	11.80	—	16.04	15.85	14.85	14.41	20.05	6.50
v out/v in LP	—	—	—	—	—	12.05	11.42	11.66	15.93	—
dh is HP (kJ/kg)	64.2	61.1	69.2	—	36.0	102.0	96.5	93.8	48.4	43.80
dh is LP (kJ/kg)	—	—	—	—	—	91.95	87.44	89.81	46.28	—

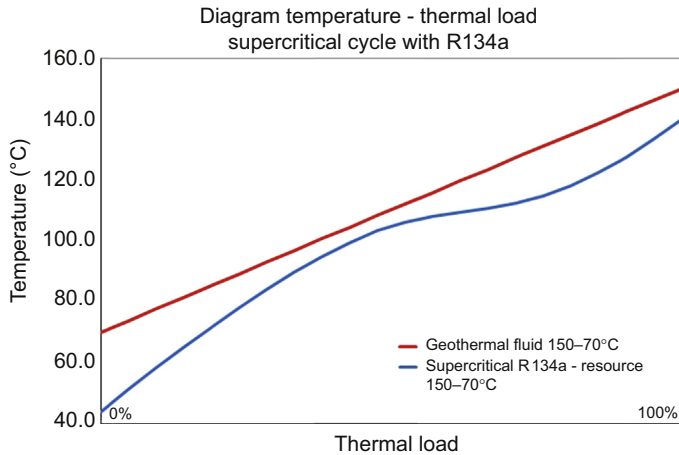


Figure 14.28 Temperature—thermal load diagram for supercritical cycle with R134a for a geothermal resource cooled from 150°C to 70°C.

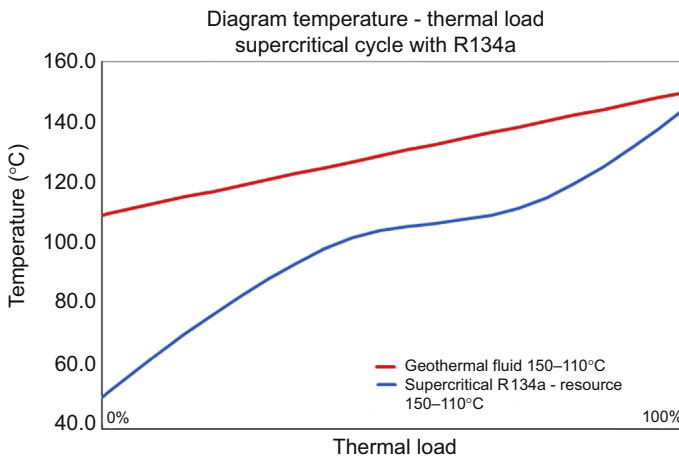


Figure 14.29 Temperature—thermal load diagram for supercritical cycle with R134a for a geothermal resource cooled from 150°C to 110°C.

limited when the resource temperature variation is relatively low, as the levels would be at similar pressure.

- Operating pressure changes significantly between the various fluids: R134a has the highest, pentane has the lowest, while the other fluids are in between. It is interesting to notice that pentane evaporation pressure can be lower than the R134a condensing pressure, as can be seen in [Figs. 14.32 and 14.33](#). The operating pressure affects the system design and shall be considered while defining the system class and rating.
- Turbine design is significantly different between the various configurations:
 - Volumetric flow at inlet and outlet might even be 10 times different between the configurations (i.e., resource 150–70°C nPentane and R134a);

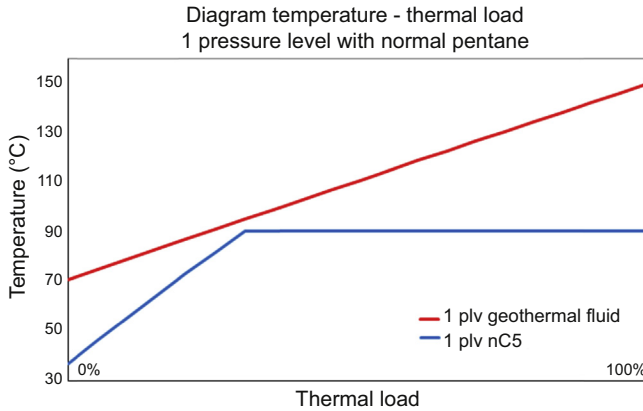


Figure 14.30 Temperature—thermal load diagram for one pressure cycle with normal pentane.

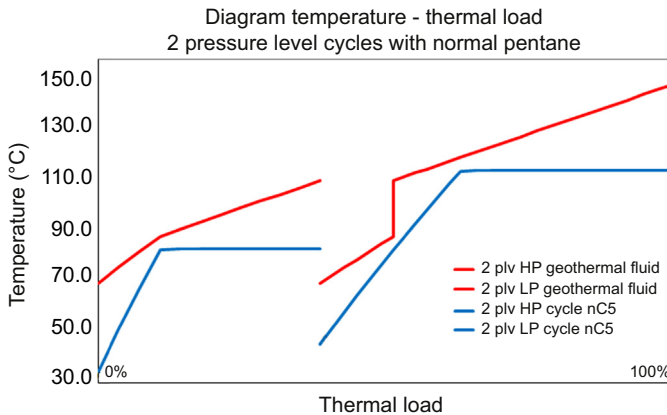


Figure 14.31 Temperature—thermal load diagram for two pressure cycles with normal pentane.

- Expansion ratio varies from 5 to 20 and varies significantly between the fluids;
- Enthalpy drop varies between 30 and 105 kJ/kg and is strictly connected to the mass weight of the organic fluid.
- Turbine selection is affected by the previously mentioned parameters:
 - Axial turbines are suitable for a wide range of configurations.
 - Radial outflow has a range of application similar to axial turbines, featuring the possibility to use lower volumetric flow at the inlet (thus, higher pressure) and the single-disk multilevel configuration.
 - Radial inflow appears to be limited in the volumetric flows (in/out), in the volumetric ratio, and in the enthalpy drop, which can be processed. Due to its nature, the optimal volumetric ratio is between 5 and 12 and the enthalpy drop is between 50 and 80 kJ/kg, while due to current market size limitation, it appears not possible to allow a high-volumetric flow at turbine inlet and outlet. As a consequence, butane is

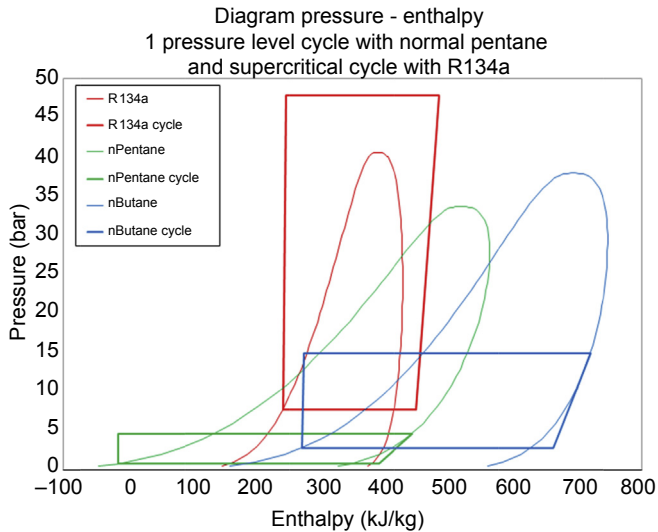


Figure 14.32 Pressure–enthalpy diagram for one pressure cycle with normal pentane and supercritical with R134a.

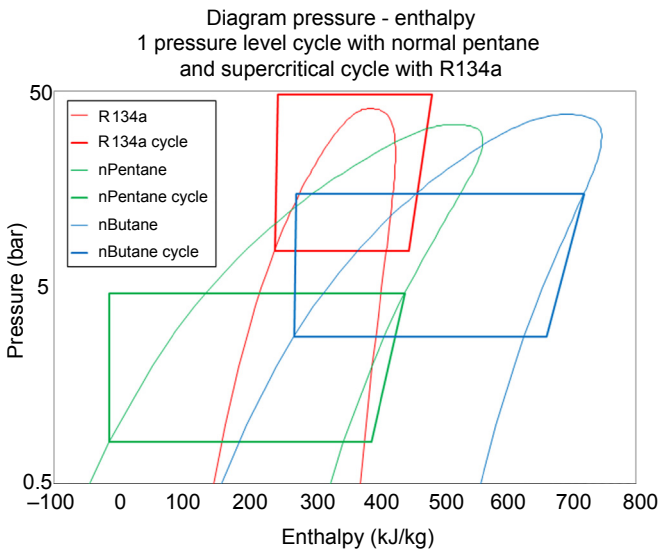


Figure 14.33 Pressure–enthalpy diagram for one pressure cycle with normal Pentane and supercritical with R134a. Pressure is in logarithmic scale.

generally preferred due to its lower volumetric flows per power produced, volumetric ratios, and enthalpy drops.

- Scroll/screw expanders are not considered as they are applicable to very small units and not comparable to the other mature technologies for power plants.

14.3 Geothermal-specific features and case studies

14.3.1 Geothermal-specific design criteria and plant features

Geothermal fluids are characterized as a solution of pure water plus dissolved minerals (i.e., Fe, Zn, Cu) and dissolved gases (i.e., H_2CO_3 , H_2S), which varies greatly field by field and well by well, as presented in [Tables 14.8 and 14.9](#).

In case of separation of the two phases, the vapor phase includes steam and gases, while the liquid phase is essentially a solution of water and dissolved minerals.

14.3.1.1 Scaling and corrosion

Due to some of the chemical components of the geothermal fluid, the exploitation of such streams may cause scaling and corrosion in geothermal plants ([Fridriksson and Thorhallsson, 2006](#)).

Scaling has three main possible natures: calcite scaling, metal sulfides scaling, and silica scaling. Calcite and metal sulfate scaling usually originate at vapor/liquid separation, thus typically inside the production well or near wellhead, more frequently than in the ORC heat exchangers. It is caused by sudden pH change due to boiling, which leads to the dissociation of the dissolved gases (i.e., H_2CO_3 and H_2S) and precipitation of calcium carbonates (CaCO_3) or metal sulfides (i.e., iron-, zinc-, copper sulfides). The boiling can happen inside the wells, at the hydrostatic level, or in correspondence with great pressure drops in the geothermal fluid (i.e., valve orifices). These kinds of scaling are thus common to all exploitation technologies of the geothermal resources, both direct and binary.

Silica solubility is instead related to the temperature of the geothermal fluid itself and decreases together with its temperature. This feature makes silica scaling a typical critical issue for binary cycles, where brine is cooled after separation. Amorphous silica and quartz (SiO_2) are formed rapidly and in large quantities when the fluid reaches the saturation point. As this phenomenon occurs while cooling the geothermal fluid, it is most likely to be formed in the heat exchanger tubes, in the injection lines, and in the injection wells ([Fig. 14.34](#)).

In order to prevent the silica scaling, acid additives and scale inhibitors are injected into the brine flow and silica in suspension is crystallized by inserting crystallizers. Diluting the alkaline brine with the geothermal steam condensate, which is rich in acid components, helps reduce silica precipitations. As for metal sulfides and calcite scaling prevention, a solution consists in keeping the geothermal fluid in liquid state at high pressure (eventually adopting pumps); in case it is not possible to maintain a liquid state, scale inhibitors are used.

Conversely, injecting acids and diluting the steam condensate may lead to metal corrosion in the various components of the system, as this is induced by fluid acidity.

Regarding the steam turbine power plant, as it has been presented in the relevant paragraph, the most sensitive part affected by these phenomena in the power unit is the turbine itself. Differently from what happens in steam turbines, for ORC binary plant the rotating equipment is not affected by this issue, as the only part of the binary

Table 14.8 Typical concentration of key chemical species from geothermal resources located in the United States (Casper and Pinchback, 1979)

Site	Fluid analyzed	Temperature (°C)	Concentration of the key species in the fluid (ppm)					
			pH	Cl ⁻	Total CO ₂	Total H ₂ S	Total NH ₃	SO ₄
Salton Sea	Unflashed	250	5.2	115,000	1,000	10–30	300	20
East Mesa	Unflashed	180–200	5.7	11,000	800	3	41	20
Heber	Unflashed	180–200	7.1	9,000	180	2	13	152
Mono – Long Valley	Unflashed	175	6.5	227	180	14	0.1	96
Baca	Flashed	171	6.8	3,770	128	6	—	59
Beowave	Flashed	132	9.3	50	209	6	3	89
Raft River	Unflashed	146	7.2	780	60	0.1	2	61

Note: As the measurements were made at different points (i.e., before and after flashing), the source fluids cannot be directly compared. Often during flashing, chloride concentration increases while CO₂ and H₂S decrease. An increase in pH will generally result.

Table 14.9 Composition of two typical brines. Resource 2 has significantly higher salinity and chlorine content

Sample	B (mg/L)	SiO ₂ (mg/L)	Na	K	Ca	Mg	CO ₃	HCO ₃	Cl	SO ₄	NO ₂	NO ₃	PO ₄	NH ₄	F	Br	Li
Resource 1	50	165	1,456	86	68	30	0	1,441	1,500	45	0.3	0.1	<0.0.1	35	6	3	7
Resource 2	2.4	250	8,750	330	60	15	0	1,064	13,250	81	<0.0.1	<0.0.1	<0.0.1	18	0	77	42

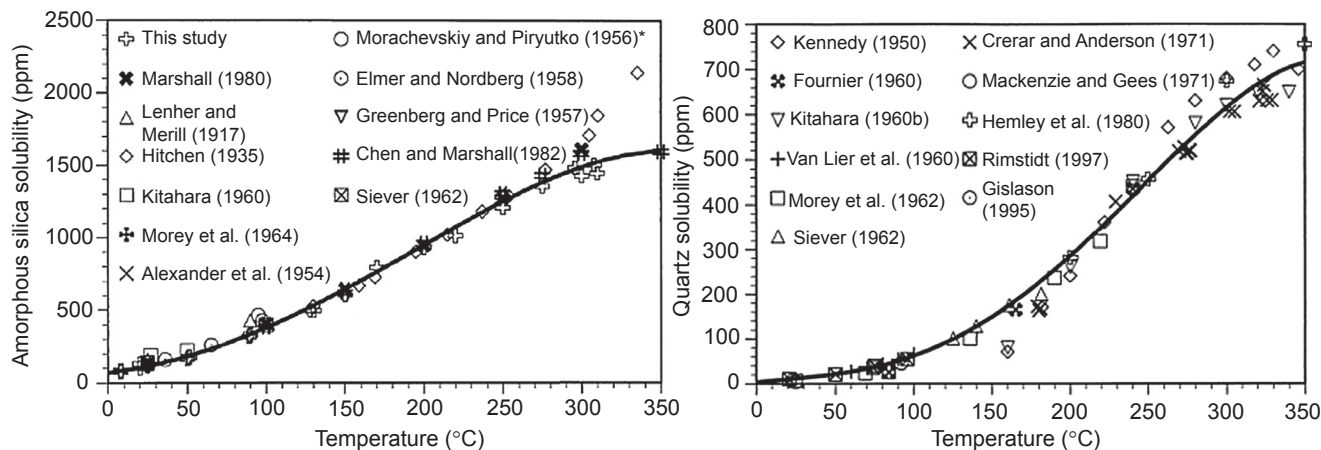


Figure 14.34 Amorphous silica (left) and quartz (right) solubility over temperature (Gunnarsson and Arnorsson, 2000).

cycle in contact with the geothermal fluid is the primary heat exchangers. Corrosion and scaling may in fact happen in the heat exchanger tubes and channels; the choice of materials is critical, and for the most aggressive fluids duplex, stainless steel and even titanium are frequently selected instead of the most common mild steel.

To mitigate corrosion effects, careful material selection should be performed at the design stage in order to ensure safe plant operability. The alkaline brine typically requires the use of mild carbon steel with a consistent corrosion allowance, while the condensing steam more likely flows in duplex or titanium tubes in order to avoid acid pitting.

Scaling affects the heat transfer process as well—it can be considered as a thermal resistance in the heat exchange between the geothermal fluid and the metal tube, decreasing the heat exchanger efficiency along the utilization time and requiring regular and intensive maintenance. When the fouling resistance becomes too relevant, the plant is shut down and the heat exchanger channel covers are opened for the visual inspection of the tubes, and eventually the mechanical or chemical cleaning of them is realized. For this reason, shell and tube heat exchangers with geothermal fluid flowing in straight tubes is the most common heat exchanger arrangement for a geothermal ORC plant. Materials and characteristics of the heat exchangers are consequently chosen according to the specific geothermal resource. The choice of the optimal velocity of the geothermal liquid flow in the tubes is determined by the trade-off between scaling, erosion, and corrosion, while the selection of materials is based on the aggressiveness of the brine or steam that is obtained in the geothermal field. Increasing the liquid velocity reduces scaling but increases corrosion and erosion. On the other hand, it increases the heat transfer convective coefficient allowing for more compact and economical components, but it also increases the pressure drop along the ORC unit and the parasitic loads, as these are directly related to the square power of the velocity.

14.3.1.2 Corrosive environment

The geothermal environment is critical for the design of electrical components due to the presence of sulfidic components: corrosion of copper electrical equipment in a geothermal environment from hydrogen sulfide contamination is a problem that must be managed starting from the design phase. Large copper current carrying items like bus bars, clamps and conductors, flexible connections, and screwed copper control wiring connections are vulnerable; furthermore, PVC insulation of the cables is not generally enough to avoid corrosion on the contained copper conductors.

Also, cadmium-plated items like nuts and bolts are affected by corrosion and produce toxic residues.

These problems can be avoided with a number of measures:

- replace copper in cables and other conductors with aluminum or other suitable materials (e.g., stainless steel)
- use tinned and epoxy painted copper for wires and other components
- use special paint
- avoid risky materials

Electrical equipment, such as printed circuit boards with plug-in copper connections associated with control, instrumentation, and protection equipment is particularly vulnerable to corrosion and failure. The correct specifications for H₂S environment on these components are mandatory for outdoor equipment, while indoor equipment must be installed in a confined and purified area (with filters, humidity and temperature controls).

14.3.1.3 *Cooling system*

ORCs for geothermal application are generally featured with dry condensing system, namely air coolers. This is substantially possible thanks to the relatively high pressure at the condenser, in the range of 0.8–1.2 bar for pentane family, 3–4 bar for butane family and R245fa, and 8–10 bar for R134a. Such condensing system has a relevant energy consumption, but there is no water consumption due to evaporation losses and blowdown as required in case a wet cooling tower is used. As such, ORC systems have the possibility for full reinjection of the geothermal fluid, with a positive effect on reservoir management throughout the years. Furthermore, direct air-cooled condenser well fits to the application in remote sites and extremely cold weather, where water management becomes a major issue. In fact, there are two main advantages of air cooling: automatic operation and performance advantage in cold weather.

Compared to biomass cogeneration and industrial heat recovery ORC applications, the geothermal binary plant is not generally located near cities or industrial areas but near the resource, which may be hundreds of kilometers from the nearest village. The possibility to operate the plant automatically in remote areas is, thus, critical for the development of geothermal power production, and the binary system is the main response to this need. Secondly, in cold climates (yearly average temperature lower than 10°C) the possibility to reduce the condensing temperature at a much lower level than what is technically possible in a water-cooled Rankine cycle, thanks to the higher saturation pressure of organic fluids (e.g., 565 mbar for pentane at 20°C condensing temperature, compared to 23 mbar for water).

14.3.1.4 *Market- and project-related features*

Similarly to what happens for all the industrial tailor-made plants, ORC plants' specific cost decreases significantly while increasing the power output and the lowest size of this technology for a greenfield project is in the range of 1 MW. The maximum size of a single module is approximately 25 MW for most of the commercial technologies.

The modular approach can help the development of the geothermal projects, as it fits the exploitation of the reservoir throughout the drilling phase, with great benefits in terms of risk profile and bankability of projects in new areas. Obviously the absence of a technology for 50+ MW single machines does not allow the economy of scale typical of big projects with steam turbines, thus the binary cycle is not competitive against the steam cycle or the combined cycle for large single modules for medium-high enthalpy resources.

With regard to the configuration of the turbine, geothermal steam and ORC turbines are significantly different: the first has a between-bearings design with horizontally split case, while the latter is overhung.

In ORC binary units the overhung configuration is the current limit while developing higher power output, even though it has the evident advantage to reduce the turbine complexity. The lower limitation is again related to the consequent high specific cost. Furthermore, the limitations in size of the components, especially heat exchangers, connected with transportation, installation, and other collateral issues, lead to a similar size limit.

For geothermal steam turbines the power output limitation is related to the available size on the market of the turbines and to the size of the project. The required number of production wells, according to the field potential, and the flexibility to accommodate resource variation along the resource exploitation time, are more difficult to manage when the plant size grows. The minimum power size is related to the high specific cost related to the turbine complexity.

As such, while exploiting geothermal fields with a great potential, geothermal steam turbine plants have historically been developed to be as large as possible, while ORC binary units have been developed with a modular approach and a progressive installation of additional power, over the time. The modular approach facilitates the field development from a business perspective and the understanding of the geothermal reservoir behavior, as it allows the geothermal developers to install additional power tailoring the plant design in accordance with the latest changes in the geothermal resource. Conversely, it leads to a negative impact on the plant specific cost.

With the aim of untapping the geothermal potential of low-temperature resources, with a different approach than what has already been presented, small-scale (<1 MW) modular ORC binary units have been engineered, produced, and presented to the market. Nonetheless, these systems have not met the market expectations yet because the specific cost is not as low as required to make them preferable, when compared to traditional modular but tailor-made solutions.

Compared to other ORC applications, due to the low temperature of the heat source and the relevant power size of the plants, the geothermal plants should take into consideration more boundary conditions.

As an example, the content of working fluid is not negligible and is usually spread over a wide area, especially when the plant is air cooled. Thus, the working fluid selection is not justified only by thermodynamics but is affected by a number of further restrictions and preferences, such as:

- local acceptance
- local regulations
- fluid flammability and associated risk
- cost of the fluid
- cost of the plant associated with the fluid choice
- availability on the market

The analysis of these additional items may lead to discard some of the suitable fluids in critical situations.

14.3.2 Examples of existing geothermal ORC power plants

14.3.2.1 Single-pressure level

Celikler Jeotermal - Pamukören (courtesy of Exergy)

When completed, the series of 22.5 MW ORC modules installed in Pamukören (Turkey) by Celikler Jeotermal will sum up to 112.5 MW (95 MW net), making this geothermal site one of the biggest in Turkey (Fig. 14.35).

The resource is a flow of water and steam separated at approximately 7.5 bar, with a bottom-hole temperature of 178°C. Each module is fed with both steam and brine in parallel on the evaporators, which feed two radial inflow expanders mounted on a common gearbox. The 1-level n-butane cycle, designed and supplied by Exergy in consortium with Atlas Copco and SPIG, grants 14.1% efficiency with a reasonably simple configuration.

Power	112.5 MW
Bottom-hole temperature	178°C
Cooling type	Air
Efficiency	14.1%

14.3.2.2 Double-pressure level with one turbine

Akca Enerji — Tosunlar (courtesy of Exergy)

The world's first binary plant featured with a double-pressure-level cycle and a single turbine with multiple admission is operating in the Tosunlar plant, owned by Akca Enerji (Fig. 14.36) near Denizli, Turkey.



Figure 14.35 Celikler Pamukören I single-pressure-level plant.
Courtesy of Exergy.



Figure 14.36 Akka Tosunlar double-pressure-level single-turbine plant.
Courtesy of Exergy.

Sited in the ancient thermal valley at about 20 km from the famous Pamukkale thermal pools, this is an example of application of a binary unit on existing geothermal wells. For 20 years the three wells have supplied steam and carbon dioxide to the greenhouses where the company produces tomatoes and other vegetables.

The resource is a low-enthalpy stream, with a corresponding bottom-hole temperature of 105°C and a separation temperature in the range of 100°C and 3.5 bar. The two-level system grants a total power of 3.5 MW (3 MW net power) developed by the radial outflow turbine in a nonrecuperative water-cooled cycle. Efficiency of the system is in the range of 10%.

The plant, supplied by Exergy, was commissioned in the first quarter of 2015.

Power	3.5 MW
Bottom-hole temperature	105°C
Cooling type	Water
Efficiency	10%

14.3.2.3 Triple-pressure level

McGuinness Hills (courtesy of Ormat)

Mc Guinness Hills was one of the first triple-pressure-level binary systems applied on a geothermal resource it was started in 2012 (Fig. 14.37).

The 44 MW gross, 38.5 MW net plant is composed of three ORC modules, two producing 17 MW and one producing 10.34 MW.



Figure 14.37 McGuinness Hills triple-pressure-level plant.
Courtesy of Ormat.

The resource is a medium-enthalpy stream, with a corresponding bottom-hole temperature of 160°C. Wells are operated through well pumps, which represent the main auxiliary load of the plant (6.1 MW, to be subtracted from the previous net power value). The fluid is discharged from the ORC for reinjection at 70°C.

Power	44.34 MW
Bottom-hole temperature	160°C
Cooling type	Water
Efficiency	10%

14.3.2.4 *Bottoming cycle*

Miravalles V (courtesy of Ormat)

A typical example of bottoming cycle is the Miravalles V plant, in Costa Rica, where the binary units are fed by part of the unused brine coming from the same well feeding a flash plant (Fig. 14.38).

The 18 MW gross, 15.75 MW net plant is independently located from the three steam plants (total of the three is 131.5 MW, summing over 150 MW with the ORC).

The resource is medium enthalpy brine, at 165°C, cooled down to 136°C by the ORC.



Figure 14.38 Miravalles V bottoming plant.
Courtesy of Ormat.

Power	18 MW
Brine temperature to ORC	165°C
Cooling type	Water

14.3.2.5 Combined cycle

Rotokawa (courtesy of Ormat)

In 1997 in Rotokawa, New Zealand, an operation began that combined a cycle using steam and binary technologies in a unique combination (Fig. 14.39). The 26 MW gross, 24 MW net plant is composed of one 14 MW steam turbine and three ORC units. The resource is a very high-enthalpy stream, with a corresponding bottom-hole temperature of approximately 330°C and a separation temperature in the range of 218.3°C at 22 bar.

Two binary units are fed by exhaust steam at the steam turbine outlet (counterpressure configuration), for a total of approximately 7.2 MW, while a third 4.4 MW binary unit exploits the liquid flow of brine, cooling it down to 150°C.

Power (steam turbine)	14.53 MW
Power (binary cycles)	11.6 MW
Steam conditions to ST	22.6 bar, 218.3°C, 134 t/h
Steam conditions to ORC	1.23 bar, 105.3°C, 132 t/h
Brine conditions to ORC	217.5°C, 304 t/h
Cooling type	Air

Kizildere II (courtesy of Zorlu)

The first geothermal power plant in the Menderes Valley, in Turkey, was built between Buharkent (Aydin) and Saraykoy (Denizli), in the area of Kizildere. At first, in 1974 a 500 kW pilot plant, and then, in 1984 a single-flash 17 MW steam turbine were supplied by the Italian manufacturer Ansaldo (Figs. 14.40 and 14.41).



Figure 14.39 Rotokawa combined cycle.
Courtesy of Ormat.

After the acquisition of the existing plant and concession by Zorlu Enerji Elektrik Üretim A.Ş., the field is under development with the installation of an approximately 80 MW combined cycle in 2013 (Kizildere II) and another unit foreseen in 2016.

Kizildere II, designed by the US-based Power Engineers, features a 60 MW triple-flash steam turbine supplied by the Japanese manufacturer Fuji and a 19 MW ORC bottoming plant supplied by TAS Energy.

The resource is a very high-enthalpy stream, with a corresponding bottom-hole temperature of 242°C and a separation temperature of 174.5°C at 8.45 bar.

The binary unit is fed by exhaust steam at HP steam turbine outlet (counterpressure configuration).

Bottom-hole temperature	242°C
Power (steam turbine)	60 MW
Power (binary cycles)	19 MW
Total auxiliaries	11 MW
Net output	68 MW
Steam conditions to HP turbine	8.45 bar, 174.5°C, 371,536 t/h (294,701 t/h steam and 76,835 t/h NCG)
Steam conditions to IP turbine	3.48 bar, 147.6°C, 128,371 t/h
Steam conditions to LP turbine	1.1 bar, 112.2°C, 213,269 t/h
Steam conditions to ORC	1.15 bar, 100.5°C, 371,536 t/h (294,701 t/h water biphasic flow and 76,835 t/h NCG)
Cooling type	Water (cooling towers)

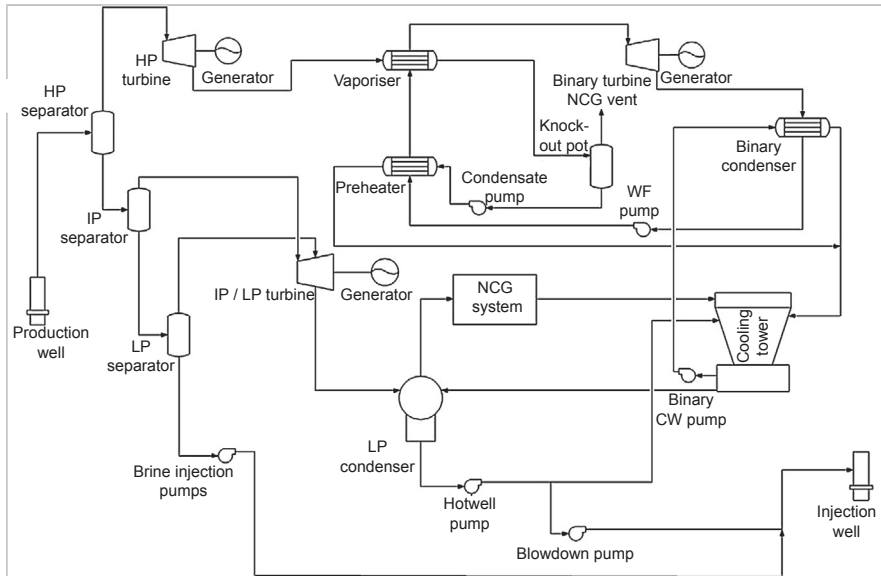


Figure 14.40 Kizildere II combined cycle simplified process flow diagram.

Lewis, W., 2014. Kizildere II: Geothermal Energy in Turkey. <http://www.ee.co.za/article/kizildere-ii-geothermal-energy-turkey.html>. Courtesy of Power Engineers.



Figure 14.41 Kizildere II combined cycle plant.

Courtesy of Zorlu.

References

- Adiprana, R., Izzuddin, Yuniarto, E., 2010. Gunung Salak geothermal power plant experience of scaling/deposit: analysis, root cause and prevention. In: Proceedings World Geothermal Congress.
- Alexander, G.B., Heston, W.M., Iler, R.K., 1954. The solubility of amorphous silica in water. *J. Phys. Chem* 58, 453–455.
- Ásgeirsson, S.D., 2009. Húsavík Power Plant Corrosion and Erosion Experience, 2008. from. P. Whittaker – Corrosion in the Kalina cycle.
- Axelsson, G., Gunnlaugsson, E., 2000. Background: geothermal utilization, management and monitoring. In: Long-term Monitoring of High- and Low Enthalpy Fields under Exploitation. WGC.
- Benderitter, Y., Cormy, G., 1990. Possible Approach to Geothermal Research and Relative Costs.
- Bertani, R., 2015. Proceedings World Geothermal Congress.
- Casper, L.A., Pinchback, T.R., 1979. Geothermal Scaling and Corrosion. ASTM.
- Chen, C.-A.T., Marshall, W., 1982. Amorphous silica solubilities IV. Behavior in pure water and aqueous sodium chloride, sodium sulfate, magnesium chloride, and magnesium sulfate up to 350°C. *Geochim. Cosmochim. Acta* 46, 279–287.
- Crerar, D.A., Anderson, G.M., 1971. Solubility and solvation reactions of quartz in dilute hydrothermal solutions. *Chem. Geol.* 8, 107–122.
- DiPippo, R., 2005. Geothermal Power Plants: Principles, Applications and Case Studies. Elsevier.
- Dickson, M.H., Fanelli, M., 2004. Cos'è L'energia Geotermica.
- Elmer, T.H., Nordberg, M.E., 1958. Solubility of silica in nitric acid solutions. *J. Amer. Ceram. Soc* 41, 517–520.
- Fournier, R.O., 1960. Solubility of quartz in water in the temperature interval from 25°C to 300°C. *Geol. Soc. Amer. Bull.* 71, 1867–1868.
- Fridriksson, T., Thorhallsson, S., 2006. Geothermal Utilization: Scaling and Corrosion. ISOR.
- Gislason, S.R., 1995. Kinetic and Thermodynamic Properties of Moganite Retrieved from Quartz and Quartz/Moganite Mixtures. RH-15–95. Science Institute, University of Iceland.
- Greenberg, S.A., Price, E.W., 1957. The solubility of silica in solutions of electrolytes. *J. Phys. Chem.* 61, 1539–1541.
- Gunnarsson, I., Arnorsson, S., 2000. Amorphous Silica Solubility and the Thermodynamic Properties of H_4SiO_4 in the Range of 0 to 350°C at Psat. Elsevier.
- Hemley, J.J., Montoya, J.W., Marinenko, J.W., Luce, R.W., 1980. Equilibria in the system $\text{Al}_2\text{O}_3\text{--SiO}_2\text{--H}_2\text{O}$ and some general implications for alteration/mineralization processes. *Econ. Geol.* 75, 210–228.
- Hitchon, S., 1935. A method for the experimental investigation of hydrothermal solutions, with notes on its application to the solubility of silica. *Trans. Inst. Min. Metall.* 44, 255–280.
- Hochstein, M.P., 1990. Classification and Assessment of Geothermal Resources.
- Islandsbanki, 2011. US Geothermal Energy Market Report.
- Kalina, A., 1984. Combined Cycle System with Novel Bottoming Cycle. ASME. Paper 84-GT-173.
- Kennedy, G.C., 1950. A portion of the system silica–water. *Econ. Geol.* 45, 629–653.
- Kitahara, S., 1960b. The solubility of quartz in the aqueous sodium chloride solutions at high temperatures and high pressures. *Rev. Phys. Chem. Japan* 30, 115–121.
- Lenher, V., Merrill, H.B., 1917. The solubility of silica. *J. Amer. Chem. Soc.* 39, 2630–2640.

- Lewis, W., 2014. Kizildere II: Geothermal Energy in Turkey. <http://www.ee.co.za/article/kizildere-ii-geothermal-energy-turkey.html>.
- Mackenzie, F.T., Gees, R., 1971. Quartz: Synthesis at earth surface conditions. *Science* 173, 533–535.
- Marshall, W., 1980. Amorphous silica solubilities—I. Behavior in aqueous sodium nitrate solutions; 25°–300°C, 0–6 molal. *Geochim. Cosmochim. Acta* 44, 907–991.
- Morachevskiy, Y.V., Piryutko, M.M., 1956. O rastvorimosti kremnevoy kisloty (On the solubility of silicic acid). *Izvestiya Akad. Nauk SSSR, Ser. khim* 8, 834.
- Morey, G.W., Fournier, R.O., Rowe, J.J., 1962. The solubility of quartz in water in the temperature interval from 25 to 300°C. *Geochim. Cosmochim. Acta* 26, 1029–1043.
- Morey, G.W., Fournier, R.O., Rowe, J.J., 1964. The solubility of amorphous silica at 25°C. *J. Geophys. Res.* 69, 1995–2002.
- Mlcak, H.A., 1996. An Introduction to the Kalina cycle, ASME International. In: Kielasa, L., Weed, G.E. (Eds.), *Proceedings of the International Joint Power Generation Conference*, vol. 30. PWR. Book No. H01077.
- Mlcak, H.A., 2001. Design and start-up of the 2 MW Kalina Cycle Orkuveita Húsavíkur geothermal power plant in Iceland. In: *European Geothermal Energy Council – 2nd Business Seminar EGEC*.
- Muffler, P., Cataldi, R., 1978. Methods for regional assessment of geothermal resources. *Geothermics* 7, 53–89.
- Nicholson, K., 1993. *Geothermal Fluids*, vol. XVIII. Springer Verlag, Berlin, p. 264.
- REFPROP 9.0. NIST Reference Fluid Thermodynamic and Transport Properties Database, Version 9.0.
- Rimstidt, J.D., 1997. Quartz solubility at low temperatures. *Geochim. Cosmochim. Acta* 61, 2553–2558.
- Sabatelli, F., October 9, 2013. Flash geothermal power plants, main features and issues. In: *EGEC Pisa*.
- Siever, R., 1962. Silica solubility 0–200°C, and the diagenesis of siliceous sediments. *J. Geol.* 70, 127–150.
- Smith, J.M., van Ness, H.C., 1975. *Introduction to chemical engineering thermodynamics*. McGraw-Hill Kogakusha, Ltd. Tokyo.
- Stefansson, V., 2005. World geothermal assessment. In: *Proceedings World Geothermal Congress*.
- UGI – Unione Geotermica Italiana, 2007. *Geothermal Energy: Yesterday, Today, Tomorrow*. Edizioni ETS.
- USGS, 1997. Ring of Fire Map. http://vulcan.wr.usgs.gov/imgs/Gif/PlateTectonics/Maps/map_plate_tectonics_world_bw.gif.
- Van Lier, J.A., de Bruyn, P.L., Overbeek, J.T.G., 1960. The solubility of quartz. *J. Phys. Chem.* 64, 1675–1682.

Biomass-fired Organic Rankine Cycle combined heat and power systems

15

A. Guercio¹, R. Bini²

¹ITI Engineering srl, Cremona, Italy; ²Turboden srl, Brescia, Italy

15.1 Introduction

Until the end of the 1990s, the biomass power market was almost exclusively served by conventional Rankine steam cycles, mainly with an application size of 2 MW electric power or more.

Conventional Rankine cycles have shown good performances and reliability but have also demonstrated strong limitations for power sizes below 2 MW because of: the reduced performance of the plant, the increased specific investment cost and the increased specific operation and maintenance costs. For this reason, in many cases the residual biomass was used in heat-only biomass boiler or even wasted.

The intuition of Turboden to apply Organic Rankine Cycle (ORC) technology to small size biomass plants opened up a new market of biomass combined heat and power (CHP) applications all over Europe, and the importance of this intuition is evidenced by the hundreds of plants now in operation.

In the last 15 years, an impressive development of biomass-fired ORC CHP systems has taken place in Europe. At present about 300 plants are in operation or under construction, mainly in Europe but also in North America and Asia. The main applications are in: district heating, pellet production, sawmills, and wood-based industries. The state of the art of the technology provides a binary cycle with the ORC associated with a biomass thermal oil boiler. The majority of the plants in operation are sized between 500kW and 2 MW electric power, corresponding to 2 MW and 8 MW thermal power respectively. The use of appropriate working fluids (the majority are silicon oils) allows the exploitation of the high temperatures available from the combustion of biomass. The results are high electric efficiency despite the relatively high temperature (80–120°C) of the hot water released at the condenser. New developments are in progress, with direct exchange solutions for small size plants, and hydrocarbons as the working fluid for larger size plants.

The biomass-fired ORC CHP systems have proven, since entering into the market, interesting features, including: high electric efficiency (18% net of ORC from thermal oil and about 15% net from biomass); very high overall efficiency (98% from thermal oil and 80% from biomass); high availability (over 98% on average for

ORCs and over 98% on average for the boiler, which can lead up to 8400 h per year of production); and a very low request for operation and maintenance (no need for the continuous presence of an operator and the operator doesn't require any particular skills). The good results from the first plants in operation in Austria, during the period 2000–2002, contributed to spread a good impression of the ORC in biomass-fired CHP, and the involvement of some specialized engineering companies (e.g., BIOS in Austria, and Gammel Engineering in Germany) supported the diffusion throughout Europe.

Small size plants imply high specific investment costs. The incentive schemes available in Austria, Germany, Italy, and then in the other European countries (see European directive 2001/77/CE) strongly contributed to the development of the market.

The biomass-fired ORC plants market has grown thanks to the reliability of the technology but also thanks to the policy mechanism of incentives available in many European countries.

The strong incentive schemes are now in a phase of progressive reduction. The next challenge of the ORC in biomass-fired CHP applications is to maintain their position in the market by reducing the specific cost of electricity production according to the reduction of the incentives. In the medium to long term, the goal is to get to grid parity, however, the grid parity in biomass applications has to be considered in a different way with respect to the other renewable energies, because the positive impact the biomass supply chain can have on the local economy.

Although biomass-fired ORCs had originally proven high reliability and good performances, in the last 15 years, there has been no apparent improvement in the ORC performances or in the overall prices of the plants.

Two main aspects have to be taken into account for the lack of cost reductions: the continuous improvement to the safety of the overall plants (due to the addition of safety and emergency devices) and to the control of emissions; and the fact that no series production has taken place, because the market is not large enough, with fragmentation due to different sizes required, often too close one to the other one.

From a performance point of view, some improvements are still possible, though some intrinsic limitations are present, i.e., fluid thermal stability, which does not allow an increase in the maximum operating temperature of the cycle.

Expected future developments could include:

1. Reduced electric size below 500 kW down to 100 kW (or even lower) to approach a new distributed market.
2. Increased size (up to 10 MW electric power) to approach what, until now, has been the "territory" of conventional steam Rankine cycles.
3. Focus on rural electrification, opening up new geographical areas in developing regions, which have a high availability of low cost biomass and insufficient electrical infrastructure to support the economic growth.

15.2 State of the art of biomass-fired Organic Rankine Cycle combined heat and power plant

15.2.1 The design concept of a combined heat and power biomass-fired plant

Biomass-fired ORC (Figs. 15.1 and 15.2) are operated as binary cycles because the working fluid and the heat carrier are different and they operate in separated circuits. In the biomass boiler, the combustion gas transfers the heat to a medium, acting as heat carrier, which is normally a synthetic thermal oil. The hot thermal oil circulates in a closed circuit and feeds the ORC, where it is cooled down and sent back to the boiler. A system of pumps maintains a continuous circulation of the thermal oil, to avoid over temperature in the boiler. The ORC operates as a “black box” for the rest of the plant, thanks to its limited interfaces; the thermal oil transfers the heat from the boiler to the ORC. The electricity produced can be delivered to the electrical grid or used locally. The heat can be used for district heating and cooling, low temperature drying processes, or to satisfy any kind of thermal request at temperatures up to 120°C. No steam production has been implemented up to now as co-generated heat in the installed ORC, though it would be possible.

The operation of the biomass-fired ORC offers many advantages in comparison with a conventional direct Rankine cycle:

1. No change of phase or high pressure levels in the boiler. The thermal oil remains liquid at atmospheric pressure raising the temperature up to 320°C and above (the normal operating pressure of thermal oil is in the range of 5–7 bar g).
2. No patented operator is needed because there is no change of phase of the thermal medium in the boiler. On the contrary, the presence of a patented operator is required by law in a number of countries if there is a change of phase in the boiler, even if it less than in the past.

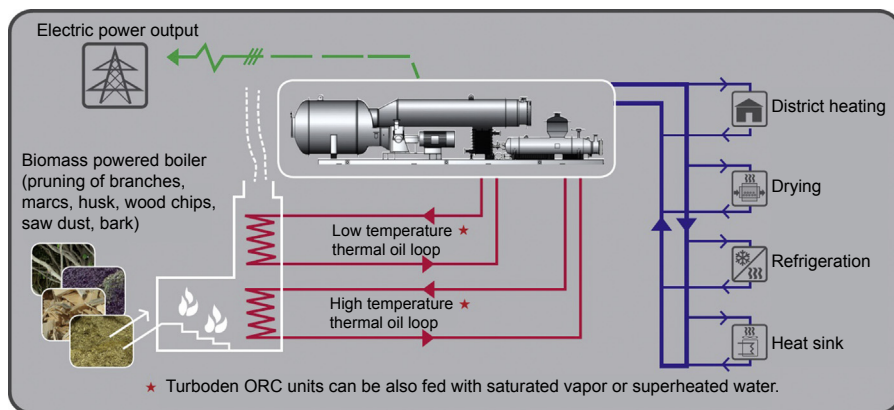


Figure 15.1 Overall biomass-fired Organic Rankine Cycle (ORC) scheme. Reproduced with permission from Turboden website. Turboden.

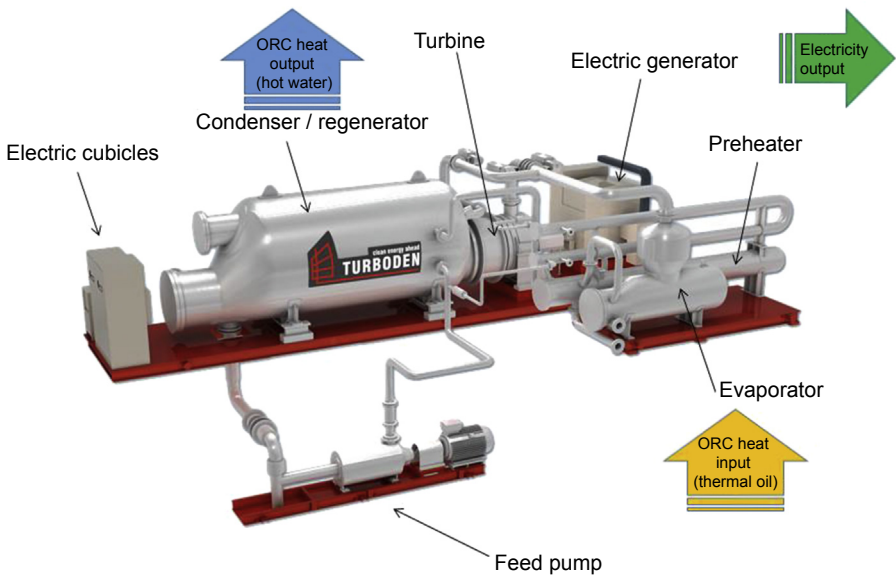


Figure 15.2 Model of a 4 MW thermal and 1 MW electric Organic Rankine Cycle (ORC). Reproduced with permission from Turboden website. Turboden.

3. Clear separation of the thermal and thermodynamic processes. This characteristic permits free choice of the biomass boiler and the ORC.

Though there are other possible configurations for the plant, using different boiler solutions and heat mediums such as, steam, hot water or, direct exchange with the hot gas, the use of a thermal oil intermediate circuit represents, at present, the state of the art and indeed the main system used.

15.2.2 The control system of the plant

There are two possible overall control methods:

1. ORC controlled by thermal demand. The thermal demand control (or pure CHP mode) is the most efficient way to exploit the biomass source. The plant is controlled by the thermal demand (whether it is district heating or a wood drying process) and the electricity production is a consequence of it. In this way the biomass fuel is modulated and not wasted, so the overall efficiency of the plant is maximized. This kind of control can be achieved simply by modulating the 3-way valve admitting the thermal oil to the ORC, to keep a certain set point of the water outlet temperature at the condenser; as soon as this temperature increases, the valve would close and vice versa. Furthermore, if the 3-way valve reduces the flow to the ORC (as in the case described previously) the return temperature to the boiler would increase and also the outlet temperature of the thermal oil. Hence the furnace control would reduce the flow of primary air and biofuel to keep the outlet temperature of the thermal oil at the required set point. In summary, two temperature controls are necessary and sufficient to

control the overall system: the water outlet temperature at the condenser and the thermal oil temperature in the boiler. These two controls act on parts that are external to the ORC, which then acts like a “heat exchanger,” transferring the heat from the thermal oil to the water and producing, of course, electricity. Inside the ORC, a working fluid pump control is implemented to adapt to different operating conditions.

2. ORC controlled by electricity demand. CHP plants are usually controlled by thermal demand and the electricity production is a sort of (profitable) subproduct. In “power-only” plants, the condensing heat is not used by a thermal consumer but is dissipated. Power-only plants are usually operated at full power to get the maximum profit from electricity production, according to the availability of biomass. Sometimes, CHP plants are also operated to get maximum electricity production and the heat is a subproduct. If this heat is not used or partly used, the condensation heat (or part of it) is dissipated.

15.2.3 The electrical grid connection

One of the advantages of a biomass-fired ORC turbine is that it can be optimized for a rotational speed of 3000 rpm, which is the rotational speed of the asynchronous electric generators in 50 Hz grids. Considering that two pole (hence 3000 rpm) Synchronous generators are not available on the market (or are excessively expensive), most of the ORCs installed for biomass application, in the range 0.5–3 MW electric power are equipped with Asynchronous electric generators. This kind of generator is very simple and efficient but requires the adoption of a power factor control system and, above all, it is not suitable to satisfy the recent requirements of Grid Codes unless expensive devices are installed. In fact, recent European Grid Codes require, to the “small” distributed production plants, to be able to support grid instabilities without disconnecting the generator. In particular, the generators must be able to support Voltage Control, Low Voltage Ride Through, and Dynamic Voltage support. To achieve this capability, either a synchronous generator (with the disadvantage of requiring a reduction gear to reduce the speed to 1500 rpm) or an asynchronous generator with an (expensive) Statcom device can be used.

15.2.4 The plant components of a conventional biomass-fired Organic Rankine Cycle with a thermal oil boiler

15.2.4.1 Lay out and operational scheme

Many manufacturers and engineering companies are present in the biomass boiler market. Some different technical solutions are possible. The following solution is based on a conventional but effective scheme. Other solutions are possible, anyway basing on the same principles (Figs. 15.3 and 15.4)

15.2.4.2 Fuel storage and handling

The capacity of the fuel storage can vary significantly depending on the context of where the plant is located. In the case of district heating plants, with no productive industrial site beside it, it is normal not to keep an operator on-site during the night

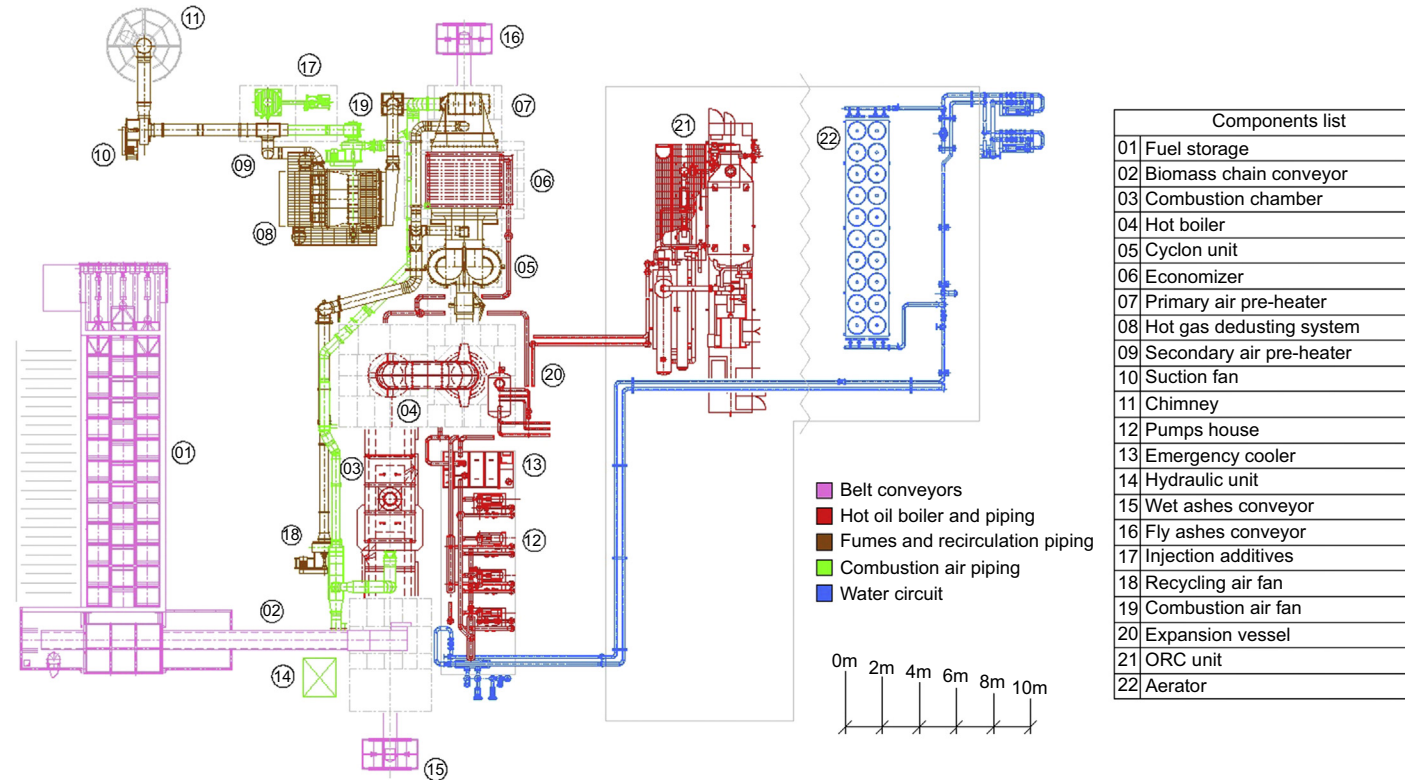


Figure 15.4 Operative scheme of a 4 MW thermal and 1 MW electric biomass-fired Organic Rankine Cycle (ORC). Adapted with permission from documentation elaborated by ITI engineering.
ITI Engineering.

and at the weekends, hence 48 h unattended autonomy is required. In some cases of highly unattended district heating plants, completely automatic systems with an autonomy of weeks have been implemented. In the case of plants associated with an industrial process, with operators present during the weekend, 6–12 h of autonomy can be sufficient. Large storage capacity means higher investment costs and higher electricity consumption for the biomass handling, so a balanced compromise has to be found.

Roughly 8 cubic meters of biomass per hour of operation are required by a 4 MW thermal and 1 MW gross electric power biomass-fired ORC.

The typical system is composed of a moving floor (Fig. 15.5) with a hydraulic-driven discharge ladder. A belt conveyor (Fig. 15.6) moves the fuel up to the mechanical pusher (Fig. 15.7) where it is introduced into the combustion chamber.

15.2.4.3 Biomass combustion section

Combustion chamber

The combustion chamber (Fig. 15.8) is designed as an adiabatic furnace and is dimensioned in order to optimize the combustion of the specified fuel types. It is typically composed of an outer shell made of carbon steel with necessary reinforcements and anchors for the application of the inside refractory shell, which is specially designed for working under furnace nominal temperatures. The furnace is normally divided into two sections: the primary combustion chamber (grate combustion chamber) and the secondary combustion chamber (postcombustion chamber).

In the primary combustion chamber, the grate for biofuel combustion is situated in the bottom of the chamber. The chamber is normally designed as a parallelepiped box and it is lined inside with refractory material. The ashes discharge and primary air distribution systems are installed in the bottom of the chamber. On the front wall there is a connection flange to insert the automatic feeding device of the grate. The opposite wall is equipped with control windows which allow visual control and the connection



Figure 15.5 Moving floor. Reproduced with permission from ITI engineering archives. ITI Engineering.



Figure 15.6 Loading belt. Reproduced with permission from ITI engineering archives. ITI Engineering.

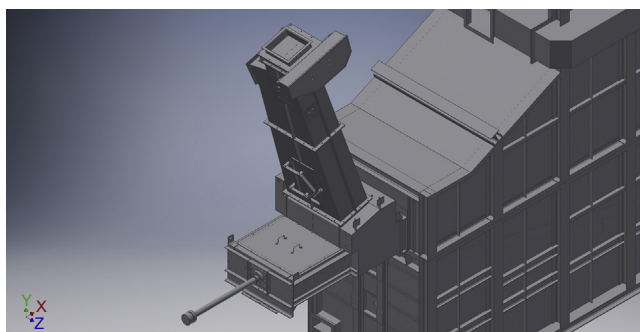


Figure 15.7 Loading hopper. Reproduced with permission from ITI engineering archives. ITI Engineering.

of a video camera for monitoring the plant from the control desk. The hopper for hot ashes is situated at the end of the chamber, where all the combustion slags are discharged; it is connected to the conveyor which brings the ashes outside.

The chamber's ceiling is sloped in order to help postcombustion gases to flow toward the outlet section; it also has a rugged steel structure to support the refractory lining. The outlet section is designed in order to optimize the mixing of gases with secondary air and recycling gas, which are injected in this section.

The secondary combustion chamber, also called postcombustion chamber, aims to guarantee the foreseen temperatures and residence time in order to reach complete combustion of all the gaseous combustion products. Gas speed is low to avoid dragging of ashes. A blending ring is positioned in the area of connection with the primary chamber in order to mix the secondary air and recycled gas. The flanges connection with the thermal oil boiler are located at the exit of the postcombustion chamber.



Figure 15.8 Combustion chamber. Reproduced with permission from ITI engineering archives. ITI Engineering.

Reciprocating grate

The grate (Figs. 15.9 and 15.10) is where the biofuel lies during the first phase of the combustion. The dimensions of the grate depend on the size of the plant and the water content in the biofuel.

Concerning the combustion process, the grate can be considered as divided into three sections: the first one at the inlet of biofuel is used as a “drying section”, where the material loses its humidity and starts to gasify; the second one is where the material burns, reaching the maximum temperature, and is defined as the “combustion section,” sometimes this section can be divided in two subsections; the third one is where the material completes its combustion and moves to the end of the grate, falling down from the discharging point into the ash recovering hopper. This final part is also called the “section for final combustion and ash discharging.” In fact the over mentioned functions are practically realized along the longitudinal axis dividing the grate in three sections.

Each section is an independent module. A trolley moves the bars of each section and creates the stroke velocity.

A primary air collector separated for each grate section guarantees the possibility to adjust the combustion air for each part of the grate. The grate structure and in particular the top deck, where the grate bars are laid and hung, is composed of strong carbon steel profiles, designed to support the weight of the bars and the burning material at the normal plant’s running conditions.

The four trolleys which support and move the bars of each section of the grate slide on high alloy steel roller supports.

The grate casing underneath the top deck is divided, by means of baffles, in four areas so that the combustion primary air can be dosed with four different rates to the burning material, giving the possibility to control and optimize the combustion.



Figure 15.9 Reciprocating grate. Reproduced with permission from ITI engineering archives. ITI Engineering.

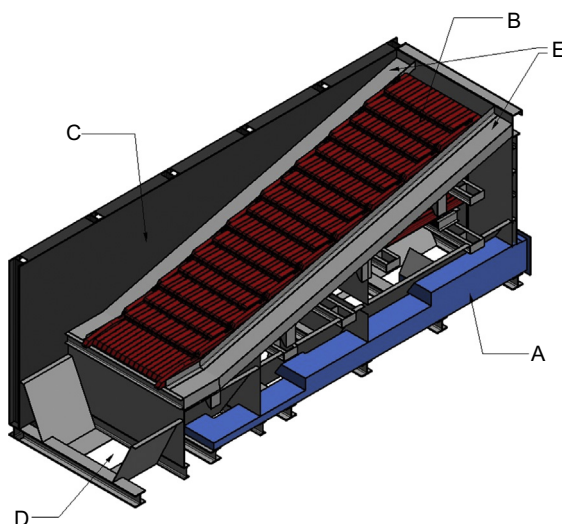


Figure 15.10 Scheme of reciprocating grate. Reproduced with permission from ITI engineering archives. ITI Engineering.

Primary and secondary combustion air

The combustion air system consists of all the necessary components for the injection of the air into the furnace, as calculated for the best combustion results. The air mass flow is divided into two parts: the primary air to be fed under the grate; and the secondary air for the postcombustion stage.

The primary air is the combustion air injected under the grate. The system is composed of an air distribution collector connected to a primary fan. Through proportional dosing valves and distribution ducting it distributes air in the lower part of the grate. There are four sections in each grate module, each one provided with an air inlet duct with a motorized proportional flap. The primary air fan motor is suitable to be driven by an inverter, in order to be able to optimize working conditions, system regulation, and power consumption. A primary air collector is integrated under the grate and consists of different distribution ducts, each one equipped with its own motorized flap for flow regulation for each section. The primary air is heated up to about 170°C by means of a heat exchanger with the exhaust gas.

The secondary air is the postcombustion air injected into the upper part of the combustion chamber and is necessary for completing the combustion process. Together with the recirculated gas it takes part in temperature and oxygen concentration controls. The secondary air fan motor is also suitable for Inverter driving, in order to be able to optimize working conditions, system regulation, and driving power consumption. The secondary air collector consists of a distribution duct which connects the fan to different intake points in the postcombustion chamber.

Gas recirculation

Part of the combustion gas produced by the furnace is recirculated after the thermal oil boiler for more efficient control of combustion products. The recirculated gas is used as a dilution gas in the postcombustion chamber for temperature and Nitrogen Oxides (NOx) control. Also some efficiency increase is achieved by using recirculated gas.

The gas recirculation system (Fig 15.11) is composed of a re-circulation gas collector and re-circulation ducting.

The recirculated gas collector consists of a distribution duct, which connects the fan to different points of air flow in the combustion chamber.

Ash removal and handling

The combustion of the biofuel on the grate produces ash and slag in two ways: ash parting and removing among the grate bars; and discharge of the slag in the last hopper at the end of the grate.

The collection and transport system to remove the ashes is composed of under grate hoppers and an ashes conveyor.

In different sections of the grate area the grate has hoppers having the double function of distributing the primary air and collecting the fine ashes falling during the grate movement. The final hopper is placed at the end of the grate for slag discharge. This hopper is lined by refractory bricks.

The slag falls directly into the main ashes conveyor designed for the transport of the entire ashes volume.

The under grate hoppers are directly connected to the grate supporting steel structure and take part in the under grate combustion air distribution system, as previously described. A chain conveyor collecting and transporting the ashes is connected to the under grate hoppers.



Figure 15.11 Re-circulation and combustion air pipes and fans. Reproduced with permission from ITI engineering archives.
ITI Engineering.

The main chain conveyor transfers the whole inert material into a recovering container.

15.2.4.4 Thermal oil boiler

The thermal oil boiler (Figs. 15.12 and 15.13) transfers the heat content in the combustion gas to the thermal oil. The temperature of the combustion gas at the inlet of the thermal oil boiler is normally about 950°C . The outlet temperature of the thermal oil directed to the ORC can rise up to 320°C , due to the use of high quality synthetic oil.

The thermal oil boiler is normally divided in two parts, the radiant and convective sections.

In the radiant section, the hot gas, due to the very high temperature, transfers the heat mainly by radiation to the heat exchanger pipes containing the thermal oil. Decreasing the combustion gas temperature the radiant efficacy becomes negligible (it is reduced by an exponent four of the absolute temperature), hence, the heat is transferred by convection in the convective section of the heat exchanger.

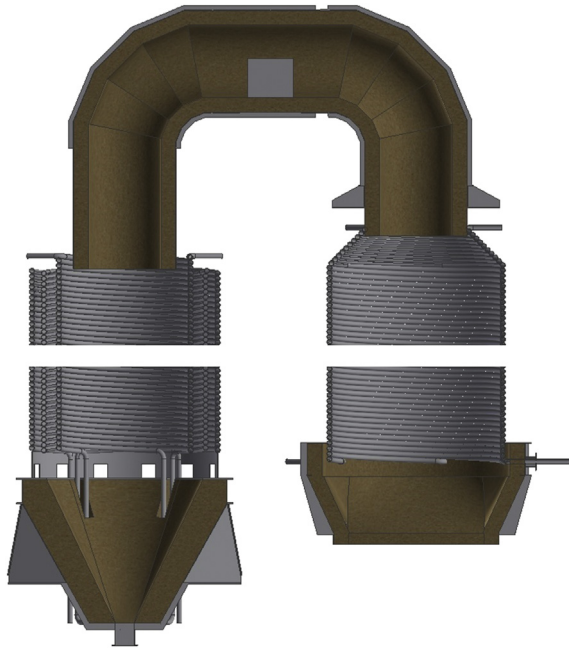


Figure 15.12 Scheme of radiant (right) and convective (left) sections of a thermal oil boiler. Adapted with permission from documentation elaborated by ITI engineering. ITI Engineering.

The last stage of the thermal oil boiler is the economizer, where the temperature of the combustion gas is reduced and the convective heat transfer requires large exchange surfaces.

The thermal oil boilers can have different shapes and geometries. A traditional and still very effective solution consists of a coil as radiant section with the hot gas passing in the center, while the convective section is composed of two or three concentric coils with the hot gas passing in the center and between them. Different and more compact solutions are possible for this section of the plant. The main advantages of the above described thermal oil boiler (using coils) are the high reliability with a wide range of low quality biomass and no need of active cleaning systems.

15.2.4.5 Air preheater

The combustion gas leaving the thermal oil boiler and economizer still contains exploitable heat. This residual heat can be transferred to the combustion air through an air preheater (Figs. 15.14 and 15.15) where the combustion gas is cooled down to heat the fresh primary and secondary air directed to the combustion chamber.

15.2.4.6 Thermal oil circuit and emergency cooling system

The thermal oil circuit (Fig. 15.16) has the scope to circulate the thermal oil and connect the biomass boiler to the ORC.



Figure 15.13 Installed thermal oil boiler. Reproduced with permission from ITI engineering archives.
ITI Engineering.

In order to maintain a continuous circulation of the thermal oil, the circulation pumps are made redundant.

The emergency cooling circuit is designed to guarantee the necessary heat dissipation in case of alarms regarding the thermal oil system. It consists of a cooling exchanger, working in bypass to the operational circuit, designed to evacuate the heat from the thermal oil through the generation of low pressure steam into the atmosphere.

15.2.4.7 Exhaust gas treatments and emissions control

The main emission values measured in biomass plants are: NO_x, Carbon Monoxide (CO), Sulfur Oxides (SO_x), Total Organic Carbon (TOC), and Particulate Matter (PM).

The formation of NO_x depends on the oxidation of the Nitrogen present in the fuel and in the combustion air. The first component is the most important, in the case of biomass, due to the high Nitrogen content of the organic matter. The most important parameter to control the NO_x is the temperature, controlled through the re-circulation of the gas. In addition, if necessary, a De-NO_x active system can be used to reduce NO_x emissions.

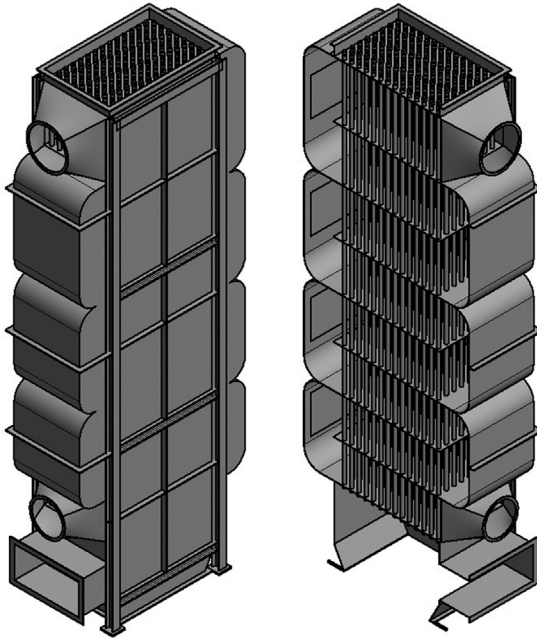


Figure 15.14 Schematic section of an air preheater. Adapted with permission from documentation elaborated by ITI engineering.
ITI Engineering.



Figure 15.15 Installed air preheater. Reproduced with permission from ITI engineering archives.
ITI Engineering.



Figure 15.16 Installed thermal oil pumps. Reproduced with permission from ITI engineering archives. ITI Engineering.

CO is generated in the first stage of the combustion and is produced by partial oxidation of the Carbon contained in the biomass. Correct design of the combustion and postcombustion chamber with an adequate residence time permits the control of the CO emissions.

The formation of SO_x depends on the sulfur content of the biofuel. Usually the biomass has a reduced content of sulfur. An active system can be installed to reduce the SO_x emissions in case there is a sulfur content in the biofuel (e.g., in some kinds of agricultural waste).

The TOC is the result of incomplete oxidation of organic macromolecules. The level of TOC formed in the combustion phase can be particularly high in the case of treated wood. The control of TOC emissions is achieved with combustion homogeneity and adequate residence time.

In case of proper combustion, the PM is formed by the residual ash from nonorganic material. An active filter is usually installed in the last section of the gas line, before the chimney (Fig. 15.17). The typical filters used in biomass combustion plants are Cyclones, Bag Filters (Fig. 15.17), and Electrostatic Precipitators.

15.2.4.8 ORC and boundary interfaces

The ORC turbogenerator (Fig. 15.18) operates according to a closed loop ORC system, producing electric power by using heat coming from an external source. The cycle also needs a cooling section, which is normally achieved using water as medium.

In some respects, an ORC turbogenerator can be considered as a “heat exchanger” between the thermal oil and the water; the heat flows through the cycle (evaporator and turbine) to the cooling water. Another output is represented by the electric power produced by the electric generator driven by the ORC turbine.

The ORC cycle automatically adapts to input heat changes in the range of some 10% power in 3–5 min.



Figure 15.17 View of the chimney and bag filter. Reproduced with permission from ITI engineering archives.
ITI Engineering.

When the ORC stops for any reason, the ORC feed pump is switched off, suddenly blocking the transfer of heat from the thermal oil to the water circuit.

Therefore, a thermal oil temperature control independent from the ORC turbogenerator should be activated in order to avoid thermal oil temperature spikes. To reach this goal, biomass boilers are usually equipped with a bypass line diverting the thermal oil flow from the ORC directly to a water cooled heat exchanger. The use of a diverter on the flue gas can intercept the main heat exchanger, thus stopping the heat flowing in the process. Nevertheless, transients and possible diverter leakages should be considered and damping methods, where relevant, should be applied.

The cooling water loop should be operated close to the nominal temperatures; a control system independent from the ORC turbogenerator normally controls the water loop.

The ORC turbogenerator always has at least one main heat exchanger to transfer heat from the thermal oil to the Rankine cycle internal working fluid.

A thermal oil valve is requested in the thermal oil circuit in order to control the flow to the ORC turbogenerator main heat exchangers. A three way valve is considered standard. The control of this valve is shared between the ORC turbogenerator Programmable Logic Control and the biomass boiler control Programmable Logic Control.

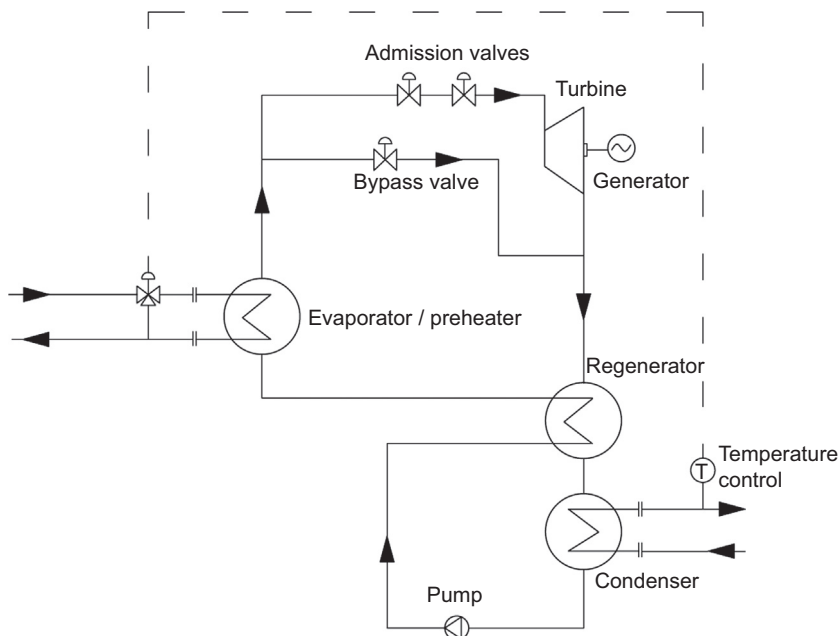


Figure 15.18 P&I Organic Rankine Cycle. Reproduced with permission from Turboden website. Turboden.

Optionally, the ORC turbogenerator can also have a second, low temperature, heat exchanger as a part of the so-called “Split system.” For this circuit a thermal oil valve is utilized in order to control the flow in the ORC.

In the ORC process, the organic working fluid flows into a closed circuit undergoing thermodynamic transformations as follows:

Preheating, evaporation and superheating if any, receiving heat from the thermal oil.

Expansion in the turbine, coupled with the electric generator.

Vapor phase cooling preheating the liquid phase, inside a regenerator. This internal heat recovery increases the overall electric efficiency of the thermodynamic cycle.

Condensation, transferring heat to the cooling water circuit.

Pumping in the working fluid feed pump.

15.2.4.9 Captive consumptions

Table 15.1 reports the consumption of electricity by the auxiliaries typically present in a biomass-fired ORC CHP 4 MW thermal and 1 MW gross electric power plant.

Hence about 17% of the gross production is used by the plant auxiliaries. If we consider the bare electricity production, this figure deteriorates the overall net performance of the plant. However, it has to be considered that in a CHP plant one important aim is to produce heat, hence the auxiliary consumption to produce this heat would be present in any case. In other words the auxiliary consumption to be ascribed to the electricity production is about 10% of the gross electricity production (i.e., thermal oil pumps and ORC auxiliary consumption).

Table 15.1 Captive electricity consumption of a biomass-fired ORC

Auxiliary consumption	Installed power (kW)	Average consumption (kW)
Biomass handling	60	15
Thermal oil pumps	150	35
Combustion air fan	75	35
Exhaust gas fan	55	35
Organic Rankine Cycle	90	50
Total	430	170

15.2.4.10 Comparison with alternative technologies

Alternative technologies

To have a better idea of the potential of the biomass-fired ORC systems, an overview of the alternative CHP technologies, using solid biomass in the range up to 10 MW electric power, is reported.

Conventional Rankine cycles

The conventional Rankine cycles using water as working fluid are the typical reference to compare with the ORC. The conventional Rankine cycle competes with the ORC in the power range between 2 MW and 8 MW electric power. The bigger the size, the better it is for the conventional Rankine steam cycle.

Below 2 MW electric power, the ORC are preferred due to a simpler operation leading to reduced operation and maintenance costs. The electric efficiencies are comparable for sizes around 2 MW electric power with rising advantages for the ORC as the size reduces, and better efficiency for conventional Rankine cycles as the size increases.

Over 8 MW electric power the conventional Rankine cycle is very competitive because of the high electric efficiency which can compensate for high operation and maintenance costs. In the range between 2 and 8 MW electric power there is indeed a real competition, with the ORC in growing competitiveness.

Biomass gasification and internal combustion engines

Biomass gasification associated with internal combustion engines are competitive in small size biomass plants (up to about 50 kW per single system), with hundreds of references in Europe (see Spanner systems). This kind of plant needs high quality wood chips. If high quality wood pellet is available as a biofuel then a very reliable system sized 180 kW electric power and 270 kW heat is present on the market with many references to its operation (see Burkhardt systems).

A good or very good quality of biomass is mandatory to ensure proper operation of these systems. On the contrary, a biomass furnace combined with an ORC is much more tolerant of the different kind and quality of biomass that can be burnt.

Stirling cycles

Though some industrial prototypes have been on the market for decades, this technology is not yet fully commercially available. A few 35 kW electric power references, associated with gasification systems, have been installed in Europe. The combustion of syngas instead of direct combustion of solid biomass reduces the fouling of the system and improves the reliability.

External fired gas turbines

This technology is one of the promising ones. A few plants have been installed and others are under construction, mainly in Italy (see Genera Biobox). The system uses an external source of heat, the gas from the biomass combustion, to operate a Brayton cycle with a gas turbine. A critical point of this system is the very high temperature heat exchanger between the hot combustion gas and the pressurized air to the turbine. Another critical aspect is that the gas turbines are typically not designed to operate with external combustion systems, so they have to be derived and modified from standard internal combustion gas turbines.

15.2.4.11 Recent evolutions and future developments of biomass-fired Organic Rankine Cycles

Large size Organic Rankine Cycles in biomass-fired plants

In the range between 300 kW and 3 MW electric power, the ORC developed for biomass applications, using silicon oil as a working fluid, performs well. However, above 3 MW electric power, some critical problems arise with the design when using the “traditional” working fluid, i.e., a silicon oil. The volumetric flow rate at the turbine outlet significantly increases (unless the condensation temperature is also increased accordingly). A large volumetric flow rate requires the dimensions of the last stage of the turbine blades to become excessively large in order to maintain a good turbine efficiency, yielding a number of design and cost problems which cause this solution to be abandoned.

By using different working fluids, such as hydrocarbons, it is possible to develop larger size ORCs maintaining similar performances and the same advantages of the smaller ones which utilize silicon oils.

On the other hand, increasing the size of conventional Rankine cycles over 2–3 MW electric power improves the performance whilst maintaining very similar fixed costs with respect to the smaller sizes.

With a constant thermal request of 20 MW as hot water at the 80°C outlet, a conventional Rankine cycle can produce 5 MW net electric power while an ORC (using current state of the art technology) can produce 4 MW. Therefore, when increasing the size of the plant, conventional Rankine cycles are more favorable.

However, the ORC may be more desirable for two other reasons: the operation of a high efficiency conventional Rankine cycle requires managing by a dedicated team of skilled workers, skills which the investor may lack; and furthermore, conventional Rankine cycles present the risk of water freezing which is not the case in an ORC plant.

At present (2015), four biomass-fired ORC sized 7 MW gross electric power are in operation with good results in North America and four others, sized between 5 and 8 MW gross electric power, are under construction in North America and Asia.

The direct exchange biomass-fired Organic Rankine Cycle power plants

The use of an intermediate medium to transfer the thermal energy from the combustion gas to the ORC offers advantages but also disadvantages as potential additional investment costs and captive electricity consumption, lowering the net efficiency.

In the last few years new ORCs with direct exchange with the hot gas have been developed. This approach was initially used in heat recovery applications (mainly in combined cycles with internal combustion engines), and is now being utilized in some biomass combustion applications.

A few biomass-fired ORC without intermediate medium carriers are in operation or under construction. The system, produced by the company Triogen, is sized 130–165 kW gross electric power and 700 kW thermal. Turboden is also developing a direct exchange biomass-fired ORC with a 600 kW electric and 2.4 MW thermal plant expected to be started up in 2017.

With respect to the equivalent binary solution, the direct exchange would target a reduction of the overall investment cost and a reduction of the captive electricity consumption.

Gas turbine and Organic Rankine Cycle through gasification and through external fired biomass combustion

The Brayton cycle, largely used in electricity production by natural gas, operates a gas turbine which expands compressed hot air heated by the internal combustion of a gaseous or liquid fuel. In the combined cycle, a steam boiler recovers the residual heat downstream of the gas turbines to produce superheated steam which operates a conventional Rankine cycle with a steam turbine. The same principle can be applied to a biomass power system in two different configurations: an Integrated Gasification Combined Cycle (IGCC) with recovery of the heat in the exhaust gas through an ORC; or an External Fired Gas Turbine (EFGT) (Fig. 15.19) with recovery of the heat in the exhaust gas through ORC.

In the first case (IGCC), the use of solid biomass can be possible through a gasification process to convert the solid biofuel into syngas. The syngas can power the gas turbine leaving the exhaust gas at a high temperature ($>500^{\circ}\text{C}$). The ORC can recover the heat in the exhaust gas to produce additional electricity, up to 25% with respect to the gas turbine power output, and residual useful heat at the requested temperature. The electric efficiency of this kind of combined plant can reach up to 40%. The overall efficiency (thermal and electric) is in the about of 70%.

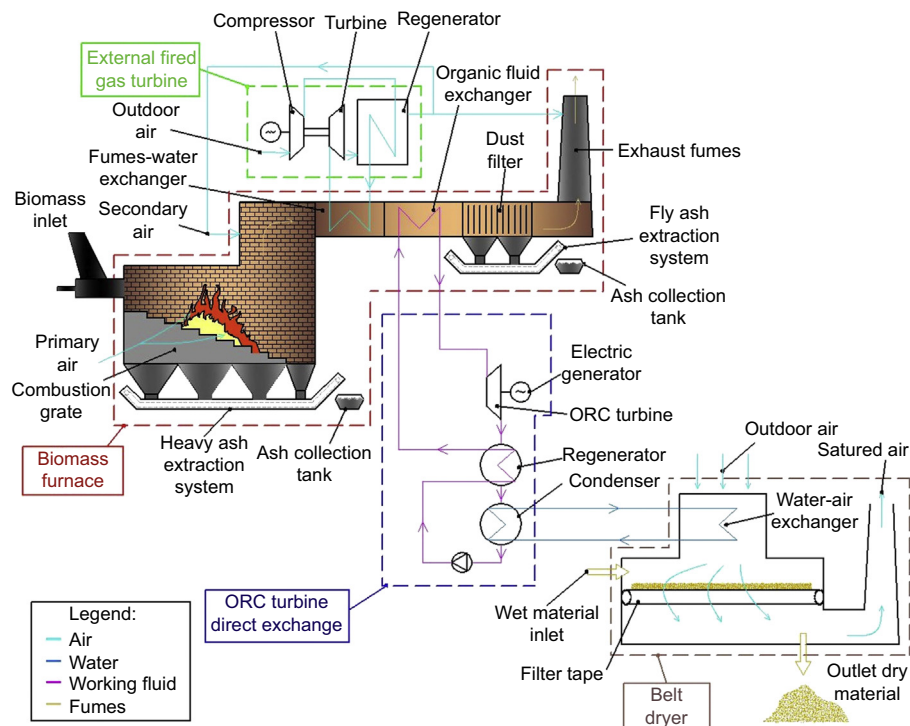


Figure 15.19 External Fired Gas Turbine with Organic Rankine Cycle (adapted with permission from the book “Il Pellet”, by Alessandro Guercio and Giuseppe Toscano, Dario Flaccovio Editore).

In the second case (EFGT), the solid biomass is burned in a biomass furnace and the hot gas is cooled by a heat exchanger heating compressed fresh air. The heated compressed air expands in a gas turbine producing electricity. The exhaust gas remains very hot after the heat exchanger ($>600^{\circ}\text{C}$), so an ORC can be applied to exploit the residual heat cooling down the gas as much as possible as well as recovering the exhaust air discharged by the turbine. In this case, the ORC can produce up to 40% with respect to the gas turbine power output and the overall electric efficiency can reach up to 30%. The overall efficiency (thermal and electric) can be close to a simply biomass-fired ORC, in the range of 80%.

15.3 Applications and references

15.3.1 Extra potentiality of the biomass-fired Organic Rankine Cycle

A CHP plant is normally designed to be operated for the wood industry, the pellet production industry, or for district heating. Often the managers of the plant are not familiar with electricity production and do not wish to assign a team of qualified operators to the management of the CHP plant. In some cases it could be seen as an interference

to the main process and to the core business of the primary process. In these cases, due to the low need for operation and maintenance and no need for qualified operators, the biomass-fired ORC is seen as a less worrying choice with respect to conventional Rankine steam cycles, in spite of lower expected economic results. For the same reasons, in larger sized power plants (up to 10 MW electric power) located in remote areas where it is not easy to find a team of skilled operators, ORC technology has a chance to gain a position in the market. As previously discussed, the freezing issue can also be a reason to discard a conventional Rankine plant in very cold countries. Also if the plant is located in an industrial area where there is easy access to skilled and qualified operators, the ORC can be still chosen because of the reduced operation and maintenance costs and consumable costs.

15.3.2 Fields of application

The main current applications of biomass-fired ORC (Figs. 15.20–15.23) are: district heating; the drying processes in the timber and wood industry; and pellet production.

The main conditions to justify biomass CHP plants are: the availability of biomass; the possibility to use or dispatch the produced electricity; and an adequate demand for thermal energy.

15.3.2.1 District heating (and cooling)

The majority of references for biomass-fired ORC CHP are in the district heating application (Table 15.2). Biomass-fired heat-only plants have been common in district heating for decades. The ORC technology has permitted the implementation of CHP systems, thanks to the possibility of adapting the plant to the new technology, without

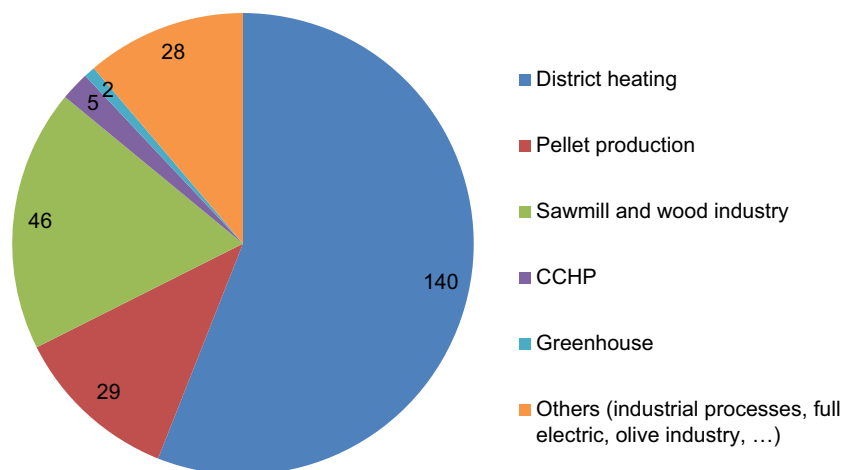


Figure 15.20 Biomass-fired Organic Rankine Cycle references per application (overall survey elaborated by the authors on the following producer: Turboden, Adoratek, GMK, Exergy, Triogen).

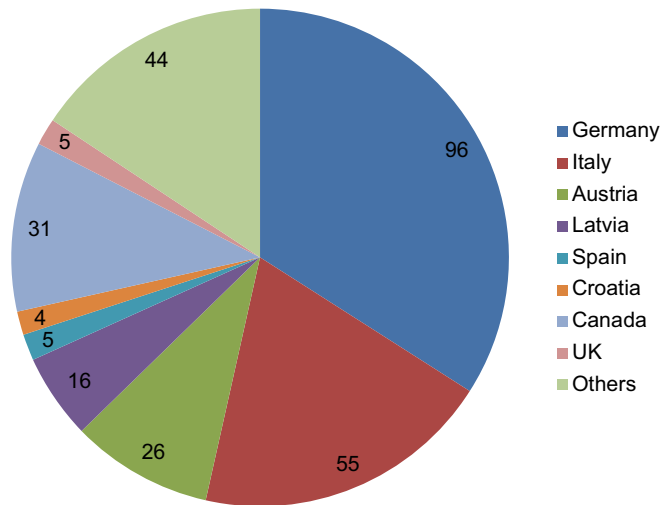


Figure 15.21 Biomass-fired Organic Rankine Cycle references per installed electric power (overall survey elaborated by the authors on the following producer: Turboden, Adoratek, GMK, Exergy, Triogen).

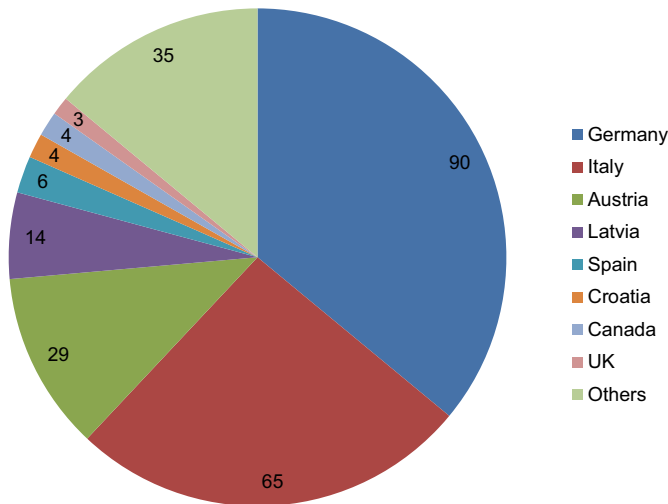


Figure 15.22 Biomass-fired Organic Rankine Cycle references per number of installations per country (overall survey elaborated by the authors on the following producer: Turboden, Adoratek, GMK, Exergy, Triogen).

the need for additional space and operators. Considering there are thousands of biomass district heating plants producing only heat, there is a big opportunity for the biomass-fired ORC to convert them in CHP plants.

An expected future development of district heating plants is to operate the grid at lower a temperature (e.g., 50–60°C instead of 80–90°C). Lowering the temperature

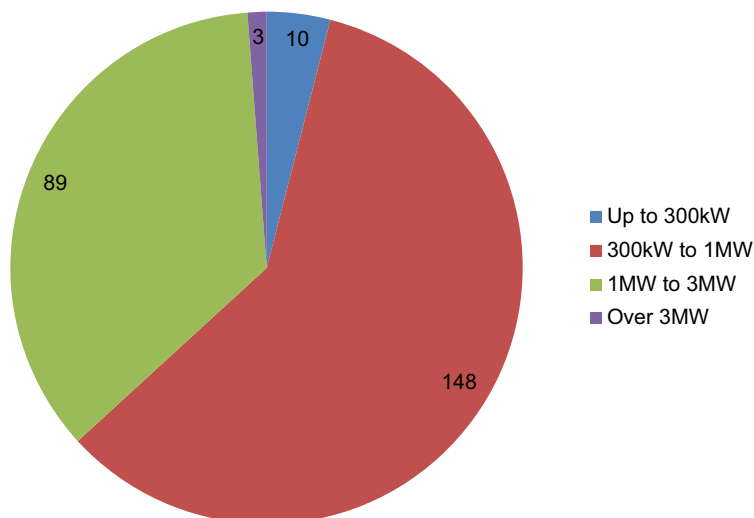


Figure 15.23 Biomass-fired Organic Rankine Cycle references per size (overall survey elaborated by the authors on the following producer: Turboden, Adoratek, GMK, Exergy, Triogen).

of the district heating gives the chance to raise the electric efficiency of the thermodynamic cycle. It would be possible to produce more cogenerative electricity with the same thermal user, reducing the specific electrical investment cost and consumption hence the specific cost of electricity production.

15.3.2.2 Pellet production

The pellet industry is relatively young. According to the AEBIOM statistical report 2015, based on a European Pellet Council (EPC) survey, in 2014 the global pellet consumption was close to 27 Mt/y (million ton per year), but just in 2005 the global pellet consumption was less than 5 Mt/y. Europe is the main consumer of pellet, with a consumption of 18.8 Mt in 2014, North America follows as the second biggest consumer with a consumption of 2.8 Mt in 2014. Europe is also the main producer with 13.5 Mt produced in 2014 while North America is the second biggest producer with a production of 8 Mt in 2014. About 5 Mt of pellet were exported from North America to Europe in 2014.

Table 15.3 show the biomass-fired ORC references in the pellet production.

The pellet production process requires thermal energy for the drying of the biomass and electricity for the process.

There are two main technologies for the drying process in the pellet production: direct drum dryer and indirect belt dryer. The competition between the two drying technologies is also the competition between the heat-only plant (at the moment no CHP technology is available in association with a direct drum dryer) and the CHP. The reason for this is that the direct drum dryer requires high temperatures (over 300°C), which is not compatible with the CHP solution. On the contrary, the indirect

Table 15.2 Biomass-fired Organic Rankine Cycle in district heating per country (overall survey on the following manufacturer: Turboden, Adoratek, GMK, Exergy, Triogen)

District heating		
Country	Number of plants	Installed electric power (MW)
Germany	40	40.1
Italy	37	32.7
Latvia	11	11
Austria	10	9.4
Switzerland	6	4
Poland	5	4.9
Belarus	4	8.9
Czech Republic	3	3.1
Estonia	2	3.2
Russia	2	3.2
Finland	2	2
Sweden	1	2.2
Bulgaria	1	1.2
Netherlands	1	1.1
Denmark	1	0.7
Greece	1	0.3

belt dryer requires low temperatures, in the range of about 90°C, which is fully compatible with the main biomass-fired CHP technologies.

The energy demand for 1 ton of pellet produced can be roughly estimated in about 4 MWh thermal and 1MWh electrical, very close to the power-to-heat ratio of the biomass-fired ORC CHP. This similar power-to-heat ratio leads to a full compatibility of the biomass-fired ORC CHP with the pellet production process. The plants in operation and under construction present a promising future.

15.3.2.3 District heating and pellet production, a smart potential integration in the European market

District heating, following the thermal request of the heat demands, needs an installed thermal capacity which will be fully used just a few hours per year, during the peak

Table 15.3 Biomass-fired ORC in pellet production per country (overall survey on the following manufacturer: Turboden, Adoratek, GMK, Exergy, Triogen)

Pellet production plant		
Country	Number of plants	Installed electric power (MW)
Germany	14	18
Spain	5	4.6
Italy	4	2.9
Poland	3	3.9
Austria	2	2.6
Croatia	2	2
Russia	1	4.5
Canada	1	3
United Kingdom	1	2.2
Czech Republic	1	1
Slovakia	1	1

hours of the coldest day. The rest of the time the thermal demand will be partial. Due to this reason, district heating normally operates 2000 to 2500 “equivalent at peak load” hours per year, with no need to implement a CHP system designed for the full capacity. The “equivalent at peak load” hours is the ratio between the annual thermal energy demanded and the installed thermal capacity. In order to improve the coefficient of utilization of the plant, raising the operative hours at full load, a thermal demand during the summer should be found. Using the excess thermal energy produced by the plant for a pellet production process can be the solution. In this way, it would be possible to operate the plant at full load for 8000 (or even more) hours per year, with a good opportunity to implement a biomass-fired CHP system.

The importance of this kind of operation is even more interesting because the produced pellet during the summer could be used to feed additional thermal users in the following winter, managed by the district heating company but not physically connected through pipes, avoiding the high costs of expanding the grid pipes to those users. The district heating company could install and operate small pellet boilers directly to the end users sites, supplying heat in the same way as if the users were connected by pipes.

15.3.2.4 Timber and wood panel industry

The wood-based industry, as a whole, represent a big potential for biomass-fired ORC CHP (Table 15.4).

Table 15.4 Biomass-fired Organic Rankine Cycle aggregate in the sawmill and wood-based industries per country (overall survey on the following manufacturer: Turboden, Adoratek, GMK, Exergy, Triogen)

Sawmills and wood-based industry		
Country	Number of plants	Installed electric power (MW)
Germany	19	23.8
Austria	7	8.9
Croatia	3	4.1
Latvia	2	3.6
Poland	2	2.5
Romania	1	1.3
Italy	1	1
Switzerland	1	1
Turkey	1	1

In sawmills there is a great availability of bark and wood residues, typically in the form of wood chips and sawdust, and there is also a high demand for electricity. The heat demand comes from the drying chambers of the timber, which can be fed by hot water at 80–90°C. The high number of references of biomass-fired ORCs in these application show the compatibility of this technology in this context.

In the wood panel industry, with production of particleboard and fiberboard, there is availability of wood wastes as virgin and treated wood. Both the electric and thermal requests are very high. The typical drying technology used are the drum dryer for particleboard production and the pneumatic dryer for fiberboard. Both drum and pneumatic dryers need high temperature heat for the drying process, about 300–400°C for the drum dryer and 150–200°C for the pneumatic dryer, and they are usually operated with direct combustion gases mixed with fresh air to get the right temperatures.

Some new developments have taken place in the particleboard production process, with the introduction of the belt dryer technology with promising results, although the requested outlet moisture of the dried particles is below 2%. This new scenario opens up an interesting market for biomass-fired ORCs, considering the belt dryer can be fed with hot water at a temperature compatible with the CHP process.

Regarding the fiberboard production, considering the requested temperature of the pneumatic dryer is in the range of 180°C, the implementation of a biomass-fired CHP could be easier. The produced heat of the CHP can be used to preheat the mixing fresh

air, introducing heat at a lower temperature. Another more interesting solution could be a new design of pneumatic dryer to operate at lower temperatures (up to 120°C), compatible with the heat production of a biomass-fired ORC.

Other production processes of wooden composite materials for packaging and construction can be similar to those described.

15.3.2.5 Full electric applications

Dedicated and exclusive electricity-only production is the least efficient way to exploit an energy source like solid biomass; it is always better to operate CHP or heat-only. Nevertheless, there could be cases in which none of the mentioned CHP solutions are possible because no thermal users are available. In these cases, if there are no alternative uses for the biomass, dedicated electricity production can be a valid alternative to the disposal of the biomass as waste.

In these cases, the biomass could be used to balance the intermittent production of other renewable sources (i.e., wind and solar) in the grid.

15.4 Current market overview and European policy: economic and environmental considerations

15.4.1 The current situation of biomass combined heat and power plants in Europe

A recent European project coordinated by AEBIOM (European Biomass Association) has identified 3172 biomass-fired plant sized at least 1 MW thermal, using wood chips, in the EU28 countries (see basisbioenergy.eu). The main countries along with their number of installed plants and their biomass consumption are:

Austria with over 550 plants and over 3 Mt of wood chips consumed;
Germany with over 470 plants and over 14 Mt of wood chips consumed;
France with over 350 plants and over 5.5 Mt of wood chips consumed;
Finland with over 550 plants and over 5.5 Mt of wood chips consumed;
Sweden with over 300 plants and over 7 Mt of wood chips consumed;
76% of the biomass-fired plants are heat-only, 21% are CHP, and 3% are dedicated power plants.

15.4.2 Social impact of electricity from biomass combined heat and power

The reduction of the investment cost of a technology in order to get it to grid parity is one of the main targets of the incentive schemes applied all over the world to renewable energy. The specific cost of electricity production from photovoltaic or wind power has significantly dropped in the last decades, while the specific cost of electricity production from biomass has remained quite constant. The biomass CHP plants

continue to need a stronger incentive with respect to solar or wind power, with minimum results on the reduction of the specific cost of electricity production.

To better understand this situation it is necessary to point out the main differences among the technologies.

Solar panels and wind mills convert solar radiation and wind directly into a single product, electricity. Furthermore, a solar panel is much simpler than an ORC; the technology of the photovoltaic cell itself is sophisticated but it can easily benefit from a mass production cost reduction compared to an ORC, which is composed of a number of different and customized components.

Biomass plants convert the biochemical content of solar radiation in to electricity and heat.

Solar and wind farms have to sustain mainly fixed capital costs due to the associated investment. Biomass plants have instead, an important cost in the biofuel, in addition to the fixed cost of the investment. If the biomass plants had to pay the same price for biomass that the solar or wind farms pay for solar radiation or the wind, the specific cost of electricity production from biomass would be competitive with respect to the conventional energy production system. Hence, the biomass itself represents an important cost to operate a biomass plant; in some cases, it is as important as the capital cost. However, the biomass is an interesting opportunity, where the biomass plant gives value to the local woods, wooden residues, and agricultural waste. A study developed in Austria (see Regionale Wertschöpfung und Beschäftigung durch Energie aus fester Biomasse. Endbericht März, 2015. Austrian Energy Agency. Auftraggeber: Klima- und Energiefonds, available as a cartoon at the following link <https://www.youtube.com/watch?v=vuk3ZhuJa2g>), compares the local impact on the job occupancy of a biomass plant with respect to a conventional fossil fuel based system. The result shows a very impressive and positive impact for the local economy. According to the AEBIOM statistical report 2015, in the EU28 there are 494,550 jobs in the bioenergy sector, 64% of them are in the solid biomass.

Obviously, these considerations are valid for every technology exploiting biomass, not simply in the CHP of a biomass-fired technology.

15.4.3 Future markets for biomass-fired Organic Rankine Cycles

The prediction of future changes is a complicated task, best approached by magicians and sorcerers than analysts, in special way when directly regarding the business related issues. Unfortunately, none of the authors of this chapter belongs to these categories but an analysis of the trends is possible anyway.

It is evident that the main driver for the diffusion of small size biomass CHP plants in Europe, where the ORC has played a very important role, has been the incentive scheme (Fig. 15.24).

The expected reduction in investment costs for ORCs has not taken place because no series production has taken place. Although an important number of plants in the range 300kW to 2 MW have been produced, this number of plant has not gained the critical mass to start a series production. The market for ORC in the biomass sector remains, at the moment, a customized market requiring/producing often similar but not

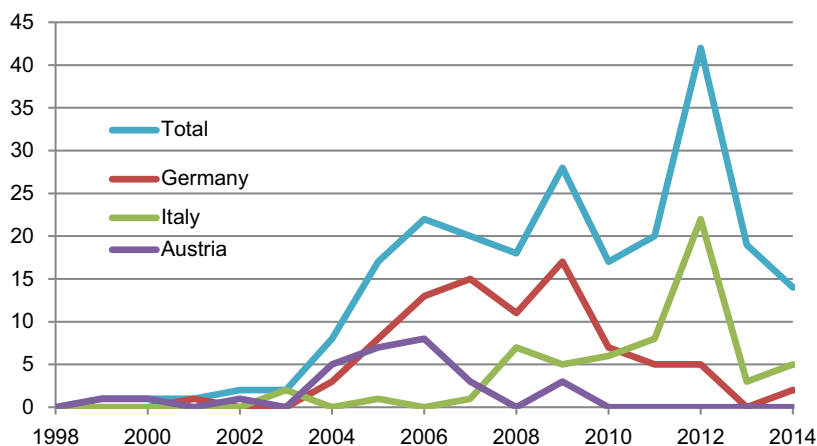


Figure 15.24 Number of installed biomass-fired Organic Rankine Cycles since 1998 (overall survey elaborated by the authors on the following producer: Turboden, Adoratek, GMK, Exergy, Triogen).

identical products. Some producers of ORCs offer a single size of plant potentially producible in series, but the number of installations are not impressive.

An important question is, if this kind of plant, after years of incentives and with no striking improvements in performance are ready to approach the market with no or reduced incentives.

Another interesting question is if the development of the technology will open up new markets, for example, larger size plants up to 10 MW electric power, until now controlled by the conventional Rankine cycles, or smaller size plants, below 200 kW electric power.

The reduced specific investment cost of the big size plants can contribute to the reduction of the specific cost of electricity production down to the market price, but it is very difficult to find adequate thermal users for big size plant. However, very small sized plants with high specific investment costs imply high production cost of electricity, but the reduction in size can permit a local consumption of heat and electricity directly to the end user.

15.5 Economic feasibility and sensitivity

15.5.1 Dimensioning a biomass-fired Organic Rankine Cycle combined heat and power plant

A biomass-fired ORC CHP system is first of all a biomass fueled plant. Most of the considerations regarding the environmental and economical sustainability, the dimensioning and sizing, and the fields of application, have a common root both with the conventional CHP systems and the baer heat production from biomass.

The dimensioning of a CHP plant starts from the characterization of the thermal demand, so the first step in the process is the same for a heat-only conventional plant. Once the thermal demand curve has been determined, it is possible to implement the CHP scheme. In this phase the different technologies can make the difference.

There are two typical shapes for the curve demand of heat:

Industrial process thermal request, with constant demand. In this case, the shape of the curve is similar to a rectangle or a succession of rectangles.

Civil application mainly for district heating and/or cooling, with very variable demand during the day and the year. In this case, the shape of the curve is similar to a rectangular triangle laid on a cathetus (Fig. 15.25).

The main features influencing the electricity production in a full cogeneration regime are: the power-to-heat ratio of the chosen technology at the demanded temperature, both at nominal and partial load; the capability of the plant itself to operate, when necessary, at partial load and varying the temperature of the discharged heat.

Once a load curve has been fixed, the equivalent hours of operation at full load is a function of the thermal size of the CHP plant. The reduction of the size will increase the equivalent hours, trending a reduction of the specific cost of electricity production. At the same time the reduction of the size will increase the specific investment cost, trending an increase of the specific cost of electricity production. So the right dimensioning of the plant has the scope to balance the thermal size to obtain the minimum specific cost of electricity production.

What can lead to a real and substantial improvement of the economic results is a modification of the load curve to increase the equivalent hours maintaining the size of the CHP. In district heating this target can be reached by finding additional thermal users during the off peak hours (for example in association with an absorption chiller

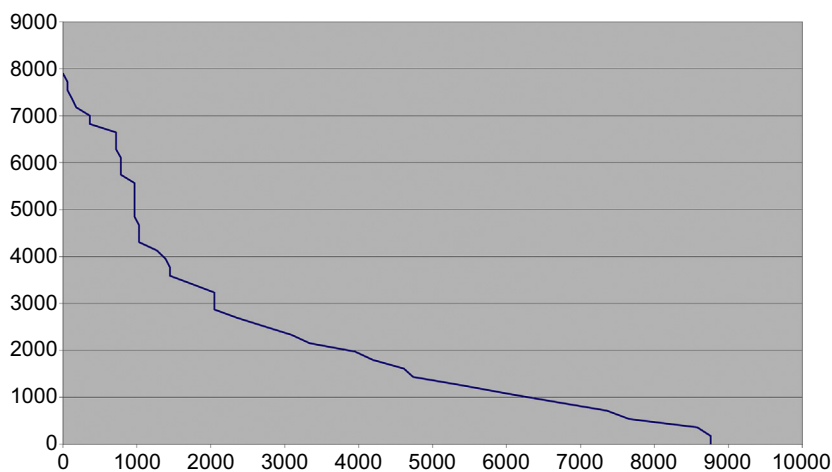


Figure 15.25 Typical sample of curve load for district heating (x-axis: Hours, y-axis: heat in kW) (elaborated by the authors).

for summer cooling or in association with an industrial thermal user which can accept heat in the off peak hours). An association with pellet production offers a very promising solution to increase the equivalent hours at peak load, using the residual heat from the district heating.

15.5.2 A differential analysis on the specific cost of electricity production

Considering that the added value offered by the ORC in a biomass-fired plant is the electricity production, the analysis of the economic sustainability to transform a biomass thermal plant into a biomass CHP plant will be conducted in a “differential” mode, where only the additional costs and revenues with respect to an equivalent heat-only plant are considered. On the contrary, if we should consider the overall operation, including the thermal part, the economic results would not be able to give evidence of the added value given by the electricity production.

15.5.3 Main economic and financial parameters considered

The CHP process converts part of the available energy from the source in to electricity, leaving the remaining heat at the disposal of the thermal users, targeting a reduced consumption of primary source with respect to the separated production of electricity and heat with “conventional systems”. In other words, the same electricity and thermal energy will be produced consuming less primary sources by a CHP plant compared to the conventional separate production of electricity and thermal energy. From an environmental point of view the sustainability of the CHP plant depends on the reduction of the use of primary sources but from an economic point of view the sustainability of the investment depends also on some other important parameters. The specific cost of electricity production has been calculated starting from the following assumptions (Tables 15.5 and 15.6):

- Capital costs

The differential investment cost compared to the equivalent heat-only plant has been considered. Table 15.5 reports the differential investment cost of a 4 MW thermal and 1 MW electrical biomass-fired ORC with respect to an equivalent 4 MW heat-only plant. The overall investment of the complete biomass-fired ORC CHP plant can be estimated to be 6,000,000 €. Generally we can consider the differential investment to be about 60% of the overall investment.

- Interest rate

The interest rate has been considered as the minimum acceptable rate of return (MARR, or hurdle rate) to motivate the investment. It has been fixed at 13% on a full equity investment.

- Price of biomass

The biomass price can vary between 10 and 25 €/MWh. A value of 15 €/MWh has been considered.

- Consumption costs

The consumption costs are mainly due to the additional consumption of biomass with respect to the equivalent heat-only plant. In the calculation of the additional request of

Table 15.5 Breakdown of a 4 MW thermal and 1 MW electric power biomass-fired Organic Rankine Cycle differential investment cost with respect to an equivalent heat-only biomass-fired plant

	€
Thermal oil boiler	700,000
Thermal oil circuit	300,000
Installation	100,000
Organic Rankine Cycle	1,300,000
Electric works	150,000
Engineering	100,000
Overall upgrade of the plant, contingency, other costs	500,000
Civil works	350,000
Total	3,500,000

biomass it has to be taken into account that a CHP plant introduces additional losses compared to an equivalent heat-only plant: reduced efficiency of the thermal oil boiler with respect to the hot water boiler; and additional auxiliary consumption due to the additional production of heat for the electricity production. Other consumption costs, which are very limited, compared to the biomass, are the consumables.

- Operation costs
The additional operation and maintenance costs are quite limited due to the reduced requirement of an ORC. A different value per size has been considered.
- Operation hours
The number of operation hours of the plant has a strong impact on the economic results. Four scenarios from 4000 h/y to 8000 h/y have been considered.
- Investment grant, taxes, and inflation.
No investment grants, taxes, or inflation have been considered.

15.5.4 Specific cost of electricity production per sizes

Table 15.7 shows the calculated specific cost of electricity production in € at different equivalent hours of operation.

In the industrial fields the equivalent hours are normally given by the specific process. In district heating the equivalent hours at full load are a function of the thermal CHP size. Reducing the size increases the equivalent hours at full load, but also the specific capital costs.

Fig. 15.26–15.28 show the composition of the specific cost of electricity production.

Table 15.6 Overall economic assumptions

	Gross electric power					
	130	300	500	1,000	2,000	5,000
Differential investment (k€)	665	1,470	1,925	3,500	5,950	10,500
Lifespan of the CHP (y)	15	15	15	15	15	15
Interest rate (%)	13	13	13	13	13	13
Consumables (€/MWh)	2	2	2	2	2	2
Operation and maintenance (€/y)	24,975	37,050	43,875	77,500	124,250	207,500
Other costs (€/y)	1,995	4,410	5,775	10,500	17,850	31,500
Fuel cost (€/MWh)	15	15	15	15	15	15
Thermal power produced (kW)	700	1,455	2,424	4,040	8,040	21,622
Gross electric power (kW)	130	300	500	1,000	2,000	5,000
Net power (kW)	125	269	448	881	1,761	4,432
ORC gross efficiency (%)	15	17	17	20	20	19
Boiler efficiency (%)	80	83	83	85	85	85
Equivalent water boiler efficiency (%)	90	90	90	90	90	90
Fuel consumption CHP [kW]	1,094	2,191	3,651	5,942	11,824	31,797
Fuel consumption water equivalent [kW]	778	1,616	2,694	4,489	8,934	24,024
Differential fuel consumption [kW]	316	574	957	1,452	2,890	7,772
Fuel to power [kW/kW]	2.5	2.1	2.1	1.6	1.6	1.8

CHP, combined heat and power; ORC, Organic Rankine Cycle.

Experience proves that 5000 h/y is the optimum equivalent at full load operating hours for a successful district heating CHP.

15.5.4.1 Sensitivity to the investment costs

The previous analysis assumes a differential investment which is valid for the implementation of the CHP solution in the design phase. In the case of modification of an existing plant, the investment costs are higher so the specific cost of electricity production rises

Table 15.7 Specific cost of electricity production in €/MWh.
Hypothesis: differential investment and differential biomass consumption with respect to an equivalent heat-only biomass plant

	Differential investment. Equivalent hours at full load [h/y]				
	4.000	5000	6.000	7000	8.000
130 kW	€ 300.9	€ 248.7	€ 213.9	€ 189.1	€170.5
300 kW	€ 283.9	€ 233.9	€ 200.6	€ 176.8	€158.9
500 kW	€ 227.7	€ 189.0	€ 163.2	€ 144.7	€130.9
1000 kW	€ 205.4	€ 169.7	€ 145.9	€ 128.8	€116.1
2000 kW	€ 177.5	€ 147.3	€ 127.2	€ 112.8	€102.1
5000 kW	€ 133.4	€ 112.4	€ 98.4	€ 88.4	€80.9

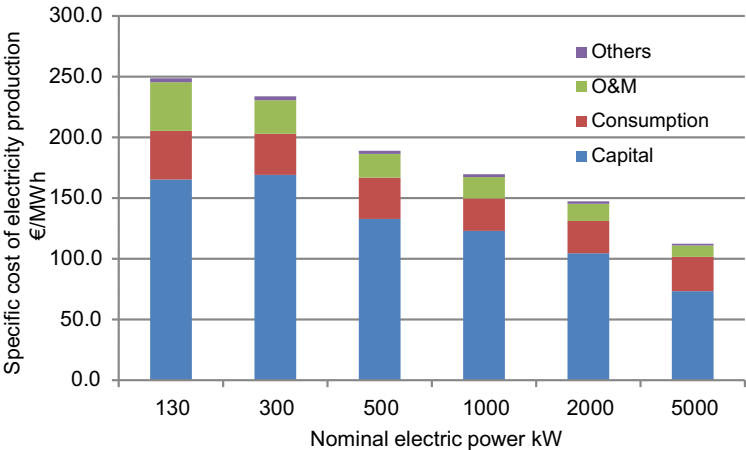


Figure 15.26 Composition of the specific cost of electricity production per size, considering 5000 equivalent at full load operative hours per year (elaborated by the authors). *O&M*, operation and maintenance.

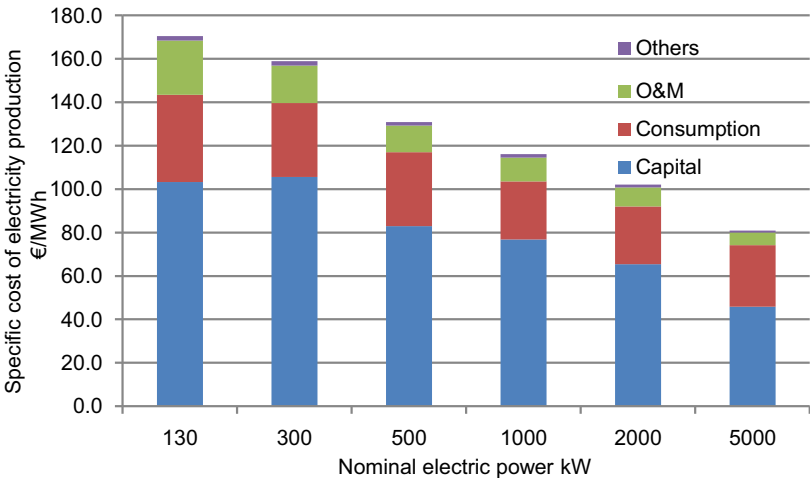


Figure 15.27 Composition of the specific cost of electricity production per size, considering 8000 equivalent at full load operative hours per year (elaborated by the authors). *O&M*, operation and maintenance.

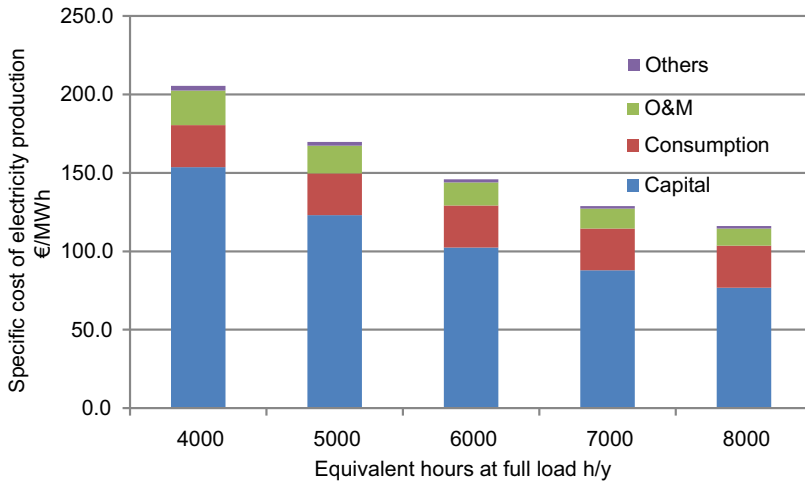


Figure 15.28 Composition of the specific cost of electricity production, for a 1 MW nominal electric power, per different equivalents at full load operative hours per year (elaborated by the authors). *O&M*, operation and maintenance.

proportionally. If we modify an existing heat-only plant then we have to charge 100% of the modification cost. Table 15.8 shows the specific cost of electricity production in the case of a biomass-fired ORC CHP assuming the overall investment costs (full replacement of the plant).

15.5.4.2 Sensitivity to thermal utilization

Considering the numbers of existing district heating plants with only-heat production, there is a very big market for the biomass-fired ORC to implement the CHP. In these

Table 15.8 Specific cost of electricity production in €/MWh.
Hypothesis: overall investment (full replacement of the plant) and differential biomass consumption with respect to an equivalent heat-only biomass plant

	Overall investment. Equivalent hours at full load [h/y]				
	4.000	5000	6.000	7000	8.000
130 kW	€ 465.2	€ 380.4	€ 323.8	€ 283.4	€253.2
300 kW	€ 452.4	€ 368.7	€ 312.9	€ 273.1	€243.2
500 kW	€ 360.1	€ 294.9	€ 251.4	€ 220.4	€197.1
1000 kW	€ 328.0	€ 267.8	€ 227.6	€ 198.1	€177.4
2000 kW	€ 281.8	€ 230.7	€ 196.7	€ 172.4	€154.2
5000 kW	€ 206.5	€ 170.9	€ 147.1	€ 130.1	€117.4

Table 15.9 Specific cost of electricity production in €/MWh.

Hypothesis: overall investment (full replacement of the plant) and differential biomass consumption with respect to an equivalent heat-only biomass plant, 8000 h/y electricity production and 4000 to 8000 h/y heat utilization

	Overall investment. Equivalent hours of heat utilization [h/y] assuming 8000 h/y of electricity production				
	4.000	5000	6.000	7000	8.000
130 kW	€ 292.3	€ 276.6	€ 266.2	€ 258.7	€ 253.2
300 kW	€ 275.2	€ 262.4	€ 253.9	€ 247.8	€ 243.2
500 kW	€ 229.1	€ 216.3	€ 207.8	€ 201.7	€ 197.1
1000 kW	€ 202.1	€ 192.2	€ 185.6	€ 180.9	€ 177.4
2000 kW	€ 178.8	€ 169.0	€ 162.4	€ 157.7	€ 154.2
5000 kW	€ 143.7	€ 133.2	€ 126.2	€ 121.2	€ 117.4

cases, the typical reduced size of the plants and the high investment costs, due to a non-differential investment, lead to a high specific cost of electricity production. To improve the economic performances and reduce the specific cost of electricity production, the installed size of the biomass-fired ORC can be raised. In this way, part of the produced heat will be dissipated but the overall performances of the plant can take advantage. Table 15.9 shows the specific cost of electricity production taking into account the overall investment costs (full replacement of the plant), considering 8000 h of electricity production per year and, respectively, from 4000 to 8000 h of heat utilization per year.

15.6 Conclusions and final considerations

The use of ORC in biomass-fired CHP systems started in the 1990s, when Turboden developed a new concept of ORC using silicon oils as the working fluid. These new types of ORCs have been able to exploit high temperatures sources, at the same time as being capable of maximizing the electric efficiency and of producing heat at a useful temperature for heating and drying processes.

The new products have developed the market of small size biomass-fired plants (between 500kW and 2 MW), which are not properly covered by conventional Rankine cycles. The incentive schemes available in Austria, Germany, Italy, and many other European countries, contributed to the fast growth of the market, peaking the number of plants started-up in 2012. At present, more than 300 biomass-fired ORC plants are in operation or are under construction, mainly in Europe, although some are in North America and Asia.

The new concept of ORC is now approaching the biomass-fired ORC market. The standard size between 500kW and 2 MW electric power has been extended in the last few years to range from 130kW to 10 MW electric power. New working fluids are being used.

However, the biomass-fired ORC market now has to face new challenges which can be played on four different fronts:

1. Maintain the present positions on the standard size market, between 500kW and 2 MW electric power.

To keep this position the biomass-fired ORC manufacturers have to achieve a reduction of the specific cost of electricity production, as a consequence of the reduction of the incentives. Until now the specific cost of electricity production has decreased just slightly from the entering of the biomass-fired ORC technology in the market. A very important role has to be played, again, by the European Institution through incentives. It is evident that biomass plants have to face the biomass cost. Biomass is an important voice of the specific cost of the electricity production but it represents at the same time an opportunity for local economies. The main battleground on this front will probably remain Europe followed by Asia and North America.

2. Look at the rural electrification, approaching new markets on remote regions, with big availability of low cost biomass, needing electricity but not properly covered by the electrical infrastructures.

In this case, stand-alone plants dedicated to local production sites or communities could represent a good opportunity. South America and Africa are prospective markets.

3. Gain new position versus the traditional conventional Rankine cycle market by growing the size of the plant up to 10 MW electric power and more.

In this case, the specific cost of electricity production can afford to access the market also with no strong incentive schemes, but it has to face the competition of the traditional Rankine cycle. The lower cost of operation and maintenance of the ORC with respect to the conventional Rankine cycle, the avoidance of freezing issues together with no need for highly skilled operators, are the main advantages offered by the ORC. South East Asia could represent an interesting opportunity for development.

4. Approach new small and very small size biomass-fired ORC, in a market potentially very big but with high investment costs normally associated with small sized plants.

A very important role can be played by the development of very low temperature district heating ($<50^{\circ}\text{C}$). In this case the market of biomass-fired ORC CHP could also be opened up to small size and low cost biomass-fired ORC. Europe could be a very important market.

Further reading

Guercio, A., Toscano, G., Pellet, I.I., 2015. Dario Flaccovio Editore (in Italian).

Guercio, A., 2015. Energy requirements for pellet production process and the role of co-generation from residues. The Turboden experience. In: Proceeding of the European Pellet Conference 2015. World Sustainable Energy Days. Wels.

- Guercio, A., 2011. Mini e micro cogenerazione a biomassa. Dario Flacovio Editore (in Italian).
- Guercio A., Impianti di piccola taglia: condizioni ideali, L'Ambiente N. 4/2009 (in Italian).
- Guercio, A., 2008. Cogenerazione; impianti a biomassa di piccola taglia con utilizzo di moduli "ORC": dimensionamento e applicazioni. Tecnologie e soluzioni per l'ambiente (in Italian).
- Bini, R., Manciana, E., Organic Rankine Cycle turbogenerators for combined heat and power production from biomass. In: 3rd Munich Discussion Meeting "Energy Conversion from Biomass Fuels Current Trends and Future Systems", 22–23 October 1996, Munich, Germany.
- Duvia, A., Tavolo, S., 2008. Application of ORC units in the pellet production field: technical-economic considerations and overview of the operational results of an ORC plant in the industry installed in Mudau (Germany). In: Proceedings of the 16th European Biomass Conference & Exhibition, Valencia, Spain.
- Ingwald, O., Thek, G., 2010. The Pellet Handbook: The Production and Thermal Utilization of Biomass Pellets. Routledge.
- Ingwald, O., Thek, G., June 2008. Cost assessment of selected decentralized CHP applications based on biomass combustion and biomass gasification. In: Proceedings of the 16th European Biomass Conference and Exhibition. ETA-Renewable Energies, Valencia (Italy).
- Ingwald, O., Gaia, M., 2005. Biomasse-Kraft-Wärme-Kopplung auf Basis des ORC-Prozesses – Stand der Technik und Möglichkeiten der Prozessoptimierung.
- Ingwald, O., Thonhofer, P., Reisenhofer, E., 2002. Description and Evaluation of the New 1,000 kWel Organic Rankine Cycle Process Integrated in the Biomass CHP Plant in Lienz, Austria, vol. 10. Euroheat & Power.
- Peretti, I., September–October 2010. ORC Technology with Biomass, its Use for Wood Pellet Production. Co-generation & On-site power production.
- Rifkin, J., 2003. The Hydrogen Economy. Tarcher.
- Righini, W., Guercio, A., et al., 2015. Biomassa legnosa, petrolio verde per il teleriscaldamento. FIPER.
- Turboden to Supply West Fraser, December 2012. Wood Bioenergy.

Solar thermal powered Organic Rankine Cycles

16

M. Orosz¹, R. Dickes²

¹Massachusetts Institute of Technology, Cambridge; ²University of Lige, Lige, Belgium

16.1 Introduction to solar Organic Rankine Cycle systems

Sunlight is the primordial energy source for most of the work that has occurred on Earth in the past 4.54 billion years. The most basic transformations are physical, e.g., sunlight evaporates water from oceans, raising it into the atmosphere and transporting it hundreds of miles to fuel global precipitation patterns. The original mechanism for converting sunlight into electro-mechanical work, however, was developed by single celled organisms, probably the progenitors of today's chloroplasts. Photosynthesis, the reduction of atmospheric carbon dioxide mediated by water and light, produced oxygen (a by-product) and energy to power cellular functions, such as DNA transcription, organelle formation, metabolism, and cell division. Over time this sunlight-powered work filled the earth's atmosphere with oxygen, creating an atmosphere similar to today's, by around 2.3 billion years ago.

In the human era, the earliest references that lay a foundation for the concept of converting sunlight into work involve a compilation of two ancient Sicilian/Greek innovations. Though likely apocryphal, the AD 2nd Century author, Lucian, reported that during the Siege of Syracuse (214–212 BC), Archimedes defended the city by setting fire to Roman ships using mirrors in a parabolic arrangement to concentrate sunlight. Nearly three centuries later, Hero of Alexandria described a device for converting heat into work with an “aeolipile” in his *Pneumatica*. His device converted thermal energy into rotary motion by means of a radial expander using two opposing steam jets emanating from a central, spinning boiler, though it is not known whether it was ever put to productive use.

In the first story, sunlight is concentrated to create heat (the autoignition temperature of wood is around 250°C), while in the second, heat creates steam in a boiler, which then expands out of orifices at opposite tangents to create rotation. When combined in this way, these two innovations embody the essence of concentrating solar power (CSP). In the midst of the Industrial Revolution, this synthesis was finally put to practice, first by French inventor Augustin Mouchot, and later by Swedish American John Ericsson, although dates of international exhibition are Ericsson first, whose solar air engine was featured at the Centennial Exhibition in Philadelphia in 1876, followed by Mouchot at the Paris Universal Exhibition in 1878.

When the first solar power plant was commissioned in 1913 in Maedi, Egypt, it was still several decades before Chapin, Fuller, and Pearson would demonstrate a working

silicon photovoltaic (PV) cell (4% efficiency, at Bell Labs in 1954). The Maedi plant, designed by American engineer Frank Shuman, used five parabolic trough collectors (PTCs), each 62 m long and 4 m wide, to concentrate the sun's rays on a boiler tube supplying a 75 kW atmospheric (low-pressure) steam engine coupled to a water pump capable of lifting 22 cubic meters of Nile water per minute ([American Inventor Uses Egypt's Sun for Power, 1916](#)). Though technologically successful, Shuman's demonstration plant never gained traction due to the onset of the first World War and the widespread availability of cheap fossil fuels, however, experimentation with solar powered motors proliferated in the ensuing decades, including: the SOMOR solar pump invented by Italians Daniele Gasperini and Ferruccio Grassi in the 1940s; a 1 kW_e Solar ORC pump installed in Mali in 1966; and a 3 kW_e Solar ORC developed by Harry Zvi Tabor and Lucien Bronicki and demonstrated to the United Nations in 1961, leading to the formation of Ormat ([Bronicki, 2013](#)). The 354 MW_e combined Solar Energy Generating System plants, operating in California, starting in 1984, established the commercial feasibility of utility-scale CSP using primarily steam Rankine power blocks, creating an industry that has over 4.5 GW_e of installed capacity in 2015. Subsequently, the commercial viability of solar-driven ORCs has been explored at many scales: in 2006, a grid-connected 1 MW_e Solar ORC plant ("Saguaro") was commissioned in Red Rock, Arizona (Southwest USA) by Arizona Public Service ([Canada et al., 2005b](#)), while more recently, the focus on solar ORC systems has tended towards smaller scale, experimental systems optimized for niche applications, as discussed in [Section 16.1.1](#).

16.1.1 Applications—grid connected power generation, desalinization, distributed power generation, cogeneration, and hybrid systems

Power from a solar ORC (SORC) can be useful in a variety of applications, from the ordinary supply of electrons via a traditional distribution grid, to islanded microgrids, to cogeneration for community or industrial use. Hybrid systems, involving other generation sources or one or more additional sources of, or uses for, thermal energy, are increasingly considered for solar ORC applications. This section highlights a range of typical uses for solar ORCs.

16.1.1.1 Grid connected power generation

There seems to be little scope for grid connected standalone solar ORC projects under the current technical and economic scenario. The 1 MW_e grid connected solar ORC, referenced in [Table 16.2](#), is an unlikely application for deployment in the future due to the recent decline in the cost of the main competing technologies, i.e., fossil fuels and solar PV. Grid scale CSP using steam Rankine, higher temperature sCO₂, or air Brayton cycles are still being commercially explored, particularly in the case where the value of the energy produced lies in its dispatchability via thermal energy storage (TES) (for more detail see [Section 16.2.3](#)). At grid scale, in 2015, PV installs for under

USD 2/W peak whereas CSP typically has a specific cost of over USD 4/W of name-plate capacity (Orosz, 2015). The cost of CSP with TES, however, remains lower than the cost of PV with electrochemical batteries at large scales; whereas large-scale batteries for shifting PV production into the evening are commercially unavailable, TES operational experience exists at the GWh scale in several CSP plants (see Table 16.1). This indicates that a solar ORC with TES may have a role to play in meeting energy needs as a dispatchable power source in a future where the grid is comprised of a high fraction of irregular, renewable sources.

16.1.1.2 Distributed power generation

Whereas the value of dispatchability in grid connected solar power plants is only beginning to gain recognition in the market, the demand variance and the need for storage of intermittent sun power is already inherent in any load-following application such as an isolated industrial or community mini-grid. Operational experience with islanded solar ORC systems is limited and commercially immature, however, recent analyses suggest that the application of solar ORC to support energy needs in remote areas for commercial or community loads may, if properly sized and designed, be economically attractive in comparison with alternative systems capable of meeting the demand dynamic, such as diesel generators (Mitterhofer and Orosz, 2015) or PV arrays with large battery storage systems. The attractiveness of the solar ORC for distributed generation can also be increased when hybrid solutions are relevant, as discussed in Section 16.1.1.5.

16.1.1.3 Desalination

Direct solar distillation of brackish water or seawater has been practiced from an early time through the coupling of a solar collector with a traditional still. Indirect desalination, through multiple stage flash distillation or reverse osmosis (RO), utilizes solar energy to derive either solar-derived electricity or mechanical work (and potentially heat) to purify water. Investigation of solar ORC desalination has included both dual use (electricity and water) and cogeneration systems, in which the water desalination mode directly couples the ORC shaft output to a high-pressure pump feeding brackish water to an RO membrane. The feedwater in these systems can be used for heat rejection from the ORC, and the increased temperature of the water improves the efficiency of the RO (Tchanche et al., 2010; Manolakos et al., 2007; Delgado-Torres and García-Rodríguez, 2007).

16.1.1.4 Irrigation

Solar-powered ORCs can also be used for irrigation duty for agricultural production. In such systems, solar energy supplied to an ORC is converted into mechanical power which is directly exploited to drive an irrigation pump. The advantages of solar water pumping include the coincidence between seasons of high solar irradiation and the demand for irrigation, and the fact that, as a load, irrigation is relatively insensitive to the diurnal intermittency of solar power (Pytilinski, 1978).

Table 16.1 Comparison of recently installed large-scale solar power plants using photovoltaic (PV) or concentrating solar power (CSP) technology, including specific costs and hours of storage (Orosz, 2015)

Plant name	Type	Nameplate (MW)	Pricetag (USD 000,000)	Reported production (GWh/year)	Storage (h)	Installed cost (USD/W)	Installed cost (USD/kWh/year)
Lalackama	PV	60	110	160	0	1.83	0.69
Chañares	PV	40	70	94	0	1.75	0.74
Desert Sunlight	PV (CdTel)	550	1900	1024	0	3.45	1.86
Crescent Dunes	CSP tower	110	975	485	10	9.09	2.01
Antelope Valley	PV (CdTel)	230	1400	623	0	6.09	2.25
Topaz	PV (CdTel)	550	2400	1053	0	4.36	2.28
Agua Caliente	PV (CdTel)	290	1800	741	0	6.21	2.43
Andasol 1	CSP trough	150	380	150	7.5	2.53	2.53
Solana	CSP trough	280	2000	600	6	7.14	3.33
Ivanpah	CSP Tower	392	2200	519	0	5.61	4.24

16.1.1.5 Hybrid solar organic Rankine cycle

Solar ORCs with or without TES may be used in conjunction with a variety of other generation technologies, some of which are simply used in parallel or potentially scheduled sequentially via a macro level control strategy. Other sources of energy include PV arrays, concentrating PV/thermal (CPVT) collectors, fuel-based generator sets, fuel cells, wind turbines, biomass boilers (Fig. 16.1), waste heat recovery, geothermal, etc. A solar ORC may also be configured to bypass heat around the ORC to directly meet thermal loads, such as industrial process heat (e.g., beverage bottle cleaning, aiding flash distillation processes, enhanced oil recovery, etc.), an absorption chiller, or building heating or hot water supplies. These configurations, while involving increasing degrees of complexity, may justify the capital expense based on fuel or battery cost savings (in the case of islanded operation), increased capacity factor, and the leveraging of locally available resources.

The benefits of hybridizing solar ORC with combustion based generators include, reduced fuel consumption (replacing fuel-derived power with solar-derived power) and the potential for improved overall fuel efficiency via recuperating waste heat from the exhaust stream of the genset. Hybridizing with PV arrays can be attractive if the daytime loads are supplied via the relatively inexpensive PV, while solar thermal production is dispatched from the TES, to supply nighttime loads, displacing the need for costly batteries. CPVT with ORC represents an opportunity to further reduce the infrastructure involved in a PV–CSP hybrid.

The capital cost of CSP collectors is especially justified when local demand for heat exists, or when available waste heat is at low temperatures that could benefit from solar boosting (e.g., from server datacenters). Some industrial processes may be supplied by CSP alone without the use of an ORC, but dynamics in load and solar resource (see Section 16.3.3) will tend to create a mismatch in the availability and requirement for heat. Excess heat from the collectors can, in this case, be exploited by an ORC, offsetting plant power consumption. Similarly, in cases where the thermal loads are seasonal (e.g., wintertime heating of buildings) the addition of an ORC can



Figure 16.1 1 MW_e Shive village electrification plant (Thermax India), a hybrid plant consisting of a concentrating solar power (CSP) collector field, steam Rankine cycle, Organic Rankine Cycle, and a backup biomass-fired boiler. Left: Thermax PTC collector. Right: GE/Calnetix 100 kW_e ORC (Thakur, 2013).

productively utilize otherwise wasted summertime CSP production. Another option making use of seasonal surplus solar resource, with or without ORC, would be to integrate a multieffect absorption chiller, although the cost of this approach compared to PV driving an electric heat pump would be worth exploring. Other hybridization scenarios are possible such as combining ORC with vapor compression cooling (Dumont et al., 2015); the key considerations in selecting and specifying the solar ORC components is the value of dispatchability and thermal products, and the costs otherwise incurred via alternate solutions. This highlights the fact that hybrid solutions tend to be unique and site specific, and one must recognize that the cost of investigating each situation and engineering the integration of multiple systems, which may require novel control strategy implementations, poses an obstacle to widespread adoption.

16.1.2 Meteorological and solar resource dynamics

As noted in the introduction to this chapter, a solar ORC obtains its heat input from the sun at the center of our solar system. While the astrophysics and celestial mechanics of this star are beyond the scope of this book, a basic overview of the functionality of the solar resource and its influence on the design and optimization of thermal power systems will be summarized.

16.1.2.1 Sunlight energy

The sun is a complex thermonuclear reactor whose mass holds the earth and other solar system objects in its gravitational field, while releasing 3.86×10^{26} J/s via the fusion of hydrogen into helium. At its outermost layers, the sun surface is maintaining a temperature of approximately 5778 K. According to Planck's well-known equation for the spectral radiance of a body at thermal equilibrium at temperature T :

$$B_{\lambda} = \frac{2hc^2}{\lambda^5} \frac{1}{e^{\frac{hc}{\lambda k_B T}} - 1} \quad (16.1)$$

(where B is the power in Watts per m^2 per nm, λ is the wavelength, k_B is the Boltzmann constant, h is the Planck constant, and c is the speed of light in the medium) the sun emanates a constant spherical beam of electromagnetic radiation with a distinct spectral signature approximating that of a blackbody at 5778 K.

16.1.2.2 The solar spectrum

Due to the size of the earth (DIA = 12,742 km) and its distance from the sun [1.496×10^8 km or 1 astronomic unit (AU)] the amount of solar energy intercepted by the earth is 1.74×10^{17} J/s. The shape of the solar spectrum is comparable to a blackbody at 5778 K, however, the actual solar spectrum is modulated by the sun's composition and partially attenuated by absorption bands in the earth's atmosphere in proportion to the depth of atmosphere traversed by a ray emanating from the sun.

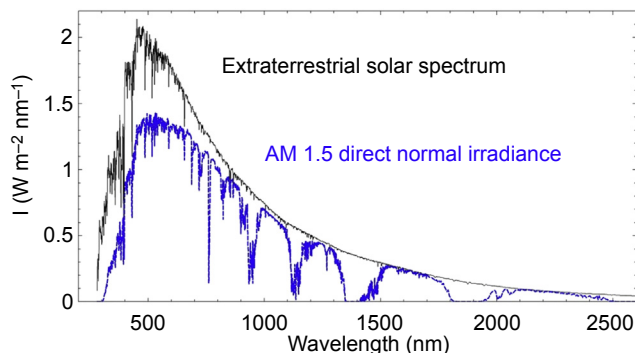


Figure 16.2 Extraterrestrial and Direct Normal Irradiance (DNI) from ASTM G173 DNI is at an air mass of 1.5 (ASTM, 2012).

Due to the rotation of the earth on an ~ 23.5 degrees tilted axis, this depth varies by latitude, seasonality, and time of day. The sunlight impinging on a flat plane at the surface of the earth is nearly collimated (the sun shape has an acceptance angle of 0.55 degrees); the intersection of a spherical beam of sunlight projected out from the sun across 1 AU distance striking the earth results in an extraterrestrial *solar constant* of approximately 1367 W/m^2 . An approximation of the direct normal irradiance (DNI—the beam component as opposed to diffuse light) solar spectrum at 1.5 times the thickness of the atmosphere is a frequently used standard for CSP known as AM1.5D (where D stands for direct, shown in Fig. 16.2). At prospective CSP sites, historical DNI measurements, obtained with a pyrheliometer, can be used to estimate local solar resources.

While the detailed characteristics of the solar spectrum have implications for the optical performance of solar collectors (specular reflectivity of primary mirrors, absorption, etc.), it is not uncommon to simply deploy the integral of the spectrum (in W/m^2), as a ready means of ascertaining power flux impinging on a collector aperture. The solar constant at the top of the atmosphere ($\sim 1367 \text{ W/m}^2$) is reduced by 25% or more by atmospheric conditions; at high DNI locations, at the earth's surface, it can reach above 1000 W/m^2 and $7.5 \text{ kWh/m}^2/\text{day}$. A more typical range for areas still considered appropriate for use of CSP is above 800 W/m^2 and $5 \text{ kWh/m}^2/\text{day}$, and standards or specifications for collector output will typically specify the DNI conditions at which the measurements were made.

16.1.2.3 Tracking

Most CSP collectors employ imaging optics that require the aperture of the collector to be normal to the sun. From dawn until dusk the sun is constantly moving in azimuth and zenith (zenith is 90-elevation, where elevation is the angle between the horizon and the sun) with respect to a fixed location on a rotating earth. Point focus systems, unlike line-focus systems (both described further in Section 16.2.1) must move to track the sun position in both azimuth and zenith coordinates (known as A-Z tracking).

In line-focus systems 2-D tracking is possible, however, the more common approach is the minimization of the cosine of the angle ϕ (between the collector aperture and the sun) by means of tracking around a single north-south or east-west axis. Compared to a horizontal surface, the increased solar irradiance on a single-axis tracking surface is approximately 10–20% or 20–30% for east-west and north-south parallel axes respectively, depending on latitude, with an additional 5–10% possible for two-axis tracking (Helwa et al., 2000; Duffie et al., 1994). Algorithms for calculating the sun position (azimuth and elevation) as a function of latitude, longitude, and time are published by National Renewable Energy Laboratory (NREL) in the USA and the Plataforma Solar de Almería (PSA) in Spain Reda and Andreas, 2008). Calculating the tilt angle for a single-axis platform in an east-west or north-south orientation CSP system involves minimizing the angle of incidence between the collector and impinging sunlight; equations for obtaining this result are widely available in the literature (Duffie et al., 1994).

16.1.2.4 Intermittency

ORCs driven by geothermal or waste heat sources can usually be designed with near constant heat input rates, or rates that vary in a predictable and controllable manner. ORCs driven exclusively or partially via solar input must contend with thermal inputs that can vary with unknown frequency and magnitude, superimposed on other fluctuations with a wide range but having a greater degree of predictability. Solar concentrators (discussed in more detail in Section 16.2), experience varying intensity of sunlight on their aperture on the timescale of seconds to minutes during cloud passing, on the timescale of hours due to the diurnal cycle, and on seasonal timescales on the basis of latitude driven changes in the time varying pathlength of rays through the atmosphere (as well as any attending angle of incidence effects). Landscape shadowing effects can have both diurnal and seasonal components. The DNI on a single-axis tracking surface for a typical cloudless day is shown in Fig. 16.3 and it is contrasted to cloudy weather at the same location; the effect of cloud passing can be seen to produce rapid changes in energy flux that require further design considerations when coupling CSP and ORC technologies (see Section 16.2.3).

16.1.2.5 Solar resource maps

The spatial distribution of the availability of beam (relatively collimated) sunlight (i.e. DNI), versus global irradiance (DNI + diffuse light) on an average daily basis (integrating the fluctuations due to local weather) per square meter for locations on earth's surface has been characterized by a combination of ground based and satellite measurements to produce useful maps for planning solar projects, an example of which is shown in Fig. 16.4:

For a more granular representation of local conditions, Typical Meteorological Year (TMY) datasets that include pyrheliometer measurements (for measuring DNI) are particularly useful for simulating the dynamic behavior of solar systems (discussed in more detail in Section 16.3.3).

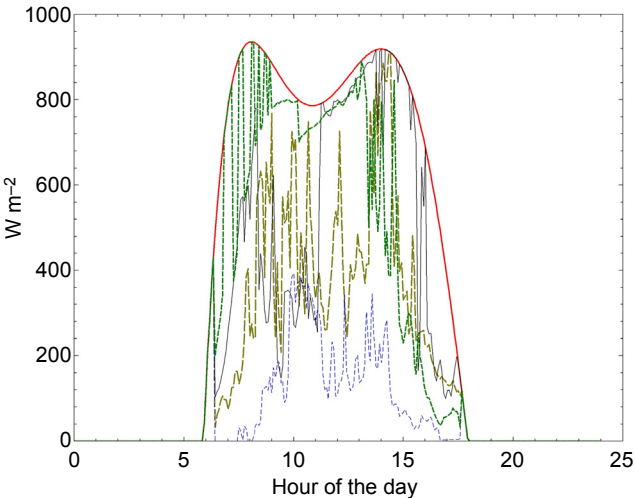


Figure 16.3 DNI on a single-axis tracking surface (Lesotho, 2009) for a cloudless day (red) and various cloudy days.
Adapted from Ireland et al. (2014).

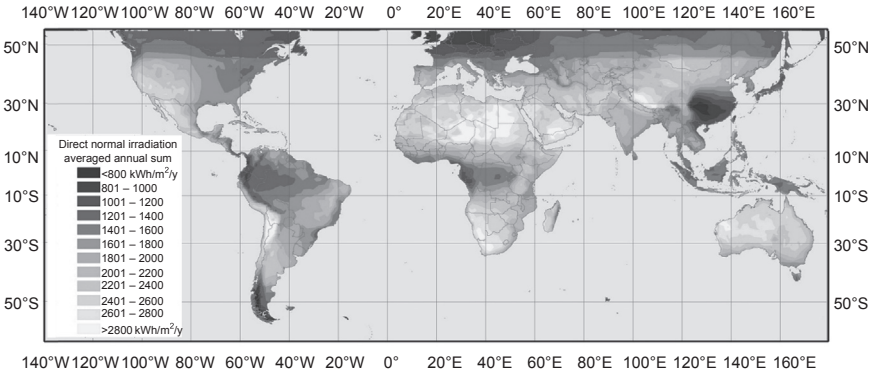


Figure 16.4 Map of direct normal irradiance (DNI) at the earth’s surface in kWh per square meter annually.
Adapted from NASA SSE 6.0 (1993–2006) and DLR (2008).

16.1.3 Installed capacity—survey of existing sites

Since the first development of heat engines, solar energy has been considered as a viable heat source. While none of the earliest experimental investigations of solar-based ORCs are in existence today, records and examples of experimental power plants are available, including unique pilot systems for R&D and commercial power generation units built and tested in the 20th century to the present. These SORC facilities range from “micro-power” generation (typically defined as lower than 1 MW_e) to large power plants of several megawatts, representing many variants of the technology.

The records for these systems are incomplete, but an effort to compile a list of known plants was undertaken by [Mueller et al. \(2016\)](#) and from this dataset of diverse solar-based ORC systems, a nonexhaustive list of experimental and commercial power plants with known characteristics is provided in [Table 16.2](#).

16.2 Solar Organic Rankine Cycle components and architecture

16.2.1 Solar thermal collectors

Solar-based ORCs use solar energy as the heat source from which to generate electricity or mechanical power. The heat is obtained by means of solar thermal collectors which intercept incoming sunlight and collect or reflect it onto a heat collection element (HCE). At the HCE, light is converted to sensible or latent heat and typically transferred to a flowing transport medium, called the heat transfer fluid (HTF). In most situations, the HTF acts as an intermediate fluid that transports heat to the ORC evaporator, however, direct generation can also be performed if the ORC working fluid is circulated through the HCE in place of a separate HTF, as discussed in [Section 16.2.2](#). The thermal efficiency of solar collectors depends significantly on the operating conditions and the insulation quality of the HCE, with values for the thermal efficiency typically ranging from 30% to 70%. For an HCE, the higher the temperature difference between the ambient air and the HCE, the higher the thermal losses.

Many types of thermal collectors have been developed in past decades and a major distinction can be made between concentrating and nonconcentrating technologies. A nonconcentrating collector has the same surface area for intercepting (aperture) and for absorbing (HCE surface) sunlight (the radiation flux onto the HCE is not increased), and a tracking system is not usually required. Both direct and diffuse portions of sunlight are exploited, and non-concentrating collectors can be well-suited for low-temperature applications. In the case of solar-based ORCs, three main technologies are used, namely solar ponds, flat plate collectors, and evacuated tube collectors.

16.2.1.1 Salt-gradient solar pond

A salt-gradient solar pond (SGSP), or simply *solar pond*, is a pool of saltwater used for collecting solar energy. Within the reservoir, a vertical salt concentration profile creates a three-layer stratification dividing the brine into an upper convective zone (UCZ) at the surface, a nonconvective zone (NZC) in the middle, and a lower convective zone (LCZ) at the bottom (see [Fig. 16.5](#)). While the top and bottom zones have a quasi-uniform density (low and high respectively) the nonconvective zone features a density profile that increases continuously from the upper to the lower boundary. As such, any natural convection is eliminated in the middle zone and a stable insulation layer is formed. During sunny periods, solar radiation passes through the layers and is absorbed by the lower zone. Thanks to the stable intermediate layer (NCZ in [Fig. 16.5](#)), the temperature of the bottom zone rises (up to 95°C) whereas the top of

Table 16.2 Nonexhaustive review of existing experimental solar Organic Rankine Cycle (SORC) facilities

Location (date)	Collector technology ^a	Collector area	Heat transfer fluid	Power output	Working fluid	Thermal storage	References
Mali (1966)	FPC	43 m ²	—	600 W	—	None	Einav (2004)
Ein Bokek, Israel (1977)	SGSP	7000 m ²	Brine	150 kW	—	Solar pond	Tabor (1981)
Pasadena, CA - USA (1978)	PDC	116.9 m ²	Toluene	30 kW	Toluene	None	Kiceniuk (1985)
Willard, NM - USA (1979)	PTC	1276 m ²	Mineral oil	19 kW	R113	Thermocline direct	Fenton et al. (1984)
Kuwai city, Kuwait (1981)	PDC	1100 m ²	Synthetic oil	100 kW/ 700 kW _{th}	Toluene	Thermocline direct	Moustafa et al. (1984)
Vignola, France (1982)	PTC	1176 m ²	Thermal oil	100 kW	Fluoroinert FC75	Thermocline direct	Simonnot et al. (1987)
Perth, Australia (1984)	PTC	—	Thermal oil	35 kW	C ₈ F ₁₆	—	Barutti et al. (1984) and Bado et al. (1979)
Beith Ha' Arava, Israel (1982)	SGSP	250,000 m ²	Brine	5 MW	—	Solar pond	Tabor and Doron (1990)
Lausanne, Switzer (2001)	LFC	100 m ³	Water	15 kW	R123/R134a	None	Kane et al. (2003)
Sendai, Japan (2002)	CPC	5.75 m ²	Water	<1 kW	R113	Buffer	Saitoh et al. (2007)
Red Rock, AZ—USA (2006)	PTC	10340 m ²	Mineral oil	1 MW	n-pentane	None	Canada et al. (2005a)
Newcastle, Australia (2006)	PTC	132 m ²	Mineral oil	6 kW	HFE 7100	n.a.	Kohlenbach et al. (2006)
Almeria, Spain (2007)	PTC	n.a.	Thermal oil	5 kW	SES36	n.a.	Galvez (2010)

Continued

Table 16.2 Continued

Location (date)	Collector technology ^a	Collector area	Heat transfer fluid	Power output	Working fluid	Thermal storage	References
Tianjin, China (2008)	FPC	0.6 m ²	R245fa	13 W	R245fa	None	Wang et al. (2011)
Tianjin, China (2008)	FPC/ETC	44 m ²	R245fa	1.7 kW	R245fa	None	Wang et al. (2010)
Morphou, Cyprus (2010)	PTC	216 m ²	Water	18 kW	R245fa	n.a.	Electrathern (2010)
Burkina Faso (2012)	SCT	180 m ²	Mineral oil	10 kW	R245fa	Two-tank direct	N'Tsoukpoe et al. (2014)
Berea, Lesotho (2012)	PTC	75 m ²	Glycol	3 kW/ 25kWth	R245fa	n.a.	Orosz (2012)
Crowley, LA—USA (2013)	PTC	1051 m ²	Water	50 kW	R245fa	Buffer	Chambers et al. (2014)
Tampa, FL—USA (2013)	PTC	n.a.	Water/ ethylene	50 kW	R245fa	PCM	Goswami et al. (2013)
Cadarache, France (2013)	PTC	550 m ²	Water	10 kW	R245fa	Thermocline direct	Rieu (2012)
Ait-Baha, Morocco (2014)	PTC	6159 m ²	Air	3 MW	n.a.	Sensible packed-bed	Ait-Baha
Rende, Italy (2014)	LFC	9780 m ²	Mineral oil	1 MW	n.a.	None	NREL
Fallon, NV—USA (2015)	PTC	656 m ²	Water	33 MW	Isobutane	None	NREL
Liège, Belgium (2015)	PTC	78 m ²	Synthetic oil	3 kW	R245fa	None	Georges et al. (2013) and Dickes et al. (2014)
Busan, Korea (2015)	ETC	n.a.	Water	1.5 kW	R245fa	n.a.	Baral et al. (2015)

^aCPC, compound parabolic collector; ETC, evacuated tube collector; FPC, flat plate collector; LFC, linear Fresnel collector; PDC, parabolic dish collector; PTC, parabolic trough collector; SCT, solar central tower; SGSP, salt-gradient solar pond.

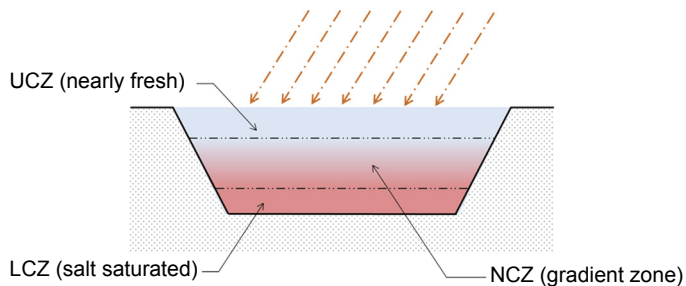


Figure 16.5 Salt-gradient solar pond. LCZ, lower convective zone; NCZ, nonconvective zone; UCZ, upper convective zone.

the pond remains close to the ambient temperature. Depths of solar ponds range from 0.5 to 5 m and large surface areas are required ($>200,000 \text{ m}^2$) for powering large-scale systems. Thermal energy is transferred to the ORC by pumping some of the hot brine to the evaporator and the upper cold water can be used as a heat sink for the ORC condenser. A key advantage of solar ponds is their ability to both collect and store thermal energy. Thanks to the high thermal inertia of the reservoir, heat power can be delivered to the ORC at a stable temperature.

16.2.1.2 Flat plate collector

A flat plate collector (FPC) is made of fluid tubes (filled with flowing HTF) connected to a darkened (high absorptivity) flat plate absorber that collects the sunlight and transfers the heat energy to the tubes. To reduce both convection and radiation losses, a transparent cover protects the absorber, while conduction losses are limited with an efficient thermal insulation of the collector casing. An example FPC architecture is shown in Fig. 16.6. Initially designed for domestic hot water generation, this technology is well-suited for low-temperature applications (below 100°C) and achieves good thermal efficiencies thanks to the limited heat losses.

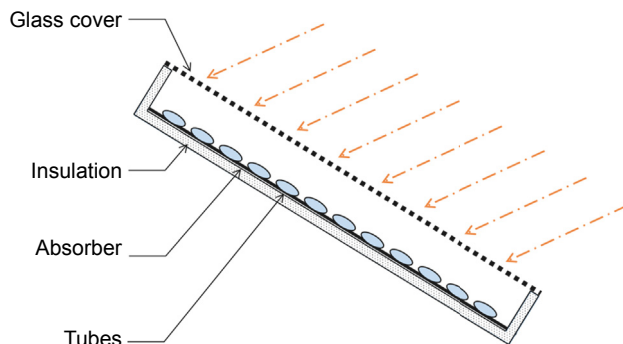


Figure 16.6 Flat plate collector.

16.2.1.3 Evacuated tube collector

To decrease heat losses at high temperature or in unfavorable weather conditions, an evacuated tube can be placed around the HCE of a solar collector. Evacuated tube collectors (ETC) can be found in two different configurations: in the first, the HTF flows directly through the tube placed in the middle of the evacuated envelope while in the second configuration, as depicted in Fig. 16.7, a heat pipe is placed in the vacuum-sealed tube and an auxiliary phase-change medium is used to transfer solar energy to the main HTF by means of an evaporation–condensation cycle. More precisely, solar radiation evaporates the auxiliary medium, after which the vapor phase naturally migrates to a condenser situated at the top of the heat pipe. The heat energy is then transferred to the main HTF, and the cooled auxiliary medium flows down the heat pipe in liquid phase. Although more complex, this mechanism permits collection of solar energy at constant temperature and avoids issues with overheating or freezing. Like flat plate collectors, ETCs exploit both direct and diffuse solar radiation, but ETCs have better thermal performance than FPCs for similar operating conditions and are suitable for a somewhat higher temperature range (up to 150°C).

In many cases, however, it is desirable to operate solar collectors at temperatures above even 150°C, and this requires use of a concentrating collector (using mirrors or lenses to focus sunlight) to increase the flux density at the HCE. Concentrating collectors therefore have a larger aperture area than HCE area, and the ratio between these two surfaces is known as the concentration ratio (C_f). Depending on the technology, the concentration ratio can be slightly larger than one or reach over one thousand. At a given operating temperature, the higher the concentration ratio, the higher the thermal efficiency. The heat loss from an HCE of a given surface area and optical properties is proportional to the average temperature difference between the HCE and the ambient environment. Therefore, for a given operating condition, the efficiency increases with the concentration ratio C_f since the losses are reduced in proportion to the heat input. Solar collectors can be designed and operated to achieve high temperatures for the heat source and thus a better thermodynamic efficiency of the ORC. Note, however, that a tradeoff must be made for this efficiency gain, as higher

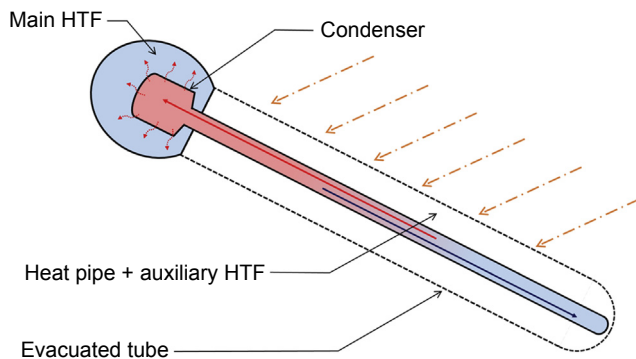


Figure 16.7 Evacuated tube collector.

temperatures at the HCE also increase thermal losses of the collector. Unlike non-concentrating technologies, concentrating collectors usually require continuous tracking to ensure an efficient focus of incoming radiation onto the HCE, and their optical imaging nature means they exploit only DNI and demonstrate poor performance in diffuse solar conditions. The most common concentrating technologies employed in SORC are presented in the following [Sections 16.2.1.4–8](#).

16.2.1.4 Parabolic trough collector

A parabolic trough collector (PTC) is a linear concentrating system made of long, parabolic-shaped mirrors and a receiver tube placed along the focal axis of the parabola. DNI is concentrated onto the receiver tube (as illustrated in [Fig. 16.8](#)), where solar energy is absorbed by the HTF. A glass envelope is often placed around the HCE to limit convection losses and further improve the collector efficiency; the annulus space between the glass envelope and the receiver tube can be under vacuum. Common PTCs achieve concentration ratios of 50, and the HTF temperature can reach up to 400°C ([Lovegrove and Stein, 2012](#)). Parabolic troughs are highly modular and can be arranged in solar fields of various sizes and architecture, however, to minimize losses, the collector axis must be oriented either in an east-west or in a north-south direction, both of which require single-axis tracking. In the case of a smaller solar field, dual-axis tracking can be used to reduce optical losses, however, this is relatively uncommon for linear concentrators.

16.2.1.5 Linear Fresnel collector

A linear Fresnel collector (LFC) is a line-focused concentrating system that reflects DNI onto an elevated stationary receiver tube (see [Fig. 16.9](#)). Unlike PTCs which consist of a continuous parabola-shaped reflector, LFCs are composed of many long strips of mirror that can be moved independently (single-axis tracking) to achieve reflection of solar radiation onto the HCE. Due to its architecture, LFCs are highly modular and can be constructed and assembled inexpensively in various-scale solar

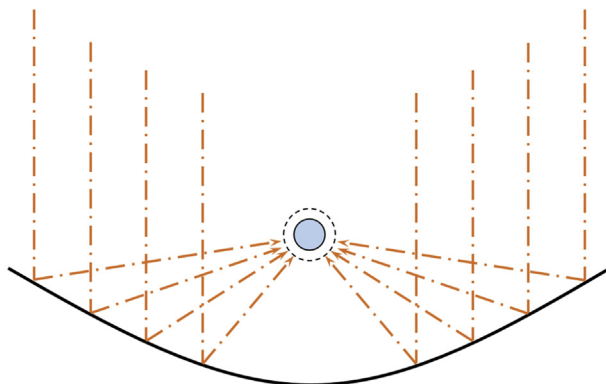


Figure 16.8 Parabolic dish/trough collectors.

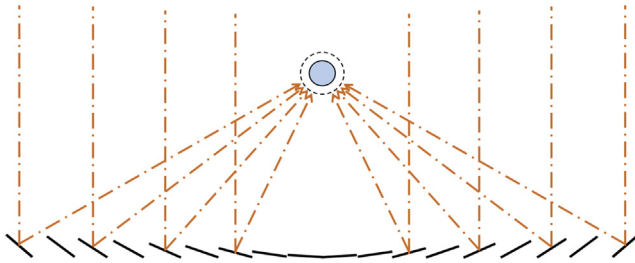


Figure 16.9 Linear Fresnel collector.

fields. Concentration ratios of LFCs without secondary optics are slightly lower than for PTCs, and LFCs are generally characterized by lower optical performance but potential cost savings.

16.2.1.6 Compound parabolic collector

A compound parabolic collector (CPC) (see Fig. 16.10) is another trough-type technology that concentrates solar energy onto a tube receiver. The reflector geometry is built by the combination of two symmetric parabolic segments with different focal lengths. This geometrical arrangement enables collection of any solar radiation entering the collector aperture within an acceptance angle (depending on geometry but ranging from 10 to 80 degrees) onto the tube receiver by means of multiple internal reflections. This important feature allows CPCs to operate without continuous tracking and to exploit both DNI and some portions of diffuse sunlight. CPCs are characterized by low concentration ratios (<5) and are well-suited for medium-temperature applications (up to 200°C). CPCs also find use as secondary down-facing reflectors in LFC systems to increase the effective concentration ratio.

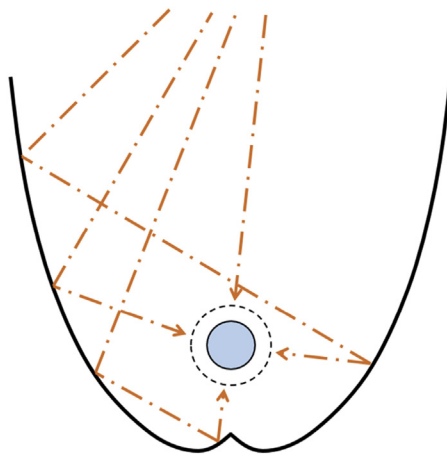


Figure 16.10 Compound parabolic collector.

16.2.1.7 Parabolic dish reflector

A parabolic dish reflector (PDR) is a point-focus system with a paraboloid geometry given by the revolution of one half of a parabola around its normal axis. Sunlight entering the collector aperture with a normal incidence is concentrated onto a heat receiver located at the focal point of the dish. Parabolic dishes exploit only DNI and require a two-axis tracking mechanism to ensure a proper focus throughout the day. Typical concentration ratios of PDRs range from 500 to 3000, making this technology suitable for high temperature applications (up to 450°C for SORCs), but unlike other collector types, PDRs are rarely connected together in a solar field. Instead, they often operate as distributed power systems with independent engine units directly located at the focal point of each collector. Due to their high temperature capabilities, ORC is not often the cycle of choice for a PDR collector, with Stirling and thermoacoustic examples being more common (Kiceniuk, 1985; Dfid, 2010; Zhang et al., 2014).

16.2.1.8 Solar central tower

A solar central tower (SCT) is another type of point-focus system that uses a field of independently actuated mirrors (called heliostats) to concentrate DNI onto a central receiver at the top of a tower (Fig. 16.11). Each heliostat is controlled with a 2D tracking mechanism calibrated to its location and physical placement relative to the tower. Solar towers achieve high concentration ratios (up to 2000) and are most often used in high-temperature large-scale steam power plants, however, some pilot projects (see Table 16.2) also use this collector technology in ORC-based power systems.

The selection of an appropriate solar collector technology for an ORC application will involve specific cost considerations, or the comparison of alternatives, along with project specifications including any limitations in mounting space, operating temperatures, and the availability of any reservoir for heat rejection (discussed further in Section 16.3.4). The main characteristics of the different collector technologies presented in this section are summarized in Table 16.3.

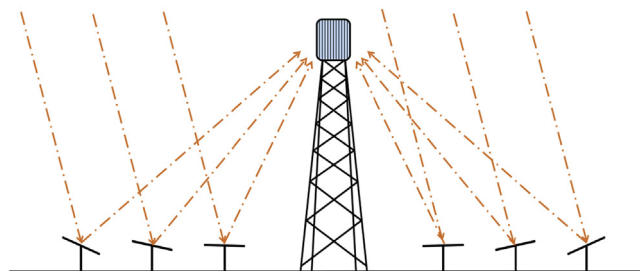


Figure 16.11 Solar tower system with heliostat array and central receiver.

Table 16.3 Solar collectors used in solar Organic Rankine Cycles (SORCs) and their characteristics (Lovegrove and Stein, 2012; Kalogirou, 2004; Weinrebe, 2007)

Collector type	SGSP	FPC	ETC	CPC	LFC	PTC	PDR	SCT
Tracking	None	None	None	None/1D	1D	1D/2D	2D	2D
Concentration ratio	1	1	1	<5	20–40	30–50	500–3000	400–2000???
Solar exploitation	Total	Total	Total	Total	Direct only	Direct only	Direct only	Direct only
Receiver temperature	<100°C	<100°C	100–150°C	100–200°C	100–300°C	100–400°C	>300°C	>300°C

CPC, compound parabolic collector; *ETC*, evacuated tube collector; *FPC*, flat plate collector; *LFC*, linear Fresnel collector; *PDR*, Parabolic dish reflector; *PTC*, parabolic trough collector; *SCT*, solar central tower; *SGSP*, salt-gradient solar pond.

16.2.2 Heat transfer fluid

In general, a flowing heat carrier fluid (HTF) is used to facilitate transfer of energy collected in the solar field to the ORC unit.

A simpler option is to directly use the working fluid of the organic Rankine cycle as the heat transport medium (Fig. 16.12 left side), referred to as *direct steam generation* (DSG), vaporizing the organic fluid within the solar collectors. This configuration avoids the cost of a heat delivery heat exchanger and the parasitic losses associated with a pump circulating a second fluid, and the simple architecture makes it convenient for use in micro-scale systems (Lovegrove and Stein, 2012). DSG is rarely utilized in medium- and large-scale SORC systems due to the large (costly) volume of organic fluid required to fill the solar field; DSG implies high-pressure operations in the solar collectors which requires a more expensive collector design and may actually increase the overall cost of the project.

The second, more common, SORC architecture employs an intermediate HTF to transport collected heat energy from the solar collectors to the ORC system. In this case, a heat exchanger between the solar loop and the ORC is used to evaporate the working fluid (heat delivery similar to that used in more traditional ORC applications), and a secondary pump circulates the HTF in the solar collectors.

The selection of an efficient and cost-effective HTF is one of the important design parameters affecting the overall power plant performance. The main solar plant HTF requirements are summarized here:

1. Low melting temperature, to avoid solidification and an adequate pumpability of the HTF during cold weather;
2. High temperature stability, to ensure the HTF integrity at high-temperature operating conditions;
3. High thermal conductivity, to maximize the heat transfer rate in the solar collectors;
4. High thermal capacity, to limit the mass flow rate required for transporting a given amount of heat power;
5. Low coefficient of expansion, to limit the volume variations of the HTF between different operating conditions;
6. Low viscosity, to reduce power consumption of circulating pumps;

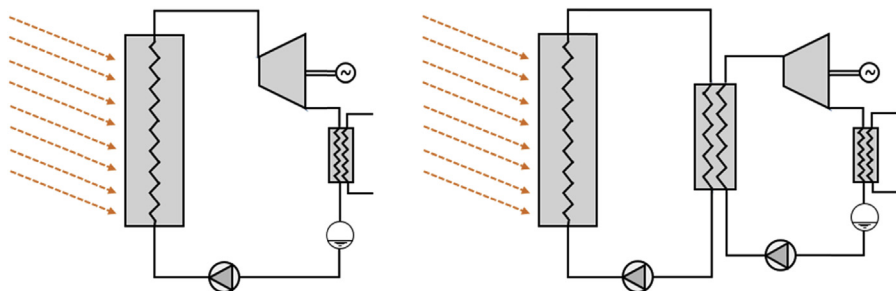


Figure 16.12 Direct steam generation (DSG) configuration (left). Heat transfer fluid (HTF) configuration (right).

7. Low corrosion, to ensure the long-term integrity of the power plant;
8. Limited hazard and environmental issues, i.e., low vapor pressure, no toxicity, limited flammability, etc.;
9. Low cost and availability within the project target market.

A common, effective, and inexpensive heat carrier used in low-medium temperature SORC is pressurized water. Aside from low cost, wide availability, and the absence of environmental issues, water has good heat transfer properties with a low viscosity and a high thermal capacity. A major drawback of water, however, is the sharp increase of pressure required to ensure a liquid-phase flow at high temperature, as shown in Fig. 16.13. Pressures in water-based solar fields easily reach 20 bar, making the installation more hazardous (from a mechanical safety perspective) and more expensive. Working HTF pressure can become a limiting factor in solar field operating temperature, which limits in turn the maximum temperature of the working fluid inside the ORC.

Low-pressure operations in the solar field can be preserved by admixture of water with soluble fluids that lower the boiling point, such as the glycol diols, or using alternative fluids such as thermal oils or other organic or inorganic materials. These HTFs can be vegetal (e.g., palm oil), synthetic (i.e., artificially-made), mineral (i.e., petroleum-derived), or liquefied salts; HTFs of these types have been developed for use in a wide range of temperature ranges and conditions (see Table 16.4). It is important to recall that HTF properties are generally temperature dependent; Table 16.4 provides one point of comparison among fluids (at 150°C) and the coefficients required to calculate the density and the specific heat capacity of the fluids in function of the temperature, i.e.,

$$\rho_T = \rho_0 + \beta_\rho T \quad cp_T = cp_0 + \beta_{cp} T \quad (16.2)$$

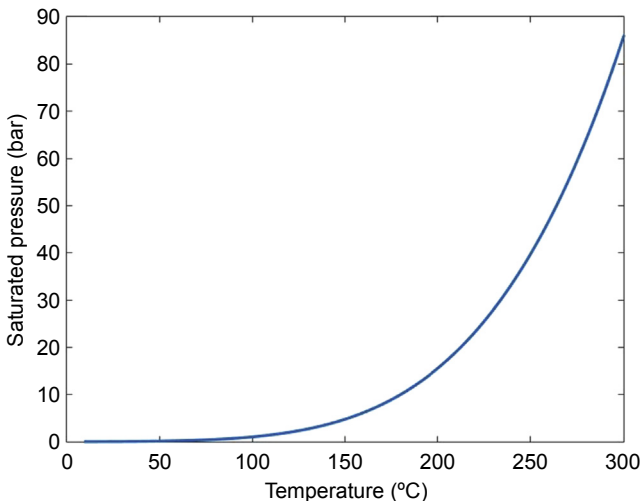


Figure 16.13 Saturated pressure of water as a function of the temperature.

Table 16.4 Nonexhaustive list of range of commercial heat transfer fluids (HTFs)

Fluid	T_{\min}	T_{\max}	$T_{\text{auto,ig}}$	$\rho_{150^{\circ}\text{C}}$	$cp_{150^{\circ}\text{C}}$	$k_{150^{\circ}\text{C}}$	$\mu_{150^{\circ}\text{C}}$	ρ_0	β_p	cp_0	β_{cp}
	(°C)	(°C)	(°C)	(kg/m ³)	(J/kg K)	(W/m K)	(cP)	(kg/m ³)	(kg/m ³ °C)	(J/kg K)	(J/kg K °C)
Water (20 bar)	—	—	—	918	4302	0.682	0.18	1024	−0.725	4099	1.49
Xceltherm 600	−29	316	349	773	2440	0.126	1.07	864	−0.607	1927	3.41
Xceltherm MK1	12	400	621	957	1916	0.121	0.59	1093	−0.942	1495	2.77
Xceltherm LV1	7	371	604	955	1944	0.120	0.70	1080	−0.835	1519	2.79
Dynalene MT	—	350	410	862	2083	0.118	1.10	972	−0.732	1772	1.72
Dynalene HT	−34	350	450	951	2033	0.113	1.51	1058	−0.715	1474	3.73
Dynalene SF	−60	315	330	789	2441	0.124	1.66	890	−0.672	1906	3.60
Dynalene SGXT	−27	176	n.a.	931	7863	0.433	7.51	1054	−0.640	3445	5.83
Dynalene 600	−65	288	n.a.	833	1517	0.130	17.00	983	−1.000	1234	1.88
Therminol 66	−3	345	399	921	2014	0.110	1.52	1028	−0.735	1475	3.65
Therminol XP	−29	315	324	795	2394	0.117	1.48	893	−0.668	1747	4.13
Therminol 59	−61	315	404	878	2110	0.110	0.74	990	−0.771	1614	3.32
Therminol 55	−54	315	343	783	2364	0.113	1.29	887	−0.705	1836	3.53
Therminol SP	−40	315	366	783	2368	0.113	1.29	888	−0.716	1836	3.54
Therminol 62	−42	325	407	859	2252	0.111	1.06	973	−0.794	1907	2.15
Therminol VP1	12	400	621	957	1913	0.121	0.59	1098	−0.972	1486	2.82
Dowtherm A	12	400	599	952	1940	0.118	0.58	1096	−0.995	1501	2.93
Dowtherm G	4	360	432	946	2000	0.111	0.96	1062	−0.775	1476	3.50
Dowtherm Q	−35	330	412	867	2058	0.104	0.45	981	−0.758	1596	3.03

Continued

Table 16.4 Continued

Fluid	T_{\min}	T_{\max}	$T_{\text{auto,ig}}$	$\rho_{150^{\circ}\text{C}}$	$cp_{150^{\circ}\text{C}}$	$k_{150^{\circ}\text{C}}$	$\mu_{150^{\circ}\text{C}}$	ρ_0	β_p	cp_0	β_{cp}
	(°C)	(°C)	(°C)	(kg/m ³)	(J/kg K)	(W/m K)	(cP)	(kg/m ³)	(kg/m ³ °C)	(J/kg K)	(J/kg K °C)
Water (20 bar)	—	—	—	918	4302	0.682	0.18	1024	−0.725	4099	1.49
Dowtherm RP	−20	350	385	937	2007	0.115	1.32	1046	−0.738	1561	2.98
Dowtherm MX	−23	330	420	868	2032	0.109	0.96	981	−0.775	1545	3.25
Dowtherm 4000 (ethylene glycol—90% vol)	−30	177	—	1031	3138	0.269	0.62	1149	−0.753	2243	5.96
Syltherm 800	−60	400	385	820	1830	0.111	1.70	960	−0.978	1574	1.71
Syltherm XLT	−111	260	350	722	2045	0.080	0.34	876	−1.027	1730	2.10
Syltherm HF	−82	260	355	740	2002	0.075	0.43	892	−1.011	1633	2.46
Paratherm HR	−11	343	416	860	2200	0.107	0.93	965	−0.746	1884	2.30
Paratherm HE	3	310	371	781	2600	0.116	2.10	872	−0.611	1791	5.06
Paratherm GLT	8	288	n.a.	781	2500	0.110	1.30	887	−0.707	1929	3.60
Paratherm NF	−43	332	366	797	2500	0.098	1.50	899	−0.683	1469	7.97
Pirobloc mineral	−10	305	n.a.	782	2374	0.131	n.a.	879	−0.649	1811	3.72
Duratherm 450	−45	232	329	774	2473	0.133	0.77	876	−0.681	2021	3.02
Duratherm 600	−10	315	360	768	2336	0.136	2.01	869	−0.672	1844	3.27
Duratherm HTO	−15	315	360	758	2288	0.135	2.07	862	−0.665	1815	3.24
Duratherm S	−66	204	436	928	1926	0.117	0.98	968	−0.263	1641	1.91
Solar salt	220	600	—	—	—	—	—	2090	−0.636	1443	0.172
Hitec salt	142	535	—	—	—	—	18	2079	−0.732	—	—

where β_p and β_{cp} are the linear coefficients of the density and the specific heat capacity correlations respectively. From Table 16.4, it can be seen that organic heat carriers have lower thermal capacities, higher viscosities, and lower thermal conductivities than pressurized water. They are limited at high temperature because of stability issues due to their molecular structures, however, even at high temperature, they can often be operated at or near atmospheric pressure, creating cost savings and avoiding the mechanical hazards of high-pressure systems. Molten salts present a good thermal stability at high temperature and properties similar to water (high thermal capacity and conductivity, and low viscosity) at low vapor pressure. However, they are characterized by high-temperature melting-points ($>150^\circ\text{C}$) which make them, in general, not suitable for ORC-based CSP systems.

Finally, besides thermophysical properties, the cost of the heat transfer carrier must be accounted in the design process of a solar power system. Price is function of the product quality, the seller, but also of the volume container. In the case of 200 L drums, cheap and low-grade HTFs are about 1–3 €/L, standard HTFs cost around 4–6 €/L, whereas high-grade fluids can cost up to 10–15 €/L.

16.2.3 Thermal energy storage

The intermittent nature of sunlight is an inherent drawback of solar power that can lead to imbalances between consumer demand and heat source availability. By adding energy storage, however, it is possible to shift excess energy from high-insolation periods to nighttime or periods of unfavorable meteorological conditions. The whole power system is thus more efficient (avoiding waste during periods where insolation outstrips demand), reliable (buffering system output during cloud passage), and flexible (higher capacity factor) despite transient external conditions. A key advantage of solar ORCs over photovoltaic technologies is the opportunity to use cost-effective thermal energy storage (TES), which stores excess heat energy in thermal rather than electrical form, in place of electrochemical batteries. TES, which is currently cheaper than commercial batteries and has a longer usable lifetime, comes in many varieties, and design/selection of the TES component of a SORC system must be undertaken with the following criteria in mind:

1. High energy density minimizes storage size;
2. High heat transfer rate permits fast storage and release of thermal energy;
3. Chemical compatibility is required between the storage medium, the container, and the HTF (if in direct contact);
4. High storage efficiency is needed over the complete charge—standby—discharge cycle; energy and exergy losses should be minimized;
5. Easy control and good flexibility;
6. Fluid selections should avoid environmental issues and limit hazards;
7. Lowest cost systems amplify advantage over electrochemical batteries.

Various TES technologies can be distinguished by the mechanism employed for storing heat energy, i.e. sensible, latent and chemical TES systems. These TES technologies are discussed in more detail in the following sections.

16.2.3.1 Sensible thermal energy storage

In sensible TES, heat storage is achieved by raising the temperature (without changing phase) of a single-phase medium. The amount of energy stored is proportional to the mass of the medium employed, its specific heat capacity, and the temperature difference between initial and final states. The storage material can either be the HTF flowing in the solar field (i.e., *direct* storage) or another medium (i.e., *indirect* storage). In the latter case, an additional heat exchanger is required to interface the SORC plant to the TES unit. Cost reductions for either direct or indirect storage can further be achieved by using inexpensive solid materials, preferably with high heat capacity, to partially fill the storage container (i.e., *packed-bed* TES). A list of common filler materials is given in Table 16.5.

Sensible TES can be integrated into SORC systems in three distinct architectures:

Single buffer

In this configuration a small volume capacity of HTF is placed in series with the solar loop (see Fig. 16.14). The buffer mitigates short fluctuations of temperatures at the outlet of the solar field (e.g., due to passing cloud cover). The storage capacity of the buffer tank is limited and is generally not used to extend operation of the SORC into nonsun periods.

Two-tank storage

Two-tank storage involves two separate reservoirs, which are used to store, respectively, hot and cold liquids (Fig. 16.15) in various system configurations. Two-tank

Table 16.5 Properties of potential solid filler materials for packed-bed storage (Kuravi et al., 2013; Singh et al., 2010; Grirate et al., 2013)

Filler material	Density (kg/m ³)	Heat capacity (J/kg K)	Conductivity (W/m K)	Thermal expansion (1e-5/K)
Concrete	2000–2400	750–900	0.4–1.5	2.5–4.5
Brick	1600–2000	850–1000	0.6–1.5	0.9–1.7
Basalt	2200–2800	800–1150	1.0–2.5	2.4–2.8
Granite	2500–2700	700–850	1.7–4.0	1.2–2.4
Limestone	2500–2800	830–1000	1.3–2.5	2.4–3.6
Marble	2600–2800	800–1150	2.0–3.0	1.7–3.6
Quartzite	2510–2860	700–1100	3.3–7.0	3.3–3.9
Sandstone	2100–2700	710–930	1.7–2.9	3.0–3.3
Aluminium	2700–2800	870–890	205–215	6.5–6.9
Cast iron	7200–7900	460–600	37–55	3.3–3.5
Steel	7750–7830	465–490	36–54	3.1–4.2

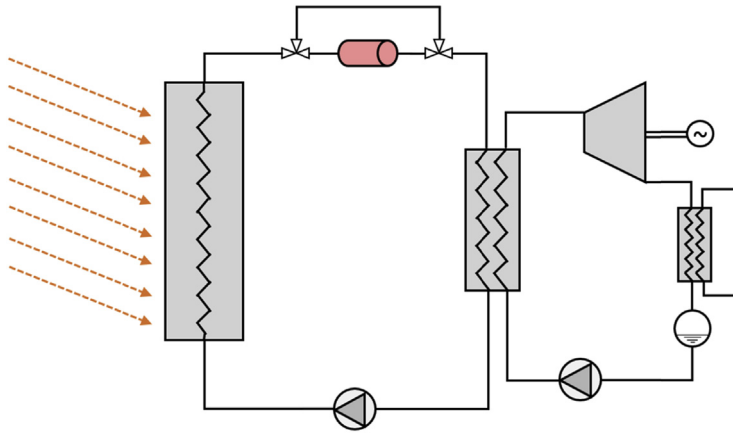


Figure 16.14 Buffer reservoir.

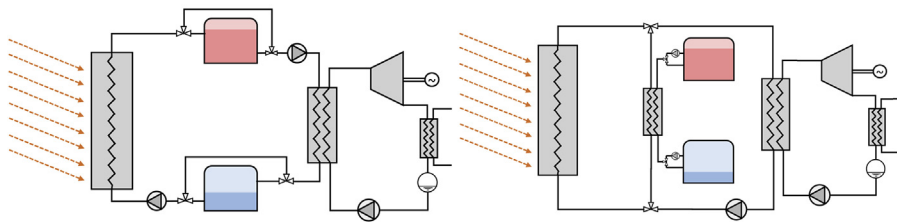


Figure 16.15 Direct (left) and indirect (right) two-tank thermal energy storage.

storage can have high thermal charge–discharge efficiencies (up to 95% if well insulated) and good operational flexibility. They are easily scalable and can be designed to widely extend the daily operational time of SORC by up to several hours.

Thermocline storage

As shown in Fig. 16.16, thermocline storage is a single tank used to store both hot and cold fluid where a natural separation is created by the density difference between the two zones of fluid. By using a single reservoir, cost reductions (up to 33% (Kolb, 2011)) can be achieved compared to two-tank storage, however, thermocline systems

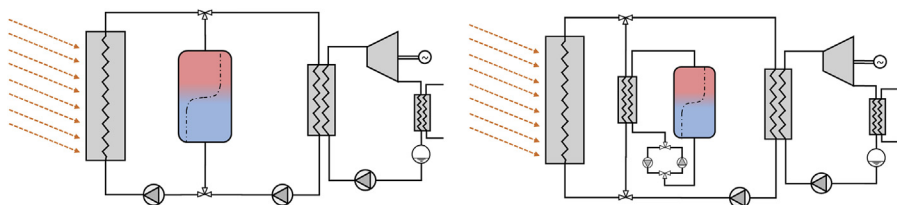


Figure 16.16 Direct (left) and indirect (right) thermocline storage.

are inherently less efficient than two-tank TES because of the imperfect separation between the hot and cold fluid. Thermal diffusion and mixing phenomena (e.g. turbulence due to flow) induce a transition zone of increasing thickness which degrades the high-temperature energy initially stored. In spite of this, thermocline TES is easily scalable and can be designed to extend the operational window of SORCs for many hours past sunset.

Overall, sensible heat storage is the most common TES technology used in SORC systems as it is simple, cost-effective, and has good heat transfer performance. However, the lower energy density ($\sim \text{kJ/m}^3$) implies large storage size compared to TES varieties discussed in [Section 16.2.3.2](#).

16.2.3.2 Latent thermal energy storage

In this design, thermal energy is stored in the latent heat of a phase-change material (PCM). Since latent energy of phase-change transitions is much higher than specific heat capacity, PCM storage has the potential for much higher energy storage density ($\sim \text{MJ/m}^3$) than sensible TES. Among the different phase-change transitions possible, solid–liquid transitions are generally preferred because of the limited volumetric expansion of the storage medium during the process. Generally encapsulation of the storage media is required to avoid mixing between the liquid-phase PCMs and the HTF.

Another key advantage of latent storage is that the phase transition is a quasi-isothermal process, a feature that facilitates TES integration and control within the SORC plant. The tradeoff, however, is the low thermal conductivity of the storage media which results in an excessive charging and discharging time for thermal storage. Faster response times can be achieved by adding high-conductivity materials (e.g., metals or graphite) within the PCM.

Media for latent storage include organic materials (e.g., paraffins and fatty acids), inorganic compounds (e.g., salt hydrates), and various eutectic mixtures (see [Table 16.6](#)). Despite its technical advantages compared to sensible technologies, latent heat storage is more expensive and still at the prototype phase.

16.2.3.3 Thermochemical thermal energy storage

Thermochemical TES relies on reversible chemical reactions to store heat energy. In the charging process, injected heat is used to drive an endothermic chemical reaction; the chemical products are later used to restore thermal energy by performing the reverse (exothermic) reaction. Examples of potential materials for thermochemical storage in CSP are provided in [Table 16.7](#). Among the different storage technologies, thermochemical TES has the highest energy density potential ($\sim \text{GJ/m}^3$) thanks to the large enthalpy change in chemical reactions. Additional advantages to thermochemical TES are quasi-isothermal storage and release, as well as storage of chemical products at ambient temperatures which largely reduces long-term thermal losses. Thermochemical storage is not yet mature, however, with high cost and technical complexity remaining barriers to commercialization.

Table 16.6 Examples of phase-change materials with their properties

Chemical formula	Medium name	Melting point (°C)	Density (kg/m ³)	Latent energy (kJ/kg)	Energy density (MJ/m ³)
C ₈ H ₈ Cl ₂	p-Xylene dichloride	100	1432	139	199
C ₈ H ₈ O ₄	Methyl fumarate	102	1370	242	332
C ₈ H ₄ (OH) ₂	Catechol	104.3	1344	207	278
C ₆ H ₄ O ₂	Quinone	115	1318	171	225
C ₈ H ₉ NO	Acetanilide	118.9	1219	222	271
C ₄ H ₄ O ₃	Succinic anhydride	119	1230	204	251
C ₆ H ₅ COOH	Benzoic acid	121.7	1266	143	181
C ₁₄ H ₁₂	Stibene	124	971	167	162
C ₆ H ₅ CONH ₂	Benzamide	127.2	1341	169	227
KNO ₃ + NaNO ₃	-	222	2257	108	244
NaNO ₂	Sodium nitrite	282	2168	212	460
NaNO ₃	Sodium nitrate	310	2257	174	393
NaOH	Sodium hydroxide	318	2130	158	337
KNO ₃	Potassium nitrate	337	2109	116	245
KOH	Potassium hydroxide	360	2100	167	351

Table 16.7 Examples of reactions for thermochemical storage

Chemical reaction	Temperature range (°C)	Energy density (GJ/m ³)
FeCO ₃ ↔ FeO + CO ₂	180–200	2.6
CH ₃ OH ↔ CO + 2H ₂	200–250	—
Ca(OH) ₂ ↔ CaO + H ₂ O	400–600	3
CaCO ₃ ↔ CaO + CO ₂	800–900	4.4
6Mn ₂ O ₃ ↔ 4Mn ₃ O ₄ + O ₂	900–1000	1

16.3 Solar Organic Rankine Cycle systems

16.3.1 Design and specification

While there may be differences in the operating temperatures, working fluids, sizes and types of pumps, expanders, and heat exchangers for an SORC system, the fundamental methods for predicting the performance of a solar-integrated ORC system are similar to the thermodynamic modeling techniques described in Chapters 1, 6, and 7. The selection of cycle parameters optimized for a solar ORC, however, is driven mainly by the cost and temperature of the available heat source and cold reservoir (air in dry or wet cooling modes, or a local water body). In particular, the optimum operating temperature of a solar-driven ORC can vary with the type of collector (described in [Section 16.2.1](#)) and its relative efficiency as a function of temperature (efficiency decreases with increasing HCE temperature). This is a fundamental aspect of solar-integrated ORC systems; there is an opposing trend between efficiency and operating temperature for any solar collector (negative derivative) as compared to a thermodynamic cycle [positive derivative (efficiency increases with increasing expander inlet temperature)]. This implies that for any collector architecture, and taking into consideration the cooling strategy at the location of the plant, there is an optimum operating temperature where the tradeoff between collector and ORC efficiency is balanced to achieve the best overall plant efficiency.

16.3.2 Steady state performance prediction of solar ORC systems

A steady state model of a solar ORC describes an instantaneous snapshot of the state of the system. On a clear day sunlight impinges on a solar collector, photons are converted to thermal energy at an efficiency calculated from optical and material properties, thermal energy is then conveyed by an HTF at a prescribed flow rate to the evaporator of an ORC, where a working fluid reaches a two-phase, saturated, or superheated state at high pressure, and mechanical work is performed when the working fluid transits through the expander. Finally the high-volume, low-pressure working fluid is condensed, heat is rejected (to ambient air, water, or a secondary thermal loop in, for example, cogeneration), and power output from the expander/generator is divided by the amount of energy captured from the sun to calculate the efficiency. System performance is analyzed assuming that all environmental variables (solar insolation, ambient temperature, etc.) remain “constant enough” over a “long enough” period of time for their effects to propagate through the system (note that the deviation of actual conditions from these assumptions can be quantified to determine the extent of validity of steady state results). This conceptual framework provides the basis for simple models, discussed in this section, and even for complex models (e.g., dynamic models, as described in [Section 16.3.3](#)).

16.3.2.1 Solar collector modeling

To determine the performance of a solar collector (and therefore quantify the HTF temperature and energy content as supplied to the ORC) it is necessary to quantify the energy input:

$$\text{Energy in} = \text{DNI} * \text{aperture of the collector} * \cos\phi \quad (16.3)$$

(where ϕ is the angle of incidence) and a few other relevant parameters which affect the heat loss terms of the model, such as the temperature and mass flow rate of the HTF entering the collector, the ambient temperature and the wind speed. A typical solar collector model will calculate the fraction of sunlight energy lost via the following optical mechanisms:

- Cosine losses (as the sunlight impinges on the aperture at an angle of incidence θ , the actual power intercepted by the collectors is $\cos \phi$, and this can lead to further losses through “walk off” of the beam past the receiver end at the collector side furthest from the sun)
- absorption or scattering at the primary or secondary mirrors (reflective coefficient)
- missing the absorber target (intercept factor)
- shadowing of aperture area (by collector structures or nearby obstructions)
- absorption or scattering at any glass envelope
- reflection off of the absorber surface (inverse of absorptivity)

After these losses are accounted for, the remaining energy is assumed to be absorbed as heat by the system, however, this heat does not entirely result in enthalpy gain of the HTF due to the inevitability of heat losses from the absorber. In typical solar collector models, such as the one developed by [Forristall \(2003\)](#), an energy balance is calculated on the HCE, taking into account its optical parameters (emissivity of absorber tube and glass glazing, if there is glazing), convection transfer at the HCE outer surface to air (as a function of ambient temperature and wind speed) and within any annulus (unless it is evacuated), and radiative losses propagating out from the absorber through any glazing. This involves a solution of the radial temperature distribution across the HCE ([Fig. 16.17](#)), taking into consideration conduction through any HCE materials and the heat transfer from the inner surface of the HCE to the HTF (as a function of the thermophysical properties of the HTF, e.g., thermal conductivity, heat capacity, viscosity, and velocity). Alternatively, empirical correlations can be used to derive the effective heat power absorbed by the fluid in function of the operating conditions ([Dickes et al., 2015](#)).

Such 1D energy balances may be performed on subsections of the HCE line and solved sequentially, where the output HTF temperature of the first node is used as the input HTF temperature for the second node, and so forth ([Fig. 16.18](#)). This method reproduces a temperature gradient along the absorber line, aggregates convection and radiation losses along the line, and estimates the outlet temperature and heat gain of the HTF, which is the relevant input parameter for the ORC model.

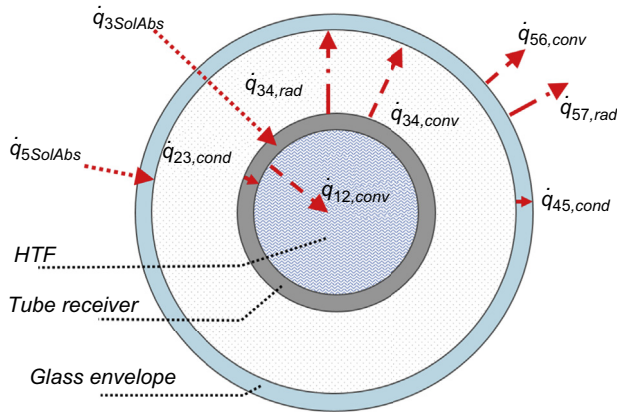


Figure 16.17 Radial temperature distribution across heat collection element boundaries beginning with the interface between the heat transfer fluid (HTF) and the inner diameter of the absorber (1-2), conduction across the absorber (2-3), radiation and convection from the outer diameter of the absorber to the inner diameter of the glass envelope (3-4), conduction across the glass envelope (4-5), and finally convection and radiation from the outer diameter of the glass envelope to the ambient air (5-6) and the sky (5-7) respectively.

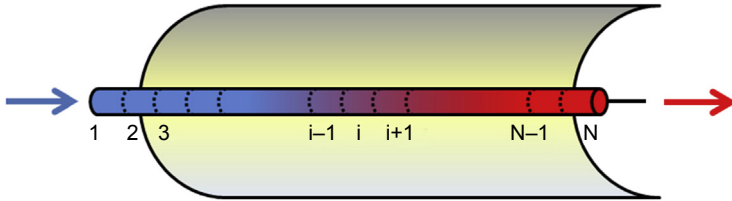


Figure 16.18 A 1D solution for energy balance is applied to sequential nodes with outlet temperatures of the n th node becoming the inlet temperature of the $n + 1$ node.

Note that the heat gain of the HTF (in Watts) divided by the original input term at the collector aperture, is the definition of solar collector efficiency:

$$\eta_{\text{col}} = \frac{\dot{m}\Delta h}{\text{DNI} \cdot A \cdot \cos \phi} \quad (16.4)$$

where ϕ is the angle of incidence of sunlight on the collector aperture.

Once the outlet temperature of the collector is known, it can be input into a detailed ORC model (iteratively, if the HTF inlet temperature of the solar loop is to be determined by the outlet temperature of the ORC vaporizer or preheater) or substituted into a simplified representation of a heat engine such as, e.g., a Chambadal-Novikov (De Parga, 2009) alternative to the Carnot efficiency approximating the operating experience of actual heat engines:

$$\eta_{\text{ORC}} = 1 - \sqrt{\frac{T_c}{T_h}} \quad (16.5)$$

where T_c and T_h are the hot source and cold sink temperatures, respectively.

The overall system efficiency is simply a product of these two component efficiencies (sunlight-to-heat and heat-to-power).

The drawback to this steady state approach lies in the assumption of steady or average DNI and average air temperature, whereas in reality these two driving parameters are constantly varying during normal operation of the ORC and “off-design” efficiencies may differ substantially from the average efficiency. At a minimum, the fluctuation in heat gain due to these changes frequently necessitates the use of thermal buffering, if not outright TES, to stabilize the inlet conditions at the ORC expander (as discussed previously). In order to consider the effects of thermal inertia (of the ORC, the collectors, or any buffering or storage components), it is necessary to make use of a dynamic modeling approach.

16.3.3 *Dynamic performance prediction of solar organic Rankine cycles with thermal energy storage using typical meteorological year data*

A thermal power plant operating from a constant heat source (such as a metered feedstock of combusting coal) is a good candidate for steady state calculations to determine typical performance parameters and specifications of major components, such as expanders and heat exchangers; in general, the system will always function at or very close to the steady state design point. A solar power plant, however, especially one that is expected to handle any load-following (such as an islanded solar microgrid), represents the opposite extreme; both energy delivery and demand will vary potentially quite far from the average values, and this points directly to the inadequacies of a steady state model.

For a solar ORC, the availability and intensity of sunlight is intermittent, and usually not synchronized with the variability in demand. If the operating temperature differential between source and sink is relatively small, as it tends to be with a solar ORC, fluctuations in ambient temperatures (and their dynamic with respect to heat availability) play a correspondingly larger role in the performance of the system.

Typical meteorological year or TMY datasets have been developed to standardize the characterization of such local fluctuations in ambient temperature and irradiance. These consist of historical weather observations for a set of 12 ‘typical’ months, usually derived from a multiyear dataset, with hourly values. This type of data provides the baseline design conditions for engineering a system that can handle dynamics.

A parametric steady state approach to characterizing thermal power generation (solving steady state models for different ambient conditions) can lead to an understanding of off-design behavior, but only a dynamic model can lead to an understanding of which *nominal design*, given the certitude of continual *off-design* conditions, optimizes for the figure of merit (typically minimized total cost per unit of energy delivered). The following sections explain the motivation and approaches used to develop dynamic models to solve optimization problems for solar ORC systems.

16.3.3.1 Conservation of energy and thermal capacitance

Energy balance, or conservation of energy, is the principal framework for modeling power systems. At steady state, the sum of inputs and outputs is equal to zero for a power block. When energy inputs and outputs of a power system do not match for every point in time, the designer can smooth these discrepancies by introducing energy storage. Thus, a solar collector array can operate at its full output, without defocusing collectors, even when this heat flux exceeds the heat flux consumed by the ORC, or an ORC can operate at full output during a brief period of cloudy weather. The difference is simply enthalpy gain (or loss) in the TES component. Even if the available (sensible) TES temperature is declining (e.g., during operation after dusk), varying the HTF flow rate can maintain constant heat flux and evaporating temperature in the ORC as long as the temperature remains above an operating threshold.

In its most simple form, a dynamic solar ORC model extends the energy balance framework by adding mathematical terms for thermal capacitance. TES is generally the largest capacitance in the system, and its relation to other system components is inherently dynamic, as its role in the power system involves either charging or discharging energy while varying its internal energy (in practice, any TES is constantly discharging through heat leakage unless it reaches equilibrium with the surroundings). These transfers of energy happen in time, and consideration of the time discretization of a dynamic model is critical to avoid numerical diffusion type errors.

16.3.3.2 Selection of model timestep

Intuitively, if the residence time of a TES tank is 30 min, a 1 h timestep will fail to conserve and balance energy flows; energy storage calculations based only on initial and final temperatures will fail to account for the increase in temperature of the HTF volume that flowed into, and then out of, the TES tank during the timestep. If a solar collector field with a network of HCEs is used with an ORC, the change in solar collector outlet temperature for a step change in HTF inlet temperature will only manifest after the travel time in the collector (and will reach steady state, if nothing else changes, only after the thermal capacity of the HCEs have equilibrated). If the timestep is shorter than the travel time in a steady state solar collector model, energy conservation residuals will ensue, because within the timestep the gradient of temperatures from inlet to outlet is resolved, when in reality the collectors did not have enough time to propagate the change in inlet temperature all the way through to the outlet. This type of numerical diffusion error is framed by the Courant-Friedrichs-Lewy (CFL) condition, which holds that, in numerical simulations using finite difference methods, the time discretization must contain the analytical phenomenological domain influenced by the initial conditions (Courant et al., 1967). Selection of an appropriate timestep as a function of the spatial discretization of components in Solar ORC dynamic simulation meeting the CFL condition can thus include:

$$\frac{\text{thermal capacity(J)}}{\text{thermal power(J/s)}} > \text{timestep} < \frac{L_{\text{HCE}}(\text{m})}{v_{\text{HTF}}(\text{m/s})} \quad (16.6)$$

(the second boundary above the timestep could be eliminated by the use of a dynamic solar collector model, similar to the approach taken with a TES tank). Other conditions, for example, volumes and flow rates in tanks, may be considered as well, but in general the consideration of dynamic simulation timestep involves the tradeoff between impractical computational effort at infinitesimal timesteps and numerical failure to converge at timesteps too large to meet the CFL condition.

16.3.3.3 Control strategy

The dynamic simulation of a solar ORC requires definition of control parameters and strategies (defining initial and operational modes), and presents an opportunity to optimize these in software before implementing them in practice. In a dynamic solar ORC simulation, the various components, including TES, are connected to each other via mass and energy flows, which may in turn depend on external conditions. Once the operational modes have been defined (e.g., by system temperatures or pressures, or by external conditions), conditional statements can be used with parameter threshold values to trigger selection between modes based on conditions for the given timestep.

The major controllable variables in a solar ORC are the flow rates of the HTF and the working fluid, the speed of the cooling fan/pump, the tracking of the collectors (on/off), and the setpoint of the expander rotational speed. Various scenarios with different operating setpoints for these components can be articulated, with real time acquisition of sensor data triggering the shift from one operational mode to another in the operation of a real system (and conditional statements embodying this behavior in the dynamic simulation).

The number of unique modes and parameter combinations triggering mode shifts are too extensive and application specific to describe comprehensively, but a few examples are given here for illustration.

Typical startup sequence

- When DNI reaches a certain threshold (e.g., 200 W/m²), solar collectors are set to tracking mode
- When temperature in the absorber of the solar collector reaches a certain threshold (depending on the application) HTF flow is initiated
- When temperature of the HTF entering the ORC vaporizer (potentially supplied from TES) reaches a certain threshold, the ORC is engaged, i.e., working fluid pump (and potentially expander variable frequency drive) and condenser cooling fan/pump are activated

Example operational considerations

- To maintain the design pressure ratio across the expander, the HTF flow rate and condenser heat rejection rate may be modulated on the basis of, for example, degrees of working fluid superheat at the expander inlet or temperature pinch in the condenser
- In the event of a cloud passing or dusk (DNI lower threshold being reached), the HTF flow in the collector field may be stopped to avoid rejecting heat at the CSP HCE, while HTF flow in the TES–ORC loop may be maintained for continuous power output (provided sufficient HTF temperature, above a set threshold, is available from the TES).

Operational systems may be shut down normally (according to a reverse of the above sequence) or due to some perturbation such as a cloud passing, low temperature in the HTF loop, or error states such as locked rotors, cavitation in the working fluid pump, excessively high temperature, etc. One specialized case of exceptional shut-down that can be easily diagnosed is frequent defocusing of a solar field due to overtemperature conditions; generally this points to an undersizing of the TES and/or the ORC components relative to the solar field in the system design.

The various thresholds deployed in the control system and the modes associated with various combinations of sensor inputs are themselves also subject to dynamic optimization. For example, [Ireland et al. \(2014\)](#) performed a parametric sweep of HTF temperature thresholds for engaging an ORC and found that system performance (in dynamic simulation of a solar ORC with TES) is highest when the ORC is only turned on when approaching the maximum allowable HTF temperature, as opposed to the minimum viable HTF temperature or some intermediate value ([Ireland et al., 2014](#)). [Mitterhofer and Orosz \(2015\)](#) conducted a parametric sweep of condenser size, temperature defect, and pressure ratios in a dynamic simulation of a pilot 3 kW_e solar ORC (installed by STG International at Eckerd College in St. Petersburg, FL) to identify optimum expander volume ratio, condenser size, temperature defect, and coolant fan effort setpoints for variable ambient temperatures, using TMY data and leveled cost as an objective function ([Mitterhofer and Orosz, 2015](#)). Observations from this study included the cost advantages of using smaller air cooled condensers with a higher temperature defect in the ORC cycle; the efficiency gains from a large condenser are outweighed by the relative expense of this component.

Because of the specificity of ambient climate conditions and project purpose and sizes, results from such studies, while informative, are typically not generalizable, and detailed analysis are required to identify optimized control strategies, operational modes, and threshold variables for each application. Furthermore, even for a given technology design, control strategies and threshold variables must be validated independently for the particular load profile and meteorological conditions experienced at each new deployment location.

16.3.4 Solar Organic Rankine Cycle optimization and economics

A physics-based representation of a solar ORC with thermal capacitance is essential for accurate prediction of performance and sizing of components. While performance and efficiency are influential metrics, several other factors may bear on the design of the system, as conceived in the context of a real-world application. The decision to deploy solar collectors with an ORC (and potentially TES) and determining appropriate sizing amongst the components, will usually be made only after evaluating specific project criteria; cost effectiveness compared to alternative options usually being foremost among them. The analysis of performance and cost of various configurations necessarily entails design engineering of the system for the particular application which, to the extent that applications vary widely and are sited across a range of locations with unique irradiance and climate characteristics, poses both a technical and economic challenge (cost of engineering

hours, time required to complete designs and dynamic simulations, etc.). These challenges have undoubtedly limited the deployment of solar ORCs historically.

16.3.5 Application engineering and system analysis

Many variables impact solar ORC project design, and it can be difficult to know where to start because the most important factors may be different in each individual case. The following list of considerations is neither comprehensive nor necessarily in order of priority but can provide a starting point for conducting a prefeasibility analysis. Before engaging in a solar ORC project, relevant information to gather can include:

- What is the location of the application? With this known, the closest station with TMY data can be used to characterize the available irradiance and ambient temperature patterns.
- What is the shape and variability of the load profile? What is the peak load (kW), total daily load (kWh), and variability in load throughout the day? What is the form of the load to be supplied (i.e., are there both thermal and electrical loads)? Is a profile of the demand well constrained in the time domain across major operating modes? Is thermal demand in the form of process or building heating, or does it require cooling? What are the target heating or cooling temperatures? Is there seasonality to the load? These data are critical for accurately parameterizing a dynamic simulation of the system and assessing the need for TES.
- Is there integration with any other thermal source (e.g., biomass, fossil fuel, geothermal, waste heat, etc), and if so, what is the capacity, availability, and cost of the alternative source? These data will influence the relative sizing of both the solar component and TES and will drive overall project economics.
- Given the temperatures involved, what type of solar collector, HTF, and ORC working fluid are most suitable?
- Given the size of the application and availability of expander—generator packages, which expander type (positive displacement or turbomachine) is suitable?
- Is the type of heat rejection (dry, wet, or water) constrained (e.g., lack of available water in desert regions), or will the decision be made on a least cost basis?
- What is the source of project finance and what are the terms, e.g., for debt financing what would be the loan tenure and interest rate?
- What is the market value of the system outputs?
- What standard alternative systems (gas burners, heat pumps, PV and battery systems, etc.) are available for the application, and what would be the total cost of deploying a competing technology?

These data and others specific to the project will inform the decision process for whether a solar ORC is an economically viable option and will guide the modeling process for deciding how to implement a solar ORC or hybrid system.

16.3.5.1 Design of Organic Rankine Cycle systems for use with solar collectors

Once the temperature regime of the system is determined, the next important specification is the selection of an ORC working fluid, which influences the expander configuration via the pressure—volume ratio of the ORC and the size of heat exchangers for thermal input and heat rejection. In a parametric study of solar ORC performance and

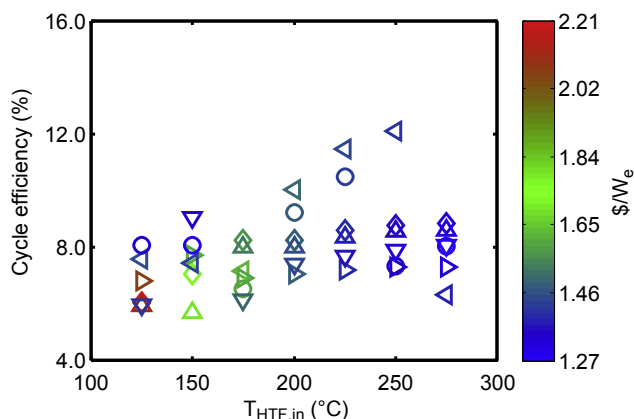


Figure 16.19 Specific cost ($\$/W_e$) and cycle efficiency for various working fluids evaluated at heat transfer fluid (HTF) inlet temperatures from 125 to 275°C for a 5 kW_e Organic Rankine Cycle. Δ , butane; \triangleright , isobutane; $<|$, R134a; \circ , R161; ∇ , R152a (Garg et al., 2015).

economics, Garg et al. (2015) investigated the specific costs of power for 16 zero-Ozone Depletion Potential (ODP) and positive condenser pressure (saturation pressure corresponding to 45°C) working fluids for HTF supply temperatures between 125 and 275°C (the top five most cost efficient fluids are shown in Fig. 16.19). This analysis showed that specific costs of electricity between 1.25 and 2 USD/W are achievable for optimized solar ORC systems using a parabolic trough solar collector, with cost advantages at increasing operating temperatures (Garg et al., 2015). Note that a significant result of this study is that cost efficiency and thermodynamic efficiency are not necessarily correlated when decisions, for example, to recuperate or not and variable condenser size/fan duty are optimized for cost.

16.3.6 Specific and levelized costs of power generation

Solar ORCs have historically been developed more often for research and demonstration purposes than for commercial applications. Where the decision to deploy depends on market forces, various financial metrics such as internal rate of return (IRR), payback period, total cost of ownership, discounted cash flow, etc., may be selected as a figure of merit for a project developer. To varying degrees, poor economic performance coupled with the necessity for complex dynamic simulation to arrive at calculated performance and optimized cost configurations may account for the scarcity of commercial solar ORC installations to date.

Specific capital costs for a nominal power output are relatively straightforward to calculate and compare among alternatives when the output is electrons (i.e., $\$/W$) but may be more difficult to assess or present in a simple metric, when the outputs are combined heat and power. Even for electricity, $\$/W$ for solar plants is typically indicated in peak Watts ($\$/W_{\text{peak}}$), whereas the daily energy generated by an equivalent nameplate capacity system could vary significantly between, for example, fixed tilt PV systems and tracking CSP systems due to the latter's higher production levels in the

morning and evening. Levelized energy costs can be calculated by dividing capital plus operating and maintenance costs by the total amount of energy produced (estimated via simulation methods), though this too is generally more useful for electricity than for thermal outputs and is difficult to assess in scenarios where the value of outputs changes (such as with time-of-use pricing for electricity).

If the objective of the project is to maximize IRR for a given amount of investment through the sale of electricity to a single off-taker, the evaluation of the project would utilize different metrics than in the case of, say, an industrial microgrid with cogeneration. In the former project, the use of storage and dynamics of time-of-use pricing would be important considerations, while in the latter the evaluation framework could be minimizing the total cost of ownership or comparison against the status quo alternative, which is likely to have a well-known cost. Projects that are designed to maximize profit through sale of energy as a commodity are therefore conceptually different from projects where the objective is to meet a particular energy demand profile at minimized cost.

Where cost minimization for a particular demand curve is sought, a general figure of merit is the net present cost (NPC) (Orosz et al., 2013):

$$\text{NPC} = I_0 + \sum_{t=0}^n \frac{O_t + M_t}{(1+r)^t} \quad (16.7)$$

where I_0 is the initial cost of the equipment, n is the service life in years, O_t and M_t represent Operating and Maintenance costs in year t , and r is the discount rate (Guth, 2009). Operating cost (O_t) is a unique function of the technology (e.g., fuel consumption) while maintenance cost (M_t) can be generalized as a function of the initial costs in two terms: a constant annual service component and a linearly increasing component for repairs due to wear with age, as shown in Eq. (16.8).

$$M_t = \frac{f}{n} + \frac{f \cdot (1-a)}{n^2} \cdot (2t-1) \quad (16.8)$$

where f is the fraction of total maintenance costs with respect to initial costs, and a is a coefficient expressing the fraction of regular service costs with respect to total maintenance costs (including incremental repairs). Various values for these coefficients can be found in the literature or in manufacturers manuals and maintenance procedures (NREL, 2013).

For demand driven projects, NPC is a valuable tool for comparison between alternative energy system configurations serving the same purpose, but other figures of merit may be preferable depending on the planner's objectives and type of available finance and the target applications of the system.

16.3.7 Optimization tools

Once a figure of merit (typically economic) is selected, the process for optimizing according to this metric involves varying system level approaches (solar ORC or

some competing solution), components, configurations, control strategies, etc., while evaluating the systems against the application conditions and known dynamics (DNI, ambient temperature, demand, and possibly time-of-use pricing). The calculation for the economic figure of merit is added to the already complex dynamic simulation of energy flows in a solar ORC or hybrid system, and in most cases an exhaustive search of the inherently irregular parameter space will be prohibitively expensive/slow to compute even using multicore cloud computing resources. This motivates the use of optimization algorithms, a diverse and specialized set of tools that can achieve maximization or minimization of an objective function with drastically reduced computational effort.

The various approaches, described in more detail in Chapter 7, include evolutionary and gradient methods, among others. The genetic algorithm (GA), inspired by biological evolution, “breeds” a population of ever more optimized solutions through successive generations, escaping the local maxima or minima that can trap gradient-ascent (“hill-climbing”) methods via “mutations” that sample more widely in the search space. Particle swarm optimization (PSO) similarly employs a population of solutions, with the candidates initially dispersed and the vector of the “swarm” in the search space is parametrically updated to move towards the “leader” (optimum metric for a given search timestep) without reference to any evolutionary operators such as “breeding”, “crossover”, or “mutation.” Once the leader is established in the monotonic region of the global optimum, the optimization can drop the swarm and switch to a faster gradient-ascent/descent from the leader’s position, however, this requires either some understanding of the search space or a metric for identification of the globally optimum ‘hill.’ GA and PSO, as well as more traditional gradient methods, can be applied to solar ORC optimization to greatly reduce computation time; for deeper analysis into their relative benefits the reader is referred to the literature ([Hassan et al., 2004](#)).

16.3.8 Case study: hybrid solar Organic Rankine Cycle microgrid system

While the recent advent of inexpensive crystalline silicon PV panels may have undermined the economic rationale for standalone solar ORC systems, viable applications for the technology exist in niches created by the need for storage, the utility of cogeneration, and the availability of inexpensive alternative supplies of thermal energy. One scenario that can meet these conditions is the deployment of a solar ORC within an isolated, hybrid microgrid consisting of PV and fossil fueled backup generation, and serving community combined heat and power loads ([Fig. 16.20](#)).

While renewable energy technologies are preferable for many reasons (long-term sustainability, emissions reductions, and even price considerations in extremely rural locations), to achieve 100% availability (capacity factor near to 1) in such a system with only PV panels and without ever resorting to a backup generator would be prohibitively expensive under the current price structure of deep cycle batteries (>250 USD/kWh). The addition of a solar ORC with TES can reduce (though not fully eliminate) the need for battery storage, but may only be economically justified in cases where a second

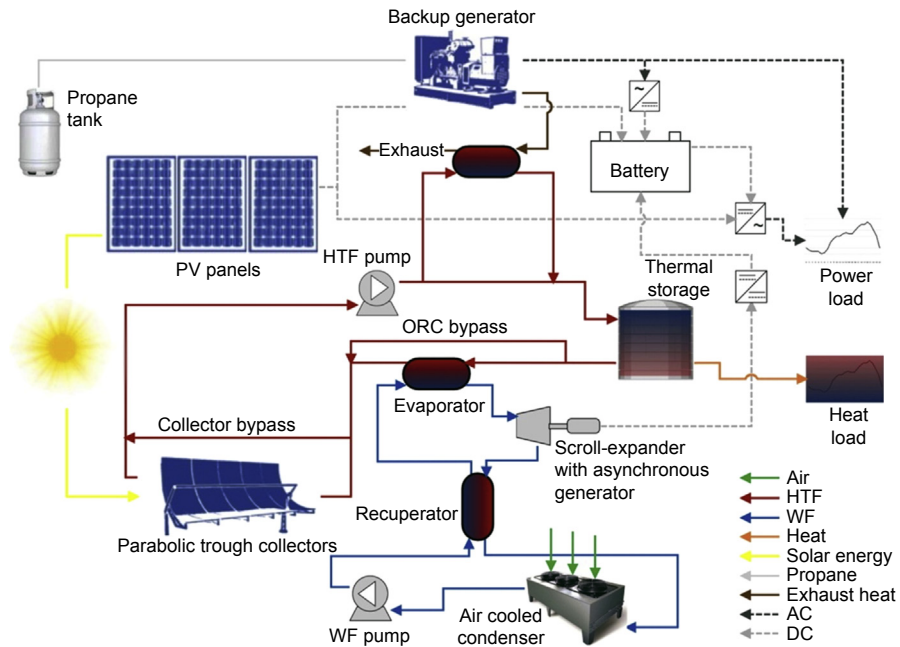


Figure 16.20 Hybrid Microgrid including photovoltaic (PV), concentrating solar power (CSP), Organic Rankine Cycle (ORC), thermal energy storage (TES), and a backup generator using liquefied petroleum gas (LPG).

Adapted from Mitterhofer, M., Orosz, M., 2015. Dynamic simulation and optimization of an experimental micro-CSP power plant. *PowerEnergy*. doi:10.1115/ES2015-49333.

use of the solar heat is specified, such as for heating institutions or dormitories. The need for a reciprocating internal combustion engine generating set to ensure high availability, however, also provides an opportunity for waste heat recovery from the approximately 60% of the fuel exergy that leaves with the exhaust (Teng and Regner, 2006). Note that while an optimum operating temperature for the ORC can be found for a given location and solar collector type (discussed in Section 16.3.1), the introduction of a second heat stream may influence the optimum operating temperature of the hybrid system due to the tradeoffs involved with a second heat exchanger and the temperature of the waste heat stream, driving the need to simulate the entire system simultaneously.

Definition of loads for a new hybrid microgrid could be derived from a survey and inventory method to predict energy consumption, but a more reliable approach would be to produce a probabilistic distribution function from a dataset of measured loads at comparable communities (i.e., ones which were only recently connected to the grid and have similar size and economic activity levels) (Orosz and Mueller, 2015). For institutional thermal loads, a building envelope model such as developed under Annex C of ISO 13790 (2008) could be parameterized for the structure of interest and exercised in dynamic simulation with local TMY data to produce a time distribution of thermal demand. Once the load profiles are established with reasonable granularity

(hourly or better), dynamic simulation of the hybrid microgrid can be performed where the allocation of PV panels, batteries, CSP collectors, and TES can be varied parametrically through an optimization method (such as PSO) within a control framework for prioritizing energy flows between components and to the load. A simple example framework for this application would be:

1. While the sun is shining, the load is supplied (via inverter) from the PV directly to the extent that PV power is sufficient to cover the load
2. If the PV power is insufficient to meet the load, the load is supplied from a battery bank (via inverter), as long as the battery storage is not depleted
3. If the PV power exceeds the load, the excess energy charges the battery bank
4. While the sun is shining the CSP collectors charge the TES, until the TES capacity is reached
5. Thermal loads are supplied by discharging the TES
6. If the TES is insufficient to supply the thermal load, a backup (fueled) source is engaged for heat production
7. If TES reaches overtemperature limits, the ORC is engaged to convert heat to electricity (except in case 9 below)
8. If the ORC is engaged while the PV is supplying power, its effect is to augment the PV power and conforms to 2 and 3 (above)
9. If the battery bank reaches a full state of charge (SOC) while PV power and/or ORC power is exceeding the load, the excess PV power is directed to a load dump or sections of the array are open circuited, and the ORC is disengaged
10. If the TES reaches overtemperature limits while case 9 holds, the CSP collectors are defocused
11. If the battery reaches a low SOC threshold while the TES is charged, the ORC is engaged
12. If the battery reaches a lowest SOC threshold while the TES is discharged and there is no PV power, the backup generator is engaged
13. If the generator is engaged and the battery state of charge or the TES SOC reaches a (design point) recharge threshold, the generator is disengaged.
14. If the generator is engaged and the sun resumes shining, the generator is disengaged (to preserve battery capacity for the solar systems).

Other special cases can be envisioned but the above is an outline of a simple hierarchy of power flows that can be considered when sizing and optimizing a hybrid microgrid and implementing its control strategy.

A one year simulation is likely to be sufficient for extrapolation across the project lifetime, as a multiyear simulation would not produce results significantly different enough to justify the additional computational effort. The annual simulation would proceed with load and TMY input at each timestep, track the SOC of the storage components, and track the cumulative fuel usage in the backup generator (which constitutes the operating cost), all while ensuring that the demand (at each timestep) is met.

If the objective function of the microgrid simulation is determination of the minimized cost-recovery tariff for electricity and heat, then for a given combination of load dynamic and location there will be some configuration of the PV, battery, CSP, TES, and ORC components that is optimum (note that under some circumstances this could be a size of zero for a particular component). When performing the optimization, it is useful to set boundaries for the parameter space to be explored, i.e., whereas the generator is sized to meet the peak load with a factor of safety, the PV

or ORC components might be varied parametrically from zero to some multiple of the peak load (not more than 5). The battery and TES components could likewise be varied from zero to some multiple of an average day's energy requirements, calculated from integrating the load profile (not more than 3).

The cost functions of all components and the financial terms of the project finance (loan tenure and interest) being known, the objective function of minimized cost-recovery tariff can be solved for with an optimization algorithm searching the tariff space in a project lifetime cash flow model accounting for initial and recurring costs: operations, maintenance, loan repayment, and battery replacement (a function of battery type and the number of charge cycles which is tracked in the dynamic simulation). Identification of the cost minimizing solution enables one to proceed with specific component selection and provides a foundation for sizing and engineering design of the microgrid. To date, the case study just described has not been realized, and therefore validation of the simulation and hybrid design approach awaits future research and piloting programs.

References

- Ait-Baha CSP Pilot Plant - Technical Datasheet.
- American Inventor Uses Egypt's Sun for Power, July 2, 1916. *Appliance Concentrates the Heat Rays and Produces Steam*. New York Times.
- ASTM, 2012. Standard tables for reference solar spectral irradiances: direct normal and hemispherical on 37° tilted surface. ASTM 1–21.
- Bado, G., Tomei, G., Angelino, T., Gaia, M., Macchi, E., 1979. The Ansaldo 35 kW solar power system. In: *Proceedings of the Silver Jubilee Congress*, pp. 1090–1094.
- Baral, S., Kim, D., Yun, E., Kim, K., 2015. Experimental and thermoeconomic analysis of small-scale solar organic rankine cycle (SORC) system. *Entropy* 17 (4), 2039–2061.
- Barutti, A., Pedrick, W.G., Angelino, G., Gaia, M., Macchi, E., 1984. Ansaldo solar thermal and photovoltaic plants located at Ballajura, western Australia. In: *Proceedings of the 8th Solar World Congress 1983, Biennial Congress of the International Solar Energy Society*, vol. 3, pp. 1572–1576.
- Bronicki, L., 2013. Short review of the long history of ORC power systems. In: *ASME ORC13*.
- Canada, S., Brosseau, D., Kolb, G., Moore, L., Cable, R., Price, H., 2005a. Status of APS 1-Mwe parabolic trough project. In: *2005 DOE Solar Energy Technologies*.
- Canada, S., Cohen, G., Cable, R., Brosseau, D., Price, H., 2005b. Parabolic Trough Organic Rankine Cycle Solar Power Plant NREL CP/-550-37077. Denver, CO.
- Chambers, T., Raush, J., Russo, B., 2014. Installation and operation of parabolic trough organic rankine cycle solar thermal power plant in south Louisiana. *Energy Procedia* 49, 1107–1116.
- Courant, R., Friedrichs, K., Lewy, H., March, 1967. On the partial difference equations of mathematical physics. *IBM Journal* 11.
- De Parga, G.A., 2009. The Curzon-Ahlborn Efficiency for Three Different Energy Converters, vol. 1, pp. 1–4.
- Delgado-Torres, A.M., García-Rodríguez, L., October 2007. Comparison of solar technologies for driving a desalination system by means of an organic Rankine cycle. *Desalination* 216 (1–3), 276–291.

- Dfid, 2010. A potential role for an AMC in supporting dish/Stirling concentrating solar power, case study annex. Advance Market Commitments for Low-carbon Development. http://www.vivideconomics.com/wp-content/uploads/2010/03/Micro_CSP_case_study.pdf.
- Dickes, R., Dumont, O., Declaye, S., Quoilin, S., Bell, I., 2014. Experimental investigation of an ORC system for a micro-solar power plant. In: Proceedings of the Purdue Conferences 2014.
- Dickes, R., Lemort, V., Quoilin, S., 2015. Semi-empirical correlation to model heat losses along solar parabolic trough collectors. In: Proceedings of ECOS 2015.
- Duffie, J.A., Beckman, W.A., Worek, W.M., 1994. Solar Engineering of Thermal Processes, second ed. Wiley.
- Dumont, O., Quoilin, S., Lemort, V., June 2015. Experimental investigation of a reversible heat pump/organic Rankine cycle unit designed to be coupled with a passive house to get a Net Zero Energy Building. International Journal of Refrigeration 54, 190–203.
- Einav, A., 2004. Solar energy research and development achievements in Israel and their practical significance. Journal of Solar Energy Engineering 126 (3), 921.
- Electratherm METU NCC Solar ORC Report. Electratherm Website, 2010.
- Fenton, D.L., Abernathy, G.H., Krivokapich, G.A., Otts, J.V., 1984. Operation and evaluation of the Willard solar thermal power irrigation system. Solar Energy 32 (6), 735–751.
- Forristall, R., 2003. Heat Transfer Analysis and Modeling of a Parabolic Trough Solar Receiver Implemented in Engineering Equation Solver. Golden, CO.
- Galvez, J.B., 2010. Powersol: Mechanical Power Generation Based on Solar Thermodynamic Engines - Final Report.
- Garg, P., Orosz, M.S., Kumar, P., Dutta, P., 2015. Thermo-economic Evaluation of ORCs for Various Working Fluids, pp. 1–16.
- Georges, E., Declaye, S., Dumont, O., Quoilin, S., Lemort, V., 2013. Design of a small-scale organic rankine cycle engine used in a solar power plant. International Journal of Low-Carbon Technologies 8 (Suppl. 1), 1–8.
- Goswami, D.Y., Stefaakos, E., Rahman, M.M., Aydin, S., Reedy, R., 2013. Design, Construction and Operation of CSP Solar Thermal Power Plants in Florida.
- Grirate, H., Zari, N., Elamrani, I., Couturier, R., Elmchaouri, A., Belcadi, S., Tochon, P., 2013. Characterization of several Moroccan rocks used as filler material for thermal energy storage in CSP power plants. Energy Procedia 49, 810–819.
- Guth, J.H., 2009. Resolving the Paradoxes of Discounting in Environmental Decisions, vol. 2008, pp. 95–114.
- Hassan, R., Cohanin, B., de Weck, O., Venter, G., 2004. A comparison of particle swarm optimization and the genetic algorithm. American Institute of Aeronautics and Astronautics 1–13.
- Helwa, N.H., Bahgat, A.B.G., El Shafee, A.M.R., El Shenawy, E.T., Bahgat, A.B.G., El Shafee, A.M.R., El Shenawy, E.T., November 2000. Maximum collectable solar energy by different solar tracking systems maximum collectable solar energy by different solar tracking systems. Energy Sources 22.
- ISO 13790:2008 Energy performance of buildings – Calculation of energy use for space heating and cooling.
- Ireland, M., Orosz, M., Brisson, J., Desideri, A., Quoilin, S., 2014. Dynamic modeling and control system definition for a micro-CSP plant coupled with thermal storage unit. In: ASME Turbo Expo 2014: Turbine Technical Conference and Exposition GT2014-27132.
- Kalogirou, S.A., 2004. Solar thermal collectors and applications. Progress in Energy and Combustion Science 30 (3), 231–295.
- Kane, M., Larrain, D., Favrat, D., Allani, Y., 2003. Small hybrid solar power system. Energy 28 (14), 1427–1443.

- Kiceniuk, T., 1985. Development of an Organic Rankine-Cycle Power Module for a Small Community.
- Kohlenbach, P., Mcevoy, S., Stein, W., Burton, A., Wong, K., Lovegrove, K., Burgess, G., Joe, W., Coventry, J., 2006. A new parabolic trough solar collector. In: Australian and New Zealand Solar Energy Society, pp. 1–8.
- Kolb, G.J., 2011. Evaluation of annual performance of 2-Tank and thermocline thermal storage systems for trough plants. *Journal of Solar Energy Engineering* 133 (3).
- Kuravi, S., Trahan, J., Goswami, D.Y., Rahman, M.M., Stefanakos, E.K., 2013. Thermal energy storage technologies and systems for concentrating solar power plants. *Progress in Energy and Combustion Science* 39 (4), 285–319.
- Lovegrove, K., Stein, W., 2012. *Concentrating Solar Power Technology - Principle, Developments and Application*. Woodhead Publishing.
- Manolakos, D., Papadakis, G., Kyritsis, S., Bouzianas, K., February 2007. Experimental evaluation of an autonomous low-temperature solar Rankine cycle system for reverse osmosis desalination. *Desalination* 203 (1–3), 366–374.
- Mitterhofer, M., Orosz, M., 2015. Dynamic simulation and optimization of an experimental micro-CSP power plant. *PowerEnergy*. <http://dx.doi.org/10.1115/ES2015-49333>.
- Moustafa, S., Hoefler, W., El-Mansy, H., Kamal, A., Jarrar, D., Hoppman, H., Zewen, H., 1984. Design specifications and application of a 100 kWe (700 kWth) cogeneration solar power plant. *Solar Energy* 32 (2), 263–269.
- Mueller, A., Orosz, M., Kumar Narasimhan, A., Kamal, R., Hemond, H., Goswami, Y., 2016. Evolution and feasibility of decentralized concentrating solar thermal power systems for modern energy access in rural areas. *MRS Energy Sustainability* 3.
- N'Tsoukpoe, K.E., Azoumah, K.Y., Clerc, E., Zmuda, J., Gaye, M., Seshie, Y.M., Kenda Nitedem, S.E., 2014. CSP4Africa: développement d'un pilote économiquement viable d'une mini-CSP pour la production d'électricité pour mini-réseau en Afrique.
- NREL, 2013. "Distributed Generation Renewable Energy Estimate of Costs (Online). Available: http://www.nrel.gov/analysis/tech_lcoe_re_cost_est.html.
- NREL - CSP Projects Review.
- Orosz, M., Mueller, A., 2015. Dynamic simulation of performance and cost of hybrid PV-CSP-LPG generator micro grids with applications to remote communities. In: *ASME Power & Energy Conference* 2015.
- Orosz, M.S., Quoilin, S., Hemond, H., 2013. Technologies for heating, cooling and powering rural health facilities in sub-Saharan Africa. *Proceedings of The Institution of Mechanical Engineers Part A-journal of Powerand Energy* 227 (7), 717–726.
- Orosz, M.S., 2012. *Thermosolar and Photovoltaic Hybridization for Small Scale Distributed Generation: Application for Powering Rural Health*. Massachusetts Institute of Technology.
- Orosz, M., 2015. Photovoltaics and concentrating solar power: why hybridization makes sense. *SPIE Newsroom* 1–4.
- Pytilinski, J.T., 1978. Solar energy installations for pumping irrigation water. *Solar Energy* 21 (4), 255–262.
- Reda, I., Andreas, A., 2008. *Solar Position Algorithm for Solar Radiation Applications*.
- Rieu, V., September 2012. A 10 kW solar power plant for rural electrification. In: *Proceedings of SolarPACES* 2012.
- Saitoh, T., Yamada, N., Wakashima, S., 2007. Solar Rankine cycle system using scroll expander. *Journal of Environmental Engineering* 2 (4), 708–719.
- Simonnot, G., Louche, A., Decanini, Y., 1987. Three years exploitation of the 100 kWe Ajaccio solar power plant. In: *Proceedings of the ISES Solar World Congress*, pp. 1588–1592.

- Singh, H., Saini, R.P., Saini, J.S., 2010. A review on packed bed solar energy storage systems. *Renewable & Sustainable Energy* 14 (3), 1059–1069.
- Tabor, H.Z., Doron, B., 1990. The Beith Ha'Arava 5 MW(e) Solar Pond Power Plant (SPPP)—Progress report. *Solar Energy* 45 (4), 247–253.
- Tabor, H., 1981. Solar ponds. *Solar Energy* 27 (3), 181–194.
- Tchanche, B.F., Lambrinos, G., Frangoudakis, a., Papadakis, G., April 2010. Exergy analysis of micro-organic Rankine power cycles for a small scale solar driven reverse osmosis desalination system. *Applied Energy* 87 (4), 1295–1306.
- Teng, H., Regner, G., 2006. Achieving high engine efficiency for heavy-duty diesel engines by waste heat recovery using supercritical organic-fluid Rankine cycle. In: SAE Pap., No. 724.
- Thakur, D., 2013. A case study on the solar biomass hybrid distributed power generation project at Shive village. In: Odisha Solar Conference.
- Wang, X.D., Zhao, L., Wang, J.L., Zhang, W.Z., Zhao, X.Z., Wu, W., March 2010. Performance evaluation of a low-temperature solar Rankine cycle system utilizing R245fa. *Solar Energy* 84 (3), 353–364.
- Wang, X.D., Zhao, L., Wang, J.L., 2011. Experimental investigation on the low-temperature solar Rankine cycle system using R245fa. *Energy Conversion and Management* 52 (2), 946–952.
- Weinrebe, 2007. Renewable energy - technology, economics and environment. In: *Solar Thermal Power Plants* (Chapter 5).
- Zhang, S., Wu, Z.H., Zhao, R.D., Yu, G.Y., Dai, W., Luo, E.C., 2014. Study on a basic unit of a double-acting thermoacoustic heat engine used for dish solar power. *Energy Conversion and Management* 85, 718–726.

Organic Rankine Cycle systems for large-scale waste heat recovery to produce electricity

17

H. Tian, G.Q. Shu

Tianjin University, Tianjin, China

Although the steam Rankine Cycle (SRC) and the Organic Rankine Cycle (ORC) share the same principle, they have many differences. ORC has been the focus of many research groups and companies in recent years due to its good performance in waste heat recovery (WHR). The comparison between ORCs and SRCs, as well as the application of ORC for WHR are elaborated in this chapter.

17.1 The comparison between Organic Rankine Cycles and steam Rankine Cycles

ORC originated from SRC by sharing the same principle but using different working fluids. Water is the only working fluid for SRC, while plenty of organic fluids are suitable for ORC. The heat source is the primary and decisive indicator for the selection between ORC and SRC. Generally, the differences in the properties of the working fluids make the ORC suitable for medium/low temperature small heat sources, while SRC is the best option for medium/high temperature large heat sources.

Common heat sources for SRCs are: coal, natural gas, oil combustion, and nuclear fission, which provide medium/high-grade heat sources with temperatures above 500°C. Given the high-energy density of these heat sources, the SRC operates well in large-scale power plants with a power range above 100 MW. Actually, the SRC systems are quite mature applications in these heat sources, with well-designed commercial systems and the mass production of components.

By contrast, ORC has few advantages over SRC under these conditions. Firstly because the critical temperatures of commonly used organic fluids (<300°C) are mostly lower than that of water (373.95°C), which limits the application of organic working fluids in high temperature conditions. Secondly, the high temperature heat source will easily cause decomposition of most regular organic fluids. Besides this, the high prices of organic fluids show economic disadvantages compared with water in these large-scale energy conversions.

As for the heat transfer coefficients (HTC) of water and commonly used organic working fluids, no obvious advantage has been revealed, since the HTC depends on

not only fluid properties but also flow properties, such as, velocity, as well as flow pass structures and arrangements. Approximate values of HTC of water and commonly used organic working fluids in forced convection are between 500 and 10,000 W/(m² K).

Although fossil fuel combustion and nuclear fission are still the major power sources, many renewable sources and technologies, such as, solar power, geothermal power, WHR, and biomass are the surging and promising ways to relieve the energy pressure on the world. Heat sources in these conditions are generally available at medium/low temperatures with a range of 90–500°C. In these applications, the organic working fluids in Rankine cycles are preferable versus steam for three reasons:

17.1.1 Organic Rankine Cycles are able to obtain higher thermal efficiency than steam Rankine Cycles

According to the slope shapes of saturation curves of fluids, major ORC working fluids are “dry” or “isotropic” fluids which do not need superheat in traditional subcritical operations. On the contrary, as a typical wet fluid, water has a negative slope on its saturation curve. So high-degree superheat is indispensable for SRC to avoid the binary phase in the expansion process. The superheat prevents water droplets from corroding the power machine and hitting the turbine blades at a high speed. However, high-degree superheat brings a greater efficiency disadvantage by reducing the evaporation temperature and the average temperature of the heating process. The low-efficiency drawback of SRC is especially obvious when the temperature difference between the hot and cold sides is small. While the temperatures of heat sources are better followed by the organic fluids with a nonrequirement of superheat, higher efficiency is thus easier to achieve. For example, the efficiency of SRC is only 11.7% when the expander inlet temperature is 200°C, which is less than that of R123 at 120°C (Li et al., 2012).

Besides better temperature matching between heat sources and working fluids, temperature differences of the ORC at the evaporators are typically less than those of SRCs. Hence, irreversibility at the evaporator of the ORC is less than that of steam ones and higher exergy efficiency can be obtained (Astolfi et al., 2014).

17.1.2 Turbo machinery of an Organic Rankine Cycle is less complicated and easier to develop than that of a steam Rankine Cycle

Firstly, as the ORC is usually a better choice in medium/low-temperature heat source conditions than the SRC, which results in a lower power capacity.

Secondly, the heat capacity and the latent heat of water are much larger than most organic fluids. For example, the latent heat of water at 100°C is 2257 kJ/kg, which is 16 times larger than that of R123 at the same temperature. Therefore, under the same

heat source condition and with the same pinch point restriction, SRC requires a much smaller mass flow rate through the power conversion process. The unconventionally small mass flow rate brings great technological difficulties in designing and manufacturing expansion components. On the contrary, most ORC systems operate with reasonable mass flow rates and allow conventional technologies to be used and a easier developing of efficient low power capacity ORC turbo machinery. Thus, the R&D time and expenses are largely reduced.

Thirdly, the critical pressure of water is higher than most organic fluids. Applying the same evaporating and condensing temperatures, the expansion ratio of SRC at the turbine outlet and inlet is significantly larger than that of ORC. For example, the ratio of water saturated pressure at 100°C to that at 20°C is about 43.35, whereas it is only 10.39 for R123 (Tian et al., 2012). In order to attain the high expansion ratio, turbines of steam cycles will inevitably be large and expensive, and even multi-stage expansion is needed since the single-stage one cannot fulfill the overall volume ratio or the power duty. On the contrary, smaller expansion ratios and lower enthalpy drops of ORC allow for a favorable turbine design, resulting in high isentropic efficiencies with a limited number of stages, a reasonable size, and hence competitive manufacturing costs (Astolfi et al., 2014).

Since high-degree superheat is needed for SRCs to avoid the binary phase in the expansion process, as well as to improve the cycle efficiency, regenerative extraction is always applied in practical applications, which increases the complexity of turbine design as well as system structure. However, in ORC systems, a regenerator between the exhaust flow from the turbine/expander and the pump outlet is enough to ensure high system efficiency by reducing the exhaust energy from the turbine/expander as well as increasing the pump outlet temperature.

17.1.3 Organic Rankine Cycle systems are much less complex than steam Rankine Cycle systems in low-grade heat conversions

Driven by the medium/low-temperature heat sources, ORC systems are able to apply much lower vaporization pressures and more reasonable mass flow rates of working fluids compared with SRCs. These are advantageous for system design and construction, when considering reliability and complexity.

It is possible for ORC systems to condense at positive pressures while the SRCs condense at negative pressures with the same sink temperature (for example, ambient temperature). Positive condensing pressure allows ORC to develop less complex and small-sized pumps, containers and pipes without worrying about the air in-leakages since no vacuum pumps and accessories are required.

Given the medium/low temperature small heat sources, these advantages make ORC systems less complex, easier to be downsized, more reliable, practical, and economical compared with SRCs.

17.2 The application of Organic Rankine Cycles for industrial waste heat recovery

Many manufacturing industries discharge large amounts of energy in the form of waste heat and it is more and more significant to recover this waste heat to achieve huge energy savings and reduce environmental impact by improving industrial energy efficiency. The industrial waste heat released from many manufacturing processes has a relatively high temperature, enough to drive a power cycle and produce electricity for on-site use or sale. The cement making, steel making, and oil refining industries operate major process plants, consuming large quantities of energy and also producing huge amounts of waste heat. As much as 20–50% of the energy used during the manufacturing processes is released to the atmosphere. However, in some cases (e.g., industrial furnaces), the energy efficiency can be improved by 10% through WHR, which means the energy efficiency can be as much as 50%. So the WHR system (WHRS) seems more and more necessary, amongst which, the ORC system has gotten more attention in recent years.

When ORC technology was compared to others (Stirling engines, Thermo-Electric, Micro SRC, and Inverted Brayton Cycle), the study highlighted that ORC is the best performing technology for heat recovery and power generation using heat sources at temperatures of 200–400°C. Obviously, ORC conversion efficiency is limited (heat-to-electricity efficiency of larger recuperated cycles ORC systems typically can reach values of up to around 20%), if compared with conventional and advanced power plant technologies, but a potential in low/medium temperature WHR exists and should be quantified. Moreover, waste heat flows are discontinuous, thus the cycle needs to be flexible. ORC systems already in function can operate at partial load conditions up to 10%, while steam cycles need more constant conditions.

F. Campana et al. (2013) conducted the first comprehensive estimate of ORC units that can be installed into the cement, steel, glass, and oil and gas industries in 27 European Union countries, based on an accurate methodology shown in Fig. 17.1, related to real plants in operation or under construction. “PCP” means “Process Capacity Parameter” in the figure. An evaluation of energy savings, depending on the number of operating hours per year and of the consequent decrease in CO₂ emission and electricity expenditure, is also provided. The study, carried out in the framework of a European research project on heat recovery in energy intensive industries, found that, in the considered scenario, up to about 20,000 GWh of thermal energy per year can be recovered and 7.6 M ton of CO₂ can be saved by the application of ORC technology to the investigated and most promising industrial sectors.

In a typical cement plant, about 35–40% of the process heat is lost from the waste heat streams including the flue gases and the ambient air stream used for cooling down the clinker. Approximately 26% of the heat input to the system is lost due to dust, clinker discharge, radiation, and convection losses from the kiln and the preheaters. A heat recovery system could be used to increase the efficiency of the cement plant and thus contribute to an emissions decrease.

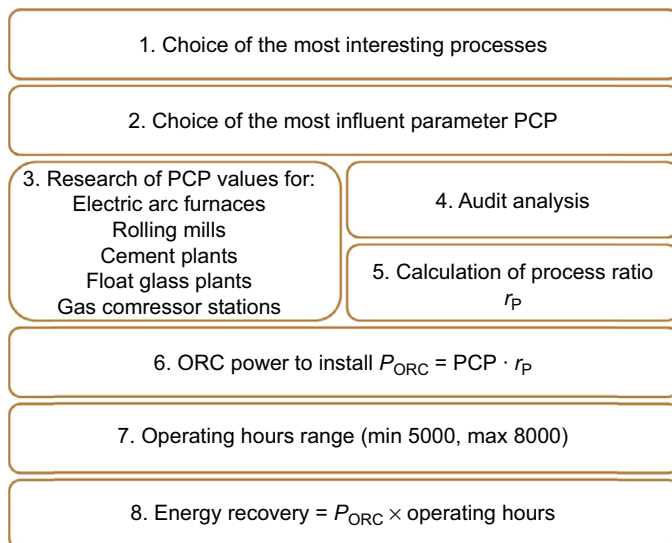


Figure 17.1 Methodology of analysis scheme (Campana et al., 2013).

S. Karellas et al. (2013) examined and compared, energetically and exergetically, two different WHR methods: a SRC, and an ORC. A parametric study proved that in the case of a newer (state of the art) cement plant with higher efficiencies, the ORC may be more advantageous than the water steam recovery cycle. Higher efficient cement plants have lower exhaust gas temperature and calculations performed showed that if the exhaust gas temperature is lower than 310°C , ORC heat recovery systems are more efficient solutions. Also, a brief economic assessment of the most efficient solution showed that WHR installations in the cement industry can contribute significantly to the reduction of the electrical consumption operating costs, thus being a very attractive investment with a payback period of up to 5 years.

The steel industry is also extremely energy-intensive. Its energy consumption accounts for about 15% of the total consumption in China, and about 68% of the energy is delivered as waste heat by flue gas and steam discharged from sintering machines, blast furnaces, converters, and reheating furnaces in steel production. Among these waste heat sources, flue gas temperature varies in the range of $200\text{--}450^\circ\text{C}$ which carries a significant amount of middle and high quality waste energy. Also, the temperature of the pressurized cooling-water leaving the furnace is generally $90\text{--}150^\circ\text{C}$. This waste hot water at a moderate temperature level is another appropriate source for heat recovery. It can be used for heating offices, buildings, or for preheating any other process if necessary. Furthermore, this moderate temperature level hot water can also be used to produce electricity. Utilizing moderate temperature steam in a conventional Rankine cycle to produce electricity is not a good choice technologically and economically. However, ORC is a promising technology for conversion of low-grade heat into electricity.

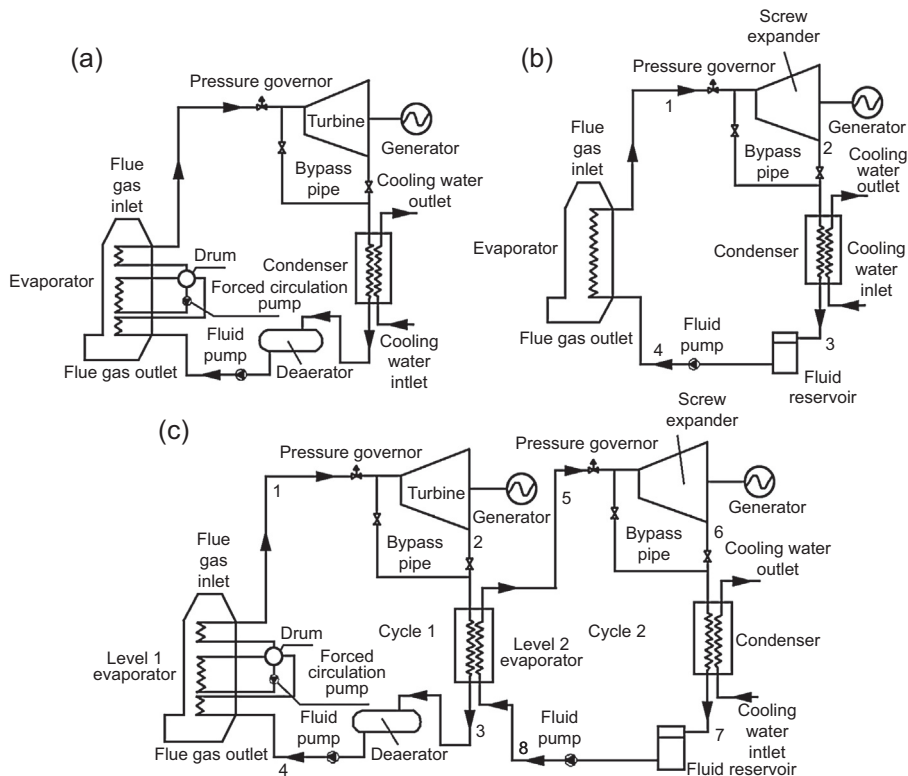


Figure 17.2 Power generation system schematics of (a) Steam Rankine Cycle, (b) Organic Rankine Cycle, and (c) steam-organic combined Rankine Cycle.

Zhang Li-hua et al. (2013) simulated three generation systems, as shown in Fig. 17.2, SRC, ORC, and steam-organic combined Rankine Cycle (S-ORC), using flue gas emissions from 200 to 450°C in iron and steel plants. To further utilize waste heat from the turbine exhaust steam of the ORC system, cascade ORC (CORC) was designed for heat sources above 300°C, whose principle is similar to that of S-ORC while water is replaced by a high boiling point organic fluid. Based on a comprehensive performance comparison, the application of the ORC using R141b is preferable for 200–300°C flue gas. For 300–450°C flue gas, CORC is an alternative technology to improve the efficiency and quality of waste heat utilization. For flue gas above 450°C, S-ORC can achieve higher efficiency and power generation than conventional SRC, with a relatively small negative pressure and high dryness of the turbine outlet steam. Hence, S-ORC can be considered as a substitute for SRC.

Conor Walsh and Thornley (2012) described the environmental and techno-economic evaluation of a case study examining the potential application of ORC to generate electricity from low-grade heat (LGH) from the stacks of a coke oven used in steel production. 21 MW of LGH was available for recovery at the plant and

resource. The results showed that 1–3% of the CO₂ emitted directly through the production of coke would be offset by installation of an ORC, with life-cycle environmental impacts (including different coal production processes) of coke production reduced by less than 1%, although this was sufficient to offset over 10,000 t on CO₂ annually. However, the amount of electricity generated was sufficient to replace all currently imported electricity and economic analysis indicated a relatively attractive discounted payback period of between three and six years, suggesting this may be a commercially viable option, which could present a relatively cost-effective method of achieving greenhouse gas savings in the process industries.

Petroleum refining also makes a good candidate for waste heat, as many processes involve cooling of large volumes of continuous, relatively clean liquid product flows.

H.C. Jung et al. (2014) investigated the technical and economic feasibility of converting waste heat from a stream of liquid kerosene which must be cooled down to control the vacuum distillation temperature. The process conditions were determined for a simple 250 kW ORC with a heat extraction loop. The pinch point technique was adopted to determine the optimum evaporation and condensation temperatures and assess the influence of the kerosene temperature at the evaporator exit on net power output. The operating conditions and performance of the ORC system were evaluated with eight potential refrigerants and refrigerant mixtures such as R123, R134a, R245fa, isobutane, butane, pentane, an equimolar mixture of butane and pentane, and a mixture of 40% isobutane and 50% butane on a mole basis. A financial model was established for the total plant cost. Results show that isobutene alone yields the best plant efficiency of 6.8% with approximately half of the kerosene flow available, and the efficiency can be increased up to 7.6% using the butane/pentane mixture. The optimum kerosene temperature at the evaporator outlet is estimated to be 70°C for all the fluid, except the butane/pentane mixture, which meets the design constraint not to disturb the existing distillation process. From simulation, the initial investment cost can be recovered within around 6.8 years as shown in the Fig. 17.3. Therefore, if the detailed engineering, component fabrication, and construction can be achieved within the cost target, the installation of a 250 kW ORC waste heat power converter on the kerosene cooling line would be technically feasible and economically viable.

Although facing some challenges on the cost and safety, an ORC system has showed us its strong point for industrial WHR.

17.3 The application of Organic Rankine Cycles for waste heat recovery on ships

Economic globalization has promoted the international flow of trade, investment, technology and financial capital, as a result of which, the globalization of the international shipping market has been further accelerated. Today, shipping is responsible for 80–90% of overall global trade. Compared to 1950, the global trade today is more than 100 times larger in terms of volume and value of goods transported. The importance and role of shipping in today's economy becomes obvious.

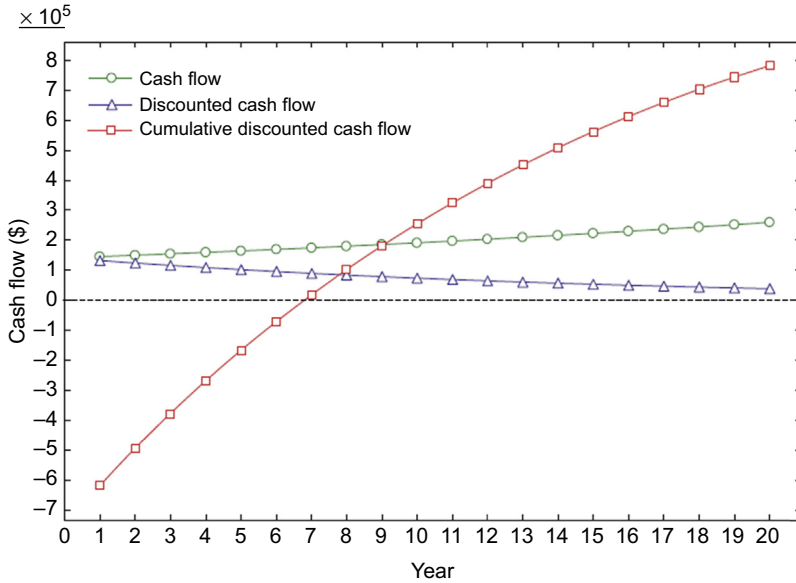


Figure 17.3 Variation of the cash flow, discounted cash flow, and cumulative discounted cash flow against the operating years.

The majority of prime movers (propulsion configuration) and auxiliary plants of ocean-going ships are diesel engines. In Germany, 96% of the ships with maximum power above 100 gross tons are supported by diesel engines. With the deterioration of energy shortage and environmental pollution problems, efficient and clean energy systems have become a hot topic for modern society.

There is a strong motivation in the marine business to increase the propulsion system energy efficiency due to increasing fuel prices and strict upcoming regulations. The International Maritime Organization (IMO) adopted Annex VI to MARPOL 73/78 in 1997 (Jing and Fan, 2010); the regulation went into effect on May 19, 2005. In 2007, the Marine Environment Protection Committee proposed the Energy Efficiency Design Index of Ships, which was a stricter requirement for pollutant emissions and efficient operations of marine engines. In October 2008, the IMO revised Annex VI, and over 53 countries implemented the regulation to address the crucial issue of the depleted energy supply and environmental deterioration.

For most marine diesel engines, less than 50% of the fuel energy is converted into useful power output, while the remaining energy is mainly lost through exhaust gas, air cooler, jacket water cooler, and other means (Shu et al., 2013). Energy balance of a typical two-stroke engine is shown in Fig. 17.4, in which we can learn the exhaust gas, air cooler, and jacket water contain significant potential to be recovered. The maximum temperature of exhaust gas produced by a two-stroke marine engine is lower than that of four-stroke diesel engine, in the range of 250–500°C, while the quantity of the former is large. Therefore, a significant amount of energy stored in exhaust gas

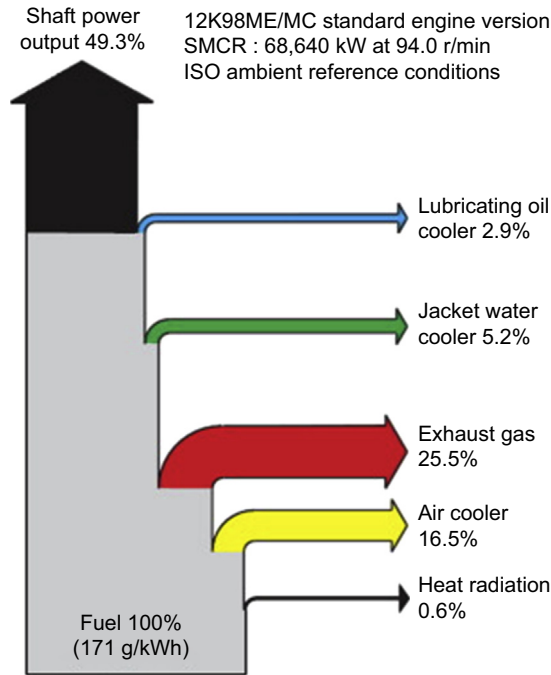


Figure 17.4 Energy balance of typical two-stroke marine engine (MAN B&W Diesel Ltd, 2005).

could be recovered. The scavenge air that enters the charger air cooler is 130–150°C, and the jacket cooling water is 70–120°C at the engine outlet.

A valuable alternative approach to improving overall energy efficiency and reducing pollutant emissions is to capture and reuse the “waste heat”, generating different types of energy needed aboard ship. Unlike the automobile operating conditions, the engine of ship especially that of large-tonnage ship usually runs at a constant speed for a long time. It is easier to make use of stable waste heat on ships compared with that of an automobile. On the other side, WHR on ship can also make use of sea water as a cooling source. The two main types of technologies used to recover waste heat from marine engines (Choi and Kim, 2013) are power turbines and bottoming SRC. Power turbines are a component that transfers enthalpy of exhaust gas into kinetic energy. Usually, the waste heat of exhaust gas recovered by a power turbine can be further utilized by means of bottoming SRC, through which can make a cascade utilization of the high-temperature exhaust gas.

SRCs have been employed for two-stroke engines, in spite of the lower temperature of the exhaust gas after the turbocharger. Ma et al. proposed and evaluated a single-pressure system, both in design conditions and at part-load (Ma et al., 2012). A detailed thermo-economic optimization of a WHRS for a two-stroke engine powered containership based on a steam cycle was proposed by Dimopoulos et al. (2011), who also investigated the exergy analysis as a means to further understand the combined

cycle (Diesel engine and WHRS) and the optimization procedure (Dimopoulos et al., 2012). SRC systems for two-stroke engines are available commercially by MAN, Wärtsilä, Mitsubishi and ABB. Most of the proposed solutions also involve the use of a turbocharger bypass in connection with a power turbine, which is particularly effective at high engine loads. The MAN B&W presented a conventional SRC system to recover waste heat of exhaust gas, which could bring a 10% increase to the engine efficiency. Wärtsilä developed a dual-pressure Rankine cycle system and observed that the engine efficiency could be improved by 11.4%. A comparison of different combined heat power (CHP) systems based on SRC was carried out by Mitsubishi heavy industries Ltd and a maximum of 5610 kW electricity can be recovered for 12K98 ME-C type engine of 69,900 kW. ABB Ltd proposed two types of recovery systems for marine diesel engines with different capacity of power outputs; these systems could efficiently utilize the waste heat from engine exhaust gas.

Recently, ORC systems have been introduced in marine applications (Shu et al., 2013). They are widely regarded as one of the most promising ways to convert low temperature waste heat into power (Larsen et al., 2013) due to the optimum thermal matching between thermal sources and thermodynamic cycles by appropriately choosing working fluids. Compared with a conventional SRC, ORCs that use a suitable organic fluids such as n-pentane or toluene in place of water have gained more attention because they allow the use of lower-temperature heat sources. Many articles about the use of ORC as WHRS coupled with four-stroke internal combustion engine (ICE) have been published, while only a few are available for ORC systems aboard ships. The first ORC system aboard a ship was installed on a car-truck carrier (Öhman and Lundqvist, 2013). The expectation was to obtain a 4–6% fuel saving using R-236fa as working fluid (Tchanche et al., 2011). Choi and Kim analyzed the performance of a dual-loop WHRS for a medium-sized containership under operational conditions (Shu et al., 2013), while Yang and Yeh (2015) analyzed the performance at part-load and transient conditions for a larger vessel. Analysis of an optimized system using the jacket cooling water as the preheating medium and the engine exhaust gas for evaporation was conducted by Song et al. (2015), and the simulation results reveal that the optimized system is technically feasible and economically attractive. These studies are of particular relevance since two-stroke engines are by far the most employed prime mover in the shipping industry in terms of installed power. Soffiato et al. (2015) proposed the ORC to recover heat associated with the jacket water, lubricating oil, and charge air cooling of the engines, while the heat from the exhaust gases is used to generate low pressure steam for the ship's internal use. In Soffiato's research, simple, regenerative, and two-stage ORC with two evaporation levels cycle are compared using six different organic fluids that are most suitable for this application, and the results show that the maximum net power output (820 kW) achieved by the two-stage ORC configuration almost doubles the simple cycle and regenerative ones (430–580 kW), but structural complexity and reliability issues may give different indications in terms of economic feasibility.

However, the ORC system has not been widely applied and was still at the stage of simulation and experiment. This is because the leakage problem has not been solved thoroughly and organic fluid is much more expensive than the water that is used in

conventional Rankine cycles. If the fresh water in the SRC system leaks to the environment, it can be supplied by a desalination system and is unable to lead to environment pollution. The ORC system will not be widely used until the leakage problem can be solved. Therefore, the application of ORC systems mainly depends on processing technology and equipment installation.

When considering the waste heat sources of different energy quality on ships, it is not reasonable to recycle the waste heat using a single method. A combination of ORC and other WHR thermodynamic cycles was usually adopted for the cascade utilization of the waste heat. Different WHR thermodynamic cycles must be determined according to the temperature range of heat source as well as the shipboard electricity, heating, cooling, and fresh water requirements. An example of WHR would be that the high temperature stage was used for electric production or mechanical power (usually SRC, ORC, and power turbine), and the low temperature stage for cooling (absorption refrigeration), fresh water (desalination), or space heating (direct heat transfer).

In our previous research (Liang et al., 2013, 2014), a novel electricity-cooling cogeneration system (ECCS) was proposed for WHR of marine engine, which not only exhibited an efficient cascade utilization of the waste heat, but also satisfied all shipboard electricity and cooling requirements. In such a cogeneration system, the SRC was used to recover the energy of jacket coolant and exhaust gas to generate electricity, an ammonia–water absorption refrigeration cycle was adopted to recycle the condensing heat in the SRC to provide cooling. However, the condensing heat in the absorption refrigeration cycle releases into the environment, which will lead to huge energy losses. Therefore, research into how to make use of the condensing heat in the absorption refrigeration cycle will be conducted. As shown in Fig. 17.5, the condenser-2 in the absorption refrigeration cycle is replaced by an expander-2, which can generate more power in the WHRS. In this way, the ORC can be irreplaceable on ships since it can improve the WHR efficiency to its maximum with the combination of other WHR technologies.

17.4 The application of Organic Rankine Cycles for waste heat recovery from Distributed Energy Systems

Distributed Energy Systems (DES) are usually a variety of small, grid-connected devices that have capacities of only 10 MW or less. Compared to conventional power stations, such as coal-fired, gas, and nuclear powered plants, as well as hydroelectric dams and large-scale solar power stations, which are centralized and often require electricity to be transmitted over long distances, DER systems are decentralized, modular, and more flexible technologies, and they are located close to the load they serve, so the energy loss in transmission can be avoided. This kind of system cannot only save a lot of energy, but can also relieve the pressure of electricity requirement, increasing the security of electricity supply. They have been valued by many developed countries and are being applied more and more in the field of supplying energy

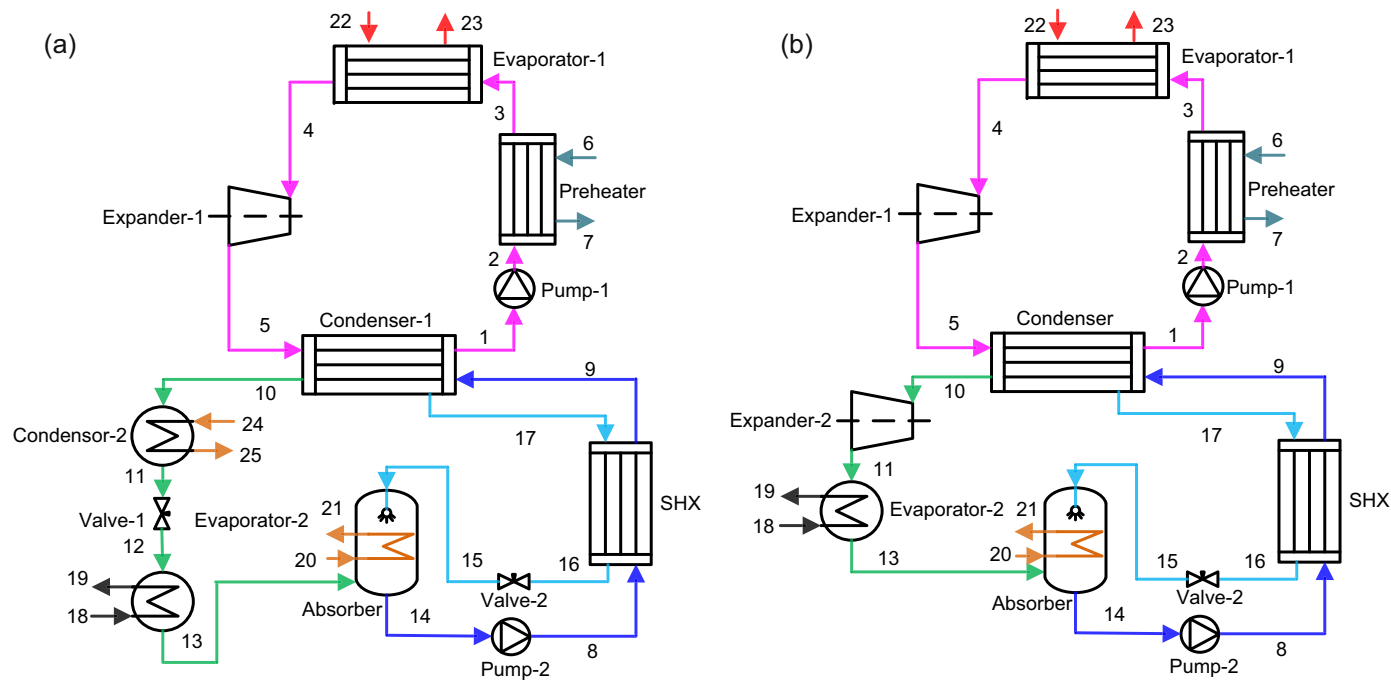


Figure 17.5 Schematic diagram of (a) electricity-cooling cogeneration system (EECS) and (b) EECS + turbine.

for buildings. Large ICE and gas turbines are two main kinds of prime engines for DES, because of its compact structure, high reliability, easy mobility, long life and other advantages. If the output power of DES is larger than 5 MW, the gas turbine is usually used; otherwise the ICE is preferred. However, the average efficiency of ICEs and gas turbines are about 30–45% and 20–42%, respectively; the rest of the energy is taken away by the exhaust, cooling water, machine oil, etc. Therein, the exhaust contains the most heat that is nearly equal to the output power of the engines, and its temperature is very high (it can be as high as 400–600°C). As a result, it is very meaningful to recover waste heat to improve the efficiency of ICEs and gas turbines.

DESs usually use the waste heat of large ICEs and gas turbines to produce heat and cooling, because they mainly serve the building, but in some places, the heat or cooling is not necessary all the year, while the electricity is. Therefore, SRCs and ORCs are a good way to recover waste heat to produce electricity. This method is not mature enough to be used in the ICEs of automobiles, because there are still many technical problems, especially miniaturization, while for the big stationary engines that are used in DES, the WHRS is more easy to apply. There are three reasons for that: firstly, because the amount of waste heat is great, the equipment of the WHRS is relative large, which is easy to find in the market; secondly, the work condition of this kind of engine is more stable; and finally, since it is stationary, there is more installation space. SRC can be easily used with a WHRS for large ICEs and gas turbines (MW-level), according to the modern technical level. There have been some WHR products with Rankine cycles for large, internal ICEs and gas turbines (MW-level). For example, MAN and Wartsila have both produced an SRC for WHR of large ICEs. Although conventional steam cycles can take better advantage of generating more power with slightly lower capital costs than ORC for the higher temperatures waste heat recovery, ORC still has many advantages. These advantages include the fact that ORC is widely studied and can be applied as a WHRS for large-scale ICEs and gas turbines.

Many researchers have compared ORC with other thermal cycles for recovering waste heat from large ICEs and gas turbines, and show the advantages of the former. Paola Bombarda et al. (2010) makes a comparison between the thermodynamic performances of the Kalina cycle and an ORC cycle as the WHRS for heat recovery from two Diesel engines, each one with an electrical power of 8900 kW; a net electric power of 1615 and 1603 kW, respectively, for the Kalina and ORC, with the working fluid hexamethyldisiloxane was calculated. R. Daniela Gewald (2012) used RC and ORC to recover the waste heat of a gaseous fuel engine, and build the math models to analyze their performance. The result showed that the use of one heat recovery steam generator for a water steam cycle may be more efficient, but requires complicated engineering in the existing plant. The research group which the writer belongs to also studied the ORC as a WHRS for a gas engine, with a rated power of 1.1 MW, and compared the ORC to an RC. The results showed that subcritical ORCs can recover heat both from exhaust and jacket water, producing more than 120 kW, at most, which is greater than the output power of the RC with positive condensing pressure. But the water SRC cannot use the heat of jacket water at most operation

conditions. The waste heat of the exhaust is enough, the jacket water preheater is needless and if it is used, the utilization of exhaust waste heat will reduce, thus increasing the final temperature of the exhaust.

When the ORC is used as the WHRS for large-scale ICEs and gas turbines, it has its own characteristics and these are discussed in detail below.

There are many organic working fluids and they have important effects on the system performance. Some working fluids have a high decomposition temperature and they can be directly heated by the exhaust of ICEs or gas turbines, while others have a low decomposed temperature, so they cannot be directly heated by the exhaust that has a temperature of more than 500°C. Therefore, a medium cycle is needed to make the high temperature heat become lower temperature and then the working fluid can be heated. The working fluids with high decomposition temperature can lead to a high thermal efficiency of the system, but they are usually very expensive (siloxanes) or flammable, and explosive (high complexity hydrocarbons like benzene, octane, toluene). The working fluids with a low decomposition temperature are usually refrigerant fluids. Although they need a Heat Transfer Fluid (HTF) loop and bring out a lower system thermal efficiency, they are cheap and safe. Most companies which produce ORCs for large ICEs and gas turbines use refrigerating fluids and a HTF loop with thermal oil. For example, a German company called [Maxxtec](#) makes the organic working fluids evaporated in a shell and tube heat exchanger by absorbing the thermal heat of the thermal oil primary circuit.

The waste heat resources of ICEs are multiple, the greatest heat comes from the exhaust, following that, it is the jacket water; many ORCs use the jacket water as a preheat source. Some ICEs have a turbocharger and the charge air has a high temperature, especially when the super charge ratio is high. The charge air needs to be cooled to a lower temperature before it flow into the cylinders, which means that this heat can also be used by the WHRS. The jacket water usually has a temperature of 80–95°C and the temperature of charge air is usually higher than 100°C. Therefore, the jacket water can be the low temperature heat source and the charge air can be the high temperature heat source at some conditions. Differently from ICEs, the exhaust is usually the only available waste heat resource of gas turbines. So the WHRS is simpler than that of ICEs.

Since the work conditions of ICEs or gas turbines are variable, the ORC also needs to work at different conditions. The WHRS is usually designed to work at the rate of the engines, so if conditions change, the performance of the ORC will become poor, and this may affect the safe operation of the WHRS. For example, if the turbine is used in the ORC system when the waste heat amount decreases, the working fluid at the evaporator outlet may contain drops which can damage the turbine blades. In order to make the system perform during different conditions and to avoid damage to the ORC system, a control strategy is necessary. Some research into control strategies for ORCs during variable working conditions has been done ([Quoilin, 2011](#); [Perales, 2012](#)). This will make the ORC more efficient and safe.

As actual products in engineering practice, an economy analysis is necessary. [Chacartegui et al. \(2009\)](#) studied combined cycles with ORC as bottoming cycles and several kinds of commercial gas turbines as top cycles. The research shows

ORCs are an interesting and competitive option when combined with high efficiency gas turbines with low exhaust temperatures or recuperative gas turbines, resulting in a topping to bottoming power ratio higher than in conventional gas–steam combined cycles. Economic analysis of ORC combined cycles shows gas turbine capital costs under 350 €/kW and ORC capital costs under 2000 €/kW would make ORC combined cycles economically interesting for medium and large-scale power generation. [R. Daniela Gewald \(2012\)](#) compared SRC and ORC to recover the waste heat of a gaseous fuel engine and also conducted an economic analysis. This revealed that despite the thermodynamic advantages of the water–steam cycles, both cycles reach the same level of costs of electricity generation which makes the consideration of detailed offers for this specific application extremely important.

Because a lot of large ICEs and gas turbines are used in DESs and the shift is towards greater use of DES, more and more companies have utilised ORC, companies include: Ormat Technologies, Israel; Turboden, Italy; ADORATEC GmbH, Germany; Maxxtec, Germany; and ElectraTherm, America. Some ORC WHRSs have been applied in engineering practice. Triogen's ORCs are operating or being installed in 10 European countries. In Finland, an ORC system was installed for a sewage gas engine in 2014, which generates 125 kW of electricity. While in Latvia, an ORC system was installed for a landfill gas engine in 2013, and produces 160 kW of electricity. The waste heat from biogas engines are also recovered by Triogen's ORC systems; 160 kW and 125 kW ORC systems for biogas engines are in operation, in Belgium and the Czech Republic, respectively ([Triogen](#)). A further Turboden project was installed in Russia (Moscow region); this heat recovery ORC unit is coupled with five MTU engines, at 2 MW each. The exhaust gas of these engines will be conveyed with thermal oil to the ORC module ([Turboden](#)). Turboden, whose ORC modules for heat recovery have a power output between 200 kW and 15 MW also has a lot of reference projects of ORC for WHR from large ICEs and gas turbines, such as heat recovery from a Solar CENTAUR gas turbine in a gas compressor station in Canada and heat recovery from a Solar TITAN 130 gas turbine in a Gas Turbine Power Plant (GTTP) in Russia (Moscow region). Other reference projects are shown in [Fig. 17.6 \(12-COM.P-21-rev\)](#):

At the gas compressor stations at 150 Mile House in British Columbia, Canada, an Energy Recovery Generation (ERG) facility based on ORC was installed to recover the waste heat of simple cycle 18.5 MW ISO General Electric PGT25 gas turbine engines driving gas compressors and 4.5 MW net electrical power could be obtained at design conditions. A simplified Process Flow Diagram of the system can be seen in [Bohl \(2009\)](#). The turbine exhaust passes through a diverter that directs it to the Bypass Stack or to the Waste Heat Oil Heater (WHOH) which make this system safer and ensures that the normal operation of the turbine is unaffected by unforeseen circumstances. The thermal oil is heated in the WHOH and then flows to the ORC, where the electricity is generated.

Compared with the application in automobiles, the ICEs and DES on ships are more likely to employ the ORC system, and with the efforts of all the researchers, ORC can contribute a lot to energy saving.

Project	ORC Module	Site	Engines
<i>Pisticci I</i>	TURBODEN 18 HR SPLIT (1.8 MWe) In operation since IV quarter 2010	Pisticci (IT)	3 x 8 MWe Wartsila Diesel engines
<i>Oxon</i>	TURBODEN 6 HR SPLIT (0.6 MWe) In operation since IV quarter 2008	Pavia (IT)	1 x 8 MWe MAN Diesel engine
<i>FinPower</i>	TURBODEN 40 HR SPLIT (3.8 MWe) In operation since II quarter 2009	Visano (IT)	1 x 7 MWe Wartsila Diesel engine
<i>Pisticci II</i>	TURBODEN 40 HR SPLIT (3.8 MWe) In operation since II quarter 2012	Pisticci (IT)	2 x 17 MWe Wartsila Diesel engines
<i>Cereal Docks</i>	TURBODEN 6 HR DIR. EXCH. (0.6 MWe) In operation since I quarter 2012	Portogruaro (IT)	1 x 7 MWe Wartsila Diesel engine
<i>Eukrasia</i>	TURBODEN 6 HR SPLIT (0.6 MWe) In operation since II quarter 2010	Catania (IT)	2 x 1 MWe JGS/GE gas engines + 3 x 0.8 MWe JGS/GE gas engines + 1 x 0.6 MWe JGS/GE gas engine
<i>Ulm</i>	TURBODEN 10 HR cogenerative (1 MWe) In operation since III quarter 2012	Senden (DE)	2 x 2 JGS/GE gas engines (+ additional heat from the process)
<i>Kempen</i>	TURBODEN 6 HR cogenerative (0.6 MWe) In operation since I quarter 2012	Kempen (DE)	Gas engines
<i>Mondopower</i>	TURBODEN 10 HR (1 MWe) In operation since I quarter 2013	Chivasso (IT)	1 x 17 MWe Wartsila Diesel engine
<i>HSY</i>	TURBODEN 14 HR (1.3 MWe) In operation since III quarter 2011	Ämmässuo (FIN)	4 x 4 MWe MWM gas engines
<i>GazProm2</i>	TURBODEN 10 HR SPLIT (0.987 MWe) Under construction	Moscow region (RU)	5 x 2 MWe MTU engines
<i>Fater</i>	TURBODEN 7 HR DIR. EXCH. (0.7 MWe) In operation since II quarter 2013	Pescara (IT)	1 x 8 MWe Wartsila Diesel engine

Figure 17.6 Reference projects of waste heat recovery systems (WHRSS) of Organic Rankine Cycles (ORCs) for internal combustion engines (ICEs) ([12-COM.P-21-rev](#)).

17.5 The application of Organic Rankine Cycles for waste heat recovery from recompression stations along pipelines

The natural gas pipeline network is a highly integrated transmission grid that delivers natural gas to and from locations. In the US, the natural gas pipeline network relies on more than 1200 recompression stations to maintain a continuous flow of natural gas between supply areas and customers. The average station is capable of moving about 700 million cubic feet (MMcf) of natural gas per day, while the largest can move as much as 4.6 billion cubic feet (Bcf) per day. Generally, the basic compressor systems in the natural gas recompression stations are comprised of two components: the “mechanical drive” that provides the shaft power that drives the compressor, and the “compressor” itself. Two types of mechanical drives are primarily in use for the recompression station today, ICEs and gas turbines. Natural gas fueled engines and turbines (mechanical drives) generate heat as a by-product. Only about one-third of the fuel energy consumed by an engine or turbine ends up as useful mechanical power, the remaining two-thirds are rejected as hot exhaust (260–540°C) or in engine cooling systems (below 70°C). In industrial or commercial CHP applications, this heat is recovered and used to provide hot water or steam for the site, dramatically improving the overall fuel use efficiency of the system. CHP is difficult to implement at pipeline compressor stations because there are very few thermal energy requirements at recompression stations, and recompression stations, in general, tend to be located in isolated locations which precludes providing the steam or hot water to an adjacent industrial or

commercial user. Recently, an alternative to recovering heat is to recover the energy in the hot exhaust to generate mechanical power or electricity through an ORC system.

In contrast to conventional steam plants (mainly developed in the 1990s), ORC systems using Hydrocarbons as working fluids (developed in the 21st century) have several advantages for recompression station applications:

1. Hydrocarbon working fluids have lower specific volumes than steam, resulting in smaller, more compact equipment.
2. Hydrocarbons condense at higher pressures than steam at the same temperature, reducing turbine size requirements and air-in leakage potential.
3. ORC condensers are typically air-cooled rather than water-cooled. This enhances applicability in remote locations where water supplies may not be readily available and eliminates disposal issues for cooling-water treatment chemicals.
4. Hydrocarbons have lower freezing points than water, eliminating condenser freeze-up concerns and allowing the condenser to transfer heat at a lower temperature, increasing cold weather performance.
5. Complex hydrocarbons such as pentane remain dry during turbine expansion while steam can form moisture droplets that cause erosion damage during high-speed collisions with turbine components.

Due to recompression stations varying widely in size and layout, ORC does not fit all of them when considering the waste heat quality and economy factor. A report ([Waste Energy Recovery](#)) by the Interstate Natural Gas Association of America (INGAA) compared the waste heat quality of ICEs and gas turbines. In addition to having the majority of their heat rejected in low temperature engine cooling systems, ICEs operate close to stoichiometric combustion conditions resulting in lower exhaust flows due to less inlet air volumes. Gas turbines, on the other hand, reject almost all of their heat in the hot exhaust gases and operate with 200–300 percent excess air, resulting in both higher exhaust temperatures and greater exhaust flow rates per horsepower output. Coupled with the fact that ICE drives are typically smaller than gas turbine compressor drives and are often grouped together in multiple units at stations that have widely fluctuating demand, ICEs do not appear to be viable near-term applications for exhaust heat recovery. Therefore, all existing compressor power recovery systems in North America have been applied to gas turbine drives. Whatmore, based on current technologies and prevailing power prices, the report proposed that minimum hurdles for economic WHR projects are: (i) total gas turbine compressor station capacity of at least 15,000 hp; and (ii) stations which operate at or more than 5250 h per year over the previous 12 months (an annual load factor at or above 60 percent). The report estimated that 90 to 100 compressor stations in the US meet these hurdles, representing approximately 500–600 MW of potential power generation capacity.

A number of companies have been actively pursuing compressor heat recovery projects over the past several years. Among them, Ormat Technologies in Reno, Nevada is the most outstanding, which has supplied ORCs to geothermal applications for close to 20 years and currently has increasing compressor recovery systems in operation or planned in the US and Canada. The INGAA arranged a list of operating and planned systems ([Tables 17.1 and 17.2](#)) based on ORC systems produced by Ormat

**Table 17.1 Waste heat to power systems applied to pipeline gas turbine drives, operating systems
(Status of Waste Heat)**

Project	Gas turbine	Turbine horsepower	Recovered power (MW)	Power purchaser	Developer/operator	Equipment	Commissioning date
TransCanada Pipeline, Gold Creek, Alberta, Canada	Rolls Royce, RB211	38,000	6.5	Alberta Power Pool	Maxim Energy	Ormat	1999
Northern Border Pipeline, St. Anthony, North Dakota	Rolls Royce, RB211	38,000	5.5	Basin Electric Cooperative	Ormat	Ormat	2006
Northern Border Pipeline, Wetonka, South Dakota	Rolls Royce, RB211	38,000	5.5	Basin Electric Cooperative	Ormat	Ormat	2007
Northern Border Pipeline, Clark, South Dakota	Rolls Royce, RB211	38,000	5.5	Basin Electric Cooperative	Ormat	Ormat	2007
Northern Border Pipeline, Estelline, South Dakota	Rolls Royce, RB211	38,000	5.5	Basin Electric Cooperative	Ormat	Ormat	2007
Alliance Pipeline, Kerrobert, Saskatchewan, Canada	GE LM2500	33,000	5.5	SaskPower	NRGreen	Ormat	5/2007
Alliance Pipeline, Loreburn, Saskatchewan, Canada	GE LM2500	33,000	5.5	SaskPower	NRGreen	Ormat	5/2008

Alliance Pipeline, Estlin, Saskatchewan, Canada	GE LM2500	33,000	5.5	SaskPower	NRGreen	Ormat	6/2008
Alliance Pipeline, Alameda, Saskatchewan, Canada	GE LM2500	33,000	5.5	SaskPower	NRGreen	Ormat	8/2008
Spectra Pipeline, 150 Mile House, BC, Canada	GE PGT20	24,000	5	BC Hydro	Enpower	Ormat	8/2008
Spectra Pipeline, Savona, BC, Canada	GE PGT20	24,000	5	BC Hydro	Enpower	Ormat	9/2008
Northern Border Pipeline, Manning, North Dakota	Rolls Royce, RB211	38,000	5.5	Basin Electric Cooperative	Ormat	Ormat	12/2008
Northern Border Pipeline, Zeeland, North Dakota	Rolls Royce, RB211	38,000	5.5	Basin Electric Cooperative	Ormat	Ormat	1/2009
Trailblazer Pipeline, Peetz, Colorado	Solar Mars 100 (2 units)	10,000* (each)	4	Highline Electric Coop	Ormat	Ormat	3/2009
Northern Border Pipeline, CS 6, North Dakota	Rolls Royce, RB211	38,000	5.5	Montana—Dakota Utilities	MDU/ Ormat	Ormat	7/2009

*Turbine capacity derated due to high altitude.

Table 17.2 Waste heat to power systems applied to pipeline gas turbine drives, planned systems
(Status of Waste Heat)

Project	Gas turbine	Turbine horsepower	Recovered power (MW)	Power purchaser	Developer/operator	Equipment	Expected commissioning date
Northern Border Pipeline, Culbertson, Montana	Rolls Royce, RB211	38,000	5.5	Basin Electric	Ormat	Ormat	2009
Northern Border Pipeline, Garvin, Minnesota	Rolls Royce, RB211	38,000	5.5	Basin Electric	Ormat	Ormat	2009
Northern Border Pipeline, CS 13, Minnesota	Rolls Royce, RB211	38,000	5.5	Great River Energy	Ormat	Ormat	2010
Kern River Pipeline, Goodsprings, Nevada	Solar Mars 100 (3 units)	$3 \times 15,000$	6	NV Energies	NV Energies	Ormat	2010
Alliance Pipeline, Windfall, Alberta, Canada			2×7	AltaLink	NRGreen	Ormat	2009
Alliance Pipeline, Morinville, Alberta, Canada			5.5	Alberta energy	NRGreen	Ormat	2009
Alliance Pipeline, Irma, Alberta, Canada	GE PGT25+	42,000	5.5	Alberta energy	NRGreen	Ormat	2009
Spectra Pipeline, Summit Lake, BC, Canada	GE PGT25	31,000	5	BC Hydro	En power	Ormat	2010
Spectra Pipeline, Hixon, BC, Canada	GE PGT25	31,000	5	BC Hydro	En power	Ormat	2010
Spectra Pipeline, Australian, BC, Canada	GE PGT25+	42,000	5	BC Hydro	En power	Ormat	2010

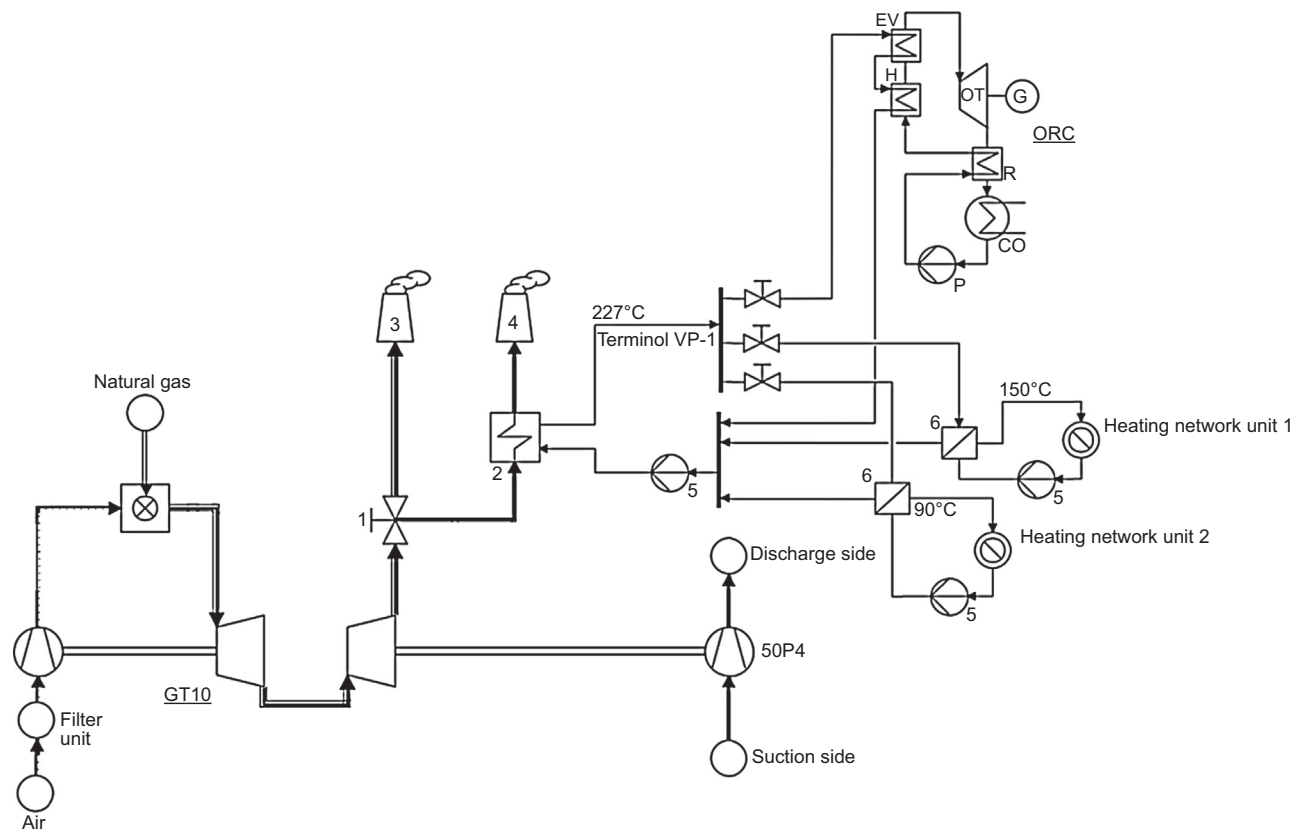


Figure 17.7 The second scenario of natural gas compressor station's waste heat recovery (Campana et al., 2013).

Technologies in a report ([Status of Waste Heat](#)). For the Northern Border Pipeline, nine stand-alone power plants were commissioned by Ormat from 2006 to 2010 in Minnesota, Montana, North Dakota and in South Dakota. Each plant is a state-of-the-art proprietary implementation following the ORC and generates approximately 5.5 MW, bringing the total generated capacity to 50 MW. With the pipelines typically running 24/7, the power plants have the capacity to serve as a baseload source of electricity powering approximately 50,000 homes, and mitigate approximately 260,000 tons of CO₂ emissions that would have been released into the atmosphere if gas was used to produce the same amount of power. The Ormat solution transfers the waste heat (about 490°C) of the Rolls-Royce RB-211 gas turbine to the working fluid of an ORC via a WHOH (tube-type heat exchangers in which thermal oil is circulated within its tubes), where the exhaust gases are cooled before venting to the atmosphere by the thermal oil flowing in the tubes. The heated oil is then used to vaporize and preheat the working fluid in the ORC systems. The power plants are air-cooled, and thus do not require a supply of water, cooling towers, or chemical additives, and has the advantage of never producing a visible plume, resulting in a low visual profile that blends into the surroundings with minimal impact to the landscape.

Some researchers study the optimal design of ORCs and working fluids selection for WHR of recompression stations. [Yilmazoglu et al. \(2014\)](#) demonstrated the feasibility of installing an ORC-based WHR in recompression stations and they analyzed a selection of working fluid to find a multicriteria optimum accounting for power, efficiency, and environmental effect. They concluded that n-pentane is the fluid which meets the optimized criteria. [Kostowski et al. \(2015\)](#) studied the technical and economic feasibility of a natural gas compressor station's WHR. Three alternative improvement strategies have been proposed: (i) installation of a heat recovery hot water generator for covering the existing heat demand of the plant; (ii) installation of a heat recovery thermal oil heater for covering the existing heat demand and driving an ORC for electricity generation; and (iii) installation of a heat recovery thermal oil heater with an ORC and gas expanders for switching into full-load operation of the gas turbine unit. Energy and exergy performance of the proposed strategies, as well as their economic feasibility have been analyzed. The second scenario (in [Fig. 17.7](#)) involving an ORC unit provides the highest local energy saving. However, its economic feasibility is not achieved under the current part-load operating conditions.

References

- 12-COM.P-21-rev, <http://www.turboden.eu/en/public/downloads/12-COM.P-21-rev.22.pdf>.
Astolfi, M., Romano, M.C., Bombarda, P., Macchi, E., 2014. Binary ORC (organic Rankine cycles) power plants for the exploitation of medium-low temperature geothermal sources – Part A: thermodynamic optimization. *Energy* 66, 423–434.
Bohl, R., 2009. Waste heat recovery from existing simple cycle gas turbine plants—a case study. In: 18th Symposium on Industrial Application of Gas Turbines (IAGT), Alberta, Canada.

- Bombarda, P., Invernizzi, M., Pietra, C., 2010. Heat recovery from diesel engines: a thermodynamic comparison between Kalina and ORC. *Applied Thermal Engineering* 30, 212–219.
- Campana, F., Bianchi, M., Branchini, L., De Pascale, A., Peretto, A., Baresi, M., Fermi, A., Rossetti, N., Vescovo, R., 2013. ORC waste heat recovery in European energy intensive industries: energy and GHG savings. *Energy Conversion and Management* 76, 244–252.
- Chacartegui, R., Sánchez, D., Muñoz, J.M., et al., 2009. Alternative ORC bottoming cycles for combined cycle power plants. *Applied Energy* 86 (10), 2162–2170.
- Choi, B.C., Kim, Y.M., 2013. Thermodynamic analysis of a dual loop heat recovery system with trilateral cycle applied to exhaust gases of internal combustion engine for propulsion of the 6800 TEU container ship. *Energy* 58, 404–416.
- Dimopoulos, G.G., Georgopoulou, C.A., Kakalis, N.M.P., 2011. Modelling and optimisation of an integrated marine combined cycle system. *ECOS* 4–7.
- Dimopoulos, G.G., Georgopoulou, C.A., Kakalis, N.M.P., 2012. The introduction of exergy analysis to the thermo-economic modelling and optimisation of a marine combined cycle system. In: *The 25th International Conference on Efficiency, Cost, Optimization and Simulation of Energy Conversion Systems and Processes*.
- Gewald, D., 2012. Waste heat recovery from a landfill gas-fired power plant. *Renewable and Sustainable Energy Reviews* 16, 1779–1789.
- Jing, G., Fan, J., 2010. Review of energy utilization technology for marine diesel engine. *Diesel Engine* 6, 1–4.
- Jung, H.C., Krumdieck, S., Vranjes, T., 2014. Feasibility assessment of refinery waste heat-to-power conversion using an organic Rankine cycle. *Energy Conversion and Management* 77, 396–407.
- Karellas, S., Leontaritis, A.-D., Panousis, G., Bellos, E., Kakaras, E., 2013. Energetic and exergetic analysis of waste heat recovery systems in the cement industry. *Energy* 58, 147–156.
- Kostowski, W.J., Kalina, J., Bargiel, P., Szuflenski, P., 2015. Energy and exergy recovery in a natural gas compressor station – a technical and economic analysis. *Energy Conversion and Management* 104, 17–31.
- Larsen, U., Pierobon, L., Haglind, F., et al., 2013. Design and optimisation of organic Rankine cycles for waste heat recovery in marine applications using the principles of natural selection. *Energy* 55, 803–812.
- Li, J., Pei, G., Li, Y., Wang, D., Ji, J., 2012. Energetic and exergetic investigation of an organic Rankine cycle at different heat source temperatures. *Energy* 38, 85–95.
- Liang, Y., Shu, G., Tian, H., et al., 2013. Analysis of an electricity–cooling cogeneration system based on RC-ARS combined cycle aboard ship. *Energy Conversion and Management* 76, 1053–1060.
- Liang, Y., Shu, G., Tian, H., et al., 2014. Theoretical analysis of a novel electricity–cooling cogeneration system (ECCS) based on cascade use of waste heat of marine engine. *Energy Conversion and Management* 85, 888–894.
- Ma, Z., Yang, D., Guo, Q., 2012. Conceptual design and performance analysis of an exhaust gas waste heat recovery system for a 10,000 TEU container ship. *Polish Maritime Research* 19 (2), 31–38.
- MAN B&W Diesel Ltd, July 2005. Thermo Efficiency System (TES) for Reduction of Fuel Consumption and CO₂ Emission. MAN B&W Diesel A/S, Copenhagen, Denmark.
- Maxxtec, <http://www.maxxtec.com/en/product/power-generation/orc-module>.
- Öhman, H., Lundqvist, P., 2013. Comparison and analysis of performance using low temperature power cycles. *Applied Thermal Engineering* 52 (1), 160–169.

- Perez, J., 2012. Towards model-based control of a steam Rankine process for engine waste heat recovery. In: IEEE Vehicle Power and Propulsion Conference (VPPC), Korea.
- Quoilin, S., 2011. Dynamic modeling and optimal control strategy of waste heat recovery organic Rankine cycles. *Applied Energy* 88, 2183–2190.
- Shu, G., Liang, Y., Wei, H., et al., 2013. A review of waste heat recovery on two-stroke IC engine aboard ships. *Renewable and Sustainable Energy Reviews* 19, 385–401.
- Soffiato, M., Frangopoulos, C.A., Manente, G., et al., 2015. Design optimization of ORC systems for waste heat recovery on board a LNG carrier. *Energy Conversion and Management* 92, 523–534.
- Song, J., Song, Y., Gu, C., 2015. Thermodynamic analysis and performance optimization of an organic Rankine cycle (ORC) waste heat recovery system for marine diesel engines. *Energy* 82, 976–985.
- Status of Waste Heat to Power Projects on Natural Gas Pipelines, Interstate Natural Gas Association of America (INGAA). <http://www.ingaa.org/File.aspx?id=9373>.
- Tchanche, B.F., Lambrinos, G., Frangoudakis, A., et al., 2011. Low-grade heat conversion into power using organic Rankine cycles—a review of various applications. *Renewable and Sustainable Energy Reviews* 15 (8), 3963–3979.
- Tian, H., Shu, G., Wei, H., Liang, X., Liu, L., 2012. Fluids and parameters optimization for the organic Rankine cycles (ORCs) used in exhaust heat recovery of internal combustion engine (ICE). *Energy* 47, 125e136.
- Triogen, <http://www.triogen.nl/references/reference-overview>.
- Turboden, <http://www.turboden.eu/en/applications/applications-heat-recovery.php>.
- Walsh, C., Thornley, P., 2012. The environmental impact and economic feasibility of introducing an organic Rankine cycle to recover low grade heat during the production of metallurgical coke. *Journal of Cleaner Production* 34, 29–37.
- Waste Energy Recovery Opportunities for Interstate Natural Gas Pipelines, Interstate Natural Gas Association of America (INGAA). <http://www.ingaa.org/file.aspx?id=6210>.
- Yang, M.H., Yeh, R.H., 2015. Thermodynamic and economic performances optimization of an organic Rankine cycle system utilizing exhaust gas of a large marine diesel engine. *Applied Energy* 149, 1–12.
- Yilmazoglu, M.Z., Amirabedin, E., Shotorban, B., 2014. Waste heat utilization in natural gas pipeline compressor stations by an organic Rankine cycle. *Energy Explor Exploit* 32 (2), 317–328.
- Zhang, L.H., Wu, L.J., Zhang, X.H., Ju, G.D., 2013. Comparison and optimization of mid-low temperature cogeneration systems for flue gas in iron and steel plants. *Journal of Iron and Steel Research International* 20 (11), 33G40.

Micro-Organic Rankine Cycle systems for domestic cogeneration

18

*R. Bracco*¹, *D. Micheli*², *R. Petrella*³, *M. Reini*², *R. Taccani*², *G. Toniato*^{4,5}

¹Centro Ricerche Fiat S.C.p.A., Orbassano, Italy; ²University of Trieste, Trieste, Italy;

³University of Udine, Udine, Italy; ⁴Kaymacor S.r.l., Legnago, Italy; ⁵Riello Group, Legnago, Italy

18.1 Requirements and main features of domestic Organic Rankine Cycle systems

The electrical efficiency of an Organic Rankine Cycle (ORC), as with any thermodynamic cycle, is a function of the temperature of the available hot and cold sources. In domestic applications, the commonly available hot sources are the combustion products of fossil fuels and/or biofuels and solar radiation. They were traditionally used for the sole purpose of providing thermal energy but they are now exploited to produce electricity. Fuels are used in cogenerators based on reciprocating or dynamic internal combustion engines or even, more rarely, on external combustion machines, mainly Stirling engines. In all of these cases, the cold source is air and/or water at ambient temperature. Solar energy can also be directly converted into electricity by photovoltaic panels.

The electrical efficiencies of all these solutions are generally higher than those obtainable by an ORC because, in the case of fuels as a primary source, the maximum temperature of the cycle is limited by the properties of the used organic fluid while, in the case of the solar energy, the limit is the temperature of the fluid heated by the flat solar panels (the use of high temperature and high concentration solar systems is not common in domestic applications). In addition, as is the case in all Rankine cycles, the eventual cogeneration of heat involves the temperature rising of the cold source of the cycle up to values higher than the ambient temperature, with a further penalization of the efficiency. While internal combustion engines of small size can achieve electrical efficiencies of around 20–30% and actual photovoltaic panels can reach values of 15–16%, a domestic ORC cycle is hardly able to exceed 10%, and will often have lower yields.

The electrical efficiency of a domestic cogenerator is not however the only matter of choice. Other features to be considered are reliability, safety, noise, emissions, versatility and, of course, the cost of purchasing and operation. The first four are definitely strengths of the ORC solution, while versatility and cost require a more comprehensive analysis.

With regard to the versatility, the advantages of Organic Rankine Cycles are:

- the option of exploiting thermal flows at low temperatures, such as the exhaust gases exiting from a boiler, or the hot water produced by thermal solar panels, to obtain electricity and sanitary water. In the first case, the dispersion of heat into the environment is reduced while, in the second case, the thermal flow which is available anyway, is converted into higher quality energy;
- efficient use of biomass in distributed cogeneration, because an important part of the transport costs can be avoided;
- the possibility of making the production of electricity less constrained by the availability of the thermal source by inserting a hot water storage between the boiler, or the solar panels, and the thermal cycle;
- in the case of prevalent exploitation of solar energy, the ability to produce thermal energy in addition to the electric one, which is the only product of the traditional not the cooled photovoltaic panels.

Note that similar results can be obtained by using also a Stirling engine, in terms of safety, noise, emissions, and electrical efficiency; electrical efficiency can be in the range 30–40% if the maximum cycle temperature is in the range 650–800°C, while it can be lower than the ORC if the size and maximum temperature are those expected for a domestic application. But, on the other hand, the adoption of Stirling engines implies important restrictions on the heat transfer to the working fluid, due to the need to concentrate it on the hot and cold pistons (with possible problems, moreover, of gas leakage and wearing of metallic surfaces, typical of reciprocating machines). However, ORC plants allow a large choice of different solutions for both heat exchangers and expanders.

With regards the economic aspects, the operation costs are very low, while those of purchase are still high, as is the case for any developing technology, when the choice offered by the market is limited. It is reasonable to assume that costs can decrease in the short to medium term due to both the technical development and the expansion of the market.

In order to better understand the possible benefits of a cogeneration system, even with low electrical efficiency, the Primary Energy Saving (PES) diagram and the Economic Recovery Index (ERI) diagram can be useful. The PES is defined as the ratio between the fuel energy saved by the cogeneration system, with respect to a conventional, separated production of the same electrical and thermal energy, and the fuel energy consumed by the conventional, separated production itself. It depends on the reference electrical, η_{er} , and thermal, η_{qr} , efficiencies assumed for the conventional production.

In Fig. 18.1 the lines at constant PES are presented in the electrical, η_e , and thermal, η_q , efficiency plane; notice that for a cogeneration system, only the region below the red line $(\eta_e + \eta_q) < 1$ is admissible.

It can be easily demonstrated that:

$$PES = 1 - \frac{1}{\frac{\eta_q}{\eta_{qr}} + \frac{\eta_e}{\eta_{er}}} \quad (18.1)$$

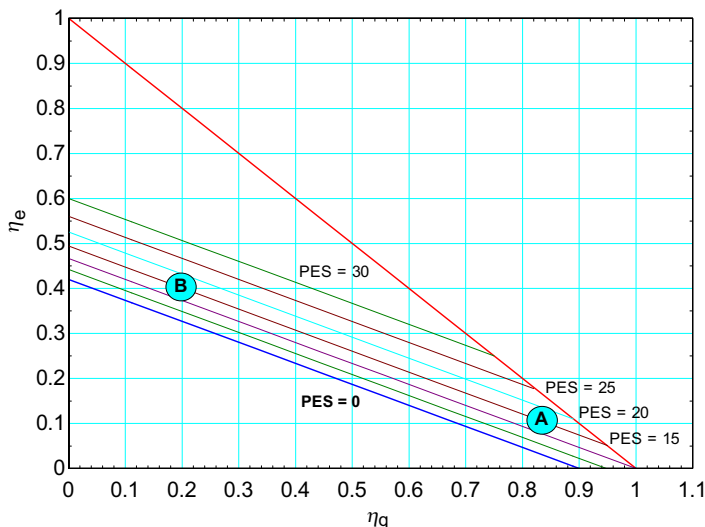


Figure 18.1 Lines at constant Primary Energy Saving (PES) in the (η_e, η_q) plane for a generic cogeneration system.

In Fig. 18.1 the following numerical values have been used for drawing all lines:

- $\eta_{qr} = 0.90$ – reference thermal efficiency of conventional systems (NG boiler);
- $\eta_{er} = 0.42$ – reference electrical efficiency of conventional suppliers (national grid).

This last value is different from that suggested by the EU (Directive, 2012/27/EU, 52.5%, if natural gas is used as a fuel). The latter can be clearly regarded as an average value for a combined cycle, sized at about 100 MWe. The owners of domestic Combined Heat and Power (CHP) systems have not generally had the option to buy electric energy directly from this kind of plant, therefore the adopted reference value has been obtained as the average efficiency of the whole Italian thermoelectric park (46–47%), reduced because of the transmission losses affecting the end users connected to the low-voltage grid (about 10%).

Notice that cogeneration systems with $\eta_e = 0.1$, or even lower (point A in Fig. 18.1) can obtain the same PES of systems with much higher electrical efficiency when their thermal efficiency (calculated taking into account the heat produced by the CHP system and actually used) are greater than 0.8. For instance, point B in Fig. 18.1 can be regarded as representative of a high-electrical efficiency CHP technology (for instance, a medium sized Internal Combustion Engine (ICE)), where only 20% of the cogenerated heat is actually exploited. In other words, an extensive utilization of the cogenerated heat is the key to a positive PES, rather than a high-electrical efficiency.

The ERI can be defined as the ratio between the money saved by the cogeneration system and the cost of the conventional separated supply of electric and thermal energy. It is affected by: the unit energy cost of the fuel for the CHP system, the unit cost of the electric and of the thermal energy for the conventional (separated)

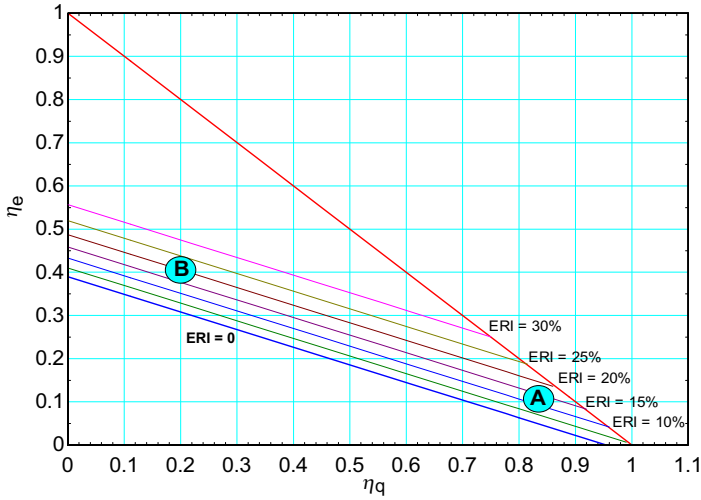


Figure 18.2 Lines at constant Economic Recovery Index (ERI) in the (η_e, η_q) plane for a generic cogeneration system.

suppliers and the capital cost of the CHP system per energy unit of the used fuel, during its life time.

In Fig. 18.2, the lines at constant ERI are presented in the (η_e, η_q) plane, using the following numerical values for drawing all lines:

- $c_F = 2.05 \times 10^{-5}$ €/kJ – unit energy cost of the fuel of the CHP system (corresponding to about 0.71 €/Nm³ of natural gas);
- $c_{Pr} = 6.11 \times 10^{-5}$ €/kJ – reference unit cost of the electric energy by conventional suppliers (corresponding to 0.22 €/kWh_e);
- $c_{qr} = 2.49 \times 10^{-5}$ €/kJ – reference unit cost of the thermal energy by conventional suppliers (it can be obtained taking into account the reference thermal efficiency previously assumed, an annual thermal demand of 20,000 kWh and a hypothetical levelized annual cost for owning and maintaining the boiler of about 150 €/year);
- $z_F = 0.33 \times 10^{-5}$ €/kJ – capital cost of the CHP system per unit of energy of the used fuel (it can be obtained taking into account the previous assumptions and a hypothetical levelized annual cost for owning and maintaining the cogeneration system of about twice the cost of the boiler).

It can be easily demonstrated that:

$$ERI = 1 - \frac{c_F + z_F}{c_{Pr}\eta_e + c_{qr}\eta_q} \quad (18.2)$$

Fig. 18.2 shows that CHP systems of the point A have a positive ERI (about 15%), while the CHP systems of the area B is slightly more convenient, in spite of their higher electrical efficiency (notice that an electrical efficiency of about 40% cannot be achieved for a CHP system of domestic size, with the actual technology, but is

possible only with systems of hundreds of kilowatts, for instance CHP internal combustion engines).

In conclusion, CHP systems with an electrical efficiency $\eta_e = 0.1$, or lower, can obtain an economic saving of about 15% if the fuel cost and the capital cost are low enough, and the reference cost for the conventional supplying of heat and power are not too low.

Let's consider a very simple example. A domestic CHP system of 1 kW_e, with electrical and thermal efficiency of 10% and 80%, respectively. Taking into account the previous hypotheses and the following additional ones:

- 2500 h/year of full load operation;
- a complete self-consumption of the produced electricity (covering in this way a part of the total annual electrical demand in the range 50–85%);
- the self-consumption of the produced heat of 95%, by means of a heat storage of proper size.

It can be easily inferred that the gross economic saving allowed by the CHP is about 2100 €/year, while the fuel cost is about 1850 €/year. The difference, 250 €/year, has to be reduced because of the additional cost for maintaining the CHP system (if any) with respect to a conventional boiler, so that the investment can be regarded to produce an annual income of about 200 €. These data demonstrate that the application of ORC in domestic application is very promising from a thermodynamic standpoint but it can only become economically attractive with the adoption of incentive schemes, for example, fuel cost reduction.

Considering the typical European domestic average yearly electricity consumption and, in particular, the Italian one (Franco Di Andrea, 2004), it emerges that the yearly need is in the range of 3000–5000 kWh. On this basis, in the case of a micro-generator operating at constant load, grid connected or integrated with an appropriate storage, the output for satisfying completely the average electrical need is, therefore, approximately 350–600 W.

When considering the ORC, constant load operation is only possible if heat is necessary and available. Normally, this is not the case as, especially in warm weather seasons, dwellings need for heat is only marginal compared to the winter period and, anyway, not enough to run the ORC with the mentioned output. Therefore, the optimal size for a domestic ORC depends on many factors, but considering also the cost and the need to dissipate a large amount of heat, it results that a power output from 300 W to 2 kW can be considered a good choice for most cases in the considered application. Bigger sizes can be chosen if multiple dwellings are connected simultaneously or in the case of particular applications where heat can be recovered from a biomass boiler, solar collector, or other heat sources.

The ORC system has to withstand different country-specific laws and rules. The operating fluid has to satisfy the rules for safety and the environment. In particular, the quantity and the pressure of the fluid in the plant has to be kept to a minimum as very stringent rules (Directive, 2014/68/UE, May 15, 2014) apply to systems where vessels can reach high pressure and explode.

The maximum operating temperature depends on the saturation temperature and on the chemical stability of the fluid. Nevertheless, problems may arise in the way heat is

transferred from the heat source to the operating fluid. When a transfer media is used, other than water, again specific laws and rules apply and its cost can be significant. Therefore, a typical choice can be a maximum temperature in the operating fluid of 130–150°C. In order to achieve a reasonable system efficiency (>3–4%), the lowest evaporating temperature should not be lower than 90–100°C.

In domestic application dimensions, noise and vibrations are very important, but the system cost is the most stringent requirement. Ideally the system should be used and installed as a traditional heat pump as it requires a heat dissipation unit as well. This unit can be demanding in terms of volume if there is no possibility to use the low temperature heat.

As for cost reduction, system components can be selected from high volume production industrial fields such as the automotive or air conditioning industry. This choice may not meet the maximum achievable performance, as the components have not been designed for the specific application, but it can be advantageous not only for the cost but in terms of reliability and maintenance as well.

In general, assuming a system efficiency of 5–8% and the design electric power output of 400–500 W, the output thermal power is expected to satisfy the typical thermal need of a central European new dwelling, provided that low temperature heat can be used.

18.2 Existing models and prototypes and comparison with solutions based on Stirling engines

At the beginning of the 21st century, various prototypes of small CHP systems based on external combustion engines (Stirling or Rankine) were studied, but only a few of them have reached the market at the present time, or are close to it. In the following section they are discussed jointly with a concise summary of their claimed, or expected performance and features (Tchanche et al., 2014; microchap.info).

- Eneftech (Switzerland) (www.eneftech.com)
 - Thermodynamic cycle/expander: Rankine with R245fa and scroll expander.
 - Electrical efficiency: up to 10% (maximum efficiency in correspondence with minimum allowed condensing temperature).
 - Thermal efficiency: up to 85%.
 - Input energy sources: heat at 120–200°C.
 - Electric power output: 5–30 kW.
 - Note: the hermetic scroll expander is integrated with the feed pump (patent no WO 2009050126 A4).
- Enogia (France) (www.enogia.com)
 - Thermodynamic cycle/expander: Rankine with R245fa (or Novec 649) and axial turbo-expander.
 - Electrical efficiency: 5–8% (R245fa) or 6–10% (Novec 649).
 - Thermal efficiency: NA
 - Input energy sources: hot liquid from 60°C (R245fa) or 110–180°C (Novec 649)/ exhaust gases at 150–500°C.

- Electric power output: 5–100 kW.
- Note: the cooling fluid in the condenser is water/glycol at 10–30°C (R245fa) or 50–80°C (Novec 649).
- Flowgroup (previously Genlec, UK) (<http://flowgroup.uk.com/>)
 - Thermodynamic cycle/expander: Rankine with organic refrigerant and scroll expander.
 - Electrical efficiency: NA
 - Thermal efficiency: NA
 - Input energy sources: natural gas.
 - Electric power output: 1 kW.
 - Note: it is currently the only truly wall-mounted micro CHP anywhere in the world.
- Powerblock (previously Otag, Germany) (<http://www.powerblock.eu>)
 - Thermodynamic cycle/expander: steam Rankine (350°C and 25–30 bar) and a single cylinder volumetric expander with two opposing pistons.
 - Electrical efficiency: 8.5–10%.
 - Thermal efficiency: 75–84%.
 - Input energy sources: natural gas.
 - Electric power output: 2 kW.
 - Note: the advantages claimed for the steam double piston, without any rotating parts, are quiet operation, low maintenance costs, and extended service intervals.
- Cogen Micro (Australia) (<http://www.cogenmicro.com/>)
 - Thermodynamic cycle/expander: steam Rankine and a single cylinder alternative volumetric expander with twin opposed piston.
 - Electrical efficiency: up to 16.5%.
 - Thermal efficiency: up to 83.5%.
 - Input energy sources: heat from solar panel/heat recovery, or natural gas.
 - Electric power output: 1–3 kW.
 - Note: in 2011 Cogen Micro appears to have left steam in favor of an ORC. The main original feature is that a reciprocating expander is used because of its expected higher volumetric expansion ratio than scroll and screw solutions.
- Kaymacor (Italy) (<http://www.kaymacor.com>)
 - Thermodynamic cycle/expander: Rankine with R245fa and scroll expander.
 - Electrical efficiency: up to 10%.
 - Thermal efficiency: up to 84%.
 - Input energy sources: heat from solar collector/heat recovery, or biomass.
 - Electric power output: 2–4 kW.
 - Note: nominal thermal power input at 145°C.
- WhisperGen (UK) (<http://www.whispergen-europe.com>)
 - Thermodynamic cycle/expander: Stirling with four cylinders.
 - Electrical efficiency: 11%.
 - Thermal efficiency: 85%.
 - Input energy sources: natural gas.
 - Electric power output: 1 kW.
 - Note: heat output with auxiliary burner 13.2–14.5 kW (at 60–80°C). No longer available on the market.
- Microgen (NL) (<http://www.microgen-engine.com/>)
 - Thermodynamic cycle/expander: Stirling with Linear Free Piston Stirling Engine (LFPSE).
 - Electrical efficiency: 12%
 - Thermal efficiency: 83–94% (condensing mode)

- Input energy sources: natural gas.
- Electric power output: 1 kW.
- Note: a similar product is also commercialized by Baxi <http://www.baxi.co.uk/>.
- Qnergy (previously Infinia, USA) (<http://www.qnergy.com/>)
 - Thermodynamic cycle/expander: Stirling with LFPSE.
 - Electrical efficiency: up to 20%.
 - Thermal efficiency: up to 82%.
 - Input energy sources: Natural gas or propane as well as wood pellets.
 - Electric power output: 3.5–7.5 kW.
 - Note: thermal energy is produced in a condensing heat exchanger so that the global efficiency with respect to the Low Heating Value of the fuel can be greater than 100%.
- Cleanergy (Sweden) (<http://cleanergy.com>)
 - Thermodynamic cycle/expander: Stirling alpha type with helium as working fluid.
 - Electrical efficiency: up to 22–25%.
 - Thermal efficiency: about 70%.
 - Input energy sources: natural gas or landfill gas, biogas, solar heat.
 - Electric power output: 2–9 kW.
 - Note: some helium leakage still occurs and the working fluid is continuously replaced from a cylinder which must be periodically replenished.

Note that the previously cited performance data have been partially extracted from commercial documents and partially inferred by numerical elaboration. In addition, the input heat sources are not the same so that comparison between the performances of different models is not always consistent. Generally speaking, the Stirling units have a higher electrical efficiency, but it can be obtained only when high temperature combustion gases are available as heat input and the cold piston is cooled at a temperature low enough (about 40°C). When the energy source is heat in the range 150–250°C and/or the cogenerated heat is needed at 80–90°C, the electrical efficiency is strongly reduced and the flexibility of the Rankine units can be advantageous.

18.3 Main technical features of domestic Organic Rankine Cycle components

The most demanding components in terms of efficiency and performance are the expander and the feed pump. As far as the first one is concerned, the use of a turbine for such small-sized expanders involves a number of disadvantages, which include: low efficiency in part-load conditions, too high a rotational speed, intolerance of moisture content in the expanded vapor, and high cost.

A possible alternative is represented by a modified commercial scroll compressor used as an expander (Zanelli and Favrat, 1994; Yanagisawa et al., 2001; Kane et al., 2003, 2007; Xiaojun et al., 2004; Lemort et al., 2006, 2009; Kim et al., 2007; Saitoh et al., 2007; Hugenroth et al., 2008; Peterson et al., 2008; Yang et al., 2008). This device is commonly hermetic, with the compressor and the electric motor in a unique sealed vessel. Both the compressor and the electric machine could operate in reverse mode, as an expander and a generator respectively, often without major

revisions. This choice is interesting because this kind of machine is produced in high volumes and therefore the cost is low. It is designed to work with refrigerants, which are very similar in physical and thermodynamic properties to the organic fluids used in ORCs. On the other hand, high expansion efficiency must also be obtained in order to avoid an unacceptable reduction of the already scarce effectiveness of low temperature ORC cycles. Such efficiency depends on the matching between some scroll characteristics (hermetic or open drive, oil-free or not, and built-in volume ratio) and operating fluids, that determine the values of volumetric efficiency, built-in pressure ratio, and heat transfer that contribute to the overall machine efficiency and mechanical losses. In the literature, adiabatic efficiency values of 60–65% (Zanelli and Favrat, 1994; Yanagisawa et al., 2001; Lemort et al., 2006; Saitoh et al., 2007) and 68–70% (Kane et al., 2003; Lemort et al., 2006, 2009; Saitoh et al., 2007), are reported. Fig. 18.3 illustrates the distribution of losses and the value of the overall efficiency calculated for a commercial compressor operating at reverse flow with R245fa as a function of the expansion ratio (Clemente et al., 2010). The higher curve takes into account only the losses connected with the expansion ratio; it can be seen that 100% efficiency is reached if the built-in pressure ratio of the machine is imposed between the

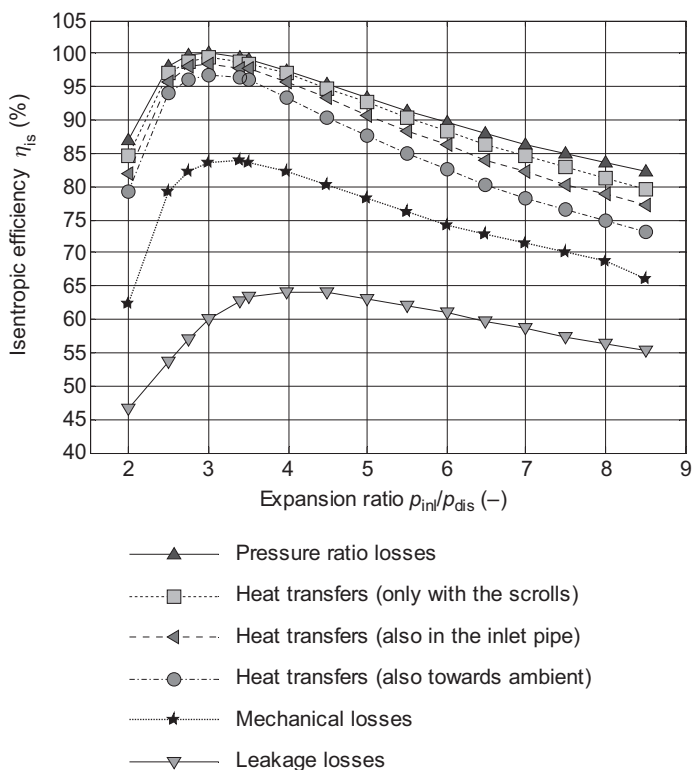


Figure 18.3 Scroll expander isentropic efficiency versus expansion ratio (fluid: R245fa) (Clemente et al., 2010).

inlet and the discharge. Otherwise, for smaller ratios, the fluid is recompressed at the discharge, while for higher ratios a part of the expansion is unexploited. When heat transfers are considered, the isentropic efficiency decreases: it can be noted that the main effect is relative to ambient losses, so the scroll expander has to be thermally insulated in order to achieve better performances. Since mechanical losses are approximately independent from the expansion ratio, they have a greater influence on the efficiency at smaller ratios, when less work is done by the fluid. Finally, the leakage can cause a great decreasing in the isentropic efficiency, as shown by the lowest curve in Fig. 18.3. The maximum value reached with these simulations is about 65%, comparable with the already cited literature data. It is interesting to note that the expansion ratio that ensures the best isentropic efficiency is greater than that defined by the machine geometry (which leads the higher curve in Fig. 18.3 to reach 100% efficiency).

The maximum efficiency and the corresponding value of expansion ratio vary with the operating fluid; Fig. 18.4 compares the performance of the same machine considered in Fig. 18.3, fed by R245fa, isopentane, and air; the trends shown for R245fa and isopentane are quite similar, with the maximum reached for a pressure ratio slightly greater than the built-in one and with the best performances achieved with the first fluid. The efficiency with air reaches the maximum at a higher expansion ratio because of the very different thermo-physical properties of this fluid.

In all cases, high expansion ratios (above 4–5) are penalized by the lower efficiency of the scroll. Fig. 18.5 shows, as an example, a set of experimental data regarding a commercial scroll compressor, used as an expander, to produce electric power in the range of 2 kW, and operating at various speeds, with R245fa as a working fluid. While the isentropic efficiency is almost independent from the speed, it decreases almost

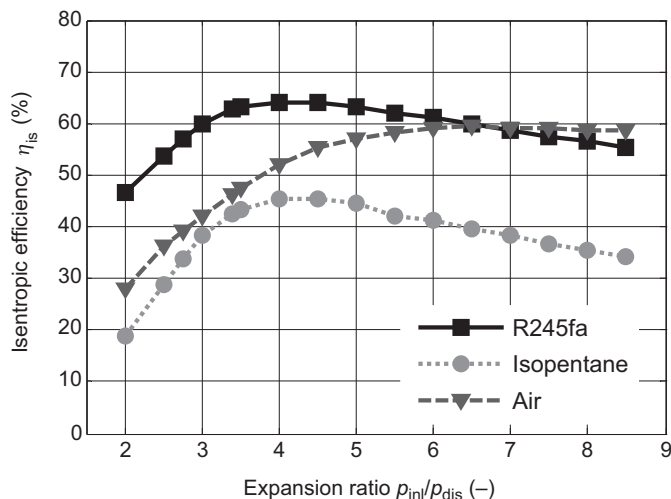


Figure 18.4 Scroll expander isentropic efficiency versus expansion ratio for three working fluids (Clemente et al., 2010).

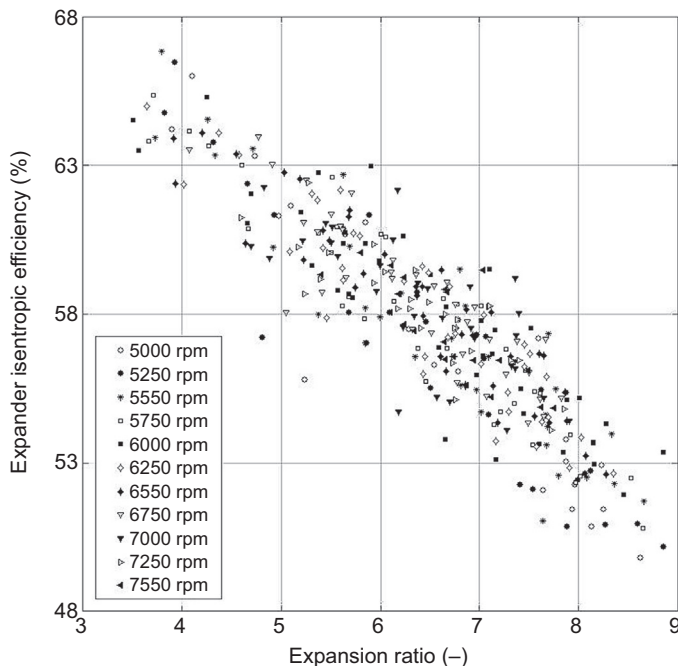


Figure 18.5 Experimental expander isentropic efficiency versus expansion ratio at various speeds (fluid: R245fa).

linearly with the expansion ratio, because it is always greater than the built-in value, showing good qualitative agreement with the corresponding theoretical data of Fig. 18.3.

This behavior, typical of the most commonly available scroll compressors that can be used as expanders, reduces the well-known thermodynamic advantage of high expansion ratio Rankine cycles, obtained by high evaporating and low condensing pressures, as shown in Fig. 18.6. In this figure, two global performance indexes are taken into account: the expander isentropic efficiency and the cycle electric efficiency. The first one is defined by:

$$\eta_{\text{exp,is}} = \frac{P_e}{\dot{m}(h_{\text{in}} - h_{\text{out,is}})} \quad (18.3)$$

where P_e is the electric power delivered by the expander, \dot{m} is the working fluid mass flow rate, h_{in} is the specific enthalpy of the fluid at the expander inlet, and $h_{\text{out,is}}$ is the specific enthalpy of the fluid after an isentropic expansion from the inlet conditions to the discharge pressure. With such a definition, the expander isentropic efficiency also accounts for mechanical and electric losses; the net power is compared to the work rate of the fluid in an ideal adiabatic expansion, within the hypothesis that kinetic energies in the expander inlet and discharge measurement sections were negligible.

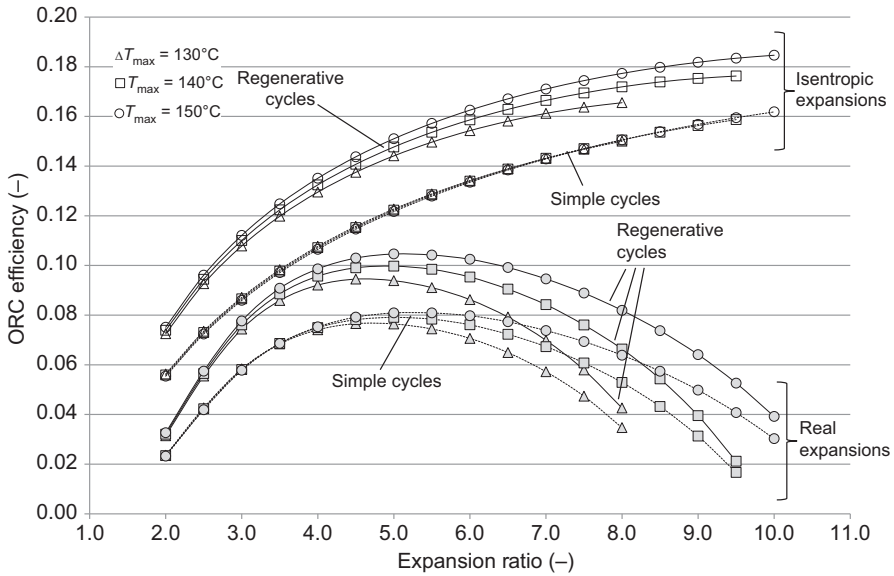


Figure 18.6 Organic Rankine Cycle (ORC) efficiency as a function of the expansion ratio. Working fluid: R245fa; condensation temperature: 40°C; expander shaft speed: 3000 rpm; maximum temperature: variable at three levels (see label); cycle arrangement: simple (dashed lines) and regenerative (continuous lines); expansion process: isentropic (empty markers) and real with variable efficiency (solid markers) (Clemente et al., 2012).

The cycle electric efficiency is defined as the ratio between the net electric power generated by the system and the heat rate absorbed by the operating fluid:

$$\eta_{\text{ORC}} = \frac{P_e - P_p}{\dot{m}(h_{\text{VG,out}} - h_{\text{VG,in}})} \quad (18.4)$$

where P_p is the power absorbed by the pump, and $h_{\text{VG,in}}$ and $h_{\text{VG,out}}$ are the specific enthalpy of the fluid at the vapor generator inlet and outlet, respectively.

The efficiency curves of an R245fa cycle are given as a function of the expansion ratio, keeping constant the values of the scroll rotational speed and of the condensation temperature, equal to 40°C, which corresponds to a discharge pressure of 2.52 bar. Three values (130, 140, and 150°C, the last one of which is considered the maximum allowable with R245fa to avoid chemical stability problems with a reasonable safety margin) have been taken into account for the maximum temperature of the cycle, assumed in both simple and regenerative arrangements. Note the difference between the cycle efficiencies calculated considering the actual expansion process taking place in the scroll machine (reported in the diagram with empty markers) and the cycle efficiencies calculated by considering an isentropic expansion (solid markers), in all the previously described conditions. The isentropic curves show the thermodynamic advantage that could be obtained by adopting higher expansion ratios, i.e., in the

considered hypothesis, by adopting higher evaporating pressures that, for a given maximum temperature, correspond to lower superheating degrees. On the other hand, however, the curves calculated considering the actual expansion processes show that high expansion ratios (above 5) are penalized by the low efficiency of the scroll. The best electrical efficiencies range between 0.105, in the regenerative case at a superheating temperature of 150°C, and 0.075, in the simple case at 130°C. But if an expander could reach its maximum isentropic efficiency at an expansion ratio of 9–10, a so equipped ORC could reach efficiency of about 0.14 in the regenerative case or of 0.12 in the simple case, together with higher values of the delivered electrical power (Clemente et al., 2012). Such results could be obtained with scroll expanders with higher built-in volume ratio, with a multistage expansion or with different types of expanders.

It must be noted that scroll compressors are not commonly oil-free, so that the actual operating fluid is a mixture of an organic fluid and a lubricant oil, with a mass concentration of oil up to about 5%. The lubricant must be chosen according to its solubility in the refrigerant and its viscosity and chemical stability at the relatively high operating temperatures reached in the functioning of the scroll as an expander. Only fully synthetic lubricants can be used and, because quite high velocities are usually reached in the circuit, the circulation of the mixture along all the system is acceptable, avoiding the need for an oil separator downstream of the expander, especially in the case where the pump requires lubrication. It must also be noted that, when an expander is directly derived from a compressor, the operation temperature limit has to be carefully checked, because the input temperature in the expander mode could be higher than the compressed fluid temperature in the compressor mode. Therefore, the lubrication conditions could be less effective, and seals and couplings may be corrupted faster thus limiting the operational life of the expander with respect to that of the original compressor.

Besides dynamic and scroll expanders, interesting results could be obtained with suitably designed reciprocating expanders (Clemente et al., 2011; Ferrara et al., 2013), as shown in Fig. 18.7, where, with reference to R245fa as working fluid, efficiency and power of a scroll expander with a best efficiency expansion ratio equal to

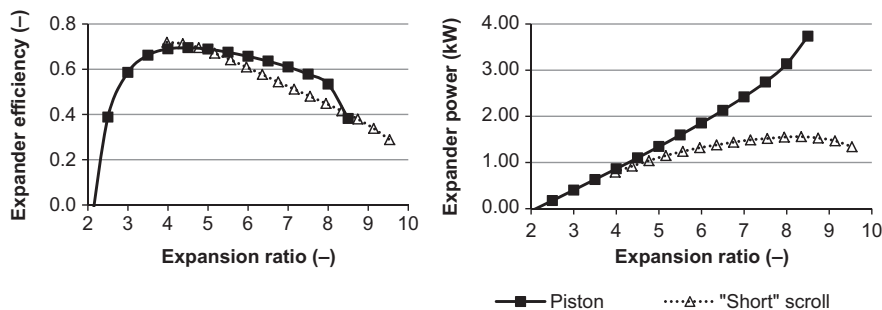


Figure 18.7 Comparison between piston and scroll expanders with R245fa at $T_{\text{cond}} = 40^\circ\text{C}$ and $T_{\text{max}} = 150^\circ\text{C}$ (Clemente et al., 2011).

3.5 and displacement of 34.31 cm^3 are compared with that of a reciprocating expander having a volumetric expansion ratio equal to 5 and displacement of 169 cm^3 .

The efficiency curves of the expanders show that the reciprocating one (Piston) allows a gradual increment of efficiency with expansion ratios greater than the scroll case optimum, up to a value after which its performance decays rapidly, and becomes lower than that of the scroll. The power curves exhibit very different shapes at high expansion ratio values; the reciprocating expander power reaches values more than twice that of the scroll. Such a behavior can be explained by taking into account that, at high expansion ratios, under-expansion operating conditions occur, so that, during the discharge phase, the working fluid pressure is suddenly reduced to the discharge value. In the reciprocating device, there is also the initial pressure of the admission phase while, on the contrary, in the scroll device, the spiral shaped wraps keep the admission and the discharge chamber apart, so that the initial pressure in the admission volume is higher than that of the discharge chamber. As a consequence, the mass of high pressure fluid introduced in the working volume in such operating conditions is lower in the scroll expander, and consequently the produced power is also lower. Such interesting results could be obtained with reciprocating expanders having a cut-off ratio (the ratio between the cylinder volume at the moment in which the admission valve is closed, minus the dead volume, and the machine displacement) and valve timing properly chosen, that is only with machines newly and properly designed. This would involve costs higher than that of the light modification needed by a commercial scroll compressor, to satisfactorily work as an expander for organic fluids.

As far as the pump is concerned, its choice has a key role in the design process of an ORC-based cogenerator (Clemente et al., 2013). Even if the most important selection criteria for a pump are the delivered flow rate and the achievable pressure increase, the choice of the best-suited technology for particular applications like the ORCs depends also on other factors, such as operating temperatures and pressures, compatibility of the fluid with the pump materials, and fluid viscosity (Smith et al., 2007). In particular, this last parameter is one of the most critical, since organic fluids feature, in most cases, a very low viscosity, that causes important leakages from the machine seals and from the pumping mechanisms, and limits the lubricating properties of the fluid itself. As an example, the influence of the fluid viscosity on the delivered flow rate of a gear pump is reported in Fig. 18.8.

While the current technology in large- and medium-scale ORC installations is represented by centrifugal feed pumps (Micheli and Reini, 2007), this solution is not suitable for smaller systems; in fact, the concurrent requirements of low flow rates and high differential pressures can be satisfied by a centrifugal machine only if multistage architectures are considered, but this option entails excessive cost and bulk (Smith et al., 2007). Positive displacement pumps appear then a more suitable alternative for domestic scale ORCs, but they involve some drawbacks such as a relatively low efficiency. Because the power consumption of the pump is an important fraction of that produced by the expander, the optimization of this component is essential to achieve an acceptable global electrical efficiency for the system.

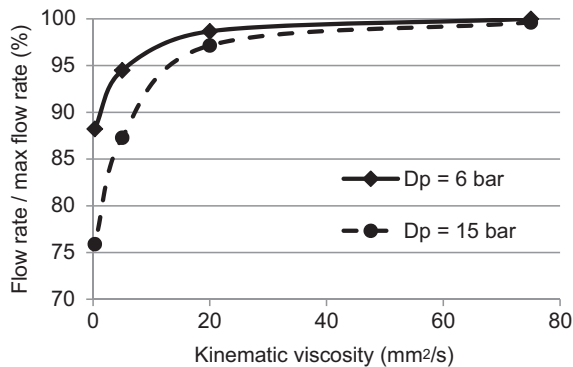


Figure 18.8 Normalized flow rate as a function of the fluid viscosity for a gear pump at nominal speed.

Only a few works relating to the feed pumps of a small-scale ORC can be found in the literature. In 1985, Bala et al. presented a paper in which they described the tests carried out on a sliding-vane pump operating with two different organic fluids, CFCs R11 and R113, now banned. The authors found that some enhancements in the pump performances can be achieved by adding a relatively small percentage (around 10%) of oil in the refrigerants, but in any case, the machine cannot reach global efficiencies (i.e., including the electric motor efficiency) higher than 0.21. In his PhD thesis, Aoun (2008) conducted an analysis on the different pumps potentially adoptable in a small-scale ORC, evaluating the main features of some commercially available positive displacement units. Only a few examples of gear, sliding-vane, and reciprocating piston machines, suitable to deliver the needed flow rate at a sufficient pressure with low-viscosity working fluids were found on the market. The working temperature of the piston type was limited to 50°C, being designed for hydraulic systems, so they could be adopted only in ORC systems that are not required to cogenerate heat at high temperatures, while the declared efficiency was very high, up to 0.78 at the best working conditions, but the datum does not include the electric motor losses. A small brass reciprocating pump installed on a small-scale ORC system is cited in Davidson (1977), which exhibited a global efficiency variable in the range 0.17–0.20. Therefore, according to Aoun (2008), diaphragm pumps represent the best-suited option for small-scale ORC applications. In these machines, the diaphragm provides a physical seal so that leakage is avoided and the maximum achievable pressures are independent from the fluid viscosity. This technology however presents a number of drawbacks. They are generally heavier and bulkier than gear or sliding-vane pumps and are also extremely sensitive to cavitation, which may cause membrane perforation (Aoun, 2008). Moreover, these devices can have very low efficiencies: for example, Declaye (2009) and Quoilin (2011) described the experimental prototype of an ORC cogenerator in which the diaphragm feed pump was not capable of reaching global efficiencies higher than 0.15–0.20 at the best working conditions, with maximum delivery pressure limited to 12 bar. This literature review confirmed that

the feed pump is a critical component of a small size ORC system, due to the difficulties connected with the handling of the organic fluids suitable for these installations, the low efficiency of commercial small-scale devices and electric motors, the high value of the ratio between the power required by the pump and the power developed by the expander, which characterizes ORC's (small-scale ones in particular), and the requirement of low cost.

Clemente et al. (2013) described a gear pumps solution which reached a good compromise between performance and cost. The pump was operating with a mixture of R245fa and lubricant, at the running conditions normally found in a small-scale ORC application. The exact percentage of oil in the mixture has to be set properly not only with respect to the pump, but also according to the expander requirements, for example, in normal conditions, a scroll expander (not oil-free type) needs a lubricant content of at least 5%.

Fig. 18.9 reports the volumetric flow rate delivered by the pump as a function of the difference of pressure between suction and discharge at various speeds; the flow rate does not collapse even at the highest values of differential pressure, despite the very low viscosity of R245fa. Performances are surely poorer of that obtainable with more viscous liquids, as fossil fuels, according to Fig. 18.8, but still acceptable for the considered applications. The corresponding trends of pump efficiency, obtained taking into account only the mechanical power absorbed by the pump (i.e., not considering the efficiency of the electric motor) are reported in Fig. 18.10. Except for the lowest velocities, when the relative influence of the leakage across the gears is larger, efficiency increases with pressure, with a stabilization around a value of 0.6 for differential pressures larger than 6 bar (below this threshold the power given to the fluid is low, but the absorbed mechanical power does not decrease with the same rate, due to the larger relative contribution of the mechanical losses). These efficiencies appear to be quite interesting, corresponding to an absorbed power of about 8–10% of the power delivered by the expander, that is a surely remarkable part, but acceptable for systems of this range of power. Note that the electric motor must be chosen very carefully, because its efficiency can be very low in the considered range of power, down to 0.3–0.4 for the cheapest units, penalizing in such cases the actual performance of the pump.

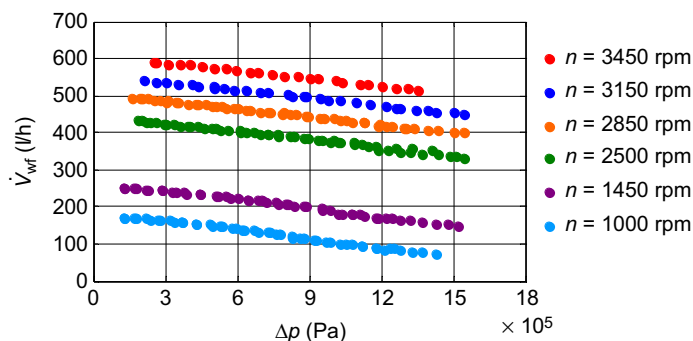


Figure 18.9 Flow rate of a gear pump as a function of the imposed differential pressure (fluid: R245fa) (Clemente et al., 2013).

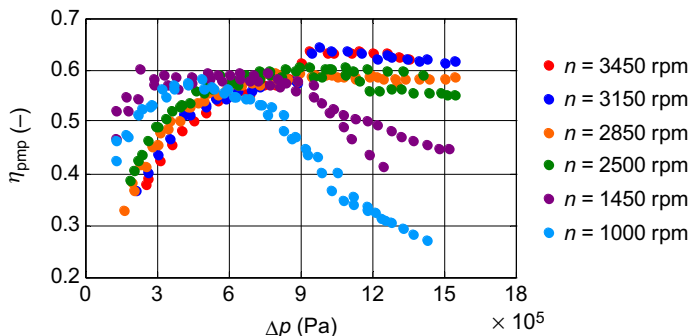


Figure 18.10 Gear pump efficiency as a function of the imposed differential pressure (fluid: R245fa) (Clemente et al., 2013).

Besides the expander and the pump, the other main components of an ORC unit are the heat exchangers and piping. Downscaling of the ORC system suggests the utilization of plate heat exchangers, instead of the shell and tube types used in big machines, if the choices regarding the general layout allow such a technical solution. To define the basic layout of a domestic ORC, the following choices must be done:

- operating fluid heated directly by the available hot source fluid (combustion product or hot water) or indirectly by means of an intermediate diathermic oil;
- simple or regenerative cycle;
- nature and temperature of the cooling fluid in the condenser;
- control strategy.

Schemes of possible arrangements are given in Fig. 18.11.

The choice between direct heating or by means of an intermediate diathermic oil is thermodynamically irrelevant, if the temperature of the heat source is high enough to make the constraint on the maximum temperature of the cycle to be affected only by the chemical–physical characteristics of the operating fluid. With intermediate oil, the evaporator stands for the boiler implemented in others ORC machines, available on the

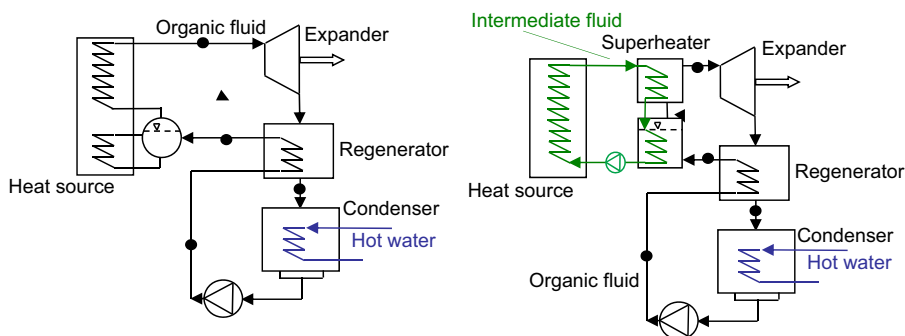


Figure 18.11 Example of Organic Rankine Cycle layout with direct and indirect heating of the working fluid.

market. Integration of an evaporator instead of a boiler makes it possible to use the same design with standardized components for all possible ORC applications: recover waste heat in small industrial processes, utilization of solar or geothermal heat, and integration with internal combustion engines or pellet boilers.

Regeneration is a possible design choice, because there is a trade-off between the thermodynamic advantage and the higher cost, bulk, and layout complication. It is well known that regeneration increases the electrical efficiency of the group (e.g., using R245fa with 150°C temperature of heat source, evaporating pressure 15 bar and 20°C temperature at the condenser, the use of a regenerator allows an overall cycle efficiency higher than 10%) but does not alter the maximum power obtained, because the shape of the cycle in the (T , s) plane does not vary, and therefore the expansion and pumping works remain unaffected. If the amount of heat saved because of the nonheating of the working fluid in liquid phase is not made available from the heat source, for example, to produce hot water in the case of cogeneration plant, then it may be preferable to give up the regeneration. The result is a more complete exploitation of the available heat in the hot source, lowering the exit temperature of the heating flow down to the achievement of technical limits or regulatory requirements, if any. In other words, if it is not possible to cool down the heat source to ambient temperature, regeneration can be very profitable.

In the condenser, the heat is exchanged with the cooling water. Full utilization of such low temperature water (in the range 20–60°C) is an essential point for the economic convenience of domestic ORC application. As a matter of fact, only in a cogenerative configuration a small ORC system can be attractive. With the use of a dry or water cooler to dissipate heat, benefits of the ORC machine are largely decreased. Two typical temperatures can be considered:

- $T_{\text{cond}} = 40^\circ\text{C}$, in order to produce hot water at a temperature sufficient for the sanitary needs or for space heating with radiant panels;
- $T_{\text{cond}} = 60^\circ\text{C}$, so that the produced hot water is compatible with the use in traditional space heating systems.

The effect of the variation of the condensing temperature on the efficiency and expansion ratio of a regenerative cycle, operating with R245fa in working conditions typical of domestic applications, are shown in Fig. 18.12.

With regards the control strategy options, it must be noted that small volumetric expanders have good efficiencies and reach the required volumetric flow rate at relatively high speeds, not compatible with the direct coupling of an alternator producing electricity at 50 or 60 Hz. Reduction gears can be conveniently replaced by static power-conditioning systems, which also allow the shaft speed of the group to be treated as a free variable, if such a solution is convenient from the control system point of view. The three-phase voltage generated by the alternator at variable frequency is converted in direct-current and then again in alternate current at the grid frequency by a power conditioning system. Fig. 18.13 shows a scroll expander shaft speed as a function of the expansion ratio for different operating conditions of a small group using R245fa.

By fixing the amount of energy introduced in the system by the evaporator at a defined temperature, and taking into account that the operating fluid mass flow rate

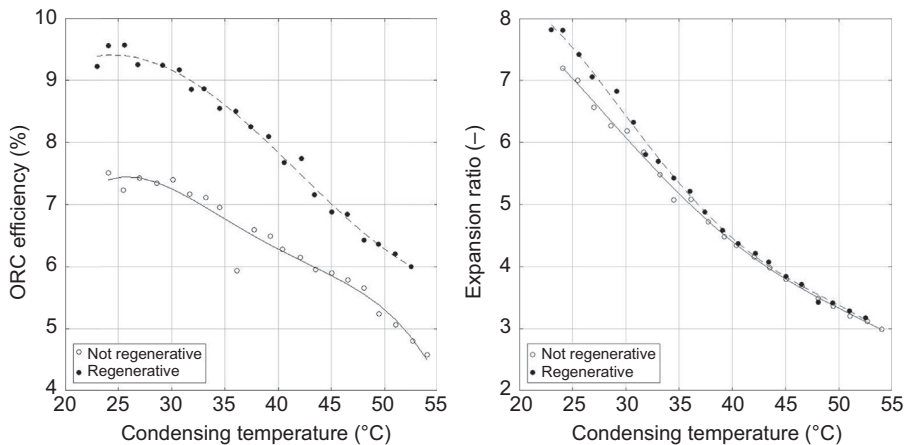


Figure 18.12 Effects of condensing temperature variation on Organic Rankine Cycle (ORC) efficiency and expansion ratio.

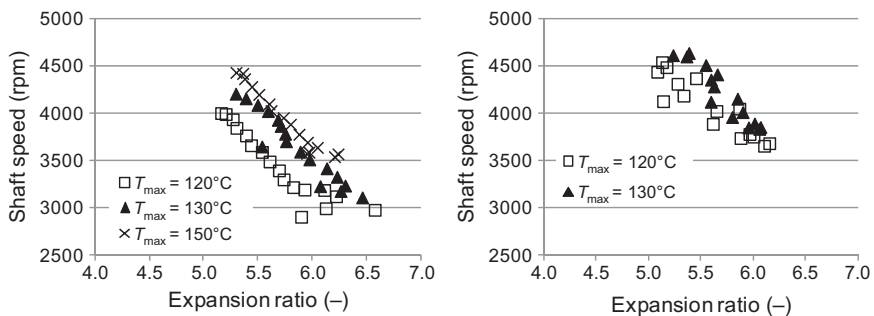


Figure 18.13 Scroll expander shaft speed as a function of the expansion ratio at different temperatures of production of vapor, for a pump shaft speed equal to 300 rpm (left) and 400 rpm (right) (Bracco et al., 2013).

is given by the pump, the expander shaft speed controls the evaporating pressure: obviously, the density of the superheated vapor must be compatible with the volumetric flow rate allowable at the inlet of the expander at a given shaft speed. Given also the condensing temperature, the evaporating pressure determines the differential pressure and as a consequence, both the expander and the cycle efficiency, as discussed in the previous paragraphs.

Expander and pump speeds are then the main control parameter of an ORC; it can be decided to use both, only one, or none of them, depending on the complexity and cost of the control system, compared with the obtainable technical and economical advantages.

The expander speed could be maintained at a constant value in every case higher than that required by the grid frequency, which assures the maximum delivered power in a

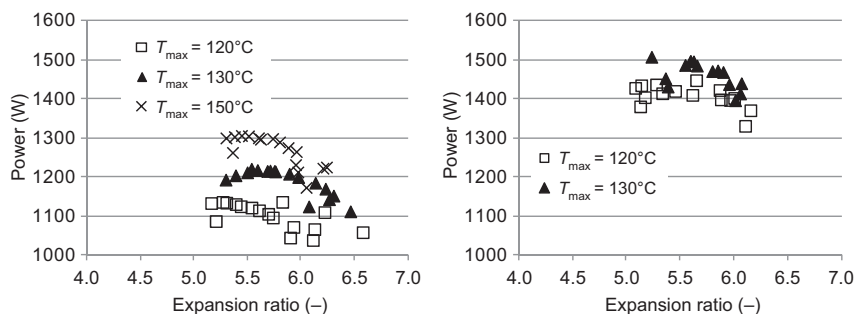


Figure 18.14 Power delivered by a scroll expander as a function of the expansion ratio at different vapor temperatures, for two pump shaft speeds 300 rpm (left) and 400 rpm (right) (Bracco et al., 2013).

range of superheating temperatures and pump speeds, as can be observed by analyzing the diagrams of Figs. 18.13 and 18.14 that refer to the same set of experimental data. The efficiency of the system should result closely to the maximum achievable values, because the combined effect of the expansion ratio, controlled by the expander speed, on both the cycle and the expander thermodynamic effectiveness results in a quite flat overall efficiency curve in a wide combination of operating conditions.

If the pump speed also has to be constant (i.e., the electric motor is simply connected to the grid, without the cost of the inverter and its control system) the group will have good efficiency close to the maximum power operating point and a limited operating range. In the case of higher availability of thermal power from the hot source, which would have required an increased pump speed, heat recovery will be limited by the reaching of the maximum allowed temperature of superheated vapor. On the contrary, in the case of lower availability that would require the decrease of pump speed, the superheating temperature will fall down towards the saturation value; full evaporation could be not assured and the group should be shut down. This fact also limits the possibility of energy recovery from low temperature sources (in the range $90\text{--}100^{\circ}\text{C}$).

It must be noted that, in the case of a pump with a constant speed, the mass flow rate of the pump must be close to the design value of the ORC group, or that the ORC must be designed according to the pump.

A very interesting option is the mechanical coupling of the pump and expander; the advantage of this is the elimination of the electric motor of the pump, whose efficiency is often very low (as previously observed), this then penalizes the performance of the group, especially in the case of low temperature heat sources and/or cogenerative configurations. The control options are more limited, i.e., it is not possible to adjust the combination of evaporating pressure and superheating temperature by varying independently, the pump and expander speeds, but the ratio of the volumetric flow rates of the two machines remains automatically constant, thus making it easier to control the vapor properties in the case of variable speed operations. The only true drawback of this technical solution is the high cost, because integrated group expander—pumps

are not actually on the market and, moreover, the most commonly available scroll expanders have a hermetic structure to avoid fluid leakage, without an external mechanical connection that allows the coupling with the pump shaft. The only small-scale ORC units adopting this solution are the units by Eneftech (previously cited) that are at the upper limit for the considered domestic application.

To target a competitive cost for a domestic application, the internal layout of the ORC unit has to be carefully designed. A modular approach should be followed, in this way, each module can be sub assembled and tested as a stand-alone component; through their integration, a very compact unit can be built.

Besides the component integration, a key role is played by the control system, in order to obtain the maximum energy saving allowed by the set of adopted components. The block diagram of a possible power and control electronics of a typical domestic ORC is shown in Fig. 18.15. The expander shaft is connected to a high-efficiency permanent magnet synchronous machine (PMSM), operating as an alternator and “fed” by a three-phase inverter.

PMSM represents the preferred solution among the electrical actuators due to specific characteristics, such as high power density, negligible (or low) rotor losses, high torque/weight ratio, robustness of the rotor structure, and possibility of flux-weakening operation (i.e., high-speed operations). In the common stator/rotor assessment, these machines are excited through permanent magnets positioned either on the surface or inside a cylindrical iron-laminated rotor body, leading to surface permanent magnet (SPM) or interior permanent magnet machines (IPM) respectively. The stator is similar to the one found in standard induction machines and hosts three-phase windings. Due to the particular arrangements of permanent magnets, SPM machines are often referred to as nonsalient machines, since the magnetic properties of the rotor, as seen from the stator windings, are more or less independent on the rotor position, i.e., the stator

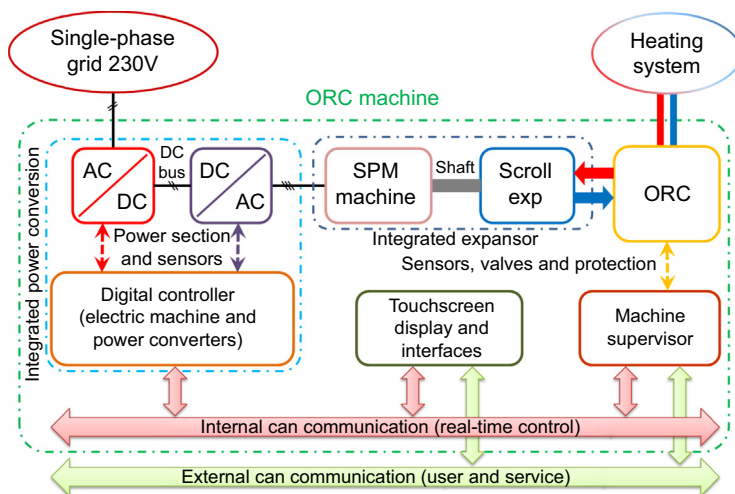


Figure 18.15 Block diagram of the power conditioning and control unit for a domestic Organic Rankine Cycle (ORC).

inductance is constant. On the other hand, IPM machines are salient rotor machines (i.e., the stator inductance is varying with the rotor position), and provide a higher torque density, increased robustness, and more efficient flux-weakening operations with respect to SPM machines.

Proper real-time control of the machine has to be adopted (i.e., sinusoidal vector control in the synchronous reference frame) in order to allow direct control of the braking torque, thus maximizing dynamics, torque to current ratio, and increasing the efficiency of the mechanical-to-electrical power conversion (Bolognani et al., 2014, 2011).

Vector control strategy can be derived directly from the dynamic voltage model of PMSM, including the torque equation. A convenient and equivalent two-phase orthogonal complex reference frame, namely the dq synchronous reference frame, oriented according to the stator flux linkage due to permanent magnet is considered and voltage equations of these two phases are written as follows:

$$\bar{u}_{dq} = R\bar{i}_{dq} + \mathbf{L} \frac{d\bar{i}_{dq}}{dt} + \omega_{me} \mathbf{J} \mathbf{L} \bar{i}_{dq} + \omega_{me} \mathbf{J} \bar{\lambda}_{mg} \quad (18.5)$$

where \bar{u}_{dq} , \bar{i}_{dq} , and $\bar{\lambda}_{mg}$ are voltage, current, and permanent magnet flux-linkage vectors, i.e.,

$$\bar{u}_{dq} = \begin{bmatrix} u_d \\ u_q \end{bmatrix}, \bar{i}_{dq} = \begin{bmatrix} i_d \\ i_q \end{bmatrix}, \bar{\lambda}_{mg} = \begin{bmatrix} \lambda_{mg} \\ 0 \end{bmatrix} \quad (18.6)$$

matrices \mathbf{L} and $\mathbf{J}\mathbf{L}$ are related to motor synchronous inductances, that is:

$$\mathbf{L} = \begin{bmatrix} L_d & 0 \\ 0 & L_q \end{bmatrix}, \mathbf{J} = \begin{bmatrix} 0 & -1 \\ 1 & 0 \end{bmatrix}, \mathbf{J}\mathbf{L} = \begin{bmatrix} 0 & -L_q \\ L_d & 0 \end{bmatrix} \quad (18.7)$$

R_s and λ_{mg} are phase resistance and permanent magnet flux-linkage respectively.

Electromagnetic torque can be easily calculated by an energy-based approach, leading to:

$$T_e = \frac{3}{2} pp [\lambda_{mg} i_q + (L_d - L_q) i_d i_q] \triangleq T_{e,PM} + T_{e,sal} \quad (18.8)$$

where pp is the number of pole-pairs of the machine. The torque is the sum of two components, the first one ($T_{e,PM}$) is proportional to the quadrature (imaginary) axis component of the stator current and to the permanent magnet flux-linkage amplitude; the second one ($T_{e,sal}$) is proportional to the product of the two components of the stator current and to the difference between the direct and quadrature inductances. In the case of SPM, this last term is zero as the inductance is constant, whereas IPM provide an additional component of the torque due to saliency.

Optimized control of PMSM is achieved by proper selection of the stator current components i_d and i_q in the synchronous reference frame as a function of the required torque and for each operating speed. Often, the maximization of the ratio between the produced torque and the current amplitude is aimed, therefore providing the reduction of copper losses in stator windings (i.e., the Maximum-Torque-Per-Ampere control strategy). Alternatively, in those applications where the operating frequency is relatively high and iron losses cannot be neglected, selection of the current space vector is done aiming at minimization of overall losses (i.e., minimum loss control strategy). This last criterion is attractive, especially in those applications where machine efficiency is of crucial performance.

As previously discussed, in order to provide a compact and efficient solution, reducing part counts and avoiding fluid leakage, the integration of the scroll expander and electric machine in a hermetic structure should be considered, i.e., without any external mechanical connection. The rated speed of the machine should be controlled to keep it below the maximum allowed value (due to mechanical limitations). Proper real-time control of the machine has to be adopted (i.e., sinusoidal vector control in the synchronous reference frame) in order to allow direct control of the braking torque, thus maximizing dynamics, torque to current ratio and increase the efficiency of the mechanical-to-electrical power conversion.

Because of the operating fluid flow inside the electric machine at a relatively high temperature, proper materials must be adopted for the permanent magnets, i.e., Samarium cobalt (SmCo), and copper for insulation.

Still with reference to the solution presented in Fig. 18.15, the electronic subsystem of the machine can be arranged into three main electronic controllers: the integrated power conversion, the machine supervisor, and touch screen display and interfaces. A high-speed Controller Area Network (CAN) communication bus allows the coordination of the three subsystems in real-time (relatively low communication latency is needed for proper machine operation). An external additional low-speed CAN communication should also be included to allow management, diagnostics, and supervising of the machine from outside. Indeed, even it is not shown in the figure, standard Ethernet, Wi-Fi, RS-232, and USB On The Go communication interfaces should also be present, together with some kind of memory card expansion slot.

The first controller, namely the integrated power conversion, is aimed at controlling the electric power flow from the electric machine to the grid. In Fig. 18.15 it is composed of two back-to-back connected three-phase (electric machine side) and single-phase (grid side) inverters, sharing a common DC bus and hosted in the main electronic board. Grid side filtering and interfacing can also be hosted in the same board, thus providing an integrated and modular solution, and reducing cabling and assembling efforts.

The second digital controller, namely the machine supervisor, can be introduced; its functions are controlling the ORC machine and providing a certain level of diagnostic features. The adopted approach is similar to the integrated power conversion electronics, featuring a main electronic board hosting the digital controller board.

Measurement of all the field sensors (i.e., temperature, pressure, flow rate, etc.), control of actuators (i.e., valves, pump, fan, etc.), and coordination with the integrated

power conversion subsystem must be implemented. Also communication with the display and interface subsystem has to be realized.

With regards interfacing with the grid, the connection of a distributed energy generation system with the public electricity grid is required to satisfy a certain number of constraints, mainly due to safety requirements and the necessity to limit the effects of the generation system on the grid operating conditions. National regulations explain and set technical rules for the connection of active and passive users to low-voltage electrical utilities.

Some technical requirements are consequence of limitations (upper and lower bounds) on the measured line voltage and frequency. Also maximum derivative in time of the power injected into the grid is required and, for power levels higher than regulation limits (i.e., 6 kW in Italy), low-voltage faults ride through response and injection of a certain active/reactive power shapes have to be guaranteed. Finally, the possibility of local disconnection command and remote control of power injection by means of net in compliance with the standards, as CEI EN 61,850, has to be foreseen.

An available option for enabling the ORC machine to be compliant with regulations, as in CEI0-21, is the use of a standard external device, generally known as an interface protection system, which allows the monitoring of main grid parameters (such as voltage and frequency) and driving an external disconnection device. Another option is to embed those functionalities inside the integrated power conversion system of the ORC machine. The last choice can be preferable for compactness, cost, reliability, and possibility of future expansion.

Electro-Magnetic-Compatibility (EMC) regulations also have to be satisfied, i.e., harmonic content of the injected current has to be limited. Both single harmonics and overall total-harmonic-distortion (THD) and weighted-THD limitations are set by, e.g., EN61000-3-2 Limits for harmonic current emissions (equipment input current ≤ 16 A per phase).

18.4 System integration

As previously mentioned, external combustion engines (like Rankine and scroll units) can in principle be integrated with almost any kind of alternative fuel, such as, biogas, syngas, or biomass (Bini and Manciana, 1996; Bolognani et al., 2014). In addition, ORC domestic cogeneration is expected to be a suitable technology for energy recovery from any kind of heat source in a temperature range 80–250°C, as it is shown in Chapters 16–20 of this book, with reference to medium and big size commercial units.

18.4.1 Solar driven domestic Organic Rankine Cycle

Regarding the specific scale of domestic applications, the integration with solar thermal collectors as a heat source is of particular interest. In Fig. 18.16 a possible solution is shown (Clemente et al., 2012), where the solar field is divided into three sections: an economizer, an evaporator, and a superheater (Delgado-Torres and García-Rodríguez, 2010). Each of them is equipped with advanced flat plate collectors based

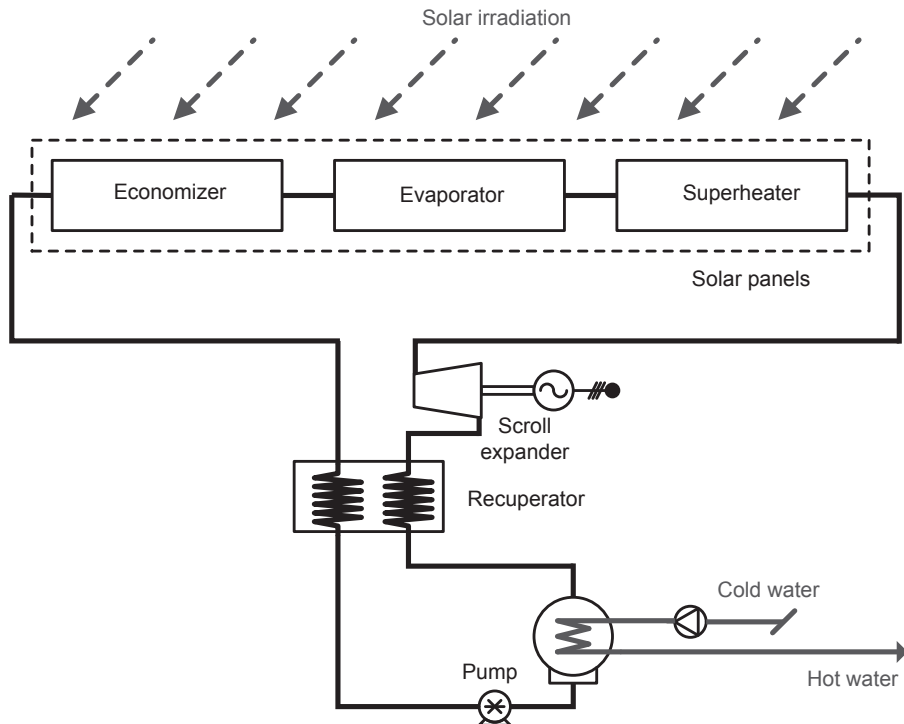


Figure 18.16 Thermodynamic lay-out of a solar-driven Organic Rankine Cycle (ORC) system (Clemente et al., 2012).

upon the evacuated tube technology. The solar thermal collector efficiency, η_{stc} , is calculated with the relation:

$$\eta_{\text{stc}} = \eta_{0a} - a_{1a} \cdot \frac{(T_f - T_{\text{amb}})}{G} - a_{2a} \cdot \frac{(T_f - T_{\text{amb}})^2}{G} \quad (18.9)$$

where G is the solar irradiance on the aperture plane of the solar collector, T_f is the mean heating temperature of the fluid flowing inside the collector, T_{amb} is the ambient temperature, η_{0a} is the optical efficiency at normal incidence of direct solar radiation and a_{1a} and a_{2a} are the coefficients of the temperature-dependent heat loss coefficient. Calculations have been carried out assuming $T_{\text{amb}} = 25^\circ\text{C}$, parameters η_{0a} , a_{1a} and a_{2a} are equal to 0.730, 1.26 W/(m² K) and 0.0041 W/(m² K²) respectively (relative to a solar collector Vitosol 300 (Clemente et al., 2012), and $G = 1000 \text{ W/m}^2$. The last value has been chosen as a design parameter for evaluating the actual energy production, the variation of the irradiance must be properly taken into account, as well as its effects on cycle parameters and expander operating conditions.

The ORC performances have been calculated assuming a flow rate of R245fa equal to 0.044 kg/s, 0.8 as recuperator efficiency and a scroll expander with design isentropic efficiency equal to 0.673.

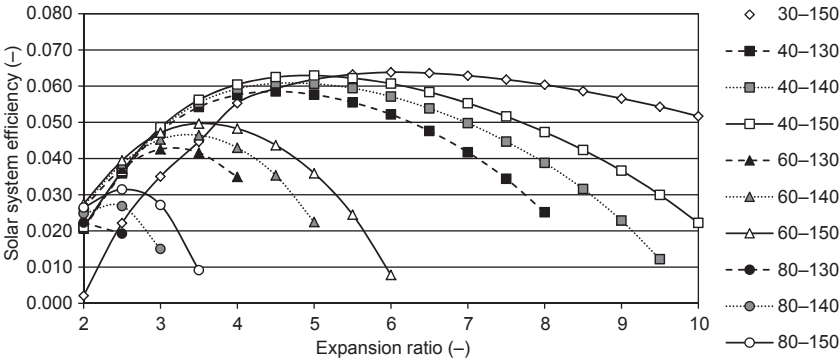


Figure 18.17 Efficiency of the solar-driven Organic Rankine Cycle (ORC) (Clemente et al., 2012). Working fluid: R245fa — Expander shaft speed: 3000 rpm — Cycle arrangement: regenerative condensation temperature: variable between 30 and 80°C (*first number in the legend*) superheating temperature: variable between 130 and 150°C (*second number in the legend*).

The total electric energy conversion efficiency of the solar system is shown in Fig. 18.17. It shows behavior very similar to the one of a stand-alone ORC, which does not take into account the solar panel effectiveness. In fact, the total electric energy conversion efficiency is the product of the efficiency of the ORC and the efficiency of the solar thermal collectors, where the latter varies in a very narrow range with the expansion ratio, if condensation and expander inlet temperature are kept constant. The higher values of the superheating temperature have been introduced in order to extend the analysis to collectors of possible future commercialization, extrapolating their efficiency with Eq. (18.9). Fig. 18.18 shows the total area of the solar thermal collectors

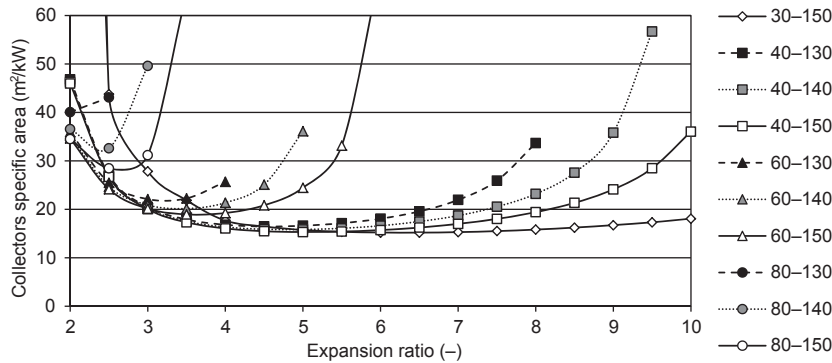


Figure 18.18 Surface of the solar collectors required to produce 1 kW_e with the Organic Rankine Cycle (ORC) (Clemente et al., 2012). Working fluid: R245fa — Expander shaft speed: 3000 rpm — Cycle arrangement: regenerative condensation temperature: variable between 30 and 80°C (*first number in the legend*) superheating temperature: variable between 130°C and 150°C (*second number in the legend*).

required to obtain 1 kW_p of electric power. It can be noted that in a wide range of expansion ratios, and within the hypothesis of reaching a vapor temperature of 130°C, a total capture area lower than 20 m² could be required to product 1 kW_p of electric power. In detail, the expansion ratio range lies between 3 and 5 when the condensation temperature is set to 60°C, between 3 and 8 when the latter is equal to 40°C.

18.4.2 Trigeneration systems based on Organic Rankine Cycle and ejector cycles

An interesting option for the development of domestic ORC systems can be a trigenerative arrangement, which consists of the integration of the CHP unit with a refrigeration cycle, able to use the waste heat from the condenser for living space cooling. This option is particularly interesting if the cogenerator produces heat which is surplus to requirements; the surplus heat is transformed into cooling energy, increasing the flexibility of the system and therefore its profitability.

At present, the market for heat powered cooling systems is extensively dominated by sorption technologies. Among these technologies, single stage Li–Br absorption chillers have reached acceptable efficiency and are compatible with moderate temperature heat sources. However for small-sized units, their cost, complexity, and volume still limit their market penetration. Therefore, the quest for alternative technologies is still open.

The energy efficiency of trigeneration units can be improved by using an ejector cooling system, in replacement of the mechanical compressor of the conventional refrigeration cycle.

As shown in Fig. 18.19, an ejector refrigeration cycle without a compressor can be summarized as follows:

- at the condenser outlet, part of the flow is directed to a pump;
- the pressurized liquid is vaporized in the generator at a relatively high temperature, and possibly superheated. Temperature depends on working fluid thermodynamic properties, and the heat supplied to the generator is the result of a waste heat recovery process;

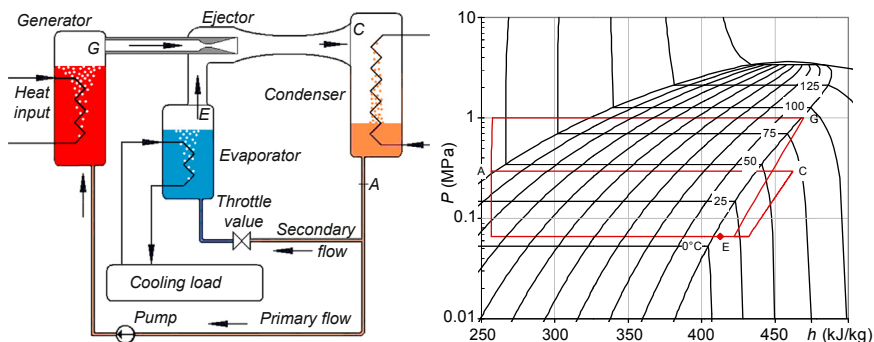


Figure 18.19 Schematic of ejector chiller and thermodynamic cycle (working fluid R245fa).

- the superheated vapor is then used in the ejector as motive fluid;
- the part of the liquid that was not taken up by the pump is expanded in the evaporator, then headed to the ejector as suction fluid;
- the mixture leaving the ejector is condensed in the condenser and the cycle is completed.

The system performance is measured by the ratio between cooling, Q_c , and motive, Q_{gen} , plus pump, W_{pump} , power, i.e.:

$$\text{COP} = \frac{Q_c}{Q_{\text{gen}} + W_{\text{pump}}} = \omega \frac{h_A - h_E}{h_G - h_A} \quad (18.10)$$

where the enthalpies have the meaning shown in the thermodynamic diagram of Fig. 18.19, and $\omega = \dot{m}_s / \dot{m}_p$ is the “entrainment ratio” between secondary and primary flow rates. For given fluid and operating temperatures, the enthalpy difference of primary and secondary flows is fixed, so Coefficient Of Performance (COP) is proportional to ω , which in turn depends on ejector geometry, operating conditions, and the working fluid. The target COP is 0.6, moving towards the COP of a single stage absorption cycle, but with a much simpler and cost-effective system. For the considered application, the maximum thermal power that can feed the ejector cycle is about 8–25 kW_{th} and the expected cooling power output is 3–10 kW_{cold} (using R245fa as working fluid).

The advantage of this kind of cycle lies in the replacement of the compressor work with a much smaller work consumed by the pump and with the heat supplied by a generator at medium temperature. Moreover, the system is made up of relatively simple components with a low manufacturing cost. The only specific piece, the ejector, has to face moderate thermal and mechanical stress and has no moving parts. It has a long history and has relatively widespread applications but, quite surprisingly, its operation still offers matter for discussion and its design is largely a trial-and-error process. To obtain good performance, a careful design of the internal ducts and enhanced testing and tuning of the system are required (ESDU 1986, Huang B. J. 1999).

The ejector is made by a nozzle, a body, a mixing chamber, and a diffuser, as shown in Fig. 18.20. The Venturi effect of a converging–diverging nozzle is used to convert the pressure energy of the motive fluid to kinetic energy, which creates a low pressure

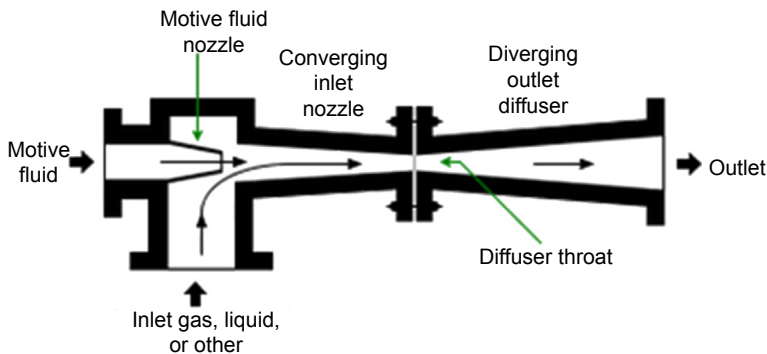


Figure 18.20 Scheme of an ejector.

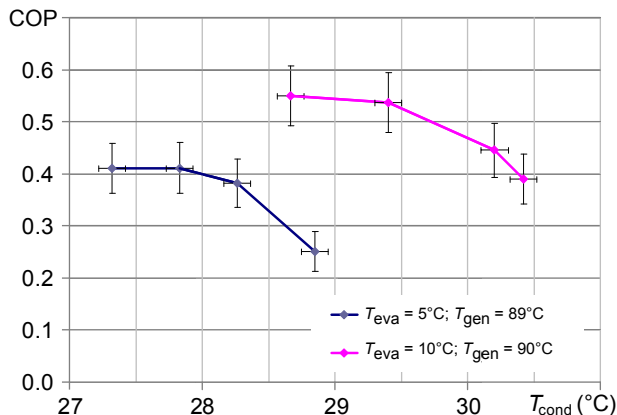


Figure 18.21 Calculated and measured performance for R245fa ejector chillers.

zone that draws in and entrains the suction fluid. After passing through the throat, the mixed fluid velocity is reduced, thus converting kinetic energy back into pressure energy. An ORC integrated ejector cycle must use the same fluid and the same pump of the ORC system.

By means of design procedures able to improve the ejector entrainment ratio (which is the fundamental performance parameter for the whole cooling system) (Eames I. W. 2002, Grazzini G. 2012), a performance level close to a COP of 0.5–0.6, typical for a single stage Li–Br chiller, can be obtained (Mazzelli F. 2014), as shown in Fig. 18.21.

The proper design of the other components should not be neglected. The heat exchangers represent a significant part of the system cost, so that their optimization in terms of temperature differences and pressure losses can greatly improve the economic viability of the system. The condenser should be most likely air cooled, requiring an energy efficient design of the air-side heat transfer surface and of the electric fan. The evaporator may deliver the cooling capacity to the conditioned space either through a water circuit or by directly cooling a suitable air flow. This second option is preferred in order to avoid an additional temperature step. In order to dehumidify the air flow, its temperature must be reduced to about 12°C, which means an evaporation temperature of 5°C, if the air flow is cooled by an intermediate water circuit, or 10°C, if the air flow passes directly through the evaporator. Fig. 18.21 shows the difference in terms of COP between these two cases, with the generator interfaced with a relatively high temperature thermal source, at about 90°C. The saturation temperature must be carefully set in order to maximize the primary flow enthalpy at the nozzle entrance. The expansion valve should be electronically managed according to a suitable control strategy.

18.5 Conclusions

Domestic cogeneration units based on ORC technology are quite different from medium and big sized units. Generally they are not equipped with a dynamic turbine,

but with volumetric expanders, often directly derived by volumetric compressors with a high volume of production. Moreover, internal regeneration is not always useful and the evaporation temperature is lower with respect to the big size units widely used in the biomass-to-energy applications. Therefore, the electrical efficiency is also lower. But these facts do not prevent the achievement of important benefits, from both an energetic and economic point of view, providing that the unit has been properly sized and that an operation strategy is used, allowing a wide usage of the cogenerated heat. As can be easily inferred, the economic benefits are higher when the capital cost of the unit is lower and the energy input is cheaper. As for cost reduction, system components can be selected from high volume production such as the automotive or air conditioning industry. Regarding the unit cost of the energy input, it can be reduced by integrating conventional fossil fuels with solar energy, or with other low cost alternative fuels. This integration can be quite easily obtained in ORC domestic units, because of the reduced temperature requirements of the heat source of the Rankine cycle.

The choice of adopting volumetric expanders, directly derived from commercially available compressors, implies some limitation in the achievable maximum efficiency. In particular, if a scroll expander is considered, a specific design for ORC applications would require higher design expansion ratios, in order of achieving the maximum isentropic efficiency of the machine in conditions where the thermodynamic efficiency of the Rankine cycle is more favorable.

As far as the pump is concerned, its choice has a key role in the design of an ORC-based cogeneration unit, since organic fluids have, in most cases, a very low viscosity, that causes important leakages from the machine seals and from the pumping mechanisms, and limits the lubricating properties of the fluid itself.

In the near future, a component cost reduction is generally expected due to a better synergy between the industrial productions of conventional components (such as, compressors or pumps) and of components with a similar structure, but specifically designed for ORC applications. Besides such a component cost reduction, the expected developments of domestic ORC systems may be mainly identified in the following two options: (1) the integration with an ejector refrigeration cycles, to obtain a CCHP (Combined Cooling Heat and Power) systems that shall better match the energy requirements of domestic users, and (2) the integration of pump, rotating expander, and electric generator in a unique hermetic structure, without any external mechanical connection. In the latter case the electric driver of the pump (often characterized by a poor efficiency) would be eliminated and a compact and efficient solution, reducing part counts and avoiding fluid leakage, would be obtained.

References

- Aoun, B., 2008. Micro Combined Heat and Power Operating on Renewable Energy for Residential Building (Ph.D. thesis). École Nationale Supérieure des Mines de Paris.
- Bala, E.J., O'Callaghan, P.W., Probert, S.D., 1985. Influence of organic working fluids on the performance of a positive-displacement pump with sliding vanes. *Applied Energy* 20, 153–159.

- Bini, R., Manciana, E., 1996. Organic Rankine cycle turbogenerators for combined heat and power production from biomass. In: Proc. 3rd Munich Discussion Meeting on "Energy Conversion from Biomass Fuels Current Trends and Future Systems", Munich, Germany.
- Bolognani, S., Petrella, R., Prearo, A., Sgarbossa, L., January–February 2011. Automatic tracking of MTPA trajectory in IPM motor drives based on AC current injection. *IEEE Transactions on Industry Applications* 47 (1), 104–114.
- Bolognani, S., Calligaro, S., Petrella, R., June 2014. Design issues and estimation errors analysis of back-EMF based position and speed observer for SPM synchronous motors. *Journal of Emerging and Selected Topics in Power Electronics* 138–145.
- Bracco, R., Clemente, S., Micheli, D., Reini, M., 2013. Experimental tests and modelization of a domestic-scale organic Rankine cycle. *Energy* 58, 107–116. Previously in Proc. of ECOS 2012.
- Clemente, S., Micheli, D., Reini, M., Taccani, R., August 7–10, 2011. Performance analysis and modeling of different volumetric expanders for small-scale organic Rankine cycles. In: Proc. of ASME 2011 5th International Conference on Energy Sustainability & 9th Fuel Cell Science, Engineering and Technology Conference, ES Fuel Cell 2011, Washington, DC, USA.
- Clemente, S., Micheli, D., Reini, M., Taccani, R., 2010. Numerical model and performance analysis of a scroll machine for ORC applications. In: Proc. ECOS 2010, Lausanne, CH.
- Clemente, S., Micheli, D., Reini, M., Taccani, R., September 2012. Energy efficiency analysis of Organic Rankine Cycles with scroll expanders for cogenerative applications. *Applied Energy* 97, 792–801.
- Clemente, S., Micheli, D., Radu, R., Toniato, G., 2013. Experimental tests on a gear pump for organic Rankine cycle applications. In: Proc. of MICROGEN III, April 2013, Napoli, pp. 15–17.
- Davidson, T.A., 1977. Design and Analysis of a 1 KW Rankine Power Cycle, Employing a Multi-vane Expander, for Use With a Low Temperature Solar Collector (Bachelor's thesis). Massachusetts Institute of Technology.
- Declaye, S., 2009. Design, Optimization and Modeling of an Organic Rankine Cycle for Waste Heat Recovery (Master's thesis). Université de Liège.
- Delgado-Torres, A.M., Garcia-Rodriguez, L., 2010. Analysis and optimization of the low-temperature solar organic Rankine cycle (ORC). *Energy Conversion and Management* 51, 2846–2856.
- Eames, I.W., 2002. A new prescription for the design of supersonic jet-pumps: the constant rate of momentum change method. *Applied Thermal Engineering* 22, 2–3.
- ESDU Ejectors and Jet Pumps Data Item 86030, 1986. ESDU International Ltd, London, UK.
- Ferrara, G., Manfrida, G., Pescioni, A., September 1, 2013. Model of a small steam engine for renewable domestic CHP (combined heat and power) system. *Energy* 58, 78–85.
- Franco Di Andrea, A.D., 2004. MISure dei Consumi di ENERgia in 110 abitazioni Italiane apparecchi di illuminazione. (Progetto MICENE).
- Grazzini, G., Milazzo, A., Paganini, D., 2012. Design of an ejector cycle refrigeration system. *Energy Conversion and Management* 54, 38–46.
- Huang, B.J., Chang, J.M., Wang, C.P., Petrenko, C.P., 1999. A 1-D analysis of ejector performance. *International Journal of Refrigeration* 22, 354–364.
- Hugenroth, J., Braun, J., Groll, E., King, G., 2008. Experimental investigation of a liquid-flooded Ericsson cycle cooler. *International Journal of Refrigeration* 31, 1241–1252.
- Kane, M., Larrain, D., Favrat, D., Allani, Y., 2003. Small hybrid solar power system. *Energy* 28 (14), 1427–1443.

- Kane, M., Favrat, D., Gay, B., Andres, O., 2007. Scroll expander Organic Rankine Cycle (ORC) efficiency boost of biogas engines. *ECOS* 2, 1017–1024.
- Kim, H.J., Ahn, J.M., Park, I., Rha, P.C., 2007. Scroll expander for power generation from a low-grade steam source. *Proceedings of IMechE* 221 (Part A), 705–711.
- Lemort, V., Teodorese, I.V., Lebrun, J., 2006. Experimental study of the integration of a scroll expander into a heat recovery Rankine cycle. In: *International Compressor Engineering Conference*. Purdue, pp. 1–8.
- Lemort, V., Quoilin, S., Cuevas, C., Lebrun, J., 2009. Testing and modeling of a scroll expander integrated into an organic Rankine cycle. *Applied Thermal Engineering* 29, 3094–3102.
- Mazzelli, F., Milazzo, A., 2014. Performance analysis of a supersonic ejector cycle working with R245fa. *International Journal of Refrigeration* 49, 79–92.
- Micheli, D., Reini, M., 2007. On bottoming a micro turbine with a micro ORC section: Part a preliminary design of the ORC expander. *ECOS* 2, 1025–1034.
microchapinfo. http://www.microchap.info/micro_chp_products.htm.
- Peterson, R.B., Wang, H., Herron, T., 2008. Performance of a small-scale regenerative Rankine power cycle employing a scroll expander. *Proceedings of IMechE* 222 (Part A), 271–282.
- Quoilin, S., 2011. Sustainable Energy Conversion Through the Use of Organic Rankine Cycles for Waste Heat Recovery and Solar Applications (Ph.D. thesis). Université de Liège.
- Saitoh, T., Yamada, N., Wakashima, S.I., 2007. Solar Rankine cycle system using scroll expander. *Journal of Environmental Engineering* 2 (4), 708–719.
- Smith, I., Stosic, N., Kovacevic, A., Langson, N., 2007. Cost effective small scale ORC systems for power recovery from low enthalpy geothermal resources. *Geothermal Resources Council Transactions* 31.
- Tchanche, B.F., Pétissans, M., Papadakis, G., Nov. 2014. Heat resources and organic Rankine cycle machines. *Renewable and Sustainable Energy* 39, 1185–1199.
- Xiaojun, G., Liansheng, L., Yuanyang, Z., Pengcheng, S., 2004. Research on a scroll expander used for recovering work in a fuel cell. *International Journal of Thermophysics* 7 (1), 1–8.
- Yanagisawa, T., Fukuta, M., Ogo, Y., Hikichi, T., 2001. Performance of an oil-free scroll-type air expander. *IMechE* C591/027/2001 167–174.
- Yang, L., Wang, J., Mangan, S., Derby, J.W., Lu, N., 2008. Mathematical model and energy efficiency analysis of a scroll-type air motor. *IAENG International Journal of Applied Mathematics* 38 (1).
- Zanelli, R., Favrat, D., 1994. Experimental investigation of a hermetic scroll expander-generator. In: *Proc. International Compressor Engineering Conference*. Purdue, pp. 459–464.

Index

'Note: Page numbers followed by “f” indicate figures and “t” indicate tables.'

A

Adoratec, 54
Aerodynamic design, 272–291
 adjoint-based gradient optimization,
 282–285, 283t, 284f, 285t
 blade geometry parametrization, 275–276
 blades design remarks, 276–278
 computational fluid-dynamics-based
 turbomachinery design, 280–282
 computational fluid-dynamics modeling,
 279–280
 evolutionary stochastic optimization,
 286–290, 287f–289f
 geometrical representation, 273–278, 274f
 robust multipoint optimization, 290–291,
 292f
 shape-optimization techniques automatic
 design, 278–291
 supersonic converging cascades, 276–277
 supersonic converging/diverging cascades,
 277–278
 transonic cascades, 276
Air cooled condensers (ACC), 71
Air-cooled heat exchangers, 455–458, 458f
Air fin exchangers, 457
AISI 316/AISI 316L steel, 133
Alternative manipulated variables, 167
ANSI/ASHRAE Standard 1997–2002, 126
Atlas Copco Group, 55, 330–331
Axial flow turbines
 design procedures peculiarities
 gas and steam turbines simple
 correlations, 301–302, 302f
 input parameters selection, 301
 efficiency correlation
 multistage turbine, 311–312, 311f–312f
 N_s effect, 308–309, 308f
 numerical correlations of efficiency, 312,
 313t

 single stage turbines, 306–311, 307f
 SP effect, 310–311, 310f
 V_r effect, 309–310, 309f
 methodology
 Axtur code, 304–306, 304f
 fluid behavior simplifying assumptions,
 303–304
 independent variables, similarity rules
 and selection, 302–303
 model validation, 313–316, 314t,
 315f–316f
 power generation sector, 299–301, 300f
Axtur code, 304–306

B

Balance of plant (BOP), 75
Bicubic interpolation, 114
Biomass-fired ORC CHP systems
 applications and references
 district heating, 550–552, 550f–551f
 district heating and pellet production,
 553–554
 extra potentiality, 549–550
 fields of application, 550–556
 full electric applications, 556
 pellet production, 552–553, 554t
 timber and wood panel industry,
 554–556, 555t
 conventional biomass-fired Organic
 Rankine Cycle, 531–549
 air preheater, 540, 542f
 alternative technologies, 546
 ash removal and handling, 538–539
 biomass combustion section, 534–535,
 536f
 biomass gasification, 546–547
 boundary interfaces, 543–545, 545f
 captive consumptions, 545, 546t
 conventional rankine cycles, 546

Biomass-fired ORC CHP systems

(Continued)

- emergency cooling system, 540–541, 543f
 - exhaust gas treatments, 541–543, 544f
 - external fired gas turbines, 547
 - fuel storage and handling, 531–534, 534f–535f
 - gas recirculation, 538, 539f
 - internal combustion engines, 546–547
 - lay out and operational scheme, 531, 532f–533f
 - primary and secondary combustion air, 537–538
 - reciprocating grate, 536, 537f
 - stirling cycles, 547
 - thermal oil boiler, 539–540, 540f–541f
 - thermal oil circuit, 540–541, 543f
 - design concept, 529–530, 529f–530f
 - economic and environmental
 - considerations, 556
 - electricity social impact, 556–557
 - Europe, 556
 - future markets, 557–558, 558f
 - economic feasibility and sensitivity
 - dimensions, 558–560, 559f
 - electricity production cost, 560
 - electricity production sizes, 561–565, 563f, 563t, 564f
 - investment costs, 562–564, 564t
 - parameters considerations, 560–561, 561t–562t
 - thermal utilization, 564–565, 565t
 - electrical grid connection, 531
 - evolutions and future developments, 547–549
 - direct exchange, 548
 - external fired gas turbine, 548–549, 549f
 - sizes, 547–548
 - overview, 527–528
 - plant control system, 530–531
- Black-box approach, 208–209
- Blade geometry, 305–306
- Brazed plate heat exchangers, 458–463, 460f
- Bundle condensation heat transfer, 442

C

- Cantilever blades, 322, 322f
- Capital budgeting analysis, 191–194
- CFC. *See* Complete Flashing Cycle (CFC)
- Complete Flashing Cycle (CFC), 84
- Composition variation, 87
- Compound parabolic collector (CPC), 584, 584f
- Concentrating solar power (CSP), 182–183, 569, 572t, 573f
- Condensation
 - heat transfer, 439–448
 - external film condensation heat transfer, 439–445, 441t, 442f
 - in-tube flow condensation heat transfer, 445–448
 - pressure, 202
 - temperature, 202
- Condensing fluid, 462–463
- Contact resistance, 399
- CoolProp library, 115
- Coupling, 166–167
- Crossing flow, 339–340, 340f
- Cycle maximum pressure, 202–203
- Cyclopentane, 135

D

- Design convective heat transfer, 407
- Directional direct-search methods, 212
- Distributed energy systems (DES), 623–627, 628f
- Dittus-Boelter correlation, 437–438
- Dividing rectangle (DIRECT) methods, 212
- Domestic cogeneration
 - requirements and features, 637–642, 639f–640f
 - stirling engines models and prototypes, 642–644, 645f–649f, 651f–653f, 655f–657f
 - system integration, 660–665
 - solar driven domestic Organic Rankine Cycle, 660–663, 661f–662f
 - trigenerative systems, 662f–665f, 663–665
- Double-pressure-level system, 498
- Dynamic modeling
 - AC/AC converters, 154
 - assumptions, 162–166
 - condenser, 163–164

- control valves, 165
- electrical/mechanical generation, 165–166
- expanders, 164
- pump models, 164–165
- recuperator, 163
- sensors, 165
- vapor generator, 162–163
- control design simulation, 155–156
- control design work-flow
 - advanced/integrated work-flows, 168–169
 - conventional work-flow, 166–168
- modica models, 158–161, 159f, 160t, 161f
- object-oriented modeling, 157–158
- overview, 153–155
- Dynamic performance prediction
 - conservation of energy, 600
 - control strategy, 601–602
 - model timestep, 600–601
 - operational considerations, 601–602
 - startup sequence, 601
 - thermal capacitance, 600

E

Economic Recovery Index (ERI), 638–640, 640f

ElectraTherm, 55–56, 55f

Electrical power, 386

Electricity-cooling cogeneration system (ECCS), 623

Equation-based object-oriented (EOO)

- method, 157–158, 161f, 207–208

Equation-oriented (EO) approach, 207–208

Euler turbine equation, 323

Evacuated tube collectors (ETC), 582–583, 582f

Evaporating fluid, 462

Evaporation/boiling heat transfer, 430–439

Exergy, 56–58, 56f–58f, 336, 336f

Exhaustive enumerative analysis, 178–179

Expander

- displacement, 382–383
- turbomachines, 73
- volumetric expanders, 73

External fluid, 410–411

F

Film boiling regime, 432

Film-wise condensation heat transfer, 440

Fixed geometry turbines, 322

Flat plate collector (FPC), 581, 581f

Flow boiling, 434–439, 435f, 439f

Fluid-dynamic analysis, 341

FluidProp, 115

Fluids

- classification, 92
- interpolation methods, 112–114
 - bicubic interpolation, 114
 - spline-based tabular look-up (SBTL) interpolation, 114
 - tabular interpolation, 112–113, 113f
 - tabular Taylor-series extrapolation, 113–114
- libraries, 115–116
 - CoolProp library, 115
 - FluidProp, 115
 - REFPROP property library, 115
 - trend, 115
 - zittau/goerlitz libraries, 116
- overview, 91
- surface tension
 - mixtures, 111
 - pure fluids, 111
- thermodynamic properties
 - cubic equation of state, 93, 101
 - equations of state, 92
 - flash routines, 97, 106
 - functions, 103–105, 104f–105f
 - IAPWS-IF97, 100–101
 - ideal-gas equation of state, 92–93
 - initial estimate values, 99–100, 100f
 - mixtures, 101–106
 - multiparameter fundamental equation of state, 93–96
 - multiparameter mixture models, 102–103
 - phase equilibria, 105–106
 - pressure–enthalpy inputs, 98–99, 99f
 - temperature–density inputs, 97–98, 98f
 - vapor–liquid equilibrium, 96
- transport properties, 106–110
 - extended corresponding states, 110
 - thermal conductivity, 108–109, 109f

Fluids (*Continued*)

- viscosity, 107–108
- viscosity/thermal conductivity, 110–111

Fouling factor, 399

Friedel correlation, 450

G

Gasketed plate heat exchangers, 458–463

General Electric (GE), 58, 59f

Geothermal energy exploitation

- binary cycles, 488–494, 489f
 - Kalina, 491–493, 491t, 492f–494f
 - pure water, 490–491, 490f
- cooling system, 516

corrosive environment, 515–516

direct cycles, 481–487

- technical/operational features, 486–487, 486f–488f

thermodynamics, 481–485, 482f–483f

features and case studies, 512–517, 513t

market- and project-related features, 516–517

ORC binary plants

- bottoming and combined cycles, 500, 501f–502f
- cycle selection, 497–503, 499f
- fluid selection, 495, 496t, 497f
- numerical example, 503–511, 505t–508t, 509f–511f
- regeneration, 500–501
- turbine technology, 501–503

ORC power plants

- bottoming cycle, 520, 521f
 - combined cycle, 521–522, 522f–523f
 - double-pressure level, 518–519, 519f
 - Pamukören, 518, 518f
 - single-pressure level, 518
 - triple-pressure level, 519–520, 520f
- overview, 473–494
- resource classification, 473–474, 475f, 475t
- resources and plant locations, 475–478, 476f, 478f, 478t–479t
- scaling and corrosion, 512–515, 514f
- technological options, 478–494, 479t, 480f
- theoretical analysis, 478–494, 479t, 480f

Geothermal steam turbines, 487

Gibbs free energy equilibrium, 124

GMK, 59

H

Heat exchangers

- air cooled condensers, 71, 71f
- basics, 407–420, 408f, 410f–413f, 415f–419f
- brazed plate, 72
- evaporators and water cooled condensers, 69–71, 70f
- heat transfer, 397–407, 398f, 400f, 400t, 401f–403f, 404t–405t
 - air-cooled heat exchangers, 455–458, 458f
- brazed plate heat exchangers, 458–463, 460f
- condensation heat transfer, 439–448
- condensing fluid, 462–463
- evaporating fluid, 462
- evaporation/boiling heat transfer, 430–439
 - flow boiling, 434–439, 435f, 439f
- gasketed plate heat exchangers, 458–463
- pipe flow pressure drop, 420–424, 423t–424t
- plain and finned tubes, 424–430, 425f, 426t–428t
- pool boiling, 430–434, 431f
- shell-and-tube heat exchangers, 451–455, 452f, 454f, 456t
- single-phase liquid flow, 461
- two-phase flow pressure drop, 448–451
- plate fin, 72
- recuperator, 72, 72f
- shell and tubes, 68–69, 68f–69f

Heat resistance, 124

Heat transfer, 379–381

Heat transfer coefficients (HTC), 87, 613–614

Heat-transfer fluid (HTF), 176–177, 587–591, 587f–588f, 589t–590t

High-level declarative modeling approach, 158

Homogeneous flow model, 449

Hybrid methods, 212

I

IAPWS-IF97, 100–101

International Maritime Organization (IMO), 620

Infeasible path approach, 209
Input parameters selection, 301
Internal fluid, 410–411
Internal leakages, 378–379, 379f–380f
Interpolation methods, 112–114
 bicubic interpolation, 114
 spline-based tabular look-up (SBTL)
 interpolation, 114
 tabular interpolation, 112–113, 113f
 tabular Taylor-series extrapolation, 113–114
ISA S75/IEC 60534 standards, 165

K

Kaplan hydro turbines, 300–301
Kiln, 132

L

Lappeenranta University of Technology,
 34–36, 35f–36f
Latent thermal energy storage
 thermochemical thermal energy storage,
 594, 595t
Levelized cost of electricity (LCOE),
 194–196
LFC. *See* Linear Fresnel collector (LFC)
Libraries, fluids, 115–116
 CoolProp library, 115
 FluidProp, 115
 REFPROP property library, 115
 trend, 115
 zittau/goerlitz libraries, 116
Linear Fresnel collector (LFC), 583–584,
 584f
Ljungström turbine, 338, 338f–339f
Low-grade heat (LGH), 618–619

M

Mass flow rate, 383–384
Material compatibility, 179–180
Mean-line preliminary design, 259–265
 guidelines, 264
 mean-line concept, 260–261
 mean-line formulation, 261–264
 optimal preliminary design, 264–265
Meridional velocity, 341
Microfin tubes, 439
Modelica software, 200
Molecular complexity, 182
Molecular mass, 182

Multiobjective optimization algorithms,
 215–217
Multiple-flash configuration, 483
Multi pressure levels cycles, 80–82, 81f
Multipressure radial outflow turbine,
 355–357, 355f–357f
Multistage radial outflow turbine,
 340f–341f
Multistage turbine, 311–312,
 311f–312f

N

National Energy Technology Laboratory
 (NETL), 198
National Physical Laboratory, Israel,
 31–33, 33f–34f
Natural convection regime, 431
Net power output, 185
Noncondensable gases (NCGs), 74–75, 75f,
 129–130, 142, 485
Nonlinear behavior, 167
Nonminimum phase response, 167
Nucleate boiling correlations, 432
Nucleate boiling regime, 431
Nusselt number, 420

O

One-dimensional flow models, 162
Optimization
 design, 173–184
 choice, 179–183
 component sizing and cycle design,
 181–183
 cost, 180–181
 cycle configuration, 178–184
 environmental impact, 180–181
 plant layout choice, 183–184, 184f
 problem analysis, 174–177, 175f
 safety concerns, 180–181
 steps, 174
 thermal stability and material
 compatibility, 179–180
 working fluid, 178–184
 numerical examples, 220–242
 biomass-fired combined heat and power
 ORC, 231–238, 232f, 234f–235f,
 237t
 geothermal field technoeconomic
 analysis, 220–231

Optimization (*Continued*)

- multiobjective optimization, 238–242, 239f–242f
- technoeconomic optimization, 225–231, 227t–228t, 229f–230f
- technothermodynamic optimization, 220–225, 221f, 223f–225f
- system optimization
 - algorithm selection, 217–220, 218f–219f
 - black-box approach, 208–209
 - capital costs, 199
 - component efficiency correlations, 190
 - condensation pressure, 202
 - condensation temperature, 202
 - cooling medium, 205
 - cycle maximum pressure, 202–203
 - directional direct-search methods, 212
 - dividing rectangle (DIRECT) methods, 212
 - environmental impact, 200
 - equation-oriented approach, 208
 - equation-oriented (EO) approach, 207–208
 - equipment cost, 196–199
 - hidden constraints, 214
 - infeasible path approach, 209
 - known constraint, 214
 - mass flow rate ratios, 205, 206t
 - multiobjective optimization algorithms, 215–217
 - objective functions, 185–200
 - off-design and dynamic behavior, 199–200
 - outlet temperature, 204–205
 - pinch-point temperature difference, 203–204
 - plant simulation, numerical approaches for, 205–208
 - population-based methods, 211–212
 - priori constraint, 214
 - problem constraints classification, 213–215
 - quantifiable *versus* nonquantifiable constraints, 213
 - random-search and simulated-annealing methods, 210–211
 - reliable *versus* unrelaxable, 213–214
 - reliable cost correlations, 196–199
 - sequential modular (SM) approach, 207
 - simplicial-search methods, 210
 - simulation based constraint, 214
 - single-objective optimization algorithms, 209–213
 - technoeconomic optimization, 191–196, 192t–193t, 194f–195f
 - technothermodynamic optimization, 185–190, 186t–188t, 189f
 - turbine inlet temperature, 203
 - variable definitions and cycle design model, 200–205, 202f, 203t
 - volume, 200
 - weight, 200

Organic Rankine Cycle (ORC)

- Adoratec, 54
- air, working fluid
 - advantages, 10–13, 11f–12f
 - poor air power cycle performance, 7–8, 7f
 - second-law analysis, 8–10, 8f–10f
 - thermodynamic processes, 6–7
- Atlas Copco Group, 55
- commercial plants, 39f–44f, 40–44
- ElectraTherm, 55–56, 55f
- Exergy, 56–58, 56f–58f
- features, 6
- General Electric (GE), 58, 59f
- GMK, 59
- integrating thermodynamics and system design
 - demonstration units, 36–37, 37f
 - Lappeenranta University of Technology, 34–36, 35f–36f
 - National Physical Laboratory, Israel, 31–33, 33f–34f
 - new cycles proposed, 37–39, 38f
 - Politecnico di Milano, 33–34, 35f
 - University of Naples, 31, 32f
- Ormat, 45–51, 46f–51f
- other entrants, 61, 62f
- software development, 63
- steam engine, 25–31
- thermodynamic issues working fluid
 - constant temperature heat sources, 16–17, 18f
 - variable temperature heat sources, 17–22, 19f–21f

- thermodynamics, 25–27
- Triogen Company, 48f, 59–60
- Turbine air systems (TAS), 60, 61f
- Turboden, 51–54, 52f–54f
- United Technologies (UTC), 60, 62f
- water, working fluid, 14–15
 - steam turbine issue, 14–15, 14f
- working fluid
 - refrigerating and air-conditioning industry, 22–24
 - selection criteria, 22–24
 - thermal stability, 24
 - thermodynamic properties requirements, 24
- Ormat, 45–51, 46f–51f
- P**
- Parabolic dish reflector (PDR), 585
- Parabolic trough collector (PTC), 583, 583f
- Parsons turbine, 337–338, 337f
- Perchlorination, 127
- Perfluorination, 127
- Perfluoro-n-hexane, 135
- Permanent magnet synchronous machine (PMSM), 657–658
- Permanent magnet synchronous machine (PMSM), 657–658
- Pinch-point temperature difference, 203–204
- Piston expanders
 - mechanical aspects, 367–369, 368f
 - principle of operation, 364–366, 365f–366f
 - technical limitations, 369
- Plain/finned tubes, 424–430, 425f, 426t–428t
- Plant layouts
 - multi pressure levels cycles, 80–82, 81f
 - single pressure level cycles, 76–80, 76f
 - subcritical cycles, 77–79, 78f
 - supercritical cycles, 79–80, 79f
 - trilateral cycles, 82–85, 82f–85f
- Politecnico di Milano, 33–34, 35f
- Population-based methods, 211–212
- Positive displacement expanders
 - achieved performance, 389f, 390
 - defined, 361
 - differences, 362–363
 - internal expansion, 362
 - moving elements motion, 362, 362f
 - oil-lubricated *versus* oil-free, 363
 - open-drive *versus* semihermetic/hermetic machines, 363
 - valves, 362–363
- integration
 - control, 393–394
 - expander preliminary design, 392–393, 393f
 - technical limitations, 392
 - technology selection, 390–392, 391f–392f
- overview, 361–363
- performance indicators
 - power performance, 387–389, 388f
 - volumetric performance, 387
- piston expanders
 - mechanical aspects, 367–369, 368f
 - principle of operation, 364–366, 365f–366f
 - technical limitations, 369
- roots expanders, 376, 376f
- scroll expanders
 - mechanical aspects, 371
 - principle of operation, 369–371, 369f–370f
 - technical limitations, 371–372
- single-screw expander, 377, 377f
- thermodynamics
 - actual internal power, 385–386
 - clearance volume losses, 381
 - displaced mass flow rate, 382–384
 - electrical power, 386
 - expander displacement, 382–383
 - frictional losses, 381
 - heat transfer, 379–381
 - internal leakages, 378–379, 379f–380f
 - losses, 377–382, 378f
 - mass flow rate, 383–384
 - mechanical/electrical power, 384–386
 - overall expander energy balance, 386
 - pressure drops, 381–382
 - shaft power, 386
 - theoretical internal power, 384–385
 - working cycle frequency, 383, 383t
- trochoidal expanders, 376–377
- twin-screw expanders, 372–374
 - mechanical aspects, 374
 - principle of operation, 372–374, 372f–373f

Positive displacement expanders (*Continued*)
 technical limitations, 374
 types, 363–377
 vane expanders, 374–376, 375f
 mechanical aspects, 374–375
 technical limitation, 375–376
 Power generation sector, 299–301, 300f
 Prandtl number, 420
 Preliminary and aerodynamic design,
 265–272
 optimal spanwise design, 271–272
 throughflow concept, 266–267, 266f
 throughflow formulation, 267–270, 270f
 throughflow/spanwise design guidelines,
 270–271
 Pressure–enthalpy inputs, 98–99, 99f
 Primary Energy Saving (PES), 638–639,
 639f
 Primary Heat Exchanger (PHE), 68
 Process Capacity Parameter (PCP), 616
 PTC. *See* Parabolic trough collector (PTC)
 Pumps, 73–74

Q

Quasiconstant velocity reaction, 143, 144f

R

Radial-axial configuration, 354–355, 354f
 Radial centrifugal turbine, 339–340
 Radial diffusers, 349
 Radial inflow turbines
 advantages, 329–330
 axial/impulse turbines, 329–330
 defined, 321
 gas-lubricated mechanical face seals,
 331–332
 gearbox and integral gear technology, 329,
 329f
 higher pressure ratios and broader areas,
 330
 large turbines, 330–331, 331f
 making, 321–322
 oil-lubricated mechanical face seals, 332
 sturdiness and reliability, 331
 thermodynamic fundamentals, 322–324,
 322f–323f, 325f
 track records, 332–333
 variable geometry nozzle guide vanes,
 326–328, 326f, 328f

Radial outflow turbines
 features and comparison, 339–354,
 340f–343f, 345f–347f, 350f, 351t,
 352f–353f
 history, 336–338
 Ljungström turbine, 338, 338f–339f
 multipressure radial outflow turbine,
 355–357, 355f–357f
 overview, 335–336, 336f
 Parsons turbine, 337–338, 337f
 radial-axial configuration, 354–355, 354f
 Random-search/simulated-annealing
 methods, 210–211
 REFPROP property library, 115
 Reinjection temperature limit, 176–177
 Response times, 166
 Reverse osmosis (RO), 571
 Reynolds-Averaged Navier-Stokes
 equations (RANS), 279
 Reynolds number, 420

S

Salt-gradient solar pond (SGSP), 578–581,
 581f
 Scaling affects, 515
 Scroll expanders
 mechanical aspects, 371
 principle of operation, 369–371,
 369f–370f
 technical limitations, 371–372
 SCT. *See* Solar central tower (SCT)
 Second law efficiency, 189
 Sequential modular (SM) approach, 207
 Sensible thermal energy storage, 592–594,
 592t
 single buffer, 592, 593f
 thermocline storage, 593–594, 593f
 two tank storage, 592–593, 593f
 SGSP. *See* Salt-gradient solar pond (SGSP)
 Shaft power, 386
 Shell-and-tube heat exchangers, 451–455,
 452f, 454f, 456t
 Silica solubility, 512
 Simplicial-search methods, 210
 Single-flash plant, 483
 Single-phase liquid flow, 461
 Single pressure level cycles, 76–80, 76f
 subcritical cycles, 76f, 77–79, 78f
 supercritical cycles, 79–80, 79f

- Single-pressure-level system, 498
 - Single stage turbines, 306–311, 307f
 - Solar central tower (SCT), 585, 585f, 586t
 - Solar Organic Rankine Cycle systems
 - application engineering and system analysis, 603–604
 - design, 603–604, 604f
 - applications, 570–574
 - desalination, 571
 - distributed power generation, 571
 - grid connected power generation, 570–571, 579t–580t
 - hybrid solar organic Rankine cycle, 573–574, 573f
 - irrigation, 571
 - economics, 602–603
 - heat transfer fluid (HTF), 587–591, 587f–588f, 589t–590t
 - hybrid microgrid system, 606–609, 607f
 - installed capacity, 577–578, 579t–580t
 - meteorological and solar resource
 - dynamics, 574–576
 - intermittency, 576, 577f
 - solar resource maps, 576, 577f
 - solar spectrum, 574–575, 575f
 - sunlight energy, 574
 - tracking, 575–576
 - optimization tools, 605–606
 - overview, 569–578
 - power generation costs, 604–605
 - solar thermal collectors, 578–585
 - compound parabolic collector (CPC), 584, 584f
 - evacuated tube collectors (ETC), 582–583, 582f
 - flat plate collector (FPC), 581, 581f
 - linear Fresnel collector (LFC), 583–584, 584f
 - parabolic dish reflector (PDR), 585
 - parabolic trough collector (PTC), 583, 583f
 - salt-gradient solar pond (SGSP), 578–581, 581f
 - solar central tower (SCT), 585, 585f, 586t
 - steady state performance prediction, 596–599
 - solar collector modeling, 597–599, 598f
 - thermal energy storage, 591–594
 - dynamic performance prediction, 599–602
 - latent thermal energy storage, 594, 595t
 - sensible thermal energy storage, 592–594
 - Spline-based tabular look-up (SBTL) interpolation, 114
 - Static tests, 131
 - Stator/rotor blades, 323
 - Steam Rankine Cycles (SRC), 613–615
 - higher thermal efficiency, 614
 - low-grade heat conversions, 615
 - turbo machinery, 614–615
 - Steam turbines, 487
 - Supercritical cycle, 500
 - Surface geometries, 447
 - Surface tension, 442
 - Synthesis optimization, 178
 - System-level models, 156
- T**
- Tabular interpolation, 112–113, 113f
 - Tabular Taylor-series extrapolation, 113–114
 - Technical options
 - equipment list, 67–75
 - air cooled condensers, 71, 71f
 - balance of plant (BOP), 75
 - brazed plate and plate fin, 72
 - evaporators and water cooled condensers, 69–71, 70f
 - expander, 72–73
 - gear boxes, 74
 - generators, 74
 - heat exchangers, 68–72
 - instrumentation, 75
 - noncondensable gas removal, 74–75, 75f
 - power electronic systems, 74
 - pumps, 73–74
 - recuperator, 72, 72f
 - shell and tubes (S&T), 68–69, 68f–69f
 - turbomachines, 73
 - volumetric expanders, 73
 - mixtures *versus* pure fluids, 86–87, 86f
 - overview, 67
 - plant layouts
 - multi pressure levels cycles, 80–82, 81f

Technical options (*Continued*)

- single pressure level cycles, 76–80, 76f
 - subcritical cycles, 77–79, 78f
 - supercritical cycles, 79–80, 79f
 - trilateral cycles, 82–85, 82f–85f
 - Technoeconomic optimization, 201
 - Temperature–density inputs, 97–98, 98f
 - Thermal stability, 179–180
 - evaluation, 126–131, 128f–129f
 - measurement system, 131–143,
 - 132f–133f, 134t
 - decomposition quantification, 136–143,
 - 138f–141f, 144f
 - vapor pressure examples, 135–136,
 - 135f–137f
 - overview, 121–124, 122f–123f
 - working fluids
 - defined, 124–125, 125f
 - thermochemical stability, 125–126
 - Thermostatic bath (B), 132
 - Titanium tetrachloride, 136
 - Transition boiling regime, 432
 - Trilateral cycles, 82–85, 83f–85f
 - Triogen Company, 48f, 59–60
 - Triple pressure level systems, 498–500
 - Tube-side industrial condensers, 446
 - Tubular Exchanger Manufacturers Association (TEMA) standard,
 - 451–454, 452f
 - Turbine air systems (TAS), 60, 61f
 - Turbine design
 - aerodynamic design, 272–291
 - adjoint-based gradient optimization,
 - 282–285, 283t, 284f, 285t
 - blade geometry parametrization,
 - 275–276
 - blades design remarks, 276–278
 - computational fluid-dynamics-based
 - turbomachinery design, 280–282
 - computational fluid-dynamics modeling,
 - 279–280
 - evolutionary stochastic optimization,
 - 286–290, 287f–289f
 - geometrical representation, 273–278,
 - 274f
 - robust multipoint optimization,
 - 290–291, 292f
 - shape-optimization techniques automatic
 - design, 278–291
 - supersonic converging cascades,
 - 276–277
 - supersonic converging/diverging
 - cascades, 277–278
 - transonic cascades, 276
 - architectures, 255–259
 - axial turbines, 257–258, 257f
 - hybrid architectures, 258–259, 259f
 - mean-line preliminary design, 259–265
 - guidelines, 264
 - mean-line concept, 260–261
 - mean-line formulation, 261–264
 - optimal preliminary design, 264–265
 - overview, 253–254, 255f
 - preliminary and aerodynamic design,
 - 265–272
 - optimal spanwise design, 271–272
 - throughflow concept, 266–267,
 - 266f
 - throughflow formulation, 267–270,
 - 270f
 - throughflow/spanwise design guidelines,
 - 270–271
 - radial-inward/centripetal turbines,
 - 256–257, 256f
 - radial-outward/centrifugal turbines, 258
 - Turbine inlet temperature, 203
 - Turbinia, 337
 - Turboden, 51–54, 52f–54f
 - Twin-screw expanders, 372–374
 - mechanical aspects, 374
 - principle of operation, 372–374,
 - 372f–373f
 - technical limitations, 374
 - Two-phase (liquid/vapor) flow, 449
 - Two-phase flow multiplier, 450
- ## U
- United Technologies (UTC), 60, 62f
 - University of Naples, 31, 32f
- ## V
- Vane expanders, 374–376, 375f
 - mechanical aspects, 374–375
 - technical limitation, 375–376
 - Vaneless diffuser, 349–350
 - Vapor–liquid equilibrium, 96
 - Velocity triangles, 308–310
 - Virgin fluid, 131–132, 136–137

W**Waste heat recovery (WHR)**

- application, 330
 - distributed energy systems (DES),
623–627, 628f
 - industrial, 616–619, 617f–618f
 - recompression stations along pipelines,
628–634, 630t–632t, 633f
 - ships, 619–623, 621f
- steam Rankine Cycles (SRC), 613–615

- higher thermal efficiency, 614
- low-grade heat conversions, 615
- turbo machinery, 614–615

Z

- Zephyr system, 27–28
- Zittau/goerlitz libraries, 116